Bulletin of Materials Science

Volume 9, January–December 1987

CONTENTS

Twin roller quenching technique and preparation of glasses of high melting ionic solids *K B R Varma* 1

Synthesis and characterization of mordenite crystals *M S Joshi and K Mohan Prabhu* 7

Non-isothermal crystallization of As_2Se_3 glass *A Giridhar, Sudha Mahadevan and A K Singh* 13

X-ray crystallographic and thermal studies on the hydrides of magnesium and its intermetallics *P Selvam, B Viswanathan, C S Swamy and V Srinivasan* 21

High resolution electron microscopy of bismuth oxides with perovskite layers *G N Subbanna and L Ganapathi* 29

Measurement of Gibbs energies of formation of CoF_2 and MnF_2 using a new composite dispersed solid electrolyte *K T Jacob and J P Hajra* 37

Influence of substrate temperature on the electrical and optical properties of amorphous germanium films *S V Chandole, Ujwala V Hulsurkar and S S Shah* 47

Hillock and island formation during annealing of gold films *M S Rahman Khan* 55

Evaluation of cumulative damage in glass fibre reinforced plastic by ultrasonic method *V K Srivastava and R Prakash* 61

Nonlinearity in gold-alkali halide-gold capacitors *S C K Misra* 67

Book Review 73

X-ray photoelectron spectroscopy studies on ethylene oxychlorination catalysts *R Vetrivel, K Seshan, K R Krishnamurthy and T S R Prasada Rao* 75

In situ photoacoustic spectroscopic studies on heterogeneous catalysts under conditions of gas flow *T Somasundaram and P Ganguly* 81

Morphological aspects of some symmetrical ammonium hydrogen tartrate crystals grown by silica gel technique *C C Desai and A N Hanchinal* 89

A study of diffusion mechanisms in sintering by shrinkage measurements *K M R Achari and R B Ramachander* 97

Dehydration and phase transformation in chrysotile asbestos-A radial distribution analysis study *A K Datta, B K Mathur, B K Samantaray and S Bhattacherjee* 103

Electrical second harmonic generation and temperature autostabilized nonlinear dielectric element in ferroelectric solid solutions $(Na_xK_{1-x})VO_3$ and $(Na_xLi_{1-x})VO_3$ *T A Patil, V M Jamadar and S H Chavan* 111

Ionic conductivity and hopping rate data for some NASICON analogues
N B Desai, K Byrappa, A B Kulkarni and G S Gopalakrishna 117

Electrical properties of the system lanthanum lead cobalt titanium oxide
Devendra Kumar, Ch. Durga Prasad and Om Parkash 123

Pressure-induced band cross-over in $Pb_{1-x}Sn_xTe$
T G Ramesh, V Shubha and P S Gopalakrishnan 131

A study of Vishnukundin coins
M Vijayakumar, M C Ganorkar, V Pandit Rao and P Gayathri 137

Alloy oxide equilibrium in the Cr-Mn-O system
S Ranganathan and J P Hajra 149

Synthesis and properties of manganese-doped barium titanate
L M Arunachalam, D Chakravorty and E C Subbarao 159

Dielectric behaviour of ZnO-based ceramic semiconductors
Subhash C Kashyap, K L Chopra and Bharat Bhushan 169

Electrical resistivity of holmium hydride films *M S Rahman Khan* 181

Electrical conductivity and transition temperature of NbN thin films
C S Menon and V S Pankajakshan 187

Optical properties of coloured transparent alumina gel monolith glasses
V Saraswati and G V Ramarao 193

Magnetic susceptibility measurements of LHP and LNP crystals
C C Desai and M S V Ramana 203

Crystallization behaviour of Metglas 2826 MB ($Fe_{40}Ni_{38}Mo_4B_{18}$)
V S Raja, Kishore and S Ranganathan 207

Preparation and properties of native oxide film anodically grown on $Hg_{0 \cdot 8}Cd_{0 \cdot 2}Te$ *F R Chavda, G Tiwari and S C Gupta* 219

Use of energy dispersive method with tungsten carbide opposed anvil high pressure set-up *A K Singh and S Usha Devi* 225

Positron annihilation in Zr-0·5 Nb alloy
D D Upadhyaya and R V Muraleedharan 235

A new formalism for representation of heat capacities of metals *J P Hajra* 241

Pyroelectric properties of lead-barium titanate and lead-strontium titanate
V M Jamadar, T A Patil and S H Chavan 249

Dielectric behaviour of glasses and glass ceramics in the system BaO-PbO-TiO_2-B_2O_3-SiO_2
R K Mandal, Ch. Durga Prasad, Om Parkash and Devendra Kumar 255

Aliovalent substitution in β-Li_2SO_4 towards conductivity enhancement
K Singh, S S Bhoga and F C Raghuwanshi 263

Kinetics of crystallization of a $Fe_{74}Co_{10}B_{16}$ glass
R P Mathur and D Akhtar 269

Undercooling studies on dispersed bismuth droplets
Sanjay Chaubey, Vakil Singh and P Ramachandrarao 277

Microhardness measurement in nonmetallic materials *V Saraswati* 287

Increase in the yield of silicon carbide whiskers from rice husk
B V Radhakrishna Bhat and G P Sanghi 295

Development of a Sievert's type gas doping apparatus
B Bandyopadhyay, A Ghoshray and N Chatterjee 305

Long term soft tissue response to metals, ceramics and composites-a comparative histopathological evaluation
Mira Mohanty, K Rathinam and C C Kartha 309

Conductivity pre-exponential factors for some new superionic conductors
N B Desai, K Byrappa, G S Gopalakrishna, S Srikantaswamy and A B Kulkarni 317

$NH_4Zr_2V_3O_{12}$ proton conductor
K Byrappa, A B Kulkarni, N B Desai and H P Jagadeesh 323

Electrical conductivity of the ferroelectric sodium vanadate, potassium vanadate, lithium vanadate and their solid solutions
T A Patil, V M Jamadar and S H Chavan 331

Transport properties of $MoSe_xTe_{2-x}$ $(0 \leqslant x \leqslant 2)$ single crystals
M K Agarwal, P D Patel and R M Joshi 337

Measurements of the microhardness and compression testing of ferroelectric lead nitrate phosphate single crystals *C C Desai and M S V Ramana* 343

Characterization of RH-sputtered garnet films *Rambilas and D Bahadur* 349

Li_2SO_4:$LiNbO_3$ binary system for solid state battery applications *K Singh* 355

Subject index 365

Author index 371

Bulletin of Materials Science

Notes on the preparation of papers

Authors wishing to have papers published in the *Bulletin of Materials Science* should send them to

The Editor, Bulletin of Materials Science, Indian Academy of Sciences, P.B. No. 8005, Bangalore 560 080.

Three copies of the paper must be submitted.

Submission of a script will be held to imply that it has not been previously published and is not under consideration for publication elsewhere; and further that, if accepted, it will not be published elsewhere.

Aims and scope

The Bulletin is devoted to the publication of topical reviews, reports on research and development activities in materials science and technology in the country, original research communications and important Notes and News.

Typescript

Papers must be typed double spaced with ample margin on all sides on one side of white bond paper of quarto size (280 × 215 mm). This also applies to the abstract, tables, figure captions and the list of references which are to be typed on separate sheets.

Title page

(1) The title of the paper must be brief and contain words useful for indexing. Serial titles are to be avoided.
(2) The names with initials of authors and the name and address of the institution where the work was done must be given.
(3) An abbreviated running title of not more than 50 letters and spaces must also be given.

Abstract

Papers must have a brief abstract of the significant results reported in the paper.

Keywords

Between 3 and 6 keywords must be provided for indexing and information retrieval.

The text

The paper must be divided into sections starting preferably with 'Introduction' and ending with 'Conclusions'. The main sections should be numbered 1, 2, etc., the sub-sections 1.1, 1.2, etc., and further sub-sections (if necessary) 1.1a, 1.1b, etc.

Tables

All tables must be numbered consecutively in arabic numerals in the order of occurrence in the text; they should be self-contained and have a descriptive title.

Figures

All figures including photographs should be numbered consecutively in arabic numerals in the order of appearance in the text. Line drawings must be in Indian ink on good quality tracing paper or Bristol board of the same size as the text paper. Lines should be sufficiently thick (axes about 0·3 mm, curves about 0·6 mm).

Units

Units and associated symbols must invariably follow SI practice.

References

References should be cited in the text by author and year, not by number. If there are more than two authors, reference should be to the first author followed by *et al* in the text. References at the end of the paper should be listed alphabetically by authors' names, followed by initials, year of publication, name of the journal (abbreviated according to the World List of Scientific Periodicals, Butterworths, London), volume number, and number of the first page. Reference to books should include: name(s) of author(s), initials, year of publication, title of the book, edition if not the first, initials and name(s) of editor(s) if any, preceded by ed(s), place of publication, publisher, and chapter or pages referred to. References to thesis must include the year, the title of the thesis, the degree for which submitted and the University.

Footnotes

Footnotes must be avoided if possible but when necessary should be numbered consecutively, and typed on a separate sheet.

Proofs

Authors are requested to prepare the manuscript carefully before submitting it for publication to minimise corrections and alterations in the proof which increase publication costs. Page proofs sent to the authors together with the reprint order form must be returned to the editorial office within two days of their receipt.

Reprints

50 reprints of each article will be supplied free of charge.

Bull. Mater. Sci., Vol. 9, No. 1, March 1987, pp. 1–5. © Printed in India.

Twin roller quenching technique and preparation of glasses of high melting ionic solids

K B R VARMA
Materials Research Laboratory, Indian Institute of Science, Bangalore 560 012, India

MS received 2 February 1987

Abstract. A rapid quenching technique with a quenching rate of roughly 10^{6}°C/sec has been developed to prepare glassy samples of ABO_3 type materials. Glasses of potassium lithium niobate have been prepared by this technique. These glasses have been characterized by x-ray diffraction, electron diffraction and differential scanning calorimetry techniques to assess the quality of the obtained glasses.

Keywords. Twin roller quenching technique; potassium lithium niobate glass.

1. Introduction

Ferroelectric-like dielectric anomalies have been reported in glassy phases of a few ABO_3 materials (Glass *et al* 1977). Several technological applications are possible for such materials and it is therefore natural to investigate whether this curious phenomenon is universal to the amorphous phases of the large class of ABO_3-type compounds. It is now widely known that glassy phases of ABO_3 materials can be obtained by several techniques, notably by fast quenching of melts using twin roller and other techniques and r.f. sputtering. While sputtering techniques are useful, it is rather difficult to obtain from this technique thick films suitable for a number of physicochemical studies. Further, non-stoichiometry of sputtered samples also creates difficulties in understanding their behaviour. Fast quenching techniques are thus quite advantageous for sample preparation. They provide high quenching rates ($\sim 10^{6}$°C sec^{-1}) and are relatively easy to fabricate. Thick and uniform flakes of glasses of many non-metallic materials can be readily prepared.

In this communication, fabrication of a twin roller quenching apparatus is described. Preparation of flaky glass samples of potassium lithium niobate (KLN) is described along with a preliminary report of the structural and thermal properties of the KLN glass.

2. Twin roller set-up

The twin roller quenching apparatus consists of two hard chrome-plated copper rollers whose dimensions were 5 cm (dia) × 10 cm (length) held together in a heavy steel frame (figure 1). One of the rollers is associated with a cone pulley arrangement and is driven by an a.c. motor with a single belt-drive to synchronize the rotation speeds of both rollers upto 3000 r.p.m. The rotation speeds of the rollers would be varied by suitably positioning them on the cone pulley arrangement. In this set-up,

---

Contribution No. 74 from Materials Research Laboratory

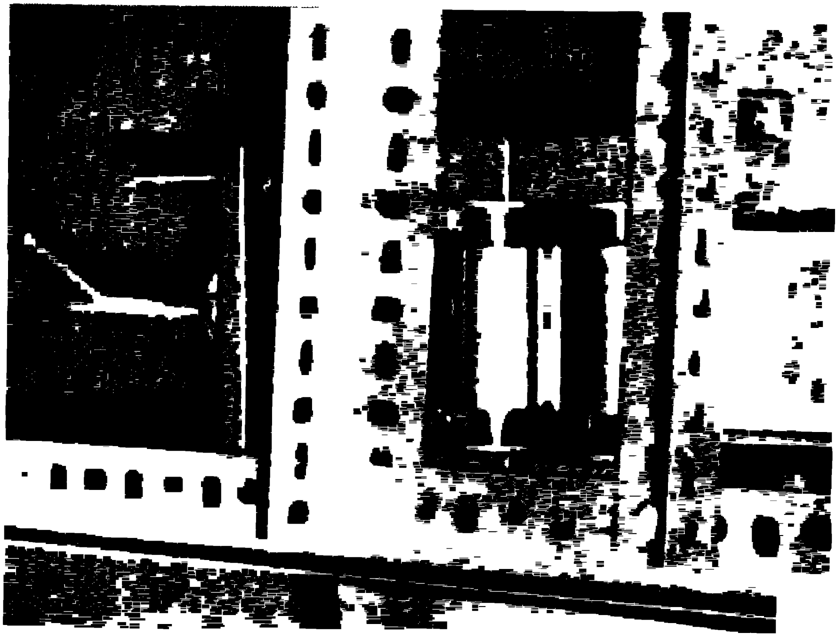

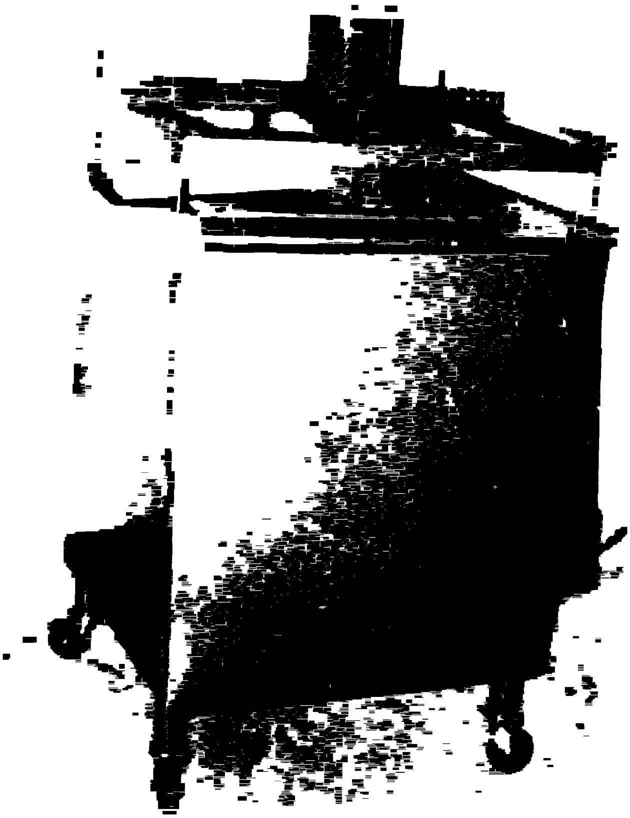

Figures 1–2 1. Top view of the twin roller assembly. **2.** The whole arrangement of twin roller set-up.

three speeds, i.e. 1500, 2000 and 3000 r.p.m. could be chosen. One of the rollers is mounted with a fixed central axis of rotation whereas the second one is spring-loaded and can be horizontally translated towards the fixed roller. This enables gap adjustment between the rollers, a feature necessary for fixing the flake thickness. This is an additional advantage of the present design. The spring system shown in figure 1 also helps in maintaining a uniform gap between the rollers during the operation of the instrument. The total set-up is shown in figure 2. It has been found possible to obtain moderately large size flakes of uniform thickness by a careful manipulation of the above parameters. Only when the molten samples wet the surface, longer ribbons of the quenched material can be obtained. The heating assembly shown in figure 2 consists of a quartz crucible with 1 mm (dia) hole. The inner surface of the crucible is wrapped with a platinum foil (which prevents contamination of the samples). The crucible is surrounded by a wire wound furnace. It is however possible to replace the furnace by a ring type gas burner, particularly while melting oxides of very high melting points. The furnace assembly is itself mounted on a sliding platform (figure 2) which is positioned on top of the roller assembly. The centering of the melt flow from the crucible is adjusted through the movement of the furnace itself along with the crucible. The present design is a modified version of a quenching set-up described by Chen and Miller (1970).

3. Potassium lithium niobate glass

Crystalline KLN ($K_3Li_2Nb_5O_{15}$) required for glass preparation was prepared starting from K_2CO_3, Li_2CO_3 and Nb_2O_5. A mixture containing alkali carbonates and Nb_2O_5 in required proportions was ground together and mixed well. It was initially heated in a platinum crucible for about 8 hr. The product was cooled and again ground to a fine powder. The powder was compacted and heated slowly to $\sim$1250 K. It was heated at this temperature for about 48 hr and slowly cooled to room temperature. The x-ray diffraction of the calcined product was examined and the formation of KLN was confirmed.

In order to make the glass, about 100 g of the powder was melted in the crucible described earlier. The temperature of the melt was raised by about 80–100 K above the melting temperature (1280 K). The melt was gently coaxed out through the capillary either by shaking or by directing a hot air blower perpendicularly over the surface of the melt in the crucible. The gentle pressure on the melt can be kept in order to maintain a continuous jet of the flowing melt. The molten jet is allowed to take the space between the rollers already set in rotation. The free fall distance of the melt before reaching the rollers is about 1 cm. The quenched flakes were collected in a tray kept just below the roller assembly.

Flakes obtained from quenching KLN were quite transparent. Their thickness could be varied from 50–100μm. The quenching rates were estimated by the procedure used by Chen and Miller (1970) and were found to be $\sim 10^5$ 10^{6}°C/sec. The flakes were examined using x-ray diffraction, high resolution electron microscopy and differential scanning calorimetry (DSC). The glassy nature of the sample is quite obvious from the broad peaks in x-ray diffraction (figure 3) and from the appearance of two broad haloes in the electron diffraction (inset in figure 4). The high resolution image shows presence of fine, short range fringes which criss-cross the entire image

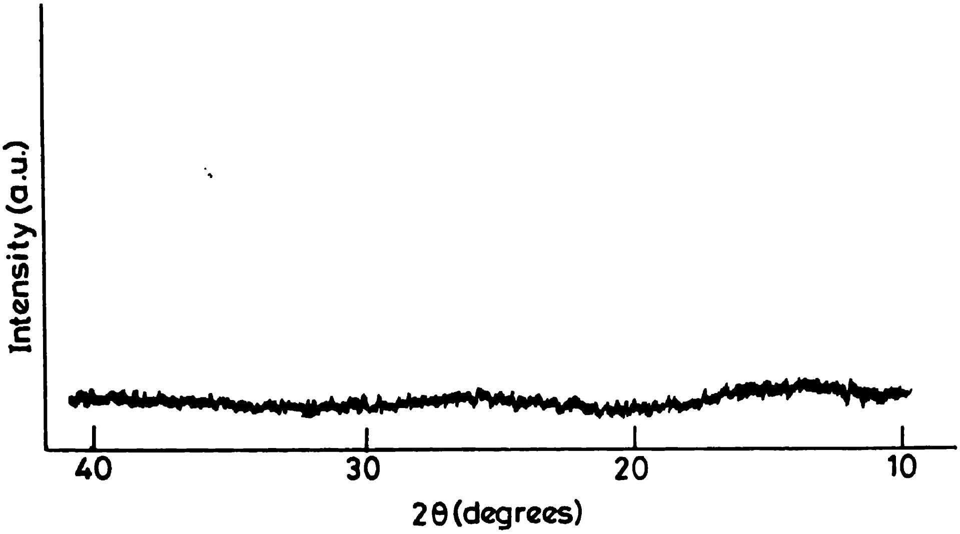

Figure 3. X-ray diffraction pattern of the quenched flake of KLN.

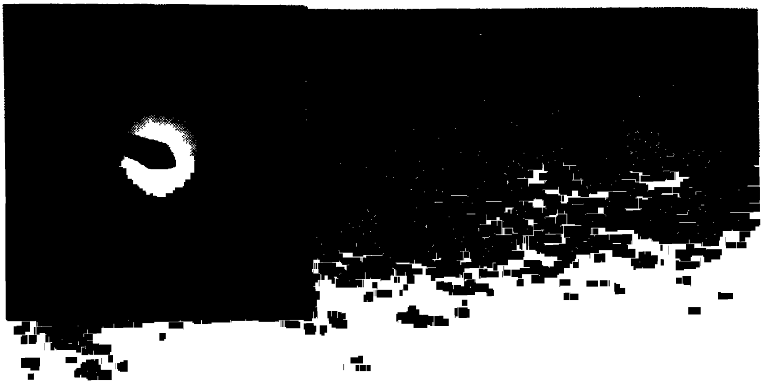

Figure 4. Electron diffraction pattern of the quenched flake of KLN.

field. Such ultra microstructures have been noted both in sputtered films (Varma *et al* 1985) and in some glassy metals.

DSC scan of the glassy sample is shown in figure 5. Glass transition occurs at 570 K and the sample crystallizes around 825 K. Crystallized samples are opaque. Unfortunately, we could not show the crystallization temperature in the above figure. However, the glassy flakes have been heated at various temperatures followed by electron microscopic studies to determine the crystallization temperature.

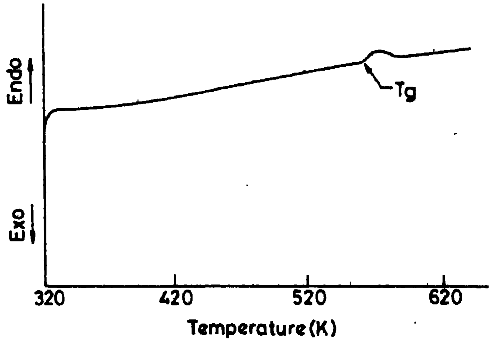

Figure 5. Typical DSC trace for as quenched flake of KLN (heating rate 20 K/min).

Further investigations are underway to determine whether the regions producing fringes are truly microcrystalline clusters and whether they correspond to the dielectrically soft units described by Lines (1977) and which give rise to dielectric anomalies. Since $LiNbO_3$ exhibits dielectric anomalies both in r.f. sputtered films and in bulk glass form, we expect similar dielectric behaviour even in mixed alkali niobates.

In conclusion, this note describes a simple rapid quenching apparatus built for obtaining glassy phases of high melting ionic solids and preparation and preliminary characterization of a typical mixed alkali niobate glass.

Acknowledgements

The author is indebted to Prof. K J Rao for helpful suggestions and critical reading of the manuscript and to Prof. C N R Rao for kind and continued encouragement.

References

Chen H S and Miller C E 1970 *Rev. Sci. Instr.* **41** 1237
Glass A M, Lines M E, Nassau K and Shiever J W 1977 *Appl. Phys. Lett.* **31** 249
Lines M E 1977 *Phys. Rev.* **B15** 388
Varma K B R, Harshavardhan K S, Rao K J and Rao C N R 1985 *Mater. Res. Bull.* **20** 315

Bull. Mater. Sci., Vol. 9, No. 1, March 1987, pp. 7–11. © Printed in India.

Synthesis and characterization of mordenite crystals

M S JOSHI and K MOHAN PRABHU
Physics Department, Sardar Patel University, Vallabh Vidyanagar 388 120, India

MS received 10 September 1986; revised 2 January 1987

Abstract. The hydrothermal synthesis of large port mordenite crystals and experimental observations are reported. Unit cell parameters are estimated as $a = 18{\cdot}142$, $b = 20{\cdot}328$ and $c = 7{\cdot}508$ Å. Prismatic and prismatic pyramidal mordenite crystals are illustrated. The average particle size computed was 8–20 μ. Adsorption capacities of synthesized mordenite crystals are 13·4% for water, 9·9% for methanol and 5·8% for benzene by weight.

Keywords. Mordenite; tetrapropylammonium bromide; prismatic pyramidal.

1. Introduction

Mordenite is a mineral zeolite, belonging to group VI and its Si/Al ratio is about 5. It has a two-dimensional channel system, designated as small port and it adsorbs only small molecules such as methane (Sand 1968) into its 12-membered ring channels (6·7 Å). The limitation on its diffusion may be because of the presence of amorphous materials or cations in the channels (Breck 1974a). Synthetic mordenite, known as large port mordenite, commonly referred to as zeolon (Sand 1969), exhibits adsorption characteristics expected for free diffusion of molecules in the 6·7 Å diameter 12-membered ring channels (Sand 1968). The high degree of stability shown by mordenite along with its high resistance to acids, finds many applications in adsorption and hydrocarbon conversion catalysis (Csicsery 1984; Burbidge *et al* 1971; Kranich *et al* 1971). Since it was first synthesised back using feldspars and alkalicarbonates its synthesis from a variety of starting materials has been reported (Barrer and Denny 1961; Coombs *et al* 1959; Senderov 1963). Chu (1973) and Chang *et al* (1975) synthesized mordenite crystals using tetraethylammonium hydroxide. Stewart and Ball (1980) used neopentylamine as templates. The present paper reports observations and results of our efforts to synthesize large port mordenite crystals using tetrapropylammonium bromide in the system Na_2O-Al_2O_3-SiO_2-H_2O at 150°C.

2. Experimental method

Colloidal silica (40% SiO_2 in water), sodium aluminate, sodium hydroxide, tetrapropylammonium bromide and double distilled water were used to prepare the gel. A known amount of TPA-Br was dissolved in double-distilled water in a large flask. Aqueous solutions of specific quantities of sodium hydroxide, sodium aluminate and colloidal silica were prepared in separate beakers. These solutions were added, one after the other drop by drop, to the TPA-Br solution in the flask and vigorously stirred during the process. The resulting solution was stirred for 3 hr. Its pH was adjusted to 12 using dilute sulphuric acid. The gel was transferred to the teflon lined autoclave vessel which was then sealed and heated to 150 ± 2°C (at 300 psi) for seven days with occasional stirring. The Berghof autoclave used in the present investigatio provides for induction-driven PTFE-protected system for stirring the reactants eve after sealing the vessel. At the end of the run, the product was filtered and washe repeatedly with double-distilled water. It was then dried at 150°C for 12 hr. Thes crystallites were characterized by the following techniques.

3. Experimental observations

3.1 *X-ray diffraction studies*

X-ray powder diffractograms were recorded in the range $2\theta = 5-75°$ using Cu radiation. From the diffractogram, *d* values and the corresponding relative intensiti were calculated. These *d* values agree with the reported values for large p mordenite (Breck 1974). Unit cell parameters were calculated as $a = 18{\cdot}142$, $b = 20{\cdot}3$ and $c = 7{\cdot}508$ Å. The crystals belong to an orthorhombic system.

3.2 *Infrared spectral studies*

Infrared spectra of our samples were recorded using KBr wafer technique in range 300–1300 cm^{-1}. Band assignment was done according to Flanigen (1976). T infrared spectrum is shown in figure 1. Bands were grouped into two classes. In class, bands were structure-sensitive and were due to internal vibrations of T

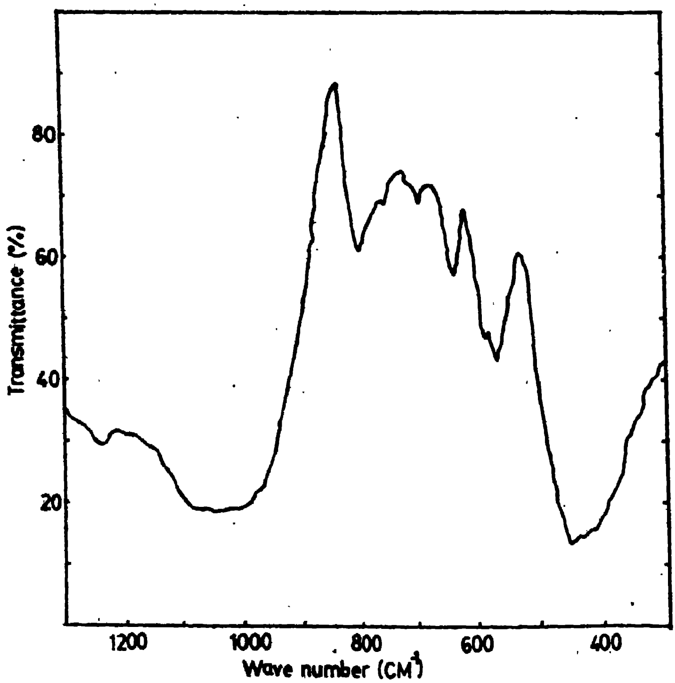

Figure 1. Infrared spectrum.

tetrahedron, the primary unit of structure. The band at 1045 cm^{-1} (vs) was caused by an asymmetric stretch and the band at 450 cm^{-1} (vs) was due to the T-O bending mode. Two bands at 755 cm^{-1} (vvw) and 696 cm^{-1} (vw) were caused by symmetric stretching modes involving tetrahedral atoms. The other class of bands was structure-sensitive. The bands at 565 cm^{-1} (ms), 585 cm^{-1} (w), 635 cm^{-1} (mw) and 1240 cm^{-1} (m sh) were due to 5-membered ring chain. The band at 800 cm^{-1} (mw) was caused by symmetric stretching mode.

3.3 *Elemental analysis*

The samples were characterized by energy dispersive analysis of x-rays (EDAX). Atomic percentages of sodium, aluminium and silicon were found to be 8·966, 12·849

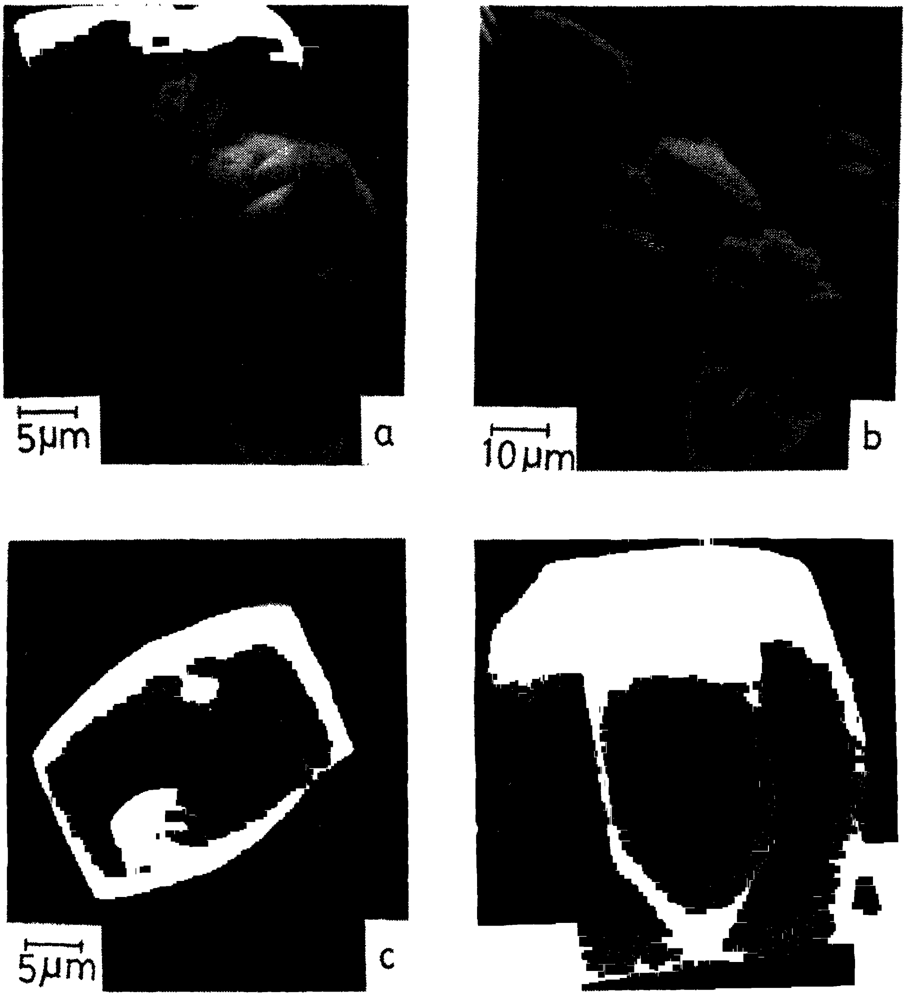

Figure 2. Scanning electron micrographs of mordenite crystals. (**a**) Crystal aggregates. (**b**) Some isolated and some aggregate crystals. (**c**) A prismatic crystal with two small crystals on its surface. (**d**) A prismatic pyramidal crystal on the surface of a prismatic crystal.

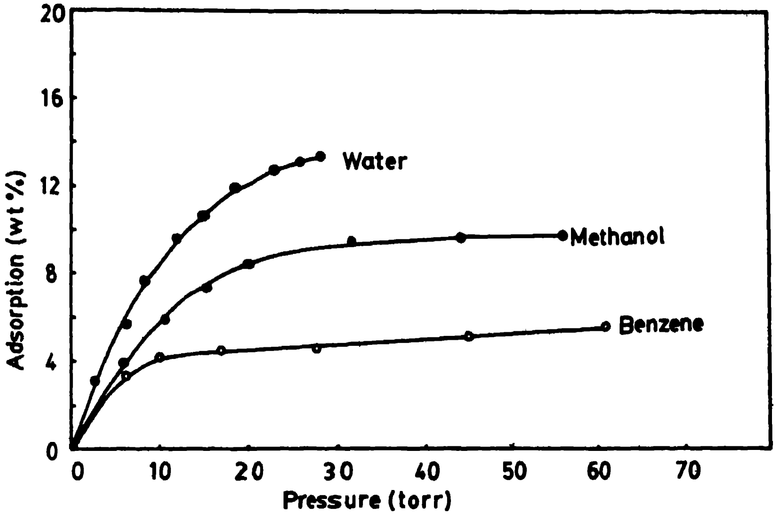

Figure 3. Adsorption curves.

and 78·185 respectively. The Si/Al ratio was 6·09. The molar oxide formula of the final product was calculated as 3·26 Na_2O. 4·67 Al_2O_3. 56·86 SiO_2. 35·20 H_2O.

3.4 *SEM studies*

The crystals were coated with gold films and examined under a scanning electron microscope. Figure 2(a) shows crystal aggregates. Some isolated and some crystal aggregates are shown in figure 2(b). A prismatic crystal with two small crystals on its surface and a prismatic pyramidal crystal on the surface of a prismatic crystal are shown in figures 2(c) and 2(d) respectively. The average particle size was calculated as 8–20 μ.

3.5 *Adsorption studies*

Using the McBain balance fabricated in this laboratory, adsorption on the calcined (at 550°C) mordenite crystals was carried out at 30°C. The adsorption curves for water, methanol and benzene are shown in figure 3. It was found that these crystals adsorb 13·4% water, 9·9% methanol and 5·8% benzene by weight.

Acknowledgement

The authors thank CSIR, New Delhi for financial support.

References

Barrer R M and Denny P J 1961 *J. Chem. Soc.* 983
Breck D W 1974a *Zeolite molecular sieves* (New York: John Wiley) pp. 124, 363

Burbidge B W, Keen I M and Eyles M K 1971 *Molecular sieve zeolites II* (*Adv. Chem. Ser.* **102**) 400
Chang C D, Lang W H and Silvestri A J 1975 U S Pat. 3894104
Chu P S 1973 U S Pat. 3766093
Coombs D S, Ellis A J, Fyfe W F and Taylor A M 1959 *Geochim. Cosmochim. Acta* **17** 53
Csicsery S M 1984 *Zeolites* 4 202
Flanigen E M 1976 *Zeolite chemistry and catalysis* (ed) J A Rabo (*Adv. Chem. Ser.* 171)
Kranich W L, Ma Y H, Sand L B, Weiss A H and Zwiebel I 1971 *Molecular sieve zeolites I* (*Adv. Chem. Ser.* **101**) 502
Sand L B 1968 *Molecular sieves* (Soc. Chem. Industry Spec. Publ.) 71
Sand L B 1969 U S Pat. 3436174
Senderov E E 1963 *Geokhimiya* **9** 848
Stewart D G and Ball W J 1980 Eur Pat. 14023

Bull. Mater. Sci., Vol. 9, No. 1, March 1987, pp. 13–19. © Printed in India.

Non-isothermal crystallization of As_2Se_3 glass

A GIRIDHAR, SUDHA MAHADEVAN and A K SINGH
Materials Science Division, National Aeronautical Laboratory, Bangalore 560 017, India

MS received 12 January 1987

Abstract. The results of non-isothermal crystallization studies performed at different heating rates on batches of As_2Se_3 glasses prepared from melts at 400°C, 600°C and 800°C are reported. The peak temperature of crystallization T_p, the enthalpy of crystallization ΔH_c and the activation energy for crystallization E_c are independent of the melt temperature used in the preparation. Bulk nucleation with three-dimensional growth of crystals is indicated for As_2Se_3. The values of ΔH_c and E_c are found to be respectively $23{\cdot}3 \pm 0{\cdot}9$ cal/g and $36{\cdot}5 \pm 0{\cdot}9$ kcal/mol for As_2Se_3.

Keywords. As_2Se_3 glass; non-isothermal crystallization; activation energy for crystal growth.

1. Introduction

The As_2Se_3 glass prepared from the congruently melting compound As_2Se_3 is one of the widely characterized chalcogenide glasses, the characterization encompassing its optical, thermal, electrical and other physical properties. It is easily prepared in bulk form by cooling (generally by quenching in cold water) the melt; the melt temperature employed in various investigations ranges from 500°C to 850°C (Henderson and Ast 1984; El Fouly and Edmond 1974; Thornburg and Johnson 1975; Moynihan *et al* 1975).

The crystallization behaviour of this glass has been studied under isothermal conditions using density and electrical conductivity measurements (Myuller and Shkolnikov 1966), x-ray methods (Majid *et al* 1974) and thermal analysis (Henderson and Ast 1984). In a preliminary non-isothermal study using DTA (El Fouly and Edmond 1974), it was observed that As_2Se_3 glasses quenched from melts at 600°C did not show any crystallization peak. However, in a later DSC study (Thornburg and Johnson 1975) on samples quenched from 600°C, crystallization exotherm was present, suggesting that the observed variance probably results from other differences in sample preparation. In order to see if there is difference in crystallization behaviour of samples quenched from melts at different temperatures, studies were made on glasses prepared from melts at 400°C, 600°C and 800°C; the results of this study are reported in this communication.

2. Experimental

Bulk glasses of As_2Se_3 were prepared by homogenization (10 g per batch) of 99·999% pure As and Se (obtained from Koch Light Co., U.K.) in appropriate atomic per cent proportions in quartz ampoules sealed in a vacuum of better than 10^{-3} torr. Homogenization was carried out under continuous agitation for 24 hr at the end of which the ampoule was quenched in cold water. Three batches of samples with melts at 400°C, 600°C and 800°C were prepared for the study.

The thermal analysis runs were carried out using a Perkin-Elmer DSC–2 differential scanning calorimeter after performing the temperature and energy calibration of the instrument using high purity tin, indium and lead supplied with the instrument. Powdered samples (typically 60 mg) were taken in crimped aluminium pans and all the measurements were referenced to an empty aluminium pan. High purity dry nitrogen was used as the purge gas.

The crystallization exotherm sets in around 540 K to 570 K depending upon the heating rate employed. All the samples were first heated in situ from 300 K to 520 K at 40 K/min and the crystallization exotherm was then recorded from 520 K onwards at the various desired heating rates starting from 0·31 K/min. The temperature of onset of crystallization increases with increasing heating rate. Therefore, the measurements could not be extended for heating rates higher than 5 K/min because, for heating rates higher than this, the melting endotherm used to set in before the completion of the crystallization exotherm. Measurements were carried out on freshly prepared and annealed (for an hour around the glass transition temperature T_g, namely, at 450 K) samples which were quenched from melts at 400°C, 600°C and 800°C.

As indicated schematically elsewhere (Sudha Mahadevan *et al* 1986) the peak temperature of crystallization was obtained as the temperature corresponding to the intersection of the two linear portions adjoining the peak. The crystallization enthalpy ΔH_c was obtained by multiplying the area of the exotherm (A) by the calibration constant C. The value of C was deduced by measuring the total area of the complete melting endotherm of high purity tin and indium and using the well-known enthalpy of melting of these standard materials. The fraction x crystallized at any temperature T is given by $x = A_T/A$, where A is the total area of the exotherm between temperature T_1 where crystallization just begins and T_2 where the crystallization is completed; A_T is the area between T_1 and T. The area measurements were made using an Autotrol AD-380 graphic system.

3. Results and discussion

The results of the present study are summarized in table 1 and figures 1–3. The values of T_p listed (table 1) for all the six batches of samples are representative values obtained for a single run at the various heating rates specified. In order to assess the spread in the value of T_p (for any given heating rate), measurements were carried out on four samples from the same batch. A spread of ±0·7% in T_p was obtained giving a standard deviation of 4. Similar measurements on four samples of another batch gave the same spread and standard deviation values. The data of table 1 indicate that T_p does not depend on the melt temperature used in the preparation because the spread in the T_p values of samples from batches with different melt temperatures is of the same magnitude as that obtained for different samples of the same batch. Also shown in table 1 are the ΔH_c values, which indicate that to within experimental errors ΔH_c is independent of the heating rate employed, a result observed in other chalcogenide glass systems also, namely, As-Sb-Se (Sudha Mahadevan *et al* 1986) and As-Ge-Te (Sugi *et al* 1971). Further ΔH_c is also found to be independent of the

Table 1. Data of T_p(K) and ΔH_c(cal/g) of As_2Se_3.

Sample details	Heating rate (K/min) 0·31	0·62	1·25	2·5	5·0	
Quenched from	560·3	572·4	584·9	599·9	619·0	T_p
400°C, fresh	22·9	22·9	23·7	24·3	23·6	ΔH_c
-do-, annealed	561·0	575·0	588·6	605·5	622·0	T_p
1 hr at T_g	23·3	23·9	24·1	24·1	—	ΔH_c
Quenched from	555·2	569·4	584·6	599·5	615·5	T_p
600°C, fresh	22·9	24·2	23·7	22·5	23·9	ΔH_c
-do-, annealed	554·4	568·9	583·2	599·0	613·0	T_p
1 hr at T_g	22·6	23·2	24·0	24·2	22·8	ΔH_c
Quenched from	553·1	566·5	582·5	597·5	614·0	T_p
800°C, fresh	22·5	23·8	24·2	23·9	24·1	ΔH_c
-do-, annealed	559·1	571·1	584·6	601·0	618·0	T_p
1 hr at T_g	22·7	23·0	22·7	23·8	23·3	ΔH_c

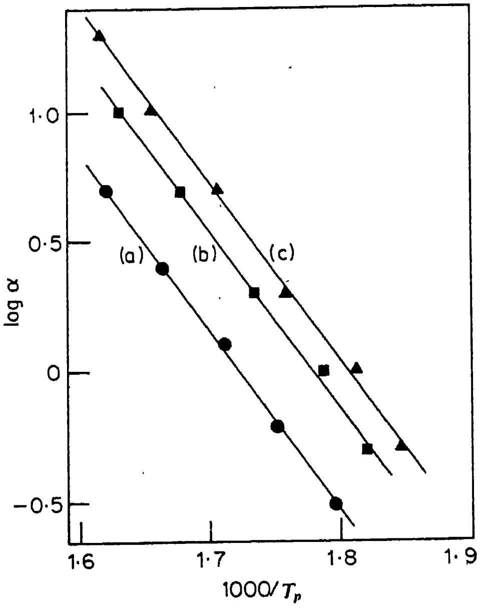

Figure 1. Log α vs $1/T_p$ for As_2Se_3 (line **a**); The solid circle denotes the mean value obtained for all the batches (table 1) at each of the heating rates; lines (**b**) and (**c**) denote the data from literature (Thornburg and Johnson 1975) on fresh and aged samples.

melt temperature used in the preparation and on the annealing treatment given to the samples; ΔH_c was found to have a value of 23·3 ± 0·9 cal/g (table 1).

It is well known (Thornburg and Johnson 1975; Kissinger 1956; Chen 1978; Yinnon and Uhlman 1983; Frahn 1983; Cadergren and Backstrom 1980; Matusita and Sikka 1979; MacFarlane 1984; Matusita and Sikka 1980; Morotta *et al* 1983) that log α vs $1/T_p$ data is linear for most glasses and the slope of this plot is related to the activation energy for crystallization. Figure 1 shows the log α vs $1/T_p$ data for the samples studied presently. Also shown in figure 1 are the T_p data from literature

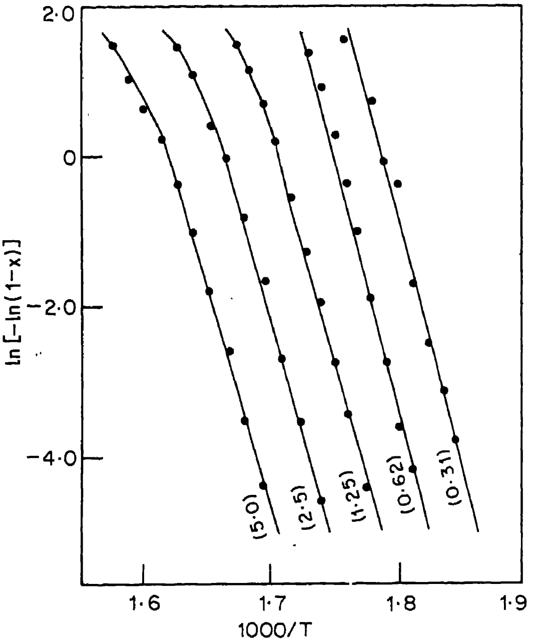

Figure 2. ln[−ln(1−x)] vs 1000/T for As_2Se_3 samples at various heating rates (K/min) indicated in parentheses.

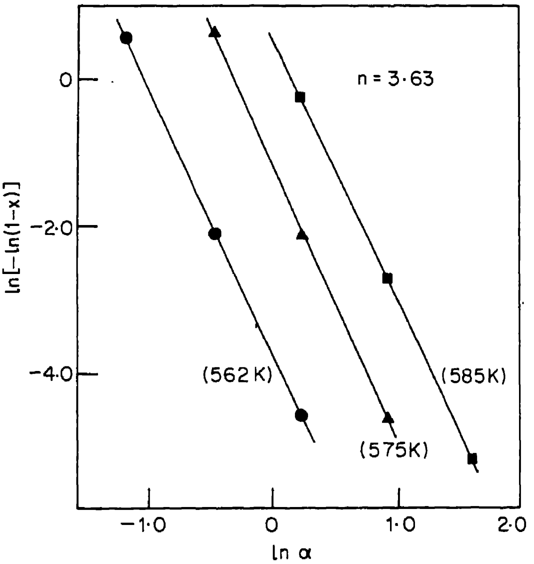

Figure 3. ln[−ln(1−x)] vs lnα for As_2Se_3 at three different temperatures.

(Thornburg and Johnson 1975) for fresh samples quenched from melt at 600°C, (figure 1, line b) and for the same samples after ageing them at room temperature for 800 days (figure 1, line c); with this ageing, a reduction of about 2% in T_p is seen. The present values of T_p for any given heating rate are systematically about 5% higher than the data of figure 1, line b. The present study shows that melt temperature does not affect the T_p values and the reason for the observed difference in T_p is attributable to other differences in preparation conditions which are yet to be identified. The present results further indicate that annealing for about an hour at T_g does not affect the values of T_p. These results are in accordance with other observations which conclude (Henderson and Ast 1984; Myüller and Shkolnikov 1966; Majid *et al* 1974) that no appreciable rearrangements or reorganisations of the atomic structure would occur in this short annealing period around T_g.

Though the values of T_p at any heating rate (figure 1, line a) are systematically slightly higher than that of figure 1, line b, the slope of the $\log \alpha$ vs $1/T_p$ data and the crystallization enthalpy agree with each other. This result is in accordance with the result reported for fresh and aged samples of As_2Se_3 (Thornburg and Johnson 1975); while the T_p values of the samples aged for 800 days are about 2% lower than that of fresh samples, the slope of the $\log \alpha$ vs $1/T_p$ line and the value of ΔH_c are unaffected.

The crystallization data obtained presently were further analyzed using a procedure suggested for non-isothermal crystallisation (Matusita *et al* 1984); this method has been successfully applied for crystallization studied on As-Sb-Se glasses (Sudha Mahadevan *et al* 1986). Referring to these papers (Matusita *et al* 1984; Matusita and Sakka 1980; Sudha Mahadevan *et al* 1986) for details of analysis and discussion, the method will be briefly outlined here and the results for As_2Se_3 presented.

For non-isothermal crystallization (Matusita *et al* 1984), the fraction x of crystals precipitated in a glass heated at a uniform rate α is related to the activation energy E_c through the relation

$$\ln[-\ln(1-x)] = -n\ln\alpha - 1{\cdot}052\, mE_c/RT + \text{constant},$$

where m and n are numerical constants having values between 1 and 4 depending on the morphology (whether it is surface or bulk crystallization and whether the crystal growth is predominantly one-, two- or three-dimensional); values of m and n for various conditions are listed (Matusita and Sakka 1980; Matusita *et al* 1984). When nuclei formed during the heating at constant rate are dominant, n is equal to $m+1$ and when nuclei formed during any heat treatment prior to the thermal analysis run are dominant, n is equal to m.

Figure 2 shows the $\ln[-\ln(1-x)]$ vs $1/T$ data at various heating rates for one of the batches of As_2Se_3 studied presently. The slope of this line (average value of the data at five heating rates, figure 2) gives a value of 112 kcal/mol for mE_c. To infer the value of m, the dimensionality of the growth, $\ln[-\ln(1-x)]$ was plotted as a function of $\ln\alpha$ at fixed temperatures. Figure 3 shows such a data for three temperatures, which gives an average value of 3·63 for the slope n. The break in the $\ln[-\ln(1-x)]$ vs $1/T$ data (figure 2) for large crystallized fractions for some heating rates has been reported and discussed for several other glass systems (Sudha Mahadevan *et al* 1986; Colemenero and Barandiarań 1978; Speyer and Risbud 1983; Shelestak *et al* 1978; Duhaj *et al* 1976; Burton and Ray 1971).

Similar analysis on other batches of As_2Se_3 gave mE_c values in the range of 112 to 118 Kcal/mol; n had values between 3·63 and 3·78 thereby giving a value of 3 for m (Matusita *et al* 1984). These values of n and m indicate that bulk nucleation with three-dimensional growth is likely in As_2Se_3, a result similar to that obtained for

$As_2Se_3-Sb_2Se_3$ glasses (Sudha Mahadevan *et al* 1986). The value of E_c is found to be 36·5 ± 0·9 kcal/mol.

It is also indicated (Illekova 1984) that in crystallization studies using non-isothermal DSC experiments, the activation energy obtained pertains to the activation energy for crystal growth. In non-isothermal measurements, generally due to a rapid temperature rise and big differences in the latent heats of nucleation and growth, the crystallization exotherm characterizes the growth of the crystalline phase from the amorphous matrix; the nucleation is more or less calorimetrically unobservable at temperatures below the crystallization exotherm or it takes place very rapidly immediately after overheating of the material, which results in the deformed beginning of the measured exotherm (Illekova 1984). Direct measurements of the activation energy for crystal growth in As_2Se_3 using electron microscopy technique (Henderson and Ast 1984) give a value of 36·8 kcal/mol. The value of 36·4 kcal/mol obtained by the present non-isothermal DSC measurements agrees well with this value.

4. Summary and conclusions

Using the DSC technique, non-isothermal crystallization has been studied at various heating rates on batches of As_2Se_3 glass prepared from melts at 400°C, 600°C and 800°C. The peak temperature of crystallization, the enthalpy of crystallization and the activation energy for crystallization are found to be independent of the melt temperature used in the preparation.

The crystallization data have been analyzed using a method suggested for non-isothermal crystallization. The results indicate bulk nucleation with three-dimensional growth of crystals for As_2Se_3. The crystallization enthalpy ΔH_c is found to be 23·3 ± 0·9 cal/g for As_2Se_3. A value of 36·5 ± 0·9 kcal/mol is obtained for the activation energy for crystallization in As_2Se_3. This value agrees well with the activation energy for crystal growth obtained by direct measurement using electron microscopy technique.

References

Burton J J and Ray R P 1971 *J. Non-Cryst. Solids* **6** 393
Cadergren M and Backstrom G 1980 *J. Non-Cryst. Solids* **37** 213
Chen H S 1978 *J. Non-Cryst. Solids* **27** 257
Colemenero J and Barandiaran J M 1978 *J. Non-Cryst. Solids* **30** 263
Duhaj P, Barancok D and Ondrejka A 1976 *J. Non-Cryst. Solids* **21** 411
El Fouly M H and Edmond J T 1974 *Phys. Status Solidi A* **21** K43
Frahn R 1983 *J. Non-Cryst. Solids* **56** 255
Henderson D H and Ast D G 1984 *J. Non-Cryst. Solids* **64** 43
Illekova E 1984 *J. Non-Cryst. Solids* **68** 153
Kissinger H E 1956 *J. Res. Natl. Bur. Stand. Sect. A* **57** 217
Macfarlane D R, Matecki M and Poulain M 1984 *J. Non-Cryst. Solids* **64** 351
Majid C A, Prager P R, Fletcher N H and Brettell J M 1974 *J. Non-Cryst. Solids* **16** 365
Matusita K and Sakka S 1979 *Phys. Chem. Glasses* **20** 81
Matusita K and Sakka S 1980 *J. Non-Cryst. Solids* **38–39** 741
Matusita K, Konatsu T and Yokota R 1984 *J. Mater. Sci.* **19** 291
Morotta A, Saiello S and Buri A.1983 *J. Non-Cryst. Solids* **57** 473
Moynihan C T, Macedo P B, Maklad M S, Mohr R K and Howard R E 1975 *J. Non-Cryst. Solids* **17** 369

Myuller R L and Shkolnikov E V 1966 in *Solid State Chem.* (ed.) Z U Borisova (New York: Plenum Press) p. 132
Shelestak L J, Charez R A and Mackenzie J D 1978 *J. Non-Cryst. Solids* **27** 83
Speyer R F and Risbud S H 1983 *Phys. Chem. Glasses* **24** 26
Sudha Mahadevan, Giridhar A and Singh A K 1986 *J. Non-Cryst. Solids* **88** 11
Sugi M, Iizima S and Kikuchi M 1971 *J. Non-Cryst. Solids* **5** 358
Thornburg D D and Johnson R I 1975 *J. Non-Cryst. Solids* **17** 2
Yinnon H and Uhlman D R 1983 *J. Non-Cryst. Solids* **54** 253

Bull. Mater. Sci., Vol. 9, No. 1, March 1987, pp. 21–27. © Printed in India.

X-ray crystallographic and thermal studies on the hydrides of magnesium and its intermetallics

P SELVAM, B VISWANATHAN, C S SWAMY and V SRINIVASAN
Department of Chemistry, Indian Institute of Technology, Madras 600 036, India

MS received 11 August 1986; revised 12 December 1986

Abstract. Magnesium nickel hydride, Mg_2NiH_4, exists in two crystallographic modifications, the low temperature phase crystallizing in monoclinic structure and the high temperature phase having a cubic structure. The phase transition (~ 510 K) was accompanied by a small composition change. The enthalpies and entropies of formation of these hydrides were calculated from the DTA data and compared with the values obtained by other methods.

Keywords. Magnesium nickel hydride; phase transition; enthalpy; entropy of formation.

1. Introduction

Among the magnesium alloys, Mg_2Ni forms a ternary hydride, Mg_2NiH_4, with favourable hydrogen content (3·6 wt. %), moderate stability and rapid kinetics (Reilly and Wiswall 1968). Its presence (Mg_2Ni) also improves the hydriding kinetics of the binary hydride, MgH_2 (Reilly and Wiswall 1968; Seiler *et al* 1980). The earliest crystallographic and thermal studies of Mg_2NiH_4 by Gavra *et al* (1979) showed a reversible allotropic phase transition around 485–520 K. There are various reports of crystallographic studies and thermal analyses on this system with a view to elucidate the crystal symmetry of the hydride as well as to identify the phase transformation (Reilly and Wiswall 1968; Gavra *et al* 1979; Mintz *et al* 1980; Schefer *et al* 1980; Hirata *et al* 1981; Darnaudery *et al* 1981; Andresen *et al* 1981; Schefer *et al* 1981; Noreus and Werner 1981, 1984; Genossar and Rudman 1981; Yvon *et al* 1981; Ono *et al* 1982a,b; Darnaudery *et al* 1983a; Noreus and Olsson 1983; Hayakawa *et al* 1984; Soubeyroux *et al* 1984a,b; Carter and Carter 1984; Gavra *et al* 1985; Zolliker *et al* 1986).

There has been a great interest in the thermodynamic properties of metal hydrides because of their importance in various technical purposes as well as in the physical understanding of metal-hydrogen reactions. Numerous experimental (Mueller *et al* 1968; Andresen and Maeland 1978; Alefeld and Volkl 1978; Bambakidis 1981; Wenzl and Labsanft 1983) and theoretical (Switendick 1972; Van Mal *et al* 1974; Lundin *et al* 1977; Gelatt *et al* 1978; Bouten and Miedema 1980) investigations on the thermodynamic aspects of the interaction of hydrogen with metals, alloys and intermetallic compounds have been reported. Experimentally the thermodynamic quantities can be obtained from pressure-composition isotherms (p-c-T) (Buchner 1978; Fischer *et al* 1978; Sandrock and Huston 1981) or from related equivalent approach of electrode potential-composition-temperature relationships or from heat capacity measurements (Flanagan and Oates 1972) or from calorimetric methods (Reilly and Wiswall 1974; Labsanft 1979; Bowerman *et al* 1979, 1980; Murray *et al* 1981, 1983; Pasturel *et al* 1982; Wenzl and Labsanft 1983). Recently Shilov *et al* (1983) suggested an alternative method based on approximate enthalpy balance equation in conjunction with differential thermal analysis (DTA).

The present investigation was undertaken to obtain information on the conflicting reports on x-ray crystallographic data for the structural modifications of Mg_2NiH_4 and the thermodynamic characteristics of the magnesium and its alloy hydrides using the DTA technique.

2. Starting materials

The sources of the samples used in the present study are BDH-GLAXO Laboratories Ltd., (India) (36 mesh, 99·5% purity) or/and SISCO Research Laboratories Pvt. Ltd. (India) (36 mesh, 99·8% purity) for magnesium, (Koch-Light Laboratories Ltd., U.K.; for nickel (100 mesh, 99·8% purity)) and SISCO Research Laboratories Pvt. Ltd. (India) for Copper (200 mesh, 99·5% purity). Commercial samples of Mg_2Ni and Mg_2Cu alloys used in the present study were supplied by the Ergenics Division of the MPD Technology Corporation, New Jersey (USA) with the designation Hystor–301 and 302 respectively. High purity argon (Iolar-1 grade) and hydrogen (Iolar-1 grade) supplied by M/s Indian Oxygen Limited with a maximum oxygen content of 2 ppm were used for the preparation and hydriding purposes respectively.

3. Experimental procedures

3.1 *Preparation of alloys and hydrides*

The alloys Mg_2Ni and Mg_2Cu were prepared by heating pure metals in the stoichiometric ratio at 1125 K and annealing it in argon for 48 hr at 825 K. The hydrides were synthesized in an autoclave with a maximum operating temperature of 673 K and a pressure of 150 atm.

3.2 *X-ray diffraction and thermal analysis*

X-ray powder diffraction measurements were carried out with or without a heating stage facility on a diffractometer (Philips model PW–1140) using CuK_α radiation. Simultaneous differential thermal and thermogravimetric analyses (DTA–TGA) were performed under 1 atm hydrogen/argon pressure using a thermogravimetric and differential thermal analysis combined unit (Stanton Redcroft thermal analyzer, model STA–780) upto 725 K with a heating rate of 10 K per min.

4. Results and discussion

4.1 *X-ray diffraction analysis*

The hydride, Mg_2NiH_4 was found to have a different crystallographic form at higher temperatures (510 K). This suggests a structural phase transition (Stucki 1983). The x-ray diffraction data of the LT-phase (room temperature) of Mg_2NiH_4 could be indexed on the basis of a monoclinic unit cell while the HT-phase (above 510 K) could be indexed on the basis of a cubic symmetry. Therefore, the Mg_2NiH_4 sample was found to undergo a structural phase transition from a LT-monoclinic to a HT-cubic phase around 510 K. The values of the least square refined cell parameters for the LT- and HT-phases obtained in the present study are given in table 1. The x-ray diffraction data obtained in the present study favour a monoclinic structure for the LT-phase and a cubic structure for the HT-phase.

Thus, the preparation conditions employed in the present study favour mainly a monoclinic structure which has a distorted cubic symmetry. The x-ray densities of the LT- and HT-forms of the samples 2·71 and 2·67 gm/cm^3 respectively are in reasonable agreement with the experimental values reported (Reilly and Wiswall 1968; Mintz *et al* 1980; Ishido *et al* 1982; Post *et al* 1984) and agree well with the calculated values (Genossar and Rudman 1981; Ono *et al* 1984).

4.2 *Differential thermal and thermogravimetric analyses*

DTA thermograms were obtained for the hydrides of Mg, Mg_2Ni and Mg_2Cu samples by heating them in the temperature range from room temperature to 725 K under hydrogen/argon atmospheres. The decomposition of the hydrides is seen by the endothermic peaks (see table 2 for the decomposition temperatures). It is seen that the hydrides decompose at lower temperatures for the intermetallic hydrides compared to the binary system MgH_2.

The decomposition temperatures in argon atmosphere are lower than those observed in the hydrogen atmosphere (refer to data given in table 2) and these values agree with the reported decomposition temperatures from pressure-composition isotherms. Hirata *et al* (1984) observed that the decomposition temperature of the hydride of Mg_2Ni can be as high as 598 K in 0·1 MPa of hydrogen pressure. Gavra *et al* (1979) reported that the decomposition temperature of Mg_2NiH_4 under 700 torr of hydrogen pressure is around 553–573 K. The results of the present study agree with these reports.

The thermal analysis of Mg_2NiH_4 carried out in 1 atm hydrogen pressure showed two endothermic peaks revealing a reversible phase transition and decomposition around 510 K and 555 K respectively (figure 1). The small endothermic peak around

Table 1. X-ray data for the LT- and HT-forms of Mg_2NiH_4 samples.

	Structure and cell parameters	
Source (Mg_2NiH_4 sample)	LT form (monoclinic)	HT form (cubic)
Synthesized	$a = 6{\cdot}581$ A° $b = 6{\cdot}400$ A° $c = 6{\cdot}499$ A° $\beta = 93{\cdot}10°$	$a = 6{\cdot}519$ A°
Hystor-301	$a = 6{\cdot}585$ A° $b = 6{\cdot}406$ A° $c = 6{\cdot}493$ A° $\beta = 93{\cdot}10°$	$a = 6{\cdot}521$ A°

Table 2. Hydrogen desorption temperatures at 1 atm (T_{des}, K) and thermodynamic properties (enthalpy, ΔH, kJ mol^{-1} H_2 and entropy, ΔS, JK^{-1} mol^{-1} H_2) for the hydrides of Mg, Mg_2Ni and Mg_2Cu from DTA data. Calorimetric and p-c-T results are given for comparison.

System	Hydride	Differential thermal analysis						Pressure–composition-isotherms			Calorimetry
		Under argon atm.			Under hydrogen atm.						
		T_{des}	$-\Delta H$	$-\Delta S$	T_{des}	$-\Delta H$	$-\Delta S$	T_{des}	$-\Delta H$	$-\Delta S$	$-\Delta H$
$Mg–H_2$	MgH_2 (BDH)	563	67·0	119·0	593	71·2	120·1	551–562	70·0–77·0	126·0–135·0	75·0
	MgH_2 (SISCO)	560	66·5	118·8	590	70·7	119·8	(Stampfer *et al* 1960; Tanguy *et al* 1976; Pedersen *et al* 1983; Post *et al* 1984; Ono *et al* 1984)			(Post *et al* 1984)
$Mg_2Ni–H_2$	Mg_2NiH_4 (Synthesized)	523	61·4	117·4	555	65·8	118·5	523–533	60·7–67·0	117·2–116·0	63·1
	Mg_2NiH_4 (Hystor–301)	528	62·1	117·6	553	65·6	118·6	(Reilly and Wiswall 1968; Lutz and De Pous 1977; Akiba *et al* 1982; Buchner *et al* 1978; Ono *et al* 1984; Darnaudery *et al* 1983b; Post *et al* 1984)			(Post *et al* 1984)
$Mg_2Cu-H_2^*$	Mg H_2 (Synthesized)	518	71·9	134·7	541	75·1	138·8	512	72·8	142·1	—
	Mg H_2 (Hystor–302)	513	71·3	134·9	538	74·7	138·9	(Reilly and Wiswall 1967; Darnaudery *et al* 1983b)			

* In this case no ternary hydride is formed but a binary hydride is formed according to the reaction (Reilly and Wiswall 1967). Enthalpy correction for the formation of Mg_2Cu alloy was made in view of the decomposition of the hydride and subsequent reaction of Mg with $MgCu_2$.

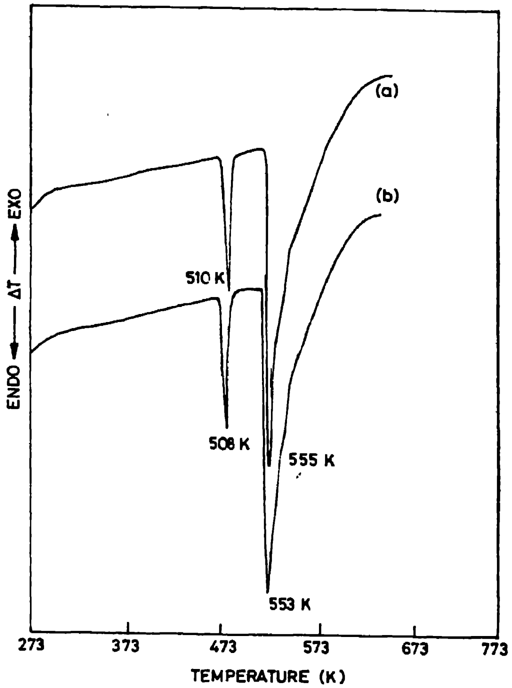

Figure 1. DTA curves for the dehydriding behaviour of Mg_2NiH_4 under hydrogen atmosphere: (**a**) Synthesized. (**b**) Hystor–301.

510 K could be attributed to the structural transition from LT-hydride form to HT-form (Gavra *et al* 1979; Hirata 1984; Noreus and Werner 1984) and is associated with a small change in the composition as observed from TGA studies. This allotropic transition appeared reversibly during repeated heating-cooling cycles. The heat change involved in the transition was calculated as 3·3 KJ mol^{-1} H_2 by Gavra *et al* (1979) employing a differential scanning calorimetry (DSC) technique. However, only one broad endotherm is observed during the decomposition of Mg_2NiH_4 in argon atmosphere. The endotherm starts at the phase transition temperature. Therefore, it is assumed that the broad endotherm is due to both the phase transition and decomposition of the hydrides. The endotherm is not separated even at a lower heating rate of 5 K per min.

TGA studies suggest that the desorbed hydrogen in Mg, Mg_2Ni and Mg_2Cu hydrides corresponds to the stoichimetry of the hydride formed. In addition, a small weight loss is observed in the case of Mg_2NiH_4 in the phase transition region suggesting a different composition of the polymorphic varieties, i.e. the LT-monoclinic phase being the stoichiometric phase (Mg_2NiH_4) and the HT-cubic phase being the sub-stoichiometric phase (Mg_2NiH_{4-x}).

Based on the method of Shilov *et al* (1983), the enthalpies and entropies of formation of the magnesium and its intermetallic hydrides were calculated from the DTA data. The calculated thermodynamic quantities along with the desorption temperatures are given in table 2. The results are comparable with the data deduced from p-c-T relationships and calorimetric measurements. However, the values calculated from DSC measurements by Gavra *et al* (1979), Ono *et al* (1982b) and Hirata (1984) are 47·3, 59·0 and 58·9 KJ mol^{-1} H_2 respectively. They are somewhat lower than the values calculated from the DTA studies or from the conventional p-c-T relationships and calorimetric measurements.

Acknowledgement

Thanks are due to the Department of Non-Conventional Energy Sources (DNES), Ministry of Energy, Government of India, New Delhi for the award of a research grant.

References

Akiba E, Nomura K, Ono S and Suda S 1982 *Int. J. Hydrogen Energy* **7** 787

Alefeld G and Volkl J 1978 *Hydrogen in metals II–Topics in applied physics* (Berlin: Springer-Verlag) vol. 29

Andresen A F, Andersen E and Pattersen K 1981 *Acta Crystallogr. Suppl. C* **A37** 152

Andresen A F and Maeland A J 1978 *Hydrides for energy storage—Proc. Int. Symp.* (Oxford: Pergamon Press)

Bambakidis G 1981 *Metal hydrides—NATO advanced study Institutes Series B: Physics* (New York: Plenum Press) vol. 76

Bouten P C P and Miedema A R 1980 *J. Less-Common Metals* **71** 147

Bowerman B S, Wulff C A, Biehl G E and Flanagan T B 1980 *J. Less-Common Metals* **73** 1

Bowerman B S, Wulff C A and Flanagan T B 1979 *Z. Phys. Chem. N.F.* **116** 197

Buchner H 1978 *Int. J. Hydrogen Energy* **3** 385

Buchner H, Bernauer O and Streub W 1978 in *Proc. Second World Hydrogen Energy Conf. on Hydrogen Energy Systems* (eds) T N Veziroglu and W Seifritz (New York: Pergamon Press) vol. 3, p. 1677

Carter G C and Carter F L 1984 in *Metal hydrogen systems* (ed) T N Veziroglu (New York: Pergamon Press)

Darnaudery J P, Pezat M, Darriet B and Hagenmuller P 1981 *Mater. Res. Bull.* **16** 1237

Darnaudery J P, Pezat M and Darriet B 1983a *J. Less-Common Metals* **92** 199

Darnaudery J P, Darriet B and Pezat M 1983b *Int. J. Hydrogen Energy* **8** 705

Fischer P, Halg W, Schlapbach L, Stucki F and Andresen A F 1978 *Mater. Res. Bull.* **13** 931

Flanagan T B and Oates W A 1972 *Ber. Bunsenges. Phys. Chem.* **76** 706

Gavra Z, Kimmel G, Gefen Y and Mintz M H 1985 *J. Appl. Phys.* **57** 4548

Gavra Z, Mintz M H, Kimmel G and Hadari Z 1979 *Inorg. Chem.* **18** 3595

Gelatt C D, Ehrenreich M and Weise J A 1978 *Phys. Rev.* **B17** 1970

Genossar J and Rudman P S 1981 *J. Phys. Chem. Solids* **42** 199

Hayakawa H, Ishido Y, Nomura K, Uruno H and Ono S 1984 *J. Less-Common Metals* **103** 277

Hirata T 1984 *Int. J. Hydrogen Energy* **9** 255

Hirata T, Matsumoto T, Amano M and Sasaki Y 1981 *J. Phys.* **F11** 521

Ishido Y, Kawamura M and Ono S 1982 *Int. J. Hydrogen Energy* **7** 173

Lebsanft E 1979 *J. Phys.* **E12** 699

Lundin C E, Lynch F E and Magee C B 1977 *J. Less-Common Metals* **56** 19

Lutz H M and De Pous 1977 in *Proc. Second Int. Cong. on Hydrogen in Metals* (Paris: Pergamon Press) vol. 1, p. 1F5

Mintz M H, Gavra Z, Kimmel G and Hadari Z 1980 *J. Less-Common Metals* **74** 263

Mueller W M, Blackledge J P and Libowitz G G 1968 *Metal hydrides* (New York: Academic Press)

Murray J J, Post M L and Taylor J B 1981 *J. Less-Common Metals* **80** 201

Murray J J, Post M L and Taylor J B 1983 *J. Less-Common Metals* **90** 65

Noreus D and Olsson L G 1983 *J. Chem. Phys.* **78** 2419

Noreus D and Werner P E 1981 *Mater. Res. Bull.* **16** 199

Noreus D and Werner P E 1984 *J. Less-Common Metals* **97** 215

Ono S, Hayakawa M, Suzuki A, Nomura K, Nishimiya N and Tabata T 1982b *J.Less-Common Metals* **88** 63

Ono S, Ishido Y, Imanari T, Tabata T, Cho Y K, Yamamoto R and Doyama M 1982a *J.Less-Common Metals* **88** 57

Ono S, Ishido Y, Akiba E, Jindo K, Saweda Y, Kitagawa I and Kakutani T 1984 in *Hydrogen energy progress V—Proc. 5th world Hydrogen energy conf.* (ed) T N Veziroglu (Toronto: Pergamon Press) p. 1291

Pasturel A, Colinet C C, Guegan A P and Achard J L 1982 *J. Less-Common Metals* **84** 73

Pedersen A S, Kjoller B, Larsen B and Vigeholm B 1983 *Int. J. Hydrogen Energy* **8** 205

Post M L, Murray J J and Taylor J B 1984 *Int. J. Hydrogen Energy* **9** 137

Reilly J J and Wiswall R H 1967 *Inorg. Chem.* **6** 2220

Reilly J J and Wiswall R H 1968 *Inorg. Chem.* **7** 2254

Reilly J J and Wiswall R H 1974 *Inorg. Chem.* **13** 218

Sandrock G D and Huston E L 1981 *Chem. Tech.* **11** 754

Schefer J, Fischer P, Halg W, Stucki F, Schlapbach L, Didisheim J J, Yvon K and Andresen A F 1980 *J. Less-Common Metals* **74** 65

Schefer J, Fischer P, Stucki F, Schlapbach L, Baerelocher Ch, Yvon K, Didisheim J J, Jorgensen J D and Andresen A F 1981 in *Prog. Rep. AF-SSP-118* (Zurich: Institut fur Reaktortechnik Eidgenossische Technische Hochschule) p. 52

Seiler A, Schlapbach L, von Waldkirch Th, Shaltiel D and Stucki F 1980 *J. Less-Common Metals* **73** 193

Shilov A L, Padurets L N and Kost M E 1983 *Russ. J. Inorg. Chem.* **57** 338

Soubeyroux J L, Fruchart D, Mikou A, Pezat M, Darriet B and Hagenmuller P 1984a *Mater. Res. Bull.* **19** 969

Soubeyroux J L, Fruchart D, Mikou A, Pezat M and Darriet B 1984b *Mater. Res. Bull.* **19** 1119

Stampfer J F, Holley C E and Suttle J F 1960 *J. Am. Chem. Soc.* **82** 3504

Stucki F 1983 *Int. J. Hydrogen Energy* **8** 49

Switendick A.C 1972 *Solid State Commun.* **8** 1463

Tanguy B, Soubeyroux J L, Pezat M, Portier J and Hagenmuller P 1976 *Mater. Res. Bull.* **11** 1441

Van Mal H H, Buschow K H J and Miedema A R 1974 *J. Less-Common Metals* **35** 65

Wenzl H and Lebsanft E 1983 *J. Phys.* **F10** 2147

Yvon K, Schefer J and Stucki F 1981 *Inorg. Chem.* **20** 2776

Zolliker P, Yvon K and Beerlocher Ch 1986 *J. Less-Common Metals* **115** 65

Bull. Mater. Sci., Vol. 9, No. 1, March 1987, pp. 29–35. © Printed in India.

High resolution electron microscopy of bismuth oxides with perovskite layers†

G N SUBBANNA and L GANAPATHI*
Materials Research Laboratory, *Solid State and Structural Chemistry Unit, Indian Institute of Science, Bangalore 560 012, India

MS received 28 January 1987

Abstract. Layered bismuth oxides of the general formula $(Bi_2O_2)^{2+}$ $(A_{n-1}B_nO_{3n+1})^{2-}$ where A = Bi or Ba, B = Ti, Fe, W and n = number of perovskite layers have been investigated by high resolution electron microscopy. Lattice images obtained for $n = 1$ to 6 members show stacking of $(n-1)$ perovskite layers sandwiched between dark bands due to the $(Bi_2O_2)^{2+}$ layers. It has been possible to resolve the perovskite layer structures in some of the oxides. A highly ordered structure is observed upto the $n = 3$ member, whereas higher members show superstructures, dislocations and stacking faults arising from the side-stepping of $(Bi_2O_2)^{2+}$ layers as well as ferroelectric domain walls.

Keywords. Electron microscopy; lattice images; defect structures; Aurivillius oxides.

1. Introduction

High resolution electron microscopy (HREM) is a powerful tool for the investigation of ultrastructure of solids in real space. Lattice imaging using an electron microscope provides novel information about the local structural defects and intergrowths which cannot otherwise be obtained from x-ray diffraction that reveals only the average structure (Anderson 1978; Rao and Thomas 1985; Rao 1985). Layered perovskite oxides containing bismuth, first described by Aurivillius (1950), have the general chemical formula $(Bi_2O_2)^{2+}$ $(A_{n-1}B_nO_{3n+1})^{2-}$ where A is a bulky cation Bi^{3+}, Ba^{2+} etc, B is a smaller cation Fe^{3+}, Ti^{4+}, W^{6+} etc and n corresponds to the number of corner-shared octahedra forming the $(A_{n-1}B_nO_{3n+1})$ perovskite layers. The crystal structure of these oxides consists of $(Bi_2O_2)^{2+}$ layers interleaved with the $(A_{n-1}B_nO_{3n+1})$ perovskite layers. All the oxides of the family are tetragonal (or with slight orthorhombic distortion) with the a and b parameters nearly equal to $\sqrt{2}a_c$, a_c being the lattice parameter of the cubic perovskite subcell. The c parameter in these solids varies progressively with increase in n. A structural projection of $n = 5$ member is shown in figure 1 to illustrate some of the structural features. Positions of the bismuth atoms of the $[Bi_2O_2]^{2+}$ layers are close to virtual A sites of the perovskite subcell. The pyramidal BiO_4 groups share edges such that the successive perovskite layers are displaced by $1/2[110]_c$. Most of these Aurivillius oxides are ferroelectrics with high Curie temperatures and large values of the spontaneous polarization (Subba Rao 1962).

Earlier electron microscope studies of the Aurivillius oxides by Hutchison *et al* (1977) revealed interesting structural defects such as antiphase boundaries, dislocations and random intergrowth of different members. In this laboratory, we have investigated several aspects of Aurivillius oxides, specially the intergrowth structures formed by them (Rao 1985; Gopalakrishnan *et al* 1984). In this paper, we present some of our HREM observations on the Aurivillius oxides chiefly containing Bi^{3+}, Ba^{2+} cations at the *A* site and Ti^{4+}, Fe^{3+} and W^{6+} cations at the *B* site.

---

†Contribution No. 73 from Materials Research Laboratory.

2. Experimental

The various oxides of the Aurivillius family with $n=1$ to 6 were prepared starting from the appropriate mixtures of Bi_2O_3, WO_3, TiO_2, Fe_2O_3 and barium carbonate. Oxides prepared along with the evaluated lattice parameters are listed in table 1. High resolution electron microscopy (HREM) work was carried out in an electron microscope (JEOL JEM 200 CX) in the top entry configuration. Thin wedge-shaped crystals lying near a hole of the holey carbon grid were selected for the study. The crystals were brought to the required orientation using the ± 30° goniometer. Images were recorded at 200 kV with a primary magnification in the range of $3–5 \times 10^5$.

3. Results and discussion

One-dimensional lattice images obtained for $n=1$ to 5 members of the family are shown in figure 2. Dark fringes correspond to the $(Bi_2O_2)^{2+}$ layers and $n-1$ fringes

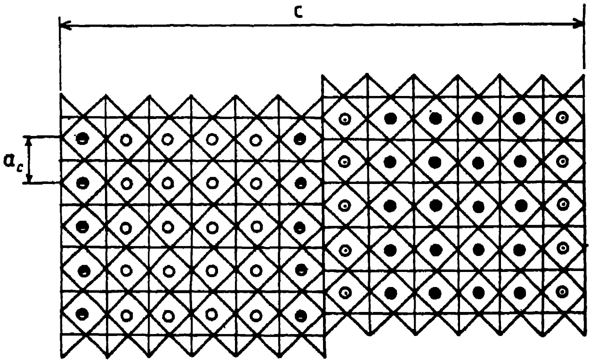

Figure 1. Structure of $Ba_2Bi_4Ti_5O_{18}$, projected on (101) of the pseudotetragonal cell. Each half of *c* are at $y=0$, and 1/2;○,● are *A* cations at $y=0$ and 1/2;◉, ⊙ are Bi in Bi_2O_2 layer at $y=0$ and 1/2.

Table 1. Unit cell parameters of bismuth oxide-layered compounds studied.

Compound	Perovskite layers	Lattice parameters (Å) *a*	*b*	*c*
Bi_2WO_6	1	5·458	5·438	16·43
$BaBi_2Nb_2O_9$	2	5·533	5·533	25·55
$Bi_4Ti_3O_{12}$	3	5·448	5·411	32·83
$Bi_5Ti_3FeO_{15}$	4	5·468	5·464	41·23
$Ba_2Bi_4Ti_5O_{18}$	5	5·514	5·526	50·37
$Bi_7Ti_3Fe_3O_{21}$	6	5·484	5·484	57·84

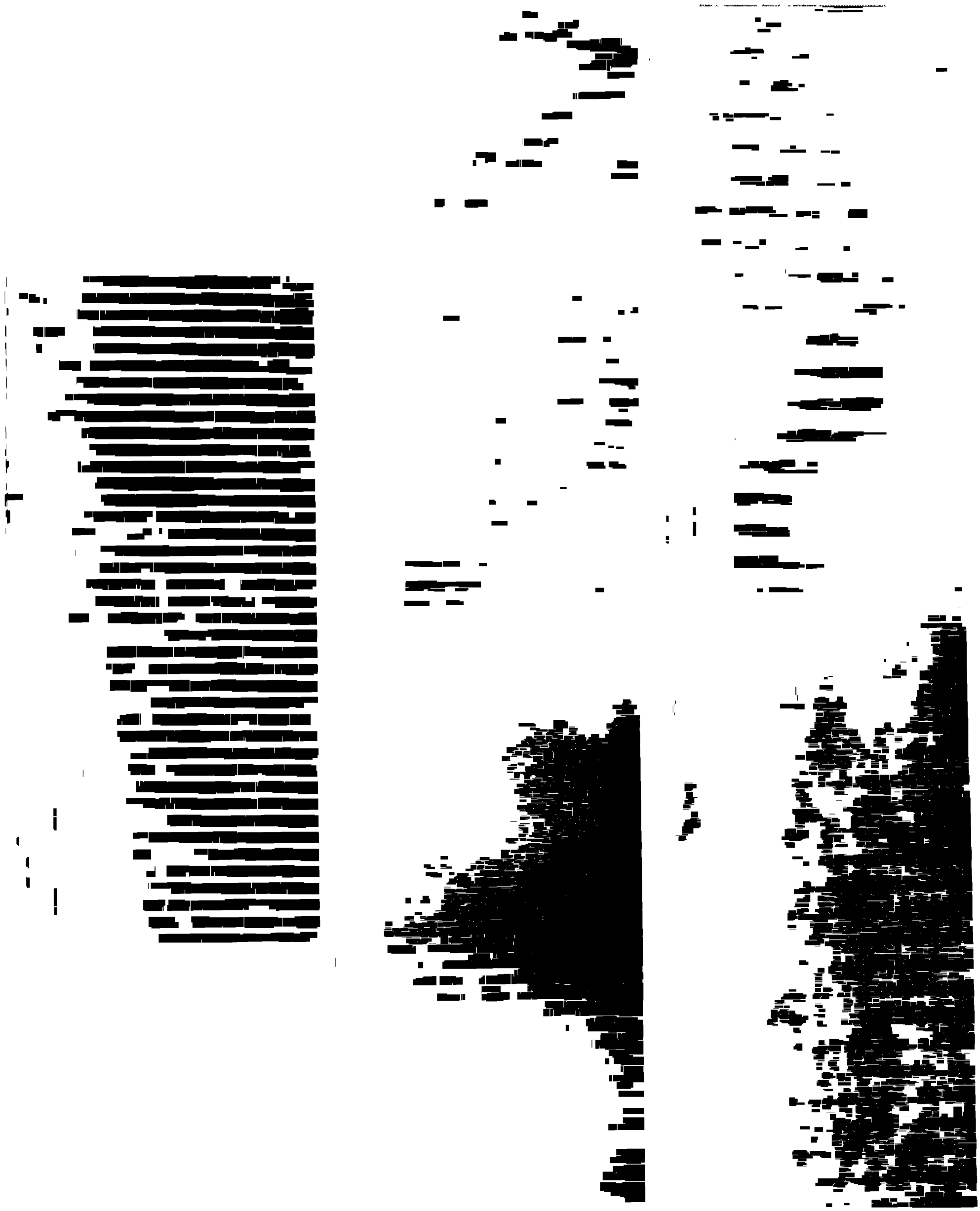

Figure 2. One-dimensional lattice images of $n=1$ to 5 members of the family. The homology in the images is clearly seen.

corresponding to perovskite layers between these two dark fringes are seen. A contrast reversal can occur in lattice images of thicker crystals. We can clearly see the homology in the images given in figure 2. Under favourable conditions, two-dimensional images (structure images) can be obtained which give a square-grid pattern of the perovskite structure with an octahedral separation of 0·38 nm. High resolution structural images obtained for Bi_2WO_6 ($n=1$) and $Bi_7Ti_3Fe_3O_{21}$ ($n=6$) are shown in figures 3 and 4 respectively. The crystal orientation in both the images is $\langle 110 \rangle$.

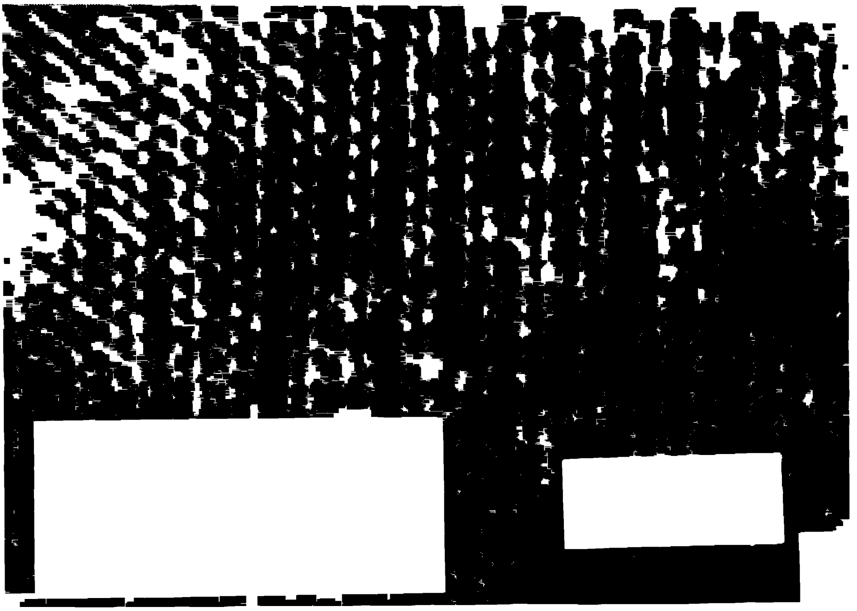

Figures 3–4. 3. HREM image of Bi_2WO_6 ($n=1$). The inset shows the projected structure matching reasonably well with the image. 4. HREM image of $Bi_7Ti_3Fe_3O_{21}$ ($n=6$). The inset shows the projected structure matching reasonably well with the image.

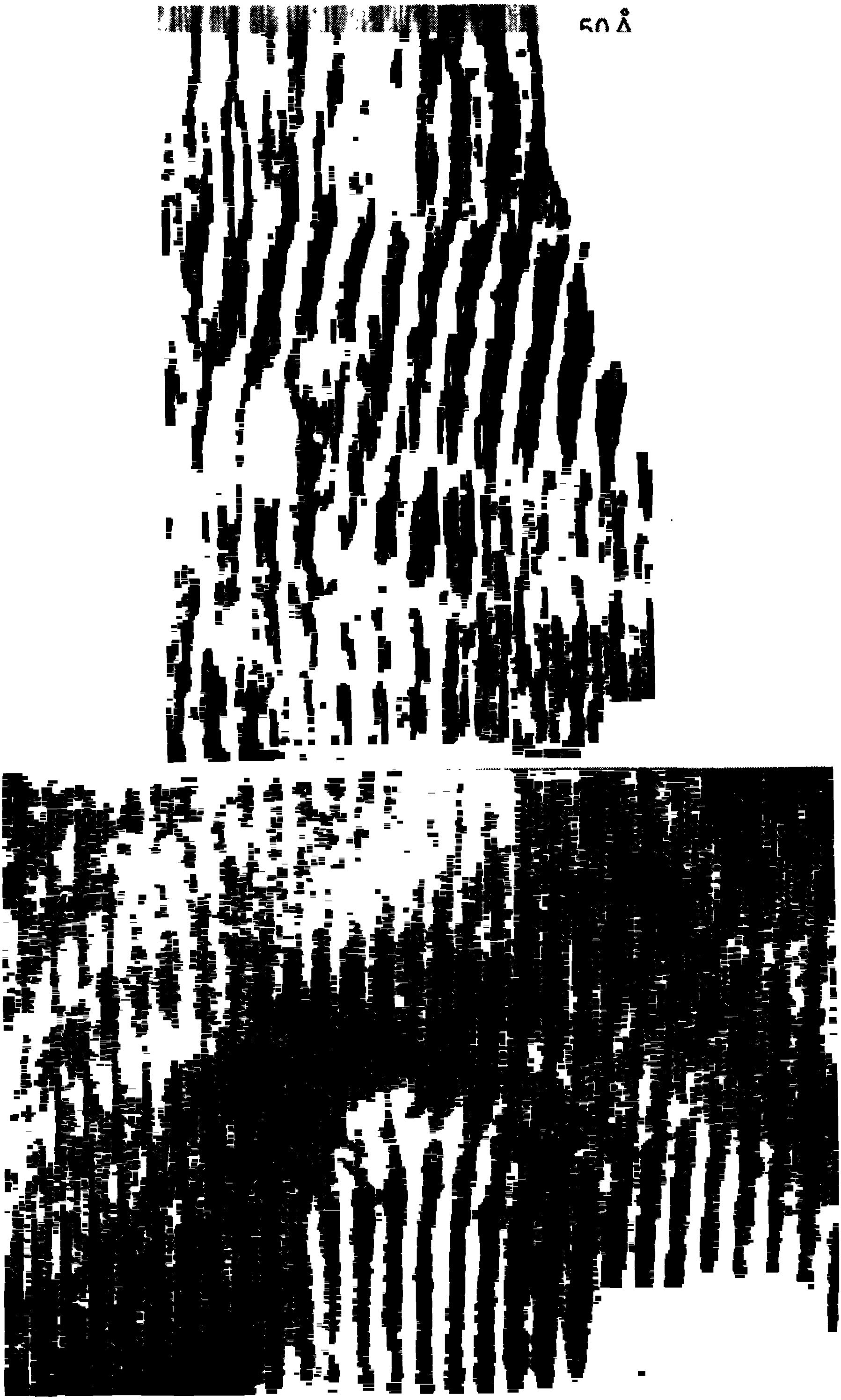

Figures 5–6. 5. Stacking fault in $Ba_2Bi_4Ti_5O_{18}$ ($n = 5$) arising from the side stepping of the $(Bi_2O_2)^{2+}$ layers. 6. Lattice image of $Bi_7Ti_3Fe_3O_{21}$ ($n = 6$) containing a dislocation. Note the associated strain field extending on either side of dislocation.

The $(Bi_2O_2)^{2+}$ layers are aligned parallel to the beam and the perovskite layers are projected along $\langle 100 \rangle$ of the cubic sub-cell. The projected structure of these oxides is shown in the insets of these figures; the HREM images can be matched with the projected images reasonably well. The structure images seem to reveal both the A and B cations as shown in figure 3. The image contrast is quite sensitive to orientation and the defocus condition, but under ideal conditions is able to yield atomic resolution. It may be noted that high resolution images of these oxides have not been described adequately in the literature hitherto (Tilley 1979).

Defect structures such as stacking faults, dislocations and antiphase boundaries are more commonly observed in the $n>3$ members of the Aurivillius family of oxides. Figure 5 illustrates the occurrence of stacking faults in a crystal of $Ba_2Bi_4Ti_5O_{18}$ ($n=5$) arising from the side-stepping of the $(Bi_2O_2)^{2+}$ layers. Edge dislocations are also frequently observed in these oxides. The image in figure 6 shows a dislocation involving the termination of two perovskite slabs and the associated strain field extending upto 12 perovskite slabs. Domains caused by twinning are expected when the material is transformed to the ferroelectric state from the high-temperature paraelectric state. Domains with complex boundaries have been observed earlier in $n=4$ and 5 members of the family (Hutchison *et al* 1977). Figure 7 shows the domains observed by us in $n=4$ member of the family. The inset shows the composite electron diffraction pattern from the two adjacent domains. The dislocations observed in these materials may be related to ferroelectric distortions.

Oxides containing Ti^{4+} and Fe^{3+} in the B-site, namely $Bi_5Ti_3FeO_{15}$ and $Bi_7Ti_3Fe_3O_{21}$ exhibit interesting superstructures in addition to the normal structure. Selected area electron diffraction (SAED) studies carried out on crystals exhibiting superstructures indicate doubling of unit cell in $Bi_5Ti_3FeO_{15}$ and tripling in $Bi_7Ti_3Fe_3O_{21}$ (Subbanna *et al* 1987). The origin of the superstructures is likely to be within the perovskite layers, possibly due to Fe/Ti ordering.

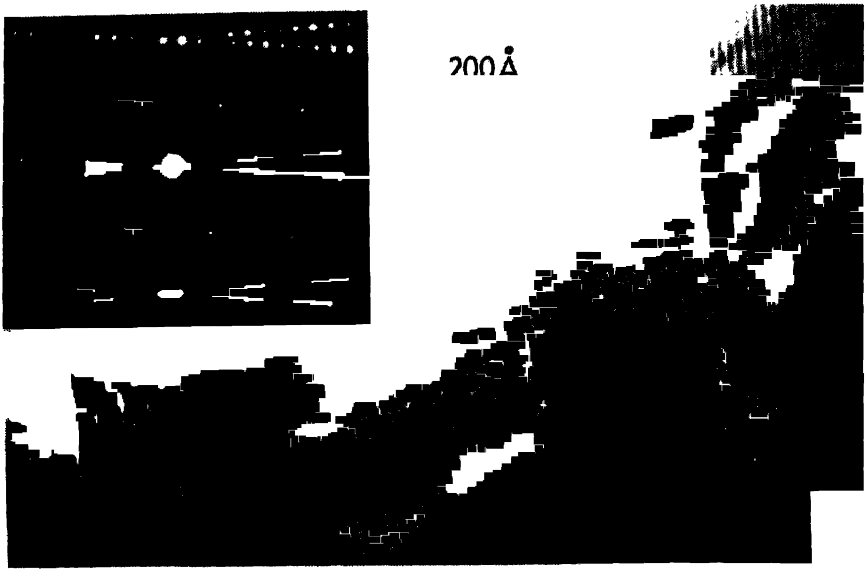

Figure 7. Lattice image of domains in $Bi_5Ti_3FeO_{15}$ ($n=4$). The inset shows the composite SAED pattern.

The formation of complex oxides as described above and other long period structures is a general phenomenon in solid state chemistry. The true complexity of these systems can only be revealed by high resolution electron microscopy. Long-range repulsive interaction arising from elastic forces is expected to be of importance in the formation of the Aurivillius family of oxides (Kikuchi 1979). The same forces also seem to be important in explaining recurrent intergrowth structures formed by adjacent members of this family of oxides (Rao 1985).

Acknowledgement

The authors thank Prof. C N R Rao for suggesting the problem and guidance.

References

Anderson J S 1978 *Proc. Indian Acad. Sci.* (*Chem. Sci.*) **87** 295
Aurivillius B 1950 *Ark. Kemi.* **2** 519
Gopalakrishnan J, Ramanan A, Rao C N R, Jefferson D A and Smith D J 1984 *J. Solid State Chem.* **55** 101
Hutchison J L, Anderson J S and Rao C N R 1977 *Proc. R. Soc. London* **A355** 301
Kikuchi T 1979 *Mater. Res. Bull.* **14** 1561
Rao C N R 1985 *Bull. Mater. Sci.* **7** 155
Rao C N R and Thomas J M 1985 *Acc. Chem. Res.* **18** 113
Subba Rao E C 1962 *J. Am. Ceram. Soc.* **45** 166
Subbanna G N, Ganapathi L, Rao C N R and Jefferson D A 1987 *Mater. Res. Bull.* **22** 205
Tilley R J D 1980 in *Chemical physics of solids and surfaces* (eds) M W Roberts and J M Thomas, Vol. 8, Specialist Periodic Report (London: Royal Society of Chemistry)

Bull. Mater. Sci., Vol. 9, No. 1, March 1987, pp. 37–46. © Printed in India.

Measurement of Gibbs energies of formation of CoF_2 and MnF_2 using a new composite dispersed solid electrolyte

K T JACOB and J P HAJRA
Department of Metallurgy, Indian Institute of Science, Bangalore 560 012, India

MS received 19 November 1986; revised 3 February 1987

Abstract. Gibbs energies of formation of CoF_2 and MnF_2 have been measured in the temperature range from 700 to 1100 K using Al_2O_3-dispersed CaF_2 solid electrolyte and $Ni + NiF_2$ as the reference electrode. The dispersed solid electrolyte has higher conductivity than pure CaF_2 thus permitting accurate measurements at lower temperatures. However, to prevent reaction between Al_2O_3 in the solid electrolyte and NiF_2 (or CoF_2) at the electrode, the dispersed solid electrolyte was coated with pure CaF_2, thus creating a composite structure. The free energies of formation of CoF_2 and MnF_2 are (± 1700) J mol^{-1};

$$\begin{aligned}\Delta G_f^\circ(CoF_2, s) &= -664{,}010 + 134{\cdot}38T \ (700\text{–}980\ K)\\ \Delta G_f^\circ(MnF_2, s) &= -848{,}270 + 129{\cdot}59T \ (700\text{–}980\ K)\\ &= -850{,}200 + 131{\cdot}56T \ (980\text{–}1100\ K)\end{aligned}$$

The third law analysis gives the enthalpy of formation of solid CoF_2 as $\Delta H^\circ(298{\cdot}15\ K) = -672{\cdot}69(\pm 0{\cdot}1)$ kJ mol^{-1}, which compares with a value of $-671{\cdot}5(\pm 4)$ kJ mol^{-1} given in Janaf tables. For solid MnF_2, $\Delta H^\circ(298{\cdot}15\ K) = -854{\cdot}97(\pm 0{\cdot}13)$ kJ mol^{-1}, which is significantly different from a value of $-803{\cdot}3$ kJ mol^{-1} given in the compilation by Barin *et al.*

Keywords. Chemical potential of fluorine; thermodynamic properties; electromotive force; enthalpy; entropy; free energy of formation.

1. Introduction

Solid state galvanic cells are extensively used for determining thermodynamic mixing properties of alloy systems (Jacob 1985). In most of the studies oxide electrodes and solid electrolytes are employed. In a few studies CaF_2 has been used as a solid electrolyte in conjunction with fluoride electrodes (Venkatraman and Hajra 1983; Egan 1985). One of the reasons for the less frequent use of fluoride solid state cells for the study of alloy thermodynamics is the lack of accurate thermochemical data on metal fluorides. Calorimetric measurements of the enthalpy of formation of CoF_2 and MnF_2 have not been reported in the literature. The free energy measurements for MnF_2 reported by Skelton and Patterson (1973) and by Rezukhina *et al* (1974) do not agree. Heat capacities and entropies of CoF_2 were measured by Catalano and Stout (1955) and Binford *et al* (1967), and those of MnF_2 by Stout and Adams (1942), and Ehlert and Hsia (1972/73). The standard heat of formation at 298·15 K can therefore be derived from accurate free energy measurements.

Recently it has been shown that a fine dispersion of inert insulating phases such as Al_2O_3 and CeO_2 in CaF_2 can increase its conductivity by two to three orders of magnitude at temperatures near 700 K. The conductivity of Al_2O_3-dispersed CaF_2 has been shown to be entirely ionic by Vaidehi *et al* (1986). One of the aims of the present study is to explore the use of Al_2O_3-dispersed CaF_2 electrolyte for thermodynamic studies, especially at lower temperatures where the response of conventional cells based on pure CaF_2 electrolyte is sluggish.

Fluorides of manganese and cobalt are used as catalysts in hydrocarbon isomerisation and polymerisation reactions. Manganese fluoride also finds application in optics and electronic industries. The knowledge of the stabilities of these fluorides would be useful in optimising the procedures for their synthesis and applications at elevated temperatures.

2. Experimental techniques

2.1 *Materials*

Ultrapure anhydrous CaF_2 (99·999%) powder was supplied by Alpha Ventron Division, USA. The alumina powder of 99·8% purity was prepared by precipitation from solution and subsequent calcination at 1400 K in air. The average particle size of Al_2O_3 was 0·02 μm. The Al_2O_3-dispersed CaF_2 electrolyte was prepared by mixing $CaF_2+Al_2O_3$ powder in an agate mortar. The CaF_2 pellets containing 2 mol% Al_2O_3 in dispersed form were made from the intimate mixture by double end compression. The composite solid electrolytes were made by sprinkling a small amount of pure CaF_2 over the lower steel plunger, then the required amount of CaF_2 containing 2 mol% Al_2O_3 mixture was added, followed again by sprinkling pure CaF_2 powder in the steel die. The upper steel plunger was then inserted and compressed to 200 MPa. The result was a composite pellet of Al_2O_3-dispersed CaF_2 with a coating of pure CaF_2, approximately 100 μm in thickness, on the two flat surfaces as shown in figure 1. The pellets were sintered under prepurified argon gas at 1400 K for up to 180 ks. The argon gas, 99·99% pure, was dried by passing through magnesium perchlorate and then through soda asbestos for removal of CO_2. The gas was subsequently deoxidised using copper at 750 and titanium at 1150 K.

Powders of Mn, Co, Ni, MnF_2, CoF_2 and NiF_2 of puratronic grade were supplied by Johnson and Matthey Chemicals Ltd. Pellets containing equimolar mixture of $Ni+NiF_2$, $Co+CoF_2$ and $Mn+MnF_2$ were prepared by compression in a steel die. Single crystals of CaF_2 were supplied by Harshaw Chemical Company.

2.2 *Apparatus and procedure*

A schematic diagram of the apparatus is shown in figure 2. The electrode pellets are spring-loaded on either side of the solid electrolyte by a system made up of alumina

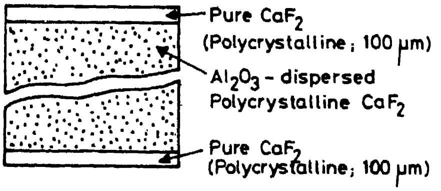

Figure 1. Structure of the composite solid electrolyte containing regions of pure CaF_2 and Al_2O_3-dispersed CaF_2.

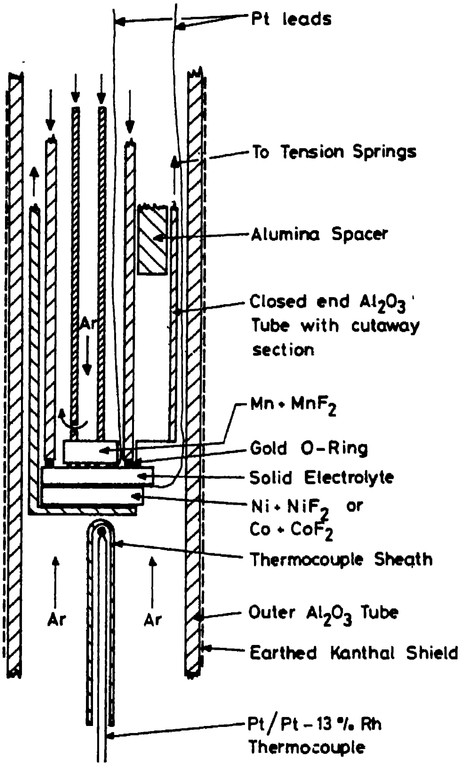

Figure 2. A schematic diagram of the apparatus used in this study.

slabs and tubes as shown in the figure. The gas phase around each electrode was separated by an alumina tube which was pressed against the CaF_2 pellet with a gold O-ring in between. The separation of the gas over each electrode was found to be essential to prevent vapour phase transport of species from one electrode to the other. The partial pressures of NiF_2, CoF_2 and MnF_2 are 0·6, 0·4 and 0·15 Pa at 1100 K. Separate streams of purified argon gas were flown past each electrode. Initially, flow rates were in the range of 4 ml s^{-1} but were reduced to 0·2 ml s^{-1} after the apparatus was completely purged. Electrical contacts to electrode pellets were made by platinum. The cell was enclosed in an outer alumina tube which was suspended in a vertical resistance furnace wound with Kanthal. The cell was electrically shielded by a Kanthal tape wound round the outer alumina tube and earthed. The temperature of the furnace was controlled to ± 1 K. The temperature was measured by a calibrated Pt/Pt–13% Rh thermocouple.

The emf of the cells was measured by a Keithley digital electrometer (model 617) with an impedance exceeding 10^{12} ohms. The reversibility of the cells was checked by passing a small current ($\sim 5\ \mu$A) in either direction through the cell and ensuring that the emfs returned to the constant initial values before titration. The emfs were reproducible on temperature cycling. The emfs were also independent of the flow rate of the inert gas at temperatures below 900 K. At higher temperatures emfs were found to be slightly dependent on the flow rate of the argon gas, presumably because of the removal of volatile fluorides. Below a flow rate of 0·4 ml s^{-1}, the emfs were not affected. The emfs of the following cells were measured as a function of temperature:

I Pt, $Mn+MnF_2 \| CaF_2+2\,mol\%\,Al_2O_3 \| Ni+NiF_2$, Pt
II Pt, $Mn+MnF_2 \| CaF_2 \| Ni+NiF_2$, Pt
III Pt, $Mn+MnF_2 \| CaF_2+2\,mol\%\,Al_2O_3 \| Co+CoF_2$, Pt
IV Pt, $Mn+MnF_2 \| CaF_2 \| Co+CoF_2$, Pt

The cells are written such that the right hand electrodes are positive. Single crystals of CaF_2 were used in cells II and IV.

Preliminary experiments with cells I and III were conducted with Al_2O_3-dispersed CaF_2 without a thin layer of pure CaF_2 on the flat surfaces of the electrolyte. It was found that the cell emf began to drop gradually after approximately 85 ks at temperatures above 1000 K. After 250 ks the emf dropped by 8 mV. Careful examination of the electrolyte/electrode interface after the experiment by electron microscope (diffraction) indicated small islands of AlF_3. This phase was found at the interface between CaF_2-2 mol% Al_2O_3 electrolyte and $Ni+NiF_2$ (or $Co+CoF_2$) electrode. Thermodynamic data suggest that the formation of AlF_3 occurs by the following reactions:

$$Al_2O_3(s)+3\,NiF_2(s)\rightarrow 2\,AlF_3(s)+3\,NiO(s);\ \Delta G^\circ_R=-92{\cdot}8\ kJ\,mol^{-1}, \quad (1)$$

$$Al_2O_3(s)+3\,CoF_2(s)\rightarrow 2\,AlF_3(s)+3\,CoO(s);\ \Delta G^\circ_R=-53{\cdot}0\ kJ\,mol^{-1}. \quad (2)$$

The contact between Al_2O_3 in the electrolyte and NiF_2 (or CoF_2) at the electrode was avoided in the subsequent experiments by using composite dispersed solid electrolytes, which had a thin coating of pure CaF_2 on the electrolyte surface. With composite solid electrolytes the emfs were stable up to 500 ks at 1100 K. All data reported in this paper were obtained using the composite dispersed solid electrolyte. Measurements with cells I and III incorporating Al_2O_3-dispersed CaF_2 composite electrolyte were conducted in the temperature range from 700 to 1100 K. Experiments using pure CaF_2 electrolyte (cells II and IV) were confined to temperatures above 950 K where the response was rapid. The electrodes in cells I and II are identical. Similarly the only difference between the cells III and IV is the composition of the electrolyte.

3. Results

The reversible emfs of cells I to IV are summarized in tables 1 and 2. The variation of emf of the cells I and II with temperature is shown in figure 3.

The emfs of the two cells are identical within experimental error, confirming that electric conduction in the biphasic dispersed solid electrolyte is entirely ionic. The reproducibility of emf at a fixed temperature is ±0·3 mV. There appears to be a change in slope of the curve at 980 K which corresponds to transformation of Mn from α to β form. The least mean squares regression analysis gives the following expression for combined emf of cells I and II:

$$E=1{,}008{\cdot}4+0{\cdot}1133T\,(\pm 0{\cdot}3)\ mV, \quad (3)$$

for the temperature range 700 to 980 K. For high temperatures (980 to 1100 K), emfs are given by

$$E=1{,}018{\cdot}4+0{\cdot}1031T\,(\pm 0{\cdot}36)\ mV. \quad (4)$$

Table 1. Emf of the cells I and II and $\Delta G_f^\circ(T)$ and $\Delta H^\circ_{298\cdot15}$ (third-law) of MnF_2.

		Pt, Mn + MnF_2 ‖ CaF_2 + 2 mol %Al_2O_3 ‖ Ni + NiF_2, Pt	
T(K)	Emf (mV)	$-\Delta G_f^\circ(MnF_2,s)$ (kJ mol^{-1})	$-\Delta H^\circ_{298\cdot15}(MnF_2,s)$ (kJ mol^{-1})
703	1088·0	757·16	854·66
757	1094·5	750·24	854·89
809	1099·6	743·34	854·82
851	1104·5	737·93	854·95
867	1107·0	735·98	855·11
900	1110·6	731·68	855·11
947	1115·5	725·51	855·04
984	1120·0	720·78	855·13
1015	1122·8	716·62	855·02
1037	1125·1	713·73	854·98
1070	1129·0	709·49	854·98
1096	1131·0	705·94	854·77
		Pt, Mn + MnF_2 ‖ CaF_2 ‖ Ni + NiF_2, Pt	
970	1118·4	722·34	855·11
1079	1130·1	708·34	854·99
1050	1127·0	712·13	855·06

Table 2. Emf of the cells III and IV and $\Delta G^\circ(T)$ and $\Delta H^\circ_{298\cdot15}$ (third-law) of CoF_2.

		Pt, Mn + MnF_2 ‖ CaF_2 + 2 mol %Al_2O_3 ‖ Co + CoF_2, Pt	
T(K)	Emf (mV)	$-\Delta G_f^\circ(CoF_2,s)$ (kJ mol^{-1})	$-\Delta H^\circ_{298\cdot15}(CoF_2,s)$ (kJ mol^{-1})
699	972·1	570·1	672·45
730	972·7	565·96	672·59
758	973·7	562·14	672·61
800	974·6	556·53	672·71
840	975·8	551·11	672·75
844	975·4	550·67	672·85
860	976·3	548·42	672·76
879	976·8	545·86	672·76
901	977·3	542·92	672·77
930	977·7	539·08	672·84
950	978·6	536·32	672·75
990	979·2	530·99	672·76
1010	979·5	528·30	672·74
1060	980·3	521·57	672·67
1080	980·4	518·92	672·67
1101	980·7	516·10	672·63
		Pt, Mn + MnF_2 ‖ CaF_2 ‖ Co + CoF_2, Pt	
966	978·9	534·96	673·54
1040	979·9	524·28	672·72
1060	980·1	521·61	672·70
1092	980·8	517·27	672·60

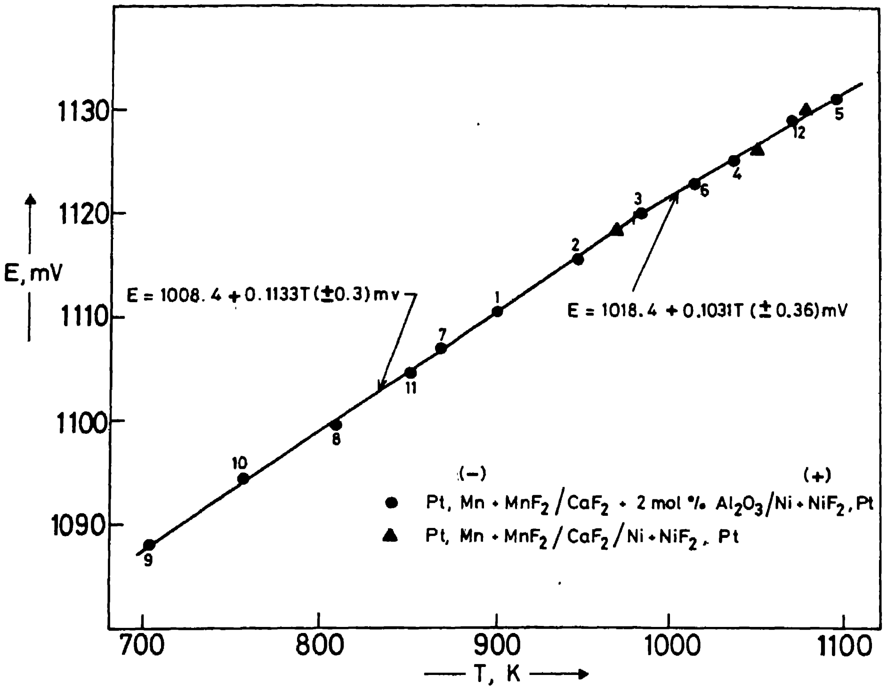

Figure 3. Variation of the emf of cells I and II with temperature.

The net reaction for cells I and II is

$$NiF_2(s) + Mn(s) = MnF_2(s) + Ni(s). \tag{5}$$

Gibbs energy change for this reaction is given by

$$\Delta G^\circ_R = \Delta G^\circ_{MnF_2} - \Delta G^\circ_{NiF_2} = -2FE, \tag{6}$$

where E is the emf in volts and F is the Faraday constant. The Gibbs energy of formation of NiF_2 is well established in the literature (Mah and Pankratz 1976). In the temperature range 700 to 1100 K, the standard Gibbs energy of formation of NiF_2 can be expressed by:

$$\Delta G^\circ_f(NiF_2, s) = -653{,}680 + 151{\cdot}46T (\pm 1650)\ \mathrm{J\ mol^{-1}}. \tag{7}$$

Combining this with (4) the standard free energy of formation of MnF_2 is obtained. For the temperature range 700 to 980 K

$$\Delta G^\circ_f(MnF_2, s) = -848{,}270 + 129{\cdot}59T (\pm 1700)\ \mathrm{J\ mol^{-1}}. \tag{8}$$

For the higher temperature range from 980 to 1100 K, ΔG°_f of MnF_2 is given by

$$\Delta G^\circ_f(MnF_2, s) = -850{,}200 + 131{\cdot}56T (\pm 1700)\ \mathrm{J\ mol^{-1}}. \tag{9}$$

The uncertainty limits are evaluated considering the errors in temperature and emf measurements as well as uncertainty in free energy of formation of NiF_2.

The temperature dependence of emfs of the cells III and IV is displayed in figure 4. Within experimental error, the emfs of both the cells are identical. Again there

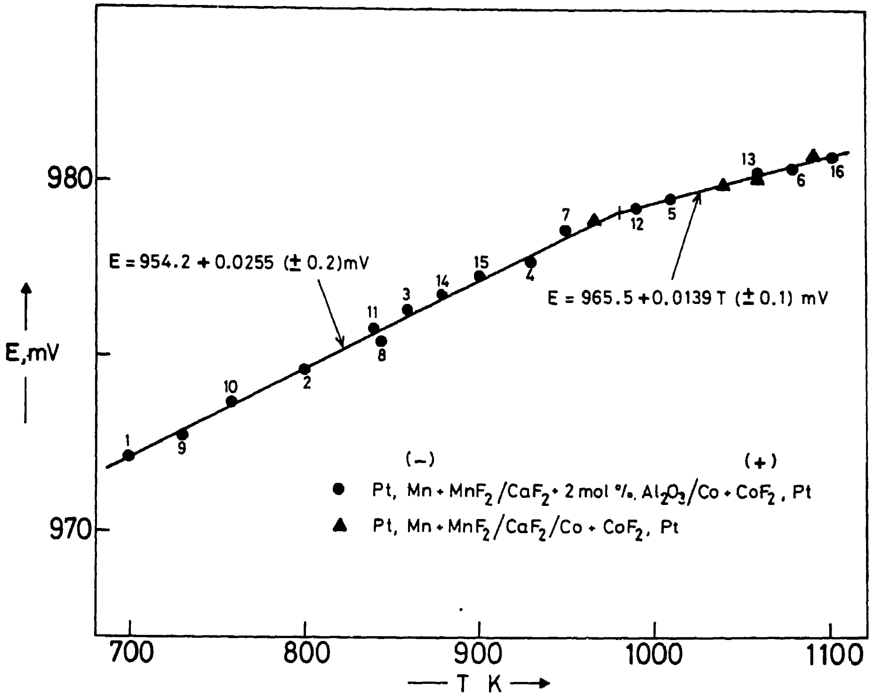

Figure 4. Temperature dependence of the emf of cells III and IV.

appears to be a change of slope at 980 K. The mean squares regression analysis gives the following expressions for the emf:

$$E = 954{\cdot}2 + 0{\cdot}0255\mathrm{T}\,(\pm 0{\cdot}2)\ \mathrm{mV}\ (700\text{–}980\ \mathrm{K}), \tag{10}$$

$$E = 965{\cdot}5 + 0{\cdot}0139\mathrm{T}\,(\pm 0{\cdot}1)\ \mathrm{mV}\ (980\text{–}1100\ \mathrm{K}). \tag{11}$$

The emf corresponds to the cell reaction

$$\mathrm{CoF_2(s) + Mn(s) = MnF_2(s) + Co(s)}, \tag{12}$$

$$\Delta G^\circ_R = \Delta G^\circ_f(\mathrm{MnF_2}) - \Delta G^\circ_f(\mathrm{CoF_2}) = -2FE. \tag{13}$$

Using values for the standard Gibbs energy of formation of MnF_2 given by (8) and (9) Gibbs energy of formation of CoF_2 can be computed from the emf of cells III and IV

$$\Delta G^\circ_f(\mathrm{CoF_2,s}) = -664{,}140 + 134{\cdot}51T(\pm 1700)\ \mathrm{J\ mol^{-1}}\ (700\text{–}980\ \mathrm{K}), \tag{14}$$

$$\Delta G^\circ_f(\mathrm{CoF_2,s}) = -663{,}880 + 134{\cdot}24T(\pm 1700)\ \mathrm{J\ mol^{-1}}\ (980\text{–}1100\ \mathrm{K}). \tag{15}$$

The coefficients of (14) and (15) are almost identical within experimental error. Since there are no transformations of either metallic cobalt or cobalt fluoride in temperature range of 700 to 1100 K, there is little theoretical justification for separate equations in this range. Therefore Gibbs energy of formation of CoF_2 is expressed as

$$\Delta G^\circ_f(\mathrm{CoF_2,s}) = -664{,}010 + 134{\cdot}38T(\pm 1700)\ \mathrm{J\ mol^{-1}}. \tag{16}$$

4. Discussion

The Gibbs energy of formation of MnF_2 obtained in this study is compared with the data reported by Rezukhina *et al* (1974) and Skelton and Patterson (1973) in figure 5. The results of this study are in excellent agreement with the data of Rezukhina *et al* (1974) obtained by using a CaF_2 cell with $Al + AlF_3$ as the reference electrode. However, the data of Skelton and Patterson (1973) obtained by using $Ni + NiF_2$ as reference electrode are more negative than the present data by approximately 4 kJ mol^{-1} at 1070 K. The smaller emfs obtained by Skelton and Patterson (1973) may be attributed to the transport of materials between electrodes via the vapour phase in their open stacked pellet assembly.

Figure 6 shows the comparison of Gibbs energy data obtained in this study for CoF_2 with values reported in the literature. The present data are in good agreement ($\pm 2{\cdot}5$ kJ mol^{-1}) with those of Chattopadhyay *et al* (1975) between 850 and 1050 K and Skelton and Patterson (1973) in the temperature range 580 to 1066 K. Both sets of data in the literature obtained using solid state cells almost identical to that employed in this study indicate a slightly more positive free energies of formation of CoF_2. Since fluorine potentials at both electrodes are similar, emfs of cells III and IV are smaller. Problems due to gas transport between electrodes are therefore, likely to be less significant.

The standard enthalpy of formation of MnF_2 at 298·15 K, calculated from the free energy of formation at different temperatures by the third law method using entropy and heat capacity functions from the literature is listed in table 1. The values of $\Delta S^\circ_{298\cdot15}$, $S^\circ_T - S^\circ_{298\cdot15}$ and $H^\circ_T - H^\circ_{298\cdot15}$ for MnF_2 are obtained from Stout and Adams (1942), Ehlert and Hsia (1972/73); the corresponding values for fluorine gas are from Stull and Prophet (1971) and those of solid Mn are from Barin *et al* (1977). The average value for ΔH°_f(298·15 K) for (MnF_2,s) obtained from this study is $-854{\cdot}97$ ($\pm 0{\cdot}13$) kJ mol^{-1}. The values of ΔH°_f(298·15 K) obtained in this study are plotted as a function of the temperature of the free energy measurement in figure 7. It

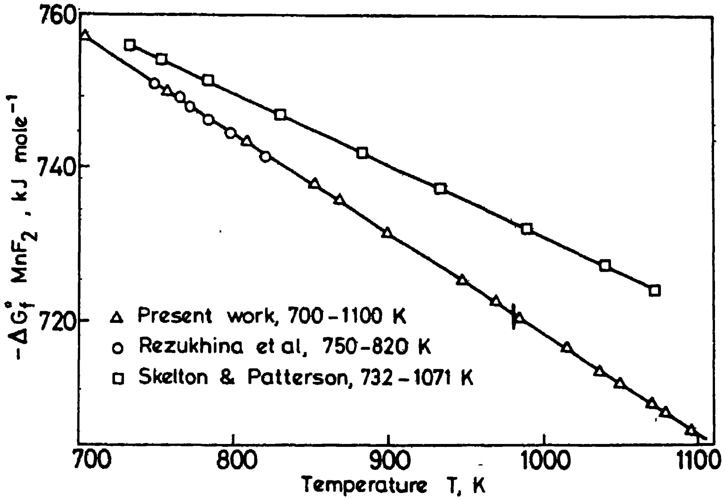

Figure 5. Gibbs energy of formation of MnF_2—Comparison with data in the literature.

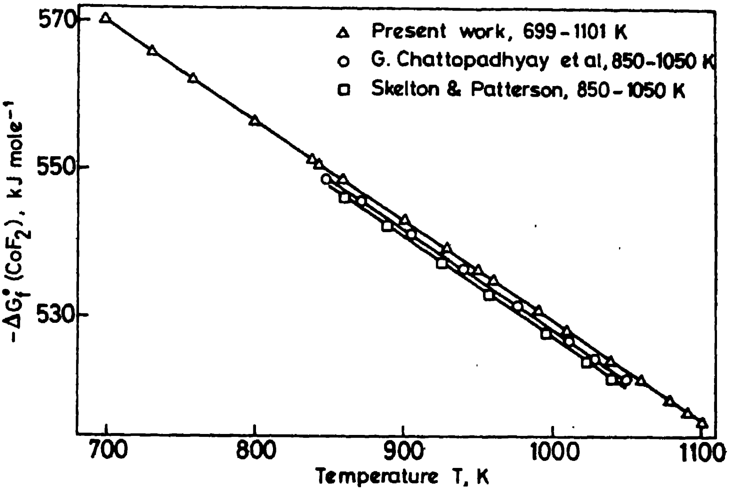

Figure 6. Comparison of free energy of formation of CoF_2 obtained in this study with previous work.

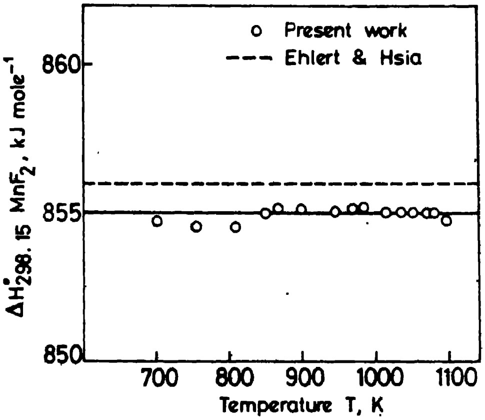

Figure 7. $\Delta H_{298\cdot15}^\circ$ (third-law) for $Mn(s) + F_2(g) = MnF_2(s)$.

is seen that the values are virtually constant throughout the temperature range suggesting the absence of systematic temperature-dependent errors in the free energy measurement. The value of ΔH_f°(298·15 K) obtained in this study is significantly more negative than the value of -795 (± 20) kJ mol^{-1} suggested by Brewer *et al* (1950), the value of -793 kJ mol^{-1} suggested by Mah (1960) or the value of -803 kJ mol^{-1} given in the compilation of Barin *et al*(1977). The results of this study are in reasonable agreement with the value of -849 ± 20 kJ mol^{-1} suggested by Ehlert and Hsia (1972/73).

The third law enthalpy of formation of CoF_2 at 298·15 K evaluated from each free energy value obtained in the study is plotted as a function of temperature in figure 8. The average value of $\Delta H_{298.15}^\circ = -672{\cdot}69$ ($\pm 0{\cdot}1$) kJ mol^{-1}, compares with a value of

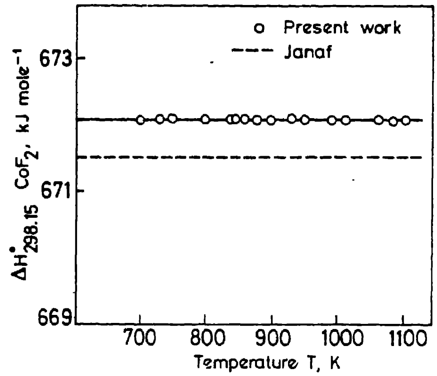

Figure 8. $\Delta H^\circ_{298\cdot15}$ (third-law) for $Co(s) + F_2(g) = CoF_2(s)$.

$-671\cdot5\,(\pm4)$ kJ mol^{-1} given in Janaf tables (Stull and Prophet 1971) based on earlier free energy measurements using gas equilibration and emf techniques.

5. Conclusion

The use of dispersed solid electrolytes in galvanic cells permits accurate measurements at temperatures lower than those permitted by conventional electrolytes. Problems arising from the interaction of the electrode materials with the dispersoid can be overcome by having a thin layer (~ 100 μm) of pure electrolyte at the contact surfaces. Such engineered composite solid electrolytes are expected to enlarge the temperature range available for thermodynamic measurements with galvanic cells in the future.

References

Barin I, Knacke O and Kubaschewski O 1977 *Thermochemical properties of inorganic substances* (Berlin: Springer-Verlag) p. 395

Binford J S Jr, Strohmenger J M and Hebert T H 1967 *J. Phys. Chem.* **71** 2404

Brewer L, Bromley L A, Gilles P W and Lofgren N L 1950 *The chemistry and metallurgy of miscellaneous materials* (ed.) L L Quill (New York: McGraw-Hill) p. 76

Catalano E and Stout J W 1955 *J. Chem. Phys.* **23** 1803

Chattopadhyay G, Karkhanavala M D and Chandrasekhariah M S 1975 *J. Electrochem. Soc.* **122** 325

Egan J J 1985 *High Temp. Sci.* **19** 111

Ehlert T C and Hsia M 1972/73 *J. Fluorine Chem.* **2** 22

Jacob K T 1985 *Thermodynamics and kinetics of metallurgical process* (eds) M Mohan Rao, K P Abraham, G N K Iyengar and R M Mallya (Calcutta: The Indian Institute of Metals) p. 91

Mah D A 1960 Bureau of Mines Report of Investigation **5600** 10

Mah D A and Pankratz L B 1976 *Bureau Mines Bull.* **665** 21

Rezukhina T N, Sisoeva T F, Holokhonova L I and Ippolitov E 1974 *J. Chem. Thermodyn.* **6** 883

Skelton W H and Patterson J W 1973 *J. Less Common Metals* **31** 47

Stout J W and Adams H E 1942 *J. Am. Chem. Soc.* **64** 1535

Stull D R and Prophet H 1971 JANAF Thermochemical Tables NSRDS NBS 37 U.S. Dept. of Commerce, Washington DC

Vaidehi N, Akila R, Shukla A K and Jacob K T 1986 *Mater. Res. Bull.* **21** 909

Venkatraman M and Hajra J P 1983 *Metall. Trans.* **14A** 2125

Bull. Mater. Sci., Vol. 9, No. 1, March 1987, pp. 47–54. © Printed in India.

Influence of substrate temperature on the electrical and optical properties of amorphous germanium films

S V CHANDOLE*, UJWALA V HULSURKAR and S S SHAH
Department of Physics, Marathwada University, Aurangabad 431 004, India
*Department of Physics, Deogiri College, Aurangabad 431 005, India

MS received 15 October 1984; revised 28 July 1986

Abstract. The influence of substrate temperature on electrical and optical properties of the amorphous germanium films deposited under well-defined conditions has been investigated. DC electrical conductivity in the temperature range of 80–573°K has been measured. In the low temperature region Mott's $T^{-1/4}$ law of conductivity is obeyed. The estimated values of T_0 and N show significant decrease with change in T_s in steps of 50°K. Similar results are seen in annealed films. The values of activation energy and optical energy increase with T_s.

Keywords. Amorphous germanium; annealing; substrate temperature; density of states; optical energy gap; d.c. electrical conductivity.

1. Introduction

Although much work has been carried out on the structural, electrical and optical properties of amorphous germanium (a-Ge), the many aspects towards a basic understanding of a-Ge have still remained a challenging problem. This is due to the strong dependence of properties such as density, structural transformation kinetics, electrical conductivity, thermopower, magneto-resistance, optical absorption and optical constants etc observed on various deposition parameters, subsequent ageing, annealing treatment and adsorption effects.

An amorphous thin film obtained by condensation of vapour atoms onto the substrate consists of various defects in the films like voids, vacancies, divacancies, dangling bonds (unsatisfied bonds) etc and these defects arise due to various preparation conditions during deposition and pre- and post-deposition treatments of the films. Thermally-activated continuous rearrangement is possible in amorphous materials if the amorphous matrix contains micropolycrystalline regions which may occur in various deposited films and if finite adatom mobility exists during the condensation process. Though the existence of the so-called ordered region of $\simeq 14$ Å dimensions (Graczyk and Choudhari 1973) hardly supports the microcrystalline nature of a-Ge films, the sharp dependence of several properties of a-Ge films on various deposition parameters (Walley 1968; Bauer and Galeener 1972; Zavetova and Koc 1972; Goebel *et al* 1973) can be understood only on the assumption of a finite adatom mobility during the condensation process of the film. Therefore, for a satisfactory interpretation of the properties, a clear understanding of the atomic rearrangement during and after deposition of a-Ge film is necessary. This is because any rearrangement in the structure of films causes a change in the number of defects thus providing a variation in the density of states in the mobility gap and therefore in the properties. Studies on the variation of angle of deposition (Chopra and Pandya 1974), annealing (Walley 1968; Brodsky *et al* 1970; Brodsky and Title 1969; Paesler *et al* 1974; Paul and Mitra 1973) and oxygenation (Walley 1968; Lecomber *et al*

1974) in a-Ge revealed a decrease in the density of states with an increasing angle of incidence, annealing temperature T_A and the presence of oxygen during deposition respectively.

We have utilized the substrate temperature as a parameter while studying the d.c. electrical conductivity of vacuum-evaporated a-Ge films in the temperature range 80–573°K. The optical absorption of samples deposited at various substrate temperatures has also been studied.

2. Experimental

2.1 *Sample preparation*

Sample films of a-Ge were prepared by evaporating intrinsic (99·99% pure) Ge from molybdenum boat onto the clean glass substrates with predeposited Al contacts held at various substrate temperatures. The six substrate temperatures chosen were in the range of 300–500°K in steps of 50°K. The angle of deposition was $\simeq 80°$. The deposition rate was $\simeq 100$ Å/sec. All evaporations were made using a conventional vacuum system with an oil diffusion pump (pressure during deposition 10^{-5} torr). Film thickness was measured using an interferometric technique. The thickness of the film was 1000–1500 Å.

2.2 *DC conductivity measurement*

The low temperature d.c. conductivity was measured by transferring sample films after deposition to the cryostat (Chandole and Shah 1981) evaluated at a pressure of 10^{-3} torr. The sample conductance was measured at various stable temperatures between room temperature and upto 130°K. While measuring the conductance, pressure contacts were used and the temperature was recorded using a calibrated copper constantan thermocouple fixed on a glass plate near the sample. High temperature d.c. conductivity was measured from room temperature to 573°K in vacuum and $\simeq 10^{-5}$ torr pressure. The sample conductance was measured at different temperatures. While measuring the conductance, pressure contacts were used. Both at low and high temperatures, conductance was measured by determining a voltage drop across a standard resistor using a d.c. micro-voltmeter TFM 12.

If the natural logarithm (ln) σ_{dc} vs $T^{-\frac{1}{4}}$ is plotted using a low temperature σ_{dc} data, we get a straight line plot, the slope of which will be $T_0^{\frac{1}{4}}$. Thus using experimentally obtained values of T_0, the values of density of states at E_F, $N\ (E_F)$ were obtained using the relation (Ambegaonkar *et al* 1971) $T_0 = 16\alpha^3/KN(E_F)$ where $\alpha = 10^7\ \text{cm}^{-1}$ and k is the Boltzmann's constant. Also by plotting $\ln \sigma_{dc}$ vs $1/T$ for high temperature σ_{dc} data, the values of E_{act} were determined for various sample films from the slope of the plots. The values of $N(E_F)$ and E_{act} are shown in table 1. The values of $\ln \sigma_{dc}$ vs $T^{-\frac{1}{4}}$ and $\ln \sigma_{dc}$ vs $1/T$ plots are shown in figures 1 and 2 respectively.

2.3 *Optical absorption*

The optical absorption of the sample films was measured using a double beam spectrometer (Cary 17D) in the near infrared range (8000–20000 Å). The refractive index

Table 1. Electrical and optical data of a-Ge films.

Substrate temperature T_s(°K)	Hopping parameter T_0(°K)	Density of states $N(E_F)$(eV^{-1} cm^{-3})	Activation energy E_{act}(eV)	Optical energy E_g^{op}(eV)
300	$5{\cdot}39 \times 10^7$	$3{\cdot}44 \times 10^{18}$	0·32	0·86
350	$7{\cdot}72 \times 10^7$	$2{\cdot}40 \times 10^{18}$	0·33	0·88
400	$1{\cdot}60 \times 10^8$	$1{\cdot}16 \times 10^{18}$	0·35	0·90
450	$1{\cdot}99 \times 10^{18}$	$9{\cdot}33 \times 10^{17}$	0·36	0·93
500	$2{\cdot}93 \times 10^8$	$6{\cdot}32 \times 10^{17}$	0·45	0·96

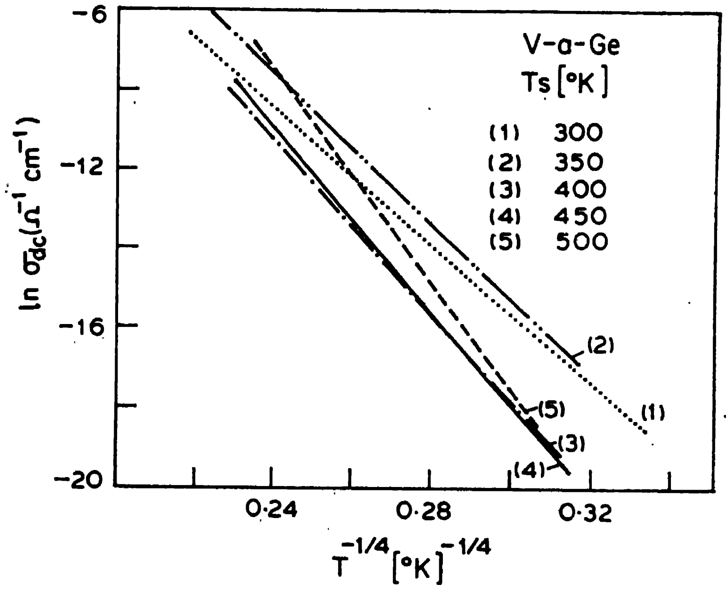

Figure 1. Low temperature measurement data plotted for a-Ge films with different T_s values.

(n) of the sample films was determined by identifying the order of interference peak obtained from transmission maximum and transmission minimum (Wales *et al* 1967). An average value of n was calculated and used for further calculation. Following Brodsky *et al* (1970) for a film of thickness, the value of transmission T is given by

$$T = \frac{(1-R_1)(1-R_2)(1-R_3)\exp(-\alpha t)}{1-R_2R_3[1-|R_1R_2+R_1R_3(1-R_2)^2|\exp(-\alpha t)]},$$

where R_1 is the film to air reflection coefficient $= [(n-1)/(n+1)]^2$, R_2 is the film substrate reflection coefficient $= [(n-n_s)/(n+n_s)]^2$, R_3 is the air to substrate reflection coefficient $= [(1-n_s)/(1+n_s)]^2$, α is the absorption-coefficient, n, the refractive index of glass and n_s is the refractive index of the film. It is found that $R_3 \ll R_2 < R_1$, so that the above formulae can be approximated to the form

$$T = (1-R_1)(1-R_2)(1-R_3)\exp(-\alpha t).$$

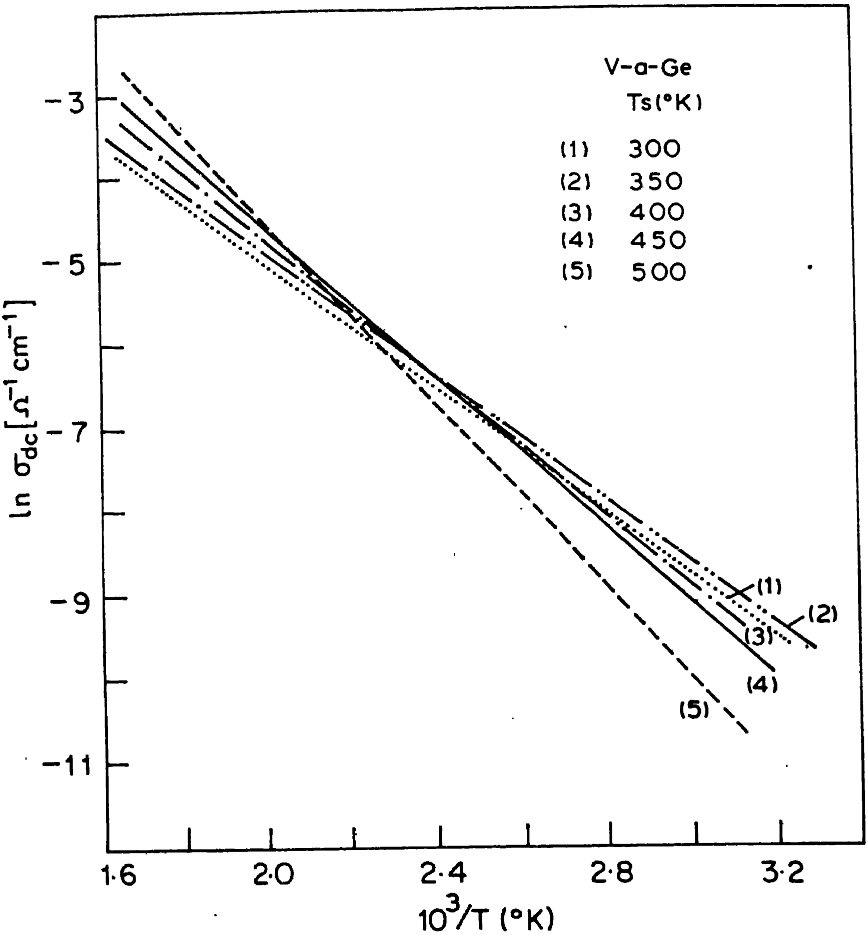

Figure 2. High temperature measurement data plotted for a-Ge films with different T_s values.

From the value of T measured experimentally, α can be calculated using the above equation. When absorption is plotted as $(\alpha h\nu)^{\frac{1}{2}}$ vs $(h\nu - E_g^{\mathrm{op}})$, a straight line fit for the above data (particularly at the high absorption region) is observed. Extrapolating this to $\alpha = 0$ gives the value of E_g^{op}. By measuring T experimentally, the plots of α vs $h\nu$ and $(\alpha h\nu)^{\frac{1}{2}}$ vs $h\nu$ for all samples were obtained to study the absorption edge and to calculate the E_g^{op} respectively. The E_g^{op} data are summarized in table 1 and plots α vs $h\nu$ and $(\alpha h\nu)^{\frac{1}{2}}$ vs $h\nu$ are shown in figures 3 and 4 respectively.

3. Results and discussion

The low temperature dependence of d.c. conductivity in a-Ge films deposited at $T_s = 300$°K and at elevated T_s is shown in figure 1. Mott's $T^{-\frac{1}{4}}$ law of conductivity is verified in each case. As the resistivity of the films increase with higher T_s values $T^{-\frac{1}{4}}$ plots shift towards the lower conductivity region. The values of T_0 obtained

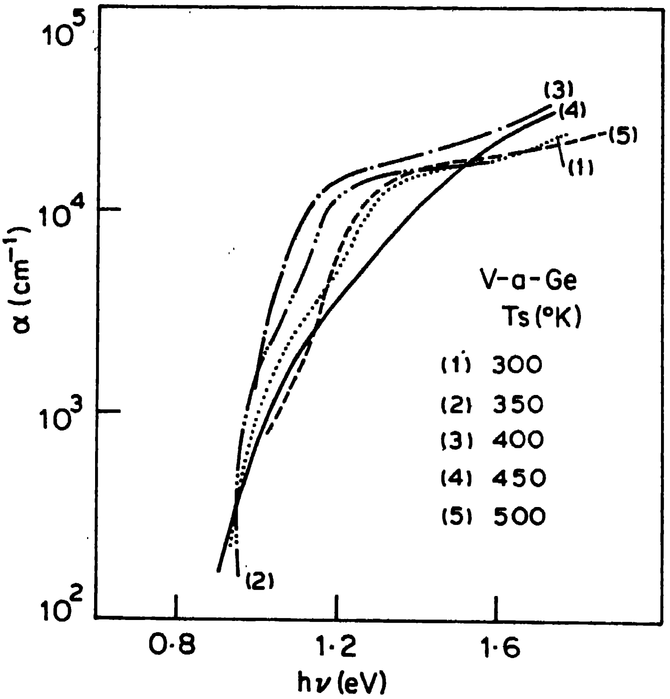

Figure 3. Absorption coefficient (α) vs photon energy ($h\nu$) plotted for a-Ge films with different T_s values.

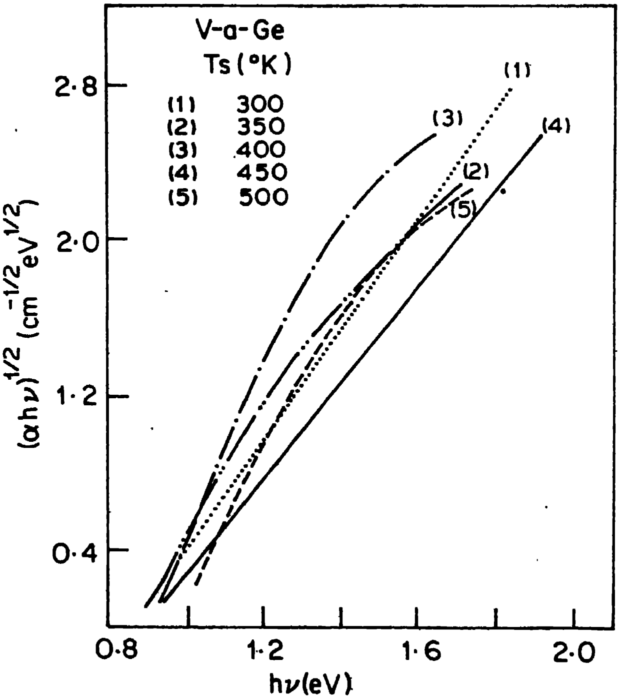

Figure 4. $(\alpha h\nu)^{\frac{1}{2}}$ vs photon energy ($h\nu$) plotted for a-Ge films with different T_s values.

from the $T^{-\frac{1}{4}}$ plots increase with increasing value of T_s. Thus $N(E_F)$ is smaller in films deposited at elevated T_s. This observation agrees with the studies on annealed (Hasegawa *et al* 1978; Paul and Mitra 1973; Narasimham 1977; Koc *et al* 1972) and oxygenated a-Ge films (Zavetova and Koc 1972; Lewis *et al* 1974; Kubler *et al* 1979). The temperature dependence of the conductivity of a-Ge films deposited at various T_s is shown in figure 2. Although the conductivities of the film with $T_s = 300°\text{K}$ and films with increased T_s differ considerably from each other, the general features of the temperature dependence behaviour are found to be similar as the value of E_{act} decreases rapidly with decreasing temperature and at the same temperature E_{act} is higher for films with higher T_s. This effect is similar to that observed in annealed (Pierce and Spicer 1971), oxygenated and obliquely deposited (Chopra and Pandya 1974) a-Ge films. The optical absorption coefficients α of the a-Ge films deposited at $T_s = 300°\text{K}$ near the fundamental absorption edge behave nearly in the same manner as that reported by Theye (1971) with increasing T_s. The curves α vs $h\nu$ and $(\alpha h\nu)^{\frac{1}{2}}$ vs $h\nu$ (figures 3 and 4 respectively) for a-Ge films shift towards higher energies. The value of E_g^{op} for a-Ge film deposited at $T_s = 300°\text{K}$ is in accordance with that reported by Theye (1971). Similar results are reported for optical absorption studies carried out over annealed (Brodsky *et al* 1970; Hasegawa and Kitagawa 1978; Koc *et al* 1972; Theye 1971, 1974; Pandya and Chopra 1976), oxygenated (Mott and Davis 1979) and obliquely deposited a-Ge films (Chopra and Pandya 1974). The shift of fundamental absorption edge towards higher energies and increase in E_g^{op} values with increasing T_s is also reported by other workers (Pandya and Chopra 1976; Theye 1970; Connell *et al* 1973; Donovan and Spicer 1970).

In general, films deposited at high T_s are of high density and coordination number but they have a fair density of impurities, voids, vacancies, dangling bonds, etc. In such cases trends of these properties with increasing film density allow the effect of dangling bonds, voids, impurities etc to be separated out from those of matrix itself. This happens at crystallization temperature because there is a gradual modification in the electrical and optical properties of films with increasing T_s below crystallization temperature. Density, refractive index, resistivity, activation energy and optical energy gap values tend to increase upto limiting values and this is characteristic of most ideal amorphous state of the matrix. Deposition of films at quite high T_s may produce high density films closer to those of the hypothetical pure perfectly co-ordinated network i.e. pure crystalline films (Connell *et al* 1973). According to Theye (1971) the ideal amorphous state and complete crystallization state of vacuum evaporated a-Ge films occur at 400°C and 500°C respectively. These limiting states have characterized E_g^{op} values as 1 eV and 0·8 eV respectively. Our films have preparation conditions similar to that of Theye (1971) and the observed changes in the electrical and optical properties of our sample films below crystallization temperature, can be interpreted as showing progressive transformation of the as-deposited film towards a most ideal amorphous state. Our annealing supports such a modification in the film structure with T_s as we obtained a value of $E_g^{op} \simeq 0{\cdot}99$ eV (comparable to $\alpha \simeq 1$ eV, a characteristic value of E_g^{op} indicating perfect amorphous state) in a-Ge annealed at $T_A = 300°\text{C}$ for 6 hr (Delit and Shah 1983).

The role of T_s determining such a transformation in the structure of the film and thereby the properties may be understood with the possible existence of finite adatom mobilities. Though adatom mobility is considered very small, it may be finite in the films deposited with the increased temperature of T_s since adatom may get more thermal activation energy from the surface of substrate compared to that of the film deposited into room temperature substrates. As a result the rearrangement may be different for different T_s. The resulting gradual change in the structure of films with T_s may be related to the probability that a high energy adatom configuration may transform to a lower energy adatom configuration during deposition of a monolayer (Connell *et al* 1973).

The fact that density of defect states at E_F decreases with increasing T_s below recrystallization temperature (table 1) supports the explanation that there is a gradual transformation of the as-deposited films towards a most ideal amorphous state with well-defined specific properties. The increase in T_0, E_{act} and E_g^{op} data with T_s (table 1) below crystallization temperature also confirms the above explanation as the data reflect the properties of the increasing amorphous state of the matrix. Similar reports on sputtered a-Ge films (Connell *et al* 1973) have shown that the main structural changes are due to densification of the structure with the elimination of voids, dangling-bonds etc.

Thus, similar to annealing and oblique deposition studies, the trends of electrical and optical properties of vacuum-evaporated a-Ge films reflect the same cycle indicating an evolution of the film structure towards an ideal amorphous state with increasing T_s below crystallization temperature ($\simeq 300°C$). For higher $T_s > 300°C$ we may expect the modification of the film structure towards recrystallization which, according to annealing studies, are expected to start at about $T_A \geqslant 400°C$. This is obvious since densification of the matrix after an ideal amorphous state will result in recrystallization of the structure. Such changes in the films with elevated T_s may be detected by performing structural studies in films with elevated T_s as seen in the case of annealed films (Theye 1971).

References

Ambegaonkar V, Halperin B I and Langer J S 1971 *Phys. Rev.* **B4** 2612
Bauer R S and Galeener F L 1972 *Solid State Commun.* **10** 1171
Brodsky M H and Title R S 1969 *Phys. Rev. Lett.* **23** 581
Brodsky M H, Title R S, Weisser K and Pettit G D 1970 *Phys. Rev.* **B1** 2632
Chopra K L and Pandya D K 1974 *Proc. Fifth Int. Conf. on Amorphous and liquid semiconductor,* (ed) J Stuke and W Brenig (London: Taylor and Francis) p 1141
Chandole S V and Shah S S 1981 *Indian J. Cryogenics* **6** 82
Chandole S V 1983 Ph.D. thesis, Marathwada University, Aurangabad
Connell G A N, Temkin R J and Paul W 1973 *Adv. Phys.* **22** 531, 643
Donovan T M and Spicer W E 1970 *Phys. Lett.* **A32** 85
Goebel H, Dettmer K and Kessler F R 1973 *Phys. Status Solidi* **A16** 61
Graczyk J F and Chaudhari P 1973 *Phys. Status Solidi* **B58** 501
Hasegawa S and Kitagawa M 1978 *Solid State Commun.* **27** 855
Hasegawa S, Yazaki S and Shimizu T 1978 *Solid State Commun.* **26** 407
Koc S, Zavetova M and Zemek J 1972 *Czech. J. Phys.* **B22** 1296
Koc S, Zavetova M and Zemek J 1972 *Thin Solid Films* **10** 165
Kubler L, Jaegle A and Koulmann J J 1979 *Phys. Status Solidi* **B95** 307
Lecomber P G, Loveland R J, Spear W E and Vaughan R A 1974 *Amorphous and liquid semiconductors* (eds) J Stuke and W Brenig (London: Taylor and Francis) p. 245
Lewis A J, Connell G A N, Paul W, Pawlik R J and Temkin R J 1974 *Tetrahedrally bonded amorphous semiconductors* (ed) M H Brodsky (New York: American Institute of Physics) p 27
Mott and Davis 1979 *Electronic process in non-crystalline materials* (Oxford: Clarendon Press) p 333
Narasimham K L 1977 Ph.D. thesis, TIFR, Bombay

Paesler M A, Agarwal S C, Hudgens S J and Fritzche H 1974 *Tetrahedrally bonded amorphous semiconductors* (eds) M H Brodsky, S Kirpatric and D Wearie (New York: American Institute of Physics) p 37

Pandya D K and Chopra K L 1976 *Phys. Status Solidi.* **A35** 725

Paul D K and Mitra S S 1973 *Phys. Rev. Lett.* **31** 1000

Pierce D T and Spicer W E 1971 *Phys. Rev. Lett.* **27** 1217

Theye M L 1970 *Opt. Commun.* **2** 329

Theye M L 1971 *Mater. Res. Bull.* **6** 103

Theye M L 1974 *Amorphous and liquid semiconductors* (eds) J Stuke and W Brenig (London: Taylor and Francis) p 479

Wales J, Lovitt G J and Hill R A 1967 *Thin Films* **1** 137

Walley P A 1968 *Thin Solid Films* **2** 327

Zavetova M and Koc S 1972 *Czech. J. Phys.* **B22** 429

Bull. Mater. Sci., Vol. 9, No. 1, March 1987, pp. 55–60. © Printed in India.

Hillock and island formation during annealing of gold films

M S RAHMAN KHAN
Department of Applied Physics and Electronics, University of Rajshahi, Rajshahi, Bangladesh

MS received 2 June 1986; revised 16 February 1987

Abstract. Kinetics of the hillock and island formation during annealing of thin gold film has been studied. The reorganisation of gold film has been distinguished in five stages in progression from the original film to the final island structure. The area occupied by the holes remained virtually constant until the removal of the metal from the substrate started. No increase in the number of holes was detected in the induction period. Hole densities decrease with increasing film thickness. Agglomerates were frequently found at the side of an enlarging hole. The hole growth rate increased steadily with temperature. The growth rate of holes eventually leads to a network structure. The catchment area increased with increasing initial film thickness.

Keywords. Hole density; Catchment area; delineation of Catchment area; hillock and island formation.

1. Introduction

The factors affecting the sintering of supported gold catalysts during catalytic oxidation are interesting and is worthy of study. But only a few observations exist of the mode of surface reorganisation in evaporated films, namely, hillock growth (Neilson *et al* 1967; Caswell *et al* 1963; Lahiri 1970; Gangulee 1970). Changes in morphology and the kinetics of agglomeration could be studied as the system is suitable for the study of the energetics and mechanism of mass transfer in supported metals. Microscopic examination of the agglomeration could clarify the relationship between the metal redistribution and the initial structure of evaporated films.

Surface diffusion-controlled space charges have been studied for thin films of gold (Brandon and Bradshow 1966). The decay of two types of step and growth of holes was observed. Caswell *et al* (1963) found that on annealing at 560°C in nitrogen for 20 min, hillocks were produced on the surface. Two different accounts have been given for hillock growth, both in terms of stress relief and the driving force. Existing work on the surface morphology annealing effects in thin films is not extensive and although some indication of the factors controlling the kinetics may be inferred, the lack of sufficient work describing the structure and energetics of such processes is apparent (Jorgensen and Wehner 1963). Two main classes of effect have been observed—agglomeration into discrete islands and surface hillock growth (Gimpi *et al* 1964). Island formation was found to occur whenever silver film on collodion support was heated to a sufficient temperature (Borel 1955). A detailed study of the metal reorganisation has been undertaken and the kinetics of the hillock and island formation has been reported in this paper.

2. Experimental details

Films were prepared by evaporation of gold wire (99·99% purity) from a tungsten filament at a pressure of about 5×10^{-6} torr. The evaporation rate was 9 nm/min. The films were deposited on freshly cleaved rocksalt, carbon-coated copper grids and silica, maintained either at room temperature or at an elevated temperature. The evaporation distance was kept at about 15 cm to ensure uniform film thickness. For transmission electron microscopy, specimens were coated with 10 nm carbon films by vacuum evaporation onto the gold deposit. The silica substrate was then dissolved in 30% hydrofluric acid and the carbon replicas were washed and mounted on copper grids.

Films on the copper grids were transferred through the atmosphere to the annealing system where they were placed in a small pyrex chamber through a polished conical glass seal. After closing the chamber, flushing of the annealing atmosphere for 15 min at a flow rate of 10-15 ml/min was sufficient to obtain a reproducible sintering behaviour. The pyrex chamber was then heated by insertion into a furnace. The sintering of films was studied by periodic cooling and removal of the samples. Cylindrical grade gases were used in all the cases. Below 10^{-2} torr of oxygen a vacuum system with air injector was used and the specimen was heated in a specially designed radiant heater within the system. The thickness of the deposited gold was measured by Tolansky's multiple beam interferometric method. The films were examined in a transmission electron microscope (Hitachi 500).

3. Results

It is convenient to distinguish five stages in the progression from the initial film to the final island structure. It should be noted that the changes in microstructure follow from the redistribution of a constant amount of material. Four features of the microstructure of the initial film were examined. The first of these, the hole density, was measured from transmission electron micrographs of the films in the thickness range 30–120 nm at a magnification of 15,000. The hole density was calculated manually over a measured area. The smaller holes were occasionally indistinguishable from multigrain boundary intersections in the thinnest films. However, this was not a serious problem for the range of thickness considered above. Hole densities were found to decrease steadily with increasing film thickness (figure 1). The mean crystallite size was 4·5 nm for 100 nm film.

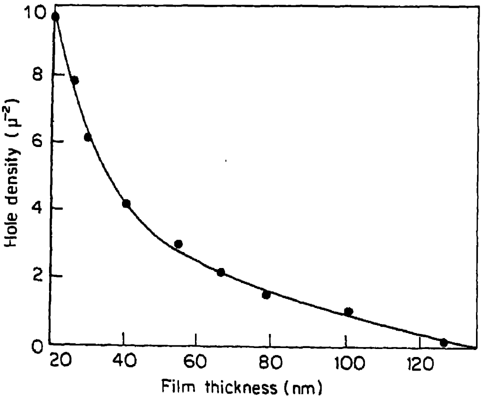

Figure 1. Dependence of hole density on film thickness.

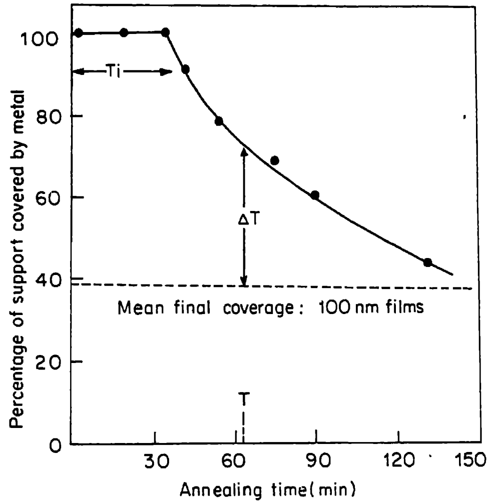

Figure 2. Variation in gold-supported area with annealing time.

Transmission electron micrographs of oxygen-annealed films showed little change initially from their original structure. The area occupied by holes remained virtually constant until removal of metal from the substrate started (figure 2). This interval is called the induction period. No increase in the number of holes was detected in this period. The length of the induction period Ti (min) was found to depend on the temperature T(K), the film thickness d(Å) and the gas environment. Agglomerates were frequently found at the side of an enlarging hole. The growing holes were irregular in shape, with multiple cups pointing upwards. The hole growth rate was measured at temperatures of 150–250°C and found to increase steadily with temperature. The growth of holes eventually leads to a network structure. Where cups at adjacent holes are close, a neck is effectively present and progressive thinning of these necks results in parting of the agglomerates into discrete islands. In some specimens, a population of much smaller islands was left between the main masses, probably by adhesion of metal to small areas of the intervening substrate. Prolonged annealing of the separated islands allowed them to slowly approach an equilibrium shape. Heating at 350°C in oxygen for about 48 hr proved sufficient to allow islands of $< 1\ \mu$ diameter to attain an approximately hemispherical character. Transmission electron microscopy did not detect grain boundaries in most islands of this size; when viewed in true dark field, a few individual islands at a time were visible by transmission through a narrow band around their complete perimeter for each alignment of the illuminating beam.

Final island densities were counted visually from micrographs for a series of films of initial thickness of 30–120 nm heated in oxygen at 200°C for several hours. The island densities decreased steadily with increasing film thickness. Only the main population of large islands was introduced; islands left behind at a later stage by adhesion to points on the substrate were thus excluded; some estimation was involved at this point. A catchment area $A_c(\mu^2)$ was defined as the main area from which a given island had withdrawn material for growth; figure 3 shows a plot of $\log_{10} A_c(\mu^2)$ against $\log_{10} d$(nm). The catchment area increased steadily with increasing initial

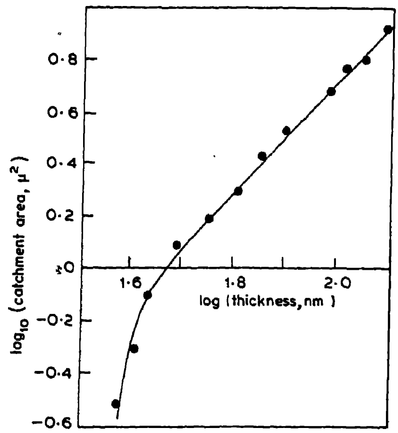

Figure 3. Relation between catchment area and initial film thickness.

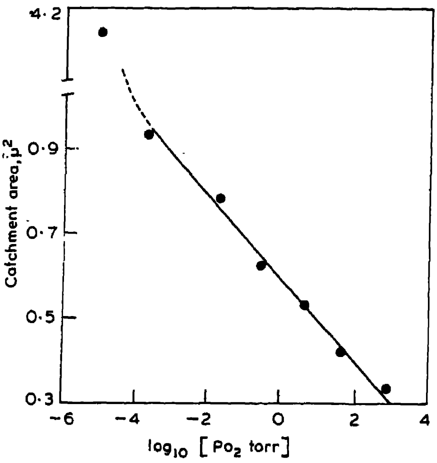

Figure 4. Relation between catchment area and oxygen partial pressure.

film thickness for all but the thinnest films and the points lie about a straight line of slope 2·21 indicating a linear relationship.

$$\log_{10} A_c = 2{\cdot}13 \log_{10} d - 5{\cdot}31$$

or

$$A_c = 4{\cdot}53 \times 10^{-6} d^2. \qquad (1)$$

The effect of oxygen partial pressure on the final island density was also determined. The results shown in figure 4 reveal that the catchment area increase as P_{O_2} decreases.

4. Discussion

The islands formed on annealing are so much larger than the crystallites in the initial film that the area from which they draw material cannot have been simply delimited by grain boundaries. The catchment area can be related to the properties of the original film. The areas form a network of adjacent polygons with varying numbers of side but with little error their dimensions may be represented conveniently as the radii, r of the tangent circles. Hence,

$$r=(A_c/\pi)^{\frac{1}{2}} \tag{2}$$

and so from (1), $A_c=4{\cdot}53\times10^{-6}\,d^2$, r should be proportional to d.

An overall picture of catchment areas in relation to film structure can now be represented (figure 5). The formation of discrete solid nuclei from the vapour followed by growth until holes left between the enlarged islands (Pashley *et al* 1964) is presented diagrammatically in figure 5a. The delineation of a catchment area by such holes is shown in figure 5b. During annealing, these delineating holes effectively close up to cut off these areas of deposit which form the final islands. The lines joining the holes cover the deposit in an irregular network. In the case of both a regular and an irregular network, the number of areas thus delimited approaches the number of holes n as $n\to\infty$. We must therefore assume that in the present case, one hole is associated with each catchment area. If $C=$islands/initial hole, then it was observed experimentally that $I/C=6$ holes were associated with each island formed. Since only one hole per island can be on the lattices delineating area, we conclude that only about 1 in 6 of the observed holes is effective.

The temperature dependence of the length of the induction period was measured, to understand the processes governing the rate of microstructural change. Solid thin films at temperature too low allow morphology change by diffusion are necessarily metastable with respect to surface energy, since they have a high specific area. The observation that freshly deposited films were nonporous removed the possibility that a description of the energetics would have to take into account the energy of internal surface area. However, the role of surface energy had still to be considered among other possible driving forces for hillock formation. The growth of hillocks during the induction period cannot be regarded as driven by surface energy alone. The deposit is also affected by mechanical interaction with the substrate; during heating, different thermal expansion will cause the stress of the high expansivity metal to become more

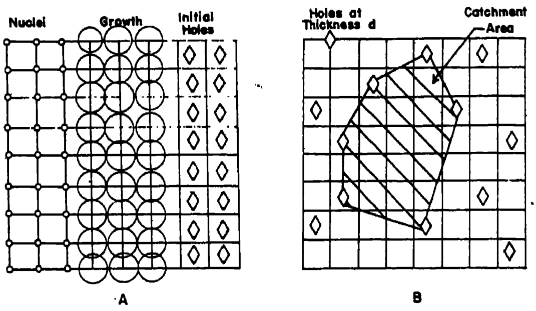

Figure 5. Delineation of the catchment area.

compressive and this may lead to the formation of surface hillocks (Lahiri 1970; Pennebaker 1968; Chaudhuri 1969).

The transfer of material to the hillock above the surface proceeds until at the end of the induction period, the hole growth begins by withdrawal of metal in the remaining thin land areas from the substrate.

5. Conclusions

Several stages of discrete island formation during the annealing of thin gold films in oxygen containing atmospheres can be accounted for in terms of capillary theories of surface topography change of the type first proposed by Mullins (1957) for grain boundary greeving. The role of compression stress, suggested by other workers to contribute to initial hillock formation, is confirmed and the kinetics of hillock growth is accounted for in terms of surface diffusion transport. Subsequently, withdrawal of the material from the substrate is again by surface diffusion and the kinetics is governed by surface energy forces. The islands remaining at the end of the agglomeration process are shown to have drawn their material from areas delineated by the network of residual holes remaining after the film was initially deposited by heterogeneous nucleation and growth from the vapour.

References

Borel J P 1955 *Mem. Soc. Vaudoise Sci. Nat.* **11** 2
Brandon R H and Bradshow F J 1966 R.A.E. (Farnborough) Rep. 66095
Caswell H L and Budo Y 1963 *J. Appl. Phys.* **34** 3461
Caswell H L, Priest J R and Budo Y 1963 *J. Appl. Phys.* **34** 3261
Chaudhuri P 1969 *IBM J. Res. Rep.* 197
Gangulee A 1970 *Philos. Mag.* **22** 865
Gimpi M L, Mcmaster A D and Fuschille N 1964 *J. Appl. Phys.* **35** 3572
Lahiri S K 1970 *J. Appl. Phys.* **41** 3172
Jorgenson G V and Wehner G K 1963 *Trans. Tenth National Vacuum Symposium*
Mullins W W 1957 *J. Appl. Phys.* **28** 355
Neilson N A, Keating K B and Miller W R 1967 *Surface Sci.* **8** 307
Pashley D W, Stewell M J, Jacibs M E and Law T W 1964 *Philos. Mag.* **10** 127
Pennebaker W B 1968 K.B.M. Res. Rep. RC-2105

Bull. Mater. Sci., Vol. 9, No. 1, March 1987, pp. 61–65. © Printed in India.

Evaluation of cumulative damage in glass fibre reinforced plastic by ultrasonic method

V K SRIVASTAVA and R PRAKASH*
Department of Mechanical Engineering, *Department of Bio-Medical Engineering, Institute of Technology, Banaras Hindu University, Varanasi 221 005, India

MS received 20 November 1986; revised 16 December 1986

Abstract. This paper presents the cumulative damage in glass fibre reinforced plastic composite during loading and unloading at regular intervals using the continuous monitoring of ultrasonic test instrument. The result shows that the ultrasonic attenuation increases with an increase in the tensile load, which provides the change in internal damage of composites.

Keywords. Cumulative damage; E-glass fibre; epoxy resin; ultrasonic technique; hounsfield tensemeter; tensile load.

1. Introduction

Ultrasonic non-destructive testing is based on the interaction of sound waves passing through a material with the structure of the material. If a material is homogeneous and of a sufficiently good quality, a sound wave will pass through it with a relatively little loss of energy. If the material is not homogeneous (i.e. if there are cracks or voids within it), the sound wave gets scattered and/or reflected at these features giving rise to (i) a greater attenuation of the transmitted beam and (ii) the presence of reflected and/or scattered waves. If a wave is to be appreciably scattered by any scattering centre the wave must have a wavelength of the order of the size of scattering centre or less (Prakash 1980). Stone and Clarke (1975) evaluated the void content by ultrasonic technique in carbon fibre reinforced plastics (CFRP). Their results show that ultrasonic attenuation is not very sensitive to fibre volume fraction. Interlaminar cracks are also occasionally present in fibre reinforced plastic composites, also ultrasonic attenuation in the same way, as voids do. Birchon (1972) tried to differentiate between voids and interlaminar cracks by observing the ultrasonic responses from these two features. Knollman *et al* (1979) determined the cumulative internal damage in filled polymers using an ultrasonic technique. Hayford *et al* (1977) presented a correlation between ultrasonic attenuation and shear strength of graphite-polyimide composite samples. Their results showed a good correlation between the initial ultrasonic attenuation values of the samples and the shear strength of these samples. The present paper describes the ultrasonic detection of cumulative damage in glass fibre reinforced plastic composite.

2. Experimental procedure

Glass fibre reinforced plastic (GRP) composites were made by hand lay-up technique. The composites (0°/90° and ±45°) were moulded by using the E-glass fibre woven mats and epoxy resin (CY-205 resin and HY-951 hardner). Epoxy resin sheets were also moulded for the present study. These GRP and epoxy resin sheets were cut to obtain flat specimens for experimentation. The test set-up used for evaluating cumulative damage in GRP composites is shown in figure 1. Tensile loading was applied using commercially available Hounsfield tensometer. A water bath made of "Perspex" fabricated sheet was used so as to fit in the tensometer and keep the gauge length portion of specimen submerged in water. The transmitter and receiver probes (10 MHz frequency) were placed on the top and bottom of the specimen and the water bath was filled with water to provide a medium for the transmission of ultrasonic energy from transmitter probe to receiver probe through the specimen. The ultrasonic attenuation values were continuously monitored by recording the peak heights of the ultrasonic signal corresponding to various loads for epoxy specimens, 0°/90° cross-ply GRP specimens and ±45° GRP specimens. The specimens were loaded maximum upto 40% of the ultimate tensile strength value for GRP composites. Readings were taken at regular intervals during loading and unloading of the specimen.

3. Results and discussion

Curves were plotted to show the variation of ultrasonic attenuation with the increasing/decreasing tensile load for epoxy specimens (figure 2), 0°/90° cross-ply GRP specimens (figure 3) and ±45° GRP specimens (figure 4). These curves show that ultrasonic attenuation increases with increasing load from the very beginning and on unloading, the attenuation values start decreasing but they do not retrace their path (i.e. the value of ultrasonic attenuation (during unloading) does not remain what it was for a particular load, during increasing load cycle). On complete unloading, the new ultrasonic attenuation value is higher than the one previously obtained for the same material, until and unless some microdamage takes place within the material. Since ultrasonic attenuation is a material parameter, it should not change. On further loading, the ultrasonic attenuation values once again starts rising and again, on unloading the values start falling as was the trend during the first loading/unloading cycle. At the end of this second cycle the ultrasonic attenuation of the material once again was higher than the previous two ultrasonic attenuation values (points A and B in figure 2). This clearly indicates that further microdamage has crept-in. In other words, the measured ultrasonic attenuation may provide the specimens under tests. For GRP specimens also, a behaviour similar to that for epoxy specimens was observed. Figure 3 shows the tensile loading vs ultrasonic attenuation curve for 0°/90° cross-ply GRP specimens and the same trend was also recorded for ±45° GRP specimens (figure 4). Our results show that ultrasonic attenuation increases with increasing tensile load, since ultrasonic attenuation is related to the amount of defects present in the material under test (Stone and Clarke 1975). It is almost certain that the loading of the specimen causes microdamages within the specimen. This damage may be in the form of a resin crazing, resin cracking or microcracks in weak fibre etc. Whatever may be the cause for higher ultrasonic attenuation, it points to the fact that the damage within the material has increased.

Figure 1. Experimental set-up of ultrasonic testing.

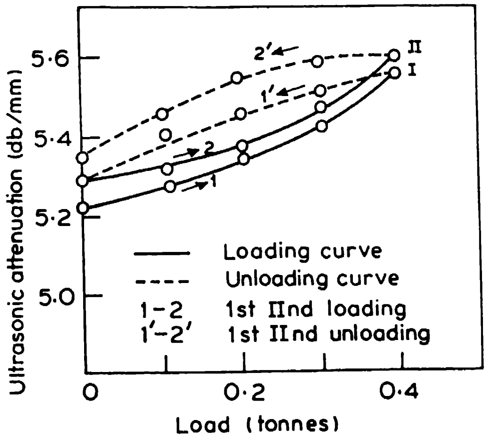

Figure 2. Ultrasonic attenuation vs tensile load of epoxy.

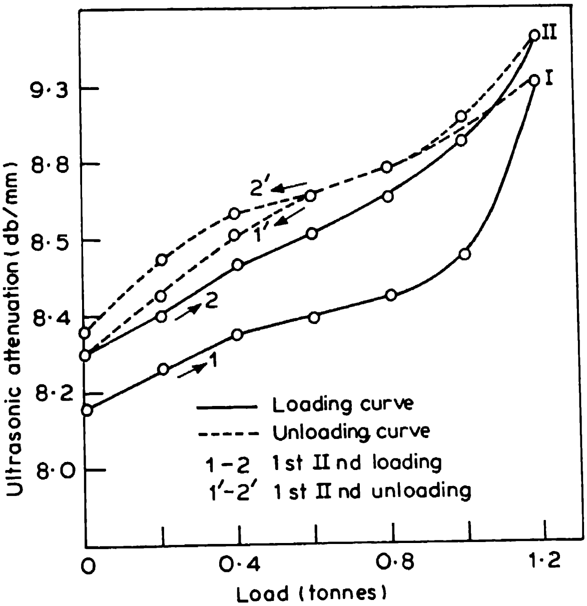

Figure 3. Ultrasonic attenuation vs tensile load of 0°/90° cross-ply GRP composites.

4. Conclusion

The study on cumulative damage in GRP composites by ultrasonic technique proves that the change in ultrasonic attenuation is due to microdamages within the material. However, the change in ultrasonic attenuation serves as a measure of cumulative damage in GRP composites i.e. $\Delta\alpha = (\alpha_u - \alpha_i)$ db/mm is proportional to the cumulative damage in GRP composites where α_u is the ultrasonic attenuation after loading/unloading cycle and α_i is the initial ultrasonic attenuation.

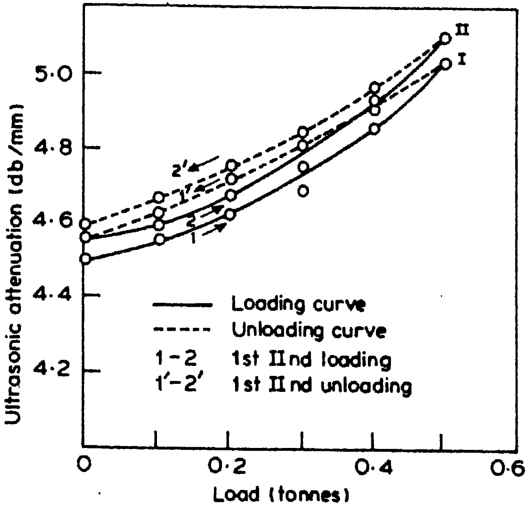

Figure 4. Ultrasonic attenuation vs tensile load of ±45° cross-ply GRP composites.

References

Birchon D 1972 *J. Chart. Mech. Eng.* **17** 54
Hayford D T, Henneke II E G and Stinchcomb 1977 *J. Composite Mater.* **11** 429
Knollman G C, Martinson R H and Bellin J L 1979 *J. Appl. Phys.* **50** 111
Prakash R 1980 *J. Compos.* **9** 217
Stone D E W and Clarke B 1975 *J. Non Destructive Testing* **7** 137

Bull. Mater. Sci., Vol. 9, No. 1, March 1987, pp. 67–72. © Printed in India.

Nonlinearity in gold-alkali halide-gold capacitors

S C K MISRA
Department of Electrical Engineering, University of Strathclyde, Glasgow, UK
Present address: National Physical Laboratory, New Delhi 110 012, India

MS received 17 October 1986

Abstract. All epitaxial gold-NaCl/NaBr-gold capacitors were fabricated on hot NaCl substrates. The dielectric properties, capacitance and loss have been measured. Severe harmonic distortion in the output current has been observed. Maximum contribution was from third and odd harmonics. The amplitude of harmonics was maximum at frequencies above the loss peak. The phenomenon has been explained on the basis of nonlinear space charge theories.

Keywords. Gold; alkali halide gold; capacitors; nonlinearity.

1. Introduction

Thin film metal insulator devices have many advantages in integrated circuits and a large number of devices using this phenomenon have been made. Frequency modulation, switching, amplification, rectification and many more interesting phenomena are available from these devices. The practical device essentially comprises of metal-semiconductor-metal structure in one form or the other. The system is made either of bulk constituents or of thin films or hybrids. The large scale integration necessarily makes use of fabrication of devices by properly masking the base silicon chip and selectively preparing resistors, capacitors and inductors as in a FET. The thin film devices made from aluminium oxide, glasses, CaF, CdS, silicon oxide etc have been studied in great detail. For device fabrication, its properties have to be controlled for a successful operation. The electrical characteristics of the metal-electrode junction are nevertheless equally important. Invariably, charge injection or polarization is associated with a metal-semiconductor and metal-insulator structure. Polarization occurs mainly due to electronic blocking of charge carriers at the boundaries and electrode. The effects have been analyzed in thin films of such materials (Breckenridge 1950; Weaver 1962; Macfarlane and Weaver 1968).

Alkali halide thin films, because of their simplicity in structure, provide an ideal specimen for this purpose. The characteristics of the ionic charge carriers responsible for polarization are very well known. The nonlinear dielectric properties and mechanism of polarization in alkali halide thin films, both polycrystalline and epitaxial, have been studied. Various materials like NaCl, NaBr, Lif etc have also been studied. The dependence of dielectric constant and losses with the applied signal and by application of a d.c. bias have been analyzed quantitatively (Weaver 1975; Misra 1975). In all the above investigations epitaxial silver film was used as the electrode for the capacitor where the charge carriers are blocked. Since the phenomenon is a metal-insulator interfacial effect it was thought that the electrode material may have some effect on the dielectric response of metal-insulator-metal device, as it does in the semiconductor-metal devices. We have prepared capacitors having epitaxial gold-alkali halide-gold structure. The dielectric properties of such devices are reported here.

2. Experimental

The gold-alkali halide (NaCl)-gold capacitor was fabricated on top of a hot NaCl crystal by a method similar to that used for silver electrode structures (Weaver 1975). The substrate temperature and the evaporation rate of gold were accordingly varied to get epitaxial gold film. Figure 1 shows the transmission electron micrograph of such a gold film (thickness 1000 Å) used as top electrode prepared at 250°C substrate temperature and 200 V/cm electric field applied across the substrate during deposition. The absence of any polycrystallinity and the presence of stacking faults and dislocations are typical of epitaxial films.

Electrical measurements were carried out by continuously maintaining the specimen under vacuum. The method of measurement of dielectric loss and capacitance was the same as used earlier (Macfarlane and Weaver 1968; Weaver 1975).

3. Results and discussion

Figures 2 and 3 show the capacitance and dielectric loss for a 5000 Å thick NaCl film capacitor with gold electrodes at temperatures 91°C, 118°C and 148°C. It can be seen

Figure 1. Electron micrograph of a 1000 A thick gold film (× 50,000).

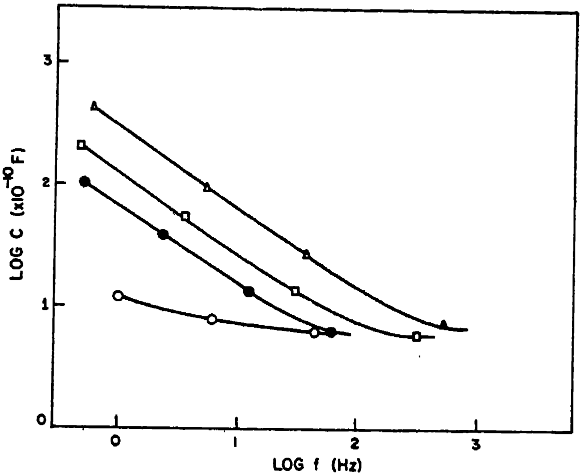

Figure 2. Variation in capacitance of epitaxial gold-NaCl-gold capacitor at ● 91°C, □ 118°C, △ 148°C, ○ room temperature.

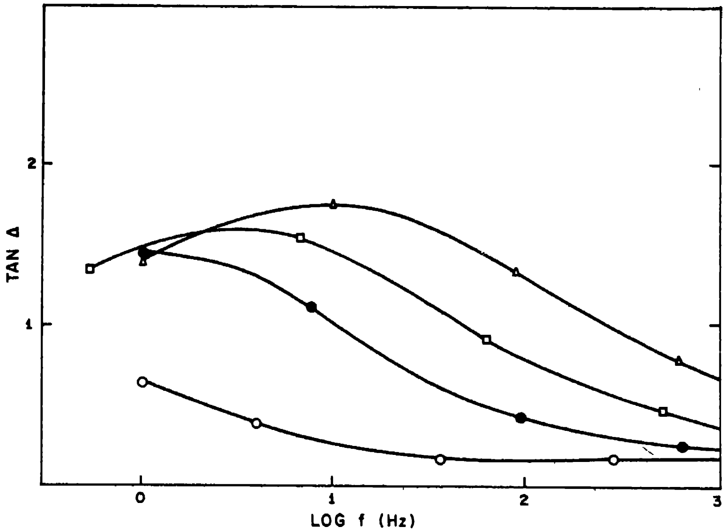

Figure 3. Variation in dielectric losses of epitaxial gold-NaCl-gold capacitor at ● 91°C, □ 118°C, △ 148°C, ○ room temperature.

that the loss peaks are broadened and shift to higher frequencies at higher temperatures. This can be attributed to the fact that the gold-NaCl interface may not be well defined, the gold film electrode deposited on NaCl film is not perfectly smooth and that the interface boundary is diffused.

However the presence of only one peak signifies the complete blocking of charge carriers at the electrodes. Figure 4 shows the Arrhenius plot for activation energy for the loss peaks depicted in figure 3. The activation energy has been deduced as 0·82 eV which is typical of migration of cation vacancies in NaCl (Macfarlane and

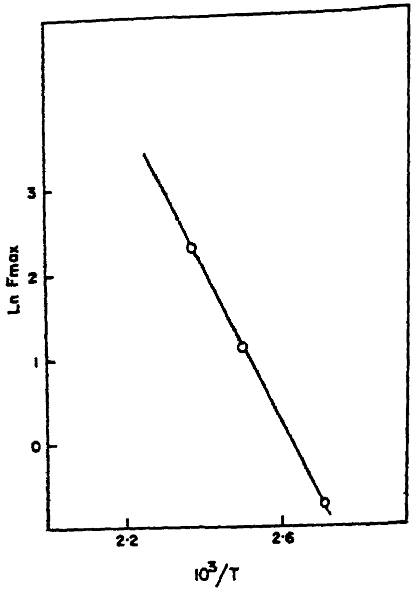

Figure 4. Arrhenius plot for activation energy.

Weaver 1968). This confirms that the only phenomenon taking place in our investigations is the migration of cation vacancies throughout the thickness of the film and thereupon complete blocking at the electrodes occur. The same conclusion was drawn while investigating the dielectric behaviour of NaBr films (Macfarlane and Weaver 1968) where the activation energy (1·05 eV) corresponding to that of migration of cation vacancies was obtained.

The capacitors exhibited a strong nonlinearity with the applied d.c. bias for any variation in the signal amplitude. The dielectric losses increased and distortion in the output waveform on application of a d.c. bias was observed. Variation in measuring the signal amplitude created a severe distortion of the output current waveform which contained distinct higher harmonics. We tried to measure the amplitude of harmonics present in the output current. A resonant filter was used in association with the phasemeter and the oscilloscope. Figure 5 shows the variation of amplitude of third harmonic of 5 Hz, 2 Hz and 20 Hz applied signal.

The loss peak for this specimen at 140°C was located around 5 Hz. From figure 5 it can be seen that the amount of the third harmonic of input signal is maximum at 5 Hz, which is the loss peak frequency. The harmonic content increased with increase in the signal amplitude.

It can be seen from figure 5 that modulation of 5 Hz signal to 15 Hz was maximum and increased tremendously with increase in the applied signal amplitude. For amplitudes in excess of 0·4 eV where the field in the capacitor was of the order of 10^6 V/M the output rises sharply and then breaks down as seen on the oscilloscope. The highest frequency at which distortion occurs increased with temperature. No contribution from second and fourth harmonic of applied signal frequency could be detected. A very mild fifth harmonic was traceable which however could not be measured.

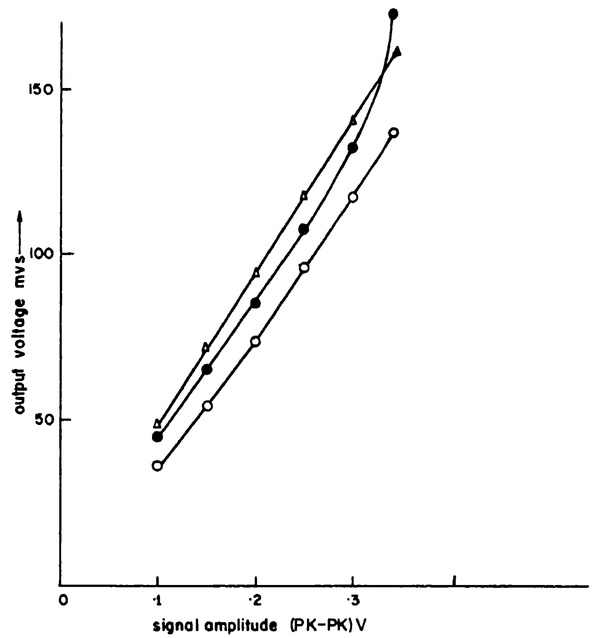

Figure 5. Variation of the amplitude of third harmonic content with amplitude of input signal in a gold NaCl-gold-capacitor at 118°C for various frequencies ● 5 Hz, ○ 2Hz, △ 20 Hz.

To explain the linear dependence of dielectric loss and capacitance on the amplitude of the signal and distortion etc the simple theory of space charge polarization can be used. These theories require that the measuring signal should be less than KT/e, which means that it should be less than 10^{-2} V. For a 1000 Å film we have used a signal in excess of 10^{-2} V and therefore only nonlinear space charge theories can be applied. The present phenomenon was earlier predicted by the nonlinear space charge theory (Misra and Stern 1975). The application of an electric field across the capacitor creates a charge build up at the electrodes. The distribution of space charge gives rise to a field gradient. The gradient itself is field-dependent. In such a case the equations used to explain the polarization are highly complex and no longer linear. This eventually leads to nonlinearity of the dielectric behaviour. The current through the specimen will therefore contain higher and odd harmonics of the input signal. Such an effect has been observed in silicon oxide films (Argall and Jonscher 1968). This type of harmonic generation has been explained by Stern and Weaver. The harmonic generation should be observed only at or below the loss peak frequency and should contain contribution from third and higher odd harmonics. The same has been observed in the present investigations. Figure 6 shows the output current waveform for the specimen of figure 5.

4. Conclusion

The present investigations on metal alkali-halide metal structures also cover those with different electrode materials. Gold was used as the blocking electrodes. The

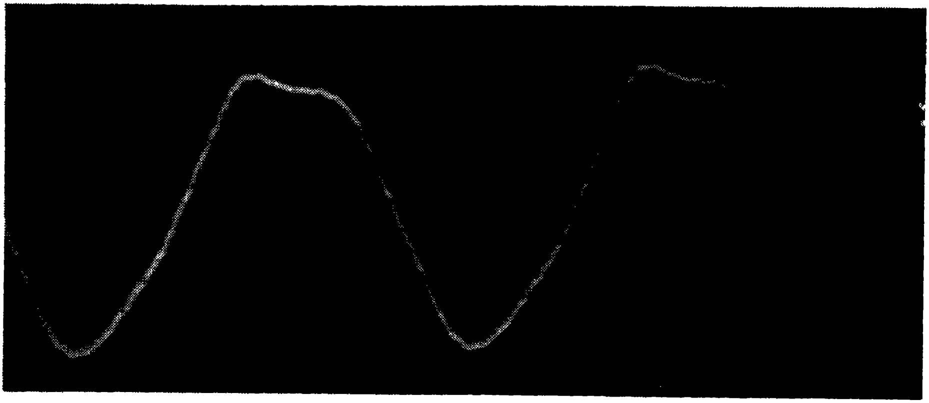

Figure 6. Output current waveform of the capacitor at 118 C, input signal 5 Hz.

results show that replacing silver by gold does not in any case change the dielectric properties of thin film capacitor. The gold-NaCl interface is slightly different from silver-NaCl interface in that the loss peaks are not as sharp as in the latter and since the low frequency polarization in alkali halides is due to the migration of cation vacancies only, the electrode material has no effect.

The strong nonlinearity associated with space charge (interfacial) polarization leads to variation of dielectric constant and losses with applied signal. Frequency modulation of input signal below and around loss peak has been observed as is expected from nonlinear theories. The investigation of frequency modulation and accurate measurement of higher harmonics can be done. Similar phenomenon can be observed in complex structure materials like silicon oxide, aluminium oxide and cadmium sulphide etc. Once the phenomenon of frequency modulation is understood, the various parameters can be controlled and practical frequency modulation devices can be prepared from simple thin film capacitors.

References

Argall F and Jonscher A K 1968 *Thin Solid Films* **2** 185
Breckenridge R G 1950 *J. Chem. Phys.* **16** 913
Macfarlane J C and Weaver C 1968 *Philos. Mag.* **18** 27
Misra S C K 1975 Ph.D. Thesis, Strathclyde University, UK
Misra S C K and Stern F 1975 *Thin Solid Films* **29** 339
Stern F and Weaver C 1970 *J. Phys.* **C3** 1736
Weaver C 1962 *Adv. Phys.* **2** 83
Weaver C and Misra S C K 1975 *Thin Solid Films* **28** 303

BOOK REVIEW

ENCYCLOPAEDIA OF MATERIALS SCIENCE AND ENGINEERING, M. B. Bever (Editor-in-Chief), 8 Volumes, Text 5552 pages + indexes 554 pages, price $ 1950, Pergamon Press, Oxford.

This encyclopaedia is a monumental eight-volume reference work covering the entire spectrum of topics dealing with the principles and practice of materials science and engineering. The coverage is such that it is useful for beginners as well as experts. The encyclopaedia is also most useful to designers and those involved in products and processes. Over 1400 engineers and scientists have contributed to the volumes.

The encyclopaedia includes the following classes of materials: metals and alloys, ceramics, glasses, other inorganic materials, polymers, elastomers, fibers, composites, wood, paper and materials of biological origin. Based on applications, materials of the following types are covered: industrial, electrical, electronic, superconducting, nuclear, energy, magnetic, biomedical, dental and building. Production, processing and fabrication aspects are discussed where necessary, besides properties and applications. Justice has been done to the physical, chemical and engineering aspects of materials. Materials-related methods and phenomena such as characterization techniques, nondestructive evaluation, surfaces and interfaces, surface coatings, joining by adhesives, welding, safety etc are described. Some general aspects, for example, mineral resources, materials policy and economics and humanistic aspects of materials are also covered.

All in all, this encyclopaedia is fantastic. It is a must in the personal library of solid state scientists, metallurgists, ceramicists, materials scientists and many others interested in materials science, engineering, processing, applications and policy. But, alas, the encyclopaedia is too expensive for individuals to buy. At least every science and engineering library must have this encyclopaedia which is a great boon to students, teachers and practitioners of the "science and engineering of materials" in the broadest sense.

Indian Institute of Science Bangalore C. N. R. Rao

1

Bull. Mater. Sci., Vol. 9, No. 2, June 1987, pp. 75–80. © Printed in India.

X-ray photoelectron spectroscopy studies on ethylene oxychlorination catalysts†

R VETRIVEL**, K SESHAN, K R KRISHNAMURTHY and
T S R PRASADA RAO*
Research Centre, Indian Petrochemicals Corporation Limited, Baroda 391 346, India
**Present address: Department of Chemistry, University of Keele, Staffordshire, UK

MS received 5 March 1987

Abstract. Copper chloride on alumina catalyst used for oxychlorination of ethylene represents a typical system where copper is in a dynamic equilibrium between Cu^+ and Cu^{++} oxidation states. Surface studies on redox, structural and compositional properties have been undertaken to monitor the changes that occur on the catalyst during use and pinpoint causes for its deactivation. For this, a fresh and a spent catalyst were been chosen for characterization. A core consisting of copper in Cu^+ state and present as $CuAlO_2$ is formed at the centre of the catalyst sphere. Formation of such a nonreversible phase under reaction conditions upsets the redox equilibrium. XPS also shows the absence of potassium in the core and its precipitation as a new phase on use, probably KCl, formed by the decomposition of active component $KCuCl_3$. These factors facilitate deactivation.

Keywords. Oxychlorination; deactivation; x-ray photoelectron spectra; $CuAlO_2$; $KCuCl_3$.

1. Introduction

The major reactions that take place in an industry producing vinyl chloride are

$$CH_2=CH_2+Cl_2\rightarrow Cl-CH_2-CH_2-Cl, \quad (1)$$

$$Cl-CH_2-CH_2-Cl\rightarrow CH_2=CH-Cl+HCl, \quad (2)$$

$$HCl+½O_2+CH_2=CH_2\rightarrow Cl-CH_2-CH_2-Cl+H_2O. \quad (3)$$

Of these, reaction (3) is an oxychlorination reaction and is an adoption of the classical Deacon reaction

$$2HCl+½O_2\rightarrow Cl_2+H_2O \quad (4)$$

catalysed by a $CuCl_2/Al_2O_3$ system (Buckley 1966). This reaction takes care of the by-product HCl formed in reaction (2) and economizes the process. Reaction (3) is basically an oxychlorination of ethylene (Allen and Clark 1971).

Fundamentally, oxychlorination is a redox reaction in which the active component copper is in a dynamic equilibrium between 1+ and 2+ oxidation states.

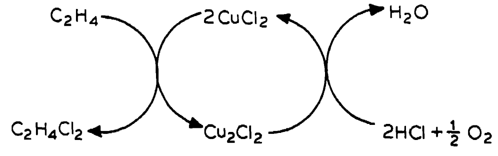

---

†IPCL Communication No. 96

*To whom all correspondence should be addressed.

An optimum balance of Cu^+ and Cu^{2+} population and their presence in easily interchangeable environments is essential for smooth functioning of the catalyst. Addition of alkalihalides (KCl for e.g.) is known to improve the Cu^+/Cu^{2+} ratios (Conner *et al* 1981).

The present investigation aims at finding out transformations that cause activity loss of the catalyst. The focal point is to monitor the oxidation states of copper which directly influences the effectiveness in the redox catalyst system. The choice of x-ray photoelectron spectroscopy (XPS) for such a study, is based on the characteristic spectra exhibited by Cu^+ and Cu^{2+} states; the Cu^{2+} species show typical shake-up satellites associated with the $2p$ 1/2 and $2p$ 3/2 energy levels, whereas these satellites are absent for Cu^+ species. The satellite structure of Cu^{2+} compounds has been attributed to the simultaneous $3d \rightarrow 4S$ transition. Such transitions are not seen for Cu^+ compounds or Cu^0 (d^{10}) (Strohmeier *et al* 1985). The absence of satellites indicates the absence of Cu^{2+} whereas their presence indicates copper to be in a mixture of 2+ and 1+ oxidation states or in 2+ state only. XPS, therefore, is a useful method to identify the fluctuations in the Cu^+/Cu^{2+} redox system and to help understand the mechanism of deactivation.

2. Experimental

X-ray photoelectron spectra of fresh and spent catalysts have been recorded on a spectrometer (VG ESCALAB III). The catalysts have also been subjected to a thorough characterization using standard techniques.

3. Results and discussion

A cross-sectional view of a fresh and spent catalyst is shown in figure 1. It is seen that the catalyst on use develops a block core, which could be easily separated physically from an outer shell. While studying the used catalyst, the inner core and the outer shell have therefore been analysed separately. What forms this core? Table 1 gives

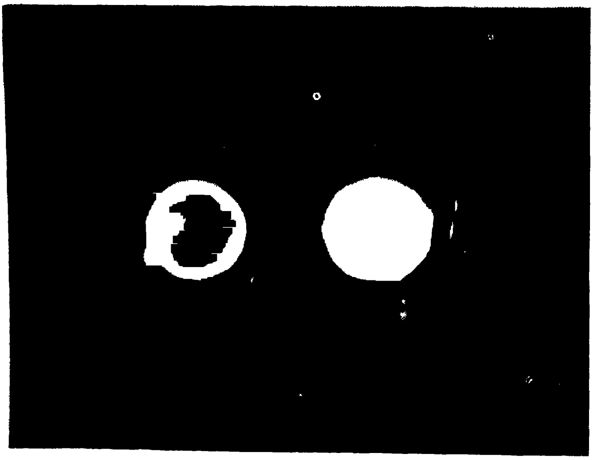

Figure 1. Cross-sectional view of fresh (right) and used (left) oxychlorination catalysts.

Table 1. Phases indentified in the catalysts.

Sample	Phases
Fresh catalyst	γ-Al_2O_3, $KCuCl_3$ $CuCl_2 \cdot 2H_2O$
Spent catalyst	
Shell	γ-Al_2O_3, $KCu\,Cl_3$, KCl $CuCl_2 \cdot 2H_2O$
Core	Al_2O_3, $CuAlO_2$

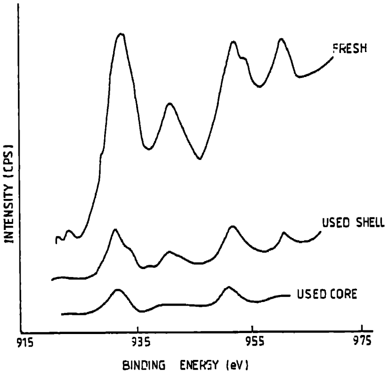

Figure 2. XP spectrum of oxychlorination catalyst (region of copper).

the phases that could be identified in the different samples by x-ray diffraction measurements. Fresh catalyst consists of the support Al_2O_3, the impregnated active component $CuCl_2 2H_2O$ and its double salt with KCl, $KCuCl_3$. The shell of used catalyst additionally contains free KCl, obviously formed by the decomposition of the double salt on use. Interestingly no KCl was observed in the core, which contained a new Cu^+ compound, $CuAlO_2$. This can only be formed by the reaction

$$Cu_2O + Al_2O_3 \rightarrow 2\,CuAlO_2. \tag{5}$$

Is this really possible under reaction temperature of around 250°C?.

A look at the spectrum of catalysts (figure 2) in the region of Cu 2*p* 1/2 and 2*p* 3/2 binding energies provides some confirmation. The binding energy values for the catalysts and that of some pure compounds for comparison, given in table 2, make it very clear that the core contains only a Cu^+ phase as indicated by the absence of satellite, whereas the shell consists of both Cu^{2+} and Cu^+ phases. Presence of the satellites and proximity of binding energy values render deconvolution of the main peaks into Cu^+ and Cu^{2+} peaks a difficult proposition and hence no attempts were made to derive any Cu^+/Cu^{2+} ratios from these curves. Temperature-programmed reduction did indicate a two-stage reduction for fresh catalyst and shell of used catalyst corresponding to reduction of different species namely Cu^{2+} and Cu^+ (Vetrivel *et al* 1987). Likewise in the case of core, a reduction maxima was observed at 710 K which has been attributed to the stable spinal phase $CuAlO_2$ undergoing reduction. The copper binding energies of 932·8 eV (2*p* 3/2) and 952·8 (2*p* 1/2), therefore, correspond to Cu^+ from the compound $CuAlO_2$.

Table 2. XPS data on the catalysts.

Sample	Binding energy (eV) 2*p* 3/2	Satellite	2*p* 1/2	Satellite	References
Cu	932·5	—	951	—	*a*
CuCl	934·6	—	954·5	—	*b*
Cu_2O	932·5	—	954·7	—	*a*
$CuCl_2$	936·4	944·9	956·2	964·8	*b*
CuO	933·8	944·0	956·3	964·8	*a*
Fresh catalyst	932·2	940·0	952·2	962·2	
Spent catalyst					
Shell	932·8	942·0	952·2	962·0	
Core	932·8	—	952·2	—	

a, McIntyre and Cook (1975); *b*, Frost *et al* (1972).

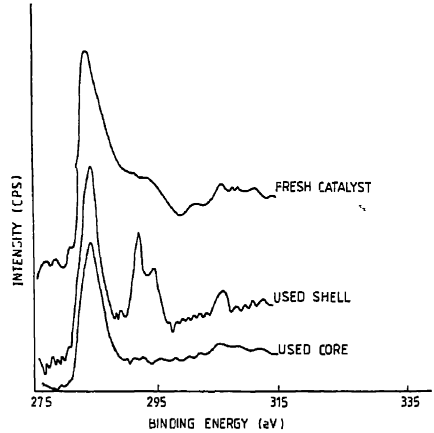

Figure 3. XP spectrum of oxychlorination catalysts (region of potassium).

The XP spectrum showing the state of the promoter potassium in the catalyst is shown in figure 3. Potassium in KCl is expected to show a doublet corresponding to 2*p* 1/2 and 2*p* 3/2 at 297 and 294 eV respectively.

In the case of a fresh catalyst the potassium 2*p* 1/2 and 2*p* 3/2 peaks appear to have shifted to a lower binding energy and hence it merges with the C_{1S} peak (285 eV). In the case of shell of the spent catalyst, potassium appears as a doublet as expected at 294 and 297 eV respectively. A shift towards a lower binding energy, in case of potassium, compared to the case of KCl is possible only if K is attached to a lesser electro-negative group. Comparison of KCl with the potassium compound present in the fresh catalyst i.e. $KCuCl_3$ shows that this is only to be expected because, in $KCuCl_3$, potassium is attached to a bulky ($CuCl_3$) group whose charge is distributed over a larger volume than in the case of Cl on KCl and hence, the former has less electro-negative influence on K than Cl.

It is surprising to note that potassium is absent in the core of the sample. Concentration profiling by energy dispersive x-ray analysis (EDXA) also indicated a migration of potassium from the bulk to the periphery of the catalyst pellet on use

(Vetrivel *et al* 1987). These observations are consistent with phase identification obtained earlier from x-ray diffraction measurements.

Figure 4 shows the XP spectra of oxychlorination catalysts in the region of chlorine. Qualitatively, the spectra of the fresh catalyst may be indicative of a bound chlorine in two different environments as shown by the doublet. The origin of two chlorine states could be attributed to the presence of two chlorine containing compounds in the fresh catalyst i.e. $CuCl_2 \cdot 2H_2O$ and $KCuCl_3$ (table 1). Further, an enrichment of the chlorine in the outer shell is evident from figure 4. This has also been confirmed by the concentration profiling of the catalysts by EDXA which showed chlorine migration from the centre to the periphery of the sphere on use.

The oxygen states in these compounds are shown in figure 5. First, the oxygen species are similar in all samples (fresh, shell core), showing a peak at 530 eV. However there appears to be an enrichment of surface oxygen in the shell compared to the fresh catalyst. This enrichment of oxygen is higher in the shell than that of the core. This is in agreement with the observation that the shell contains both +2 and +1 copper states while copper in the core is present exclusively in +1 state as $CuAlO_2$.

A very stable compound like $CuAlO_2$ is an inactive phase for the redox oxychlorination catalysts. This is because of the prime requirement that copper should be available in an optimum Cu^+/Cu^{++} ratio and an easily interchangeable environment does not hold good once the difficultly reducible or oxidisable phase like $CuAlO_2$ is formed. What is the cause of its formation? Being an oxidation reaction, improper intraparticle heat transfer can cause sufficiently high local temperature and help a reaction of the type $Cu_2O + Al_2O_3 \rightarrow 2\,CuAlO_2$ otherwise known to occur around 1270 K. The presence of copper as Cu^+ in the core could be due to oxygen diffusibility limitations in the interior of the core. There is tremendous porosity loss in the core indicated by the values of total pore volume (shell 0·43 ml/g) and core

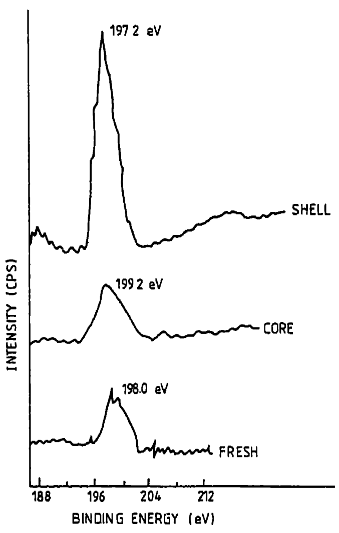

Figure 4. XP spectrum of oxychlorination catalyst (region of chlorine).

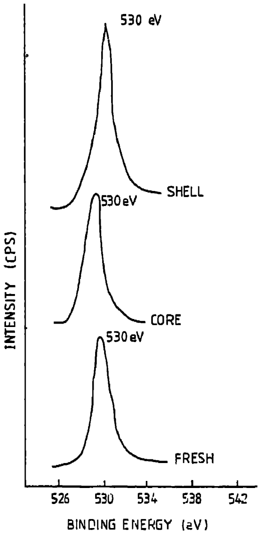

Figure 5. XP spectrum of oxychlorination catalyst (region of oxygen).

(0·09 ml/g)). This is to be expected because of the formation of a crystalline compound like $CuAlO_2$ and its sintering and growth to larger crystallites caused by the high local temperatures. In order to confirm these limitations to oxygen diffusivity, temperature-programmed oxidations were carried out and it was observed that oxidation was relatively easier when the core was crushed to a very fine powder in comparison to the situation when the core was taken as it was, proving that it is difficult for oxygen to penetrate the core due to its reduced porosity.

4. Conclusion

Deactivation in oxychlorination catalysts seems to be facilitated by preferential formation of a Cu^+ phase, $CuAlO_2$, in the core of the catalyst, on use, upsetting the Cu^+/Cu^{++} redox equilibrium. This is a thermally stable phase and formed as a solid solution between Cu_2O and Al_2O_3 due to the high oxothermicity of the reaction resulting in high local temperatures and the oxygen diffusibility limitations to the core caused by the reduction in porosity due to sintering of the core. Such a stable $CuAlO_2$ phase cannot be active for oxychlorination catalysts, where easy changes in oxidation states of copper are essential. Deactivation is also facilitated by decomposition of the active double salt $KCuCl_3$ and precipitation of free KCl followed by migration of potassium and chlorine from the core to periphery. There is also an enrichment of oxygen in the shell compared to the core obviously due to the diffusion limitations to the core.

References

Allen J A and Clark A J 1971 *Rev. Pure Appl. Chem.* **21** 145
Buckley J A 1966 *Chem. Eng.* **73(24)** 102
Conner Wm.c, Pieters W J M and Signorelli A J 1981 *Appl. Catal.* **11** 59
Frost D C, Ishitani A and McDowell C A 1972 *Mol. Phys.* **24** 861
McIntyre N S and Cook M G 1975 *Anal. Chem.* **47** 2208
Strohmeier B R, Leyden D E L, Field R S and Hercules 1985 *J. Catal.* **94** 514
Vetrivel R, Seshan K, Rao K V, Krishnamurthy K R and Prasada Rao T S R 1987 (to be published)

Bull. Mater. Sci., Vol. 9, No. 2, June 1987, pp. 81–87. © Printed in India.

In situ photoacoustic spectroscopic studies on heterogeneous catalysts under conditions of gas flow*

T SOMASUNDARAM and P GANGULY
Solid State and Structural Chemistry Unit, Indian Institute of Science,
Bangalore 560 012, India

MS received 31 March 1987

Abstract. An all-glass open photoacoustic cell through which gases can be passed without affecting the signal has been described. The cell has been characterized for various chopping frequencies and temperatures. Several heterogeneous catalytic reactions have been studied under conditions of gas flow at elevated temperatures and the potential application of this method in the field of heterogeneous catalysis has been pointed out.

Keywords. Photoacoustic spectroscopy; open photoacoustic cell; heterogeneous catalyst; catalytic reactions.

1. Introduction

In the last decade or so there has been a revived interest in the study of photoacoustic (PA) effect from condensed matter (Ganguly and Rao 1981; Tam 1986), after the pioneering work of Bell (1881) on the 'sonorousness' of the materials under the influence of intermittent light. This revival of interest was mainly due to the belief that the PA effect could be gainfully employed to obtain optical spectra of materials like gels and translucent solids which are normally inaccessible to the conventional spectroscopic techniques. Secondly it was believed that even thermal properties could be studied because of the dependence of the PA signal on thermal parameters. There have been several occasions where the belief has come true. Hence, there has been enormous growth since the revival in various branches of PA effect. Optical spectra have been recorded on powdered and light scattering materials (Monahan and Nolle 1977); thermal properties have been studied by Adams and Kirkbright (1977); phase transitions studied (Somasundaram *et al* 1986). Besides these applications there have been photoacoustic microscopic studies (Wickramasinghe *et al* 1978; Wong *et al* 1978), biological studies (Balasubramanian and Mohan Rao 1981) and surface studies (Low and Parodi 1980; Somasundaram *et al* 1987). The main advantage of using PAS for spectroscopic studies is the fact that the sample preparation is not very critical and in principle spectra can be recorded even from opaque solids. The disadvantages are the saturation effect and the difficulty in getting a quantitative measure of absorption coefficient β. Taking all these into account it was believed that the area of photoacoustic spectroscopy would be especially useful in the study of surfaces and more specifically those of catalysts which have high surface area. The high surface area of catalysts essentially increases the signal intensities (due to the possible increase in efficient heat transfer) and reduces the saturation effects.

---

*Communication No. 428 from the Solid State and Structural Chemistry Unit.

One of the distinguishing features of PAS is that the positioning of the detector is not very crucial as far as the geometry with respect to the incident light is concerned. This flexibility of the detector position gives rise to the idea that perhaps the geometry of the cell may be changed so as to allow the study of catalysts under more realistic conditions. One such early study was by Kanstad and Nordal (1978) who proposed that a membrane could be used to separate the catalytic reactor cell from the microphone. The PA signal (I_{PA}) generated in the reactor may then be transmitted to the microphone through the membrane. Others have proposed a design in which the catalyst could be transferred from the reaction chamber to the PA cell (Low and Parodi 1980). In all the studies the spectra were taken in a closed cell.

We have recently reported that gas-microphone PA signal may be recorded without significant loss of intensity even if the cell is open to the atmosphere or a gas is flowing through it (Ganguly and Somasundaram 1987). This suggests immediately that PA spectra may be obtained from a sample *in situ* under catalytic conditions. We have designed a cell in which we have been able to record PA spectra upto 800 K, using a gas microphone, and study the spectra of catalysts under catalytic conditions. In this communication we report the characterization of an all-glass cell for the study at various frequencies and temperatures along with some of the experiments carried out by us using visible light. We believe the method will be of interest especially to those engaged in heterogeneous catalysis.

2. Experimental

2.1 *Description of the cell*

The cell used for this study shown in figure 1, has been fabricated from glass and consists of a cylindrical sample chamber of 15 mm dia and 6 mm height. Three capillaries are attached to the sample chamber each of roughly 15 cm in length. Two of these have internal diameter of 0·5 mm while the other has an internal diameter of 2 mm. The last capillary is attached to the microphone. The smaller capillaries are used for gas inlet and outlet. The capillaries are joined to the sample chamber such that the sample (taken as a powder) is below the joints and the gas flow does not affect the sample in the sense that it is not blown out of the cell. With the dimensions given the signal amplitude is not changed by more than 5% when the cell is closed, open or when a gas is flowing through the cell for frequencies greater than or equal

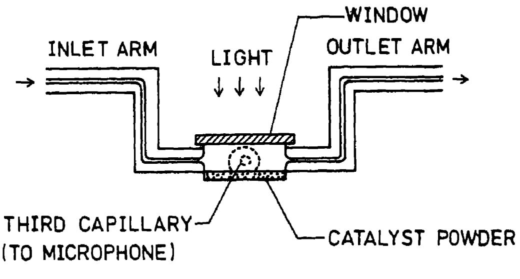

Figure 1. The all-glass open photoacoustic cell used for the catalytic studies under gas flow conditions.

to 15 Hz (Ganguly and Somasundaram 1987). For frequencies lower than this there is a decrease.

The microphone connected to the sample chamber through the 2 mm dia capillary is GR 1961 electret condenser microphone. The microphone is in turn connected to a x-y recorder through a lock-in-amplifier. The microphone has a flat frequency response. The cell is immersed in refractory alumina powder, inside a furnace, with the top of the cell kept clear for illumination. There is practically no signal from empty cell for wavelength (λ) above 400 nm for all temperatures. Studies below $\lambda = 400$ nm carried out have taken into account the contributions from the cell and variations in the power spectrum. However, the results below $\lambda = 400$ nm are not quantitative, especially at high temperatures. The catalyst under study is taken as a fine powder and loaded into the sample chamber through one of the capillaries. For studies under catalytic conditions a gas such as nitrogen is passed after mixing with the vapours of the reactant. Care is taken to see that there is no condensation of liquids in the capillaries before and after reaction. In the studies described here the products have neither been analysed nor collected as the interest is only to study the changes in the catalyst and demonstrate the feasibility of PAS for studies under catalytic conditions.

2.2 *Characterization of the cell*

In figure 2 the frequency dependence of the signal is shown for carbon black powder. Between 10 and 100 Hz the signal from carbon black shows the expected inverse frequency dependence. Similar behaviour is seen even when a gas flows through the cell at ~1·2 cc/sec. The upturn at higher frequencies is associated probably with the onset of Helmholtz resonance. In figure 3 the intensity of the signal from carbon black at several temperatures is plotted against the reciprocal of the temperature.

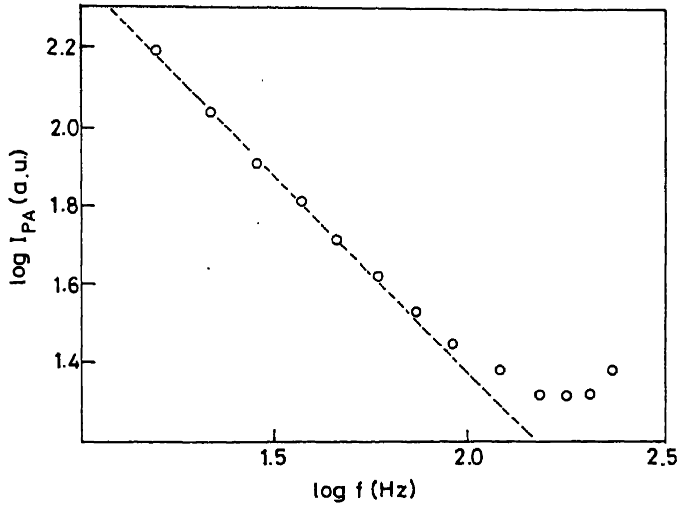

Figure 2. Frequency dependence of the PA signal of carbon black powder in the open PA cell under no gas flow condition. The dotted line shows the expected f^{-1} dependence and circles represent experimental data points.

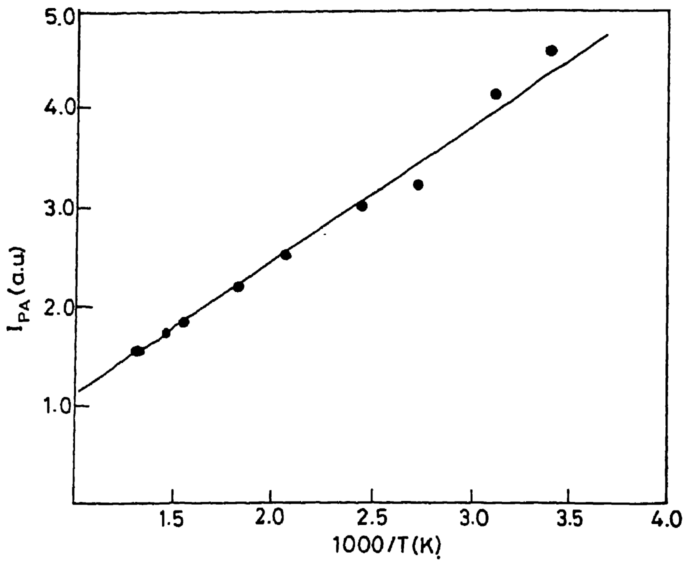

Figure 3. Variation of I_{PA} as a function of temperature for carbon black sample in the open PA cell under no gas flow conditions. The line is the best fit obtained for the data points.

The linear plot is in accordance with the currently accepted model due essentially to Rosencwaig and Gersho (1976). The power spectrum recorded at various temperatures is actually identical above $\lambda = 400$ nm except for the decrease in intensity as a function of temperature. These results show that the cell can be used for various studies without any difficulties. Even the Helmholtz resonance can be used successfully to enhance the signal if frequency dependence study is not required.

3. Results and discussion

3.1 *Studies with catalysts*

3.1a *CuO-ZnO*: A catalyst with the nominal composition $Cu_{0\cdot 2}Zn_{0\cdot 8}O$ prepared by the decomposition of nitrates has been studied in an atmosphere of N_2-CH_3OH (10:1 molar ratio) at various temperatures. The flow-rate of the mixture has been 1·5 cc/sec. The spectra are independent of flow-rate and chopping frequency in the range studied (flow rates upto ~2 cc/sec and chopping frequency 10–100 Hz). Such independence is found with all the other systems studied. In figure 4 the spectra obtained at various temperatures in the presence of the reactant mixture are shown. The development of a feature around 500 K is similar to that observed by optical spectroscopy of these catalysts reduced at 250°C in hydrogen and attributed to the presence of Cu^+ species (Bulko *et al* 1979). At higher temperatures this band is missing and the intensity of the photoacoustic signal is independent of the wavelength below 400 nm, perhaps due to the formation of metallic Cu. The absorption at higher energies is probably due to ZnO.

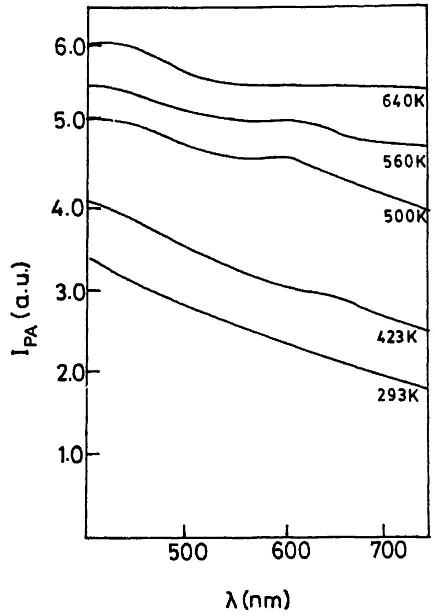

Figure 4. Normalized PA spectra of $Cu_{0.2}Zn_{0.8}O$ catalyst under various experimental conditions. Flow-rate: ~1·5 cc/sec of N_2-CH_3OH in the ratio 10:1. Temperature at which the spectrum is recorded is indicated against each curve.

3.1b *Acetone-alumina*: An alumina catalyst (surface area 190 m^2/g) has been studied in the presence of acetone vapour at various temperatures. In figure 5 we show the PA spectra obtained in the presence of a flowing stream of acetone-N_2 mixture (in the molar ratio 1:8). Curve A in figure 5 is the spectrum of the catalyst alone at room temperature while curve B is the spectrum in the presence of acetone. The increased signal below 400 nm in curve B must be attributed to the presence of acetone. When the temperature is raised, a prominent shoulder is seen around 350 nm at 370 K. With further increase in temperature the catalyst attains a strawish brown colour which intensifies as the temperature is increased. The PA spectra at 400 and 500 K are shown as curves D and E. The shoulder around 350 nm in curve C may be attributed to the formation of mesityl oxide (Rao 1967) which polymerizes further to give the yellowish brown product on the surface.

3.1c *Chromia-alumina catalyst*: In figure 6 the spectrum obtained from a 5% $Cr^{6+}-Al_2O_3$ catalyst is shown. At room temperature the air-fired catalyst is yellow in colour due to the presence of Cr^{6+} ions. The PA signal at room temperature shows no features due to Cr^{3+} ions. The PA signal is saturated below 420 nm for the catalyst at room temperature. In the presence of a flowing stream of N_2-isopropanol mixture (10:1 molar ratio) the spectrum is unaffected up to about 370 K. The feature due to Cr^{3+} ion starts appearing around 400 K. Around this temperature it is noticed that the signal shows a continuous increase below 400 nm instead of being saturated. This may be attributed to the formation of acetone. By recording the spectra of the effluent gas in another cell in which there is no catalyst one could

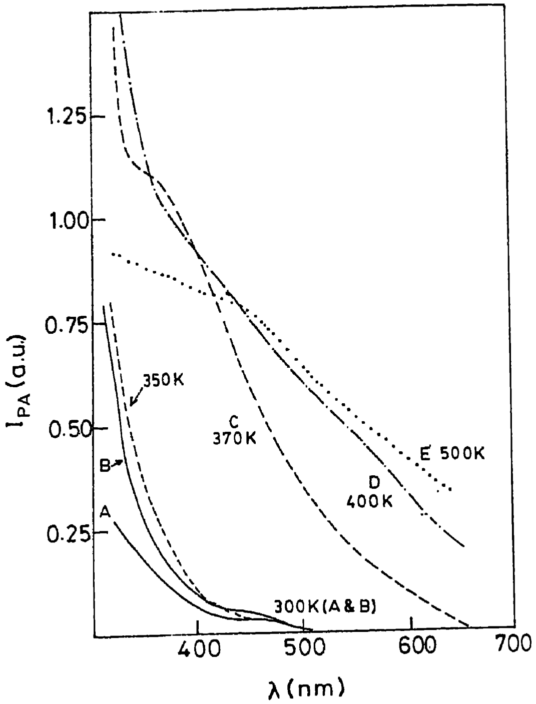

Figure 5. Normalized PA spectra of alumina catalyst under various experimental conditions. Flow-rate: 1·55 cc/sec of N_2-acetone in the ratio 8 : 1. A: catalyst only; B: catalyst with gas flow. The temperature at which the spectrum is recorded is indicated against each curve.

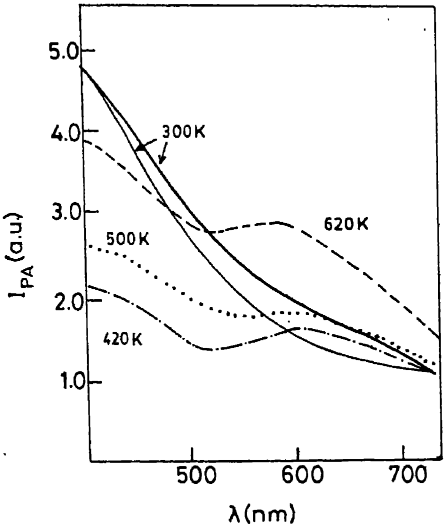

Figure 6. Normalized PA spectra of 5% $Cr^{6+}-Al_2O_3$ under various experimental conditions. Thin and thick lines represent catalyst and catalyst with gas flow at 300 K, respectively. Flow-rate: ~1·2 cc/sec of N_2-isopropanol in the ratio 10 : 1. Temperature is indicated against each curve.

ascertain whether the acetone is in the gaseous phase or adsorbed on the catalyst. With further increase in temperature the Cr^{3+} feature becomes more prominent and the charge-transfer band due to Cr^{6+} ion is much reduced in intensity.

4. Conclusion

The present study indicates the possibility of using PA spectroscopy for studying reactions under real catalytic conditions. By appropriately designing the cell, for example all quartz cell, even the UV region where most of the organic reactants absorb, can be studied at still higher temperatures. The difference between the adsorbed species and species present in the gas phase can also be made. These kind of studies are suitable especially for species which form only under the gas-flow conditions or decompose when the catalyst is cooled down to room temperature. By analysing the products either chemically or by attaching the PA spectrometer to a gas chromatograph the products of the reaction can be identified very easily. Further work is in progress on these lines.

Acknowledgement

One of the authors (TS) is thankful to CSIR, New Delhi for a fellowship.

References

Adams M J and Kirkbright G F 1977 *Analyst (London)* **102** 678
Balasubramanian D and Mohan Rao Ch 1981 *Photochem. Photobiol.* **34** 749
Bell A G 1881 *Philos. Mag.* **11** 510
Bulko J B, Herman R G, Klier K and Simmons G W 1979 *J. Phys. Chem.* **83** 3118
Ganguly P and Rao C N R 1981 *Proc. Indian Acad. Sci. (Chem. Sci.)* **90** 153
Ganguly P and Somasundaram T 1987 *Proc. Indian Acad. Sci. (Chem. Sci.)* (Communicated)
Low M J D and Parodi G A 1980 *Appl. Spectrosc.* **34** 76
Monahan E M and Nolle A W 1977 *J. Appl. Phys.* **48** 3519
Kanstad S O and Nordal P E 1978 *Opt. Commun.* **26** 367
Rao C N R 1967 in *Ultraviolet and visible spectroscopy* (New York: Plenum) p. 18
Rosencwaig A and Gersho A 1976 *J. Appl. Phys.* **47** 64
Somasundaram T, Ganguly P and Rao C N R 1986 *J. Phys.* **C19** 2137
Somasundaram T, Ganguly P and Rao C N R 1987 *Zeolites* (in print)
Tam A C 1986 *Rev. Mod. Phys.* **58** 381
Wickramasinghe H K, Bray R C, Jipson V, Quate C F and Salcedo J R 1978 *Appl. Phys. Lett.* **33** 923
Wong Y H, Thomas R L and Hawkins G F 1978 *Appl. Phys. Lett.* **32** 538

Bull. Mater. Sci., Vol. 9, No. 2, June 1987, pp. 89–96. © Printed in India.

Morphological aspects of some symmetrical ammonium hydrogen tartrate crystals grown by silica gel technique

C C DESAI and A N HANCHINAL
Department of Physics, Sardar Patel University, Vallabh Vidyanagar 388 120, India

MS received 30 December 1986; revised 26 February 1987

Abstract. Ammonium hydrogen tartrate single crystals have been prepared by the reaction of NH_4Cl and tartaric acid in silica gel. The morphology of some as-grown symmetrical crystals has been studied by optical microscopy. The growth morphology studies indicate that the grown crystals are needle-shaped, orthorhombic disphenoidal and tetrahedral disphenoidal. The growth mechanism has been assessed.

Keywords. Ammonium hydrogen tartrate; single crystal; gel method; morphology; habit modification.

1. Introduction

Crystals show a wide variety of morphology. Questions relating to variations and the relationship of different morphologies to the growth conditions of crystals have been a long and stimulating problem. The relationship between morphologies of crystals and the growth conditions would help in understanding the kinetics processes of the growth mechanism. The morphology and morphology modifications of a variety of crystals have been studied earlier (Burton *et al* 1951; Mullin 1961; Hartman 1969; Elwell and Scheel 1975).

Ammonium hydrogen tartrate (AHT), $NH_4HC_4H_4O_6$ crystals show many interesting physical properties such as ferroelectricity, piezoelectricity, optical and other characteristics. They are used for controlling laser emission (Pipree and Koblova 1967). The efficiency of AHT crystals in different modulation and defocusing systems is characterized by their electro-optical coefficients. The optimal conditions for the growth of large transparent crystals of AHT in silica gels and the results affecting the nucleation by altering the gel parameters have earlier been reported by Desai and Hanchinal (1983, 1985). This paper explains the morphological variations in AHT crystals and its relation to growth conditions.

2. Experimental

Single crystals of AHT were grown by the gel technique. The growth process involves the subsequent diffusion of ammonium chloride into a gel in which tartaric acid is diffused before. Due to the slow diffusion of NH_4Cl in the gel, the reaction region advances gradually into the gel from the gel solution interface. The colourless transparent crystals upto $20 \times 5 \times 3$ mm^3 in size have been grown in about 2–3 weeks. The crystals were harvested by physical removal from the gel and examined by scanning electron microscope, x-ray diffraction, density measurements and thermogravimetric analysis and were confirmed to be AHT. They belong to the orthorhombic crystal system and have lattice parameters $a_0 = 0{\cdot}7640 \pm 0{\cdot}0002$ nm, $b_0 = 1{\cdot}3441 \pm 0{\cdot}0003$ nm and $c_0 = 0{\cdot}7029 \pm 0{\cdot}0002$ nm and its space group is $P2_12_12_1$, and have 4 molecules per unit cell. The density of AHT is 1·636 g cm^{-3}. The crystals do not contain any water molecules as seen from differential scanning calorimetric (DSC) curves. Defect properties of AHT crystals were studied by using a chemical etching technique. A solution of $SrCl_2$ (1·0 M) was used as an etchant which produces well-defined rectangular shaped etch pits at the emergent sites of dislocations on the cleaved (100) face. The dislocation density was found to be $2{\cdot}1 \times 10^3$ cm^{-2}. The morphology of the crystals has been studied by optical microscopy. The results are based on the statistical average of five sets of experiments.

3. Results

In the present investigation, crystals with different morphologies were obtained at different depths in the growing test tubes and at different growth conditions. The morphology of the grown crystals is affected mainly by the concentration of the feed (NH_4Cl) solution and the pH of the system. Three types of morphologies of AHT crystals were observed namely (i) prismatic needle-shaped crystals, (ii) orthorhombic disphenoidal crystals and (iii) disphenoidal tetrahedral crystals.

3.1 *Prismatic needle-shaped crystals*

Usually the nucleation of this type of crystals initiates in the region OA (figure 1a), just below the gel-interface. They start growing from a bunch of nucleii with the diffusion of feed solution into the gel. With lapse of time, the thickness of the crystal increases with faster growth rate along [001] direction, which is the growth direction of AHT crystals of different habits. The growth of needle is mainly due to the presence of diffusion field around the crystal tips of the needle and the crystals grow into the supersaturated solution whereas the sides of the crystals are in contact with a largely exhausted solution. The typical prismatic needle-shaped crystals are illustrated in figure 1b. The development of the morphology is schematically shown in figure 1c and it is seen that (100), (110), (130) and $(11\bar{1})$ are well-developed faces and the $(1\bar{1}0)$ face is fairly developed. The crystals are quite transparent with lusterou faces. These characteristics speak of good quality and perfection of these crystals.

3.2 *Orthorhombic disphenoidal crystals*

In this category, two types of crystals, rod-like orthorhombic and plate-like ortho rhombic, are obtained. Fairly high concentrations of 2·0 M to 3·5 M NH_4Cl fee solutions and a fairly large amount of this solution at pH between 3 and 4·5 (figur 2a) gave rise to a rod-like orthorhombic disphenoidal type of crystals as shown i figure 2b, whereas the concentration of feed solution between 0·5 M and 2·0 M at p less than 2 (figure 3a) gave rise to a platelet orthorhombic disphenoidal type o crystals as shown in figure 3b. The usual regions of crystal growth in the test tube are clearly illustrated in figures 2a and 3a. The morphology of these two types o crystals is depicted in figures 2c and 3c.

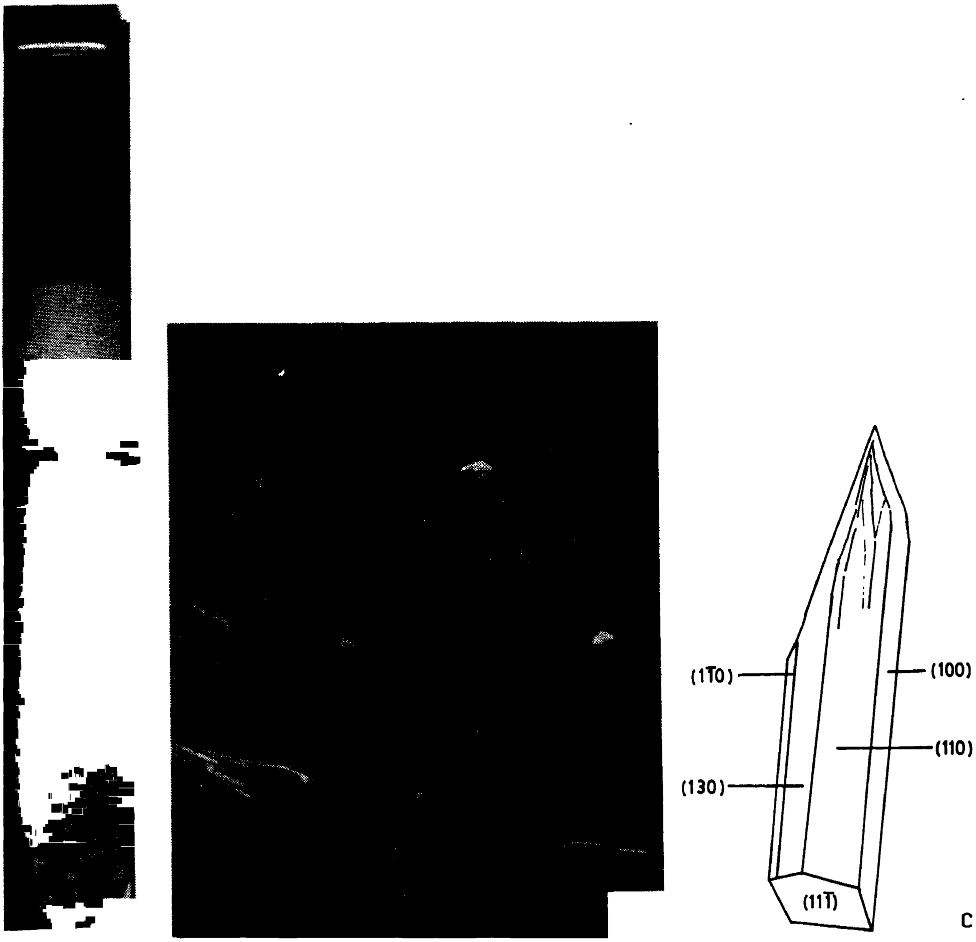

Figure 1. (× 50) **a.** Transparent AHT crystals growing in a silica gel medium. The nucleation initiates in the OA region. **b.** Some of the typical prismatic needle-shaped crystals. **c.** Schematic representation of the crystal morphology.

In rod-like disphenoidal crystals the (100), (110), (11$\bar{1}$), ($\bar{1}\bar{1}$0) and ($\bar{1}\bar{1}$1) faces are large and dominating while the (113) and (130) faces are very small. Gel incorporation inclusion is often used in these crystals without affecting their morphology. These inclusions reduce their transparency.

In plate-like disphenoidal crystals, the prominent faces are (100), (111), (11$\bar{1}$), (2$\bar{1}$3), while (110) and ($\bar{1}$10) faces are not well developed. Most of them are fairly transparent.

3.3 *Disphenoidal tetrahedral crystals*

These crystals usually appear at the top of the interface and at the extreme bottom of the glass test tube as illustrated in figure 4a. Within a limited distance above the gel interface, supersaturation takes place because of a spontaneous liberation of liquid

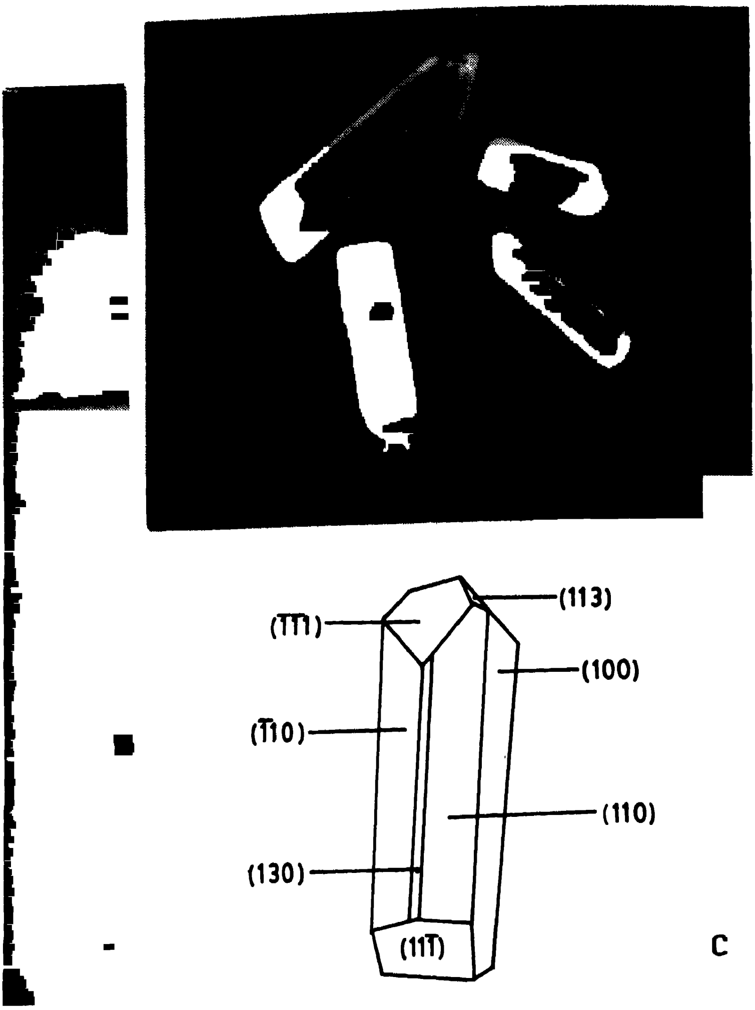

Figure 2. (× 50) **a.** AHT rod-like orthorhombic disphenoidal crystals growing at pH 4. **b.** Typical crystals. **c.** Schematic representation.

from the gel (tartaric acid). This is called 'syneresis' which is one of the important properties of gels. Syneresis is also considered as an internal dehydration. It produces shrinking of the gel thereby changing its pore size. The formation of this type of crystals is believed to be due to lack of place to grow further. At the top of the interface, within a limited distance when nucleation initiates along the [001] directions, the interface perforces to stop the growth. At the bottom, when nucleation takes place within a very short distance from the bottom of the test tubes, the bottom of the tube stops the growth. The limited growth develops only in (111) and $(\bar{1}\bar{1}1)$ faces, and sometimes with slightly developed (113) face. A couple of such crystals are illustrated in figure 4b and schematically represented in figure 4c. These crystals are transparent.

Occasionally cusps are observed due to the lateral growth of crystals in the test tube. In cusp-like cavities, the gel has been separated from the growing crystals.

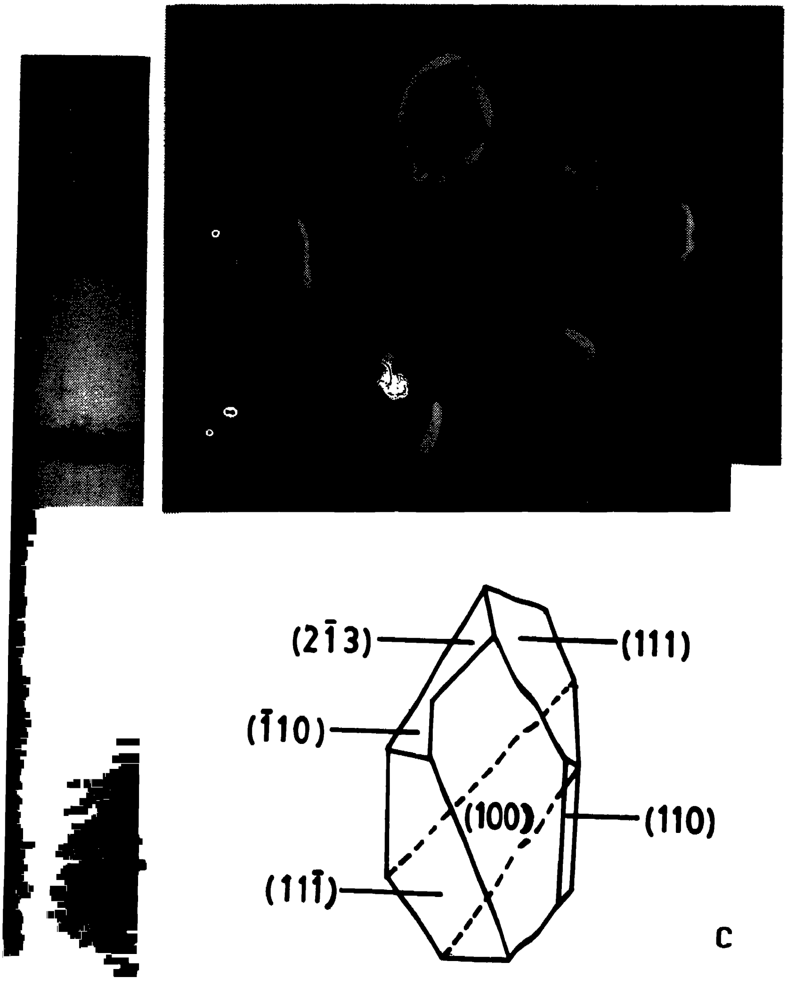

Figure 3. (× 50) **a.** AHT platelet orthorhombic disphenoidal crystals growing in silica gel at pH 2. The nucleation initiates in CD region. **b.** Platelet crystals of AHT. **c.** Schematic representation of the crystal morphology.

These are presumably the outcome of gel displacement from the pressure of advancing growth surface.

The *c*-axis is the growth axis of AHT crystals. Hence, whenever isolated crystals are grown, irrespective of their orientation with respect to the vertical axis of the test tube, they always grow along *c*-axis. In many cases the growth of the axis of isolated crystals is normal to each other. In addition, there are several other factors which influence the morphology and size of the growing crystals such as gel temperature, gel aging, gel density, gel pH, concentration of feed solution, specific gravity of gel mixture, etc. It is therefore desirable to consider a few of the above factors in details.

3.4 *Influence of gel pH*

The effect of gel pH on the morphology of grown crystals was studied by keeping all

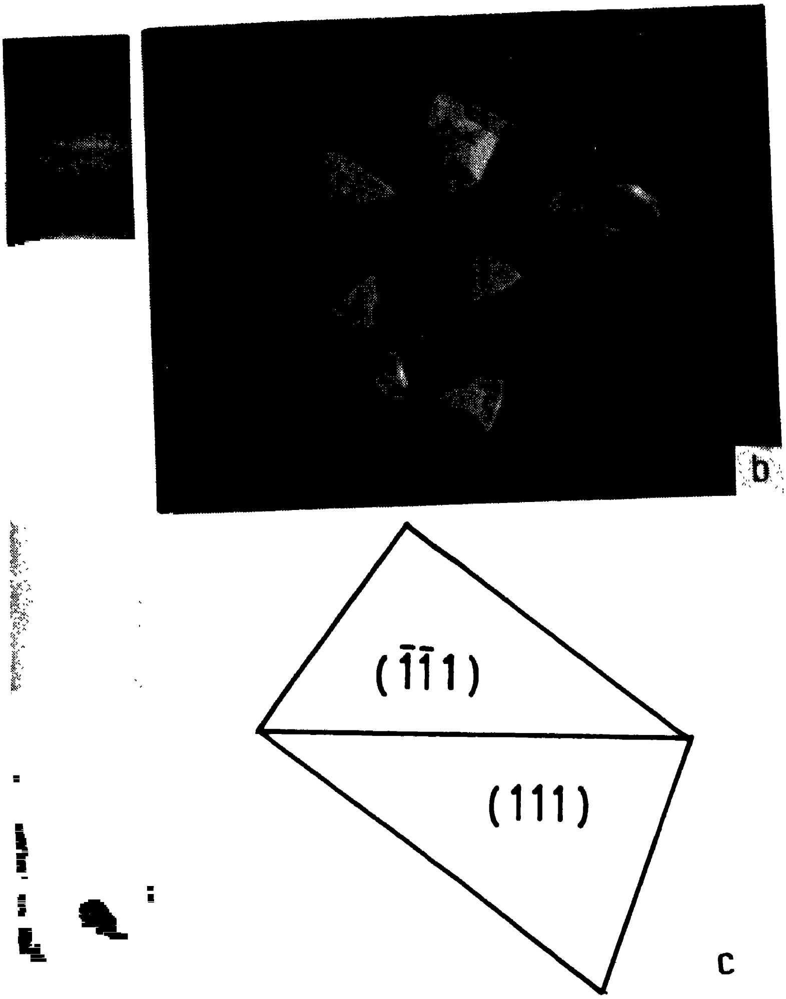

Figure 4. (× 50) **a.** Transparent tetrahedral crystals growing at the bottom of the tube. **b.** Disphenoidal tetrahedral crystals. **c.** Schematic representation of the tetrahedral crystal morphology.

other factors constant. Before gelation, the pH value of the gel mixture (gel + tartaric acid) was determined by a pH meter for a known concentration of feed solution, viz 2·0 M. The effect of gel pH was studied and the results are as follows: pH range between 4·5 and 7·0 gave rise to prismatic needle-shaped crystals, while rod-like orthorhombic disphenoidal crystals obtained between 2·0 and 4·5 pH and pH < 2·0 was responsible for the formation of plate-like sphenoidal crystals.

3.5 *Effect of feed solution*

The effect of concentration of feed (NH_4Cl) solution on the morphology and size of growing crystals was studied by keeping all other parameters constant and varying the concentration of feed solution. It is observed that increasing the concentration of feed solution increases the linear growth along the [001] direction for needle-shaped and disphenoidal crystals. Needle-shaped crystals are translucent and geometrically well-defined. The quality of these crystals deteriorates with an increase in the concentration of feed solution. Disphenoidal crystals are transparent and increase in size with the increase of concentration of feed solution.

4. Discussion

Habit modification depends on the phenomenon occurring on crystal surfaces. Diffusion of molecules on the surfaces of growing crystals is an important parameter in this regard. The relative rates of surface diffusion on basal and prism faces are responsible for determining the habit in the very early stages of growth. Crystal habit is governed by the interaction between its surface and the diffusion field. Once the habit has been established, the diffusion field around it will orient itself to conform to the crystal symmetry and tend to maintain it.

The parameters such as concentration of feed solution, pH of gel, impurities in the solvent, temperature etc have considerable influence on the diffusion rate (or growth rate) which ultimately influences the crystal morphology. In a steady state of concentration gradients, diffusion rate also becomes steady which favour the growth of well-developed crystals. However, a relatively slower growth rate along one direction results in the growth of platelet disphenoidal crystals (figure 3a). Preferentially faster growth rate in one particular direction viz *c*-axis, leads to the formation of prismatic needle-shaped crystals (figure 1a). At moderate supersaturation of feed solutions, crystals continue to develop as a tetrahedral disphenoidal crystals (figure 4a). In such cases the excess materials arriving at the edges and corners of the crystals is redistributed over the surface by surface diffusion.

5. Conclusions

Transparent prismatic needle-shaped crystals are obtained. Platelets and rod-like orthorhombic and tetrahedral sphenoidal crystals are obtained under different growth conditions. Increasing concentration of feed solutions increases the linear growth along [001] direction for needle-shaped and disphenoidal crystals. Generally crystals are transparent, but opaque crystals result in the event of gel inclusion. Restricted amount of gel inclusion takes place in rod-like disphenoidal crystals. Gels set with tartaric acid give better crystals than those set with mineral acids.

Acknowledgements

One of the authors (CCD) is grateful to the University Grants Commission, New Delhi, for financial assistance. Thanks are also due to Dr K C Desai and Mrs Lila K Desai (Belleville, New Jersey) for their interest and encouragement.

References

Burton W K, Cabrera N and Frank F C 1951 *Philos. Trans. R. Soc. London* **A243** 299
Desai C C and Hanchinal A N 1983 *Cryst. Res. Technol.* **18** 1499

Desai C C and Hanchinal A N 1985 *Surface Technol.* **25** 69
Elwell D and Scheel H J 1975 *Crystal growth from high temperature solutions* (London: Academic Press)
Hartman P 1969 *Growth of crystals* (ed.) N N Shifftal (New York: Consultants Bureau) p. 8
Mullin J W 1961 *Crystallization* (London: Butterworths)
Pipree L V and Koblova M M 1967 *Radio Eng. Electron. Phys.* (*Engl. Transl.*) **12** 503

Bull. Mater. Sci., Vol. 9, No. 2, June 1987, pp. 97–101. © Printed in India.

A study of diffusion mechanisms in sintering by shrinkage measurements

K M R ACHARI* and R B RAMACHANDER
Department of Physics, Osmania University, Hyderabad 500 007, India
*Department of Physics, Loyola Academy, Secunderabad 500 010, India

MS received 16 December 1986; revised 14 April 1987

Abstract. Shrinkage measurement is important in the study of sintering to ascertain the operative mechanism. Surface area reduction is related to shrinkage with the help of which operative mechanisms at different temperatures are inferred. Densification during sintering is mainly related to volume diffusion, grain boundary diffusion and plastic flow.

Keywords. Diffusion mechanism; sintering; shrinkage measurements.

1. Introduction

Sintering mechanism in copper has long been disputed. To establish the operative mechanisms at different stages both model (Coble 1961) and real experimental like dilatometric (Akechi and Hara 1979; Masuda and Watanabe 1981) as well as fractographic results (Slesar *et al* 1982) have been reported. In this paper the fractional shrinkages of copper powder compacts are related to normalized specific surface area reduction and also to the ratio of radius of the neck size to the radius of the particle. From the calculated values of inverse slopes and neck size exponents, the operative mechanisms are reported.

2. Theory

The radius of neck curvature (ρ) between two spherical particles is related (Kingery and Berg 1955) to the neck contact area (x) and the radius of the particle (r) as

$$\rho = x^2/2r \qquad \text{or} \qquad x/r = (2\rho/r)^{\frac{1}{2}}. \tag{1}$$

The ratio of x and r is connected to the sintering time (t) (German and Munir 1975) as

$$(x/r)^N = Bt, \tag{2}$$

where B is a constant containing parameters like material transport properties and the particle size, while N represents the characteristic mechanism The above relation can be written as

$$x/r = (Bt)^{1/N}. \tag{3}$$

Eliminating x/r from (1) and (3) one obtains

$$2\rho/r = (Bt)^{2/N}$$

or

$$\rho = (r/2)(B)^{2/N}\, t^{2/N}. \tag{4}$$

For the particles of same size, r is a constant and therefore

$$\rho \propto t^{2/N}.$$

The relation between the fractional shrinkage ($\Delta L/L_0$) and (ρ) is deduced (Kingery and Berg 1955) as

$$\rho/r=(\Delta L/L_0)=x/2r^2 \tag{5}$$

using (4) and (5)

$$\rho/r=(\Delta L/L_0)=(B)^{2/N}/2\ t^{2/N}. \tag{6}$$

Kingery and Berg (1955) have also obtained another form of relation

$$\Delta L/L_0=k\,t^n, \tag{7}$$

which is similar to (6) deduced in its form

where $(B)^{2/N}/2=k$ and $2/N=n$.

So, $$\Delta L/L_0=k\,t^{2/N}. \tag{8}$$

If N takes a value 5, then $n=0{\cdot}4$ as found experimentally for volume diffusion by Kingery and Berg (1955) for spherical particles i.e.,

$$\Delta L/L_0=kt^{0\cdot 4}. \tag{9}$$

Hence, we can have a relation

$$\rho/r=\Delta L/L_0=x^2/2r^2=kt^{0\cdot 4}. \tag{10}$$

To evaluate activation energy for volume diffusion (Lee 1972) the relation with fractional shrinkage f used, is

$$\Delta L/L_0=f=\mathrm{const}\,(t/T)\exp(-mQ_v/kT), \tag{11}$$

connecting sintering temperature (T), activation energy (Q_v) for volume diffusion and the exponent m. Here Lee (1972) assumed that $m=(l/2l+1)$ and has taken for spherical particles $l=2$ and got $m=0{\cdot}4$. Lee (1972) experimentally confirmed this exponent by plotting $\ln f$ vs $\ln t$ for constant T and evaluating the slope as 0·4 which agrees with above assumption of l for Niobium. With a view to verify the value of m for copper the authors (Achari *et al* 1986) have plotted $\ln f$ vs $\ln t$ at constant T and found the value as 0·46.

Further the normalized specific surface area reduction ($\Delta S/S_0$) is related as

$$\Delta S/S_0=(x/r)^{m'}. \tag{12}$$

In another paper German and Munir (1975) have also expressed

$$\Delta S/S_0=k'(Bt)^{m'/N}. \tag{13}$$

Here k', m' and N are constants for a given set of conditions, which are dictated by the controlling mechanism. Examination of (13) reveals that a plot of $\log(\Delta S/S_0)$ vs $\log t$ will give the characteristic value of the inverse slope N/m' if a single mechanism is operative. The expected values for each individual mechanism (German and Munir 1975) are given in table 1. Using (5) and (12) the fractional shrinkage is related to ($\Delta S/S_0$) as

$$(\Delta S/S_0)\propto(x/r)^{m'}=[(2\Delta L/L_0)^{\frac{1}{2}}]^{m'}$$

Table 1. Relation between mechanism and N/m' (German and Munir 1975).

Mechanism	Densification	Neck size exponent N	Appropriate value of N/m'
Viscous flow or plastic flow	Yes	2	1·1
Evaporation condensation	No	3	1·5
Volume diffusion	Yes	5	2·7
Grain boundary diffusion	Yes	6	3·3
Surface diffusion	No	7	3·5

1 hence

$$(x/r)^{m'} = [(2\Delta L/L_0)^{\frac{1}{2}}]^{m'} = ck'(Bt)^{m'/n}, \tag{14}$$

ere c is another constant.

Iere one is left with two alternatives. A plot of

$$\log(\Delta S/S_0) = \log(r_0^2 = r^2)/r_0^2 \text{ vs } \log t$$

n (13) which yields a value of N/m' based on which the operative mechanism can inferred or a plot of log (x/r) vs log t from (14) can be made to yield a value of N.

Experimental details

pper powder was pressed into pellets using a metallic die. These pellets were ered for different hours of duration at different temperatures. The initial diameter he pressed compact is (L_0). The change in diameter (ΔL) was measured. The tional shrinkage $(\Delta L/L_0)$ was calculated. The first plot of $\log[(r_0^2 - r^2)/r_0^2]$ vs $\log t$ hown in figure 1. Also the plot of $\log(x/r) = \log(2\Delta L/L_0)^{\frac{1}{2}}$ vs $\log t$ is shown in re 2.

Results and discussion

xpected the plots of (14) and (15) are straight lines for 873 K, 973 K and 1273 K not for 1073 K and 1173 K. For these graphs the reduction in surface area ted as $\log(r^2 - r_0^2)/r_0^2$ and $\log x/r$ continuously increases with respect to the ering duration (figures 1 and 2). The inverse slopes of these lines and the neck size nents help to confirm the operative mechanisms at the respective temperatures opper as shown in table 2.

he graphs at 1073 K and 1173 K show unexpected deviations. In both the figures, ally the 1073 K graph is linear. But it bends around the sintering duration of 0 sec, when the grain boundary diffusion terminates as could be seen from the rse slope in table 2. The slope of second segment confirms the anomalous nsion of copper due to pore coalescence already reported (Schreiner and Tusche). In figure 2 the line at 1173 K shows a sharp rise of $\log x/r$ compared to other es. This indicates maximum shrinkage at this temperature for the sample in ormity with volume diffusion (Masuda and Watanabe 1981).

figure 1 the reduction in surface area for the sample at 1173 K do not show

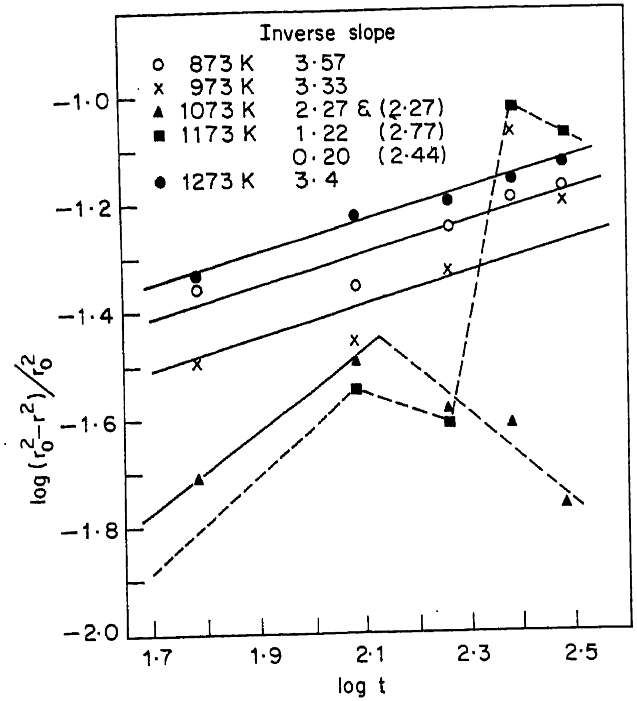

Figure 1. Plot of $\log(r_0^2 - r^2)/r_0^2$ vs $\log t$.

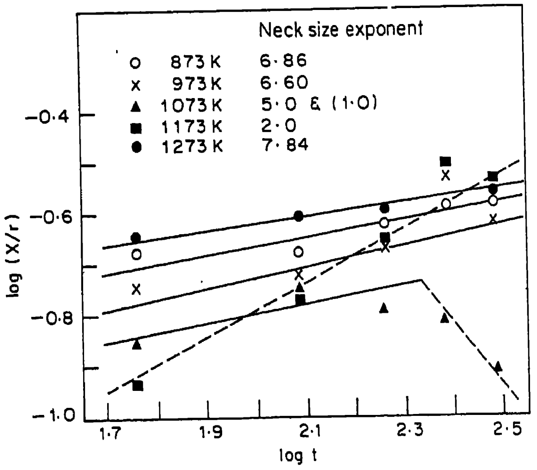

Figure 2. Plot of $\log(x/r)$ vs $\log t$.

continuous increase. It decreases from 72000 sec to 10800 sec, as well as from 15400 sec to 18000 sec of sintering duration. The calculated inverse slopes indicate plastic flow for these regions. But for copper at this temperature volume diffusion is reported to occur (Masuda and Watanabe 1981). We have also observed a maximum densification of the samples (Achari *et al* 1987) at 1173 K. However the locked-up

Table 2. Different mechanisms evaluated at different temperatures.

Temperature $T(K)$	Sintering duration (sec)	Inverse slope (N/m')	Neck size exponent (N)	Mechanisms
873	Total	3·57	6·86	Surface diffusion
973	—do—	3·33	6·60	Volume diffusion
1073	Upto 12600	2·27	5·0	—do—
	Beyond	(2·27)	(1·0)	(Plastic flow starts)
1173	Upto 7200	1·22	2·0	Plastic flow
	7200 to 10800	(2·77)	—	(expansion and/or volume diffusion)
	10800 to 15400	(0·20)	—	(Plastic flow)
	15400 to 18000	(2·44)	—	(Expansion and/or volume diffusion)
1273	Total	3·4	7·84	Volume and/or grain boundary diffusions.

stresses in the grains, during compacting the powder at high pressures, are released subsequently at 1173 K while sintering by the plastic flow mechanism (Slesar *et al* 1982). Further, it is felt that the contribution from volume diffusion perhaps is masked by the plastic flow in the above regions under consideration.

5. Conclusions

(i) The fractional shrinkages are related to reduction in surface area and also to the ratio of radius of neck to the radius of the particle. (ii) Anomalous expansion of the sample at 1073 K confirms pore coalescence. (iii) Plastic flow is suggested along with volume diffusion around 1173 K. (iv) The effect of sintering duration on shrinkage is related to different operative mechanisms.

Acknowledgements

The authors are thankful to Prof. Anwarur Rahman, Department of Physics, Osmania University and to Mr V Raghavender Rao, Mr A D Manohar and Mr G Sundara Sarma for their assistance while carrying out the work at DMRL.

References

Achari K M R, Reddy M B and Ramachander R B 1986 *J. Mater. Sci.* (Communicated)
Achari K M R, Reddy M B and Ramachander R B 1987 *J. Mater. Sci.* (Communicated)
Akechi K and Hara Z 1979 *Sintering—New developments* (ed) M M Ristic (Amsterdam: Elsevier)
Coble R L 1961 *J. Appl. Phys.* **32** 787
German R M and Munir Z A 1975a *Mater. Sci. Res.* **10** 249
German R M and Munir Z A 1975b *Mater. Sci. Res.* **10** 259
Kingery W D and Berg M 1955 *J. Appl. Phys.* **20** 1205
Lee D N 1972 *Mater. Sci. Res.* **6** 261
Masuda Y and Watanabe R 1981 *Sci. Sintering* **13** 117
Schreiner H and Tusche R 1982 (*Proc. 25th Int. Round Table Conference on Sintering*)
Slesar M, Besterci M and Dudrova E 1982 *Sci. Sintering* **14** 21

Bull. Mater. Sci., Vol. 9, No. 2, June 1987, pp. 103–110. © Printed in India.

Dehydration and phase transformation in chrysotile asbestos—A radial distribution analysis study

A K DATTA, B K MATHUR, B K SAMANTARAY and S BHATTACHERJEE
Department of Physics, Indian Institute of Technology, Kharagpur 721 302, India

MS received 25 November 1986; revised 2 January 1987

Abstract. Radial distribution analysis of x-ray intensities diffracted by chrysotile samples untreated and treated at different temperatures upto 900°C has been carried out. Interatomic distances, coordination numbers, mean square displacements and the interatomic coupling constants for different pairs of atoms have been calculated from the radial distribution curves. The interatomic distances and octahedral co-ordination number is found to decrease marginally upto 640°C and thereafter decrease steadily upto 800°C. The hydroxyl water is completely expelled from the structure and the original chrysotile structure breaks down. The entire process of dehydration has been interpreted in terms of RDF data.

Keywords. Dehydration; phase transformation; chrysotile asbestos; radial distribution.

1. Introduction

Chrysotile asbestos is of great scientific interest and commercial value because of its complexity of structure and multiplicity of uses. It belongs to the serpentine group of clay minerals with 1 : 1 layers which curl into cylindrical rolls. Its ideal structural formula is $Mg_3Si_2O_5(OH)_4$ for half a unit cell. It is built up of alternate half layers of silicate and brucite. Misfit between the two results in curvature with the longer brucite layer lying on the convex side. The curved layers form cylindrical fibrils with the *a*-axis along the fibre axis, *b* along the circumference and *c* along the radius of the fibres (Brindley and Brown 1980). The crystal chemical state of water in this mineral can be classified into two distinct groups characterized by hygroscopic (or adsorbed) and hydroxyl according to their nature and location in the structure. It is well established that these water molecules play a dominant role at different stages of dehydration resulting in significant transformation of structural and physical properties (Datta *et al* 1986; Datta and Bhattacherjee 1986).

The dehydration transformation mechanism in chrysotile has been studied by various workers using the usual x-ray powder diffraction method supported by IR and TEM studies (Hey and Bannister 1948; Brindley and Zussman 1957; Martin 1977; Santos and Yada 1979; Glasser *et al* 1962). Broadly, the results of these works show that chrysotile with loss of structural water transforms into an anhydride phase around 600°C followed by the formation of forsterite. Finally above 800°C the anhydrous phase recrystallizes into enstatite. However, the exact nature of the entire sequence of this transformation mechanism is yet to be fully understood.

From the review of literature, it is clear that notwithstanding the industrial potential and geochemical importance of this mineral, its x-ray crystallography and structure remain disputed till date owing to nonavailability of single crystal of suitable size. The problem is further complicated by the poorly crystalline form of this mineral which produces ill-defined powder patterns marked by large number of overlapping diffused broad lines rendering the application of usual powder method difficult for structural study. The problem becomes still more acute in the case of dehydration products which are still less crystalline with higher concentration of disorders. Because of these facts the problem is still open and calls for a better approach for investigating the structural details, especially in these poorly crystalline transient products from their x-ray diffraction patterns. To a large extent most of the difficulties encountered in the analysis of these types of poorly crystalline materials can be surmounted by adopting the technique of radial distribution analysis which is considered to be one of the most powerful and suitable tools for the study of less crystalline, amorphous and highly disordered systems (Leonard 1977; Lokanatha *et al* 1984, 1985). This approach is relatively new for clay minerals. In recent decades several workers (Leonard 1977; Lokanatha *et al* 1984, 1985; De *et al* 1986) have applied this technique successfully for structural analysis of several clay minerals and their poorly crystalline dehydration products. They have been able to explain the transformation mechanism in a much better way compared to any existing standard methods. Hence in the present work this technique has been applied to study the transformation process in a sample of chrysotile.

2. Experimental methods

2.1 *Sample preparation*

A sample of chrysotile from Cuddapah was selected for the present investigation. For testing the purity and identification of the sample, chemical and x-ray analyses were carried out and the results have been reported earlier (Datta *et al* 1986). Chemical analysis revealed the presence of Al_2O_3, FeO and TiO_2 in traces besides the principal constituents SiO_2 and MgO. X-ray analysis showed the traces of quartz. The sample was finely powdered and sieved through a 325 mesh screen. Then it was divided into several parts and heated separately for 5 hr each at temperatures 580, 640, 700, 750, 800 and 900°C respectively. Heated samples were then cooled in a desiccator to avoid the absorption of moisture and rehydration.

2.2 *Determination of intensities and radial distribution function*

The sample preparation for recording diffraction patterns was similar to that described by Mitra and Bhattacherjee (1969). Recording of intensities in the angular range 4° to 120° (2θ) and subsequent corrections for different factors were carried out as described by Lokanatha *et al* (1985). Following the same procedure as outlined by these authors, the corrected intensities were scaled to electron units. Finally the radial distribution function (RDF) for a polyatomic system was obtained by using the equation

$$4\pi r^2 \rho_e(r) = 4\pi r^2 \rho_{0e} + (2r/\pi) \int_0^\infty \mathrm{Si}(S) M_1(S) M_2(S) M_3(S) \sin rS \, dS,$$

where the symbols have usual meanings (Lokanatha *et al* 1985).

In the present case, the value of the damping factor b was adjusted till the ripples in the low angle region were considerably reduced. After several trials an optimum value of $b=0{\cdot}001$ Å^2 was assumed. The RDF obtained from Fourier inversion curves, representing the intensity distribution in reciprocal space using the above equation, shows peaks at radial distances corresponding to different nearest neighbour positions. Some of the overlapped peaks have been resolved by fitting Gaussian profiles to individual peaks. The coupling constants associated with various interatomic distances of untreated as well as dehydrated products were calculated following the procedure of Kaplow *et al* (1968) to obtain an approximate idea of the relative strength of the bonds. The values of coordination numbers with dehydration for the first three nearest neighbours have been calculated by measuring the area under the peaks of the untreated and treated chrysotile sample at different temperatures.

3. Results and discussion

The RDF curves for untreated and treated samples at different temperatures are shown in figure 1. Results of the calculations made from RDF curves are shown in tables 1 to 3. It is observed that the first peak occurs at $r=1{\cdot}61$ Å which corresponds to Si-O bond distance as reported in literature. It is interesting to note that unlike Lokanatha *et al* (1984, 1985) who observed the Si-O bond distances in fibrous silicate minerals to be much higher than the usual value as reported by Smith (1954), the present value is much closer to the value generally considered to be standard. Comparing this result with that of Lokanatha *et al* (1984, 1985), we conclude that substitution of Si, by trivalent ions which is attributed to the observed higher values in fibrous palygorskite and sepiolite, is less in chrysotile sample. The coordination number calculated from the area under the peak is 3·92 (∼4) which confirms the tetrahedral coordination of silicon atoms as expected. Hence, the first peak can be associated with the tetrahedral group forming Si-O network in silicate minerals. The coordination number remains practically unaltered with marginal changes at 640°C and 800°C establishing the stability of silicate layer. This observation is in conformity with the stepwise transformations in chrysotile fibres leading to the formation of forsterite and enstatite as revealed by x-ray, DTA and IR studies (Datta *et al* 1986). As reported by Datta *et al* (1986), the first stage extends upto about 640°C when dehydration starts with the expulsion of hydroxyl water. Beyond 750°C, there is a rapid recrystallization to forsterite and enstatite. The marginal increase in the value of the coordination number in two successive steps at 640°C and 750°C respectively is certainly associated with the formation of new phases and indicates a better coordination in these new crystalline phases. The near constancy of the Si-O bond distance and coordination number reaffirms the earlier observations made by Brindley (1980) that the Si-O bonds and consequently the tetrahedral silicate layer are more stable than the metal oxygen parts forming the octahedral groups and maintain the structural continuity of the different phases with the parent matter and do not collapse even at high temperatures.

The second and the third peaks can be similarly associated with Mg-O bonds forming octahedral groups with values 1·98 Å and 2·33 Å and coordination numbers 5·5 and 5·4 respectively. These values of the Mg-O bond distances and their coordination numbers are slightly less than the standard values. These marginal deviations

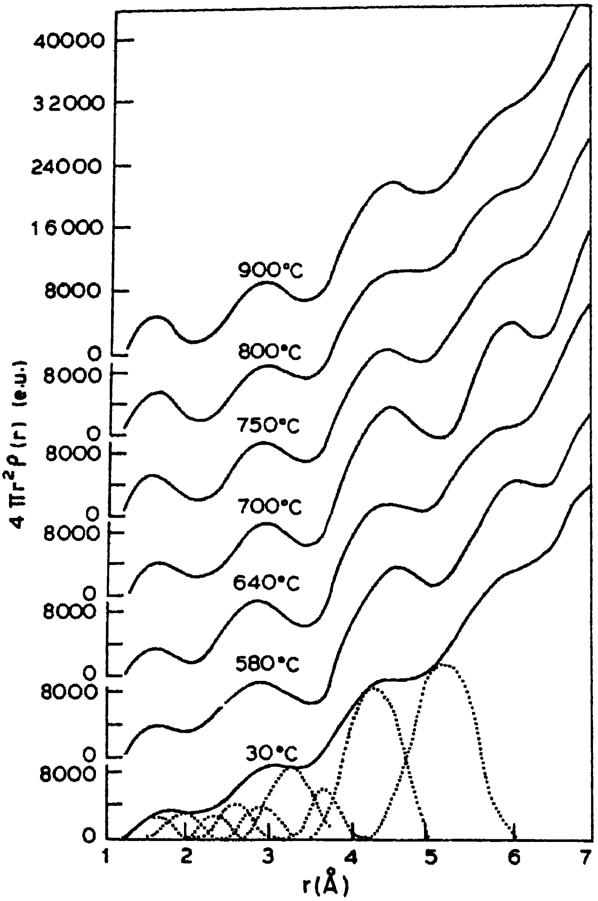

Figure 1. Radial distribution function curves for untreated and treated chrysotile at different temperatures. For the sake of clarity, the origins of the successive curves have been shifted by 10000 e.u. along the ordinate.

Table 1. Variation of interatomic distances (Å) of chrysotile sample with dehydration.

	Interatomic distances (Å)						
Peak Number	30°C	580°C	640°C	700°C	750°C	800°C	900°C
Si-O	1·61	1·61	1·60	1·60	1·60	1·60	1·60
Mg-O_I	1·98	1·97	1·96	1·96	1·95	1·95	1·95
Mg-O_{II}	2·32	2·32	2·30	2·18	2·20	2·34	2·20
O-O	2·61	2·60	2·58	2·59	2·61	2·61	2·62
O-O	2·95	2·90	2·92	2·94	2·94	2·94	2·98
Si-Si	3·34	3·34	3·35	3·32	3·36	3·37	3·38
Mg-Si	3·70	3·74	3·72	3·66	3·70	3·73	3·74
Mg-Si	4·34	4·32	4·30	4·30	4·32	4·32	4·31
Si-Si	5·18	5·18	5·18	5·18	5·18	5·19	5·20

Table 2. Variation of the coordination numbers with dehydration for the first three neighbours.

Peak Number	Coordination numbers 30°C	580°C	640°C	700°C	750°C	800°C	900°C
Si-O	3·92	3·92	3·94	3·94	3·94	3·96	3·96
Mg-O_I	5·50	5·40	5·30	4·90	4·40	4·40	4·60
Mg-O_{II}	5·40	5·40	5·30	4·90	4·70	4·60	4·70

of bond distances and coordination numbers can very well be ascribed to the presence of vacancies in the octahedral sites which are invariably present and are greater in this type of trioctahedral silicate minerals. These vacancies are likely to upset the equilibrium of the bond forces resulting in this deviation from theoretically expected values which is necessary to adjust the octahedral coordination to a stable configuration. All other peaks listed in table 1 have been resolved and identified by comparing with the standard interatomic distances reported by Sueno *et al* (1973).

Unlike Si-O distances, most of the remaining interatomic distances, in general, are observed to decrease only marginally and irregularly with gradual dehydration upto 640°C. However, above this temperature the changes become appreciable in a few cases, especially the Mg-O distance at 700°C. These initial marginal variations which are most likely due to expulsion of some adsorbed water, are of no consequence from structural point of view.

It is observed from table 1 that different bond lengths in the present sample do not vary regularly by any appreciable amount with dehydration which starts actually from around 568°C and continues slowly upto 768°C as revealed by the DTA curve (Datta *et al* 1986). These variations of bond lengths may be considered to be insignificant for all practical purposes. Thus we can say that the structure remains almost stable even upto 640°C because of this slow rate of dehydration as was observed by Martin (1977). The minor changes at 640°C is obviously due to the commencement of loss of structural water. Below 640°C the sample consists primarily of chrysotile and hence this particular feature can be attributed to chrysotile alone. Hereafter, forsterite starts developing slowly followed by the rapid formation of enstatite at 800°C and above. Hence above 640°C the entire diffraction pattern considered for calculation of RDF, is due to the contribution of an admixture of anhydrous or amorphous chrysotile, crystalline forsterite and enstatite. However, the relative abundance of the different constituents will depend on the temperature above 600°C. The existence of this multiphase system above 600°C or so is borne out by x-ray and DTA observations (Datta *et al* 1986) and renders the analysis very difficult. Hence above 600°C, whatever values of the lattice parameters are obtained, should preferably be considered as a weighted statistical average which is averaged over all the three phases and their relative proportions. However, since the conversion rate is rather slow at the initial stage, we can quite justifiably consider the main constituent to be chrysotile and hence the parameters obtained also related primarily to this mineral below 700°C.

It is interesting to note that even at 700°C almost all the interatomic distances may be considered to remain more or less the same for all practical purposes barring however Mg-O_{II} distances which change significantly. This drastic change in the

Table 3. Variation of the coupling constants and root mean square displacement of the chrysotile sample with dehydration.

Peak Number	Coupling constant (c.c) and r.m.s displacement ($(u^2)^{\frac{1}{2}}$) in Å													
	30°C		580°C		640°C		700°C		750°C		800°C		900°C	
	c.c.	$\langle u^2\rangle^{\frac{1}{2}}$	c.c.	$\langle u^2\rangle^{\frac{1}{2}}$	c.c.	$\langle u^2\rangle^{\frac{1}{2}}$	c.c.	$\langle u^2\rangle^{\frac{1}{2}}$	c.c.	$\langle u^2\rangle^{\frac{1}{2}}$	c.c.	$\langle u^2\rangle^{\frac{1}{2}}$	c.c.	$\langle u^2\rangle^{\frac{1}{2}}$
Si-O	0·405	0·28	0·411	0·28	0·374	0·27	0·374	0·27	0·366	0·26	0·376	0·26	0·371	0·26
Mg-O_I	0·550	0·38	0·544	0·37	0·513	0·37	0·499	0·36	0·535	0·38	0·579	0·40	0·599	0·42
Mg-O_{II}	0·507	0·35	0·514	0·35	0·458	0·33	0·458	0·33	0·450	0·32	0·521	0·36	0·514	0·36
O-O	0·666	0·46	0·676	0·46	0·624	0·45	0·597	0·43	0·605	0·43	0·623	0·43	0·585	0·41
O-O	0·666	0·46	0·647	0·44	0·611	0·44	0·583	0·42	0·591	0·42	0·608	0·42	0·628	0·44
Si-Si	0·608	0·42	0·602	0·41	0·569	0·41	0·583	0·42	0·591	0·42	0·608	0·42	0·599	0·42
Mg-Si	0·811	0·56	0·794	0·54	0·736	0·53	0·708	0·51	0·718	0·51	0·739	0·51	0·728	0·51
Mg-Si	1·0	0·69	1·0	0·68	1·0	0·72	1·0	0·72	1·0	0·71	1·0	0·69	1·0	0·70
Si-Si	0·797	0·55	0·852	0·58	0·805	0·58	0·777	0·56	0·746	0·53	0·768	0·53	0·771	0·54

value of interatomic distance between the farthest oxygen from Mg atom occupying the octahedral layer, primarily in the dehydrated chrysotile, leads to the collapse of chrysotile structure. The process is followed by simultaneous conversion of a major fraction to amorphous state and a minor fraction into crystalline forsterite. This observation on instability of structural organization of Mg is in agreement with the results obtained by Lokanatha *et al* (1984, 1985) and several other earlier workers. Increase of all the interatomic distances above 700°C clearly demonstrates the formation of the crystalline forsterite followed by forsterite and enstatite both at the final stage.

Table 2 shows that Si-O coordination number remains constant till 750°C and from 800°C there is an increase in the same. This is obviously due to the formation of crystalline enstatite which also results in sharpening of electron density function. This is also supported by the fact that the x-ray diffraction patterns of the sample heated at this temperature exhibit prominent peaks of enstatite corresponding to $d = 2{\cdot}91$, 2·55, 2·31 Å respectively along with the peaks of forsterite and chrysotile (Datta *et al* 1986). The DTA curve also showed an exothermal peak at the same temperature indicating recrystallization of the sample. It is observed that the octahedral coordination number decreases marginally, like the interatomic distances upto 640°C with dehydration; thereafter changes steadily and attains the minimum average value of about 4·5 around 800°C. This clearly demonstrates that all hydroxyl water is completely expelled from the structure at 800°C as is evidenced from the DTA curve. The original chrysotile structure breaks down and a part of it subsequently recrystallizes, in addition to forsterite, into a crystalline enstatite whose yield proportion goes on increasing with temperature. Thus the disorder starts in the octahedrally coordinated magnesium atoms which are reorganized primarily into tetrahedral coordination as was observed in palygorskite and sepiolite by Lokanatha *et al* (1984, 1985). The slightly higher value compared to those reported in case of palygorskite and sepiolite may be attributed to the complex multiphase system existing in this temperature range in the present sample.

An attempt has been made to calculate the coupling constants and the root mean square displacements ($\langle u^2 \rangle^{\frac{1}{2}}$) associated with the various interatomic distances of untreated as well as the dehydrated products following the methods of Morimoto (1958) and Kaplow (1972). The calculated values of $\langle u^2 \rangle^{\frac{1}{2}}$ and the coupling constants tabulated in table 3 reveal that the strongest bondings are between Si-O, Mg-O and Si-Si. With an increase in temperature, there is no appreciable variation in the $\langle u^2 \rangle^{\frac{1}{2}}$ values and consequently no significant change in the strength of the bonds even upto 640°C. This fact lends further support to our earlier observation that the structure remains stable upto this temperature without any significant disorder being introduced by dehydration. However, at higher temperatures, $\langle u^2 \rangle^{\frac{1}{2}}$ values corresponding to Mg-O are found to increase and consequently the strength decreases. This is somewhat expected and is in conformity with other results. But the variations of $\langle u^2 \rangle^{\frac{1}{2}}$ values for other atom pairs are too insignificant to draw any definite conclusion on the structure except that the couplings of these atom pairs remain more or less unchanged in the new phases developed at temperatures above 700°C.

4. Conclusion

The results of RDF analysis of the observed diffraction pattern enable us to arrive at certain valuable conclusions on the structural reorganization of atoms in the different stages of thermal treatment of chrysotile samples. It is clear that upto about 600°C there is no significant change and only above 700°C, significant changes occur owing to the completion of dehydration and subsequent development of the various phases. These observations agree well with the results of DTA, IR, TEM and x-ray studies (Datta *et al* 1986).

References

Brindley G W and Brown G 1980 *Crystal structures of clay minerals and their x-ray identification* (London: Mineralogical Society) p. 13
Brindley G W and Zussman J 1957 *Am. Mineral.* **42** 461
Datta A K and Bhattacherjee S 1986 *J. Mater. Sci.* **21** 1041
Datta A K, Samantaray B K and Bhattacherjee S 1986 *Bull. Mater. Sci.* **8** 497
De A K, Mathur B K, Samantaray B K and Bhattacherjee S 1986 *Trans. Indian Ceram. Soc.* **45** 14
Glasser L S D, Glasser F P and Taylor H F W 1962 *Q. Rev. Chem. Soc.* **16** 343
Hey M H and Bannister F A 1948 *Mineral. Mag.* **28** 333
Kaplow R 1972 *Interatomic potentials and stimulation of lattice defects* (ed) P O GehPen (London: Plenum Press)
Kaplow R, Rowe T A and Averbach B L 1968 *Phys. Rev.* **168** 1068
Leonard A J 1977 *J. Am. Ceram. Soc.* **60** 37
Lokanatha S, Mathur B K, Samantaray B K and Bhattacherjee S 1984 *J. Mater. Sci. Lett.* **3** 1105
Lokanatha S, Mathur B K, Samantaray B K and Bhattacherjee S 1985 *Z. Kristallogr.* **171** 69
Martin C J 1977 *Mineral. Mag.* **41** 453
Mitra G B and Bhattacherjee S 1969 *Am. Mineral.* **54** 1409
Morimoto H 1958 *J. Phys. Soc. (Jpn)* **13** 1015
Santos H D S and Yada K 1979 *Clays Clay Miner.* **27** 161
Smith J V 1954 *Acta Crystallogr.* **7** 479
Sueno S, Cameron M, Papike J J and Prewitt C T 1973 *Am. Mineral.* **58** 649

Bull. Mater. Sci., Vol. 9, No. 2, June 1987, pp. 111–115. © Printed in India.

Electrical second harmonic generation and temperature autostabilized nonlinear dielectric element in ferroelectric solid solutions $(Na_xK_{1-x})VO_3$ and $(Na_xLi_{1-x})VO_3$

T A PATIL, V M JAMADAR* and S H CHAVAN**†
Department of Physics, Vivekanand College, Kolhapur 416 002, India
*D K Mahavidyalaya, Ichalkaranji 416 115, India
**Department of Physics, Shivaji University, Kolhapur 416 004, India

MS received 9 February 1987; revised 3 April 1987

Abstract. Second harmonic generation and temperature autostabilized nonlinear dielectric element (TANDEL) effect have been studied for ferroelectric solid solutions $(Na_xK_{1-x})VO_3$ and $(Na_xLi_{1-x})VO_3$ in the vicinity of the Curie temperature. The generated second harmonic is linear for low biasing d.c. fields with zero off-set. The deviations from linear behaviour and a sharp decrease in the amplitude of second harmonic is observed at higher d.c. bias voltages. The TANDEL elements, in the autostabilized state, adjust their impedance against the variation of applied a.c. voltage. The observed zero off-set might be due to the presence of defects which give internal bias and generate second harmonic.

Keywords. Ferroelectrics; second harmonic generation; thermoautostabilized state (TANDEL).

1. Introduction

Second harmonic generation (SHG) in the autostabilized state has been studied by Malek *et al* (1964) for TGS from the harmonic analysis of current response. Similar effect has been observed for barium titanate and potassium dihydrogen phosphate by Miller (1964). Abe *et al* (1971) studied SHG for triglycine sulphate using external temperature arrangement and observed zero off-set. They suggested the use of TGS in electrometer circuit. Mansing and Eswar Prasad (1977) studied SHG and TANDEL effects in triglycine sulphate and suggested that the zero off-set might be due to the presence of defects which in turn give rise to an internal bias. Chavan and Patil (1980) reported that the defects and dislocations in the crystal give rise to an internal bias for TGSe and TGS-Se.

Our studies on SHG and TANDEL effects for ferroelectric solid solutions sodium-potassium vanadate $(Na_xK_{1-x})VO_3$ and sodium-lithium vanadate $(Na_xLi_{1-x})VO_3$ are reported in this paper.

2. Experimental

The crystalline solids of sodium vanadate ($NaVO_3$), potassium vanadate (KVO_3) and lithium vanadate ($LiVO_3$) were prepared from a stoichiometric mixture of $M_2^+CO_3$ ($M^+ = $ Na, K and Li) and V_2O_5. This mixture was heated in a platinum crucible inside a globar furnace at 750°C for 4 hr and then allowed to cool up to room temperature. The solid solutions of $(Na_xK_{1-x})VO_3$ and $(Na_xLi_{1-x})VO_3$ were prepared from their respective vanadates by firing in the platinum crucible at 900°C for 3 hr and then allowed the furnace to cool. The samples formed were confirmed by scanning them on x-ray diffractometer. The pellets of the solid solutions in the form of discs (diameter 1 cm and thickness about 1 mm) were prepared by applying 5 tonnes pressure using a hydraulic press. These pellets were sintered on a platinum foil at 500°C for 3 hr. The two sides of the pellets were coated with a thin layer of silver paste for good electrical contact.

---

†To whom all correspondence should be addressed.

The experimental set-up (figure 1) is similar to that used by Mansing and Eswar Prasad (1977) and Chavan and Patil (1980). We have studied voltage response of TANDEL elements of $(Na_xK_{1-x})VO_3$ and $(Na_xLi_{1-x})VO_3$ with a pure resistor of 10 ohm connected in series with them. A frequency of 10 kHz was used during the entire course of study. The experiments were carried out near the Curie temperatures of different samples using a temperature controller arrangement. The Curie temperatures of these samples were investigated by using a modified form of Sawyer and Tower (1930) circuit. The investigated Curie temperatures of $(Na_{0\cdot75}K_{0\cdot25})VO_3$, $(Na_{0\cdot50}K_{0\cdot50})VO_3$ and $(Na_{0\cdot25}K_{0\cdot75})VO_3$ are 425, 460 and 485°C respectively and of $(Na_{0\cdot75}Li_{0\cdot25})VO_3$, $(Na_{0\cdot50}Li_{0\cdot50})VO_3$ and $(Na_{0\cdot25}Li_{0\cdot75})VO_3$ are 490, 470 and 445°C respectively. The second harmonic voltage response for TANDEL elements of $(Na_{0\cdot50}K_{0\cdot50})VO_3$ is shown in figure 2. The other compositions of sodium-potassium vanadate series also show similar nature as in figure 2. The second harmonic voltage response for TANDEL elements of $(Na_{0\cdot50}Li_{0\cdot50})VO_3$ is shown in figure 3. The other compositions of sodium-lithium vanadate series also show similar type of graphical nature as in figure 3.

3. Results and discussion

Figures 2 and 3 show that the generated second harmonic is linear with applied d.c. voltage for low biasing fields in accordance with equation (1) given by Mansing and Eswar Prasad (1977), viz

$$V_{sh} = 6\omega\, CRd\, BP_0\, P_\omega^2 \cos 2\omega t, \qquad (1)$$

where C is the capacitance of the TANDEL element, d the thickness of the pellet, R

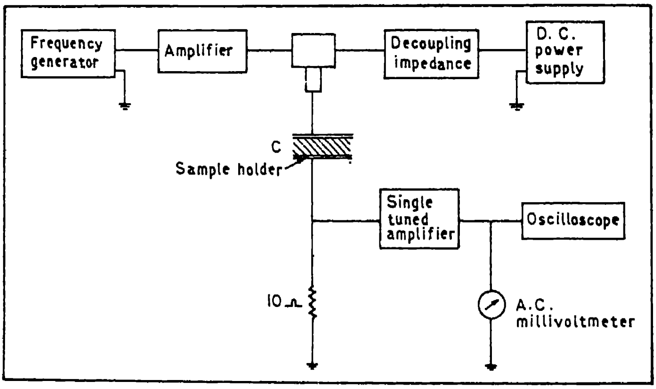

Figure 1. Experimental set-up.

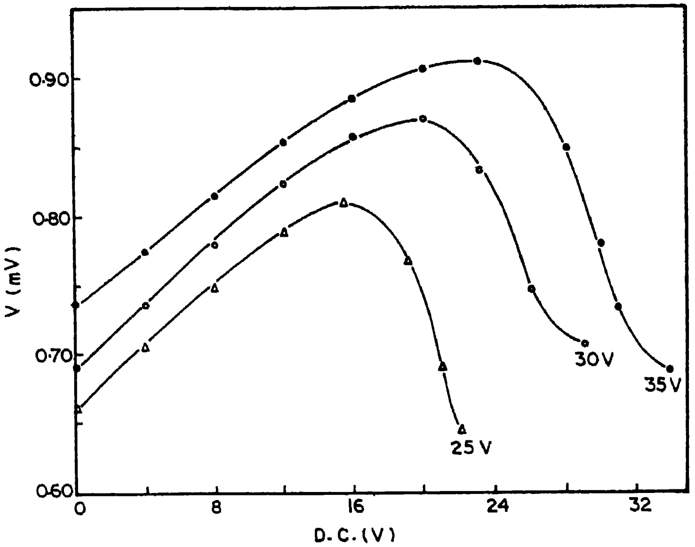

Figure 2. Variation of second harmonic voltage with D.C. bias for different a.c. voltages for $(Na_{0\cdot 50}K_{0\cdot 50})VO_3$.

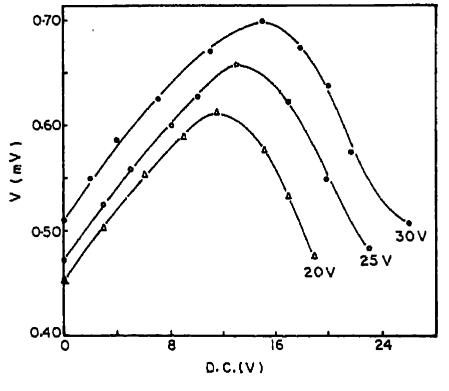

Figure 3. Variation of second harmonic voltage with d.c. bias for different a.c. voltages for $(Na_{0\cdot 50}Li_{0\cdot 50})VO_3$.

the small series resistance, ω the sinusoidal frequency and B the material specific constant. From (1) the generated second harmonic is proportional to polarization P_0 (which is proportional to applied d.c. bias) and to P_ω^2 (which is proportional to the square of the applied a.c. voltage). Similar results were reported by Malek *et al* (1964) and Mansing and Eswar Prasad (1977) for TGS and by Chavan and Patil (1980) for TGSe and TGS-Se. The region over which the second harmonic is linear with the applied d.c. bias can be extended by increasing the a.c. voltages. This is due to the fact that for low biasing fields the polarization is counteracted by d.c. bias fields so that the second harmonic is generated.

At higher biasing voltages a deviation from linear behaviour and a sharp decrease in the amplitude of second harmonic is observed for TANDEL elements $(Na_xK_{1-x})VO_3$ and $(Na_xLi_{1-x})VO_3$. At high d.c. fields the polarization is counteracted to the extent at which the elements fall out of the state of autostabilization. Higher d.c. bias is required to drive the TANDEL elements out of the state of autostabilization for higher a.c. voltages. This can be explained from the impedance voltage hysteresis given by Malek *et al* (1964).

The generated second harmonic should be proportional to the square of the applied a.c. voltage according to (1). But in the present studies, as also in the work of Mansing and Eswar Prasad (1977) and of Chavan and Patil (1980), no such variation was observed perhaps due to the basic TANDEL behaviour. The TANDEL element adjusts its impedance against the variations of applied a.c. voltage, so that the product CP_ω^2 in (1) remains constant which is in agreement with the theory of TANDEL given by Dvorak *et al* (1964). From figures 2 and 3 it is clear that when the d.c. bias voltage is zero there is still some second harmonic output. This is in agreement with the results of Abe *et al* (1971), Mansing and Eswar Prasad (1977) and of Chavan and Patil (1980). This zero off-set might be due to the presence of defects, giving rise to an internal bias, which in turn generates second harmonic. Table 1 summarizes our observations of threshold peak voltage for transition to the autostabilized state, amplitude of a.c. signal used for different samples, magnitude of second harmonic at zero bias and magnitude of d.c. bias at which samples go out of the autostabilized state.

Table 1. Values of various parameters of $(Na_xK_{1-x})VO_3$ and $(Na_xLi_{1-x})VO_3$ solid solutions.

Sample	Threshold peak voltage for autostabilization (*V*)	Peak a.c. voltage (*V*)	Magnitude of second harmonic at zero bias (*mV*)	Magnitude of d.c. bias for going out of autostabilization (*V*)
$(Na_{0\cdot75}K_{0\cdot25})VO_3$	18	25	0·70	14·0
		30	0·75	18·5
		35	0·78	23·0
$(Na_{0\cdot50}K_{0\cdot50})VO_3$	16·5	25	0·66	15·5
		30	0·69	20·0
		35	0·74	23·0
$(Na_{0\cdot25}K_{0\cdot75})VO_3$	14	25	0·62	17·0
		30	0·65	20·5
		35	0·69	24·5
$(Na_{0\cdot75}Li_{0\cdot25})VO_3$	10	20	0·42	12·0
		25	0·44	14·5
		30	0·50	17·0
$(Na_{0\cdot50}Li_{0\cdot50})VO_3$	12	20	0·45	11·5
		25	0·47	13·0
		30	0·51	15·0
$(Na_{0\cdot25}Li_{0\cdot75})VO_3$	14·5	20	0·49	9·0
		25	0·50	12·0
		30	0·53	14·0

The following observations could be noted

(i) The threshold peak voltage for transition to the autostabilized state and the magnitude of zero off-set increases as the proportion of $NaVO_3$ increases in the solid solution $(Na_xK_{1-x})VO_3$ and decreases in the solid solution $(Na_xLi_{1-x})VO_3$.

(ii) The zero off-set might have been caused due to the presence of defects, giving rise to an internal bias, which generates second harmonic.

(iii) Higher d.c. bias is required to drive the ferroelectric solid solutions out of the state of autostabilization at higher a.c. voltage.

(iv) The d.c. bias voltage that drives the TANDEL element out of autostabilization increases as the proportion of $NaVO_3$ in the solid solution $(Na_xK_{1-x})VO_3$ decreases and in the solid solution $(Na_xLi_{1-x})VO_3$ increases.

(v) Our results establish that the solid solutions $(Na_xK_{1-x})VO_3$ and $(Na_xLi_{1-x})VO_3$ can be used as TANDEL elements.

References

Abe Z, Koto Y and Furuhate Y 1971 *Rev. Sci. Instrum.* **42** 805
Chavan S and Patil R 1980 *Pramana—J. Phys.* **15** 85
Dvorak V, Malek Z, Mastner J, Janovec V and Glanc A 1964 *J. Appl. Phys.* **35** 1875
Malek Z, Mastner J, Hridlicka J and Janta J 1964 *Solid State Electron.* **7** 655
Mansing A and Eswar Prasad S 1977 *J. Phys. Chem. Solids* **38** 1207
Miller R 1964 *Phys. Rev.* **A134** 1313
Sawyer C and Tower C 1930 *Phys. Rev.* **35** 269

Bull. Mater. Sci. Vol. 9, No. 2, June 1987, pp. 117–121. © Printed in India.

Ionic conductivity and hopping rate data for some NASICON analogues

N B DESAI*, K BYRAPPA, A B KULKARNI* and
G S GOPALAKRISHNA
Department of Geology, University of Mysore, Manasagangotri, Mysore 570 006, India
*Department of Physics, Gulbarga University, Gulbarga 585 106, India

MS received 30 December 1986; revised 20 March 1987

Abstract. The a.c. conductivity of ionic materials shows two regions of frequency-dependent conductivity over a wide range of frequencies. Jonscher's law of dielectric response for ionic conductors enables us to characterize the conductivities. The region of low frequency dispersion approximates to a frequency-independent plateau enabling us to obtain the d.c. conductivity. In some other conductors, the presence of low-frequency dispersion cannot be neglected while determining the effective d.c. conductivity. We have used this method to extract the d.c. conductivity and hopping rate as well as to estimate concentrations of the mobile ions (carriers) in some NASICON analogues.

Keywords. Nasicon analogues; superionic conductors; solid electrolytes; hopping rate; frequency dispersion; jump frequency; mobile ion concentration.

1. Introduction

Superionic materials are being extensively investigated in recent years in view of their potential value as solid electrolytes in solid state battery systems. The ionic conductivity and other related characteristics are usually studied by a.c. techniques to avoid the necessity of developing non-blocking electrodes needed for d.c. measurements. Recently it has been suggested that a.c. conductivity data could be used to extract the hopping rates of ions in superionic materials. This technique has been applied on Na β''-alumina, $LiGaO_2$ and Ag/Na-mixed alkali β-alumina single crystals. These investigations enable us to study the role of carrier mobility and mobile ion concentrations in determining the net ionic conductivity of a particular material (Almond *et al* 1982, 1983, 1984; Almond and West 1985). In the present paper similar studies have been carried out on NASICON analogues.

NASICON (sodium superionic conductor — $Na_{1+x}Zr_2Si_xP_{3-x}O_{12}$, $0<x<3$) has been the most popular material for many years. Owing to problems connected with the synthesis, lack of stoichiometry in the final products, lack of single crystals, zirconium deficiency etc NASICON analogues (preferably pure phosphates having more simple structures and stoichiometric in composition), in the form of single crystals are being preferred.

The dielectric loss $\chi''(\omega)$ and the real part of the dielectric constant $\chi'(\omega)$ can be expressed as follows (Jonscher 1978):

$$\chi''(\omega) \propto (\omega/\omega_p)^{n_1-1} + (\omega/\omega_p)^{n_2-1}, \tag{1}$$

$$\chi''(\omega) \equiv \sigma(\omega)/\varepsilon_0(\omega), \tag{2}$$

for the hopping ion conductors and conducting solids (dipolar dielectrics) where ω_p denotes the characteristic frequency of the dielectric loss peak. The change in the conductive response from low to high frequency dispersion occurs where $\omega \approx \omega_p$. Using (1) and (2), and by identifying ω_p with the thermally activated (with an activation energy E_a) ion hopping rate, one can express the d.c. conductivity (Huggins 1975) as

$$\sigma(0) = K\,\omega_p = [Ne^2a^2/kT]\,\gamma C(\mathrm{i}-c)\,\omega_p. \tag{3}$$

The magnitude of the constant $K = \sigma(0)/\omega_p$ is largely a measure of the mobile ion concentration. γ is a geometrical factor that may include a correlation factor, C is the concentration of mobile ions on N equivalent lattice sites per unit volume, a is the hopping distance and e is the electronic charge. The thermally-activated mobile ion concentration C is the basis of the Arrhenius relation for the superionic materials. One can further analyze the a.c. conductivity as a function of the measuring frequency ω as expressed by the following equation:

$$\sigma(\omega) = K\,\omega_p{}^{1-n_1}\,\omega^{n_1} + K\,\omega_p{}^{1-n_2}\,\omega^{n_2}. \tag{4}$$

The plots of $\log_{10}\sigma(\omega)$ vs $\log_{10}\omega$ give slopes n_1 and n_2 which are non-zero in most materials studied by us. This contradicts the earlier assumption $n_1 = 0$ and $n_2 = n$ (Hill and Jonscher 1979). The tangents of $\log_{10}\sigma(\omega)$ vs $\log_{10}\omega$ plots intersect at $\omega = \omega_p$, where the conductivity equals $2\sigma(0)$. Hence one can extract the d.c. conductivity from the a.c. conductivity data. Further analysis of d.c. conductivity $\sigma(0)$ enables an assessment of the carrier mobility and mobile ion concentration in the superionic material. Based on the values of n_1 and n_2, one can classify the materials into three categories (i) those with no conductivity plateau, (ii) those with well-developed conductivity plateau and (iii) those with intermediate conductivity plateau.

2. Synthesis

NASICON analogues—$NaNi_2ZrP_3O_{12}$, $Na_2(La,Co)TiP_3O_{12}$ and $Na_2(La,Al)TiP_3O_{12}$ were synthesized in the form of small single crystals according to the method described earlier (Byrappa and Gopalakrishna 1985; Byrappa *et al* 1985, 1986).

3. Complex impedance measurements

The complex impedance measurements were carried out according to the technique reported earlier (Hodge *et al* 1976). The NASICON analogue crystals were powdered and pressed into pellets by applying 77·2 MN/m^2 pressure. The pellets (10 mm dia, 3 mm thick and 85 to 90% compactness) were provided with blocking silver electrodes on either side. These pellets were sintered in a vacuum chamber (10^{-2} torr) at 300°C. A capacitance bridge (General Radio 1620-B) was used in the present work. The pellets were placed inside an evacuated (10^{-2} torr) tubular furnace (with a three-terminal arrangement) whose temperature could be controlled with an accuracy of ± 1°C. The ionic conductivity measurements were carried out within the frequency range d.c. to 1 MHz and within the temperature range of room temperature to 330°C. Low frequency dispersion, high frequency dispersion and electrode polarization are evident in the conductivity data. The corresponding log $\sigma(\omega)$ vs $\log\omega$ plots are given in figures 1 and 2. The calculated values of ω_p, $\sigma(o)$, $\sigma(\omega_p)$, n_1, n_2 and K are given in table 1.

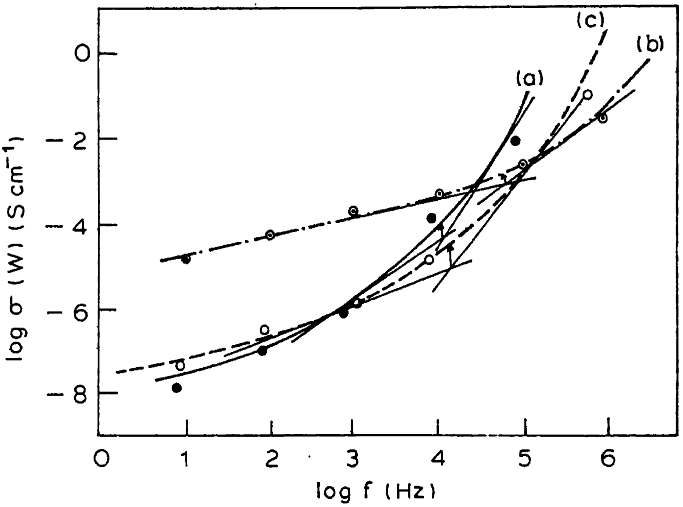

Figure 1. Log $\sigma(\omega)$ vs log ω plot for (**a**) $NaNi_2ZrP_3O_{12}$ at 60°C. (**b**) $NaNi_2ZrP_3O_{12}$ at 300°C and (**c**) $Na_2(La,Al)TiP_3O_{12}$ at 85°C.

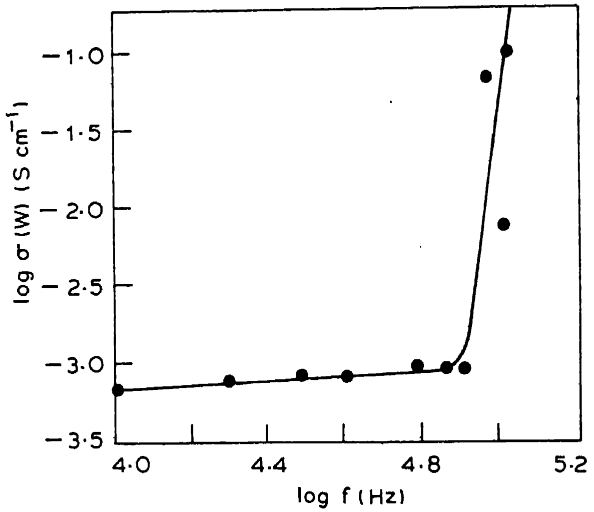

Figure 2. Log $\sigma(\omega)$ vs log ω plot for $Na_2(La,Co)TiP_3O_{12}$ at 220°C.

Table 1. Hopping rate data for NASICON analogues

Compound	T (°C)	ω_p (1/2)	$\sigma(0)$ (S cm^{-1})	(ω_p) (S cm^{-1})	n_1	n_2	K (ΩCmHz)$^{-1}$	E_a (eV)
$NaNi_2ZrP_3O_{12}$	60	634333	$3{\cdot}1 \times 10^{-5}$	$6{\cdot}3 \times 10^{-5}$	0·8	1·0	$4{\cdot}8 \times 10^{-10}$	0·6
	300	100000	$1{\cdot}99 \times 10^{-4}$	$5{\cdot}01 \times 10^{-4}$	0·4	1·06	$1{\cdot}9 \times 10^{-9}$	0·6
$Na_2(La,Co)TiP_3O_{12}$	220	75857	$7{\cdot}58 \times 10^{-4}$	—	0	4·0	$9{\cdot}98 \times 10^{-9}$	0·7
$Na_2(La,Al)TiP_3O_{12}$	85	10000	$1{\cdot}0 \times 10^{-5}$	$2{\cdot}51 \times 10^{-5}$	0·6	1·13	$1{\cdot}0 \times 10^{-10}$	0·62

4. Discussion

Almond *et al* (1984) reported two distinct regions of low and high frequency dispersion at high and low temperature regions for Na β''-alumina. In the case of $LiGaO_2$ and Na/Ag β-alumina, the corresponding regions were displayed at 856 K (and below) and 294 K (and below) respectively. Such low and high frequency dispersions have been observed in most of our materials at various temperatures (figures 1 and 2).

The slopes of the plots of log $\sigma(\omega)$ vs log ω in the high frequency dispersion regions vary from 1·00 to 1·50. The values of n_2 correspond to $n_2=2$ for an electrode response that may be simulated by a Debye-like series RC element. The change in the conductivity response from low to high frequency dispersion occurs at $\omega \approx \omega_p$. This region shifts to higher frequencies with increasing temperature, thus confirming the thermal activation of ω_p.

The magnitude of the constant K ($K=\sigma(0)/\omega_p$ equation (2)) is a measure of the mobile ion concentration. From table 1, it is seen that the values of K range from 10^{-12} to $10^{-9}\Omega^{-1}\,cm^{-1}\,Hz^{-1}$. Almond *et al* (1984) reported the following values of K for different materials:

Na β''-alumina	$1{\cdot}5\times10^{-12}\,\Omega^{-1}\,cm^{-1}\,Hz^{-1}$,
$LiGaO_2$	$1{\cdot}5\times10^{-14}\,\Omega^{-1}\,cm^{-1}\,Hz^{-1}$,
Na/Ag β-alumina	$5{\cdot}0\times10^{-13}\,\Omega^{-1}\,cm^{-1}\,Hz^{-1}$.

The NASICON analogues reported in this work show relatively higher mobile ion concentrations.

Based on the values of n_1 and n_2, the NASICON analogues have been classified into categories I and II mentioned by Almond *et al* (1984). We have observed that $NaNi_2ZrP_3O_{12}$ (at 90°C) and Na_2 (La, Co) TiP_3O_{12} belong to category I; surprisingly, $NaNi_2ZrP_3O_{12}$ becomes a material pertaining to category II at 300°C. Such a phenomenon could be explained in terms of variation in jump distance a, geometrical correlation factor and the number of available equivalent sites N per unit volume for a particular superionic as a function of temperature. Larger K values in the NASICON analogues of this work indicate to some extent a higher jump frequency, larger jump distance and a higher correlation factor. In the high frequency dispersion region, the power-law dispersion is attributed to the presence of many-body excitations in the superionic system (Ngai *et al* 1979; Dissodo and Hill 1979). The low frequency dispersion involves translational motion of ions. This dispersion may be caused by the presence of impurities and crystalline imperfections that impede the motion of ions through the lattice (Jonscher 1978). Yoshikado *et al* (1982) have shown that the low frequency dispersion in hollandite is dependent on crystalline perfection, whereas Dissado and Hill (1983) attribute the low frequency dispersion to the restricted ionic motion, i.e. in one or two dimensions. On the other hand, the high frequency dispersion and high ionic conductivity in NASICON analogues vis-a-vis Na β-alumina can be attributed to a cooperative event involving many neighbouring ions. Dygas and Brodwin (1986) carried out measurements on the frequency dependent conductivity of NASICON ceramics in the microwave region showing a lower charge correlation factor $f_c=\sigma(0)/\sigma(\omega)$ for low temperature regions.

The hopping rates for NASICON analogues vary in the order of 10^4 to 10^5 which is slightly lower than that of Na β''-alumina single crystals. This may be due to the polycrystalline nature of the NASICON analogues. The grain boundaries in polycrystalline material may decrease the hopping rate.

The values of d.c. conductivity in NASICON analogues appear in general to be smaller than that of Na β''-alumina. By further appropriate substitutions (for example, the replacement of Ti with Zr and Hf) of various elements within the framework of NASICON analogues, one can achieve higher conductivity. This work is in progress and will be reported separately.

The low frequency dispersion in the dielectric loss $\chi''(\omega)$ and the real part of the dielectric constant, $\chi'(\omega)$ are related by the Kramers-Kronig relation:

$$\chi''(\omega)/\chi'(\omega) = \mathrm{Cot}\ (n_1\pi/2). \qquad (5)$$

Appreciable values of n_1 for some of the NASICON analogues (table 1) indicate smaller χ''/χ' values. Larger χ'' values indicate higher absorption of energy by the dielectric material. Small values of n_1 in some of NASICON analogues indicate that the material does not absorb energy and instead allows it to flow through, which is an essential and important feature of a superionic conductor.

References

Almond D P and West A R 1985 *J. Electroanal. Chem.* **186** 17

Almond D P, Duncan G K and West A R 1983 *Solid State Ionics* **8** 159

Almond D P, Hunter C C and West A R 1984 *J. Mater. Sci.* **19** 3236

Almond D P, West A R and Grant R J 1982 *Solid State Commun.* **44** 1277

Byrappa K and Gopalakrishna G S 1985 *Prog. Cryst. Growth Charact.* **11** 89

Byrappa K, Gopalakrishna G S, Kulkarni A B and Venkatachalapathy V 1985 *J. Less Com. Metals* **110** 441

Byrappa K, Kulkarni A B and Gopalakrishna G S 1986 *J. Mater. Sci. Lett.* **5** 408, 519

Dissado L A and Hill R M 1979 *Nature* (*London*) **279** 685

Dissado L A and Hill R M 1983 Private Communication

Dygas J R and Brodwin M E 1986 *Solid State Ionics* **18/19** 981

Hill R M and Jonscher A K 1979 *J. Non-Cryst. Solids* **32** 53

Hodge J M, Ingran M D and West A R 1976 *J. Electroanal. Chem.* **74** 125

Huggins R A 1975 *Diffusion in solids, recent developments* (eds) A S Nowick and J J Burton (London: Academic Press)

Jonscher A K 1978 *Philos. Mag.* **B38** 587

Ngai K L, Jonscher A K and White C T 1979 *Nature* (*London*) **277** 185

Yoshikado S, Ohachi T, Taniguchi I, Onada Y, Watanabe M and Fuziki Y 1982 *Solid State Ionics* **7** 335

Bull. Mater. Sci., Vol. 9, No. 2, June 1987, pp. 123–130. © Printed in India.

Electrical properties of the system lanthanum lead cobalt titanium oxide

DEVENDRA KUMAR†, Ch. DURGA PRASAD and
OM PARKASH*
School of Materials Science and Technology, †Department of Ceramic Engineering,
Institute of Technology, Banaras Hindu University, Varanasi 221 005, India

MS received 1 April 1987

Abstract. Measurements of DC electrical resistivity and Seebeck coefficient on the perovskite system $La_{1-x}Pb_{x-\delta}\ Co_{1-x}Ti_xO_{3-\delta}$ for $0{\cdot}2 \leqslant x \leqslant 0{\cdot}9$ have been made in the temperature range 300–800 K. AC conductivity, $\sigma_{a.c.}$, of all the samples were measured as a function of temperature (300–573 K) and frequency (1 kHz–1 MHz). DC resistivity behaviour of all the samples is similar. However, the resistivity value, which varies over 5–6 orders of magnitude, depends on both the composition x and the structure of the samples. All the samples exhibit p-type electronic conduction. The value of Seebeck coefficient, α, for samples with $x \leqslant 0{\cdot}5$ initially increases with temperature up to a particular temperature. Above this temperature, the behaviour of α for samples with $x \leqslant 0{\cdot}5$ and for samples with $x > 0{\cdot}5$ over the entire temperature range is similar to that of La CoO_3. All the samples exhibit frequency-dependent a.c. conductivity at low temperatures.

Keywords. Perovskite; resistivity; Seebeck coefficient; hopping; lanthanum lead cobalt titanium oxide

1. Introduction

Lanthanum cobaltate, $LaCoO_3$, exhibits interesting electrical and magnetic properties due to co-existence of low-spin and high-spin cobalt ions in it (Raccah and Goodenough 1967; Bhide *et al* 1972). Cobalt ions which exist in the diamagnetic low-spin configuration $t_{2g}^6 e_g^0$ at very low temperatures transform to paramagnetic high-spin state $t_{2g}^4 e_g^2$ upto 200 K. Above this temperature, electron transfer occurs from the high-spin Co^{3+} ions to low-spin Co^{III} ions to give intermediate charge transfer states like Co^{2+}, Co^{IV} etc. Around 1200 K, $LaCoO_3$ undergoes a first order transition from localized to collective behaviour of d-electrons.

Replacement of La^{3+} in $LaCoO_3$ by Sr^{2+} changes its properties remarkably (Bhide *et al* 1975). Thus the system $La_{1-x}Sr_xCoO_3$ becomes ferromagnetic at low temperatures for $x > 0{\cdot}125$ due to Co^{4+}-O-Co^{3+} interactions; Co^{4+} ions being generated by Sr^{2+} substitution to maintain electrical neutrality. However, if the electrical neutrality is maintained by the simultaneous substitution of Ti^{4+} for Co^{3+} in the above system, no ferromagnetism is observed as indicated by the studies of electron-transport properties and Mössbauer spectra of the system $La_{1-x}Sr_x Co_{1-x}Ti_xO_3$ $(0{\cdot}0 \leqslant x \leqslant 0{\cdot}5)$ (Bahadur and Om Parkash 1983; Kumar *et al* 1985). This is due to the absence of Co^{4+}-O-Co^{3+} links in this system. Further, the localized character of d-electrons increases with increasing x. On the other hand, substitution of Ti^{4+} for Co^{3+} in $LaCoO_3$ gives rise to high-spin Co^{2+} ions in order to maintain a charge neutrality in the system $LaCo_{1-x}Ti_xO_3$ $(0 < x \leqslant 0{\cdot}5)$.

Recently formation of solid solution $La_{1-x}Pb_xCo_{1-x}Ti_xO_3$ has been reported for all values of x (Om Parkash *et al* 1987). These samples had some lead deficiency in them. In this paper we report the detailed electrical properties of this system in the composition range $0{\cdot}20 \leqslant x \leqslant 0{\cdot}90$.

---

*To whom all correspondence should be addressed.

2. Experimental

All the samples were prepared by ceramic method starting with AR grade lanthanum oxalate, lead monoxide, cobalt oxalate and titanium dioxide. The method of preparation has been reported earlier (Om Parkash *et al* 1987). Formation of a single phase in all the samples was established by x-ray diffraction. Chemical analysis was carried out using an atomic absorption spectrophotometer (Perkin-Elmer). Total concentration of cobalt was also determined gravimetrically using the mercury thiocyanate method. Both the results were identical. DC resistivity and Seebeck coefficient was measured as a function of temperature on sintered pellets pressed between spring-loaded platinum foils employing a digital electrometer (Keithley 616). AC conductivity of sintered pellets coated with silver paint on both sides was measured using an impedance analyzer (HP 4192 LF) as a function of temperature and frequency.

3. Results and discussion

All the samples in the study were single phase materials. Analysis of x-ray diffraction data showed that the overall symmetry was rhombohedral for $x \leqslant 0{\cdot}30$; cubic for $0{\cdot}30 < x \leqslant 0{\cdot}80$ and tetragonal for $x \geqslant 0{\cdot}90$. In an earlier report, composition with $x = 0{\cdot}30$ has been reported to have a cubic symmetry (Om Parkash *et al* 1987). A more careful analysis shows that it has a slight rhombohedral distortion with $a = 5{\cdot}525$ Å and $\alpha = 60^\circ.10'$. Similarly compositions with $0{\cdot}5 \leqslant x \leqslant 0{\cdot}8$, have an overall cubic symmetry. However, the asymmetry of diffraction lines shows that these samples have a slight tetragonal distortion with c/a ratio very close to one. This is further supported by the observed anomalies in their behaviour of dielectric constant as a function of temperature (Om Parkash *et al* 1987). Similar results have also been reported in the case of lanthanum-substituted lead zirconate titanate (Wolters and Burggraaf 1974).

Chemical analysis indicates that all the samples were lead-deficient. This is due to the loss of PbO during calcination and sintering. Once prepared, it was found that these samples are thermally stable at high temperatures (~ 1100 K) where no detectable loss in weight was observed even after heating for several hours.

Effect of substitution of Ti^{4+} and Pb^{2+} on the valence state of cobalt ions in $LaCoO_3$ can be viewed as follows: alone substitution of Ti^{4+} promotes the generation of divalent cobalt ions, Co^{2+}, as mentioned in §1. However, the simultaneous substitution of Pb^{2+} (on La^{3+} site) along with Ti^{4+} (on Co^{3+} site) reverses this process by forcing the cobalt ions to remain in the trivalent state. Due to loss of PbO during preparation, the proportionate amount of Pb^{2+} is less than Ti^{4+} as represented in the formula $La_{1-x}Pb_xTi_xO_3$ in all the samples. Therefore, the reversal of Co^{2+} to Co^{3+} as mentioned above may not be complete. It implies that some cobalt ions are in the divalent state similar to that in the system $LaCo_{1-x}Ti_xO_3$ at least upto $x \leqslant 0{\cdot}50$. Exact determination of relative concentrations of Co^{2+} and Co^{3+} ions was not possible by iodimetry due to the complex nature of the system. We can write the chemical formula of our samples as $La_{1-x}Pb_{x-\delta}Co^{3+}_{1-x-y}\,Co^{2+}_{y}Ti^{4+}_{x}O_{3-\delta-y/2}$. Values of δ for all the samples are given in table 1. It is interesting to note that the δ value is 0·21 for samples with $x > 0·50$. The density of all the samples determined by water displacement method is given in table 1.

Typical plots of Seebeck coefficient, α, as a function of temperature, T, are shown in figure 1. All the samples were found to have positive values of α over the entire

Table 1. Lead deficiency δ, density and activation energy E_a for conduction for various samples in the system $La_{1-x}Pb_{x-\delta}Co_{1-x}Ti_xO_{3-\delta}$ $(0·2 \leqslant x \leqslant 0·9)$

x	δ	Density (g/cc)	E_a (eV)
0·20	0·16	6·18	0·30
0·30	0·20	6·23	0·48
0·40	0·23	6·28	0·46
0·50	0·25	6·59	0·41
0·60	0·20	6·92	0·47
0·70	0·21	6·97	0·58
0·80	0·21	7·16	0·65
0·90	0·21	7·20	0·55

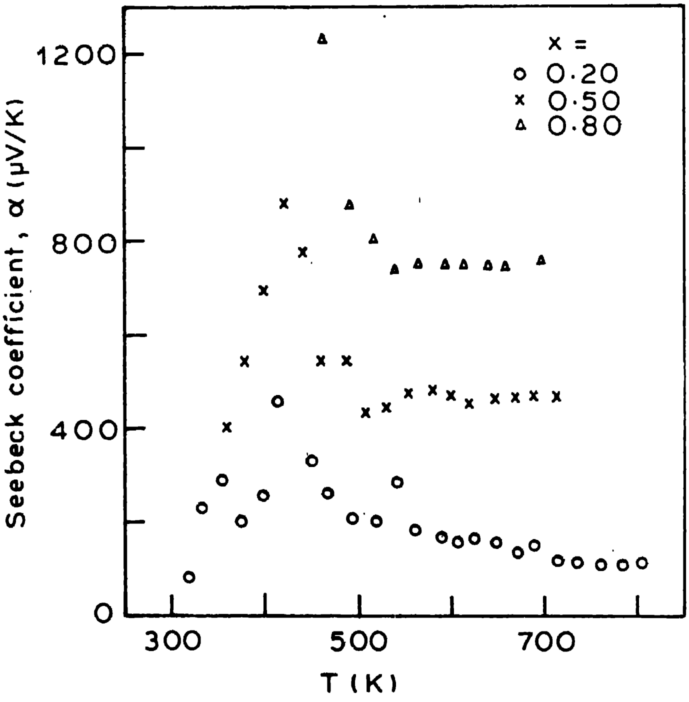

Figure 1. Variation of Seebeck coefficient α with temperature for samples with $x = 0·20$, 0·50 and 0·80 in the system $La_{1-x}Pb_{x-\delta}Co_{1-x}Ti_xO_{3-\delta}$.

range of temperature indicating that the holes are the majority charge carriers. For $0{\cdot}20 \leqslant x \leqslant 0{\cdot}50$, α initially increases with the increasing temperature and peaks at a particular temperature T_α. Above T_α, α decreases and finally becomes constant with respect to temperature. For $x > 0{\cdot}50$, α initially decreases rapidly with temperature and finally becomes constant with respect to temperature similar to samples with $x \leqslant 0{\cdot}50$. Measurements of α below 400 K were not possible for $x > 0{\cdot}50$ because of their high resistivity. The value of α increases with x. Variation of log $\rho_{\mathrm{d.c}}$ with $1000/T$ for all the samples is shown in figure 2. The resistance of the samples was found to be independent of time at a steady temperature in the temperature range of measurements. This indicates that the electrical conductivity is mainly electronic in nature. Two regions are observed in log $\rho_{\mathrm{d.c}}$ vs $1000/T$ plots of all the samples. The resistivity in region 1 decreases sharply with temperature in accordance with the Arrhenius relationship:

$$\rho = \rho_{01} \exp(-E_a/(kT)), \tag{1}$$

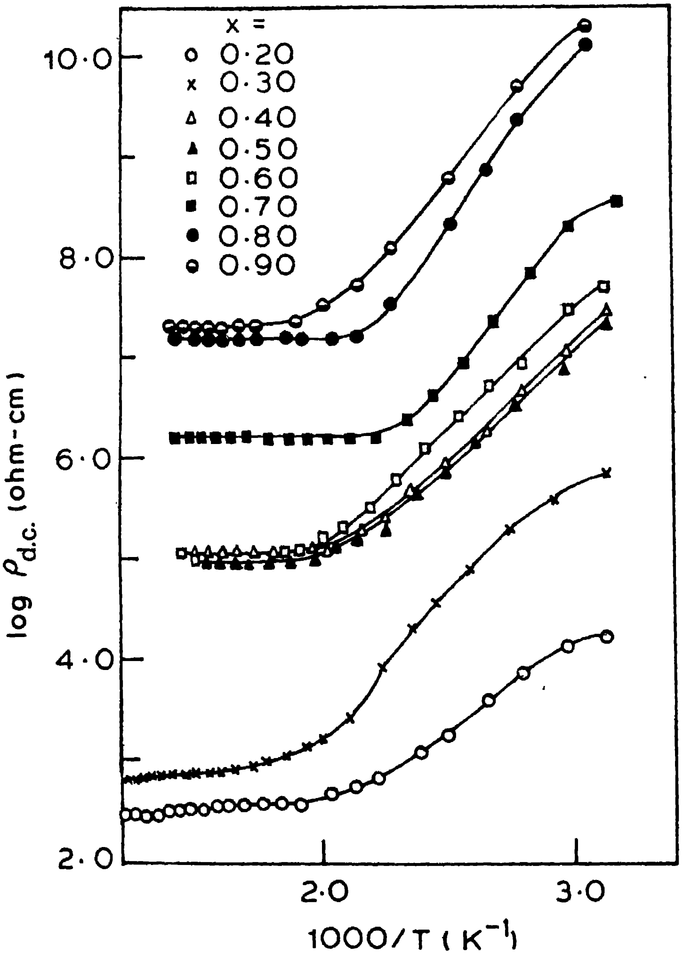

Figure 2. Variation of log $\rho_{\mathrm{d.c}}$ vs $1000/T$ for various samples in the system $\mathrm{La}_{1-x}\mathrm{Pb}_{x-\delta}\mathrm{Co}_{1-x}\mathrm{Ti}_x\mathrm{O}_{3-\delta}$.

where E_a is the activation energy for conduction in this region. Values of E_a obtained by least square fitting of data are given in table 1. For samples with $x \leqslant 0{\cdot}3$, a slight decrease in the resistivity is observed with increasing temperature in region 2, while resistivity is almost independent of temperature for all the other samples in this region. In almost all the samples region 2 starts from 450 K onwards. The resistivity value increases with x. Variations of $\rho_{0\text{I}}$, $\rho_{0\text{II}}$ and E_a with x are shown in figure 3.

The a.c. conductivity ($\sigma_{\text{a.c.}}$) was measured as a function of temperature and frequency (f). Typical plots of $\log \sigma_{\text{a.c.}}$ vs $\log f$ at a few selected temperatures for samples with $x = 0{\cdot}20$, $0{\cdot}30$ and $0{\cdot}70$ are shown in figure 4. It is observed that all the samples exhibit frequency-independent $\sigma_{\text{a.c}}$ for $T \geqslant 473$ K. This temperature is greater than T_α, the temperature of maximum Seebeck coefficient for all the samples. At lower temperatures, frequency dependence of a.c. conductivity was observed above a certain frequency below which it is frequency-independent. This frequency shifts to a higher value with increasing temperature. The variation of log $\sigma_{\text{a.c}}$ (1 kHz) with $1000/T$ for some of the samples is shown in figure 5.

DC electrical resistivity behaviour over the entire temperature range and variation of Seebeck coefficient, α, with temperature above T_α are similar to $LaCoO_3$ for all the samples. The increasing value of both these parameters with x shows that conduction is mainly due to $3d$ electrons of cobalt ions in this system. Electron transport properties of $LaCoO_3$ have been reported earlier (Bhide *et al* 1972). It is a p-type semiconductor in which low-spin Co^{III} ($t_{2g}^6 e_g^0$) ions are separated from high-spin Co^{3+} ($t_{2g}^4 e_g^2$) ions by approximately 0·08 eV. As $LaCoO_3$ is heated from very low temperature, low-spin Co^{III} ions transform to high-spin Co^{3+} ions upto 200 K. Activation energy of conduction in this region is 0·1 eV. Between 200 and 400 K, electron transfer occurs between Co^{III} and Co^{3+} ions generating an intermediate charge transfer states Co^{2+}, Co^{IV} etc. Activation energy of conduction in this region is $\sim 0{\cdot}2$ eV which represents the gap between filled t_{2g}^6 orbitals and empty σ^* band formed from e_g orbitals. Between 400 and 650 K, short range ordering of low-spin

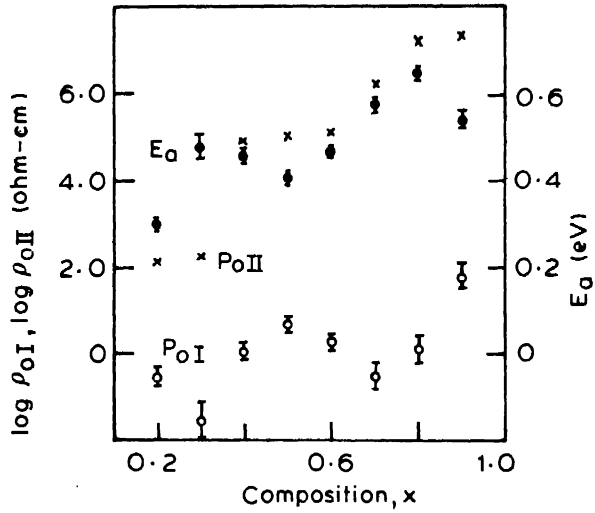

Figure 3. Variation of log $\rho_{0\text{I}}$ (O) log $\rho_{0\text{II}}$ (×) and E_a (●) with composition x in the system $La_{1-x}Pb_{x-\delta}Co_{1-x}Ti_xO_{3-\delta}$.

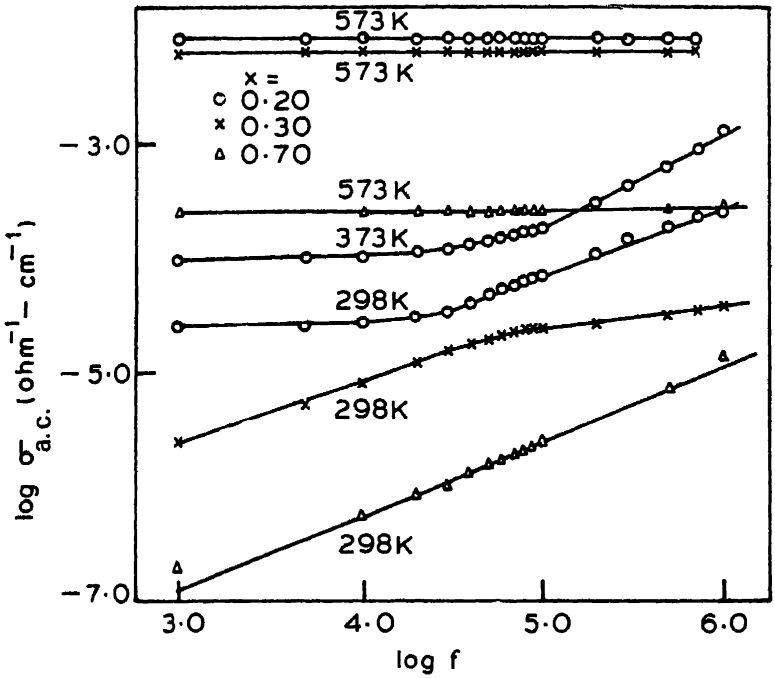

Figure 4. Variation of log $\sigma_{a.c}$ vs log f for samples with $x=0{\cdot}20$, 0·30 and 0·70 at temperatures $T=298$ and 573 K in the system $La_{1-x}Pb_{x-\delta}Co_{1-x}Ti_xO_{3-\delta}$.

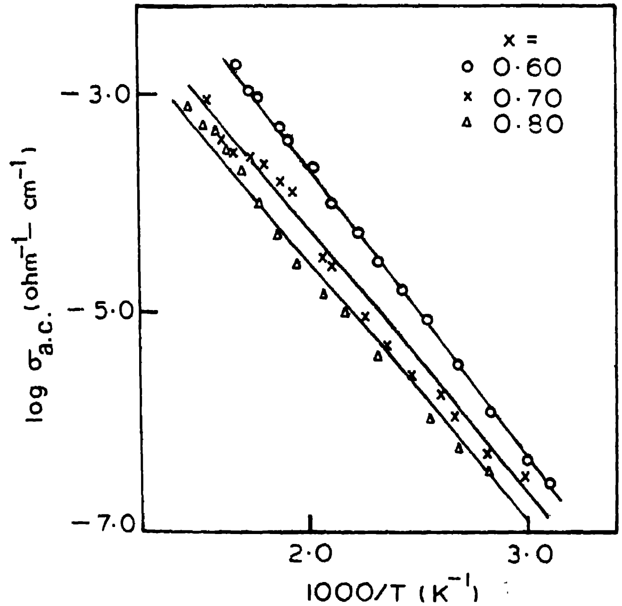

Figure 5. Variation of log $\sigma_{a.c}$ vs $1000/T$ for samples with $x=0{\cdot}60$, 0·70 and 0·80 in the system $La_{1-x}Pb_{x-\delta}Co_{1-x}Ti_xO_{3-\delta}$.

and high-spin ions occurs leading to a sharp decrease in resistivity with an activation energy of 0·54 eV. The sharp decrease in resistivity is ascribed to the small difference in energy (E_0) between low-spin and high-spin ions and to entropy associated with random spin directions (Rao *et al* 1975). Beyond 650 K resistivity changes slightly indicating almost saturation of charge carriers and finally it undergoes a first-order transition from localized to collective behaviour of *d*-electrons at 1210 K. Both electrons and holes contribute to conduction in $LaCoO_3$. The electrons are present in orbitals of e_g symmetry and holes in orbitals of t_{2g} symmetry. Their total numbers (trapped plus mobile) are equal. The *p*-type character of $LaCoO_3$ in the temperature range 300–1200 K shows mobility of holes is greater than that of electrons. In our system, for $x \leqslant 0{\cdot}5$, there are some divalent cobalt ions which act as donors. Therefore electron contribution to α increases at low temperatures. This accounts for the small values of α for these values of x. The contribution due to electrons decreases sharply upto T_α accounting for an overall increase in α. Above T_α, the behaviour is essentially similar to that of $LaCoO_3$. Increase of α below T_α may also be due to contribution of hopping of charge carriers among localized sites to the total conductivity. This hopping will be variable in nature due to random distribution of cobalt ions responsible for conduction. In this regime, α would increase with increasing T as observed experimentally (Mott and Davis 1979). Conduction occurs in the extended states above T_α. This is further supported by our results of a.c conductivity, $\sigma_{\text{a.c}}$ as a function of frequency at various temperatures (figure 4). AC conductivity is independent of frequency at temperatures greater than 473 K indicating conduction in the extended states. It is to be noted that T_α for all the samples is either less than or equal to 473 K. Below this temperature, the observed frequency dependent of a.c. conductivity in a certain frequency range also shows that there are two contributions to the observed a.c. conductivity: (i) due to conduction in the extended states which is frequency-independent and (ii) frequency dependence contribution due to hopping among localized sites. The second contribution varies according to the relation $\sigma_{\text{a.c.}} \propto \omega^s$ where s is a weak function of frequency at a particular temperature. The value of s lies within the range 0·4 to 0·7 for various samples at room temperatures. The value of s decreases with increasing temperature.

The regions of low activation energy of conduction (upto 400 K) of $LaCoO_3$ are not observed in all our samples. This may be due to slight changes in the values of crystal field splitting, Δ_{cf}, which occur due to substitution of Pb^{2+} and Ti^{4+} in $LaCoO_3$ in various amounts. The generation of Co^{3+} from Co^{III} and subsequent electron transfer from Co^{III} to Co^{3+} seems to be complete at lower temperatures as compared to $LaCoO_3$ due to such a change. Region I in our samples correspond to 400–650 K region of electrical conduction in $LaCoO_3$. Activation energies observed in this region are close to that observed in $LaCoO_3$. Above region I, a region indicating saturation of charge carriers similar to that in $LaCoO_3$ (for $T > 650$ K) is observed in all the samples. This shows that conduction process is similar to that in $LaCoO_3$ above T_α. Only the order of conductivity changes. There are two factors affecting the magnitude of conductivity. One is the decreasing concentration of cobalt ions which decreases conductivity with increasing x as mentioned earlier. The other factor is the change of structure with composition. As is clear from figure 3, E_a and $\rho_{0\text{II}}$ change considerably wherever the structure changes.

We would like to compare the behaviour of the present system with those of

$La_{1-x}Sr_xCoO_3$, $LaCo_{1-x}Ti_xO_3$ and $La_{1-x}Sr_xCo_{1-x}Ti_xO_3$. In $La_{1-x}Sr_xCoO_3$ and $LaCo_{1-x}Ti_xO_3$, the substitutions of Sr^{2+} and Ti^{3+} respectively generate Co^{4+} ions and Co^{2+} ions to maintain the overall charge neutrality. Due to the change of valence state of cobalt ions, the properties of these two systems are considerably different from that of $LaCoO_3$ (Bhide *et al* 1975; Bahadur and Om Parkash 1983; Kumar *et al* 1986). In $La_{1-x}Sr_xCo_{1-x}Ti_xO_3$, due to simultaneous substitution of Sr^{2+} and Ti^{4+}, though the valence state of cobalt ions remains the same (Kumar *et al* 1986), the electron transport properties are different from that of $LaCoO_3$. This is due to replacement of La^{3+} by Sr^{2+} which increases both the overlap integrals b^{σ} and b^{π} (Goodenough 1974). In the present system replacement of La^{3+} by Pb^{2+} does not affect these parameters much and hence the behaviour of 3*d*-electrons of cobalt ions. Therefore, the behaviour is very similar to that of $LaCoO_3$ except that due to random distribution of cobalt ions, hopping conduction seems to contribute partly to the electron transport in this system. Hopping conduction has also been observed in other systems mentioned above.

Acknowledgements

The authors express their gratitude to Prof. C N R Rao for useful discussions and constant encouragement. We are thankful to Dr Lakshman Pandey for useful discussions during these investigations. Thanks are due to the Department of Science and Technology, Government of India for financial assistance.

References

Bahadur D and Om Parkash 1983 *J. Solid State Chem.* **46** 197

Bhide V G, Rajoria D S, Rao G R and Rao C N R 1972 *Phys. Rev.* **B6** 1021

Bhide V G, Rajoria D S, Rao C N R, Rao G R and Jadhao V G 1975 *Phys. Rev.* **B12** 2832

Goodenough J B 1974 *Solid state chemistry* (ed) C N R Rao (New York: Marcel Dekker) pp 348

Kumar V, Singru R M, Om Parkash and Bahadur D 1985 *Phys. Status Solidi* **B128** 223

Mott N F and Davis E A 1979 *Electronic processes in non-crystalline materials* (Oxford: Clarendon Press) 2nd ed., pp 239

Om Parkash, Prasad C D and Kumar D 1987 *J. Solid State Chem.* (in press)

Raccah P M and Goodenough J B 1967 *Phys. Rev.* **155** 932

Rao C N R, Bhide V G and Mott N F 1975 *Philos. Mag.* **32** 1277

Wolters M and Burggraaf A J 1974 *Phys. Status Solidi* **A24** 341

Bull. Mater. Sci., Vol. 9, No. 2, June 1987, pp. 131–136. © Printed in India.

Pressure-induced band cross-over in $Pb_{1-x}Sn_xTe$

T G RAMESH, V SHUBHA and P S GOPALAKRISHNAN
Materials Science Division, National Aeronautical Laboratory, Bangalore 560 017, India

MS received 27 March 1987

Abstract. Resistivity and thermoelectric power studies have been carried out on two semiconductor alloy systems viz $Pb_{0.8}Sn_{0.2}Te$ and $Pb_{0.6}Sn_{0.4}Te$ up to 35 kbar pressure. Thermoelectric power and resistivity data on $Pb_{0.8}Sn_{0.2}Te$ indicate that the energy gap $E_g = E_{L_6^-} - E_{L_6^+}$ decreases with pressure resulting in a zero gap state near 35 kbar pressure. TEP studies on the alloy system $Pb_{0.6}Sn_{0.4}Te$ provide direct evidence for a pressure induced $L_6^- \rightarrow L_6^+$ cross over transition.

Keywords. Thermoelectric power; band cross-over; narrow gap semi-conductors; lead tin telluride.

1. Introduction

The semiconducting alloy system $Pb_{1-x}Sn_xTe$ has received considerable attention in recent years in view of its importance as an infrared detector material and also as a thermoelectric material (Ravich *et al* 1970). It is known that these solids are semiconductors having a rocksalt crystal structure throughout the range $0 \leqslant x \leqslant 1$. Band structure calculations (Conklin *et al* 1965) show that the valence and conduction band extrema in the Pb salts occur at the L-point in the Brillouin zone. In PbTe the conduction band is L_6^- while L_6^+ is the valence band. Since these bands have only a two-fold spin degeneracy, it is a semiconductor. Due to relativistic effects, alloying with SnTe results in a reduction of the energy gap $E_g = E_{L_6^-} - E_{L_6^+}$ (Verie 1973). According to the band model proposed by Dimmock *et al* (1966), E_g decreases upon alloying and beyond a certain concentration the valence and conduction bands cross over and exchange roles. The application of pressure also leads to a reduction of the principal energy gap E_g. Akimov *et al* (1978) used galvanomagnetic and oscillatory effects as a means for determining the energy band parameters of $Pb_{1-x}Sn_xTe$ alloys with $x = 0{\cdot}18$ and $0{\cdot}23$ under pressure. These authors found that there is a pressure-induced transition to the zero gap state in these alloy systems. A considerable increase in the hole relaxation time was observed on transition to the zero gap state under pressure which was attributed to a reduction in the density of states and an increase in the Fermi energy. These authors also found that at a particular pressure there is an inversion in the band structure.

In this paper we report some new measurements of TEP and resistivity behaviour of the alloy systems $Pb_{0.6}Sn_{0.4}Te$ and $Pb_{0.8}Sn_{0.2}Te$ upto 35 kbar pressure. The pressure behaviour of TEP in $Pb_{0.6}Sn_{0.4}Te$ gives clear evidence for a pressure-induced L_6^- to L_6^+ cross-over near 13 kbar at ambient temperature, whereas the $Pb_{0.8}Sn_{0.2}Te$ system approaches a zero gap state near 35 kbar. The temperature behaviour of TEP and resistivity at different pressures strongly suggest that these systems are degenerate semiconductors.

2. Experimental procedure

Samples of $Pb_{0\cdot8}Sn_{0\cdot2}Te$ and $Pb_{0\cdot6}Sn_{0\cdot4}Te$ were prepared by taking the stoichiometric ratios of high purity PbTe and SnTe and melting the mixture. The mixture was homogenized by repeated melting. Crystals of these samples were then grown using the Bridgman technique. The techniques for high resolution TEP measurement in a piston-cylinder apparatus under controlled conditions of both temperature and temperature gradient have been described elsewhere (Shubha and Ramesh 1986a,b). The experimental data were collected in the teflon cell arrangement with silicone fluid as the pressure-transmitting medium (Shubha and Ramesh 1986a).

3. Results

3.1 $Pb_{0\cdot6}Sn_{0\cdot4}Te$

The variation of TEP and resistivity with pressure near ambient temperature is shown in figure 1. The samples are *p*-type and TEP exhibits a marked pressure dependence with a minima near 13 kbar. Resistivity, however, continuously decreases with pressure with no feature near 13 kbar. We attribute the minima in the TEP vs pressure graph to the pressure induced $L_6^- - L_6^+$ cross-over transition. The isotherms of TEP vs pressure upto 150°C are given in figure 2. It may be noted that the pressure corresponding to the minimum in the TEP vs pressure plot shifts to higher values with increase in temperature. This is related to the temperature variation of the principal energy gap $E_g = E_{L_6^-} - E_{L_6^+}$ which will be discussed later. In contrast, the isotherms of resistivity (figure 3) do not show any features near the pressure corresponding to the band cross-over.

The temperature behaviour of the resistivity at different pressures for the

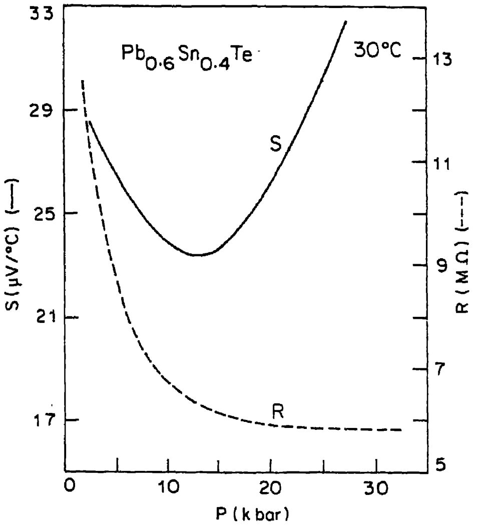

Figure 1. Resistivity (dashed curve) and thermopower (solid line) vs pressure in $Pb_{0\cdot6}Sn_{0\cdot4}Te$.

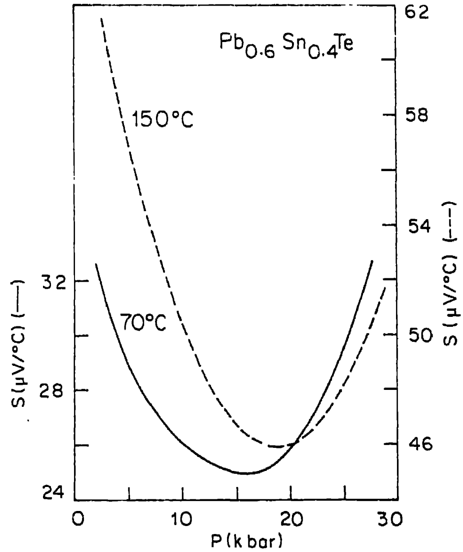

Figure 2. Isotherms of TEP variation with pressure.

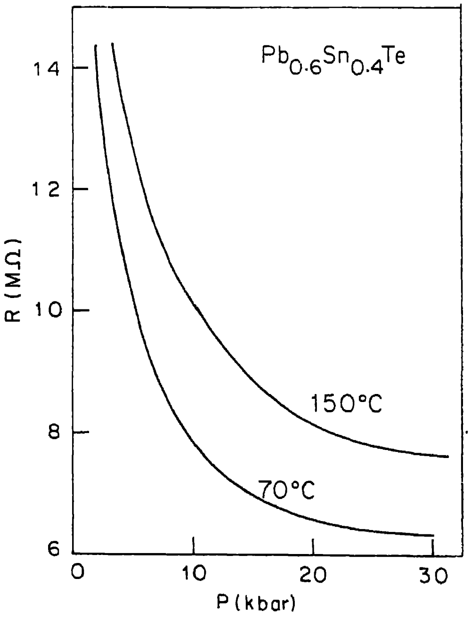

Figure 3. Isotherms of resistivity variation with pressure.

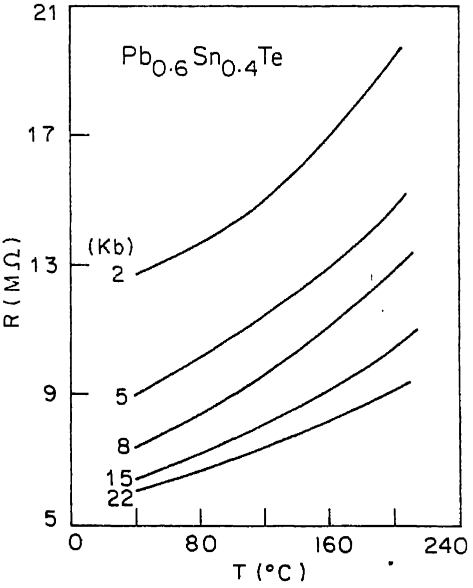

Figure 4. Resistivity vs temperature at different pressures.

$Pb_{0.6}Sn_{0.4}Te$ system is given in figure 4. The positive temperature coefficient of resistivity clearly points out that the samples under study are degenerate semiconductors. The positive temperature coefficient of TEP (dashed curves in figure 5) also supports this view.

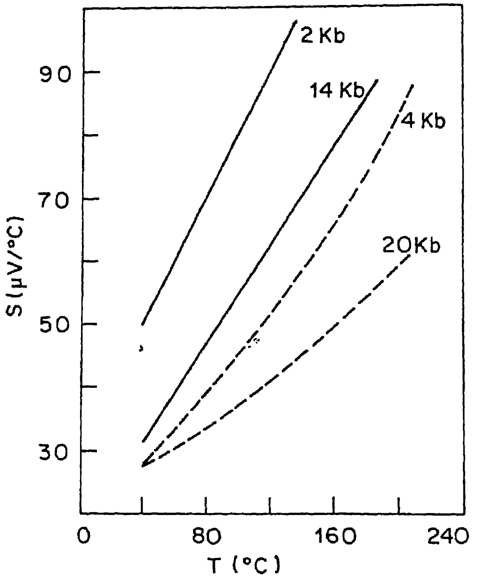

Figure 5. TEP variation with temperature in $Pb_{0.6}Sn_{0.4}Te$ (dashed lines) and $Pb_{0.8}Sn_{0.2}Te$ (solid lines).

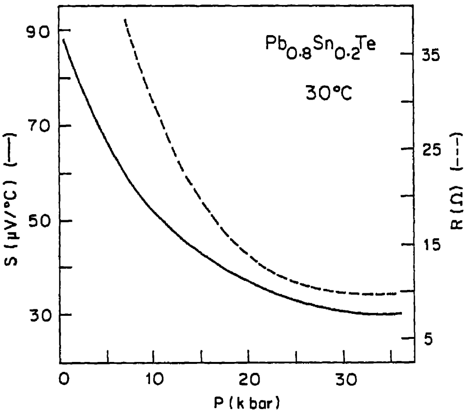

Figure 6. Resistivity (dashed curve) and thermopower (solid line) vs pressure in $Pb_{0.8}Sn_{0.2}Te$.

3.2 $Pb_{0.8}Sn_{0.2}Te$

Figure 6 presents the TEP and resistivity data for $Pb_{0.8}Sn_{0.2}Te$ as a function of pressure. Both TEP and resistivity continuously decrease with pressure upto 35 kbar. This alloy system has a higher energy gap $E_g = 220$ MeV as compared to the $Pb_{0.6}Sn_{0.4}Te$ system ($E_g \simeq 110$ MeV) and a comparison with the TEP data in figure 1 suggests that in this system a zero gap state is reached around 35 kbar. The band cross-over would occur at a higher pressure. The temperature behaviour of TEP (solid line in figure 5) differs from that of $Pb_{0.6}Sn_{0.4}Te$ (dashed curves in figure 5) in which it is highly linear. The isobars at 2 and 14 kbars are well separated from each other compared to the isobars at 4 and 20 kbars of $Pb_{0.6}Sn_{0.4}Te$ because in the latter case TEP is a double-valued function of pressure due to the band cross-over. The temperature behaviour of resistivity is very similar to that in the $Pb_{0.6}Sn_{0.4}Te$ system (figure 4).

4. Discussion

It is now well established that lead chalcogenide alloys exhibit a pressure-induced semiconductor-semiconductor transition corresponding to the $L_6^- - L_6^+$ cross-over. Earlier resistivity measurements at different temperatures under pressure did not permit clear conclusions about a band-crossing induced by pressure (Melngailis *et al* 1970). Strong evidence for a cross-over however came by the observation of the emission wave length λ of a PbTe-rich alloy diode laser subjected to high pressures at 77°K (Martinez 1973c). The emission wavelength increases upto 20 μm, followed by an extinction with increasing pressure and then by the reappearence of laser emission in the high pressure region. These results are in complete conformity with the band model proposed by Dimmock *et al* (1966). According to this model, dE_g/dP changes sign from negative to positive values in going from an inverted band ordering to a normal situation.

The present TEP and resistivity measurements under pressure can also be understood on the basis of the Dimmock model. The temperature behaviour of both resistivity and TEP (figures 4 and 5) imply that the semiconducting samples are highly degenerate. Further, the Hall effect measurements under pressure (Martinez 1973b) clearly show that the carrier concentration is more or less independent of pressure. Thus the resistivity variation with pressure is the inverse of the mobility variation. Martinez (1973b) noted that the pressure dependence of the mobility is quite different for *n*-and *p*-type samples of equivalent carrier concentrations. In particular, for *p*-type samples the mobility does not reach the expected maximum value near $E_g = 0$ and gets shifted considerably towards the negative gaps i.e. towards the region where the band ordering is reversed. Thus the resistivity continues to decrease with pressure even after the cross-over transition (figures 1 and 3).

In contrast to the resistivity behaviour TEP variation gives clear evidence for the band cross-over in the $Pb_{0\cdot 6}Sn_{0\cdot 4}Te$ system (figures 1 and 2). We interpret these results using the TEP expression appropriate to metallic samples as these systems are highly degenerate. Then the variation of TEP with pressure mainly stems from the dependence of the Fermi energy E_F on the energy gap with the condition that the carrier concentration remains unchanged with pressure. Model calculations on the behaviour of Fermi energy for a given number of carriers, when the gap is varying (either due to pressure or alloying) in Kane type band structures have been performed by Martinez (1973a). These calculations show that the Fermi energy E_F passes through a maximum at $E_g = 0$. Figure 7 gives the schematic diagram of band inversion induced by pressure appropriate to lead salts. Figure 8 shows the variation of Fermi level as a function of E_g (or pressure) for a given carrier concentration. It is clear that as TEP is inversely related to E_F, TEP should exhibit a minimum near the band cross-over transition. At ambient pressures $Pb_{0\cdot 6}Sn_{0\cdot 4}Te$ has the band ordering with L_6^- as the conduction band and L_6^+ as the valence band. Since $E_g = E_{L_6^-} - E_{L_6^+}$ decreases with pressure (dE_g/dP is negative), TEP also decreases with

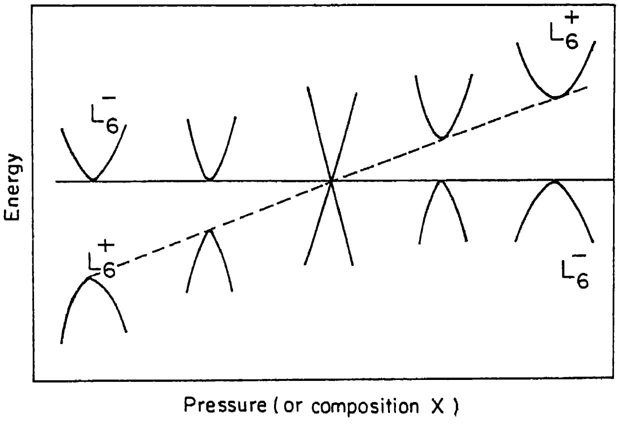

Figure 7. Schematic energy band structure for $Pb_{1-x}Sn_xTe$.

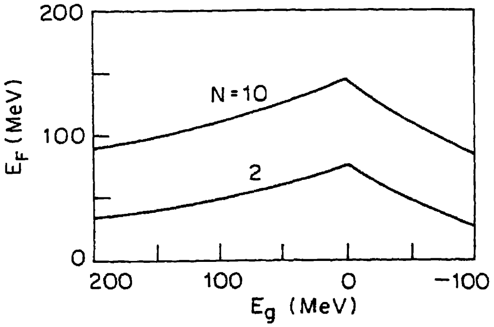

Figure 8. Variation of Fermi energy as a function of E_g for a given carrier concentration N (in $10^{18}\,\mathrm{cm}^{-3}$ units).

pressure. After the cross-over $\mathrm{d}E_g/\mathrm{d}P$ becomes positive and TEP increases with pressure. Using the reported values of $E_g \approx 110\,\mathrm{MeV}$ at 300°K and $\mathrm{d}E_g/\mathrm{d}P = -8{\cdot}6\,\mathrm{MeV/kbar}$ (Martinez 1973a), E_g should become zero near 12·8 kbar. This correlates well with the present experimental observation of the minimum in TEP vs pressure curve near 13 kbar (figure 2) which we attribute to the band cross-over transition. The shift in the pressure corresponding to the minimum with temperature (figure 2) can be understood by noting that the temperature coefficient of E_g is positive for the lead rich alloys (Dimmock *et al* 1966). With increasing temperature E_g increases and therefore the pressure required to reach the zero gap state should also increase. Thus we can account for the shift towards higher pressures in the TEP vs pressure plot with increasing temperature.

Acknowledgement

The authors thank Mr K Jagannatha Rao for skilled assistance in the experimental work.

References

Akimov B A, Vadkhva R S and Chudinov S M 1978 *Sov. Phys. Semicond.* **12** 1146
Conklin J B, Johnson L E and Pratt G W 1965 *Phys. Rev.* **A137** 1282
Dimmock J O, Melngailis I and Strauss A J 1966 *Phys. Rev. Lett.* **16** 1193
Martinez G 1973a *Phys. Rev.* **B8** 4678
Martinez G 1973b *Phys. Rev.* **B8** 4686
Martinez G 1973c *Phys. Rev.* **B8** 4693
Melngailis J, Harman T C and Kafalas J A 1972 in *Proc. Int. Conf. on the Physics of IV–VI Compounds*, Philadelphia
Ravich Yu I, Efimova B A and Smirnov I A 1970 *Semiconducting lead chalcogenides* (New York, London: Plenum Press)
Shubha V and Ramesh T G 1986a *Rev. Sci. Instrum.* **57** 473
Shubha V and Ramesh T G 1986b *High Temp. High Press.* **18** 311
Verie C 1973 in *New developments in semiconductors* (eds) P R Wallace, R Harris and M J Zuckermann (Leiden: Noordoff Int. Pub.) p. 510

Bull. Mater. Sci., Vol. 9, No. 2, June 1987, pp. 137–147. © Printed in India.

A study of Vishnukundin coins

M VIJAYAKUMAR*, M C GANORKAR, V PANDIT RAO and P GAYATHRI
*Defence Metallurgical Research Laboratory, Kanchanbagh, Hyderabad 500 258, India
Division of Scientific Studies, Birla Archaeological and Cultural Research Institute, Hyderabad 500 036, India

MS received 27 February 1987

Abstract. Three types of Vishnukundin coins belonging to Andhra region were subjected to chemical and microstructural studies. The source of the ores used, the nature of the alloy and the techniques employed have been inferred from the data obtained. Trace elemental data have shown that the coins were made of unrefined metal which was also confirmed by electron microprobe results.

Keywords. Coin; Vishnukundin; chemical analysis; microstructural study.

1. Introduction

Vishnukundins were a major dynasty since the fall of the Satavahanas which enjoyed imperial status over the entire Andhra region including Kalinga (Orissa) and some parts of Maharastra. The period of Vishnukundin rule was about 140 years from 475 A.D. During their rule, they have issued a number of coins some of which have been studied (Rama Rao 1963; Hegde 1975).

The Birla Archaeological and Cultural Research Institute (BACRI) obtained about 500 coins belonging to the Vishnukundin period from a local antique dealer. The Andhra Pradesh State Department of Archaeology and Museums (SDAM) also has a number of Vishnukundin coins obtained through excavation, exploration and treasure troves from various parts of Andhra Pradesh. Compositional and microstructural study of these coins can provide a clue to the materials used and the distinctive techniques employed during the period in making the coins. Viewing with this hindsight, it is also possible to gauge the technological competence and expertise available in the various regions. We have chosen the following three types of Vishnukundin coins for a detailed investigation: (a) BACRI coins said to be obtained from the Nalgonda area, though details are not known clearly. (b) Kesaragutta coins obtained from the Kesaragutta excavations, Ranga Reddy district, AP by the State Department of Archaeology and Museums, and (c) Tangadupalli coins obtained from a treasure trove at Tangadupalli Village, Nellimarla taluka, Vizianagaram District, AP again by the State Department of Archaeology and Museums.

All the three types of coins were round in shape and showed a lion in a circle on the obverse and a sankha flanked by lampstands on either side inside a rayed circle on the reverse, which is typical of the designs on the coins of Vishnukundin period (figure 1). BACRI coins had surface cracks and were covered with red and black incrustations. Most of the Kesaragutta and Tangadupalli coins on the other hand were in fairly good condition, and legends and designs could be clearly seen. A few had surface cracks. Greenish and black incrustations were also noticed.

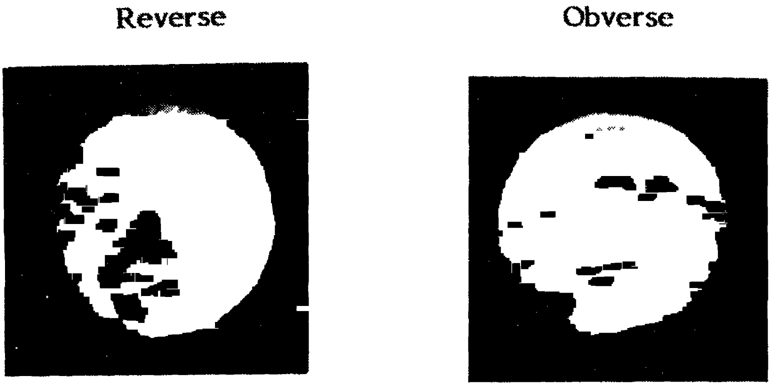

A. BACRI coins

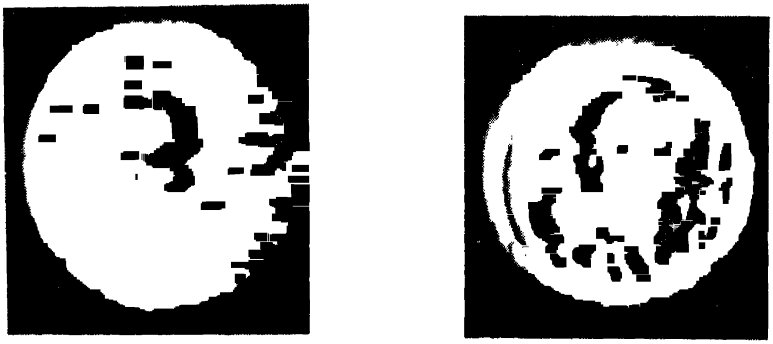

B. Kesaragutta coins

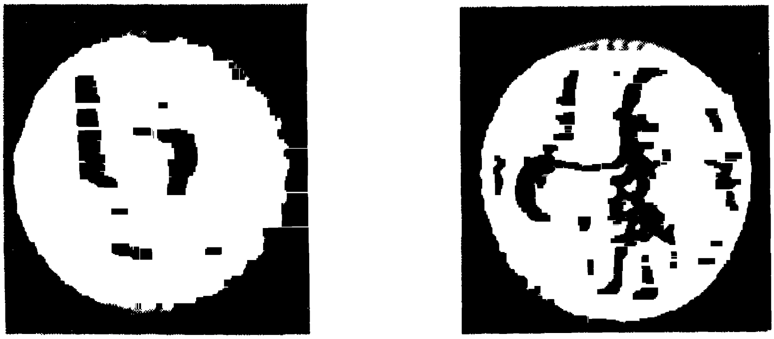

C. T coins

Figure 1. Photographs of the BACRI, Kesaragutta and Tangadupalli coins.

This paper presents the details of our investigation on chemical and microstructural aspects of these coins of the Vishnukundin period.

2. Experimental

About 1–5 mg of the coin samples were obtained with the help of microdriller from the rim of each coin after removing the surface incrustations carefully. The samples thus obtained were screened by the use of a medium Hilger-Watts large quartz spectrograph to know the composition qualitatively. The quantitative chemical analyses were carried out using an atomic absorption spectrophotometer (Perkin Elmer 2380).

Microstructural studies were carried out on a cut cross-section of the coins after mounting the pieces in Bakelite, polishing and etching it with ferric chloride. All microchemical studies were done using a scanning electron probe microanalyzer, (Camebax-Micro) equipped with a microprocessor-controlled wavelength dispersive spectrometer system for x-ray analysis.

3. Results and discussion

3.1 *Physical measurements*

Table 1 summarizes physical measurements of the Vishnukundin coins. The coins of the BACRI museum are significantly thinner and smaller than the Kesaragutta and Tangadupalli Vishnukundin coins. The average weight of the BACRI coins is about 3·34 g and the average maximum and minimum diameters, 1·55 cm and 1·48 cm respectively. The thickness is not uniform throughout the coin. The average weights

Table 1. Physical measurements data of Vishnukundin copper coins.

Weight (g)	Maximum diameter (cm)	Minimum diameter (cm)	Thickness (cm)
	BACRI coins		
2·944	1·53	1·50	0·32
3·241	1·40	1·35	0·46
3·024	1·50	1·50	0·31
3·902	1·55	1·48	0·47
3·735	1·71	1·55	0·34
4·175	1·53	1·48	0·57
	Kesaragutta coins		
6·722	2·10	2·00	0·48
5·140	1·89	1·85	0·39
6·063	2·00	1·85	0·41
6·010	1·87	1·81	0·41
	Tangadupalli coins		
6·522	2·10	2·03	0·41
6·759	2·50	2·30	0·40
6·840	2·30	2·25	0·48
5·851	1·98	1·97	0·39

of Kesaragutta and Tangadupalli coins are about 5·98 g and 6·49 g respectively which are heavier compared to the BACRI museum coins. The average maximum and minimum diameters of the Kesaragutta coins are 1·97 cm and 1·88 cm respectively and the average thickness is 0·42 cm. For Tangadupalli coins, the average maximum diameters are 2·22 cm and 2·14 cm respectively, and the thickness is 0·42 cm. The thickness is almost uniform throughout the coin.

3.2 *Chemical composition*

Table 2 contains the chemical composition of 6 representative coins out of 200 coins of the BACRI museum, along with those of 4 Kesaragutta coins and 4 Tangadupalli coins. Analyses have been carried out to delineate the range of composition for each of the two major, one minor and a few trace elements, i.e. Cu, Sn, Fe, Co, Pb, Ag, Cr.

The material of all the three types of coins was found to be Cu-Sn bronze. The Cu-Sn ratio in the coins from three places varied from 2·58 to 3·79. The analytical values show the presence of tin upto 20–25%. These results were further confirmed by electron probe microanalysis. It appears that the Cu:Sn ratio is almost perfectly maintained to mint the bronze coins or the so-called tin money in all coins of three different places of this dynasty. The main object of adding tin to the copper in ancient metallurgy is for work hardening and improved castings (Agarwal 1969; Catling 1977; Scott 1980).

The chemical analysis of Vishnukundin copper coins showed appreciable quantity of iron (table 2). Although iron is present in some coins upto 11·92%, the coins are not attracted by magnet. On the contrary, the analysis of Paunar* coins of the same dynasty was shown to contain iron upto 23% and are attracted by magnet; it was

Table 2. Chemical composition of Vishnukundin copper coins.

Cu%	Sn%	Fe%	Co%	Pb%	Ag%	Cr%	Cu/Sn
			BACRI museum coins				
76·22	21·02	2·18	—	0·45	0·04	0·09	3·62
72·73	24·53	1·46	0·26	0·50	—	0·23	2·96
74·13	20·67	3·33	0·33	0·50	0·04	0·25	3·59
72·06	22·07	2·75	0·99	0·67	0·05	0·15	3·26
77·87	20·50	0·44	0·38	0·44	0·02	0·30	3·79
72·02	24·73	2·47	0·13	0·21	0·02	0·08	2·91
			Kesaragutta coins				
71·57	24·17	3·68	0·02	0·18	0·02	0·01	2·96
73·80	22·08	3·75	0·01	0·11	0·03	0·01	3·34
71·60	24·15	4·03	0·01	0·17	0·04	0·02	2·96
72·50	23·99	3·13	0·02	0·15	0·02	0·01	3·02
			Tangadupalli coins				
72·56	23·07	3·98	0·10	0·12	0·03	0·02	3·15
73·97	22·03	3·39	0·02	0·25	0·02	0·02	3·36
73·50	21·81	5·65	0·05	0·21	0·03	0·01	3·37
63·25	24·56	11·92	0·08	0·18	0·02	0·02	2·58

---

*Paunar (20°·27′N, 78°·41′E), a village in the Wardha Taluka of Wardha Dist., Maharashtra, India suggested that those coins were alloyed with iron and some contained iron ore (Hegde 1975).

The presence of trace elements (see table 2) associated with the coins of all the places suggests that no elaborate treatment was carried out for refining the metals/ores.

3.3 *Microstructural studies*

Figures 2 and 3 show the optical micrographs and the x-ray elemental distribution maps for the cross-section of a BACRI coin. The cross-section exhibits a three-layered structure. The right side of figure 2A shows the completely corroded layer, and the centre, the partially corroded one. The interior region is shown in figure 2B. The microstructure in figures 2 and 3 clearly reveals a two-phase structure in the interior as well as partially corroded regions. Quantitative electron probe micro-analysis indicates the composition of the light etching phase to be Cu-15 wt% Sn, and that of matrix phase to be Cu-25 wt% Sn in the interior region. The composition of the matrix phase in the outer regions, however, is found to be 28 wt% Cu-51 wt% Sn-3 wt% Fe-O ($Cu_2O + 2SnO_2$) thus showing it to be an oxide phase formed probably because of weathering due to bad preservation of the coin. Iron particles containing about 2–8 wt% Cu, appearing as black features in figure 2B and white inclusions in the absorbed current image in figure 3 are also seen in the interior region. The microstructure of the inner and the partially corroded layer also shows a few sulphide particles of size $< 5\ \mu m$. Its composition in the inner region is Cu-14 wt% Fe-26 wt% S, and in the outer region, Cu-19 wt% S.

The microstructure of the Tangadupalli coin is shown in figure 4. Figure 4A indicates equiaxed, well-refined grains with a fine dispersion of precipitates in the grains. Iron particles (black features in figure 4B), pure copper regions enveloped by dark green phases (figure 4C) and grey particles (figure 4A) are also seen in the microstructure. The greenish phases appear as big lumps, sometimes as big as 1 mm in diameter, while grey phases appear as small inclusions throughout the matrix. Microprobe studies indicate that the matrix is Cu-25 wt% Sn, the dark green phases are copper and tin oxides of uncertain composition, and the grey inclusions are sulphide ore particles having Cu-13 wt% Fe-28 wt% S. The greenish phase and pure copper regions contain a small amount of iron also. The elemental distribution maps of a region near a dark green feature in figure 5 clearly show the iron particles and sulphide inclusions along with copper and tin rich regions of the greenish phase.

Material-wise, Kesaragutta coin appears to be the same as the Tangadupalli coin but for one major difference in that the microstructures, shown in figure 6, do not indicate any refined grains. Similar to the Tangadupalli coin, the microstructure shows pure copper regions surrounded by dark green phases, iron particulates and sulphide ore inclusions of same composition.

Chemical and microstructural evidence strongly suggests that the starting materials used are the same for Tangadupalli and Kesaragutta coins. The sulphide particles present have a composition close to that of bornite, Cu_5FeS_4, suggesting that bornite ore, available only in the Agnigundala area of Nallakonda, Guntur District (AP) was the source of copper. It was also confirmed by geologists that the minerological zoning (depthwise) was observed in the Nallakonda block and surface sections were rich in bornite followed by chalcopyrite and galena at depth (Rama

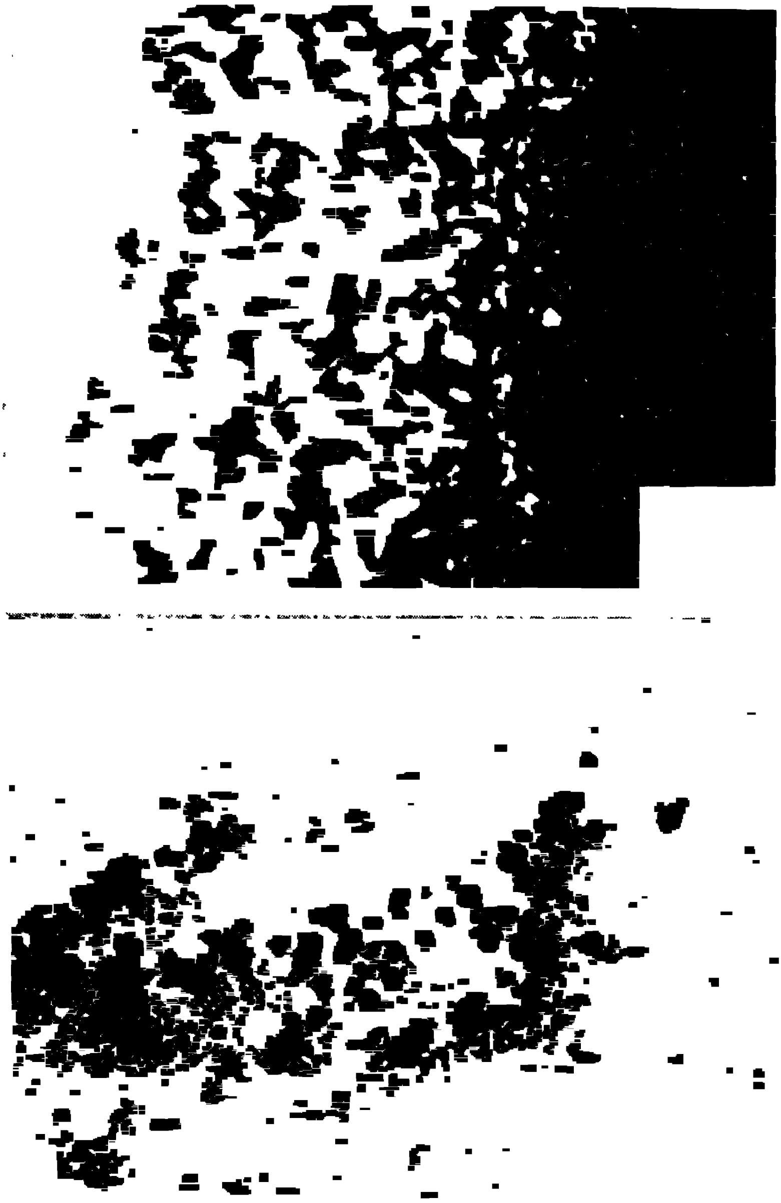

Figure 2. Photomicrographs of a cross-section of BACRI coin.

Rao 1952). The presence of copper-tin-oxide regions indicates that cassiterite, an oxide ore of tin was used as the source of tin. This is so because tin oxide has a melting point of 1630°C compared to 231·9°C of pure tin, and hence is likely to be left undissolved at the temperatures used for making copper. It is probable that copper and tin ores were intimately mixed, partially oxidized, and then reduced to get the alloy. Such a method is likely to leave copper-tin-oxide regions noticed in the microstructure of both Tangadupalli and Kesaragutta coins. BACRI coin, on the

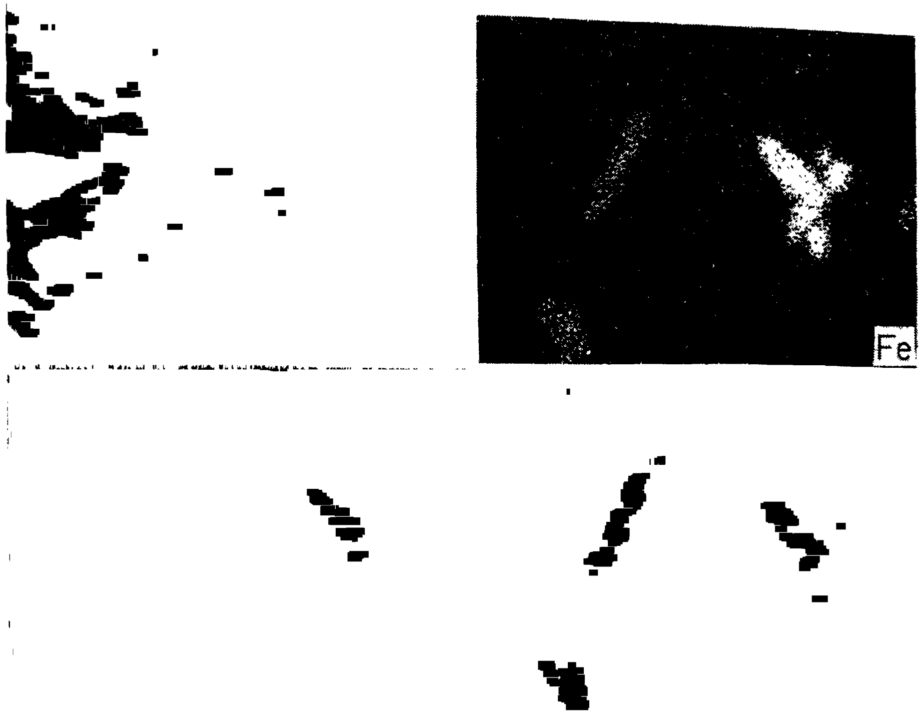

Figure 3. X-ray elemental distribution maps of a BACRI coin.

other hand, does not show any tin oxide particles left in the matrix, indicating that pure tin itself has possibly been used in making the alloy. The difference in the source of raw materials and their processing for Tangadupalli and Kesaragutta coins on the one hand, and BACRI coins on the other are also borne out by the difference in the Pb, Co and Cr content of the coins (see table 2). It is also interesting to note that silica inclusions are not seen in the microstructure. Thus the ores have been processed well to remove all the extraneous material.

The solubility of iron in bronze is very low. So, iron present in the copper ore has precipitated in the matrix. In fact, in many of the copper coins, it is very likely that the total iron present has come only from the copper ore as a consequence of bad melting practice rather than by deliberate addition as has been suggested earlier (Hegde 1975).

Microstructure of the BACRI coin suggests it to be in the as-cast condition. In the partially corroded regions, however, twinning was observed, suggesting that this outer layer has been worked and later annealed. The composition indicates that the light etching alpha phase is present in a matrix of $(\alpha+\delta)$. Tangadupalli coin, however, appears to have been worked and annealed resulting in well-refined grain structure as shown in figure 4A. Annealing in high tin bronze is known to result in the precipitation of ε phase as a fine dispersion (Reeves *et al* 1953), and this is also noticed in the microstructure. Micrographs in figure 6 showing the acicular α-needles in a matrix of δ-phase indicate a martensitic type of structure produced by water quenching of tin bronze with about 25 wt% Sn after annealing at 700–750°C i.e. in the β-region of the

Figure 4. Photomicrographs of a cross-section of a Tangadupalli coin.

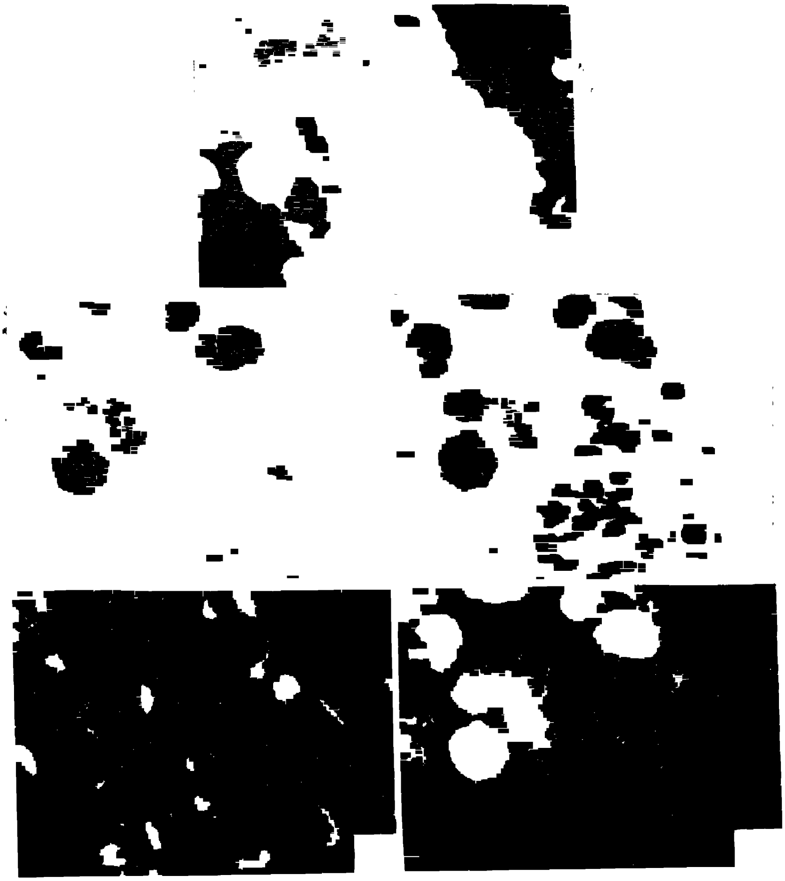

Figure 5. X-ray elemental distribution maps of a Tangadupalli coin.

phase diagram (Reeves *et al* 1953). This sort of acicularity disappears slowly tempering resulting in the type of structure shown in figure 4 for the Tangadup coin. Soaking in the β-range and quenching in the case of bronzes contain > 20 wt% Sn helps to soften the alloy (Reeves *et al* 1953).

In conclusion, it appears that while BACRI coins are made by alloying meta copper and tin as starting materials, Tangadupalli and Kesaragutta coins are m by direct mixing of the ores of copper and tin and processing them together. In b cases, the presence of sulphide particles of composition close to that of bor suggests that local copper ores were used. It is not yet clear as to how exactly coins were fabricated from the alloy melt of high tin containing bronzes which quite brittle in nature, even though the evidence presented suggests that a cer amount of processing has been done on the alloy to make the coins.

Acknowledgements

The authors are thankful to Dr V V Krishna Sastry, Director, S Ramakanth Curator and Dr Mir Fazaluddin Ali Khan, coin keeper of Andhra Pradesh S

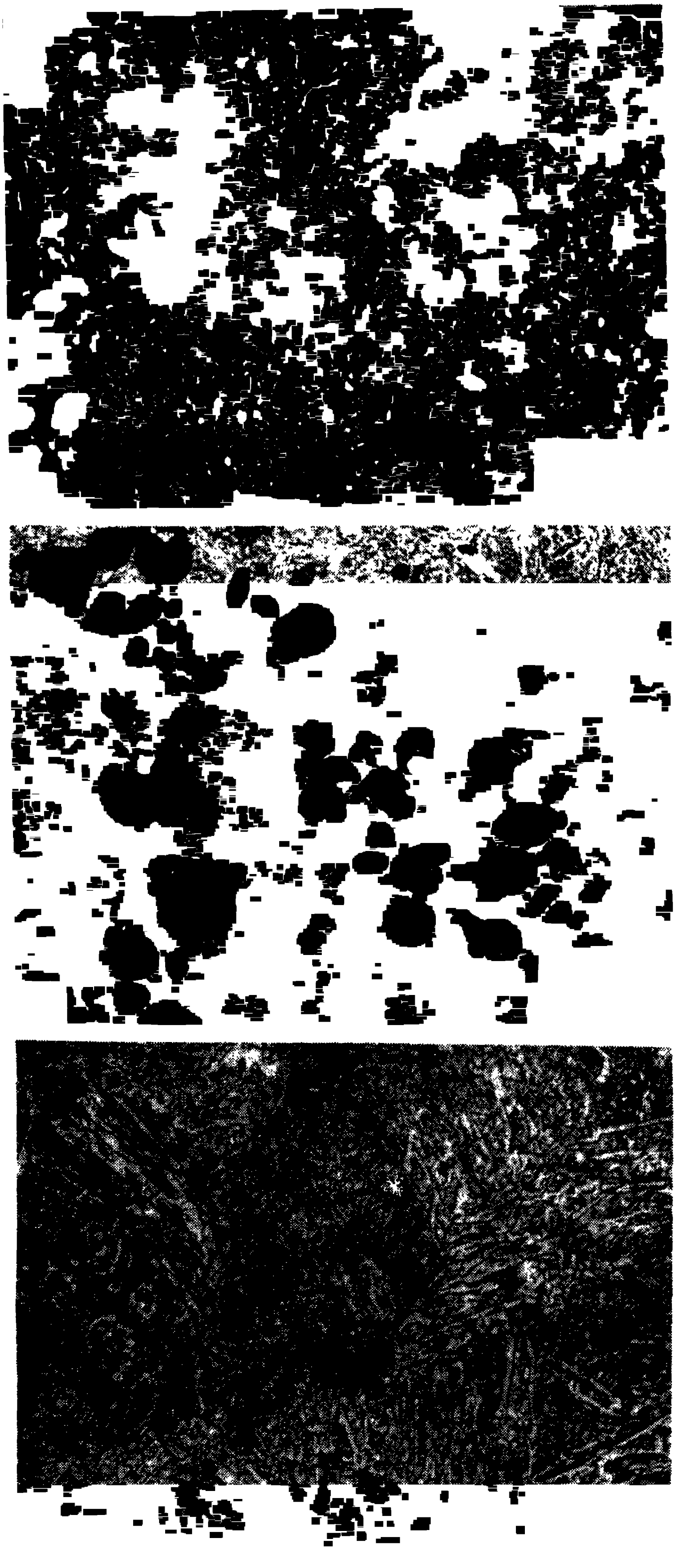

Figure 6. Photomicrographs of a cross-section of a Kesaragutta coin.

Department of Archaeology and Museums for their kind co-operation in making the samples available for analyses, and for valuable suggestions. The authors are also thankful to Dr B R Rao of Geological Survey of India for permitting us to use the emission spectrograph. We are grateful to the Director, DMRL for providing the facilities to carry out metallurgical studies.

References

Agarwal D P 1969 *The copper bronze age in India*, (ed) Md Abdul Waheed Khan (Hyderabad: Department of Archeology) 109–204
Catling H W and Jones R E 1977 *Archaeometry* 57
Hegde K T M 1975 *J. Numis. Soc. India* 180
Rama Rao M 1963 *AP Govt. Archeol. Ser.* 10
Rama Rao K and Appavadhanulu K 1952 *Q.J. Geol. Min. Metall. Soc. India* **24** 75
Reeves M R, Bowden J S and Cuthbertson J W 1953 *Met. Ind.* **82** 40
Scott D A 1980 *Stud. Conserv.* **25** 157

Bull. Mater. Sci., Vol. 9, No. 2, June 1987, pp. 149–158. © Printed in India.

Alloy oxide equilibria in the Cr-Mn-O system

S RANGANATHAN and J P HAJRA
Department of Metallurgy, Indian Institute of Science, Bangalore 560 012, India

MS received 17 March 1987

Abstract. The phase boundaries of the Cr-Mn-O system have been investigated by alloy-oxide equilibria at 1173 and 1273 K and by isopiestic technique at 1323 K. The oxide phases which coexist in equilibrium with the Cr-Mn alloys are determined by x-ray diffraction studies. The results of the experiments indicate the presence of MnO in equilibrium with Mn-rich alloy whereas $MnCr_2O_4$ and Cr_2O_3 phases coexist with almost pure Cr. A three-phase equilibrium consisting of $MnCr_2O_4$ and MnO phases has been detected at the alloy composition $X_{Mn}=0{\cdot}252$ at 1323 K. The composition of the alloy delineates the phase boundaries in the isothermal sections of the system. The results are interpreted by thermodynamic analysis of the Cr-Mn-O system using the data from the isopiestic measurements and those available in the literature.

Keywords. Cr-Mn-O; alloy oxide equilibria; isopiestic technique.

1. Introduction

Chromium and manganese are important components of high temperature alloys. Alloys containing the elements undergo oxidation with the formation of spinel phases during high temperature applications. Information regarding the various types of phases which exist in the Cr-Mn-O system, the stability and proportions of the phases as a function of composition and temperature is important in assessing the applicability of the alloys as high temperature materials. An understanding of the stability of these phases is also important in various thermodynamic studies involving solid state galvanic cells. No studies on thermodynamics and phase equilibria in the system have so far been reported in the literature. Investigations have been carried out to identify various oxide phases and delineate the phase boundaries in the Cr-Mn-O system in equilibrium with Cr-Mn alloys as a function of alloy composition and temperature. The equilibrium phases have been detected by x-ray diffraction studies and the results obtained in the experiments have been interpreted by thermodynamic analysis of the system.

2. Experimental aspects

2.1 *Materials and preparation*

The metals, chromium and manganese were 99·99% pure and supplied by Johnson and Matthey Chemicals, UK and Alfa Products of Thiokal Corporation, USA, respectively. The alloys were prepared by melting weighed quantities of the metals in a recrystallized alumina crucible using a high frequency generator under an atmosphere of pure argon. The gas was purified by passing it over calcium granules heated to 873 K. The alloys were analysed using a Shimadzu spectrophotometer

(UV-visible) after oxidizing a solution containing the alloy to a mixture of permanganate and dichromate as described by Vogel (1969).

Manganese oxide was prepared by reducing Mn_2O_3 in a stream of hydrogen at 1273 K. Manganese chromate was prepared by heating a mixture of potassium manganese chloride, K_2MnCl_4 and lithium chromium oxide, $LiCrO_2$ at 873 K in an atmosphere of pure nitrogen which was dried by passing it over phosphorus pentoxide as described by Busch (1980). Chromium oxide, Cr_2O_3, was prepared by decomposition of chromium carbonate at 1073 K in air. The oxides obtained were then confirmed using an x-ray diffractograph by comparing with *d*-spacing data available in the literature.

3. Apparatus and procedure

A mixture of an alloy of given composition and a small amount of oxide was repeatedly mixed and ground in an agate mortar to ensure intimate contact between the reactant phases. The alloy-oxide system was heterogenous in nature and fine grinding followed by mixing prior to pelletization was required to enhance the slow solid state diffusion process. The alloy + oxide mixture was pelletized using a steel die to a pellet of about 7 mm dia. The pellet was then enclosed in an outer pellet of MnO as shown in figure 1. Manganese, being a volatile component in the alloys at the temperatures under investigation, the outer pellet of MnO restricts the loss of Mn due to vaporization. The pellet was then introduced in a quartz capsule which was evacuated and filled with argon. It was then re-evacuated and sealed. The quartz capsule was placed carefully in the even temperature zone of a furnace for 720 hr. The furnace zone was controlled within ± 1 K. The time required for the alloy + oxide system to reach equilibrium was determined by several trial runs. At the end of this period, the quartz capsule was quenched in water and the alloy + oxide pellet inside the outer MnO pellet was recovered carefully. An x-ray diffractograph of pellet was then taken after grinding and polishing the surface, to identify the oxide phase present in equilibrium with the alloy at the experimental temperature. Grinding of the alloy + oxide pellet is necessary to avoid any MnO particles adhering to the surface. The equilibrium experiments were carried out at 1173 and 1273 K. Since the alloy phase cannot be separately analysed due to fineness of the grinding and intimate mixing of the reactants, a small quantity of the oxide phase was used to ensure insignificant compositional changes during the experiments. Each alloy composition had been repeated with starting oxide phase as either MnO or $MnCr_2O_4$ separately irrespective of the resultant equilibrium phase as shown in table 1. These repeat experiments were required to ascertain the composition of the alloys in equilibrium with the oxide phases. No side reaction between MnO in the alloy + oxide pellet and quartz was detected by x-ray diffraction studies.

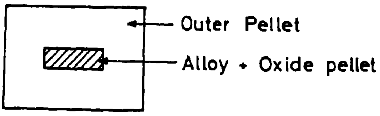

Figure 1. Schematic sketch of an alloy + oxide pellet inserted in a pellet of MnO used in the alloy-oxide equilibrium experiments.

Table 1. Results of the alloy oxide equilibria at 1173 K and 1273 K.

Composition X_{Mn}		0·0		0·264		0·416		0·526		0·579		0·672		0·689		0·735		0·899	
Starting oxide		$MnCr_2O_4$	MnO	$MnCr_2O_4$	MnO	$MnCr_2O_4$	MnO	$MnCr_2O_4$	MnO	$MnCr_2O_4$	MnO	$MnCr_2O_4$	MnO	$MnCr_2O_4$	MnO	$MnCr_2O_4$	MnO	$MnCr_2O_4$	MnO
Final oxide phase at	1173 K	—	—	MnO	MnO	MnO	MnO	MnO	MnO	—	—	MnO	MnO	MnO	MnO	MnO	MnO	MnO	MnO
	1273 K	Cr_2O_3 $MnCr_2O_4$	Cr_2O_3 $MnCr_2O_4$	—	MnO	MnO	MnO	—	MnO	—	MnO	—	MnO	MnO	MnO	MnO	MnO	MnO	MnO

4. Isopiestic experiments

A number of alloys were used in the isopiestic experiments in order to establish the compositions of the alloys and the corresponding oxide phases in equilibrium at 1323 K. In these experiments, two alloy pellets of different compositions and an alloy pellet mixed with a small quantity of Cr_2O_3 were taken in the upper part of a quartz capsule as shown in figure 2. The lower part of the capsule contained a pellet of pure Mn. A chromel-alumel thermocouple attached close to it measured the temperature of the pellet. The capsule was then held vertically in a furnace such that the upper part containing the alloy pellets was in the even temperature zone of the furnace. An

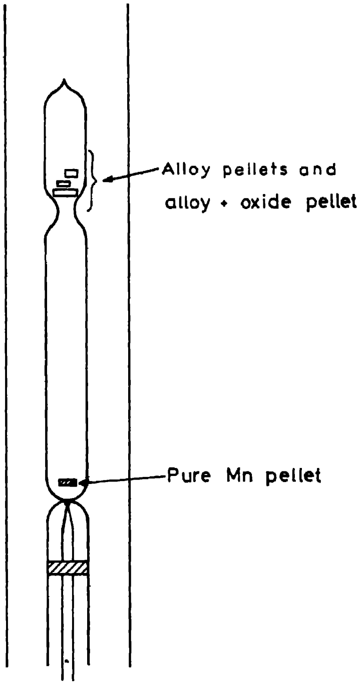

Figure 2. Schematic sketch depicting the experimental set-up for the isopiestic technique.

additional chromel-alumel thermocouple placed in the zone measured the temperature of the alloy sample. The temperature of the Mn pellet dictated the partial pressure of Mn in the capsule. The system was considered to be in equilibrium as the composition of the alloys placed in the upper part of the capsule approached that of an equilibrium value. The temperature distribution in the furnace was such that the manganese pellet was at a lower temperature than that of the alloy pellets. After the equilibrium which required 500 hr, the capsule was quenched in air. The compositions of the alloy pellets were then determined by chemical analysis using a spectrophotometer as already described. The alloy + oxide pellet was then subjected to x-ray analysis to determine the oxide phase present as shown in table 2. Since two alloy pellets reached the same composition starting from different initial compositions, the composition of the alloy in the alloy + oxide pellet was considered to be the same as that of the other alloy pellets. The initial composition of the alloy in the alloy + oxide pellet was chosen fairly close to those of the other two so that the same equilibrium value could be achieved in the samples. An added advantage of the method is that, apart from the alloy + oxide equilibrium studies, thermodynamics of the Cr-Mn system could also be determined simultaneously. One set of experimental results is reported in table 2. This constitutes a part of a major programme on the determination of thermodynamic properties of Mn-based systems, the details of which are to be published elsewhere.

5. Results and discussion

The tie line compositions of Cr-Mn alloys in equilibrium with the corresponding oxide phases at 1173 and 1273 K are summarized in table 1 and those at 1323 K in table 2. These data indicate that for alloys $X_{Cr} \simeq 1{\cdot}0$, the stable oxide phases are Cr_2O_3 and $MnCr_2O_4$ irrespective of the starting oxide phase used in the equilibrium experiments. However, as the Mn content of the alloy is increased close to $X_{Mn} = 0{\cdot}252$, $MnCr_2O_4$ is recognized to be the only oxide phase in equilibrium as determined by the isopiestic technique at 1323 K. The alloy-oxide system exhibits

Table 2. Results of isopiestic experiments at temperature 1323 K Starting oxide phase (in all cases): Cr_2O_3.

Composition X_{Mn}	Final oxide phases
0·04	$MnCr_2O_4$ Cr_2O_3
0·067	$MnCr_2O_4$
0·152	$MnCr_2O_4$
0·188	$MnCr_2O_4$
0·215	$MnCr_2O_4$
0·233	$MnCr_2O_4$
0·252	MnO $MnCr_2O_4$
0·337	MnO
0·392	MnO
0·570	MnO
0·586	MnO

similar trends as X_{Mn} tends to 0·252 independent of the starting oxide phase used in the experiments. However, the change-over of the type of oxide phase from $MnCr_2O_4$ to MnO occurs when $X_{Mn} = 0{\cdot}252$ as shown in tables 1 and 2. The change-over composition is considered to be an important feature which essentially determines the existence of the three-phase equilibrium in the Cr-Mn-O system. Tables 1 and 2 further indicate the existence of a MnO phase in equilibrium with the alloys as X_{Mn} is increased beyond the change-over composition. These compositions roughly demarcate the phase boundaries in the Cr-Mn-O system in terms of the type of oxide phase which coexist in equilibrium with the Cr-Mn alloys as a function of alloy composition and temperature. The results summarized in tables 1 and 2 have been interpreted by thermodynamic calculation in the subsequent section.

6. Thermodynamic analysis

The determination of the isothermal sections of the Cr-Mn-O system is based on equilibrium calculation and information from the constituent binaries. Various alloy phases and their phase boundaries in the Cr-Mn system as a function of composition and temperature were recently computed by Venkataraman and Neuman (1986). These phase designations and boundaries are adopted in the present study. The composition of the alloy in equilibrium with the oxide phases has been determined from thermodynamic properties of the Cr-Mn alloys and equilibrium constants of the following reactions:

$$Mn = \tfrac{1}{2}O_2(g) = MnO(s), \tag{1}$$

$$2Cr + \tfrac{3}{2}O_2(g) = Cr_2O_3(s), \tag{2}$$

$$Mn + 2Cr + 2O_2(g) = MnCr_2O_4. \tag{3}$$

The equilibrium constants of (1), (2) and (3) at 1173, 1273 and 1323 K are obtained from the standard free energy of formation of MnO and $MnCr_2O_4$ respectively. The standard free energy of formation of MnO is obtained from Barin and Knacke (1973) and Barin *et al* (1977) and those of Cr_2O_3 and $MnCr_2O_4$ are available from Chase *et al* (1975) and Jacob (Private Communication) respectively. In order to evaluate the stability of the oxides as a function of alloy composition in the Cr-Mn-O system, thermodynamic properties of the Cr-Mn alloys have been used as reported by Eremenko *et al* (1968) and Jacob (1985) and those from the present isopiestic studies at 1323 K. Thermodynamic properties of the Cr-Mn system have been studied by Eremenko *et al* (1968) at 1023 K using a fused salt emf technique. Their results indicate positive deviations from Raoult's law. In the absence of any enthalpy data or data based on second law evaluation, the activity data as reported by Eremenko *et al* (1968) are used with reference to β Mn as standard state. The calculation assumes the excess free energy property of the Cr-Mn system to be independent of temperature. Figure 3 depicts the variation of $-\log P_{O_2}$ as a function of alloy composition at 1323 K which describes the stability range of various oxides in the Cr-Mn-O system. It also shows that the free energy change of the MnO phase coincides with that of $MnCr_2O_4$ at $X_{Mn} = 0{\cdot}29$ at this temperature. The calculated values of the change-over composition using the data of Eremenko *et al* (1968) at 1173 and 1273 K are 0·26 and 0·25 respectively. More recently thermodynamic properties of the Cr-Mn

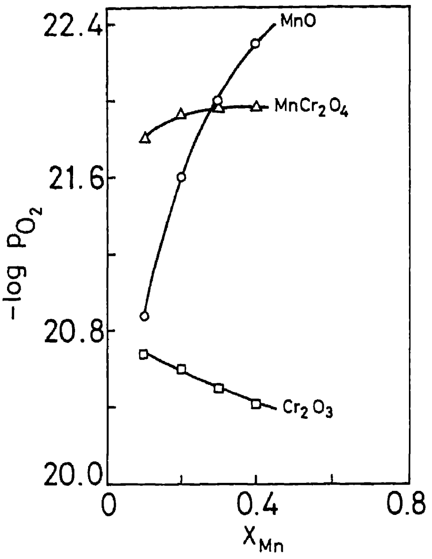

Figure 3. Logarithm of partial pressure of oxygen as a function of composition of the Cr-Mn alloys using the extrapolated data of Eremenko *et al* (1968) at 1323 K.

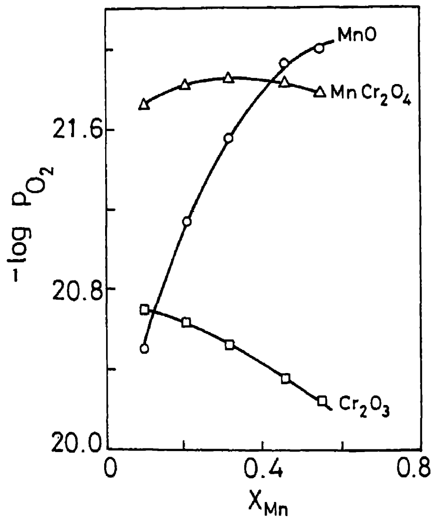

Figure 4. Logarithm of partial pressure of oxygen as a function of alloy composition based on the activity data determined by Jacob (1985) at 1323 K.

system for Cr rich b.c.c. solid solution have been measured by Jacob (1985) using Knudsen effusion cell in the temperature range of 1200 to 1500 K. The calculated relationship between the stabilities of the oxide phases and alloy composition at 1323 K based on his data is presented in figure 4. The change-over composition at this temperature may be noted as $X_{Mn} = 0{\cdot}43$. The corresponding calculated X_{Mn} values at 1173 and 1273 K are 0·41 and 0·38 respectively.

The thermodynamic data of the Cr-Mn system based on the present investigation using isopiestic technique at 1323 K are expressed in terms of the activity coefficients of Mn and Cr, in the range of $0<X_{\mathrm{Mn}}<0{\cdot}65$ as

$$\gamma_{\mathrm{Mn}}=2{\cdot}504-1{\cdot}927X_{\mathrm{Mn}}. \tag{4}$$

and

$$\ln\gamma_{\mathrm{Cr}}=1/0{\cdot}2305[-0{\cdot}7695\ln(1-X_{\mathrm{Mn}})+\ln(1-0{\cdot}769\,X_{\mathrm{Mn}})]. \tag{5}$$

Figure 5 depicts the variation of $-\log P_{O_2}$ as a function of alloy composition using (4) and (5) in conjunction with (1), (2) and (3). The calculated change-over composition exists at $X_{\mathrm{Mn}}=0{\cdot}22$. The latter thermodynamically calculated value is in excellent agreement with $X_{\mathrm{Mn}}=0{\cdot}252$ which is obtained from alloy-oxide equilibria followed by x-ray diffraction studies as reported in table 2. The change-over composition is considered to be important, as it delineates the phase boundaries of the Cr-Mn-O system. The existence of the three-phase equilibrium at this composition would make the coexistent partial pressure of oxygen imparted by the alloy + MnO to be equal to that by the $MnCr_2O_4$ + alloy phases at 1323 K. Therefore using (1), (3), (4) and (5) at $X_{\mathrm{Mn}}=0{\cdot}252$, the standard free energy of formation of $MnCr_2O_4$ has been assessed and found to be $-1133{\cdot}86$ kJ mole^{-1}. This compares favourably with a value of $-1129{\cdot}68$ kJ mole^{-1} as given by Jacob (Private Communication) at 1323 K.

The existence of the other three phase equilibria between Cr, $MnCr_2O_4$ and Cr_2O_3 phases is indicated in tables 1 and 2. Table 3 shows that for an alloy of almost pure Cr, $X_{\mathrm{Mn}}=0{\cdot}0001$ at 1323 K, the $MnCr_2O_4$ and Cr_2O_3 phases coexist in equilibrium. In this dilute solution range, the activity coefficients of Cr and Mn in the alloy are used based on (4) and (5) such that X_{Mn} tends to unity, γ_{Cr} tends to 1·0 and γ_{Mn} approaches a value of 2·504 at 1323 K. The Cr-rich alloy, however, retains about 4 at % Mn as reported in table 2. This is considered to be due to lack of

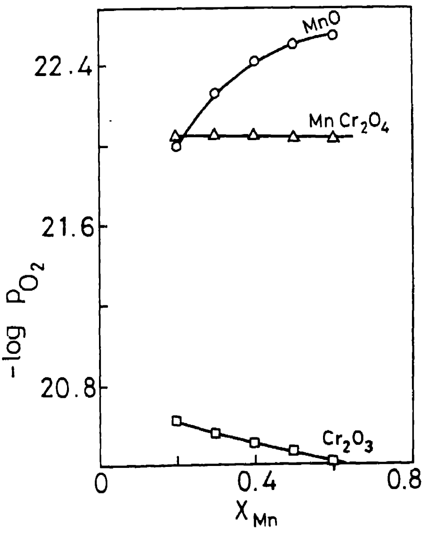

Figure 5. Variation of logarithm of partial pressure of oxygen with the composition of Cr-Mn alloys based on the activity data determined by the isopiestic technique at 1323 K.

Table 3. Three phase equilibrium involving Cr, Cr_2O_3 and $MnCr_2O_4$.

X_{Mn}	P_{O_2} $MnCr_2O_4$, atm.	P_{O_2}, Cr_2O_3 atm.
0·001	$9{\cdot}52\times10^{-23}$	$1{\cdot}78\times10^{-21}$
0·0001	$3{\cdot}00\times10^{-21}$	$1{\cdot}78\times10^{-21}$

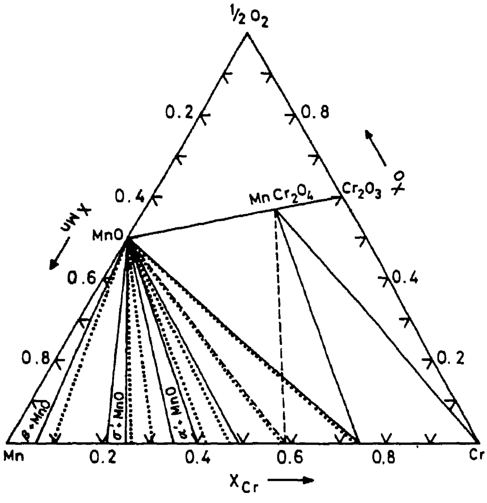

Figure 6. Isothermal section of the Cr–Mn–O system at 1173 K. Comparison between the present data (. . . .) and those calculated based on the activity data of Eremenko *et al* (1968) (———) and Jacob (1985) (– – –).

thermodynamic equilibrium. It may be mentioned that the starting composition of the alloy was about 6 at % Mn mixed with Cr_2O_3 which is expected to be extremely slow in giving up its Mn content to reach an equilibrium state containing alloy + $MnCr_2O_4$ phases.

The samples containing either Cr + $MnCr_2O_4$ or Cr + MnO, as reported in table 1, reach equilibrium under the experimental conditions used in the alloy-oxide equilibrium studies. Consequently the existence of the equilibrium phases, $MnCr_2O_4$ and Cr_2O_3, has been detected by x-ray analysis of the samples irrespective of their starting oxide phases. The tie line compositions of the Cr-Mn alloys summarized in tables 1 and 2 are shown along with the thermodynamically calculated values in the isothermal sections of the Cr-Mn-O system. Figures 6, 7 and 8 denote the isothermal sections at 1173, 1273 and 1323 K, respectively.

The alloy-oxide equilibria and thermodynamic studies indicate the presence of MnO predominently in the Mn-rich compositions and $MnCr_2O_4$ and Cr_2O_3 in the three-phase equilibrium with almost pure Cr. The change-over of the chromate to MnO phase occurs when $X_{Mn} = 0{\cdot}252$ at 1323 K which decides the other three phase equilibria in the Cr-Mn-O system.

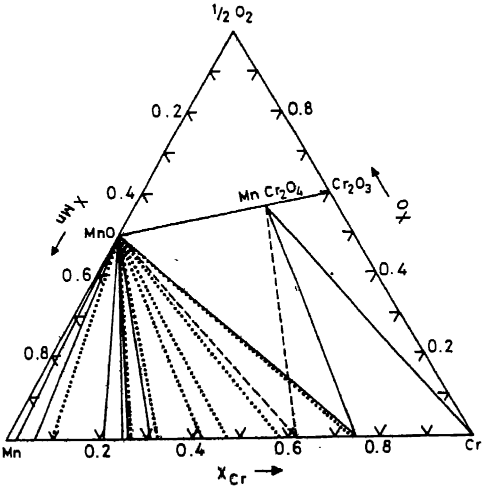

Figure 7. Isothermal section of the Cr-Mn-O system at 1273 K. Comparison between the present data (. . .) and thermodynamically calculated values based on the data of Eremenko *et al* (1968) (———) and Jacob (1985) (---).

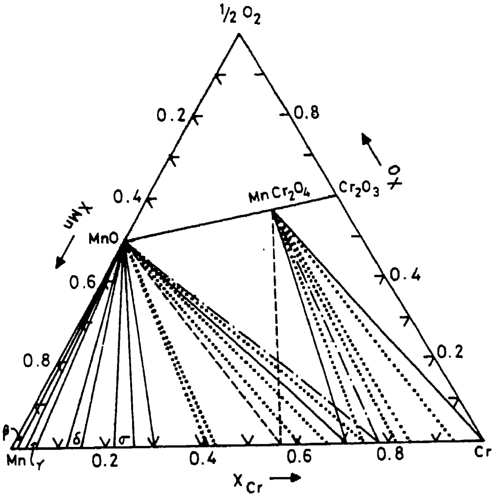

Figure 8. Isothermal section of the Cr-Mn-O system at 1323 K. Comparison between the data of the present work (—·—isopiestic experiment; . . . . alloy-oxide equilibrium) with values derived based on Eremenko *et al* (1968) (———) and Jacob (1985) (---).

Acknowledgements

The authors are grateful to the University Grants Commission for financial support.

References

Barin I and Knacke O 1973 *Thermochemical properties of inorganic substances* (Berlin: Springer Verlag)

Barin I, Knacke O and Kubaschewski O 1977 *Thermochemical properties of inorganic substances* (Berlin: Springer Verlag) Supplement

Busch D H 1980 *Inorganic synthesis* (New York: John Wiley) Vol. 20
Chase M W, Wrnutt J L, Prophet H and Mcdonald R A 1975 *J. Phys. Chem. Ref. Data* **4** 92
Eremenko V M, Lukashenko G M and Sidorko V R 1968 *Russ. J. Phys. Chem.* **42** 343
Jacob K T 1985 *Z. Metallkde* **76** 415
Venkataraman M and Neuman J P 1986 *Bull. Alloy Phase Diagrams* 7 457
Vogel A I 1969 *Quantitative inorganic chemistry* (London: ELBS & Longman)

Bull. Mater. Sci., Vol. 9, No. 3, August 1987, pp. 159–168. © Printed in India.

Synthesis and properties of manganese-doped barium titanate

L M ARUNACHALAM†, D CHAKRAVORTY†† and E C SUBBARAO*
Indian Institute of Technology, Kanpur 208 016, India
†Present address: Department of Metallurgy, Indian Institute of Technology, Madras 600 036, India
††Present address: Indian Association for the Cultivation of Science, Calcutta 700 032, India
*Present address: Tata Research Development and Design Centre, Pune 411 001, India

MS received 2 May 1987

Abstract. An oxalate route for the production of $BaTiO_3$ has been modified to incorporate Mn (upto 2%) as a dopant and the reaction sequence has been studied. The resulting Mn-doped $BaTiO_3$ exhibits a dielectric constant with an increasing insensitivity to temperature and applied a.c. field as the Mn content is increased. These samples possess a high electrical resistivity even after treatment in hydrogen at 1100°C and are therefore suitable as dielectric for multilayer capacitors with base metal electrodes.

Keywords. Mn-doping; domain stabilization; base metal electrodes; barium titanate; oxalate route; capacitors.

1. Introduction

Barium titanate ($BaTiO_3$) is by far the most extensively studied ceramic dielectric material (Jona and Shirane 1962). Conventional ceramic processing poses problems for the preparation of reproducible, high purity $BaTiO_3$ and for the incorporation of small amounts of desired impurities. Clabaugh *et al* (1956) described a method to prepare the high purity $BaTiO_3$ from barium titanyl oxalate tetrahydrate (BTO) and Desu (1979) had adapted this route to incorporate small amounts of manganese into $BaTiO_3$.

The rapidly escalating cost of established silver electrodes for the ceramic capacitors has forced the use of base metals such as nickel as electrode. However, a disc or multilayer capacitor with nickel electrode has to be heat-treated in a low oxygen content atmosphere to prevent the oxidation of nickel. Under these conditions (of low P_{O_2} and high temperature), $BaTiO_3$ becomes conducting due to the formation of Ti^{3+} ions accompanying the creation of oxygen ion vacancies. It has been found that the incorporation of Mn into $BaTiO_3$ lattice prevents the reduction of $BaTiO_3$ when it is fired in an atmosphere reducing enough to inhibit the oxidation of Ni (Ainger and Herbert 1959; Herbert 1963, 1965; Burn and Meher 1975; Daniels 1976; Burn 1978, 1979; Hagemann 1978a, b; Desu 1979; Subbarao 1979; Hagemann and Ihrig 1979; Desu and Subbarao 1980a, b).

Manganese can exist in three valences: 2^+, 3^+ and 4^+. The oxygen vacancy concentration on incorporation of Mn into $BaTiO_3$ varies with the valency of Mn as follows:

---

†To whom all correspondence should be addressed.

$$\mathrm{BaTi_{1-x}Mn_x^{4+}O_3 \rightarrow BaTi_{1-x}Mn_x^{3+}O_{3-(x/2)}} + \frac{x}{4}\mathrm{O_2}\uparrow, \tag{1}$$

$$\rightarrow \mathrm{BaTi_{1-x}Mn_x^{2+}O_{3-x}} + \frac{x}{2}\mathrm{O_2}\uparrow. \tag{2}$$

The presence of oxygen ion vacancies in reduced, undoped $BaTiO_3$ was found to decrease the Curie temperature (by 40–50°C for every 10^{20} oxygen ion vacancies cm^{-3}) (Hardtl and Wernicke 1972) and enhance the dielectric losses. On the other hand, incorporation of Mn in the Ti^{4+} site in $BaTiO_3$ was reported to decrease the Curie temperature by 10°C/1% Mn when sintered in an air atmosphere and by 40–50° C/1% Mn when sintered in low oxygen atmosphere ($P_{O_2} \simeq 10^{-12}$) (Hagemann 1978a; Burn 1979; Hagemann and Ihrig 1979). At the same time, Mn addition reduces the permittivity and loss factor (Burn 1979).

Since Mn-doped $BaTiO_3$ has been found to be the most satisfactory dielectric for capacitors with base metal electrodes (BME), a detailed study was undertaken in the present work to establish the mechanism underlying the proper incorporation and amount of Mn into the $BaTiO_3$ lattice, so that the desired dielectric properties (high resistivity, low $\tan\delta$, low dependence of permittivity on applied a.c. field and on temperature etc) for this application could be achieved.

2. Experimental

2.1 *Materials*

The raw materials used were barium chloride dihydrate and oxalic acid dihydrate (both from Sarabhai Chemicals), titanium tetrachloride and manganese carbonate (from Reidel de Haven, Germany). All of them are more than 99·5% pure. Either distilled or deionized water was used for preparing the solutions.

2.2 *Specimen preparation*

High purity $BaTiO_3$ and manganese-doped $BaTiO_3$ were prepared from the complex barium titanyl oxalate and manganese-doped barium titanyl oxalate respectively. A mixed solution of barium chloride and titanium tetrachloride was allowed to drip slowly into a hot (80–85°C) vigorously stirred solution of oxalic acid. The precipitated oxalate was filtered hot, washed several times with distilled water and acetone, and air-dried at 150°C. The precipitate was calcined at 900°C for 2 hr and care was taken to remove the chloride ions from the calcined powder.

The calcined powder was mixed with about 4 wt% of 25% polyvinyl acetate solution, dried and pressed under a hydraulic pressure of 5 kbar (75,000 psi) into cylindrical discs of either 12·5 mm or 9 mm dia. Sintering was carried out in air at 1350°C for 2 hr. The power to the furnace was switched off during cooling. For the domain stabilization studies, the discs were annealed in two different conditions: (i) in ultra-high pure argon at 800°C for 10 min with furnace cooling and (ii) in air at 1100°C for 10 min and quenched to room temperature to establish the oxygen defect equilibria within the system. To define the conditions suitable for the BME capacitors, the discs were annealed in H_2 at 1100°C for 10 min with furnace cooling. For capacitance and resistivity measurements, all the discs were polished to obtain clean and parallel surfaces and electroded with air-dry silver paint.

2.3 *Characterization*

The DTA and TGA studies were carried out on a MOM derivatograph. The IR spectra were obtained on a Perkin Elmer 580 spectrometer. The X-ray diffraction data were recorded on a Philips diffractometer using CuK_α radiation. The dielectric properties were measured on a General Radio 1620-A capacitance bridge assembly. The electrical resistivity was measured on a General Radio 1650-A impedance bridge and a General Radio megaohm bridge.

3. Results and discussion

A method for effectively incorporating Mn into $BaTiO_3$ lattice and the dielectric behaviour of the resulting compositions are presented here.

3.1 *Preparation of Mn-doped $BaTiO_3$*

3.1a *Pure $BaTiO_3$*: To start with, pure $BaTiO_3$ was prepared by the BTO route, following the method of Clabaugh *et al* (1956) and was subjected to a DTA/TGA study (figure 1). A number of reaction schemes have been proposed for the decomposition of BTO to $BaTiO_3$ (Saburi 1959; Strizbkov *et al* 1960; Gallagher and Schery 1963; Gallagher and Thomson 1965; Gopalakrishna Murthy *et al* 1975). The present results did not fit any of these schemes and could be explained only by the reaction sequence proposed below:

$$\mathrm{BaTiO(C_2O_4)_2\cdot 4H_2O} \xrightarrow[-(\mathrm{4H_2O,\ CO})]{\text{upto }250^\circ\mathrm{C}} \mathrm{BaTiO(C_2O_4)\cdot CO_2\cdot \tfrac{1}{2}O_2}$$

$$\xrightarrow[-3\,\mathrm{CO}]{400^\circ\mathrm{C}} \mathrm{BaTiO\cdot 2O_2} \xrightarrow[-\mathrm{O_2}]{800^\circ\mathrm{C}} \mathrm{BaTiO_3}. \qquad (3)$$

The weight losses calculated from (3) are compared with the observed values at different temperature ranges (table 1) which substantiate the above reaction sequence. The x-ray pattern of the calcined material showed the expected tetragonal $BaTiO_3$ phase only. The room temperature dielectric constant of this material, after calcination and sintering, was high (about 4000) suggesting fine grain size.

3.1b *Mn-doped $BaTiO_3$—Method 1*: In a minor modification of Clabaugh *et al*'s (1956) method, solutions of chlorides of barium, titanium and manganese were mixed in requisite proportion, and the mixed solution was added drop-wise to the oxalic acid solution. The precipitate was white, as in the case of undoped BTO. Compared to the instantaneous precipitation of pure BTO when drops of the chloride solutions

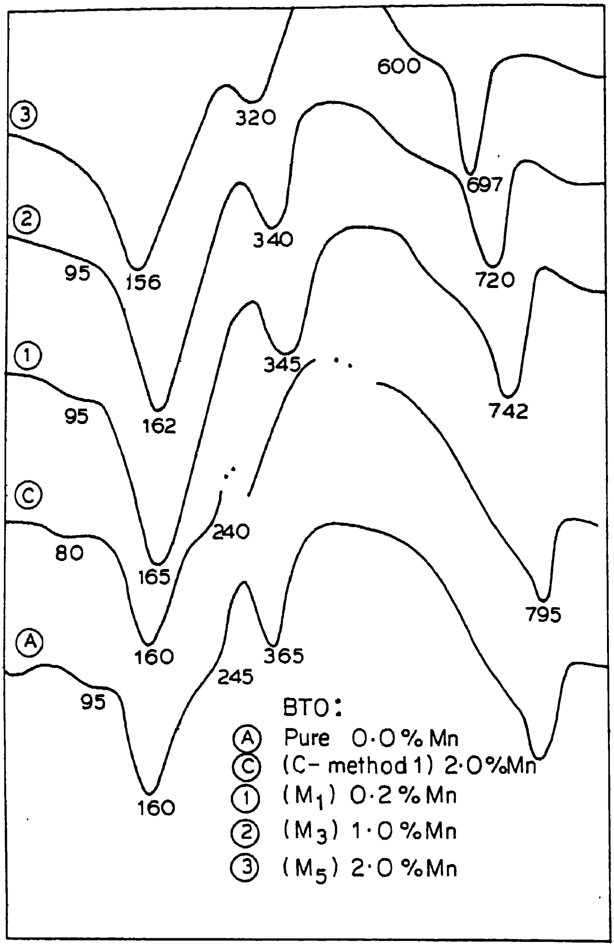

Figure 1. DTA of pure and Mn-doped barium titanyl oxalates.

Table 1. Comparison of the weight losses of BTO, observed and calculated.

Decomposition	Weight loss (%)		Temperature (°C)
	Calculated	Observed	
Dehydration of BTO and low temperature decomposition of BTO	22·24	20·25	Upto 250
Main oxalate decomposition	18·69	19·50	About 400
Final decomposition to $BaTiO_3$	7·11	6·75	About 800
Total weight loss	48·09	46·50	

touched the oxalate solution, there was a delay in the start of the precipitate formation when Mn was present in the chloride mixture added to oxalic acid. This observation is discussed later. The DTA and IR study did not reveal any difference between the doped and undoped BTO, raising a doubt as to whether Mn was at all incorporated in the $BaTiO_3$ lattice at this stage. However, the doped samples, after calcination and sintering, did exhibit a brown colour. The room temperature dielectric constant of 1% Mn sample was higher than that of the undoped and the 2% Mn-doped samples (figure 2). This behaviour may be contrasted with the steady decrease in dielectric constant with Mn content when the samples are prepared from $BaCO_3 + TiO_2 + MnCO_3$ by conventional ceramic processing but the trend is comparable to samples of $BaTiO_3$ doped with La, which is known to be a donor impurity (Hagemann 1978a) (figure 2). These higher values may be due to the donor mode of Mn incorporation or due to grain growth inhibition by Mn oxides present at grain boundaries. The Curie temperature of the three samples is nearly the same. These confusing set of results raise a question about the presence of Mn in $BaTiO_3$, its location, valence state and amount. The following experiments were undertaken to throw light on these issues.

3.1c *Mn-doped* $BaTiO_3$*—Experiments leading to Method 2*: In the first experiment, barium oxalate was precipitated by adding barium chloride solution, drop-wise to the oxalic acid solution. To this precipitate $MnCl_2$ solution was added drop-wise, when it was observed that gradually the entire barium oxalate precipitate disappeared, leaving a clear solution.

In the second experiment, hydrated titanyl oxalate was formed by adding the $TiCl_4$ solution, drop-wise to oxalic acid solution. To this precipitate was added a solution of manganese chloride or carbonate drop-wise when the titanyl oxalate precipitate was found to partially redissolve.

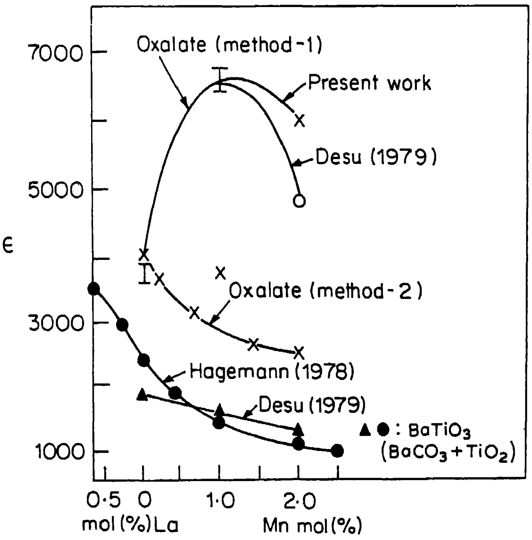

Figure 2. Variation of room temperature permittivity of $BaTiO_3$ with concentration of La and Mn dopant.

The dissolution of the barium and titanyl oxalate precipitates on coming into contact with $MnCl_2$ or manganese oxalate explains the delay in precipitate formation when chlorides of Ba, Ti and Mn were added to oxalate, referred to in the first method.

In the third experiment, $TiCl_4$ was added drop-wise to the clear solution containing Ba and Mn oxalates, described in the first experiment above. There was an instant reddish brown colour and reddish brown precipitate simultaneously formed. This is in sharp contrast to the white precipitate obtained when a mixture of all the three chlorides is added to the oxalic solution in the first method. The formation of a coloured precipitate may be indicative of the incorporation of Mn into the $BaTiO_3$ lattice.

Based on the insight gained from the above three experiments, the final compositions used in the present study were prepared as follows (designated as method 2). A requisite amount of $MnCl_2$ solution was added to the oxalic acid solution. To this, a mixture of Ba and Ti chlorides was added drop-wise. A reddish brown precipitate was formed, the intensity of the colour increasing with increasing Mn content. These samples are designated M_1 to M_5 containing 0·2, 0·6, 1·0, 1·4 and 2·0% Mn respectively.

All the DTA peaks are gradually shifted to lower temperatures as Mn concentration increases from 0 (A) to 2% (M_5), except the dehydration peak at about 160°C (figure 1). The small peaks at 95° and 245°C in pure BTO gradually disappear in samples with increasing Mn content. A peak whose sharpness increases with Mn content appears at about 600°C in Mn-doped samples and is attributed to the oxidation of lower oxides of Mn to Mn_2O_3. The Ti-O peak in the IR spectra appears at 507 cm^{-1} in pure BTO (A) and at 520 cm^{-1} in M_5 (containing 2% Mn).

The shifts in DTA peaks and IR spectra, as well as colouring of the precipitate prepared by the second method is in sharp contrast to the data for samples prepared by the first method, suggesting that Mn is indeed incorporated in BTO prepared by the second method. Further confirmation is provided by the steady decrease in room temperature dielectric constant with Mn content, similar to the trend observed by Hagemann (1978a) and Desu (1979) for Mn-doped $BaTiO_3$ prepared from $BaCO_3 + TiO_2$ (figure 2). Hagemann (1978a) reported that donor impurities (e.g. La) increases the dielectric constant of $BaTiO_3$ while acceptor type impurities (e.g. Fe, Mn) decrease the same, which suggests that Mn is in the acceptor mode in samples prepared by the second method.

The X-ray diffraction patterns are unaffected by Mn addition (upto 2% studied). With 2% Mn addition, the Curie temperature decreased by 5°C, when the samples were sintered in air or oxygen but decreased by about 15°C when the samples were sintered and quenched in argon ($P_{O_2} = 10^{-12}$ atm). The trend of variation of T_c with Mn addition and with P_{O_2} observed here is in agreement with the earlier reports (Hagemann 1978a; Burn 1979; Hagemann and Ihrig 1979) but the magnitude of change obtained in the present work is smaller.

3.2 *Dielectric behaviour of Mn-doped $BaTiO_3$*

3.2a *Variation with temperature*: The temperature dependence of dielectric constant of pure (A) and Mn-doped $BaTiO_3$ (M_1 to M_5) prepared by the second method is shown in figure 3. The dielectric constant at all temperatures decreases

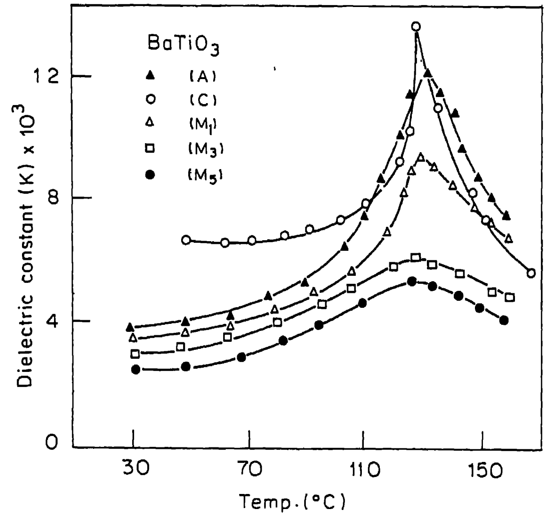

Figure 3. Variation of dielectric constant of Mn-doped $BaTiO_3$ with temperature.

with Mn content. However, for sample *C* containing 2% Mn, made by the first method, not only is the dielectric constant at room temperature very high but at Curie point exhibits a sharp peak, suggesting that Mn may be serving as a grain growth inhibitor or as a donor impurity in these samples. The Curie temperatures shift by only a small amount with Mn content.

3.2b *Variation with a.c. field*: Besides the stability of dielectric constant with temperature change discussed above, another important property sought in a multilayer capacitor material is the stability of dielectric constant with applied a.c. field. The change in dielectric constant (at room temperature) with applied a.c. field (upto 500 V/cm) for samples of pure (A) and Mn-doped $BaTiO_3$ (M_1 to M_5) prepared by the second method is shown in figure 4. The susceptibility of dielectric constant to applied a.c. field decreases remarkably with increasing Mn content. This trend can be further enhanced by quenching the samples from a high temperature in air atmosphere (e.g. 1100°C) (figure 4a) or by sintering and quenching samples from 1300°C in argon ($P_{O_2} = 10^{-12}$ atm.) (figure 4b). On the other hand, sintering and quenching from a high temperature in oxygen atmosphere was more deleterious than treatment in air with or without quenching (figure 4b). The corresponding changes in dielectric loss (tan δ) are shown in figures 5a and 5b.

The importance of proper preparation method is demonstrated strikingly by comparing the samples *C* (prepared by the first method) and M_5 (prepared by the second method), both containing 2% Mn, as far as the effect of the a.c. field on their dielectric constant is concerned (figure 4). With normal furnace cooling or quenching from high temperatures, sample *C* exhibited a dielectric behaviour close to that of undoped sample (A). Only on heat treating under low P_{O_2} (10^{-12} atm.) did this sample exhibit an acceptable dielectric response to the applied a.c. field.

The insensitivity of the dielectric constant to the applied a.c. field has been termed by Hagemann (1978) as domain stabilization, which is brought about by the formation of a transition metal (e.g. Mn)-oxygen ion vacancy (TM-V_O) assemblies (Lambeck and

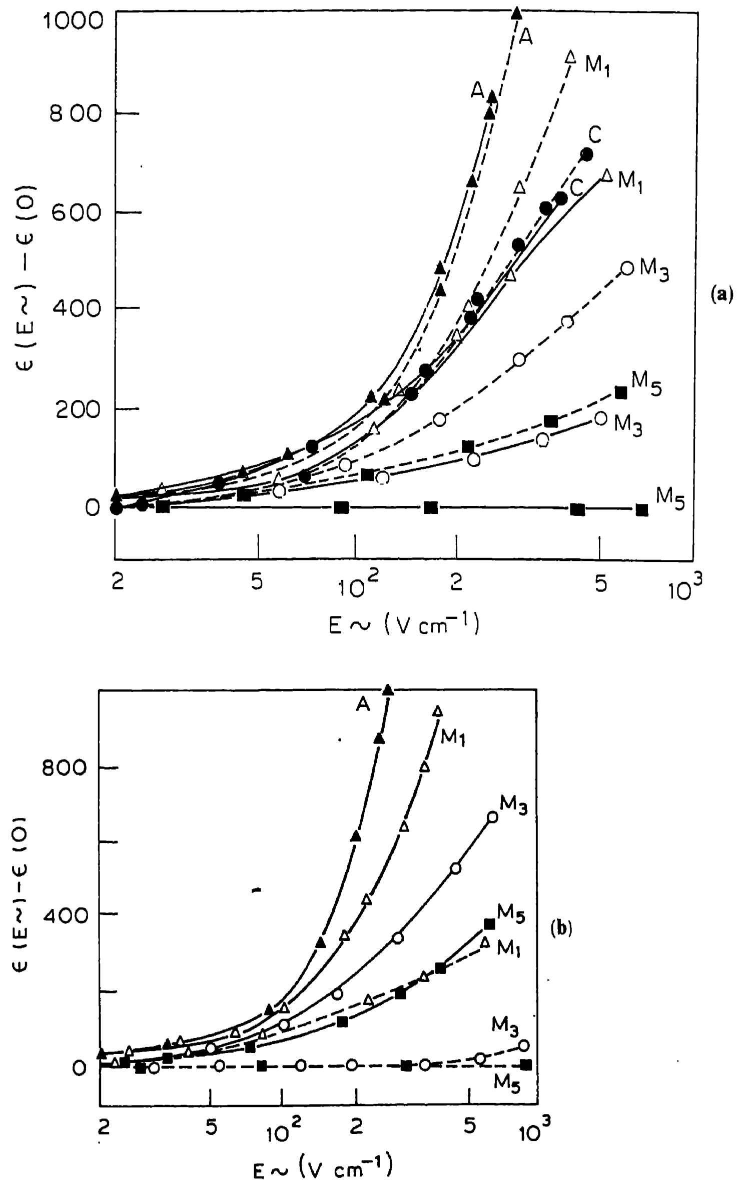

Figure 4. Dependence of ϵ of Mn-doped $BaTiO_3$ on the amplitude of the external a.c. field ($T=28°C$, $f=1$ kHz). **a.** Sintered in air, with and without annealing (-----) and quenched in air (———). **b.** Sintered, annealed and quenched in argon (-----) and in oxygen (———).

Jonker 1978). The formation of these assemblies is facilitated by the presence of Mn of a lower valency in Ti^{4+} sites in the $BaTiO_3$ lattice and an enhanced concentration of oxygen ion vacancies. These processes are clearly favoured by quenching from high temperatures in air but not in oxygen (to retain the higher equilibrium defect concentration corresponding to that temperature) and by heat treating at low P_{O_2}, thus accounting for the observed dielectric behaviour.

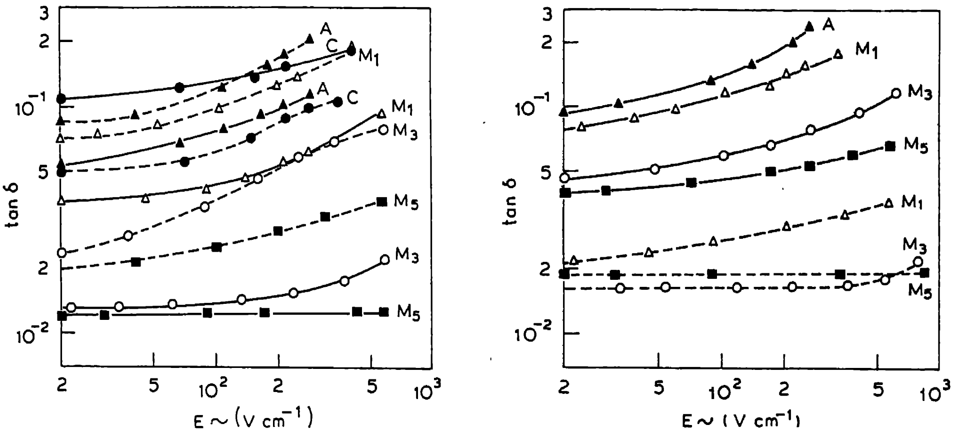

(a) (b)

Figure 5. Dependence of tan δ of Mn-doped $BaTiO_3$ on the amplitude of the external a.c. field (T = 28°C, f = 1 kHz). **a.** Sintered in air, with and without annealing (-----) and quenched in air (———). **b.** Sintered, annealed and quenched in argon (-----) and in oxygen (———).

3.2c *Behaviour in hydrogen atmosphere*: A multilayer capacitor with base metal electrodes is fired in a reducing atmosphere (with a very low P_{O_2}) to prevent the oxidation of the base metal (e.g. Ni). Under these conditions, the dielectric material should not get reduced i.e. it should sufficiently retain the high electrical resistivity. For this purpose, the samples were subjected to a harsher treatment by exposing them to pure hydrogen at 900°C and 1100°C and cooling them in the same atmosphere. The electrical resistivity, dielectric constant and tan δ of these samples at room temperature are listed in table 2. Clearly, the incorporation of Mn(~0·6%) ensures an adequate electrical resistivity of $BaTiO_3$ samples even under these extreme conditions employed.

4. Conclusions

(i) A proper preparation method is essential to achieve the necessary dielectric properties of ceramic $BaTiO_3$ for use with base metal electrodes. (ii) A method has

Table 2. Effect of annealing in H_2, 900°C/10 min and 1100°C/10 min on electrical resistivity (ρ), dielectric constant (K) and dielectric loss (tan δ).

Compositions (% Mn)	900°C/10 min.			1100°C/10 min.		
	log ρ	K	tan δ	log ρ	K	tan δ
A (0)	5·0	2900	0·15	2·0	—	—
M_1 (0·2)	5·0	2140	0·15	3·5	—	—
M_2 (0·6)	8·2	2450	0·09	7·0	1975	0·15
M_3 (1·0)	8·2	2520	0·07	7·5	2400	0·12
M_4 (1·4)	9·0	2750	0·07	8·0	2520	0·10
M_5 (2·0)	9·0	3500	0·06	8·2	2600	0·10

also been developed to incorporate Mn into the $BaTiO_3$ lattice, by modifying the barium titanyl oxalate route. (iii) The Mn-doped $BaTiO_3$ prepared in this manner exhibits dielectric properties which are relatively insensitive to temperature and applied a.c. field (upto 500 V/cm) and possesses a high electrical resistivity even after treatment in H_2 at 1100°C and thereby is eminently suitable for multilayer capacitors with base metal electrodes. (iv) The dielectric constant is insensitive to the applied a.c. field if the samples are quenched from 1300°C in air atmosphere (but not in oxygen) or are given a heat treatment at a low P_{O_2} at the same temperature.

Acknowledgements

The authors are grateful to Mrs T A Padmavathi Sankar, Mr V P Srivastava, Mr S C Barthwal and Mr K Umesh Kumar for their assistance and to the Department of Electronics, Government of India, for financial support.

References

Ainger F W and Herbert J M 1959 *Trans. Br. Ceram. Soc.* **58** 410
Burn I 1978 *Am. Ceram. Soc. Bull.* **57** 600
Burn I 1979 *J. Mater. Sci.* **14** 2453
Burn I and Meher G H 1975 *J. Mater. Sci.* **10** 633
Clabaugh W S, Swiggard E M and Gilchrist R 1956 *J. Res. Natl. Bur. Stand.* **56** 289
Daniels J M 1976 *Philips Res. Rep.* **31** 505
Desu S B 1979 M. Tech. Thesis, IIT, Kanpur
Desu S B and Subbarao E C 1980a *J. Mater. Sci.* **15** 2113
Desu S B and Subbarao E C 1980b *Adv. Ceram.* 1 189
Gallagher P K and Schery F 1963 *J. Am. Ceram. Soc.* **46** 567
Gallagher P K and Thomson J 1965 *J. Am. Ceram. Soc.* **48** 644
Gopalakrishna Murthy H S, Subbarao N and Narayan Kutty T R 1975 *J. Inorg. Nucl. Chem.* **37** 891
Hagemann H J 1978a *J. Phys.* **C11** 3333
Hagemann H J 1978b *Ber. deut. Keram. Ges.* **55** 353
Hagemann H J and Ihrig H 1979 *Phys. Rev.* **B20** 3871
Härdtl K H and Wernicke R 1972 *Solid State Commun.* **10** 153
Herbert J M 1963 *Trans. Br. Ceram. Soc.* **62** 645
Herbert J M 1965 Proc. IEE **122** 1474
Jona F and Shirane G 1962 *Ferroelectric crystals* (London: Pergamon Press)
Lambeck P V and Jonker G H 1978 *Ferroelectrics* **22** 729
Saburi O 1959 *J. Phys. Soc. Jpn.* **14** 1159
Strizbkov B V, Lapitskiv A V and Blasov L G 1960 *Zh. Prikla. Khim.* **33** 2009
Subbarao E C 1979 *Proc. symp. sintering and sintered products* (Bombay: DAE) p. 1

Bull. Mater. Sci., Vol. 9, No. 3, August 1987, pp. 169–180. © Printed in India.

Dielectric behaviour of ZnO-based ceramic semiconductors

SUBHASH C KASHYAP†, K L CHOPRA* and BHARAT BHUSHAN**
Centre for Materials Science and Technology, Indian Institute of Technology, New Delhi 110 016, India
*Indian Institute of Technology, Kharagpur 721 302, India
**Present address: Semiconductor Complex Ltd., Chandigarh, India

MS received 9 June 1987

Abstract. The effect of composition, sintering parameters, frequency and temperature on the dielectric parameters of ZnO-based ceramic semiconductors (cersems) having small amounts of Bi_2O_3, Sb_2O_3, CoO, MnO_2, La_2O_3 and/or Cr_2O_3 has been investigated. The unusually high dielectric constant of these composites, arising due to a two-phase microstructure has been explained on the basis of a depletion layer model. The agreement in values of barrier height and donor concentration calculated from $C^{-2}-V$ plot, Hall measurement and I-V characteristics of these cersems supports the validity of barrier and depletion layer models. The depletion and inter-granular layers are estimated to be nearly 10^2 nm and 1–2 nm respectively. The observed variation of dielectric constant/capacitance with sintering parameters and temperature of measurement has also been explained on the basis of simplified microstructure and depletion layers. The loss peak (f_{max}) observed at 300 kHz remains practically unaltered with change in composition and sintering parameters. The observed dielectric dispersion in the range 10^2–10^6 Hz, exhibiting multiple relaxation times and activation energy of relaxation process as 0·36 eV, has been explained on the basis of Debye-type relaxation process originating due to trapping/detrapping and possibly due to scattering of carriers in the depletion regions.

Keywords. Dielectrics; ceramic semiconductors; zinc oxide; relaxation phenomena; varistors.

1. Introduction

Zinc oxide-based ceramic semiconductors (cersems), prepared by sintering of ZnO with one or more of the oxide additives like Bi_2O_3, BaO, Sb_2O_3, CoO, MnO_2 and/or Cr_2O_3 are known to exhibit a remarkable nonlinear current (I)-voltage (V) characteristics given by $I = KV^{\alpha}$, where the exponent α having a typical value of 50 is a measure of nonlinearity (Matsuoka 1971; Levinson and Philipp 1975; Mukae *et al* 1977; Bhushan *et al* 1981; Eda *et al* 1983). Microstructurally a ZnO nonlinear cersem is a two-phase composite having semiconducting/conducting ZnO grains embedded in thin insulating intergranular layers of additives of varying thickness estimated to lie between 10 nm and 1 μm (Matsuoka 1971; Levinson and Philipp 1975, 1976; Morris 1976; Clarke 1978; Santhanam *et al* 1979). Owing to their large current-carrying capacity and quick response time these composites find tremendous application potential as varistors.

There are only a few reports which exclusively discuss the dielectric properties of ZnO cersems (Delaney and Kaiser 1967; Levinson and Philipp 1976, 1978; Matsuura and Yamaoki 1977; Chopra *et al* 1983). In some other cases only a mention of strikingly high dielectric constant and/or appearance of loss peak at or nearly at 300 kHz has been made (Eda *et al* 1980; Bhushan *et al* 1981). The observed broad peak in dielectric loss ($\tan\delta$) vs frequency curve could not be attributed to any single model. Whereas Levinson and Philipp (1976, 1978) rejected the Maxwell-Wagner model of interfacial polarization at temperatures other than 4 K, and explained the observed dispersion on the basis of defect-states model. Matsuura and Yamaoki (1977) simulated the Maxwell-Wagner model to fit the observed loss curves of ZnO varistors. In some cases the estimated high value of dielectric constant (~ 1000) and the capacitance value of 0·18 μF/cm^2/grain have been ascribed to the insulating inter-granular layers (Matsuoka 1971; Levinson and Philipp 1975; Morris 1976).

---

†To whom all correspondence should be addressed.

In order to understand the role of microstructure, composition and inter-granular potential barrier on the observed dielectric properties of ZnO-based cersems, these composites have been systematically investigated in the present study. Results of the effect of composition and sintering parameters on the dielectric properties and dependence of dielectric parameters on frequency, temperature and bias voltage are discussed.

2. Experimental

Zinc oxide cersems having different combinations of additives were prepared by a standard ceramic sintering technique. Mechanically polished and ultrasonically cleaned samples were annealed at 200°C in a vacuum of about 10^{-5} torr for 30 min so that any adsorbed gases or volatile impurities are removed. Dielectric constant (ε') and dielectric loss ($\tan\delta$) of the composites were measured at different temperatures ranging from 200 to 400 K in the frequency range of 10^2 to 10^6 Hz by employing an LCR bridge and a Wayne-Kerr bridge. That the measurements are not affected by the electrode capacitance is confirmed by the observation that the dielectric parameters thus measured are independent of sample thickness. Bias dependence of capacitance was plotted at a fixed frequency of 10^6 Hz using a C-V plotter (Plotomatic 715 MSI Electronics).

The composition (elemental) analysis and depth profile of various cersems were obtained by Auger electron spectroscopy technique using a super SAM 590A instrument. An electron beam of 0·2 μ diameter with 0–10 kV energy was used in scanning mode. Analysis could be done in both the spot as well as scanning mode, with a spatial resolution of about 0·2 μ. The depth profile of various constituent elements was achieved by etching with a calibrated 5 kV argon ion beam of 300 μ diameter which could be rastered over different areas ranging from 1×1 mm^2 to 10×10 mm^2.

3. Results and discussion

3.1 *High dielectric constant and depletion layer model*

The values of capacitance and dielectric constant of various cersems having different compositions and prepared under varied experimental conditions are presented in table 1. It can be seen that the composites showing linear *I-V* characteristics exhibit

Table 1. Capacitance/dielectric constant of various ZnO cersems measured at 10^3 Hz.

Sample	Sintering temperature (°C)	Capacitance/cm^2 (sample thickness = 1 mm) (pF/cm^2)	Capacitance (μF/cm^2/G.B.)	Dielectric constant
ZnO-Cr_2O_3	1200	24	—	26^L
ZnO-CoO	1200	20	—	22^L
ZnO-Bi_2O_3,M	800	17	—	19^L
ZnO-Bi_2O_3,M	900	570	0·20	450^N
ZnO-Bi_2O_3,M	1000	1000	0·22	820^N
ZnO-Bi_2O_3,M	1200	2600	0·27	2080^N
ZnO-CoO-La_2O_3	1200	3700	0·26	2960^N

L, linear (ohmic) system; N, nonlinear (nonohmic) system; M, multicomponent.

values of dielectric constant (ε') which are comparable to those for the constituent oxides ($\varepsilon' = 10$ to 30), whereas all the cersems exhibiting nonlinear characteristics have shown higher values ($\sim 10^3$) of dielectric constant. A typical multicomponent composite of ZnO, having 0·5 mol% of each of the additives including Bi_2O_3, MnO_2, CoO and Sb_2O_3, hereafter referred to as ZnO-Bi_2O_3, M, sintered at 1200°C has a dielectric constant of 2080 whereas its constituents have values of dielectric constant below 30.

It may be noted that the nonlinear behaviour in cersems is caused by a two-phase microstructure and that only nonlinear cersems have a strikingly high value of dielectric constant. This implies that a two-phase microstructure is a pre-requisite for observing abnormally high values of dielectric constant. In order to quantitatively account for the observed value of dielectric constant/capacitance, the two-phase microstructure can be idealized as depicted in figure 1a and further simplified, as in figure 1b, by neglecting the contribution of interfaces which are perpendicular to

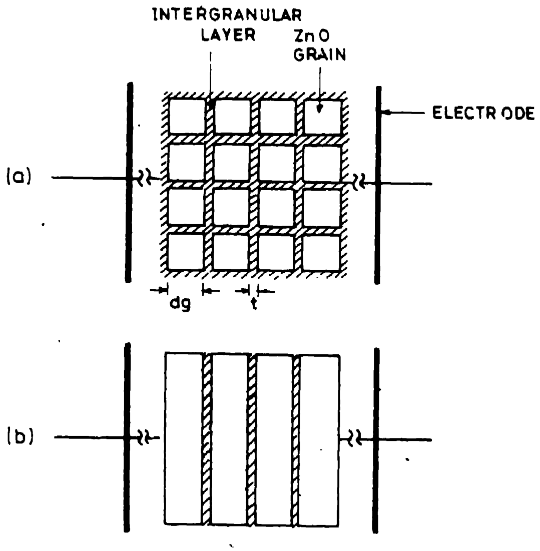

Figure 1. Sketch of an equivalent microstructure of a ZnO multicomponent nonlinear cersem.

electrodes. The total cross-section of the grains in each column, parallel to an electrode, is approximated to the area of the electrode itself, for nearly 1 nm thick intergranular layer can be neglected in comparison to the grain size of 10 μm.

A sequential mild etching with extremely low rates (1 nm/min) followed by an Auger scan was performed to carry out the depth profile. Etching was preferred over ion-induced depth-profiling due to charging of the specimen by ion-beam and extreme thinness of the intergranular layer in question. Typical Auger scans on both the unetched and etched surfaces are shown in figure 2. It is interesting to note that the carbon signal appearing due to contamination of the sample surface and Bi signal ($N_6O_{4,5}O_{4,5}$: 101 eV) vanish and the Zn signal ($M_1M_{4,5}M_{4,5}$: 107 eV) enhances after ion etching. This implies that ZnO grains are initially coated with a Bi_2O_3-rich layer and the thickness of the intergranular layers is nearly 1 to 2 nm.

Using the expression for the capacitance of a cersem in the simplified geometry of figure 1b, the value of C/area $= \varepsilon_0\varepsilon'/nt$, (where ε' is the dielectric constant of additives ($\sim$20), t, the thickness of intergranular layer and n, the number of intergranular layers per mm) comes out to be about 10^5 PF/cm^2 (for a sample with $n=50$, $t=1$ nm, this is about two order of magnitude higher than the observed value. It is therefore clear that thicker dielectric layers are required to arrive at the observed value. Such insulating layers are expected to be present in the form of depletion

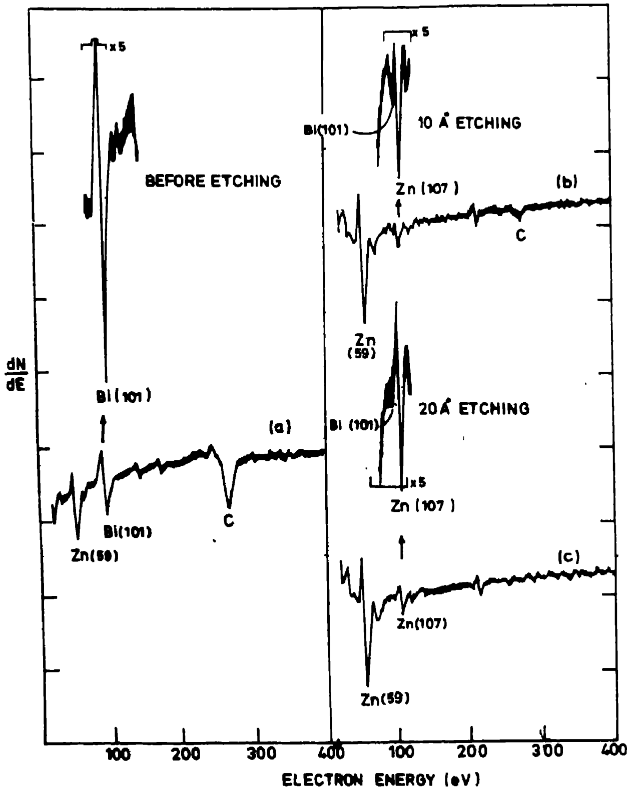

Figure 2. Auger electron spectra of ZnO-Bi_2O_3 (2 wt.%) cersem taken at different depths with sequential ion etching: **a.** Before etching. **b.** 10 Å etching and **c.** 20 Å etching.

layers in the conducting ZnO grains originating at grain intergranular interfaces due to trapping of charge carriers by the surface states/traps and defects present at/near the interface.

In the present case, where two junctions are placed back to back with each other, the total capacitance can be written as

$$(1/C - 1/2\,C_0)^2 = 2(\phi_0 + V)/E\varepsilon_0 \varepsilon n_0, \tag{1}$$

where

$$C = e\varepsilon_0 \varepsilon n_0 / 2(\phi_0 \pm V)^{1/2},$$

and

$$\tfrac{1}{2}C_0 = (2\phi_0 / e\varepsilon_0 \varepsilon n_0), \tag{2}$$

Here C represents the capacitance/junction, n_0, the carrier concentration and ϕ_0, the barrier height.

The width of depletion layer (X_0) and interface charge density (Q) can be estimated using the following standard relations

$$x_0 = (2\varepsilon_0 \varepsilon \phi_0 / e n_0)^{\frac{1}{2}}, \tag{3}$$

$$Q = 2eX_0 n_0. \tag{4}$$

As expected from (1), the plot of $(1/C - 1/2C_0)^2$ vs V of a ZnO-Bi_2O_3, M cersem, shown in figure 3, is a straight line which confirms the barrier model. The values of n_0 and ϕ_0 calculated from the slope and intercept on the voltage axis, respectively, are found to be $2{\cdot}26 \times 10^{18}\,\mathrm{cm}^{-3}$ and 0·85 eV. The density of states N_s at the interface between the ZnO grain and the intergranular layer as estimated from $N_s = (2N_d \varepsilon_s \varepsilon_0 \phi_0 / q)^{\frac{1}{2}}$ is found to be $4{\cdot}61 \times 10^{12}\,\mathrm{cm}^{-2}$. Nearly the same value of n was

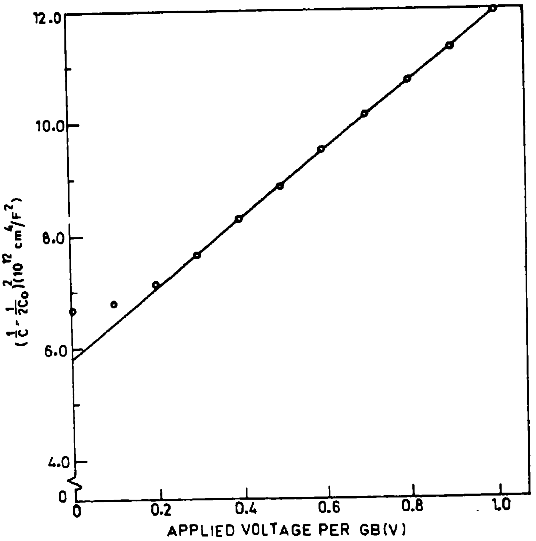

Figure 3. Variation of $\left(\frac{1}{C} - \frac{1}{2C_0}\right)^2$ vs applied voltage per grain boundary of a ZnO multicomponent cersem.

found from the Hall measurements. Also the depletion layer width and capacitance/junction/cm^2 have been calculated to be 60 nm and about 0·15 μF respectively. The latter agrees well with the observed values given in table 1.

Figure 4 shows the variation of dielectric constant of ZnO-Bi$_2$O$_3$, M with sintering temperature. It is clear from table 1 and figure 4 that the dielectric constant of the composite increases monotonically with sintering temperature. The observed increase in grain size with sintering temperature (figure 4) helps in explaining the variation of dielectric constant. Higher sintering temperature increases the grain size i.e. lowers n and hence nt resulting in higher values of observed capacitance/cm^2 and dielectric constant. Experimentally observed values of 0·2 to 0·3 μF/cm^2/junction for capacitance agree well with the calculated values. The low values of dielectric constant for linear cersems like ZnO-CoO, ZnO-Cr$_2$O$_3$ and ZnO-Bi$_2$O$_3$, M sintered at 800°C are understandable because in these systems of microstructurally randomly dispersed constituents there are no segregated intergranular layers between conducting ZnO grains and depletion layers in ZnO grains.

3.2 *Dielectric dispersion at room temperature*

The frequency dependence of the capacitance, the dielectric constant (ε') and $\tan\delta$ $(=\varepsilon''/\varepsilon')$, where complex dielectric constant $\varepsilon=\varepsilon-j\varepsilon''$, has been carried out for nonlinear cersems of various compositions.

The frequency dependence of capacitance and dielectric constant for a binary ZnO-Bi$_2$O$_3$ cersem having a low value (~ 6) of nonlinearity parameter is plotted in figure 5. In this case capacitance shows a dispersion in the entire frequency range with its value decreasing with frequency. Similar variation is exhibited by $\tan\delta$ up to a frequency of 10^4 Hz.

A dissipation maxima ($\tan\delta_{\max}$) is evident at a frequency of 3×10^5 Hz. The variation of ε' and $\tan\delta$ as a function of frequency for a ZnO-Bi$_2$O$_3$, M cersem is plotted in figure 6. The value of ε' decreases slowly with increasing frequency up to

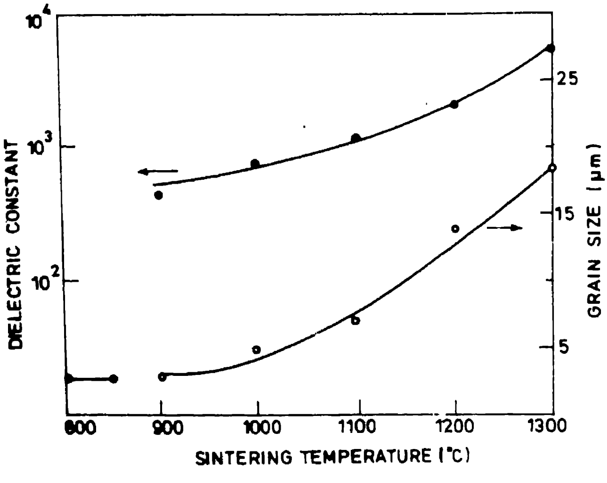

Figure 4. Variation of dielectric constant and grain size with sintering temperature of a ZnO multicomponent cersem.

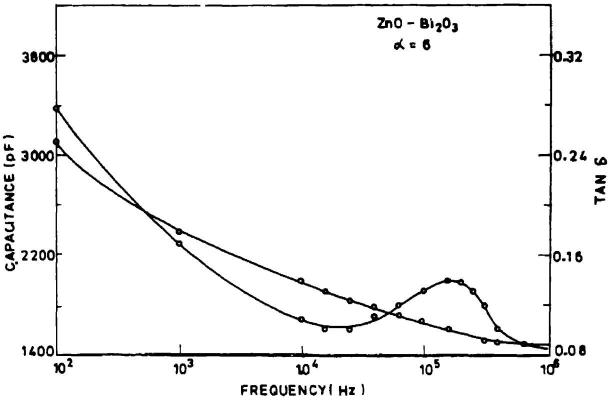

Figure 5. Variation of capacitance and tan δ of a binary cersem with frequency.

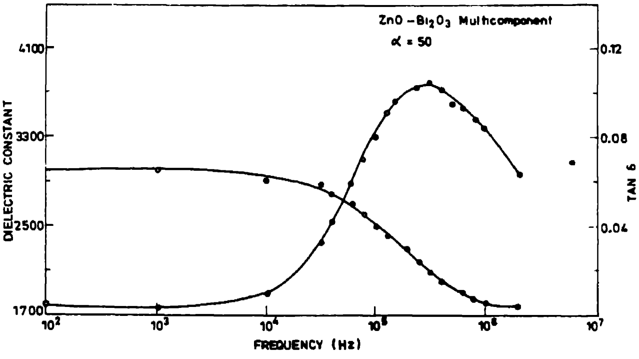

Figure 6. Frequency dependence of dielectric constant (ε') and tan δ of the multicomponent cersem.

about 10^5 Hz and exhibits a noticeably sharper drop in the frequency range 10^5–10^6 Hz. The value of tan δ is very small at low frequencies and does not vary significantly up to a frequency of about 10^4 Hz. Beyond this frequency tan δ increases rapidly and exhibits a maxima around 3×10^5 Hz at room temperature.

It is noteworthy that while the value of capacitance, dielectric constant (ε') and tan δ at low frequencies is dependent on composition and fabrication process, tan $\delta_{\max}$ remains practically unaltered (observed at 3×10^5 Hz) with changes in composition and sintering parameters (Bhushan *et al* 1981). Even in degraded ZnO-Bi_2O_3, M ceramics, Eda (1984) reported the peaking of tan δ at the same frequency of 300 kHz.

Dielectric dispersion can be explained on the basis of Debye-type relaxation by drawing Cole-Cole plot (plot of ε' vs ε'') exhibiting a single or multiple relaxation times. In the present case a Cole-Cole plot for a high nonlinearity cersem is shown in figure 7. It is observed that the experimental data lie on a circular arc centred at a point below the ε'' axis. This suggests a distribution of relaxation times. The value of $n(n = 2\theta/\pi)$ has been found to be about 0·2 which corresponds to a distribution of relaxation time extending over one or two orders of magnitude. Such a Debye-type of relaxation may be attributed to an orientational polarization (Daniel 1967),

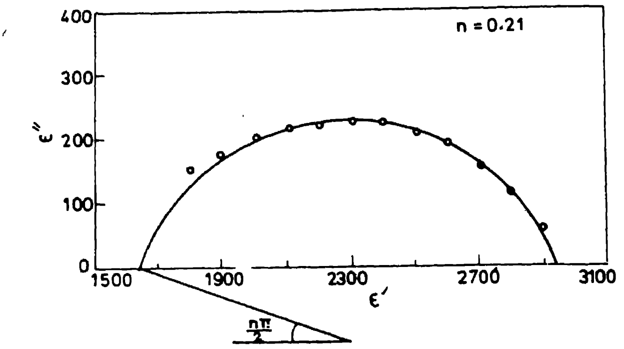

Figure 7. Cole-cole plot for ε' and ε'' of the multicomponent cersem of figure 6.

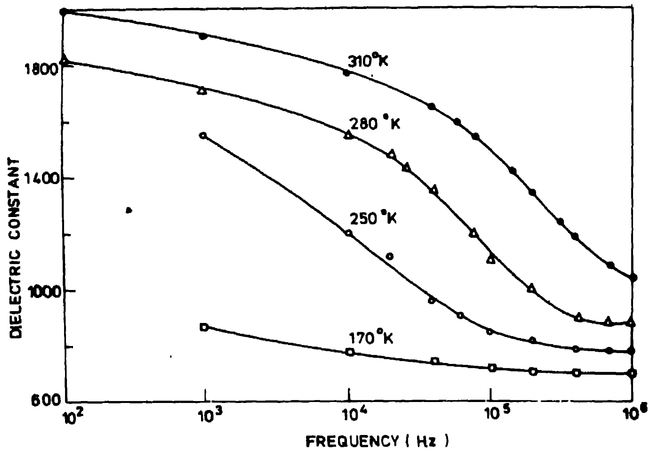

Figure 8. Frequency dependence of dielectric constant of the multicomponent cersem measured at different temperatures.

interfacial polarization (Maxwell-Wagner Model) (Volger 1960) or an electronic phenomena such as hopping, trapping and detrapping of carriers (Jonscher 1981).

In the case of ZnO nonlinear cersems, as shown in figures 5 and 6, the peak position of $\tan\delta$ is independent of composition, and the dielectric constant increases monotonically with temperature (figure 8). Furthermore, these observations cannot be accounted for by orientational polarization because this type of polarization is composition-dependent and the dielectric constant of a material in this case is known to be inversely proportional to temperature (Meakins 1961).

According to interfacial polarization theory, often applied to polycrystalline semiconductors having regions (d_i), of different electrical conductivity (σ_i), and dielectric constant (ε_i), the values of dielectric constants ε_∞ (at $w=\infty$) and ε_s (at $w=0$), are expressed as

$$\varepsilon_\infty = \sum d_i \Big/ \sum (d_i/\varepsilon_i), \tag{5}$$

$$\varepsilon_s = \frac{\left\{\sum d_i\right\}\left\{\sum (d_i \varepsilon_i/\sigma_i^2)\right\}}{\left\{\sum (d_i/\sigma_i)^2\right\}} \tag{6}$$

In the present case the composite is simply assumed to be a mixture of two materials—ZnO grains and depletion regions including intergranular layers. As already established, the depletion layer d_1, is very thin as compared to ZnO grain d_2. Assuming that the intrinsic dielectric constant of the thin layer (most of it extending into ZnO as a depletion layer) has the same value as in the grain ε_2, the expression for ε_∞ reduces to $\varepsilon_\infty = \varepsilon_z = 10$. Since the resistance of the blocking layer has a high value $(d_1\rho_1 \gg d_2\rho_2)$, the expression for ε_s reduces to $\varepsilon_s = (d_2/d_1)\varepsilon_2 = 10 \times 10^{-5}$ m/ 10^{-7} m $= 1000$, which is nearly half the observed value (figure 6). In this case the loss-factor peaking at frequency ω is expressed as

$$\tan\delta = (d_2/d_1)[\omega\tau_\delta/(1+\omega^2\tau_\delta^2)], \tag{7}$$

where τ_δ, the relaxation time at loss angle, δ, is written as

$$\tau_\delta = (\varepsilon_\infty/\varepsilon_s)^{\frac{1}{2}}\, \varepsilon_0 \frac{\varepsilon_2 d_2 + \varepsilon_2 d_1}{\sigma_2 d_2 + \sigma_2 d_2} \tag{8}$$

Using $\sigma_1 = 10^{-10}$ mho cm^{-1}, $\sigma_2 = 1$ mho cm^{-1}, $\varepsilon_0 = 8{\cdot}845 \times 10^{-12}$ F m^{-1}, an $\tan\delta_{\max} = 0{\cdot}14$, the value of $f_{\max}$ $(\omega_{\max}/2)$ is calculated to be nearly 10^{10} Hz, a valu which is five orders of magnitude higher than the one obtained experimentally. It is therefore, concluded that the Maxwell-Wagner theory of interfacial polarizatio cannot satisfactorily explain the observed dielectric behaviour.

The dielectric loss ($\tan\delta$) vs frequency plots at different temperatures is shown i figure 9. The peak position shifts towards lower frequency with decrease in th temperature of measurement. The above data have been replotted as $f_{\max}$ (th frequency at which $\tan\delta_{\max}$ occurs) vs $1/T$ in figure 10. An activation energy o

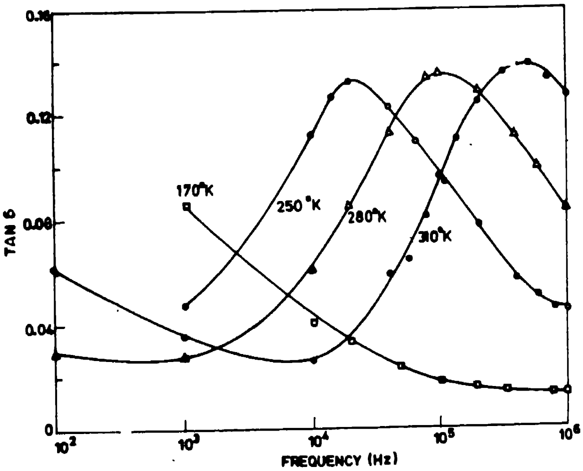

Figure 9. Variation of $\tan\delta$ with frequency of a ZnO multicomponent cersem measured different temperatures.

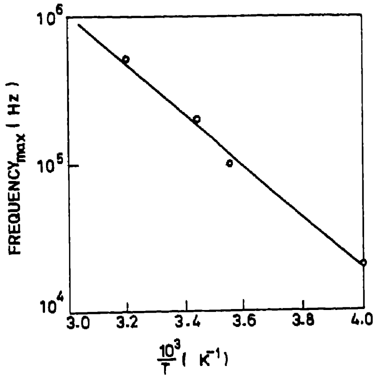

Figure 10. Variation of dissipation factor peak frequency (f_{max}) with inverse temperature of the multicomponent cersem.

0·36 eV, a value in agreement with the one due to Levinson and Philipp (1976), has been estimated from this curve for the dielectric relaxation process giving rise to loss peak.

The observed thermally-activated dissipation peak can be attributed to trapping/detrapping of carriers in the interface states. In the case of insulators and amorphous semiconductors exhibiting a broad distribution of relaxation times (as indeed observed in the present case) the dielectric loss is attributed to the hopping of electrons between localized defect states (Elliot 1984). A similar behaviour observed in *p-n* junction has also been explained on the basis of trapping/detrapping model by Barsony and Jonscher (1978).

It is therefore established that the observed dielectric dispersion of ZnO cersems is caused due to hopping, trapping and detrapping of electrons in the energy states lying in intergranular/depletion layers.

3.3 *Temperature dependence of dielectric constant/capacitance*

It is known that the energy difference between the bottom of the conduction band and the Fermi level E_F is proportional to [ln $(N_C/N_D)T$], where N_C is the effective density of states and N_D the donor density. As such, in ZnO with a high donor density, Fermi level is not expected to change significantly with increase in temperature from 100 to 300 K. This in turn will leave the barrier height (ϕ_0) unchanged in this temperature range. The carrier concentration n, as evident from (9) increases with the temperature

$$n=(2N_D)^{\frac{1}{2}} \left(\frac{2\pi m^* kT}{h^2}\right)^{\frac{3}{4}} \exp(-E_d/2KT) \tag{9}$$

where E_d is the ionization energy of donors. The invariance of ϕ_0 and increase of n with change in temperature from 100 to 300 K has been observed by the present authors. It can therefore be inferred from (3) that the thickness of a depletion layer which is inversely proportional to the square root of carrier concentration, decreases with increase in temperature and results in the increase of dielectric constant/capacitance as indeed observed (figures 8 and 11).

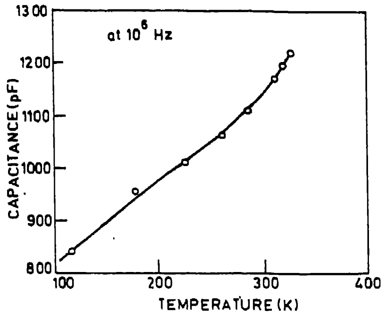

Figure 11. Variation of capacitance with measurement temperature of a Z multicomponent cersem.

4. Conclusions

(i) Zinc oxide-based nonlinear cersems exhibit extremely high dielectric consta (upto nearly 3×10^3) as compared to the linear cersems and the individual cc stituents (up to 30). Such a high dielectric constant arises solely because of a tw phase microstructure.

(ii) The observed high value of dielectric constant has been explained on the ba of depletion layers existing at grain-intergranular interfaces and extending into Z grains. Typical thickness of a depletion layer has been estimated to be approximat 10^2 nm. The thickness of an intergranular layer using Auger electron spectrosco however, has been determined to be 1 to 2 nm only.

(iii) The dielectric constant of the cersems has been found to depend on the gra size of conducting ZnO (which in turn is a function of sintering temperatu Increase in sintering temperature results in the increase of both the grain-size and dielectric constant. The increase in dielectric constant has been successfully explai on the basis of the depletion layer model and the simplified microstructure of cersems.

(iv) The dielectric constant (ε') and dielectric loss ($\tan\delta$) exhibit a dispersion in frequency range of 10^2 to 10^6 Hz. While the values of ε' and $\tan\delta$ are quite sensit to fabrication process at low frequencies, the $\tan\delta$ peak position remains practic unaltered with change in composition or sintering parameters. The dispers associated with a distribution of relaxation times is explained on the basis of Deb type relaxation process caused due to trapping/detrapping of electrons in the st available in depletion layer and interface.

(v) The monotonic increase in dielectric constant/capacitance with temperature the range of 170 to 310 K, has been attributed to the change in width of the deplet layer brought about by the change in carrier concentration.

Acknowledgement

One of the authors (BB) wishes to acknowledge the financial support from the Ind Institute of Technology, Delhi.

References

Barsony I and Jonscher A K 1978 *Solid State Electron* **21** 471
Bhushan B, Kashyap S C and Chopra K L 1981 *Appl. Phys. Lett.* **38** 160
Bhushan B, Kashyap S C and Chopra K L 1981 *J. Appl. Phys.* **53** 2932
Chopra K L, Bhushan B and Kashyap S C 1983 *J. Appl. Phys.* **54** 1610
Clarke D R 1978 *J. Appl. Phys.* **49** 2407
Daniel V V 1967 *Dielectric relaxation* (New York: Academic Press)
Delaney R A and Kaiser H D 1967 *J. Electrochem. Soc.* **114** 833
Eda K 1984 *J. Appl. Phys.* **56** 2948
Eda K, Iga A and Matsuoka M 1980 *J. Appl. Phys.* **51** 2678
Eda K, Eguchi H, Okinaka H and Matsuoka M 1983 *Jpn. J. Appl. Phys.* **22** 202
Elliot S R 1984 *Physics of amorphous materials* (London: Longman)
Jonscher A K 1981 *6th Progress Report of Chelsea Dielectric Group* (London: University Press)
Levinson L M and Philipp H R 1975 *J. Appl. Phys.* **46** 1332
Levinson L M and Philipp H R 1976 *J. Appl. Phys.* **47** 1117 and 3116
Levinson L M and Philipp H R 1978 *J. Appl. Phys.* **49** 6142
Matsuoka M 1971 *Jpn. J. Appl. Phys.* **10** 736
Matsuura M and Yamaoki H 1977 *Jpn. J. Appl. Phys.* **16** 1261
Meakins R J 1961 *Progress in dielectrics* (London: Heywood) vol. 3
Morris W G 1976 *J. Vac. Sci. Technol.* **13** 926
Mukae K, Tsude K and Nagasawa I 1977 *Jpn. J. Appl. Phys.* **16** 1361
Santhanam A T, Gupta T K and Carlson W G 1979 *J. Appl. Phys.* **50** 852
Volger J 1960 *Progress in semiconductors* (ed.) A F Gibson (New York: John Wiley) vol. 4

Bull. Mater. Sci., Vol. 9, No. 3, August 1987, pp. 181–185. © Printed in India.

Electrical resistivity of holmium hydride films

M S RAHMAN KHAN
Department of Applied Physics and Electronics, University of Rajshahi, Rajshahi
Bangladesh

MS received 2 June 1986; revised 3 March 1987

Abstract. The electrical resistivity and temperature coefficient of resistance o polycrystalline holmium hydride films, grown on glass slides, have been measured in vacuc Experimental results show that the resistivity decreases with decreasing film thickness. Th resistivity of 200 Å holmium dihydride film is less than that of the parent metal. Th observed behaviour of the thickness dependence of the resistivity has been explained i terms of the structural phase change.

Keywords. Holmium hydride films; electrical resistivity; temperature coefficient c resistance.

1. Introduction

Although considerable work has been done on the electrical properties of thin film of metal (Chopra 1969; Maissel and Glang 1970; Samble 1983), not much is know about the thin films of rare earth metals and their hydrides. It was therefore fe worthwhile to carry out some investigations on the electrical properties of the film grown from holmium which is one of the heavy rare earth metals.

Conductivity measurements have earlier been made on most of the rare eart metals and their hydrides in the bulk form (Heckman 1969; Kubota and Walla 1963). The results show a wide variation of conductivity of the Ho-H syste depending upon its composition, e.g. the nonstoichiometric dihydride has high conductivity than the parent metal.

The electronic properties of rare earth hydrides are usually discussed in terms either protonic hydrogen model or the anionic hydrogen model (Libowitz 1968; B and Gayer 1966; Heckman 1969; Colvin *et al* 1960). In the former, the hydrog contributes an electron to the system's conduction band, while in the anionic mod it extracts one. It has been shown that when holmium metal (having an h.c. structure) is thermally evaporated, the condensed film form f.c.c. dihydrides up 200 Å thickness (Khan and Miller 1979; Curzon and Chlebeck 1972; Curzon a Singh 1975; Gasgnier *et al* 1974). Films thicker than 820 Å have h.c.p. bulk structu while films of intermediate thickness have a mixed phase (f.c.c. dihydride + h.c metal). This paper aims at reporting the anomalous behaviour of the resistivity of t film prepared from holmium and to correlate them with the structural stud mentioned above.

2. Experimental

Thin films of holmium hydride (thickness range 70–900 Å) were prepared by vacu evaporation of holmium wire (99·9% purity, Koch Light, U.K.) onto precleaned sc glass microscope slides at a pressure of about 10^{-6} torr. The materials were evaporated from helical tungsten filament.

Making reliable electrical contact to the films is always a problem, but this was overcome by constructing 4 spring-loaded flat ended copper rods (0·15 cm diameter) fixed with the mask so that they could be easily adjusted to make good electrical contact with the predeposited nichrome electrode on the substrate. The system was found to give a satisfactory ohmic contact to the film in the temperature range 77°K to 573°K. By using suitable masks, nichrome films of about 1500 Å thickness were deposited on the previously cleaned substrates to form contact electrodes and were found very effective. Contacts to the films were made by evaporating the holmium hydride films over the predeposited nichrome electrodes.

The resistance measurement in this work was carried out employing a conventional four-probe technique (Vander Pauw 1958). A constant current in the range 200–500 μA was passed through the specimen between two probes and the voltage developed between the other two probes was measured. The voltage across the two potential probes was measured using a d.c. microvoltmeter sensitive to 100 μV. The current was measured with an electrometer sensitive to 10^{-14} amps. The resistivity value for a film of a particular thickness was reproducible, when the observations were repeated on the films of the same thickness grown under identical conditions. The film temperature was varied by using a specially designed radiant heater and was measured by a $T_1 - T_2$ chromel alumel thermocouple. The temperature between the ambient and the liquid nitrogen was achieved by using a conduction cooled cryostat, a very simple device constructed in the laboratory. The film thickness was determined by Tolansky's multiple beam interferometric method.

3. Results and discussions

The electrical resistivity (at 77°K and in the range 293–573°K) and the temperature coefficient of resistance of the polycrystalline films grown from holmium are discussed here. The structure of the same films has been determined by electron diffraction studies (Khan and Miller 1979) and attempts have been made to correlate the dependence of the electrical resistivity and structures on thickness.

The thickness dependence of the electrical resistivity of holmium hydride films at room temperature is shown in figure 1. The resistivity of the films thinner than 70 Å could not be accurately measured because of their discontinuous structures (Khan 1976). The curve of figure 1 is reproducible to within experimental error. The non-stoichiometric characteristics of the rare earth hydride, especially dihydride and the lack of knowledge of the exact composition (i.e. H/Ho atomic ratio) of the film made it difficult to precisely explain the behaviour of resistivity vs thickness curve. However, attempts have been made to put forward arguments and evidences to explain the characteristics on the basis of bulk dihydride resistivity, our own structural investigations and the observed resistivity values.

An examination of the curve shows its anomalous behaviour. The salient features of the resistivity thickness curve are (i) the resistivity has a minimum value of 60 $\mu\Omega$-cm at a film thickness of about 200 Å and increases for thinner films and (ii) an abnormal increase occurs in the resistivity of the films thicker than 200 Å and continues to increase until it becomes nearly constant at 900 Å.

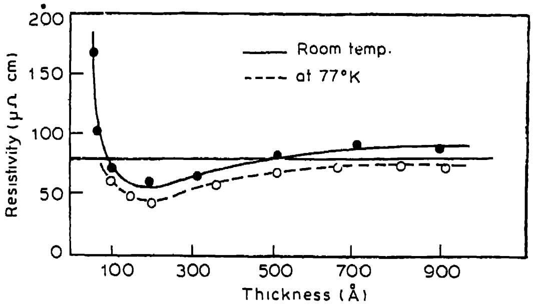

Figure 1. Thickness dependence of resistivity of holmium hydride films (70–900 Å).

An interesting feature of the experimental results is that the resistivity of 200 Å film (60 μΩ-cm) is less than that of the parent metal (for bulk Ho, $\rho = 81$ μΩ-cm). This clearly indicates that 200 Å film (holmium dihydride) is a better electrical conductor than the parent metal, which is similar to the behaviour of gadolinium dihydride films (Khan 1976) and holmium dihydride bulk materials (Heckman 1969). In the bulk Ho-H systems, the f.c.c. dihydride phase exists in the composition range H/Ho (atomic ratio) = 1·95–2·24 (Libowitz 1965). Structural investigations by Khan and Miller (1979) indicated that the films in the thickness range 70–200 Å are f.c.c. dihydrides and the thickness of 200 Å marks the boundary between single phase f.c.c. dihydride and mixed phase (f.c.c. dihydride + h.c.p. metal) and has the minimum resistivity value (60 μΩ-cm), which agrees with the resistivity behaviour of bulk holmium dihydride (Heckman 1969).

It may be seen from figure 1 that the resistivity of films in the thickness range 200–900 Å (which have mixed phase) is higher than 60 μΩ-cm, which is again in agreement with the bulk Ho-H system. The increase in resistivity with the decrease of thickness in the range 70–200 Å (which has a continuous structure) is due to the nonstoichiometric composition of holmium dihydride which may exist over the above thickness range. The sharp rise in resistivity below 70 Å thickness is due to the discontinuous structure of the film. As the thickness of the film was increased to 900 Å (which is almost h.c.p. Ho) the resistivity attained nearly a constant value (93 μΩ-cm). This value is consistent with the known bulk resistivity (81 μΩ-cm). The somewhat higher values (15%) of resistivity for the thicker films compared with the bulk metal can be attributed to inherent film defects such as point defects, vacancies, grain boundaries, dislocations etc. The resistivity of the films in the thickness range 70–99 Å at 77°K is shown by the dashed curve (figure 1). The lower values of the resistivity at liquid nitrogen temperature are generally expected (Gillam *et al* 1955) and characterizes the metallic nature of the films.

The variation of resistance with temperature was measured for five films of thickness range 140 to 900 Å. Typical data are shown in figure 2, in which the resistivity of the films has been plotted as a function of temperature for heating rate 2–3°K/min. The resistivity was measured over the temperature range of 293–573°K at intervals of 50°K. The increase in resistivity with temperature was found to be linear for films thicker than 140 Å.

The general behaviour of the temperature dependence of resistivity indicates the conduction as metallic (Chaudhury and Pal 1975). The temperature coefficient of

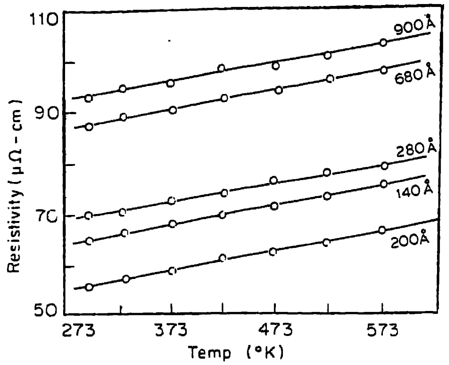

Figure 2. Variation of resistivity with temperature of holmium hydride films.

Table 1. Temperature coefficient of resistance (TCR) values of holmium hydride films.

Film thickness (Å)	TCR(°K)
140	0·00019
200	0·00020
280	0·00022
680	0·00020
900	0·00016

resistance (TCR) of the films was measured in the range 273–343°K by thermally cycling the films to allow for small changes in their electrical characteristics. The observed TCR values are recorded in table 1. There is no TCR data available for comparison (even on bulk material).

The curious feature of the results is that the resistivity of the films of limiting thickness (200 Å) is less than that of the bulk parent metal. The anomalous resistivity behaviour can be explained quite satisfactorily on the basis of the nonstoichiometric composition and consequently on the thickness dependence of the structural phase of dihydride films. The composition of the films could not be given due to experimental problems but could be well inferred from the structural investigations (Khan and Miller 1979; Khan 1976) where the diffraction pattern clearly shows that the intensities of the different reflections varied over the thickness range 200–900 Å. The resistivity of the bulk rare earth dihydride is highly dependent on nonstoichiometric composition (Heckman 1969; Colvin *et al* 1960) and it is evident from the present experimental results that the resistivity depends on the structural phase (which is again dependent on thickness). The resistivity results are quite in agreement with terbium hydride films (Khan 1977) and with the behaviour of the bulk rare earth dihydride resistivity (Heckman 1969; Colvin *et al* 1960).

4. Conclusion

The effective thickness dependence of the resistivity of the holmium hydride films can be assumed to arise from a superposition of several factors, namely, the usual surface scattering component, structural phase change, nonstoichiometric composition of the dihydride phase and the coexistence of the dihydride and metallic phase in certain thickness range. The temperature dependence of resistivity and TCR values indicate, generally, metallic conduction characteristics.

References

Bos W G and Gayer K H 1966 *J. Nucl. Mater.* **18** 1
Chopra K L 1969 *Thin film phenomena,* (New York; McGraw Hill)
Choudhury S and Pal A K 1975 *J. Phys.* **D8** 1311
Colvin R V, Legvold S and Spedding F H 1960 *Phys. Rev.* **120** 741
Curzon A E and Chlebeck H G 1972 *J. Less Common Metals* **37** 411
Curzon A E and Singh O 1975 *J. Less Common Metals* **39** 227
Gasgnier M, Ghys J, Schiffmacher G, Henry C and Caro P E 1974 *J. Less Common Metals* **34** 131
Gillam E J, Preston J S and Williams B 1955 *Philos. Mag.* **46** 1051
Heckman R C 1969 Sandia Laboratories SC-RR-69-571
Khan M S R 1976 *Growth and structure of epitaxial rare earth hydride,* Ph.D. Thesis, University of London
Khan M S R 1977 *J. Bangladesh Acad. Sci.* **1** 1
Khan M S R and Miller R F 1979 *J. Phys.* **D12** 271
Kubota Y and Wallace W E 1963 *J. Chem. Phys.* **39** 1285
Libowitz G G 1965 *Solid state chemistry of binary metal hydrides* (New York: Benjamin Inc.)
Libowitz G G 1968 *Metal hydrides* (New York; Academic Press)
Maissel L I and Glang R 1970 *Handbook of thin film technolcgy* (New York: McGraw Hill)
Samble J R 1983 *Thin Solid Films* **106** 321
Vander Pauw 1958 *Philips Res. Rep.* **13** 1

Bull. Mater. Sci., Vol. 9, No. 3, August 1987, pp. 187–191. © Printed in India.

Electrical conductivity and transition temperature of NbN thin films

C S MENON* and V S PANKAJAKSHAN
Department of Physics, University of Calicut, Calicut 673 635, India
*Present address: Department of Physics (Materials Science), Gandhiji University, Kottayam 686 002, India

MS received 8 September 1986; revised 21 February 1987

Abstract. Niobium nitride thin films are grown using reactive RF sputtering technique for four different partial nitrogen pressures in argon atmosphere. The superconducting transition temperature of the films has been measured. The films exhibit a negative temperature coefficient of resistivity. The electrical characterization of the films has been carried out and the conductivity measured between room temperature and liquid nitrogen temperature. This is fitted using T^p law.

Keywords. Niobium nitride; thin film; sputtering; super-conducting transition temperature.

1. Introduction

Aschermann *et al* (1941) discovered that niobium nitride (NbN) has a cubic structure and has a relatively high superconducting transition temperature. We have employed the RF reactive sputtering method (Wolf *et al* 1980) for the deposition of NbN films. In this method, while sputtering is done in an atmosphere of nitrogen and argon, the ionized nitrogen combines with niobium atom and NbN is deposited onto the substrate. The deposition parameters like substrate temperature, deposition rate and partial pressures of reactive gases influence the stoichiometry of NbN films (Bacon *et al* 1983).

NbN is a technologically promising material in the fabrication of Josephson junction devices (Classen 1984) and submillimeter wave detectors (Carr *et al* 1984). The critical current and field characteristics studies of NbN were mainly done by Ashkin *et al* (1984).

In the present work we have made use of the reactive RF sputtering technique to produce NbN films at different partial nitrogen pressures. It is observed that the values of superconducting transition temperature T_c, sheet resistivity R and resistance ratio $\beta(=R_{300}/R_{77})$ depend considerably on the partial nitrogen pressures. The electrical conductivity of the films was measured in the temperature range 77 K and 305 K and fitted using a T^p law.

2. Experimental details

The sputtering apparatus consists of a stainless steel chamber evacuated by a rotary pump and a 10 cm diffusion pump. A niobium disc (99·9% pure) was placed over the stainless steel cathode and an RF potential was applied to the cathode.

Quartz substrates of 25 × 5 mm were washed with detergent, water and distilled water. Subsequently they were agitated in an acetone bath in an ultrasonic cleaning device and dried in an oven. They were then placed above the cathode at a distance of 4 cm. In all cases the substrate temperature was kept at 475°C.

When the residual gas pressure in the chamber was 1×10^{-6} torr, dry nitrogen was introduced into it and the desired pressure was maintained. Pure argon gas was then introduced and the total pressure was kept at 8×10^{-3} torr in all cases. Pre-sputtering for 30 min was effected with a closed shutter which was opened for 30 min and the films deposited. When the sputtering was complete the needle valve in the argon gas line was closed and the nitrogen pressure was again checked.

The voltage and current leads were connected to the sample using indium soft bonding. The sample was placed in a copper chamber containing liquid helium. The temperature was measured by a calibrated germanium resistance thermometer. The transition temperature was measured by simultaneously plotting the potential across the voltage leads and the potential across the germanium sensor on a chart recorder. The transition temperature T_c was measured as that temperature at which the resistance of the sample was half the normal value. The transition width ΔT_c was the temperature difference between 90% and 10% values of the normalized resistance of the sample.

For measuring the voltage-current characteristics between room temperature and liquid nitrogen temperature, the samples were cooled by keeping them in a liquid nitrogen cryostat.

For different current through the samples, the potential across the voltage leads was measured by a digital multimeter (model HIL 2645) at different temperatures. The temperature of the films was measured using a copper-constantan thermocouple.

3. Results and discussion

Figure 1 shows a representative voltage-current characteristic of the sputtered NbN films for partial nitrogen pressure of 2×10^{-3} torr at different temperatures. It is seen

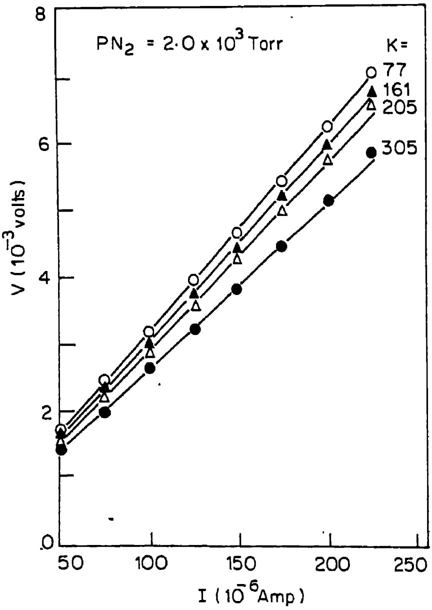

Figure 1. Voltage current characteristics at various temperatures for $P_{N_2} = 2 \times 10^{-3}$ torr.

that the resistivity increases with increasing partial nitrogen pressures while the same decreases with increasing temperature. The conductivity σ of the films was found out from the characteristic curves for various temperatures. A plot between $\log_e \sigma$ vs $\log_e T$ as shown in figure 2 is a straight line. These experimental points are fitted using a T^P law. This agrees with the observations of Ayer and Rose (1973). The P values obtained from the slopes of the temperature-conductivity graphs showed an increase from 0·07 to 0·26 as the partial nitrogen pressure increased from 2×10^{-3} to 6×10^{-3} torr. Since all P values were positive, all the NbN films showed a negative temperature coefficient of resistivity (TCR). The TCR is more negative for films prepared with higher nitrogen pressures. The calculated resistance ratio β for these samples is less than unity indicating that these films are possibly granular or of the columnar void structure (Cukauskas *et al* 1985). Keskar *et al* (1971) obtained a nearly constant unity value for β in this range of pressures. Table 1 shows the T_c and ΔT_c for different samples. Figure 3 shows a representative T_c graph of the NbN film grown at partial nitrogen pressure of 2×10^{-3} torr.

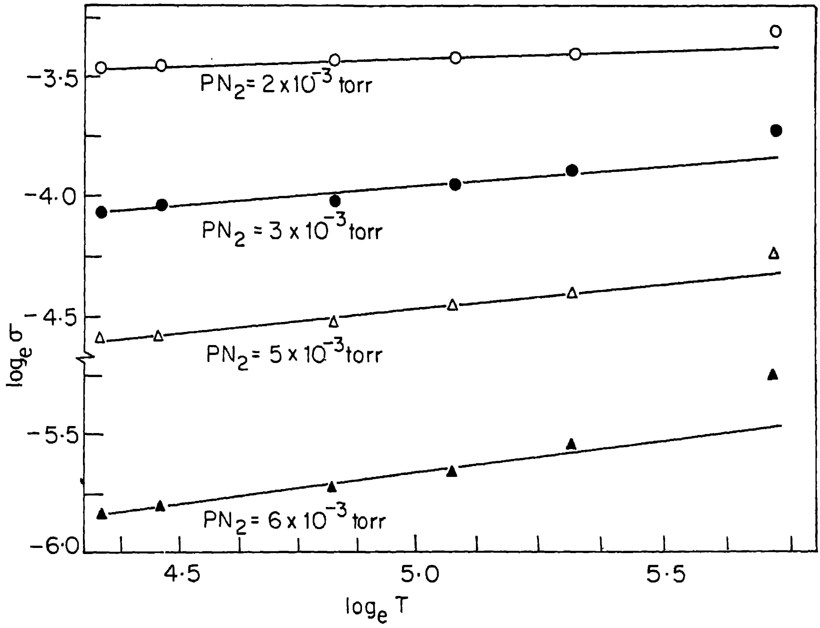

Figure 2. $\log_e \sigma$ vs $\log_e T$ for various partial nitrogen pressures.

Table 1. Superconducting transition temperature T_c and ΔT_c of NbN films at different partial nitrogen pressures PN_2.

$PN_2 \times 10^{-3}$ torr	T_c(K)	ΔT_c(K)
2	11·4	0·5
3	9·0	0·5
5	6·4	0·6
6	4·8	1·0

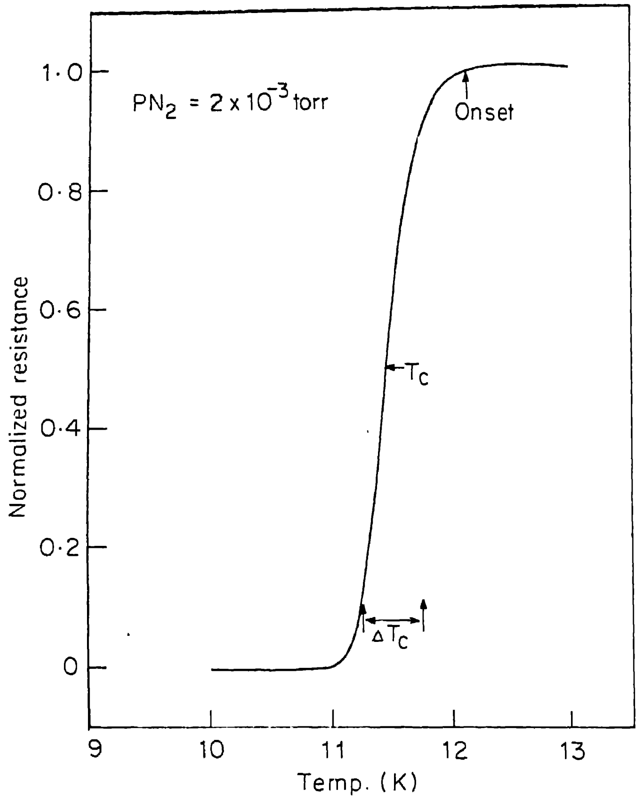

Figure 3. Superconducting transition temperature T_c graph of NbN film at partial nitrogen pressure $P_{N_2} = 2 \times 10^{-3}$ torr.

4. Conclusion

NbN films have been prepared by reactive RF sputtering technique at different partial nitrogen pressures. The films exhibit a wide range of electrical and superconducting properties which depend mainly on the partial nitrogen pressure in argon atmosphere. The films prepared on a partial nitrogen pressure of 2×10^{-3} torr have a better T_c of 11·4 K. The transition width is broad for films prepared at 6×10^{-3} torr pressure.

The conductivity of the films between room temperature and 77 K is found to obey the relation $\sigma \propto T^P$. The resistance ratio β for the films is less than unity.

Acknowledgement

The authors thank Prof. S C K Nair for his keen interest and encouragement.

References

Aschermann G, Fridrich E, Justi E and Kramer J 1941 *Z. Phys.* **42** 349
Ashkin M. Gavaler J R and Greggi J 1984 *J. Appl. Phys.* **55** 1044

Ayer W J Jr and Rose K 1973 *Phys. Lett.* **A45** 333

Bacon D D, English A T, Nakahara S, Peters S, Schreiber H, Sinclair W R and Van Dover R B 1983 *J. Appl. Phys.* **54** 6509

Carr G L, Karecki D R and Perkowitz S 1984 *J. Appl. Phys.* **55** 3892

Classen J H 1984 *J. Appl. Phys.* **55** 3367

Cukauskas E J, Carter W L and Quadri S B 1985 *J. Appl. Phys.* **57** 2538

Keskar K S, Yamashita T and Onodera Y 1971 *J. Appl. Phys.* **10** 370

Wolf S A, Singer K L, Cukauskas E J, Francavilla T L and Skelton E F 1980 *J. Vac. Sci. Technol.* **17** 411

Bull. Mater. Sci., Vol. 9, No. 3, August 1987, pp. 193–202. © Printed in India.

Optical properties of coloured transparent alumina gel monolith glasses

V SARASWATI and G V RAMARAO
Materials Development Laboratory, Indira Gandhi Centre for Atomic Research, Kalpakkam 603 102, India

MS received 26 March 1987; revised 27 May 1987

Abstract. Optical properties of transparent alumina prepared through gel process at room temperature and coloured with dopants have been studied. The absorption bands, molar absorptivity, effect of concentration and the dependence of oxidation state of copper on the copper content and water content are similar to the random network glasses. The ultraviolet absorption edge at lower energies confirm the disordered nature of the transition phase aluminas γ and δ. The absorption bands in the visible suggest the octahedral symmetry of oxygen around aluminum.

Keywords. Optical properties; transparent alumina; coloured alumina gel; alumina gel; xerogels; transparent ceramic.

1. Introduction

Gel-processed materials have evoked considerable interest in recent years owing to the novel features they exhibit. It has become feasible to prepare transparent ceramics at low temperatures which otherwise could be produced only at high temperatures and pressures. A transparent porous alumina was first prepared by Yoldas (1975) using the gelation process initiated by Roy (1969). A gel-processed silica glass was found to have certain properties different from the melt-quenched conventional silica though both exhibited a random network arrangement of atoms (Yoldas 1982). Alumina prepared from the metal organic alkoxide was found to be polymeric and partially crystalline (Saraswati *et al* 1987). Transition metal ions incorporated in materials show absorption in the visible and have been used as probes for the local structure (Sigel 1977). The alumina gels could be easily coloured at room temperature with iron, copper or organic dyes. The optical properties of these transparent and coloured gel monoliths have been studied for the first time in the ultraviolet, visible and near-infrared regions and are reported in this paper. The colour centres identified due to copper can also help in the study of photochromic silver halide glasses in which copper is added to improve the sensitivity.

2. Experiment and results

2.1 *Preparation of the gel monoliths*

The gel was prepared by hot hydrolysis and polycondensation of aluminum isopropoxide using a procedure described by Yoldas (1975). The microstructure and properties of the gel depend upon the process parameters such as the amount of water added for hydrolysis, the nature and amount of the acid catalyst. After several trials for obtaining crack-free clear gel monoliths, we found the best molar ratio for alkoxide : water : acid to be 1 : 100 : 0·3. The slow evaporation of the gel in a flat dish produced monolithic glass-like discs. These are called xerogels.

A drop of a dye solution coloured the gel blue or red depending on the dye added. Transition metal ions could be introduced either as salts or metal powders. Pure copper or iron powders were added at room temperature. They took about 48 hr to colour and penetrate into the layers of boehmite (alumina gel). Iron-doped gels were yellow whereas the copper-doped were colourless, blue or green depending on the concentration of copper and the amount of chloride ions in the gel (indicated by the pH value). The dopant concentration was analysed spectrochemically and is given in table 1.

2.2 *Transmission and absorption in the xerogels*

A double-beam Hitachi spectrophotometer was used for recording the transmission and absorption in the IR, visible and UV region of wavelengths (200–2600 nm). No polishing or surface treatment was done, or required, as the surface was naturally smooth and glossy owing to the fine size of particles and pores. The thickness of samples ranged from 0·1 to 0·5 mm. Scattering losses were found to be negligible as seen from the difference spectra with a similar sample in the reference beam. The doped gels were found to be less transparent as compared to the undoped alumina. Physical properties like density, X-ray diffraction, IR absorption and microhardness remained unaffected within experimental errors and compared well with earlier

Table 1. Molar absorptivity in doped alumina gels.

Dopant colour	Conc. ppm	Thickness (mm)	Abs edge (nm)	Abs max (nm)	ε litre mol^{-1} cm^{-1}
Fe, d^5	8000	0·36	340		3800
Yellow				480	46
Cu, d^{10}	1000	0·24	240		10^4
Colourless					
Cu, d^9	5000	0·2	360	730	54·9
Light blue					
Cu, d^9	8540	0·2	330	840	480
bluish green					
Cu, d^9	8550	0·2	360		3900
green				880	580
acidic				390	78
Cu, d^9	6900	0·5	330		2400
Turquoise				730	110
Cu, d^9	6900	0·5	330		2400
heated 400°C				720	70
γ phase					
Cu, d^9	6900	0·44	240		2900
heated 950°C				285	280
δ phase				390	80
Sample, 2	1000	0·24		380	20
exposed for 30 min,					
at 100°C					
Yellow				880	76

measurements (Saraswati and Rama Rao 1986). The absorption edge, measured at $T \sim 0{\cdot}1\%$, was found to have shifted to longer wavelengths in the doped xerogels. The absorption edges in the UV, the absorption bands in the visible and the molar absorptivity calculated are all listed in table 1. Figure 1 shows the spectra in the dye doped xerogel. The colourless, copper-doped xerogels showed no absorption in the visible for concentration of copper less than 1000 ppm, whereas the green and blue xerogels (concentration = 6900 ppm) exhibited a broad band centred between 720 and 900 nm depending on the concentration of copper ions and the chloride content. Figure 2 exposes the results. Absorption band shifts towards longer wavelength with increase in copper and chlorine content. The chloride ion comes from the hydrochloric acid, which is added to catalyse the gelation of boehmite. The pH value of the acidic gels were between 2 and 4 and the resultant xerogel was yellowish green, the yellowness increasing with increasing chlorine content. In the visible, one more band at ~380 nm appears with increasing chlorine content. Two more weak absorptions at 510 and 470 nm have been observed in some xerogels with copper. The lack of colour and the absence of absorption for ion concentration of copper (< 1000 ppm) was attributed to the monovalent state of copper, which has an electronic configuration d^{10} and hence cannot have a *d-d* transition in the visible.

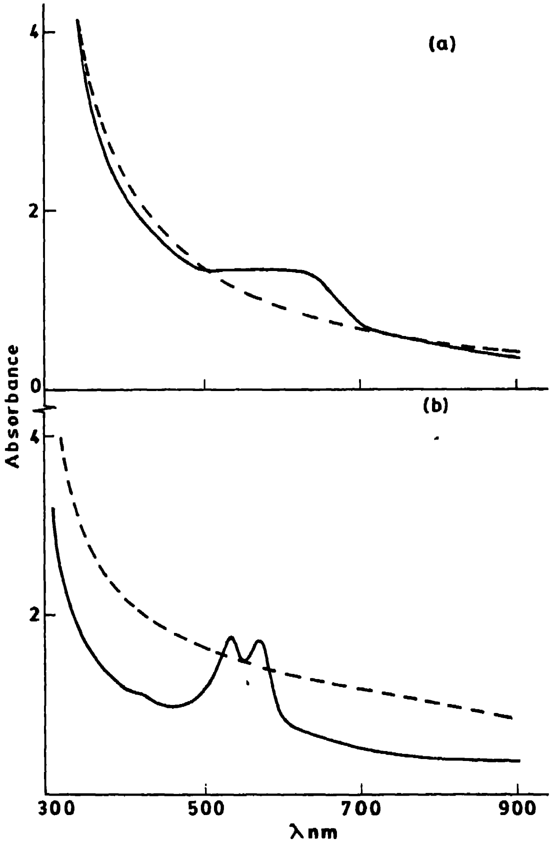

Figure 1. Absorption in boehmite xerogel doped with **a.** Blue dye. **b.** Red dye. The dashed curve is for the γ-Al_2O_3 phase in the same, heated to 700°C.

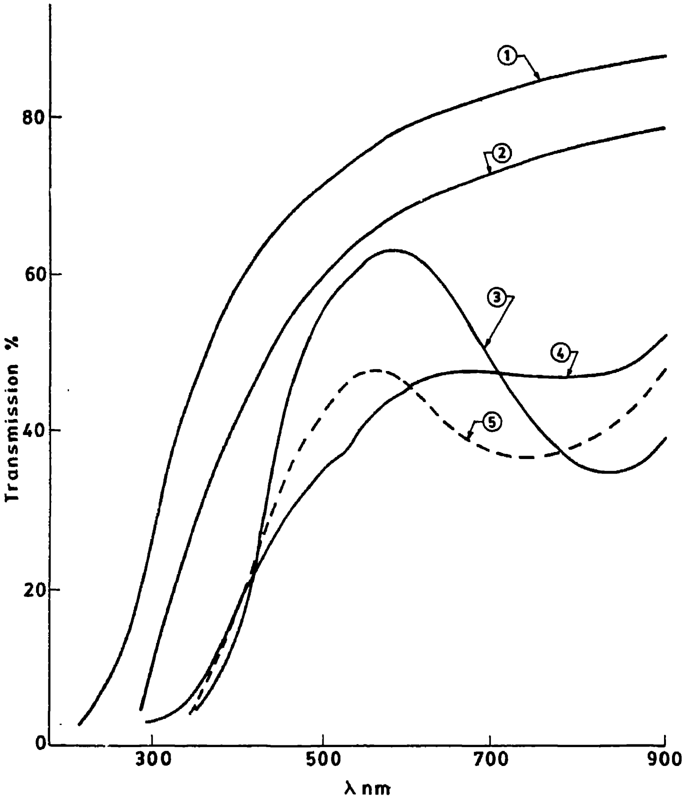

Figure 2. Influence of copper concentration on transmission spectra. Copper content of (1) and (2) < 1000 ppm, (3) 8550 ppm (4) 5000 ppm and (5) sample 3 heated at 500°C for 10 hr.

On slight heating (60–100°C), under an infrared lamp the xerogel turned bright yellow and the glow lasted for a long time after switching off the heating. The spectrum taken in the 'yellow state' of the xerogel for different duration of heating is indicated in figure 3a. The overall transmission improved considerably from 17 to 46% with dehydration and also the oxidation state changed to bivalent copper (d^9) as seen by the absorption maximum at ~800 nm. When the chlorine content is greater on dehydration, another peak at 380 nm appears. The dehydration effect can also be seen at room temperature. Light green xerogels turn yellowish in the desiccator.

In the near-infrared region, from 1000 to 2600 nm, all the doped xerogels exhibit similar spectra. The transmission is better and two absorption bands at ~1·4 and 1·9 μm, due to the combinational overtones from OH^- ions of the water molecules are observed.

2.3 *Transition phases of the xerogels*

The xerogel of alumina is boehmite, AlOOH. On heating in air, the transition phases of alumina were obtained. The γ alumina phase is formed at temperatures between 400–800°C and the δ phase at 900–1000°C. The crystalline, α phase was obtained

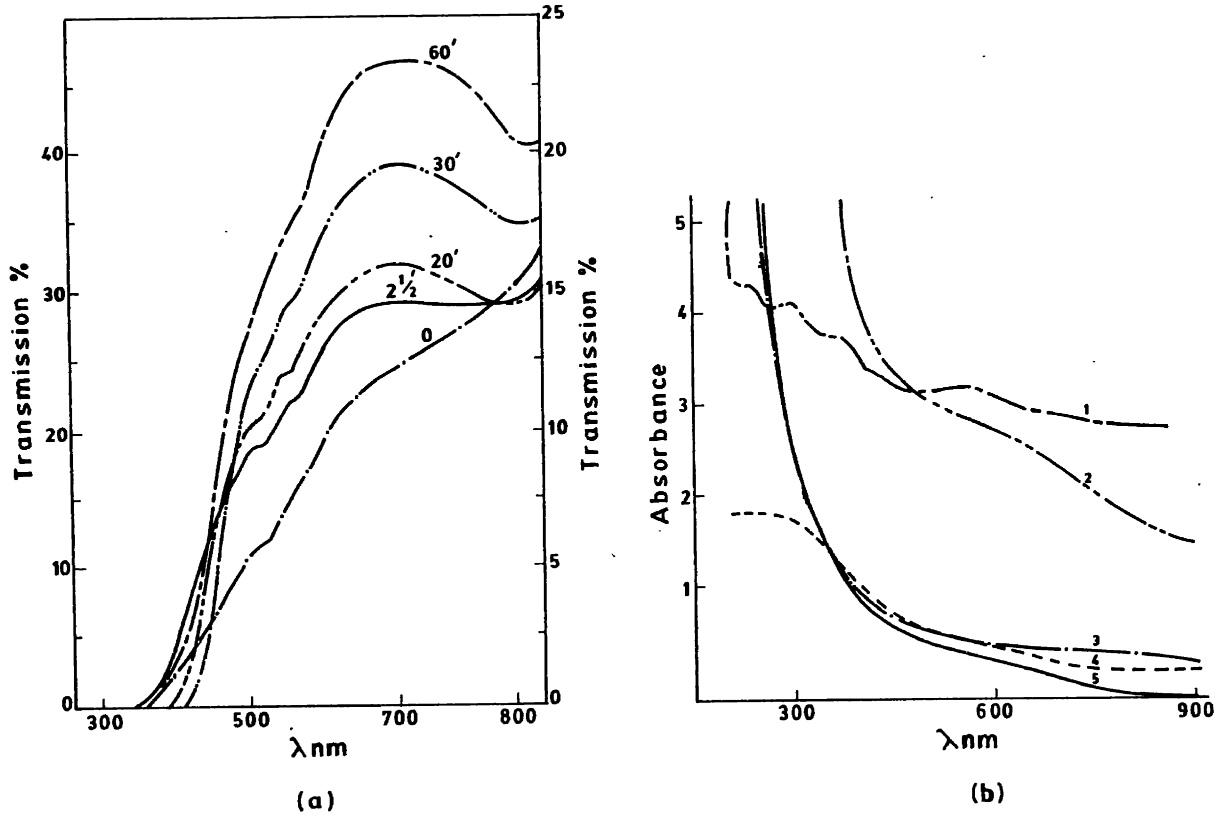

Figure 3. **a.** Change in transmission spectra on heating a colorless copper doped gel at 100°C. Numbers denote the duration of heating in minutes. **b.** Absorption in the undoped alumina (1) Sintered pellet, (2) δ-Al_2O_3 (1000°C), (3) γ-Al_2O_3 (600°C), (4) boehmite and (5) γ-Al_2O_3 (800°C).

above 1200°C. The xerogels did not crack when the heating rate was 300° per hour. The xerogels remained transparent upto 950°C and turned opaque above 1000°C. Figure 3b shows the shift in the absorption edge in the UV in the undoped alumina xerogel. For the doped gels, the trend was almost the same. On heating the colours changed. The dyes lost the colour at 700°C, may be due to the decomposition of organic molecules. All the copper gels were pale blue above 900°C. The transmission in the visible is not very different, but considerably improved in the near infra region owing to the absence of absorption due to the water molecules (figure 4). The UV absorption edge in the γ phase did not vary much from the boehmite phase in the doped gels but the δ phase (950°C) was very different. For all the low concentration doped materials the edge was at a longer wavelength, 360 nm and had a kink at $\sim$550 nm (figure 3b) which could be due to the mixture of δ and another phase, say θ or α. The microstructure and X-ray diffraction also support the mixture of another phase in these. For a turquoise, Cu doped gel (6900 ppm) in the δ phase, a sharp peak at 285 nm and broad peak at 380 nm also appeared. The 285 nm peak disappeared with time (in a week) and this could be due to the instability of the monovalent copper. The 380 nm peak is due to a Cu-Cl complex (similar to D band of Paul). Figure 5 shows these peaks. Heating at 1300°C for 12 hr, all the doped xerogels became white, thin, more dense and crystalline (α phase). The xerogels became opaque due to the increasing size of the inhomogeneities. In the absorption (the spectra was noisy) weak bands at 585, 420, 290 and 240 nm were observed in all xerogels, irrespective of dopant. The gel also lost its smooth, glossy appearance.

On heating at 1500°C for 90 hr, the gel pieces became $\sim$78% dense. The absorption could not be recorded. The microstructure showed the formation of fine grains of micron size. In a sintered pellet weak peaks at 560, 375 and 300 nm were observed. The absorption edge also shifted to higher energies as expected.

2.4 *Calculation of the molar absorptivity*

The light beam incident on a specimen can be reflected, scattered, absorbed and transmitted. As mentioned earlier, the scattering as seen from the difference spectra was negligible. Spectrophotometers record the absorption as percentage transmission or optical density, OD. The attenuation of light on passing through a thickness X of the material is given by $a = 2{\cdot}303\ \mathrm{OD}\ X^{-1}$ where a is the absorptivity. The

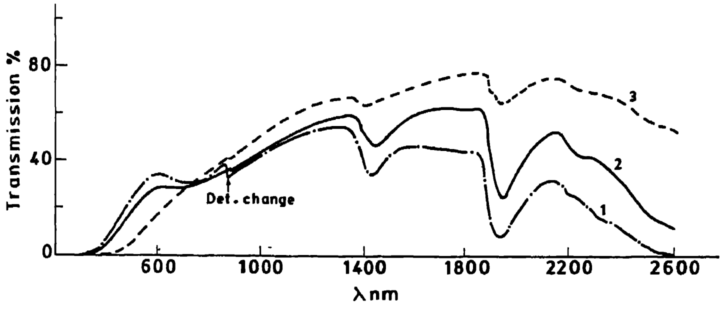

Figure 4. Transmission spectra in a turquoise, Cu-doped alumina; (1) boehmite phase, (2) γ phase and (3) δ phase.

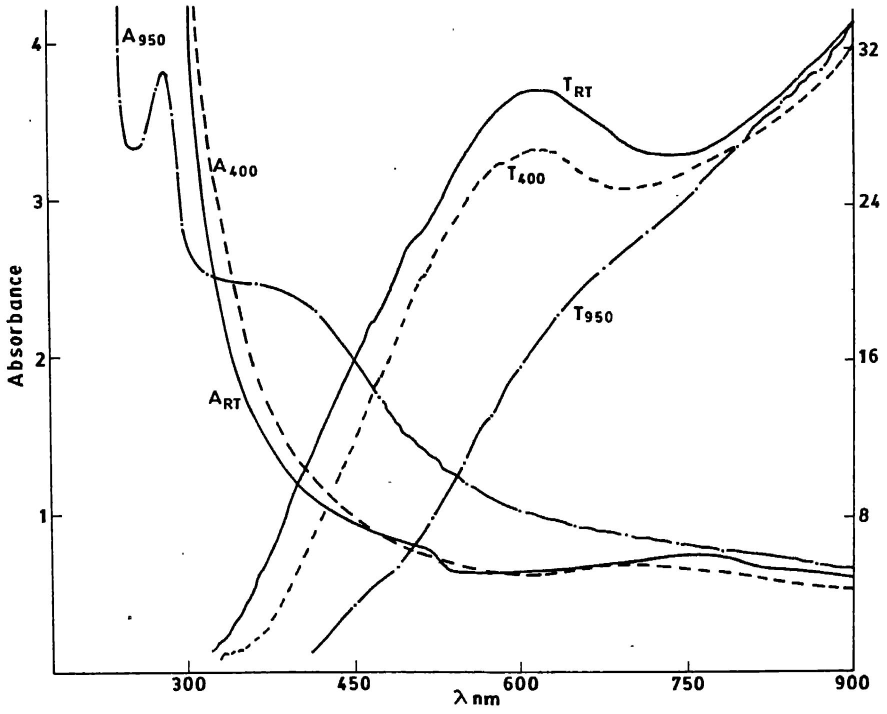

Figure 5. Absorption in the turquoise sample showing the peaks at 285 and 380 nm.

optical absorption produced by a given concentration of dissolved impurities is expressed (Wong and Angell 1976) in terms of molar absorptivity ε as,

$$\varepsilon = 2{\cdot}303 \text{ OD } C^{-1} X^{-1},$$

where C is the concentration of the absorbing ion in g moles per litre. Hence the unit of ε is litres mol^{-1} cm^{-1} throughout.

To get a correct idea of ε, very thin samples must be used. As ceramic samples are brittle we used samples ~0·15–0·5 mm thick. Thin films of the gel solution coated on glass showed that the variation due to thickness was negligible. The calculated molar absorptivity are in table 1. As it is proportional to the concentration, one should expect a linear variation. This is found to be exactly so. With the presence of chloride ions, the absorptivity will be greater as ascertained from observations.

3. Discussion

Our X-ray diffraction results in the xerogels showed broad diffuse bands and a partially crystalline structure as in a polymer.

3.1 *Absorption in the UV region*

The ultraviolet absorption in the alumina xerogel arise from (i) absorption intrinsic to the electronic excitation of the Al-O network and (ii) absorption from dopants, especially the charge transfer spectra of transition metal ions. Xerogel of boehmite consists of molecules that form long chain polymers with the hydroxyl group at the ends of chain. Aluminum atom is in the octahedral environment of oxygen (Saraswati *et al* 1987). As the gel is porous ($\sim 60\%$ porosity) with large surface area, the unsaturated bonds give rise to tail states in the valence and conduction band and lower the energy gap. Impurities, especially transition metal ions, lower it further. Hence, on both accounts, the absorption edge in the ultraviolet will be at longer wavelengths and is observed to be so (table 1). The absorption edge results from the excitation of valence band electrons to unoccupied high energy states such as exciton or conduction band levels. For crystalline corundum, the main absorption edge was found to be 8·55 eV (Arakawa and Williams 1968) and 6·8 eV for the anodized film (amorphous). Our results also show that in the crystalline phase the edge moves to higher energies whereas in the γ and δ phases they are at 5·16 eV and 3·75 eV. Thus we have evidence that the γ and δ phases are disordered. In the δ alumina phase mixture of other phases had been inferred from microstructure. Furthermore, the coarsening of the crystallites and the increased covalency with change in the oxygen network rearrangement, can shift the edge to longer wavelengths. The transition metal ions like Fe and Cu also shift the edge lower to 3·65 eV due to the tail end defect states near the bands. In the δ alumina phase in one of the copper-doped samples the absorption bands at 285 nm and 380 nm could both be due to the charge transfer transitions. The 380 nm band is dependent on the presence of chlorine and can be attributed to π-d charge transfer, the transfer of an electron from filled ligand orbital. The molar absorptivity was higher for the 285 nm band, which, because of its instability could be attributed to Cu^{+} charge transfer absorption. From these, again the octahedral coordination of oxygen around aluminum becomes evident.

3.2 *Visible absorption*

When transition metal ions are introduced in a material, the energy levels of the free ions are split and shifted by the electrostatic fields of the nearest neighbour anions, the ligands. As the field of the metal ion falls off rapidly with distance (r^{-5}) only adjacent interactions need to be considered (Sigel 1977). Hence broad features of crystalline and noncrystalline materials would be similar as long as the short range interactions are similar. Generally, octahedral or tetrahedral coordination by the ligands are noticed with probable distortions of symmetry configuration. When the transition metal ion has an incomplete d shell, as for Fe^{3+} (d^5) and Cu^{2+} (d^9) transition between the crystal field split d levels are possible and these are responsible for the optical absorption band. All the d-d transitions are forbidden by Laporte rule. However, the transitions are weakly allowed if mixing of the $3d$ band with metal $4p$ or ligand p orbitals can take place. The topological disorder in a noncrystalline network can make this possible. The forbidden transitions have weak extinction coefficients (or molar absorptivity). In the tetrahedral coordination, more of mixing is possible compared to octahedral resulting in an increased intensity of absorption. The energy of the absorption band is also dependent on the charge state of the metal ion, coordination and nature of ligand atoms. Thus, local structural information can be gathered from absorption spectra, which normally occurs in the visible for internal transitions between d electron levels. Boehmite gel with iron showed an absorption maximum at 480 nm ($\varepsilon = 46$) comparing with the value of Bamford (1961) for trivalent Fe in the octahedral environment of oxygen atoms.

The molar absorptivity of copper widely varied depending on the concentration of copper and chloride ion. Paul (1970) had studied in detail the absorption of Cu^{++} and Cu^{+} in aqueous solutions containing HCl and borate glasses containing NaCl. We have observed that (i) with an increase in the copper concentration the bivalent state of copper is preferred. The absorption maximum shifts to longer wavelengths from 720 to 840 nm. The molar absorptivity increase is linear with concentration; (ii) with dehydration, monovalent copper ion becomes unstable and the oxidation state changes to bivalent and (iii) with an increase in the chloride content the color of the gel changes, absorption is more intense and shifts to near infra at 900 nm. Another peak at 380 nm also appears.

Interestingly enough most of these observations were noted for copper in glasses by Paul (1970). The influence of chloride ion is very strong and was attributed to the formation of chlorocomplexes. The layered structure of boehmite and the porosity of material with large surface area have enabled the xerogel to form complexes with H_2O, Cl^- and O^{--} ligands. These could also be responsible for the other weak absorptions seen at 510 and 470 nm. The complexes suggested were $[Cu(OH)(H_2O)_5]^{1+}$, $[CuCl(H_2O)_5]^{1+}$, $[CuCl_2(H_2O)_4]$, etc. The shift of the absorption maximum to higher wavelengths was suggested as due to a reduction in copper-halide distances. The enhanced intensity is attributed to a larger distortion of the octahedron. Cu^{++} is a d^9 ion and experiences a strong Jahn-Teller distortion. Hence the coordination polyhedra is usually a tetragonally-distorted octahedron. The transition ${}^2\Gamma 3(D) \rightarrow {}^2\Gamma 5(D)$, results in an asymmetric band around 800 nm and usually consists of 2 or 3 overlapping symmetrical bands. This absorption is more or less a signature to the presence of bivalent copper. Cu^{+} being a d^{10} ion is not expected to have ligand field band in the visible and no absorption due to this in the range 300–1400 nm was observed. Cu^{+} has charge transfer (oxide-copper) spectrum at ~240 nm, similar to Cu^{++} and it is not possible to identify them separately.

In the $\gamma\, Al_2O_3$ phase, the absorption band was centred around 720 nm and in the $\delta\, Al_2O_3$ phase, the ultraviolet range peaks at 285 nm, 390 nm and the edge at 240 nm could be observed. These indicate the penetration of copper into the matrix, possibly at the Al sites, leading to the conclusion that Al is octahedrally surrounded by O ions atleast upto the γ phase. The structural investigations had also shown (Saraswati *et al* 1987) that the $\gamma\, Al_2O_3$ was cubic and octahedral arrangement was evident from IR.

3.3 *Infrared region of absorption*

The optical absorption of oxide glasses in the near and middle region is determined by collective vibration of molecules and atoms in the network. Absorption correspond to transition in the vibrational energy levels. The absorptions at 1·44 and 1·94 μm are vibrational overtones and combinations linked to the OH^- ion of the absorbed water mols at the surface. In the $\gamma\, Al_2O_3$ and $\delta\, Al_2O_3$ these bands were again observed, slightly shifted and with a shoulder at 1·42, 1·38, 1·93 and 1·88 μm. As the shift is also to lower wavelengths (higher energies) a possibility is that these are bonded and intrinsic to the $\delta\, Al_2O_3$ phase as had been suggested earlier by Leonard *et al* (1967).

4. Conclusions

From our results on the optical transmission and absorption in the doped gel monolith glasses, we arrive at the conclusions that (i) the transition phase aluminas γAl_2O_3 and δAl_2O_3 are disordered, (ii) γ and δ aluminas could have water associated with them intrinsically and (iii) the optical behaviour of copper doped gels are identical to those of the random network glasses. The concentration of copper affects the oxidations state, absorption wavelengths and intensity. The chloride ions influence the wavelength and intensity of absorption of copper. Desorption of water affects the stability and oxidation state of copper.

References

Arakawa E T and Williams M W 1968 *J. Phys. Chem. Solids* **29** 735
Bamford C R 1961 *Phys. Chem. Glasses* **2** 163
Leonard A J, Vancanvelaer F and Fripat J J 1967 *J. Phys. Chem.* **71** 697
Paul A 1970 *Phys. Chem. Glasses* **11** 159
Roy R 1969 *J. Am. Ceram. Soc.* **52** 344
Saraswati V and Ramarao G V 1986 *J. Mater. Sci. Lett.* **5** 1
Saraswati V, Rao G V N and Ramarao G V 1987 *J. Mater. Sci.* **22** 2529
Sigel Jr G H 1977 *Treatise in materials science and technology* (eds) M Tomazawa and R H Doremus (New York: Academic Press) vol. **12** 5
Wong J and Angell C A 1976 *Glass structure by spectroscopy* (New York: Marcel-Dekker Inc) Chapt. 6
Yoldas B E 1975 *Am. Soc. Ceram. Bull.* **54** 286
Yoldas B E 1982 *J. Non-Cryst. Solids* **51** 105

Bull. Mater. Sci., Vol. 9, No. 3, August 1987, pp. 203–205. © Printed in India.

Magnetic susceptibility measurements of LHP and LNP crystals

C C DESAI and M S V RAMANA
Department of Physics, Sardar Patel University, Vallabh Vidyanagar 388 120, India

MS received 5 February 1987; revised 6 June 1987

Abstract. Ferroelectric single crystals such as lead hydrogen phosphate (LHP) and dihydrated lead nitrate phosphate (LNP) have been derived from the diffusion of lead nitrate into the set gel containing orthophosphoric acid. By employing Faraday's Gouy balance technique, the magnetic susceptibilities of LHP and LNP have been determined. It has been observed that (i) the gram and molar susceptibilities are independent of magnetic field, (ii) χ_M of LNP materials are greater than that of LHP materials and (iii) the positive values of magnetic susceptibilities suggest that LHP and LNP are paramagnetic materials.

Keywords. Silica gels; ferroelectric; Gouy balance; magnetic susceptibility; lead hydrogen phosphate; lead nitrate phosphate.

1. Introduction

The study of magnetic susceptibility at different magnetic fields is an important tool to probe into the magnetic properties of materials. Considerable amount of work along these lines has been carried out on a variety of materials, e.g. scheelite compound (Godbole 1982) and tin iodates (Desai and Rai 1983) yielding valuable information. LHP and LNP crystals are of considerable interest, particularly in basic studies of their phase transitions and of their ferroelectric, optical and other pertinent characteristics. The information on magnetic properties of ferroelectric crystals, such as LHP and LNP is meagre. In this paper, we report magnetic susceptibilities of these crystals using the Faraday Gouy balance technique.

2. Experimental

Single crystals of LHP and LNP were grown using the controlled reaction between lead nitrate and orthophosphoric acid solutions. The crystals were examined by EDAX, X-ray diffraction and density measurements; these techniques confirmed that they were LHP (monoclinic, space group $P2/a$) and LNP (monoclinic, space group $P2_1/c$).

The magnetic susceptibility of these crystals was measured using the Faraday method (Bates 1951). The finely powdered crystals of LHP and LNP were packed in a Gouy tube of known magnetic susceptibility. This tube was hung between two powerful electromagnetic pole pieces of a Gouy balance whose accuracy was 10^{-5} g. Initially, the samples were weighted accurately in the absence of the magnetic field. The magnetic field was increased by increasing the current from 3 to 7 amp through the coils and the corresponding magnetic field strength was measured with a Gauss meter. The change in weight, i.e. reduced mass of samples, after applying the magnetic field was measured.

The positive gram susceptibility, χ_g, characteristic of a paramagnetic material was determined using the formula

$$\chi_g = (\alpha + \beta\, dw)/w \tag{1}$$

where α is a constant which represents the correction factor due to displacement of air, β the constant for a glass container at a given current, w the weight of the sample, dw the change in weight when a magnetic field is applied. The gram susceptibility of the material was multiplied by its molecular mass to obtain molar susceptibility (χ_M).

3. Results and discussion

LHP and LNP grown crystals are usually transparent, white in colour and are rectangular in shape. These crystals are finely ground and the resulting powder (particle size 150 μm) were packed in a Gouy tube of known magnetic susceptibility. The experiments on magnetic susceptibility measurements were repeated five times and the average change in weight was computed for a given current. The accuracy in the measurement of reduced mass was ±5%. The readings of the Gouy balance were recorded when the values became steady. The values were quite consistent and reproducible.

As the magnetic field increases, the change in weight, i.e. the reduced weight also increases. The plot of magnetic susceptibility, χ against magnetic field (H) is illustrated in figure 1. From this figure it is clear that (i) when magnetic field is applied the reduced weight of all samples is increased, (ii) the magnetic susceptibilities (χ_g and χ_M) are independent of the current, (iii) χ_M of LNP samples are greater than that of LHP samples, and (iv) the positive values of the susceptibilities thereby suggest that LHP and LNP are paramagnetic materials. This may be attributed to the presence of lead (unfilled p shells) in them.

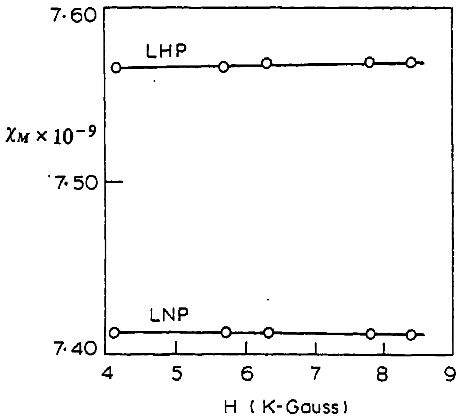

Figure 1. Plots of magnetic susceptibility (χ_M) against magnetic field (H) for LHP and LNP crystals.

Acknowledgements

The authors thank CSIR, New Delhi for financial assistance. One of us (CCD) is grateful to Mrs Gangaba Desai for her keen interest.

References

Bates L F 1957 *Modern magnetism* (Cambridge: University Press) pp 101–109

Desai C C and Rai J L 1983 *J. Mater. Sci. Lett.* **2** 467

Godbole R S 1982 *Growth and characterization of tungstate group crystals*, Ph.D. thesis, Sardar Patel University, Vallabh Vidyanagar

Bull. Mater. Sci., Vol. 9, No. 3, August 1987, pp. 207–217. © Printed in India.

Crystallization behaviour of Metglas 2826 MB ($Fe_{40}Ni_{38}Mo_4B_{18}$)

V S RAJA, KISHORE and S RANGANATHAN
Department of Metallurgy, Indian Institute of Science, Bangalore 560 012, India

MS received 21 May 1987

Abstract. Differential scanning calorimetry, x-ray diffraction and transmission electron microscopy have been employed to determine the thermal stability and identify the crystalline phases on devitrification of Metglas 2826 MB. The glass crystallizes into γ-FeNiMo and fcc $(FeNi)_{23}B_6$ with activation energies of 270 and 375 kJ mol^{-1} respectively. The reactions are primary and polymorphic in nature. The influence of Mo towards crystallization of $Fe_{40}Ni_{40}B_{20}$ has been to enhance the formation of the fcc $(FeNi)_{23}B_6$ phase in preference to orthorhombic $(FeNi)_3B$ phase and to raise the thermal stability of the amorphous state.

Keywords. Crystallization; Kissinger plot; microstructure; metallic glass.

1. Introduction

The crystallization study of metallic glasses is of interest as it provides a means to understand the nucleation and growth processes in undercooled melts and determine the thermal stability of glasses (Ranganathan and Banerjee 1984; Ranganathan and Suryanarayana 1985). It also derives interest from the fact that a number of metastable phases can be synthesized through this route. We have studied the thermal and chemical stability of a series of Fe-Ni-B glasses and this study of Metglas 2826 MB forms a part of it (Raja 1986).

Metglas 2826 MB ($Fe_{40}Ni_{38}Mo_4B_{18}$), a product of Allied Corporation (USA), has drawn considerable interest towards understanding its thermal stability (Antonione *et al* 1978, 1981; Azam *et al* 1979; Mizgalski *et al* 1981; Nicolai *et al* 1981; Battezzati *et al* 1982; Cumbrera *et al* 1982a, b; Menon and Suryanarayana 1985).

Employing non-isothermal DSC measurements, Antonione *et al* (1978) reported two-stage crystallization processes at 703 K and 777 K having activation energies of 296 and 334 kJ mol^{-1} respectively for the first and second crystallization reactions. However, Majumdar and Nigam (1980) and Cumbrera *et al* (1982b) observed a three-stage crystallization of the glass. DTA measurement by Majumdar and Nigam (1980) showed crystallization peaks at 728, 810 and 863 K. Cumbrera *et al* (1982b) determined activation energies both from Kissinger (288 and 355 kJ mol^{-1}) and isothermal (288 and 451 kJ mol^{-1}) methods using DTA, DSC and resistivity measurements for the first two crystallization processes. It may be noted that the activation energy deduced from the isothermal method for the second crystallization differs significantly from that obtained by the Kissinger method.

Mizgalski *et al* (1981) studied the sequence of crystallization using XRD. Their studies indicate that the first phase to crystallize from the glass is the fcc $(FeNi)_{23}B_6$, followed by the formation of a γ-FeNiMo solid solution. At high temperature $(FeNi)_3B$-bct phase was produced. An orthorhombic $(FeNi)_3B$ phase was found in samples annealed in a vacuum of 2×10^{-5} torr. Interestingly, Battezzati *et al* (1982) reported the presence of an orthorhombic Ni_3B phase in Metglas 2826 MB annealed at about 1000 K even without subjecting the glass to vacuum.

The observations by Nicolai *et al* (1981) are interesting in this context. They interpreted their DSC and Guinier high temperature camera experiments to indicate several stages of reaction. Phase separation was observed as a precrystallization process. The first crystal to form was γ-FeNiMo solid solution. This was followed by the formation of fcc $(FeNi)_{23}B_6$ phase by a peritectoid reaction of the γ-phase with the remaining glass of composition $(FeNiMo)_{75}B_{25}$. Eventhough reactions other than primary, eutectic and polymorphic have been speculated upon in the literature (Ranganathan and Banerjee 1984), this is the first time that a peritectoid reaction has been claimed to occur.

In a limited but direct microstructural study by TEM, Cumbrera *et al* (1982a) observed the appearance of γ-FeNiMo followed by fcc $(FeNi)_{23}B_6$. Subsequent heating to high temperature led to a stable phase whose structure was not determined.

Menon and Suryanarayana (1985) have recently brought out the difference between the crystallization behaviour of the vapour deposited and liquid quenched Metglas 2826 MB using TEM. The vapour-deposited glass leads to a fcc solid solution, which is different from the γ-FeNiMo phase formed during annealing. Furthermore, it has been pointed out that the vapour-deposited glass yields a simple cubic phase instead of the fcc boride phase crystallizing in melt quenched glass.

As seen above, the review of the literature on Metglas 2826 MB shows that, in spite of extensive work, diverse views exist among several investigators regarding the crystallization process. The present study is undertaken to address the following points over which differences exist in the literature: (a) the number of stages of crystallization (two, three or more); (b) the order of appearance of the crystalline phase (γ-FeNiMo and $(FeNiMo)_{23}B_6$)); (c) the nature of the second stage of crystallization (Polymorphic or peritectoid); (d) the possibility of phase separation preceding crystallization.

2. Experimental procedure

Metglas 2826 MB obtained from Allied Corporation, USA was in the form of ribbons of width 15 mm and thickness 35 μm. The nominal composition in atomic percentage was $Fe_{40}Ni_{38}Mo_4B_{18}$. A Perkin Elmer DSC 2C was used to determine the crystallization temperatures. In order to get a true value of crystallization temperature free from the thermal gradients of the instrument, the method of Meisel and Cote (1983) was adopted. The phases present in the annealed samples were analysed using a Philips 1140 x-ray diffractometer (XRD) with CoKα radiation of wavelength 0·17902 nm. The microstructures were observed under a Philips 301 electron microscope operating at 100 kV. Thin samples for transmission electron microscopy were obtained using a Tenupol twin jet electropolisher controlled by Struers variable potential stabilizer. A good polishing was obtained with an electrolyte of 20% methanol and 80% sulphuric acid maintained at −10°C and with an operating DC volt of 10.

3. Results and discussion

3.1 *Differential scanning calorimetry*

The glass subjected to constant heating rates in DSC for 10, 20, 40 and 80 K min^{-1}

between 320 and 1000 K exhibited two exothermic peaks (the typical DSC trace for the heating rate 10 K min^{-1} is shown in figure 1). This agrees with the results of Antonione *et al* (1978) but shows disagreement with other results which reported three (Majumdar and Nigam 1980; Cumbrera *et al* 1982b) and four (Nicolai *et al* 1981) exothermic peaks. However, it can be noted that the peak temperatures for the first and second peaks reported by these investigators agree well with the present values. Additional support for the two-stage crystallization is found in the fact that for a variety of (FeNiMo)B glasses, Antonione *et al* (1980) have found only two stages. The nature of crystalline phases formed under these peaks will be discussed in §§ 3·2 and 3·3 using XRD and TEM.

The peak shift with heating rates has been exploited to determine the activation energy for crystallization employing Kissinger's (1957) equation

$$\ln \beta/T_p^2 = -E_c/RT_p + C, \tag{1}$$

where β, T_p, E_c and C respectively represent the heating rate, peak temperature, apparent activation energy and a constant. The Kissinger plots of $\ln \beta/T_p^2$ vs $1/T_p$ are shown in figure 2. The E_c values turn out to be 270 and 375 kJ mol^{-1} respectively for the first and second crystallization processes. The values compared with earlier results reported in the literature are given in table 1. In a majority of the cases the present values agree with the earlier reported results. However, two differences can be noticed: (i) Nicolai *et al* (1981) reported higher values of activation energies for both the transitions and (ii) Cumbrera *et al* (1982b) estimated a higher value from the isothermal kinetics for the second crystallization reaction. It should be remarked that the activation energy determined by Cumbrera *et al* (1982b) using non-isothermal kinetics is in close agreement with the present results. It is also relevant to note that though the apparent activation energies obtained through DSC and microscopy techniques have been widely employed to compare the thermal stabilities of amorphous alloys, Berkenpas *et al* (1986) expressed reservation towards meaningful interpretation of the crystallization mechanisms.

3.2 *X-ray diffraction*

The phases crystallizing out during the first and second exothermic reactions are

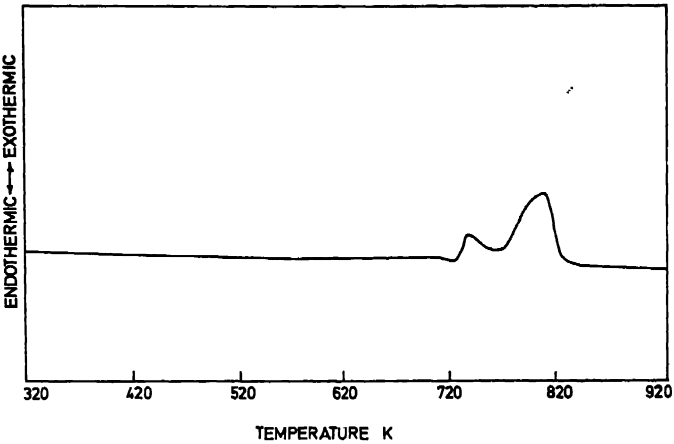

Figure 1. DSC trace of Metglas 2826 MB for the heating rate of 10 K min^{-1}.

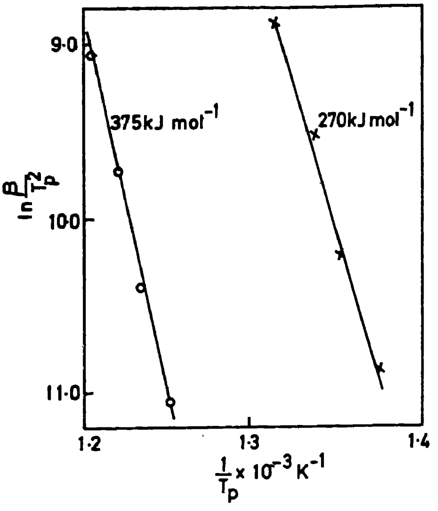

Figure 2. Kissinger plots for the first and second crystallization process.

Table 1. Comparison of activation energies for the crystallization of Metglas 2826 MB.

MS I kJ mol^{-1}	MS II kJ mol^{-1}	Method of determination	References
270	375	Kissinger	Present work
296	334	Ozawa	Antonione *et al* (1978)
*403	415	Kissinger	Nicolai *et. al* (1981)
288	355	Kissinger	Cumbrera *et al* (1982b)
288	451	Isothermal kinetics	—"—

*The values correspond to the second and third peaks, where γ-FeNiMo and fcc $(FeNi)_{23}B_6$ are reported, whereas these phases have been found to crystallize under first and second peaks of the DSC curve according to other investigators.

identified by heating the glass till the end of the peaks in DSC, cooling it back to room temperature with a cooling rate of 320 K min^{-1} and subsequently analysing it in XRD. Phase transition in the crystallized glass, if any, at high temperature is identified by heating the glass in DSC upto 1000 K. These XRD results are summarized in figure 3. The XRD of the amorphous alloy is extremely broad (figure 3a). The k value $(=4\pi \sin\theta/\lambda)$ determined from the half width of the half maxima turns out to be 31·1 nm^{-1}. The broad peak becomes sharper in the case of the sample annealed till the end of the first peak of the DSC trace (figure 3b). The peak corresponds to (111) of γ-FeNiMo phase with the lattice parameter 0·358 nm. The other peaks are not visible owing to the low volume of γ-FeNiMo present in the sample. Distinct peaks appear in the x-ray diffractogram (figure 3c) of the glass annealed till the end of the second exothermic peak which are indexed satisfactorily on the basis of fcc $(FeNi)_{23}B_6$ phase with $a = 1{\cdot}061$ nm. It should be noted that the peak corresponding to (111) of γ-FeNiMo phase merges with that of (333) of $(FeNi)_{23}B_6$ in this case. The glass annealed upto 1000 K shows significant volume of γ-FeNiMo phase which might have transformed from fcc $(FeNi)_{23}B_6$ boride phase.

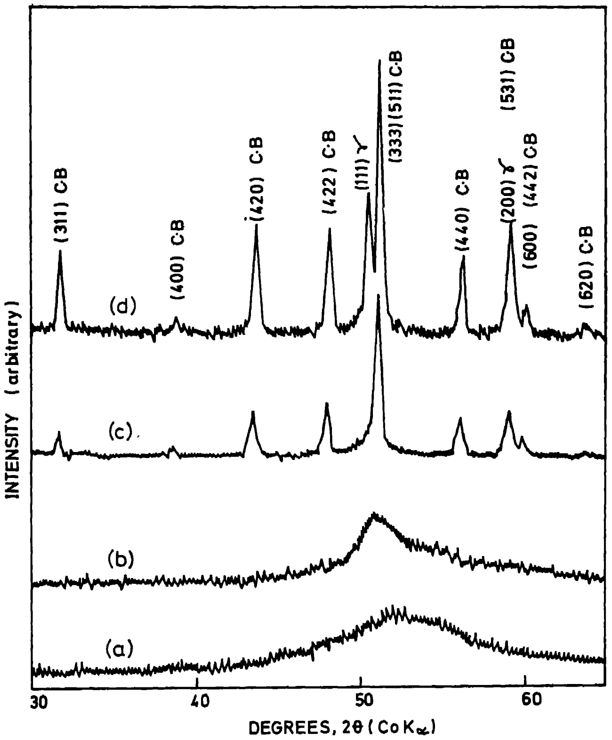

Figure 3. X-ray diffractograms showing the sequence of crystallization: (**a**) amorphous (**b**) heated upto 760 K (**c**) heated upto 860 K and (**d**) heated upto 1000 K. (C.B. refers to cubic boride).

3.3 *Transmission electron microscopy*

The microstructure and the corresponding selected area diffraction (SAD) pattern of the as-received amorphous alloy is shown are figure 4. The glass possesses a mottled structure and the unusually broad halo rings (especially the first ring) complement the XRD of the amorphous alloy shown in figure 3a. This may be attributed to phase separation. Such an instance of phase separation in an as-quenched glass has earlier been reported in Fe-B alloys by Walter and Bartram (1978). However, the mottled structure may be due to the preferential dissolution during electropolishing. Cumbrera *et al* (1982a) have indeed explained their microstructure on this basis. As has been observed by Walter and Bartram (1978), two sets of haloes are not detected in this glass. Further, there was no evidence for two glass transition temperatures. Thus incipient phase separation remains only a possibility, without adequate evidence. It has to be pointed out that among the many investigators, only Nicolai *et al* (1981) have postulated phase separation.

The development of microstructure has been studied for the isothermal annealing at 773 K using TEM. Figure 5 shows the microstructure, SAD pattern and dark field image (corresponding to the second ring of the pattern) for the glass annealed for 15 min at 773 K. The SAD pattern can be indexed satisfactorily for γ-FeNiMo phase with $a = 0{\cdot}358$ nm and the dark field image reveals almost spherical crystals

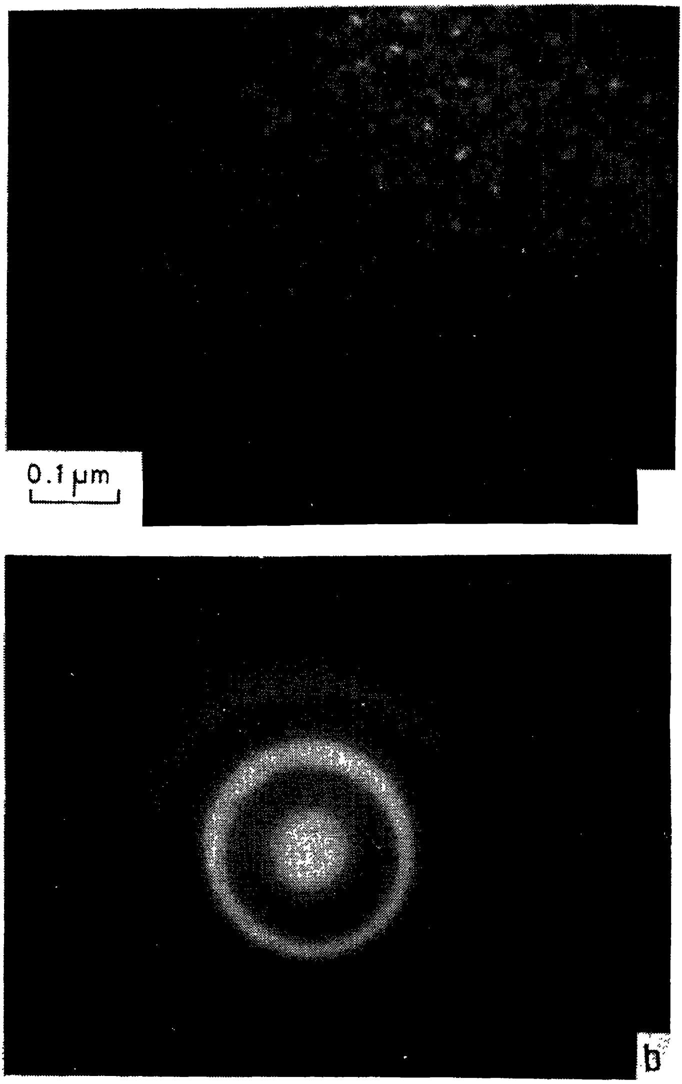

Figure 4. **a.** Bright field image. **b.** SAD pattern of the amorphous alloy. Note the mottled structure in the micrograph.

embedded in the matrix. The fcc $(FeNi)_{23}B_6$ crystals start emerging from the specimen annealed for 30 min and their number and size increase with time. A complete crystallization is noticed in the alloy annealed for 120 min. Figure 6 shows the microstructure of the partially crystallized glass (773 K, 45 min). The crystals possess a faceted morphology. Figure 7 shows the bright field image, SAD pattern and the dark field image of the fully crystallized (773 K, 120 min) glass. On close examination some of the fcc $(FeNi)_{23}B_6$ crystals exhibit twins/faults in them.

Figure 5. **a.** Bright field image. **b.** Corresponding SAD pattern. **c.** Dark field image of the glass annealed at 773 K for 15 min. The continuous rings belong to γ-FeNiMo phase.

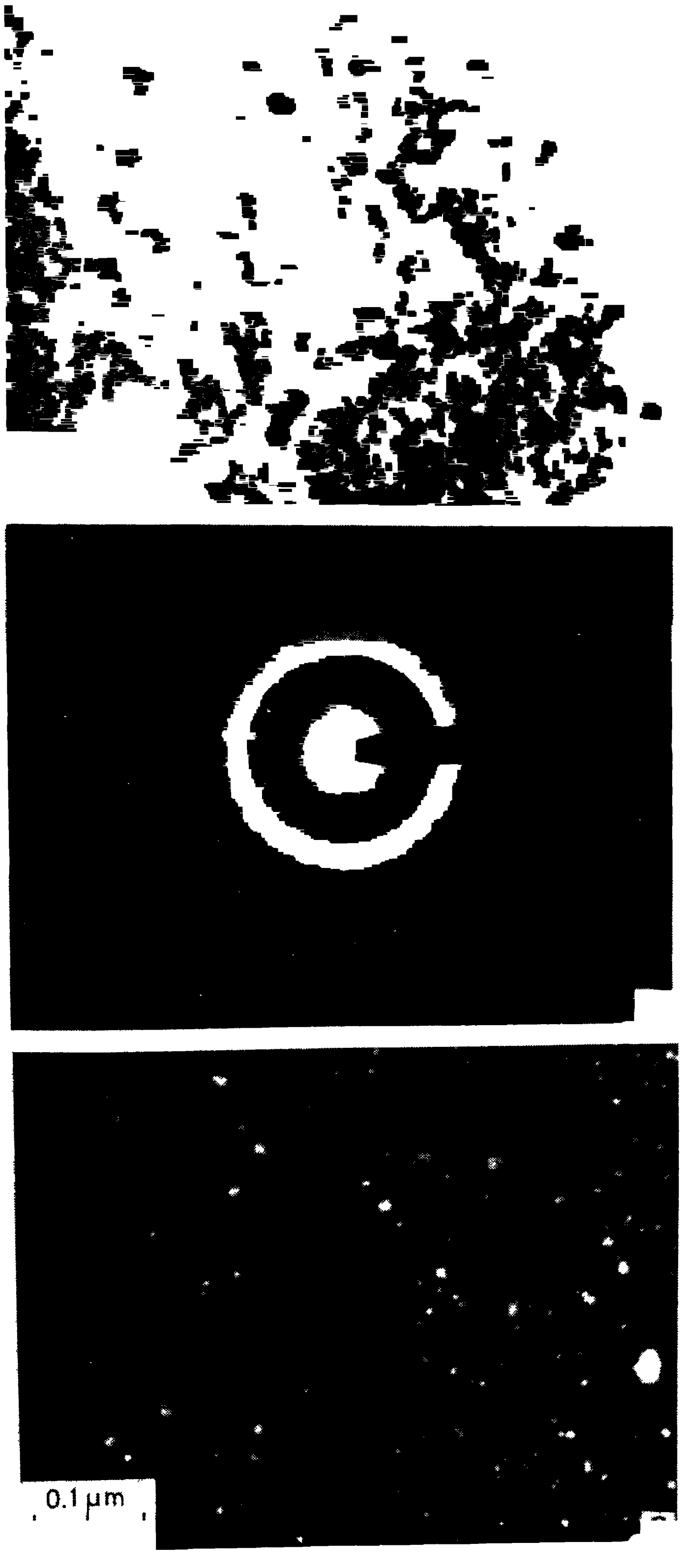
0.1 µm

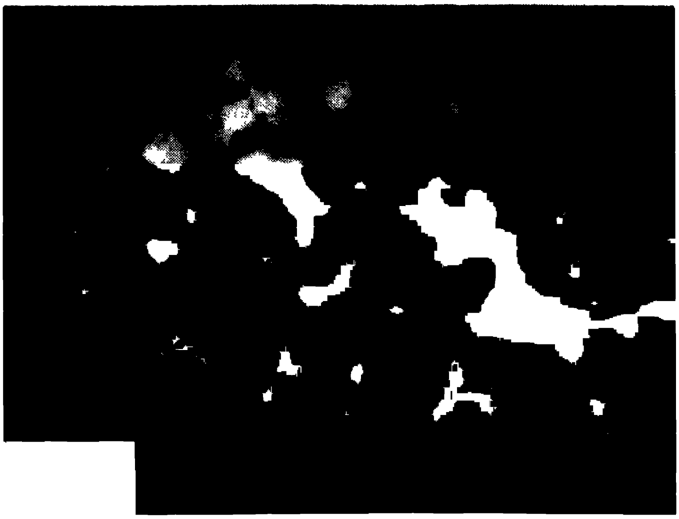

Figure 6: Well grown fcc $(FeNi)_{23}B_6$ crystals in the glass annealed at 773 K for 45 min.

Interestingly, fcc $(FeNi)_{23}B_6$ crystals grow with the same morphology at low temperature (723 K, 60 min) as illustrated by the micrograph of figure 8.

The following scheme of sequence of phase transition in Metglas 2826 MB can be derived from the DSC, XRD and TEM studies.

Amorphous→γ-FeNiMo + amorphous
(primary crystallization)
→γ-FeNiMo + fcc $(FeNi)_{23}B_6$
(polymorphic crystallization)
→γ-FeNiMo + fcc $(FeNi)_{23}B_6$
(volume of γ-FeNiMo found increasing at the expense of fcc $(FeNi)_{23}B_6$ phase).

It can be noted that fcc $(FeNi)_{23}B_6$ phase is metastable (Herold and Koster 1978) and hence can transform into γ-FeNiMo phase. The sequence of formation of γ-FeNiMo followed by fcc $(FeNi)_{23}B_6$ is in accordance with the observations of Nicolai *et al* (1981) and Cumbrera *et al* (1982a). However, Mizgalski *et al* (1981) reported a different sequence as follows

Amorphous→fcc $(FeNi)_{23}B_6$ + amorphous
→fcc $(FeNi)_{23}B_6$ + γ-FeNiMo→
fcc $(FeNi)_{23}B_6$ + γ-FeNiMo + bct$(FeNi)_3B_6$.

Comparing the above sequences of crystallization with the present one indicates that they have not identified the initial formation of γ-FeNiMo from the glass but have reported the phase transition from fcc $(FeNi)_{23}B_6$ to γ-(FeNiMo) phase in the crystallized glass.

Figure 7. **a.** Microstructure. **b.** SAD pattern. **c.** Dark field image of the fully crystallized glass (annealing treatment 773 K, 120 min).

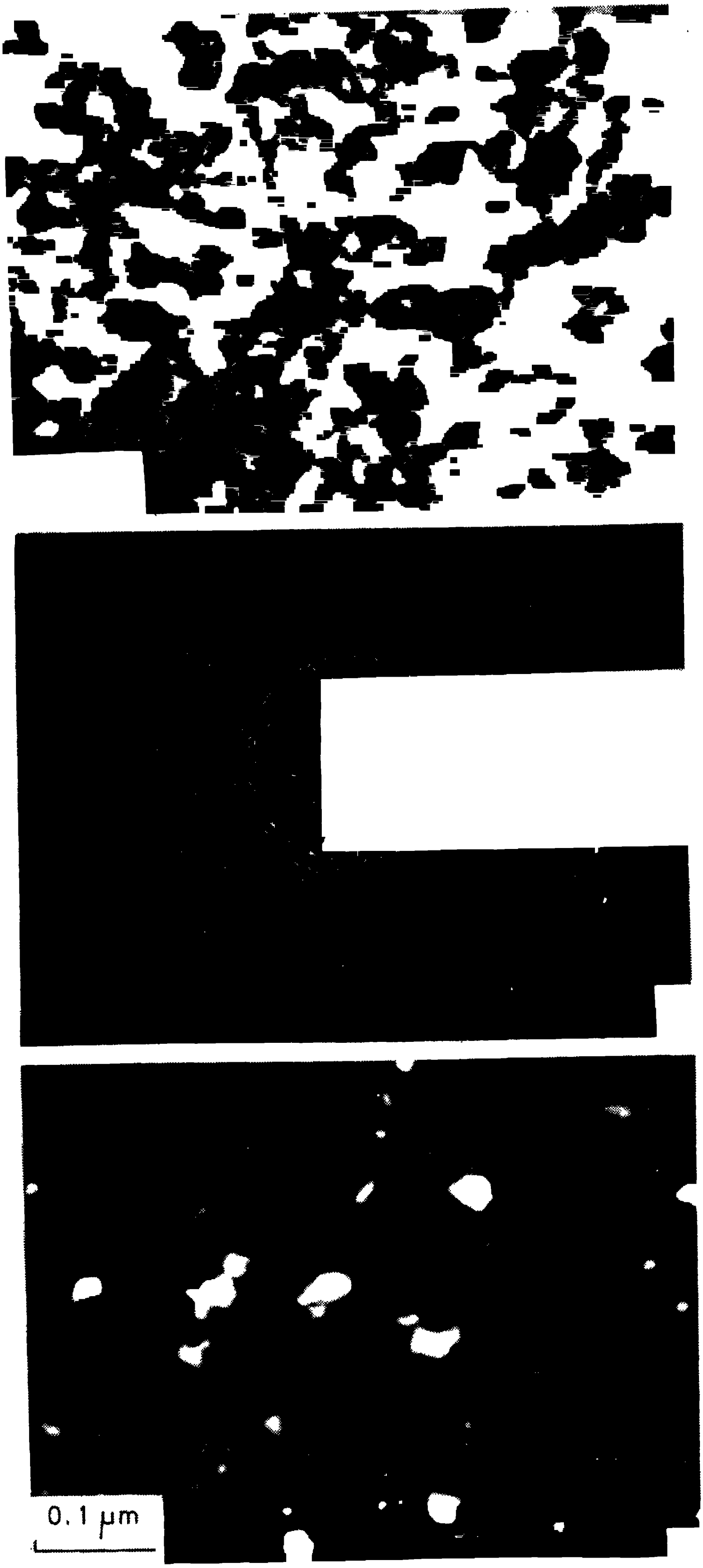

Figure 7.

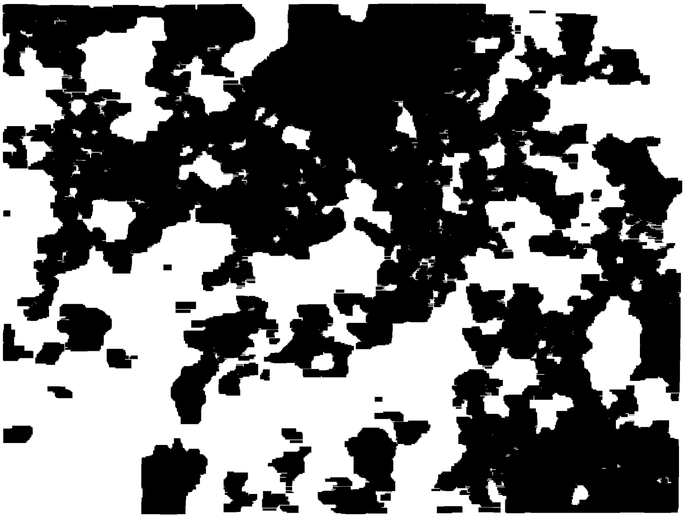

Figure 8. Microstructure of Metglas 2826 MB annealed for 60 min at 723 K.

In addition to the γ and boride phases, Mizgalski *et al* (1981) noticed the formation of bct $(FeNi)_3B$ above 950 K and Battezzati *et al* (1982) identified an orthorhombic Ni_3B phase at about 1000 K. However, the present study does not indicate any of the two phases either in x-ray or in TEM studies. Interestingly, neither Nicolai *et al* (1981) nor Menon and Suryanarayana (1985) found the presence of bct $(FeNi)_3B$ and orthorhombic Ni_3B phases.

The influence of Mo towards the crystallization of FeNiB glasses is more striking when the crystallization characteristics of $Fe_{40}Ni_{40}B_{20}$ glass is compared with that of Metglas 2826 MB. Raja (1986) has reported that the glass $Fe_{40}Ni_{40}B_{20}$ crystallizes into four types of crystals. The first two of them are eutectic mixtures of γ-FeNi + orthorhombic $(FeNi)_3B$ and γ-FeNi + fcc $(FeNi)_{23}B_6$ and the third and the fourth are a single phase γ-FeNi solid solution and an unknown Fe-rich phase. Although we find fcc $(FeNi)_{23}B_6$ phase in $Fe_{40}Ni_{40}B_{20}$, its volume fraction is $< 5\%$ (could not be identified by x-ray diffraction and was possible to detect only in TEM). Hence it is very obvious that Mo enhances the formation of a fcc $(FeNi)_{23}B_6$ phase in preference to the orthorhombic $(FeNi)_3B$ phase. Further, in the presence of Mo, crystallization takes place by simple two-stage processes in contrast to the complex single-stage crystallization in Mo-free $Fe_{40}Ni_{40}B_{20}$ glass simultaneously imparting a thermal stability to the glass.

4. Conclusions

(i) XRD and TEM studies have indicated that the glass crystallizes in two stages into γ-FeNiMo followed by fcc $(FeNi)_{23}B_6$. The same sequence is reported by Nicolai *et al* (1981) and Cumbrera *et al* (1982a). Additional stages observed by other investigators are due to the transformation of the crystalline state to more stable states.

(ii) The γ-FeNiMo phase forms by the primary mode as noted by Nicolai *et al*

(1981), while the fcc $(FeNi)_{23}B_6$ forms by a polymorphic mode and not by the peritectoid mode as suggested by Nicolai *et al* (1981).

(iii) The activation energies for the devitrification of the glass into γ-FeNiMo and fcc $(FeNi)_{23}B_6$ phases respectively turn out to be 270 and 375 kJ mol^{-1} from the Kissinger plots.

(iv) Though the appearance of the pseudograin structure and the broad XRD peak can be attributed to the incipient phase separation of the glass during melt quenching itself, it is felt that the evidence for phase separation is not strong.

(v) It is confirmed that the addition of molybdenum enhances the thermal stability of (FeNiB) glasses and leads to the formation of fcc $(FeNi)_{23}B_6$ in preference to orthorhombic $(FeNi)_3B$.

Acknowledgements

The authors are thankful to the Department of Science and Technology, Government of India for financial assistance.

References

Antonione C, Battezzati L, Lucci A, Riontino G and Venturello G 1978 *Scr. Metall.* **12** 1011

Antonione C, Battezzati L, Lucci A, Riontino G, Tabasso M C and Venturello G 1980 *J. Phys. (Paris)* **C41** 131

Antonione C, Battezzati L, Lucci A, Riontino G and Venturello G 1981 *La Metall.* **73** 118

Azam N, Lenaour L, Rivera C, Grosjean P, Sacovy P and Delaplace J 1979 *J. Nucl. Mater.* **83** 298

Battezzati L, Antonione C and Cossolo A 1982 *Z. Metallkd.* **73** 185

Berkenpas M B, Barnard J A, Ramanujam R V and Aaronson H I 1986 *Scr. Metall.* **20** 323

Cumbrera F L, Millan M, Conde A, Marquez R and Vigier P 1982a *J. Mater. Sci.* **17** 861

Cumbrera F L, Miranda H, Conde A, Marquez R and Vigier P 1982b *J. Mater. Sci.* **17** 2677

Herold U and Koster U 1978 *Z. Metallkd.* **69** 326

Kissinger H E 1957 *Anal. Chem.* **29** 1702

Majumdar A K and Nigam A K 1980 *J. Appl. Phys.* **51** 4218

Meisel L V and Cote P J 1983 *Acta Metall.* **31** 1053

Menon J and Suryanarayana C 1985 *Z. Metallkd.* **76** 802

Mizgalski K P, Inal O T, Yost P G and Karnowsky M M 1981 *J. Mater. Sci.* **16** 3357

Nicolai H P, Kopmann G and Frommeyer G 1981 *Z. Metallkd.* **72** 558

Raja V S 1986 *Thermal and chemical stabilities of three Fe-Ni-B metallic glasses*, Ph.D. Thesis, Indian Institute of Science, Bangalore

Ranganathan S and Banerjee S 1984 *Metallic glasses—production, properties and application* (ed.) T R Anantharaman (Switzerland: Trans-Tech Publications) p 147

Ranganathan S and Suryanarayana C 1985 *Mater. Sci. Forum* **4** 173

Walter J L and Bartram S F 1978 *Rapidly quenched metals* (ed.) B Cantor (London: The Metal Society) Vol. 1, p 307

Bull. Mater. Sci., Vol. 9, No. 3, August 1987, pp. 219–223. © Printed in India.

Preparation and properties of native oxide film anodically grown on $Hg_{0.8}Cd_{0.2}Te$

F R CHAVDA, G TIWARI and S C GUPTA
Solid State Physics Laboratory, Lucknow Road, Delhi 110 007, India

MS received 1 February 1985; revised 5 February 1987

Abstract. The process for forming the anodic oxide on $Hg_{0.8}Cd_{0.2}Te$ using a constant voltage d.c. source is studied. The electrolyte is composed of 0·1 N KOH, 90% ethylene glycol and 10% water. Good, uniform, transparent and reproducible films are obtained when the pH of the solution is adjusted between 7 and 8 by using oxalic acid. The anodic oxide film shows an anti-reflection effect. HCl and NH_4OH etch the oxide well and give a smooth polished surface of $Hg_{0.8}Cd_{0.2}Te$.

Keywords. Anodic oxide; mercury cadmium telluride; pH value; native oxide; II–VI compounds.

1. Introduction

The pseudo-binary alloy $Hg_{0.8}Cd_{0.2}Te$ is one of the most important semiconducting material for infrared applications. Photoconductive detectors, photodiodes, metal-insulator-semiconductors (MIS) diodes and charge coupled devices (CCDs) have been made using this material for the 8–14 μm atmospheric window. The performance of these opto-electronic devices is closely related to the surface properties. It is limited by the surface leakage current as well as the electrical and the chemical stability of $Hg_{0.8}Cd_{0.2}Te$. It is, therefore, necessary to passivate the surface of this material. Native oxide film anodically grown on $Hg_{0.8}Cd_{0.2}Te$ has been used for surface passivation and preparation of MIS structure by various workers (Willardson and Beer 1981; Catagnus and Baker 1979; Dornhaus and Nimtz 1983). However, the chemical and optical properties of the film are not well reported in the literature. In this paper we describe the procedure for forming the anodic oxide film on $Hg_{0.8}Cd_{0.2}Te$ under constant voltage source. The chemical behaviour of the film to various organic and inorganic solvents and the antireflection effect of the film are also examined and discussed.

2. Anodization procedure

The $Hg_{0.8}Cd_{0.2}Te$ wafers used were both of *n* and *p*-types with carrier concentration in the range 10^{15}–10^{17} cm^{-3} and with a random orientation. These crystals were obtained from New England Research Centre, USA. The surface of the wafers was prepared by first lapping with 3–5 μm Al_2O_3 powder and then with 0·5 μm powder. The lapped surface was then etched by a standard procedure for MCT using 2% Br_2+ methanol solution prior to anodization to remove the damaged surface.

The set-up used for anodic oxidation is shown in figure 1. A graphite rod is used as the cathode. The electrolyte is a mixture of 0·1 N KOH + 90% ethylene glycol and 10% H_2O. The anodic oxidation is carried out under normal light condition at room

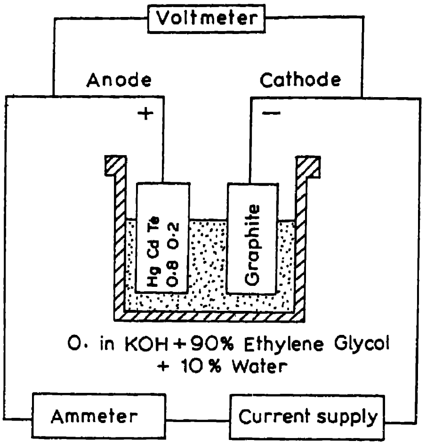

Figure 1. Systematic arrangement for anodizing $Hg_{0\cdot8}Cd_{0\cdot2}Te$.

temperature using a constant voltage d.c. source. The cell voltage and the current are measured with time. The pH value of the prepared solution is found to be 12 and is alkaline in nature. The film grown in this solution at a current density 1 mA/cm^2 showed matte appearance. To improve the quality of the film, the parameters—the pH of the solution and the current density are varied and the effects are investigated. The pH value of the solution is varied from 5 to 11 by adding oxalic acid. The initial current density is varied from 0·2 mA/cm^2 to 2 mA/cm^2. During the growth it is observed that good, uniform shining and reproducible films are obtained when the pH is in the range 7–8 and current density 0·5–1 mA/cm^2. For further experiments the pH was kept equal to 8 and initial current density to 1 mA/cm^2. After anodization the samples are rinsed in deionized water for a few seconds and then dried in pure nitrogen gas flow. Figure 2 shows a typical example of the behaviour of the current and the voltage as a function of time during the anodization. The voltage increases linearly with time and saturates to the previously set value. The current decreases rapidly and then becomes a small constant value depending on the voltage. The reason for this small constant residual current is not established.

3. Film properties

The oxide film grown at the optimum value of pH 8 and initial current density 1 mA/cm^2 are shining and transparent for all cell voltages upto 25 V. The thickness of the oxide films as a function of cell voltage is determined by optical interferometry using the standard formula. A relation between the cell voltage and the thickness of the film is shown in figure 3 along with the colour of the film obtained at these cell voltages. The colour chart is similar to that obtained for anodic oxide of $Pb_{0\cdot94}Sn_{0\cdot06}Se$ (Gupta and Richter 1983) and SiO_2 (Ghandhi 1985). The thickness of the oxide film is also calculated theoretically by using the colour chart of SiO_2 and the following relation

$$n_1 t_1 = n_2 t_2, \tag{1}$$

where n_1 and n_2 are the indices of refraction for SiO_2 and oxide of MCT respectively

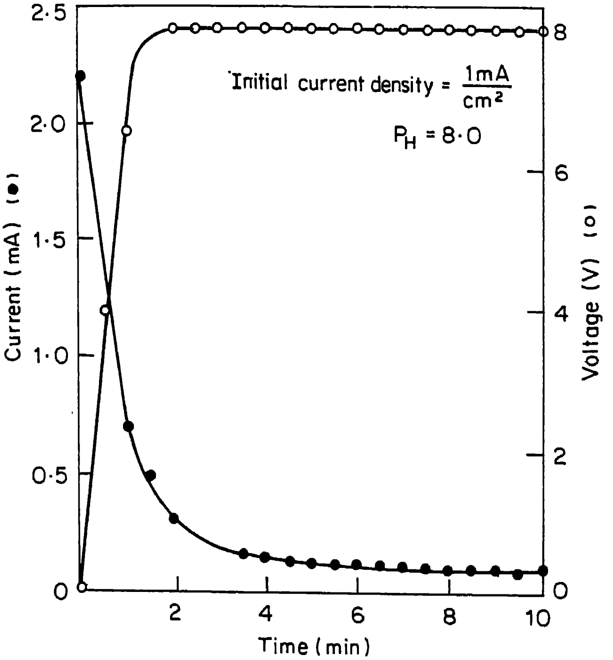

Figure 2. Time dependence of voltage and current during anodization under constant voltage d.c. source.

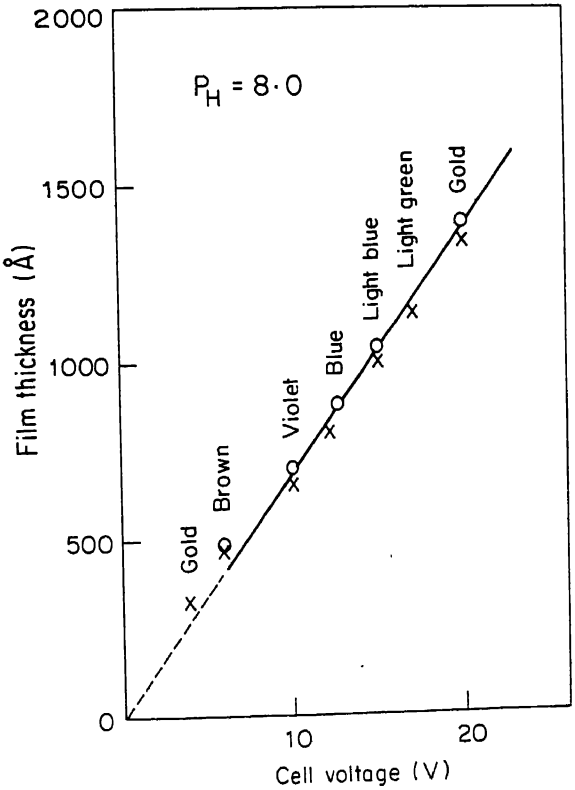

Figure 3. Oxide film thickness and its colour vs cell voltage at a current density 1 mA/cm^2.

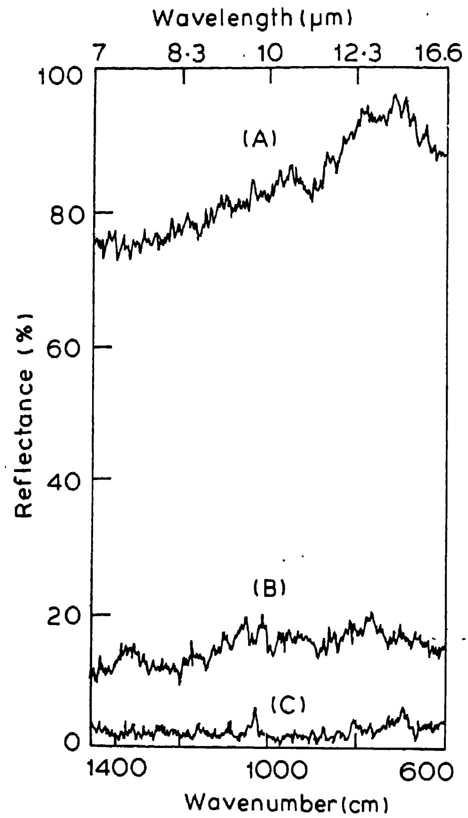

Figure 4. Reflectance vs wavelength for $Hg_{0\cdot8}Cd_{0\cdot2}Te$ with and without oxide. Curve (A) is the reference signal and curves (C) and (B) are with and without oxide films.

and t_1 and t_2, the respective thicknesses. In the calculation of the refractive index of SiO_2, (n_1) is taken to be 1·48 and the refractive index of oxide grown is taken as 2·18 assuming that the main component of the anodic oxide is TeO_2. As shown, there is a fairly good agreement between the experimental and the theoretical value of different cell voltages. The refractive index of TeO_2 is nearly equal to that of ZnS (Debenham 1984) and ZnS is used as an anti-reflection coating in the range 7–16·6 μm. This leads us to measure the reflectivity of the oxide film and compare with that of unoxidized samples of MCT. The anodic oxide film shows an anti-reflection effect. The results are shown in figure 4 which substantiate our assumption that the main component of the anodic film of MCT is TeO_2. The growth of 1000 Å thick TeO_2 consumes about 1500 Å of MCT.

The anodic oxides are not chemically attacked by organic solvents such as acetone, benzene, trichloroethylene, glycol, methanol, ethanol and carbon tetrachloride. The transparent film is easy to etch. The solubility properties of the oxide in acid and alkaline solutions and the surface obtained after etching are given in table 1. It is clear from the table that HCl or NH_4OH easily dissolves the oxide and gives a smooth polished surface. HCl or NH_4OH can therefore be used to delineate the oxide film to any shape using standard photolithography.

Table 1. Solubility of the anodic oxide film in acid and alkaline solutions and surface of the crystal after etching.

Solution	Solubility	Etched surface
HCl	Easily dissolves	Smooth polished surface
HNO_3	Fast action	A layer remains
H_2So_4	Slowly dissolves	Not smooth
HF	Slowly dissolves	A layer remains
HBr_2	Slowly dissolves	Rough
NH_4OH	Easily dissolves	Smooth polished surface
NaOH	Slowly dissolves	Not smooth
KOH	Dissolves very very slowly	A layer remains

4. Conclusion

The condition of forming a good anodically oxidized film on $Hg_{0\cdot8}Cd_{0\cdot2}Te$ is studied. The electrolyte composed of 0·1 N KOH, 90% ethylene glycol, 10% H_2O when adjusted to pH = 7 to 8 gives good transparent film for cell voltages upto 25 V. HCl and NH_4OH can be used as a useful etchant to delineate the oxide film to any shape.

Acknowledgement

The results reported in this paper were presented at the National Symposium on Thin Film Science and Technology, Bangalore, January 1985.

References

Catagnus P C and Baker C T U S 1979 Pat. 3,977,018

Debenham M 1984 *Appl. Opt.* **23** 2238

Dornhaus R and Nimtz G 1983 in *Springer tracts in modern physics* (ed.) R Hohler (Berlin: Springer Verlag) vol. 98 p. 119

Ghandhi S K 1983 *VLSI fabrication principles, silicon and gallium arsenide* (New York: John Wiley) p. 371

Gupta S C and Richter H J 1983 *J. Electrochem. Soc.* **130** 1469

Willardson R K and Beer A C 1981 *Semiconductors and semimetals* (New York: Academic Press) vol. 18

Bull. Mater. Sci., Vol. 9, No. 3, August 1987, pp. 225–233. © Printed in India.

Use of energy dispersive method with tungsten carbide opposed anvil high pressure set-up

A K SINGH and S USHA DEVI
Materials Science Division, National Aeronautical Laboratory, Bangalore 560 017, India

MS received 14 April 1987

Abstract. The use of energy dispersive method has been discussed to record the X-ray diffraction data from a tungsten carbide opposed anvil high pressure set-up. It is pointed out that a proper collimation of the incident and the diffracted beams can eliminate the scattering from the gasket material. This results in an appreciable improvement in the quality of the recorded diffraction data. The choice of the various parameters has been discussed. The data on sodium chloride are presented in support of this analysis.

Keywords. High pressure studies; energy-dispersive method; beam divergence; gasket scattering.

1. Introduction

The energy dispersive method has been used extensively in recent years in recording X-ray diffraction data from specimens under high pressure. This method offers high speed of data collection and has been used mostly with diamond anvil cells. In this paper we have discussed the use of energy dispersive method in recording the diffraction data from tungsten carbide opposed anvil set-up. Freud and LaMori (1969), while discussing the use of an energy-dispersive technique with a split-die belt apparatus, suggested a configuration of the specimen, and the incident and the diffracted beams, which can eliminate the unwanted scattering from the gasket material. However, Freud and LaMori (1969) neither analysed this aspect in detail nor perform any experiments using the geometry they suggested. Since their geometry is also applicable to the tungsten carbide opposed anvil set-up, a detailed analysis has been presented in this paper. The high pressure data on sodium chloride gathered with a tungsten carbide opposed anvil set-up under the Freud-LaMori geometry are presented to support the analysis given in this paper.

2. General considerations

The working principle of a tungsten carbide anvil high pressure cell for X-ray diffraction work (Jamieson and Lawson 1962; Perez-Albuerne *et al* 1964; McWhan and Bond 1964) is shown schematically in figure 1. The powdered specimen is contained in a hole at the centre of a X-ray transparent gasket (boron, boron-epoxy, beryllium) typically 3 mm in diameter and about 0·2 mm thick. The specimen is pressurized by loading the gasket-specimen assembly between the tips of two tungsten carbide anvils. A collimated x-ray beam, normal to the direction of the applied load, passes through the gap between the anvils and illuminates the specimen. The commonly used angle dispersive method employs MoK radiation, and the diffraction pattern is recorded on a photographic film. The use of energy

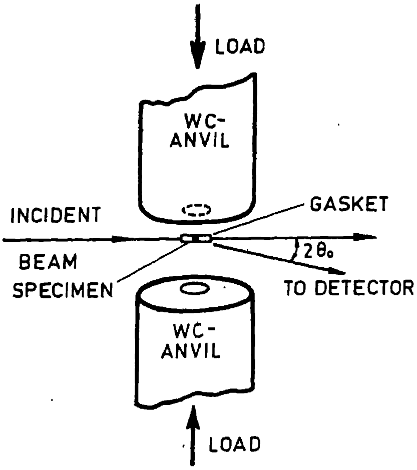

Figure 1. Working principle of a tungsten carbide opposed anvil set-up for X-ray diffraction work.

dispersive method discussed here requires white (continuous) radiation from either molybdenum or tungsten target. A solid state detector is placed at a fixed 2θ ($=2\theta_0$) to detect the entire range of energy spectrum in the direction $2\theta_0$. The diffraction peaks which appear at different energies are recorded simultaneously. The *d*-spacing of a set of planes with indices (*hkl*) is given by

$$d\,(hkl)=hc/2E\sin\theta_0, \tag{1}$$

where *E*, *h* and *c* are respectively the energy at the diffraction maximum, the Planck's constant and the velocity of light.

3. Beam divergence

The divergences (termed radial divergences) of the incident and the diffracted beams (in a plane perpendicular to the loading direction and passing through the centre of the gasket) along with the other parameters used in further discussion are marked on figure 2. The divergence of the incident beam, α_i and the dimension, $2a$, of the specimen region at the centre, bathed by the incident X-ray beam are given by

$$\alpha_i=W_i/L_i, \tag{2}$$
$$2a=\alpha_i(L_i+l_i). \tag{3}$$

The symbols appearing in (2) and (3) are explained in figure 2. The above equations are valid for the condition $2r>\alpha_i(L_i+l_i)$ where r is the radius of the specimen. It will become clear from the later discussions that the analysis under this condition alone is of interest. In deriving (2) and (3) it is assumed that the focal spot is larger than $\alpha_i(D_i+L_i)$. This condition is satisfied if a conventional X-ray tube is used. However, microfocus or fine focus X-ray tubes provide focal spots which are 100 μ or less in size. In such cases α_i is smaller than the value given by (2). It can be easily shown that in this case α_i is given by

$$\alpha_i=(f_1+W_i)/(2L_i+D_i), \tag{4}$$

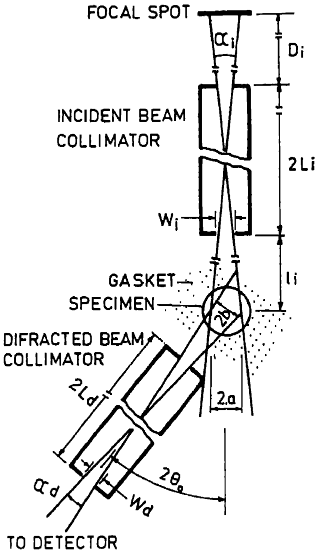

Figure 2. Arrangement for restricting the incident and the diffracted beam divergences.

where f_1 is the dimension of the focal spot in the plane of figure 2, and D_i is the distance between the focal spot and the nearest pinhole of the collimator.

The expressions for the radial divergence, α_d, of the diffracted beam, and $2b$, the width of the region (at the centre of the specimen) *seen* by the detector can be obtained by replacing suffix i in (2) and (3) by d. The resulting expressions for α_d and $2b$ are valid if the detector surface size is greater than $\alpha_d(L_d + D_d)$. This condition is always satisfied in practice.

The incident and the diffracted beams possess divergences also in the plane normal to the plane of figure 2. These are termed axial divergences and are denoted by β_i and β_d. The values of β_i and β_d depend on the gasket thickness, t, and the shape of the collimator pinhole. If the pinhole is circular and $t \geqslant 2a$, then $\beta_i = \alpha_i$. For $t < 2a$, β_i is given by

$$\beta_i = (W_i + t)/(2L_i + l_i). \tag{5}$$

These results are valid only if the axial dimension of the focal spot is greater than $\alpha_i(L_i + D_i)$. Similar consideration of the geometry of the diffracted beam collimator shows that for $t \geqslant 2b$, $\beta_d = \alpha_d$. For $t < 2b$, an expression for β_i can be obtained by simply replacing suffix i in (5) by d.

4. Scattering from the gasket

The origin of scattering from the gasket material in energy-dispersive mode of data collection can be understood from figure 3. Since the divergences of the incident and the diffracted beams are small (rarely exceeding a few milliradians), the regions of the gasket and the specimen illuminated by the incident beam can be considered to be bound by parallel lines AB and CD, the distance between the two being $2a$. Similarly, the illuminated region from where the scattered radiation reaches the detector is

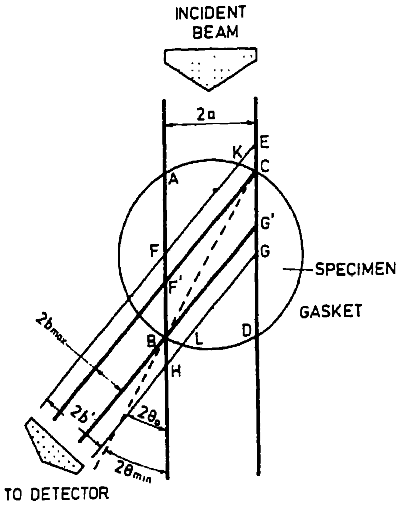

Figure 3. Origin of the scattering from the gasket material. The scattered radiation from the gasket region ECK and LHB reaches the detector.

bound by parallel lines EF and GH separated by $2b'$. Clearly, the regions ECK and LHB contribute to the scattering from the gasket material. This contribution results in a high background if boron or boron epoxy gasket is used, and produces diffraction lines if beryllium gasket is used. The assumption that AB || CD and EF || GH has been made only to define the regions illuminated by the incident beam, and the illuminated region *seen* by the detector. This is a very good approximation in view of the small divergences involved in such experiments.

It is possible, by reducing the divergence of the receiving slit, to arrive at a value of $2b$ for a given set of values of $2a$, $2\theta_0$ and the radius r of the specimen such that the regions ECK and LHB do not exist. Such a situation is shown in figure 3; a region, CG′ BF′ only of the specimen illuminated by the incident beam is *seen* by the detector. In such a case the scattering from the gasket material is eliminated. The radiation scattered by the specimen passes through the gasket before reaching the detector, and interacts with the gasket material producing a rescattered radiation which reaches the detector. However, the intensity of the rescattered radiation is very small as compared with the intensity of radiation produced by the scattering of the primary incident beam, and can be neglected. Thus, the diffraction data gathered in the absence of regions ECK and LHB will be practically free from the scattering from the gasket material.

The separation, $2b_{\max}$, between the lines CF′ and G′B is the maximum value of $2b$ (for a given set of values of $2a$, $2\theta_0$ and r) which can lead to the absence of regions ECK and LHB. It is seen from figure 3 that the situation resulting in the absence of the scattering from the gasket material can arise only if $2\theta_0 > 2\theta_{\min}$, where $2\theta_{\min}$ is the angle ABC. Noting that $AC = 2a$, $BC = 2r$, and the angle CAB is a right angle, $2\theta_{\min}$ is given by

$$\sin 2\theta_{\min} = a/r. \tag{6}$$

For $2\theta_0 > 2\theta_{\min}$, the relation connecting the various quantities can be obtained by considering the triangle CF′B. Noting that CF′, F′B and BC equal respectively $2a/\sin 2\theta_0$, $2b_{\max}/\sin 2\theta_0$ and $2r$, the following relation can be written,

$$a^2+b_{\max}^2+2ab_{\max}\cos 2\theta_0-r^2\sin^2 2\theta_0=0. \tag{7}$$

At $2\theta_0=2\theta_{\min}$, $2b_{\max}=0$. The value of $2b_{\max}$ increases with increasing value of $2\theta_0$ and reaches a maximum value at $2\theta_0=90°$. At $2\theta_0=4\theta_{\min}$, $2b_{\max}=2a$.

It is instructive to estimate the numerical values of the various parameters discussed so far. On substituting a reasonable set of values ($l_i=7{\cdot}5$ mm, $L_i=75$ mm and $W_i=0{\cdot}15$ mm) for the various quantities in (1) and (2), $\alpha_i=2$ mrad and $2a=0{\cdot}17$ mm are obtained. Assuming $r=0{\cdot}5$ mm, $2\theta_{\min}\simeq 10°$ is calculated from (6). In experiments with either molybdenum or tungsten target, $2\theta_0$ is set at 20°. Thus, the condition $2\theta_0>2\theta_{\min}$ is satisfied. The value of $2b_{\max}$ as calculated from (7) is 0·16 mm. A diffracted beam collimator with essentially the same dimension as those given above for the incident beam collimator will be required for $2b_{\max}=0{\cdot}16$ mm. With a fine focus tube, it is possible to further reduce α_i without appreciable reduction in the intensity of the incident beam.

5. Specimen size optimization

The intensity of the diffracted beam is proportional to the volume of the specimen. However, the larger the size of the specimen, the larger is the reduction in the intensity of the diffracted beam, because of the absorption factor. By considering the specimen volume and absorption factor effects for a geometry required to eliminate gasket scattering it can be shown (appendix) that the diffracted beam intensity reaches a maximum when,

$$2a=2b=-(\sin 2\theta_0 \ln \cos 2\theta_0)/\mu(1-\cos 2\theta_0), \tag{8}$$

where μ is the linear absorption coefficient of the sample material. Since the absorption coefficient depends strongly on the energy of the radiation, it is not possible to choose a single set of values of $2a$ and $2b$ in accordance with (8) which will be valid for the entire energy range. In most cases, the diffraction data are collected in the energy range approximately 10 to 40 keV. The optimum values of $2a$ and $2b$ may be chosen at 25 keV, an energy in the middle of useful energy range. Even this criterion may often lead to $2a$-value which is unacceptable from other considerations. For example, $r\leqslant 0{\cdot}5$ mm, for the gaskets of 3 mm dia. Further, from practical consideration $2a$ and $2b$ should be in the range 0·1–0·2 mm. Obviously, the optimum value of $2a$ obtained from (8) will be unacceptable if it falls grossly outside this range. The optimum value of $2a$ for low (high) absorbing materials is too large (small) to be achieved in practice. For the optimum value of $2a$ to be in the range 0·1–0·2 mm at $2\theta_0=20$, μ-value should be in the range 35 cm^{-1} to 17·5 cm^{-1}.

The effective absorption coefficient of highly absorbing materials can be brought in the desired range by diluting it with the appropriate proportion of low absorbing material. For example, for niobium $\mu=385\ \text{cm}^{-1}$ at 24·9 keV, the corresponding value of $2a$ from (8) being 0·009 mm. However, diluting niobium powder with sodium chloride in the weight ratio 1 : 3 gives $\mu=35\ \text{cm}^{-1}$. It is fortuitous that sodium chloride is used as a pressure marker.

6. Experimental results

The analysis proposed in this paper was verified by gathering the energy-dispersive data on sodium chloride. A pair of tungsten carbide anvils with the flat face diameter of 3 mm was used to pressurize the specimen. The experiments were conducted using both boron-epoxy and beryllium gaskets. In either case, the gasket was 3 mm in diameter and 0·3 mm thick with a central hole of 1 mm dia. The X-ray source was a Enraf-Nonius generator with fine focus tungsten target sealed tube operated at 20 mA and 60 kV. The data were collected at $2\theta_0 = 18°$ using a Si(Li) solid state X-ray detector from Ortec and the associated electronics Ortec 6230. A counting time of 8000 sec was used. First, the data were gathered (with both boron-epoxy and beryllium gaskets) by setting the incident and the diffracted beam divergences such that $2a = 2b \simeq 0{\cdot}6$ mm. Next, the divergences were reduced such that $2a = 2b \simeq 0{\cdot}3$ mm and the experiments repeated.

The data gathered with boron-epoxy gaskets are shown in figure 4. The inset shows the data with large divergence ($2a = 2b \simeq 0{\cdot}6$ mm). Only the first two strong peaks are seen on a large background. The data under the condition $2a = 2b \simeq 0{\cdot}3$ mm clearly show the first five strong peaks of sodium chloride on a relatively low general background. The data with beryllium gasket under the condition $2a = 2b \simeq 0{\cdot}6$ mm are shown in the inset of figure 5. The strong beryllium lines are seen together with the sodium chloride lines. In practice the interference from the beryllium lines can pose serious problems. The reduction of the divergences of the incident and the diffracted beams results in a considerable improvement of the diffraction patterns. The intensity of the beryllium line drops considerably. Ideally, the beryllium lines should be absent. However, in figure 5, (101) beryllium line appears with a very low intensity presumably because of small misalignment.

7. Discussion

The tungsten carbide opposed anvil set-up was extensively used in sixties and early seventies in high pressure x-ray diffraction studies. The gasket made from

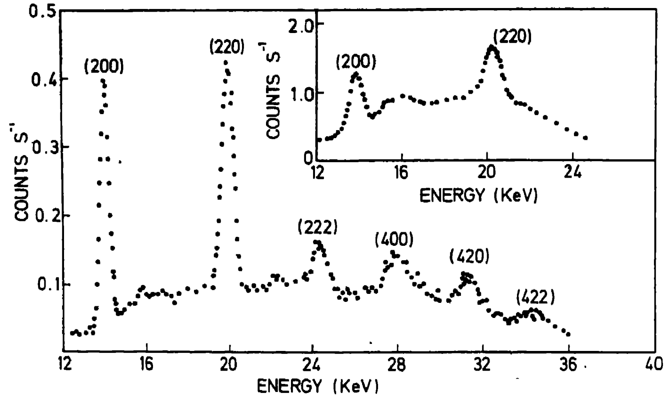

Figure 4. Sodium chloride data recorded with boron-epoxy gasket under the conditions $2a = 2b \simeq 0{\cdot}3$ mm, and $2\theta_0 = 18°$. The inset shows the data recorded with $2a = 2b \simeq 0{\cdot}6$ mm.

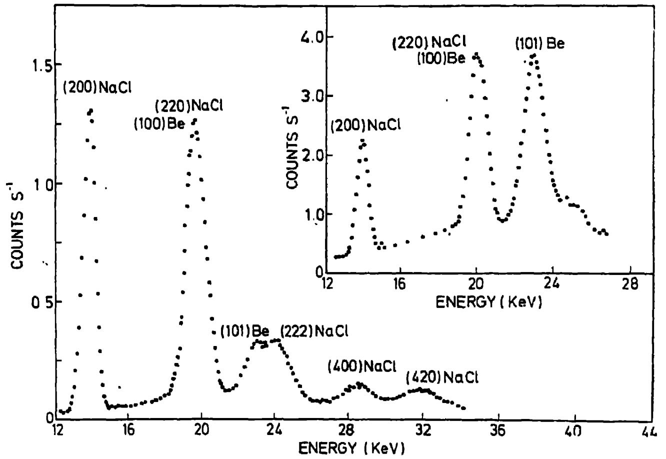

Figure 5. Sodium chloride data recorded with beryllium gasket under the conditions $2a=2b\simeq 0{\cdot}3$ mm. and $2\theta_0=18^\circ$. The inset shows the data recorded with $2a=2b\simeq 0{\cdot}6$ mm.

amorphous boron (or amorphous boron and epoxy mixture) was used to contain the specimen. The set-up was inexpensive and extremely easy to operate. It provided a good control over the small pressure increments. The method, however, suffered from two major drawbacks. Firstly, the pressure on the specimen was not truly hydrostatic, and this introduced systematic errors in the pressure-volume curve derived from X-ray measurements (Singh 1978). Secondly, the X-ray scattering from the gasket material produced high background. These drawbacks outweighed the advantages of lower cost and ease of operation, and this method was discarded in favour of other methods such as diamond anvil cell.

Halleck and Olinger (1974) solved the problems arising from the non-hydrostatic pressure distribution on the specimen by replacing boron gaskets by beryllium gaskets. The use of beryllium gaskets made it possible to seal fluid together with the specimen and generate truly hydrostatic pressure. This proved to be an important improvement in the tungsten carbide opposed anvil technique. The background scattering, however, did not decrease appreciably with the use of beryllium gaskets. The diffraction lines from beryllium gasket added further complications.

The present analysis of the Freud-LaMori geometry indicates that a proper choice of the divergences of the incident and diffracted beams can lead to a situation wherein the radiation scattered from the gasket material does not enter the detector. This results in an improved peak-to-background ratio if boron-epoxy gasket is used, and eliminates unwanted diffraction lines from beryllium, if beryllium gaskets are used.

It may be noted that any degree of collimation cannot give this result if photographic film is used to record the diffraction pattern. In principle, angle dispersive method with a scintillation or a proportional counter detector can give this result at $\theta > \theta_{\min}$. However, the use of a scintillation or a proportional counter is not practicable because of the extremely low count rate produced by the diffracted beam in angle dispersive mode. The use of the energy-dispersive method is crucial in realizing in practice the geometry discussed in this paper.

8. Conclusion

The present analysis of Freud-LaMori geometry and the data collected under these conditions clearly indicate that the scattering from the gasket material reaching the detector can be eliminated by suitably limiting the divergences of the incident and the diffracted beams. Thus, the use of beryllium gasket with fluid pressure transmitter, and Freud-LaMori geometry for data collection using energy dispersive method eliminates both the major drawbacks of the tungsten carbide opposed anvil set-up. It is hoped that with these improvements, the tungsten carbide opposed anvil set-up will prove to be a reliable method of recording X-ray diffraction data from the specimen pressurized up to 15 GPa.

Acknowledgement

The authors thank Dr R V Krishnan for many helpful discussions.

Appendix

Let the x- and y-axes be respectively along OU and OV (figure 6). Clearly,

$$OU\,(\equiv 2\bar{a}) = 2a/\sin 2\theta_0, \tag{9}$$

$$OV\,(\equiv 2\bar{b}) = 2b/\sin 2\theta_0. \tag{10}$$

Consider an area element $dxdy$ at N with coordinates (x,y). The incident ray $L'N$, is scattered by element $(dxdy)$ along NP' parallel to x-axis. Neglecting small path lengths $L'L$ and PP', the total path length, l, in the specimen is given by,

$$\begin{aligned} l &= LN + NP; = (LM + MN) + (QS - QN + SP); \\ &= (x\cos 2\theta_0 + y) + (2\bar{a} - x + ST\cos 2\theta_0); \\ &= (x\cos 2\theta_0 + y) + (2\bar{a} - x) + (UT - US)\cos 2\theta_0; \\ &= 2\bar{a} + 2\bar{b}\cos 2\theta_0 - (x - y)\,(1 - \cos 2\theta_0). \end{aligned} \tag{11}$$

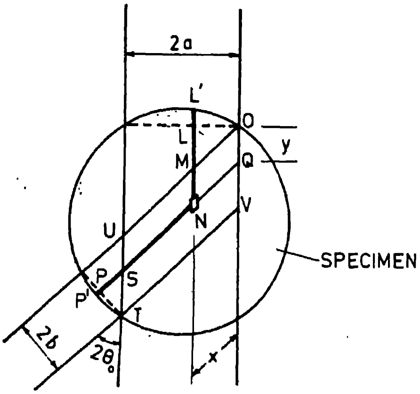

Figure 6. The X-ray beam path length in the specimen.

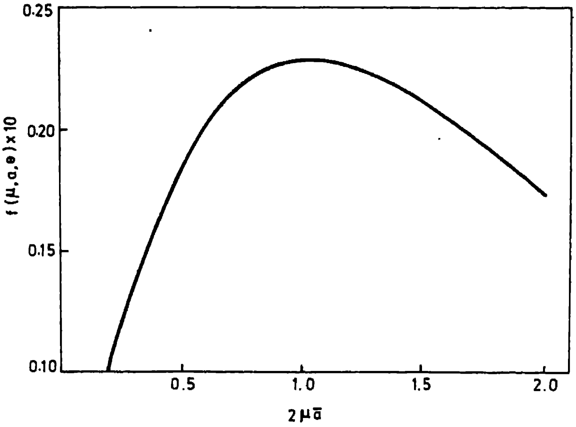

Figure 7. A plot of $f(\mu,\bar a,\theta)$ vs $2\mu\bar a$.

In deriving (11), the following equalities in addition to (9) and (10) have been used;

$$QS = OU = 2\bar a;\ UT = OV = 2\bar b;$$

$$OQ = MN = US = y;\ QN = OM = x.$$

The intensity of the radiation scattered from $(\mathrm{d}x\mathrm{d}y)$ along NP' is proportional to the volume element $(\mathrm{d}x\mathrm{d}y)t$ (where t is the thickness of the cylindrical specimen) and $\exp(-\mu l)$. The total intensity reaching the detector is given by

$$I = C\int_0^{2\bar a}\int_0^{2\bar b}(\exp - \mu l)\,\mathrm{d}x\,\mathrm{d}y$$

On substituting for l from (11) and integrating, the following expression is obtained,

$$I = [K/\mu^2(1-\cos 2\theta_0)^2]\, f(\bar a,\mu,\theta_0)\, f(\bar b,\mu,\theta_0) \tag{12}$$

where

$$f(\bar a,\mu,\theta_0) = \exp(-2\mu\bar a\cos 2\theta_0) - \exp(-2\mu\bar a).$$

It can be easily shown that I reaches a maximum value when,

$$2\bar a = 2\bar b = -\ln(\cos 2\theta_0)/\mu(1-\cos 2\theta_0)$$

The variation of $f(\bar a,\mu,\theta)$ with $\bar a\mu$ is shown in figure 7.

References

Freud P J and LaMori P N 1969 *Trans. Am. Crystallogr. Assoc.* **5** 155
Halleck P M and Olinger B 1974 *Rev. Sci. Instrum.* **45** 1408
Jamieson J C and Lawson A W 1962 *J. Appl. Phys.* **33** 776
McWhan D B and Bond W L 1964 *Rev. Sci. Instrum.* **35** 626
Perez-Albuerne E A, Forsgren K F and Drickamer H G 1964 *Rev. Sci. Instrum.* **35** 29
Singh A K 1978 *High Temp-High Pressures* **10** 641

Bull. Mater. Sci., Vol. 9, No. 3, August 1987, pp. 235–239. © Printed in India.

Positron annihilation in Zr-0·5 Nb alloy

D D UPADHYAYA and R V MURALEEDHARAN*
Metallurgy Division, *Physical Metallurgy Division, Bhabha Atomic Research Centre, Bombay 400 085, India

MS received 1 December 1986; revised 20 June 1987

Abstract. The measurement of coincidence counting rate at the peak of the angular correlation curve shows a considerable difference between the recovery behaviour of cold-worked Zr-0·5 Nb alloy from that reported for pure zirconium. This difference in behaviour illustrates the point-defect activity during the course of isochronal annealing in this alloy. The recovery spectrum can be understood in terms of the vacancy-solute entrapment upto about 250°C. In the next stage the release and clustering effects of vacancies are indicated prior to their elimination. The study thus demonstrates the effect of alloying element on the defect mobility and associated point defect interactions in Zr.

Keywords. Positron annihilation; 2γ-angular correlation; cold-work recovery; dilute zirconium alloys.

1. Introduction

Positron annihilation spectroscopy (PAS) is a powerful nuclear technique for characterization of the defect microstructure in solids. For metals and alloys, the positron probe is very sensitive to changes in local electron density near the lattice defects, especially the vacancy type of structural imperfections. This selective nature of interaction makes it an important complementary and also a nondestructive research tool. It has helped in advancing the fundamental understanding of various metallurgical phenomena to a great advantage (Doyama 1984; Krishnan and Upadhyaya 1985). The mechanism of electron-positron annihilation and details of measurement techniques have been discussed by various authors (West 1973; Hautojarvi 1979; Upadhyaya 1985).

The present work is an investigation of the defect recovery behaviour of a dilute solid-solution composition of Zr-Nb system as studied by γ-γ angular correlation technique. These alloys are of interest in nuclear industry as cladding, coolant and pressure tube material. The thermomechanical processing parameters largely control the microstructural development and need to be studied in detail employing different techniques. Considering, for example, during thermal annealing of cold-worked metals the successive process steps recognised are recovery, recrystallization and grain-growth. These stages are conventionally followed in the form of changes observed in the average property parameters like hardness, resistivity etc. Supplementing these measurements with a defect-specific quantity like the positron annihilation parameter, greatly enhances the accuracy of the proposed annealing mechanism. The present results being on the latter aspect alone, demonstrate the mechanism of vacancy elimination in the presence of aliovalent impurity atoms in the lattice. A dilute solution composition was selected to prevent solute clustering effects.

2. Experimental

The alloy was prepared by melting together sponge purity Zr (purity better than 99·7%) and zone-refined niobium (nominal purity 99·95%) in an electric arc furnace under pure argon atmosphere. The alloy button thus produced was encapsulated in a silica tube (under a vacuum better than 10^{-4} torr) and given an homogenization treatment at 1000°C for 24 hr. It was then sealed in a copper tube and hot-rolled at 700°C down to about 1 mm thin plate form. Such plates were then subjected to crystallization annealing (600°C/48 hr) and finally cold-rolled to give a thickness reduction of about 30%.

Square cross-section (15 mm) samples were machined out of these strips for various isochronal annealing treatments upto a temperature of 350°C. A duration of 30 min was used at each annealing temperature (under argon atmosphere). Although the as machined samples were reasonably flat, an attempt to improve the surface finish by the usual metallographic techniques was found to change the results considerably. Therefore, before mounting onto the positron apparatus the only surface preparation process followed was by electro-polishing the samples in a dilute sulphuric acid bath and cleaning by rinsing in water and methanol.

The angular correlation was measured using a standard linear-slit configuration (Upadhyaya 1985). The angular resolution of the system was adjusted to be 1 mrad. The positron source used was ^{64}Cu of ~1 Ci strength, prepared by irradiation in CIRUS reactor. The angular distribution spectrum ($N(\theta)$ vs θ) of coincidence counts was obtained for about 22 mrad across $\theta=0$. A suitable data collection time at each angle was selected to achieve a good statistics and measurements were repeated 2 to 3 times for each sample. Data were normalized for equal area after the background and source decay corrections.

3. Results and discussion

Figure 1 shows the normalized peak value of 2γ-angular correlation curves of positron annihilation radiation in 30% cold-rolled Zr-0·5 Nb as a function of isochronal annealing temperature. A gradual fall in the peak count rate was observed upto 250°C and then a small increase in value in the range 250 to about 325°C. Above this temperature a further decreasing trend was observed. Positron experiments were not followed beyond 350°C annealing, in the recrystallization and grain-growth regime of the alloy.

Taking the Brandt and Paulin (1977) relationship, the energetic positron ($E_\beta^{\max}=$ 0·7 MeV) from ^{64}Cu source has a range of 58 μm in the Zr samples. Therefore the changes introduced in the annihilation events due to surface oxide contamination etc will be within the limits of experimental errors. However, substantial changes were observed on ground and polished samples, which was thus avoided for the entire set of measurements reported here. This can readily be ascribed to the sample being subjected to plastic deformation by mechanical polishing. This has been clearly demonstrated very recently (again by PAS-experiments) by Waber and Park (1986). Their positron lifetime results on mechanically polished single crystals of iron, enabled the mapping of dislocation-density profile. It showed that the abrasion damage extends to about 25 μm from the surface.

Cold work produces two types of lattice defects in metals; (i) point defects which

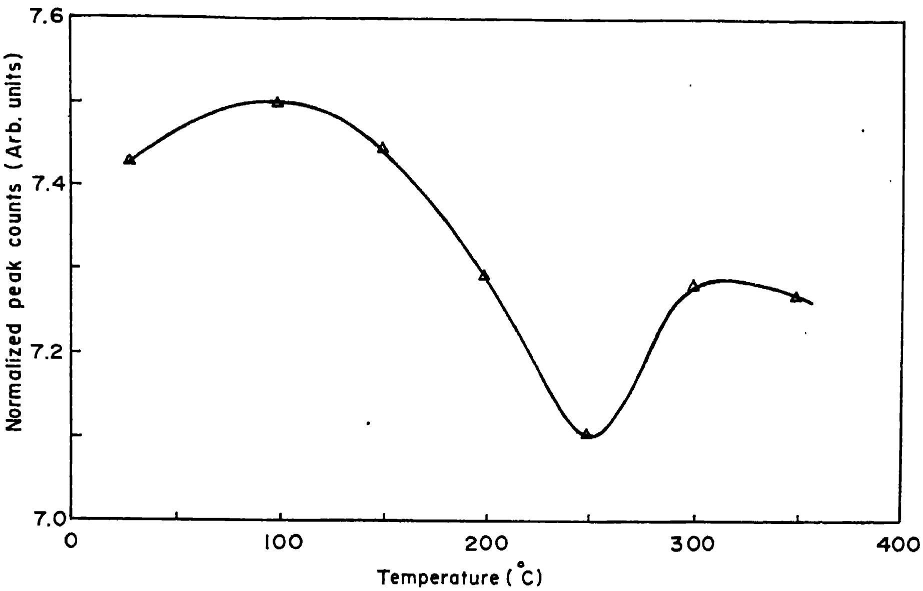

Figure 1. Coincidence counts at the peak of the angular correlation curve as a function of isochronal annealing temperature for Zr-0·5 alloy.

are mobile at temperatures close to room temperature (vacancies), and those are mobile at low temperatures (say interstitials) and (ii) dislocations which are randomly distributed initially, but get reorganized (during recovery temperature range) in arrays and later annihilate during recrystallization ($\simeq$0·2–0·5 Tm ranges). In the deformed lattice the region containing a point defect such as an isolated vacancy is deficient in ion core and hence deficient in higher energy core electrons. A positron trapped in the attractive potential of the vacancy has a higher probability of annihilation with lower momentum conduction electrons (Seeger 1976; Byrne 1980). This effect is revealed in the form of rise in the peak counting rate, $N(0)$ of 2γ-angular correlation events. Similarly, the vacancy agglomerates and dislocations etc are other effective positron traps. Any change, for instance, during annealing in the concentration and configuration of the defect species involved is thus monitored by the relative magnitude of the integral parameter $N(0)$.

Positron trapping by vacancies is strongly affected by the presence of impurities (which are also attracted into these defects forming various vacancy-impurity complexes). Results on several dilute alloy systems have shown that the specific trapping rate for vacancies is much reduced when bound to a higher valent impurity, e.g. Ge in Cu (Doyama *et al* 1974), Sn in Au (Shirai *et al* 1979) and In, Sb again in Cu (Bosse *et al* 1986) etc. Another special attribute of positron probe is to exhibit a higher degree of sensitivity for charge modification at individual lattice sites: such as for transition metal impurity atoms in Cu (Doyama *et al* 1973) or electron density variations due to 'charge transfer effects' in some binary alloys (Kubica *et al* 1975; Tsuchiya and Tamaki 1978).

The impurity size also influences the recovery of cold-rolled metals. As an example, for Ni the solutes which are largely oversized (like Sb, As and Pb) were found to induce a strong vacancy clustering effect whereas other solutes have a very weak or no effect for such defect agglomeration (Dlubek *et al* 1979; Brummer and Dlubek 1985). In the case of iron, the carbon impurity traps the vacancies and these carbon-vacancy pairs then dissociate at about 500 K. This acts as a source of free vacancies which then move and form clusters (Brandt and Dupasquier 1973). In general, the activation energy for diffusion of solute in dilute alloys seems to bear a direct dependence on the ratio of charge to size (e/a) parameter (Tiwari *et al* 1980).

The recovery behaviour of pure zirconium above room temperature was studied earlier by resistometry (Pande *et al* 1972) and by positron lifetime measurements (Tanigawa *et al* 1982). In either case, essentially a continuous decrease in resistivity or mean lifetime was observed, representing only the vacancy migration and recrystallization processes being operative. The electron irradiated α-Zr also showed a similar continuous recovery (Hood *et al* 1977), whereas for Zr-0·5 Nb alloy a multiple peak pattern was observed (Batra *et al* 1984).

In the present case, the initial rise can be understood to be associated with the onset of free vacancy migration (Hood *et al* 1984). After about 100°C stage we visualize a defect configuration of the type of single vacancy being trapped at Nb impurity atoms. Since Nb is an undersized atom, and has an excess positive charge (pentavalent) with the result that the migrating vacancy will have a greater probability for being trapped at it. Now, as mentioned above, the positrons will show a lower affinity for such a vacancy (bound to a higher valent impurity site). Thus, in contrast to pure zirconium, the Nb-bound vacancy in the alloy partially nullifies the charge imbalance and results in the depletion of the vacancy cause effect. With increasing temperature and up to 250°C, the steady decrease in the peak count rate merely signifies an increase in the concentration of such solute-decorated vacancies. The number of multiple defect aggregates is generally negligible in dilute alloys (Bosse *et al* 1986).

Concerning the rise in peak parameter above 250°C, it is likely to be due to the release of the solute-bound vacancies and their clustering effect. Moreover, these clusters become unstable and are eliminated on dissociation at about 325°C. Above this temperature the recovery spectrum follows the same pattern as for pure Zr. Thus the difference in behaviour is only with respect to the dip in the recovery curve (figure 1) at 250°C in Zr-0·5 Nb. This corresponds to the binding energy of impurity-vacancy complexes in the alloy. The detrapping mechanism suggested above 250°C is in conformity with the results on Zr-Sn system (Anand *et al* 1985). The temperature range of 500 K (for Zn-Sn) is also in fairly good agreement for the present alloy composition.

The present investigation shows that with the help of angular correlation measurements an explicit analysis of the processes occurring during the annealing of the point defects in metals is possible. Moreover, in the context of plastically defected metals the location of the recovery stages and their intensities essentially depend upon the degree of deformation and on the purity of the sample. Therefore in order to understand the detailed mechanism of recovery process, similar studies need to be extended to a series of other alloy systems as a function of cold-work parameter and also the solute parameters like its size, valency and concentration.

4. Conclusions

(i) Positron annihilation measurements have been utilized to monitor the isochronal recovery of Zr-0·5 Nb alloy specimens. Positron probe has a selective sensitivity towards vacancy-like defects and vacancy-agglomerates. These experiments thus greatly help in resolving the recovery process by identifying the participating defect species.

(ii) In contrast to the continuous recovery spectrum reported for α-Zr, a distinctively two-stage process was indicated in the presence of Nb impurity. The mobile vacancies above 50°C get trapped by the solute atoms and remain bound upto about 250°C. The solute-vacancy binding energy being the controlling factor for the release of free vacancies, which, with increasing temperature migrate and form clusters.

(iii) The dissociation of these vacancy clusters is activated by thermal stimulation above 325°C. These are subsequently absorbed at dislocation sinks. Finally the stages of recrystallization and grain growth take over.

Acknowledgements

The authors are thankful to Dr C K Gupta and Dr M K Asundi for their keen interest in the work and to Dr S K Sikka and Dr S M Sharma for extending the experimental facility. Thanks are also due to Dr B M Pande, Dr M S Anand, Dr G P Tiwari and Shri I S Batra for many useful discussions.

References

Anand M S, Mansel W, Wallner G and Weck W 1985 *Radiat. Eff.* **89** 179

Batra I S, Dedek U and Dwarschak F 1984 *Radiat. Eff.* **82** 295

Bosse H, Sager A, Luhr-Tanek W and Hehenkamp Th 1986 *J. Phys.* **F16** 1337

Brandt W and Dupasquier A 1983 *Positron solid state physics* (Amsterdam: North-Holland) p. 677

Brandt W and Paulin R 1977 *Phys. Rev.* **B15** 2511

Brummer O and Dlubek G 1985 *Progress in materials analysis* (eds) M Grasserbauer and W Wegscheider (New York: Springer-Verlag) Vol. 2 p. 187

Byrne J G 1980 *Scr. Metall.* **14** 3

Dlubek G, Brummer O, Meyendorf N, Hautojarvi P, Vehanen A and Yli-Kauppila J 1979 *J. Phys.* **F9** 1961

Doyama M 1984 *Trans. Indian Inst. Met.* **37** 170

Doyama M, Nanao S, Kuribayashi K and Tanigawa S 1973 *J. Phys.* **F3** L 125

Doyama M, Kuribayashi K, Nanao S and Tanigawa S 1974 *Appl. Phys.* **4** 153

Hautojarvi P 1979 *Positron in solids: Topics in current physics* (Heidelberg: Springer-Verlag) Vol. 12 p. 7

Hood G M, Eldrup M and Mogensen O E 1977 *Radiat. Eff.* **32** 11

Hood G M, Schiultz R J and Jackman J A 1984 *J. Nucl. Mater.* **126** 79

Krishnan R and Upadhyaya D D 1985 *Pramana-J. Phys.* **24** 351

Kubica P, McKee T A, Stewart A T and Stott M J 1975 *Phys. Rev.* **B11** 11

Pande B M, Anand M S and Agarwala R P 1972 *Phys. Status Solidi* **A10** K 137

Seeger A 1976 *Frontiers in materials science* (eds) L E Murr and C Stein (New York: Marcel Dekker) p. 177

Shirai Y, Nakata K, Narita N, Furukawa F and Takamura J 1979 *Proc. 5th Int. Conf. on Positron annihilation* (eds) R R Hasiguti and K Fujiwara (Sendai: Japan Inst. Metals) p. 209

Tanigawa S, Shinta I and Iriyama H 1982 *Proc. 6th Int. Conf. on Positron annihilation* (eds) P G Coleman, S C Sharma and L M Diana (Amsterdam: North-Holland) p. 401

Tiwari G P, Hoshino K, Iijima Y and Hirano K 1980 *Scr. Metall.* **14** 735

Tsuchiya Y and Tamaki S 1978 *J. Phys.* **F8** L 29

Upadhyaya D D 1985 *Studies on sintering kinetics, positron annihilation and thermoluminescence properties of nuclear oxide ceramics*, Ph. D. Thesis, Kumaun University.

Waber J T and Park Y 1986 *J. Mater. Sci. Lett.* **5** 163

West R N 1973 *Adv. Phys.* **22** 263

Bull. Mater. Sci., Vol. 9, No. 3, August 1987, pp. 241–247. © Printed in India.

A new formalism for representation of heat capacities of metals

J P HAJRA
Department of Metallurgy, Indian Institute of Science, Bangalore 560 012, India

MS received 1 April 1987; revised 10 June 1987

Abstract. The applicability of a function involving geometrical progression of temperature in interpreting the heat capacities of metals has been studied. The constants of the function have been described in terms of vibrational, electronic and magnetic contributions to heat capacities. The equation may be useful in representing heat capacity of metals.

Keywords. Vibrational constant; magnetic constant; electronic heat capacities.

1. Introduction

Various empirical mathematical equations are used for presentation of heat capacities of metals as a function of temperature. Although extrapolation of heat capacities with respect of temperature sometimes leads to difficulties, the equations are important in determining the thermodynamic properties of metals.

2. Formalisms consisting of two and three parameters

Heat capacities of solid metals and intermetallic compounds at elevated temperature are frequently expressed by a linear form of function

$$C_p = A + BT, \tag{1}$$

where A and B are constants and evaluated by least mean squares regressional analysis of the experimental values over a specified range of temperature. The choice of an equation depends on the temperature range and the way in which the slope of the C_p curve varies. Sometimes, heat capacity shows pronounced curvature at low temperature and becomes linear at high temperature. In such cases, a three-parameter form of equation,

$$C_p = A' + B'T + C'T^{-2} \tag{2}$$

is generally preferred as proposed by Kelley (1960). The equations are purely empirical in nature and limited to a range of temperature of the data from which they have been derived. Apart from (1) and (2), an additional term of the form $d'T^2$ or $dT^{1/2}$ has also been incorporated by Kubaschawski *et al* (1979) in deriving heat capacities of various metals and inorganic substances. Battezzati and Garrone (1984) recently observed that the ΔC_p between the undercooled melt and solid equilibrium phases of metallic glass forming alloys decreases with increase in temperature. The variation of the C_p data as a function of temperature is considered by them to be either linear or intermediate between linear and hyperbolic. The hyperbolic type of representation is denoted by

$$C_p = x + y/T, \tag{3}$$

where x and y are constants.

2.1 *The present equation*

The dependence of heat capacity on temperature is usually expressible in the form of polynominals, as already mentioned, and the corresponding coefficients which are important in describing the behaviour as a function of temperature. The present study investigates the form of function

$$C_p = a/(1+bT), \tag{4}$$

where a and b are constants and are to be evaluated for a particular system under consideration.

3. Results and discussion

The applicability of the equation has been studied carefully choosing the selected C_p values of several metals from Hultgren *et al* (1973). For comparison, the constants involved in (1), (2) and (3) have also been evaluated using least means squares regressional analysis of the experimental values computed by Hultgren *et al* (1973). The evaluated constants for (1), (2), (3) and (4) are computed in table 1 along with their respective standard deviations. The magnitude of the standard deviations for metals, such as Ag, Au, βCo, Cu, Ni, Zn and Cr at the stated temperature range, show that the data derived by the present equation are in good agreement with those of the experimental values of Hultgren *et al* (1973). The hyperbolic function shows consistently higher standard deviations for all the metals than those derived by (1), (2) and (4). Although comparable deviations from experimental values have been registered by (1), (2) and (4) for α, Co and Pt, the present equation exhibits somewhat higher values for α Mn than those derived by (1) and (2). The deviations, however, are generally considered to lie within the range of experimental error. Figure 1 presents the comparison of C_p values for some of the metals which are derived by (1), (2) and (4) and the experimental data reported by Hultgren *et al* (1973).

4. Physical interpretation and form of the present equation

The constants a and b of the expanded form of the present equation may be interpreted by considering the vibrational, electronic and magnetic contributions to heat capacity. Equation (4) may be expanded in power series of T as

$$C_p = a/(1+bT) = a(1-bT) \tag{5}$$

The empirical approach by Weiss and Tauer (1956) and Hofmann *et al* (1956) is to split up the experimental specific heat data in additive vibrational, electronic and magnetic contributions. The vibrational contribution to the specific heat is calculated from Debye model as described by Kittel (1976) as

$$C_v = 9R(1/x)^3 \int_0^x \frac{x^4 . e^x}{(e^x-1)^2}\,dx, \tag{6}$$

where $x = \theta/T$ and θ is the Debye temperature. A good description of C_v can be obtained if θ is known accurately. The Debye temperature θ, has however been

Table 1. Least mean squares regressional values of the constants involved in (1), (2), (3) and (4) and the standard deviations.

Metals and temp. range (K)	A, $\{A\}$ $[X]$(a)(J mol^{-1} deg^{-1})		$B \times 10^3$, $[Y] \times 10$,	$\{B\} \times 10^3$ $(b) \times 10^4$	$\{C'\} \times 10^{-5}$ (J mol^{-1} deg)	Standard deviation, (J mol^{-1} deg^{-1}) for equation			
						(1)	(2)	(3)	(4)
Ag	22·9712,	21·852	6·8945	7·9211	1·1066	0·2230	0·0846	1·044	0·0826
298·15–1200	31·829,	23·6872	−2·2974,	−2·0552					
Au	21·3499,	21·3499	7·5727,	7·5727	1·748	0·4666	0·4666	1·268	0·399
298·15–1300	31·2024	23·7083	−2·147,	−1·8326					
β Co	12·4127	−3·725	25·1037,	36·485	43·4198	0·5892	0·187	1·394	0·05
700–1200	58·573,	21·6776	−20·494	−4·145					
Cu	22·2544,	21·4853	6·8911,	7·5539	0·8155	0·4271	0·42195	1·1998	0·2281
298·15–1300	31·6067,	23·0742	−2·51137,	−2·0478					
Ni	14·8068	1·6581	34·5031,	52·8163	8·1215	1·11954	0·9088	1·8041	0·7736
298·15–631	46·233,	20·3778	−6·6148,	−7·0723					
Zn	22·0969,	20·7349	10·6609	12·5112	0·835	0·1291	0·0421	0·5887	0·041
298·15–692·73	31·9918	22·8971	−2·0904,	−3·2538					
α Co	20·2809,	21·5299	15·5506,	13·8629	0·7727	0·1292	0·0665	0·588	0·191
298·15–700	34·969,	21·8342	−3·1598,	−4·3380					
Cr	18·7293,	17·6574	14·5825,	15·2659	1·5923	0·71107	0·6632	4·041	0·6016
298·15–1900	44·453,	23·0204	−8·0296,	−2·8151					
Pt	24·3443	24·373	5·263,	5·2458	−0·04385	0·0998	0·1027	1·415	0·192
298·15–2000	34·122,	25·1709	−3·174,	−1·4567					
αMn	22·0455,	24·4097	15·8271,	13·3212	−0·9264	0·3934	0·1995	1·0331	0·515
298·15–980	40·605	24·183	−46·419,	−3·7300					

Note: The first set of constants of equations (1), (2), (3) and (4) are represented by A, $\{A'\}$, $[x]$ and (a) respectively. The dimensions for the second set of constants: BJ mol^{-1} deg^{-2} $\{B'\}$ J mol^{-1} deg^{-2} and $[y]$ J mol^{-1}.

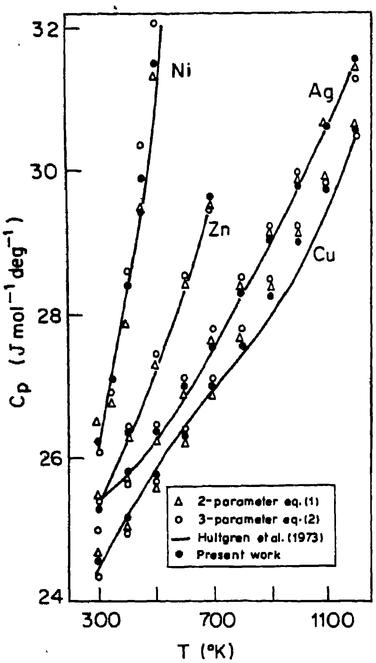

Figure 1. Comparison of heat capacities of metals between the experimental values and those derived from the models.

shown by Desorbo (1954) to vary with experimental temperature for many metals due to lattice irregularities and crystal structure. The variation of θ with temperature has further been found by Desorbo (1954) to be significant between 0 and 20 K and almost linear with slight positive slope in the neighbourhood of 100 K. Because of this variation and in the absence of any other experimental data, θ for various metals has been selected as shown in table 2. To calculate C_v, the temperature is assumed to be 298·15 K, as the C_p data for various metals are quoted from that temperature. Table 2 shows that a reasonable agreement exists between the Debye values at 298·15 K and a values of the present equation. The latter values are considered to be closer to the Debye values than those derived by (1), (2) and (3).

The correction due to lattice dilation, $(C_p - C_v)$ is small compared to C_v and the following empirical equation as suggested by Kaufman *et al* (1963) is used as an approximation over the entire range of temperature as

$$C_d = 10^{-4}\, C_v T. \tag{7}$$

Table 2. Comparison between a values of (4) and Debye heat capacities Cv at 298·15 K.

Metals	Ag	Au	Co(α)	Cu	Ni	Zn	Cr	Pt	Mn
Debye temp. θ, (K)	225	164	445	339	456	310	402	229	450
Cv 298·15 K ($\mathrm{J\,mol^{-1}\,deg^{-1}}$)	24·26	24·57	22·32	23·38	22·13	23·63	22·698	24·195	21·2
a equation (4) ($\mathrm{J\,mol^{-1}\,deg^{-1}}$)	23·687	23·708	21·834	23·074	20·377	22·89	23·02	25·17	24·18

Table 3. Comparison between *ab* values of (5) with the lattice dilation and electronic specific heat values of metals.

Metals	$(\gamma_e + C_v) \times 10^4$, (J mol^{-1} deg^{-2})	$ab \times 10^4$, (J mol^{-1} deg^{-2})
Ag	30·53	48·68
Au	31·85	43·44
Co (α)	69·77	94·71
Cu	30·33	47·25
Ni	92·42	144·11
Cr	38·6	64·80
Pt	90·42	36·6
Mn	147·7	90·20

The other coefficient of T from theoretical consideration is the electronic specific heat, γ_e, and expressed from the free electron model (6) as described by Hofmann *et al* (1956) as

$$C_e = \gamma_e T. \tag{8}$$

The latter values for various metals are obtained from Hultgren *et al* (1973). The coefficients of T, $(10^{-4}\, C_v + \gamma_e)$ from (7) and (8) are compared with *ab* terms of the expanded function (5) in table 3. The two sets of data compare favourably despite various uncertainties. Since low temperature electronic heat values are used, uncertainties lie the way they may vary with temperature. Although the .C_v values have been calculated from Debye function (equation (6)) at 298·15 K to be used in (7), the overall lattice dilation values will not change significantly with increase in temperature relative to 298·15 K. Table 3 also shows that the *ab* values of the present equation for various metals are closer to the $(10^{-4}\, C_v + \gamma_e)$ values than the

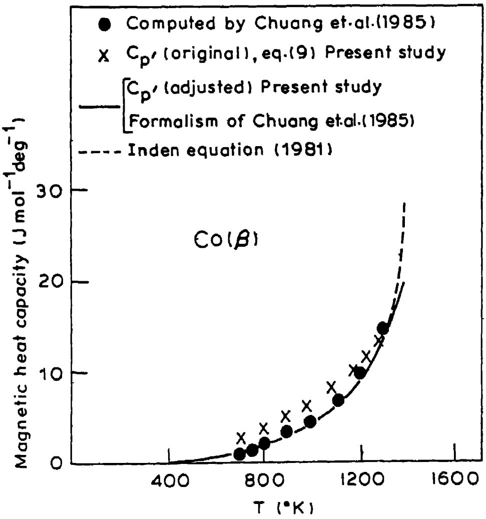

Figure 2. Magnetic specific heat for β cobalt. Comparison between the derived values and those from the experiment.

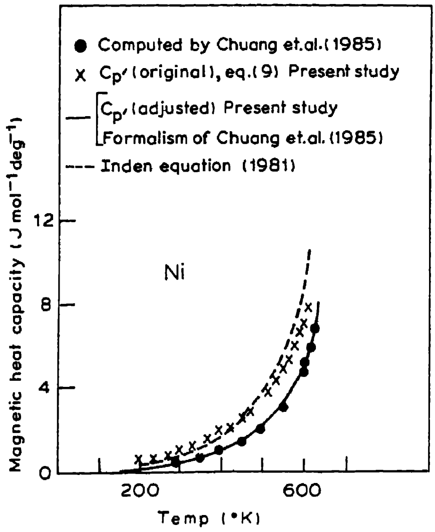

Figure 3. Magnetic specific heat for nickel. Comparison between the derived values and those from the experiment.

corresponding coefficients of T of (1) and (2). The rest of the present function may be expressed as

$$C'_p = [a/(1+bT)] - a(1-bT) = ab^2T^2/(1+bT). \tag{9}$$

The applicability of the equation has been studied carefully choosing the selected values of the magnetic specific heats of Co (β) and Ni computed by Chuang *et al* (1985) below the curie temperature. The equation records somewhat higher values than the experimental data as shown in figures 2 and 3. The figures show that the magnetic contribution to heat capacity cannot be calculated directly by using (9). This is considered to be due to the increased vibrational effects which is difficult to separate from the magnetic contributions. It may be noted that at 298·15 K, the Debye values of various metals do not exceed the value of $3R$ which corresponds to the maximum frequency of vibration of atoms v_m. Since C_v increases with increase in temperature, the coefficients of higher powers of T of the expanded function (5) are expected to be associated with atomic vibration. To study the suitability of the function (9), regressional analysis of the magnetic heat capacities of Co (β) and Ni has been carried out. The least mean squares regressional values of a and b along with the standard deviations are computed as follows:

	a (J mol^{-1} deg^{-1})	$b \times 10^4$	Standard deviation (J mol^{-1} deg^{-1})
Co (β)	3·968	−6·35	0·035
Ni	1·6883	−13·33	0·024

The adjusted C_p (magnetic) values as derived by (9) are in good agreement with those of the experimental values as shown in figures 2 and 3. Since the equation with different sets of constants interprets the magnetic properties of the metals, the form of the function is considered to be adequate below the curie temperature. The magnetic transition, however, is described by Belov (1961) as a second-order transformation and C_p at curie temperature being a discontinuous function the present equation cannot be extrapolated beyond the curie temperature. It may be mentioned that the regressional analysis of the experimental C_p data for Co (β) and Ni has been carried out as reported in table 1, in the temperature range of 700 to 1200 K and 298·15 K to 631 K respectively. The applicability of the present equation is, therefore, restricted to the temperature range where the data have been fitted. Empirical mathematical equations consisting of adjustable parameters have been proposed by Chuang *et al* (1985) and Inden (1981) for the magnetic contribution to the specific heats of pure metals. The derived values from the formalisms are also shown in figures 2 and 3 for Co (β) and Ni respectively; the values are found to coincide with the adjusted C_p (magnetic) values from (9).

Table 1 further indicates that the present equation records lower values of standard deviations than those derived by the conventional two- and three-parameter equations. Since the applicability of the equation spans over a fairly wide temperature range, the equation is considered to be useful in interpolation of heat capacity values and evaluation of various thermodynamic functions of the metals.

5. Conclusions

The present equation offers an alternative expression to two- and three-parameter functions for representation of heat capacities of metals. The constants of the equation are susceptible to physical interpretation based on vibrational, electronic and magnetic contributions to heat capacity.

References

Battezzati L and Garrone E 1984 *Z. Metallkd.* **75** 305

Belov K P 1961 *Magnetic transitions* (New York: Consultants Bureau) p. 1

Chuang Y Y, Schmid R and Chang Y A 1985 *Metall. Trans.* **16** 153

Desorbo W 1954 *Acta Metall.* **2** 274

Hofmann J A, Paskin A, Tauer K J and Weiss R J 1956 *J. Phys. Chem. Solids* **1** 45

Hultgren R, Desai P D, Hawkins D T, Gleiser M, Kelly K K and Wagman D P 1973 *Selected values of the thermodynamic properties of the elements* (Ohio: ASM)

Inden G 1981 *Physica* **B103** 82

Kaufman L, Clougherty E V and Weiss R J 1963 *Acta Metall.* **11** 323

Kelly K K 1960 *Contribution to the data on theoretical metallurgy* U. S. Bur. Mines Bull. p. 584

Kittel C 1976 *Introduction to solid state physics* (New York: John Wiley) 5th ed.

Kubaschewski O and Alcock C B 1979 *Metal thermochem* (Oxford: Pergamon Press) 5th ed.

Weiss R J and Tauer K J 1956 *Phys. Rev.* **102** 1490

Bull. Mater. Sci., Vol. 9, No. 4, November 1987, pp. 249–253. © Printed in India.

Pyroelectric properties of lead-barium titanate and lead-strontium titanate

V M JAMADAR, T A PATIL* and S H CHAVAN**
Department of Physics, Dattajirao Kadam Mahavidyalay, Ichalkaranji 416 115, India
*Vivekanand College, Kolhapur 416 002, India
**Department of Physics, Shivaji University, Kolhapur 416 004, India

MS received 1 June 1987; revised 21 August 1987

Abstract. Pyroelectric properties of poled solid solutions of lead-barium titanate and lead-strontium titanate have been investigated in the temperature range covering their transition points. The values of pyroelectric current and coefficients of $(Pb_x-Ba_{1-x})TiO_3$ and $(Pb_x-Sr_{1-x})TiO_3 (x = 0{\cdot}8-0{\cdot}5)$ show a sharp peak at the Curie temperature. It is observed that these values change with Ba or Sr concentration in the respective solid solutions.

Keywords. Titanate solid solutions; pyroelectric behaviour; phase transition.

1. Introduction

The primary pyroelectricity is defined as the change of polarization of a dielectric with the temperature after eliminating polarization effects produced by thermal strains which accompany the temperature changes according to the terminology introduced by Cady (1946). There is, in general, some contribution to the polarization change with temperature due to the thermal expansion or contraction of the dielectric. Pearls *et al* (1958) and Tawfik (1969) have reported that the secondary effect in $BaTiO_3$ is small. Primary pyroelectricity in ferroelectric ceramics can arise from two factors: (i) the primary effect of aligned domains and (ii) switching of domains by 180°.

The pyroelectric effect in barium titanate ceramic was studied by Lang *et al* (1969). A dynamic method has been devised by Chynoweth (1956) to measure pyroelectric effect in barium titanate. Temperature dependence of pyroelectric current in potassium nitrate has been studied by Sawada *et al* (1961). The pyroelectric current measurements and effects of poling and of light illumination upon pyroelectric current in SbSI were found by Imai *et al* (1966). A direct method for measuring the pyroelectric coefficients and application to a nsec response time detector $(Sr_x-Ba_{1-x})Nb_2O_6$ was described by Byer and Roundy (1972). Pyroelectric properties were studied by Vasileva (1977) in triglycine sulphate and by Tawfik (1974) in the polarized specimen of sodium acetylacetonate. Dielectric and pyroelectric properties of triglycine sulphate polystyrene composite were studied by Mansingh and Sreenivas (1983). Similar properties were studied by Mathur *et al* (1981) in TGS, TGFS etc and by Yuhan (1984) in ferroelectric single crystal series $(K_x-Na_{1-x})_{0{\cdot}4}(Sr_y-Ba_{1-y})_{0{\cdot}8}Nb_2O_6$. Pyroelectric materials have also been reviewed recently by Srinivasan (1984).

The present investigation aims to report the variation of pyroelectric current and coefficients with temperature in the poled solid solutions of $(Pb_x-Ba_{1-x})TiO_3$ and

---

**Address for communication

$(Pb_x-Sr_{1-x})TiO_3$. These solid solutions, being ferroelectric materials, exhibit interesting pyroelectric properties and have practical applications as pyroelectric detectors which are of special interest.

2. Experimental

Lead titanate ceramics were prepared from a mixture of lead carbonate and titanium dioxide with 1:1 molar proportions and heated in platinum crucible in globar furnace upto 1200°C for 4 hr by the method reported by Sawada *et al* (1950). Similarly $BaTiO_3$ and $SrTiO_3$ ceramics were prepared.

Solid solutions $(Pb_x-Ba_{1-x})TiO_3$ were prepared from a mixture of $PbTiO_3$ and $BaTiO_3$ having molar proportions of $(x=0{\cdot}8-0{\cdot}5)$ and heated in globar furnace at 1200°C for 4 hr in a platinum crucible. The solid solutions $(Pb_x-Sr_{1-x})TiO_3$ $(x=0{\cdot}8-0{\cdot}5)$ were similarly prepared.

The X-ray powder diffractions of our samples confirm that homogeneous solid solutions have been formed. The pellets of these solid solutions having thickness of about 1 mm and diameter 1 cm were prepared under a pressure of 5 tonnes by using a hydraulic machine. The test samples were made by sintering these pellets at 750°C. The two end-faces of these test samples were made conducting by applying silver paint and were placed in the sample holder fabricated in our laboratory.

The experimental set-up consists of a furnace, electronically regulated power supply to provide d.c. electric field, a digital d.c. micro-voltmeter (VMV 15), a pico-ammeter adaptor for VMV 15 and a digital multimeter. The test sample was polarized for 10 min at room temperature by a constant d.c. electric field of 1 kV/cm. To eliminate the current due to the space charge, the test sample electrodes were short-circuited for 30 min before the pyroelectric measurements. This poled sample was slowly heated in a furnace and the pyroelectric current was measured with a digital d.c. micro-voltmeter (VMV 15) connected to the pico-ammeter adaptor at various temperatures and the corresponding time was also noted for calculating the rate of heating. The heating rate was determined from the graph of temperature against time and was found to be nearly 3°C/min. The pyroelectric coefficients were calculated by the direct method suggested by Byer and Roundy (1972) and Mansingh *et al* (1983), which is more straightforward than the dynamic method.

3. Results and discussion

The results of the measurements of the pyroelectric current and coefficients in solid solutions of $(Pb_x-Ba_{1-x})TiO_3$ and $(Pb_x-Sr_{1-x})TiO_3$ obey the equation given by Chynoweth (1956)

$$i=A[(\mathrm{d}P_s/\mathrm{d}T)(\mathrm{d}T/\mathrm{d}t)], \tag{1}$$

where i is the pyroelectric current, P_s the spontaneous polarization, $(\mathrm{d}T/\mathrm{d}t)$ the rate of heating, A the area of the ceramic material and $(\mathrm{d}P_s/\mathrm{d}T)$ the pyroelectric coefficient.

The pyroelectric current response for ferroelectric solid solutions of $(Pb_x-Ba_{1-x})TiO_3$ and $(Pb_x-Sr_{1-x})TiO_3$ on heating at the rate ~3°C/min are shown in figures 1 and 2. The pyroelectric current produced in solid solutions

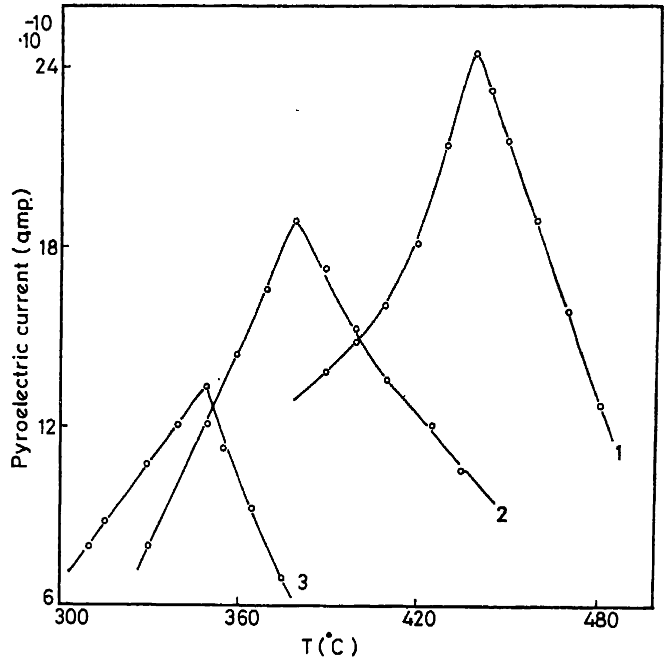

Figure 1. Temperature dependence of the pyroelectric current in poled sample 1. $(Pb_{0·8}-Ba_{0·2})TiO_3$, 2. $(Pb_{0·6}-Ba_{0·4})TiO_3$ and $(Pb_{0·5}-Ba_{0·5})TiO_3$.

(figures 1 and 2) arose as a consequence of the change in polarization of a ceramic when it underwent a variation in its temperature.

From figures 1 and 2 it is clear that the pyroelectric current shows a peak at 440, 380 and 350°C for different molar proportions of $(Pb_x-Ba_{1-x})TiO_3$ and at 340, 200 and 125°C for different molar proportions of $(Pb_x-Ba_{1-x})TiO_3$. The above temperatures indicate Curie temperatures of the respective solid solutions which are consistent with the Curie temperatures determined by the hysteresis loop method and the dielectric constant measurements. These solid solutions belong to the polar class below their Curie temperatures while above they are non-polar.

Table 1 summarizes the observations on the pyroelectric current and pyroelectric coefficients at the Curie temperatures of the solid solutions.

Table 1 reveals that the pyroelectric current and the coefficients increase as the proportion of $PbTiO_3$ increases in the respective solid solutions of $(Pb_x-Ba_{1-x})TiO_3$ and $(Pb_x-Sr_{1-x})TiO_3$.

4. Conclusions

It seems that 440, 380 and 350°C are the Curie temperatures for molar proportions of $(Pb_x-Ba_{1-x})TiO_3$ with ($x=0·8$, 0·6 and 0·5) and for different molar proportions of $(Pb_x-Sr_{1-x})TiO_3$; 340, 200 and 125°C are the Curie temperatures. Pyroelectric current and coefficients increase with the proportion of $PbTiO_3$ in solid solution.

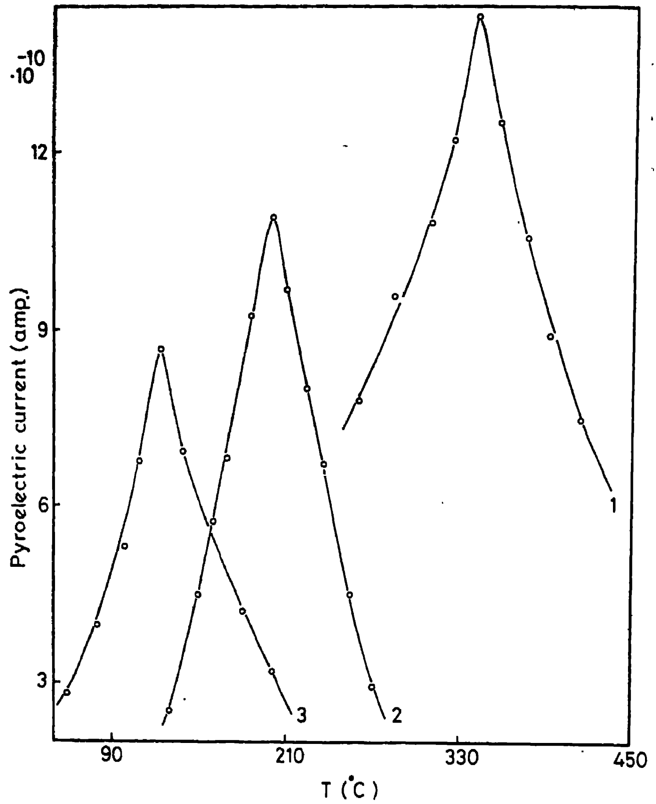

Figure 2. Temperature dependence of the pyroelectric current in poled sample 1. $(Pb_{0\cdot8}-Sr_{0\cdot2})TiO_3$, 2. $(Pb_{0\cdot6}-Sr_{0\cdot4})TiO_3$, and 3. $(Pb_{0\cdot5}-Sr_{0\cdot5})TiO_3$.

Table 1. Values of various parameters for different $PbTiO_3$, $BaTiO_3$ and $SrTiO_3$ solid solutions.

Substance	Pyroelectric current 10^{-10}A/cm^2	Pyroelectric coefficient 10^{-9}C/cm^2/°C	Curie temp. (°C)
$(Pb_{0\cdot8}-Ba_{0\cdot2})TiO_3$	24·3	58·3	440
$(Pb_{0\cdot6}-Ba_{0\cdot4})TiO_3$	18·8	28·2	380
$(Pb_{0\cdot5}-Ba_{0\cdot5})TiO_3$	13·3	24·0	350
$(Pb_{0\cdot8}-Sr_{0\cdot2})TiO_3$	14·2	37·0	340
$(Pb_{0\cdot6}-Sr_{0\cdot4})TiO_3$	10·8	19·5	200
$(Pb_{0\cdot5}-Sr_{0\cdot5})TiO_3$	8·6	17·9	125

References

Byer R L and Roundy C B 1972 *Ferroelectrics* **3** 333
Cady W G 1946 *Piezoelectricity* (New York: McGraw-Hill)
Chynoweth A G 1956 *J. Appl. Phys.* **27** 78
Imai K, Kawada S and Ida M 1966 *J. Phys. Soc. Jpn* **21** 1855
Lang S B, Rice L H and Shaw S A 1969 *J. Appl. Phys.* **40** 4335

Mansingh A and Sreenivas K 1983 *Ferroelectr. Lett. Sec.* **1** 67
Mathur S C, Baira A Y and Singh H 1981 *Ferroelectrics* **39** 1197
Pearls T A, Diesel T J and Dobrov W I 1958 *Appl. Phys.* **29** 1297
Sawada S and Nomura S 1950 *Rep. Inst. Sci. Tech. Tokyo Univ.* **4** 217
Sawada S, Nomura S and Asao Y 1961 *J. Phys. Soc. Jpn.* **16** 2486
Srinivasan M R 1984 *Bull. Mater. Sci.* **6** 317
Tawfik A 1969 M.Sc. Thesis, Physics Department, Faculty of Science, Cairo University
Tawfik A 1974 *Indian J. Phys.* **48** 294
Vasileva L D 1977 *Vestn Kiev Politekhn. In. Ta Ser Radio electron* **14** 18
Yuhan Xu 1984 *Ferroelectr. Lett. Sec.* **2** 189

Bull. Mater. Sci., Vol. 9, No. 4, November 1987, pp. 255–262. © Printed in India.

Dielectric behaviour of glasses and glass ceramics in the system BaO-PbO-TiO_2-B_2O_3-SiO_2

R K MANDAL, Ch. DURGA PRASAD, OM PARKASH and DEVENDRA KUMAR*
School of Materials Science and Technology, *Department of Ceramic Engineering, Institute of Technology, Banaras Hindu University, Varanasi 221 005, India

MS received 15 June 1987; revised 3 September 1987

Abstract. Glasses with varying molar ratios of PbO/BaO in the system BaO-PbO-TiO_2-B_2O_3-SiO_2 were prepared keeping $(BaO+PbO)/TiO_2$ ratio equal to one. The glasses were ceramized by two-stage heat treatment. X-ray diffraction indicates that $PbTiO_3$ crystallizes in lead-rich glasses while $BaTiO_3$ precipitates in barium-rich compositions. Solid solution $(Ba, Pb)TiO_3$ does not seem to crystallize over the entire range of compositions. Simultaneous presence of PbO and BaO in the initial glass composition reduces the yield of ferroelectric phase. Dielectric properties have been interpreted in terms of microstructural features.

Keywords. Glass ceramics; ferroelectric; dielectric constant.

1. Introduction

Glass ceramic processing provides an efficient way of producing uniform fine grains of a crystalline phase in a pore-free glassy matrix (McMillan 1979). These microstructural features, being highly desirable in ferroelectric ceramics, attracted the attention of many workers in the sixties to study ferroelectric glass ceramics (Bergeron 1961; Herczog 1964; Grossman and Isard 1969a). The amount of ferroelectric phase and its microstructure can be precisely controlled by choosing a suitable initial glass composition and a heat treatment schedule. Since ferroelectric ceramics possess useful properties in the solid solution form, efforts were made to precipitate the ferroelectric phase in the solid solution form in the glass ceramics. Herczog (1964) attempted to replace Ba in $BaTiO_3$ by various ions such as Ca^{2+}, Sr^{2+} and Pb^{2+} etc by incorporating oxides of these ions in the initial glass composition. It was reported that only a limited amount of substitution was possible and the effects of such substitutions were similar to that in the polycrystalline materials. However, a recent publication by Herczog (1984) indicates that the substitution of Ba by Sr or of Ti by Zr is ineffective in modifying the properties as they crystallize in a different phase. Various glass ceramics containing ferroelectric phases have been reviewed recently by Om Parkash *et al* (1986b).

Grossman and Isard (1969b) reported the formation of $PbTiO_3$ during ceramization of glass in the system PbO-BaO-TiO_2-B_2O_3 using X-ray diffraction (XRD). Lynch and Shelby (1984) studied the same compositions as studied by Grossman and Isard (1969a, b) and confirmed the precipitation of $PbTiO_3$ using dilatometry. Om Parkash *et al* (1986a) studied the ceramization of a glass composition 21 BaO-21 PbO-42 TiO_2-10 B_2O_3-6 SiO_2 (mole %) and confirmed the formation of $BaTiO_3$ on heat treatment. As is clear from this glass composition, an adequate amount of TiO_2 was used to react with both BaO and PbO while glass compositions studied by earlier workers did not contain requisite amount of TiO_2 i.e. the $(BaO+PbO)/TiO_2$

ratio was < 1. This led us to the conjecture that ferroelectric phase crystallizing out during heat treatment depends on the (BaO + PbO)/TiO_2 and BaO/PbO molar ratios. In this paper we report the dielectric behaviour of glasses and glass ceramics in the system BaO-PbO-TiO_2-B_2O_3-SiO_2 where the (BaO + PbO)/TiO_2 ratio is kept equal to one while the BaO/PbO ratio is varied.

2. Experimental

Glasses were prepared using AR grade PbO, $BaCO_3$, TiO_2, SiO_2 and H_3BO_3. Batches weighing 25 g were mixed in an agate mortar using acetone. The dry powders were transferred to high alumina crucibles. The crucibles were heated to a temperature in the range 1350–1550 K depending on the composition to melt the mass. The molten mass was held at this temperature for about half an hour with intermittent stirring to homogenize the melt. The melt was quenched by pouring into an aluminium mould and pressing with a thick aluminium plate. The transparent glass discs were quickly transferred to another pre-heated furnace maintained at 500–600 K for annealing. The annealed samples were furnace-cooled after half an hour. The compositions of various glasses are given in table 1.

The amorphisity of glasses was confirmed by X-ray diffraction. The samples were given two-stage heat treatment based on DTA studies and earlier results (Om Parkash *et al* 1986a). The two stages correspond to the nucleation and growth of ferroelectric crystalline phase. All the glass samples were heated at 860 K for 30 min (nucleation stage) and 960 K for 3 hr (growth stage).

X-ray diffraction patterns were recorded using an X-ray diffractometer (JEOL) using Cu–K_α radiation. For microstructural studies, samples were polished, ground and etched using 10% boiling HCl. Surface was coated with Au–Pd alloy and the microstructures were observed using a scanning electron microscope (Philips PSEM 500). For dielectric measurements, samples were ground to a thickness of 0·5–1·0 mm and air-dried silver paint was applied on both the faces. Dielectric measurements were made using an impedance analyzer (HP 4192A LF) as a function of temperature and frequency in the temperature range 300–760 K. Temperature was stabilized within ± 1°C before each measurement.

3. Results and discussion

Plots of dielectric constant, ε, and $\tan\delta$ at 1 kHz, 10 kHz and 100 kHz as a function of temperature for glass sample no. 2 are shown in figure 1. All the glasses listed in

Table 1. Composition of various glasses.

Glass No.	Composition (mol %)				
	PbO	BaO	TiO_2	B_2O_3	SiO_2
1	42	0	42	10	6
2	31·5	10·5	42	10	6
3	10·5	31·5	42	16	0
4	10·5	31·5	42	13	3
5	10·5	31·5	42	10	6
6	0	42	42	10	6

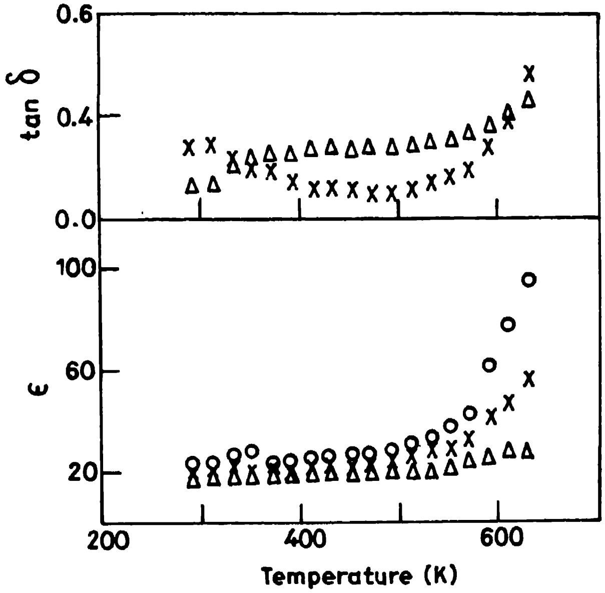

Figure 1. Variation of dielectric constant (ε) and dielectric loss (tan δ) with temperature of glass no. 2 at 1 kHz (O), 10 kHz (×) and 100 kHz (Δ)

table 1 have a value of dielectric constant in the range 15–25 at 300 K and 1 kHz. These values agree with the results reported earlier (Skanavi and Kashtanova 1957). Values of dielectric constant change very little up to a particular temperature, T_a, above which they increase very sharply. Lead-rich glasses (1 and 2) show this rapid increase at lower temperature as compared to barium-rich glasses (3 to 6). Values of tan δ are in the range 0·10–0·20 for these glasses which seem to be high in alkali-free glasses. But this may be attributed to space charge polarization. Variation of tan δ with temperature is similar to that of ε. Both ε and tan δ show little frequency dispersion below T_a which become quite pronounced above it.

Figures 2 and 3 show the variation of dielectric constant, ε and tan δ with temperature at 1 kHz, 10 kHz and 100 kHz of glass ceramics 2C and 3C respectively. It is interesting to note that the dielectric constant of glass ceramics 1C and 2C (figure 2) is not much higher than that of the parent glasses while barium-rich compositions show significant enhancement of dielectric constant over the parent glasses (figure 3). This can be understood in terms of different crystalline phases which develop during ceramization. Lead-rich compositions contain $PbTiO_3$ and Ba-rich compositions contain $BaTiO_3$ crystalline phase. This is supported by the X-ray diffraction data of these samples. Due to the higher dielectric constant of $BaTiO_3$, Ba-rich compositions show higher values of ε. Variation of ε with temperature is similar to the parent glasses i.e. ε changes very little with temperature below a particular temperature and thereafter rises very rapidly. A similar trend is observed in tan δ vs T plots.

Variation of ε with frequency at a few selected temperatures is shown in figure 4 for glass ceramic nos. 2C and 5C respectively. Stronger dispersion is observed in the range 1 kHz–100 kHz beyond which ε seems to level off with frequency in these as

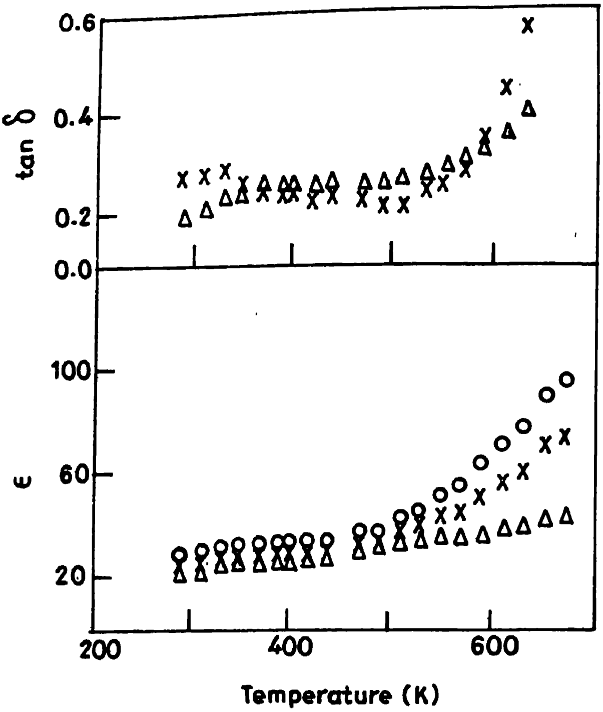

Figure 2. Variation of dielectric constant (ε) and dielectric loss (tan δ) with temperature of glass ceramic 2C at 1 kHz (○), 10 kHz (×) and 100 kHz (△)

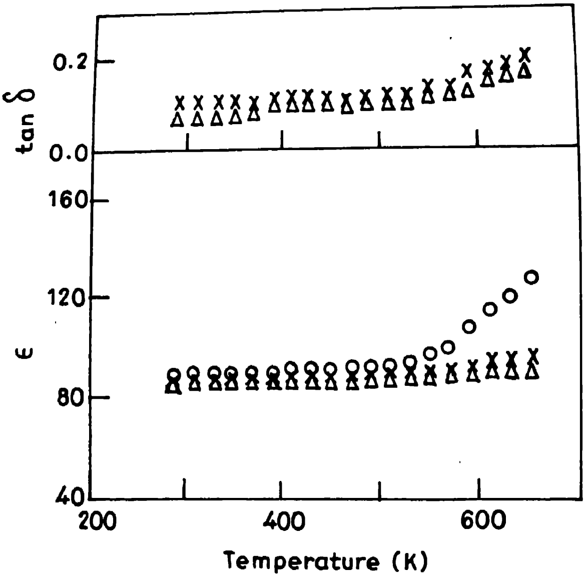

Figure 3. Variation of dielectric constant (ε) and dielectric loss (tan δ) with temperature of glass ceramic 3C at 1 kHz (○), 10 kHz (×) and 100 kHz (△).

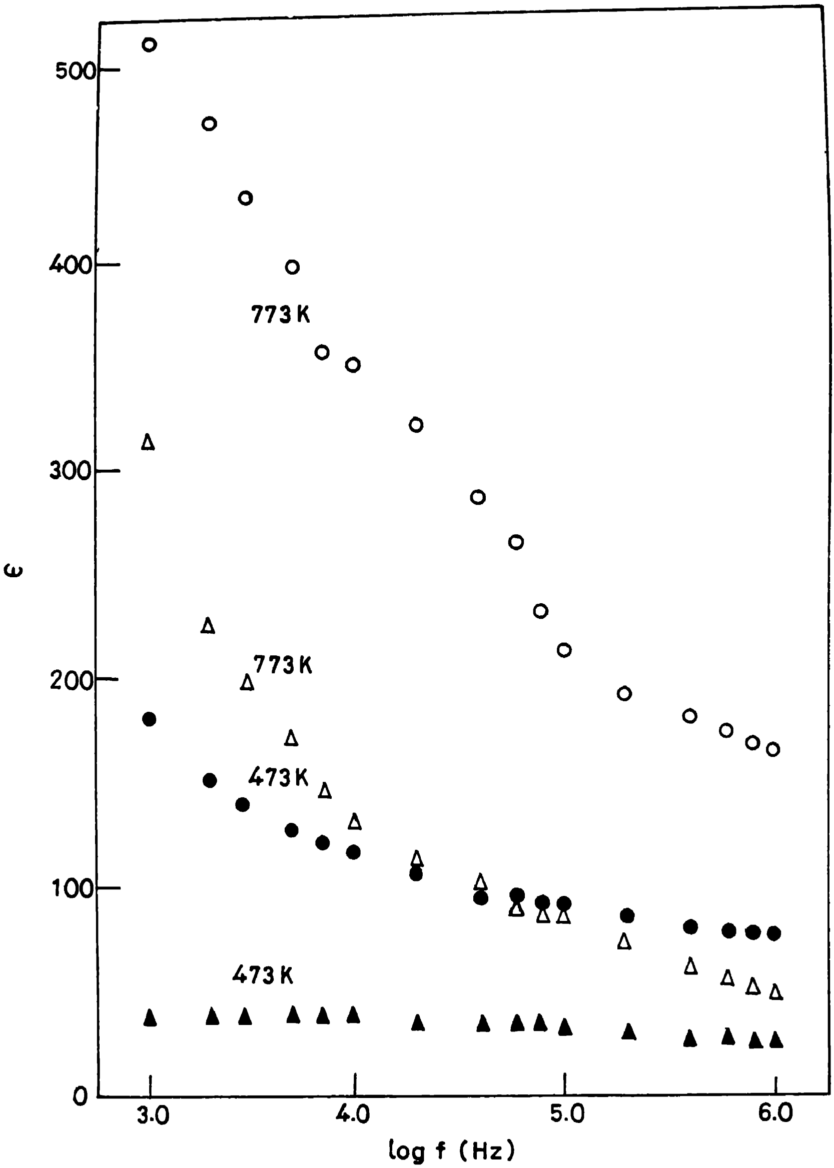

Figure 4. Variation of dielectric constant (ε) with frequency at few selected temperatures of glass ceramics 2C (▲,△) and 5C (●, ○)

well as in other compositions. The frequency dependence becomes stronger with increasing temperature. Strong dispersion in the 1 kHz–100 kHz range indicates contribution of space charge and orientational polarization to the observed dielectric constant.

Figures 5(a) and 5(b) show the scanning electron micrographs of the glass ceramic samples 2C and 5C respectively. Particle size is in the range (0·8–10 μm) for sample 2C and (0·8–6 μm) for sample 5C. Distribution of particles is uniform in 5C as

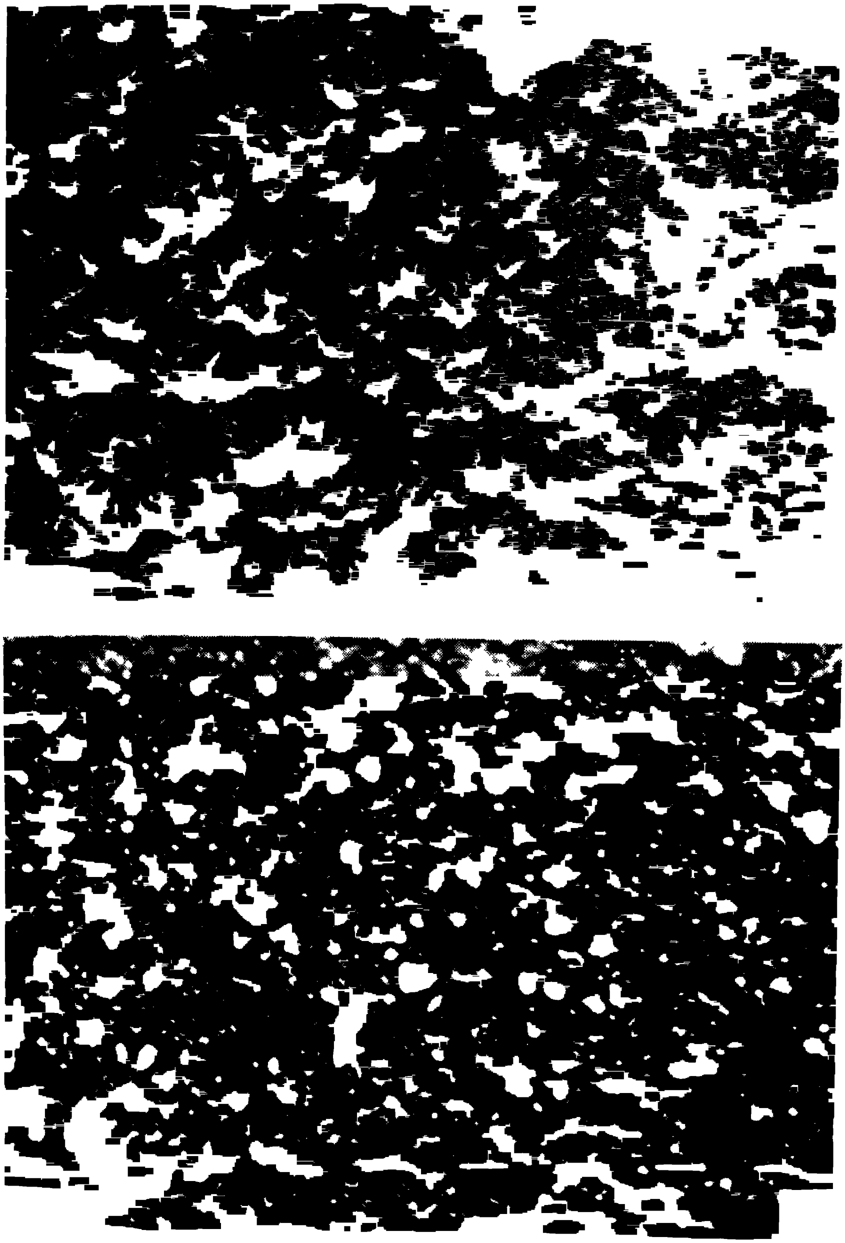

Figure 5. Scanning electron micrograph of glass ceramic. a. 2C b. 5C

compared to 2C. Volume fraction of ferroelectric crystalline phase is smaller in 2C compared to 5C.

The observed dielectric behaviour of various glass ceramics can be understood on the basis of their microstructure. Those samples with uniform distribution of fine particles show very little variation in the dielectric constant upto quite high temperatures whereas samples with very non-uniform distribution of irregular size particles show significant variation of ε. The absence of peak in ε vs T plots is due to the clamping of fine crystallites in rigid glassy matrix (Lynch and Shelby 1984). Samples with a few large crystallites, 3C and 4C do show small anomalies around 400 K which is close to the Curie temperature of $BaTiO_3$. It is observed from microstructural studies that the volume fraction of ferroelectric phase is quite small (less than 20 volume %). This is in conformity with the results reported earlier in an attempt to precipitate (Ba–Sr)TiO_3 in the glassy matrix (Herczog 1984). Attempts to produce a solid solution resulted in precipitation of a different phase lowering the yield of ferroelectric phase.

The absence of peak in ε vs T plots of lead-rich samples can be understood as follows: On ceramization, two or more phases develop. The dielectric constant of these glass ceramics is not much higher than that of parent glass. This, as well as the microstructural studies, indicate that the volume fraction of $PbTiO_3$ is quite small. As these samples are heated, dielectric constant changes very little up to ~ 600 K and thereafter it increases rapidly due to space charge polarization effects. The contribution of these effects seems to dominate over that due to $PbTiO_3$ beyond this temperature and hence masks the normal anomaly observed in $PbTiO_3$.

4. Conclusions

The main conclusions of these investigations are:

(i) The ferroelectric phase crystallising out during ceramization of glasses in the system PbO-BaO-TiO_2-B_2O_3-SiO_2 depends on the PbO/BaO ratio if the $(PbO+BaO)/TiO_2$ ratio is 1:1. For $PbO/BaO > 1$, $PbTiO_3$ crystallizes out while for $PbO/BaO \leqslant 1$, $BaTiO_3$ separates out during heat treatment.

(ii) Crystallization of solid solution (Ba,Pb)TiO_3 does not occur during ceramization. Reasons for this are not clear at the moment. Such attempts on the other hand reduce the yield of the ferroelectric phase. Further, the distribution of the crystallites is non-uniform and they are of varying sizes and shapes. These microstructural features impair the properties of resulting glass ceramics.

Acknowledgements

One of the authors (CDP) is thankful to UGC, New Delhi for a research fellowship. We are thankful to Dr Lakshman Pandey for useful discussion. Thanks are due to the Solid State and Structural Chemistry Unit, Indian Institute of Science, Bangalore for providing XRD facility and the National Electron Microscopy Facility, Banaras Hindu University, Varanasi for extending the scanning electron microscope facility.

References

Bergeron C G 1961 *Crystallization of perovskite lead titanate from glass*, Ph.D. Thesis, University of Illinois

Grossman D G and Isard J O 1969a *J. Am. Ceram. Soc.* **52** 230

Grossman D G and Isard J O 1969b *J. Mater. Sci.* **4** 1059

Herczog A 1964 *J. Am. Ceram. Soc.* **47** 107

Herczog A 1984 *J. Am. Ceram. Soc.* **67** 484

Layton M M and Herczog A 1967 *J. Am. Ceram. Soc.* **50** 369

Lynch S M and Shelby J E 1984 *J. Am. Ceram. Soc.* **67** 424
McMillan P W 1979 *Glass ceramics* (London: Acàdemic Press) (2nd ed.)
Om Parkash, Devendra Kumar and Rajagopalan R 1986a *Bull. Mater. Sci.* **8** 13
Om Parkash, Devendra Kumar and Lakshman Pandey 1986b *Bull. Mater. Sci.* **8** 557
Skanavi G I and Kashtanova A M 1957 *Sov. Phys. Tech. Phys.* **2** 1645

Bull. Mater. Sci., Vol. 9, No. 4, November 1987, pp. 263–267. © Printed in India.

Aliovalent substitution in β-Li_2SO_4 towards conductivity enhancement

K SINGH, S S BHOGA and F C RAGHUWANSHI
Department of Physics, Nagpur University, Nagpur 440 010, India

MS received 25 May 1987; revised 20 July 1987

Abstract. Aliovalent sulphates were selected for substitution in β-Li_2SO_4 at 6% vacancy concentration. The results show that if the guest ions are substituted on the basis of the criteria given for the formation of a solid solution, then it is possible to achieve a considerable enhancement in conductivity especially in the case of isostructural materials.

Keywords. Aliovalent substitution; conductivity enhancement.

1. Introduction

Solid electrolytes have attracted attention due to their potential use in several technical applications. The prospects for developing an ideal solid electrolyte are good and it is necessary to determine the conditions of the atomic arrangement for this purpose.

The sulphate-based solid electrolytes differ in some respects from the other solid electrolyte materials. An advantage is that many mono- and divalent cations have high mobility in them and thus increasing the choice of anode material in power sources (Heed *et al* 1975).

Amongst all the sulphates studied so far, lithium sulphate is a well-studied solid electrolyte (Benrath and Drekopf 1921; Kvist and Lunden 1965; Kvist 1966, 1967; Heed *et al* 1977). It undergoes a phase transition from a monoclinic to cubic structure at 848 K. Its high temperature form has very high ionic conductivity, comparable to the molten salts (Kvist and Lunden 1965). The effect on the ionic conductivity of substitution of divalent cations Mg^{2+}, Ca^{2+} and Zn^{2+} for Li^+ in the high temperature form of Li_2SO_4 has been investigated (Heed *et al* 1977). Monoclinic Li_2SO_4 has low electrical conductivity at ambient temperatures. Its electrical conductivity has been studied in the monoclinic phase from 550 K to 848 K (Deshpande and Singh 1982).

According to Kimura and Greenblatt (1984), an addition of small quantity of trivalent sulphate enhances the conductivity of β-Li_2SO_4. Similar effect has been reported in Na_2SO_4 (Murray and Secco 1978; Höfer and Esyel 1981; Saito *et al* 1984) and K_2SO_4 (Natarajan and Secco 1975). The maximum conductivity was obtained for 7% vacancy concentration for Na_2SO_4 (Höfer and Esyel 1981). Using the same concept, different vacancy concentrations were calculated for β-Li_2SO_4.

In the present investigation, the effect on the ionic conductivity of the partial substitution of Li^+ by divalent cations Ca^{2+}, Ba^{2+} and Mg^{2+} in β-Li_2SO_4 has been studied to determine whether such a replacement would enhance the ionic conductivity, as a result of the increased vacancies in the cation sublattice described by $Li_{2-2x}M_x^{2+}\square_x SO_4$.

2. Experimental

The starting materials Li_2SO_4, $MgSO_4$, $CaSO_4$ and $BaSO_4$ with purity greater than 99% procured from AG Fluka, Germany and Sarabhai Chemical, India, were dried at 423 K for 24 hr. Divalent sulphate (6·3 mol%) was added to the lithium sulphate. The mode of sample preparation was the same as reported earlier (Deshpande *et al* 1986). X-ray diffraction results of these samples confirm the solid solubility upto 6·5 mol%.

For electrical conductivity measurements, the specimen was prepared in rectangular shape of dimensions 7 × 5 × 3 mm. Aluminium foils were used to provide a good ohmic contact.

The AC conductivity was measured as a function of frequency (10 Hz to 10 MHz) at various temperatures in the range 740–550 K during the cooling cycle, using an impedance analyzer (Hewlett Packard 4192A) at 5 mV oscillator level.

3. Results and discussion

In the present investigation, β-Li_2SO_4, in quenched form, showed a frequency-independent behaviour of impedance in the frequency range 5 to 13 MHz. Ljungmark (1974) also reported similar results in the case of β-Li_2SO_4. Even after doping, the impedance of β-Li_2SO_4 remained frequency-independent (figure 1).

The solid electrolytes in which the conductivity does not vary with frequency are considered as ideal solid electrolytes and their properties are simulated by a single parallel resistance capacitance element (Macedo *et al* 1972).

As reported earlier, doping with an aliovalent can help to enhance the ionic conductivity of the host solid electrolytes. Thus, to make a systematic study and to derive conclusions, only those divalents were considered which showed an increase in the conductivity of β-Li_2SO_4 (monoclinic) low conductivity phase.

Here, Ca^{2+} being quite bigger in size (0·99 Å) in comparison with Li^+ (0·67 Å), enhances electrical conductivity in the temperature range 550 to 740 K by an order of magnitude. To understand the role of Ca^{2+} towards increase in conductivity, $CaSO_4$ was added in different concentration. This effect, illustrated in figure 2, shows that conductivity increases with increasing temperature. This is attributed to the hopping of cations due to thermal energy. Figure 2 also shows that conductivity increases with increasing vacancy concentration upto 6%. This is because of the

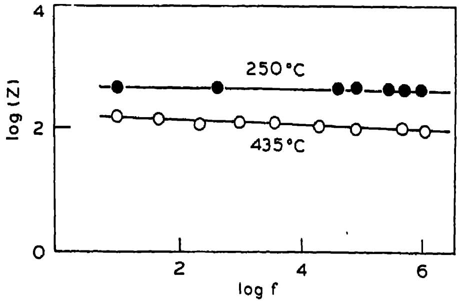

Figure 1. Variation of log Z vs log f for 6·3 mol% of $CaSO_4$.

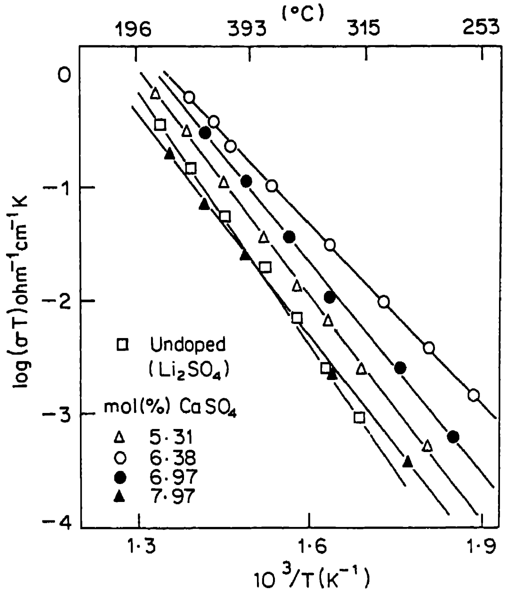

Figure 2. Effect of variation of $CaSO_4$ content on the electrical conductivity of β-Li_2SO_4.

increasing concentration of cation vacancies in $Li_{2-2x}Ca_x\square_xSO_4$ upto the solubility limit and replacement of Li^+ by Ca^{2+}, which in turn, expands the lattice of β-Li_2SO_4. Beyond 6% vacancy concentration, conductivity decreases because at low vacancy concentration, no interactions between mobile ion vacancies take place. At high vacancy concentration, the interaction between the lithium ion vacancies increases decreasing the mobility. With increasing vacancy concentration, greater paths for lithium migration are created. On the other hand the mobility of the ions is reduced by interactions such as cluster formation and ordering in the cation sublattice (Höfer and Esyel 1981). When conductivity attains a maximum at 6% vacancy concentration, these opposite effects cancel each other. Also with increasing concentration of Ca^{2+}, the concentration of vacancies increases whereas the concentration of mobile lithium cations is decreased continuously (here Li^+ ions are considered solely to be mobile ions on account of its smaller size and low equivalent weight compared to Ca^{2+}).

Figure 3 displays the variation of log σ as a function of vacancy concentration. For constant vacancy concentration (6%), conductivity increases with temperature.

Maximum conductivity was achieved by doping β-Li_2SO_4 with $CaSO_4$ for 6% vacancy and the necessary molar composition of $CaSO_4$ which was found to be 6·3 mol% was added to study the role of other divalents.

For 6% vacancy concentration, Li_2SO_4 and MSO_4 (M = Mg, Ca, Ba) have been compared (figure 4). It is seen that addition of MSO_4 increases the conductivity of the β-Li_2SO_4 because the presence of the divalent ion increases the cation migration energy (Natarajan and Secco 1975). It is also clear that $CaSO_4$-containing specimen shows the highest conductivity. The doping with Mg^{2+} slightly increases the conductivity at lower temperature, but decreases at higher temperature. The higher conductivity of Ba^{2+}-doped Li_2SO_4 sample may be due to its larger ionic size

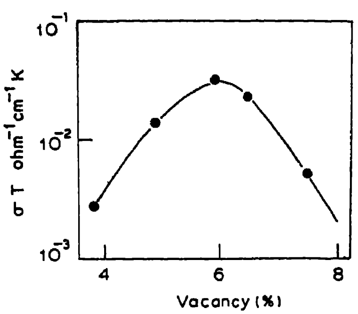

Figure 3. Variation of conductivity with vacancy concentration at 623 K.

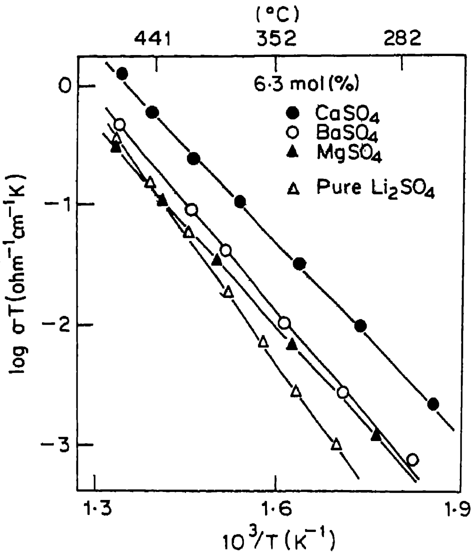

Figure 4. Effect of MSO$_4$ (M = Mg, Ca and Ba) on the electrical conductivity of β-Li$_2$SO$_4$.

compared to Mg^{2+} which might be attributed to its attraction towards the dislocation in the salt. Barium ion is mobile along the grain boundaries. Similar effect has been reported in the literature (Ljubnov and Lunden 1966) for K$_2$SO$_4$ when added in monoclinic Li$_2$SO$_4$. The larger size of the guest ion leads to an expansion of the lattice and hence the formation of a more open structure giving higher conductivity in the host Li$_2$SO$_4$. At the same time, the highly massive Ba^{2+} ions may obstruct the conduction pathways of mobile cations and hence reduce the conductivity. Thus ionic size might be the predominant factor contributing to the conductivity features of doped Li$_2$SO$_4$. Similar effect has been reported by Natarajan and Secco (1975) which is quite contrary to the reports of Höfer *et al* (1978).

On the basis of the previous discussion it can be concluded that only in the case of CaSO$_4$ substitution the ionic conduction of substituted Li$_{2-2x}$Ca$_x$ $\square_x$SO$_4$ phase increased by an order of magnitude in comparison with Li$_2$SO$_4$.

More effective enhancement of the ionic conductivity has been reported in Na_2SO_4 (Höfer *et al* 1978), which is probably due to the structural differences of sodium and lithium host compounds. It is interesting to note that doping does not give considerable importance for the size of ions, but gives special consideration to isostructural compounds, as it is in the present case, that both Li_2SO_4 and $CaSO_4$, are monoclinic.

Acknowledgements

The authors (SSB and FCR) thank CSIR and UGC respectively for financial support.

References

Benrath A and Drekopf K 1921 *Z. Phys. Chem.* **99** 57

Deshpande V K and Singh K 1982 *Solid State Ionics* **6** 151

Deshpande V K, Raghuwanshi F C and Singh K 1986 *Solid State Ionics* **18, 19** 378

Heed B, Lunden A and Schroeder K 1975 *10th Intersoc. Energy Conv. Eng. Conf.* IECEC'75 RECORD p. 613

Heed B, Lunden A and Schroeder K 1977 *Electrochim. Acta.* **22** 705

Höfer H H and Esyel W 1981 *J. Solid State Chem.* **36** 365

Höfer H H, Esyel W and Alpen U V 1978 *Mater. Res. Bull.* **13** 265

Kimura N and Greenblatt M 1984 *Mater. Res. Bull.* **19** 1653

Kvist A 1966 *Z. Naturforsch.* **A21** 1221

Kvist A 1967 *Z. Naturforsch.* **A22** 208

Kvist A and Lunden A 1965 *Z. Naturforsch.* **A22** 235

Ljungmark H 1974 Ph.D. thesis, Goteborg University, Sweden

Ljubnov V and Lunden A 1966 *Z. Naturforsch.* **A21** 1592

Macedo P B, Moynihan C T and Bose R 1972 *Phys. Chem. Glasses* **13** 171

Murray R M and Secco E A 1978 *Can. J. Chem.* **56** 2616

Natarajan M and Secco E A 1975 *Can. J. Chem.* **53** 1542

Saito Y, Maruyama T and Kobayushi K 1984 *Solid State Ionics* **14** 265

Bull. Mater. Sci., Vol. 9, No. 4, November 1987, pp. 269–275. © Printed in India.

Kinetics of crystallization of a $Fe_{74}Co_{10}B_{16}$ glass

R P MATHUR and D AKHTAR
Defence Metallurgical Research Laboratory, Hyderabad 500 258, India

MS received 29 June 1987

Abstract. Differential scanning calorimetry (DSC) technique has been employed to study the crystallization kinetics of a $Fe_{74}Co_{10}B_{16}$ glass. Crystallization of $Fe_{74}Co_{10}B_{16}$ glass is known to occur in two distinct stages. It was possible to separate out the isothermal kinetics of both the crystallization stages through a thermal treatment scheme in the DSC. The crystallization processes are interpreted in the light of the kinetic data obtained.

Keywords. Metallic glass; crystallization; incubation time; activation energy; Avrami exponent.

1. Introduction

Continuous heating of $Fe_{74}Co_{10}B_{16}$ glass in a differential scanning calorimeter (DSC) exhibits two exothermic events (Akhtar *et al* 1986) which are separated by a temperature interval of 84 K at a heating rate of 20 K/min. It has been shown (Mathur *et al* 1987) that the first event corresponds to the precipitation of α-Fe from the amorphous matrix and the second event corresponds to the crystallization of the remaining amorphous phase into Fe_3B and Co_2B phases.

In the present study, isothermal kinetics of both the crystallization events of $Fe_{74}Co_{10}B_{16}$ glass have been investigated using the DSC technique. A thermal treatment scheme in the DSC comprising isothermal anneals at two temperatures, given to the same specimen (Akhtar 1986), was employed. The crystallization processes are interpreted in the light of the kinetic data obtained.

2. Experimental

Details of the preparation of $Fe_{74}Co_{10}B_{16}$ glass ribbons are given elsewhere (Akhtar *et al* 1986; Mathur *et al* 1987). DSC experiments were carried out in an advanced thermal analysis system, the computerized DuPont 1090. This instrument allowed a good control over the temperatures of isothermal scans. It heats up to the temperature set for isothermal scan at the maximum possible heating rate. Typically, a temperature of 500°C could be arrived at in 3–4 min starting from room temperature. The data could be stored, processed and compared, thus making it simple to produce plots for accurate comparison.

3. Results and discussion

Typical continuous heating DSC thermogram obtained at a heating rate of 20 K/min is shown in figure 1a. The two exothermic peaks observed in the DSC thermogram reveal two stages of crystallization of the $Fe_{74}Co_{10}B_{16}$ glass as discussed earlier. To determine the kinetics of the crystallization processes, a two-step isothermal

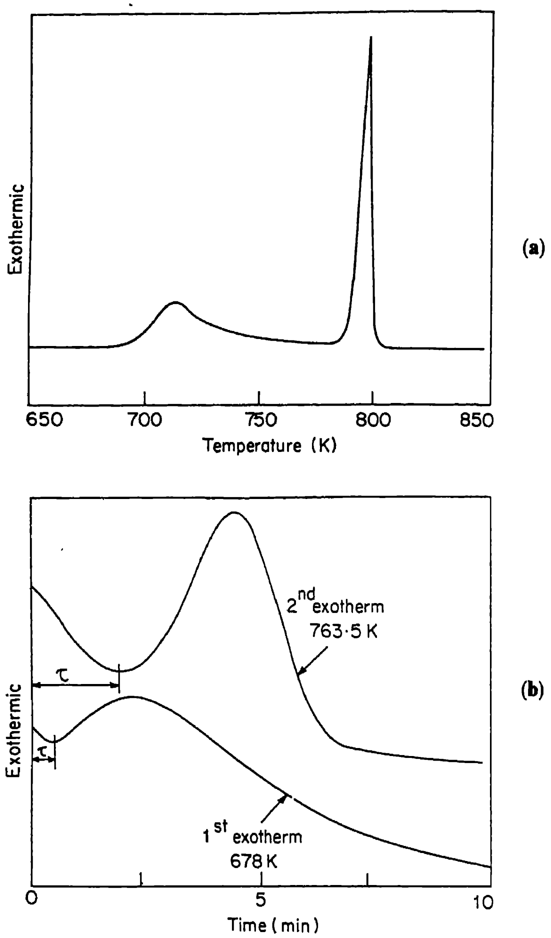

Figure 1. **a.** Crystallization exotherms obtained at a heating rate of 20 K/min. **b.** Typical isothermal exotherms depicting the incubation period, τ.

treatment was devised. The first isothermal anneals were carried out in the temperature range 678 K to 685 K. Anneals at higher temperatures could not be carried out because of the normally encountered difficulty of the incubation time falling short of the instrument transient time. At temperatures lower than 678 K, because of slow transformation rates, the exotherm tended to flatten out. In the temperature range of investigation, the base line became linear after the end of the instrument transient and a well-defined isothermal exotherm could be obtained. After completion of the first stage of crystallization, the base line in the isothermal thermogram became parallel to the time axis indicating an undetectable rate of exothermic reaction.

The second crystallization event did not occur at a detectable rate at the first annealing temperatures. Thus it was necessary to heat the specimen rapidly to the temperatures of second isothermal anneals in order to study the isothermal kinetics of the second event. The second anneals were performed in the temperature range 763·5 K to 772·5 K, the upper and lower temperature limits being again governed by the factors described above. Observation of a well-defined incubation period for the second anneal suggested that (i) the formation of α-phase was complete before the second annealing temperature was arrived at and (ii) during the heating-up period between the two annealing treatments, the second crystallization event did not start. Operation of either of these processes would have caused the disappearance of the incubation period.

The incubation period was taken as the time interval between the specimen reaching the annealing temperature and the start of the transformation. The start of the transformation was taken as that instant at which the base line first deviated from linearity. Typical isothermal exotherms depicting the incubation period, τ for both the stages of crystallization are shown in figure 1b. The incubation times observed at some annealing temperatures are listed in table 1 for both the crystallization events. The observed decrease in the incubation period with increasing annealing temperature was in keeping with the fact that at temperatures below the nose of the time – temperature-transformation curve for crystallization, the nucleation rate increases with increasing temperature, resulting in a decrease in the incubation period (Scott and Ramachandrarao 1977).

The kinetics of the two crystallization processes were analysed in terms of the following expression of the generalized theory of phase transformations (Burke 1965)

$$x = 1 - \exp(-bt^n),$$

where x is the fraction transformed in time t, b is a rate constant and n the Avrami exponent. The fraction transformed x at any time t was determined as the ratio $A(t)/A(\text{tot})$ where $A(t)$ and $A(\text{tot})$ are the area under the isothermal exotherm up to time t and the total area of the exotherm respectively. Plots of x vs time at different temperatures yielded sigmoidal curves, shown in figures 2a and 2b for the first and second crystallization events respectively.

The activation energy of the crystallization processes was evaluated from the isothermal exotherms making use of the Arrhenius relation

$$t_x = t_o \exp(E/RT),$$

where t_x is the time required for the transformation of fraction x at temperature T and E is the activation energy. The plots of t_x ($x = 0{\cdot}3$, $0{\cdot}5$ and $0{\cdot}8$) against $1/T$ are shown in figures 3a and 3b for the first and second stages of crystallization respectively. Calculated values of activation energy are depicted in the figures. The Avrami exponent n was determined by evaluating the slope of the plots of $\ln[-\ln(1-x)]$ against $\ln t$. Such plots are shown in figures 4a and 4b for the first and second cry-

Table 1. Values of incubation times at some annealing temperatures.

I stage		II stage	
Temperature (K)	Incubation time (min)	Temperature (K)	Incubation time (min)
678	0·35	763·5	1·8
682·5	0·25	767	0·65
685	0·2	768	0·5
		772·5	0·3

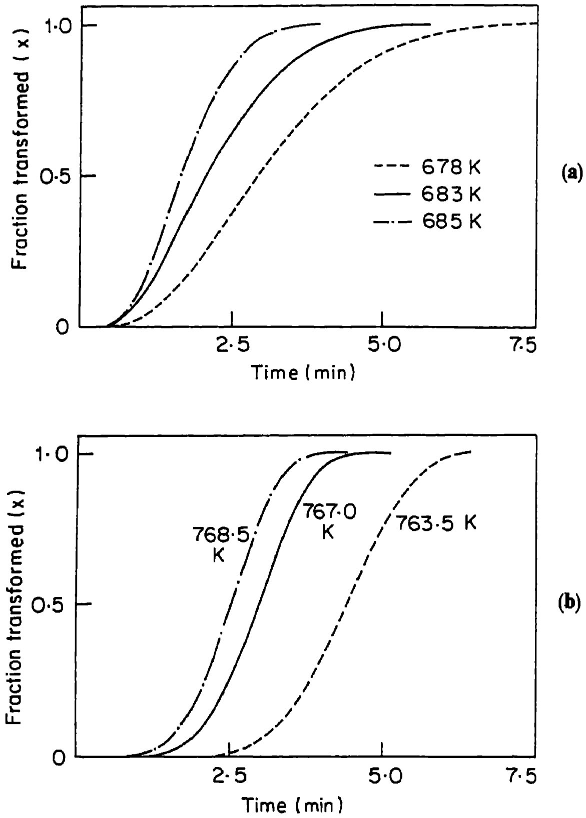

Figure 2. Some of the sigmoidal curves for **a.** first crystallization stage and **b.** second crystallization stage.

stallization events respectively. Estimated values of the Avrami exponent are also depicted in the figures.

The crystallization kinetics of iron-based metallic glasses containing boron have been studied by various investigators (Greer 1982; Chang and Marti 1983; Baburaj *et al* 1985; Miranda *et al* 1986a, b), particularly because of the favourable properties of these glasses. Activation energy values ranging from 2·4–2·5 eV (Greer 1982; Baburaj *et al* 1985) to 3·7–3·8 eV (Chang and Marti 1983; Akhtar 1986) have been obtained for the precipitation of α-Fe phase. Our activation energy of 3·2–3·3 eV for the first stage of crystallization of $Fe_{74}Co_{10}B_{16}$ glass lies within the range of reported values. Activation energies of 4·8 and 5·2 eV reported by other investigators (Miranda *et al* 1986a, b), however, appear to be too high for the primary crystallization process. A comparison of activation energies for the second crystallization event would not be proper since the structure/composition of the phase(s) corresponding to this stage is not similar. In $Fe_{74}Co_{10}B_{16}$ glass, Fe_3B and Co_2B phases are formed simultaneously in the second stage which requires an average activation energy of 5·2–5·7 eV. The effective activation energy of crystallization is determined by both nucleation and growth processes. It is therefore not possible to attach any physical significance to the values of the activation energies. It is noteworthy that the activation energy

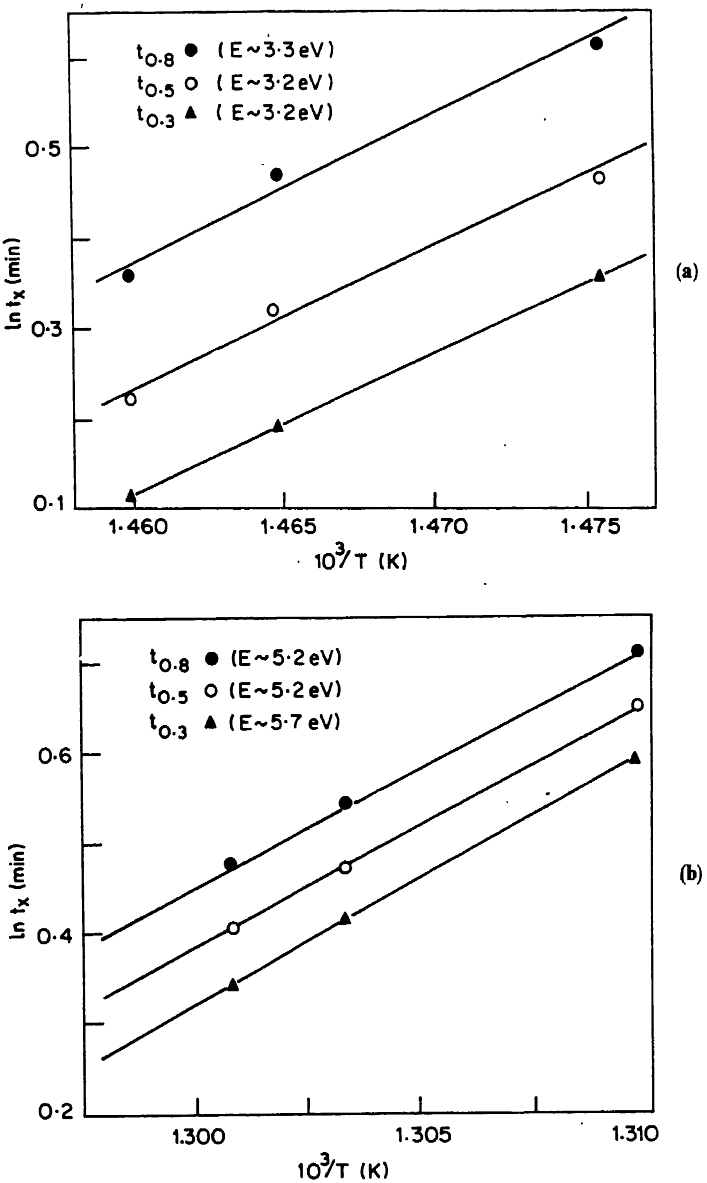

Figure 3. Plots of $\ln t_x$ against $1/T$ for **a.** first crystallization stage and **b.** second crystallization stage.

values are much larger than those expected for simple diffusive processes and may be taken as an indication of the complexity of the crystallization kinetics on which such factors as diffusion, nucleation mechanisms and interface processes may exert an influence.

For the primary crystallization process, the value of the Avrami exponent $n = 2{\cdot}2$ estimated in the present investigation is slightly lower than the value of 2·5 obtained for Metglas 2605 SC (Akhtar 1986) but higher than the values of 2·0 and 1·7 obtained

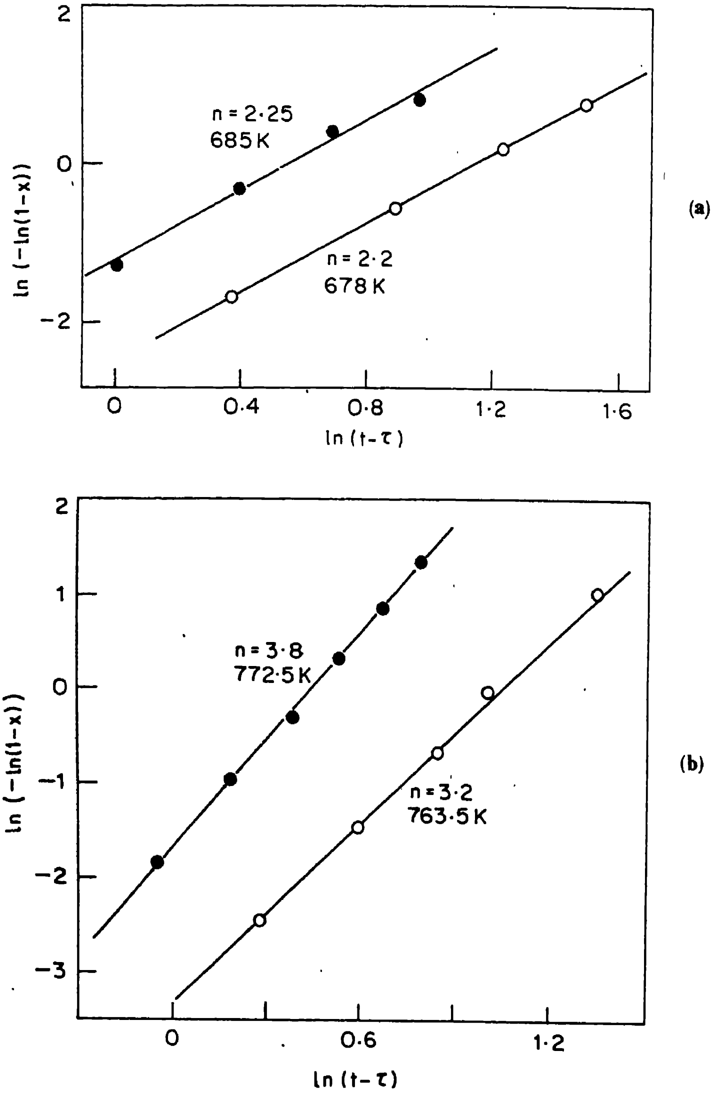

Figure 4. Plots of $\ln[-\ln(1-x)]$ against $\ln(t-\tau)$ for **a.** first crystallization stage and **b.** second crystallization stage.

for primary crystallization of Metglas 2605 CO (Baburaj *et al* 1985) and Metglas 2826A (Von Heimendahl and Kuglstatter 1981). Let us consider the expression for n (Christian 1975)

$$n = a + pd,$$

where $p = 1$ for linear growth, $p = 1/2$ for parabolic growth; $d = 1$, 2 or 3 for one; two- or three-dimensional growth; $a = 0$ for no nucleation (i.e. zero nucleation rate), $a = 1$ for constant nucleation rate, $0 < a < 1$ for a decreasing nucleation rate and $a > 1$ for an increasing nucleation rate. Our n value of 2·2 for the primary crystallization of $Fe_{74}Co_{10}B_{16}$ glass is thus indicative of a process involving nucleation at a decreasing rate with time and a parabolic growth. For the second crystallization stage, the values of n obtained in the present investigation vary from 3·2 to 3·8. A direct interpretation of these values is not possible because these Avrami exponents correspond to the formation of both Fe_3B and Co_2B phases in the second stage. Nevertheless, they imply a nucleation rate which decreases with time and a linear growth process.

4. Conclusions

It was possible to separate out the isothermal kinetics of both the crystallization stages of $Fe_{74}Co_{10}B_{16}$ glass. The kinetic data thus obtained imply a decreasing nucleation rate (with time) and a parabolic growth for the first crystallization stage and a decreasing nucleation rate (with time) and a linear growth process for the second crystallization stage.

Acknowledgements

Thanks are due to Mr V N Murthy and Dr P Subrahmaniam for their help in preparation of the alloy.

References

Akhtar D 1986 *Scr. Metall.* **20** 983

Akhtar D, Murthy V N, Subrahmaniam P and Jagannathan R 1986 *J. Mater. Sci. Lett.* **5** 1148

Baburaj E G, Dey G K, Patni M J and Krishnan R 1985 *Scr. Metall.* **19** 305

Burke J 1965 *Kinetics of phase transformation in metals* (Oxford: Pergamon Press)

Chang C F and Marti J 1983 *J. Mater. Sci.* **18** 2297

Christian J W 1975 *The theory of phase transformation in metals and alloys*' (Oxford: Pergamon Press)

Greer A L 1982 *Acta Metall.* **30** 171

Mathur R P, Murthy V N, Akhtar D, Subrahmaniam P and Jagannathan R 1987 *J. Mater. Sci. Lett.* **6** (in press)

Miranda H, Conde C, Conde A and Marquez R 1986a *Mater. Lett.* **4** 226

Miranda H, Conde C, Conde A and Marquez R 1986b *Mater. Lett.* **4** 442

Scott M G and Ramachandrarao P 1977 *Mater. Sci. Eng.* **29** 137

Von Heimendahl M and Kuglstatter G 1981 *J. Mater. Sci.* **16** 2405

Bull. Mater. Sci., Vol. 9, No. 4, November 1987, pp. 277–285. © Printed in India.

Undercooling studies on dispersed bismuth droplets

SANJAY CHAUBEY, VAKIL SINGH and P RAMACHANDRARAO*
Department of Metallurgical Engineering, *School of Materials Science and Technology, Institute of Technology, Banaras Hindu University, Varanasi 221 005, India

MS received 18 April 1987; revised 2 July 1987

Abstract. In the zinc-bismuth system, a monotectic reaction occurs at 689 K and 0·6 at.% Bi composition. Rapid solidification of the as-cast monotectic alloy led to a micromorphology in which bismuth was uniformly and bimodally distributed as small droplets in the zinc matrix. Statistical analysis of the electron micrographs obtained from different transparent regions of the foils revealed that the size of most of the droplets was about 6 nm. These droplets undercooled by 132 K. An analysis of the nucleation rate measurements shows that the activation energy barrier to nucleation is of the order of 39·8 kcal/mol at the maximum undercooling.

Keywords. Undercooling; nucleation; bismuth.

1. Introduction

The phenomenon of undercooling exhibited by liquid metals and alloys below their thermodynamic freezing temperature has been given due importance by materials scientists. Heterogeneities present within the bulk melt usually initiate crystal nucleation at low undercooling. However, various experimental techniques for extending the limit of undercooling are now available (Vonnegut 1948; Turnbull 1950; Duwez *et al* 1960; Southin and Chadwick 1978; Lacy *et al* 1981). The droplet dispersal technique proposed by Vonnegut (1948) and later employed by Turnbull (1950, 1952) and coworkers (Turnbull and Cech 1950) is an effective technique for extending the range of observable undercooling. One of the useful techniques for inducing large undercooling in bulk melts is the glass slag technique in which the melt is under the cover of a fluid glass slag in a crucible (Fehling and Scheil 1962). By repeated melting and freezing under the glass flux, drastic undercooling is achieved in the melt. An emulsification technique in which the droplets are supported in aromatic oils and stabilized by reaction with organic peroxides and organic acid modifiers was developed by Rasmussen and Loper (1975). Such an emulsification procedure segregates heterogeneities present in the bulk melt into a small fraction of the droplet population and permits measurement of the undercooling in the presence of different types of surface layers. Southin and Chadwick (1978) employed the so-called liquid-entrapment technique, described previously by Wang and Smith (1950), for the enhancement of the degree of undercooling. Binary eutectic or monotectic alloy systems are best suited for this technique. The composition of the alloy is adjusted such that the equilibrium structure contains a small fraction of either one of the monotectic phases or the eutectic mixture. Subsequent annealing, at temperatures between the solidus and liquidus of the alloy, for sufficient time leads to the formation of droplets within the solid matrix grains. Such isolated droplets, free from heterogeneities, undercool enormously and can even produce metastable phases (Ramachandrarao *et al* 1979). In monotectic alloy systems isolated droplets of the second phase can also be produced through the process of rapid solidification (Chattopadhyay and Ramachandrarao 1980).

In the present study, the conventional gun-technique of rapid solidification is employed for the formation of isolated bismuth droplets in zinc matrix. The undercooling behaviour of such entrapped droplets has been characterized and discussed in the light of earlier work and the available models for heterogeneous nucleation of melts.

2. Experimental

Zn-0·6 at.% Bi monotectic alloy and Zn-9·69 at.% Bi hypermonotectic alloy were prepared by melting the accurately weighed components together in a graphite crucible under an argon atmosphere. The alloys were made from 5 N purity metals. The alloy melt was vigorously shaken and then it was allowed to solidify in the crucible under an argon gas cover.

Small alloy pieces weighing approximately 20 mg were cut from the bulk alloy and were rapidly solidified using the gun-technique in order to disperse Bi in the Zn-matrix in the form of small droplets. The resultant product was in the form of irregular foils, which were transparent in many places to the electron beam. Electron microscopy of the foils was carried out and the micrographs were analyzed to arrive at the statistical size distribution of Bi droplets.

Using a differential scanning calorimeter (Perkin Elmer DSC II) and about 10 mg of the rapidly solidified foils, thermograms were recorded at heating and cooling rates of 2·5 K/min to study the undercooling behaviour and nucleation kinetics of Bi droplets. The lower and upper temperature limits of the DSC II were set at 323 K and 570 K respectively. In every run empty Al sample pan with cover served as a reference. Argon gas was used for purging throughout the experiment.

3. Results

Statistical analysis of electron micrographs obtained from different transparent regions of the foils reveals that the size of most of the Bi droplets is of the order of 6 nm (figure 1). However, in thicker sections some bigger droplets were also seen in the micrographs but they were few in number. The size of the bigger droplets was not less than 25 nm. In thin sections of the rapidly solidified product fine scale distribution was observed, whereas in thicker sections a bimodal distribution consisting of coarse as well as fine particles was observed. A typical micrograph is shown in figure 2(a, b). Several of the big Bi particles show faceting (figure 2b).

Undercooling behaviour restricted to well-defined exothermic crystallization events is illustrated in figures 3–6. Figures 3 and 4 present DSC thermograms for rapidly solidified Zn-0·6 at.% Bi and Zn-9·69 at.% Bi respectively. Figures 5 and 6 present DSC thermograms for as-cast Zn-0·6 at.% Bi and Zn-9·69 at.% Bi respectively. The melting temperature, T_L, recorded in the thermograms of figures 3–6 is 528 ± 1 K which simply represents the melting of Bi-rich droplets entrapped in Zn-matrix. Apart from this melting transition at 528 K one more small endothermic transition appears at ~440 K. By successive heating and cooling of the sample the area under the peak appearing at 440 K increases slightly. After the third cycle there

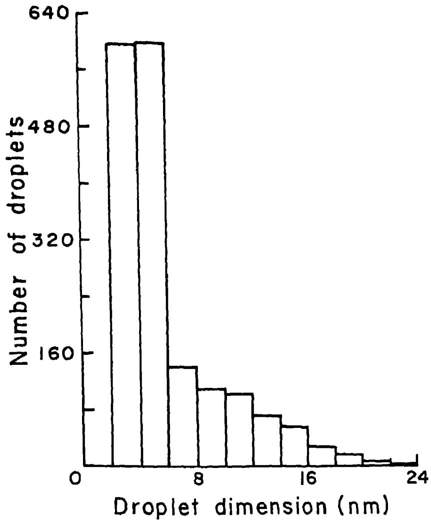

Figure 1. Histogram showing the droplet size distribution.

is an almost negligible increase in the area. Cooling thermograms in figures 3 and 4 show a number of exothermic peaks, the last one appearing at 397–396 K. The largest undercooling achieved is 132 K which is equivalent to about 0·25 T_L, where T_L is the liquidus temperature. Several experiments have shown that the number and position of exothermic peaks change. However, the position of last exothermic peak appearing at 397 K remains unchanged. Thermograms of figures 5 and 6 have been recorded for comparing the behaviour of rapidly solidified foils with the as-cast ones. As in figures 3 and 4, thermograms of figures 5 and 6 also show a number of exothermic peaks, the last one appearing at 398–397 K. As far as the highest degree of undercooling is concerned it is of the same order of magnitude as in the case of its rapidly solidified counterpart. Except for the last peak occurring at 397 K, the number and the position of other exothermic peaks change from sample to sample.

4. Discussion

The experimental results obtained in this work clearly show that crystallization of Bi-rich droplets entrapped in Zn-matrix occurs through several nucleation events. It is worthwhile to note that there is a close resemblance between the observations on slowly cooled samples of as-cast and rapidly solidified Zn-Bi alloys. Rapid solidification possibly restricts the layering mechanism in liquid monotectic alloys and results in granulation of Bi (Chattopadhyay and Ramachandrarao 1980). These granules or droplets are distributed on a coarse scale in thicker portion whereas fine scale distribution is observed in thin portion of the rapidly solidified product. Most of the active nucleants which are responsible for lesser undercoolings are restricted to within bigger and coarser droplets leaving the finer ones relatively free. A number of exothermic peaks at different temperatures indicate the presence of different types of heterogeneities, each becoming effective at different undercoolings.

Bulk samples of Bi were undercooled more than 60° when melted in a flux of

Figure 2. Electron micrographs showing dispersion of Bi particles. **a.** fine scale distribution and **b.** bimodal distribution.

$SnCl_2 + ZnCl_2$ (Bosio *et al* 1961). The maximum recorded undercooling, $\Delta T = 132$, is greater than the value reported by Turnbull and Cech (1950) which is 90°, but is less than the value reported by Perepezko (1984) which is 227°. According to Turnbull and Cech (1950) homogeneous nucleation for any metal was said to occur at approximately 0·2 T_L, T_L being the melting temperature. However, this limit does not seem to be appropriate. The substantial undercooling recorded in the present investigation may be understood as a consequence of surface catalytic effect and implies that the Zn-matrix containing Bi dispersion provides a suitable surface for catalyzing the nucleation of fine Bi droplets which are supposed to be relatively free from heterogeneities. The nucleation events occurring at lesser undercoolings are also heterogeneous in nature but impurity-aided. Fine Bi droplets exhibiting larger undercooling are clean and are in contact with only solid Zn surface. Therefore, it is appropriate to call the responsible nucleation process as clean heterogeneous nucleation (Southin and Chadwick 1978). The unspecified surface layer formed during emulsification in the experiments of Perepezko (1984) is less catalytic than the

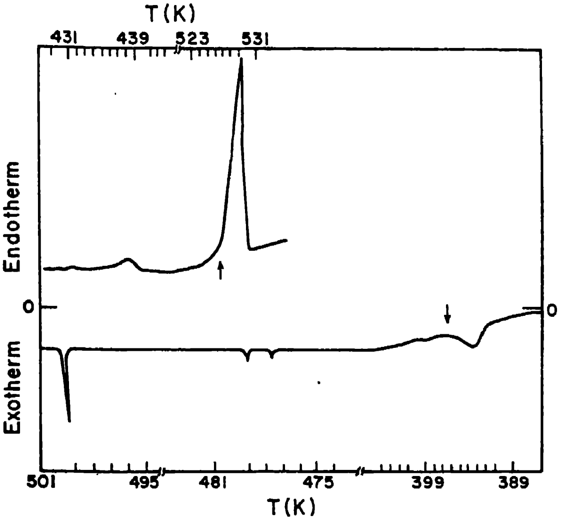

Figure 3. Thermogram for rapidly solidified Zn-0·6 at.% Bi recorded at the heating and cooling rates of 2·5 K min^{-1}. The transformation temperatures are marked by an arrow.

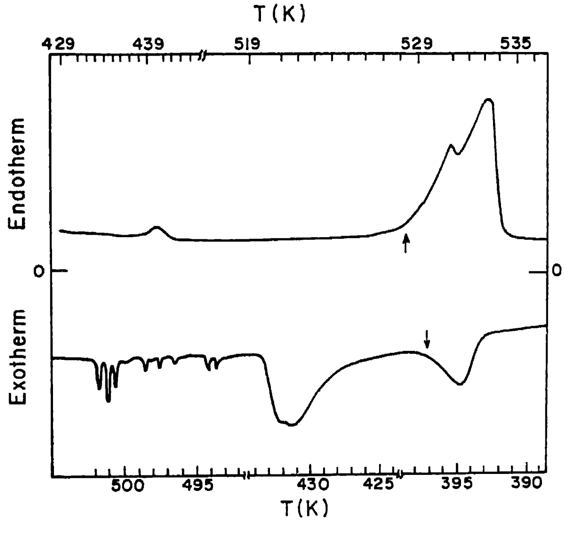

Figure 4. Thermogram for rapidly solidified Zn-9·69 at.% Bi recorded at the heating and cooling rates of 2·5 K min^{-1}. The transformation temperatures are marked by an arrow.

solid Zn surface of the present case and hence results in the highest level of undercooling for Bi reported till date.

The observation of the endothermic transition at 528 ± 1 K in the case of as-cast as well as rapidly solidified product of the Zn-Bi alloy is in accord with the phase diagram of Zn-Bi system (Hansen 1958). A notable feature observed in the thermograms of figures 3–6 is the appearance of one more endothermic transition at 440 K. This temperature did not correspond to the melting points of oxides of bismuth

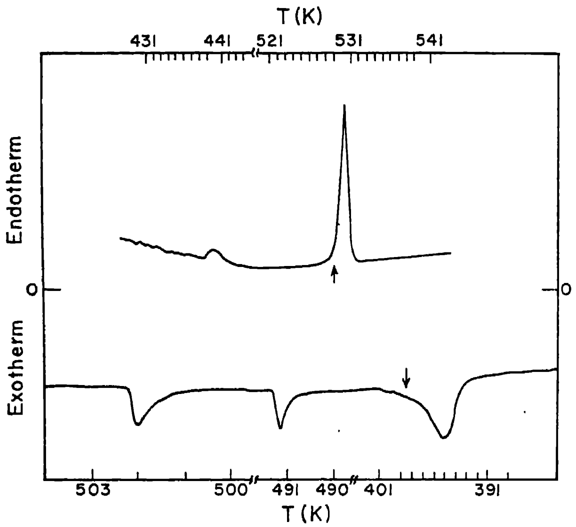

Figure 5. Thermogram for the as-cast Zn-0·6 at.% Bi recorded at the heating and cooling rates of 2·5 K $\min^{-1}$. The transformation temperatures are marked by an arrow.

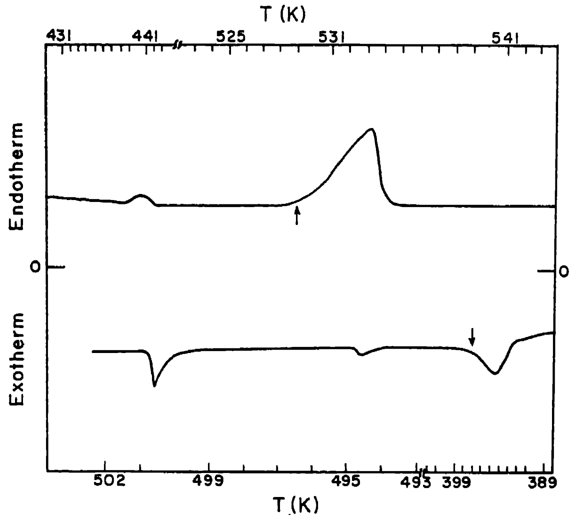

Figure 6. Thermogram for the as-cast Zn-9·69 at.% Bi recorded at the heating and cooling rates of 2·5 K $\min^{-1}$. The transformation temperatures are marked by an arrow.

(Weast 1977) and so the presence of any oxide of bismuth was ruled out. However, Bi is reported to undergo several polymorphic transformations (Perepezko 1980). A clear inspection of the areas under the two melting transitions indicates that the volume fraction of the phase appearing at 440 K is less than 5% of the total. X-ray diffraction studies did not give a clear evidence for the presence of a polymorph of Bi. However, it may not be possible to detect any polymorph by X-ray diffraction since the volume fraction of the phase is too small. Perepezko (1980) has already suggested that at high undercooling solidification is initiated by the nucleation of Bi with different crystal structures. For the additional endotherm observed at 447 K he argued that the structural modification may be the Bi (II) phase.

If it is assumed that only one nucleation event per droplet is enough for solidification of each fine droplet, the heat released for a droplet solidification in a DSC will be the same as for any other droplet and hence the amount of heat released is a direct measure of the number of droplets to solidify. Following the base line correction employed by earlier workers (Scott and Ramachandrarao 1977) the total area under the cooling thermogram from any time t_1, A_{t_1} gives a measure of the number of droplets unsolidified at time t_1, N_{t_1}. After a short interval of time Δt, the area left, $A_{t_1+\Delta t}$, is a measure of the number of droplets still unsolidified, $N_{t_1+\Delta t}$. In a constant cooling experiment it has been shown that the nucleation rate per droplet during a small time interval Δt is (Wood and Walton 1970; Rasmussen and Loper 1976)

$$J_s = -\frac{1}{\Delta t}\ln\left(\frac{A_{t_1+\Delta t}}{A_{t_1}}\right). \tag{1}$$

The nucleation rate thus calculated corresponds to some average temperature of the sample during the time interval Δt. Because of slow cooling rate, sample temperature does not change appreciably over the time interval Δt. The nucleation rate per droplet, J_s, where s is the average droplet surface area, has been calculated for thermograms recorded at a cooling rate of 2·5 K/min.

In the approximation of a spherical nucleus the temperature dependence of the nucleation rate for the constant cooling experiment is given by the expression (Turnbull 1952)

$$J = A\exp(-\Delta G^*/kT), \tag{2}$$

where ΔG^* is the thermodynamic barrier to nucleation and A is a factor which is practically insensitive to small changes of temperature. For heterogeneous nucleation process A is of the order of $10^{25\pm1}$ sec^{-1} cm^{-2}, whereas for homogeneous nucleation it is of the order of $10^{33\pm1}$ sec^{-1} cm^{-3} (Turnbull 1950). For the homogeneous nucleation process

$$\Delta G^* = 16\pi\sigma^3/3\Delta G_v^2. \tag{3}$$

For the heterogeneous nucleation process

$$\Delta G^* = \frac{16\pi\sigma^3}{3\Delta G_v^2}f(\theta), \tag{4}$$

where $f(\theta) = \frac{1}{4}(2 - 3\cos\theta + \cos^3\theta)$, θ being the contact angle. σ and ΔG_v in (3) and (4) are solid-liquid interfacial tension and volume free energy change during crystallization respectively.

Recently Lele *et al* (1985) developed the following novel expression for ΔG accompanying crystallization of an undercooled melt

$$\Delta G = \Delta S_f\,\Delta T - [\Delta C_{pf}\,\Delta T^2/(T_f + T)]. \tag{5}$$

Table 1. Comparison between the observed and calculated ΔG values for undercooled liquid bismuth.

T	ΔT (K)	ΔG(Bi) (Olesinski and Abbaschian) (cal/mol)	ΔG(Bi) (Lele *et al* 1985) (cal/mol)
514	30	148	148
499	45	222	223
484	60	295	297
469	75	367	371
454	90	441	445
439	105	513	518
424	120	585	592
409	135	656	666
394	150	726	739

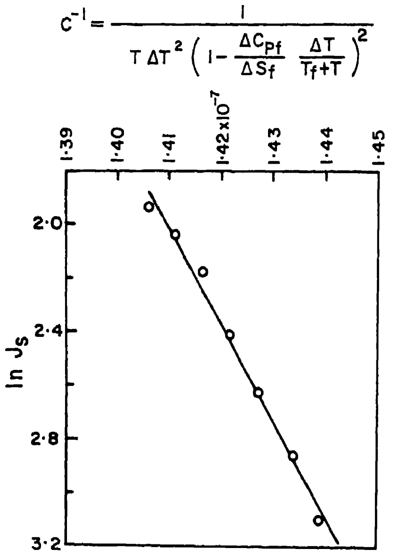

Figure 7. Temperature dependence of the nucleation rate.

ΔS_f and ΔC_{pf} in the above equation are entropy and heat capacity differences between the liquid and solid at the melting point. Suitability of the above equation has been checked with the help of an analytical equation for the Gibbs-free energy change for Bi which is written as (Olesinski and Abbaschian 1986)

$$\Delta G(\text{Bi}) = 4198 + 108{\cdot}96T + 15{\cdot}234 \times 10^{-3}T^2 - 19{\cdot}9493T\ln T + 2{\cdot}05 \times 10^5 T^{-1} J/\text{mol}. \qquad (6)$$

Table 1 shows the comparison between the ΔG values calculated using (5) and (6) separately. From table 1 it is clear that even at higher undercoolings the agreement between both the values is quite satisfactory.

Combining (2), (4) and (5) we have the following expression for the heterogeneous nucleation process

$$J = A \exp\left[-\frac{16\pi\sigma^3 f(\theta)}{3k\Delta S_f^2 C}\right], \tag{7}$$

where $$C = T\Delta T^2 \left[\frac{\Delta C_{pf}}{.\Delta S_f} . \frac{\Delta T}{(T_f + T)}\right]^2 .$$

From (7) it is clear that there must be a linear relationship between ln J and C^{-1}. Values of ln J_s calculated using (1) have been plotted against the temperature function, C^{-1}, in figure (7). As expected, a linear behaviour is observed over a range of the long tail on the thermogram which enabled us to arrive at the value of 39·8 kcal/mol for ΔG^*.

The present study shows that a reduction in the size of the droplets alone is not a sufficient requirement for enhancing the degree of undercooling in the present technique. The undercooling achieved is strongly dependent on the surface activity of the matrix entrapping the droplet. Experiments on Bi suspended in other matrices by a similar technique will throw further light on the inherent undercooling tendency of Bi.

Acknowledgements

The authors gratefully acknowledge the helpful discussions they had with their colleagues Prof. S Lele and Dr K S Dubey. They also acknowledge with thanks the experimental facilities extended by Prof. S Ranganathan and the assistance rendered by Dr K Chattopadhyay.

References

Bosio L, Defrain A and Ebelboin L 1961 *Compt. Rand.* **253** 2343
Chattopadhyay K and Ramachandrarao P 1980 *J. Mater. Sci.* **15** 685
Duwez P, Willens R H and Klement W 1960 *J. Appl. Phys.* **31** 1136
Fehling J and Scheil E 1962 *Z. Metallkde.* **53** 593
Hansen P M 1958 *Constitution of binary alloys* (New York: McGraw Hill)
Lacy L L, Robinson M B and Rathz T J 1981 *J. Cryst. Growth* **51** 47
Lele S, Dubey K S and Ramachandrarao P 1985 *Curr. Sci.* **54** 994
Olesinski R W and Abbaschian G J 1986 *Bull. Alloy Phase Diagrams* 7 535
Perepezko J H 1980 in: *Rapid solidification processings: principles and technologies Proc. Second Int. Conf.*, (eds) R Mehrabian, B H Kear and M Cohen (Virginia: Claitor's Publishing Division) p. 56
Perepezko J H 1984 *Mater. Sci. Eng.* **65** 125
Ramachandrarao P, Lal K, Singh A Deo and Chattopadhyay K 1979 *Mater. Sci. Eng.* **41** 259
Rasmussen D H and Loper C R 1975 *Acta. Metall.* **23** 1215
Rasmussen D H and Loper C R Jr 1976 *Acta. Metall.* **24** 117
Scott M G and Ramachandrarao P 1977 *Mater. Sci. Eng.* **29** 137
Southin R T and Chadwick G A 1978 *Acta. Metall.* **26** 223
Turnbull D 1950 *J. Appl. Phys.* **21** 1022
Turnbull D 1952 *J. Chem. Phys.* **20** 411
Turnbull D and Cech R E 1950 *J. Appl. Phys.* **21** 804
Vonnegut B 1948 *J. Colloid. Sci.* **3** 563
Wang C C and Smith C S 1950 *Trans. AIME* **188** 136
Weast R C 1977 *CRC handbook of chemistry and physics* (Cleveland: CRC Press) 58th Ed.
Wood G R and Walton A G 1970 *J. Appl. Phys.* **41** 3027

Bull. Mater. Sci., Vol. 9, No. 4, November 1987, pp. 287–294. © Printed in India.

Microhardness measurement in nonmetallic materials

V SARASWATI
Materials Development Laboratory, Indira Gandhi Center for Atomic Research, Kalpakkam 603 102, India

MS received 11 May 1987; revised 3 September 1987

Abstract. The load dependence of Vicker's indentation hardness has been measured in some non-metallic materials and thin foils. A load of 100 g appears to be appropriate for comparing materials. Foil thickness, especially for soft metals like copper, must be at least twenty times the impression diagonal to get a correct value of hardness. The Meyer index varies for materials and can be used for comparison because it seems to pertain to the nature of chemical bonds. The index for boron carbide is similar to glass as was expected by Rice.

Keywords. Indentation hardness; microhardness; Vickers hardness; non-metallic materials.

1. Introduction

Hardness measurements are commonly carried out to estimate the mechanical strength of a material as it is a measure of resistance against plastic deformation. A microhardness tester using a Vickers or Knoops indenter is a compact machine which can give a quick and qualitative estimate of the hardness number. The resistance to penetration by a sharp indenter is the measure of hardness. Apart from being a strength microprobe it correlates other physical properties as well, such as the presence of other phases, inhomogeneity, anisotropy and surface conditions of a material (Gilman 1973). As the required size of material is small, it is a convenient method. But there are practical difficulties in its usage and comparison with results available in the literature, because the loads used are different. In the microhardness range (< 1 kg load) the hardness number VHN is found to be a function of load applied, especially for non-metallic materials (Buckle 1959). In this work different non-metallic materials have been compared. Hard and brittle materials like the carbides, noncrystalline glasses, polymers and also metals have been used for measurements. Polycrystalline materials have been used to avoid anisotropy effects in comparison. It is felt that Meyer index can be used for comparing materials because it pertains to the nature of the chemical bond. Boron compounds, though crystalline, show amorphous-like behaviour (Golikova and Samatov 1983). The conduction mechanism in boron carbide was similar to amorphous semiconductors (Saraswati *et al* 1985). In this study the Meyer index of boron carbide is found to be similar to the random network glasses.

2. Experiment

The materials compared are sintered boron carbide, tungsten carbide, a metglass, sodalime glass, a plastic, araldite mould aluminum and copper foils to represent soft, hard materials, crystalline ceramics and non-crystalline glasses. The carbide pellets, in which the reflectivity was low, were polished with a diamond paste of 0·25 μm grit size. Mechanical polishing affects the results. It was not adopted unless found necessary. The density of the tungsten carbide pellet was 98% of the theoretical density. The boron carbide pellets were 92% and 95% dense and the grain sizes were about 5 μ and 10 μ respectively. The metallic glass was a piece from a ribbon, 300 μm thick. The copper foils were of thickness 400 and 1200 μm. The thin foil was 99·9% pure whereas the thick one was of commercial grade. The aluminum sheet was 2 mm thick. A 3 mm thick plastic piece and a well-aged araldite mould represent the polymers. The surface was ultrasonically cleaned with water for plastic and glass and swabbed with dilute acid for copper to remove the oxide layer. A Leitz microhardness tester with a diamond pyramidal indenter was used. The load could be varied from 5 to 500 g in fixed steps. The load duration could be varied. When the duration was changed from 10 to 50 sec or more no appreciable change was detected. Hence it was kept at 25 sec throughout the study. For each load an average of atleast ten impressions were recorded for measuring the length of impression diagonal to d. The hardness was calculated using the formula

$$H = 1854{\cdot}4\,(P/d^2), \tag{1}$$

where P is the load expressed in g, d is in microns and H in kg/mm^2. Ridging and sinking of material on unloading result in impressions which are not square but are convex or concave (Buckle 1959). These affect the diagonal length measurements to an extent of 10%. Errors also arise due to poor reflectivity, numerical aperture etc. When the impression is small, the percentage error is greater.

3. Results and discussion

3.1 *Influence of heterogeneities*

The influence of porosity and heterogeneities in the hardness values were noticed in the carbides as can be seen from figure 1 which shows a plot of hardness against the load applied in the carbides and a reference steel metal. The hardness is higher for a denser boron carbide. The humps seen for a boron carbide and tungsten carbide are attributed to impure phases present, which were noticed earlier (Saraswati 1987) in microstructure and radiation damage study. When a material contains precipitates or other heterogeneities the hardness can increase. This will create fluctuations in the hardness values and produce humps. Irradiation reduced the hardness further (Saraswati and Rao 1985). A load of 200 to 300 g produced a good impression. For smaller loads the impression was small and the measurement error was large whereas for loads of 500 g or more cracks appeared and reduced the hardness. Hardness variation due to load had also been observed earlier (Buckle 1959). In tungsten carbide cracks appeared above 200 g load.

3.2 *Surface and thickness effects*

In metglass ($Fe_{40}Ni_{40}B_{20}$) and sodalime glass polishing was found to reduce the inhomogeneities and hardness value as denoted by the smoothened humps (figure 2). It is understandable if the heterogeneity was on the surface. As the glasses are quenched from the melt inhomogeneities are likely. In the metglass the hardness

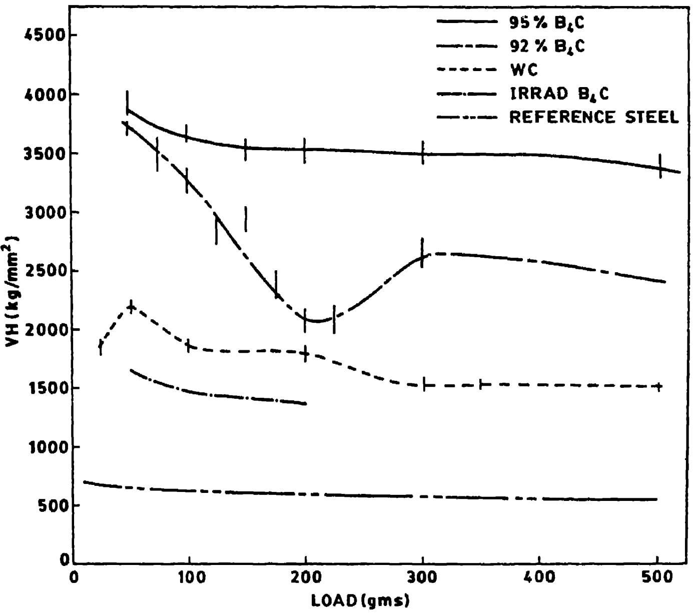

Figure 1. Hardness measurements in carbides.

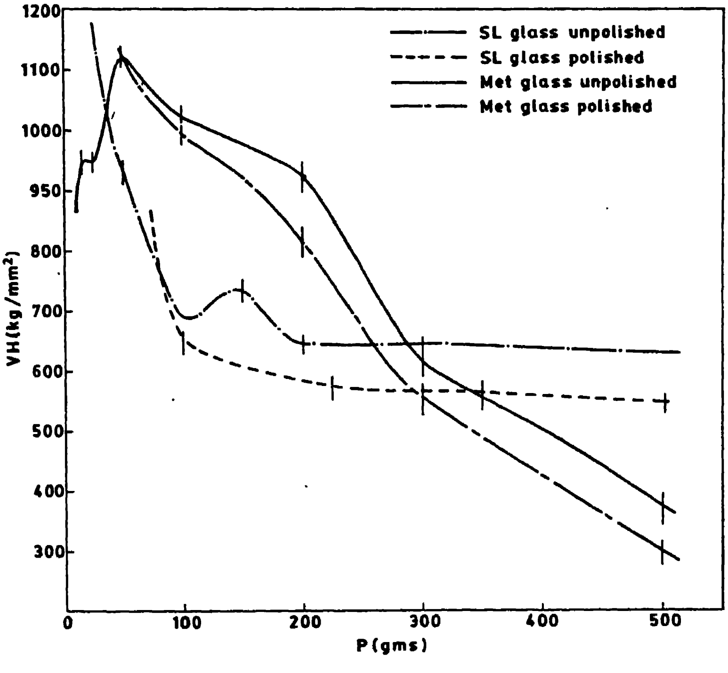

Figure 2. Effect of polishing in glasses.

continued to decrease with increase in the load. In soda lime glass hardness approached a steady value above 100 g. Comparison of a thin and thick foil showed the influence of thickness in copper. The specimen thickness normally recommended is about ten times the diagonal. At 15 g load, d was 13 μm for both the thin and the thick foil. At 25 g, d was 21 μm for the thin foil which is about 1/20th the thickness of the foil but the hardness was lower. As the load increased the hardness number reduced rapidly. The impression was highly concave indicating severe sinking of the material. There was a visible depression in the foil as there was no resistance to deformation. Adhesion was also noticed. During plastic flow adhesion takes place in softer metals when the elastic stresses are smaller. In harder specimens elastic recovery breaks any such effect.

Thin foils of metals and alloys are normally used in some investigations because grinding these for TEM observations is easier. As is seen here the impression diagonal when compared to or is a large percentage of thickness erroneous results will be obtained unless the load is small. But very low loads such as 20 or 50 g can give an elevated value. The best suited load appears to be 100 g and hence materials investigated should have a reasonable thickness depending on the hardness of the material.

3.3 *Appropriate load*

At small loads i.e. <50 g, hardness increased rapidly in all materials. The exact load at which this happens depends on the material and normally appeared at impression diagonals less than 10 μm. This appeared to be due to surface, which might contain adsorbed gases or moisture or remnants of occluded abrasives or due to intrinsic difference in the surface and bulk density. One possibility is that equation (1) which

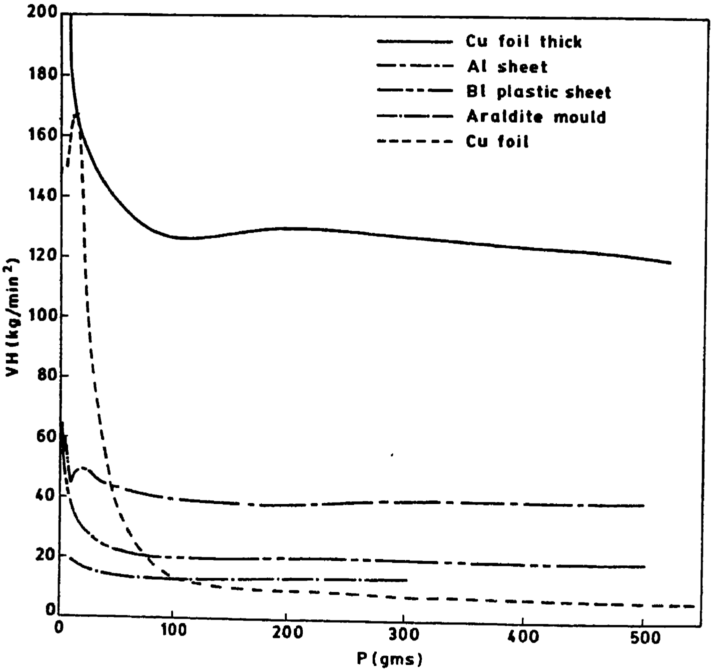

Figure 3. Vickers hardness in polymers and copper foils.

is derived for a plastic contact may not be valid at low loads when the contact is elastic. Several other explanations given which hold specially for metals were Orowan's model of workhardening and coherent regions suggested by Buckle (1973).

An empirical formula of Meyer states that load is related to impression diagonal as

$$P = ad^n, \tag{2}$$

where n is the Meyer index. Comparing with (1)

$$H = bd^{n-2}. \tag{3}$$

Thus hardness is independent of load only when $n = 2$. From (2) we can see that a plot of $\log P$ vs $\log d$ should be a straight line with slope n. Figure 4 shows the plot for various materials investigated. The hard materials are on the left and the polymers are on the right in this diagram. The slopes deviate from 2. The values are listed in table 1. The metals have an index close to 2, whereas the oxide glasses and ceramics have a low value of $n = 1{\cdot}66$. The metglass and polymers exhibit an intermediate value of 1·85. The differing n values had been observed earlier and attempts were made to modify (2) by incorporating other powers of d in an empirical way. It is felt that n is related to the chemical bond. In a metal, impurity and defects determine whether a material is soft or hard, whereas in a covalent compound the intrinsic strengths of the chemical bond determine its hardness. Gilman (1973) had shown that hardness vs elastic modulus had a slope of 1 for metals compared to 3/2 for semiconductors and covalently-bonded materials. The difference arises because the flow rate in metals is limited primarily by the interaction between dislocations, whereas in covalent crystals it is limited by the interaction between dislocation and chemical bonds in the compound i.e. short range (atomic) interactions are involved

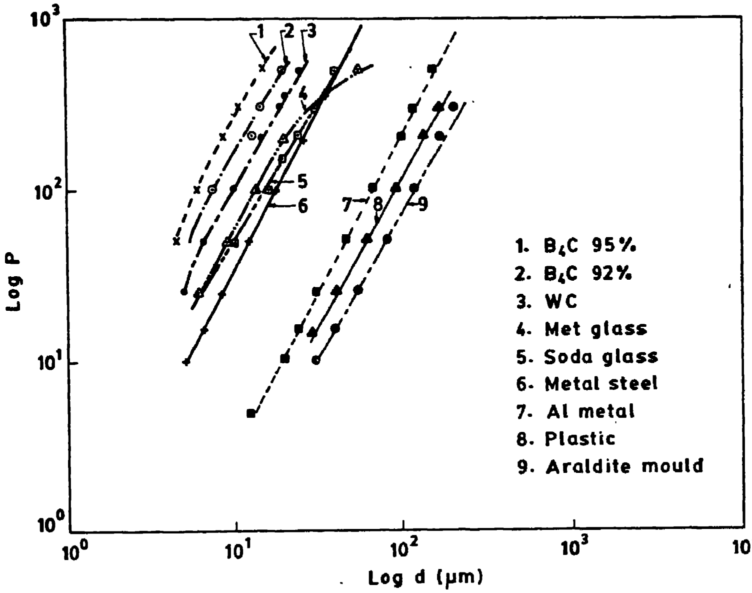

Figure 4. Load vs diagonal in various materials.

Table 1. Hardness at different loads and the slope of log *P* vs log *d*.

Material	Thickness	HV 200*	HV 100†	HV 50	HV(20)	Slope $n \pm {\cdot}01$
B_4C 95%	2 mm	3525	3650	3875		1·68
B_4C 92%	2 mm	3100	3250	3700		1·66
WC	3 mm	1800	1900	2200		1·66
Ref steel	5 mm	600	625	650		1·96
copper	1200 μm	130	127	137	>200	
copper	400 μm	10	14	37	167	
aluminum	2 mm	38	40	43	>50	1·92
plastic	3 mm	20	20	20	>60	1·80
araldite	1 cm	14	14	14	20	1·82
sl glass polished	2 mm	570	650	>800		1·66
sl glass unpolished	2 mm	640	680	930	>1000	1·66
Metglass polished	300 μm	815	1000	1120		1·81
Metglass unpolished	300 μm	925	1025	1110		

*HVX refers to hardness at a load X g.
†The deviation between HV 200 and HV 100 is the lowest.

in covalent materials whereas longer range (elastic) interactions are pertinent in metals. This is because the covalent bonds are highly stereospecific. Hence plastic characteristics will be closely connected with electronic characteristics of covalent materials. This can explain the difference in the Meyer index. It is also noted that the curves are linear in the load range 100 to 200 g even for plastics in which the hardness is low. The hardness values at different loads are compared in table 1. If one considers a standard load for all materials, 100 g is appropriate except for hard carbides for which 200 g is probably better.

3.4 *Hardness of boron carbide*

A material accommodates indentation by slipping around the sides of the indenter or by compressing radially under the indenter. For ductile metals the microhardness H is related to the uniaxial flow stress Y as $H = CY$ where C is the constraint factor (Tabor 1951). For ductile metals $C = 3$, whereas for polymers and glasses it is less than 3. It is so because, in the region of indentation (influence zone), the plastic and elastic strains are comparable for non-metals whereas the strain is essentially plastic for ductile metals. An elastoplastic interpretation is needed when the material displaced by the indenter is accommodated elastically by the surrounding medium. This was taken into account by Marsh (1964) and Johnson (1970). Thus, materials can be distinguished as those with high E/Y (e.g. metals) and those with low E/Y (non-metals like glass or polymers) because of the following reasons: (i) metals are dense whereas the non-metals are not and so can be compressible under an indentation load, (ii) metals prefer deformation by slip whereas non-metals prefer compression and a uniform stress distribution as in liquids and (iii) metals normally have a long range order whereas order is short ranged in glasses and partial in polymers.

For glasses and polymers Marsh (1970) derived an expression

$$H/Y = 0{\cdot}28 + 0{\cdot}60 \ln 0{\cdot}7\, E/Y. \qquad (4)$$

From this expression we get $E/Y=133$ when $H/Y=3$. This represents the critical value for distinguishing the low and high E/Y regimes. Steels have E/Y in the range 300 to 1000 depending upon the composition while glasses and polymers have E/Y near 25. This variation is to be ascribed to their atomic structure and chemical bonds. The demarcating value for H/E is 0·02 (metals have lower and non-metals higher). Many covalent ceramics are found to deform by slip or twinning like metals (Rice 1973) though H/E is $>0{\cdot}02$. Hence Rice (1973) suggested that low E/Y materials should be further distinguished as those with low E as for polymers and those with large Y as for covalent crystalline ceramics like the carbides. H/E is 0·07–0·09 for boron carbide from experimental values. Table 1 shows that boron carbide is similar to glasses if the Meyer index is a criterion. Hence Rice's suggestion appears valid. Moreover several properties of boron carbide are akin to amorphous materials. It is a semiconductor with hopping electron conduction (Saraswati *et al* 1985) and has a temperature-dependent susceptibility (Saraswati and Paulose 1987).

Boron carbide has a hardness next only to diamond. Its structure consists of interconnected B_{12} icosahedra in layers linked by C-B-C chains. Boron and carbon contain *p* electrons in their outer orbitals and they are responsible for the high covalency of B-C bond. Hence sintering of this ceramic is difficult and is possible only close to the melting point, 2300°C. Gilman (1973) has shown that for carbides a correlation between chemical bond and hardness can be expected because strong chemical forces inhibit dislocation movements. The heat of formation was found to be proportional to the hardness. According to Samsonov (1970), the high value of hardness in carbides is connected with the localization of valence electrons at nuclei with the formation of stable sp^3 configuration which determines the rigidity and direction of chemical bonds. In the configuration-localization model of Samsonov (1970), the hardness of carbides is determined by the probability of stable sp^3 configuration of valence electrons being formed at the C atoms and this depends on the donor-acceptor properties of the constituent metal. When a carbide is formed, the non-localized electrons of the metal are transferred to C atoms and are maintained there by the exchange interaction, stabilizing the sp^3 configuration of C. This sp^3 configuration stability accounts for the hardness of boron carbide and diamond. Brittleness is also associated with the localization of electrons. Plastic deformation decreases with decreasing localization and increasing sp^3 configuration stability. The high strength and melting point of boron carbide are attributed to this.

4. Conclusions

From the experimental observations it is concluded that (i) Vicker's microhardness numbers in non-metals increase at low loads independent of the surface finish and in all materials. At loads of 300 g or more, appearance of cracks reduces the hardness. A load of 100 g seems to be appropriate for comparing materials. For soft materials the specimen thickness should be atleast 15–20 times the diagonal impression length at this load. (ii) The metglasses normally come as ribbons, few hundred microns thick. The impression diagonal is small because the metglasses are hard. The inhomogeneity of the material can be tested using the load variation of hardness. (iii) The Meyer index varies for materials and can be used for comparison. Highly covalent boron carbide and sodalime glass have similar index probably because of the similar sp character of the bonds.

Acknowledgement

The author thanks Dr P Rodriguez for his comments and suggestions.

References

Buckle H 1959 *Metall. Rev.* **4** 49

Buckle H 1973 *The science of hardness testing and its research applications* (eds) J H Westbrook and H Conrad (Ohio: ASM) p. 453

Gilman J J 1973 *The science of hardness testing and its research applications* (eds) J H Westbrook and H Conrad (Ohio: ASM) p. 51

Golikova O A and Samatov H 1983 *Phys. Status Solidi A* **77** 449

Johnson K L 1970 *J. Mech. Phys. Solids* **18** 115

Marsh D M 1964 *Proc. R. Soc. London* **A279** 420

Rice R W 1973 *The science of hardness testing and its research applications* (eds) J H Westbrook and H Conrad (Ohio: ASM) p. 117

Samsonov G V 1970 *Refractory carbides* (New York: Consultants Bureau)

Saraswati V 1987 *Nucl. Instrum. Methods* **B23** 347

Saraswati V and Rao G V N 1985 *J. Mater. Sci. Lett.* **4** 260

Saraswati V and Paulose P L 1987 *J. Less Common Metals* **128** 185

Saraswati V, Nandedkar R V and Radhakrishnan T R 1985 *Proc. of Solid State Symp. Nagpur* (Bombay: BARC) **C28** 123

Tabor D 1951 *The hardness of metals* (Oxford: Clarendon Press)

Bull. Mater. Sci., Vol. 9, No. 4, November 1987, pp. 295–303. © Printed in India.

Increase in the yield of silicon carbide whiskers from rice husk

B V RADHAKRISHNA BHAT and G P SANGHI*

Defence Metallurgical Research Laboratory, Kanchanbagh, Hyderabad 500 258, India

*Present address: Defence Research and Development Laboratory, Hyderabad 500 258, India

MS received 18 May 1987; revised 7 July 1987

Abstract. Favourable conditions for the growth of good quality silicon carbide (SiC) whiskers from rice husk have been discussed in the light of available evidence on the probable growth mechanism and the theoretical understanding of the same. Preliminary results indicate an increase in whisker yield at lower temperatures and coarsening of whiskers with longer duration of conversion.

Keywords. Silicon carbide whiskers; rice husk; vapour-liquid-solid process.

1. Introduction

Silicon carbide whiskers have emerged as an attractive reinforcement in both metal and ceramic matrix composites. Silicon carbide whisker-reinforced aluminium is the topic of many recent research papers (Nair *et al* 1985; Flom and Arsenault 1986; David 1985; Vogelsang *et al* 1986) after the original one by Divecha *et al* (1981) and is reported to be a strategic material. Silicon carbide whiskers have been reported to be useful in enhancing the strength, fracture toughness and reliability of ceramic matrix composites (Sudarshan and Musikant 1985; Tiegs and Bacher 1986). All this has become possible due to the development of processes to produce silicon carbide whiskers on a commercial scale. Table 1 gives the properties of these whiskers as reported in literature (Sudarshan and Musikant 1985).

Milewski *et al* (1985) listed various methods that have been reported to be useful in producing SiC whiskers. One of them is the process developed by Lee and Cutler (1975) in the University of Utah wherein it was demonstrated that SiC may be produced by the pyrolysis of rice husk yielding part of the product in the form of whiskers. Although various authors (Milewski *et al* 1973; Lakiza and Dyban 1982) have described this process, the optimum parameters for a higher yield of whiskers in the product are not mentioned in the literature probably due to the commercial interests involved. In this paper, an attempt has been made to discuss the probable whisker growth mechanism and the favourable conditions for enhancing the yield of whiskers in the light of available evidence and the theoretical understanding of the process. Preliminary work has in fact proved the validity of some of the suggested favourable conditions.

2. Process

Rice husk, a waste product of rice milling, is an ideal raw material for silicon carbide production, since in natural form it contains amorphous silica and carbon in a finely mixed form. The typical composition of rice husk and its ash (Bechtold *et al* 1982) is

Table 1. Properties of commercially available SiC whiskers.

Material	Manufacturer	Density (g/cc)	Diameter (μm)	Length (μm)	Tensile strength (MPa)	Tensile modulus (GPa)
SILAR SC-9	ARCO Metals Greer. SC USA	3·20	0·6	10–80 (80 wt%)	6895	689
SCW-1	Tateho Chemical Ind. Co., Japan	3·21	0·1–0·5	10–40	20685	483

Table 2. Typical composition of rice husk and its ash.

Compound	Weight (%)
Raw rice husk analysis	
Organics	59·5
Carbon	18·8
Ash	20·6–21·7
Ash residue analysis	
SiO_2	96·27
K_2O	1·10
SO_3	0·57
P_2O_5	0·39
MgO	0·35
Na_2O	0·25
Fe_2O	0·10
Al_2O	0·10
TiO_2	0·08

given in table 2. The main steps involved in the formation of silicon carbide from rice husk are shown in figure 1.

The reaction steps have been discussed in detail earlier (Lee and Cutler 1975; Bechtold *et al* 1982). The silicon carbide formation occurs by the reaction

$$SiO_2 + 3C \rightarrow SiC + 2CO, \qquad (1)$$

where excess carbon is available. But, due to the uneven distribution of silica within the rice husk (Sharma *et al* 1984; Bechtold *et al* 1982) it may proceed through any of the following steps:

$$SiO_2 + C \rightarrow SiO + CO, \qquad (2)$$
$$SiO + 2C \rightarrow SiC + CO, \qquad (3)$$
$$SiO + 3CO \rightarrow SiC + 2CO_2, \qquad (4)$$
$$SiO + CO \rightarrow SiC + O_2. \qquad (5)$$

Lee and Cutler (1975) suggested that the reaction proceeds mainly via the gas phase and the rate-controlling step is the carbothermal reduction of silica to form SiO and CO (equation (2)). Bechtold *et al* (1982) concluded that the excess carbon in the interior cell-walls leads to the formation of silicon carbide particulates by the solid state reaction (1) above, while the silicon carbide whiskers grow on the outer cell-walls by the vapour phase reactions (2), (3), (4) and (5).

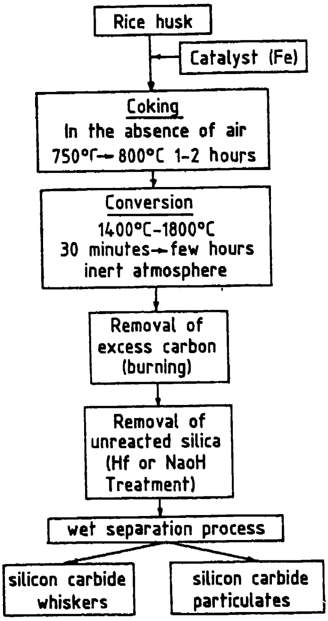

Figure 1. Steps in the formation of silicon carbide whiskers from rice husk.

3. Evidence for the probable growth mechanism

There are two important mechanisms of whisker growth from vapour phase, namely the Frank mechanism and the vapour-liquid-solid (VLS) mechanism (Evans 1972). The former suggests that whiskers contain one or more screw dislocations parallel to their growth axes and the steps or ledges due to the dislocations at the whisker tips provide the energetically-favoured sites for growth to continue. The latter postulates that the presence of small liquid droplet acts as a preferred site for whisker growth at the tip of each whisker.

Observations by various authors in regard to silicon carbide formation from rice husk (Lee and Cutler 1975; Lakiza and Dyban Yu 1982; Bechtold *et al* 1982) and the studies concerning the structure of whiskers produced from rice husk (Nutt 1984; Sharma *et al* 1984) have provided an insight into the most probable growth mechanism operating in this process.

Nutt (1984) discussed the various types of defects found in the silicon carbide whiskers grown from rice husk. Frank mechanism was ruled out due to the absence of axial screw dislocations in any of the whiskers. The abundance of cavities observed in the core regions of these whiskers points to the possibility of a two-stage growth process in which a whisker grows rapidly in length by the VLS mechanism followed by a slower lateral growth by some other mechanism. The cavities could arise from the entrapment of carbon monoxide gas evolved during the rapid growth period. Subsequent lateral growth at slower rates might account for the absence of cavities outside the whisker core region. The radial partial dislocations associated with the cavities are attributed to the nucleation of faulted regions near the whisker core, followed by crystal growth in radial directions. Sharma *et al* (1984) also observed a similar high density of planar defects and hollow whiskers, concluding that their work provides limited support to the VLS mechanism as spheres were sometimes found on the whisker tips.

It was concluded by earlier workers (Lee and Cutler 1975; Bechtold *et al* 1982; Lakiza and Dyban Yu 1982) that the whisker growth occurs from the vapour phase while Lakiza and Dyban Yu (1982) confirm the presence of spheroidal whisker tips suggesting a VLS mechanism of whisker growth. Although Lee and Cutler (1975) have not mentioned about the whisker growth mechanism, the photograph of whiskers presented by them clearly shows whiskers ending with spherical tips. Hence, various evidences mentioned above largely suggest VLS mechanism, combined with possibly other less important mechanisms depending upon changing parameters. A better understanding of the VLS mechanism is therefore expected to give a higher yield of whiskers. Evans (1972) gave a detailed analysis of the VLS mechanism and outlined the parameters essential for this growth mechanism to operate while Milewski *et al* (1985) and George and John (1985) described a VLS process of growing silicon carbide whiskers.

4. Suggested conditions for favourable growth

Whisker growth from vapour phase is essentially a preferential nucleation and preferential growth process. To increase whisker yield, both nucleation and growth must be controlled. The thermodynamics, kinetics, temperature, gas flow rates, availability and concentration of growth species, Si/C ratio and a free space to grow are some of the important considerations.

4.1 *Temperature*

To control nucleation, i.e. to promote heterogeneous nucleation and to avoid homogeneous nucleation, it is necessary to control supersaturation and provide preferential nucleation sites. Higher supersaturations lead to spontaneous homogeneous nucleation and higher temperatures will lead to higher supersaturations. A temperature slightly above the equilibrium temperature of the reaction responsible for SiC formation must therefore help in avoiding homogeneous nucleation. An increase in temperature, apart from increasing the supersaturation level, usually reduces the contact angle between the alloy droplet and the substrate and eventually a smooth film growth can result (Evans 1972). Lakiza and Dyban Yu (1982) also suggested lower temperatures for a different reason. They believe that higher temperatures favour the formation of crystalline SiO_2 and silicates which are more stable and less reactive thus effectively hindering SiC formation.

4.2 *Atmosphere*

Bechtold *et al* (1982) discussed the inert atmosphere to be used for the conversion. Argon is the inert gas used in their process for conversion. Nitrogen can be used, but at lower temperatures it has the tendency to react to form silicon nitride. Carbon monoxide can also be used but large concentrations can inhibit the reaction as it is a product of reaction nos. (1), (2) and (3). Hydrogen can also be used, but offers no real advantage even though it might help to increase the SiO concentration by the reaction

$$SiO_2 + H_2 \rightarrow SiO + H_2O. \qquad (6)$$

Vacuum will be unfavourable to whisker growth as it will remove the vapours containing the whisker growth species. Being a vapour phase reaction, even the flow rates of the inert or reducing gases supplied through the sample must be kept low to prevent sweeping the gaseous reactants away from the growth site. Fast moving gases can also destabilize the liquid droplet at the whisker tip and hinder whisker growth. The composition of the gases must be adjusted so as to provide a correct Si/C ratio for whisker growth.

4.3 *Catalyst*

A catalyst must be selected so as to form an alloy droplet at the conversion temperature with the reacting species and must have the correct distribution coefficient between the liquid and the solid whisker. It must also have a low vapour pressure at the growth temperature. Lee and Cutler (1975) used Fe as a catalyst, while Milewski *et al* (1985) mention 304 stainless steel as the catalyst. George and John (1985) tried a Mn-Ni-Co alloy as the catalyst.

4.4 *Conversion chamber design*

A proper growth chamber is essential to ensure (i) a substrate for the whiskers to nucleate, (ii) a free space for the whiskers to grow and (iii) a system to introduce the inert gases without disturbing the growing whiskers. Milewski *et al* (1985) and George and John (1985) described a growth chamber for their VLS process. We suggest an improved version of the same as depicted in figure 2, wherein the growth substrate plates have been made horizontal and the SiO generators have been kept on the sides. The horizontal plates are expected to give better stability for the liquid droplet on the whisker tips apart from providing a surface for uniform distribution of catalyst and sufficient free space for the whiskers to grow. Finely ground coked rice husk can be substituted for the fine mixture of SiO_2 and carbon (Milewski *et al* 1985)

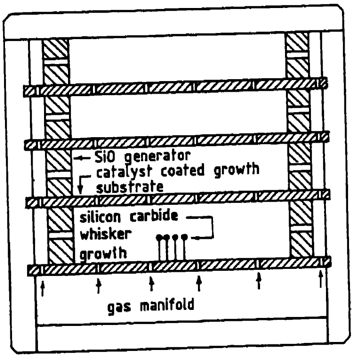
SiO generator
catalyst coated growth substrate
silicon carbide whisker growth
gas manifold

Figure 2. Whisker growth chamber design.

and impregnated into the porous bricks acting as SiO generators. The holes provided in the substrate plates and the SiO generators will help in the proper distribution of the gases prevailing within the chamber.

4.5 *Duration at high temperature*

Since whisker growth rates can be as high as a few mm/sec, the duration must be just sufficient for the whiskers to grow to their full lengths between the substrate plates. A duration longer than what is necessary will only lead to coarsening of the whiskers and also secondary whisker growth may occur leading to interlocking which is not desirable. It is also essential to keep the temperature constant throughout the whisker growth duration as any fluctuation can give rise to complications in terms of droplet stability, whisker diameter variation etc.

5. Experimental results

Preliminary studies were carried out to assess the feasibility of producing silicon carbide whiskers from rice husk. Rice husk obtained from local sources was dried and treated by soaking it in 3 wt% $FeSO_4$ solution at 75°C for 1 hr. $FeSO_4$ was then drained out and the husk was then soaked in 10 wt% NH_3 solution for 1 hr at room temperature. After soaking the husk was washed with water and dried at 110°C for 5 hr. This was then coked at 700°C for 30 min. Oxidation was prevented by covering the layer of rice husk with a thin layer of petroleum coke. The weight loss due to coking was 55%.

Coaked rice husk was heat-treated in two batches of 200 g each in a H_2 atmosphere furnace. One of them was treated at 1600°C for 30 min while the other was treated at 1500°C for 2 hr. The heat-treated samples were purified by burning off the excess carbon and leaching out the unreacted SiO_2 by boiling in NaOH solution. The filtered and dried product was analysed by X-ray diffraction. Samples of coked rice husk and the final product were also studied by SEM. X-ray diffraction data confirmed that the product was silicon carbide of the β polytype.

SEM analysis showed that the coked rice husk maintains its skeletal structure (figure 3) and that the final product is a mixture of submicron size silicon carbide particulates and whiskers. While the whisker content is very less (figure 4) in the sample treated at higher temperature there is a visible increase in the content of whiskers in the lower temperature treated sample (figure 5). Comparison of figures 4 and 5 reveals coarsening of whiskers in the longer duration treated sample. There is a frequent change in diameter and growth direction of whiskers in the longer duration treated sample, possibly due to fluctuations in temperature and the non-availability of free space for the whiskers to grow straight.

6. Conclusion

Experimental evidence and observations of the various authors available in literature suggest VLS mechanism to be the most probable mechanism operating in the growth of silicon carbide whiskers from rice husk. Even if VLS mechanism is not the only operating mechanism, it is felt that by promoting favourable conditions for the VLS

Figure 3. Scanning electron micrograph of coked rice husk.

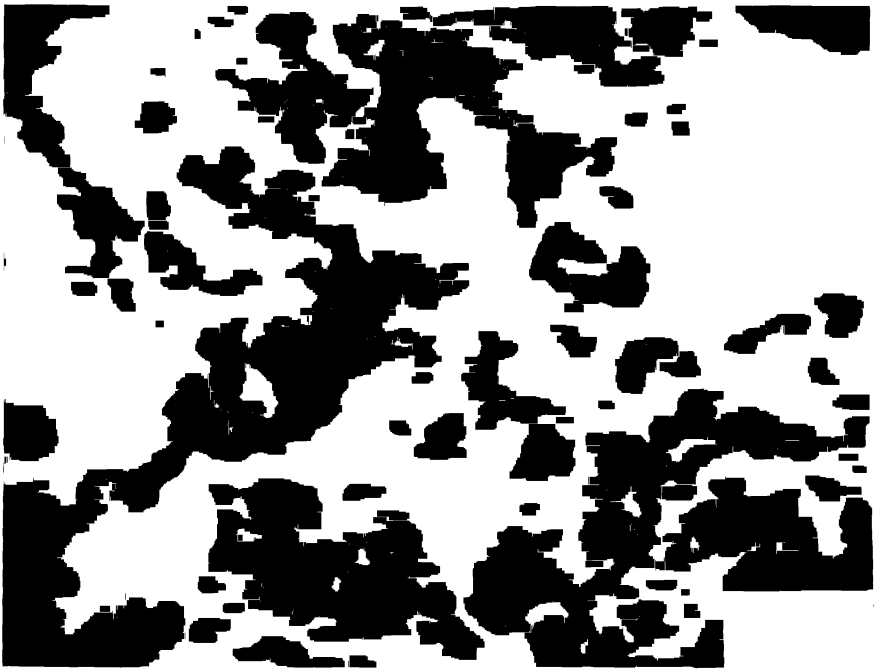

Figure 4. Scanning electron micrograph of silicon carbide formed at 1600°C (30 min duration).

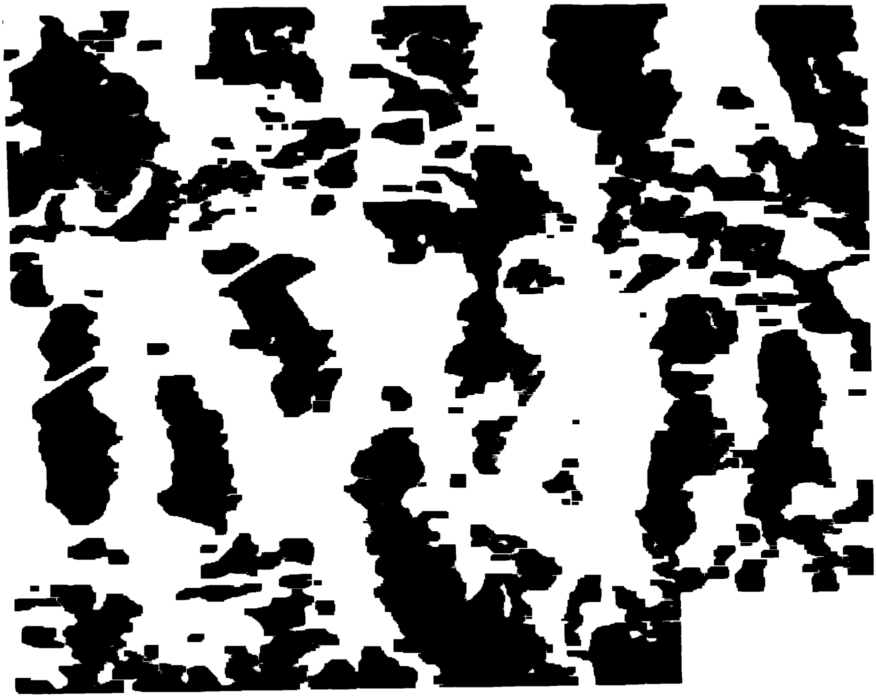

Figure 5. Scanning electron micrograph of silicon carbide formed at 1500°C (2 hr duration).

mechanism, it will, however, be possible to increase the yield of good quality silicon carbide whiskers from rice husk. Preliminary experimental work confirms some of these ideas.

Acknowledgements

The authors are grateful to Dr P Rama Rao for encouragement. Experimental assistance of Mr P Balakrishna, (Nuclear Fuel Complex, Hyderabad), Mr Y V Rama Krishna and Mr K Ramanjaneyulu is gratefully acknowledged.

References

Bechtold B C, Beatly R L and Cook J L 1982 *Progress in science and engineering of composites* (eds) Tsuyoshi Hayashi, Kozo Kawata and Sokichi Umakawa; (Tokyo: The Japan Society for Composite Materials) p. 113–120

David M L 1985 *Metall. Trans.* **A16** 1105

Divecha A P, Fishman S G and Karmarkar S D 1981 *J. Met.* **33** 12

Evans C C 1972 *M and B monograph ME/8 whiskers* (ed) J Gordon Cook (London: Mills and Boon Ltd) Chapt. 1, 2 and 3

Flom Y and Arsenault R J 1986 *J. Met.* **38** 31

George Hurly F and John Petrovic J 1985 *Advanced composites conference proceedings* (Michigan: American Society for Metals) p. 207–212

Lakiza S N and Dyban Yu P 1982 *Sov. Powder Met. Met. Ceram.* **21** 117

Lee J G and Cutler I B 1975 *Ceram. Bull.* **2** 195

Vogelsang M, Arsenault R J and Fisher R M 1986 *Metall. Trans.* **A17** 379
Milewski J V, Gac F D, Petrovic J J and Skaggs S R 1985 *J. Mater. Sci.* **20** 1160
Milewski J V, Sandstrom J C and Brown W S 1973 *Silicon carbide* (eds) R C Marshall, J W Faust Jr and C E Ryan (Columbia: University of South Carolina Press) p. 634
Nair S V, Tien J K and Bates R C 1985 *Int. Met. Rev.* **30** 275
Nutt S R 1984 *J. Am. Ceram. Soc.* **67** 428
Sharma N K, Wendell W S and Zangwill A 1984 *J. Am. Ceram. Soc.* **67** 715
Sudarshan S C and Soloman M 1985 *Ceram. Eng. Sci. Proc.* **6** 663
Tiegs T N and Bacher P F 1986 *Ceram. Eng. Sci. Proc.* **7** 1182

Bull. Mater. Sci., Vol. 9, No. 4, November 1987, pp. 305–308. © Printed in India.

Development of a Sievert's type gas doping apparatus

B BANDYOPADHYAY, A GHOSHRAY and N CHATTERJEE
Saha Institute of Nuclear Physics, Calcutta 700 009, India

MS received 14 April 1987

Abstract. A high pressure and high temperature Sievert's type gas doping apparatus using indigenous components has been designed and fabricated for preparing metal hydrides. This has been tested by preparing vanadium hydride $VH_{0.8}$. Proton NMR of this hydride has been observed and compared with earlier reports.

Keywords. Metal hydrides; hydriding apparatus.

1. Introduction

Recently, research on hydrogen in metals has attracted considerable attention both from theoretical as well as applied points of view. The electronic and magnetic properties of hydrides of some transition metals and their intermetallic compounds are being studied. These materials are normally hydrided at elevated temperatures in the presence of hydrogen at a high pressure and the hydriding reaction is therefore done in a closed chamber called the hydriding apparatus. We have designed and fabricated a Sievert's type hydriding apparatus (Mueller *et al* 1968) using indigenous components and the hydriding experiment has been successfully carried out in the apparatus.

The working range of temperature and pressure for the hydriding apparatus to be fabricated has to be suitably selected for the particular systems of interest. The phase diagrams of different hydrides provide the appropriate temperatures and pressures for their synthesis. In our case, however, the availability of components as well as the ease of fabrication also had to be considered and finally an apparatus was set up where hydriding experiments at a pressure of upto 3·5 MPa and in the temperature range from room temperature to 700°C were carried out.

2. Development

Figure 1 shows the details of the apparatus consisting of four main parts, viz the purifiers, the reservoir, the reactor chamber and the manometer with a standard volume. Different parts were connected by stainless steel tubes (i.d. = 4 mm) using compression type fittings. The inner volume of the tubes was reduced by inserting ceramic capillaries throughout the length. Only needle-type valves were used in our system. The valves were thoroughly checked before connecting to the system. While working with hydrogen, the complete gas-line manifold has to be absolutely leak-proof and leak tests should be conducted from time to time. The whole system was tested for leak-proof at 5 MPa. Also a vacuum of the order of 10^{-6} torr could be achieved and maintained throughout the manifold.

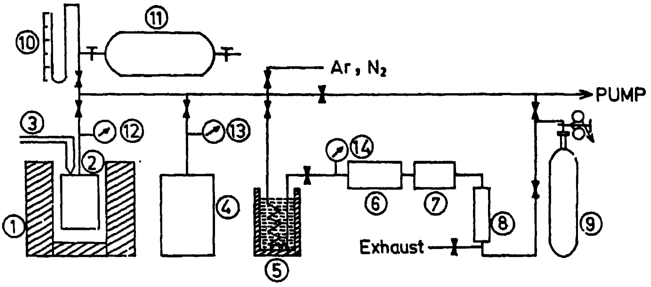

Figure 1. The hydriding apparatus. (1) furnace, (2) reactor chamber, (3) thermo-couple, (4) reservoir, (5) liquid N_2 trap, (6) activated charcoal container, (7) KOH pellet container, (8) silica gel column, (9) H_2 cylinder, (10) Hg manometer with scale, (11) standard volume and (12–14) pressure gauges.

2.1 *Purifier*

The hydrogen gas (IOLAR-2), supplied by the Indian Oxygen Limited, contains various impurities such as nitrogen (100 VPM), oxygen (4 VPM), moisture (4 VPM), oxides of carbon and nitrogen (2 VPM) and trace amounts of hydrocarbon and sulphur components. These impurities often exert an undesirable influence on the preparation of hydrides. For example, nitrogen and oxygen may create films of nitride and oxide respectively on the material surface preventing diffusion of hydrogen into the bulk. Some hydrides tend to lose their hydrogen concentration in the presence of moisture. Other impurities, in general, may adversely affect the hydriding process by surface poisoning.

To remove the impurities, hydrogen from the cylinder was made to pass slowly through a train of purifiers before reaching the reactor chamber. Moisture was removed by using a column of dehydrated silica gel. Potassium hydroxide pellets were packed in a horizontal column to remove carbon-dioxide through the reaction, $KOH+CO_2 \rightarrow KHCO_3$. Powdered activated charcoal was used as nitrogen getter. Finally, heavier gaseous impurities were arrested in a liquid nitrogen trap.

2.2 *Reservoir*

Purified and measured quantities of hydrogen can be stored here, if necessary. Pressure of the gas is measured using a Bourdon-type gauge.

2.3 *Reactor chamber*

Figure 2 illustrates the reactor chamber suitably designed to run for a number of heating and cooling cycles at high temperatures and pressures in an absolutely leak-proof condition. The whole chamber was cut out from a 62 mm rod of stainless steel which is the best chosen material for the reactor because of its hardness, small thermal expansion coefficient, low porosity and low gas absorption coefficient. Flange-type sealing with a metal gasket was used. Flat copper gasket, earlier annealed in hydrogen atmosphere and polished, was placed between the two circular

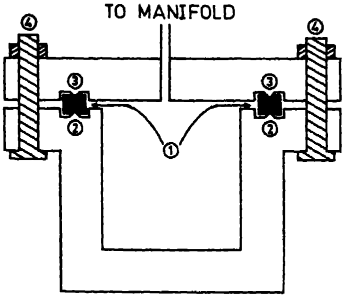

Figure 2. Cross-sectional view of the reactor chamber. (1) Cu gasket, (2 and 3) ridges on upper and lower flanges and (4) nuts and bolts.

ridges of the upper and the lower flanges. Of the various types of sealing tried, this was felt the most suitable method of sealing the reactor to work at a high pressure and a temperature as high as 700°C. Stainless steel bolts and nuts were used to maintain equal thermal expansion. The reactor chamber was also connected to a Bourdon-type pressure gauge.

2.4 *Manometer*

Concentration of hydrogen in the hydride samples was measured from the amount of gas evolved by thermally degassing a portion of the hydride sample in the reactor chamber and then by using PVT relations. The pressure of the evolved gas was measured from the mercury manometer. The volumes of the reactor chamber and the manometer were accurately measured by PV relations with the help of the manometer and a standard volume which is a cylindrical glass chamber with stop-cocks at both ends. The manometer and the standard volume were connected to the reactor chamber through capillary tubes of copper. The volume of the reservoir was 95 cc and that of the reactor chamber was 28·6 cc. The standard volume was 133·7 cc and the manometer had a volume of 8·2 cc.

3. Experiment

The gas doping apparatus which was fabricated was tested by hydriding pure vanadium. About 1 g of vanadium in pressed pellet form was etched in a solution of dilute hydrochloric acid and ethyl alcohol. After proper washing and drying, the pellet was taken in the reactor chamber, which was then connected to the manifold. The reactor chamber was then evacuated and flushed several times with hydrogen. The sample was completely outgassed and annealed by holding it for several hours in a dynamic vacuum at 500°C. Just after degassing, pure hydrogen was slowly injected into the reactor chamber from the reservoir. The rate of increment of pressure inside the reactor chamber, due to hydrogen injection, was less than 5 mm/min, as observed in the manometer. At this stage, the furnace temperature was lowered down to 450°C and a desired amount of hydrogen gas was loaded in the reactor. The reactor was then slowly cooled down to room temperature.

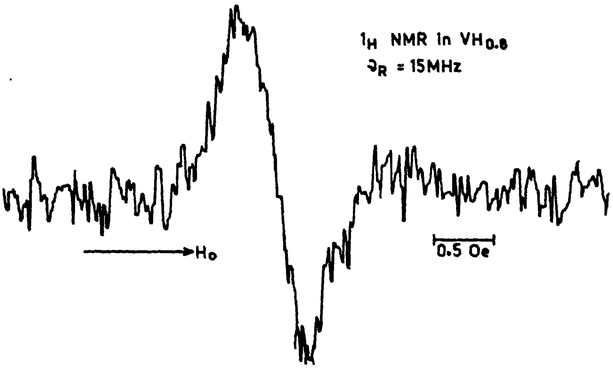

Figure 3. Absorption derivative of ^1H NMR in $VH_{0{\cdot}8}$ at room temperature.

The sample was again completely outgassed at 500°C and loaded with hydrogen in the same manner as described above. This method of hydriding and dehydriding the sample was repeated five to six times to activate the metal and finally the same procedure was followed to obtain the desired metal-to-hydrogen ratio in the hydride of vanadium. The reactor was then disconnected from the manifold, cooled in liquid nitrogen and the hydride was taken out and stored in normal atmosphere.

The vanadium hydride, VH_x, thus prepared, was then ready for measurements. The value of x, the molar hydrogen concentration was measured several times, each time by completely degassing about 0·1 g of hydride at 500°C in the previously evacuated reactor chamber. The pressure developed due to hydrogen liberated from the hydride was observed in the manometer. Using PVT relation, the value of x was calculated as $0{\cdot}8 \pm 0{\cdot}1$.

Proton NMR line of the above $VH_{0{\cdot}8}$ was observed in a cw wideline NMR spectrometer using proton-free probe. The line width at room temperature was very narrow, about 0·5 gauss (figure 3), as reported earlier (Zamir and Cotts 1964) for similar hydrides. Thus our fabricated gas-line manifold was tested for successful loading of hydrogen gas under high temperature and high pressure in a properly prepared host metal lattice.

Acknowledgement

The authors thank Dr K Ghoshray, Mr N Banerjee, Mr D R Sikdar and Mr A Biswas for their advice and active participation in fabricating the apparatus.

References

Mueller W M, Blackledge J P and Libowitz G G 1968 *Metal hydrides* (New York and London: Academic Press) p. 151

Zamir D and Cotts R M 1964 *Phys. Rev.* **134** A666

Bull. Mater. Sci., Vol. 9, No. 5, December 1987, pp. 309–315. © Printed in India.

Long term soft tissue response to metals, ceramics and composites—a comparative histopathological evaluation

MIRA MOHANTY†, K RATHINAM* and C C KARTHA**
Divisions of Pathophysiology, *Toxicological Screening of Materials, BMT Wing, **Pathology, Sree Chitra Tirunal Institute for Medical Sciences and Technology, Trivandrum 695 012, India

MS received 2 July 1987; revised 10 October 1987

Abstract. Soft tissue reaction to metals, ceramics and composites was investigated over a long period. Titanium, nitrided titanium, ruby, sapphire and carbon-carbon composite materials were used. Histological response was uniform for all materials despite their differing chemical and physical properties.

Keywords. Soft tissue reaction; metals; composites; ceramics; long term evaluation; biocompatibility.

1. Introduction

In recent years, there has been great progress in the development of prosthetic devices for implantation. Metals, ceramics and lately composites have found wide applications in surgery. Among metals, the excellent corrosion resistance and good strength of titanium has proved it to be very useful as an orthopaedic implant. Ceramics have been tested and applied clinically in humans as prosthesis in orthopaedics and dentistry. Currently, sapphire is being tested as disc material in artificial heart valves with nitrided titanium as cage material. Carbon-carbon composite finds wide application as orthotic devices, artificial limbs, tendon replacements, dental and maxillofacial implants. Considering a variety of future clinical applications, a comparative long-term study of these materials seemed to be of importance. In this paper a long term histological study of tissue reaction to five different materials, possessing different chemical and physical properties, is being presented.

2. Materials and methods

The materials investigated were titanium, nitrided titanium, sapphire, ruby and carbon-carbon composite. All materials were of uniform shape of 10 mm × 1 mm rods. The implants were sterilized by autoclaving prior to surgery and all surgical procedures were performed under general anaesthesia and under sterile conditions. Two rods of each material were implanted at different sites, in the paravertebral muscle of one side, with negative controls (proved non-toxic) in the contra-lateral side of rabbits.

The animals were observed closely for any acute post-surgical inflammatory response during the first 2 weeks of post-implantation period. At specific time intervals, the animals were sacrificed by exanguination. The implants were retrieved with surrounding tissue of approximately 2 cm thickness on all sides and were immediately placed in 10% buffered neutral formalin for fixation. The next day, each implant was removed carefully from the muscle and a gross examination of the implant as well as the site of implantation was made. Thick pieces (1 mm) of muscle all around the implant site were processed by the conventional method for paraffin embedding. Thin sections stained with haematoxylin and eosin were examined by light microscopy. The histological response was evaluated according to the scoring method of Turner *et al* (1973).

---

†To whom all correspondence should be addressed

3. Results

3.1 *Gross observations*

No acute post-surgical inflammatory reaction was observed in any animal. All implants at the end of 7 days were freely movable and not attached to the underlying muscle. The surface of all implants was smooth and the site of implantation showed a neat edge in the muscle. The implants and the surrounding muscle at the end of 6 weeks and 12 weeks showed a similar picture except in the case of carbon-carbon composite showing black discoloration of adjacent muscle, at the end of 6 months. All implants except titanium wire had a soft white material adherent to the surface. It was difficult to remove ruby, sapphire and nitrided titanium from the muscle after a year.

3.2 *Microscopic observations*

For most part the microscopic observations of the materials tested were uniform (table 1). At 7 days, there was moderate to marked necrosis of the skeletal muscle, with accompanying chronic inflammation (figure 1). Macrophages, lymphocytes and giant cells formed the cellular infiltrate. Repair was evident in the periphery by the

Table 1. 7 days post-implantation, histopathological evaluation of adjacent muscle.

Histopathology	Titanium	Nitrided titanium	Sapphire	Ruby	Carbon-carbon composite
Muscle necrosis	2+	2+	3+	3+	2+
Giant cells	2+	1+	3+	1+	2+
Lymphocytes	1+	0	2+	1+	0
Neutrophils	0	0	0	0	0
Eosinophils	0	0	0	0	0
Macrophages	2+	1+	3+	1+	1+
Foreign body debris	1+	1+	0	0	1+
Fibroblasts	3+	3+	2+	3+	3+
Fibrosis	1+	0	1+	2+	0
Fatty change	±	±	0	0	0
Haemorrhage	1+	0	±	0	±
Oedema	0	0	0	0	0

Scoring: Based on a 0 to 3+ scale; 0 = item not present; ± = item occasionally present; + = item present to a mild degree; 2+ = item present to a moderate degree; 3+ = item present to a marked degree.

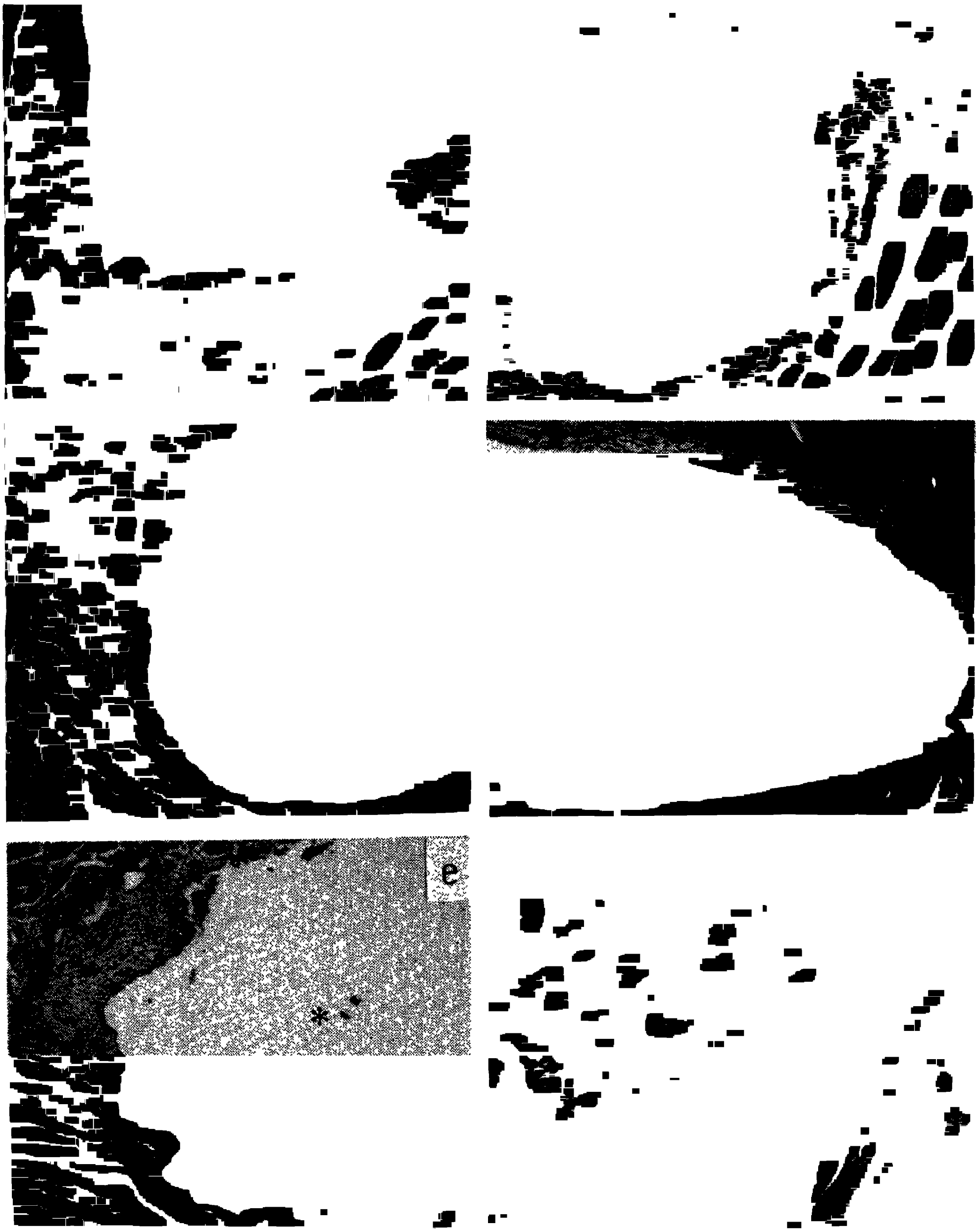

Figure 1. Light microscopic picture of tissue reaction around implants at 7 days (× 60). a. Titanium, b. Nitrided titanium, c. Sapphire, d. Ruby, e. Carbon-carbon composite and f. Higher magnification of tissue around titanium showing necrotic fragments of muscle and inflammatory cells (× 150).

presence of immature fibroblasts and a few mature fibrocytes. Comparatively, the reaction to sapphire was of a higher degree.

By 6 weeks, the inflammation had cleared up. A capsule consisting of mature collagen with a few fibrocytes was seen surrounding all implants (figure 2). No

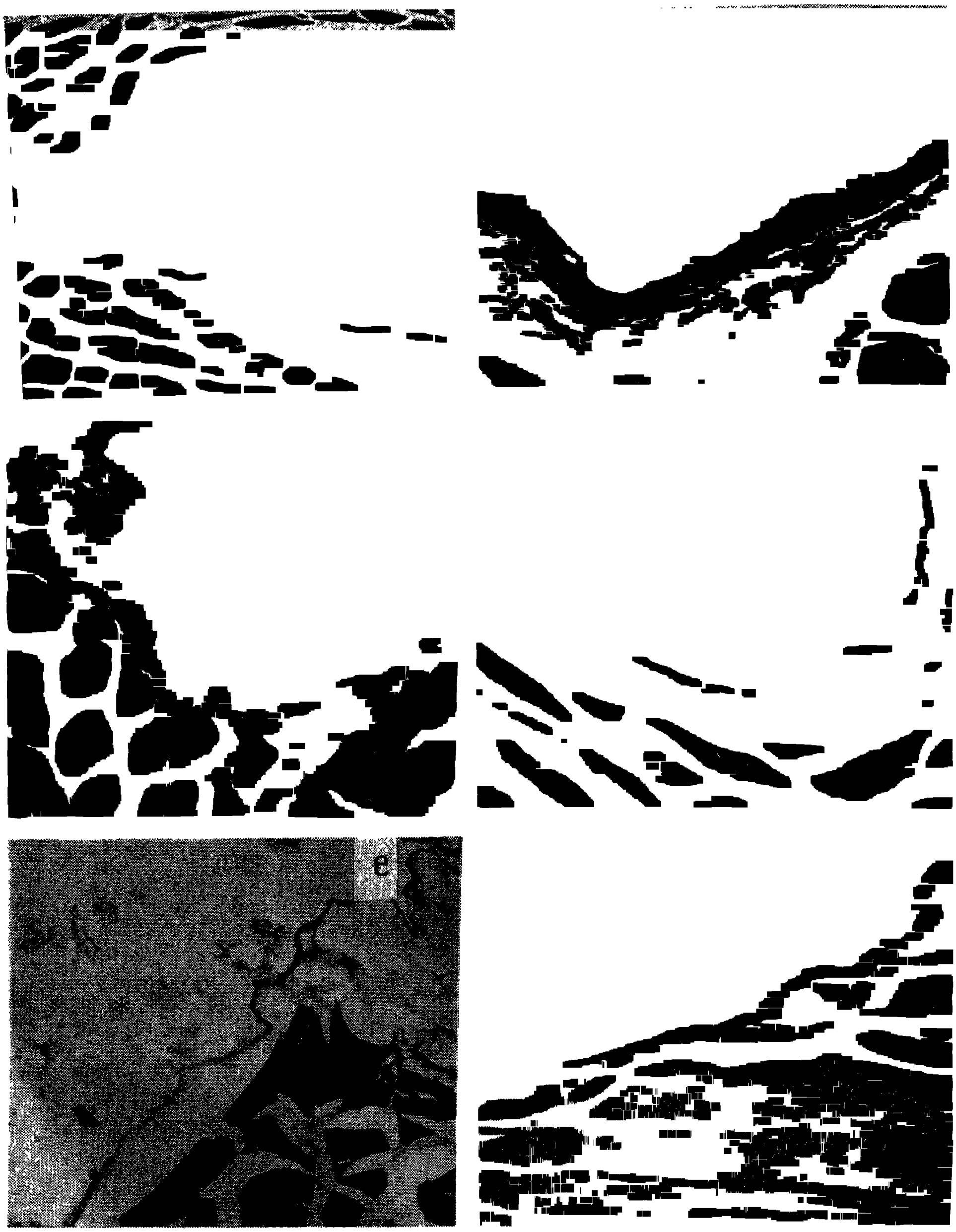

Figure 2. Photomicrograph of implant site at 6 weeks post implantation showing thir fibrous capsule (×150). **a.** Low magnification picture of capsule around titaniun (×60), **b.** Titanium, **c.** Nitrided titanium, **d.** Sapphire, **e.** Ruby and **f.** Carbon carbon composite.

inflammatory cells were noted. The fibrous tissue adjacent to nitrided titanium an carbon-carbon composites was reduced to thin fibrils of collagen at certain place having been separated off the surface of the implants.

The capsule decreased in thickness with time, till finally a very thin strip of con pressed collagen remained surrounding the nitrided titanium, ruby and sapphire at 1 year (figure 3). At all time intervals, particles of titanium and carbon were seen scattered in adjacent soft tissue (figure 4). These were golden yellow and black titanium and black carbon particles. At no time during this study, there was any evidence of tumours adjacent to the implants.

4. Discussion

The purpose of this study was to investigate the biological response of soft tissue to long term implantation of metals, ceramics and composite materials. Semi-quantitative histopathological evaluations were used to describe the tissue reactions.

The ideal biocompatible material for the construction of surgical prosthesis should not be toxic, allergic or carcinogenic. Nor should it cause any local inflammation, but should at most cause a thin encapsulation of the process. The response of inflammation, followed by repair, noted at 7 days, 6 weeks and 12 weeks in all implants, was due to the irritation and presence of a foreign body, rather than any toxic influence upon the surrounding soft tissue. The general histological trend of decreasing capsule thickness is typical of a reaction to a biologically acceptable material (Laing *et al* 1967). A similar observation has been made in the present study where there has been a failure to elicit any long term inflammation.

A soft white material was noted on the surface of implants at 6 months. This material resembles the layer or amorphous substance known to separate cells and extracellular fibrillar material from the surface of the implant (Albrektsson *et al* 1982). While removing the implant from the muscle, the adhesion between the two is

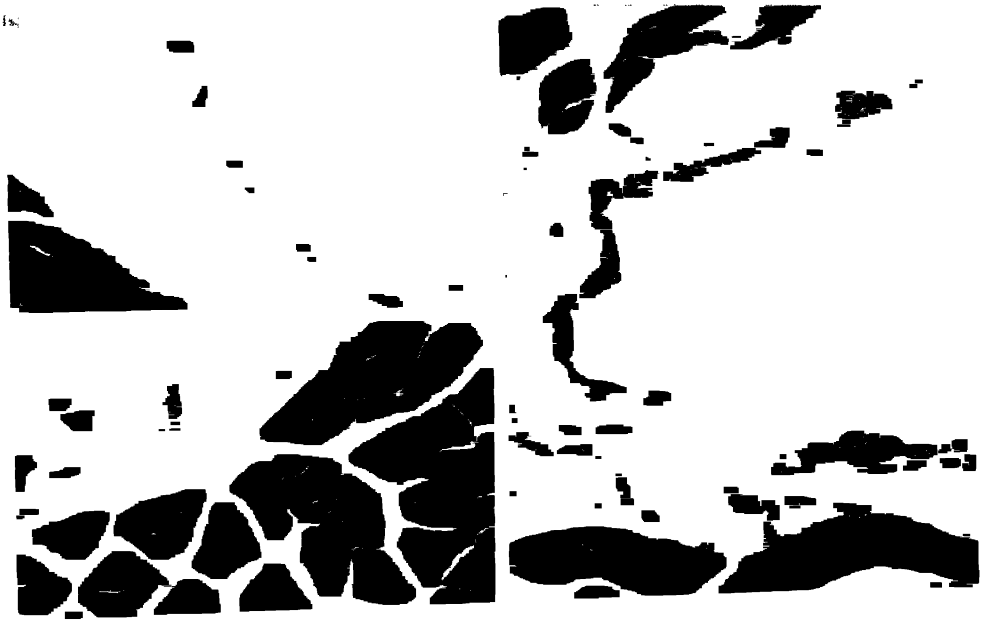

Figure 3. Photomicrograph of implant site at one year post-implantation (× 150). **a.** Nitrided titanium, **b.** Sapphire and **c.** Ruby.

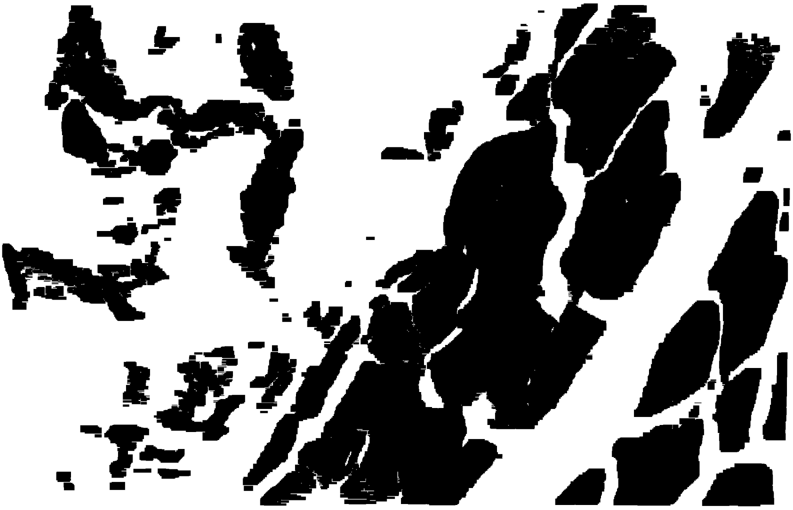

Figure 4. Photomicrograph of black carbon particles at the site of carbon-carbon composite implant, 6 months post-implantation (× 150).

broken and fine collagen fibrils (remnants of the bond) are seen in the histological sections. This type of adhesion may not be useful either in load-bearing situations or in mechanical stress, but it may be desirable in other applications such as replacement of ossicular chain and its transmucosal applications (Hench and Wilson 1984). It has been noted in this study that nitrided titanium forms a bond with adjacent tissue quite early at 6 weeks and may be termed as a type 3 biomaterial which is surface-reactive (Hench and Ethridge 1982). When this material is used as a rigid housing in heart valves (Chitra Heart Valve) the valve is anchored firmly to the surrounding cardiac tissue within a short time, thus improving the interfacial stability.

Increased amounts of titanium have been found in nonosseous tissue adjacent to the titanium implants in man and in rabbits (Meachim and Williams 1973). Though particles of titanium and carbon were found in tissues adjacent to the implanted area in the present study there was no evidence of toxic reaction around them. A notable feature was the absence of debri of sapphire, which makes it a good material for various intravascular biomaterial applications.

Though ceramics are strong and extremely hard, they have not been applied much for use in prosthetic devices. Brittleness and loss of strength in saline as well as when implanted in soft tissue have led to a conservative approach (Lynch 1982). However, in this study the soft tissue response to ceramics has been excellent over one year.

To conclude, our present study confirms the uniform tissue tolerance (biocompatibility) to the implanted metals, ceramics and composites in paravertebral muscle of rabbits.

References

Albrektsson T, Bramemark P I, Hansson H A, Ivarsson B and Jonsson U 1982 *Adv. Biomater.* 4 167

Hench L L and Ethridge E C 1982 in *Biomaterials—an interfacial approach* (New York, London: Academic Press) Chapter 1, p. 3

Hench L L and Wilson J 1984 *Science* **226** 630
Laing P, Ferguson A and Hodge E 1967 *J. Biomed. Mater. Res.* **1** 135
Lynch W 1982 in *Implants. Reconstructing the human body* (New York: Van Nostrand) Chapter 1, p. 18
Meachim G and Williams D F 1973 *J. Biomed. Mater. Res.* 7 555
Turner J E, Laurence W H and Autian J 1973 *J. Biomed. Mater. Res.* 7 39

Bull. Mater. Sci., Vol. 9, No. 5, December 1987, pp. 317–321. © Printed in India.

Conductivity pre-exponential factors for some new superionic conductors

N B DESAI*, K BYRAPPA†, G S GOPALAKRISHNA,
S SRIKANTASWAMY and A B KULKARNI*
Department of Geology, University of Mysore, Manasagangotri, Mysore 570 006, India
*Department of Physics, University of Gulbarga, Gulbarga 585 006, India

MS received 11 May 1987; revised 8 September 1987

Abstract. The pre-exponential factors obtained from the ionic conductivity studies on $Na_2(La,Al)ZrP_3O_{12}$, $Na_2(La,Al)TiP_3O_{12}$, $NH_4Zr_2V_3O_{12}$ and $AlPO_4:Li^+$ have been analysed. The compensation law has been found to be valid for these materials indicating that the entropy is directly related to the activation energy. The $1/\alpha$ vs β plots show straight lines for most of the superionic materials except for a few and this variation has been discussed.

Keywords. Nasicon analogues; superionic conductors; pre-exponential factor; Meyer-Neldel rule.

1. Introduction

Solid ionic conductors are of immense scientific and technological interest. They are used in fuel cells, oxygen and specific ion sensors and electrochromic displays (Hagenmuller and Van Gool 1978; Vashishta *et al* 1979; Takahashi and Kozawa 1980). Many solid electrolytes with high ionic conductivity comparable to that of Na β-alumina have been reported (Liang 1973; Hu *et al* 1977; Bankamp and Huggins 1978). The ionic conductivity and hopping rate data for some Nasicon analogues have been reported earlier (Desai *et al* 1987). In this paper the extrapolation of the pre-exponential factors from the ionic conductivity data has been carried out on a wide range of materials like $Na_2(La,Al)ZrP_3O_{12}$; $Na_2(La,Al)TiP_3O_{12}$, $NH_4Zr_2V_3O_{12}$ and $AlPO_4$: Li^+. The first two compounds have been reported earlier as Nasicon analogues (Byrappa *et al* 1985), the third one as a new fast proton conductor (Byrappa *et al* 1987a) and the last one is an interesting new material reported recently (Byrappa *et al* 1987b). $AlPO_4$ shows a covalent bonding and has six polymorphic modifications. The seventh polymorphic modification with 100% ionic bonding and a conducting ion like Li^+ in its composition has been reported earlier (Byrappa *et al* 1986a, b). The Meyer-Neldel rule or the compensation law applied to all these materials show that the entropy is directly related to the activation energy.

2. Experimental method

The synthesis and characterization of all these superionics have been reported earlier (Byrappa and Gopalakrishna 1985; Byrappa *et al* 1985, 1987a,b). Similarly the experimental method of complex impedance measurements has been given earlier (Desai *et al* 1987).

---

†To whom all correspondence should be addressed.

3. Results and discussion

The ionic conductivity in superionics can be expressed as

$$\sigma=\sigma_0/T[\exp(-E/kT), \tag{1}$$

where E is the activation energy, T the temperature, k the Boltzman's constant and σ_0 the pre-exponential factor. The conductivity pre-exponential factor σ_0 can be expressed as

$$\sigma_0=Ne^2a^2C(1-C)\gamma k^{-1}\omega_0\exp(S/k) \tag{2}$$

$$\sigma_0=k\omega_0\exp(S/k) \tag{3}$$

$$\text{Therefore}\quad \log\sigma_0=S/k+\log(k\omega_0), \tag{4}$$

where e is the electronic charge, a the hopping rate, γ the constant depending upon the number of possible jumps available for a particular ion, ω_0 the vibrational frequency of the mobile ions, N the number of equivalent sites per unit volume, C the concentration of mobile ions and S the entropy (Almond *et al* 1983). It has been reported that for a wide range of materials the magnitude of the pre-exponential factor σ_0 and the activation energy E are related by the Meyer-Neldel rule

$$\log\sigma_0=\alpha E+\beta, \tag{5}$$

where α and β are constants (Weichman and Kuzel 1970; Roberts and Thomas 1974; Dosdale and Brook 1978). The study of Meyer-Neldel rule helps to rationally understand the activation entropies. It has been shown that in Ag^+ ion conducting glasses (Almond and West 1986), the entropies and activation energy values for ionic conduction can be expressed as

$$S=E/T_d, \tag{6}$$

where T_d is the effective temperature corresponding to an order-disorder transition in mobile ion sub-lattice. From (1) and (4) we get

$$\alpha=1/kT\text{ and }\beta=\log\sigma T. \tag{7}$$

Similarly from (4) and (6) we get

$$\log\sigma_0=(E/kT_d)+\log k\omega_0. \tag{8}$$

By combining these equations with the Meyer-Neldel rule (equation (5)) we get

$$\alpha=1/kT_d;\ \beta=\log\omega_0. \tag{9}$$

The applicability of the Meyer-Neldel rule to the materials synthesized by the present authors and the role of α and β in understanding the mobile ion conduction mechanism have been critically examined in this paper. Table 1 gives the values of E and $\log\sigma_0$ for $Na_2(La,Al)ZrP_3O_{12}$, $Na_2(La,Al)TiP_3O_{12}$, $NH_4Zr_2V_3O_{12}$ and $AlPO_4$: Li^+. The values of E have been plotted against $\log\sigma_0$ (figure 1). The linear relationship E vs $\log\sigma_0$ indicates that T_d and C are the same for members of a particular family of superionic materials. The slope of the straight lines in the E vs $\log\sigma_0$ plots can be used to evaluate T_d. The curvatures in the conductivity plots generally indicate an ordered-disordered transition. The pre-exponential factors were obtained for all these compounds from the ionic conductivity data measured within a wide range of temperature (room temperature to 550° K). Similarly the activation

Table 1. Interdependance of the concentration, pre-exponential factor and activation energy.

Compound	Concentration* (wt %)		log σ_0	E (eV)
$NH_4Zr_2V_3O_{12}$	25·00	ZrO_2	1·90	0·43
	27·50		2·39	0·55
	28·75		2·69	0·70
	31·25		4·99	1·20
	35·00		7·49	2·22
$Na_2(La, Al)ZrP_3O_{12}$	7·18	La_2O_3	0·65	0·15
	7·80		1·30	0·30
	8·12		2·60	0·75
	9·02		3·40	1·00
	9·92		4·99	1·50
	10·78		6·94	2·10
$Na_2(La, Al)TiP_3O_{12}$	2·15	La_2O_3	−0·37	0·75
	3·23		−2·61	0·50
	5·02		5·86	1·50
	5·39		6·29	1·60
	6·46		0·54	0·80
	6·85		−3·80	0·30
$AlPO_4$: Li^+	0·55	Li_2O	−3·00	0·30
	0·95		−1·39	0·22
	1·36		1·52	0·15
	1·77		2·30	0·14
	2·18		3·00	0·10

*Concentration of the component in the nutrient

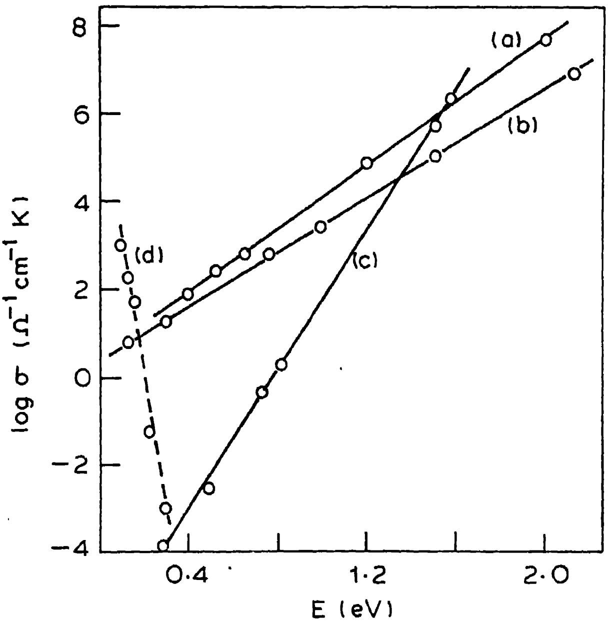

Figure 1. Log σ_0 against E plot for some superionic conductors. **a.** $NH_4Zr_2V_3O_{12}$, **b.** $Na_2(La, Al)ZrP_3O_{12}$, **c.** $Na_2(La, Al)TiP_3O_{12}$ and **d.** $AlPO_4{:}Li^+$.

Table 2. Values of α and β for some superionic materials.

Compound	$\alpha = 1/T_a k$	$1/\alpha$	$\beta = \log(k\omega_0)$
$NH_4Zr_2V_3O_{12}$	3·25	0·31	1·00
$Na_2(La,Al)TiP_3O_{12}$	7·76	0·13	−6·00
$Na(La,Al)ZrP_3O_{12}$	2·75	0·36	2·50
AgI-fly Ash	10·00	0·10	−3·50
Na_2SO_4-$In(SO_4)_3$	6·50	0·15	−1·50
Na_2SO_4-$La(SO_4)_3$	8·00	0·12	−2·62
$AlPO_4$: Li^+	2·90	0·03	6·00
AgI-Ag oxysalt glass	9·00	0·11	2·10
AgI-AgBr	7·60	0·13	−1·50
Na_2SO_4-Na_2WO_4	7·00	0·14	−4·25
$Y:Na_2SO_4$	9·99	0·10	0·65
$Li_{3+x}V_{1-x}Ti_xO_4$	17·36	0·05	−4·06
$AgI + Pb^{2+}$	19·53	0·05	−9·12
$Na_{1+x}Zr_{2-x}In_xP_3O_{12}$	16·50	0·06	−7·82
$Li_{2+x}C_{1-x}B_xO_3$	8·69	0·11	−2·17

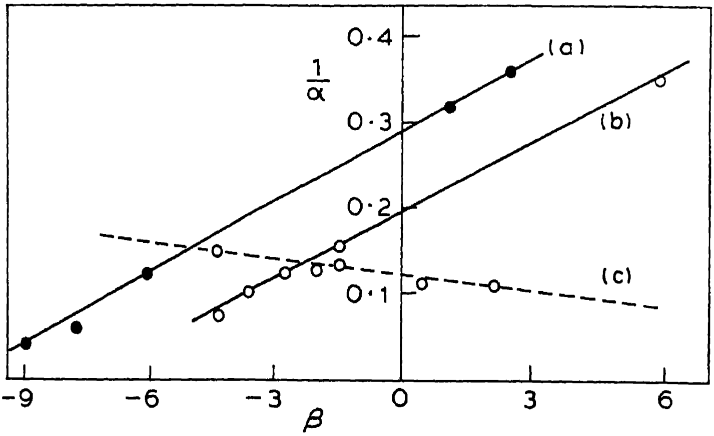

Figure 2. $\frac{1}{\alpha}$ against β plot for some superionic conductors. **a.** $Na_2(La,Al)TiP_3O_{12}$; $Na_2(La,Al)ZrP_3O_{12}$; $NH_4Zr_2V_3O_{12}$; AgI-Pb^{2+}; $Na_{1+x}Zr_{2-x}In_xP_3O_{12}$ systems. **b.** AgI-fly Ash; Na_2SO_4-$La_2(SO_4)_3$; Na_2SO_4-$In(SO_4)_3$; $AlPO_4$: Li^+; $Li_{3+x}V_{1-x}Ti_xO_4$; $Li_{2+x}C_{1-x}B_xO_3$ systems. **c.** Na_2SO_4-Na_2WO_4; AgI-AgBr; AgI-Ag oxysalt glass; $Y:Na_2SO_4$ systems.

energy values were obtained from the Arrhenius plots given earlier (Byrappa *et al* 1987c). It is found that the Meyer-Neldel rule is applicable to all the four compounds indicating that the pre-exponential factor increases exponentially with E except in the case of $AlPO_4$:Li^+ where it decreases exponentially with E. Such a decreasing trend in the $\log \sigma_0$ vs E has been reported for several ion-exchanged β-alumina (Whittingham and Huggins 1972). The decrease in the values of $\log \sigma_0$ with E is attributed to a small negative entropy of the activation. On the other hand, the first three materials showing an increase in the pre-exponential factor with E have been compared to AgI-Ag oxysalt glasses and Lisicon (Almond *et al* 1985). It is interesting to note that $Na_2(La,Al)ZrP_3O_{12}$, $Na_2(La,Al)TiP_3O_{12}$ are the fast ionic conductors and $NH_4Zr_2V_3O_{12}$ is a fast proton conductor. The positive slope of $\log \sigma_0$ vs E

indicates an increase in the values of conductivity pre-exponential factor with E. The pellets of $Na_2(La, Al)ZrP_3O_{12}$ and $Na_2(La, Al)TiP_3O_{12}$ have been prepared with and without polyvinyl alcohol, but the log σ_0 vs E plots are the same for both and hence the binding medium (in this case polyvinyl alcohol) does not hinder the mobility of the ions. Table 2 gives the values of α and β for some known superionics available in the literature (Prakash and Gopalan 1985; Shahi and Wagner 1982; Saito *et al* 1984; Rodger *et al* 1985; Shahi *et al* 1986; Delmas *et al* 1981; Shannon *et al* 1977), as well as for the present compounds. The plots of $1/\alpha$ vs β show three straight lines. Lines (a) and (b) appear almost parallel with a positive slope, whereas line (c) has a negative slope. The positive slope of $1/\alpha$ vs β plot (figure 2) indicates an increase in the disordering temperature T_d with an increase in the values of $\log(k\omega_0)$. On the other hand the negative slope indicates a decrease in T_d with an increase in the values of $\log(k\omega_0)$. These results appear to be surprising and such a behaviour may be explained in terms of the varying concentration of selective cations in the composition, x, C, conduction mechanism, etc.

Acknowledgements

The authors thank UGC, New Delhi for financial assistance.

References

Almond D P and West A R 1986 *Solid State Ionics* **18/19** 1105

Almond D P, Duncan G K and West A R 1983 *Solid State Ionics* **8** 159

Almond D P, Duncan G K and West A R 1985 *J. Non-Cryst. Solids* 74 285

Bankamp B A and Huggins R A 1978 *Mater. Res. Bull.* **13** 23

Byrappa K and Gopalakrishna G S 1985 *Prog. Cryst. Growth Charact.* **11** 89

Byrappa K, Gopalakrishna G S, Venkatachalapathy V and Kulkarni A B 1985 *J. Less Common Metals* **110** 441

Byrappa K, Srikantaswamy S and Shashidhara Prasad J 1986a *J. Mater. Sci. Lett.* **5** 690

Byrappa K, Shashidhara Prasad J and Srikantaswamy S 1986b *J. Cryst. Growth* **79** 232

Byrappa K, Kulkarni A B, Desai N B and Srikantaswamy S 1987a in: *Current trends in the physics of materials* (ed.) M Youssuf (Singapore: World Scientific Publishers)

Byrappa K, Kulkarni A B, Srikantaswamy S and Desai N B 1987b *J. Mater. Sci. Lett.* **6** 980

Byrappa K, Gopalakrishna G S, Kulkarni A B and Desai N B 1987c *J. Less Common Metals* **138** 1

Delmas C, Viala J C, Zeuoga R, LeFlem G, Hagenmuller P, Cherkaoui F and Brochu R 1981 *Solid State Ionics* **3/4** 209

Desai N B, Byrappa K, Kulkarni A B and Gopalakrishna G S 1987 *Bull. Mater. Sci.* **9** 117

Dosdale T and Brook R J 1978 *J. Mater. Sci.* **13** 167

Hagenmuller P and Van Gool W 1978 *Solid electrolytes* (New York: Academic Press)

Hu Y W, Raistrick I D and Huggins R A 1977 *J. Electrochem. Soc.* **124** 1240

Liang C C 1973 *J. Electrochem. Soc.* **120** 1289

Prakash G and Gopalan S 1985 *Development and characterization of Na_2SO_4 based fast ion conductors*, M.Tech Thesis, IIT Kanpur, India

Roberts C G and Thomas D G 1974 *J. Phys.* **C7** 2312

Rodger A R, Kuwano J and West A R 1985 *Solid State Ionics* **15** 185

Saito Y, Maruyama T and Kobayashi K 1984 *Solid State Ionics* **14** 265

Shahi K and Wagner J B 1982 *J. Solid State Chem.* **42** 107

Shahi K, Weppner W and Rabenau A 1986 *Phys. Status Solidi* **A93** 171

Shannon R D, Taylor B E, English A D and Berzins T 1977 *Electrochim. Acta* **22** 783

Takahashi T and Kozawa A 1980 *Application of solid electrolytes* (Cleveland: JEC press)

Vashishta P, Mundy J N and Shenoy G K 1979 *Fast ion transport in solids* (Amsterdam: North Holland)

Weichman F L and Kuzel R 1970 *Can. J. Phys.* **48** 63

Whittingham M S and Huggins R A 1972 *Solid State Chem. NBS Spl. Pub.* **364** 139

Bull. Mater. Sci., Vol. 9, No. 5, December 1987, pp. 323–330. © Printed in India.

$NH_4Zr_2V_3O_{12}$ proton conductor

K BYRAPPA†, A B KULKARNI*, N B DESAI* and H P JAGADEESH
Department of Geology, University of Mysore, Manasagangotri, Mysore 570 006, India
*Department of Physics, Gulbarga University, Gulbarga 585 006, India

MS received 15 June 1987; revised 29 October 1987

Abstract. $NH_4Zr_2V_3O_{12}$, a new proton conductor, has been synthesized by flux, melt and hydrothermal methods. The crystals were subjected to X-ray diffraction, differential thermal analysis, infrared spectroscopy and impedance measurements.

Keywords. $NH_4Zr_2V_3O_{12}$; proton conductor.

1. Introduction

The growth and study of vanadates is not as popular as silicates, sulphates or phosphates, probably because of their limited use in modern technology. Vanadates have been synthesized only recently. The growth of vanadates by hydrothermal technique is also not known due to various reasons. An attempt was therefore made to synthesize some new vanadates with a device potential and various methods like flux, melt, solution and hydrothermal have been studied.

There has been a great interest in superionics including the fast proton conductors in recent years. The fast ionic and fast proton conductors are used in high temperature solid state batteries, fuel cells, hydrolysis cells, high energy density batteries and charge transport in complex biophysical systems. The features of proton conduction in solids are unique due to the missing electron cloud. There are very few anhydrous proton conductors reported so far like NH_4 β-alumina, NH_4 zeolite, $LiN_2H_5SO_4$, LiH_2PO_4, $N_2H_6SO_4$, $(NH_4)_3H(SO_4)_2$, $NH_4Zr_2P_3O_{12}$, $HZr_2P_3O_{12}$ etc (Chandra 1984; Kreuer *et al* 1982; Clearfield *et al* 1984; Rudolf *et al* 1985; Subramanian *et al* 1984). An attempt has been made to find out new conductors with high proton conductivity. This paper reports the synthesis and characterization of a new proton conductor $NH_4Zr_2V_3O_{12}$.

2. Synthesis

Almost all the vanadates found in literature have been synthesized by the flux method. Here, an attempt has been made to develop $NH_4Zr_2V_3O_{12}$ by flux, melt and hydrothermal techniques. These methods have been critically evaluated and the advantages and disadvantages of each method have been discussed. Vanadates from solutions could not be synthesized due to lack of a suitable acid media. However, $NH_4Zr_2V_3O_{12}$ could be synthesized by using a saturated aqueous solution of $(NH_3)_2CO_3$ and such studies are in progress.

---

†To whom all correspondence should be addressed.

2.1 *Flux method*

Synthesis of vanadates by this method is not new and in most cases V_2O_5 is used as a flux along with PbO and PbF_2. Wanklyn (1986) studied the growth of vanadate crystals by the flux method. Normally the starting components and the flux agents are taken in a platinum crucible and the mixture is heated up to 850°C followed by a slow cooling at 1 to 5°C per hour. The present authors have obtained well-developed crystals of $NH_4Zr_2V_3O_{12}$ (figure 1a).

2.2 *Melt technique*

This technique is more suitable because of its simplicity and good results. The starting components such as NH_4VO_3, ZrO_2 were taken in the desired molar ratio in a platinum crucible kept inside the reactor whose temperature could be controlled with high accuracy. The crucible was initially heated up to 600°C, held overnight and subsequently the temperature of the crucible was raised up to 950°C and held for a few hours leading to the formation of a homogeneous melt which was slowly cooled to the room temperature in different phases. By this method the growth parameters like the temperature of the initial heating, temperature of the melt, cooling rate, molar ratio etc can be controlled. It is therefore necessary to consider these parameters otherwise and a slight change in any one of them could change the resulting product. The crystals obtained by this technique are superior in quality compared to those obtained from flux growth. They were steel grey in colour, small tabular and often flaky with metallic lustre and perfect basal cleavages (figure 1b).

2.3 *Hydrothermal method*

Hydrothermal synthesis of complex vanadates has not been reported so far. A series of experiments were therefore conducted by this method to obtain $NH_4Zr_2V_3O_{12}$ crystals. Although, initial experiments with a varying molar ratio of the nutrient components yielded only a crystalline powder without any external morphology, we were able to finally synthesize small needle-like crystals of $NH_4Zr_2V_3O_{12}$ under the following conditions: temperature 250°C, pressure 200 atm, NH_4VO_3 5 g and HCOOH (2·0 M) 6 ml. The experiments were carried out for 8 days using teflon liners in Morey-type autoclaves of capacity 50 ml. Since crystallization occurred due to spontaneous nucleation, the furnace temperature was slowly increased to control the nucleation rate (nearly 5°C per hour). The main drawback of this method is the small size of the crystals (figure 1c).

3. Characterization

$NH_4Zr_2V_3O_{12}$ crystals were characterized through various techniques like XRD, DTA, IR-spectroscopy and complex impedance measurements.

X-ray powder diffraction patterns were recorded using X-ray diffractometer (JEOL, model JDX 8P) with a monochromatic FeK_α ($\lambda - 1{\cdot}934$ Å) as the source. The structure was found to be monoclinic with cell parameters $a = 12{\cdot}19$, $b = 11{\cdot}81$, $c = 15{\cdot}15$ Å, $\beta = 101{\cdot}96°$ and $V = 2133{\cdot}71$ Å^3. Table 1 gives the powder diffraction pattern for $NH_4Zr_2V_3O_{12}$ crystals.

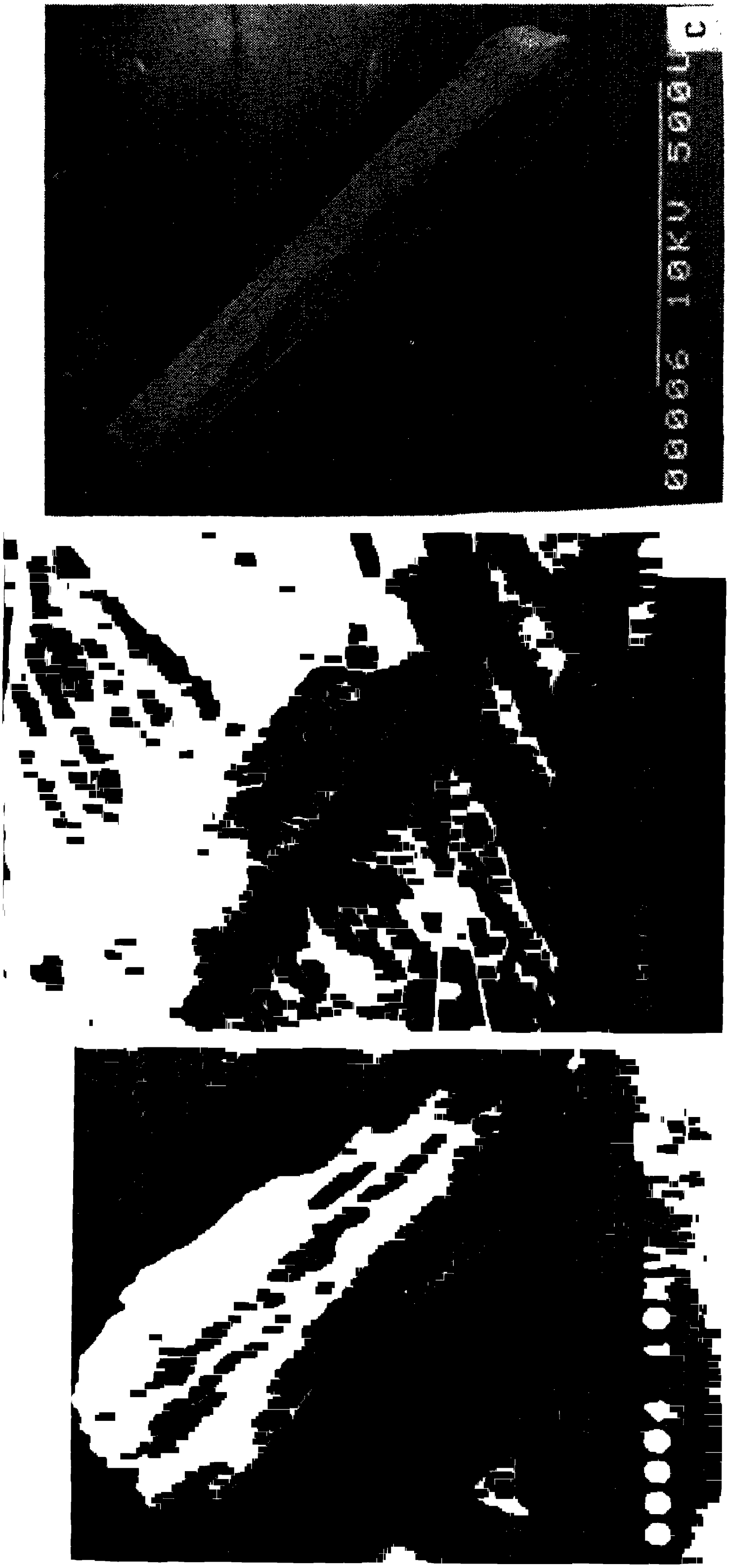

Figure 1. **a–c.** $NH_4Zr_2V_3O_{12}$ crystals. **a.** Flux grown **b.** Melt grown **c.** Hydrothermally grown.

Table 1. X-ray powder diffraction pattern for $NH_4Zr_2V_3O_{12}$.

I	d_o	d_c	hkl
6	14·817	14·434	100
8	12·190	—	010
8	11·556	—	001
8	8·882	9·017	101
10	8·382	—	011
10	7·935	—	—
11	7·058	7·217	111/200
8	6·842	—	—
5	6·542	—	—
15	6·016	6·108	020
6	5·068	5·057	121
3	4·979	4·909	112
8	4·794	4·8112	300
100	4·381	4·4280	301
15	4·105	4·0723	030
11	3·862	3·8490	003
8	3·676	3·6711	013
15	3·562	3·5578	113
24	3·405	3·3962	203
8	3·148	3·1766	023
8	2·970	2·9683	223
27	2·880	2·8868	004
10	2·761	2·7576	114
8	2·638	2·6325	403
6	2·609	2·6090	024
8	2·527	2·5286	242
11	2·480	2·4754	304
5	2·382	2·3925	043
13	2·278	2·2710	243
6	2·234	2·2389	254
16	2·186	2·2086	342

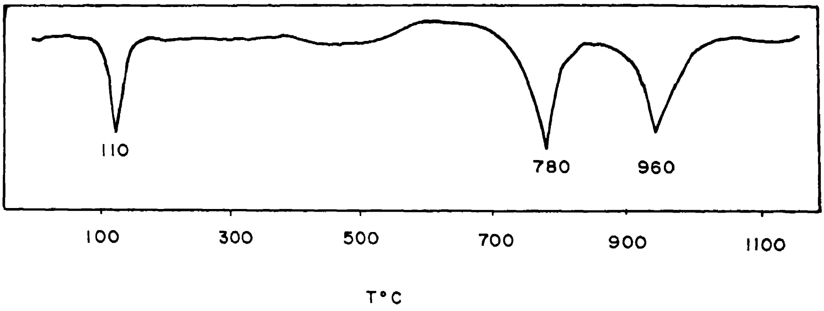

Figure 2. DTA curve for $NH_4Zr_2V_3O_{12}$ crystals.

The DTA curve (figure 2) was recorded using an apparatus (Stanton Redcroft, model DTA 673–4) with a temperature programmer and a potentiometric recorder (model RE-571–20). The sample holder was platinum and Al_2O_3 was used as a standard. The heating rate was 5°C per min. $NH_4Zr_2V_3O_{12}$ crystals show multiple phase transitions at temperatures 110°, 780° and melts at 960°C. The phase transition at 110°C was also confirmed through impedance measurements. Efforts are being made to shift the first phase transition temperature at 110°C to a much higher temperature to make the material more suitable for battery applications by introducing some selective dopants into the composition of $NH_4Zr_2V_3O_{12}$.

The infrared spectrum of $NH_4Zr_2V_3O_{12}$ (figure 3) was recorded in the range 4000 to 400 cm^{-1} using a spectrophotometer (Specord 75 IR, GDR) with liquid paraffin. It is well known that orthovanadates with a T_d symmetry have four fundamental vibrations namely $\nu_1(A_1)$, 870 cm^{-1}, $\nu_2(E)$, 345 cm^{-1}, $\nu_3(F_2)$, 825 cm^{-1} and $\nu_4(F_2)$, 480 cm^{-1} (Nakamoto 1966). $NH_4Zr_2V_3O_{12}$ crystals show a characteristic strong absorption for $(NH_4)^+$ at 3250 cm^{-1}. On the whole the absorption bands are not sharp for this compound and this happens in most of the vanadates.

The impedance was measured for $NH_4Zr_2V_3O_{12}$ crystals taken in the form of pellets (10 mm dia., 2 to 3 mm thickness, 85 to 90% compactness and pressure 5 ton sq. cm^{-1}). The pellets were sintered in a vacuum chamber at 300°C. A capacitance bridge (General Radio model 160B) was used. The conductivity was measured at varying a.c. internal frequency range and the proton conductivity measured as a function of temperature. The Arrhenius plot in figure 3 shows a high proton conductivity of the order of 10^{-3} and 10^{-1} per ohm/cm at 100°C. Beyond this temperature the proton conductivity falls down sharply due to the phase transition at 110°C and raises again steadily above 220°C. The proton conductivity value obtained for $NH_4Zr_2V_3O_{12}$ is much higher than the proton conductivity values reported for NH_4-zeolites, NH_4 β''-alumina and other related compounds. The conduction mechanism is $(NH_4)^+$ migration as in NH_4-zeolites and NH_4 β''-alumina. As seen in figure 4, there is a discontinuity in the Arrhenius plot of $NH_4Zr_2V_3O_{12}$ and similar discontinuities in the Arrhenius plots have been reported earlier in various proton conductors (Chandra 1984; Subramanian *et al* 1984). However, such factors were earlier explained in terms of the loss of water in the compound. In the present case, there is no such loss of water (normally occurring above 100°C) and also the loss of ammonia (occurring above 500°C). The corresponding activation energy values were calculated from the slopes of the Arrhenius plots (0·3 eV and 0·75 eV respectively for the low temperature and high temperature regions).

The complex admittance plots (conductance G vs susceptance B) were obtained over a wide range of frequency for a number of samples of $NH_4Zr_2V_3O_{12}$ crystals and a plot is given in figure 5 which shows a semi-circle whose centre is slightly below the G axis. The angle between the diameter of the semi-circle and the G axis is around 35° which can be explained on the basis of the dispersion of the relaxation time that occurs in the polycrystalline material (Bayard and Barna 1978; Almond *et al* 1984). This also shows that the intergranular impedance or the grain boundary effects are negligible compared to the bulk impedance of the sample.

4. Conclusions

A new proton conductor, $NH_4Zr_2V_3O_{12}$ has been synthesized by various methods. The melt grown crystals are quite superior in quality with metallic lustre and flaky to massive in habit. It crystallizes in the monoclinic system and shows multiple phase transitions at 110°C and 780°C. Its high proton conductivity makes it a prospective material for fuel cells.

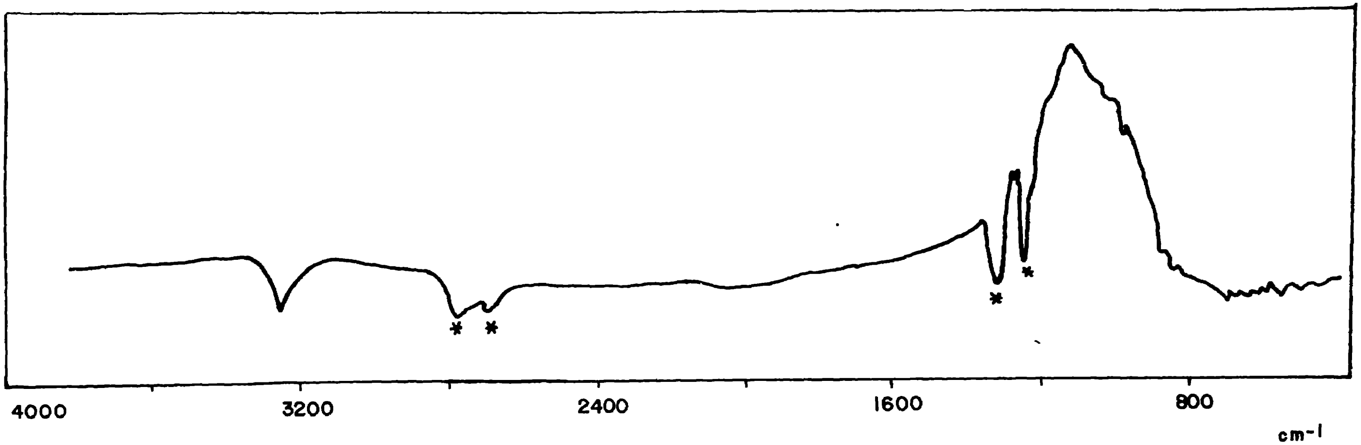

Figure 3. IR-spectrum for $NH_4Zr_2V_3O_{12}$ crystals.

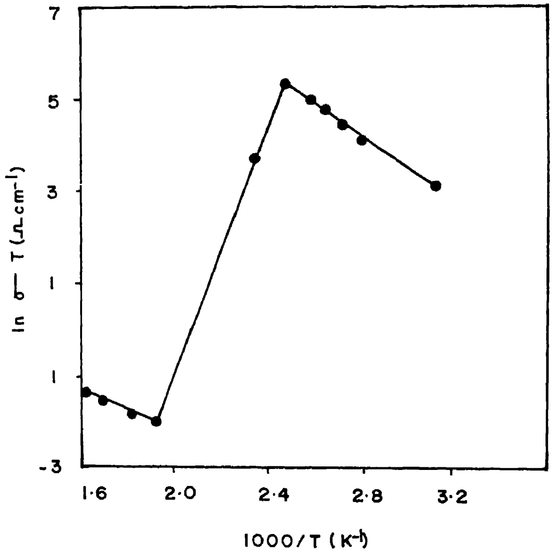

Figure 4. Arrhenius plot for $NH_4Zr_2V_3O_{12}$.

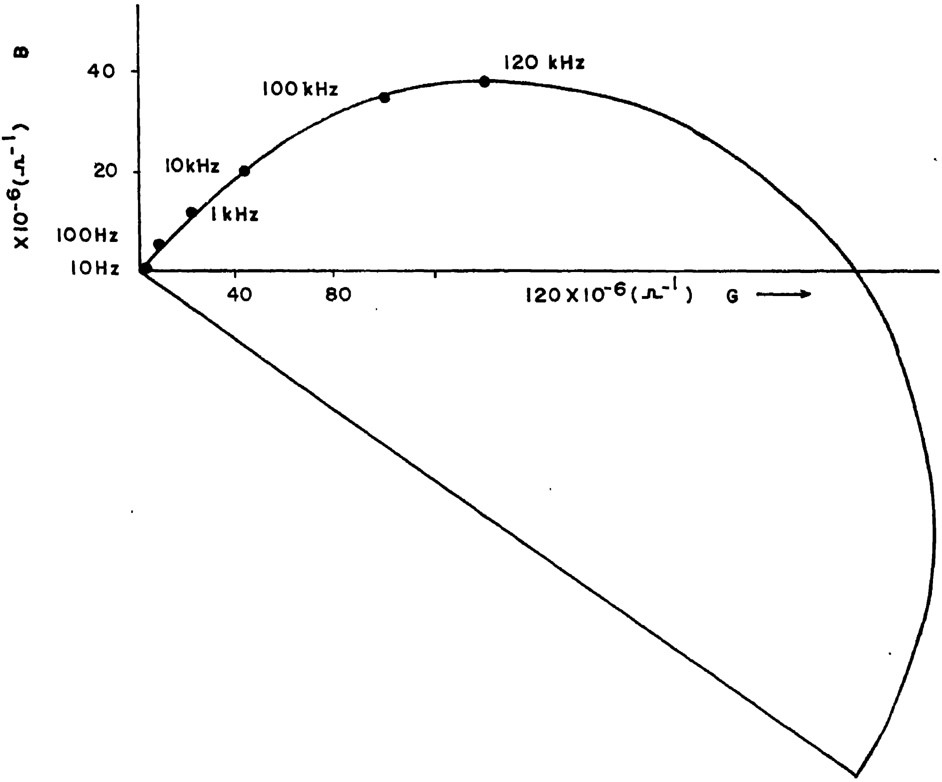

Figure 5. Complex admittance plot for $NH_4Zr_2V_3O_{12}$ at 100°C.

Acknowledgements

The author (HPJ) thanks UGC, New Delhi for a fellowship.

References

Almond D P, Hunter C C and West A R 1984 *J. Mater. Sci.* **19** 3236
Bayard M L and Barna G G 1978 *J. Electroanal. Chem.* **91** 201
Chandra S 1984 in: *Materials science forum* (Switzerland: Trans. Tech publications) vol. 1 p 153
Clearfield A, Roberts B D and Subramanian M A 1984 *Mater. Res. Bull.* **19** 219
Kreuer K D, Weppner W and Rabenau A 1982 *Mater. Res. Bull.* **17** 501
Nakamoto K 1966 *Infrared spectra of inorganic and co-ordination compounds* (Moscow: Mir)
Rudolf P R, Subramanian M A, Clearfield A and Jorgensen J D 1985 *Solid State Ionics* **17** 337
Subramanian M A, Roberts B D and Clearfield A 1984 *Mater. Res. Bull.* **19** 1471
Wanklyn B M 1986 List of flux grown crystals, Univ. of Oxford, Physics Dept. Oxford (private communication)

Bull. Mater. Sci., Vol. 9, No. 5, December 1987, pp. 331–336. © Printed in India.

Electrical conductivity of the ferroelectric sodium vanadate, potassium vanadate, lithium vanadate and their solid solutions

T A PATIL, V M JAMADAR* and S H CHAVAN†
Department of Physics, Vivekanand College, Kolhapur 416 002, India
*D K Mahavidyalaya, Ichalkaranji 416 115, India
†Department of Physics, Shivaji University, Kolhapur 416 004, India

MS received 19 October 1987

Abstract. The d.c. electrical conductivity of sodium vanadate, potassium vanadate, lithium vanadate and their solid solutions sodium-potassium vanadate, sodium-lithium vanadate were measured by a two-probe method in the temperature range covering their transition points. These materials show sharp change in conductivity at their phase transition temperatures. In sodium, potassium and lithium vanadates an exponential increase in d.c. conductivity is observed in ferroelectric region while discontinuities are observed above the transition temperatures. The activation energy in paraelectric state of the solid solutions is found to be higher than in ferroelectric state. In solid solutions the activation energy depends upon sodium vanadate concentration.

Keywords. Ferroelectrics; conductivity; phase transition; activation energy.

1. Introduction

Grawford (1959) reported that almost all ferroelectric materials which possess a high Curie temperature lose their piezoelectric properties at temperatures considerably below their Curie points. Guruvich and Rez (1960) showed that the loss of piezoelectric properties of these materials was due to the increase in electrical conductivity at high temperatures. Electrical transport studies on heavy rare-earth tungstates were reported by Verma and Lal (1981) who showed that they are mixed ionic-electronic conductors. Lal *et al* (1982) reported the electrical transport in heavy rare-earth iron garnets. Kanchan Gaur and Lal (1985, 1986) reported the electrical transport in light and heavy rare-earth vanadates.

The present paper reports the variation of d.c. electrical conductivity with temperature of sodium vanadate ($NaVO_3$), potassium vanadate (KVO_3), lithium vanadate ($LiVO_3$) and their solid solutions, sodium-potassium vanadate ($(Na_x\text{-}K_{1-x})VO_3$) and sodium-lithium vanadate ($(Na_x\text{-}Li_{1-x})VO_3$).

2. Experimental

Crystalline solids of sodium vanadate, potassium vanadate and lithium vanadate were prepared from a stoichiometric mixture of $M_2^+CO_3$ ($M^+ = $ Na, K and Li) and vanadium pentoxide (V_2O_5). This mixture was heated in a platinum crucible at 750°C for 4 hr inside a globar furnace and then cooled to room temperature. The solid solutions of $(Na_x\text{-}K_{1-x})VO_3$ and $(Na_x\text{-}Li_{1-x})VO_3$ were prepared from their respective vanadates by firing in the platinum crucible at 900°C for 3 hr and then allowed to furnace cool. The samples formed were confirmed by scanning them on X-ray diffractometer. The sample pellets were prepared in the form of discs (diameter 1 cm and thickness about 1 mm) by applying a 5 ton pressure using a hydraulic press. These pellets were sintered on a platinum foil at 500°C for 3 hr. The two sides of these sintered pellets were coated with a thin layer of silver paste for good electrical contact.

---

† To whom all correspondence should be addressed.

The experimental set-up consisted of a globar furnace, a digital DC microvoltmeter (VMV 15) with a Pico-ammeter adaptor, a transistorized power supply unit to provide d.c. electric field and a temperature controller arrangement. Current through the pellets was measured as a function of applied d.c. electric field at a constant temperature and the current density J was plotted against the applied electric field E. Three such plots are shown in figure 1. The current density J varies linearly with E up to the critical field and then the variation becomes nonlinear. For further study of d.c. conductivity the value of d.c. electric field is chosen (10 V) to fall within the critical field. The d.c. conductivity measurements were based on the d.c. resistivity data obtained by the two-probe method. A d.c. voltage of 10 V was applied across the pellet holder in series with Pico-ammeter. The pellet holder was heated slowly in the furnace and d.c. resistivity measurements were taken in the temperature regions covering the transition points of the samples. The resistivity data were used to calculate the d.c. conductivity.

3. Results and discussion

The variation of conductivity σ with temperature T can be represented by the general relation

$$\sigma=\sigma_0 \exp(-\Delta E/KT),$$

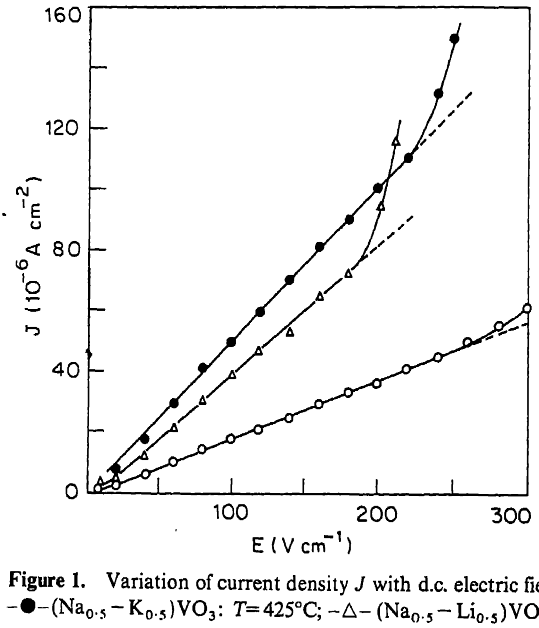

Figure 1. Variation of current density J with d.c. electric field E [–O– $NaVO_3$: $T=325$°C; –●–$(Na_{0.5}-K_{0.5})VO_3$: $T=425$°C; –Δ– $(Na_{0.5}-Li_{0.5})VO_3$: $T=425$°C].

where ΔE is the activation energy, σ_0 the constant and K the Boltzmann constant. The variation of $\log \sigma$ with $1/T$ for $NaVO_3$, KVO_3 and $LiVO_3$ is shown in figure 2 while figures 3 and 4 show such variations for solid solutions $(Na_x\text{-}K_{1-x})VO_3$ and $(Na_x\text{-}Li_{1-x})VO_3$ respectively. To determine whether the conductivity is ionic, electronic or mixed, the variation of d.c. conductivity with time is studied at a constant temperature using electrodes which block ionic conduction. For pure ionic conduction, conductivity decreases with time and tends to zero after a long time while for a pure electronic conductor, the conductivity is independent of time. In the case of mixed conduction, conductivity first decreases with time and then remains constant at some finite value. The variation of $\log \sigma$ with $\log t$ is shown in figure 5 for $NaVO_3$, $(Na_{0\cdot5}\text{-}K_{0\cdot5})$ VO_3 and $(Na_{0\cdot5}\text{-}Li_{0\cdot5})$ VO_3.

It is clear from figure 2 that for $NaVO_3$, KVO_3 and $LiVO_3$ an exponential increase in d.c. conductivity is observed only up to transition temperature (T_c) and thereafter there are discontinuities. The nature of conductivity below the transition temperature is ionic. In figures 3 and 4 the conductivity increases exponentially and a sharp change in conductivity is observed at the transition temperatures (T_c) of the respective solid solutions. These transition temperatures (T_c) are ferroelectric Curie temperatures of the respective samples which we have investigated by the hysteresis loop method and the dielectric constant measurements. For solid solutions $(Na_x\text{-}K_{1-x})VO_3$ and $(Na_x\text{-}Li_{1-x})VO_3$ the graphical variation of $\log \sigma$ with $\log t$ shows that the conductivity below T_c is of mixed type (partially ionic and electronic) (figure 5) and

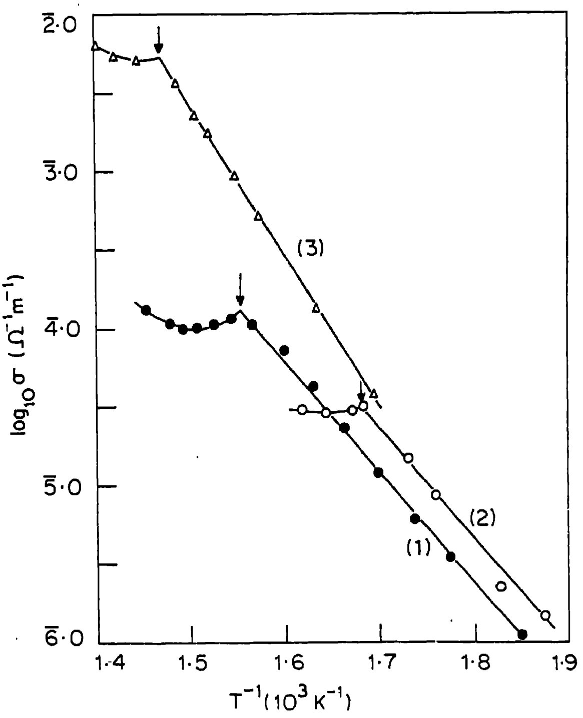

Figure 2. Variation of logarithmic conductivity σ with $1/T$ for **1.** $NaVO_3$, **2.** KVO_3 and **3.** $LiVO_3$.

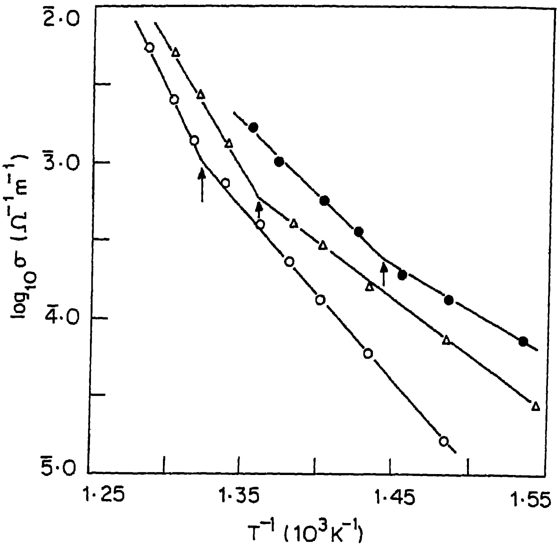

Figure 3. Variation of logarithmic conductivity σ with $1/T$ for $(Na_x-K_{1-x})VO_3$ [-●- $(Na_{0\cdot75}-K_{0\cdot25})VO_3$; -Δ- $(Na_{0\cdot50}-K_{0\cdot50})VO_3$; -O- $(Na_{0\cdot25}-K_{0\cdot75})VO_3$].

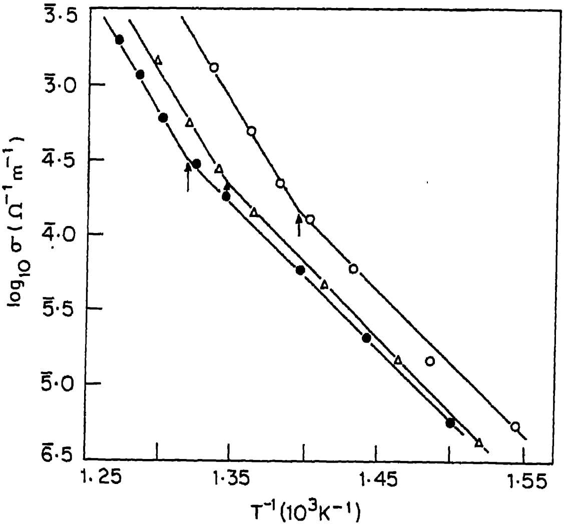

Figure 4. Variation of logarithmic conductivity σ with $1/T$ for $(Na_x-Li_{1-x})VO_3$ [-●- $(Na_{0\cdot75}-Li_{0\cdot25})VO_3$; -Δ- $(Na_{0\cdot50}-Li_{0\cdot50})VO_3$; -O- $(Na_{0\cdot25}-Li_{0\cdot75})VO_3$].

above T_c the electronic conduction dominates over the ionic conduction. The activation energies are evaluated from the slope of $\log\sigma$ against $1/T$ plot and their values are summarized in table 1.

In the paraelectric state of the solid solutions the activation energy is higher than in ferroelectric state.

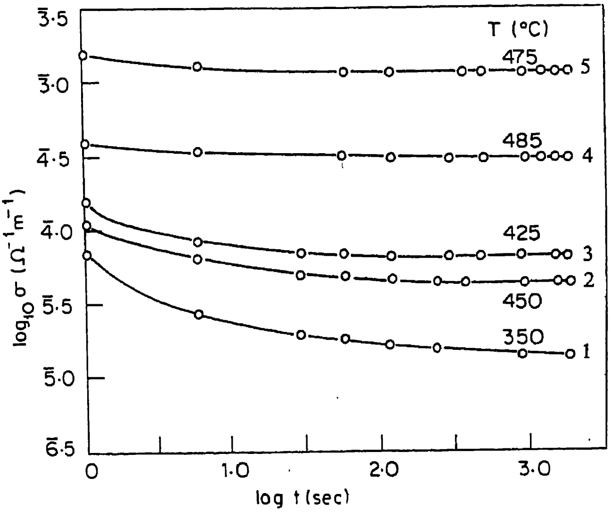

Figure 5. Variation of $\log\sigma$ with $\log t$ for 1. $NaVO_3$, 3, 5. $(Na_{0.5}K_{0.5})VO_3$ and 2, 4 $(Na_{0.5}Li_{0.5})VO_3$.

Table 1. Activation energies and Curie temperatures of different samples.

Sample	Activation energy (eV)		Curie temperature (°C)	Density of pellet (g cm^{-3})
	Ferro-state	Para-state		
$NaVO_3$	1·39	—	370	2·69
KVO_3	1·51	—	322	2·67
$LiVO_3$	1·92	—	407	2·81
$(Na_{0.75}\text{-}K_{0.25})VO_3$	1·12	1·85	420	2·48
$(Na_{0.50}\text{-}K_{0.50})VO_3$	1·38	2·69	462	2·61
$(Na_{0.25}\text{-}K_{0.75})VO_3$	2·14	3·96	483	2·23
$(Na_{0.75}\text{-}Li_{0.25})VO_3$	1·88	3·32	485	2·64
$(Na_{0.50}\text{-}Li_{0.50})VO_3$	1·98	3·12	470	2·56
$(Na_{0.25}\text{-}Li_{0.75})VO_3$	1·96	3·17	444	2·39

Experimental densities of the pellets of sodium vanadate, potassium vanadate and lithium vanadate relative to their crystal densities are 0·92, 0·93 and 0·92 respectively.

4. Conclusions

(i) For $NaVO_3$, KVO_3 and $LiVO_3$, discontinuities are observed above the transition temperature and conductivity increases exponentially in ferroelectric region. The nature of electrical conductivity is ionic below the transition temperature.

(ii) The electrical conductivity of all the materials shows a sharp change at the phase transition temperature, indicating the ferroelectric Curie temperatures of the respective materials.

(iii) For solid solutions the nature of electrical conductivity below the transition temperatures is of mixed type (partially ionic and electronic) and above this temperature it is electronic.

(iv) The activation energy of the solid solutions is higher in the paraelectric state than in the ferroelectric state and it depends upon the sodium vanadate concentration.

References

Grawford A 1959 *Br. Commun. and Electron.* **6** 516
Guruvich V and Rez I 1960 *Sov. Phys. Solid State* (*Engl. Transl.*) **2** 624
Kanchan Gaur and Lal H 1985 *J. Mater. Sci.* **20** 3167
Kanchan Gaur and Lal H 1986 *J. Mater. Sci.* **21** 2289
Lal H, Verma B and Yadav V 1982 *J. Mater. Sci.* **17** 3317
Verma B and Lal H 1981 *Mater. Res. Bull.* **16** 1579

Bull. Mater. Sci., Vol. 9, No. 5, December 1987, pp. 337–341. © Printed in India.

Transport properties of $MoSe_xTe_{2-x}$ $(0 \leqslant x \leqslant 2)$ single crystals

M K AGARWAL, P D PATEL and R M JOSHI
Department of Physics, Sardar Patel University, Vallabh Vidyanagar 388 120, India

MS received 13 August 1986; revised 16 September 1987

Abstract. The layer type $MoSe_xTe_{2-x}$ $(0 \leqslant x \leqslant 2)$ have been grown in single crystalline form by chemical vapour transport technique using bromine as the transporting agent. The electrical resistivity and Hall mobility perpendicular to the *c*-axis of the crystals were measured at room temperature. The variation of the Seeback coefficient with temperature was also investigated.

Keywords. Electrical resistivity; Hall mobility; thermoelectric power; $MoSe_xTe_{2-x}$ $(0 \leqslant x \leqslant 2)$ single crystals.

1. Introduction

Recently, transition metal dichalcogenides have attracted much attention because of their possible applications as lubricants, switching devices and photoelectrochemical solar energy converters. They form a wide range of solid solutions (Schneemeyer and Sienko 1980; Mentzen and Sienko 1976) either with mixed metals or with mixed chalcogenide compositions. The crystals of transition metal dichalcogenide are of layered type, each layer being a sandwich of chalcogen-metal-chalcogen sheets. The metal-chalcogen bonding is partly ionic and partly covalent whereas the interlayer bonds are of van der Waal's type. These VIB–VIA group of compounds have been studied extensively for their electrical properties (Wilson and Yoffe 1969; Brixner 1963; Mansfield and Salam 1953). Studies have also been made on mixed systems such as $(Mo/W)Te_2$, $(Mo/W)Se_2$ (Revolinsky and Beerntsen 1964), $(W/Mo/Te)Se_2$ (Brixner and Teufer 1963) and $Mo(S/Se)_2$ (Agarwal and Talele 1986). However, no attempt has been made to investigate the variation of the properties like resistivity, Hall coefficient and thermoelectric power with composition for $Mo(Se/Te)_2$ solid solutions in the single crystalline form. The present paper reports a study of these properties for $Mo(Se/Te)_2$ single crystals grown by chemical vapour transport technique.

2. Experimental

Single crystals of $MoSe_xTe_{2-x}$ $(0 \leqslant x \leqslant 2)$ were prepared from 99·999% pure molybdenum, selenium and tellurium. Powdered starting material in the required composition was taken in a quartz ampoule and vacuum-sealed with a residual air of 10^{-5} torr. The powder was thoroughly mixed and distributed along the length of horizontally held ampoule. The charge was slowly heated over 72 hr to 700°C. At this stage a reaction product was obtained in the form of free flowing shining polycrystalline material. The ampoule and the product were thoroughly mixed by shaking. Large single crystals were found to grow after heating the ampoule at appropriate temperatures for about 2–7 days (table 1). These crystals were characterized for their structure and composition.

The electrical resistivity and Hall coefficients of the crystals were determined using the standard method of Van der Pauw (1958). Electrical contacts were provided by conducting silver paste and thin copper wires attached to the periphery of a thin flat crystal. Seeback coefficient was measured using an integral method. The specimen holder used for the measurement is shown in figure 1.

3. Results and discussion

A detailed study of the variation of d.c. resistivity, ρ (ohm cm) as a function of the crystal composition reveals that the resistivity increases non-linearly with the increasing selenium content in the solid solution $MoSe_xTe_{2-x}$ $(0 \leqslant x \leqslant 2)$ as shown in figure 2. The room temperature (30°C) resistivities of $MoSe_2$ and $MoTe_2$ have been obtained as 9·5 and 0·25 Ω cm respectively. These results agree with those reported earlier (Revolinsky and Beerntsen 1964; Lepetit 1965). The resistivity value is found to increase as the selenium content increases in the solid solution. Analogus behaviour is observed in the case of WSe_xTe_{2-x} system (Champion 1965).

In order to judge the semiconducting nature of $MoSe_xTe_{2-x}$ $(0 \leqslant x \leqslant 2)$, the Hall effect was measured. The Hall mobility, μ_H was determined using Van der Pauw's method for various compositions at room temperature. The Hall coefficient R_H and

Table 1.

Nominal composition (X)		Reaction temperature (°C)	Growth temperature (°C)	Growth time (hr)
$MoTe_2$	0·0	700	650	72
	0·5	900	800	48
	1·0	800	670	96
	1·5	880	720	168
$MoSe_2$	2·0	900	800	120

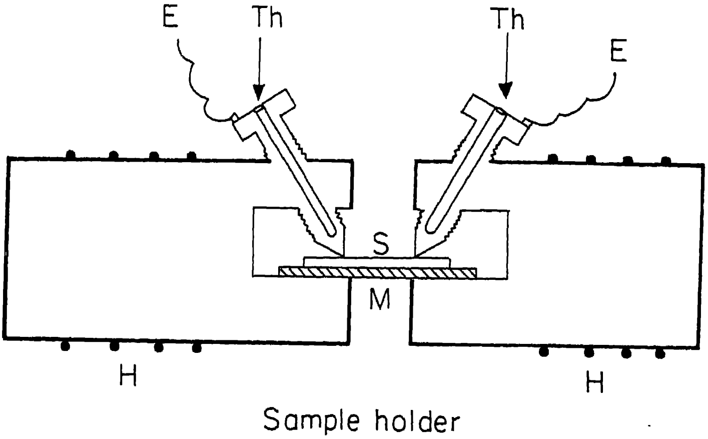

Figure 1. Schematic diagram of the sample holder for Seeback coefficient measurements. H, Heater, Th, Thermocouples E, Electrodes, S, Sample M, Mica sheet.

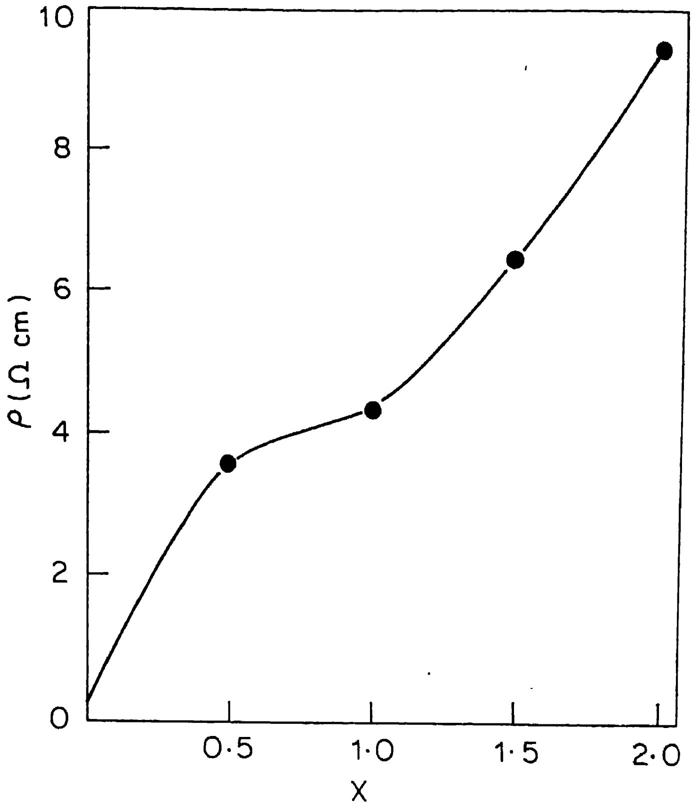

Figure 2. Variation of resistivity (ρ) as a function of composition X at $T = 30°C$.

the carrier concentration n were also calculated assuming the single carrier conduction model using the relations

$$\mu_H = R_H/\rho \text{ and } n = -1/eR_H,$$

where e is the electronic charge. The variation of μ_H, R_H and n with the composition of MoSe$_x$Te$_{2-x}$ is shown in figure 3. It is observed that Hall mobility increases with increasing selenium content. As resistivity also increases with increasing selenium content in the crystal, it is concluded that the Hall coefficient increases and hence carrier concentration decreases as we go from $MoTe_2$ to $MoSe_2$.

It is interesting to note that the optical band gap determined from the spectral response of the crystals increases with increasing selenium content in the MoSe$_x$Te$_{2-x}$ system (Agarwal *et al* 1987). The atomic radius decreases as we go from Te (1·37 Å) to Se (1·17 Å) leading to changes in the band strengths and hence in the structure. Further the electro-negativity of the atoms increases from Te (2·1) to Se (2·4) thereby indicating an increase in the ionic nature of the bonding. As a result, an increase in the resistivity and a decrease in the effective carrier concentration should be expected which agree with the experimental observations.

Thermoelectric measurements were made in the temperature range 40 to 200°C. The variation in the Seeback coefficient S with temperature for MoSe$_x$Te$_{2-x}$ system

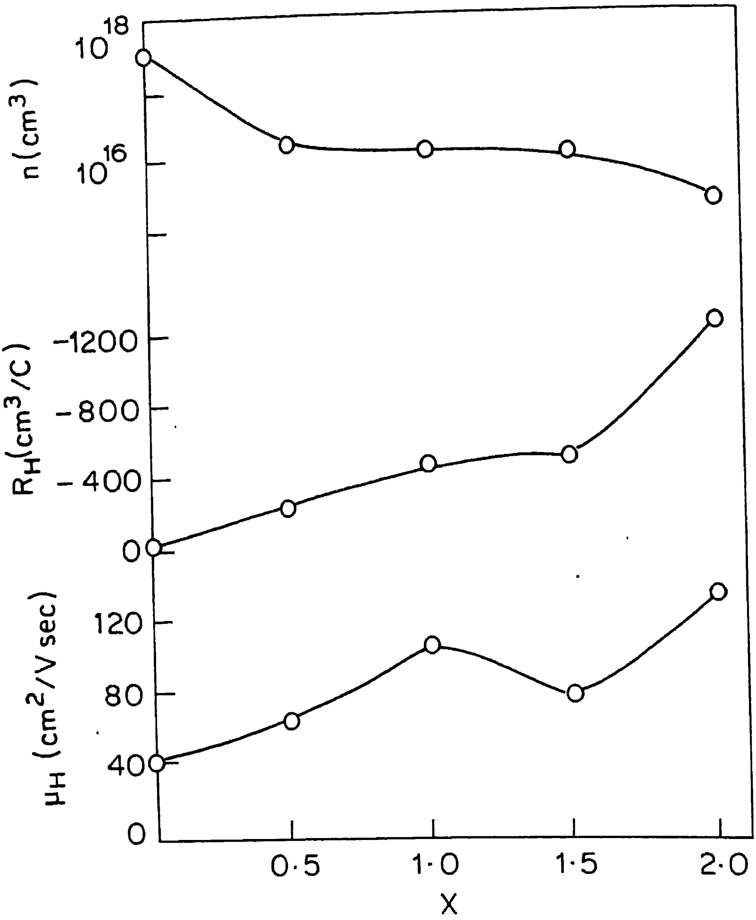

Figure 3. Variation of Hall mobility (μ_H), Hall coefficient (R_H) and carrier concentration (n) as a function of composition X at $T = 30°C$.

is shown in figure 4. The value of S increases initially with temperature and then decreases to a nearly constant value. The nature of variation is identical for all compositions in the $MoSe_xTe_{2-x}$ system except that the peak value of Seeback coefficient occurs at different temperature. The existence of a peak in S vs temperature plot and its relation to the variation in concentration and mobility of charge carriers needs to be investigated. However, it is worth noting that S showed a negative value for all compositions of the solid solution throughout the temperature range in the present study indicating the crystals to be n-type semiconductors.

Acknowledgement

One of the authors (RMJ) is thankful to the University Grants Commission, New Delhi for financial assistance.

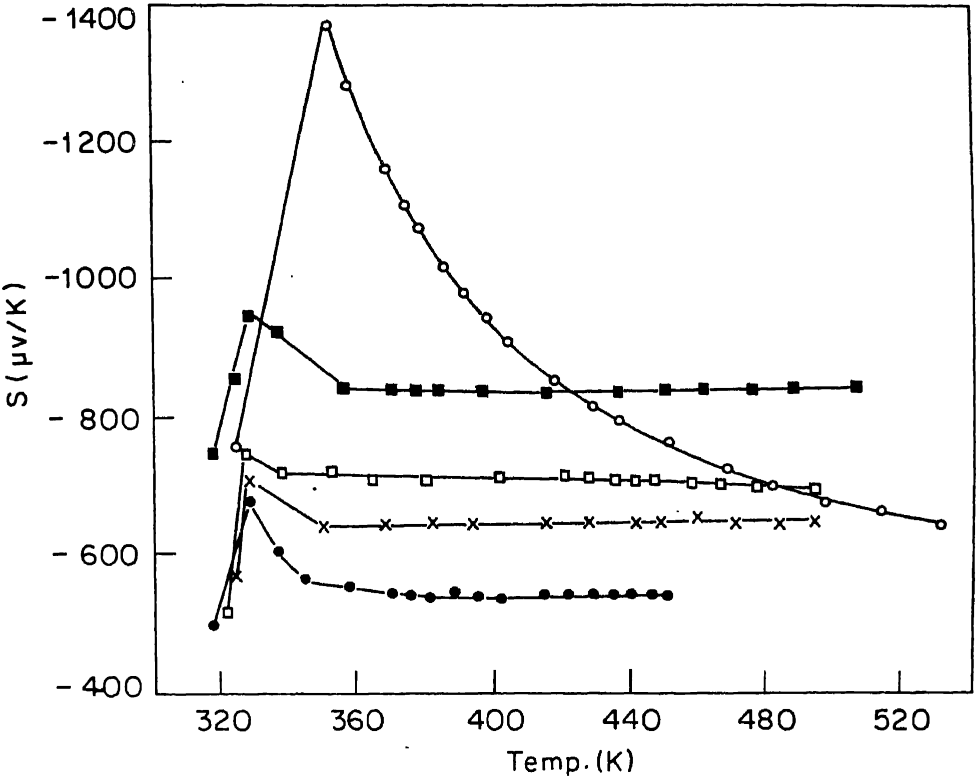

Figure 4. Seeback coefficient as a function of temperature for $MoSe_xTe_{2-x}$ system.

References

Agarwal M K and Talele L T 1986 *Solid State Commun.*
Agarwal M K, Patel P D and Joshi R M 1987 *Cryst. Res. Technol.*
Brixner L H 1963 *J. Electrochem. Soc.* **110** 298
Brixner L H and Teufer G 1963 *Inorg. Chem.* **2** 992
Champion J A 1965 *Br. J. Appl. Phys.* **16** 1035
Lepetit A 1965 *J. Phys.* **26** 175
Mansfield R and Salam A 1953 *Proc. Phys. Soc.* **66** 377
Mentzen B F and Sienko M J 1976 *Inorg. Chem.* **15** 2198
Revolinsky E and Beerntsen D 1964 *J. Appl. Phys.* **35** 2086
Schneemeyer L F and Sienko M J 1980 *Inorg. Chem.* **19** 789
Van der Pauw L J 1958 *Phillips Res. Rep.* **13** 1
Wilson J A and Yoffe A D 1969 *Adv. Phys.* **18** 193

Bull. Mater. Sci., Vol. 9, No. 5, December 1987, pp. 343–348. © Printed in India.

Measurements of the microhardness and compression testing of ferroelectric lead nitrate phosphate single crystals

C C DESAI and M S V RAMANA
Department of Physics, Sardar Patel University, Vallabh Vidyanagar 388 120, India

MS received 4 July 1987; revised 28 September 1987

Abstract. Ferroelectric crystals of lead nitrate phosphate (LNP) have been grown employing the controlled reaction between lead nitrate and orthophosphoric acid. The microhardness of LNP crystals has been determined. The effect of annealing and quenching on the mechanical properties of these crystals has been studied.

Keywords. Hardness; indentation; plasticity; cracks; indentation mark; compression; microhardness.

1. Introduction

Hardness is an important solid state property (Buckle 1959) commonly studied to determine the mechanical strength and other properties of materials. Point indentation techniques such as Vicker's pyramidal test, Hertz test and Knoop test have been commonly used to study glide, deformation anisotropy, cracks, etc in various materials. The Vicker's test is reliable for hardness measurements since it is independent of pre-existing surface flaw conditions (Haranoh *et al* 1982), is less time-consuming (Weber and Matzke 1984) and can yield a better statistical average with fewer indentations. Katakov and Yamada (1977) studied the yield strength and dislocation mobility of KCl-KBr solid solution single crystals. Grigorovish (1968) showed that microhardness is sensitive to the indented surface symmetry and its energy. Plendle and Gieliese (1962) correlated the hardness of several crystals with their lattice energy. Julg (1978) drew quantitative information about the bond strength from hardness values.

Ferroelectric lead nitrate phosphate (LNP) crystals show many interesting physical properties such as piezoelectric, optical and other characteristics. They are used in transducers and many linear and nonlinear mechanical devices. They are also suitable for verifying the microscopic theory of ferroelectricity. Data concerning the mechanical properties of LNP crystals have not so far been reported in the literature. In this paper, the results of our studies on the mechanical properties derived from plastic deformation are presented. The results of compression testing up to breaking point of the crystal are also described.

2. Experimental

Single crystals of LNP were grown using the controlled reaction between H_3PO_4 and $Pb(NO_3)_2$ by diffusion in silica gels (Desai and Ramana 1987). The crystals were examined by scanning electron microprobe analysis, X-ray diffraction, density measurements and thermogravimetric analysis. These techniques confirmed that they were LNP (monoclinic, space group $P2_1/c$). The LNP crystals ($6 \times 4 \times 3\ mm^3$) with smooth surfaces and free from microstructures were selected and indentation studies were made on as-grown (001) surface with the indentor diagonal along [010] and [100] directions. These were made on dislocation-free regions using a microhardness indentor (Vicker's model 6270). The pyramidal diamond indentor is fixed to the front lens of the reproducing objective whose optical data are those of the standard 32/0·65 apochromats. The hardness tester with an optical device to indicate the testing load was attached to an incident-light microscope (Vicker's projection microscope), with the vertical illuminator replacing a standard objective. An indentation load (10 to 100 g) can be used for this model. The indentation impression was measured by using a filer micrometer eyepiece which resembled the standard micrometer eyepiece in design, with a least count of 10 μm. To measure the diagonal of the impression and the length of the cracks, a high power objective replaced the reproducing objective of the indentor. The value of microhardness (Vickers hardness numerals, VHN) was calculated using the expression

$$\mathrm{VHN} = 1{\cdot}854\, P/d^2, \tag{1}$$

where P is the applied load in kg and d the mean diagonal length of the indentor impression in mm.

The probable mean error was calculated based on 10 indentations for a given plane and environment. Due to slight deviation from the normal incidence of the indentor on the crystal surface, two of the four vertices of the indentation impression were not well-defined on some of the samples and in such cases the measurements of length of diagonals were not accurate. To minimize the error, half diagonals were measured. The samples were maintained at 100°C for 24 hr and cooled to room temperature at 5°C hr^{-1} to anneal the crystal. The crystals were kept at different quenching temperatures for a fixed period and quenched to room temperature.

The applied pressure per unit volume of the crystal necessary for breaking was determined using a compression testing machine (Instron). For this purpose, visible transparent LNP crystals were selected and their dimensions were carefully determined using a travelling microscope. The crystal was placed between the two compression heads of the Instron machine, the upper head being slowly moved downword at a uniform speed of 0·5 cm min^{-1} and the record chart speed was 50 cm min^{-1}. The load applied and the resulting compression were recorded for various crystals. The upper head of the compression was moved until the crystal was crushed at the end of the plastic limit.

3. Observations and discussion

3.1 *Microhardness testing*

It was difficult to obtain cleaved surfaces of LNP crystal and therefore plane surfaces, microscopically free from signs of any damage, were chosen for indentation. Figure 1 shows the impression of an indentation inflicted on the (001) as-grown surfaces of the crystals at load of 30 g, the indented impression being approximately square. It also shows that several cracks or median vents grow simultaneously from the concentration points, the sharp indentation edges. No preferred directions of venting were observed as in the case of anisotropic materials where the vents tend to have a preferred orientation (Dekker and Rieck 1974). Even for low loads, the deformation was too severe and near the indentation mark, the displaced matter

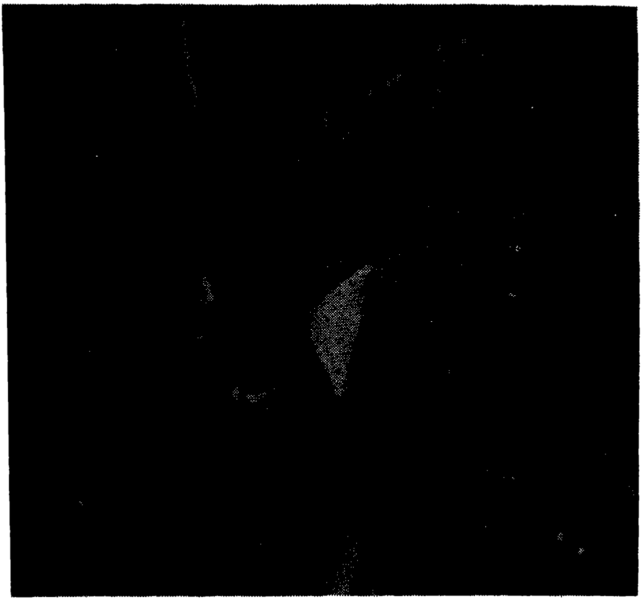

Figure 1. Typical indentation mark on (001) as-grown surface of LNP crystal (×200).

chipped off as observed on the minerals. However, this chipping off does not change the size of the indentation mark, if diagonal ends can still be observed. The basic sequence of the crack propagation events is explained below (Lawn and Wilshaw 1975).

The sharp point of the indentor produces an elastic deformation and at some threshold, a deformation-induced flow suddenly develops into a small crack, the median vent on a plane containing the contact axis and the increase in load causes further stable growth of the median vents. On unloading, the median vents begin to close but do not heal. Relaxation of deformation materials within the contact zone, just before the removal of the indentor, superimposes intense residual tensile stresses upon the applied load and extending cracks called "lateral vents" begin to appear sideways. The lateral vents continue to extend and cause chipping.

The present experimental data fit equation (1) well in the load range studied (10 to 80 g). Microhardness measurements revealed that VHN is independent of loading time or dwell time but is a function of an indentor load. The variation of hardness with load for quenched, annealed and room temperature samples is illustrated in figure 2. In all cases it was observed that microhardness increases with load giving a sharp maximum at 25 g and consistency in VHN are revealed after 50 g. The absolute value of VHN in the case of quenched sample is greater than that of specimens at room temperature and annealed crystals.

During indentation, the indentor penetrates to a depth comparable to (or greater than) the thickness of the distorted zone. Since this zone is pierced by the indentor, its effect will be marked at comparatively low loads, consequently a noticeable increase in VHN is observed in the beginning, when the chipping of the material from the surface is very intense. As the depth of impression of the diamond pyramid increases with load, the effect of distorted zone decreases and hence the load dependence of microhardness is less. This explains that the variation of VHN with load is

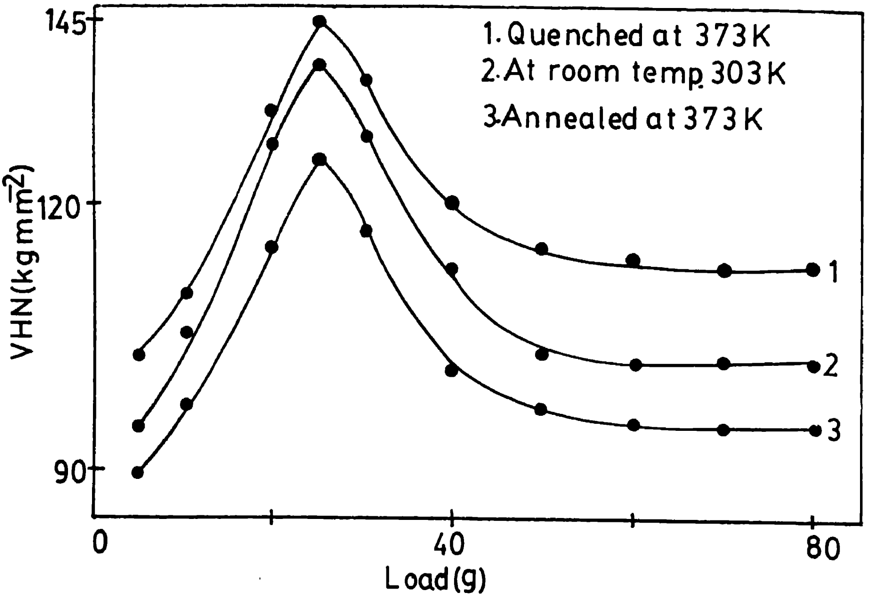

Figure 2. Plots of Vickers hardness numerals (VHN) against loads for (i) quenched, (ii) room temperature and (iii) annealed samples.

almost zero beyond 50 g. For large loads (above 50 g) when the indentor reaches a depth at which undistorted material exists, the microhardness is independent of load. Figure 2 also illustrates that annealing decreases the hardness whereas quenching increases the hardness for all loadings on (001) as-grown surfaces. This may be attributed to the quenching process as it introduces a large number of line and point defects and also results in the creation of internal stresses. Annealing, on the other hand, is a thermally activated process which leads to an arrangement of the existing dislocations and other defects into low energy configuration or total or partial annihilation.

The graph of $\log P$ vs $\log d$ (figure 3) gives two straight lines with different slopes for quenched, annealed and room temperature samples. VHN for all samples increases up to 25 g then decreases up to 50 g. Correspondingly, the $\log P$ vs $\log d$ plots give two straight lines in all cases with slopes 2·1 and 1·1 at low and high loadings for (001) as-grown surfaces which proves the validity of the Mayer's equation

$$P = ad^n, \tag{2}$$

where P is the load applied (g), d the observed length of indentation mark (mm) and a (standard hardness) and n are constants. Though $n = 2$ is satisfied in the initial conditions, the concept of Onitsch (1947) seems to be more appropriate, i.e. if $n > 2$ the hardness number decreases with increase in load but if $n < 2$, hardness increases as load increases.

3.2 *Instron compression testing*

The plot of Instron compression recorded obtained for LNP single crystals is shown in figure 4. It is observed that when the crystal is pressed perpendicular to the (001) plane, Hooke's law is obeyed in the complete region upto breaking point without

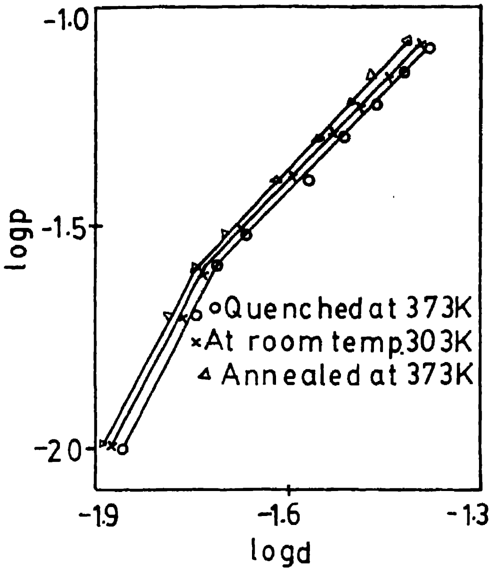

Figure 3. Graphs of log P against log d for (i) quenched (○) (ii) room temperature (×) and (iii) annealed samples (△).

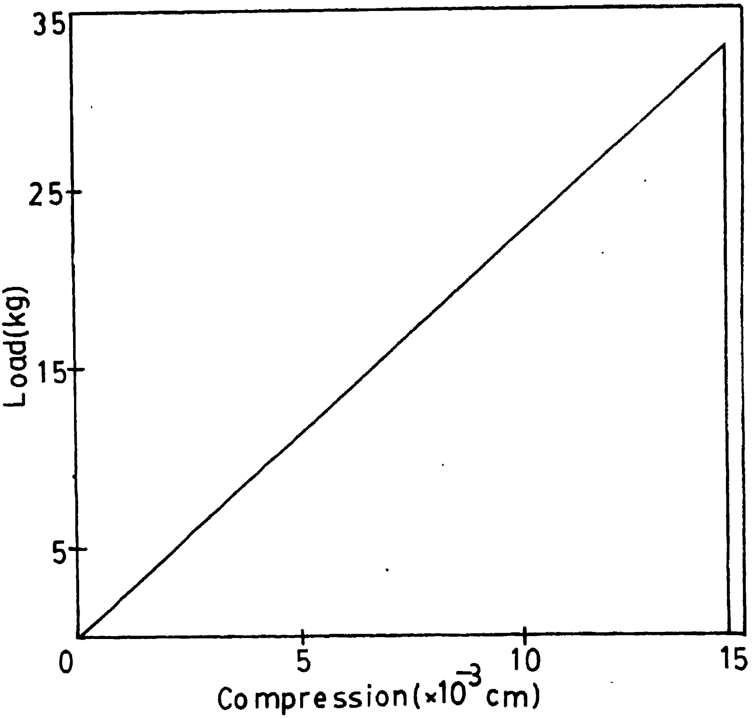

Figure 4. Instron plot of applied load vs compression for (001) as-grown surface.

Table 1. Determination of Young's modulus of LNP crystals (crystal plane: 001)

Crystal thickness (cm)	Crystal area (cm^2)	Compressibility (cm)	Load ($\times 10^6$ dynes)	Strain	Stress (kg cm^{-2})	Young's modulus ($\times 10^9$ dynes cm^{-2})
0·109	0·1888	0·0184	49	0·1688	259·4	1·5370
0·086	0·1281	0·0145	33	0·1686	256·3	1·5321

passing through a plastic region and the crystals just get randomly crushed into microbits. Crystals with different thickness were taken and the corresponding stress and strain were determined and the Young's modulus of LNP evaluated. The results are shown in table 1.

The present work suggests that (i) LNP crystals are highly brittle, because even at low indentation loads, fracture occurs at stress concentration points, (ii) VHN of LNP crystals is dependent on the applied load but is independent of the duration of loading, (iii) quenching increases the hardness of LNP crystals whereas annealing decreases the hardness, (iv) thermal treatment influences the dislocation mobility as a result of changes in the state and distribution of point defects in the crystal lattice and (v) Young's modulus of LNP crystals is $1{\cdot}53 \times 10^9$ dynes cm^{-2}.

Acknowledgements

The authors thank CSIR, New Delhi for financial assistance. One of us (CCD) thanks Mrs Aruna Desai and Mr Vishnu Desai (USA) for their interest.

References

Buckle H 1959 *Met. Rev.* **4** 49
Desai C C and Ramana M S V 1987 *Cryst. Res. Technol.* **22** 731
Dekker E H and Rieck G D 1974 *J. Mater. Sci.* **9** 1839
Grigorovish V K 1968 (Moscow: Scleromenry, Nauka) USSR pp 71–76
Haranoh T, Ishikawa H, Shinkai N and Mizuhashi M 1982 *J. Mater. Sci.* **12** 595
Julg A 1978 *Phys. Chem. Miner.* **3** 139
Katakov T and Yamada T 1977 *J. Appl. Phys.* **16** 1119
Lawn B and Wilshaw R 1975 *J. Mater. Sci.* **10** 1049
Onitsch E M 1947 *Microskopie* **2** 131
Plendle J N and Gieliese P J 1962 *Phys. Rev.* **125** 828
Weber W J and Matzke H 1984 *J. Mater. Sci.* **19** 2533

Bull. Mater. Sci., Vol. 9, No. 5, December 1987, pp. 349–353. © Printed in India.

Characterization of RF-sputtered garnet films

RAMBILAS and D BAHADUR
Advanced Centre for Materials Science, Indian Institute of Technology, Kanpur 208 016, India

MS received 2 November 1987

Abstract. Noncrystalline garnet films of nominal composition $Y_3Fe_5O_{12}$ and $Y_2GdFe_5O_{12}$ were synthesized by RF sputtering. The AC and DC resistivity data have been discussed in line with the model of Mott and Davis where conduction occurs through excitation of carriers into localized states at the band edges and hopping at energies close to the band tails.

Keywords. RF sputtering; garnet films.

1. Introduction

Noncrystalline garnets have been synthesized by several methods and characterized before and after crystallization (Popma and Van Diepen 1974; Roy *et al* 1985; Bahadur and Rai 1980). Thin films made by spray pyrolysis (Bahadur *et al* 1986), flash evaporation (Bahadur *et al* 1984) or reactive sputtering (Sawatzky and Kay 1968) yielded an amorphous structure, which upon suitable heat treatment, gave crystalline garnets. Such films showed very interesting structural, electronic and magnetic properties. Garnet films of nominal composition $Y_3Fe_5O_{12}$ (YIG) and $Y_2GdFe_5O_{12}$ (Gd-YIG) by r.f. sputtering and their structural and electronic properties were studied, the results of which are presented here.

2. Experimental

Thin films were made by r.f. sputtering of the hot-pressed target of appropriate composition by Nordiko NM-400 sputtering module on quartz substrates. Gold electrodes were deposited on the film for thickness as well as for electrical measurements. The standard error in thickness measurement is ±20 Å. The thickness of YIG and Gd-YIG films on which all measurements were carried out were 1400 Å and 1300 Å respectively.

The X-ray diffractions were recorded for the as-prepared and heat-treated samples with a Rich-Seifert isodebyeflex 2002 diffractometer with Cu-K_α target between 2θ values of 25° and 50°. Electron micrographs and diffractions were recorded with a transmission electron microscope (Philips 301). The AC and DC resistivity were measured with a Keithley electrometer and HP impedance bridge (model HP 4192A). I-V characteristics were recorded at intermittent temperatures to see its linearity.

3. Results and discussion

The as-prepared films are amorphous as determined by X-ray diffraction. Partial crystallization occurs only for samples heat-treated above 800°C for both the YIG and Gd-YIG compositions. It may be noted that the spray-pyrolysed films of the same composition crystallise at 650°C (Bahadur *et al* 1986). Therefore it appears that the r.f. sputtered films are more stable. Secondly, for the spray-pyrolysed films we observe the exsolution of Fe_2O_3 phase along with garnet phase for all the heat treatments we had tried (Bahadur *et al* 1986). In the case of r.f. sputtered films it had been possible to index all the lines to garnet phase for a particular heat treatment. Table 1 lists the *d*- and possible *hkl* values for the sample Gd-YIG heat-treated in two different conditions. When heat-treated at 1100°C for 1 hr, it gives strong lines of both the garnet and orthoferrite phase. The same sample when heat-treated at 1000°C for 2 hr gives a single garnet phase. In this case 1000°C appears as the right growth temperature for the garnet phase. Figure 1 shows a typical electron micrograph for the sample Gd-YIG heat-treated at 700°C. The inset shows its selected area

Table 1. X-ray diffraction data for Gd-YIG film heat-treated in two different conditions (data taken only between $2\theta = 25°$ and $2\theta = 50°C$).

Heat treated at 1000°C for 2 hr		Heat treated at 1100°C for 1 hr	
d value	*hkl*	*d* value	*hkl*
2·96 (S)	400	3·32 (S)	321
2·76 (S)	420	3·02 (S)	400
2·51 (M)	422	2·90 (W)	—
2·19 (W)	440	2·80 (W)	420*
2·09 (W)	532	2·70 (S)	*
1·83 (S)	444	—	—

Note: *hkl* values are w.r.t. YIG phase; The intensity is given in brackets: S, strong; M, medium; W, weak.

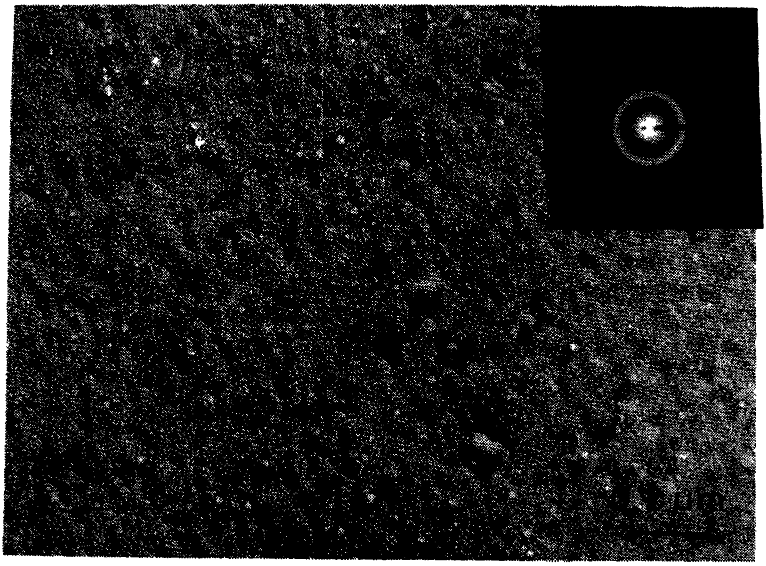

Figure 1. Electron micrograph of nominal composition $Y_2GdFe_5O_{12}$ heat-treated at 700°C for 1 hr. Inset shows the corresponding electron diffraction.

electron diffraction from which an amorphous structure is evident. The micrograph exhibits a fairly homogeneous structure. Figure 2 shows the plot of log ρ_{DC} vs $1000/T$ for YIG and Gd-YIG and figure 3 the representative plot of log ρ_{AC} vs $\log f$ for the sample Gd-YIG at two different temperatures. The activation energies evaluated from figure 2 and S values from figure 3 along with temperature ranges are given in table 2.

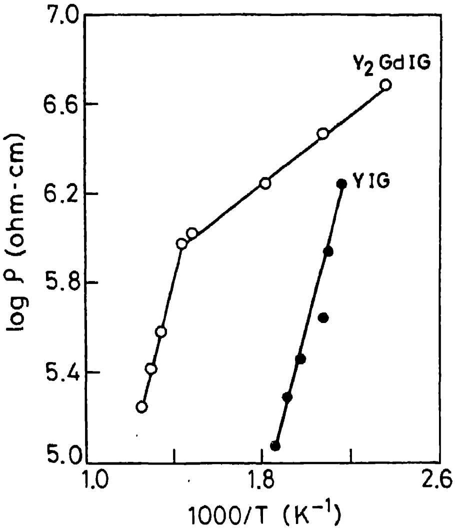

Figure 2. Plot of $\log \rho_{d.c.}$ vs 1000 T for films of nominal composition $Y_3Fe_5O_{12}$ and $Y_2GdFe_5O_{12}$.

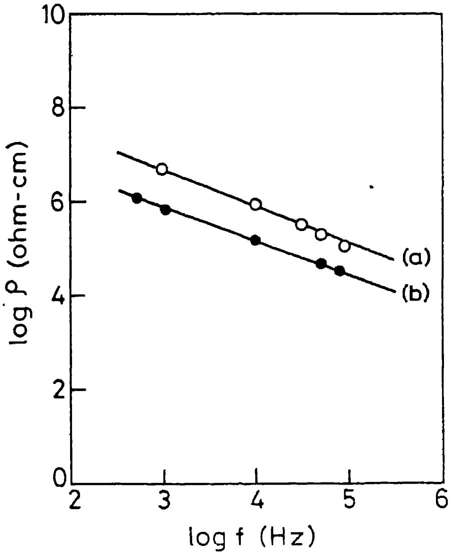

Figure 3. Plot of $\log \rho_{a.c.}$ vs $\log f$ for film of nominal composition $Y_2GdFe_5O_{12}$ at temperatures **a.** 380° K and **b.** 650° K.

Table 2. Activation energies and S values in different ranges for films of YIG and Y_2GdIG.

Sample	Thickness (Å)	Range (K)	Activation energies (eV)	S-values
YIG	1400	420–600	0·34	0·62 (670 K) 0·93 (RT)
Y_2GdIG	1300	420–690	0·07	0·8 (380 K)
		690–770	0·34	0·75 (650 K)

Note: The parentheses of the last column gives the temperature of measurement.

The sample Gd-YIG exhibits two activation energies whereas the YIG sample gives a single activation energy for the temperature range studied. The value of E_a for YIG is the same as that observed for Gd-YIG in the high temperature region. A similar observation has been made in bulk YIG and Gd-YIG (Bahadur *et al* 1981). It appears, therefore, that the localized sites through which hopping occurs are essentially the same. However, for lower temperature region where Gd-YIG exhibits an activation energy of 0·07 eV, Gd-substitution may be responsible for the generation of some new localized states which is closer to the fermi level. Another noteworthy feature of the DC resistivity data is the lower values of resistivity and activation energies compared to the bulk sample. Lowering of activation energies was similarly observed in flash-evaporated garnet films (Bahadur *et al* 1984). This is attributed to the tails of localized states and the band of compensated levels in amorphous systems which could lower the activation energies. It is interesting that the frequency dependence of resistivity varies approximately as σ^S where S lies between 0·6 and 1.

In the light of these results, it is possible to assign the electronic conduction due to the excitation of carriers into localized states at the band edges and hopping at energies close to band tails (Mott and Davis 1980; Nagels 1979). In this model a narrow tail of localized states at the extremities of the valence and conduction band and a band of localized levels near the middle of the gap exist. According to this, three conduction mechanisms are possible: (i) The extended state conduction, which demands a frequency-independent conductivity is ruled out, (ii) the conduction in localized states at the fermi energy may not be operative as indicated by the exponential dependence of $\rho(f)$ with temperature and (iii) this is then a characteristic of conduction in band tails which appears to be the mode of conduction in the system.

Acknowledgement

Financial support by the Department of Atomic Energy, Government of India is acknowledged.

References

Bahadur D and Rai K N 1980 *Mater. Res. Bull.* **15** 510
Bahadur D, Roy D and Ram S 1986 *Adv. Ceram.* **16** 651
Bahadur D, Roy D, Singh B and Saran D 1984 *Bull. Mater. Sci.* **6** 53
Bahadur D, Prakash O and Kumar D 1981 *Bull. Mater. Sci.* **3** 325

Mott N F and Davis E A 1980 *Electronic processes in noncrystalline materials* (Oxford: Clarendon Press) p. 199

Nagels D 1979 in: *Amorphous semiconductors* (ed) M H Brodsky (Berlin: Heidelberg and New York: Springer Verlag)

Popma J A and Vandiepen A M 1974 *Mater. Res. Bull.* **9** 1119

Roy D, Bhatnagar R and Bahadur D 1985 *J. Mater. Sci.* **20** 157

Sawatzky K and Kay E 1968 *J. Appl. Phys.* **39** 4700

Bull. Mater. Sci., Vol. 9, No. 5, December 1987, pp. 355–363. © Printed in India.

Li_2SO_4: $LiNbO_3$ binary system for solid state battery applications

K SINGH
Department of Physics, Nagpur University, Nagpur 440 010, India

MS received 7 September 1987; revised 12 November 1987

Abstract. Different compositions in the Li_2SO_4-$LiNbO_3$ system have been prepared by adopting the twin roller quenching technique. The electrical conductivity has been measured and the sample with 20 mole% $LiNbO_3$ exhibited maximum conductivity at 573 K. The results have been explained on the basis of XRD, SEM data and vacancy concentration. A number of solid state electrochemical cells were fabricated by varying the electrolyte composition, using Li-metal and MnO_2 as anode and cathode respectively. The 80 Li_2SO_4:20 $LiNbO_3$ composition gave the best cell performance.

Keywords. Dispersed solid electrolytes; characterization; cell voltage and current.

1. Introduction

In recent years solid electrolytes have gained importance because of their potential application in many technological devices. Lithium-conducting solid electrolyte is advantageous as it produces a greater cell voltage because of the highly electropositive nature of lithium. In addition, several cathode materials can be employed in lithium-transporting systems, because of their relatively high lithium diffusion coefficient.

Lithium sulphate is a well-known ionic conductor. It undergoes a phase transition from monoclinic (β-phase) to cubic (α-phase) structure at 848 K. In the high temperature α-phase, it has high conductivity, comparable to molten salts (Kvist and Lunden 1965). The high conducting α-phase has a fcc structure (space group $F\bar{4}$-3m) with sulphate ions situated at the origin and the oxygen atoms rotationally disordered about the sulphur atom. The highly mobile Li^+ ions, which occupy the $\pm(\frac{1}{4}, \frac{1}{4}, \frac{1}{4})$ positions in the lattice, are the charge carriers and it has been suggested that the rotational freedom of the sulphate group facilitates cation mobility (Nilsson *et al* 1980; Aronsson *et al* 1981).

β-Li_2SO_4 has a monoclinic structure (space group $P2_{1/a}$) (Mellander and Nilsson 1983) and exhibits low ionic conductivity (Deshpande and Singh 1982). The phase diagrams of many binary sulphate systems with Li_2SO_4 as one component have been studied (Schroeder and Kvist 1969; Schroeder *et al* 1972; Schroeder 1975). It has been reported that highly conducting phases can be obtained for binary systems of lithium sulphate with Na_2SO_4 and Ag_2SO_4 at a lower temperature (Heed *et al* 1977).

The equilibrium phase diagram of Li_2O:Nb_2O_5 determined by Reisman and Holtzberg (1958) shows that $LiNbO_3$ exists as a single phase over a narrow range of composition (figure 1). The single phase compound $LiNbO_3$ crystallizes from the melt at the melting point 1526 K with an exact stoichiometric ratio of atoms at 50 mole% Li_2O.

Charge transport mechanism in single crystals of $LiNbO_3$ has been investigated at higher temperature ($T > 623$ K) (Jorgensen and Bartlett 1969; Bergmann 1968) and the conductivity at 973 K has been found to be electronic at low oxygen partial

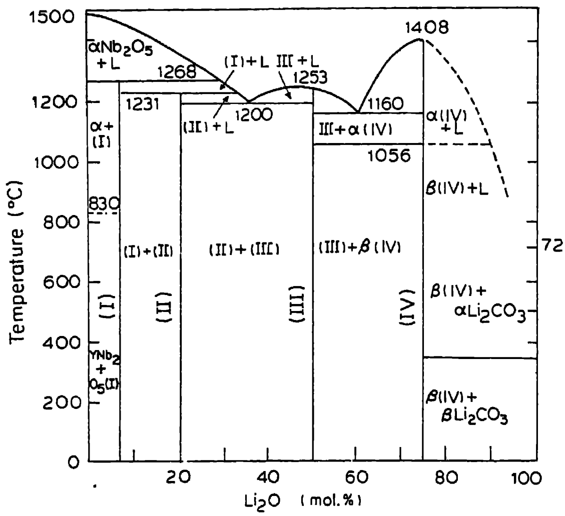

Figure 1. Phase diagram of Li_2O-Nb_2O_5 system.

pressure and ionic at one atmosphere of oxygen. They have also reported that ionic conductivity could be increased by a factor of ten by adding Li_2O. Bergmann (1968) also proposed a considerable fraction of ionic conductivity using stoichiometric $LiNbO_3$.

Although many solid state electrochemical cells have been reported, attempts to use lithium sulphate-based solid electrolytes are few. Kanda *et al* (1982) tried a composition of 80·8 Li_2SO_4:19·2 $LiNbO_3$ in Li/MnO_2 solid state cell. Their cell of 0·8 mm thickness gave an open circuit voltage of 2·65–3·4 V. It may be useful to identify the composition with maximum conductivity in the solid solution series. With this in view, the present investigation was aimed at the study of electrical conductivity of the Li_2SO_4:$LiNbO_3$ binary system, and the composition with the highest conductivity was used in an electrochemical cell.

2. Experimental

2.1 *Material preparation*

The compounds used were Li_2SO_4, Li_2CO_3 and Nb_2O_5 (99% pure) procured from A G Fluka, Germany. These initial ingredients were dried in a platinum crucible. Dried Li_2CO_3 and Nb_2O_5 (used to grow single crystals of $LiNbO_3$) were mixed and ground in an agate mortar. The mixture was taken in a 50 ml flat bottom platinum crucible covered with a platinum lid. The mixture was heated in the Gallenkamp furnace. The temperature of the furnace was raised at the rate of 313 K per hour up to 1073 K after which the lid was removed. Then the temperature was raised at the same rate to 1173 K where the mixture was sintered for about 12 hr. During sintering, Li_2CO_3 decomposes and gives CO_2 to produce Li_2O according to the reaction

$$Li_2CO_3 \rightarrow Li_2O + CO_2\uparrow.$$

The temperature was further raised at the same rate to 1573 K which is well above the melting point of Li_2CO_3. $LiNbO_3$ is formed according to the reaction

$$Li_2O + Nb_2O_5 = 2\,LiNbO_3.$$

The melt kept at this temperature for 12 hr was then cooled at a slow rate of 278 K per hour to the eutectic temperature of 1433 K. During cooling, there was spontaneous nucleation of the melt at many points so that a number of crystals were formed at the surface on solidification. From 1433 K the crystals were cooled at a faster rate of 313 K per hour to 1373 K and at this temperature, the crystals were annealed in atmosphere. It has been noticed that approximately square-shaped crystals were formed on the surface in the central region of the crucible. The crystals were clear, colourless and transparent, but in the outer regions they were pale yellow in colour.

The crystals mechanically taken out from the central region were about 2 × 2 × 1 mm in dimension. The extent of $LiNbO_3$ formation was determined by the X-ray diffraction technique.

The single crystals of $LiNbO_3$ were ground in an agate mortar under acetone and dried well at around 393 K. This powder was further used to prepare the Li_2SO_4: $LiNbO_3$ pseudo binary compositions.

The weighed quantity of Li_2SO_4 and $LiNbO_3$ of compositions 100:00, 95:5, 90:10, 80:20, 70:30, 50:50 and 30:70 mole% were ground separately. Later, the $LiNbO_3$ powder was taken in platinum crucible and introduced in an electric furnace at 1533 K. It was kept at this temperature for an hour. After this, the well ground Li_2SO_4 powder was added to the melt of $LiNbO_3$. The crucible was maintained at 1533 K for 10 to 15 min. After shaking, the melt was poured on the line contact of twin rollers made of stainless steel.

Thin flakes were obtained from the quenched liquid. Other compositions were similarly prepared. The samples were characterized by X-ray diffraction technique.

2.2 *Electrical conductivity*

The samples were obtained in the form of thin flakes and hence could not withstand the pressure of the sample holder. Therefore, these flakes were finely crushed and pelletized at 10 ton/cm^2 and these pellets were used for electrical conductivity measurements. To ensure good ohmic contact, thin aluminium foils were used before loading the sample in the sample holder (Deshpande and Singh 1982). The a.c. electrical conductivity was measured in air as a function of frequency (10 Hz–13 MHz) at various temperatures in the range 393–753 K during the cooling cycle, with the Hewlett Packard 4192ALF impedance analyser at 5 mV oscillator level. The temperature was controlled to 273 ± 1 K with Eurotherm (UK) temperature controller.

2.3 *Electrochemical cell*

The solid state electrochemical cells were fabricated by pressing together the compounds sequentially at room temperature in 1·2 cm dia. stainless steel die. A weighed amount of cathode powder was pressed at about 10 ton/cm^2. A weighed amount of Li_2SO_4 : $LiNbO_3$ (80:20) powder was dispersed on the surface of the pre-

pressed cathode, levelled and pressed at about the same pressure as mentioned above. Finally, a thin lithium foil of appropriate dimension was pressed against the pellet as an anode in a glove bag filled with argon gas. The cell thus obtained was placed in a stainless steel cell holder (figure 2).

3. Results and discussion

When Li_2SO_4 (LS) and $LiNbO_3$ (LN) were melted together and quenched rapidly, LN remained separated at the bottom of the crucible. Since LS and LN are not isostructural, this system is pseudobinary. The melting point of LN (1526 K) is much higher than that of LS (1133 K). Thus when (90:10) LS:LN was melted together, the LN-rich phase was obtained due to the evaporation of LS which was confirmed by XRD (table 1a). For this composition, the conductivity was quite low due to the increased phase separation. Thus in the case of 80:20 (LS:LN), LN was melted first at 1526 K and then LS was added to the melt. To overcome evaporation losses, the melt was thoroughly shaken before rapid quenching.

Figure 3 depicts the plots of $\log \sigma T$ vs $10^3/T$ for pure LS, LN and different binary compositions. In general, the conductivity increases with rise in temperature. The conductivity of LS is higher than that for LN. This is due to the lower melting point and phase transition temperature ($T_c = 848$ K) of LS as compared to LN ($T_c = 1483$ K).

The functional dependence of $\log \sigma T$ on mole% of LN at 553 K (figure 4) shows maximum conductivity at 20 mole% of LN. It is seen from XRD data (tables 2 and 3) that only a few peaks of LN appear. SEM study (figure 5) revealed the presence of finely dispersed $LiNbO_3$ in the Li_2SO_4 matrix. This in turn gives rise to more interfacial area between the grains probably contributing to the conductivity. The present results are similar to the results of the composite solid electrolyte system such as AgI-Al_2O_3 (Liang 1973; Chowdhary *et al* 1985; Poulsen 1985). A conductivity maximum has also been found for the two-phase regions in the system with two ionic conductors AgI-AgBr (Shahi and Wagner 1980, 1984; Maier 1985) $Li_2SO_4:CaSO_4$ (Careem and Dissanayake 1986) and $Li_2SO_4:Li_2CO_3$ (Dissanayake and Mellander 1986). The increase in conductivity in these cases had been attributed to conduction in the interface region between the two phases.

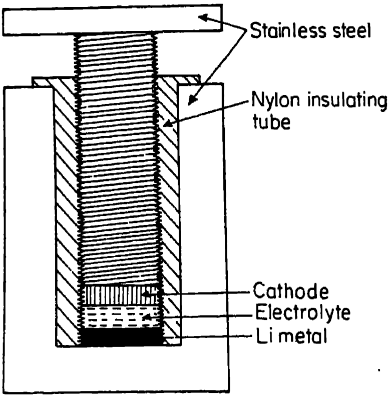

Figure 2. Solid state electrochemical cell assembly.

Table 1. Comparison of the experimentally obtained *d* values with that of the ASTM data for 90 mole% Li_2SO_4 and 10 mole% $LiNbO_3$.

Observed			ASTM		Observed phase	*hkl*
2θ	*d*	I/I_0	*d*	I/I_0		
22·0	4·0401	100·00	4·04	100	LS	002
25·35	3·5201	14·54	3·520	04	$LS\cdot H_2O$	111
28·0	3·1866	39·35	3·18	30	LS	112
32·7	2·7385	43·24	2·730	64	LN	100
33·4	2·6067	17·14	2·603	6	$LS\cdot H_2O$	200, 003
34·7	2·5851	43·24	2·5801	37	LN	110
36·1	2·4830	21·38	2·479	20	LS	020
36·8	2·3799	27·14	2·377	06	$LS\cdot H_2O$	$\bar{2}12$
37·4	2·4044	11·16	2·402	10	LS	$\bar{3}11$
38·6	2·3324	4·93	2·339	16	$LS\cdot H_2O$	$\bar{1}13$
39·1	2·3037	7·40	2·300	7·3	LN	006
40·7	2·2168	9·35	2·211	2·0	LS	121
42·6	2·1222	28·57	2·120	18·4	LN	202
46·4	1·9569	9·35	1·950	2	$LS\cdot H_2O$	004
48·3	1·8842	16·36	1·884	4	LS	$\bar{4}03$
55·9	1·6447	9·74	1·641	36	LN	122
61·0	1·5166	7·79	1·514	21	LN	241
62·2	1·4924	14·80	1·491	4	LS	$\bar{4}05$

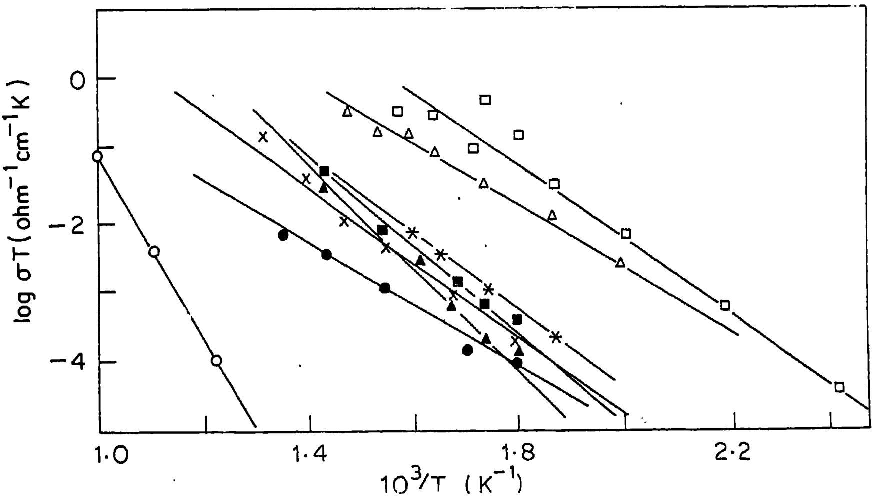

Figure 3. Variation of log σT vs $10^3/T$ for Li_2SO_4:$LiNbO_3$. -●- 100:00; -×-95:05; -▲-90:10; -□-80:20; -△-70:30; -■-50:50; -*-30:70; -○-00:100.

Li/MnO_2 cells using different electrolytes have been fabricated. From table 4 it is evident that the 80 Li_2SO_4 : 20 $LiNbO_3$ system, giving maximum conductivity in the series, offered better electrochemical cell performance compared to other solid electrolytes developed in our laboratory. In spite of the higher conductivity exhibited

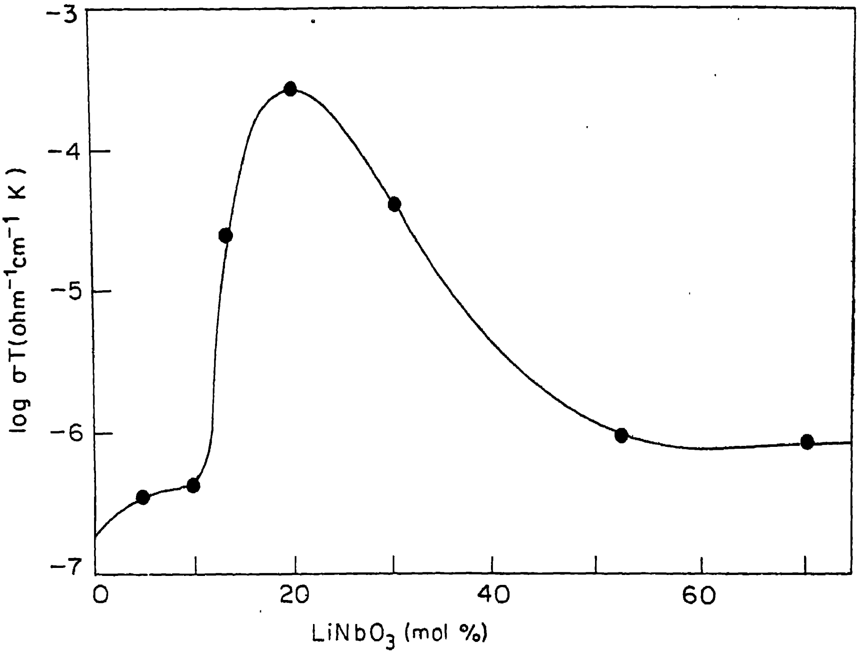

Figure 4. Functional dependence of logσT vs mol. % of LiNbO$_3$.

Table 2. Comparison of the experimentally obtained d values with that of the ASTM data for 80 mole% Li$_2$SO$_4$ and 20 mole% LiNbO$_3$.

Observed			ASTM		Observed phase	hkl
2θ	d	I/I_0	d	I/I_0		
21·5	4·1329	100·00	4·133	95	LS·H$_2$O	011
23·2	3·8338	70·45	3·83	85	LS·H$_2$O	101
25·1	3·6926	95·65	3·696	35	LS·H$_2$O	$\bar{1}02$
30·4	2·9402	51·13	2·944	50	LS·H$_2$O	112
32·8	2·7302	55·11	2·730	64·2	LN	014
33·6	2·6671	16·47	2·666	16	LS·H$_2$O	$\bar{1}03$
37·6	2·3921	7·95	2·396	10	LS·H$_2$O	112
38·6	2·3324	12·72	2·339	16	LS·H$_2$O	$\bar{1}13$
39·3	2·2924	15·34	2·295	20	LS·H$_2$O	210, 013
40·0	2·2539	7·95	2·254	8	LS·H$_2$O	$\bar{2}12$
41·0	2·2012	9·65	2·202	12	LS·H$_2$O	122
45·3	2·0018	4·54	2·001	6	LS·H$_2$O	$\bar{2}13$
48·6	1·8733	12·50	1·875	6	LS	$\bar{4}13$
50·8	1·7972	4·54	1·797	6	LS·H$_2$O	$\bar{1}13$, $\bar{3}02$
54·0	1·6980	7·38	1·697	2	LS	123
57·0	1·6165	5·11	1·616	2	LS	130
59·1	1·5631	5·68	1·565	2	LS	$\bar{4}22$, 131
78·4	1·2068	5·11	1·206	9	LN	218

by the Li$_2$SO$_4$: LiOH : LiF system, its cell performance is not as good as that of 80 Li$_2$SO$_4$: 20 LiNbO$_3$. Thus high conductivity is not the only criteria for obtaining a good cell.

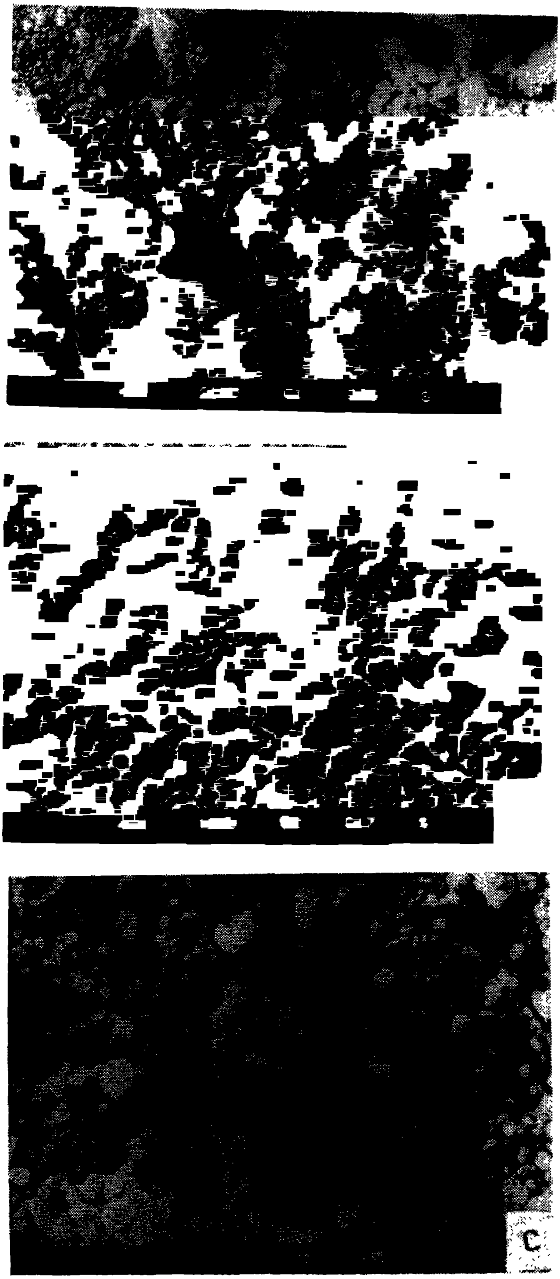

Figure 5. Scanning electron micrographs of $LiNbO_3 : Li_2SO_4$ system.

Table 3. Comparison of the experimentally obtained *d* values with that of the ASTM data for 70 mole% Li_2SO_4 and 30 mole% $LiNbO_3$.

Observed			ASTM			
2θ	d	I/I_0	d	I/I_0	Observed phase	*hkl*
23·2	3·8338	14·34	3·837	85	LS · H_2O	101
25·0	3·5617	22·22	3·559	90	LS · H_2O	110
25·5	3·4930	7·87	3·49	20	LS	111
28·2	3·1644	25·85	3·16	40	LS	201
29·2	3·0532	17·57	3·049	60	LS · H_2O	012
32·7	2·7385	16·16	2·730	64·2	LN	014
36·2	2·4813	6·85	2·479	16·0	LS	020
42·7	2·1175	100·00	2·120	18·40	LN	202
61·9	1·4989	32·59	1·495	4·0	LS	510
78·4	1·2197	7·6147	1·217	5·5	LN	312

Table 4. Conductivity and cell performance for various solid electrolytes.

		Cell Li/SE/MnO_2		
Solid electrolyte	Condition	O.C.V. (V)	Short circuit current (μA)	AC conductivity (bulk) at 553 K $ohm^{-1}\,cm^{-1}$ K
Li_2SO_4	Powder	3·2	0·22	$2{\cdot}70 \times 10^{-7}$
$LiNbO_3$	Single crystal	1·6	0·02	$1{\cdot}53 \times 10^{-7}$
7 Li_2SO_4 : 3 $LiNbO_3$	Powder	3·22	0·00	$3{\cdot}71 \times 10^{-5}$
8 Li_2SO_4 : 2 $LiNbO_3$	Powder	3·55	10·00	$2{\cdot}74 \times 10^{-4}$
8·08 Li_2SO_4 : 1·92 $LiNbO_3$*	Powder	2·65–3·40 (16 h)	—	—
6 Li_2SO_4 : 4 Li_2CO_3	Powder	3·60	1·4	$7{\cdot}19 \times 10^{-4}$
Li_2SO_4 : LiOH : LiF	Powder	3·183	0·069	$2{\cdot}27 \times 10^{-2}$
Li_2O : B_2O_3 : Ag_2SO_4	Powder	2·00	0·00254	$1{\cdot}2 \times 10^{-3}$

*Kanda *et al* (1982).

References

Aronsson R, Knape G, Lunden A, Nilsson L and Torell L 1981 *Solid State Ionics* **5** 445

Bergmann G 1968 *Solid State Commun.* **6** 77

Careem M A and Dissanayake M A K L 1986 *Proc. Regional Workshop on Materials for Solid State Batteries* (ed) B V R Chawdhary and S Radhakrishna (Singapore: World Scientific Co) p. 286

Chowdhary P, Tare V B and Wagner Jr J B 1985 *J. Electrochem. Soc.* **132** 123

Deshpande V K and Singh K 1982 *Solid State Ionics* **6** 151

Dissanayake M A K L and Mellander B E 1986 *Solid State Ionics* **21** 279

Heed B, Lunden A and Schroeder K 1977 *Electrochim. Acta* **22** 705

Jorgensen P J and Bartlett R W 1969 *J. Phys. Chem. Solids* **30** 2639

Kanda M, Yamada S, Shirogami T, Sato Y and Takamura T 1982 *J. Appl. Electrochem.* **12** 599

Kvist A and Lunden A 1965 *Z. Naturforsch.* **229** 235

Liang C C 1973 *J. Electrochem. Soc.* **120** 1289

Maier J and Ber Bunsenges 1985 *Phys. Chem.* **89** 355

Mellander B E and Nilsson L 1983 *Z. Naturforsch.* **A38** 1396

Nilsson L, Thomas J O and Tofield B C 1980 *J. Phys.* **C13** 6441

Poulsen F W 1985 *Transport structure relations in fast ion and mixed conductors* (eds) F W Poulsen, N H Andersen, K Clausen, S Skaarup and O T Sorenson (Roskilde: Riso National Laboratory) p. 67

Reismen A and Holtzberg F 1958 *J. Am. Chem. Soc.* **80** 6503

Schroeder K 1975 Ph.D. Thesis, Chalmers University of Technology, Goteborg, Sweden

Schroeder K and Kvist A 1969 *Z. Naturforsch.* **A24** 844

Schroeder K, Kvist A and Ljungmark H 1972 *Z. Naturforsch.* **A27** 1252

Shahi K and Wagner Jr J B 1980 *Appl. Phys. Lett.* **37** 157

Shahi K and Wagner Jr J B 1984 *Solid State Ionics* **12** 511

Bulletin of Materials Science

Volume 9, January–December 1987

SUBJECT INDEX

Activation energy
  Kinetics of crystallization of a $Fe_{74}Co_{10}B_{16}$ glass 269
  Electrical conductivity of the ferroelectric sodium vanadate, potassium vanadate, lithium vanadate and their solid solutions 331
Activation energy for crystal growth
  Non-isothermal crystallization of As_2Se_3 glass 13
Aliovalent substitution
  Aliovalent substitution in β-Li_2SO_4 towards conductivity enhancement 263
Alkali halide gold
  Nonlinearity in gold-alkali halide-gold capacitors 67
Alloy oxide equilibria
  Alloy oxide equilibria in the Cr-Mn-O system 149
Alumina gel
  Optical properties of coloured transparent alumina gel monolith glasses 193
Ammonium hydrogen tartrate
  Morphological aspects of some symmetrical ammonium hydrogen tartrate crystals grown by silica gel technique 89
Amorphous germanium
  Influence of substrate temperature on the electrical and optical properties of amorphous germanium films 47
Annealing
  Influence of substrate temperature on the electrical and optical properties of amorphous germanium films 47
Anodic oxide
  Preparation and properties of native oxide film anodically grown on $Hg_{0.8}Cd_{0.2}Te$ 219
As_2Se_3 glass
  Non-isothermal crystallization of As_2Se_3 glass 13
Aurivillius oxides
  High resolution electron microscopy of bismuth oxides with perovskite layers 29
Avrami exponent
  Kinetics of crystallization of a $Fe_{74}Co_{10}B_{16}$ glass 269

Band cross-over
  Pressure-induced band cross-over in $Pb_{1-x}Sn_xTe$ 131
Barium titanate
  Synthesis and properties of manganese-doped barium titanate 159
Base metal electrodes
  Synthesis and properties of manganese-doped barium titanate 159
Beam divergence
  Use of energy dispersive method with tungsten carbide opposed anvil high pressure set-up 225
Biocompatability
  Long term soft tissue response to metals, ceramics and composites—a comparative histopathological evaluation 309
Bismuth
  Undercooling studies on dispersed bismuth droplets 277
Book review 73

Capacitors
  Nonlinearity in gold-alkali halide-gold capacitors 67
  Synthesis and properties of manganese-doped barium titanate 159
Catalytic reactions
  In situ photoacoustic spectroscopic studies on heterogeneous catalysts under conditions of gas flow 81
Catchment area
  Hillock and island formation during annealing of gold films 55
Cell voltage and current
  Li_2SO_4:$LiNbO_3$ binary system for solid state battery applications 355
Ceramics
  Long term soft tissue response to metals, ceramics and composites—a comparative histopathological evaluation 309
Ceramic semiconductors
  Dielectric behaviour of ZnO-based ceramic semiconductors 169
Characterization
  Li_2SO_4:$LiNbO_3$ binary system for solid state battery applications 355
Chemical analysis
  A study of Vishnukundin coins 137
Chemical potential of fluorine
  Measurement of Gibbs energies of formation of CoF_2 and MnF_2 using a new composite dispersed solid electrolyte 37

Chrysotile asbestos
  Dehydration and phase transformation in chrysotile asbestos—A radial distribution analysis study 103
Coin
  A study of Vishnukundin coins 137
Cold-work recovery
  Positron annihilation in Zr-0·5 Nb alloy 235
Coloured alumina gel
  Optical properties of coloured transparent alumina gel monolith glasses 193
Composites
  Long term soft tissue response to metals, ceramics and composites—a comparative histopathological evaluation 355
II–VI compounds
  Preparation and properties of native oxide film anodically grown on $Hg_{0\cdot8}Cd_{0\cdot2}Te$ 219
Compression
  Measurements of the microhardness and compression testing of ferroelectric lead nitrate phosphate single crystals 343
Conductivity
  Electrical conductivity of the ferroelectric sodium vanadate, potassium vanadate, lithium vanadate and their solid solutions 331
Conductivity enhancement
  Aliovalent substitution in β-Li_2SO_4 towards conductivity enhancement 263
Cracks
  Measurements of the microhardness and compression testing of ferroelectric lead nitrate phosphate single crystals 343
Cr-Mn-O
  Alloy oxide equilibria in the Cr-Mn-O system 149
Crystallization
  Crystallization behaviour of Metglas 2826 MB ($Fe_{40}Ni_{38}Mo_4B_{18}$) 207
  Kinetics of crystallization of a $Fe_{74}Co_{10}B_{16}$ glass 269
$CuAlO_2$
  X-ray photoelectron spectroscopy studies on ethylene oxychlorination catalysts 75
Cumulative damage
  Evaluation of cumulative damage in glass fibre reinforced plastic by ultrasonic method 61

d.c. electrical conductivity
  Influence of substrate temperature on the electrical and optical properties of amorphous germanium films 47
Deactivation
  X-ray photoelectron spectroscopy studies on ethylene oxychlorination catalysts 75
Defect structures
  High resolution electron microscopy of bismuth oxides with perovskite layers 29
Dehydration
  Dehydration and phase transformation in chrysotile asbestos—A radial distribution analysis study 103
Delineation of catchment area
  Hillock and island formation during annealing of gold films 55
Density of states
  Influence of substrate temperature on the electrical and optical properties of amorphous germanium films 47
Dielectric constant
  Dielectric behaviour of glasses and glass ceramics in the system BaO-PbO-TiO_2-B_2O_3-SiO_2 255
Dielectrics
  Dielectric behaviour of ZnO-based ceramic semiconductors 169
Diffusion mechanism
  A study of diffusion mechanisms in sintering by shrinkage measurements 97
Dilute zirconium alloys
  Positron annihilation in Zr-0·5 Nb alloy 235
Dispersed solid electrolytes
  Li_2SO_4:$LiNbO_3$ binary system for solid state battery applications 355
Domain stabilization
  Synthesis and properties of manganese-doped barium titanate 159

E-glass fibre
  Evaluation of cumulative damage in glass fibre reinforced plastic by ultrasonic method 61
Electrical resistivity
  Electrical resistivity of holmium hydride films 181
  Transport properties of $MoSe_xTe_{2-x}$ $(0 \leqslant x \leqslant 2)$ single crystals 337
Electromotive force
  Measurement of Gibbs energies of formation of CoF_2 and MnF_2 using a new composite dispersed solid electrolyte 37
Electronic heat capacities
  A new formalism for representation of heat capacities of metals 241
Electron microscopy
  High resolution electron microscopy of bismuth oxides with perovskite layers 29
Energy-dispersive method
  Use of energy dispersive method with tungsten carbide opposed anvil high pressure set-up 225
Enthalpy
  X-ray crystallographic and thermal studies on the hydrides of magnesium and its intermetallics 21
  Measurement of Gibbs energies of formation of CoF_2 and MnF_2 using a new composite dispersed solid electrolyte 37

Entropy
  Measurement of Gibbs energies of formation of CoF_2 and MnF_2 using a new composite dispersed solid electrolyte 37
Entropy of formation
  X-ray crystallographic and thermal studies on the hydrides of magnesium and its intermetallics 21
Epoxy resin
  Evaluation of cumulative damage in glass fibre reinforced plastic by ultrasonic method 61

Ferroelectric
  Magnetic susceptibility measurements of LHP and LNP crystals 203
  Dielectric behaviour of glasses and glass ceramics in the system $BaO\text{-}PbO\text{-}TiO_2\text{-}B_2O_3\text{-}SiO_2$ 255
Ferroelectrics
  Electrical second harmonic generation and temperature autostabilized nonlinear dielectric element in ferroelectric solid solutions $(Na_xK_{1-x})VO_3$ and $(Na_xLi_{1-x})VO_3$ 111
  Electrical conductivity of the ferroelectric sodium vanadate, potassium vanadate, lithium vanadate and their solid solutions 331
Free energy of formation
  Measurement of Gibbs energies of formation of CoF_2 and MnF_2 using a new composite dispersed solid electrolyte 37
Frequency dispersion
  Ionic conductivity and hopping rate data for some NASICON analogues 117

Garnet films
  Characterization of RF-sputtered garnet films 349
Gasket scattering
  Use of energy dispersive method with tungsten carbide opposed anvil high pressure set-up 225
Gel method
  Morphological aspects of some symmetrical ammonium hydrogen tartrate crystals grown by silica gel technique 89
Glass ceramics
  Dielectric behaviour of glasses and glass ceramics in the system $BaO\text{-}PbO\text{-}TiO_2\text{-}B_2O_3\text{-}SiO_2$ 255
Gold
  Nonlinearity in gold-alkali halide-gold capacitors 67
Gouy balance
  Magnetic susceptibility measurements of LHP and LNP crystals 203

Habit modification
  Morphological aspects of some symmetrical ammonium hydrogen tartrate crystals grown by silica gel technique 89
Hall mobility
  Transport properties of $MoSe_xTe_{2-x}$ $(0\leqslant x\leqslant 2)$ single crystals 337
Hardness
  Measurements of the microhardness and compression testing of ferroelectric lead nitrate phosphate single crystals 343
Heterogeneous catalyst
  In situ photoacoustic spectroscopic studies on heterogeneous catalysts under conditions of gas flow 81
High pressure studies
  Use of energy dispersive method with tungsten carbide opposed anvil high pressure set-up 225
Hillock and island formation
  Hillock and island formation during annealing of gold films 55
Hole density
  Hillock and island formation during annealing of gold films 55
Holmium hydride films
  Electrical resistivity of holmium hydride films 181
Hopping
  Electrical properties of the system lanthanum lead cobalt titanium oxide 123
Hopping rate
  Ionic conductivity and hopping rate data for some NASICON analogues 117
Hounsfield tensemeter
  Evaluation of cumulative damage in glass fibre reinforced plastic by ultrasonic method 61
Hydriding apparatus
  Development of a Sievert's type gas doping apparatus 305

Incubation time
  Kinetics of crystallization of a $Fe_{74}Co_{10}B_{16}$ glass 269
Indentation
  Measurements of the microhardness and compression testing of ferroelectric lead nitrate phosphate single crystals 343
Indentation hardness
  Microhardness measurement in nonmetallic materials 287
Indentation mark
  Measurements of the microhardness and compression testing of ferroelectric lead nitrate phosphate single crystals 343
Isopiestic technique
  Alloy oxide equilibria in the Cr-Mn-O system 149

Jump frequency
  Ionic conductivity and hopping rate data for some NASICON analogues 117

$KCuCl_3$
  X-ray photoelectron spectroscopy studies on ethylene oxychlorination catalysts 75
Kissinger plot
  Crystallization behaviour of Metglas 2826 MB ($Fe_{40}Ni_{38}Mo_4B_{18}$) 207
Lanthanum lead cobalt titanium oxide
  Electrical properties of the system lanthanum lead cobalt titanium oxide 123
Lattice images
  High resolution electron microscopy of bismuth oxides with perovskite layers 29
Lead hydrogen phosphate
  Magnetic susceptibility measurements of LHP and LNP crystals 203
Lead nitrate phosphate
  Magnetic susceptibility measurements of LHP and LNP crystals 203
Lead tin telluride
  Pressure-induced band cross-over in $Pb_{1-x}Sn_xTe$ 131
Long term evaluation
  Long term soft tissue response to metals, ceramics and composites—a comparative histopathological evaluation 309

Magnesium nickel hydride
  X-ray crystallographic and thermal studies on the hydrides of magnesium and its intermetallics 21
Magnetic constant
  A new formalism for representation of heat capacities of metals 241
Magnetic susceptibility
  Magnetic susceptibility measurements of LHP and LNP crystals 203
Mercury cadmium telluride
  Preparation and properties of native oxide film anodically grown on $Hg_{0.8}Cd_{0.2}Te$ 219
Metal hydrides
  Development of a Sievert's type gas doping apparatus 305
Metallic glass
  Crystallization behaviour of Metglas 2826 MB ($Fe_{40}Ni_{38}Mo_4B_{18}$) 207
  Kinetics of crystallization of a $Fe_{74}Co_{10}B_{16}$ glass 269
Metals
  Long term soft tissue response to metals, ceramics and composites—a comparative histopathological evaluation 309
Meyer-Neldel rule
  Conductivity pre-exponential factors for some new superionic conductors 317
Microhardness
  Microhardness measurement in nonmetallic materials 287
  Measurements of the microhardness and compression testing of ferroelectric lead nitrate phosphate single crystals 343
Microstructural study
  A study of Vishnukundin coins 137
Microstructure
  Crystallization behaviour of Metglas 2826 MB ($Fe_{40}Ni_{38}Mo_4B_{18}$) 207
Mn-doping
  Synthesis and properties of manganese-doped barium titanate 159
Mobile ion concentration
  Ionic conductivity and hopping rate data for some NASICON analogues 117
Mordenite
  Synthesis and characterization of mordenite crystals 7
Morphology
  Morphological aspects of some symmetrical ammonium hydrogen tartrate crystals grown by silica gel technique 89
$MoSe_xTe_{2-x}$ ($0 \leqslant x \leqslant 2$) single crystals
  Transport properties of $MoSe_xTe_{2-x}(0 \leqslant x \leqslant 2)$ single crystals 337

Narrow gap semiconductors
  Pressure-induced band cross-over in $Pb_{1-x}Sn_xTe$ 131
Nasicon analogues
  Ionic conductivity and hopping rate data for some NASICON analogues 117
  Conductivity pre-exponential factors for some new superionic conductors 317
Native oxide
  Preparation and properties of native oxide film anodically grown on $Hg_{0.8}Cd_{0.2}Te$ 219
$NH_4Zr_2V_3O_{12}$
  $NH_4Zr_2V_3O_{12}$ proton conductor 323
Niobium nitride
  Electrical conductivity and transition temperature of NbN thin films 187
Non-isothermal crystallization
  Non-isothermal crystallization of As_2Se_3 glass 13
Nonlinearity
  Nonlinearity in gold-alkali halide-gold capacitors 67
Nonmetallic materials
  Microhardness measurement in nonmetallic materials 287
Nucleation
  Undercooling studies on dispersed bismuth droplets 277

Open photoacoustic cell
  In situ photoacoustic spectroscopic studies on heterogeneous catalysts under conditions of gas flow 81

Optical energy gap
  Influence of substrate temperature on the electrical and optical properties of amorphous germanium films 47
Optical properties
  Optical properties of coloured transparent alumina gel monolith glasses 193
Oxalate route
  Synthesis and properties of manganese-doped barium titanate 159
Oxychlorination
  X-ray photoelectron spectroscopy studies on ethylene oxychlorination catalysts 75

Perovskite
  Electrical properties of the system lanthanum lead cobalt titanium oxide 123
Phase transformation
  Dehydration and phase transformation in chrysotile asbestos—A radial distribution analysis study 103
Phase transition
  X-ray crystallographic and thermal studies on the hydrides of magnesium and its intermetallics 21
  Pyroelectric properties of lead-barium titanate and lead-strontium titanate 249
  Electrical conductivity of the ferroelectric sodium vanadate, potassium vanadate, lithium vanadate and their solid solutions 331
Photoacoustic spectroscopy
  In situ photoacoustic spectroscopic studies on heterogeneous catalysts under conditions of gas flow 81
pH value
  Preparation and properties of native oxide film anodically grown on $Hg_{0\cdot8}Cd_{0\cdot2}Te$ 219
Plasticity
  Measurements of the microhardness and compression testing of ferroelectric lead nitrate phosphate single crystals 343
Positron annihilation
  Positron annihilation in Zr–0·5 Nb alloy 235
Potassium lithium niobate glass
  Twin roller quenching technique and preparation of glasses of high melting ionic solids 1
Pre-exponential factor
  Conductivity pre-exponential factors for some new superionic conductors 317
Prismatic pyramidal
  Synthesis and characterization of mordenite crystals 7
Proton conductor
  $NH_4Zr_2V_3O_{12}$ proton conductor 323
Pyroelectric behaviour
  Pyroelectric properties of lead-barium titanate and lead-strontium titanate 249

Radial distribution
  Dehydration and phase transformation in chrysotile asbestos—A radial distribution analysis study 103
Relaxation phenomena
  Dielectric behaviour of ZnO-based ceramic semiconductors 169
Resistivity
  Electrical properties of the system lanthanum lead cobalt titanium oxide 123
RF sputtering
  Characterization of RF-sputtered garnet films 349
Rice husk
  Increase in the yield of silicon carbide whiskers from rice husk 295

Second harmonic generation
  Electrical second harmonic generation and temperature auto-stabilized nonlinear dielectric element in ferroelectric solid solutions $(Na_xK_{1-x})VO_3$ and $(Na_xLi_{1-x})VO_3$ 111
Seebeck coefficient
  Electrical properties of the system lanthanum lead cobalt titanium oxide 123
Shrinkage measurements
  A study of diffusion mechanisms in sintering by shrinkage measurements 97
Silica gels
  Magnetic susceptibility measurements of LHP and LNP crystals 203
Silicon carbide whiskers
  Increase in the yield of silicon carbide whiskers from rice husk 295
Single crystal
  Morphological aspects of some symmetrical ammonium hydrogen tartrate crystals grown by silica gel technique 89
Sintering
  A study of diffusion mechanisms in sintering by shrinkage measurements 97
Soft tissue reaction
  Long term soft tissue response to metals, ceramics and composites—a comparative histopathological evaluation 309
Solid electrolytes
  Ionic conductivity and hopping rate data for some NASICON analogues 117
Solid tissue reaction
  Long term soft tissue response to metals, ceramics and composites—a comparative histopathological evaluation 309
Sputtering
  Electrical conductivity and transition temperature of NbN thin films 187
Substrate temperature
  Influence of substrate temperature on the electrical and optical properties of amorphous germanium films 47

Superconducting transition temperature
  Electrical conductivity and transition temperature of NbN thin films 187
Superionic conductors
  Ionic conductivity and hopping rate data for some NASICON analogues 117
  Conductivity pre-exponential factors for some new superionic conductors 317

Temperature coefficient of resistance
  Electrical resistivity of holmium hydride films 181
Tensile load
  Evaluation of cumulative damage in glass fibre reinforced plastic by ultrasonic method 61
Tetrapropylammonium bromide
  Synthesis and characterization of mordenite crystals 7
Thermoautostabilized state (TANDEL)
  Electrical second harmonic generation and temperature autostabilized nonlinear dielectric element in ferroelectric solid solutions $(Na_xK_{1-x})VO_3$ and $(Na_xLi_{1-x})VO_3$ 111
Thermodynamic properties
  Measurement of Gibbs energies of formation of CoF_2 and MnF_2 using a new composite dispersed solid electrolyte 37
Thermoelectric power
  Pressure-induced band cross-over in $Pb_{1-x}Sn_xTe$ 131
  Transport properties of $MoSe_xTe_{2-x}$ $(0 \leqslant x \leqslant 2)$ single crystals 337
Thin film
  Electrical conductivity and transition temperature of NbN thin films 187
Titanate solid solutions
  Pyroelectric properties of lead-barium titanate and lead-strontium titanate 249
Transparent alumina
  Optical properties of coloured transparent alumina gel monolith glasses 193
Transparent ceramic
  Optical properties of coloured transparent alumina gel monolith glasses 193
Twin roller quenching technique
  Twin roller quenching technique and preparation of glasses of high melting ionic solids 1

Ultrasonic technique
  Evaluation of cumulative damage in glass fibre reinforced plastic by ultrasonic method 61
Undercooling
  Undercooling studies on dispersed bismuth droplets 277

Vapour-liquid-solid process
  Increase in the yield of silicon carbide whiskers from rice husk 295
Varsitors
  Dielectric behaviour of ZnO-based ceramic semiconductors 169
Vibrational constant
  A new formalism for representation of heat capacities of metals 241
Vickers hardness
  Microhardness measurement in nonmetallic materials 287
Vishnukundin
  A study of Vishnukundin coins 137

Xerogels
  Optical properties of coloured transparent alumina gel monolith glasses 193
X-ray photoelectron spectra
  X-ray photoelectron spectroscopy studies on ethylene oxychlorination catalysts 75

2γ-angular correlation
  Positron annihilation in Zr-0·5 Nb alloy 235

Zinc oxide
  Dielectric behaviour of ZnO-based ceramic semiconductors 169

AUTHOR INDEX

Achari K M R
  A study of diffusion mechanisms in sintering by shrinkage measurements 97
Agarwal M K
  Transport properties of $\mathrm{MoSe_xTe_{2-x}}$ $(0 \leqslant x \leqslant 2)$ single crystals 337
Akhtar D
  see Mathur R P 269
Arunachalam L M
  Synthesis and properties of manganese-doped barium titanate 159

Bahadur D
  see Rambilas 349
Bandyopadhyay B
  Development of a Sievert's type gas doping apparatus 305
Bhat B V Radhakrishna
  Increase in the yield of silicon carbide whiskers from rice husk 295
Bhattacherjee S
  see Datta A K 103
Bhoga S S
  see Singh K 263
Bhushan Bharat
  see Kashyap C Subhash 169
Byrappa K
  see Desai N B 117
  see Desai N B 317
  $\mathrm{NH_4Zr_2V_3O_{12}}$ proton conductor 323

Chakravorty D
  see Arunachalam L M 159
Chandole S V
  Influence of substrate temperature on the electrical and optical properties of amorphous germanium films 47
Chatterjee N
  see Bandyopadhyay B 305
Chaubey Sanjay
  Undercooling studies on dispersed bismuth droplets 277
Chavan S H
  see Patil T A 111
  see Jamadar V M 249
  see Patil T A 331
Chavda F R
  Preparation and properties of native oxide film anodically grown on $\mathrm{Hg_{0\cdot8}Cd_{0\cdot2}Te}$ 219
Chopra K L
  see Kashyap C Subhash 169

Datta A K
  Dehydration and phase transformation in chrysotile asbestos—A radial distribution analysis study 103
Desai C C
  Morphological aspects of some symmetrical ammonium hydrogen tartrate crystals grown by silica gel technique 89
  Magnetic susceptibility measurements of LHP and LNP crystals 203
  Measurements of the microhardness and compression testing of ferroelectric lead nitrate phosphate single crystals 343
Desai N B
  Ionic conductivity and hopping rate data for some NASICON analogues 117
  Conductivity pre-exponential factors for some new superionic conductors 317
  see Byrappa K 323

Ganapathi L
  see Subbanna G N 29
Ganguly P
  see Somasundaram T 81
Ganorkar M C
  see Vijayakumar M 137
Gayathri P
  see Vijayakumar M 137
Ghoshray A
  see Bandyopadhyay B 305
Giridhar A
  Non-isothermal crystallization of $\mathrm{As_2Se_3}$ glass 13
Gopalakrishna G S
  see Desai N B 117
  see Desai N B 317
Gopalakrishnan P S
  see Ramesh T G 131
Gupta S C
  see Chavda F R 219

Hajra J P
  see Jacob K T 37
  see Ranganathan S 149
  A new formalism for representation of heat capacities of metals 241
Hanchinal A N
  see Desai C C 89

Jacob K T
  Measurement of Gibbs energies of formation of $\mathrm{CoF_2}$ and $\mathrm{MnF_2}$ using a new composite dispersed solid electrolyte 37
Jagadeesh H P
  see Byrappa K 323

Jamadar V M
  see Patil T A 111
  Pyroelectric properties of lead-barium titanate and lead-strontium titanate 249
  see Patil T A 331
Joshi M S
  Synthesis and characterization of mordenite crystals 7
Joshi R M
  see Agarwal M K 337

Kartha C C
  see Mira Mohanty 309
Kashyap C Subhash
  Dielectric behaviour of ZnO-based ceramic semiconductors 169
Khan M S Rahman
  Hillock and island formation during annealing of gold films 55
  Electrical resistivity of holmium hydride films 181
Kishore
  see Raja V S 207
Krishnamurthy K R
  see Vetrivel R 75
Kulkarni A B
  see Desai N B 117
  see Desai N B 317
  see Byrappa K 323
Kumar Devendra
  Electrical properties of the system lanthanum lead cobalt titanium oxide 123
  see Mandal R K 255

Mandal R K
  Dielectric behaviour of glasses and glass ceramics in the system BaO-PbO-TiO_2-B_2O_3-SiO_2 255
Mathur B K
  see Datta A K 103
Mathur R P
  Kinetics of crystallization of a $Fe_{74}Co_{10}B_{16}$ glass 269
Menon C S
  Electrical conductivity and transition temperature of NbN thin films 187
Mira Mohanty
  Long term soft tissue response to metals, ceramics and composites—a comparative histopathological evaluation 309
Misra S C K
  Nonlinearity in gold-alkali halide-gold capacitors 67
Muraleedharan R V
  see Upadhyaya D D 235

Pankajakshan V S
  see Menon C S 187
Parkash Om
  see Kumar Devendra 123
  see Mandal R K 255
Patel P D
  see Agarwal M K 337
Patil T A
  Electrical second harmonic generation and temperature auto-stabilized nonlinear dielectric element in ferroelectric solid solutions $(Na_xK_{1-x})VO_3$ and $(Na_xLi_{1-x})VO_3$ 111
  see Jamadar V M 249
  Electrical conductivity of the ferroelectric sodium vanadate, potassium vanadate, lithium vanadate and their solid solutions 331
Prabhu K Mohan
  see Joshi M S 7
Prakash R
  see Srivastava V K 61
Prasad Ch Durga
  see Kumar Devendra 123
  see Mandal R K 255

Raghuwanshi F C
  see Singh K 263
Raja V S
  Crystallization behaviour of Metglas 2826 MB $(Fe_{40}Ni_{38}Mo_4B_{18})$ 207
Ramachander R B
  see Achari K M R 97
Ramachandrarao P
  see Chaubey Sanjay 277
Ramana M S V
  see Desai C C 203
  see Desai C C 343
Ramarao G V
  see Saraswati V 193
Rambilas
  Characterization of RF-sputtered garnet films 349
Ramesh T G
  Pressure-induced band cross-over in $Pb_{1-x}Sn_xTe$ 131
Ranganathan S
  Alloy oxide equilibria in the Cr-Mn-O system 149
  see Raja V S 207
Rao T S R Prasada
  see Vetrivel R 75
Rao V Pandit
  see Vijayakumar M 137
Rathinam K
  see Mira Mohanty 309

Samantaray B K
  see Datta A K 103
Sanghi G P
  see Bhat B V Radhakrishna 295

Saraswati V
  Optical properties of coloured transparent alumina gel monolith glasses 193
  Microhardness measurement in nonmetallic materials 287
Selvam P
  X-ray crystallographic and thermal studies on the hydrides of magnesium and its intermetallics 21
Seshan K
  see Vetrivel R 75
Shah S S
  see Chandole S V 47
Shubha V
  see Ramesh T G 131
Singh A K
  see Giridhar A 13
  Use of energy dispersive method with tungsten carbide opposed anvil high pressure set-up 225
Singh K
  Aliovalent substitution in β-Li_2SO_4 towards conductivity enhancement 263
  Li_2SO_4:$LiNbO_3$ binary system for solid state battery applications 355
Singh Vakil
  see Chaubey Sanjay 277
Somasundaram T
  In situ photoacoustic spectroscopic studies on heterogeneous catalysts under conditions of gas flow 81
Srikantaswamy S
  see Desai N B 317
Srinivasan V
  see Selvam P 21
Srivastava V K
  Evaluation of cumulative damage in glass fibre reinforced plastic by ultrasonic method 61
Subbanna G N
  High resolution electron microscopy of bismuth oxides with perovskite layers 29
Subbarao E C
  see Arunachalam L M 159
Sudha Mahadevan
  see Giridhar A 13
Swamy C S
  see Selvam P 21

Tiwari G
  see Chavda F R 219

Ujwala V Hulsurkar
  see Chandole S V 47
Upadhyaya D D
  Positron annihilation in Zr-0·5 Nb alloy 235
Usha Devi S
  see Singh A K 225

Varma K B R
  Twin roller quenching technique and preparation of glasses of high melting ionic solids 1
Vetrivel R
  X-ray photoelectron spectroscopy studies on ethylene oxychlorination catalysts 75
Vijayakumar M
  A study of Vishnukundin coins 137
Viswanathan B
  see Selvam P 21

($T_s = 473°$ K) were p-type with a carrier concentration of $4{\cdot}8 \times 10^{18}$ cm^{-3} and Hall mobility, 110 cm^{2}V^{-1}sec^{-1}. These films did not exhibit any photoresponse, probably due to the low mobility of charge carriers, high carrier concentration and p-type conduction.

The films were annealed at 700° K in arsenic vapour at 1 atm pressure, to compensate the native acceptors. After annealing, the films were found to be n-type with carrier concentration $6{\cdot}2 \times 10^{17}$ cm^{-3} and mobility $1{\cdot}4 \times 10^3$ cm^{2}V^{-1}sec^{-1} and exhibited good photoresponse.

2.2 *Photoconductive measurements*

The annealed $InAs_{0\cdot3}Sb_{0\cdot7}$ films with dimensions 0·2 cm × 0·2 cm × 1 μm were used for photoconductive measurements. The electrical contacts were provided by evaporating indium and attaching silver leads using indium solder.

The blackbody photoconductive response of the films was measured using the experimental set-up shown in figure 1. A blackbody (Model 11-210) obtained from M/s Barnes Engineering Company, USA was used as a radiation source. A variable mechanical chopper (Barnes Model 11-200/201-10A and 10C) placed between the source and the sample film, modulated the radiation frequency in the range 10 Hz to 10 kHz. The film sample was mounted in a specially designed cryostat and the temperature was controlled by a temperature controller (Specac 20-100) with an accuracy of ±1°K in the temperature range, 80°K to 303°K. A CaF_2 infrared transmitting window was fixed to the cryostat with 90° field of view. The film sample i.e. the detector was connected in series with load resistor and a bias power supply. The signal voltage (V_s) developed across the detector due to the incident radiant power from the blackbody was measured using a lock-in amplifier (Princeton Applied Research, model 124A) with a plug-in (PAR 184) pre-amplifier.

The measurements were repeated by varying the blackbody temperature from 333° K to 673° K, maintaining the detector always at 80° K.

The spectral response of the detector was measured using a monochromator (M/s Central Electronics Limited, New Delhi, model HM104) with interchangeable

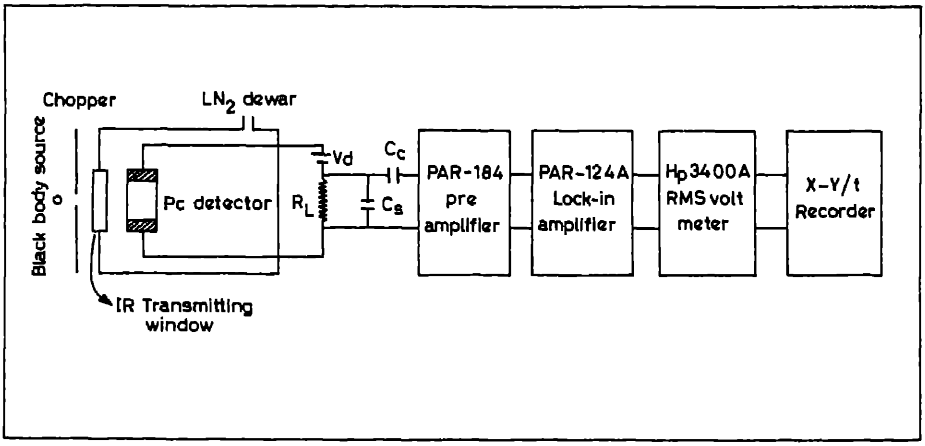

Figure 1. Experimental set-up for photoconductive measurements.

gratings in the wavelength range 2 μm to 10 μm. The detector temperature was varie from 80°K to 303°K.

The noise voltage of the detector in the frequency range 10 Hz to 10 kHz wa measured using a voltmeter (Hewlett Packard 3400A RMS) with a full scale accurac of ±1%.

The photoresponsivity (R) of the detector, was determined using the relation,

$$R = V_s/H A \qquad ($$

where H is the irradiance on the plane of the detector and A is the effective area of tl detector.

In order to specify the effect of noise on the performance of the detector, an ar independent figure of merit, D^*, was evaluated using the relation (Kruse *et al* 196

$$D^* = (1/H)(V_s/V_n)(\Delta f/A)^{1/2}, \qquad ($$

where V_n is the noise voltage and Δf the electrical bandwidth.

3. Results and discussion

The variation of blackbody photoresponse with its temperature is shown in figure The responsivity slowly increases with increasing blackbody temperature and th saturates beyond 500° K. The initial increase is due to the increase of photon fl density. The blackbody temperature was therefore fixed at 500° K for studyi responsivity and detectivity.

From the measured spectral response of the detector, D^* was calculated and plott against wavelength. D^* showed a maximum around 8 μm (figure 3). Further, t detectivity was high at 80° K and decreased as the temperature increased. This may due to the substantial increase of the thermally generated charge carriers whi overshadow the photogenerated charge carriers resulting in the decrease of signal-t noise ratio.

The variation of detectivity with frequency and temperature is shown in figure 4. I observed that the detectivity is frequency-dependent up to about 200 Hz and th

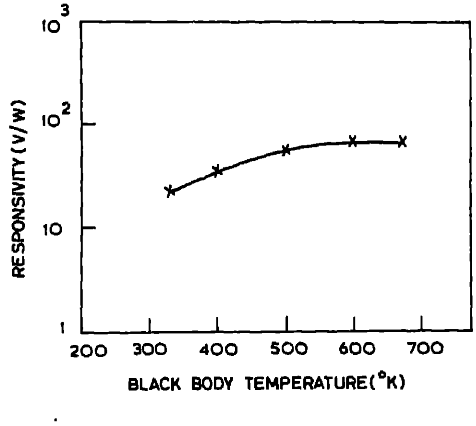

Figure 2. Variation of photoresponse with blackbody temperature.

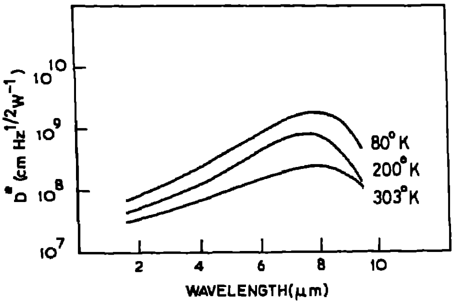

Figure 3. Variation of detectivity (D^*) with wavelength.

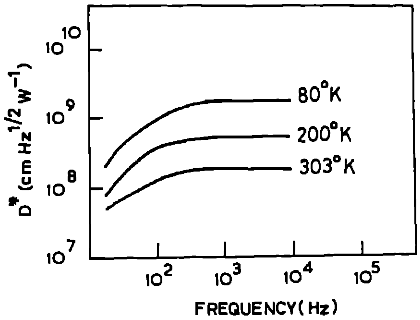

Figure 4. Variation of detectivity (D^*) with frequency.

becomes independent. At low frequencies the detectivity is generally limited by $1/f$ noise arising due to the presence of potential barriers at the electrical contacts, surface or interior (Hanafi and van der Ziel 1978) of the sample. In the present case, the potential barriers appearing at the electrical contacts were taken as negligible, because the contacts used were perfectly ohmic. Also, the surface states contribution to $1/f$ noise was reduced by depositing antireflecting layer (polystyrene) on the surface of the detector, i.e. the low value of $1/f$ noise (figure 4) was mostly due to the interior potential barriers of the semiconducting film which was polycrystalline in nature. At frequencies > 200 Hz, the detectivity is limited by amplifier or generation-recombination (g-r) noise. Because of the use of a low noise amplifier and a proper design of the electronic circuit, the amplifier noise may be taken as negligible in the present study. The g-r noise is generally proportional to the minority carrier density and is dependent on the nature of conduction and the quality of the films. In the present film samples (i.e. detectors), even after annealing, there are likely to be some uncompensated native defects which act as recombination centres, contributing significantly to the g-r noise and limiting the detectivity. The performance of the detector however, can be improved by preparing films free from impurities and defects and having a low minority carrier concentration. The g-r noise decreases with increasing temperature (figure 4), because the majority carrier concentration increases at higher temperatures.

4. Conclusions

$InAs_{0.3}Sb_{0.7}$ films were deposited on glass and mica substrates held at 473° K using discrete evaporation at a pressure of 10^{-6} torr. As-deposited films were p-type and did not exhibit photoresponse. The films were annealed in arsenic ambient to convert them to n-type. The annealed films exhibited high mobility and good photoresponse. The photoresponse of annealed n-type films were studied as a function of frequency, wavelength and detector temperature. The performance of the detector was limited by $1/f$ noise at low frequencies (< 200 Hz) and then g-r noise at higher frequencies. The detector showed maximum detectivity ($2{\cdot}78 \times 10^9$ cm Hz$^{1/2}$ watt^{-1}) at 80° K around 8 μm. The performance of the detector may be improved by preparing epitaxial films free from defects and impurities.

Acknowledgement

The authors are grateful to the Department of Science and Technology, New Delhi, financial assistance.

References

Andrews A M, Chenug D T, Gertner E R and Longo J T 1975 *J. Vac. Sci. Technol.* **13** 961

Bubalac L O, Andrews A M, Gertner E R and Chenug D T 1980 *Appl. Phys. Lett.* **36** 734

Chenug D T, Andrews A M, Gertner E R, Williams G M, Clarke J E, Pasko J G and Longo J T 1977 *A Phys. Lett.* **30** 587

Clawson A R, Lile D L and Wieder H H 1972 *J. Vac. Sci. Technol.* **9** 976

Gertner E R, Andrews A M, Bubalac L O, Chenug D T, Ludowise M J and Riedel R A 1979 *J. Elect Mater.* **8** 545

Hanafi H I and van der Ziel A 1978 *Solid State Electron.* **21** 1019

Kruse P W, McGlauchlin L D and McQuistan R B 1962 *Elements of infrared technology: Genera transmission and detection* (New York: John Wiley) p. 271

Raja Reddy M, Srinivasulu Naidu B and Jayarama Reddy P 1984a *Proc. Int. Conf. Metallurgical Coati* San Diego, USA

Raja Reddy M, Srinivasulu Naidu B and Jayarama Reddy P 1984b *Ntl. Symp. Instrumentation*, Kash India

Raja Reddy M, Srinivasulu Naidu B and Jayarama Reddy P 1984c *Proc. Sixth Int. Conf. Thin F* (Lausanne: Elsevier) Stockholm, Sweden

Wieder H H and Clawson A R 1973 *Thin Solid Films* **15** 217

Bull. Mater. Sci., Vol. 8, No. 3, June 1986, pp. 379–384. © Printed in India.

R.F. magnetron sputtered tungsten carbide thin films

P K SRIVASTAVA, V D VANKAR and K L CHOPRA

Department of Physics and Centre for Materials Science and Technology, Indian Institute Technology, New Delhi 110016, India

Abstract. Thin films of tungsten carbide have been deposited on stainless steel substra held at 500°C by r.f. reactive magnetron sputtering in two different modes of introducing arg and acetylene gases called normal and high rate mode. A single phase fcc-WC is formed in t normal mode whereas a mixture of A-15-W_3C, hexagonal-WC and graphitic- and diamor carbon is found in the high rate mode. A microhardness value as high as 3200 $\mathrm{kgf/mm^2}$ (compared to the bulk value of 1800 $\mathrm{kgf/mm^2}$) is obtained in the film deposited by norn mode.

Keywords. Tungsten carbide; magnetron sputtering

1. Introduction

High rate reactive magnetron sputtering process for thin film deposition is importa for industrial applications. Several workers (Aronson *et al* 1980; Schiller *et al* 198 Kaiza *et al* 1981) have developed such techniques to deposit thin films of vario transition metal carbides, nitrides, oxides etc for wear-resistant and protective coatin on various substrates like cemented carbide tools, high speed steel, copper and copp alloys. Efforts to enhance the deposition rate by effective control of the flow of reacti gases into sputtering chamber have been made. The processes that occur on tl magnetron target surface are dependent on the interaction between sputter produc and reactive gaseous products as well as on the degree of coverage of the reactic products obtained on the target. Generally in reactive sputtering, the target metal ge carburized, nitrided or oxidized by the reactive gases and subsequently sputtered at lo rates since the sputtering yield for carbides, nitrides or oxides is much lower than tho of the corresponding metals. Schiller *et al* (1980) deposited various compounds wi very high rates by using a dc magnetron-plasmatron system in such a way th practically complete separation of solid component sputtering at the target and of tl reaction of the produced particles with the gaseous component during condensatic occurs on the substrate. They were able to sputter various compounds with very hi rate ($\sim 1\,\mu$m/min for Ta_2O_5). Recently Scherer and Wirz (1984) used a simil configuration for sputtering of Al_2O_3.

We have prepared tungsten carbide films by reactive r.f. magnetron sputtering (stainless steel substrates. The substrate temperature, flow of gases and bias potential the cathode were controlled to obtain hard adherent coatings. Two different modes introducing argon and acetylene gases were studied. In one, called the normal mo (NM), the two gases were homogeneously mixed in the plasma region whereas in t other, called the high rate mode (HRM), separate zones of argon and acetylene we created by controlling the flow of the two gases such that the carbide formation on t tungsten target could be reduced (Srivastava *et al* 1985). The WC_X films formed in both the modes were analyzed by x-ray diffraction (XRD) and Auger electron spectroscopy (AES) for their structure and compositional analysis. The microhardness was measured by Vicker's microhardness tester fitted onto Carl Zeiss optical microscope. The indents produced during the microhardness measurements were also analyzed in a scanning electron microscope (SEM).

2. Experimental details

Figure 1 shows the magnetron sputtering system used for deposition of tungsten carbide films on stainless steel substrates held at 500°C in the normal mode (a) and in the high rate mode (b). Preparation of substrates for deposition and various conditions for sputtering is reported elsewhere (Srivastava *et al* 1984). Flow rates of argon and acetylene gases were maintained at 30 scc/min and 6 scc/min, respectively for both systems. An r.f. power density of 4.5 watt/cm^2 was maintained during sputtering. This developed a target bias voltage of 500 volts. For each run, the substrate temperature, flow of gases and the bias potential developed on the cathode were kept constant. Under similar conditions the deposition rate of tungsten films and tungsten carbide films in normal and high rate mode are 825, 600 and 825 Å/min respectively.

An x-ray diffractometer (Philips PW 1730/10) was used for x-ray analysis in $\theta - 2\theta$ scan mode using CuK_{α_1} (1·54 Å) radiation and 1°/min scan speed. For compositional analysis, a scanning Auger microprobe (PH1 590) with electron beam of 0·2 μm diameter was used. The sputter depth profile was performed with an ion gun of $\sim$ 200 μm diameter operated at 5 kV and current density 600 μA/cm^2.

3. Results and discussion

Figure 2 shows the XRD profiles for 4·2 μm thick films deposited at 500°C in the normal mode (a) and in the high rate mode (b). The maximum grain size as calculated from the broadening of x-ray peaks is $\sim$ 300 Å for both types of films. Since at different temperatures the structure and composition of the film are different, correlation of the grain size variation with temperature is not possible. The interplanar spacings *d* were calculated from the XRD and compared with standard data (ASTM data cards). The NM films deposited at 500°C on stainless steel are cubic tungsten monocarbide (f.c.c. B1 structure) while the HRM films deposited at 500°C are a mixutre of various phases, namely A-15 W_3C, hexagonal WC, graphitic carbon and diamond carbon.

Figure (3a) shows the AES traces of the surface of WC_X films which is a typical feature of all the films sputtered in both modes. Oxygen ($KL_{2,3}L_{2,3}$-512 eV) is a major impurity on the surface. The presence of carbon is indicated by a peak ($KL_{2,3}L_{2,3}$-271 eV) which has a characteristic shape suggesting the formation of graphitic phase on the surface. Inside the bulk of the NM film the shape of this peak changes and additional features at 252 eV and 260 eV appear (figure 3b). Such features are characteristic of carbide phase formation (Moyoshi and Bucklay 1982). Similar peaks at 252 eV and 260 eV appear in the HRM films but these peaks are not very sharp suggesting that the carbide phase formation is not complete and a mixture of graphitic and carbidic phases are present (figure 3c). Thus XRD and AES profiles are found consistent with each other. AES

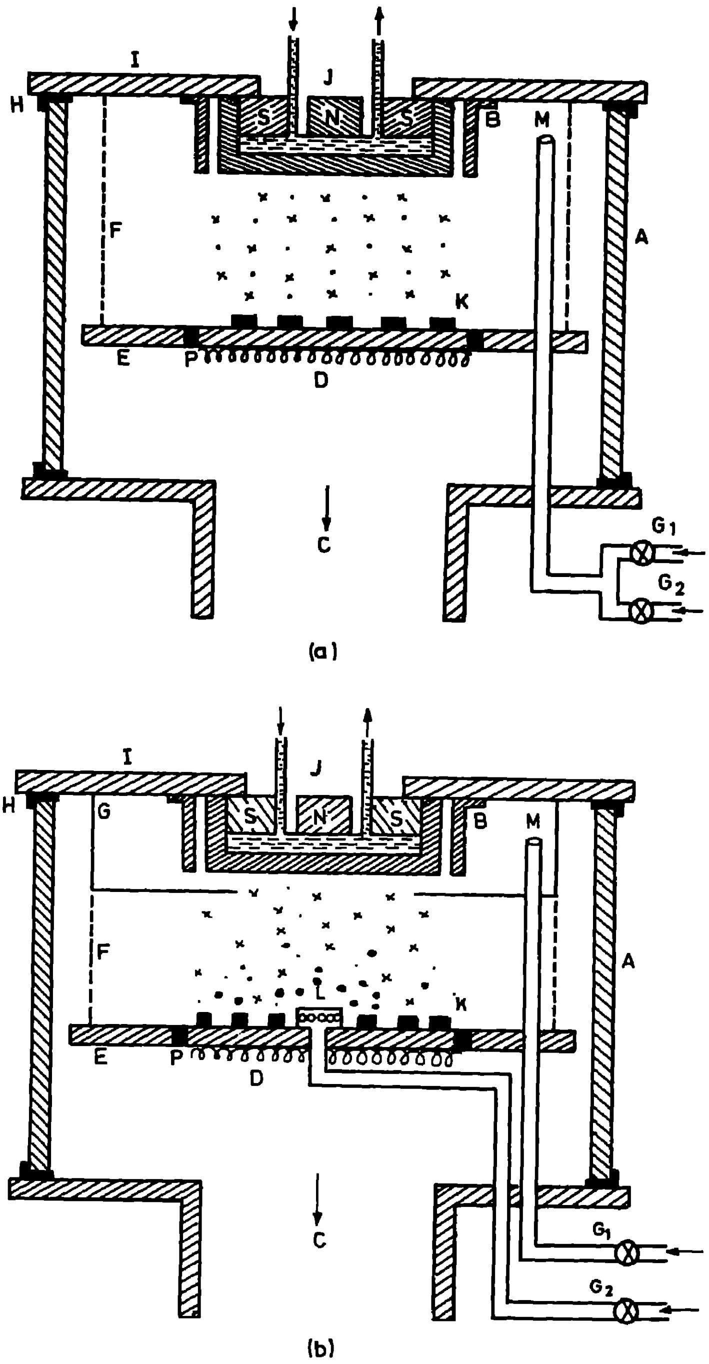

Figure 1. Schematic diagram of reactive r.f. magnetron system in (**a**) normal mode, (**b**) hig rate mode showing metallic belljar (A), target shield (B), vacuum pump (C), substrate heater (D grounded base plate (E), perforated aluminium mesh (F), aluminium metallic partition (G L gasket for vacuum sealing (H), top plate (I), target (J), substrate (K), opening of reactive ga (L), opening of inert gas (M), insulator ring (P), and precision needle valves (G$_1$ and G$_2$).

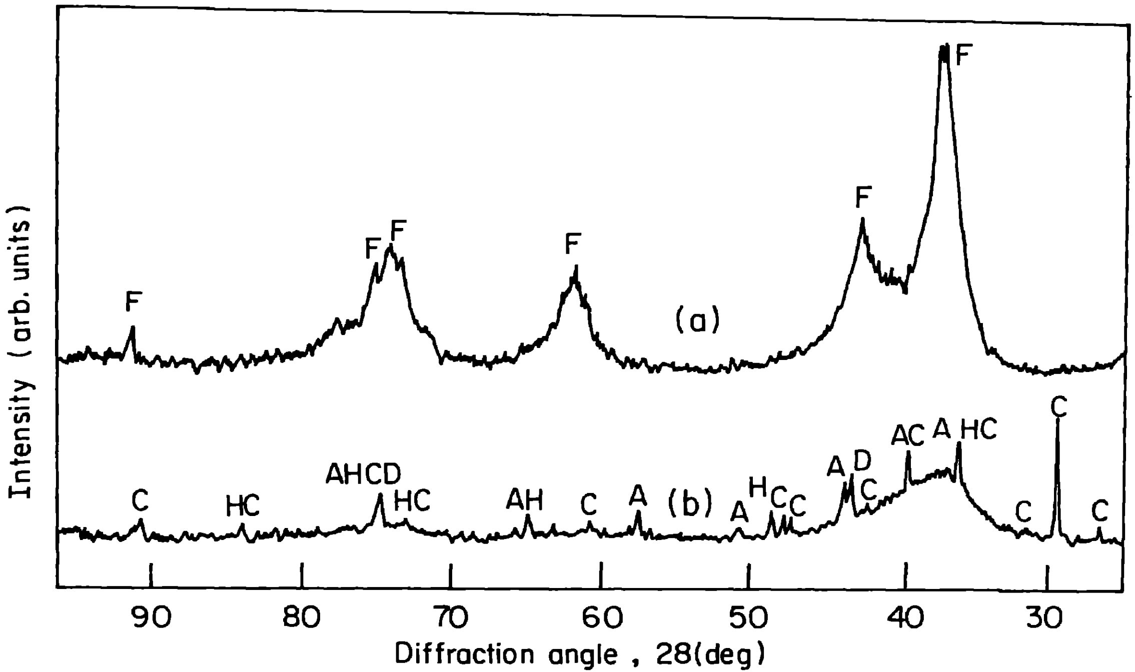

Figure 2. X-ray diffraction profiles of WC_x films prepared on stainless steel substrates at 500°C in (a) normal mode, (b) high rate mode showing A-15 W_3C phase (A), hexagonal WC phase (H), graphitic carbon (C) and diamond carbon phase (D), and fcc WC_x phase (F).

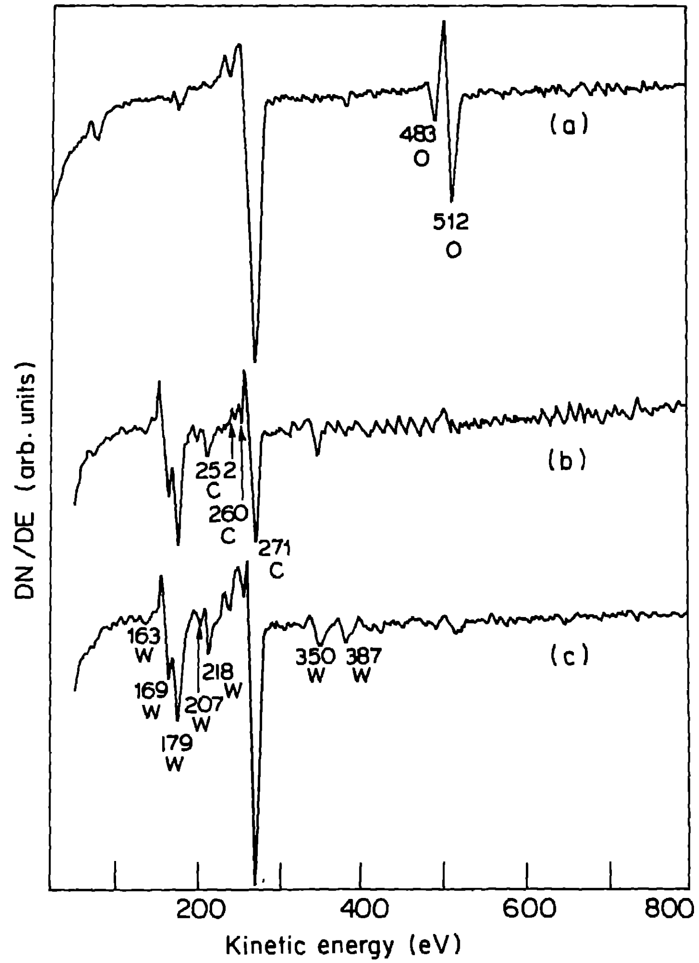

Figure 3. AES profile of WC_x films deposited at 500°C on stainless steel substrate at (a) an surface of HRM films, (b) 100 Å depth from the surface of NM films, and (c) 100 Å depth from th surface of HRM films.

analysis yields the composition of these films as 50 % W, 50 % C for NM films, and 40 W, 60 % C for HRM films.

The microhardness of the films has been measured by Vicker's microhardne indentor and value of 3200 and 2365 kgf/mm^2 is observed at 10 g load for NM and HR films respectively. It should be noted that the bulk hardness of tungsten carbi (hexagonal phase) is 1800 kgf/mm^2. The higher values observed in NM films may be d to fine grain size and B1 fcc crystal structure. HRM films crack during the microhardne measurement and a circular crack pattern is developed around the indentation. T number of the cirlces increases with increasing load and three concentric circles a formed at a load of 160 g. In the case of NM films such cracks around the indentation a not observed.

The XRD and AES studies suggest that the HRM films have excess free carbon graphitic and diamond form which is dispersed in W_3C (A-15 phase) and WC (hexagon phase) resulting in brittle films (as observed in microhardness measurements) which develop cracks at higher loads. On the other hand, NM films have single phase and are less brittle and, therefore, do not crack at loads as high as 160 g.

4. Conclusions

(i) Rates of deposition of WC_X films as high as that of pure tungsten have been achieved by dividing the inert and reactive gases in separate zones and controlling their flow patterns in such a way that the carbide formation on target surface is avoided.
(ii) W_3C (A-15 phase), WC (hexagonal) and carbon (graphitic and diamond form) are obtained in the films prepared in the modified geometry whereas in the normal geometry a single phase fcc tungsten monocarbide is formed.
(iii) A microhardness value as high as 3200 kgf/mm^2 at 10 g load has been obtained in single phase fcc WC_X films whereas the films containing a mixture of phases and dispersed carbon have lower microhardness (2365 kgf/mm^2) at 10 g load.

Acknowledgements

The authors are grateful to the Department of Science and Technology, New Delhi, for financial support, to Dr K C Nagpal for help and advice with x-ray diffraction work, to M Bhatnagar for AES work, to Vandana Agrawal and R S Rastogi for technical discussion.

References

Aronson A J, Chen D and Class W H 1980 *Thin Solid Films* **72** 535
ASTM Data Card Nos. 20-1316, 5-728, 22-1069, 6-675
Kaiza K, Tsunetaka S and Mitsunori K 1981 *Thin Solid Films* **78** 41
Moyashi and Bucklay D H 1982 *Appl. Surf. Sci.* **10** 357
Scherer M and Wirz P 1984 *Thin Solid Films* **119** 203
Schiller S, Heisig U, Strumptel K and Sieber W 1980 *Vakuumtechnik* **30** 1
Schiller S, Beister G and Sieber W 1984 *Thin Solid Films* **111** 259
Srivastava P K, Rao T V, Vankar V D and Chopra K L 1984 *J. Vac. Sci. Technol.* **A2** 1261
Srivastava P K, Vankar V D and Chopra K L 1985 *J. Vac. Sci. Technol.* **A3** 2129

Bull. Mater. Sci., Vol. 8, No. 3, June 1986, pp. 385–389. © Printed in India.

Cobalt oxide-iron oxide selective coatings for high temperature applications

C S UMA, L K MALHOTRA and K L CHOPRA
Department of Physics, Indian Institute of Technology, New Delhi 110016, India

MS received 1 January 1985; revised 9 January 1986

Abstract. Cobalt oxide-iron oxide coatings on stainless steel have been prepared by spra pyrolysis technique. These coatings have absorptance (α) = 0·94 and emittance (ε_{100}) = 0·2 which are much better values than for cobalt oxide or iron oxide alone on stainless stee substrates. The coatings have been found to be stable for temperatures upto 400°C.

Keywords. Selective coatings; absorptance; emittance; cobalt-iron oxide

1. Introduction

The spectral profile of an ideal absorber surface in a photothermal converter for sola spectrum comprises of a low reflectance region from 0·3–2·0 μm and a high reflectanc at higher wavelength. Such a spectral profile can be generated in many ways by using combination of thin film materials (selective coatings). An absorber-reflector tanden structure is one of the important selective coatings. The tandem structure is made up o a thin layer of a material (which absorbs the solar radiation but is transparent i infrared) on a metal having a high infrared reflectance and hence low emittance.

Cobalt oxide as an absorber layer has been studied by many workers (Kokoropoula *et al* 1959; Gillette 1960; Kruidhoff and Van der Leij 1979; McDonald 1980; Smith *et a* 1980; Chidambaram *et al* 1982) on a variety of substrates like polished nickel, silve platinum and stainless steel. Different techniques such as thermal oxidation, elec trodeposition and spray pyrolysis have been utilized to deposit thin cobalt oxide layer The resulting absorber/reflector tandem structure gives integrated absorptance in th range 0·87–0·92 and thermal emittance ~ 0·14–0·24. The reflectance spectrum of suc an oxide coating on metal substrate shows a rise around 1·05 μm which limits th ultimate integrated absorptance. Addition of other materials like cobalt sulphid (Chidambaram *et al* 1982) modifies the reflectance spectrum but the presence sulphide reduces the stability of the coating to ~ 250°C. If this modification is achieve by the addition of another stable oxide, a higher stability is expected. Such combination of cobalt oxide-iron oxide was studied by Kruidhoff and Van der Le (1980) by thermally oxidizing an electroplated layer of Fe and Co. Iron oxide has lowe refractive index compared to cobalt oxide and hence one expects such a combination give rise to a high absorptance. However, an integrated absorptance of only 0·90 an thermal emittance of 0·3 was obtained by these workers. The coatings were found to stable up to 300°C. In the present work a simple spray process has been used to prepa cobalt oxide-iron coatings on stainless steel. The results are presented in the followi section.

2. Experimental details

The coatings were prepared by spray pyrolysing aqueous solution of cobalt nitrate and ferric nitrate on stainless steel substrates. The substrates were initially cleaned by a mild scrubbing with detergent, thoroughly washed with water and then chemically etched for 2–3 min at 60°C in a solution having 200–250 g/l of sodium dichromate and 20–30 ml/l of sulphuric acid. This was followed by cleaning with distilled water. Good, uniform and adherent coatings were obtained at a deposition temperature of ~ 170°C. Various parameters like volume of the solution sprayed, concentration of cobalt nitrate and ferric nitrate solution, spray rate were optimized to give the best values of absorptance and emittance.

Total reflectance was measured using a Hitachi 330 spectrophotometer with an integrating sphere attachment. Freshly prepared MgO was used as a standard. The absorptance (α) was calculated by integrating the reflectance data over AM 1·5 spectrum. The emittance (ε) was measured by using the standard radiometric method. The temperature of measurement was kept at 100°C. The stability of the coating was tested by annealing in air at 400°C and 500°C for 24 hr and in a separate test, by boiling in a 5% NaCl solution. The absorption and emittance were measured before and after each test.

Electron diffraction analysis was carried out using AEI/EM 802 transmission electron microscope. A scanning auger microprobe (PHI 590A) was used to determine the composition of the coating.

3. Results and discussion

Figure 1 shows the reflectance spectra of cobalt oxide, iron oxide and cobalt oxide-iron oxide coatings on stainless steel. The deposition parameters for all the coatings have

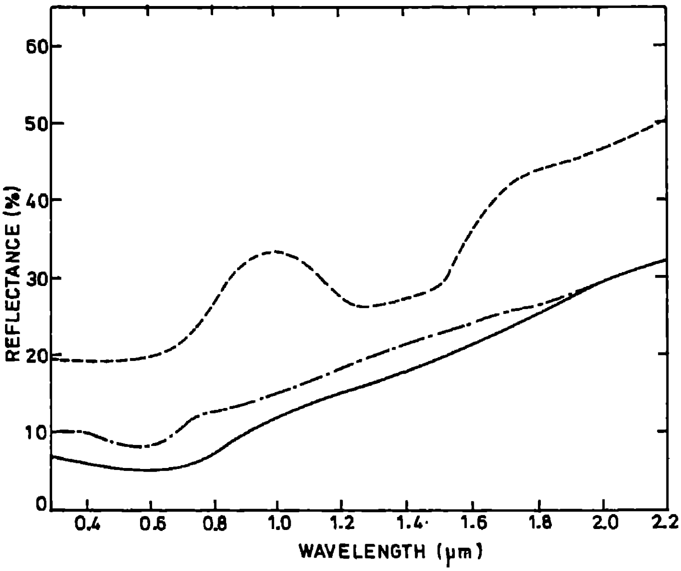

Figure 1. Reflectance spectrum of cobalt oxide (– – – – –), cobalt oxide-iron oxide (———) and iron oxide (—·——·—) for the same deposition parameters.

been kept similar for comparison. The characteristic rise in reflectance spectrum of cobalt oxide is quite evident. The coating with this reflectance spectrum has $\alpha = 0{\cdot}80$ only and $\varepsilon_{100} \sim 0{\cdot}15$. The optimized values of α and ε for cobalt oxide/stainless steel were 0·89 and 0·2 respectively. Since iron-oxide has a lower refractive index than cobalt oxide, one expects cobalt oxide-iron oxide coatings to have lower reflectance and hence higher absorptance. Incorporation of iron oxide thus decreases the reflectance in the entire spectral range of interest and particularly around 1·05 μm and consequently α goes up to 0·94. The emittance has a value of 0·20. The reflectance spectrum of iron oxide alone is also shown. This coating has $\alpha = 0{\cdot}89$. This indicates that the higher absorption in cobalt-oxide iron oxide is partly due to the inherent low reflectance of this material compared to either cobalt oxide or iron oxide and partly due to textural effects. Dependance of absorptance and emittance on the volume of solution sprayed (and hence the thickness of the absorber layer) for a particular concentration is shown in figure 2. The absorption initially rises and then saturates to a value of 0·94. This value is limited by the front surface reflection of the absorber layer. As expected, emittance increases with thickness of the absorber layer.

The coatings were stable upto 400°C. When heated upto 500°C in air for 24 hr, the absorptance decreased to 0·91 and emittance increased to 0·22. The reflectance spectrum of such a heated sample is shown in figure 3.

Auger analysis showed the presence of Fe, Co and O. The composition profile as a function of etch time is shown in figure 4. The ion etching was done using a differentially pumped ion gun with Ar^+ ions (ion beam voltage ~ 3 KV, current density ~ 600 μ Amp/cm^2, raster area 2 mm x 2 mm, corresponding to a precalibrated etch rate of 120 A/min of Ta_2O_5). The depth profile was started after sputter cleaning. The percentage of iron was greater than that of cobalt throughout the film. Electron diffraction studies showed these coatings to consist of Fe_2O_3 and CoO with slight traces of Fe_3O_4. Fe_2O_3 and CoO are known to be the stable oxide of Fe–O and Co–O systems. The general decomposition mechanism of aqueous solution of salts is similar

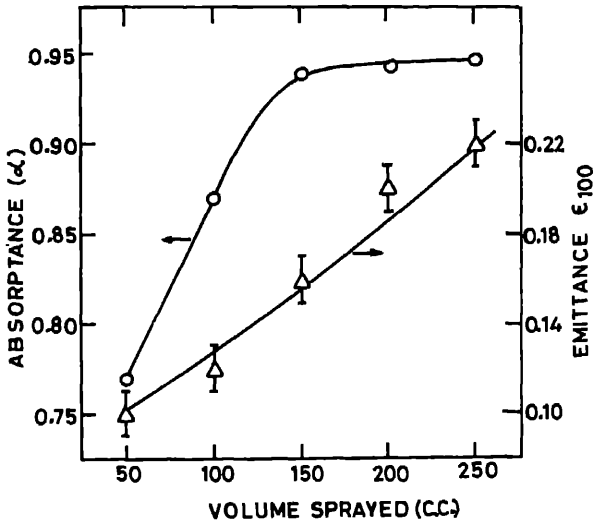

Figure 2. Dependance of absorptance and emittance on the amount of absorptance an emittance on the amount of volume of solution sprayed.

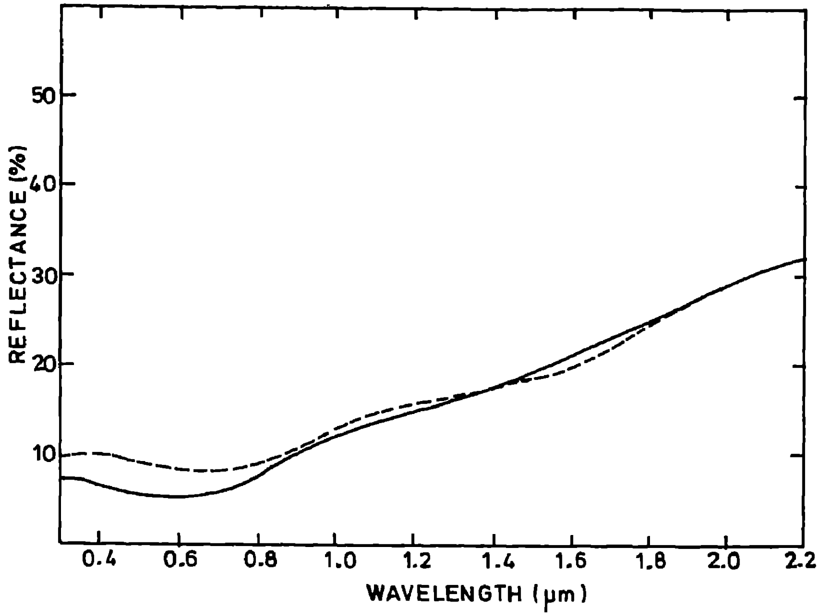

Figure 3. Change in reflectance spectrum of cobalt oxide-iron oxide coating on stainless steel after heating (------) at 500°C for 24 hr in air. (———) is reflectance spectrum before heating.

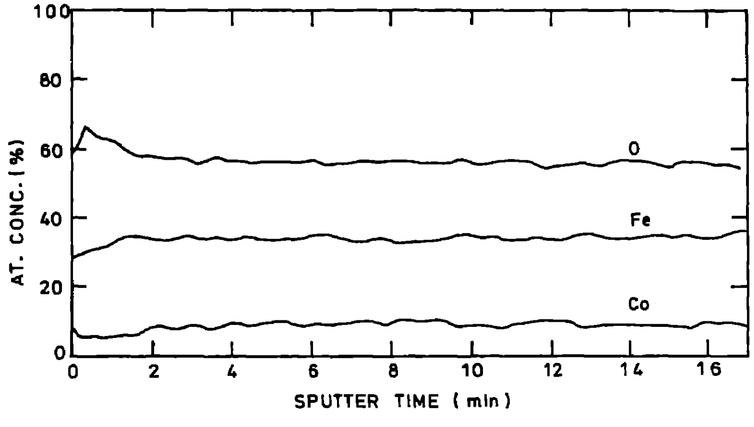

Figure 4. Auger depth profile showing the variation of Fe, Co and O concentrations with depth.

to that of decomposition of salts in air. The following chemical reactions lead to the formation of CoO and Fe_2O_3.

$$2\,Co(NO_3)_2 \text{——} 2\,CoO + 4\,NO_2 + O_2$$
$$4\,Fe(NO_2)_3 \text{——} 2\,Fe_2O_3 + 12\,NO_2 + 3O_2$$

This explains the presence of the above mentioned oxides in the bulk of the coating.

4. Conclusions

Mixed oxides of cobalt and iron have been prepared on stainless steel by spray pyrolysis. The integrated absorptance of the mixed oxide is 0·94 which is higher than that of either cobalt oxide ($\alpha = 0{\cdot}80$) or iron oxide ($\alpha = 0{\cdot}89$) on stainless steel obtained under similar conditions. The emittance increases slightly from 0·15 for pure cobal oxide to 0·20 for mixed oxide. As far as stability is concerned, cobalt oxide coatings are stable upto 600°C whereas the mixed oxide coatings of cobalt and iron are stable only upto 400°C.

References

Chidambaram K, Malhotra L K and Chopra K L 1982 *Thin Solid Films* **87** 365
Chaudhary C and Sehgal H K 1982 *Solar Energy* **28** 25
Gillette R B 1960 *Solar Energy* **4** 24
Kokoropoulos P, Salam E and Daniels F 1959 *Solar Energy* **3** 19
Kruidhof W and Van der Leij M 1979 *Solar Energy Mater.* **2** 69
McDonald G E 1980 *Thin Solid Films* **72** 83
Smith G B, Ignatiev A and Zajac G 1980 *J. Appl. Phys.* **51** 4186

Bull. Mater. Sci., Vol. 8, No. 3, June 1986, pp. 391–396. © Printed in India.

Transistors made in laser recrystallized polysilicon on insulator films

S CHANDRASEKHAR, P R APTE and S K ROY

Solid State Electronics Group, Tata Institute of Fundamental Research, Bombay 400005, India

Abstract. LPCVD polycrystalline silicon films were deposited on thermally oxidized silicon as well as on LPCVD silicon nitride deposited on silicon. A CW argon ion laser was used to recrystallize the polysilicon film into large grains (grain size from 5 μm to 40 μm). Boron was then implanted and standard N-channel silicon gate process and N-channel metal gate process were carried out to realise MOSFETs on this material. Channel mobilities upto 450 cm^2/V-sec for electrons have been measured. This thin film MOSFET has a four-terminal structure with a top and a bottom gate and the influence of one gate on the drain current due to the other gate has been investigated. Comparison of the I_D–V_D curves of the devices with physical models was found in good agreement.

Keywords. Recrystallisation; semiconductor; silicon; laser; MOSFET; silicon-gate process.

1. Introduction

Polycrystalline silicon formed by low pressure chemical vapour deposition (LPCVD) is commonly used in integrated circuits for interconnections, gate electrodes and resistors. However, the relatively small grain size (of the order of 500 Å) tend to limit its application since the grain boundaries usually affect the transport properties. The earliest MOSFETS fabricated on thin films of polysilicon have shown poor mobilities and transconductances (Kamins 1972). It has now been well demonstrated that the grai size of polysilicon deposited on thermally-oxidized silicon can be increased dramatically by annealing the material with either a scanning cw laser beam (Gat *et al* 1978 Kamins *et al* 1980) or a heated graphite strip (Tsaur *et al* 1981). The grain size can be a large as 100 μm by 100 μm extending through the thickness of the film. This ha generated a considerable amount of work (Lam *et al* 1982; Colinge *et al* 1983) devote to the fabrication of device-worthy silicon-on-insulator (SOI) films as an alternative t the classical silicon-on-sapphire (SOS). A variety of applications such as large flat pane displays and 3-D integrated circuits offer a significant promise for the future.

We report here our results of MOSFETS made by laser recrystallization.

2. Experimental

The samples were made on 2 inch diameter P type ⟨100⟩ silicon wafers. A 1 μm thic oxide was grown in steam ambient and a 500 nm thick film of polysilicon was deposite by low pressure chemical vapour deposition (LPCVD) of silane. A capping layer of silico nitride was then deposited by LPCVD of dichlorosilane and ammonia. The thickness the nitride was 60 nm which gives the optimum antireflection effect for the two las wavelengths (488 nm and 514·5 nm) used in the recrystallization. The wafers were then recrystallized using a cw argon ion laser operating in the multiline mode. The substrate was heated to 350°C on a vacuum held chuck and the laser beam was scanned in a serpentine fashion using an X-Y mirror galvanometer deflection system. A plano convex lens of focal length 250 mm was used to focus the beam on to the substrate to give a spot size of about 60 to 70 μm. The scan speed was 10 cm/sec with spacing between successive scan lines of about 20 μm. The laser power used was between 11 W and 13 W.

As a result of the recrystallisation, long crystallites (upto 40 μm in length, 5 to 10 μm in width) were formed in a chevron shape. The capping nitride was then stripped in hot phosphoric acid. Boron was implanted into the large grain silicon at 80 keV to a dose of 1×10^{12} ions/cm^2. (This dose was calculated to make the recrystallised polysilicon p-type with an average concentration of $1\text{-}2 \times 10^{16}$ atoms/cm^2). Standard N-MOS silicon gate process was carried out from this stage. A 100 nm silicon nitride was deposited, active areas of transistors defined by photolithography and nitride etched in a CF4 plasma. Local oxidation was then carried out to convert the unwanted polysilicon into oxide. The nitride was then stripped, a gate oxide of 100 nm was grown at 1050°C in oxygen, 0·5 μm polysilicon was deposited and patterned into gates. The source, drain and gates were then doped by $POCl_3$ at 975°C. After opening contact holes, aluminium was evaporated and patterned. The devices were then sintered at 500°C in N_2 for 45 min. Figure 1 shows the cross-section of the completed structure. Some wafers were processed for N-MOS meal gate devices.

3. Results and discussion

The MOSFET device characteristics were measured with an automated measurement system controlled by a desktop computer. Figure 2 shows a typical drain current I_D versus drain voltage V_D family of curves as a function of the top gate voltage V_{G1} for a particular bottom gate voltage V_{G2}. Referring back to figure 1, we notice that the 1 μm silicon dioxide on which the recrystallized film is sitting acts as a second gate dielectric with the underlying support of silicon as the gate electrode. This four-terminal structure of the laser recrystallized film is thus unique and consequently, the device has two channels for current to flow from source to drain—a top channel below gate 1 and a bottom channel above gate 2.

The MOSFET, now called MISIMFET (metal-insulator-semiconductor-insulator-metal), has therefore four cases of operation:

(i) When the voltages on both gates are large and negative the silicon below the gates are accumulated and the transistor is in the OFF state.
(ii) The voltage on one gate forms an inversion layer (i.e. a channel) while the other gate is in accumulation.
(iii) The voltage on one gate forms a channel while the other gate forms a depleted region.
(iv) Both the gate voltages are such that a channel is formed below each gate.

The drain current I_D therefore is a function of drain voltage V_D, gate 1 voltage V_{G1} and gate 2 voltage V_{G2}. This dependence can be seen in figure 3 which is the I_D–V_{G1} curve for a small drain voltage ($V_D = 100$ mV) as a function of the back gate voltage V_{G2}. For

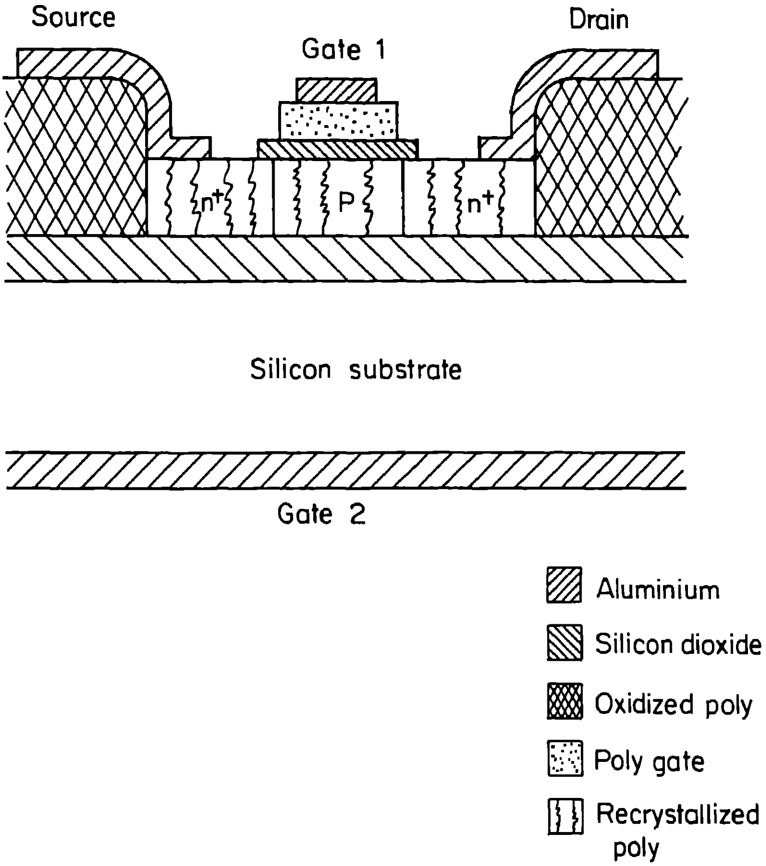

Figure 1. Cross-sectional view of completed MOSFET on laser recrystallized polysilicon.

$V_{G2} < -45$ V and $V_{G1} < -4$ V, we see the drain current is practically zero. This is case 1 above, when both channels are OFF. For $V_{G1} > -4$ V and $V_{G2} < -45$ V, the drain current starts increasing showing that channel 1 has inverted while channel 2 is still off For $V_{G2} > -45$ V and $V_{G1} < -4$ V, we see that the drain current again increases showing that channel 2 has inverted while channel 1 is off. This is case 2. For $V_{G1} \geqslant -3$ V and $V_{G2} \geqslant -35$ V both channels are conducting and we have case 4. Case 3 fall between these two voltage limits.

The expression for the drain current when channel 2 is accumulated is

$$I_D = \mu \frac{W}{L} C_{01} (V_G - V_{T1}) V_D,$$

where μ is the mobility, W and L are the device width and length, C_{01} is the gate capacitance, V_D is the drain voltage ($=$ 100 mV), V_{T1} is the turn on voltage of channel 1 The slope is

$$\partial I_D / \partial V_G = \mu \frac{W}{L} C_{01} V_D$$

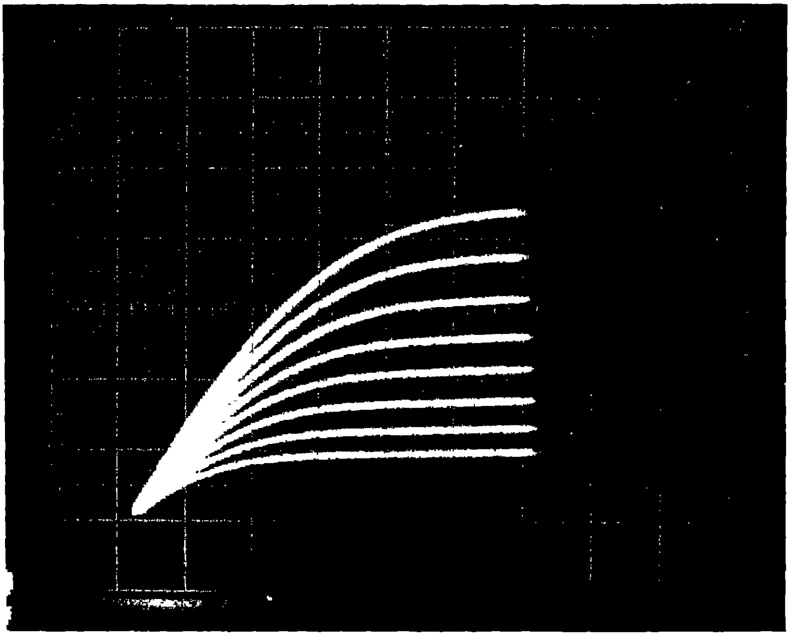

Figure 2. Photograph of the I_D–V_D characteristics of the *n*-channel Si gate MOSFET as a function of front gate voltage V_{G1} for a fixed back gate voltage V_{G2}

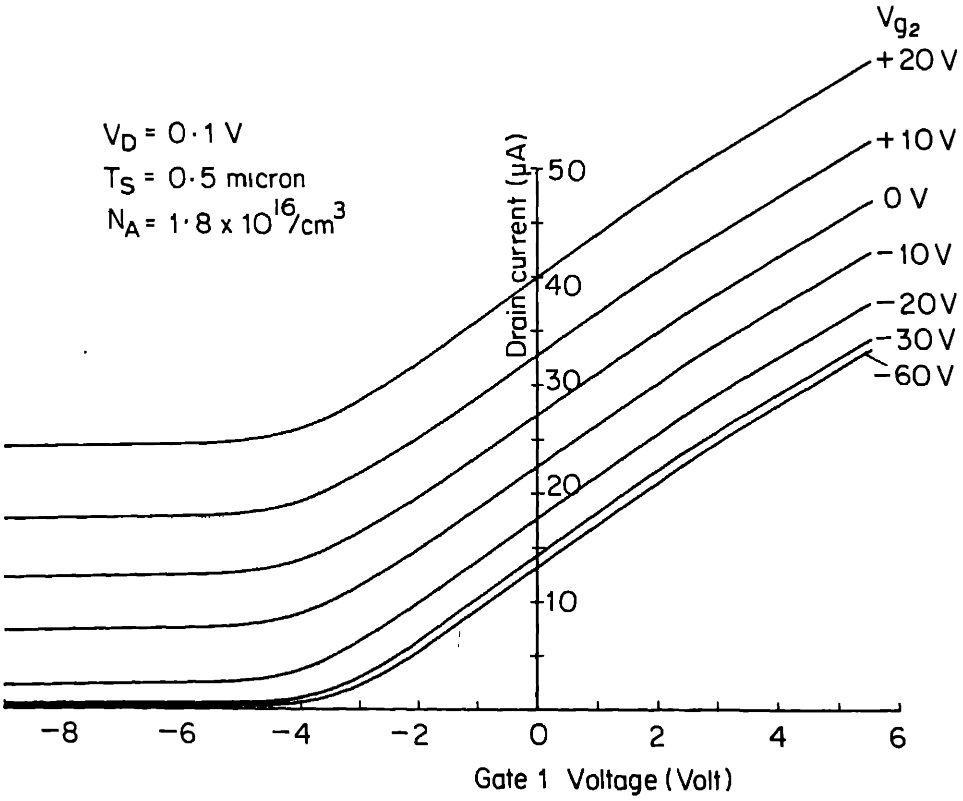

Figure 3. Drain current vs front gate voltage V_{G1} as a function of back gate voltage V_{G2}.

and the intercept is V_{T1}. We have measured mobilities from 250 cm^2/V-sec to 450 cm^2/V-sec with the front channel threshold voltage of −3·2 to −3·5 V and back channel threshold voltage of −30 V to −35 V.

There have been two models proposed in literature for explaining the I_D–V_D behaviour of the MISIM structure, one by Lim and Fossum (1984) and the other by Barth *et al* (1983). The second model is exact while the first one makes some approximations. Both models take into consideration the fact that silicon is finite in extent (0·5 μm in our case) and so far a given impurity concentration, the depletion regions from the top and the bottom will meet at some point making the entire film depleted. As a result, there is "communication" between the top and bottom gates, thereby controlling the drain current. We have matched our data with the Barth-Apte-Angell model and this is shown in figure 4 with a good fit.

Since our device has a W of 100 μm and L of 20 μm, there are a couple of grain boundaries in the active region of the transistor perpendicular to the current flow. The mobility and threshold voltages are thus modulated by these grain boundary charges and this gives a small error to our modelling effort. We have taken care of these effects by a voltage-dependant mobility (as can be seen in figure 3, where the slope is not constant).

The parameters which were used to fit the data are the mobilities $\mu n_1 = 295$ cm^2/V-sec of front channel and $\mu n_2 = 310$ cm^2/V-sec of back channel, V_{FB1}, the front channel flat band voltage of −6·1 V and V_{FB2}, the back channel flat band voltage of −52 V. The front gate oxide is 1000 Å while the back gate oxide is 1 μm.

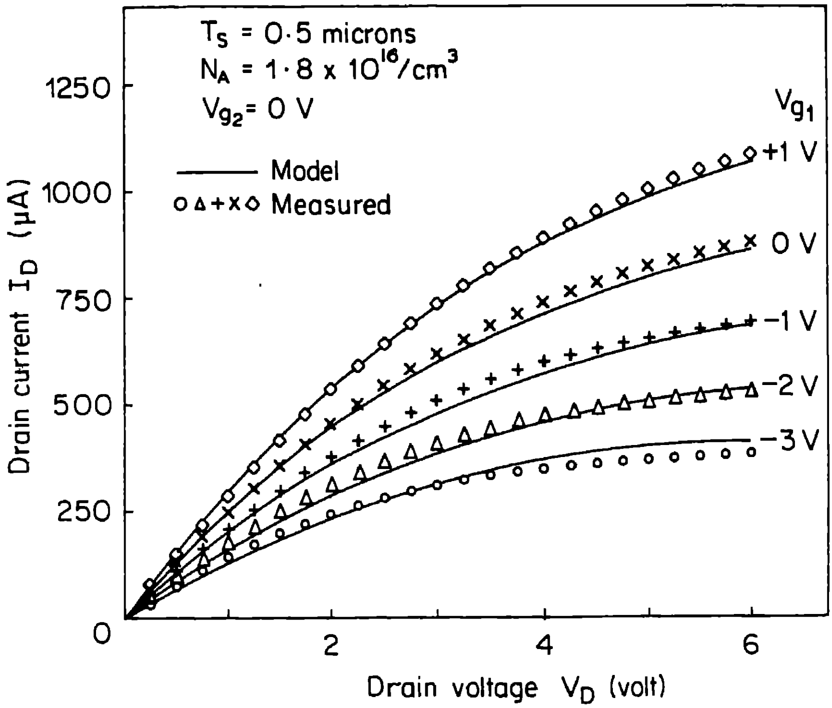

Figure 4. Experimental and calculated I_D–V_D curves for the MISIMFET.

4. Conclusions

We have fabricated N-channel silicon gate and metal gate MOSFETS by recrystallization, using a CW laser beam, LPCVD polysilicon deposited on thermally oxidized silicon. Surface electron mobilities upto 450 cm^2/V-sec have been measured. We have demonstrated the 4-terminal behaviour of our structure and applied a model to explain the I_D–V_D curves as functions of the two gate voltages. Laser beam recrystallized polysilicon films on insulators have a bright future for realising device-worthy silicon-on-insulator films and making 3-D integrated circuits.

Acknowledgements

The authors are grateful to the Department of Science and Technology for financing the laser. The authors would like to thank Prof. K V Ramanathan for his keen interest and continuous encouragement during the course of this investigation.

References

Barth P W, Apte P R and Angell J B 1983 *IEEE Trans. Electron Devices* **ED-30** 1717
Colinge J P, Demoulin E, Bensahel D, Auvert G and Morel H 1983 *IEEE Electron Device Lett.* **EDL-4** 75
Gat A, Gerzberg L, Gibbons J F, Magee T J, Peng J and Hong J D 1978 *Appl. Phys. Lett.* **33** 775
Kamins T I 1972 *Solid State Electron.* **15** 789
Kamins T I, Lee K F and Gibbons J F 1980 *Appl. Phys. Lett.* **36** 550
Lam H W, Sobczak Z P, Pinizotto R F and Tasch A F Jr 1982 *IEEE Trans. Electron Devices* **ED-29** 389
Lim H-K and Fossum J G 1984 *IEEE Trans. Electron Devices* **ED-31** 401
Tsaur B-Y, Fan J C C, Geiss M W, Silversmith D J and Mountain R 1981 *Appl. Phys. Lett.* **39** 561

Bull. Mater. Sci., Vol. 8, No. 3, June 1986, pp. 397–405. © Printed in India.

Effect of bulk and thin film dielectric overlay on the characteristics of microstrip rejection filter and simple microstriplines

K VIJAYA, M L JADHAV, S A GANGAL and R N KAREKAR
Department of Physics, University of Poona, Pune 411 007, India

Abstract. The changes in the characteristics of microstrip rejection filter and simple microstriplines due to bulk and thin film dielectric overlay are reported in this paper. Al_2O_3 overlay both bulk and thin film increases the Q of the filter. All other overlays decrease the Q. TiO_2 thin film shows improvement in Q whereas with bulk TiO_2 the filtering property is not observed. The effect of overlays on simple lines is to reduce the transmission without much effect in the reflection.

Keywords. Microstrip rejection filter; simple microstriplines; dielectric overlay; thin films

1. Introduction

The structure of the microstripline may lend itself to the study of microwave properties of materials in the thin film form by using overlay/underlay techniques which result in a change in the effective dielectric constant (Farrar and Adams 1974; Pande and Karekar 1976; Pande 1976).

For a given dielectric substrate the characteristic impedance (Z_0) of the microstripline is governed by the w/h ratio where w is the width of the line on top of the substrate and h is the dielectric thickness (Wheeler 1965). The impedance of the measuring system is normally 50 Ω. Thus for maximum power transfer the value of Z_0 should also be 50 Ω. For alumina substrate with $\varepsilon = 9{\cdot}6$, Z_0 is 50 Ω for w/h ratio of about 1 (Gupta and Singh 1974).

Open microstrip resonators are often employed in MIC techniques as absorption filters. One form is the standard half-wave resonator, open at both sides and coupled over a quarter wavelength with the main transmission line (figure 2). In the design of coupled microstrip structures the odd-mode impedance value is often used (Mullard Tech. Comm. 1972) for arriving at the coupling and the corresponding geometry. Unfortunately a considerable portion of the odd mode field exists in the air (Weirather 1974) which leads to fringing fields and radiative losses, particularly in open circuit resonators. The overlay technique, using Bi_2O_3 overlay on Au microstrip circuits (Pande 1976), is reported to be one of the solutions to this problem.

The aim of the present work is to fabricate copper microstriplines and rejection filter and study their transmission and reflection properties with and without overlay of various dielectric materials. From these observations the properties viz the characteristic impedance, Q, rejection, etc are calculated.

2. Experimental

The microstrip lines were obtained using chromium/copper on standard 1″ × 1″ × 0·025″ 99·66 % pure alumina substrates. Initially a thin film of chromium (thickness ~ 300 Å) was vacuum-evaporated at about 2×10^{-5} torr onto heated alumina substrates, the substrate temperature being optimized to 100°C for best adhesion.

After cooling the substrates to room temperature copper was deposited onto the Cr to a thickness of approximately 3000 Å in the same cycle. After repeating the process on the other side of the alumina substrate, the thickness of Cu was increased to about 5 μ by electroplating in a $CuSO_4$-H_2SO_4 bath using the arrangement shown in figure 1. The bath required about 2 litres of plating solution ($CuSO_4$—200 g/l, H_2SO_4—56 g/l, potash alum 12 g/l).

The size of the anode was twice that of the cathode so as to obtain a uniform field around the cathode. The pH of the solution was approximately 2. This electroplating system was optimized to obtain a uniform pinhole free deposit which did not oxidize easily. For a fixed separation between the electrodes (7·5 cm) and for a fixed voltage (10 V) a current of 80 mA gave the best films. When run for 30 min, a thickness of 5 μ was obtained.

The rejection filters and microstriplines were photolithographically delineated on one side of these metallized substrate. The geometry was arrived at by using the standard tables and curves reported by Wheeler (1965) and Bryant and Weiss (1978). We designed a $\lambda/2$ open circuit resonant, single section maximally flat rejection filter (see figure 2) without overlay, at $f = 9{\cdot}57$ GHz, $\lambda_g = 1{\cdot}271$ with bandwidth of 2 %. In addition stripline masks of different widths were used to study the effect of width on Z_0 and to optimize the mask width.

For circuit evaluation, the microstrip circuits were mounted in resilient contact MIC test fixture. The performance of the filter and microstripline was evaluated using a network analyser (Hewlett-Packard 8410B). On this system the amplitude as well as the phase of the reflection and transmission coefficients can be measured. Using Smith chart overlay fixed on the polar display, direct evaluation of the input impedance (Z_{in}) is

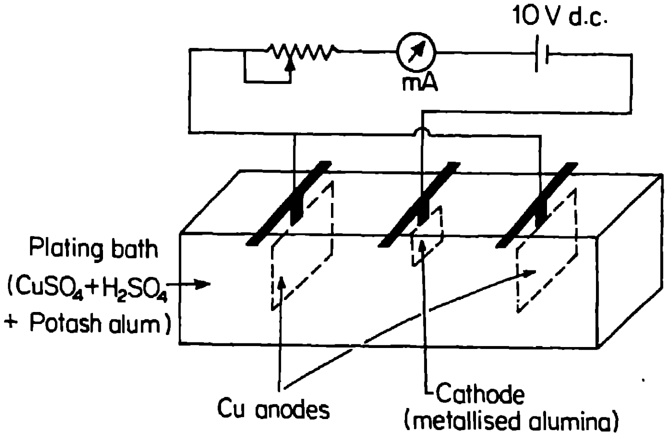

Figure 1. Arrangement for copper electroplating.

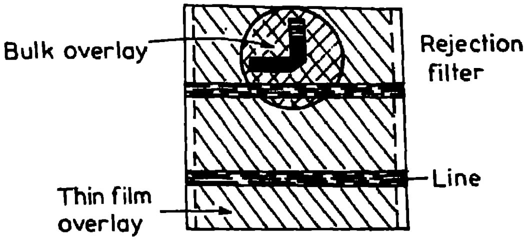

Figure 2. Sketch of the rejection filter and single microstripline with thin film overla (λ_g = 1·271 cm).

possible. The Z_{in} data, obtained in the frequency range of 2 to 12 GHz, were used t calculate the characteristic impedance Z_0 of the microstripline, using the equation

$$Z_{in} = Z_0\left(\frac{Z_L + Z_0 \tan\beta l}{Z_0 + jZ_L \tan\beta l}\right) \quad (1$$

where Z_L is the load impedance = 50 Ω, β is the propagation constant and l is the lengt of the stripline. Both the bulk and thin film overlays were tried on the filters an microstriplines. The bulk overlays of Bi_2O_3, TiO_2 and ZnS were in pellet form (abo 1 cm in diameter and 2 mm thick). Those of Al_2O_3 and 0211 corning glass were in th form of plates of size 2 cm × 1 cm. The thickness was 0·5 mm for corning glass an 0·26 mm for Al_2O_3. In any case the dimensions of these bulk overlays were such th they covered the entire coupline area of the filter.

For the film overlays, Al_2O_3, Bi_2O_3, TiO_2 and ZnS and PAN were tried. Al_2O_3 w deposited by chemical vapour deposition. The substrates were heated in a nitroge atmosphere to 375°C and a mixture of aluminium isopropoxide (Al $(OC_3H_7)_3$) vapou and N_2 gas was passed over them. Due to the pyrolysis of $Al(OC_3H_7)_3$ at 375°C, Al_2 is deposited on the substrate. Bi_2O_3 films were obtained by vacuum evaporation bismuth and subsequent oxidation in atmospheric air at a temperature of 165°C f about 90 min, and also by reactive ion plating. These overlays of Al_2O_3 and Bi_2O_3 ha some problem of oxidation and peeling because of the heat treatment required. Ti and ZnS were obtained by vacuum evaporation without much difficulty. PAN (po acrylo-nitrate) films were obtained by plasma polymerization. In all the cases the a covered by overlay was such that it covered the whole substrate except for the cont areas as shown in figure 2.

3. Results and discussion

3.1 *Rejection filter*

Figure 3 shows the typical curves of rejection (db) (i.e. transmission) vs frequency the filter with and without bulk overlay for various overlay materials. Figure 4 sh rejection vs frequency curves for filters with thin film overlay. It is seen from figu that the bulk overlays shift the centre frequency (f_0) to the lower frequency side. Ex for Al_2O_3 all other overlays have the effect of reducing the Q. TiO_2 overlay decre the transmission at all frequencies from 8–12 GHz and the sample does not show f

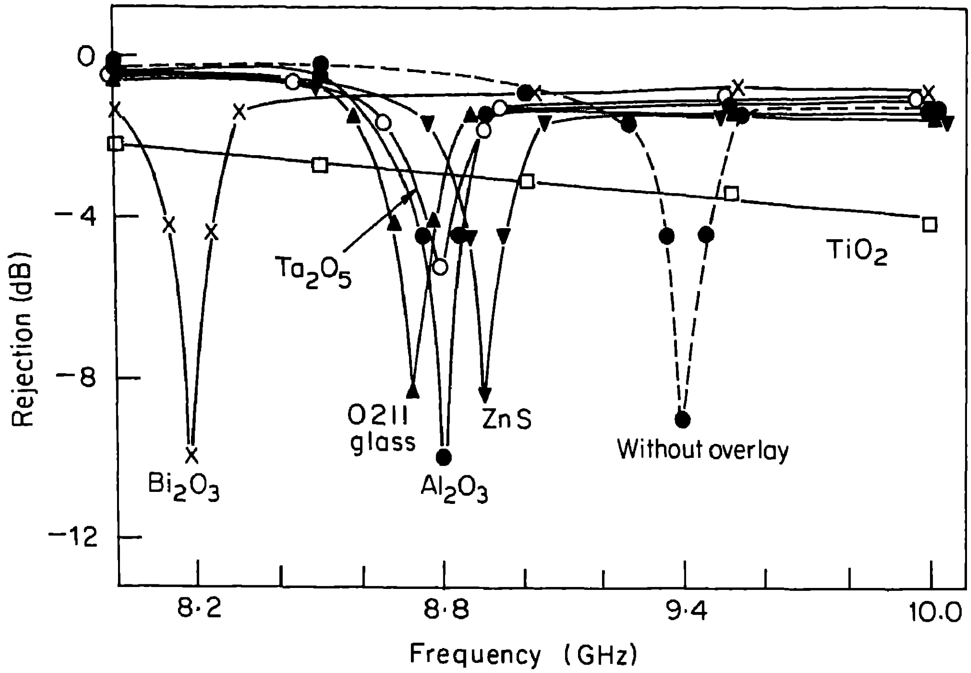

Figure 3. Graph of rejection (db) vs frequency (GHz) for rejection filter with and without bulk overlay.

properties. This shows that the higher thickness of the overlay in some way makes the filter more lossy. This may be due to the presence of some other higher modes, like surface waves. The thickness effect was studied only for Bi_2O_3 bulk overlay which shows improvement in *Q* (even compared to the one without overlay) at a lower thickness of 0·9 mm.

Table 1a gives the data of *Q* for filter with and without Al_2O_3 and 0211 corning glass bulk overlay. It shows that there is an increase in *Q* and rejection after Al_2O_3 bulk overlay (except in one sample). This shows that the overlay has tightened the coupling and reduced the losses. For 0211 glass there is decrease in *Q* for all the samples. Table 1b gives the data for other bulk overlays.

From figure 4 (for the thin film overlay) it is seen that for Al_2O_3 (thickness ~ 4000 Å deposited by CVD) there is a shift in frequency and also improvement in *Q* from 84·08 to 112. Bi_2O_3, TiO_2 and Ta_2O_5 do not show any shift in frequency. TiO_2 film of thickness 900 Å also shows improvement in *Q* from 158·5 to 172·9. Thin film overlay of TiO_2 is better than bulk TiO_2 overlay. For Bi_2O_3 and Ta_2O_5 there is decrease in *Q*, for Bi_2O_3 from 189 to 118 and for Ta_2O_5 from 188 to 156·6. ZnS films reacted with copper, spoiling the microstrip structure itself, so the effect of ZnS thin film overlay could not be studied. Plasma-polymerized PAN overlay gave rise to shift in f_0 from 9·52 to 9·49 and decrease in *Q* from 190 to 158.

An attempt was also made to use the frequency shift and *Q* of filters with overlay to get an idea about the material properties of the overlay. The procedure was as follows.

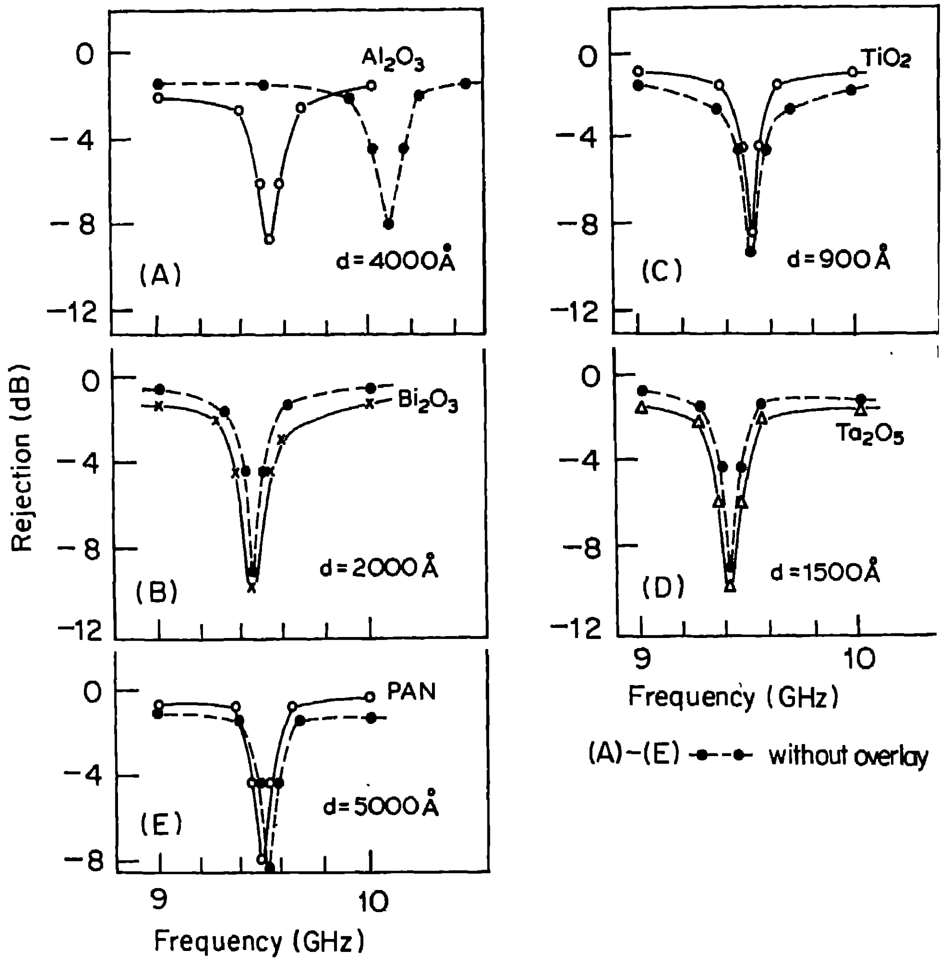

Figure 4. Graph of rejection (db) vs frequency (GHz) for rejection filter with and witho thin film overlay.

The ε_{eff} of the stripline without overlay was calculated using the formula of Owe (1976).

$$\varepsilon_{\text{eff}} = \frac{\varepsilon_r + 1}{2}\left\{1 + \frac{29{\cdot}98}{Z_0}\left(\frac{2}{\varepsilon_r + 1}\right)^{1/2}\left(\frac{\varepsilon_r - 1}{\varepsilon_r + 1}\right)\left(\ln\frac{\pi}{2} + \frac{1}{\varepsilon_r}\ln\frac{4}{\pi}\right)\right\}^2 \quad ($$

where $\varepsilon_r = 9{\cdot}6$, the dielectric constant of the alumina substrate. Z_0 was assumed to 50 Ω as an approximation. From this formula ε_{eff} without overlay comes out to be 6·0 Using this value of ε_{eff} and the experimental resonant frequency f_0 without overlay, t guide wavelength λ_g was calculated for each sample using the relation,

$$\lambda_g = \frac{\lambda_0}{\sqrt{\varepsilon_{\text{eff}}}},$$

λ_0 is the free space λ_0 (c/f_0). This is done to account for changes in λ_g due to delineati

Table 1a. Data of Q and rejection of filter with and without bulk Al_2O_3 and 0211 glass overlays

	Without overlay			Bulk overlay of Al_2O_3 and 0211 glass					
				Al_2O_3			0211 glass		
Sample No.	f_0 GHz	Q	Rej db	f_0 GHz	Q	Rej db	f_0 GHz	Q	Rej db
3	9·64	160	4·9	9·05	181	5·4			
41	9·47	145·6	4·9	8·82	147	5·6	8·72	96·8	4·3
44	9·51	158·5	6·1	8·78	175·6	6·1	8·76	109·5	4·5
48	9·52	190·4	5·4	8·94	149	5·4	8·67	123·8	4·8
53	9·40	188·0	6·1	8·80	251·4	6·9	8·72	158·5	5·4
B	9·57	106·3	3·9	8·92	111·5	4·5	8·81	80·10	3·9
D	9·65	175·4	4·9	8·88	253·8	6·1	8·87	108·75	4·9
H	9·71	107·8	3·9	9·19	13·13	4·5	9·0	90·0	4·1
I	9·56	73·5	3·0	8·85	126·4	3·9	8·82	76·7	3·0
Average values	$\varepsilon_{\text{eff}} = 6{\cdot}077$ $\tan\delta_{\text{eff}} = 5{\cdot}7 \times 10^{-3}$ $\sigma_{\text{eff}} = 2{\cdot}99 \times 10^{-9}\,℧\text{-cm}$			$\varepsilon_{\text{eff}} = 7{\cdot}169$ $\tan\delta_{\text{eff}} = 3{\cdot}94 \times 10^{-3}$ $\sigma_{\text{eff}} = 3{\cdot}98 \times 10^{-9}\,℧\text{-cm}$			$\varepsilon_{\text{eff}} = 7{\cdot}19$ $\tan\delta_{\text{eff}} = 9{\cdot}19 \times 10^{-3}$ $\sigma_{\text{eff}} = 1{\cdot}70 \times 10^{-9}\,℧\text{-cm}$		

Table 1b. Data of Q and rejection of filter with other bulk overlays

Without overlay			Bulk overlays of											
			Bi_2O_3			ZnS								
f_0 GHz	Q	Rej db	f_0 GHz	Q	Rej db	f_0 GHz	Q	Rej db	f_0 GHz	Q	Rej db	f_0 GHz	Q	Rej db
9·64	160	4·9	8·52	31·5	1·4	9·12	102	3·9	8·79	46·3	2·2	No filter characteristics		
9·52	190·4	5·4	9·28	42·2	3·2									
9·40	188	6·1	8·18	204·5	6·9							No filter characteristics		
			(thin pellet)											
			$\varepsilon_{\text{eff}} = 7{\cdot}5$			$\varepsilon_{\text{eff}} = 6{\cdot}7$			$\varepsilon_{\text{eff}} = 7{\cdot}3$					

As a result of overlay, ε_{eff} will change to $(\varepsilon_{\text{eff}})_0$, thus changing the resonant frequency to $(f_0)_0$. Hence by knowing experimental $(f_0)_0$ and calculated $(\lambda_g)_0$ and using equation (3) again one can get $(\varepsilon_{\text{eff}})_0$. The values of $(\varepsilon_{\text{eff}})_0$ thus calculated are given in tables 1a and 1b.

From the experimental value of Q, the effective loss tangent of the overall configuration can be calculated using the relation

$$\tan\delta = 1/Q. \tag{4}$$

Some typical values are given in tables 1a and 1b. Assuming the rejection filter to be a parallel resonant circuit the effective conductivity can be estimated to a first approximation using the formula for parallel resonant circuits.

$$\sigma_{\text{eff}} \approx Q/\omega\, \varepsilon_{\text{eff}}. \tag{5}$$

It is seen that with overlay there is a reduction in the effective $\tan\delta$ as compared to the one without overlay. Only $\tan\delta$ of Al_2O_3 is available in literature and is $\sim 6 \times 10^{-4}$. Our values are effective and further analysis is being done to separate the dielectric properties from the effective values.

3.2 *Single microstriplines*

Figure 5 shows the variation of Z_0 with frequency in the range of 2 to 12 GHz for microstriplines with widths varying from 18 to 28 mils. It is seen that Z_0 varies in the range of 20 Ω to 95 Ω randomly about the expected value of 50 ohms. Although some sort of oscillatory behaviour is observed, it is difficult to relate this to width variation. In all cases, except for the 18 mils line the scatter is more pronounced at the higher

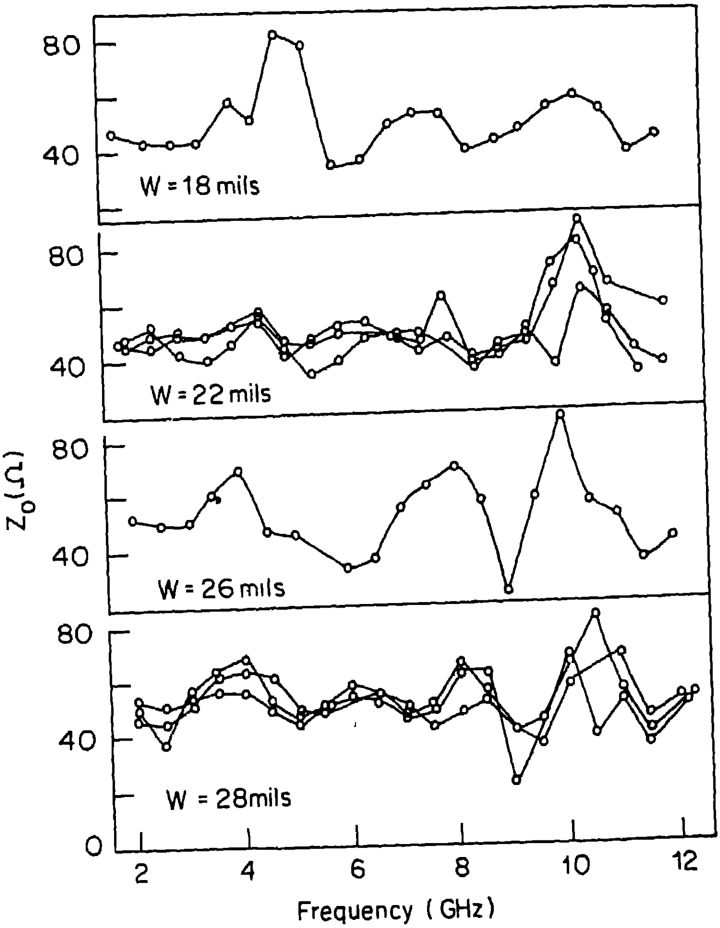

Figure 5. Variation of characteristic impedance (Z_0) with frequency for striplines o different widths.

frequencies (8–12 GHz). In the microwave range, Z_0 is expected to show a steady increase with frequency (Krage and Haddad 1972). This is because of the change in the effective dielectric constant with frequency and also changes in the resistivity of conductor material.

The observed random variation of Z_0 with frequency could be due to the contacts between the microstrip and the ommni spectra (OSM) launchers which are actually co-axial to microstrip connectors used to connect the microstrip to the rest of the measuring system. Bianco *et al* (1976) characterized the effect of launcher on a system of microstrips and active devices. They too report random oscillatory behaviour of the scattering parameter S_{11} and S_{22}. Since the results are heavily affected by launcher discontinuities, there seems to be no justification to discuss the frequency dependance of Z_0 in any further depth.

3.2a *Overlay effects on losses*: In order to study the effect of overlay on the losses present in the microstripline the power reflection and transmission coefficients were studied for both bulk and thin film overlays. The typical graphs of ρ^2 and T^2 versus frequency for bulk overlay effect are shown in figure 6. In all cases except for TiO_2 the reflection reduced as a result of bulk overlay. The transmission is also slightly reduced except in TiO_2, where it reduced almost by 50 %. However, the values of ρ^2 and T^2 are very critically dependant on size and position of the overlays. Since thin film overlays had to be tried on different samples only ΔT and $\Delta\rho$ were studied as a result of overlay. Only PAN (reactive ion-plated), Bi_2O_3 and TiO_2 showed increased average transmission as shown in table 2. The reflection coefficient measured at 8 GHz did not show much change (within variability limits). More careful experimentation is needed after considering the effect of discontinuities and variabilities.

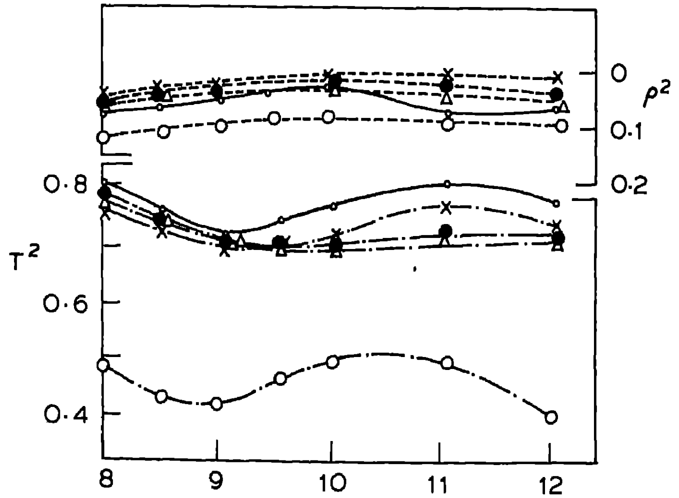

Figure 6. Variation of transmission and reflection coefficients as a function of frequency for single stripline with and without bulk overlay. (●) Al_2O_3; (×) Bi_2O_3; (Δ) 0211 glass; (O) TiO_2.

Table 2. Effect of thin film overlay on microstripline, ρ^2 and T^2

Material	ΔT^2 (average)	$\Delta\rho^2$ (8 GHz)
PAN	$+0{\cdot}09$	$-0{\cdot}04$
TiO_2	$+0{\cdot}13$	0
ZnS	$-0{\cdot}67$	—
Bi_2O_3 (oxidized)	$-0{\cdot}05$	0
Bi_2O_3 (reactive ion-plated)	$+0{\cdot}13$	$-0{\cdot}004$
Al_2O_3 (CVD)	$-0{\cdot}05$	—

Acknowledgements

The authors gratefully acknowledge the permission given by Mr R P Arora of
Pune for the extensive use of network analyser. Thanks are also due to Mr D Che
for helping in CVD of Al_2O_3. The authors also acknowledge the financial assistance fr
the Department of Science and Technology, New Delhi.

References

Bianco B *et al* 1976 *IEEE Trans. Instrum. Meas.* **1M-25** 320
Bryant T G and Weiss J A 1978 *IEEE Trans. Microwave Theory Tech.* **MTT-16** 1021
Farrar A and Adams A T 1974 *IEEE Trans. Microwave Theory Tech.* **MTT-22** 889
Gupta K C and Singh A 1974 *Microwave integrated circuits* (New York: Wiley, Eastern) p. 13
Krage M K and Haddad G I 1972 *IEEE Trans. Microwave Theory Tech.* **MTT-20** 678
Mullard Tech. Commun. No. 116 1972 p. 117–187
Owens R P 1976 *Radio Electron. Eng.* **46** 360
Pande M K and Karekar R N 1976 *IEEE Trans. Microwave Theory Tech.* **MTT-24** 262
Pande M K 1976 Ph.D. Thesis, Poona University, Pune
Weirather R R 1974 *IEEE Trans. Microwave Theory* (*Lett.*) **MTT-22** 70
Wheeler A 1965 *IEEE Trans. Microwave Theory Tech.* **MTT-13** 172

Bull Mater Sci., Vol. 8, No. 3, June 1986, pp. 407–413. © Printed in India.

Thermoelectroluminescence in thin films of zinc and copper phthalocyanines

L N TRIPATHI and Y MISRA
Department of Physics, University of Gorakhpur, Gorakhpur 273 001, India

Abstract. Thermoelectroluminescence studies were performed on zinc phthalocyanine and copper phthalocyanine films deposited on transparent and conducting glass substrate. The EL glow curves were recorded. The trap depths and frequency factors have also been determined using three different methods.

Keywords. Thermoelectroluminescence; zinc phthalocyanines; copper phthalocyanines

1. Introduction

Thermoelectroluminescence (TEL) is one of the thermally stimulated processes to study the thermal activation of inorganic and organic phosphors under a super-imposed d.c. or a.c. electric fields. This method gives information about the traps and their distribution like the simple glow curve experiment, viz thermoluminescence (TL) o thermally stimulated current (TSC) or thermally stimulated electron emission (TSEE experiments. Trapping action in EL processes can be understood by studying the E brightness as a function of temperature.

In organic hydrocarbons, the temperature dependence of space charge limite current in d.c. electroluminescence has been studied in anthracene (Nakada an Ishahara 1964; Bierman 1963) and metal-free phthalocyanines (Heilmeir and Warfel 1963). Thermally stimulated current measurements on the trapping levels of coppe phthalocyanine have been reported by Hoshino (1981). No attempt, has, however, bee made to determine parameters such as trap depths and recombination rate constants o frequency factors in ZnPc and CuPc. The present study attempts to record the TE glow peaks for these materials to determine the above parameters.

2. Theoretical

EL brightness is strongly dependent on the variation in temperature, which in tu brings about a number of changes; for example, electrons/holes are detrapped released and the mean trapping time of the carriers is also affected. The degree ionization of the trap levels also affects the potential in the space charge region. T increase of brightness at a particular field frequency may be due to release electrons/holes at a particular temperature, which interact with excitons leading enhanced EL. These electrons may associate themselves with holes supplied from t positive contact forming excitons which decay radiatively giving EL emission. Th carriers released from the traps are over and above those which are injected from t electrode contacts during the positive half cycles and which eventually form space-charge region leading to the formation of excitons. The release from traps, therefore, depends both on temperature and time. It therefore becomes necessary to consider the effect of temperature and the frequency of the alternating voltage together.

Chukova (1972), Johnson *et al* (1956) and Haake (1955) showed that the effect of temperature and frequency on EL brightness can be expressed by the relation

$$f = S \exp(-E/kT), \tag{1}$$

where E is the trap activation energy, S the frequency factor or carrier attempt to escape frequency, f the frequency of the electric field and T, the temperature at which the brightness is maximum.

If the experiment is performed at a number of frequencies $f_1, f_2, f_3 \ldots$ at a constant fixed voltage and $T_1, T_2, T_3 \ldots$ be the corresponding temperatures of maximum brightness for a particular peak, then the slope of the line drawn between $\log f$ and $1/T$ would give $-E/K$ and the intercept on the $\log f$ axis would give logs. From these data, E and S could be found out.

There is a second approach to determine the trap depth. If the experiment is performed at different heating rates, a particular peak is shifted towards the higher temperature side at a higher rate of heating. The shift in EL brightness is also expected with change in frequency of the field. At higher frequencies the peak would shift towards higher temperature side. Therefore, the different maxima at a particular frequency f, can be represented by an equation similar to (1)

$$f_1 = S_n \exp(-E_n/kT_n), \tag{2}$$

where E_n is the energy of the nth trap corresponding to temperature T_n and S_n is the frequency factor for that trap.

If the experiment is repeated at another frequency f_2 but at the same voltage, then

$$f_2 = S_n \exp(-E_n/kT'_n), \tag{3}$$

where T'_n is the new temperature at which the new peak maxima occur. From (2) and (3), we have

$$E_n = K \frac{(\log f_1 - \log f_2)}{\left(\frac{1}{T'_n} - \frac{1}{T_n}\right)}. \tag{4}$$

S can now be calculated from (2) and (3).

We use a third method known as the initial rise method to determine trap depth. Here, the probability that the electrons/holes will be excited by thermal energy is proportional to $\exp(-E/kT)$. At lower temperatures, a smaller number of electrons/holes will be released and their number will increase with increase in temperature. After reaching a maximum, it falls as the traps are depleted. The resulting TL curve has a single peak, the peak maxima denoting the depth of the level. If $\log I$ (at a constant frequency and voltage) versus $1/T$ is plotted, we could get a straight line, which would give the trap depth. The peak shape and the temperature of peak maxima depend not only on the intrinsic parameters such as E and S, but also on the heating rate, the intensity of EL emission and also on the concentration of traps and excitons. Several types of traps with different activation energies usually result in several TL peaks which may superimpose. There may be as many glow peaks as the number of trap levels in the TEL curve. The brightness maxima correspond to the exhaustion of certain group of trap levels.

3. Measuring arrangement and procedure

All the TEL curves were recorded above 200°K. The phosphor samples were in the form of thin films. The EL cell was fixed on a metallic plate of the cryostat, over which a heating element was wound, thin mica sheet providing an insulation.

The temperature of the EL cell was measured by a chromel-alumel thermocouple. One junction of the thermocouple was securely fixed in the metallic electrode of the cell using thin mica insulation and the other junction was dipped in ice. The EMF generated in the thermocouple was recorded by a digital multimeter and the value of corresponding temperature was computed from the standard table with an accuracy of 1°C. The heating rate was adjusted at 0·68°K/sec by controlling the current in the heating coil.

To obtain EL, the cell terminal was connected to a wide band amplifier capable of giving a.c. voltages upto 1000 V and frequencies from 1 Hz to 10 kHz. The integrated light output was measured using photomultiplier tube (1P21) operated by a stabilized power supply unit giving voltages upto 1200 V. The output terminals of the photomultiplier tube were connected to a multiflex galvanometer of current sensitivity 10^{-9} amp/mm to record the relative intensity in arbitrary scale.

For recording TEL emission, 500 V (r.m.s.) was applied between the plate of the EL cell and the heating was then started. The light output was recorded at 3 field frequencies, 1·5, 2·0 and 2·5 kHz respectively for every sample.

4. Results and discussion

The TEL glow curves for ZnPc and CuPc are shown in figures 1 and 2 respectively. The maxima of the brightness temperature curves are seen to shift to lower temperatures with increasing field frequencies. In inorganic systems so far known, the peak maxima are reported to shift towards the higher temperature side (Tripathi *et al* 1982). Normally such systems have a majority of electron traps. This probably implies that in ZnPc and CuPc, the presence of hole traps might cause this behaviour.

The log f versus $1/T$ plots for each sample show a straight line. This gives the tra depth directly and intercept the value of S. The calculated values of E and S ar shown in table 1 for each system.

Trap depths have also been calculated using equation (4) at three differen frequencies 1·5, 2·0 and 2·5 kHz and the results are presented in table 1. The initial ris method (log B versus $1/T$) curves are shown in figures 5 and 6 and the values of E ar shown in table 1. The value of S for each sample is of the order of 10^6 sec^{-1}.

Hwang and Kao (1974) studied the d.c. electroluminescence and its temperatur dependence in anthracene single crystals and reported one glow peak maxima at 313°K This has been interpreted as arising due to competing behaviour of two types o processes: (i) due to exciton-trapped-exciton interaction and (ii) due to exciton carrie interaction. The exciton-trapped-exciton interaction dominates at temperatures lowe

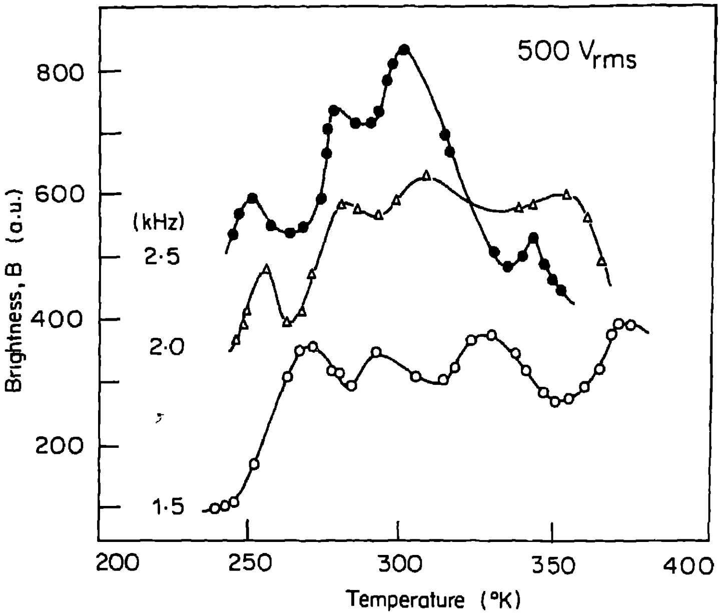

Figure 1. TEL curves for ZnPc (150 nm thick).

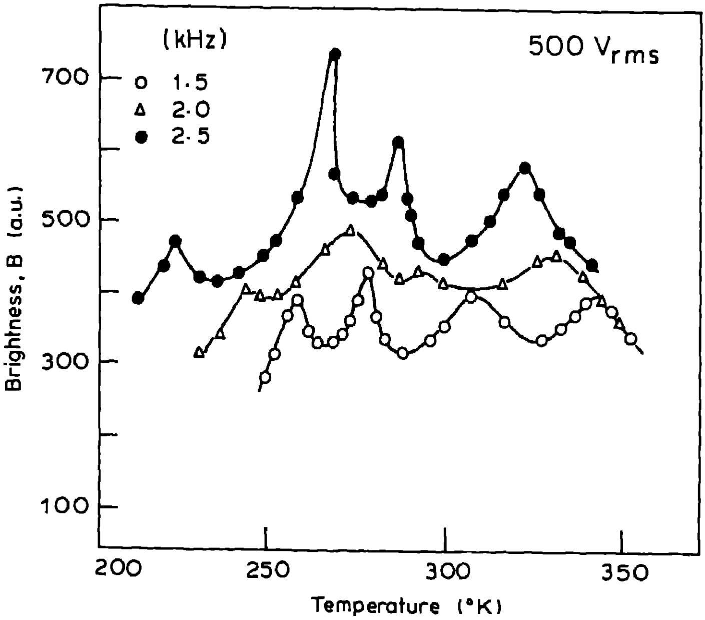

Figure 2. TEL curves for CuPc film (200 nm thick).

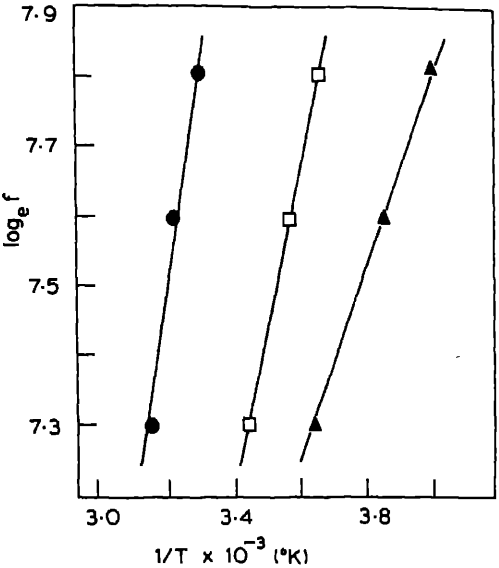

Figure 3. Log f vs $1/T$ for ZnPc film (200 nm thick).

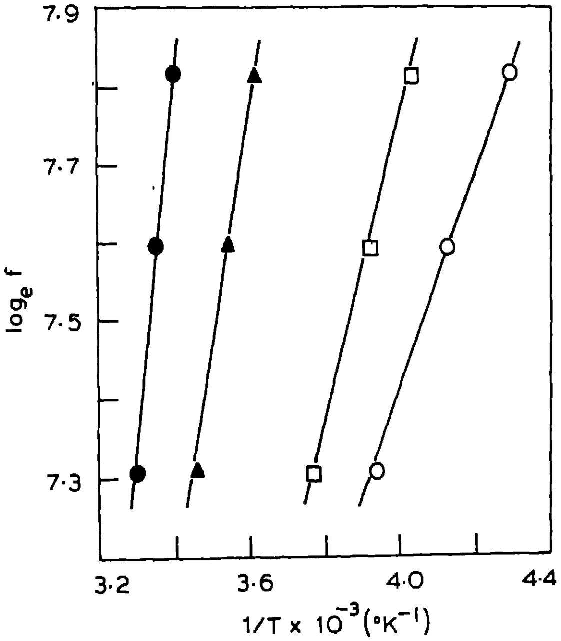

Figure 4. Log f vs $1/T$ for CuPc film (200 nm thick)

Table 1. Values of trap depths E and the frequency factor S ZnPc and CuPc

Phosphor film	From glow curve at low temperature trap depth (eV)			Trap depth (TEL) log f vs $1/T$	Trap depth log B vs $1/T$	Escape frequency (sec^{-1})
	f_1-f_2	f_2-f_3	f_3-f_4			
ZnPc	0·10	0·12	0·11	0·14	0·16	10^6
	0·21	0·21	0·21	0·22	0·23	
	0·50	0·47	0·49	0·26	0·27	
CuPc	0·14	0·07	0·08	0·13	0·16	10^6
	0·16	0·19	0·17	0·16	0·18	
	0·36	0·27	0·29	0·24	0·25	
	0·83	1·16	—	0·74	—	

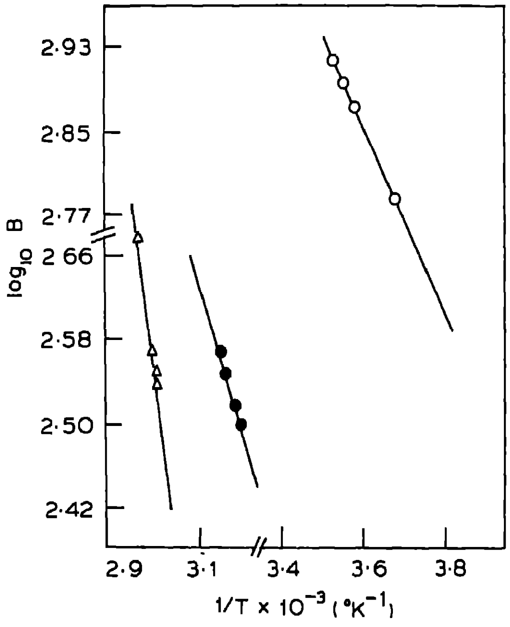

Figure 5. Log B vs $1/T$ for ZnPc.

maximum while the exciton carrier interaction dominates at higher res.

emperature range shown, we find four peaks corresponding to 4 groups of oth the materials.

e pointed out that in EL experiment, the phosphors are excited by photons at ratures for some time to fill the trap levels with electrons/holes and later the re is raised to get the stored energy released. But no such excitation was done ent study. The EL radiation itself acts as excitation source for filling the traps

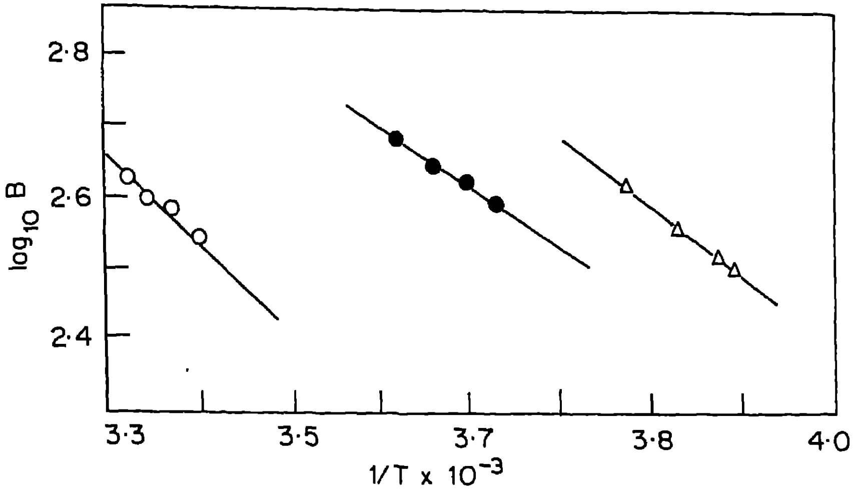

Figure 6. Log B vs $1/T$ for CuPc.

and these trapped electrons/holes are released by the combined action of fie frequency and temperature.

References

Bierman A 1963 *Phys. Rev.* **130** 2226
Chukova Y P 1972 *Electrolum. Proc., P. N. Lebedev Phys. Institute,* **50** 97
Haake C H 1957 *J. Electrochem. Soc.* **104** 291
Heilmeir G H and Warfeld G 1963 *J. Chem. Phys.* **38** 163
Hoshino Y 1981 *J. Appl. Phys.* **52** 5655
Hwang W and Kao K C 1974 *J. Chem. Phys.* **60** 3845
Johnson P D, Piper W W and Williams F E 1956 *J. Electrochem. Soc.* **103** 221
Nakada I and Ishahara Y 1964 *J. Phys. Soc. Jpn* **19** 695
Tripathi L N, Chaube B R and Misra C P 1982 *Pramana* (*J. Phys.*) **19** 385

Bull. Mater. Sci., Vol. 8, No. 3, June 1986, pp. 415–418. © Printed in India.

Characterization of Pb_3O_4 films by electrochemical techniques

M SHARON, SUDHIR KUMAR and S R JAWALEKAR*

Department of Chemistry, *Department of Electrical Engineering, Indian Institute
Technology, Bombay 400 076, India

Abstract. The band gap of semiconductor is determined by photovoltage spectrum. T photovoltage sign shows the semiconductor to be of *n*-type conductivity. Mott-Schottky pl gives the position of Fermi level, the approximate position of band edges, donor density in t semiconductor and space charge layer thickness. The results agree with other reported value

Keywords. Electrochemistry; photovoltage; photoelectrochemical

1. Introduction

The practical application of the concepts of semiconductor electrochemistry is still not sufficiently developed field, although sufficient information regarding its characteristic is available since the last two decades. In many semiconductors, electrochemica characterization has been used successfully (Faktor *et al* 1980) to determine band ga donor density, space charge layer width, absorption coefficient, type of conductivit carrier concentration, composition, diffusion length etc. In the present investigation the semiconductor Pb_3O_4 is characterized by photovoltage spectrum and capacitance voltage characteristics.

2. Experimental details

The Pb_3O_4 films (thickness 6·3 μm) were obtained by annealing the electrodeposited β PbO_2 films on nickel substrates for 24 hr at 450°C (Sharon *et al* 1984c). These film exhibited low conductivity ($\sim 10^{-4}\ \mathrm{ohm}^{-1}\,\mathrm{cm}^{-1}$). The photovoltage spectrum wa obtained by measuring the open circuit photovoltage between Pb_3O_4 electrode an platinum counterelectrode dipped in redox electrolyte IO_3^-/I^- (0·2 M) at differen wavelengths of light (200–800 nm). The semiconductor electrode was illuminated b xenon arc lamp (Oriel, 500 W) through a monochromator (Oriel) keeping the cell 7·8 c away from the latter. Capacitance-voltage characteristics were studied with the thre electrode system i.e. semiconductor, platinum and saturated calomel electrode (SCE) a reference dipped in buffer solution (pH = 7). The capacitance was measured by LC bridge (Systronics) at various electrode potentials (vs SCE) of semiconductor electrode AnalaR grade of chemicals were used in all the experiments without any furthe purification. All the solutions were prepared in triple distilled water.

3. Results and discussion

The criteria for electrolyte selection, validity of photovoltage spectrum for band-gap determination and interpretation of Mott-Schottky plot are discussed below.

3.1 *Electrolyte selection*

The criteria for the most suitable electrolyte in contact with semiconductor are that it should not react chemically with the semiconductor and should produce sufficient band bending. Based on earlier studies (Sharon *et al* 1984c), the redox couple IO_3^-/I^- (0·2 M, pH = 7) satisfies both the conditions. Therefore, IO_3^-/I^- was selected for further studies.

3.2 *Photovoltage spectrum*

Open-circuit photovoltages of the photoelectrochemical (PEC) system Pb_3O_4/IO_3^-, I^-/Pt were measured at various wavelengths of light. The photovoltage sign gives conductivity type of semiconductor (Peter 1983; Faktor *et al* 1980). In this system anodic behaviour of photovoltage of the semiconductor was observed which indicates its *n*-type of conductivity.

A plot of photovoltage against the wavelength of light is shown in figure 1. The absorption edge of the spectrum gives the band-gap value 2·12 eV which is in good agreement with the value of 2·18 eV reported earlier (Pamfilov *et al* 1967). This value is also comparable with that measured earlier by photocurrent method (E_g = 2·0 eV) (Sharon *et al* 1984a) and reflectance spectrum (Sharon *et al* 1984b) (E_g = 2·1 eV). The exact explanation of photovoltage spectrum is not available till date. However, Williams

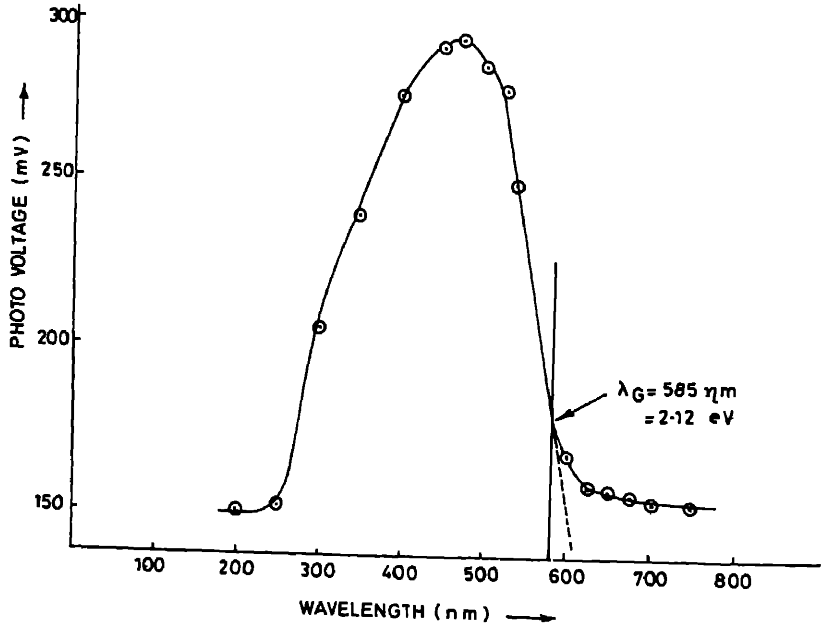

Figure 1. Photovoltage vs wavelength of light for the system n-Pb_3O_4/IO_3^-, I^-/Pt to determine the band gap of Pb_3O_4.

(1959) observed that the photovoltage spectra of ZnO and CdSe exactly behave as optical density vs wavelength plot and give similar absorption edge. This can be explained as follows:

Based on the equation for the generation rate $g_p(x)$ as a function of depth (x) for the semiconductor electrolyte junction (Myamlin and Plaskov 1967)

$$g_p(x) = P(1-R)\alpha \exp(-\alpha x),$$

an expression for small signal photovoltage is given as (Faktor *et al* 1980),

$$KP\left[\frac{(1-R)\alpha L_p}{1+L_p}\right]$$

where K is the constant for the given material; P, the photon flux; R, the surface reflectivity; α, the absorption coefficient and L_p = hole diffusion length. In the above expression, if $\alpha \cdot L_p \ll 1$ which is always true when band gap is not too low, $V_{ph} = KP(1-R)L_p \times \alpha$. At constant photon flux $KP(1-R)L_p = A$ = constant $V_{ph} = A\alpha$. Hence, V_{ph} is directly related to α and consequently shows the same spectral distribution.

3.3. *Capacitance-voltage characteristics*

The capacitance-voltage characteristics were studied by using the well-established Mott-Schottky plot for semi-conductor-electrolyte junction (Gerischer 1979). The $(\text{capacitance})^{-2}$ vs electrode potential plot for the electrochemical system Pb_3O_4/buffer solution (pH = 7)/Pt is given in figure 2. The condition when electrode potential is equal to zero gives the flat-band potential. The value of flat-band potential (V_{fb}) as obtained from this plot is −0·405 V vs SCE which is comparable to that reported

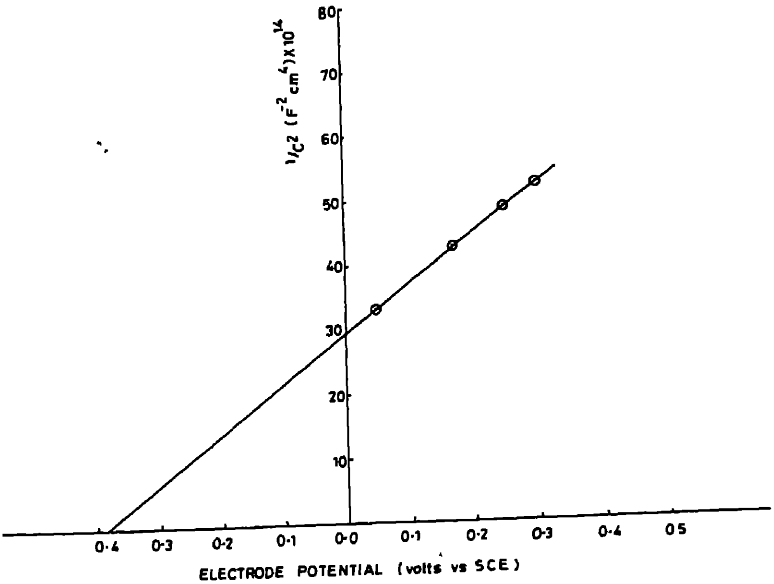

Figure 2. Mott-Schottky plot for the system n-Pb_3O_4/Buffer solution (pH = 7)/Pt to study capacitance voltage characteristics. Electrode potential is measured with respect to saturated calomel electrode (SCE).

earlier (i.e. −0·31 V vs SCE) using photocurrent method (Sharon *et al* 1984a) f polycrystalline Pb_3O_4 pellets.

The flat band potential gives the position of Fermi-level in semiconductors. T position of Fermi-level with respect to vacuum level is given by

$$E_F = eV_{fb}\,(\text{vs SCE}) - 4{\cdot}781\ \text{eV (Gerischer 1975)}$$
$$= 4{\cdot}376\ \text{eV}$$

In highly doped semiconductors the Fermi level position lies 0·1 eV below that conduction band edge (Scaife 1980). However, these Pb_3O_4 films have low conductivi Therefore, if we assume this difference as 0·2 eV, the approximate positions conduction and valence band edges can be given as −4·176 eV and −6·356 respectively. The donor density in the semiconductor is calculated from the slope Mott-Schottky plot (figure 2). Using the reported value of dielectric constant ($\varepsilon = 15$) Pb_3O_4 (Oehme 1964) the donor density is calculated to be $1{\cdot}19 \times 10^{-16}\ \text{cm}^{-3}$. Putti the appropriate values of donor density, dielectric constant and flat band potential, t space charge layer width in semiconductor was calculated to be $7{\cdot}80 \times 10^{-5}$ cm.

4. Conclusions

The electrochemical characterization methods are fast and much less complicat Specially the band gap measurement is very simple and reliable. The value of (−0·405 V vs SCE) is also in good agreement with that of determined by photocurre method (−0·31 V vs SCE). However, detailed studies are needed to explain the ex behaviour of photovoltage spectrum and this is now in progress.

Acknowledgement

We are grateful to CSIR for providing a research grant to complete this project. One us (SK) is specially thankful to the Director, IIT, Bombay for a research fellowshi

References

Faktor M M, Ambridge T, Elliott C R and Regnault J C 1980 *Current topics in material science* (ed.) E Ka (Amsterdam: North-Holland) Vol. 6, p. 1

Gerischer H 1979 *Topics in applied physics* (Solar Energy Conversion) (ed.) B O Seraphin (Berlin: Sprin Verlag) Vol. 31, p. 214

Gerischer H 1975 *J. Electroanal. Chem. Interf. Electrochem.* **58** 263

Myamlin V A and Plaskov Y V 1967 *Electrochemistry of semiconductors* (New York: Plenum Press) p.

Oehme F 1964 *Chemiker Ztg.* **88** 657 (*Chem. Abstr.* **61** 15459f)

Pamfilov A V, Evanchevka E G and Drogomeretskie P V 1967 *Russ. J. Phys. Chem.* **41** 565

Peter M 1983 *J. Electroanal. Chem. Interf. Electrochem.* **144** 315

Scaife D E 1980 *Solar Energy* **25** 41

Sharon M, Kumar S, Sathe N P and Jawalekar S R 1984a *Renewable energy sources*, (ed) T N Vezir (Amsterdam: Elsevier) p. 321

Sharon M, Kumar S, Sathe N P and Jawalekar S R 1984b *Solar Cells* **12** 353

Sharon M, Kumar S and Jawalekar S R 1984c *Proc. Symp. photovoltaic materials and devices*

Williams R 1959 *J. Chem. Phys.* **32** 1505

Bull. Mater. Sci., Vol. 8, No. 3, June 1986, pp. 419–422. © Printed in India.

Electrochemical bath deposition technique: Deposition of CdS thin films

S H PAWAR, C H BHOSALE and L P DESHMUKH
Department of Physics, Shivaji University, Kolhapur 416 004, India

Abstract. Cadmium sulphide thin films have been deposited onto chromium plated stainless steel substrates under the influence of electric field. The various deposition parameters such as speed of rotation of the substrates, temperature of the chemical bath, molar concentrations of solution and the strength of the electric field were kept at optimized conditions. The electrochemical photovoltaic (ECPV) cells are formed with CdS film electrodes. The properties of CdS films and ECPV cells are monitored with selective values of the electric field employed in the controlled precipitation technique. This relatively new technique is described and the possible film formation mechanism suggested.

Keywords. Anodic chemical film; cathodic chemical film; electrochemical photovoltaic cells.

1. Introduction

Recent investigations have developed considerable interest in CdS thin film due to its intermediate band gap, high absorption coefficient and considerable energy conversion efficiency. This resulted from the discovery of Ellis *et al* (1976) that photodecomposition of CdS can be quenched by adding polysulphides to the aqueous solution. Much work has been done on the CdS thin films and their use in electrochemical photovoltaic (ECPV) cells. Various preparative and post-preparative treatments have been given to CdS photoanode (Lokhande *et al* 1983; Mukherjee and Das 1980) to improve the performance and efficiency of these cells.

In this investigation an attempt has been made to improve the ouput current and voltage of the ECPV cell formed with CdS photoanode, prepared under the influence of an electric field. This paper also presents the formation mechanism of CdS film prepared anodically and cathodically.

2. Experimental

The reaction mixture was prepared as under: 20 c.c. of desired molar $CdSO_4$ solution was taken in 250 c.c. beaker and an appropriate amount of 14 M liquor ammonia was slowly added into it at room temperature, with continuous stirring, to redissolve the white precipitate of $Cd(OH)_2$. The pH of the deposition mixture was adjusted to 10. The mixture was then diluted to a total volume of 120 c.c. by adding double-distilled water. This reaction vessel containing the turbid solution of $Cd(OH)_2$ was kept in an oil bath maintained at 90°C. The ultrasonically-cleaned chromium-plated stainless-steel substrates fixed in a specially designed substrate holder were rotated by 75 r.p.m. a.c. motor, in a reaction vessel for 30 min at 85°C. The desired molar thiourea solution was added into the reaction vessel at the rate of 0·7 ml/min. Before adding thiourea an electric field of proper magnitude was applied between chromium plated stainless steel substrates and a ring-shaped stainless steel electrode, the distance between the electrode and the substrate being 1 cm. The CdS film was deposited onto the chromium-plated stainless steel substrates first with positive bias (by applying positive potential to the substrates), and then cathodically (by applying negative potential to the substrates) by applying d.c. 900 mV voltage. The current maintained during the deposition was 0·15 mA. The films so deposited were taken out of the reaction vessel, washed several times with double-distilled water, dried and then heated in a furnace for an hour at 200°C. The photoanode area was defined by the coal tar.

The ECPV cell was formed simply by immersing the photoanode and the counter electrode in an electrolyte. Platinum was used as a counter electrode in the cell and the properties of the films were investigated.

3. Results and discussion

The method of formation of thin films by controlled precipitation technique, also called chemical bath deposition technique, was modified by employing additional electric fields between conducting substrates and the counter electrode made up of chemically inert metallic cylinder. The chemical mixture was stirred into the electric cylindrical cell. The CdS films were formed by sustaining the conducting substrates both at positive and negative potentials, known as anodic and cathodic chemical films respectively.

A systematic investigation was made to reveal the role of the preparative parameters such as speed of rotation of substrates, temperature of the electrochemical bath, pH of the solution, strength of electric field etc on the properties of the films. It was found that, at low speeds of substrates (50-60 rpm), films were thick, nonspecular, and nonuniform. At higher speed (150 rpm), films were thin, specular and adhesive, while at intermediate speeds (70–80 rpm), films were smooth, specularly reflecting, adhesive and uniform. The films formed on the stationary substrates were porous, powdery, thick and nonuniform. Rotation of substrates into the electric cylindrical cell may help to increase the deposition of CdS molecules on the substrates, affecting the quality of the film.

The dissociation of complex and anion compounds depends on the temperature of the electrochemical bath. The optimum temperature of the electrochemical bath, for the growth of CdS films, was determined as 85 ± 5°C. Similarly the concentrations of the chemical ingredients used, the strength of the electric field and the pH of the mixture were optimized.

In chemical bath deposition technique, Kaur *et al* (1980) suggested the growth mechanism for CdS film formation, according to which, film formation takes place either by ion-by-ion condensation of Cd^{2+} and S^{2-} ions or by adsorption of colloidal CdS particles formed in the reaction mixture. Formation of CdS nuclei by combination of ions on the substrate surface requires some catalytic solid phase on the substrate surface, which can preferentially adsorb Cd^{2+} or S^{2-} ions to form CdS.

In our electrochemical bath deposition technique, the above mechanism was modified by applying electric field. The CdS molecules thus formed are in dispersed state due to the stirring of the chemical mixture. Generally the dispersed CdS and CdSe molecules exhibit negative charges. These negatively-charged particles under the influence of electric field are bound to attract or repel from the electrically-energized substrate electrode, depending on its polarity. The influence of the electric field on the growth mechanism of CdS and CdSe films was earlier studied by Ueno *et al* (1983) in electrophoretic technique. In the present investigation, chromium-plated stainless steel substrate dipped in a suspension of $Cd(OH)_2$ has a layer of $Cd(OH)_2$ on it, which acts as a catalytic solid phase, to stimulate the decomposition of thiourea. Decomposition of thiourea in the deposition mixture supplies S^{2-} ions which then combine with $Cd(OH)_2$ to form CdS molecule. It is therefore quite obvious that, if positive potential is given to the conducting substrates, these negatively-charged CdS molecules attract towards the substrates and get deposited on the substrates. Thus the growth of CdS thin film takes place molecule-by-molecule. The rate of deposition of CdS molecules on the substrate surface is increased due to the application of electric field with substrates at the positive potential. Stirring of the solution under the influence of electric field increases the rate of deposition of CdS molecules on the substrates.

For cathodic chemical CdS films, the rate of deposition of CdS molecules onto the substrate surface is decreased. This automatically decreases the deposition rate of CdS molecules on the substrate surface, but at the same time the deposition rate of CdS molecules on the ring shaped metallic counter electrode is increased as it is at the positive potential. It is thus clear that the anodic films are more adherent, physically coherent and smoother than the latter.

The properties of CdS films were studied by the method of semiconductor-electrolyte junction. In the present investigation, ECPV cells, termed as Cr/CdS-NaOH-Na_2S-S/Pt, were fabricated with both anodic and cathodic chemical CdS films. The current-voltage (I – V) characteristics, both in dark and light for anodic and cathodic

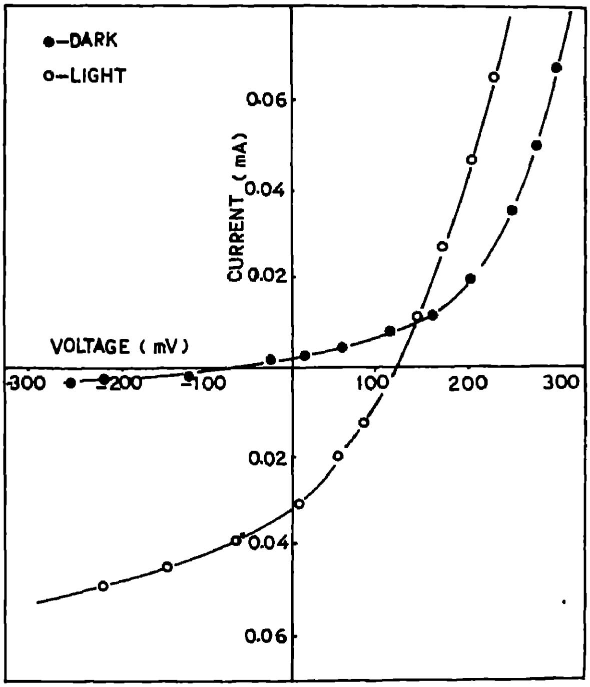

Figure 1. Current-voltage characteristics in the dark and light for the ECPV cell formed with anodic chemical CdS film.

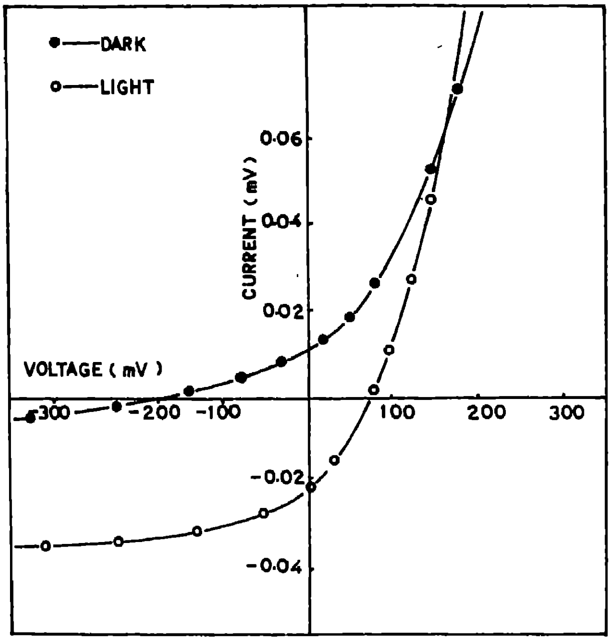

Figure 2. Current-voltage characteristics in the dark and light for the ECPV cell formed with cathodic chemical CdS film.

chemical CdS films are, shown in figures 1 and 2 respectively. It is seen that the photovoltaic output performance for the ECPV cell formed with anodic chemical CdS films is better than that formed with the cathodic chemical CdS film. This is attributed to the superiority of the anodic chemical CdS film.

Acknowledgements

The authors are grateful to the University Grants Commission, New Delhi for financial support. One of the authors (CHB) is indebted to Rayat Shikshan Sanstha, Satara for granting study leave.

References

Ellis A B, Kaiser S W and Wrighton M S 1976 *J. Am. Chem. Soc.* **98** 1635
Kaur I, Pandya D K and Chopra K L 1980 *J. Electrochem. Soc.* **127** 943
Lokhande C D, Uplane M D and Pawar S H 1983 *Indian J. Pure Appl. Phys.* **21** 78
Mukherjee M K and Das S K 1980 *Proc. National Solar Energy Conversion* (Madras: Allied Publishers) 326
Ueno Y, Minoura H, Nishikawa T and Masayasu T 1983 *J. Electrochem. Soc.* **130** 43

Bull. Mater. Sci., Vol. 8, No. 3, June 1986, pp. 423–426. © Printed in India.

Spray pyrolytic deposition of $CuBiS_2$ thin films

S H PAWAR, A J PAWAR and P N BHOSALE

Department of Physics, Shivaji University, Kolhapur 416004, India

Abstract. Thin films of $CuBiS_2$ have been deposited on glass substrates using spray pyrolysis technique. The effect of substrate temperature on the growth of $CuBiS_2$ thin films is studied in the range of 150 to 400°C. The best quality films are grown at substrate temperature 250°C with 0·1 M composition. Other preparative parameters like spray rate, pressure, height of the solution, etc are optimized with respect to substrate temperature. Some optical and electrical properties of $CuBiS_2$ films are also studied and reported.

Keywords. Spray pyrolysis technique; ternary chalcogenide films; spray rate.

1. Introduction

Ternary systems of the compound semiconductors are particularly interesting because of their technological applications in thin film devices and photovoltaic energy converters. Among the ternary semiconducting materials sulphur-containing compounds occupies an important place. These compounds can be prepared by employing various deposition methods, namely vacuum evaporation, chemical bath deposition, spray pyrolysis etc (Austin *et al* 1956; Rajebhosale and Pawar 1978; Pawar and Uplane 1983).

Spray pyrolysis technique has been successfully used in the deposition of a number of chalcogenide semiconductors (Feigelson *et al* 1977). However, no information is available on the preparation of $CuBiS_2$ thin films of the type I-III-VI_2 by spray pyrolysis technique. In the present study $CuBiS_2$ thin films were deposited on glass substrates to study the conditions for obtaining pure, uniform and adherent films of $CuBiS_2$. The effect of preparative parameters on optical and electrical properties of grown $CuBiS_2$ films has also been studied.

2. Experimental

Thin films of $CuBiS_2$ were deposited on ultrasonically cleaned glass substrates, employing spray pyrolysis technique (Chamberlin and Skarman 1966; Pawar *et al* 1985). The basic ingredients used were cuprous chloride (CuCl), bismuth trichloride ($BiCl_3$) and thiourea [$(NH_2)_2CS$].

The starting solution was prepared by adding 100 c.c. of 0·1 M CuCl solution into 100 cc of 0·1 M $BiCl_3$ solution to maintain a Cu : Bi ratio of 1 : 1. Then 200 cc of 0·1 M thiourea solution was added to the solution to obtain a CuBi : S ratio of 1 : 2. This starting solution was sprayed through a specially designed glass nozzle. Air was used to atomize the spray. The substrate temperature was varied from 150°C to 400°C with an interval of 50°C. Fast cooling was used at the termination of spray, as slow cooling produces film with higher resistivity, possibly because of the reaction with oxygen in air over a longer time used in cooling (Feigelson *et al* 1977). The films were taken out and preserved for further study.

Films prepared at different substrate temperatures are described as S_{150}, S_{200}, S_{250}, S_{300}, S_{350} and S_{400}, the subscripts denoting the substrate temperature. The bandgap of the deposited material was determined by taking optical absorption using a monochromator (Carl Zeiss Jena). The resistivity was measured employing routine techniques. Thermovoltage of the films was recorded by using d.c. microvoltameter (P.P.9004) in the temperature range between 300 K and 450 K.

3. Results and discussion

The $CuBiS_2$ thin films were prepared by spray-pyrolysis technique. The aqueous complex solution was fed via an atomizer to hot substrates, where they decompose forming a heat-resistant compound of the copper, bismuth and sulphur. The reaction is as follows:

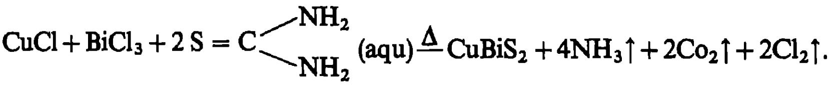

$$CuCl + BiCl_3 + 2\,S = C\begin{matrix} \diagup NH_2 \\ \diagdown NH_2 \end{matrix}\ (\text{aqu}) \xrightarrow{\Delta} CuBiS_2 + 4NH_3\uparrow + 2Co_2\uparrow + 2Cl_2\uparrow.$$

The decomposition of the complex compound depends on substrate temperature, spray rate, height of solution etc. It is observed that at lower temperature the films are powdery and porous in nature indicating that the decomposition of the complex compound is not complete. As substrate temperature increases, the decomposition rate increases. At higher substrate temperatures thin reflecting films are obtained which is ascribed to the evaporation rate of initial ingredients reducing the volumetric proportion of Cu, Bi and S in the film. The same effect is observed when the spray rate is high (10 cc/min) and the substrate temperature suddenly drops reducing the decomposition rate of the solution. When the spray rate is low the evaporation is high reducing the thickness of the thin film.

The $CuBiS_2$ thin films prepared by spray pyrolysis technique at different substrate temperatures are found to be uniform and adhere tightly to the substrate. However, the thickness of the films decreases with increase in the substrate temperature (Ugai *et al* 1978) which is attributed to the increase in evaporation rate of the initial products. The crystallinity of the films increases with substrate temperature. In order to optimize the substrate temperature of the films their optical and electrical properties were studied.

3.1 *Optical and electrical properties*

The optical absorption of the films was recorded in the wavelength range between 400 nm and 800 nm. The absorption coefficient α attained a minimum value at higher wavelength region and increases with decrease in wavelength (λ). This is attributed to the absorption edge of the semiconductor and homogeneity of the film. α lies in the order of $10^{-4}\ cm^{-1}$ indicating that the material is of direct energy gap in accordance with the pure Bi_2S_3 and Cu_2S compounds. Figure 1 shows the variation of $(\alpha h\nu)^2$ versus energy for the typical sample S_{250}. The linear extrapolation of this curve to the energy axis gives the value of optical gap of the film. In the present study the value of bandgap (E_g) obtained is 1·65 eV, which is somewhat larger than the bandgap of Bi_2S_3 (1·4 eV)

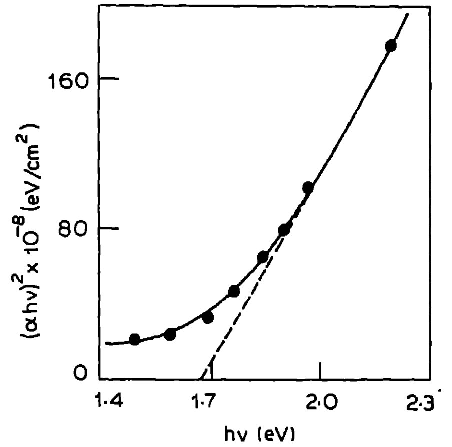

Figure 1. Plot of $(\alpha h\nu)^2$ versus energy $(h\nu)$ for a typical sample S_{250}.

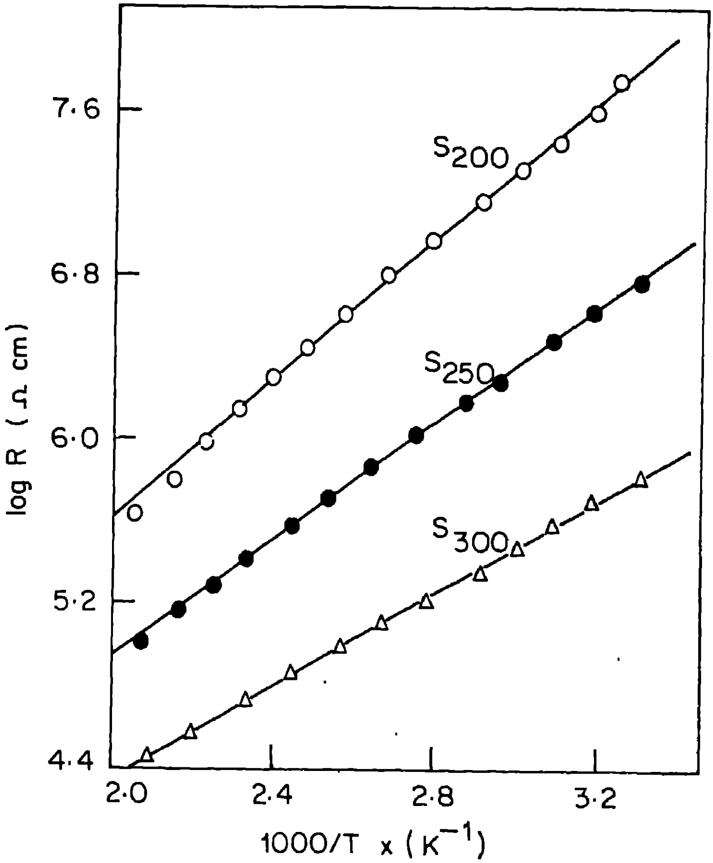

Figure 2. Variation of log R versus $1/T$ for the samples S_{200}, S_{250}, S_{300}.

(Pawar *et al* 1983) and Cu_2S (1·2 eV) (Mytton 1974). At higher substrate temperature excessive evaporation from the film takes place giving a nearly ionic ratio of 1:1:2. Beyond 450°C of substrate temperature, the evaporation rate of sulphur increases thereby forming the oxides of copper and bismuth. Better quality films were obtained between the substrate temperatures of 250°C and 300°C.

The dark resistivity measurements were carried out in the range between 300°k and 600°k. Figure 2 shows the variation of log R with the reciprocal of temperature for typical samples S_{200}, S_{250} and S_{300}. Films prepared at lower substrate temperature show greater resistance than films prepared at higher substrate temperature. Resistance decreases with increase in temperature confirming that $CuBiS_2$ is a semiconducting material. The activation energies for the samples S_{200}, S_{250} and S_{300} are 0·64 eV, 0·52 eV and 0·40 eV respectively. In the present investigation the resistivity of the films lies in the range of 10^4 to 10^7 ohm-cm.

Thermovoltage of the films was recorded to understand the conductivity and the as- grown $CuBiS_2$ thin films showed n-type conduction.

Acknowledgements

The authors are grateful to the University Grants Commission, New Delhi for financial support. One of the authors (AJP) is indebted to Rayat Shikshan Sanstha, Satara for granting study leave.

References

Austin I G, Goodman C H L and Pengelly A E 1956 *Electrochem. Soc.* **103** 609
Chamberlin R R and Skarman J S 1966 *J. Electrochem. Soc.* **113** 86
Feigelson R S, N' Dioye A, Yin Shaiw-Yih and Bube R-H 1977 *J. Appl. Phys.* **48** 3162
Mytton R J 1974 *Solar Energy* **16** 33
Pawar S H and Uplane M D 1983 *Solar Cell* **10** 177
Pawar S H, Bhosale P N, Uplane M D and Tamhankar S P 1983 *Thin Solid Films* **110** 165
Pawar S H, Uplane M D, Pawar S K and Desai J S 1985 *J. Shivaji Univ.*
Rajebhosale M R and S H Pawar 1978 *J. Shivaji Univ.* **18** 45
Ugai Ya A, Semenov V N and Averbakh E M 1978 *Izv. Nauk SSIR, Neorgani Cheskie Materialy* **14** 1529

Bull. Mater. Sci., Vol. 8, No. 3, June 1986, pp. 427–431. © Printed in India.

Preparation and properties of $Bi_{2-x}As_xS_3$ thin films by solution-gas interface technique

S H PAWAR and P N BHOSALE

Department of Physics, Shivaji University, Kolhapur 416 004, India

Abstract. The solution gas interface technique by which thin films of $Bi_{2-x}As_xS_3$ were deposited is described in this paper. The semiconducting properties of the interface grown $Bi_{2-x}As_xS_3$ thin films are studied. The optical absorption, dark resistivity and thermoelectric power of the films were studied and results are reported.

Keywords. Solution-gas interface technique; $Bi_{2-x}As_xS_3$ films; resistivity.

1. Introduction

During the last few years, mixed semiconductors, especially chalcogenides, have been extensively studied because of their proven and potential applications in thin film technology. Among the compound semiconductors, sulphides of arsenic, antimony and bismuth are important due to their photoconductive and photovoltaic properties (George and Radhakrishnan 1979; Curran *et al* 1982; Bhattacharya and Pramanik 1982; Andreichin 1970; Ghosh and Verma 1979). We have recently reported the growth of thin films of As_2S_3, Sb_2S_3 and Bi_2S_3 by our newly developed solution-gas interface (SGI) technique (Pawar and Bhosale 1984; Pawar *et al* 1983). Thin films of these compounds can be obtained by vacuum evaporation, spray pyrolysis, dip and dry and solution growth techniques (Ghosh and Verma 1979; Pawar *et al* 1984; Nayak *et al* 1982; Pramanik and Bhattacharya 1980). Amongst these techniques SGI technique is relatively new, inexpensive, simple and convenient for the deposition of uniform large area thin films. In order to devise a simple method of controlling the composition of the individual metal ions in the chemically grown films, we have studied their optical and transport properties and the results are reported in this paper. These results are used to deduce the variation in optical gap (E_g) as a function of composition (x).

The mixed Bi_2S_3-As_2S_3 system can be one of the promising materials for the photovoltaic energy conversion, because of the availability of the bandgap between 1·4 eV and 2·4 eV to cover the maximum portion of the solar spectrum. Therefore, attempts have been made to establish the feasibility of producing this system in thin film form using SGI technique and to investigate the energy gap and dark resistivity of the material as a function of x.

2. Experimental

Thin films of $Bi_{2-x}As_xS_3$ were deposited onto the glass substrates in the following manner. The solutions were prepared using analar grade bismuth and arsenic salts by adding together clear solutions of $BiCl_3$, $3H_2O$ (0·1 M) and $AsCl_3$ (0·1 M) in the volumetric ratio by varying the relative proportion of $BiCl_3$ and $AsCl_3$ so as to get Bi : As ratio from $x = 0$–2. The solutions were mixed thoroughly and the final solution was exposed to hydrogen sulphide (H_2S) gas. The experimental set-up was described earlier (Pawar *et al* 1983; Pawar and Bhosale 1984). In brief, it consists of a gas chamber filled with pure and dry H_2S gas at a desired pressure, solution container which is specially designed to remove the solution from its bottom without disturbing the solution surface and uniform gas exposure unit. Cleaned and dry glass substrates (size 2·5 cm × 1 cm) which were kept on a rectangular glass stand in the container were immersed in the solution. The solution was exposed to H_2S gas. A thin solid film is formed at the interface of the solution and gas. The solution is drained slowly from the bottom of the solution container and a uniform large area film remained on the glass substrates. The films were washed, dried and preserved in dark desiccator for further study. The films prepared with different Bi : As ratios are denoted as, $S_{2\cdot0:0\cdot0}$, $S_{1\cdot5.0\cdot5}$, $S_{1\cdot0:1\cdot0}$, $S_{0\cdot5:1\cdot5}$ and $S_{0\cdot0:2\cdot0}$, where subscripts denote the Bi : As ion ratios. The band gap of the deposited material was determined by recording the absorption spectrum in the wavelength range between 4000 and 8000 A° using a spectrophotometer (Carl Zeiss Jena). The dark resistivity measurements were carried out in the temperature range between 300 and 600 K, while thermovoltage was recorded in the temperature range between 300 and 450 K using d.c. microvoltameter (PP 9004).

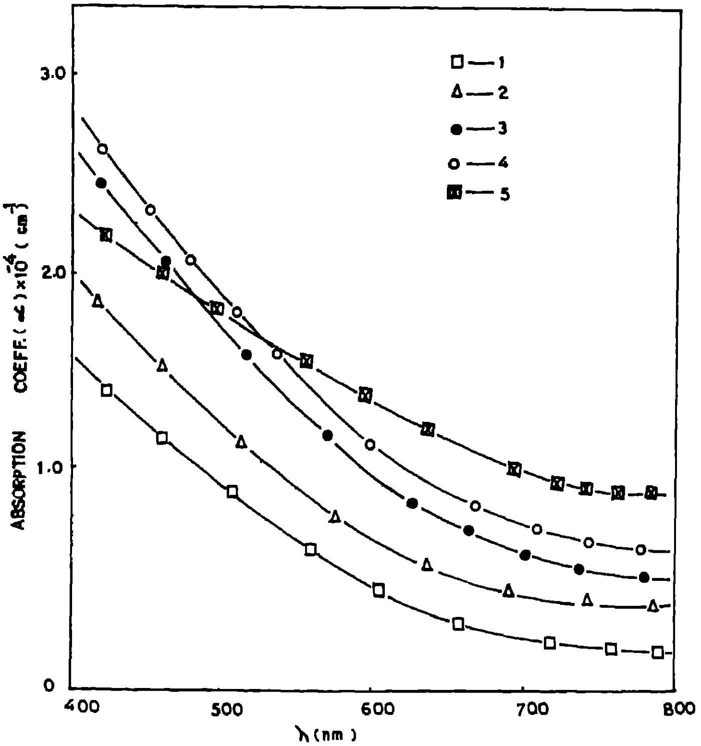

Figure 1. Variation of absorption coefficient α as a function of wavelength (λ) for the samples, (1) $S_{2\cdot0.0\cdot0}$ (2) $S_{1\cdot5:0\cdot5}$ (3) $S_{1\cdot0.1\cdot0}$ (4) $S_{0\cdot5,1\cdot5}$ (5) $S_{0\cdot0:2\cdot0}$.

3. Results and discussion

It is well known that the fifth group elements Bi, Sb and As have a strong affinity towards chalcogen ions and form stable chalcogenide compounds. Based on the experimental evidence a new deposition method is being proposed for the mixed thin film semiconductors. Similar to solution growth techniques, the growth of $Bi_{2-x}As_xS_3$ thin films takes place at the interface of the solution and gas. Due to cation-anion interaction of the arsenic, bismuth and sulphide ions a thin solid film of mixed $Bi_{2-x}As_xS_3$ is formed at the interface of solution and gas.

The quality and uniformity of the $Bi_{2-x}As_xS_3$ thin films prepared by the SGI technique depend on various preparative conditions, including the composition of the mixed solution, pH, surface tension, temperature, gas exposure time and gas pressure. Keeping all these parameters constant the composition of $AsCl_3$ and $BiCl_3$ solutions was taken to vary from 0–2. The $Bi_{2-x}As_xS_3$ thin films in the present investigation were formed using 0·1 M bismuth and arsenic chloride solutions with pH range between 2 and 4 at room temperature.

Variation of absorption coefficient (α) with wavelength (λ) is shown in figure 1. The steep fall in α is ascribed to the absorption edge of the semiconductor. The value of α for all the films lies in the order of 10^{-4} cm^{-1} which is characteristic of the direct transition. Figure 1 shows that the absorption edge shifts towards the shorter wavelength side with increase in the arsenic composition in the film. This reveals that the bandgap of $Bi_{2-x}As_xS_3$ film increases with increasing composition of arsenic in the film. Figure 2 shows that the variation of $(\alpha h\nu)^2$ vs photon energy ($h\nu$) for a typical film

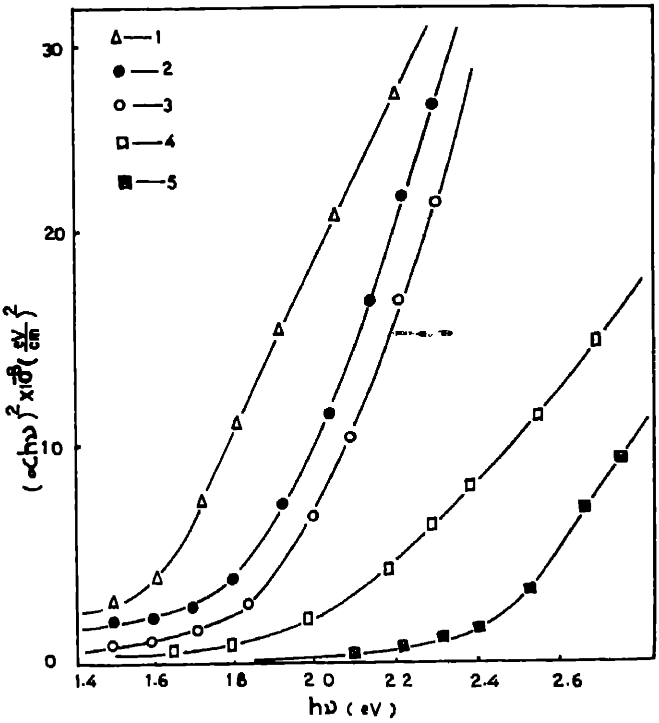

Figure 2. Plots of $(\alpha h\nu)^2$ vs ($h\nu$) for the samples. Details same as in figure 1.

is linear and shows strong absorption near the bandgap region. Extrapolation of this plot to energy axis gave the bandgap varying from 1·5 eV for pure Bi_2S_3 to 2·42 eV for pure As_2S_3 thin films. Figure 3 shows the experimental curve of E_g vs x. The dependence of energy gap E_g on x is obtained from the position of the symmetry point x which has been selected in accordance with the values for pure compounds of Bi_2S_3 and As_2S_3.

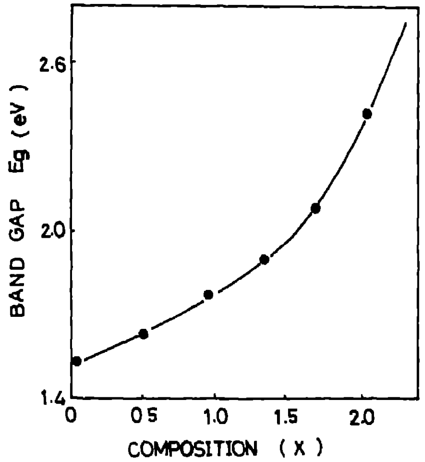

Figure 3. Variation of bandgap (E_g) as a function of composition (x) for $Bi_{2-x}As_xS_3$ films.

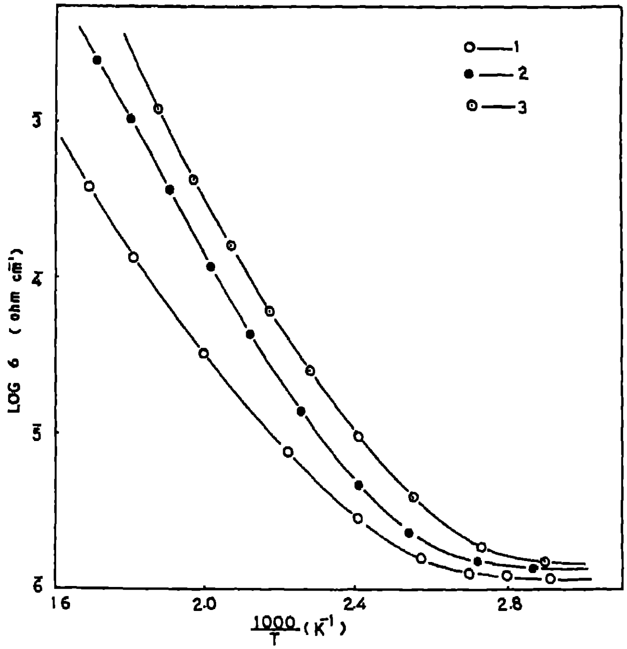

Figure 4. Plot of log σ vs $1/T$ for the typical samples (1) $S_{2\cdot0.0\cdot0}$ (2) $S_{1\cdot0.1\cdot0}$ (3) $S_{0\cdot0\cdot2\,0}$.

The nonlinear variation of E_g with x is similar to the results reported by other workers in case of $Cd_{1-x}Zn_xS$ thin films (Agnihotri and Gupta 1979; Mbow *et al* 1982).

In the present investigation variation of resistivity with reciprocal of temperature is studied for all films. The films have high electrical resistance in comparison to single crystals of Bi_2S_3 and As_2S_3 (Andreichin 1970; Bhattacharya and Pramanik 1982). The resistivity lies in the range of 10^8 to 10^9 ohm cm at room temperature. The resistance is generally high for films prepared by solution growth techniques, presumably due to the discontinuity and thickness of the films. The activation energy of the films deposited by SGI technique is high as compared to single crystals, perhaps due to high specific resistivity. The plot of log σ vs $1/T$ for three typical samples are shown in figure 4. The slope of the plots gives two activation energies at lower and higher temperature region which can be attributed as follows. At higher temperatures, excessive evaporation of sulphur from the films takes place with a pronounced reduction in resistance (Krishnamoorthy and Shivakumar 1984), while at lower temperature conduction of electrons takes place in the extrinsic region of the semiconductor. The $Bi_{2-x}As_xS_3$ films show *n*-type conduction in accordance with pure Bi_2S_3 thin films.

Acknowledgements

Authors are grateful to the Department of Non-Conventional Energy Sources (DNES), Ministry of Energy, Govt. of India for financial assistance. They would like to thank Mr S K Jamadar and the Energy Conversion group for experimental help.

References

Agnihotri O P and Gupta B K 1979 *Jpn J. Appl. Phys.* **18** 141
Andreichin R 1970 *J. Non-Crystall. Solids* **4** 73
Bhattacharya R N and Pramanik P 1982 *J. Electrochem. Soc.* **129** 332
Curran J S, Philippe R, Joseph J and Gagnaire 1982 *Chem. Phys. Lett.* **89** 511
George J and Radhakrishnan M K 1979 *Solid State Commun.* **33** 987
Ghosh C and Verma B P 1979 *Thin Solid Films* **60** 61
Gildert L, Kline J M and Mattox D M 1961 *J. Phys-Chem. Solids* **18** 286
Krishnamoorthy P A and Shivakumar G K 1984 *Mater. Lett.* **2** 223
Mbow C M, Cohen C W and Laplaze D 1982 *Thin Solid Films* **87** 141
Nayak B B, Acharya H N, Chaudhury T K and Mitra G B 1982 *Thin Solid Films* **92** 309
Pawar S H and Bhosale P N 1984 *Mater. Chem. Phys.* **11** 461
Pawar S H, Bhosale P N, Uplane M D and Tamhankar S P 1983a *Thin Solid Films* **110** 165
Pawar S H, Bhosale P N, Deshmukh L P and Uplane M D 1984a *Thin Solid Films* (In press)
Pawar S H, Bhosale P N, Tamhankar S P and Uplane M D 1983b *Ind. J. Pure & Appl. Phys.* **21** 665
Pawar S H, Tamhankar S P and Lokhande C D 1984b *Mater. Chem. Phys.* **11** 401
Pramanik P and Bhattacharya R N 1980 *J. Electrochem. Soc.* **127** 2087

Bull. Mater. Sci., Vol. 8, No. 3, June 1986, pp. 433–438. © Printed in India.

Electron microscopy study of chemically deposited Ni-P films

S V S TYAGI, V K TANDON and S RAY*

Department of Physics, * Department of Metallurgy, University of Roorkee, Roorkee 247 667, India

Abstract. The structure of electroless thin films of Ni-P has been studied. The microstructure and the selected area diffraction pattern of the samples reveal that certain samples transform to crystalline Ni with P in solid solution by nucleation and growth, whereas others transform to crystalline state by growth alone. The former set of thin films having a P-content of 19–21 at.% is characterized as amorphous. Films with a P-content of 13–15 at.% fall in the latter category and are characterized as microcrystalline. Those with a P-content of 16–18 at.% contain both amorphous and microcrystalline regions.

Keywords. Amorphous; microcrystalline; electroless; nickel-phosphorous; electron microscopy.

1. Introduction

Electroless deposition of Ni with different metalloids like P, B etc has produced both crystalline and amorphous thin films depending upon the composition of the bath (Pai and Marton 1972; Gorbunova *et al* 1973; Hedgecock *et al* 1975; Yamasaki *et al* 1981; Cortiju and Schlesinger 1983). These metalloids have very restricted solid solubilities in Ni (Maeda 1970). When the amount of metalloid exceeds the limit of solid solubility, the film at equilibrium has a suitable precipitate containing the excess metalloid in the matrix of Ni with the metalloid upto the limit of solid solution. However, electroless deposition, being a low temperature process, the system is constrained to remain in a single non-equilibrium phase due to its kinetic limitations.

As the metalloid content increases beyond the solubility limit, they produce excessive strain in the crystalline structure resulting in a higher density of defects (Graham *et al* 1965). Normally one expects that the defects increase with increase in metalloid content and the system becomes microcrystalline. Moreover, when the metalloid content is increased beyond a limit, it becomes difficult to retain the long range order and the system passes into a non-equilibrium amorphous state.

To distinguish between the as-deposited state of an amorphous sample and that of a microcrystalline sample is a difficult task, because responses which are similar to the diffraction studies in the two states. Bagley and Turnbull (1970) provided the first conceptual framework by arguing that on heating, a microcrystalline sample will undergo grain growth to pass on to a crystalline state but the amorphous sample can transform only by nucleation and growth. While there will be a critical temperature only above which it is possible to surmount the activation barrier for nucleation, for the microcrystalline samples the grain growth will take place at all temperatures depending upon the magnitude of the diffusion coefficient.

In the present investigation we have examined the thin films of electroless deposited Ni-P alloys with different P-contents. The thin films were subjected to electron microscopy while heating on the stage of the microscope. The electron micrographs and selected area diffraction pattern (SAD) of the films with different P contents were analyzed to determine the nature of the as-deposited electroless films. Makhsoos *et al* (1978) undertook similar investigations on electrodeposited films by heating the samples with electron beam itself. However, the extent of heating could not be determined in their investigation. In the present study the sample temperature was monitored throughout.

2. Experimental

The Ni-P films were deposited using electroless deposition technique. The details of the bath and conditions are given in table 1. The concentration of components in the solution was optimized to get a deposition rate of about 800 Å/min. The glass slides, used as substrates, were first washed with liquid detergent (Teepol), then by acid and degreased with hot NaOH solution. Finally substrates were washed with hot double distilled water. For deposition, these properly cleaned substrates were given a sensitizing treatment (by dipping in a 1% $SnCl_2$ solution for 60 sec) and activation treatment (by dipping in a 0·1% $PdCl_2$ solution for 30 sec). The film was deposited for about 40 sec for examination under transmission electron microscope.

The samples were chemically analyzed by using wet chemical method, the accuracy of which is less than ±1%. Transmission electron microscopy (Philips model EM 400 T/ST with a heating holder PW 6592) was carried out and the general form of the holder was similar to that of other holders for the goniometer stage.

3. Results and discussion

Ni-P samples have been deposited by varying the amount of the reducing agent, NaH_2PO_2, in the bath so that the composition falls in three ranges—sample I containing 13–15 at.% of P, sample II 16–18 at.% P and sample III 19–21 at.% P. The composition of the deposits could not be controlled more closely due to limited facilities.

The electron micrograph of sample I is shown in figure 1. The deposit shows unevenness, but the SAD as in figure 2 shows a diffuse ring at $2\theta = 1{\cdot}063°$ and $\Delta 2\theta = 0{\cdot}08°$. If it is assumed to be microcrystalline the lattice parameter is approximately 3·46 Å on the average. However, the diffuse ring may have been a characteristic of an amorphous state; while heating this sample the width of the diffuse ring decreases continuously leading to rather sharp rings as given in figure 3 showing

Table 1. Bath and conditions of Ni-P films

Plating variables	g/l of H_2O	
$NiSO_4 \cdot 7H_2O$	24	pH-(8·5–9·5)
$(NH_4)_2SO_4$	50	adjusted with NH_4OH
$Na_3C_6H_5O_7 \cdot 2H_2O$	88	temperature-85 ± 2°C
NaH_2PO_2	(10–45)	No stirring

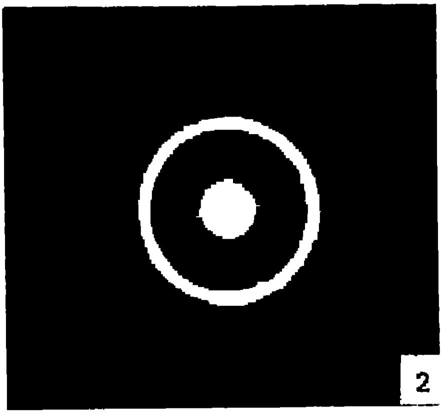

2

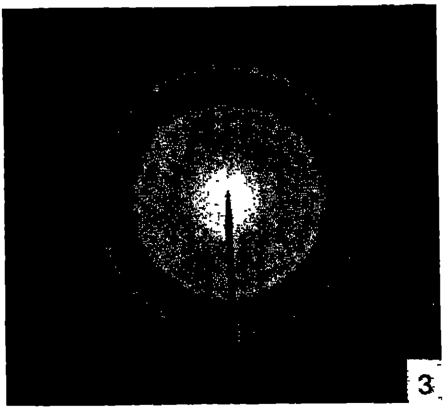

3

Figures 1–3. Electron micrograph and SAD of Ni-P sample I (13–15 at. %). **1, 2.** As-deposited state. **3.** Heated at 350°C for 2 min.

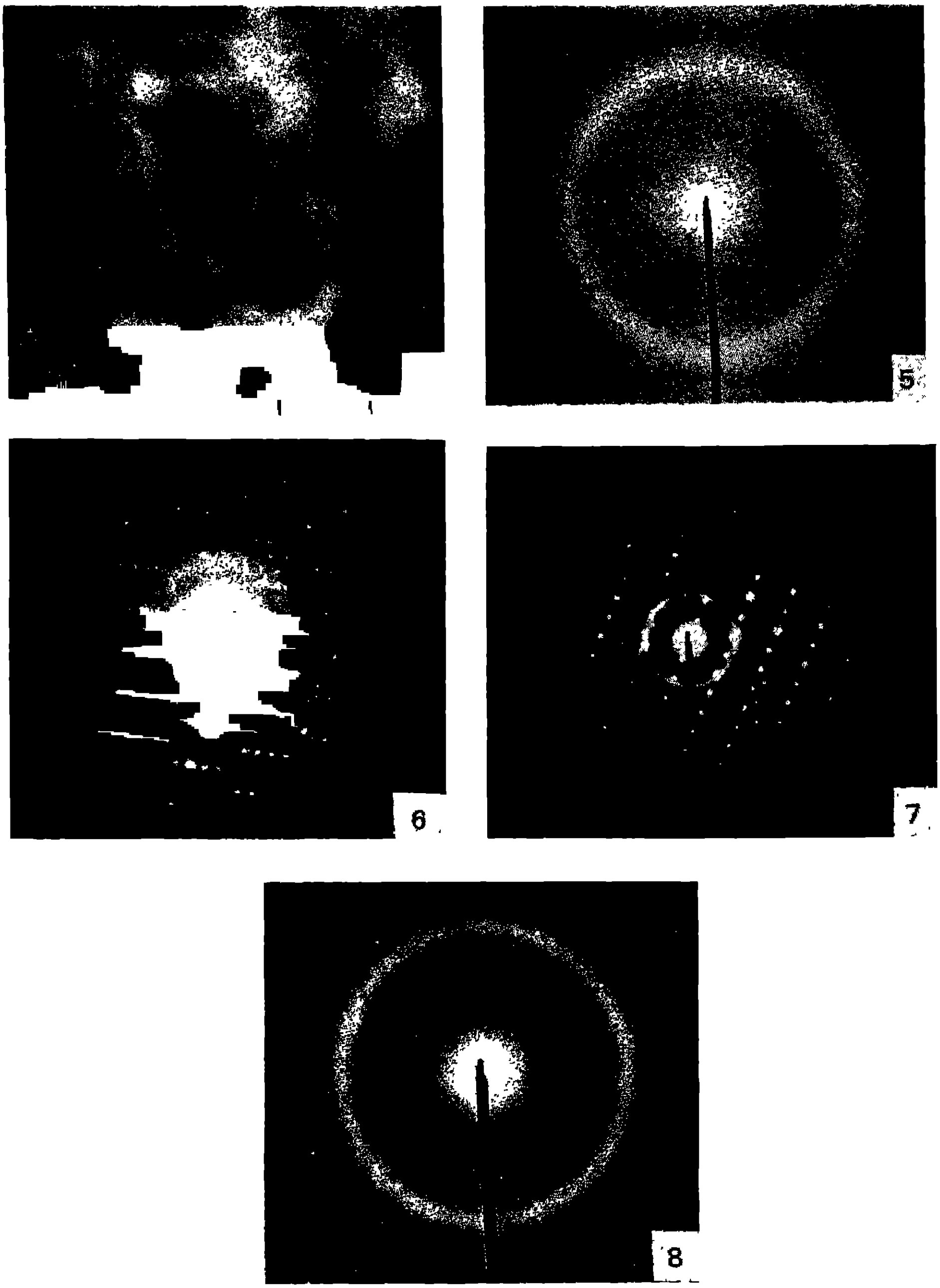

Figures 4–8. Electron micrograph and SAD of Ni-P sample II. **4–7.** 16–18 at.%. **4, 5.** As-deposited state. **6.** Heated at 340°C for 2 min. **7.** Heated at 340°C for 2 min in a region different from that of **6.** **8.** 19–21 at.% in as-deposited state.

the SAD of sample I heated to 350°C for 2 min in TEM. The reduction in broadening may be attributed to the lowering of defect density and growth of the grains in microcrystalline state. Following the arguments of Bagley and Turnbull (1970), we believe that the sample class I is not in amorphous state but in a microcrystalline state.

The electron micrographs of as-deposited sample II and its SAD pattern are shown in figures 4 and 5. The SAD pattern has a diffuse ring at $2\theta = 1{\cdot}057°$ and its width $\Delta 2\theta = 0{\cdot}13°$. Clearly it is identical to that observed for as-deposited sample I excepting for a slight shift in the position of the ring and an increase in width. If the sample is microcrystalline, the higher P content of the sample will change the lattice parameter causing a shift in position of the ring. The resulting strain may also have been accommodated by larger concentration of defects and reduced grain size. Thus, the diffraction ring has a higher width. But again SAD may be attributed to that of an amorphous state.

On heating sample II to 340°C and holding it for 2 min certain areas of the sample showed an SAD pattern as given in figure 6. The SAD pattern shows broad diffuse rings superimposed over a spot pattern. The retention of width at a high temperature (340°C) is in sharp contrast with the behaviour observed in sample I. Thus in sample II there is a barrier to the change in state from the one characterized by the broad diffuse ring. In addition, the spot pattern is characteristic of a crystalline state with a crystallite size exceeding the width of focus. It can be inferred that in this region of the sample, an amorphous state transforms to a crystalline state by nucleation and growth. However, in certain other regions of this sample one observes continuous sharpening of broad rings, resulting in sharp rings superimposed on the spot pattern (figure 7). This region appears to consist of microcrystallites and a crystallite of size greater than the size of focus indicating a grain growth and an abnormal grain growth. Sample II contains both amorphous and microcrystalline regions, which may have resulted due to the variation of P distribution from one region to the other.

Sample III shows an SAD pattern (figure 8) and again consists of a broad diffuse ring with $2\theta = 1{\cdot}055°$ and $\Delta 2\theta = 0{\cdot}16°$. The position of the ring has slightly been shifted and the width increased obviously due to an increase in P content. However, it is not possible to infer about the structural state of the sample from this SAD pattern. On heating this sample to 345°C and holding for 2 min, one observes superposition of broad diffuse rings on the spot pattern similar to that observed in some regions of sample II.

4. Conclusions

The electron microscopy study of the Ni-P samples containing 13–21 at.% P shows that the as-deposited film passes from a microcrystalline state to amorphous state with increasing P content. At intermediate compositions the microcrystalline and amorphous state co-exist. But it is not clear whether it is a result of composition variation or whether it is possible to achieve these two states together at the same composition. In the composition range of 19–21 at.% P it is amorphous. Several investigations have noted that the samples with low-P are crystalline (Yamasaki *et al* 1981). Thus, it appears that with increase of P, the as-deposited Ni passes from crystalline to microcrystalline state continuously and then beyond a certain composition to an amorphous state.

Acknowledgements

The authors are highly grateful to Dr Kailash Chandra for all facilities at the University Service and Instrumentation Centre and to Dr R C Bembi for chemical analysis of the samples. Thanks are also due to Mr N K Saini for transmission electron microscopy.

References

Bagley B G and Turnbull D 1970 *Acta Metall.* **18** 857
Cortiju R O and Schlesinger M 1983 *J. Electrochem. Soc.* **130** 2341
Gorbunova K M, Ivanov M V and Moiseev V P 1973 *J. Electrochem. Soc.* **120** 613
Graham A B, Lindsay R W and Read J 1965 *J. Electrochem. Soc.* **112** 401
Hedgecock N, Tung P and Schlesinger M 1975 *J. Electrochem. Soc.* **122** 866
Maeda H 1970 *J. Phys. Soc. Jpn* **29** 311
Makhsoos E V, Thomas E L and Toth L E 1978 *Metall. Trans.* **A9** 1449
Pai S T and Marton J P 1972 *J. Appl. Phys.* **43** 282
Yamasaki T, Izumi H and Sunada H 1981 *Scripta Met.* **15** 177

Bull. Mater. Sci., Vol. 8, No. 4, October 1986, pp. 439–448.
© Printed in India.

Liquid phase epitaxy growth of GaAs: Si by temperature difference method

C C WEI, Y K SU, C C CHANG and S C LU
Research Institute of Electronic and Electrical Engineering, National Cheng Kung University, Tainan, Taiwan, Republic of China

MS received 26 October 1985

Abstract. The LPE growth of a horizontal sliding system by temperature difference method is used to grow single and multiple layers of GaAs compounds from dilute solution. The weight ratio of Si to Ga solvent is 10^{-4} wt%. The growth rate, surface morphology, carrier concentration and Hall mobility are studied. Relationship between the above properties and the growth temperature and temperature difference (ΔT) is also discussed. In general, the present results appear quite consistent with the diffusion limited model. The growth rate can be precisely controlled. The stability of the solid-liquid interface can be obtained in the epilayer growth at a constant temperature of the system which can avoid the effect of constitutional supercooling. Under proper control, a perfect epilayer and multiple smooth layers can be obtained.

Keywords. Liquid phase epitaxy; GaAs : Si doping; temperature difference method; growth rate; surface morphology; carrier concentration; Hall mobility.

1. Introduction

Liquid phase epitaxy (LPE) is a technique normally used to grow single or multiple layers of III–V compound semiconductor materials from dilute solution. It can also be used to grow other materials, such as II–VI compounds and magnetic materials, and offers good quality epilayers for devices such as injection lasers, solar cells, varactor, LED and FET etc.

The steady state temperature difference method with horizontal sliding boat system was adopted in this experiment (Nishizawa and Okuno 1978). This technique is easier for temperature control compared with the transient method. The desired thickness of epilayers can be obtained by precisely controlling the growth time. The other advantage associated with this method is that constitutional supercooling can be avoided (Long *et al* 1974; Tiller 1968). In this experiment, silicon was used as the *n*-type dopant. The weight ratio of Si to Ga solvent was 10^{-4} wt%. The Cr-doped semi-insulated GaAs wafer was used for substrate which was oriented on the (100) crystal plane. Gallium was used as a solvent and GaAs polycrystal wafer was adopted as the source.

The growth rate, surface morphology, Hall mobility and carrier concentration were measured. Relationship between the above properties and growth temperature and ΔT (temperature difference between substrate and source) is also discussed.

The growth temperature and temperature difference ranged from 650°C to 800°C and from 4·5°C to 25·7°C respectively. The thickness of epilayer ranged from 1 μm to 20 μm.

2. Growth apparatus and measurements

The schematic diagram of the apparatus is shown in figure 1. The princ components are graphite boat, quartz tube, gold-coating transparent furnace, purifier, vacuum system and exhaust system. Small quartz tubes were used as pı pull rod, graphite boat holder and thermal couple protector. Since temperaı difference method was adopted (Nishizawa and Okuno 1978) the tungsten filar should be designed and wound around crucibles as heater. Certainly, a sı cylindrical quartz tube was needed to cover the environment of graphite crucibl obtain a more uniform temperature distribution.

Gold-coating transparent furnace can be tuned to a constant temperature wi ± 1°C over 70% of its length. The boat was set in the middle of the furnace for n stable temperature. Only one zone was needed.

Vacuum system had a cold trap with liquid nitrogen for preventing the oil vaṗ from contaminating the system.

After loading the boat and substrate, the reactor was flushed with flowing evacuated and then backfilled with purified H_2. A slow flowing H_2 (about 0·5 liı min) was used as purge (30 min) and the furnace was then moved into the positio boat. The furnace temperature was increased gradually to the growth temperat After the stable operating temperature was reached, ΔT was established betv substrate and source with AC power supply. A few minutes later, the substrate pushed to contact source solution and the desired LPE layers were grown. Du the growth run, the variation of the system temperature was kept within ±0·5°(less. After the growth run ended, the substrate was pushed out of the solution, furnace moved away and the boat cooled to room temperature. Hydrogen stopped and then the growth was finished.

When the epilayer was grown, the surface morphology and cleavage surface oı epilayer were examined by optical microscopy. The carrier concentration and

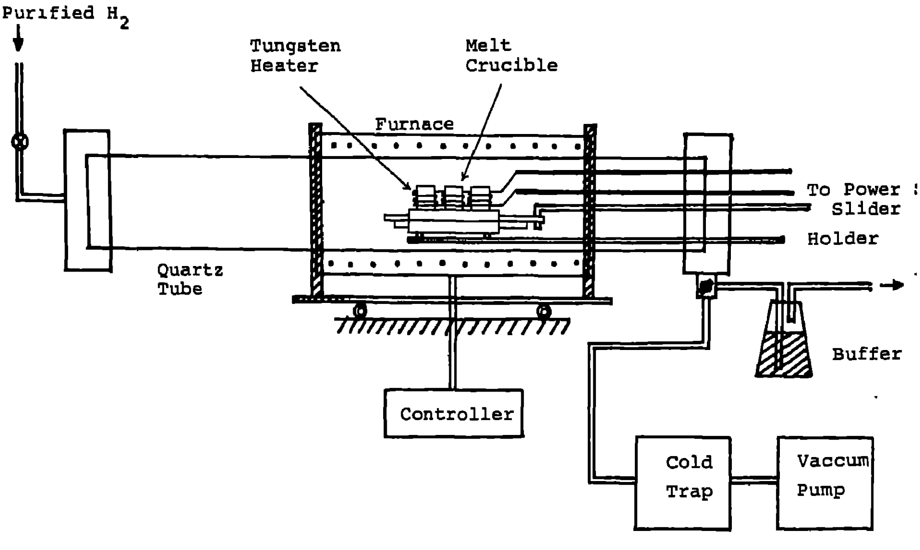

Figure 1. The apparatus of horizontal system for temperature difference method.

mobility was measured with van der Pauw measurement and Hall effect. The multilayer Ge/Au/Ni (about 400 Å/2500 Å/400 Å), evaporated onto the wafer surface, was used for ohmic contacts.

3. Results and discussion

3.1 *Growth rate*

With a solution temperature of 704·5–725·7°C, a substrate temperature of 700°C and a growth time of 4 hr, the thickness vs temperature difference ΔT between the source and the substrate is shown in figure 2. The experimental data are compared with theoretical values (Long *et al* 1974; Hsieh 1980). It can be shown that the thickness of epilayer increases as ΔT is increased. The furnace temperature was varied from 650°C to 800°C ($\Delta T = 18{\cdot}8$ C, growth time = 1 hr) and the thickness vs growth temperature is shown in figure 3. It is assumed that the diffusion constant is determined by growth temperature (T_G) (dashed curve) and that it is determined by growth temperature and temperature difference between the source and the substrate (i.e. $T_G + \Delta T$) (dashed line b). The experimental data in figure 2 are more consistent in the latter case.

The growth rate of epilayer was apparently proportional to the growth time in our measurement (see figure 4). Further, the carrier concentration showed a strong dependence on the value of ΔT. Two interesting experimental results are shown in figure 5. Figure 5(a) shows that two layers were grown on substrate in the same solution and at the same growth temperature but ΔT was different during the epilayer growth. The first and the second layers were grown with a temperature difference of 25·7°C and 11·2°C respectively for 2 hr. The growth temperature was set at 700°C and the height of the solution was 0·34 cm. The thickness of the second layer was greater than the normal growth, because the temperature difference was

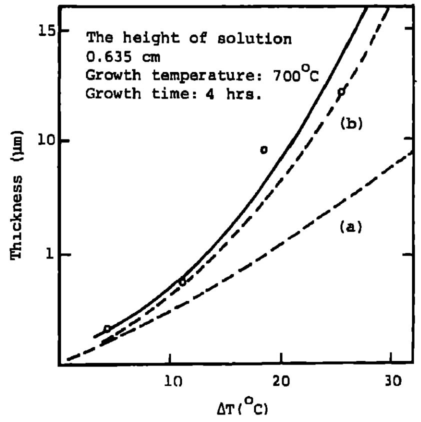

Figure 2. Epilayer thickness vs temperature difference (ΔT) curve. The dashed lines are the theoretical data and the solid line is the experimental data.

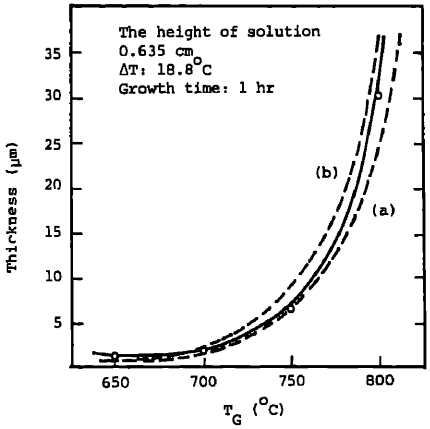

Figure 3. Epilayer thickness vs growth temperature curve. The dashed lines are the theoretical data and the solid line is the experimental data.

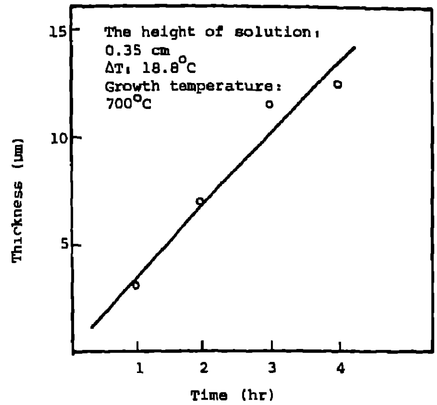

Figure 4. Epilayer thickness vs time

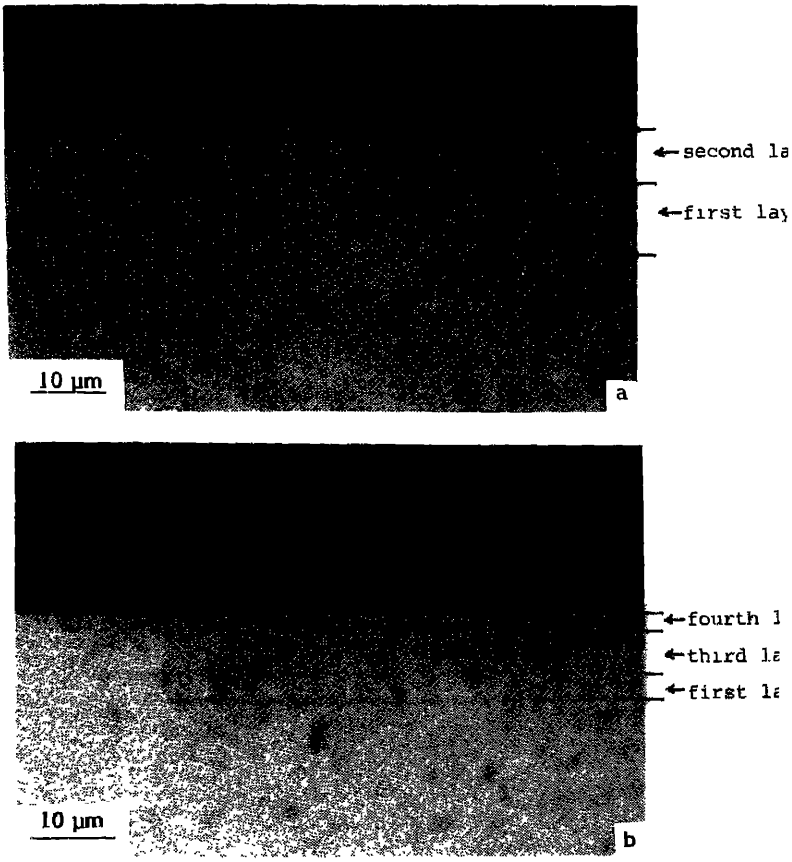

Figure 5. Cleavage surface of grown layer. (a) Double epilayers ($T_G = 700°$ C, W= ΔT:t=25·7°C:2 hr then 11·2° C:2 hr). (b) Multilayer ($T_G = 700°$ C, W= ΔT:t=25·7° C:1 hr, 11·2° C:1 hr, 18·8° C:1 hr then 4·5° C:1 hr).

reduced from 25·7°C to 11·2°C producing the condition of equilibrium cooling step cooling in the solution.

A similar condition is shown in figure 5b. The temperature difference was 2. 11·2, 18·8 and 4·5°C respectively for 1 hr during each growth. Here, it appears t the fourth layer is much thicker than the normal growth, while the first layer is qu thinner than the normal growth, although the secondary layer has disappeared. M back etching seems to have occurred when the temperature difference changed fr 11·2°C to 18·8°C.

3.2 *Electric characteristics of epilayers*

Figure 6 shows the dependence of resistivity and Hall mobility on carr concentration. The dashed line from Sze (1981) shows the dependence of resistiv and Hall mobility on impurity concentration which can be compared with c experimental data. The Hall mobility and the resistivity of experimental data a lower than the comparative values of dashed lines. Perhaps it is influenced by the dopant because Si is an amphoteric impurity in GaAs layers (Casey and Pani 1978). Since carrier concentration is $n = N_D - N_A$ for n-type material and the impur

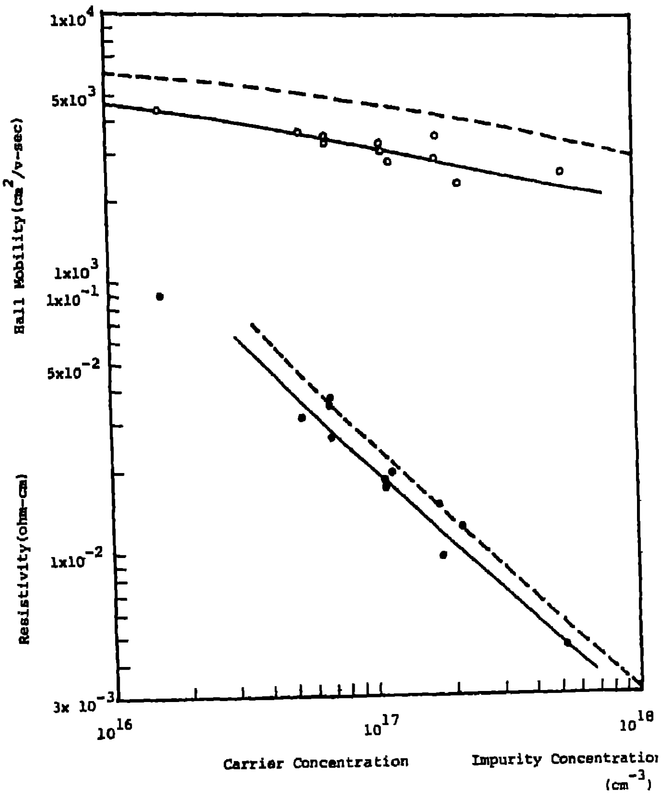

Figure 6. Dependence of resistivity and Hall mobility on carrier concentration (sm circles) and impurity concentration (dashed lines).

concentration is $C_B = N_D + N_A$, the carrier concentration is lower than impurity concentration. In our measurements the carrier concentration decreased with increasing growth temperature and ΔT. It may be that the solution ahead of the advancing interface gets depleted of Si, as a result of the limited diffusion of Si for faster growth rate. Certainly, the As vacancy may increase with temperature, but its influence is much less than the depletion effect of Si about 700°C.

For the depletion effect of Si, the carrier concentration decreased with increasing ΔT (figure 7). Hall mobility increased as ΔT increased (figure 8). The inhibition of constitutional supercooling also helps in increasing the Hall mobility. The saturation of this curve may be due to the increasing domination of As vacancy. The same is the

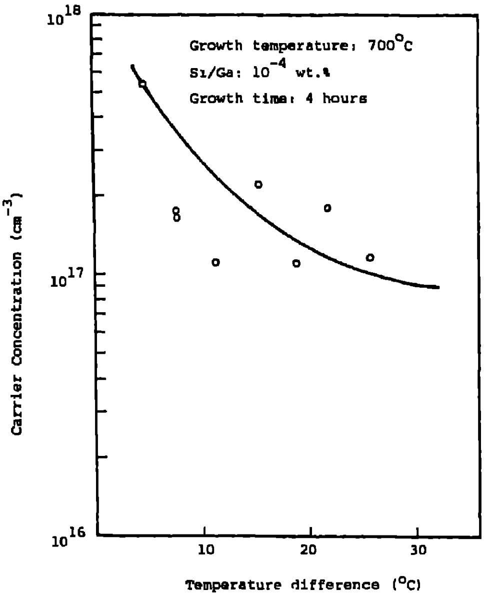

Figure 7. Dependence of carrier concentration on the temperature difference between source and substrate.

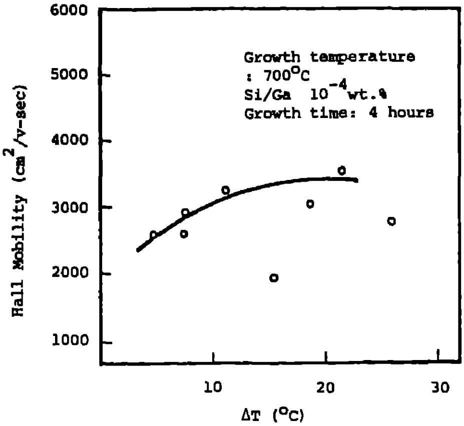

Figure 8. Dependence of Hall mobility on the temperature difference between source and substrate.

reason for the changes of carrier concentration and Hall mobility followed by th variation of growth temperature. From figures 9 and 10 similar results can be found When the variation of growth time was used as a parameter, a minimum carrie concentration and a maximum Hall mobility were measured in the vicinity of 2 h growth (figures 11 and 12).

3.3 *Surface morphology*

Figures 13(a) to 13(d) show some pictures of the surface grown at 700°C for 4 hr. The temperature difference was 4·5, 11·2, 18·8 and 25·7°C respectively. On the scale of

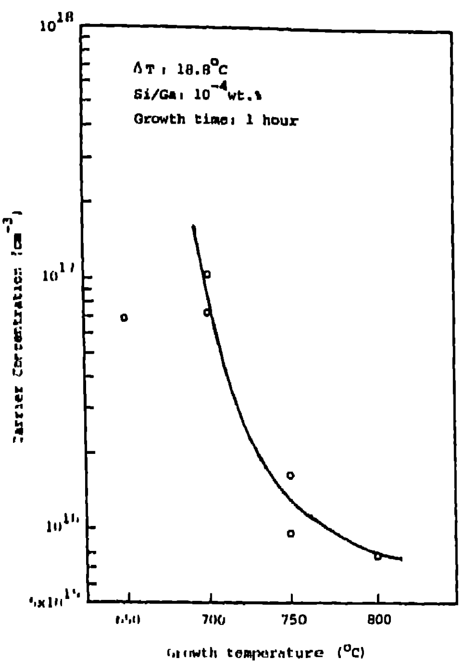

Figure 9. Dependence of carrier concentration on the growth temperature.

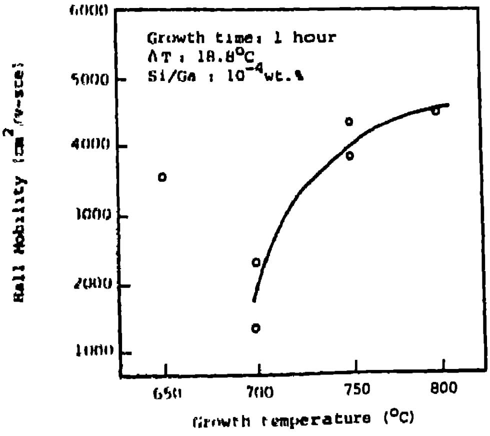

Figure 10. Dependence of Hall mobility on the growth temperature.

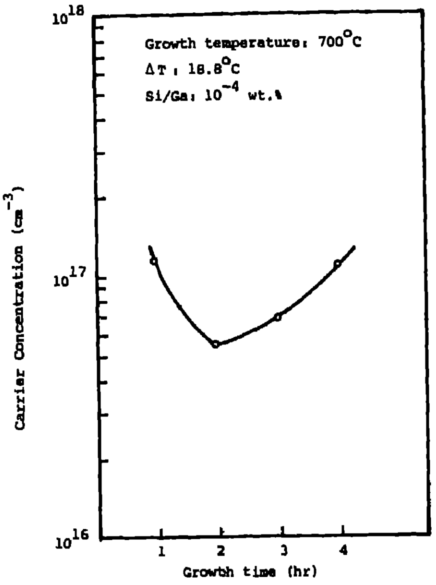

Figure 11. Dependence of carrier concentration on the growth time.

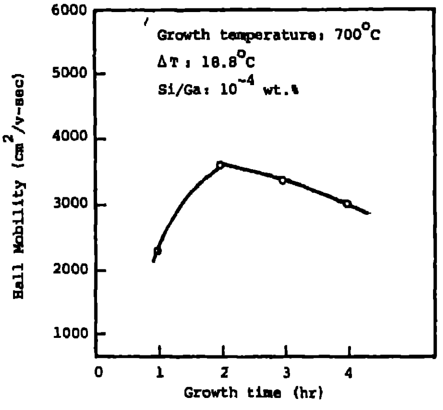

Figure 12. Dependence of Hall mobility on the growth time.

those photographs, the surface has a rough appearance although both to the eye a at higher magnifications the surface appeared smooth. Those photographs of hig magnification are shown in figures 13(e) and 13(f) with temperature difference 4·5°C and 18·8°C. It is found that with higher ΔT, the surface morphology is be because the constitutional supercooling is inhibited more for the higher ΔT.

4. Conclusion

The LPE growth was studied using the temperature difference method. The epil with uniform doping was grown. The results show that the electric characteris and the thickness of the epilayer strongly depend on the growth temperature and

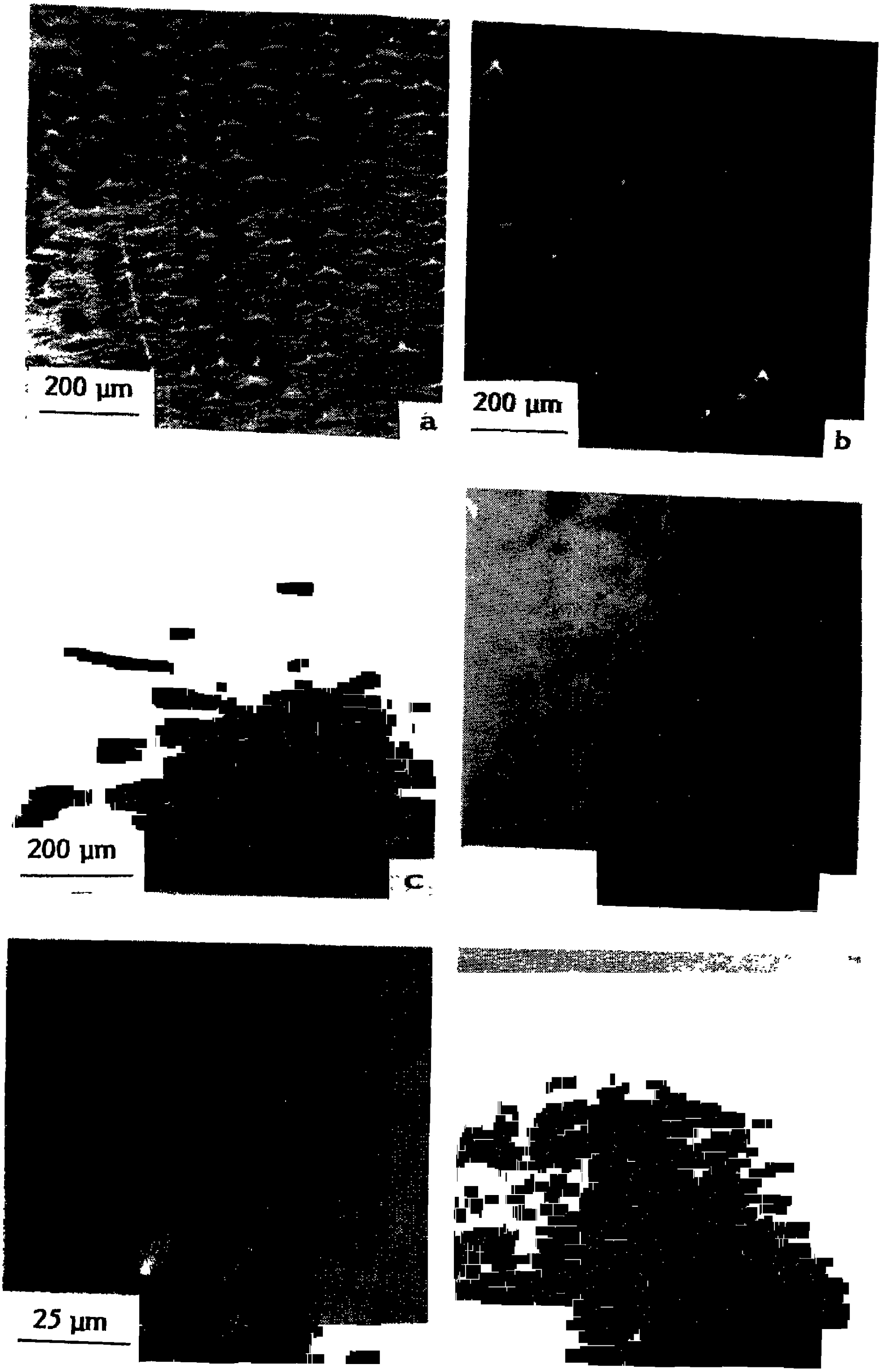

Figure 13. Photomicrographs of the substrate morphology T_G=700°C, W=0·635 cm, t=4 hr, (a) ΔT=4·5°C, (b) ΔT= 11·2°C, (c) ΔT= 18·8°C, (d) ΔT=25·7°C, (e) higher

temperature difference. With proper control, a perfect epilayer and multiple smoot layers can be obtained.

Even the thickness is limited by edge effects. However, the uniformity of thickne is well away from the edge. Therefore by utilizing a larger size of substrate epilayer better uniformity suitable for fabrication of devices can be obtained.

In general, diffusion limited model is consistent with this experiment. The grow rate can be controlled well. The stability of solid-liquid interface can be acquired constant temperature of system, which can avoid the effect of constitution supercooling.

As the solution ahead of the advancing interface becomes depleted of Si, t reducing carrier concentration can be obtained at higher growth rate. Due to t effect, it increases the complication of epilayer growth. Although the variation of vacancy influences the carrier concentration, depletion effect dominates the grow temperature about 700°C. With proper control, a perfect epilayer can be obtaine

Acknowledgements

The authors gratefully acknowledge Dr T S Wu for his fruitful discussions a suggestions. The authors also thank National Science Council, Republic of China financial support of this research project.

References

Casey Jr H C and Panish M B 1978 *Heterostructure lasers*, Part B (New York: Academic Press) p 1

Hsieh J J 1980 *Handbook on semiconductors* (eds) T S Moss and S P Keller (Amsterdam, New Y Oxford: North-Holland) Vol. 2, p 418

Long S I, Ballantyne J M and Eastman L F 1974 *J. Cryst. Growth* **26** 13

Nishizawa J and Okuno Y 1978 RIEC Technical Report TR–41, April

Sze S M 1981 *Physics of semiconductor devices* (New York: John Wiley) pp 29–33

Tiller W A 1968 *J. Cryst. Growth* **2** 69

Bull. Mater. Sci., Vol. 8, No. 4, October 1986, pp. 449–452.
© Printed in India.

X-ray diffraction study of epitaxial zinc and cadmium films prepared b hot-wall technique

A V KULKARNI and R PRATAP*
D B J College, Chiplun 415 605, India
*Department of Physics, University of Bombay, Vidyanagari, Bombay 400 098, India

MS received 12 May 1986

Abstract. Hot-wall technique greatly improves the quality of zinc and cadmium films deposited on glass substrate. At substrate temperature the growth of such films is wel ordered, showing highly preferred orientation along c-axis. However, if the substrate temperature is increased beyond certain limit, we get polycrystalline growth of the films This shows that the growth of zinc and cadmium films on glass substrate strongly depends on the substrate temperature.

Keywords. X-ray diffraction; epitaxial growth; hot-wall technique; zinc films; cadmium films.

1. Introduction

The conventional method of vacuum deposition of cadmium films does not give good quality homogeneous films deposited on glass substrate (Bandopadhyay and Pal 1979). We have already shown that, by using the hot-wall technique, good quality cadmium films consisting of large crystal domains with only [002] orientation, can be obtained (Kulkarni *et al* 1984). The present paper reports the effect of elevated substrate temperature on the epitaxial growth of zinc as well as cadmium films. The growth process is strongly influenced by the temperature as well as the nature of the substrate. Cadmium films deposited on NaCl (100) single crystal substrate show preferred orientations in [101], [102], [103] and [002] directions in decreasing order (Kulkarni *et al* 1984). The polycrystalline nature of the films deposited on this substrate is due to the lattice mismatch and relative positioning of cadmium atoms (Chopra 1969). However, if an amorphous substrate like glass is used, the lattice mismatch plays a smaller role in the growth process. After initial deposition of few atomic layers of the film, the auto-epitaxy plays an important role in further development of the film structure. Thus, we get ordered structure with highly preferred orientation. It is also observed that a vacuum of the order of 10^{-5} torr is suitable for such growth.

2. Experimental

The apparatus used to deposit cadmium and zinc films was essentially the same as described earlier (Kulkarni *et al* 1984). The only modification was to replace corning glass tube with quartz tube having larger dimensions (height 6·0 cm; outer dia. 2·9 cm; inner dia. 2·6 cm). Cadmium metal (purity 6N) (obtained from Koch-Light Laboratories, UK) and zinc metal (purity, 5N) (from Fluk A G, Buchs, Switzerland) were used as source material for depositing the films. The vacuum during deposition was maintained at 2×10^{-5} torr. Cleaned glass substrates were used to deposit all the films. The thickness of the films was determined by gravimetric method and for the purpose a Mettler, M5, balance with sensitivity 1μ g was used.

3. Results and Discussion

Visual observation showed that all the films deposited on the glass were continuous and shining like mirror at the back of the films, while the front surfaces had silvery-white shine. To understand the film structure, x-ray diffractometry was carried out using fully computerised, SIEMENS-RE 2400 diffractometer. During x-ray scanning, the sample was kept rotating at a constant speed of 30 rev/min about an axis perpendicular to its plane and passing through its centre. This gave an overall picture of the complete film structure.

Figure 1 shows the XRD patterns of cadmium and zinc films deposited by HWT at different substrate temperatures. Tables 1 and 2 give the relative intensities of the

Table 1. X-ray diffraction measurement on cadmium films prepared by HWT on glass substrate.

	Relative intensity (%)		
hkl	70° < Ts* < 80°C	100° < Ts < 110°C	ASTM-data
002	100	100	65
100	–	2·5	32
101	–	32·2	100
102	–	12·4 ($K\alpha_1$)	32
102	–	6·7 ($K\alpha_2$)	–
103	–	15·4 ($K\alpha_1$)	26
103	–	8·3 ($K\alpha_2$)	–
004	9·4 ($K\alpha_1$)	23·5 ($K\alpha_1$)	3
004	5·0 ($K\alpha_2$)	12·3 ($K\alpha_2$)	–

*T_s, Substrate temperature.

Table 2. X-ray diffraction measurement on zinc films prepared by HWT on glass substrate.

	Relative intensity (%)		
hkl	40° < Ts < 50°C	60° < Ts < 70°	ASTM-data
002	100	100	53
100	0·4	0·7	40
101	0·2	1·9 ($K\alpha_1$)	100
101	–	1·1 ($K\alpha_2$)	–
102	–	2·6 ($K\alpha_1$)	28
102	–	1·6 ($K\alpha_2$)	–
103	0·1	4·1 ($K\alpha_1$)	25
103	–	2·2 ($K\alpha_2$)	–
110	–	0·2	21
004	9·4 ($K\alpha_1$)	17·6 ($K\alpha_1$)	2
004	4·7 ($K\alpha_2$)	10·2 ($K\alpha_2$)	–
112	–	0·7	23
200	–	0·2	5

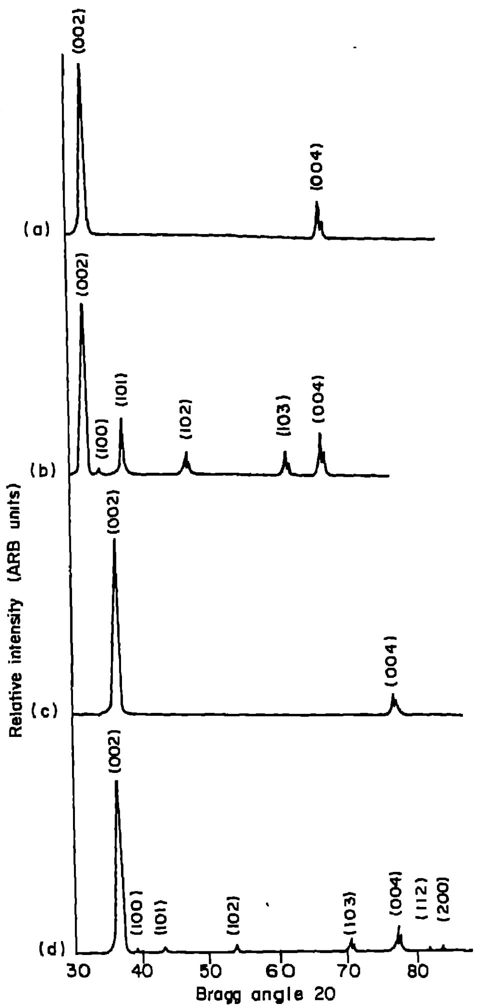

Figure 1. X-ray diffraction pattern (obtained with CuKα radiation) for the films deposited onto glass substrate by HWT. (**a**) Cd film (70° < T_s < 80°C); (**b**) Cd film (100° < T_s < 110°C); (**c**) Zn film (40° < T_s < 50°C); (**d**) Zn film (60° < T_s < 70°C). T_s = substrate temperature.

peaks observed for cadmium and zinc films respectively. Figures 1a, c indicate that the film structure is well ordered with perfect epitaxial growth along [002] direction. The diffraction pattern at elevated substrate temperature (100–110°C) clearly shows the appearance of Cd peaks corresponding to the planes (100), (101) and so on (figure 1b). This shows that cadmium films deposited at elevated temperature (approximately greater than one third of the melting point of the metal) are polycrystalline. Similar trend is observed in zinc films deposited at higher substrate temperature (60–70° C) (figure 1d), the newly appeared reflection peaks (showing polycrystalline nature of the film) have very low intensity. Such preferentially oriented growth of zinc films along [002] direction has also been reported in the thickness range 500–5000 Å (Nandi *et al* 1978). But the perfect epitaxial growth (figure 1c) in zinc films

Table 3. Deposition parameters of the films prepared by HWT

Film	Temperature (°C)			Thickness (μm)	Growth rate (μm/hr)
	Source	Wall	Substrate		
Cd	400–450	375–425	70–80	5·2	25
Cd	450–500	400–450	100–110	4·5	35
Zn	500–550	300–400	40–50	6·5	39
Zn	550–600	350–450	60–70	2·3	45

has been observed for the first time in thick films at the substrate temperature 40–50° C.

Table 3 gives the deposition parameters for cadmium and zinc films. The films are thick, the thickness being in the range 2 to 6 μm. The rate of deposition is in the range of 25 to 45 μm/hr. Single heating coil was used to heat the quartz tube and therefore, the source and wall temperatures could not be precisely defined. The glass substrate was radiation-heated from the same heating coil.

4. Conclusion

By using hot-wall technique, thick zinc and cadmium films having perfec orientation can be deposited on glass substrate, keeping the substrate temperatur sufficiently low (below one third of the melting point of the metal). We have als shown that such films usually consist of large crystallites (~5 μm) (Kulkarni *et a* 1984). Thus, this simple version of HWT is useful wherever highly epitaxial on (eve thick) films of cadmium and zinc are required.

Acknowledgements

The diffractometer facility was provided by the Tata Institute of Fundamenta Research, Bombay. One of us (AVK) gratefully acknowledge the fellowship awarde by the University Grants Commission, New Delhi. The authorities of DBJ Colleg Chiplun, were kind enough to grant AVK the necessary study leave to take up th fellowship.

References

Bandopadhyay S K and Pal A K 1979 *J. Mater. Sci.* **14** 2989
Chopra K L 1969 Thin film phenomena (New York: McGraw-Hill) 226
Kulkarni A V, Bose S and Pratap R 1984 *Thin Solid Films* **120** L73–L77
Nandi R K, Suchitra Sen and Sen-Gupta P 1978 *Thin Solid Films* **51** 141

Bull. Mater. Sci., Vol. 8, No. 4, October 1986, pp. 453–465.
© Printed in India.

Concept of thermodynamic capacity

R AKILA*†, K T JACOB* and A K SHUKLA**
*Department of Metallurgy, *†Materials Research Laboratory,
**Solid State and Structural Chemistry Unit, Indian Institute of Science, Bangalor
560 012, India.

MS received 15 April 1986

Abstract. The thermodynamic capacity of a species (C_i) in a homogeneous phase is define as $(\partial n_i/\partial \mu_i)_{P,T,n_j}$ where n_i is the total number of moles of i per unit quantity of the systen irrespective of the actual system chemistry and μ_i is its chemical potential. Based on thi definition, the thermodynamic capacity of oxygen in non-reactive and reactive gas mixture and in binary and ternary liquid solutions has been computed. For reactive gas mixture containing stable chemical species which do not undergo significant dissociation such a $CO+CO_2$, H_2+H_2O and H_2+CO_2, the capacity curves show a maximum at equimola ratio and a minimum at higher oxygen potentials. If one of the chemical species partl dissociates as in the case of H_2S in H_2+H_2S mixtures or SO_3 in SO_2+SO_3 mixtures capacity curves do not exhibit such maxima and minima, especially at high temperatures. I would be difficult to produce stable oxygen fugacities when the capacity has a low value, fo example at compositions near the minimum. Oxygen capacities of non-ideal liquid solutions, Cu–O and Cu–O–Sn, and heterogeneous systems formed at saturation with the respective oxides are discussed.

Keywords. Thermodynamic capacity; ideal gas mixture; reactive gas mixture; condensed phase.

1. Introduction

While the concept of thermodynamic potential is well established and widely used in chemical literature, the corresponding capacity function has not been discussed in the textbooks on thermodynamics (Prigogine and Defay 1954; Swalin 1972; Kestin 1979; Lupis 1983). As such, chemical potentials are appropriate to determine the direction of transport of a species or of a reaction in a chemical system. However, being an intensity factor, chemical potentials do not provide any information on the amount of species transported or on the extent of reaction, even in the absence of kinetic restrictions. A suitably defined capacity factor can be useful in quantifying the amount of a species that can be drawn from a chemical reservoir at a specified chemical potential. Consider, for example, the synthesis of a non-stoichiometric oxide or a Magneli phase at high temperatures by equilibrating the solid with a flowing gas of defined oxygen potential. As oxygen is being added or removed from the oxide, the oxygen potential of the gas phase will usually change. If an $Ar+O_2$ mixture with $p_{O_2} < 10^{-4}$ atm is used for controlling the stoichiometry, the change in oxygen potential of the gas accompanying a finite oxygen exchange with the solid will be very large. In other words, the gas phase is unable to supply or remove any significant amount of oxygen from the solid at a defined potential. The oxygen capacity of the $Ar+O_2$ mixture may therefore be considered to be low at these low oxygen partial pressures. A gas mixture consisting of $CO+CO_2$ or H_2+H_2O may have higher capacity to supply or remove oxygen at low potentials. The purpose of this communication is to define thermodynamic capacity and to illustrate its variation for some typical systems. A potential application of the concept in high temperature material synthesis and solid state device research is projected.

2. Definition of thermodynamic capacity

Just as the electrical potential increases as electrons are put into a condenser, the chemical potential of a species increases in a homogeneous medium with the addition of that species. While the electrical potential rises linearly with charge, the chemical potential increases logarithmically with concentration for ideal or dilute solutions. The thermodynamic capacity of a species (i) in a homogeneous phase may be defined by the expression,

$$C_i = (\partial n_i/\partial \mu_i)_{P,T,n_{j(j\neq i)}}, \tag{1}$$

where n_i is the total moles of i in any state of chemical combination per unit amount of the phase and μ_i is the chemical potential of i. Thermodynamic capacity of species i may be visualized as the moles of i that is added or removed from a specified quantity of a homogeneous system when the chemical potential of i is given a unit increment or decrement.

It is interesting to explore the variation of thermodynamic capacity with composition for an ideal gas mixture ($Ar + O_2$), reactive gas mixtures usually used in chemical synthesis ($CO + CO_2$, $H_2 + H_2O$, $SO_2 + SO_3$, $H_2 + CO_2$ and $H_2 + H_2S$) and condensed phase solutions (Cu–O and Cu–O–Sn). For simple mixtures, analytical expressions may be derived relating capacity and composition. However, in systems containing several complex species, numerical procedures are more convenient. In the numerical technique, one starts with a preset composition and computes the chemical potential of species i. The chemical potential is then incremented by a small amount and the new composition is computed. From the change in composition, the amount of the species added is calculated. The capacity

$$C_i = \Delta n_i/\Delta \mu_i.$$

3. Capacity of an ideal gas mixture

An example of a simple gas mixture is $Ar + O_2$. In the ideal gas approximation, chemical potential of oxygen in the mixture is given by

$$\mu_{O_2} = \mu^{\circ}_{O_2} + RT \ln p_{O_2}. \tag{2}$$

Implicit differentiation gives

$$d\mu_{O_2} = (RT/p_{O_2})\, dp_{O_2}. \tag{3}$$

The partial pressure of oxygen is defined by

$$p_{O_2} = n_{O_2}/(n_{O_2} + n_{Ar}). \tag{4}$$

This on differentiation gives

$$dp_{O_2} = (p_{Ar}/n)\, dn_{O_2} = (p_{Ar}RT/PV)\, dn_{O_2}, \tag{5}$$

where $n = n_{O_2} + n_{Ar}$ is the total moles of oxygen plus argon in the gas and P is th total pressure. Combining (3) and (5), one gets

$$C_{O_2} = \frac{dn_{O_2}}{d\mu_{O_2}} = \frac{p_{O_2}PV}{(RT)^2 p_{Ar}} = \frac{p_{O_2}PV}{(RT)^2(P - p_{O_2})} = \frac{p_{O_2}V}{(RT)^2[1-(p_{O_2}/P)]}. \quad (6$$

When $p_{O_2} \ll P$, the thermodynamic capacity of oxygen is proportional to the oxyge partial pressure. As p_{O_2} tends to P, the infinite capacity of pure oxygen i approached.

In the numerical procedure for the calculation of C_{O_2}, the relative chemica potential is computed for an initial mixture of n_{O_2} moles of O_2 and n_{Ar} moles of A using (4). The chemical potential is then changed by 100 or 1000 cals by addition o removal of oxygen. This changes the number of moles of oxygen in the system b Δn_{O_2}, which is given by

$$\Delta n_{O_2} = \frac{[p'_{O_2}(n_{Ar} + n_{O_2}) - n_{O_2}]}{(1 - p'_{O_2})}, \quad (7)$$

where p'_{O_2} is the new oxygen partial pressure, corresponding to μ'_{O_2}. The thermodynamic capacity is given by

$$C_{O_2} = \Delta n_{O_2}/(\mu'_{O_2} - \mu_{O_2}). \quad (8)$$

The calculations have been carried out per mole of the mixture. The variation of $\log C_{O_2}$ with $\log p_{O_2}$ is shown in figure 1 at 1 atm total pressure for different temperatures. Both analytical and numerical techniques give essentially the same result.

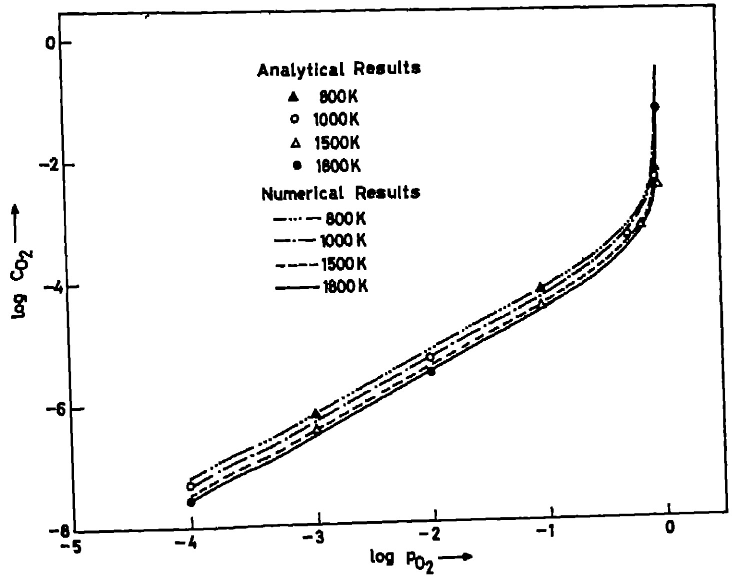

Figure 1. Variation of the thermodynamic capacity, C_{O_2}, with p_{O_2} in $Ar + O_2$ gas mixture at different temperatures.

4. Reactive gas mixtures containing stable species

4.1 $CO+CO_2$ mixtures

In a $CO+CO_2$ gas mixture, the system is buffered against changes in oxygen potential by the formation or dissociation of CO_2 according to the reaction

$$CO_2 \rightarrow CO + 1/2\, O_2. \tag{9}$$

The equilibrium constant K is given by

$$K = (p_{CO}/p_{CO_2})\, p_{O_2}^{1/2}. \tag{10}$$

Based on the approach similar to the one used for an $Ar+O_2$ mixture, the thermodynamic capacity of oxygen, C_{O_2}, at a given oxygen partial pressure p_{O_2} can be approximated by

$$C_{O_2} = \frac{V}{(RT)^2}\left[p_{O_2} + \frac{P(p_{O_2}/K^2)^{1/2}}{4[1+(p_{O_2}/K^2)^{1/2}]^2}\right]\frac{1}{(1-p_{O_2}/P)}. \tag{11}$$

At $p_{O_2} \simeq K^2$ or a p_{CO}/p_{CO_2} ratio equal to unity, C_{O_2} is a maximum. A minimum in capacity is observed at a value of p_{O_2} given by

$$p_{O_2} \simeq \tfrac{1}{4}(P^{2/3} K^{2/3}), \tag{12}$$

or

$$\frac{p_{CO_2}}{p_{CO}} \simeq \tfrac{1}{4}(P^{1/3} K^{-2/3}). \tag{13}$$

In the numerical technique, we consider a starting gaseous mixture of carbon dioxide, carbon monoxide and oxygen with initial number of moles of the species being n_{CO_2}, n_{CO} and n_{O_2} respectively. The equilibrium composition at a given temperature may be reached by the decomposition of a certain amount of CO_2, say α, according to the reaction (9). Each of the partial pressures in (10) may be expressed in terms of mole fractions of the particular species. For example

$$p_{CO_2} = \frac{n_{CO_2} - \alpha}{n_{CO_2} + n_{CO} + n_{O_2} + \alpha/2}. \tag{14}$$

Substituting for the partial pressures in (10), the value of α is given by the solution of the equation

$$\begin{aligned} &\alpha^3(1-K^2)/2 + \alpha^2(1-K^2)(n_{O_2}+n_{CO}) + \alpha[K^2 n_{CO_2}(3/2 n_{CO_2} + 2n_{CO} + 2n_{O_2}) \\ &+ n_{CO}(n_{CO}/2 + 2n_{O_2})] - [K^2 n_{CO_2}^2(n_{CO_2} + n_{CO} + n_{O_2}) - n_{CO}^2 n_{O_2}] = 0. \end{aligned} \tag{15}$$

Let Δn_{O_2} be the change in total number of moles of oxygen corresponding to a change in chemical potential by 1000 calories. Equilibrium is reached by the formation of x additional moles of CO_2. The new values of the partial pressures are represented as p'_{CO_2}, p'_{CO} and p'_{O_2}. The values of x and Δn_{O_2} are then given by the expressions

$$x = (n_{CO} + \alpha) - \frac{p'_{CO}(n_{CO_2} + n_{CO})}{(1 - p'_{O_2})} \tag{16}$$

and

$$\Delta n'_{O_2} = \left(\frac{n_{CO}}{2} - n_{O_2}\right) - \frac{(n_{CO_2} + n_{CO})(p'_{CO} - 2p'_{O_2})}{2(1 - p'_{O_2})} . \qquad (17$$

Hence

$$C_{O_2} = \Delta n'_{O_2} / \Delta \mu_{O_2} . \qquad (18$$

Two separate cases of $CO + CO_2 + O_2$ mixtures can be considered. In the first case the equilibrium O_2 concentration is generated solely by the dissociation of CO_2 in a $CO + CO_2$ mixture. For this case, initial oxygen $n_{O_2} = 0$. In the second case, the equilibrium CO is generated by dissociation of CO_2 in a $CO_2 + O_2$ mixture and therefore $n_{CO} = 0$.

Case 1: When $n_{O_2} = 0$, the expressions (15) and (17) reduce to

$$\alpha^3(1 - K^2)/2 + \alpha^2 n_{CO}(1 - K^2) + \alpha[(3/2)K^2 n^2_{CO_2} + 2K^2 n_{CO_2} n_{CO} + n^2_{CO}/2] - K^2 n^2_{CO_2}(n_{CO_2} + n_{CO}) = 0, \tag{19}$$

$$\Delta n_{O_2} = \frac{n_{CO}}{2} - \frac{(n_{CO_2} + n_{CO})(p'_{CO} - 2p'_{O_2})}{2(1 - p'_{O_2})} . \tag{20}$$

When n_{CO} is large, p'_{CO} is also large, therefore $\Delta n'_{O_2}$ is small. As n_{CO} decreases, p'_{CO} also decreases. However, $\Delta n'_{O_2}$ increases with decreasing n_{CO}. As the ratio n_{CO_2}/n_{CO} approaches unity, the value of $\Delta n'_{O_2}$ and hence the thermodynamic capacity increases. A maximum value is obtained at a ratio of one. With increasing value of the n_{CO_2}/n_{CO} ratio, capacity decreases and passes through a minimum. It is difficult to control oxygen potential near the minimum in capacity. Other systems should be considered if it is necessary to control oxygen potential in this range.

Case 2: When $n_{CO} = 0$, i.e. at very high oxygen potentials, decomposition of CO_2 alone cannot account for the free oxygen in the system. The starting mixture would therefore have CO_2 and O_2 as the initial species, the CO content at equilibrium being set up by dissociation of CO_2. Then α and $\Delta n'_{O_2}$ are given by the solutions of

$$\alpha^3(1 - K^2)/2 + \alpha^2(1 - K^2)n_{O_2} + \alpha[(3/2)K^2 n^2_{CO_2} + 2K^2 n_{CO_2} n_{O_2}] - K^2 n^2_{CO_2}(n_{CO_2} + n_{O_2}) = 0 \tag{21}$$

and

$$\Delta n'_{O_2} = \frac{(2p'_{O_2} - p'_{CO}) n_{CO_2}}{2(1 - p'_{O_2})} - n_{O_2} \tag{22}$$

respectively. As n_{O_2} and p'_{O_2} increase, the thermodynamic capacity of oxygen increases. For pure oxygen, the capacity will be infinite.

Figure 2 gives the thermodynamic capacity of oxygen as a function of the equilibrium n_{CO_2}/n_{CO} ratio per mole of gas mixture. The equilibrium constants were taken from the Janaf tables (Stull and Prophet 1971). The values given by the analytic expression (11) and the numerical technique match well. The plot shows a peak at a 1:1 ratio, where the system is buffered well against changes in oxygen potential. At higher oxygen potentials, the capacity coincides with that of an $Ar + O_2$ mixture as shown in figure 3. The capacity values at 1500 K are tabulated for various input compositions in table 1.

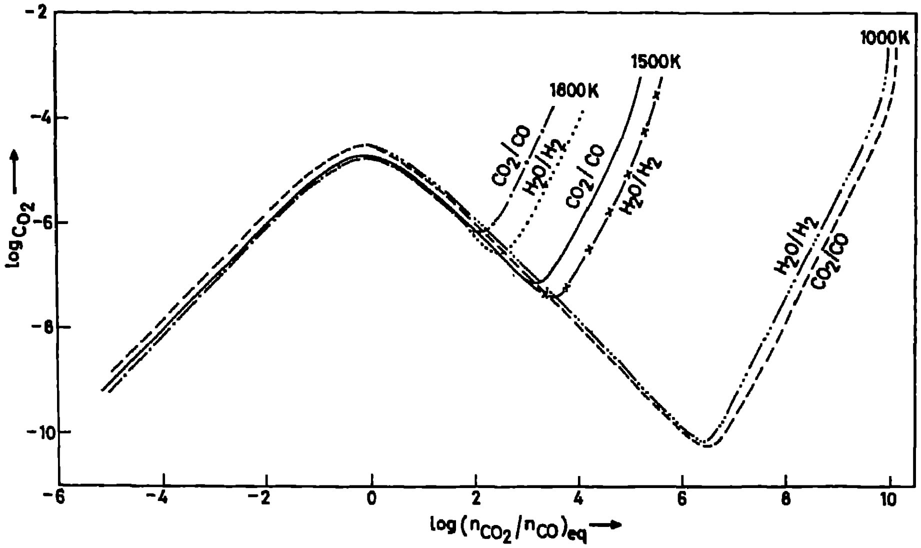

Figure 2. Variation of C_{O_2} with the equilibrium n_{CO_2}/n_{CO} or n_{H_2O}/n_{H_2} ratios at various temperatures.

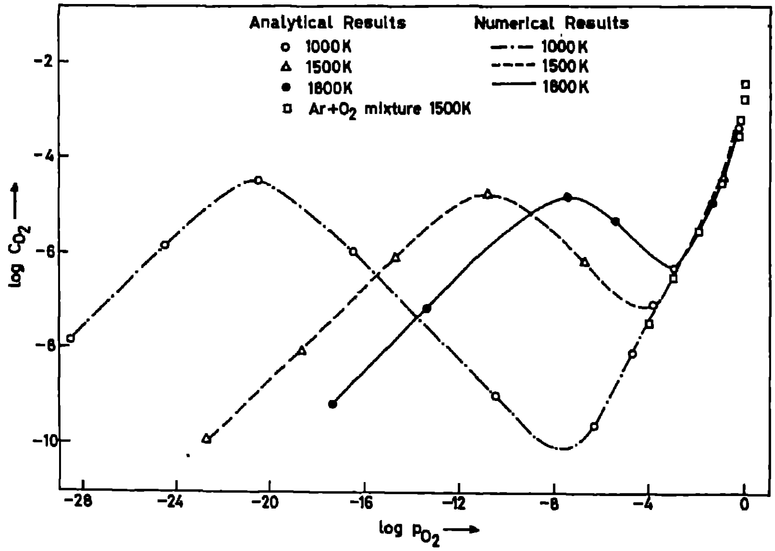

Figure 3. Variation of C_{O_2} as a function of log p_{O_2} in a CO+CO_2 gas mixture at various temperatures.

4.2 H_2+H_2O mixtures

The procedure for calculating C_{O_2} is similar to that for a CO+CO_2 gas mixture. As seen in figure 2, the small differences in the values of the equilibrium constants for the dissociation reactions in the two gas mixtures give rise to significant differences in the values of C_{O_2} only at higher oxygen potentials.

Table 1. Values of thermodynamic capacity of oxygen in a $CO+CO_2$ mixture for defined values of the equilibrium ratio n_{CO_2}/n_{CO} in the input mixture at 1500 K, obtained by the numerical technique.

n_{CO_2}/n_{CO}	p_{O_2} atm	C_{O_2} moles/cal
10^{-7}	$2{\cdot}13\times10^{-25}$	$1{\cdot}19\times10^{-10}$
10^{-5}	$2{\cdot}13\times10^{-21}$	$8{\cdot}94\times10^{-10}$
10^{-3}	$2{\cdot}13\times10^{-17}$	$9{\cdot}15\times10^{-8}$
10^{-1}	$2{\cdot}13\times10^{-13}$	$7{\cdot}45\times10^{-6}$
1	$2{\cdot}13\times10^{-11}$	$2{\cdot}10\times10^{-5}$
10	$2{\cdot}13\times10^{-9}$	$6{\cdot}49\times10^{-6}$
$2{\cdot}59\times10^{3}$	$1{\cdot}43\times10^{-4}$	$8{\cdot}72\times10^{-8}$
$2{\cdot}16\times10^{4}$	$9{\cdot}92\times10^{-3}$	$4{\cdot}03\times10^{-6}$
$6{\cdot}53\times10^{4}$	$9{\cdot}09\times10^{-2}$	$4{\cdot}17\times10^{-5}$
$1{\cdot}53\times10^{5}$	$0{\cdot}5$	$6{\cdot}68\times10^{-4}$

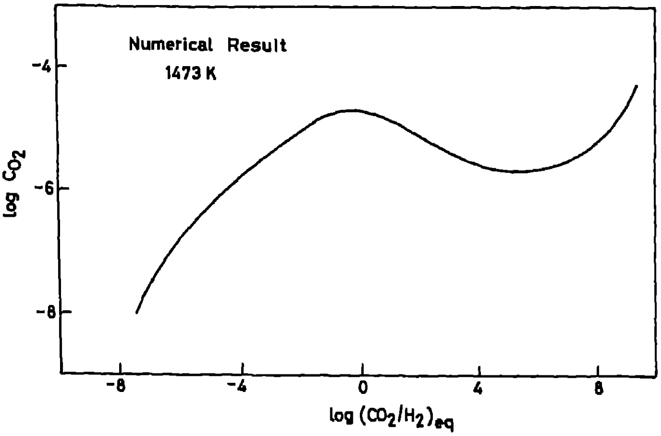

Figure 4. Dependence of C_{O_2} on n_{CO_2}/n_{H_2} at 1473 K.

4.3 H_2+CO_2 *mixtures*

The equilibrium gas composition at 1473 K was calculated considering the species CO_2, CO, H_2O, H_2 and CH_4, using the SOLGAS program (Eriksson 1971). The oxygen capacity was then computed using the numerical procedure. As seen from figure 4, a peak is seen at a ratio of n_{CO_2}/n_{H_2} equal to unity, at which the equilibrium n_{CO_2}/n_{CO} and n_{H_2O}/n_{H_2} values are also close to one. The trend is similar to that for other reactive gas mixtures.

5. Reactive gas mixtures containing unstable species

5.1 SO_2+SO_3 *mixtures*

The equilibrium constant for the decomposition of SO_3 is large even at a low temperature of 1000 K. Figure 5 gives the C_{O_2}values in an SO_2+SO_3 mixture as a

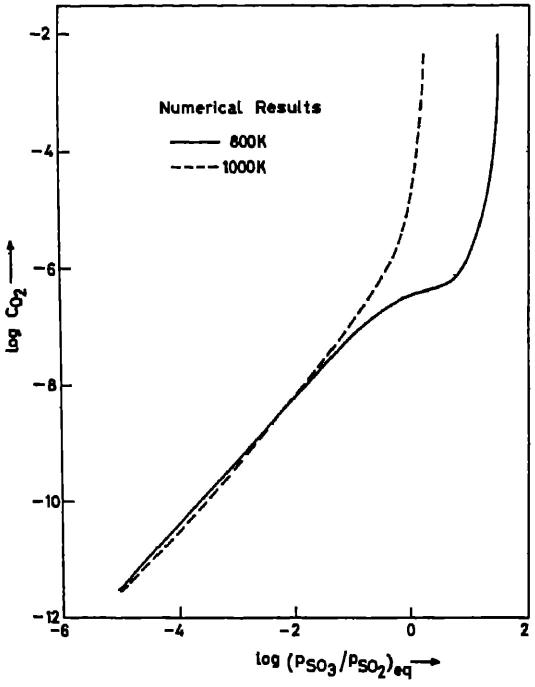

Figure 5. Variation of C_{O_2} with equilibrium n_{SO_3}/n_{SO_2} in an SO_2+SO_3 gas mixture at 800 K and 1000 K.

function of the equilibrium n_{SO_3}/n_{SO_2} ratio. No peak is observed even at 1000 K and it is not clearly defined at 800 K. For identical ratios of n_{SO_3}/n_{SO_2} and n_{CO_2}/n_{CO} at a given temperature, the thermodynamic capacity of oxygen in an SO_2+SO_3 mixture is lower.

5.2 H_2+H_2S mixtures

The thermodynamic capacity of sulphur C_{S_2} in a H_2+H_2S gas mixture at temperatures of 800, 1000, 1500 and 1800 K has been calculated on similar lines. The peak again occurs at a ratio of unity as seen in figure 6. At higher temperatures where H_2S is unstable, no peak is seen and the capacity continuously increases.

6. Condensed phase calculations

In the copper-oxygen system, when oxygen is added to molten copper, its chemical potential rises. However, more oxygen is required at higher potentials to produce a given rise and the capacity increases with increasing oxygen content. While the mathematical equation referring to this curve has no upper limit, there are very real chemical limits. When the oxygen potential exceeds −32,860 cals at 1373 K, Cu_2O will precipitate as a separate phase. Attempts to increase the oxygen content of molten copper will result in the formation of Cu_2O, which is equivalent to a "leak" at

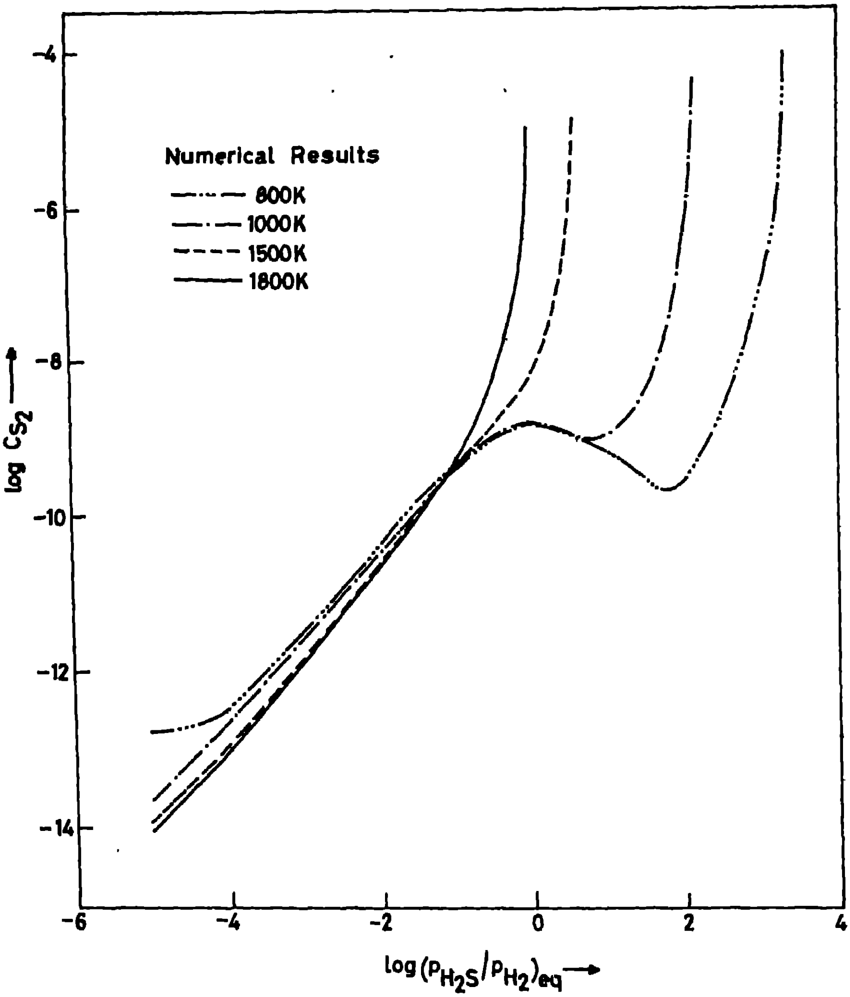

Figure 6. Thermodynamic capacity of sulphur in an H_2+H_2S gas mixture at different temperatures.

this level into another phase with unlimited capacity. The whole copper can be oxidized at this potential.

Similarly, if copper contained dissolved tin, it would not be possible to raise the oxygen potential above the value corresponding to the formation of SnO_2. The oxygen potential for the formation of SnO_2 will be a function of the tin concentration. Here, the leak is to another oxide SnO_2. As the tin concentration decreases due to the formation of SnO_2 the permissible oxygen potential in the metal goes up. Since the oxygen potential does not remain constant during the formation of SnO_2, the capacity does not go to infinity as in the Cu–O system, but increases to a very large value at the saturation solubility limit for oxygen at the given tin concentration.

6.1 *Molten Cu–O system*

Dissolution of oxygen in molten copper may be represented by the reaction

$$1/2\,\mathrm{O}_2 \rightarrow [\mathrm{O}] \qquad (23)$$

where ΔG°, the free energy change associated with the above reaction is given by (Jacob and Jeffes 1971)

$$\Delta G^\circ = RT\left(\frac{\ln(\%\,\mathrm{O}\,f_\mathrm{O}^\mathrm{O})}{p_{\mathrm{O}_2}^{1/2}}\right) = -20{,}542 + 1{\cdot}723\,\mathrm{T}\ \mathrm{cal/g.at.} \qquad (24)$$

The standard state for dissolved oxygen is chosen such that a_O = atom % O as atom % O→0. The variation of the Henrian activity coefficient of oxygen with concentration at 1373 K is given by

$$\log f_\mathrm{O}^\mathrm{O} = -0{\cdot}042\ (\mathrm{at}\ \%\ \mathrm{O}) \qquad (25)$$

Differentiating (24) with respect to the change in number of moles of oxygen, $\mathrm{d}n_{\mathrm{O}_2}$, the thermodynamic capacity, $\mathrm{C}_{\mathrm{O}_2}$, is given by the expression

$$\mathrm{C}_{\mathrm{O}_2} = \frac{\mathrm{d}n_{\mathrm{O}_2}}{\mathrm{d}\mu_{\mathrm{O}_2}} = \frac{X_{\mathrm{O}_2}}{2RT(1 + 2\varepsilon_\mathrm{O}^\mathrm{O} X_{\mathrm{O}_2})}, \qquad (26)$$

where X_{O_2} is the oxygen content in molten copper expressed as a mole fraction of O_2 and $\varepsilon_\mathrm{O}^\mathrm{O}$ is the self interaction parameter, $(\partial \ln f_\mathrm{O}/\partial X_\mathrm{O})_{X_\mathrm{O}\rightarrow 0}$.

In the numerical technique, the equilibrium constant K for (23) given by

$$K = a_\mathrm{O}/p_{\mathrm{O}_2}^{1/2} \qquad (27)$$

was used to calculate the oxygen partial pressure in equilibrium with a given amount of dissolved oxygen in molten copper. The chemical potential of oxygen was then incremented by 100 cals and the new oxygen content computed. The analytic and numerical results agree well. The saturation solubility limit for oxygen corresponding to the formation of $\mathrm{Cu_2O}$ at 1373 K is 2·4 atom % O. As seen from figure 7, the

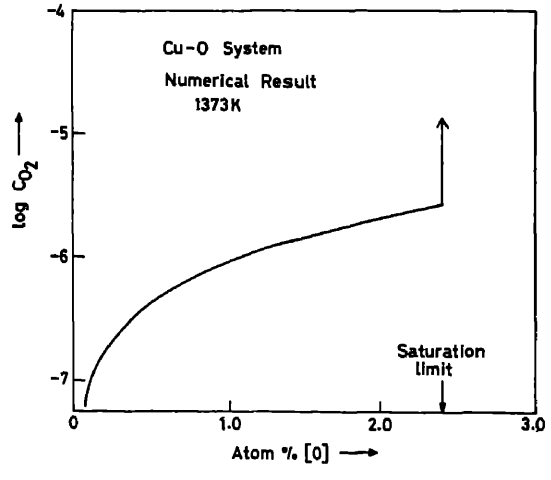

Figure 7. $\mathrm{C}_{\mathrm{O}_2}$ as a function of dissolved oxygen in molten copper at 1373 K.

thermodynamic capacity, C_{O_2}, plotted as a function of dissolved oxygen in copp expressed in atom % becomes infinite at the saturation value. The phase mixtu Cu–O + Cu_2O provides a composition invariant buffer for oxygen.

6.2 *Molten Cu–O–Sn system*

The calculations were done at 1373 K for various alloy compositions in the ran 1–14 atom % Sn. The interaction parameter ε_O^{Sn} is (Jacob *et al* 1970)

$$\varepsilon_O^{Sn} = \left(\frac{\partial \ln f_O}{\partial X_{Sn}}\right)_{X_{Sn}, X_O \to 0} = -4\cdot 6. \qquad (2$$

The corresponding expression for log f_O is

$$\log f_O = -0\cdot 042\,(\text{atom \% O}) - \frac{4\cdot 6}{2\cdot 303} X_{Sn}. \qquad (2$$

The activity coefficient of tin in molten copper is given by (Jacob *et al* 1970)

$$\log \gamma_{Sn} = (-1\cdot 38 + 3\cdot 333\, X_{Sn})\, X_{Cu}^2 \qquad (3$$

Combining (24) with the free energy of formation of SnO_2, the free energy change fo the reaction

$$Sn + 2[O] \rightarrow SnO_2 \qquad (31$$

is

$$\Delta G^\circ = -98{,}566 + 47\cdot 174\ T\ \text{cal/mol} \qquad (3$$

The upper limit to the oxygen activity corresponding to saturation can thus b calculated. The capacity values for various oxygen contents upto the saturation limi were computed by the numerical technique. At saturation, the formation o SnO_2 provides an additional sink for oxygen. The analytic expression for capacity o oxygen in saturated solutions of Cu–Sn is obtained as shown below:

$$\frac{d\mu_{O_2}}{dX_{Sn}} = \frac{d}{dX_{Sn}}(\ln X_{Sn}\gamma_{Sn})$$

$$= -\frac{RT}{X_{Sn}} - RT\left(\frac{d\ln\gamma_{Sn}}{dX_{Sn}}\right). \qquad (33$$

Now $\quad dX_{Sn} = -dX_{SnO_2} = -dn_{O_2}. \qquad (34$

Hence

$$C_{O_2} = \frac{dn_{O_2}}{d\mu_{O_2}} = \frac{X_{Sn}}{RT\{1 + 2\cdot 303 X_{Sn}(1 - X_{Sn})(2\cdot 76 + 3\cdot 333[1 - 3X_{Sn}])\}}. \qquad (35$$

At saturation the rise in capacity is by 2–3 orders of magnitude as shown in figure The capacity of the two-phase mixture of SnO_2 and the homogeneous solution i larger than that of the single phase alloy. The saturation oxygen concentration in th ternary alloy increases as the tin concentration decreases. The oxygen capacit therefore does not go to infinity at saturation. As the tin concentration in the alloy i

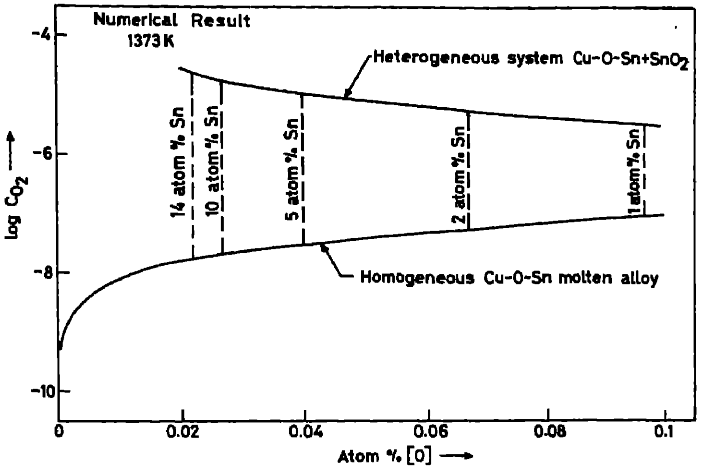

Figure 8. Variation of C_{O_2} with the concentration of dissolved oxygen in Cu–Sn allo different compositions at 1373 K.

depleted by the formation of SnO_2, the thermodynamic capacity of oxygen va along the upper curve corresponding to the two-phase mixture. This exan illustrates a composition variant two phase buffer.

7. Applications

In the preparation of inorganic solids of controlled compositions, the samples often equilibrated with a gas phase of controlled chemical potential. If thermodynamic capacity of the gas is low, then a large volume of the gas is requi unless the amount of oxygen to be exchanged is small. Similarly, when using mixtures containing molecules that differ considerably in molecular weights, a $H_2 + H_2S$ mixtures, the flow rate must be kept high to minimize thermal segregat The experiments using large volumes of high purity gases are inherently expens Sometimes disposal of large volumes of toxic gases can also be problematic solution to the problem is to use a recirculating system which provides regeneration of the gas to the required composition. Solid state sensors can be pla in the recirculating stream to ensure that the composition is maintained at pr values. In gas mixtures, for the control of oxygen potential, injection or withdra of oxygen from the stream can be accomplished by an electrochemical oxygen pu Coulometric oxygen pumps depend on Faraday's law relating current to oxygen and are based on solid electrolytes with mobile oxygen ions. In principle the pum similar to a sensor. The sensor operates in open circuit mode while the pu operates in the non-zero current mode. The current through the oxygen pump ca regulated by the emf feedback from the solid state sensor. The feedback amplifica may be automated. It can be shown that the correct value of the pump curre related to the thermodynamic capacity of oxygen in the gas

$$I = \frac{4Fn_V}{1-\bar{t}_e}\int_{\mu'_{O_2}}^{\mu''_{O_2}} \frac{C_{O_2}}{V}\, d\mu_{O_2}$$

where n_V is the volume flow rate of the gas, μ'_{O_2} and μ''_{O_2} are the actual and pres chemical potentials of oxygen in the gas, $\bar{t}_e$ is the average electronic transferenc number of the solid electrolyte and C_{O_2}/V is the oxygen capacity of the gas per un volume. The pumping current is a highly nonlinear function of oxygen partia pressure.

8. Conclusion

A new thermodynamic variable, thermodynamic capacity, which is a measure of th ability of a chemical system to exchange a species without a change in its chemica potential, has been proposed. The variation of thermodynamic capacity for ideal an non-ideal solutions and systems with strong and weak compounds have bee computed using analytical and numerical techniques. The capacities in two-phas heterogeneous systems are illustrated using Cu–O + Cu_2O and Cu–O–Sn + SnO_2 a examples. Multiphase systems can be devised that have higher thermodynami capacity than homogeneous phases. The concept of thermodynamic capacity i useful in high temperature chemical vapour transport and solid state device incorporating electrochemical pumps.

References

Eriksson G 1971 *Acta Chem. Scand.* **25** 2651

Jacob K T and Jeffes J H E 1971 *Trans. Inst. Min. Metall.* **C80** 32

Jacob K T, Seshadri S K and Richardson F D 1970 *Trans. Inst. Min. Metall.* **C79** 274

Kestin J 1979 *A course in thermodynamics* (Washington: McGraw Hill) Vols 1 and 2

Lupis C H P 1983 *Chemical thermodynamics of materials* (New York: North Holland)

Prigogine I and Defay R 1954 *Chemical thermodynamics* (London: Longmans, Green and Co.)

Stull D R and Prophet H 1971 *JANAF thermochemical tables*, 2nd ed. NSRDS-NBS37, U.S. Department of Commerce, Washington D C

Swalin R A 1972 *Thermodynamics of solids* (New York: John Wiley)

Bull. Mater. Sci., Vol. 8, No. 4, October 1986, pp. 467–470.
© Printed in India.

Growth of low dislocation density single crystals of nickel

S K KHANNA and K GOVINDA RAJAN
Materials Science Laboratory, Indira Gandhi Centre for Atomic Research, Kalpakkan 603 102, India

MS received 16 January 1986; revised 24 April 1986

Abstract. Low dislocation density single crystals of nickel have been grown at high ambient pressure by the Czochralski method. X-ray Laue picture shows that the crystals are strain-free. The dislocation density was determined to be $< 10^3/\mathrm{cm}^2$ by the etching procedure. It was found that the necking and cone regions are very critical in the dislocation introduction in the crystals. An increase in the ambient pressure used during the growth seems to aid the crystal quality.

Keywords. Nickel crystals; high pressure growth; Czochralski technique.

1. Introduction

The physical properties of the crystalline materials are sensitive to the presence of lattice imperfections such as dislocations which may be present in the as-grown crystals. A significant contribution was made by Dash (1958) who discovered the method of eliminating dislocations in the melt-grown crystals. A thin neck is grown on top of the growing crystal by employing large pulling rates. The line defects in the neck grow out to the nearby surface. Moreover, only a very small number of dislocation lines are allowed from the seed crystal. Dash's technique is particularly suitable for growing nearly perfect single crystals of metals where the necking procedure will ensure a sufficiently small temperature gradient in the main body of the crystal. We have employed this procedure to grow low dislocation density single crystals of nickel. The other objective of the present work has been to study the influence of higher ambient pressure on the quality of the crystal.

2. Experimental details

We have employed the Czochralski technique for the growth of single crystals where the crystal cools in an unconstrained manner thus making it possible to produce low dislocation density crystals. Moreover, the necking procedure can be employed, and the shape of the growing crystal can be controlled to a considerable extent. The details of the main equipment used for the Czochralski growth have been described elsewhere (Khanna *et al* 1986). The initial charge in the form of pellets (99·99% pure nickel) was placed in an alumina crucible which was completely supported by a graphite container. A 99·99% pure nickel wire was used for the seed. The system was filled with high purity argon to a pressure of 6 bars. The seed crystal was carefully wetted in the melt before initiating the crystal pulling. The seed crystal and the crucible were rotated in the opposite direction at 10 rpm. This was done to intermix the molten mass and to ensure a constant circumferential temperature. A thin neck of 0·4 mm was grown on the top of the crystal. The diameter was controlled only by continuously monitoring the melt temperature, and the pulling speed during the growth was maintained at a constant level of 0·2 mm/min. This way it was ensured that there were no sudden mechanical shocks given to the solid-liquid interface. The pulling speed v_p does not coincide with the growth rate V. As the crystal grows, the melt level lowers. The two rates are related to each other by the following relation (Paorici 1982)

$$V = \frac{V_p}{1 - [(\rho_s/\rho_L)(d_s/d_L)^2]}$$

where d_s, d_L are diameters of the growing crystal and the melt in the crucible, ρ_s and ρ_L are the densities of nickel in solid and liquid phases. The crucible lift rate was fixed at 0·02 mm/min. On completion of the growth the crystal was cooled down very slowly at 10°C/min to avoid dislocation generation due to thermal gradients.

3. Results and discussion

By using high pressure Czochralski technique we have grown single crystals of nickel (6 mm diameter and 25 mm long). Single crystallinity was examined by exposing the crystal to the x-ray beam and recording the Laue back reflection picture. Figure 1 shows that the crystal is both a single crystal and strain-free. The nickel crystals reported so far (Hayashi *et al* 1974; Kuriyama *et al* 1977) have been grown from melt either in vacuum or in an inert gas environment maintained at 1 atm. pressure. The dislocation density reported in these crystals was fairly high (Hayashi *et al* 1974). In order to find out the dislocation density of the present high pressure Czochralski grown crystals, these were cut normal to the growth axis and then characterized by metallographic techniques. The crystals were mechanically polished by using diamond paste down to a 3 μm surface finish and etched in a solution of HNO_3 and acetic acid (Brandes 1983). The dislocation density was measured by first identifying those etch pits which were due to dislocations. For this the crystal surface was successively etched and the continuity of etch pits was followed. Etching resulted in well-defined etch pits which were triangular in shape (figure 2) and which persisted even after the removal of successive layers from the crystal surface. Slight roughness of the etched surface, seen in the photograph, could be due to the effects of mechanical polishing. We have used only upto 3 μm grain size diamond paste. This procedure yielded an estimate of $< 10^3$ dislocations/cm^2, indicating that the crystal grown in an argon gas atmosphere at a pressure slightly higher than the ambient is of good quality. Low dislocation density was obtained by eliminating the dislocations from the seed crystal in the neck, and the dislocations can be reintroduced if the diameter of the cone region is not controlled. The growth of the cone region was very important for obtaining low dislocation density single crystals of nickel. The cone region was grown such that the top angle was small. The cone could thus grow out with minimum dislocations. On the other hand, with large top angles, the internal stresses in the growing crystal would have been high and that would cause dislocation generation in the cone region. With dislocations being kept at minimum level in the cone region, further growth of the crystal was accomplished such that the crystal diameter stayed more or less constant. With this the dislocation multiplication in the lower part of the crystal was prevented to a great extent.

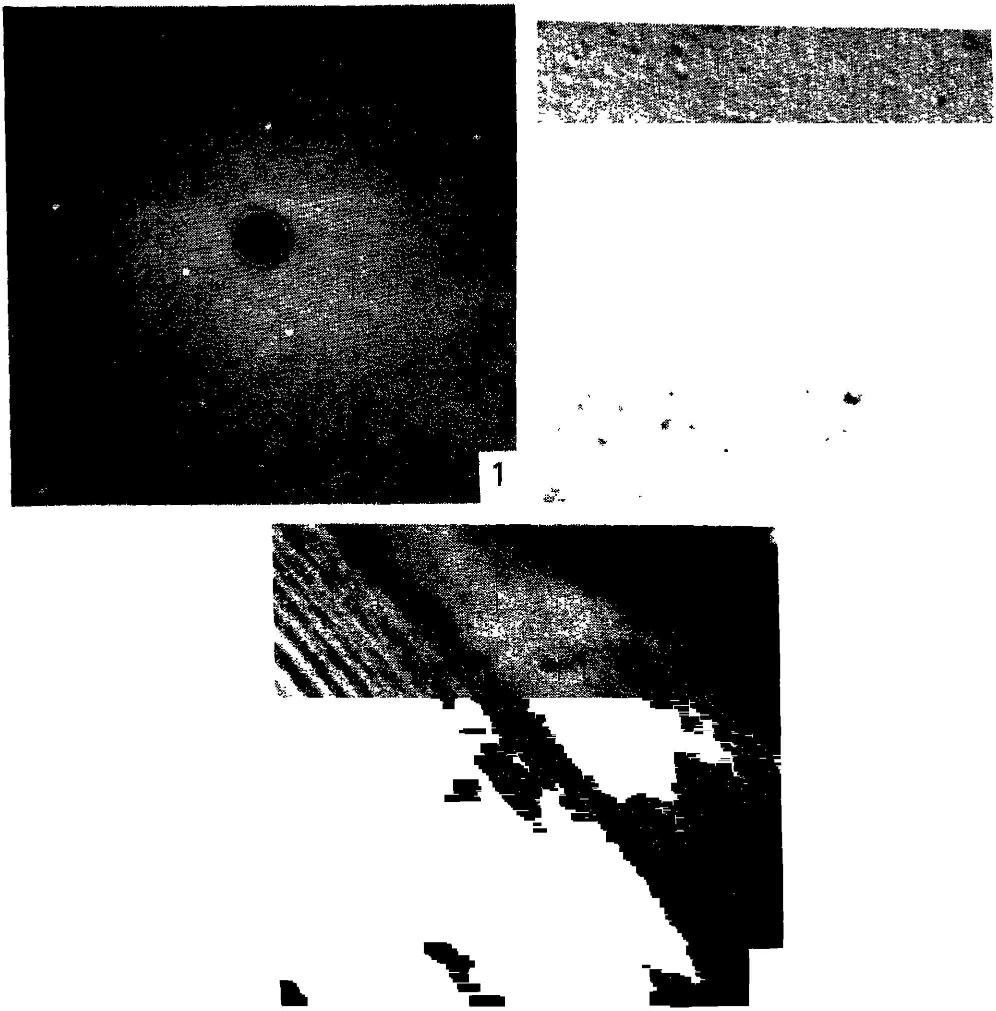

Figures 1–3. 1. X-ray back reflection picture of single crystal of nickel. 2. Dislocation etch pits in nickel crystal. 3. Radial growth striations in nickel single crystal.

Striations observed normal to the growth axis <111> (figure 3) showed the shape of the solid-liquid interface. No axial growth striations were observed. Since the crystals were not doped with any other material, these striations are not due to the solute variations. These were found to be not periodic over the length of the crystal and were observed at an extremely small number of places. The unintentional dopants that might exist in 99·99% pure nickel will, on the other hand, give rise to striations which will be periodic over the entire length of the crystal. Also no discoloration of the alumina crucible material was observed after the growth experiments, implying that there was no reaction of nickel with Al_2O_3 crucible. The spacing between the two adjoining striations was measured to be 2–3 μm. These striations can be attributed to the possible thermal fluctuations present across the interface due to the thermal and temperature gradients commonly used in the growth of single crystals of nick are not very low to eliminate thermal convection. A spacing of the abo mentioned magnitude is typical of such fluctuations. Although low temperatu gradients in the crystal were favourable for the low dislocation density growth, with su low temperature gradients in the melt, the melt convection reduces making the he transfer from the crucible wall to the crystal interface small. Subsequently it becar very difficult to control the crystal diameter.

Low dislocation density ($<10^3$ dislocations/cm^2) observed in nickel single cryst grown in argon gas at 6 bar pressure indicates that the high ambient pressure dc not reduce the quality of the crystal. On the other hand, the crystal is mechanica extremely soft at its melting temperature and a slight ambient pressure perha prevents dislocation generation by reducing the thermal stresses at the interfa Compared to the vacuum-grown crystals these crystals have lower dislocati density and their microstructure does not show any grain boundaries.

4. Conclusions

Strain-free single crystals of nickel have been grown at 6 bar inert gas pressure. T slight hydrostatic pressure environment and the necking are found to improve t crystal quality. The dislocation density of these crystals was determined to be l than 10^3 dislocations/cm^2.

Acknowledgement

The authors are thankful to Shri M Sekar for assistance in the experiments and S G V N Rao for help in x-ray work.

References

Brandes E A 1983 *Smithells metals reference book* (London: Butterworths) p. 10

Dash W C 1958 *J. Appl. Phys.* **29** 736

Hayashi S, Echigoya J, Hariu H, Sato T, Nakamichi T and Yamamoto M 1974 *J. Cryst. Growth* **2** 422–425

Khanna S K, Sekar M, Michael David A, Govinda Rajan K and Bhaskar Rao P 1986 *Pramana (J. P* **26** 151

Kuriyama M, Boettinger M J and Burdette H E 1977 *Advances in x-ray analysis* (New York: Plenum P (eds) H F McMuradie, C S Barrett, J B Newkirk and C O Rund Vol. 20, p. 245

Pamplin B R 1975 *Crystal growth* (New York: Pergamon Press)

Paorici C 1982 *Proc. international school on synthesis, crystal growth and characterization* (ed) K (Amsterdam: North-Holland) p. 170

Bull. Mater. Sci., Vol. 8, No. 4, October 1986, pp. 471–478.
© Printed in India.

Emission spectrographic technique for the quantitative determinatio of trace elements in granitic rocks

A EL BIALY, M RASMY*, L A GUIRGUIS** and W MOUSSA
Women's College, Ain Shams University, Cairo, Egypt
*Earth Sciences Laboratories, National Research Centre, Cairo, Egypt
**Nuclear Materials Corporation, Cairo, Egypt

MS received 14 March 1985; revised 29 July 1985

Abstract. An emission spectrographic technique was developed to estimate 16 trace elemen in some samples of Egyptian granite. The detection limits were: 0·1 ppm for Pb, Ba, Mo, C Cr, Yb and Ni, 0·3 ppm for Sn, Ga and Be, 1 ppm for Co, Sc and V, 3 ppm for Bi and Y an 10 ppm for La. The relative deviation of the two-thirds limits ranges between ± 1·5 and ± 24·

Keywords. Emission spectrography; granitic rocks; trace elements.

1. Introduction

Crystalline rocks, including igneous and metamorphic types, constitute more than 95 % of the earth's crust. Granites are the most common igneous rocks. Many valuable or deposits are genetically related to granitic rocks. Therefore, the determination of trac elements in granite is essential for both genetic and economic reasons. The technique o spectrographic analysis of granites has drawn the attention of a great number o authors (Ahrens and Taylor 1961; Sighinolfi 1966; Peter 1969; Fleischer 1972; Goku 1975; Watson and Russell 1978). Granites are coarse-grained acid igneous rocks whic are mainly composed of alkali feldspars, acid plagioclases, mica and some othe accessory minerals. Granites contain high SiO_2 content (usually above 65 %) and are therefore considered acidic and responsible for the dense silica bands in spectrographic analysis. Besides, the increased ratio of alkalies perceptibly lowers the arc temperature These factors give rise to a dense background and low sensitivity of the analysed elements.

The aim of the present work is to develop a specific technique by which arcing conditions of granite are improved and sensitivities of the elements increased.

2. Experimental

The emission spectrographic technique was developed to determine 16 trace elements in some samples of Egyptian granite using a Zeiss Jena grating spectrograph. Graphite was used as a buffering material while CdF_2 was added as a carrier. The current intensity was 1·4 A, time was 50 sec and Pd was used as the internal standard for most elements.

The optimum conditions of spectrographic analysis of granite can be achieved by studying some factors. These are discussed in this paper.

.1 *Electrode type*

or practical reasons, only rod-type graphite electrodes were experimented. Four orms of each of the sample and counter electrodes were alternatively tested. These orms are similar to the Ringsdroff types (RW0006, RW0021, RW0068, RW0070, W0083, RW0028 and RW0067) with tip angles 20° and 30°. The best forms that gave ood burning conditions and high line intensities are those similar to the sample form W0021 and counter form RW0028. The electrodes (electrode gap: 3·5 mm) were haped from JMC specpure graphite rods. These are shown in figure 1 and are given the

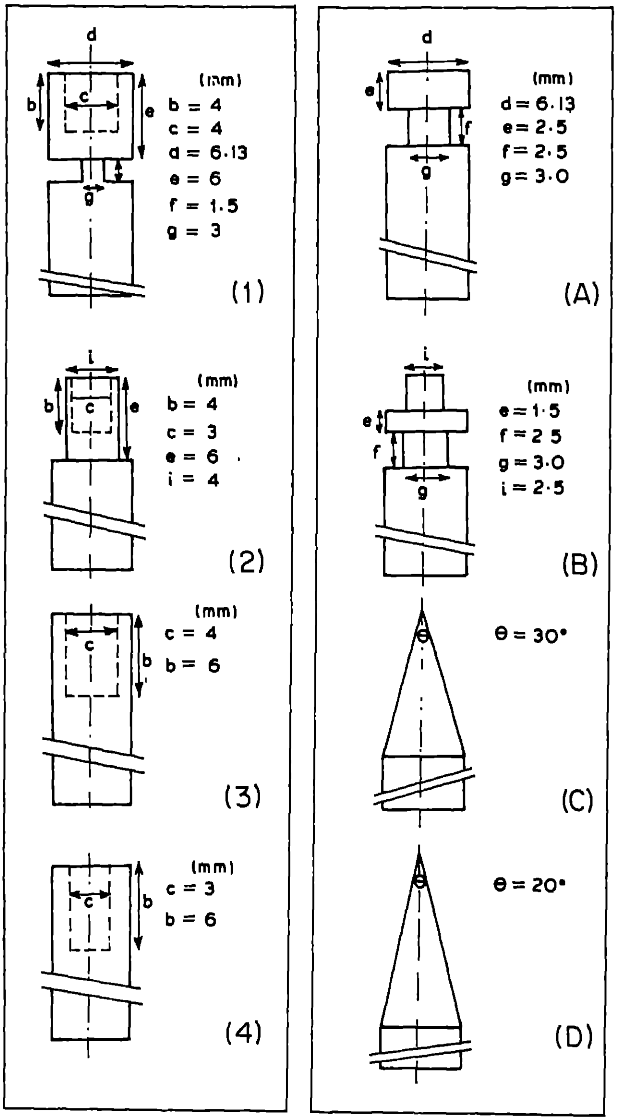

(a) (b)

Figure 1. Electrode shape.

symbols 1, 2, 3 and 4 for sample electrodes (anode) and A, B, C and D for coı electrodes (cathode) respectively.

2.2 *Current intensity*

According to Bowmans (1966) the intensities of the spectral lines are influenced b arc current. It is important to obtain the best current intensity to have a smooth buı arc and a stable arc spot.

The dependence of the current densities of the test lines: Ba: 455·40 Ti: 337·280 nm, Cr: 425·434 nm, Zr: 339·198 nm, Zn: 328·233 nm, V: 437·92 Pb: 283·307 nm, Mo: 317·035 nm, Be: 213·042 nm, Yb: 328·937 nm and Y: 332·78 on the arc current from 6 to 15 A is represented graphically in figure 2. It is clear th line densities increase gradually with current intensity. Moreover some of the rare elements such as Y and Yb did not appear except at a high current intensity (12 A) best practical current intensity was 14 A.

2.3 *Buffers and carriers*

A wide range of additives was used. They include graphite powder, alkali and alk earth carbonates and halides, oxides of Mg, Zn, Zr and Ga as well as heavy ı halides (Rasmy 1983) in varying ratios. It was observed that the best buffer and c are graphite powder and cadmium fluoride respectively. The ideal mixing rat sample, graphite and CdF_2 is 2:2:1. Figure 3 shows a moving plate study at 1 intervals for three cases, from which the following can be concluded:

(a) When the sample is arced alone, the distillation period exceeds 160 sec till the volatile elements, e.g. Y, attain their peaks.
(b) When a mixture of equal amounts of the sample and graphite powder is arce distillation period is rather shortened and arcing is improved. However, some eler like Y and Mo exhibit double peaks.
(c) When the ideal mixture of the sample, graphite and CdF_2 is arced, the distill period is greatly shortened. Each element exhibits one peak and all peaks appear d the first 50 seconds of arcing. Besides, densities of spectral lines of the elemen perceptibly increased. It seems that the most suitable exposure time is 50 sec, by time a reasonable background intensity is developed.

2.4 *Sample preparation*

Samples of granite, each about 2 kg, were crushed by hammering. Small represen samples were prepared by quartering method and ground to about 200 mesh usi agate mortar. Contamination was always avoided.

2.5 *Synthetic standards*

A matrix was prepared, the composition of which is close to the average composit granite given by Wedepohl (1969). The small content of Mn, Ti and P oxide excluded as P_2O_5 was not provided as a specpure chemical while Mn and Ti ar added as a part of the trace elements to be analysed. After thorough mixing matrix components, they were sintered in a platinum dish at 1200°C for 6 hr, c and ground to 200 mesh. The final composition of the matrix was expected

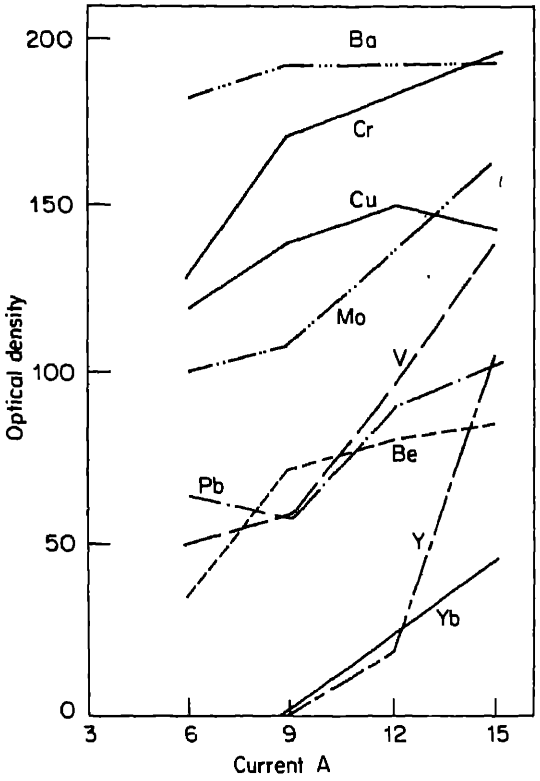

Figure 2. Current effect.

72·91 % SiO_2, 14·02 % Al_2O_3, 2·56 % Fe_2O_3, 0·53 % MgO, 1·35 % CaO, 3·12 % Na_2O and 5·52 % K_2O.

The first standard, containing 3000 ppm of each of the trace ingradients, was prepared from the calculated amount of JMC Spectromel No. 1 mixture containing 1·18 % of 53 different trace elements, to which the corresponding amounts of the oxides of Y, La and Yb are added and finally diluted with the weighed amount of the matrix. From this first standard, other standards containing 1000, 300, 100 . . . down to 0·1 ppm of the trace elements were prepared by successive dilution with the matrix.

2.6 *Internal standard*

An amount equivalent to 100 ppm palladium, as chloride, was added to each of the samples and standards for internal standardization. The intensities of the less volatile elements (Ahrens and Taylor 1961) are related to that of Pd. No other internal standard could be used for volatile elements including Ga, Pb, Cu and Sn. They were related to their adjacent background.

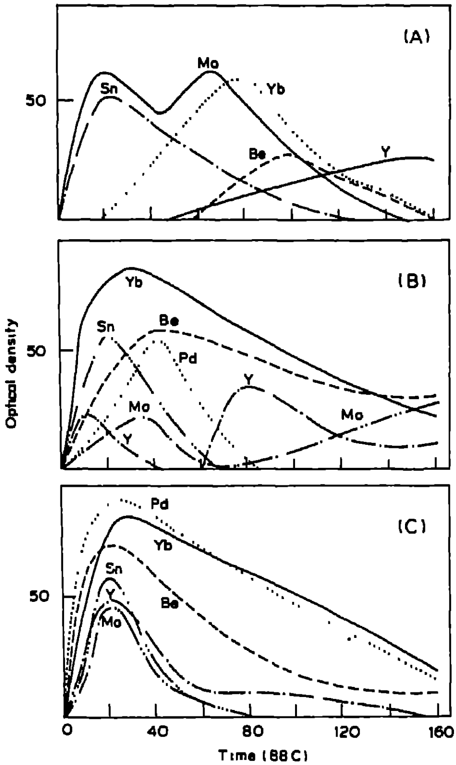

Figure 3. Time-intensity diagrams of granite standard with about 100 ppm traces sho the effect of buffer and carrier: (A) Standard alone, (B) Standard: Buffer 1/1, (C) Stan Buffer: CdF_2 2/2/1.

2.7 *Slit width adjustments*

The slit width of the spectrograph is of great importance when the background effe considered. The background intensity, due to continuous radiation, increases with width. Therefore the slit must be adjusted to give maximum line intensity reasonable background. The granitic sample was arced using variable values of width such as 10, 12, 14 and 16 μ. It is clear from the results obtained (figure 4) that slit width of 12 μ was most preferable, considering the exposure time of 50 sec and o conditions.

2.8 *Calibration and evaluation*

Calibration curves were drawn by plotting blackness D of some Fe spectral lines aga their log intensities using a six-step diminisher with 100, 40, 16, 10, 6 and transmissions. Four curves were drawn covering the whole wavelength r 282–456 nm (figure 5). The background correction was made using the relation give Mika and Torok (1974).

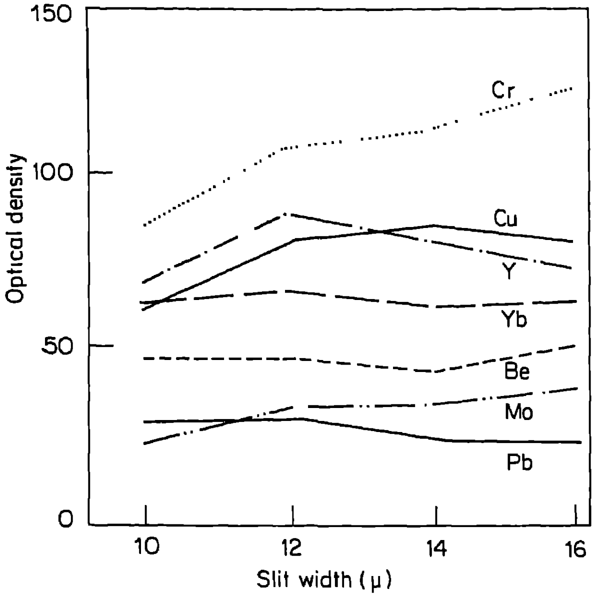

Figure 4. Effect of slit width.

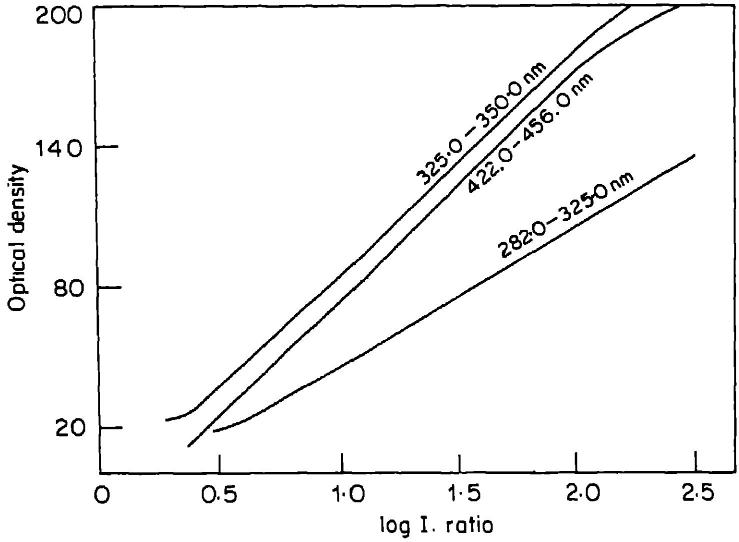

Figure 5. Sample of the calibration curves.

Working curves were drawn between log intensity ratio and log concentration (figure 6). The trace elements content of the analyzed granite samples and its implications were discussed in detail by El Bialy *et al* (1984). The analytical lines and detection limits of the analysed elements of our work and that of Gokun (1975) (the best available compatible work) are shown in table 1.

Table 1 shows that the improvements in the minimum detection limit are a 1000 for Pb, Mo, Cu, Yb, Ni, Cr and Ba, 333·33 for Ga and Be, 100 for Co, 33·33 for Y and 16·66 for Sn.

2.9 *Precision and accuracy*

Precision expressed as the standard deviation *S* and the relative deviation *C* at thirds limits is shown in table 2 using data obtained by arcing granite rock star distributed by the U.S. Geological survey, as an unknown sample. The deviation *S* ranges between ± 0·02 and ± 1·9 ppm while the relative deviation

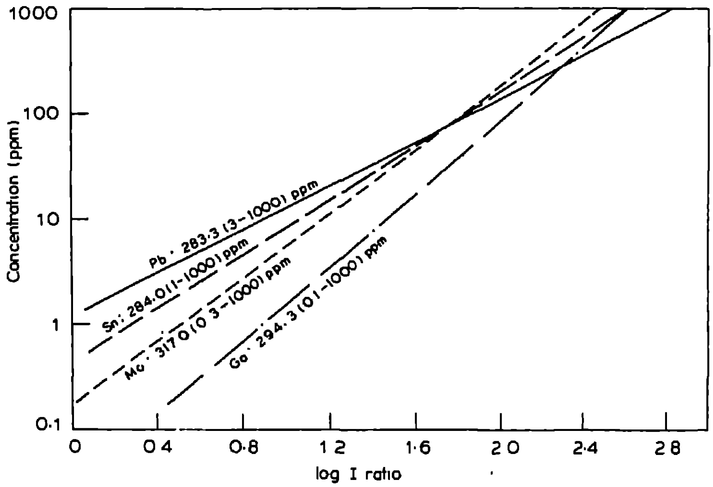

Figure 6. Samples of working curves for the determination of Pb, Sn, Mo an

Table 1. Detection limits and wavelength of spectral lines of the analysed eler present work compared to that of Gokun (1975)

Element	Wave-length (nm)	Detection limit (ppm)		Element	Wave-length (nm)	Detectic (pp
		Present work	Gokun (1975)			Present work
Pb	283·307	0·1	100	Ga	294·364	0·3
Mo	317·035	0·1	100	Be	313·042	0·3
Cu	327·396	0·1	100	Co	345·351	1
Yb	328·937	0·1	N.D.	Sc	424·683	1
Ni	341·477	0·1	100	V	437·924	1
Cr	425·434	0·1	100	Bi	306.772	3
Ba	455·404	0·1	100	Y	332·788	3
Sn	283·999	0·3	5	La	433·347	10

N.D. not detected.

Table 2. Results of analysis of granite rock standard USGS-G_2 together with standard deviations (S) and relative deviation (C)

Element	Flanagan (1973)	Present work	S	C
Be	2·6	3·1	0·70	24·7
Ga	22	18	1·9	11·5
Cu	11·7	10·27	1·58	13·8
Mo	0·36	0·5	0·06	11·5
Y	12	11·1	1·69	15·25
Yb	0·88	0·8	0·15	18·8
Sn	1·5	1·33	0·02	1·5
Cr	7	5·3	0·77	14·5
Sc	3·7	3·22	0·16	5·08

between ± 1·5 and ± 24·7. As shown in table 2, the present values of trace element G_2, are in good agreement with earlier values (Flanagan 1973). This shows that accuracy of the method is satisfactory. Moreover the reported relative deviation val in table 2 for all the elements are much better than the value of 25% given by Go (1975).

References

Ahrens L H and Taylor S R 1961 *Spectrochemical analysis* (London: Addison-Wesley) 2nd edn

Bowmans P W J M 1966 *Theory of spectrochemical excitation* (London: Hilger Watts) pp 192

El Bialy A, Rasmy M N, Guirguis L A and Moussa W 1984 *Bull. Nat. Res. Council* (*Cairo*) (accep

Flanagan F J 1973 *Geochim. Cosmoch. Acta* **37** 1189

Fleischer M 1972 *Science* **199** 6

Gokun V N 1975 *Tr. Akad. Nauk USSR* **35** 105

Mika J and Torok T 1974 *Analytical emission spectroscopy Fundamentals* (*Hung*), Eng. Transl. P A F (London: Butterworth)

Peter S 1969 *Math. Nakur. Wiss. Reibe* 1, 8, 8 971

Rasmy M 1983 *Bull. Nat. Res. Council* (Cairo)

Sighinolfi G P 1966 *Period Minerel Rome* 35, 3 769

Watson A F and Russell G U 1978 *Spectrochim. Acta part* 2, 33, 5 173

Wedepohl K H (ed.) 1969 *Data of geochemistry* (Berlin: Springer) Vol. 1

Bull. Mater. Sci., Vol. 8, No. 4, October 1986, pp. 479–488.
© Printed in India.

Determination of oxygen to metal ratio of U-Pu mixed oxides by x- diffraction

RAVI VERMA and P R ROY
Radiometallurgy Division, Bhabha Atomic Research Centre, Bombay 400 085, India

MS received 13 March 1986

Abstract. The possibility of measuring the oxygen-metal ratio (O/M) of U-Pu m oxides by x-ray diffraction technique has been explored. In single-phase U-Pu mixed o the lattice parameter vs O/M plots for different plutonium concentrations are draw interpolation of lattice parameter values between those of UO_2, PuO_2 and Pu_2O_3. plots are then used for determining the O/Ms of unknown samples against experimentally measured lattice parameter values. In two-phase mixed oxides, the fractions of the two phases are determined from the intensities of their selected diffra lines. The O/M of the mixed oxide is then given by the mole average of the individual of the two phases.

Keywords. Oxygen-metal ratio; uranium plutonium oxides; x-ray diffraction.

1. Introduction

The oxygen-to-metal ratio (O/M) is an important parameter governing m properties of the U-Pu mixed oxide fuels. It is well known that deviation f stoichiometry assists in the sintering of mixed oxide compacts (Belle 1961; Lay 1 The O/M also affects fuel properties such as thermal conductivity (Zebroski 1965; Gibby 1969) and melting point (Lyon and Baily 1965). Diffusion coeffici and vapour pressures have also been reported to change by 3 or more orde magnitude for a minor change of 0·02 in the O/M near the value of 2·00 (Ma 1976). A knowledge of O/M of the mixed oxide fuel, therefore, is very essential.

A variety of O/M measurement techniques have been developed and used ove past several years with varying degree of success. Lyon (1963) reviewed sever these techniques and recommended a thermogravimetry method of measurement. McNeilly and Chikalla (1971) improved upon the two-step me and suggested a single heat treatment of the sample at 1073 K for 6 hr i atmosphere of Ar–8% H_2 passed over a water trap maintained at 273 K. method has an accuracy of ±0·002. The thermogravimetry method require accurate balance, a furnace and a gas handling system which make it difficu adopt it as an on-line method of O/M measurement in a commercial fuel produ plant. Lattice parameter measurement can be conveniently used to measure O/ single-phase mixed oxides. In this paper, different methods of O/M measure based on x-ray diffraction analysis are presented for single-phase and for two- mixed oxides. The results of O/M measurements obtained using these method discussed.

2. U-Pu-O system

Before discussing the x-ray methods, it is worthwhile to examine some relationships in the ternary U-Pu-O system. Since the recommended fuel for metal fast breeder reactors is a hypostoichiometric mixed oxide, the discussion would be restricted only to this region of the ternary phase diagram.

The phase diagram in figure 1 (Markin and Street 1967) shows that for plutonium concentrations less than 30–35%, the hypostoichiometric mixed oxide exists as a single fcc phase. The remarkable ability of the mixed oxide to lose oxygen without undergoing a phase transformation is attributed to the conversion of Pu^{4+} ions to Pu^{3+} ions. The O/M limit of the single phase region corresponds to a state in which all the plutonium in the mixed oxide is reduced to Pu^{3+}. Uranium, on the other hand, remains tetravalent throughout the reduction of the mixed oxide. For plutonium concentrations more than 30–35%, the hypostoichiometric mixed oxide exists as a mixture of two phases—the stoichiometric $MO_{2 \cdot 00}$ phase and a substoichiometric MO_{2-x} phase. The O/M of the latter phase corresponds to all the plutonium in Pu^{3+} state. The phases, $MO_{2 \cdot 00}$ and MO_{2-x}, have the fcc structure upto a plutonium concentration of 50% (Brett and Russell 1963), beyond which the MO_{2-x} phase shows a bcc structure (Brett and Russell 1963; Dean 1965). Further, it has been shown (Dean *et al* 1970) that the hypostoichiometric mixed oxide containing 76% plutonium shows a rhombohedral phase in equilibrium with the fcc $MO_{2 \cdot 00}$ phase. The O/M of the rhombohedral phase is reported to be 1·70, which means that only a part of plutonium in this phase exists in Pu^{3+} state.

3. Methods

3.1 *Single-phase mixed oxide*

The x-ray diffraction method for determining O/M in a single-phase mixed oxide is based on finding a correlation between the lattice parameter and the O/M of the

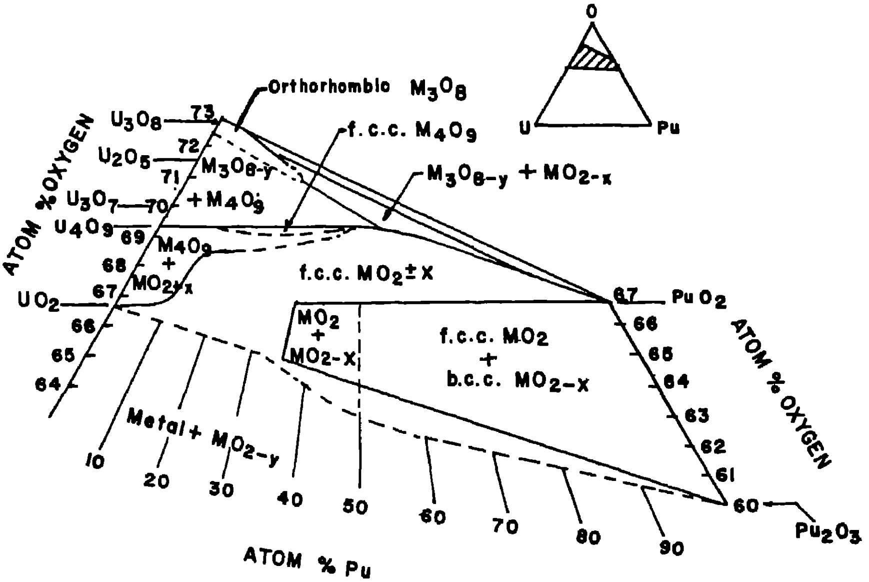

Figure 1. A section of U-Pu-O ternary equilibrium diagram.

mixed oxide. Lattice parameter values determined by the x-ray diffraction techniq are plotted against O/M values measured by the thermogravimetric method f different plutonium concentrations of the mixed oxide (Dean and Pascard 196 Blank *et al* 1967; Markin and Street 1967). These plots are then used to obtain t O/M values for unknown samples.

The lattice parameter vs O/M plots for different plutonium concentrations ca also be drawn on the basis of the following consideration.

The lattice parameter of a stoichiometric mixed oxide varies linearly with plut nium content from UO_2 to PuO_2 (Mufford and Ellingor 1958). Dean *et al* (197 showed that the lattice parameter of a fully reduced mixed oxide (i.e. all plutonium Pu^{3+} state) varies linearly with plutonium content, from UO_2 to Pu_2O_3. Furthe there is ample evidence (Dean and Pascard 1967; Blank *et al* 1967; Markin and Stre 1967) indicating that the lattice parameter of a mixed oxide of given plutoniu concentration varies linearly with its oxygen content. These observations sugge that, in general, the lattice parameter of a hypostoichiometric mixed oxide can obtained by linear interpolation between the lattice parameter values of UO_2, Pu and Pu_2O_3. Details of the interpolation are shown in figure 2. Dean's latti parameter vs plutonium content plot for fully reduced mixed oxide (line a in t

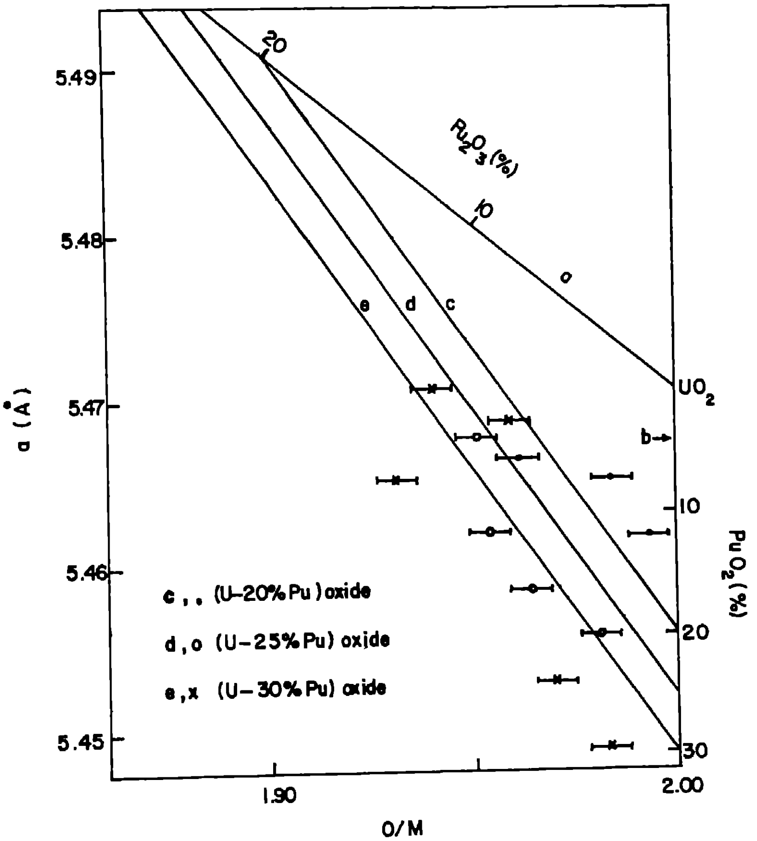

Figure 2. Dependence of lattice parameter on O/M for different compositions of the si phase mixed oxide; theoretical plots (—) and the experimental data points.

figure) is drawn by assigning limit stoichiometry according to the trivalent state plutonium, to each composition of the limiting phase. The linear variation of t lattice parameter with the PuO_2 content of the stoichiometric mixed oxide is plott as line b. Since the lattice parameter vs O/M plot for a mixed oxide of giv plutonium concentration, say $U_{1-c}Pu_c$ oxide, is also a straight line (Dean a Pascard 1967; Blank *et al* 1967; Markin and Street 1967), the plot is simply obtain by joining with a straight line the limit compositions, $U_{1-c}Pu_cO_{2-0\cdot5c}$ on plot a a $U_{1-c}Pu_cO_{2\cdot00}$ on plot b. This way the lattice parameter vs O/M plots for differe plutonium concentrations of the mixed oxide are drawn. By knowing the latti parameter of a mixed oxide of known plutonium concentration its O/M can obtained from a suitable plot in figure 2.

3.2 *Two-phase mixed oxide*

The overall O/M of a mixed oxide consisting of two phases can be obtained l taking the weighted mean of the individual O/Ms of the two phases. If m denotes tl mole fraction of MO_{2-x} phase in a mixture of $MO_{2\cdot00}$ and MO_{2-x} phases, tl overall O/M of the mixed oxide will be given by

$$\begin{aligned} O/M &= (1-m)\times 2\cdot00 + m\,(2-x) \qquad (\\ &= 2\cdot00 - mx \end{aligned}$$

To find the O/M of a two-phase mixed oxide, therefore, the values of x and m shoul be known. The deviation from stoichiometry of the MO_{2-x} phase is given, based o the trivalent state of plutonium, as

$$x = 0\cdot5\, C_{Pu}/(C_U + C_{Pu}) \qquad (:$$

where C_U and C_{Pu} are atomic concentrations of uranium and plutonium in tł mixed oxide.

In the MO_{2-x} phase containing 76% plutonium, all the plutonium do not exist i the trivalent state as shown by Dean *et al* (1970). The departure from stoichiometr in this phase, therefore, is not given by (2). This phase has been shown to have a O/M of 1·70 (Dean *et al* 1970), and so, an x equal to 0·3. The value of m can b obtained experimentally by measuring the x-ray line intensities of some selecte reflections of the two phases as described below.

The ratio of the volumes of two phases, α and β in a mixture is given in terms c the integrated intensities of their selected x-ray reflections, as

$$V_\alpha/V_\beta = \frac{I_\alpha(hkl)}{I_\beta(h'k'l')}\,\frac{K_\alpha(hkl)}{K_\beta(h'k'l')} \qquad (3$$

where $K(hkl)$ is a factor characteristic of the selected reflection (hkl) and the crysta structure of the particular phase.

In mixed oxides having 35 to 50% plutonium, both $MO_{2\cdot00}$ and MO_{2-x} phase have a fluorite-type cubic structure. Their lattice parameter values are nearly th same. They differ in their oxygen contents, but this is not of much consequence in s far as the K factors of the two phases are concerned since the atomic scattering facto of oxygen is much smaller than those of uranium and plutonium. Thus, for a give reflection (hkl), the K factor values for the two phases can be regarded as equal

$$K_\alpha(hkl) = K_\beta(hkl).$$

ed oxides containing more than 50% Pu, the bcc structure of the MO_{2-x} is in fact identical in atomic arrangement to the fluorite structure of the $_{0}$ phase, except that the vacancies in its oxygen sublattice are ordered, giving a bcc super lattice (Gardner *et al* 1965). Thus, for the same reasons as ced in the preceding paragraph, for a given reflection (*hkl*), the *K* factors for $_{0}$ and MO_{2-x} phases can be regarded as equal.

x-ray diffraction pattern of hypostoichiometric mixed oxide containing 76% ium is shown in figure 3. It is seen that the lines of the rhombohedral MO_{2-x} closely precede the corresponding lines of the cubic $MO_{2\cdot 00}$ phase. Because of w symmetry of the rhombohedral structure *vis-a-vis* the cubic structure, some lines are split into two. It has been shown (Dean *et al* 1970) that the ohedral structure of the MO_{2-x} phase is a slightly distorted form of the e structure of the $MO_{2\cdot 00}$ phase (rhombohedral: $a=5\cdot5087$ Å and $\alpha=89\cdot525°$; $a=5\cdot4147$ Å, $\alpha=90°$). Therefore, the *K* factors for equivalent reflections of $_{-x}$ and $MO_{2\cdot 00}$ phases should be nearly equal. In the case of the split lines of ombohedral phase, the combined *K* factor for the pair of split lines is equal to factor for the corresponding single line of the cubic phase. The {200} line of the bohedral phase is not split into two (figure 3). Therefore,

$$K_r\{200\}=K_c\{200\}.$$

the subscripts *r* and *c* denote rhombohedral and cubic phases respectively. us, for all compositions of the mixed oxide,

$$K_{MO_{2\cdot 00}}(hkl)=K_{MO_{2-x}}(hkl),$$

(*hkl*) can be any reflection for mixed oxides containing 35 to 50% plutonium

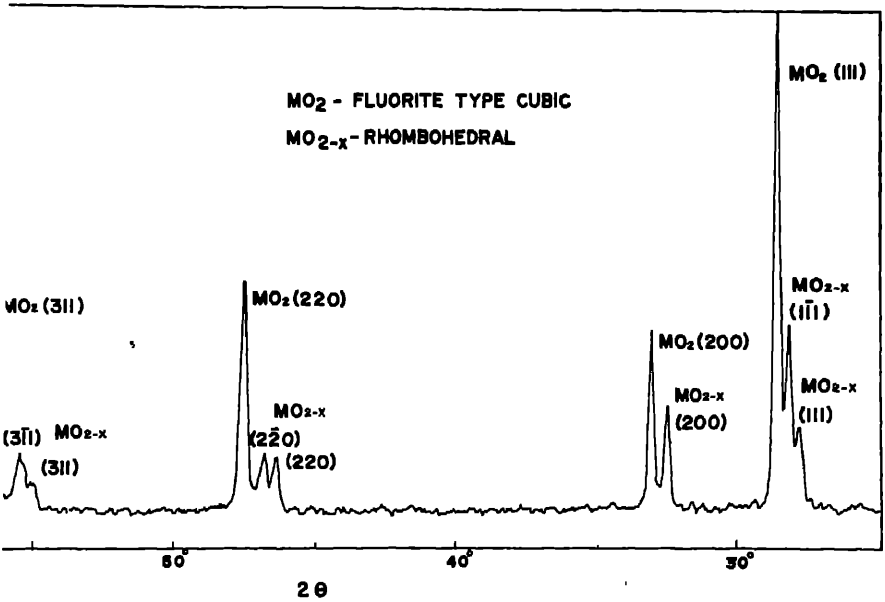

Figure 3. Recorded trace of (U0·24 Pu0·76) O_{2-x} diffraction pattern by CuK_α radiation.

and only the {200} reflection in case of mixed oxide containing 76% plutonium. Using the above equality in (3), one gets

$$V_\alpha/V_\beta = I_\alpha(hkl)/I_\beta(hkl). \tag{4}$$

The subscripts α and β represent the MO_{2-x} and the $MO_{2\cdot00}$ phases respectively. Since all the different crystal structures associated with MO_{2-x} phases are closely related to the flourite-type cubic structure of the $MO_{2\cdot00}$ phase, both these phases will have the same number of molecules per unit cell or per unit volume. Now, if m_α and m_β represent the number of moles of MO_{2-x} and $MO_{2\cdot00}$ phases, respectively, in a given mixed oxide sample, then

$$m_\alpha/m_\beta = V_\alpha/V_\beta.$$

Substitution from (4) gives

$$m_\alpha/m_\beta = I_\alpha(hkl)/I_\beta(hkl),$$

or

$$m = m_\alpha/(m_\alpha + m_\beta) = I_\alpha(hkl)/[I_\alpha(hkl) + I_\beta(hkl)], \tag{5}$$

where m is mole fraction of the MO_{2-x} phase in the mixed oxide. Knowing the values of x and m from (2) and (5) respectively, the O/M of unknown mixed oxide can be obtained from (1).

With the help of (1) m vs O/M plots for three different mixed oxide compositions U–35, 50 and 76% Pu, have been drawn in figure 4. The values of O/M for unknown

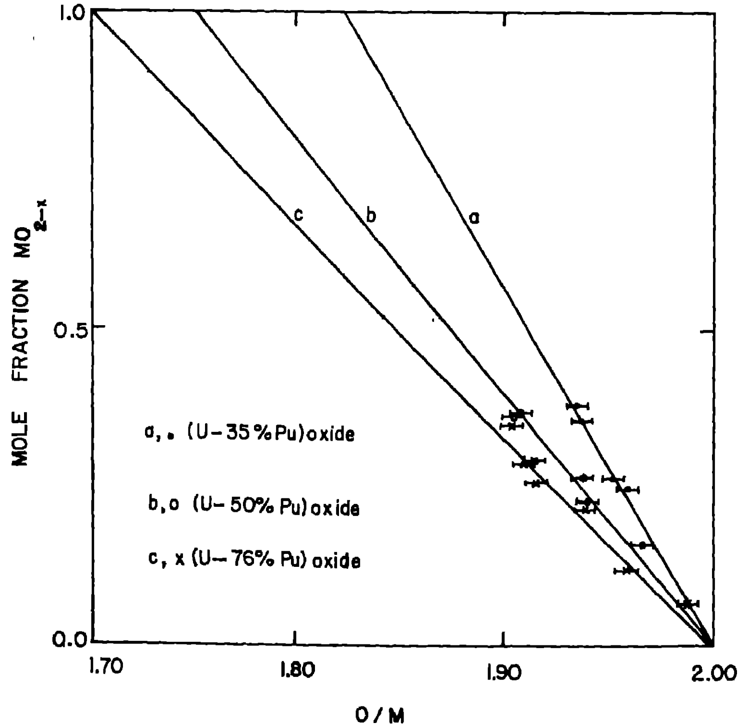

Figure 4. Amount of substoichiometric phase versus overall O/M of the two-phase mixed oxide; theoretical plots (—) and experimental data points (—o—)

mixed oxides belonging to these compositions can be read from these plots against their *m* values obtained from (5).

4. Experimental

Mixed pellets of compositions UO_2–20, 25, 30, 35, 50 and 76% PuO_2 were homogenized at 2073 K for 30 hr in a dry (100 ppm moisture) Ar + 8% H_2 atmosphere. The measurement of O/Ms of representative pellets by the thermogravimetric method showed that all the mixed oxides were highly reduced The process of O/M measurement by the thermogravimetric method adjusts the O/M of the mixed oxide pellet to 2·00. These O/M adjusted pellets are free from oxygen inhomogeneity and other phases and are thus suitable for assessing the metal atom homogeneity in the mixed oxides by the x-ray diffraction technique. X-ray diffraction patterns of all the O/M adjusted pellets showed sharp lines belonging to a single fcc phase. They also showed well-resolved ($K\alpha_1$–$K\alpha_2$) doublets for the (531 reflection, confirming that all the mixed oxides were well homogenized.

As-homogenized (non adjusted) pellets were heated at 373 K in air. For each of th various mixed oxide compositions, one pellet was removed from the furnace afte every 15 min of heating and stored in an inert atmosphere. This was continued ti the last set of pellets was removed. Thus, pellets of different O/Ms were obtained i all the mixed oxide compositions. Each of these pellets was broken into two halves one half was used to determine O/M by the thermogravimetric method and the othe half was used to record the x-ray diffraction pattern. For mixed oxides containing 20 25 and 30% plutonium (single-phase mixed oxides) precise lattice parameter value were determined by 'extrapolation' method using high angle lines. For mixed oxide containing 35 and 50% plutonium, the {311} reflection and in the case of mixe oxide containing 76% plutonium, the {200} reflection was recorded at a slo scanning speed of 1/8° in 2θ/min. These reflections consisted of two peaks eacl corresponding to the $MO_{2\cdot00}$ and the MO_{2-x} phases. The integrated peak intensitie $I_{MO_{2\cdot00}}$ and $I_{MO_{2-x}}$ were obtained by measuring areas under individual peak profile In mixed oxide containing 35% plutonium, however, the two peaks overlapped eac other as shown in figure 5 and measuring the area under the individual peak wa very difficult. This difficulty was overcome by correcting the peak profiles for th instrumental broadening by line profile analysis technique described elsewhe (Verma 1983). The measured integrated intensities were substituted in (5) to obta mole fractions of the MO_{2-x} phase in mixed oxide samples of different compositio

5. Results and discussion

The experimental data points based on measured lattice parameter and O/M valu of the single phase mixed oxides are plotted in figure 2. It is seen that the data poi are scattered not too closely on both sides of the theoretical lattice parameter O/M plots. The O/M values of various mixed oxide samples were also obtain against the respective measured lattice parameter values from these theoretical plo The differences between the O/M values thus obtained and the O/M valu measured by the thermogravimetric method are plotted against the latter in figure

In the case of two-phase mixed oxides, the experimental data points based

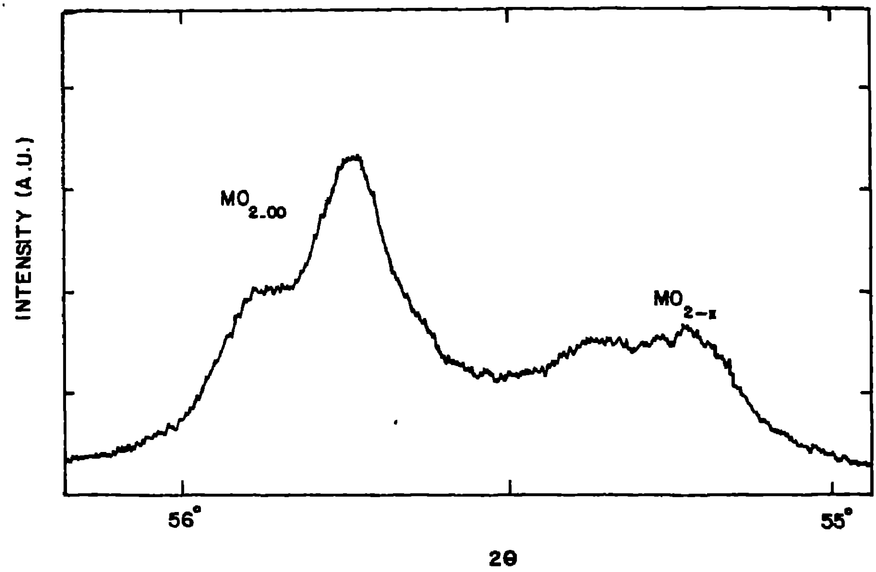

Figure 5. (311) Reflection profile recorded from (UO_2-35% PuO_2) mixed compact sintere in a reducing atmosphere.

measured MO_{2-x} phase fractions and O/M values obtained by thermogravimetri method are plotted in figure 4. The data points in this case fit the theoretical MO_{2-} phase fraction versus O/M plots fairly well. The differences in the O/M value obtained from the theoretical plots and those measured by the thermogravimetri method are plotted against the latter in figure 6.

It could be seen that the differences between the calculated and the measured O/M values are larger in the case of single phase mixed oxides than those of two-phas mixed oxides. The points in figures 6a and 6b show standard deviations of ±0·0 and ±0·005 respectively, from the O/M values measured by the thermogravimetri method. The thermogravimetric method of O/M measurement being the referenc method in this study, the O/M values obtained by this method may be treated a absolute. The standard deviations of ±0·01 and ±0·005, therefore, represent th accuracies of O/M measurement by the x-ray method in the context of single-phas and two-phase mixed oxides respectively. The accuracy of the x-ray method i single-phase mixed oxides is thus rather poor whereas in two-phase mixed oxides th accuracy of this method is comparable to that reported for the thermogravimetri method.

An O/M measurement by the x-ray method takes less than an hour which is muc shorter a period as compared to 6–8 hr required by the thermogravimetric metho

6. Conclusions

The x-ray diffraction technique provides a convenient method for measuring th O/M of U-Pu mixed oxides. In single-phase mixed oxides (Pu < 30%), the x-ra method is based on measurement of the lattice parameter of the mixed oxide. Th

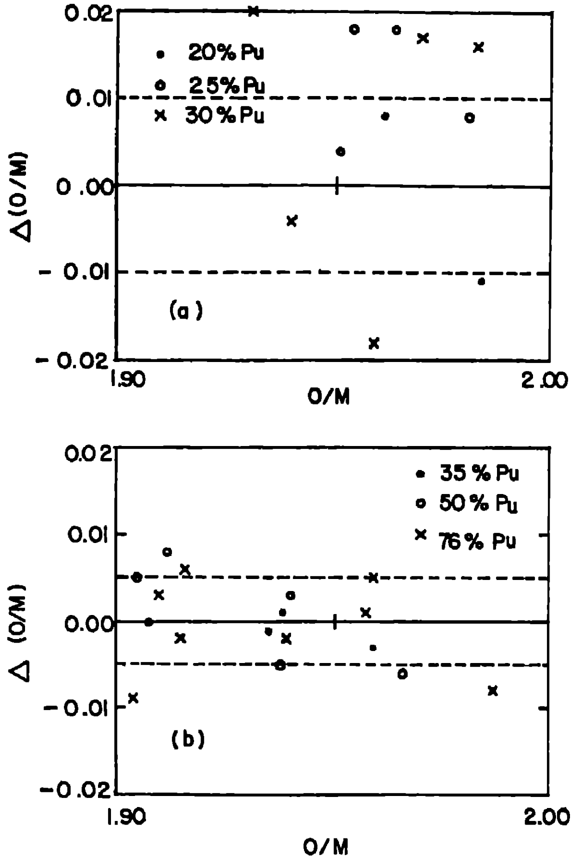

Figure 6. Difference in O/M determined by x-ray method and that determined b thermogravimetric method versus the latter; (a) single-phase mixed oxides, (b) two-phas mixed oxides.

accuracy of the method is approximately ±0·01 which is poor compared to that o the thermogravimetric method.

For two-phase mixed oxides, the x-ray method of O/M measurement is based o measuring the volume fractions of the stoichiometric and the sub-stoichiometri phases in the mixed oxide. In this case the x-ray method has an accuracy of ±0·005 which is comparable to that reported for the thermogravimetric method.

As compared to the thermogravimetric method, the x-ray method is faster, non destructive and does not require a furnace or gas handling system. The method ca be easily automated for on-line applications.

References

Belle J 1961 Uranium dioxide: Properties and nuclear applications Naval Reactors, Division of Reacto Development, USAEC

Blank H, Benedict U and Sari C 1967 in Technical Report Series (Vienna:IAEA) No. 79 p. 56

Brett N H and Russell L E 1963 *Trans. J. Br. Ceram. Soc.* **62** 97

Dean G 1965 *Proc. 3rd Int. Conf. on Plutonium* (ed) A E Kay and M B Waldron (London: Chapman and Hall)

Dean G and Pascard R 1967 in Technical Report Series (Vienna:IAEA) No. 79 p. 56

Dean G *et al* 1970 *Proc. 4th Int. Conf. on Plutonium and other actinides Santa Fe, New Mexico* (ed) William N Miner (New York: Metallurgical Society)

Gardner E R, Markin T L and Street R S 1965 *J. Inorg. Nucl. Chem.* **27** 541

Gibby R L 1969 Battelle Northwest (USA) Report BNWL 927

Lay K W 1971 *J. Am. Ceram. Soc.* **54** 18

Lyon W L 1963 General Electric (USA) Report GEAP 4271

Lyon W L and Bailey W E 1965 *Trans. Am. Nucl. Soc.* **8** 376

Markin T L and Street R S 1967 *J. Inorg. Nucl. Chem.* **29** 2265

Matzke H J 1976 in *Plutonium and other actinides* (Amsterdam: North Holland) p. 801

McNeilly C E and Chikella T D 1971 *J. Nucl. Mater.* **39** 77

Mufford R N R and Ellinger F H 1958 *J. Am. Ceram. Soc.* **80** 2023

Schmidt H E 1968 Progress Report 4, European Institute for Transuranium Elements

Van Craeynest J C and Weilbacher J C 1968 *J. Nucl. Mater.* **26** 132

Varma R 1983 *J. Nucl. Mater.* **118** 325

Zebroski E L, Lyon W L and Baily W E 1965 Int. Conf. on Safety, Fuels and Core Design in Large Fast Breeder Reactors, Argonne

Bull. Mater. Sci., Vol. 8, No. 4, October 1986, pp. 489–496.
© Printed in India.

Kinetics of calcium molybdate crystallization

N M BATRA and S K ARORA
Department of Physics, Sardar Patel University, Vallabh Vidyanagar 388 120, India

MS received 17 June 1985; revised 24 October 1985

Abstract. Kinetics of crystallization of calcium molybdate from unstirred molten solutio of lithium chloride of low to medium supersaturation in platinum crucibles by the process continuous cooling at 5° C hr^{-1} from temperatures $T_0 = 700$ and 750° C are investigate The crystal size measured by optical microscopy for different crystallization periods revea that both crystal length and width generally increase with cooling period. The degree crystallization α_p also increases with cooling period, attaining a maximum of 0·90. Th diffusion rate constants, K_{Dl} at 700 and 750°C are 0·0776 and 0·1138 respectively. The effe of variation of the crystallization temperature on the crystal size and their number is als studied.

Keywords. Calcium molybdate; crystallization kinetics.

1. Introduction

Crystallization of inorganic materials from high temperature solution has bee studied by many workers (Laudise 1963; Kroger 1964; White 1964; Schroedger an Linares 1966; Elwell and Scheel 1975). Alkaline earth metal molybdates and tungstate have been prepared by crystallization from lithium chloride and sodium tungstat or molybdate metals (Groot 1947; Moon 1948; Klick 1949; Anikin 1956; Va Uitert 1960; Ouwetjes 1965; Packter and Roy 1971). Packter and Roy (1973, 197 1975) studied some of the crystallization kinetics of alkaline earth metal compound Kinetics of precipitation of alkaline earth metal molybdates have also been briefl studied (Packter 1977). However, only preliminary reports on the kinetics of crysta growth of calcium molybdate are available in literature and therefore we hav undertaken further studies of the crystallization kinetics of calcium molybdate fro an unstirred supersaturated solution in molten lithium chloride. These results ar reported here.

2. Experimental

2.1 *Materials*

The chemicals used were $CaMoO_4$ powder (ICN Pharmaceuticals, New York) an hydrated LiCl (Burgoyne, Bombay). A 100 ml platinum crucible was employed t hold the growth charge.

2.2 *Solubility*

Calcium molybdate solubilities in LiCl melt at 650 to 900°C were determined b supersaturation method. For this purpose, lithium chloride powder (5 g) was melte in a platinum crucible and the temperature was measured with a chromel/alumel thermocouple and controlled using a variable voltage transformer. Increasing amounts of ground metal molybdate were then added to the molten solvent until a saturated solution was attained; the solution was considered saturated when traces of excess solute were visible at the bottom of the crucible. The solubility was thus determined from the weight of solute dissolved.

2.3 *Crystallization*

From the solubility data, appropriate quantities of flux and solute were weighed, mixed thoroughly using a pestle and mortar and then packed into the platinum crucible with a loosely fitting lid to prevent excessive evaporation. The saturated solutions were prepared at temperature, given by

$$T_l = T_0 + \Delta T,$$

where T_0 is the temperature at which the crystallization is intended to be studied and $\Delta T = 50°\mathrm{C}$. The charge was heated at T_l for an hour. The furnace was then rapidly cooled to the crystallization temperature T_0 and then soaked for an hour. After soaking, it was cooled at a uniform rate of $5°\,\mathrm{C\,hr^{-1}}$ for different periods ranging from 1 to 17 hr, after which the crucible was withdrawn from the furnace and the undissolved crystals were separated from the solidified matrix by leaching with hot distilled water. The crystallization was studied at $T_0 = 700$ and 750°C and the crystals were characterized essentially by EDAX and XRD. Crystal sizes were measured by optical microscopy.

Crystallization was next studied at $T_0 = 650$, 700 and 750°C, but the charge was cooled from T_0 to the eutectic (550°C) at $5°\mathrm{C\,hr^{-1}}$. The furnace power was then turned off and the crucible allowed to cool to room temperature. The effect of variation of crystallization temperature on the final crystal sizes and number was also studied.

3. Observations and discussion

The solubility of calcium molybdate at different temperatures is shown in figure 1. The observed increase in solubility with temperature is quite favourable for the crystal growth. The charge was deliberately heated at 50°C above T_0, to ensure removal of any undissolved excess nuclei which might have remained at T_0; failure to carry this out usually resulted in considerable spurious nucleation. Calcium molybdate crystallized as tetragonal bipyramids with well-developed (011) faces. The average crystal lengths l_t and widths w_t were both measured using a travelling microscope (least count 0·001 cm). The l_t (cm) vs t (hr) and the w_t (cm) vs t (hr) plots are shown in figure 2. One observes that the crystal size increases with increasing crystallization period and the growth rate is higher at larger temperatures. However, after about 10 hr of cooling the change in crystal size was very small, giving a final, almost consistent size, l_{fin} and w_{fin}. Probably, the limiting growth rate is imposed by surface kinetic processes, such as dissolution, ledge integration of kinks and steady removal of solvent molecules from the surface. At times, spontaneous nucleation of further crystals might also limit the experimental, maximum feasible, growth rate (Laudise 1963).

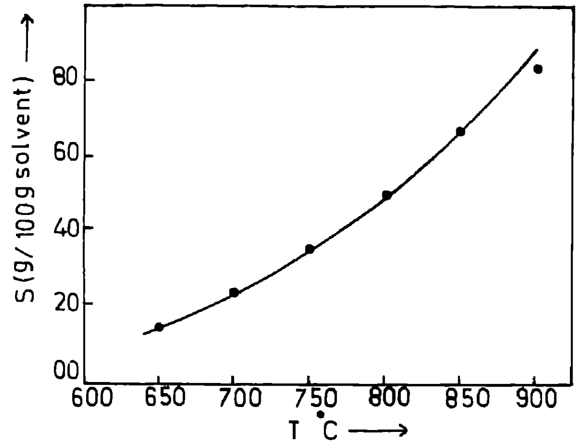

Figure 1. Solubility of $CaMoO_4$ in LiCl at different temperatures.

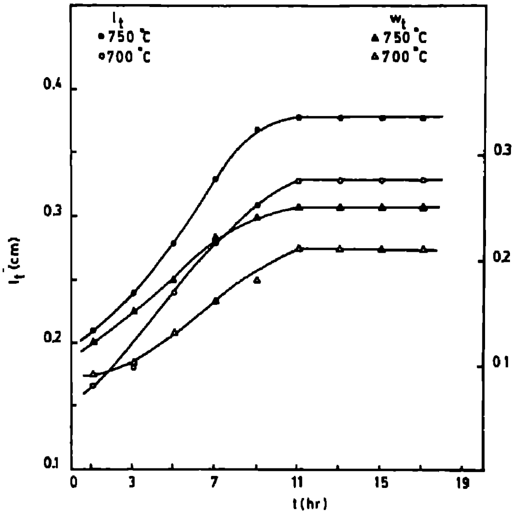

Figure 2. Variation of average crystal length and width at different cooling periods f 700° and 750°C.

The degree of crystallization, α_t, measured by the ratio between the amount substance crystallized to the total amount able to crystallize, is defined as (Nielse 1964)

$$\alpha_t=(C_0-C_t)/(C_0-S), \quad (1$$

where C_0 is the concentration at $t=0$, C_t the instantaneous concentration an $S(=C_{sat})$ the solubility. One can also write,

$$\alpha_t=l_t^3/l_{fin}^3 \quad ($$

where l_t and l_{fin} are instantaneous and final lengths, respectively. It is evident that since l_t is sensitive to the cooling time (figure 2), α_t becomes a function of the crystallization period and this relationship for 700° and 750°C is plotted in figure 3a, α_t increases monotonically with time, reaching $>0{\cdot}9$ after about 9 hr of crystallization.

Crystal growth rates in unstirred solutions of low permeability are generally controlled by the rate of diffusion of material on different growth faces. The deposition rate of the metal salt ions on growing surfaces from low viscosity LiCl melt, at any time, would then be expressed by the relation (Mullin 1961; Nielsen 1964; Treybal 1968)

$$\frac{\mathrm{d}l}{\mathrm{d}t} = \frac{2\,\mathrm{Sh}\Phi_1(\varepsilon)D\Delta C_t}{l_t}\,\frac{\rho_f}{\rho_x},\ \frac{\mathrm{cm}}{\mathrm{sec}} \tag{3}$$

where Sh is the Sherwood dimensionless function, $\Phi_1(\varepsilon)$ an overall shape permeability factor, D the diffusion coefficient of metal salt ion, Ca^{+2}, ΔC_t the instantaneous excess $\mathrm{CaMoO_4}$ concentration expressed in g/g solution ($\mathrm{d}l/\mathrm{d}t$ however depends on α_t through ΔC_t), ρ_x the crystal density and ρ_f the fluxed-melt density.

In the present case of unstirred molten solution where the natural convection is very poor, $\mathrm{Sh} \simeq 2$ (Treybal 1968), one obtains

$$\mathrm{d}l/\mathrm{d}t = (2\,K_{Dl}\Delta C_t)/l_t,\ \mathrm{cm/sec}, \tag{4}$$

where K_{Dl} is the rate constant (dependent on the permeability factor) for diffusion-controlled growth of the longer crystal-pyramid side. A general solution of equation

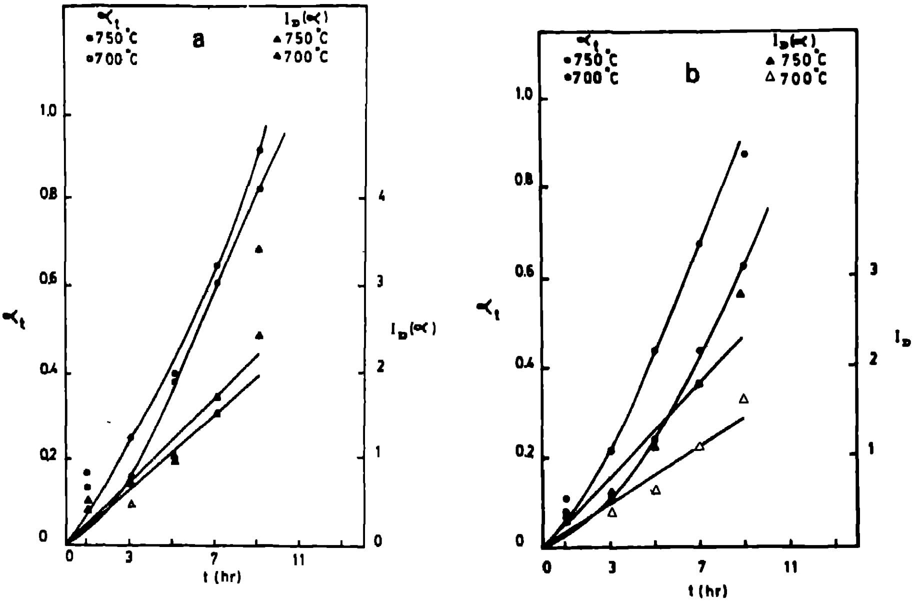

Figure 3. Degree of crystallization α_t and I_D (α) at different cooling periods for 700° and 750°C. **a.** for length **b.** for width.

(4) for all α_t values can be given as,

$$I_D(\alpha) = \int_0^{\infty} \frac{d\alpha}{\alpha^{1/3}(1-\alpha)} = \left(\frac{12K_{Dl}\Delta C_0}{l^2_{\text{fin}}}\right) t = t/K_D. \tag{5}$$

The rate constant of metal salt deposition K_D, having the dimension of time, contains all physical constants of the process, including K_{Dl}, ΔC_0 and l^2_{fin}. Furthermore, $I_D(\alpha)$ is identified as the dimensionless time, or chronomal, which is a characteristic parameter for diffusion-controlled and polynuclear-layer controlled growth mechanisms. It signifies that if the size of a particle is known at a certain time, one can calculate at constant concentration the time at which it started with zero size. The integral in (5) can be solved using standard methods (Lamer and Dinegar 1950) to give

$$I_D(\alpha) = \tfrac{1}{2}\ln\left[\frac{(1-\alpha)}{(1-\alpha^{1/3})^3}\right] - \sqrt{3}\tan^{-1}\left[\frac{\sqrt{3}}{1+2\alpha^{-1/3}}\right]. \tag{6}$$

This equation predicts the overall kinetics of crystallization. The value of diffusion chronomal $I_D(\alpha)$ obtained with the help of Nielsen's table (Nielsen 1964) are plotted with time as shown in figure 3a for 700° and 750°C respectively. The two plots are seen to be linear upto $\alpha_t \simeq 0{\cdot}61$ for 700°C and $\alpha_t \simeq 0{\cdot}65$ for 750°C. Similarly expressing the rate of diffusion-controlled growth of the shorter side of the crystal bipyramid as

$$dw/dt = (2K_{D_w}\Delta C_t)/w_t, \ \text{cm/sec} \tag{7}$$

the Nielsen's relation for this case would be

$$I_D(\alpha) = \left(\frac{12K_{D_w}\Delta C_0}{w^2_{\text{fin}}}\right) t = t/K_D\,, \tag{8}$$

α_t and $I_D(\alpha)$ vs t(hr) plots are shown in figure 3b. Both the plots are linear upto $\alpha_t \simeq 0{\cdot}44$ and $\alpha_t \simeq 0{\cdot}68$ for 700° and 750°C respectively.

It is interesting to find the rate constant K_{Dl} and K_{D_w} at different crystallization temperatures from $I_D(\alpha)$ vs t(hr) plots using the relation,

$$K_{Dl} = \frac{\text{Grad}[I_D(\alpha) \text{ vs } t \text{ plot}] \times l^2_{\text{fin}}}{12\Delta C_0} \frac{\text{cm}^2}{\text{sec}} \tag{9}$$

and

$$K_{D_w} = \frac{\text{Grad}[I_D(\alpha) \text{ vs } t \text{ plot}] \times \omega^2_{\text{fin}}}{12\Delta C_0} \frac{\text{cm}^2}{\text{sec}}. \tag{10}$$

The required ΔC_0 values were estimated from solubility vs temperature data (figure 1), and the results are shown in table 1.

In order that a crystal may grow from solution, the solute must essentially be transported through the solution to the growing surface, desolvated and arranged in conformity with the crystal structure. Therefore, both diffusion and convection are important in controlling the growth velocity. But, when the crystal was relatively smaller than say about 10 μ, convection may be neglected in view of the very low velocity of growth fronts in normal gravity fields. At this stage, when convection is insignificant, crystal growth takes place principally due to Fick's steady diffusional concentration gradients. The fact that this state is established around the crystal at a much faster rate than the rate at which the solution in its close vicinity would be replenished, has been proved by Nielsen (1964). This also explains the initially faster growth rate. Such a situation, on an average, exists in the present case upto about 63% (corresponding to $\alpha_t \simeq 0{\cdot}61$ at 700° and 0·65 at 750°C) and the remaining growth may, however, be surface-reaction-controlled, approximated by

$$l_t^3 = l_0^3 + K_R(t - t_0),$$

where K_R is the surface-reaction rate constant.

The fact that the remaining 37% of growth occurs by surface-reaction needs confirmation. This could not be done experimentally because it is not possible to measure the surface tension of solid substances, though some attempts have been made in this direction (Kuznetsov 1957) with non-convincing results. Nonetheless, the fact that the lateral growth rate is diffusion-controlled to only about 44% is corroborative of the pyramidal morphology of the crystal with its C-axis much larger than either lateral axis.

Further, to understand the effect of crystallization temperature on the final crystal size and the crystal numbers, the final crystal lengths (l_{fin}) and widths (w_{fin}) were measured, and the number N of crystals that grew from 100 g solution was

Table 1. Initial excess solute concentration ΔC_0 and rate constant at different temperatures

Temp. (°C)	ΔC_0 (g/g solution)	Rate constant (cm^2 sec^{-1}) $10^{-4}K_{Dl}$	$10^{-4}K_{Dw}$
700	0·069	0·0776	0·0234
750	0·071	0·1138	0·0526

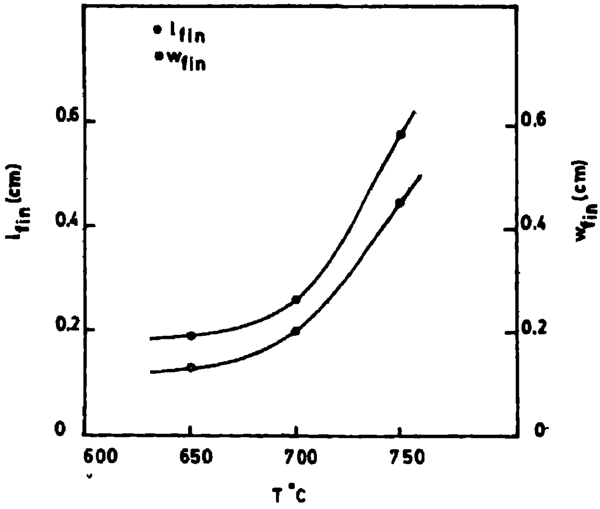

Figure 4. Variation of final crystal length and width at different crystallization temperatures.

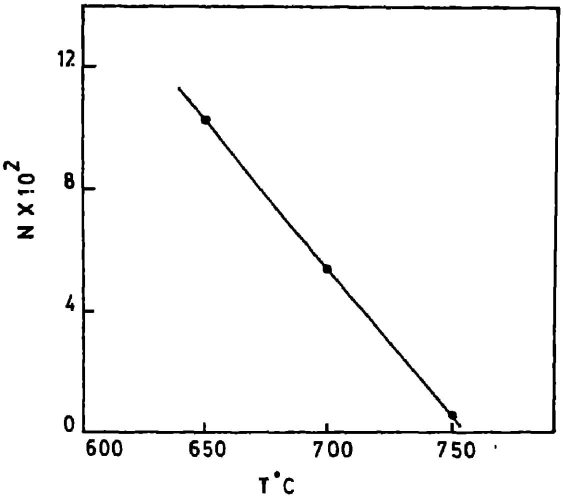

Figure 5. Variation in crystal numbers at different crystallization temperatures.

determined from the average crystal lengths using the relation (Roy and Packt 1980)

$$N=(\Delta w_{tot}/\rho_x f_s l_{fin}^3)\ 100\ \mathrm{g\ solution}^{-1}, \quad (1$$

where Δw_{tot} is the total weight of crystals forming from 100 g solution cooled ov the temperature range T_0 to T_{eut} (eutectic temperature=550°C), ρ_x is the cryst density and f_s is the shape factor determined by the volume V,

$$V=f_s l^3. \quad (1$$

The effect is shown graphically in figures 4 and 5, revealing that the crystal si increases while the crystal number decreases with increasing crystallizati temperature. This supports the general expectation that the smaller the crystal nuc concentration the larger will be the crystal size in a growth process.

Acknowledgement

One of the authors (NMB) thanks UGC, New Delhi for a fellowship.

References

Anikin I N 1956 *Dokl. Akad. Nauk.* **110** 259
Elwell D and Scheel H J 1975 *Crystal growth from high temperature solutions* (London: Academic Pr
Groot W DE 1947 *Phillips Tech. Rev.* **9** 321
Klick C C 1949 *Phys. Rev.* **75** 1606
Kroger F A 1964 *Chemistry of imperfect crystals* (Amsterdam: North Holland) p. 31
Kuznetsov V D 1957 *Surface energy of solids* (London: HMSO) translated from Russian.
Lamer V K and Dinegar R H 1950 *J. Am. Chem. Soc.* **72** 4847
Laudise R A 1963 *The art and science of growing crystals*, (ed) J J Gilman (New York: John Wiley) p

Moon R J 1948 *Phillips Tech. Rev.* **73** 1210
Mullin J W 1961 *Crystallization* (London: Butterworths) ch. 3
Nielsen A E 1964 *Kinetics of precipitation* (Oxford: Pergamon) ch.3
Ouwetjes J C 1965 *Mod. Mater.* **5** 188
Packter A and Roy B N 1971 *Kristall. Tech.* **6** 39
Packter A and Roy B N 1974 *Kristall. Tech.* **9** 1361
Packter A and Roy B N 1975 *Kristall. Tech.* **10** 385
Packter A and Roy B N 1973 *J. Cryst. Growth* **18** 86
Packter A 1977 *Kristall Tech.* **12** 729
Roy B N and Packter A 1980 *J. Cryst. Growth* **49** 368
Schroedger J B and Linares R C 1966 *Prog. Ceram. Sci.* **4** 195
Treybal R E 1968 *Mass transfer operation* (New York: McGraw Hill) ch. 3
Van Uitert L G 1960 *J. Appl. Phys.* **31** 328
White E A D 1964 *Tech. Inorg. Chem.* **4** 31

Bull. Mater. Sci., Vol. 8, No. 4, October 1986, pp. 497–503.
© Printed in India.

Thermal transformation in a chrysotile asbestos

A K DATTA, B K SAMANTARAY and S BHATTACHERJEE
Department of Physics, Indian Institute of Technology, Kharagpur 721 302, India

MS received 19 December 1985

Abstract. Structural changes accompanying thermal transformation in a chrysoti asbestos sample of Indian origin upto a temperature of 900°C have been investigated by x-ra method. The changes in lattice parameters have been systematically measured by applying least square refinement technique and the crystallite size and strain defects at different stag have been estimated by line profile analysis of the diffraction peaks. The present study al confirms the earlier results on stepwise transformation of chrysotile fibres. This sequence transformation has been explained assuming two different types of crystallites as reported kaolinite.

Keywords. Dehydration; transformation; chrysotile; asbestos; x-ray diffraction.

1. Introduction

Chrysotile asbestos is of great scientific interest and commercial value because of i complex structure and multiple uses. It belongs to the serpentine group of cl minerals with 1:1 layers which curl into cylindrical rolls. Its ideal formula per ha unit cell is $Mg_3Si_2O_5(OH)_4$ and is built up of alternate half layers of silicate ar brucite (magnesium hydroxide). Misfit between the two half layers results curvature with the longer brucite layer lying on the convex side. The curved laye form cylindrical fibrils with the *a*–axis along the fibre axis, *b* along the circumferen and *c* along the radius of the fibres (Brindley and Brown 1980).

Several studies have been reported (Brindley and Zussman 1957; Glasser *et* 1962; Martin 1977; Hey and Bannister 1948; Santos and Yadà 1979) using differe methods. These results show that chrysotile with the loss of structural wat transforms into an anhydrous phase around 600°C followed by formation of fc sterite. Finally above 810°C the anhydrous phase recrystallizes into enstati However, the exact nature of the entire sequence of this transformation mechanism yet to be fully understood.

No attempt has so far been made to study this transformation by applying t technique of line profile analysis for estimating the extent of lattice defects which a likely to increase with temperature in this type of mineral with cylindrical structu Systematic estimation of the crystallite size and strain defects which are present this type of sample with curved structure as described earlier, in conjunction w accurate measurements of the changes of lattice parameters from the x-1 diffraction patterns at different temperatures may reveal several new informati which might suggest a satisfactory model of the entire sequence of t transformation. The present work reports the results of studies carried out o chrysotile sample of Indian origin following this approach.

2. Experimental methods

2.1 *Chemical and differential thermal analysis*

A specimen of chrysotile from Cuddapah (India) was selected for the presen investigation. The sample was silky fibrous in form and about 1 to 2 cm long. Th average chemical composition of the sample is shown in table 1. The result of th thermal analysis is shown in figure 1. It consists of a strong and broad endotherma band with peak at about 660°C followed by a sharp exothermal peak at 814°C characteristic of chrysotile. The broad endothermal peak is, however, marked by a number of small humps resembling necks on either side of the peak corresponding to 595, 715 and 753°C respectively. The finely powdered samples were heated below and above the DTA peak temperatures at 580, 640, 700, 750, 800 and 900°C respectively each for 5 hr.

Table 1. Chemical analysis of chrysotile sample at room temperature.

Component	Percentage
SiO_2	36·72
Al_2O_3	Trace
Fe_2O_3	2·48
FeO	Trace
TiO_2	Trace
MnO	0·04
CaO	1·50
MgO	40·10
Na_2O	0·07
K_2O	0·04
H_2O	18·53

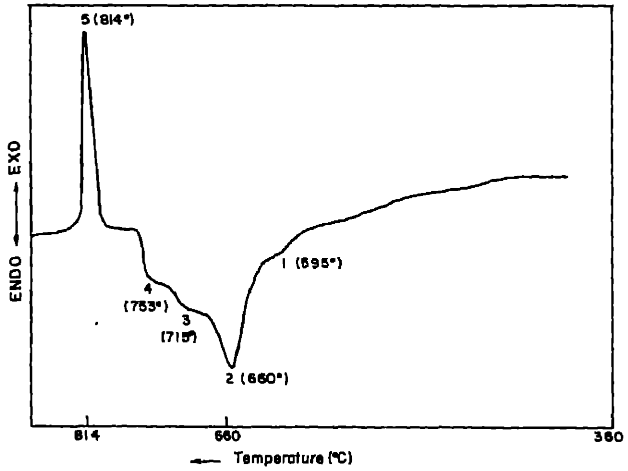

Figure 1. Differential thermal analysis curve of chrysotile.

2.2 *X-ray diffraction analysis*

The sample preparation and the x-ray diffraction techniques followed were similar t those described earlier (Mitra and Bhattacherjee 1969, 1970). X-ray Debye Scherr powder photographs were taken and from the observed *d*-values, the changes i lattice parameters were studied by adopting Ito's (1949) method followed by a lea square refinement using LAPOD programme (Langford and Marriner 1973).

Diffraction profiles of the samples were recorded in a Norelco x-ray diffractomet at a scanning speed of 1/4°/min (2θ) using CuK_α radiation. Crystallite size an microstrain were obtained from the variance of the corrected line profiles and usin the relation (Mitra 1965)

$$\frac{W\cos\theta}{\lambda\sigma}=\frac{1}{2\pi^2 P}+\frac{\lambda n^2}{\sigma\cos\theta}\frac{\langle e^2\rangle}{d^2},$$

where W is the variance in (2θ) unit of the line profile, P is the apparent crystallit size in the direction normal to the reflecting planes with interplanar spacing d; σ i the angular range of the profile; $\langle e^2\rangle$ the mean square strain and θ the Bragg angl of reflection. Thus a plot of $W\cos\theta/\lambda\sigma$ against $\lambda n^2/\sigma\cos\theta\, d^2$ will be a straight lin whose slope gives $\langle e^2\rangle$ and the intercept $P\,(=t/k)$ where t is the true particle siz and k is the Scherrer constant.

The partially overlapped lines were resolved accurately by following the method o Mitra and Bhattacherjee (1970) and corrected for instrumental broadening by usin the profiles of standard silicon sample. The values of crystallite size along the radia direction and the microstrain values were determined from the variance range plot o the (002), (004), (008) and (0010) reflections. The mean values of these parameters ar shown in table 2.

3. Results and discussion

The broad endothermal peak which extends between 568–768°C and marked b several small maxima clearly indicates that dehydration takes place in several steps It is quite likely that there are different groups of particles affected at different stages The sharp exothermal peak at 814°C indicates that rapid recrystallization occurs a this temperature. These results are in conformity with those of the previous worker as mentioned earlier. The x-ray diffraction patterns of samples heated upto 580°C

Table 2. Values of crystallite size and r.m.s. strain as obtained from variance analysis of (001) line profiles of chrysotile asbestos.

Temperature (°C)	Crystallite size (Å)	r.m.s. strain $\langle e^2\rangle^{1/2}\times 10^3$
30	425	1·894
580	615	0·245
640	705	0·653
700	1010	0·334
750	2850	0·733
800	730	0·699
900	625	0·698

exhibited the usual lines, characteristic of chrysotile only. However, the patterns of samples at 640, 700 and 750°C were marked by prominent peaks of forsterite also at 3·88, 3·72, 2·77, 2·81 and 2·46 Å in addition to the existing lines of chrysotile. On the other hand, diffraction patterns of the samples at 800 and 900°C contained, besides these peaks of foresterite and chrysotile, characteristic peaks of enstatite at 2·91, 2·55, 2·31 Å respectively. These observations clearly indicate that chrysotile is converted to forsterite and enstatite in steps during this thermal transformation. During dehydration a part of chrysotile is converted to forsterite only, corresponding to the endothermal peak while partial conversion of chrysotile to both forsterite and enstatite takes place at higher temperatures which correspond to the exothermal region.

Table 3 shows the refined values of the lattice parameters of samples heated to different temperatures. Since prolonged heating even for 100 hr at high temperatures does not fully convert chrysotile (Brindley and Hayami 1965), heating for 5 hr in the present case converts only 40% at 800°C. Hence quite justifiably, the lattice parameters measured from the patterns of samples at higher temperatures and shown in table 2, are considered to be that of the unaffected chrysotile. The room temperature data clearly demonstrate the monoclinic symmetry of the present sample. Table 2 shows that the a-values initially decrease systematically up to 640°C and thereafter increase gradually till 900°C. The b-values also follow the same pattern of variation. On the other hand c-values increase steadily till 750°C beyond which they decrease slowly up to 900°C. However, the b-values do not follow any systematic variation. Thus the temperature variation of lattice parameters in general shows a contraction along the axial a-direction up to 640°C accompanied by an expansion in the radial c-direction up to 750°C. Contraction of the lattice in general and along the fibre axis, in particular, has been observed in fibrous chain silicate clay minerals (Bhattacherjee and Lokanatha 1984). Hence the present results are on expected lines.

On heating cavities possibly open up (Martin 1977) resulting in decrease of curvature of the rolled layers. This may lead to an extension of c along the radial direction with release of strain and subsequent increase in crystallite size upto 750°C as shown in table 3. The curvature along the surface is likely to change nonuniformly resulting in irregular variation of b with dehydration and perhaps is responsible for the slight increase of a-values above 640°C. It may be noted here that this process relates only to chrysotile sample and its dehydration products as the measurements are on the pattern of chrysotile only. After completion of dehydration above 750°C,

Table 3. Variation of lattice parameters of chrysotile with temperature.

Temperature (°C)	a(Å)	b(Å)	c(Å)	β(deg)
30	5·4158	9·1959	14·5424	95·46
580	5·3529	9·1610	14·8328	90·62
640	5·3433	9·4868	14·8435	89·88
700	5·3667	9·5028	15·0812	90·47
750	5·3736	9·5146	15·1236	92·10
800	5·3927	9·4628	15·0560	95·39
900	5·4022	9·5318	14·9318	96·12

the process proceeds at a faster rate due to mutual migration of Mg and Si ions leading to the conversion of greater proportion of chrysotile to forsterite and enstatite. The straightening of the lattice probably causes slight decrease of *c*-values and increase of *a*-values. However, these points need further convincing explanation which is not possible at the present state of our knowledge.

A possible alternative explanation of the gradual transformation of the chrysotile sample into forsterite and enstatite in various steps can be given by assuming the existence of two types of crystallites, namely type I and type II, type I being more prone to dehydration than II as reported in kaolinite (Mitra and Bhattacherjee 1969). At lower temperatures only crystallites of type I get dehydrated and as temperature increases, more and more of type II get affected, while the already affected type I crystallites get converted into forsterite. The reaction rate increases above 800°C and conversion to enstatite also starts. This process will continue unabated even beyond 900°C till the conversion is complete.

The electron micrographs of the samples clearly reveal the usual cylindrical form of the fibres. Measurements of the length and width of the fibrils from the micrographs show that the average length is of the order of 20,000 Å whereas the breadth is about 2000 Å. Dimensions of the fibrils are not changed appreciably at the initial stage of heating. However at very high temperatures (900°C) the fibres collapse and take the form of lumps possibly due to the formation of forsterite and enstatite. Two representative micrographs of the samples, one at room temperature and the other at 900°C (at magnification 50,000) have been shown in figures 2a, b to illustrate these characteristics.

The values of the crystallite size giving the thickness of the layers along the radial *c*-direction and the corresponding microstrain as calculated from the variance analysis of the 001 reflections are shown in table 3. It is seen that the crystallite size increases rapidly from about 400 Å at room temperature to 2800 Å at 750°C beyond which the size falls sharply. The corresponding strain values show a gradual decrease till 700°C and thereafter statistically remain more or less the same upto 900°C. Since the diffraction peaks of forsterite were too small to be accurately measured for variance-range analysis, a rough estimate of the crystallite size has been made from the integral width of the peaks. It has been observed that the crystallite size of forsterite remains almost the same at about 400 Å in the temperature range 640–750°C which corresponds to the endothermal peak in the DTA. Thereafter the size rises sharply in two successive jumps to 700 and 1000 Å at 800 and 900°C respectively. It can be inferred from these data that there is sharp increase of crystallite size accompanied by decrease of microstrain of the forsterite product above 750°C which marks the end of dehydration and the beginning of recrystallization as shown by DTA. The rapid growth may be attributed to annealing effect at such high temperature. The rapid fall in crystallite size of chrysotile accompanied by increase of size of forsterite above 750°C is indicative of conversion to forsterite at a faster rate and larger proportion above 750°C. Also the rapid growth of size of the forsterite suggests that defects are removed from the converted forsterite in this temperature range.

As has been observed (Ball and Taylor 1961) and recently confirmed by several workers (Santos and Yada 1979; Martin 1977) the dehydration of chrysotile goes through several steps. In the first stage there is a removal of the hydroxyl ions, in the second stage there is a slow growth of forsterite because of SiO_2 rich regions

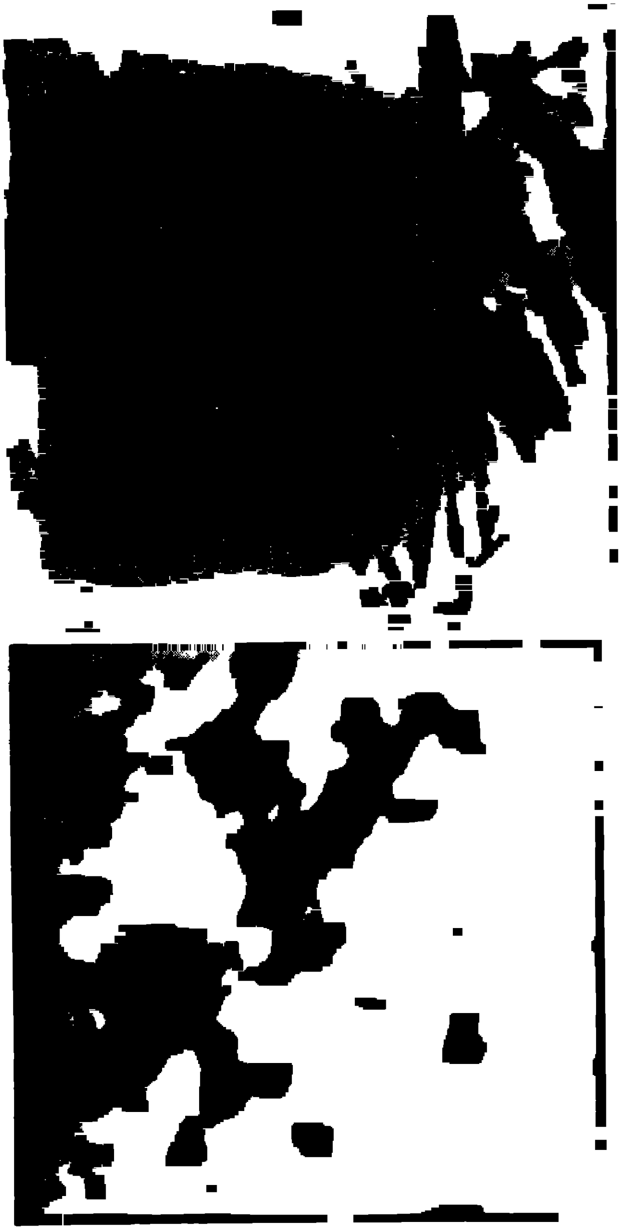

Figure 2. Transmission electronmicrographs of chrysotile sample at different temperatures (a) 30°C. (b) 900°C. × 50,000

inhibiting further recrystallization and a rapid formation of forsterite and enstatite through mutual migration of Mg and Si ions at high temperatures beyond 800°C.

The present observations also confirm the stepwise transformations of the chrysotile fibres leading to the formation of forsterite and enstatite as discussed. However, the present study shows that in the first stage which extends upto about 640°C when dehydration starts with the expulsion of hydroxyl water, the lattice transforms rather slowly mainly due to the contributions of the first type o crystallites. At the next stage which extends upto 750 marking the completion o dehydration, slow conversion of the already affected crystallites of type I int forsterite starts while more of type II gets dehydrated with further lattic transformation accompanied by increase of crystallite size in the radial directio owing to release of strain consequent upon possible opening up of cavities in th curved layer as mentioned earlier. This process continues till 750°C. In the final stag beyond 750°C, rapid recrystallization of the already affected crystallites int forsterite and enstatite takes place with changes of a and c in reverse direction Consequently the size of chrysotile reduces at the expense of development of mor forsterite and enstatite as revealed by the gradual increase of forsterite and enstatit peaks. As the process continues more and more of type II crystallites are converte till the process is complete.

References

Ball M C and Taylor H F W 1961 *Mineral. Mag.* **32** 754

Bhattacherjee S and Lokanatha S 1984 *Trans. Indian Ceram. Soc.* **43** 149

Brindley G W and Brown G 1980 *Crystal structure of clay minerals and their x-ray identificatio* (London: Mineralogical Society) p 13

Brindley G W and Hayami R 1965 *Mineral. Mag.* **35** 189

Brindley G W and Zussman J 1957 *Am. Mineral.* **42** 461

Glasser L S D, Glasser F P and Taylor H F W 1962 *Q. Rev. Chem. Soc.* **16** 343

Hey M H and Bannister F A 1948 *Mineral. Mag.* **28** 333

Ito T 1949 *Nature (London)* **164** 755

Langford J I and Marriner G F 1973 Powder pattern programmes, Univ. of Birmingham, Dept. of Physic

Martin C J 1977 *Mineral Mag.* **41** 453

Mitra G B 1965 *Acta Crystallogr.* **18** 464

Mitra G B and Bhattacherjee S 1969 *Am. Mineral* **54** 1409

Mitra G B and Bhattacherjee S 1970 *Acta Crystallogr.* **B26** 2124

Santos H D S and Yada K 1979 *Clays Clay Miner.* **27** 161

Bull. Mater. Sci., Vol. 8, No. 4, October 1986, pp. 505–509.
© Printed in India.

Effect of H^+ ion irradiation on surface morphology of $Fe_{40}Ni_{40}B$ metallic glass

A J K PRASAD and VAKIL SINGH*
School of Materials Science and Technology, *Department of Metallurgical Engineeri
Banaras Hindu University, Varanasi 221 005, India

MS received 26 June 1986

Abstract. The effect of irradiation by H^+ ions on surface modifications of metallic gla $Fe_{40}Ni_{40}B_{20}$, in the as-quenched, structurally relaxed and crystallized state, has be studied. Swollen regions develop on the surface of the as-quenched and structurally relax specimens, whereas blisters form on the surface of the crystallized specimen, under identic conditions of irradiation. The results are explained in terms of the distribution of hydrog in the amorphous and crystallized conditions.

Keywords. Metallic glass; H^+ ion irradiation; surface morphology.

1. Introduction

The effect of irradiation by gaseous ions like He^+, Ar^+ and H^+ on amorphous allo has been reviewed by Nandedkar and Tyagi (1984) and the irradiation effect has bee found to be strongly influenced by a number of factors such as the state of th material, specific composition, the implanting ion and the defects resulting fro irradiation.

The present study aims at bringing out the effect of H^+ ion implantation on th surface morphology of $Fe_{40}Ni_{40}B_{20}$ metallic glass in three different states, namel as-quenched, structurally relaxed and crystallized.

2. Experimental

Amorphous $Fe_{40}Ni_{40}B_{20}$ (Vitrovac 0040), 12 mm wide and 40 μm thick ribbon wa used. Segments (20 mm long) were vacuum sealed ($\simeq 10^{-3}$ torr) and annealed a 423 ± 2 K and 723 ± 2 K separately for 40 min to cause structural relaxation an crystallization respectively in the material (Toloui *et al* 1985). The complet amorphous nature of the structurally relaxed specimen was confirmed by x-ra diffraction.

The as-quenched, structurally relaxed and crystallized specimens were subjected t pre-irradiation electropolishing in an electrolyte containing acetic acid an perchloric acid in 10:1 proportion at 15 V. Irradiation was carried out with H^+ ion of 250 keV to a fluence in the range of 2×10^{18} to 4×10^{18} ions/cm^2 using a mas analyzed and collimated beam of 3 mm diameter from an AN-400 Vandegra accelerator as described earlier (Yadava *et al* 1980).

The changes in surface morphology of the specimens resulting from H^+ io irradiation were examined by using a scanning electron microscope (Philips PSE 500).

3. Results

The scanning electron micrographs in figures 1–3 respectively show the surface features of the as-quenched, structurally-relaxed and crystallized specimens of $Fe_{40}Ni_{40}B_{20}$ metallic glass following implantation of H^+ ions to a fluence of 4×10^{18} ions/cm^2. A large number of swollen regions developed on the irradiated surfaces of the as-quenched and structurally relaxed specimens and consequently the irradiated surface became rough (figures 1 and 2). The average size of the swollen regions developed on the surface of the structurally relaxed specimen (figure 2a) is smaller than that developed on the surface of the as-quenched specimen (figure 1a).

The dark regions in figures 2a, b arise from excessive localized swelling of the matrix around them. The enlarged views of the irradiated surfaces of the as-quenched and structurally relaxed specimens in figures 1b and 2b respectively show that tiny globular features are associated with the swollen surface of the as-quenched specimen (figure 1b), however, no such features are seen on the swollen surface of the structurally relaxed specimen (figure 2b).

Contrary to these observations, in the case of crystallised specimen, distinct blisters are seen on the surface following H^+ ion implantation (figure 3a). The domes of the blisters (figure 3b) appear quite smooth.

4. Discussion

The implanted H^+ ions produce defects through displacement damage process before they get thermalized at short depths in the near-surface region. Vacancy like defects produced in the amorphous specimens are usually unstable and collapse into the distributed free volume. The major fraction of the implanted hydrogen remains entrapped, particularly in the thin irradiation-affected zone of the amorphous specimens due to increase in the free volume and absence of any potential trapping site and preferential path, to cause inward migration of hydrogen below the irradiation affected zone. Due to neutron irradiation the amorphous $Fe_{40}Ni_{40}B_{20}$ has been found to dissociate into small amorphous regions enriched with boron to approach $(Fe, Ni)_3B$ composition and others depleted of boron (Gerling *et al* 1983; Toloui *et al* 1985). Localized stress fields with tensile and compressive stress systems have also been reported to develop simultaneously (Toloui *et al* 1985). Similar compositional fluctuations and stress fields could develop in this material on irradiation by H^+ ions. High concentration of hydrogen and its clustering at preferred sites in localized regions, with favourable chemical composition and stress system, results in formation of gas bubbles in those regions. The growth and consequent coalescence of the underlying gas bubbles, below those seen as tiny globules at the surface, result in formation of swollen regions (figure 1b).

The smaller size of the swollen regions on the surface of the structurally-relaxed specimen (figure 2a), as compared to the as-quenched one (figure 1a) may be attributed to relatively lower concentration of hydrogen in the irradiation affected zone of the structurally-relaxed specimen. It may occur due to a wider distribution of hydrogen even below the irradiation zone because of the presence of pre-irradiation chemical inhomogenities which have higher solubility for hydrogen in the structurally-relaxed condition. Also the solubility and diffusivity of hydrogen in the

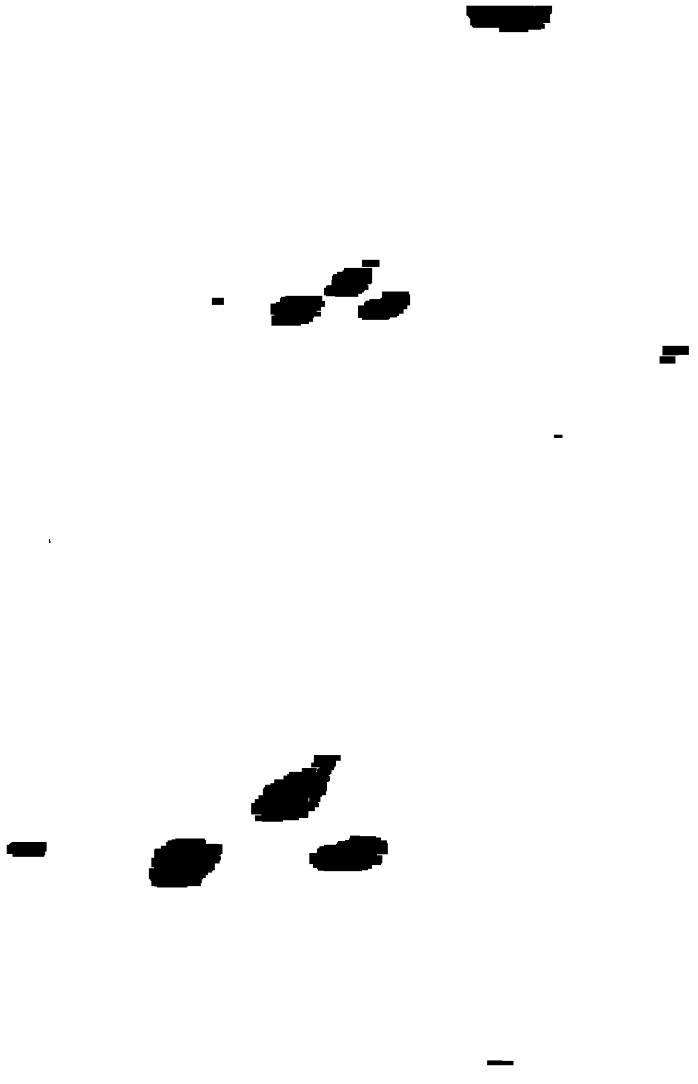

Figures 3a,b. Crystallized.

structurally-relaxed condition would be less than that in the as-quenched state a $Fe_{40}Ni_{40}P_{14}B_6$ (Lin and Johnson 1982). The absence of globules on the swo surface of the structurally-relaxed specimen (figure 2b) may thus be attributed to low concentration of hydrogen in the irradiation-affected zone and hence the sma number of gas bubbles. Swollen features have also been observed earlier in H^+ irradiated amorphous $Ni_{40}Fe_6Co_{20}$ $Cr_{12}Mo_6$ B_{16} (Yadava *et al* 1981) but at a m higher fluence of 1×10^{19} H^+ ions/cm^2. It may be attributed to the higher resista of amorphous $Ni_{40}Fe_6Co_{20}Cr_{12}Mo_6B_{16}$ against irradiation-induced decomposit because of its complex chemical composition. The formation of blisters on surface of the crystallized specimen, following H^+ ion implantation (figure 3) may due to the crystalline nature of the material. Crystallization of amorph $Fe_{40}Ni_{40}B_{20}$ results in the formation of different phases such as ν (Fe-Ni), (Fe, Ni and (Fe, Ni)$_{23}$B$_6$ of varying sizes. Since hydrogen resides in interstitial positions in metals and alloys and diffuses by jumps between the interstitial sites, the solubility and diffusivity of hydrogen would be different in the various crystalline phases, depending upon the size, number and interconnectivity of the interstitial sites per unit cell. The distribution of implanted hydrogen would not be limited only to the irradiation-affected zone, but also below the irradiation zone because of the high solubility of hydrogen in some of the crystalline phases referred to above. The wide distribution of implanted hydrogen in the crystallized state of the material is further favoured by the interphase boundaries. Though the defect sites produced in the irradiated region would act as trap sites for hydrogen, the interaction of hydrogen with defect sites in metals is weak and hence the interphase boundaries, in particular those associated with tensile stress fields and triple junctions with triaxial stresses would be potential sites for trapping of hydrogen in the crystallized specimen.

The high concentration of hydrogen above a critical level at potential trapping sites, at a depth of several hundred Å from the surface, results in nucleation of gas bubbles. The coalescence of bubbles leads to the formation of penny-shaped cavities. The increase in cavity pressure leads to plastic bulging of the thin layer of material above the cavity to form blisters on the surface of the crystallized specimen (figure 3). Formation of blisters on the surface of the crystallized $Fe_{40}Ni_{40}B_{20}$ following H^+ ion implantation in the present investigation is in agreement with the earlier observation made in the crystallized $Ni_{40}Fe_6Co_{20}Cr_{12}Mo_6B_{16}$ (Yadava *et al* 1981).

Acknowledgements

The authors are grateful to Prof. T R Anantharaman, for his encouragement and interest in the work. Useful discussions with Prof. P Ramachandra Rao, Prof. C Suryanarayana and Prof. S Lele are gratefully acknowledged.

References

Gerling R, Schimansky F P and Wagner R 1983 *Scr. Metall.* **17** 203

Lin R W and Johnson H H 1982 *J. Non-Cryst. Sol.* **51** 45

Nandedkar R V and Tyagi A K 1984 in *Metallic glasses* (ed) T R Anantharaman (Switzerland: Trans. Tech. Pub.) p. 165

Yadava R D S, Singh N I, Nigam A K and Singh Vakil 1980 *J. Nucl. Mater.* **92** 366

Yadava R D S, Singh N I, Nigam A K and Singh Vakil 1981 *J. Nucl. Mater.* **101** 124

Toloui B, Kursumovic A and Cahn R W 1985 *Scr. Metall.* **19** 947

Bull. Mater. Sci., Vol. 8, No. 4, October 1986, pp. 511–517.
© Printed in India.

Periodic crystallization of barium oxalate in silica hydrogel

S M DHARMA PRAKASH and P MOHAN RAO
Department of Physics, Mangalore University, Mangala Gangothri, Mangalore 574 199, India

MS received 1 March 1986; revised 5 May 1986

Abstract. The experimental conditions for obtaining periodic crystallization of barium oxalate in silica hydrogel are investigated. The Liesegang rings formed by the reaction of oxalic acid and barium chloride are studied. The dependence of velocity constant and the spacing coefficient on pH, concentrations of inner and outer electrolytes and temperature have also been studied and a possible mechanism for the behaviour is suggested. The deviations from Isemura's general observations are interpreted by considering the microcrystals constituting the rings and the irreversibility of inner and outer electrolytes.

Keywords. Barium oxalate; silica hydrogel; periodic crystallization.

1. Introduction

Periodic precipitation in the form of concentric rings was first observed by Liesegang (1896) during his experiments of chemical reactions in gels. Several theories of Liesegang ring phenomenon have been proposed viz the supersaturation theory (Ostwald 1897; Wagner 1950), the absorption theory (Bradford 1922; Dhar and Chatterji 1922; Shinohara 1970), the coagulation theory (Dhar and Chatterji 1922), the diffusion wave theory (Ostwald 1925), the comprehensive theory (Hedges 1932) and the flocculation theory (Shinohara 1970). All these theories only partially explain the experimental observations. Two laws govern Liesegang phenomenon. The first one is the spacing law given by Jablczynski (1923)

$$X_n = aS^n,$$

where X_n is the distance of the nth ring from the origin of diffusion, and a and S are constants, S being known as the spacing coefficient. The second law is the time law of Morce and Pierce (1903),

$$(X_n/t_n^{1/2}) = K$$

where X_n is the distance to which the precipitate penetrates in time t_n and K is the velocity constant.

The present paper reports our investigation of the conditions for obtaining periodic crystallization of barium oxalate in silica hydro gel. The effects of various factors like the temperature, the concentration of the inner and outer reactants and the pH of the gel medium are considered.

2. Experimental

Experiments were carried out in corning glass test tubes (inner diameter 2·5 cm, length 25 cm). The chemicals used were: sodium metasilicate, oxalic acid (AR) and

$BaCl_2 \cdot 2H_2O$ (AR). The gel was set by mixing sodium metasilicate solution of specific gravity, 1·03 with aqueous solution of 0·5 M oxalic acid in proportions such that the pH of the resulting solutions lay at 4·15, 4·35, 4·55, 4·75 and 4·95 measured immediately after mixing. Barium chloride solutions of 0·7, 0·5, 0·3 and 0·1 M concentration were carefully poured into the tubes over the set gel. The experiments were performed at 31, 37, 43 and 49°C. Cathetometer was used for measuring the position of the rings. Well-spaced rings were nucleated after 20–30 minutes. The time of formation and distance of each ring was recorded. The constants K and S for individual rings and hence for each experimental tube were computed. The Liesegang rings formed in the range are displayed in figure 1.

3. Observations and discussion

In accordance with the time law of Jablczynski (1923), the velocity constant K is independent of X_n and t_n. Similarly the spacing co-efficient S is independent of the order of the ring according to the spacing law of Morce and Pierce (1903). But it is observed that both K and S depend on the concentration of the inner and outer electrolytes and their diffusion coefficients.

3.1 *Variation of K and S with pH*

In figure 2, time and space constants are plotted against pH of the reaction medium, taking temperature and concentration of the outer electrolyte as fixed parameters. The graphs reveal that as the pH of the gel medium increases, the velocity constants (K) and the space constants (S) decrease. The points on the graph for S at different temperatures overlap and show small changes in the value of S with temperature.

Though the pH is the measure of acidity of the gel, it also indicates the concentration of inner electrolyte (or oxalate ions in the present case). Hence, for a particular concentration of the outer electrolyte both K and S decrease almost linearly with increase in the concentration of the inner electrolyte. Similar results have been reported from the studies of Liesegang phenomena of various systems (Gnanam *et al* 1979; Kanniah *et al* 1979; Arora *et al* 1982). Thus the inner electrolyte also plays an important role in the Liesegang phenomenon (Matalon and Packter 1955).

The observed decrease of K can be attributed to the increased hardness of the gel which in turn decreases the diffusion rate and increases the time of ring formation. The decrease of S in the present study may be explained as follows: At higher pH, though a lesser amount of Ba^{2+} ions diffuse through the pores of the hardened gel, the concentration of the uniformly spread oxalate ions is quite high. So, when a ring is formed, oxalate ions in the immediate vicinity would be sufficient to complete the reaction with the incoming barium ions. The region from which the oxalate ions diffuse upwards is small and consequently the rings tend to form more closely separated in harder gels, thereby showing relatively lower values of S.

3.2 *Variation in space and time constants with the concentration of the outer electrolyte*

Figure 3 depicts the variation of K and S with the change in the concentration of feed solution at different pH of the reaction medium and different temperatures.

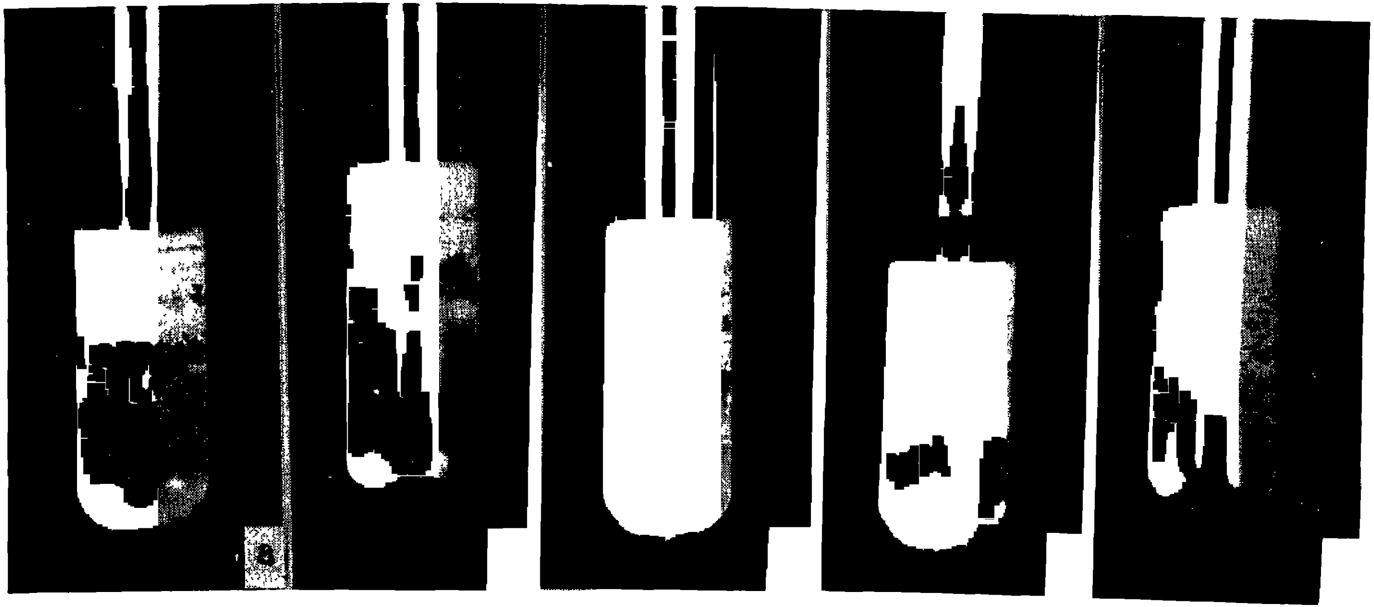

Figure 1. Liesegang rings formed in gel at room temperature (31°C) 0·5 M oxalic acid as inner and (a) 0·1, (b) 0·3, (c) 0·5, (d) 0·7 M barium chloride as outer electrolytes (e) band of precipitation in the gel of basic pH.

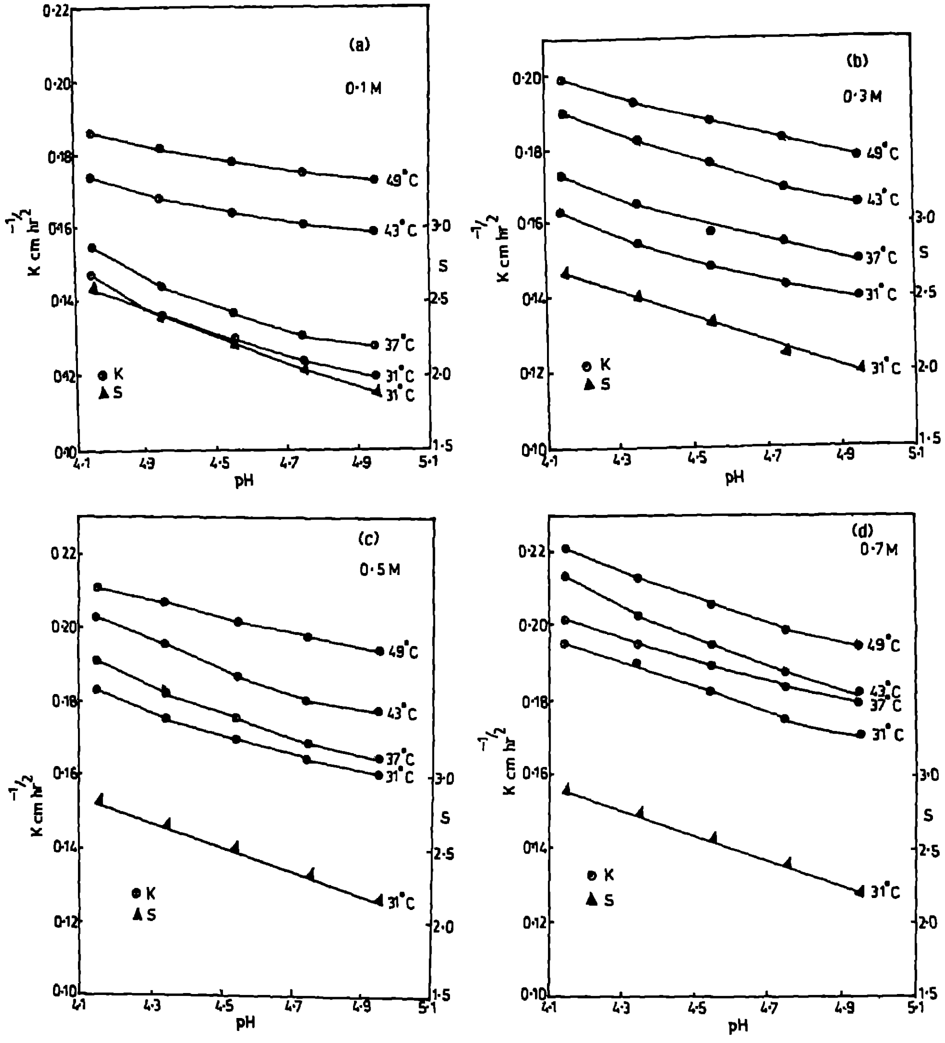

Figure 2. Plot of time constant K and space constant S against gel pH at various temperatures using (a) 0·1 M (b) 0·3 M (c) 0·5 M (d) 0·7 M $BaCl_2$ solutions.

With increased concentration, the diffusion rate of Ba^{2+} ions is enhanced which explains the greater value of velocity constant K. When a larger amount of outer electrolyte diffuses fast into the system containing uniformly distributed inner electrolyte, precipitation begins at the interface and the ring formation occurs below the interface, the growth of which is facilitated from the stoichiometric interior ions diffusing up to the position of the nucleated ring to provide nutrients to the growing crystals. This leaves a larger space below the ring which is depleted of inner electrolyte. Therefore, for the next ring to nucleate, the outer ions have to cross over this barren depletion region to meet with the other reactant. Since the passage is clear without any inner electrolyte, and Ba^{2+} ions diffuse more rapidly, it leads to increase in K.

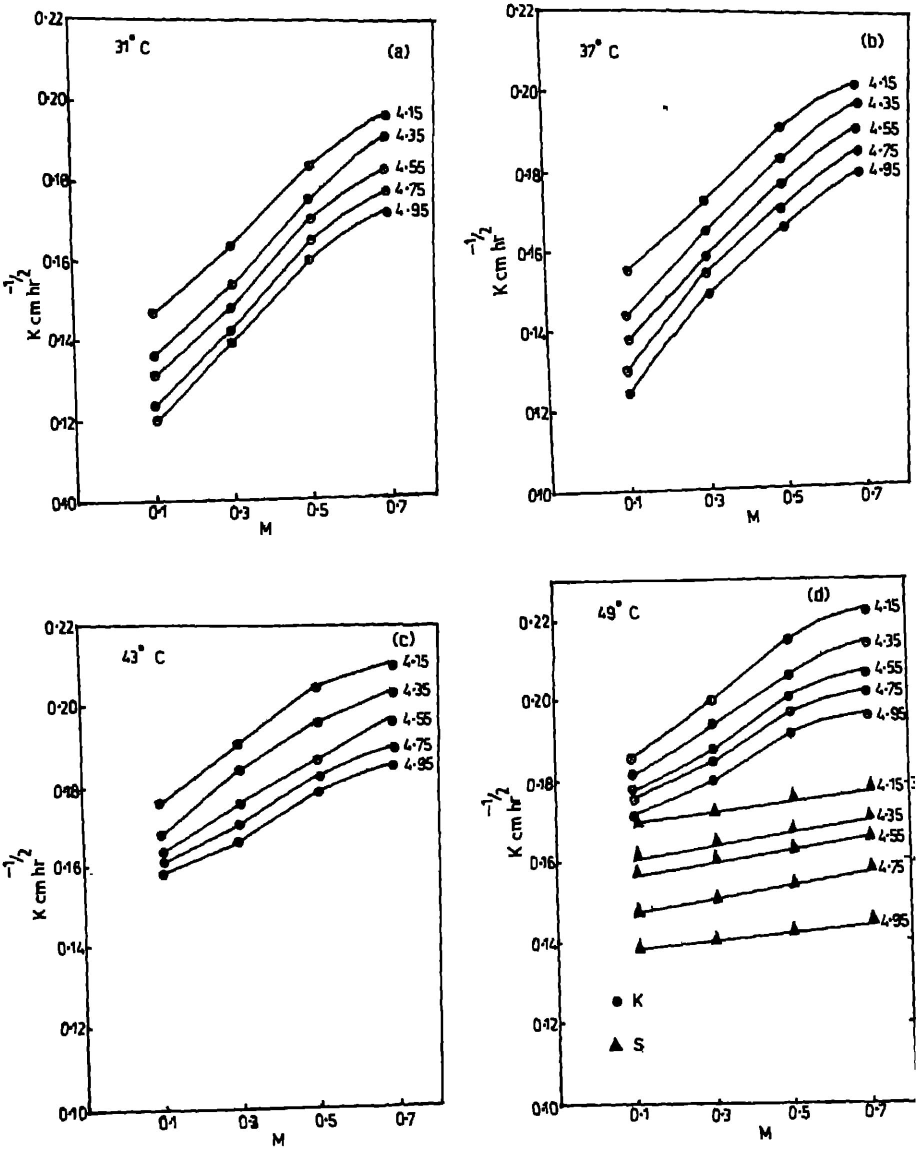

Figure 3. Plot of time constant *K* against concentration of $BaCl_2$ as outer electrolyte us different pH values at (a) 31°C (b) 37°C (c) 43°C (d) 49°C as well as space constant.

According to Isemura (1939), as the concentration of the outer electrol increases, the number of bands also increases and the successive interval betwe them decreases. Barium oxalate rings exhibit a different behaviour so that the to number of bands formed does not vary but the spacings between them increa noticeably with higher concentrations of barium chloride. The contradiction of o results when compared to Isemura's observation can be understood if we consid the nature of rings in both the cases. In amorphous or microcrystalline rings t articles do not tend to grow up after the ring formation, whereas in gs the nucleated crystals do receive nutrients from larger distance rowth of the already nucleated crystal is energetically favourable. This er separation between crystalline rings.

n of K and S with temperature

ws the plot of *K* versus temperature and figure 5 the plot of *S* versus The increased diffusion rate at higher temperature may be responsible ase in velocity constant. There is no appreciable change of space h change of temperature for a given pH and outer electrolyte

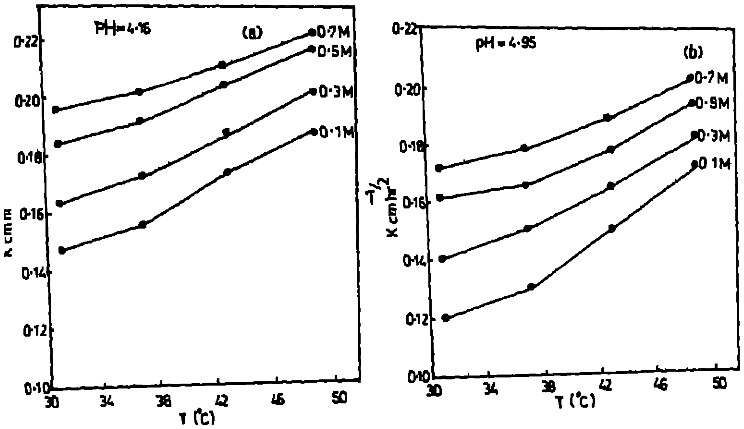

ure 4. Plot of time constant *K* against temperature using different concentration of the er electrolyte at pH values of (a) 4·15 and (b) 4·95.

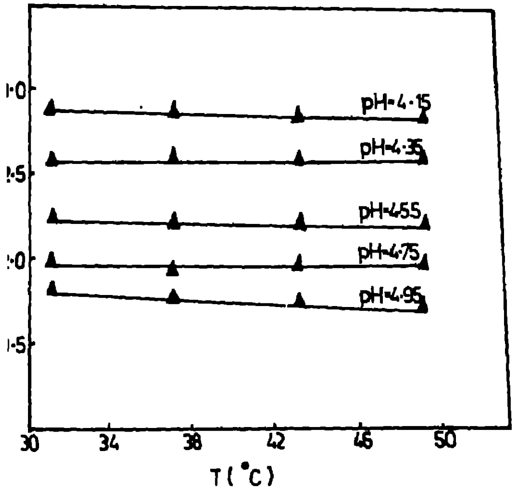

re 5. Plot of space constant *S* against temperature at different pH values.

concentration. This may be because of the competitive increase in the rate c diffusion of both the electrolytes.

Another interesting observation is that the barium chloride incorporated gel fe with oxalic acid as the supernatent solution produces no rings but only dens precipitation. This again contradicts Isemura's (1939) results according to which th interchanging of the reactants (as inner and outer electrolytes) will not affect th appearance of periodic precipitation. The nonappearance of rings when $BaCl_2$ i impregnated with the gel is perhaps due to non-diffusion of the heavier barium ions in the upward direction with sufficient velocity required for the ring formation. The continuous diffusion of oxalate ions from the top results in continuous precipitation.

References

Arora S K, Tomy Abraham and Godebole 1982 *Crystal Res. Technol.* **17** 979
Bradford S C 1922 *Kolloid Zh.* **30** 364
Dhar N R and Chatterji A C 1922 *Kolloid Zh.* **31** 151
Gnanam F D, Krishnan S, Ramasamy P and Laddha G S 1979 *J. Colloid Interface Sci.* **73** 193
Hedges E 1932 *Liesegang and other periodic structures* (London: Chapman)
Isemura T 1939 *Bull. Chem. Soc. Jpn* **14** 179
Jablczynski K 1923 *Bull. Chem. Soc. France* **33** 1592
Kannaiah N, Gnanam F D and Ramasamy P 1979 *J. Colloid Interface Sci.* **80** 377
Liesegang R E 1896 *Naturwiss Wochemschr* **11** 353
Matalon R and Packter A 1955 *J. Colloid Sci.* **10** 46
Morce H W and Pierce G W 1903 *J. Phys. Chem.* **45** 589
Ostwald W 1897 *Lchrbuch der allgemeinen Chemie*, Leipzig 788
Ostwald W 1925 *Kolloid Zh* **36** 380
Shinohara S 1970 *J. Phys. Soc. Jpn* **29** 1073
Wagner C 1950 *J. Colloid Sci.* **5** 85

Bull. Mater. Sci., Vol. 8, No. 4, October 1986, pp. 519–525.
© Printed in India.

Studies on etching of gel-grown barium oxalate dihydrate crystals

S M DHARMAPRAKASH and P MOHAN RAO
Department of Physics, Mangalore University, Mangala Gangotri 574 199, India.

Abstract. Etch pits produced by selective etchants such as 1 M HCl, 1 M HNO_3, 4 M $BaCl_2$, 4 M NH_4Cl and 4 M NH_4Cl–1 M HCl solutions on the as-grown {110} faces of barium oxalate dihydrate crystals are illustrated and explained. The kinetics of etching is studied. From Arrhenius plots, the activation energy of etching and the pre-exponential factor are computed. An empirical equation governing the kinetics has been suggested.

Keywords. Etching; gel growth; barium oxalate dihydrate.

1. Introduction

Etching technique is a powerful tool to study the nature of crystal dislocation Gilman and Johnston (1956) and Keith and Gilman (1960) showed that etch pits nucleate at the points of emergence of dislocations and other defects on the crystal surfaces. Though a voluminous literature can be cited on the study of dislocations by chemical etching, a generally complex etching mechanism (Batterman 1957; Gatos and Lavine 1960; Warikose *et al* 1962) which is at variance with the material and the etchant, is not understood properly to-date. Hence, a trial and error method is adopted for the determination of suitable etchant for a material. Since there exists no report in the literature about etching studies on barium oxalate dihydrate crystals i was considered better to subject the crystals to various dislocation etchants.

The present study reports the effect of etching parameters like temperature composition and time on selective etch rate with the different etchants used. All th etching experiments were conducted on as-grown {110} faces.

2. Experimental procedure

The barium oxalate dihydrate crystals employed for etching studies were grown b the gel method (Dharmaprakash and Mohan Rao 1985). A number of AnalaR grad chemical reagents were examined for possible use as dislocation etchant; viz HCl HNO_3, $BaCl_2$, NH_4Cl. It was felt necessary to establish the reliability of an etchan to determine the dislocation on crystal faces, for which microscopic examination wa made of the successively etched faces. Etch pit size was determined by taking a average of measurements on a number of etch pits at a constant magnification usin a filar micrometer eye piece fitted to the optical microscope. Crystals were etched a different constant temperatures between room temperature (31°C) and 49°C Temperature was controlled using a bath regulated within ±0·5°C. Etch rate fo different compositions of the etchants was calculated from a number measurements of the pit size.

3. Observations, results and discussion

Figures 1–3 depict the etch patterns produced by 1 M hydrochloric acid, 1 M nitr acid and 4 M barium chloride after etching for 30 seconds. The etch patte produced by 4 M ammonium chloride after etching for one minute is shown in figure 4. Figure 5 represents etch pits formed by a mixture of 1 M HCl and 4 M NH_4Cl after 30 seconds. It can be seen from these figures that the etch pit morphology depends on the nature of etchant used. Some shallow pits on the etched planes are seen together with deep ones. Micropits are also found (figures 1, 2 and 5) which indicate the general dissolution of the surface, because point defects are too sensitive to etching. Individual pits, not endowed with regular symmetry, are formed some of which are flat-bottomed and the others point-bottomed. Such shallow, flat and micropits formed during etching need not necessarily be related to the sites of dislocation intersection with the surface. Point defect clusters, impurity inclusions, surface damage, foreign particles on the surface, and other often in tractable factors, may also lead to the formation of pits on the habit faces. In order to test whether the etch pits are produced at the emergent sites of dislocation, successive etching is tried with each of the etchants. Successive etching results in pit widening and deepening in all the etchants, thus providing reliability of etchants. Some of the etch pits on the same face are not of the same size and depth. This discrepancy can be explained by the studies of Patel and Desai (1965) who postulated that, while the surface is dissolved by the micropit mechanism, new layers are exposed during continued etching, which means that new end points of defects terminating in the layer just below the cleavage face are attacked by the etchants. At the sites of these newly exposed defects the etch points are therefore bound to form. The time lag in the formation of pits is responsible for the non-uniform sizes of etch. In figures 2–4 the point bottoms of some of the rectangular shaped pyramidal pits are shifted from their geometric centre. The eccentricities of the pits can be explained by postulating the existence of inclined dislocation lines in the body of the crystal (Patel 1961). When the etchant attacks the dislocation sites, the pits thus produced will follow the dislocation lines into the body of the crystal. If the dislocation lines are perpendicular to the face, symmetric pits will be produced. On the other hand, for inclined dislocation lines asymmetric pits will result. When a series of dislocations lying in the same slip plane meet a barrier such as a grain boundary, the dislocation pile-up takes place. The row of etch pits shown in figure 6 represents such an example of the pile-up.

In order to study the kinetics of etching in barium oxalate dihydrate crystals, the etch rates are determined at various temperatures for different concentrations of the etchants. The plots of logarithm of etch rate $\ln R$ vs reciprocal temperature T^{-1} of the etchant in the temperature range 31–49°C for 1 M HNO_3, 1 M HCl, 4 M $BaCl_2$, 4 M NH_4Cl and a mixture of 4 M NH_4Cl and 1 M HCl are illustrated in figures 7, 8 and 9. Evidently the curves follow the Arrhenius equation:

$$R = A\exp(-E/KT),$$

where A is the pre-exponential factor, E the activation energy of the etching process, K the Boltzmann's constant and T the temperature of etchant. From these Arrhenius plots, the values of activation energy and pre-exponential factor are calculated and the results are presented in table 1.

The faster etch rate in NH_4Cl–HCl may be because the fast etching is not sensitive to the energies of the atoms at the surface or to their geometrical configuration (Gatos 1975). It may be the fact that the chemical reaction and diffusion both operate simultaneously making the etching or dissolution process less sensitive to

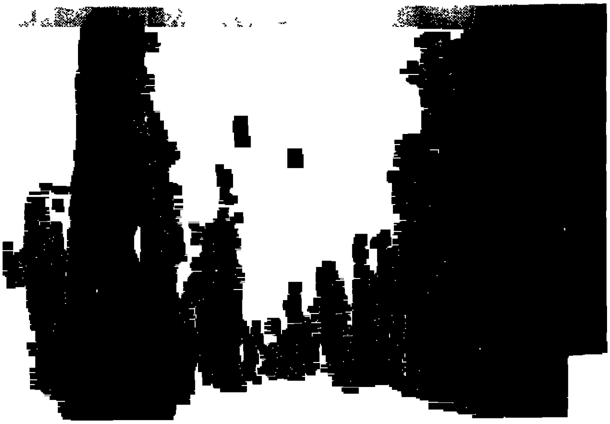

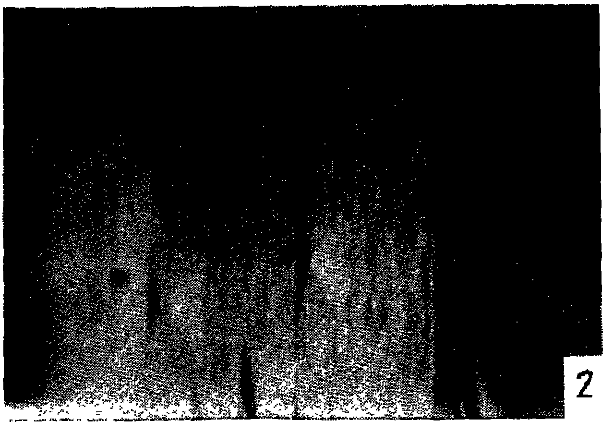

2

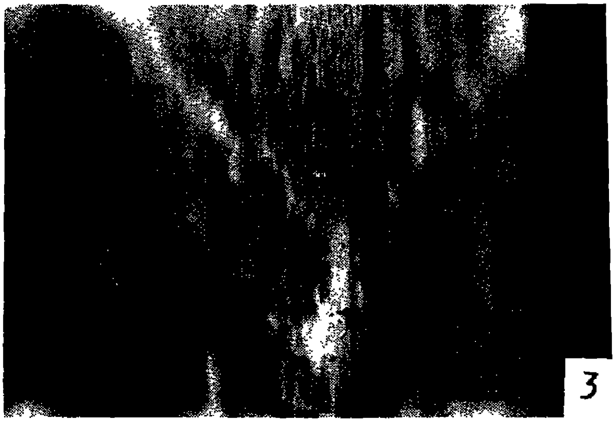

3

Figures 1–3. Etch patterns produced (at 30 sec) by: 1. 1 M HCl. 2. 1 M HNO_3. 3. 4 $BaCl_2$.

temperature change, thus giving a very low value of activation energy. As the etchi proceeds, etchants such as HCl, HNO_3 react with crystals to form oxalic acid, wh in turn dissolves in water. Therefore these dissolutions are reaction rate-controll Among the etchants presently investigated, the etch rate in $BaCl_2$ is low giving

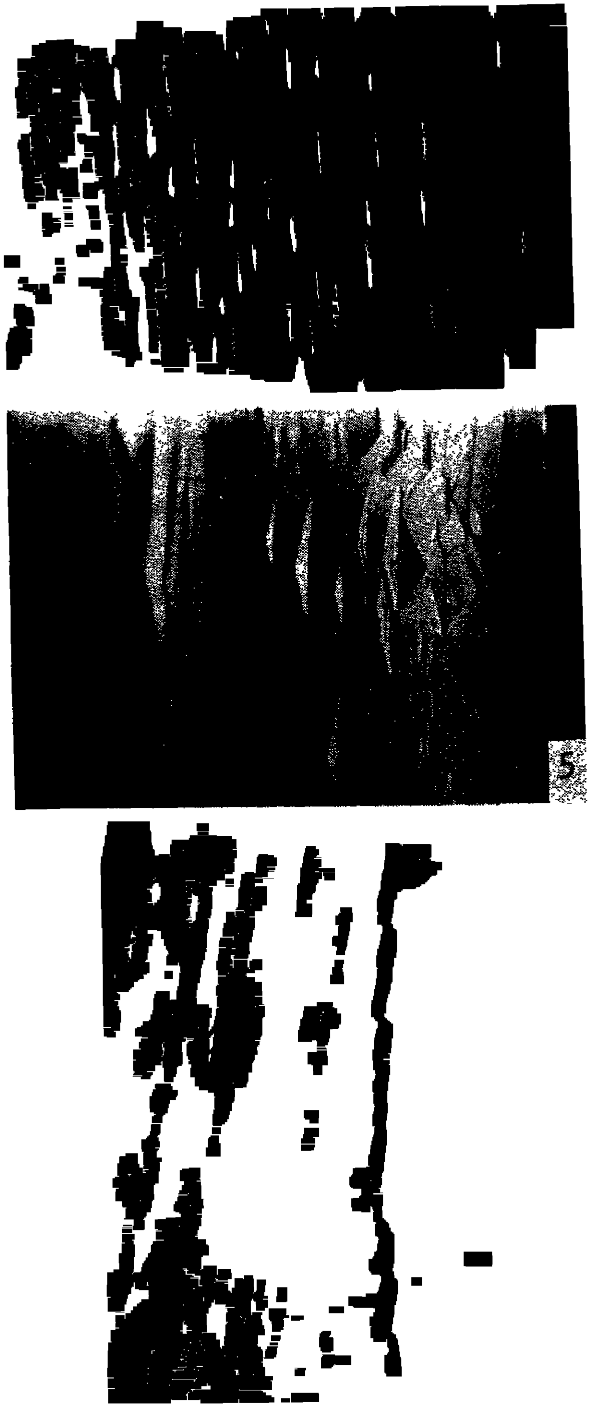

Figures 4–6. **4, 5.** Etch patterns produced (at 30 sec) by. **4.** 4 M NH_4Cl. **5.** 4 $NH_4Cl + 1$ M HCl. **6.** A row of etch pits on a surface etched with 4 M NH_4Cl (1 min)

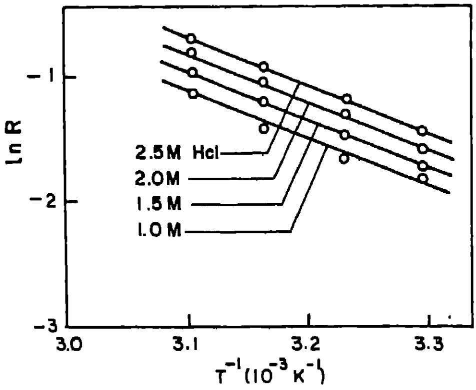

Figure 7. Plot of ln$R$ against reciprocal temperature for HCl

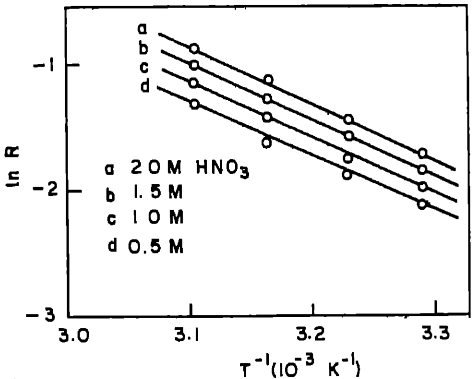

Figure 8. Plot of ln$R$ against reciprocal temperature for HNO_3

highest activation energy. Also the dissolution in $BaCl_2$ is diffusion-controll because of the common ion of the solution and the solvent. The observation tl high activation energy characterizes diffusion-controlled dissolution (as of barii oxalate in barium chloride) is contrary to the observation by Abramson and K (1939) and Tuck (1975) on certain semiconductor materials in which the activat energy for a diffusion process was found to be less than that for a chemical reacti controlled dissolution. It follows, therefore, that the other conclusion of Tuck (19 that the diffusion-controlled mechanism of dissolution is not sensitive to change temperature is contradicted in the present situation. The values of activation ene are independent of acid concentration (table 1) indicating the dependence of etch rate on temperature alone. Further, since the value of pre-exponential facto increases with increasing acid concentration, it implies that A has to be the funct of etch concentration. Figure 10 illustrates the graph of ln$A$ vs ln$C$ from which A be expressed by the empirical relations

$$A = 11{\cdot}896\, C^{0{\cdot}3143}; \quad A = 10{\cdot}8519\, C^{0{\cdot}4444}$$

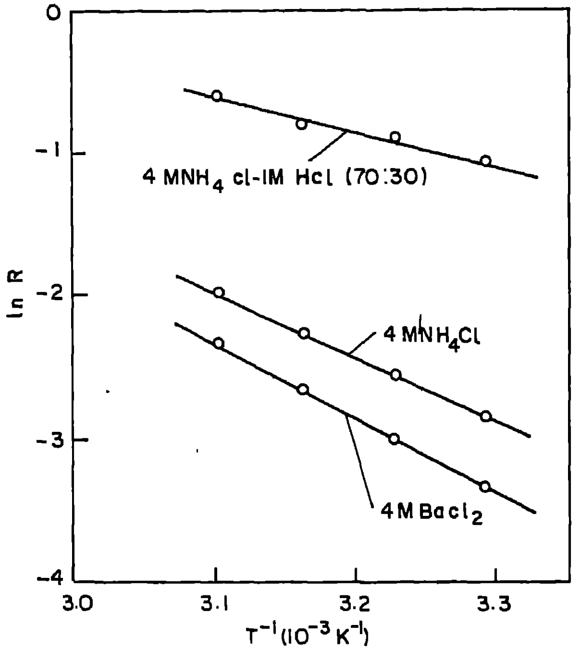

Figure 9. Plot of ln$R$ against reciprocal temperature for $BaCl_2$, NH_4Cl and NH_4Cl–HCl

Table 1. Activation energies and pre-exponential factors calculated from Arrhenius plots.

Dislocation etchants	Etchant concentration (M)	Activation energy E (in ev)	Arrehenius pre-exponential factor ($\times 10^4$)
HNO_3	0·5	0·36	12·53
	1·0	0·36	14·64
	1·5	0·36	16·33
	2·0	0·36	18·84
HCl	1·0	0·34	5·87
	1·5	0·34	6·82
	2·0	0·34	7·77
	2·5	0·34	8·93
NH_4Cl	4	0·38	10·28
$BaCl_2$	4	0·44	92·72
NH_4Cl and HCl	4	0·22	00·13

in the case of HNO_3 and HCl respectively. This would enable us to represent the dissolution of barium oxalate dihydrate crystals by writing the Arrhenius equation in the form

$$R = 11{\cdot}896\ C^{0{\cdot}3143} \exp(-E/KT);$$
$$R = 10{\cdot}8510\ C^{0{\cdot}4444} \exp(-E/KT),$$

where C is the etch concentration of HNO_3 and HCl respectively.

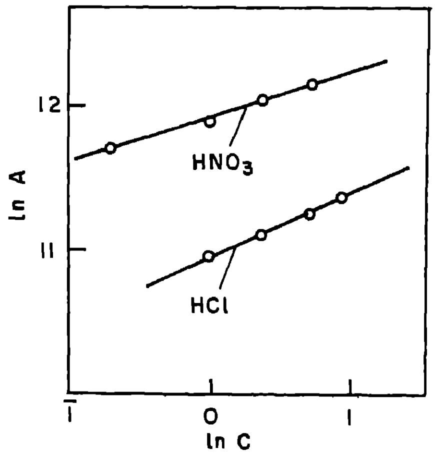

Figure 10. Plot of ln$A$ vs ln$C$

References

Abramson M B and King C V 1939 *J. Am. Ceramic Soc.* **61** 2290

Batterman E P 1957 *J. Appl. Phys.* **28** 1236

Dharmaprakash S M and Mohan Rao P 1985 *J. Mater. Sci. Lett.* **4** 787

Gatos H C 1975 *Crystal growth and characterization* (eds) R Ueda and J B Mullin (Amsterdam: North Holland)

Gatos H C and Lavine M C 1960 *J. Appl. Phys.* **31** 743

Gilman J J and Johnston W G 1956 *J. Appl. Phys.* **27** 1018

Keith R E and Gilman J J 1960 *Acta Metall.* **8** 1

Patel A R 1961 *Physica* **27** 1097

Patel A R and Desai C C 1965 *Acta Crystallogr.* **18** 373

Tuck B 1975 *J. Mater. Sci.* **10** 321

Warikose E P, Lavine M C, Mariano A N and Gatos H C 1962 *J. Appl. Phys.* **33** 690

Bull. Mater. Sci., Vol. 8, No. 4, October 1986, pp. 527–530.
© Printed in India.

Determination of molecular weight distribution of polyethylene terephthalate by gelpermeation chromatography

K SREENIVASAN and PRABHA D NAIR
Biomedical Technology Wing, Sree Chitra Tirunal Institute for Medical Sciences and Technology, Poojapura, Trivandrum 695 012, India.

MS received 18 March 1985; revised 25 April 1986

Abstract. Gel permeation chromatography was used to determine the molecular weight distribution of polyethylene terephthalate. Chloroform was used as the mobile phase. The average molecular weights calculated from the chromatogram closely agree with the known values of the samples used in this experiment.

Keywords. Polyethylene terephthalate; gel permeation chromatography; Styragel.

1. Introduction

A knowledge of molecular weight distribution (MWD) of a polymer is important for understanding the relationship between its structure and properties. Gel permeation chromatography (GPC) is commonly used for determining the MWD. However, the number of solvents which could be used for polyethylene terephthalate (PET) in conjuction with GPC is limited due to the insoluble nature of the polymer in most solvents. Phenols and mixed solvents containing phenols as one of the constituents have been widely used as solvents for PET (Panaris and Pallas 1970; Ede 1971 Didely 1972). The analysis requires, in certain cases, higher temperatures and often affects the detector response of the instrument. Moreover, the use of phenols as the mobile phase drastically affects the performance of the crosslinked polystyrene gel which are widely used as GPC column material (Snyder and Kirkland 1979) Recently hexafluoroisopropanol (HFIP) has been used as a GPC solvent for PET (Drott 1977). However, HFIP is incompatible with low pore size as well as old crosslinked polystyrene packings (Drott 1977; Snyder and Kirkland 1979). Furthe the toxic hazards of HFIP are still not clearly known despite its wide use as a solven for a variety of polymers. Also, the high cost of HFIP restricts its use as a routin solvent for PET.

In this paper, we describe a GPC method using chloroform as the mobile phase fo determining the MWD and average molecular weights of PET.

2. Experimental

2.1 *Materials*

PET samples were from SITRA, India, Analytical grade phenol and chloroform fro BDH, India.

2.2 *Method*

About 25 mg of the PET samples were dissolved in 10 ml of chloroform-phenol mixture (1:1 V/V) at about 50°C. One ml of this solution was diluted with 4 ml o chloroform and filtered through a millipore membrane. 100 μl of the solutions were used for the analysis.

2.3 *Chromatography*

The instrument employed consisted of a solvent delivery pump (Waters Associates Model 6000A), 440 absorbance detector, U6K injector and a set of five μ Styrage columns of pore size 10^5, 10^4, 10^3, 500 and 100 Å (particle size 10 μm). Freshly distilled chloroform at a flow rate of 1 ml/min was used as the mobile phase and columns effluents were monitored at 254 nm. The columns were calibrated using polystyrene standards (Waters Associates Inc, USA) in chloroform.

2.4 *Calibration curve*

0·1% solutions of polystyrene standards in chloroform were prepared. Peak averag molecular weights of the standards chosen were 2,40,000, 1,10,000, 50,000, 9,000 an 4,000. These solutions were filtered and 100 μl of the filtered solution were injecte into the chromatograph. Chromatography was performed under the same condition as used for the samples above. The retention time of each standard i.e. from the sta of the injection to the maximum of the chromatographic peak was plotted on th linear x-axis on semilog paper vs the corresponding value on the logarithmic y-ax of the peak molecular weight of the respective standard. A smooth curve was draw through the points plotted to obtain the calibration curve.

2.5 *Computation*

The direct calibration method was employed for determining the weight averag molecular weight of the PET samples. The data obtained were computed as in DS (1974). The retention times for the start (t_1) and finish (t_2) of the polym chromatogram were marked and a baseline drawn from t_1 to t_2. Peak heights of equally spaced points along the GPC curve were measured and tabulated under t headings: col.1: retention time; col.2: height (mm); col.3: molecular weight; col. col.2/col.3; col.5: col.2 × col.3. The molecular weight averages were determined by t following equations

$$M_n = \Sigma \text{ col.2}/\Sigma \text{ col.4},$$

$$M_w = \Sigma \text{ col.5}/\Sigma \text{ col.2}.$$

The equations are based on the theoretical equation

$$\bar{M}^* = \sum_0^i NiMi^b / \sum_0^i NiMi^{b-1},$$

Where b is a constant, any whole integer, and $\bar{M}^* = M_n$, when $b = 1$, M_w when $b =$ M_z when $b = 3$, respectively.

3. Results and discussion

Figure 1 shows a typical chromatogram of PET in the mobile phase. The number average and the weight average molecular weights were determined from the chromatogram according to the method discussed above and summarized in table 1.

Table 1 also gives the known values of viscosity average molecular weights M_v of the three PET samples A, B and C. The molecular weights obtained by the GPC method can be said to be in good agreement with the known values of M_v as it is known that M_v lies between M_n and M_w but closer to M_w (Allcock and Lampe 1981).

PET is widely used commercially and as a biomedical polymer. In this context, it should be noted that subtle batch-to-batch variation in MWD and molecular weights of PET can cause significant differences in end use performances. The

Table 1. Molecular weights of PET samples

Sample	Number average molecular weight (M_n)	Viscosity average molecular weight (M_v)	Weight average molecular weight (M_w)	Dispersity (M_w/M_n)
A	24,000	54,767	58,175	2·42
B	25,000	40,553	54,669	2·19
C	24,009	56,099	62,147	2·59

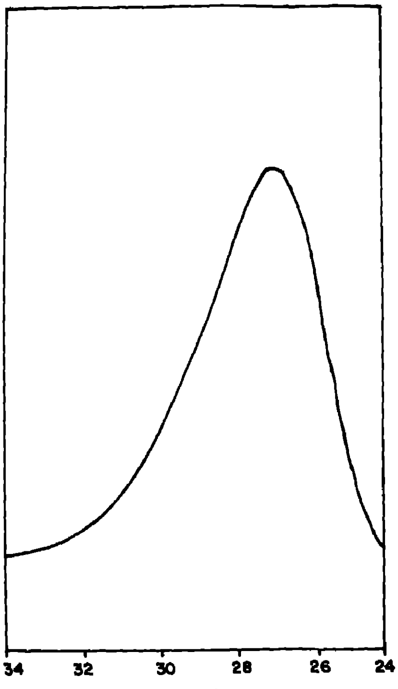

Figure 1. A representative chromatogram of PET.

dependability of a number of properties such as mechanical strength, glass transition temperature etc on MWD and molecular weight further emphasize the need for a simple and rapid method for the determination of molecular weights and dispersity.

Light scattering and viscometric methods, which are also used for molecular weight determinations, however require extensive sample preparation and are too cumbersome for routine determinations. Further, these techniques are incapable of providing any information on MWD.

The hydrodynamic volume of PET molecules in chloroform relative to the conformational status in other good solvents and solvent mixtures has not been assessed. However, the close agreement of the data obtained from the present method with the known values of the viscosity average molecular weight of the samples indicates the absence of any substantial deviation of molecular size in chloroform.

A small quantity of phenol introduced along with the samples elutes after a considerable time and does not interfere with the analysis.

4. Conclusion

The reported method allows the MWD determination of PET at ambient temperature without affecting the efficiency of the crosslinked polytyrene gel columns.

Acknowledgement

The authors thank Mr G S Bhuvaneshwar for the PET samples.

References

Allcock H R and Lampe F W 1981 *Contemporary polymer chemistry* (New Jersey: Prentice-Hall) p. 388

Didely M A 1972 *J. Appl. Polym. Sci.* 16 493

Drott E E 1977 *Chromatographic science series* (ed.) Jack Cazes (New York: Marcel-Dekker) Vol. 8, p. 41

DSO 1974 Waters Associates Application brief, DSO 47, April

Ede P S 1971 *J. Chromatogr. Sci.* 9 275

Panaris R and Pallas G 1970 *J. Polym. Sci.* 16 493

Snyder L R and Kirkland J J 1979 *Introduction to modern liquid chromatography* (New York: Wiley-Interscience) Ch. 12

Bull. Mater. Sci., Vol. 8, No. 4, October 1986, pp. 531–534.
© Printed in India.

Space charge limited currents in chlorazole black E dye

J P S CHAUHAN, D C DUBE and S C MATHUR
Department of Physics, Indian Institute of Technology, Hauz Khas, New Delhi 11001
India

MS received 19 September 1985; revised 18 January 1986

Abstract. Space-charge-limited-currents have been studied in Chlorazole Black E (CB dye to understand the current-voltage relationship and the nature and distribution of tra present in the dye. Three distinct regions of voltage-current characteristics have be observed probably for the first time. The results have been discussed on the basis of carri injection theory. There are non-uniformly distributed deep as well as shallow traps.

Keywords. Space-charge-limited-current; traps; carrier injection; chlorazole black E dye.

1. Introduction

Photovoltaic studies on merocyanine dyes (Morel *et al* 1983; Morel *et al* 1978) ha generated a lot of interest in the studies of electrical properties of organic dy Sharma (1985) collected the various organic solar cells studied so far along with the efficiencies, open-circuit voltages, fill factors and stabilities. These cells use polycrystalline thin film. Though a lot of work has been done on organic dye sol cells (Kudo and Moriizumi 1981; Chamberlain *et al* 1981; Kudo *et al* 19 Yoshimura *et al* 1981; Chamberlain *et al* 1982; Skotheim *et al* 1982; Chauhan *et* 1983; Sharma *et al* 1983; Loutfy *et al* 1983; Sharma 1985), very little attention has far been paid towards studying other electrical properties of the dyes. An importa parameter controlling the photovoltages in thin film solar cells and the electri conductivity of solids is the nature of the traps. In most organic molecular cryst the trap distribution is Gaussian (Silinsh 1970; Silinsh *et al* 1974; Nespurek a Silinsh 1976; Silinsh *et al* 1978). However other types of distribution cannot be ru out. The nature of the traps is reflected in the current-voltage relationship. A study space-charge-limited-current (SCLC) is considered a good probe into the nature a distribution of traps. We have therefore studied the current-voltage characteristics CBE dye. Since thin films of dyes in solar cells are polycrystalline our interest lie the study of polycrystalline samples. Therefore powder compacts of unpurified well as purified material were used for the present studies. The results have been u to understand the nature of the traps and their distribution in the dye.

2. Experimental

The CBE dye obtained from Sigma Chemical Company, USA was only 50% p Since the presence of impurities in organic dyes is a major impediment in investigation of their electrical properties, the dye was subjected to fur purification by chemical precipitation, column chromatography and sublima techniques. For chemical precipitation, a saturated solution of CBE dye prepared in triple distilled dimethyl formamide and filtered to remove the insol impurities. The pure dye was precipitated out by adding chloroform to the filtrate. This process, repeated three times, gave a high purity material but the yield was low. For chromatographic purification, the dye purified by chemical technique, was dissolved in a mixture of propanol, acetone, triple distilled water and acetic acid in 5:5:3:1 ratio. Finally the dye was sublimed under a vacuum of 10^{-6} torr. Unfortunately the dye could not be put to zone refining. But the purity of the dye was estimated to be better than 99·99%. For space-charge-limited-current studies thin pellets were prepared in a evacuable die (Pye Unicam). The pressure applied to the die, having ½ inch diameter was 10 tons. In some preliminary studies it was found that the conductivity of the CBE dye pellet became constant at a pelletising pressure of 10 tons and more. It was also noted that the pelletising pressure does not effect the I-V characteristics at these pressures. The thickness of the samples prepared ranged between 0·09 mm and 0·16 mm. The measuring set-up consisted of a conductivity cell (Chauhan *et al* 1983), a regulated power supply and an electrometer (Keithley 610C). The measurement of current as a function of applied field was taken in dark at room temperature (~300°K). The samples were cycled six times with electric field and all the measurements were taken under steady state conditions. No hysteresis was observed on increasing and decreasing the field. Also no aging effect was observed on I-V curves.

3. Results and discussion

Figure 1 shows the current-voltage characteristics of unpurified and purified samples. The applied electric field was cycled between 300 volts/cm and 12000 volts/cm. As

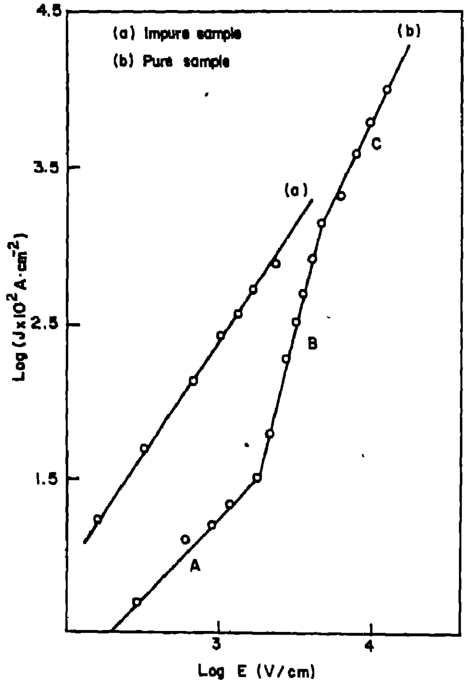

Figure 1. Log J–log E plot for chlorazole black E dye.

can be seen the current-voltage curve, for unpurified sample, follows a straight lir on a log-log plot, having a slope of 1·5 yielding $J \propto E^{3/2}$. For purified sample tl current-voltage curve on log-log plot can be divided into three distinct straight lin marked A, B and C. Straight line A extends upto $E = 1800$ volts/cm and has a slop of 0·96 ($\simeq 1$) indicating an ohmic behaviour. Line B has a slope of 3·4. It starts fro $E = 1800$ volts/cm and extends upto $E = 4500$ volts/cm. The third region starts fro $E = 4500$ volts/cm and extends upto 12000 volts/cm.

It is reported (Lyons and Gutmann 1967; Kao and Hwang 1981) that in trap-fr solids and in solids having only the shallow traps the injected currents follow an law after the ohmic region. But when there are shallow as well as deep traps and tl distribution of the traps is nonuniform, the current varies as E^n where $n > 2$. This the situation presently observed for the region marked B. In case there are shallow well as deep traps and the trap distribution is uniform the injected current vari exponentially with the applied field. Further it has also been reported (Silinsh 19 that the constancy of slope in the log J vs log E curve in the superlinear region of t current-voltage characteristic (region B) with $n > 2$ within a wide range of fie intensity values is an absolutely indispensable condition for the validity of t exponential distribution of traps. In the region C the injected current follows an law. This suggests that at this stage all the traps are filled and the injection is in t conduction band only. In this situation the injected currents follow the Chi Langmuir law, a situation consistent with our observation in region C. So far ther no other study on the traps in chlorazole black E dye which we can use to cro check our conclusions.

Further studies on the CBE dye are in progress and will be reported elsewher

Acknowledgement

Authors wish to thank Professor M L Gulrajani for many useful discussi regarding the purification of the dye. Our thanks are also due to Mr Bala Dut estimating the purity of vacuum sublimed dye.

References

Chamberlain G A 1982 *J. Appl. Phys.* **53** 9

Chamberlain G A, Cooney P J and Dennison S 1981 *Nature (London)* **289** 45

Chauhan J P S, Rai R C, Tripathi A K and Mathur S C 1983 *J. Mater. Sc. Lett.* **2** 149

Kao K C and Hwang W E 1981 *Electrical transport in solids* (New York: Pergaman Press) pp 145

Kudo K and Moriizumi T 1981 *Jpn. J. Appl. Phys.* **20** L553

Kudo K, Shinohara T, Moriizumi T, Iriyama K and Sugi M 1981 *Jpn. J. Appl. Phys.* **20** 135

Loutfy R O, Shing Y H and Murti D K 1983 *Solar Cells* **5** 331

Lyons L E and Gutmann F 1967 *Organic semiconductors* (New York: John Wiley) pp. 558

Morel D L, Ghosh A K, Feng T, Stogryn E L, Purwin P E, Shaw R F and Fishman C 1978 *Appl. Lett.* **328** 495

Morel D L, Stogryn E L, Ghosh A K, Feng T, Purwin P E, Shaw R F and Fishman C 1983 *J. Phys.* **88** 923

Nespurek S and Silinsh E A 1976 *Phys. Status Solidi* **A34** 747

Sharma G D 1985 *Photovoltaic studies on some organic dyes*, Ph.D thesis, Department of Physics, Institute of Technology, New Delhi

Sharma G D, Tripathi A K, Mathur S C and Dube D C 1983 *J. Mater. Sc. Lett.* **2** 433

Silinsh E A 1970 *Phys. Status Solidi* **A3** 817

Silinsh E A, Jurgis A, Gailis A K and Taure L F 1974 Electrical properties of organic solids, Summer School, Karpacz, Wroclaw, p. 40

Silinsh E A, Muzikante I J and Taure L F 1978 Electrical and related properties of organic solids, Paper of Int. Conf., Karpacz, Poland, p. 71

Skotheim T, Yang J M, Otvos J and Klein M P 1982 *J. Chem. Phys.* 77 6144

Yoshimura T, Kiyota K, Ueda H and Tanaka M 1981 *Jpn. J. Appl. Phys.* **20** 1671

Bull. Mater. Sci., Vol. 8, No. 4, October 1986, pp. 535–539.
© Printed in India.

Microstrip losses with Al_2O_3 overlay

K K JOSHI, C DHANAVANTRI, S A GANGAL and R N KAREKAR
Department of Physics, University of Poona, Pune 411 007, India

MS received 19 December 1985; revised 20 June 1986

Abstract. Microstriplines were coated with Al_2O_3 by chemical vapour deposition to ge homogeneous thin film overlay. The paper reports the decrease in the total power loss i such microstrips. The frequency response from 2–6 GHz is studied for the overlay effect.

Keywords. Microstrip; attenuation; microwave power; overlay; aluminium oxide; chemica vapour deposition.

1. Introduction

Open microstrip is the most convenient type of transmission line for fabricatin hybrid and monolithic microwave integrated circuits (MICs). This inhomogeneou open structure has quasi-TEM mode of propagation with electric lines of forc dispersing into air which contribute to radiation losses. Pucel *et al* (1968) has give an expression for conductor and dielectric losses of microstrips. Denlinger (196 expressed radiation loss from microstrip resonator as a function of effective dielectr constant (ε_{eff}), substrate thickness (h) and a free space wavelength (λ_0). The ε depends on the substrate dielectric constant and the distribution of field betwee substrate and air. This distribution is a function of frequency due to contribution higher order modes propagating which are unavoidable because of its structu (Young and Sobol 1974).

The fringing fields from microstrip are often used for coupling the power betwe two close-by strips. The dielectric overlay technique can be used to improve t coupling and directivity as analyzed by Haupt and Delysh (1974), Speilman (197 and Lee (1974). Speilman (1974) reported theoretical analysis for machined alumi stuck on overlay on the alumina substrate; this study of course cannot be direc applied to thin film overlay. Experimental observations on thin film overlay nicrome (Weirather 1974) and Bi_2O_3 (Karekar and Pande 1976) have been report the latter showing an improvement in the quality factor (Q) of rejection filter. Bo the overlays are inhomogeneous with Al_2O_3 substrate.

Only thin film Al_2O_3 overlay can give a near homogeneous structure which reported in this study. The improvement in the parameters of microstrip resonat and couplers can be analyzed if the effect of overlay on parameters of a sin microstrip (like characteristic impedance (Z_0), attenuation and radiation) is kno The total loss of power which includes attenuation and radiation is studied h using transmission and return loss observations, with swept frequency techniq (2–6 GHz) using WILTRON, computer-aided scalar network analyzer. The effec overlay on total loss is studied and is further analyzed to distinguish between effect of overlay on reducing radiation and the effect giving better matching du Z_0 changes.

2. Experimental

Alumina substrates (1 inch × 1 inch Alsimag 772) were locally metallized (at IIT, Bombay) by Cr-Au successive vacuum evaporation. The thickness of gold film was then increased by electroplating upto 8 μ. The three masks for three-line patterns and one mask for five-line pattern were prepared and photolithographically delineated on the substrate. For each mask three sample sets were taken, out of which sixteen lines could be finally used for this experiment. The Al_2O_3 homogeneous overlay was deposited on these patterns by metal organic chemical vapour deposition (MOCVD). The MOCVD system consisted of a resistively heated horizontal flow system (Dhanvantri *et al* 1985). Aluminium isopropoxide was used as a reactant material. The thickness of the overlay was kept constant at nearly 3000 Å. The microwave measurements of transmission and return loss (RL) were performed on a WILTRON network analyzer with an HP-85 microcomputer for correcting the system errors. This gives high accuracy of 56 dB ± 1·5 dB (i.e. the limiting power level is about $\pm 10^{-6}$ mW).

3. Results and discussion

Figure 1 shows a typical transmission and return loss curves before and after overlay, measured using the same connectors, transitions and other components. The average improvement in transmission measured for 16 lines is 0·3 dB over the frequency range of 2–6 GHz. For the same samples and frequency range the average decrease in RL is 5·6 dB which is further used to calculate the power reflection coefficient (ρ^2).

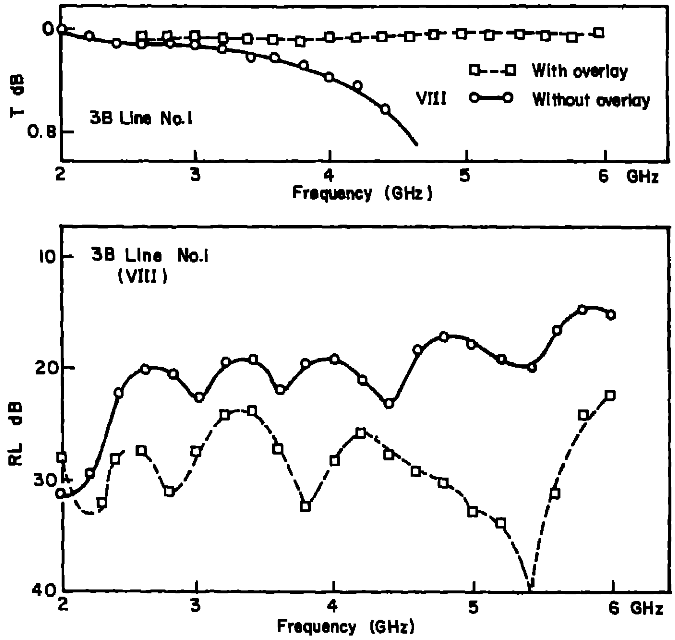

Figure 1. Typical transmission and return loss curves with and without Al_2O_3 overlay.

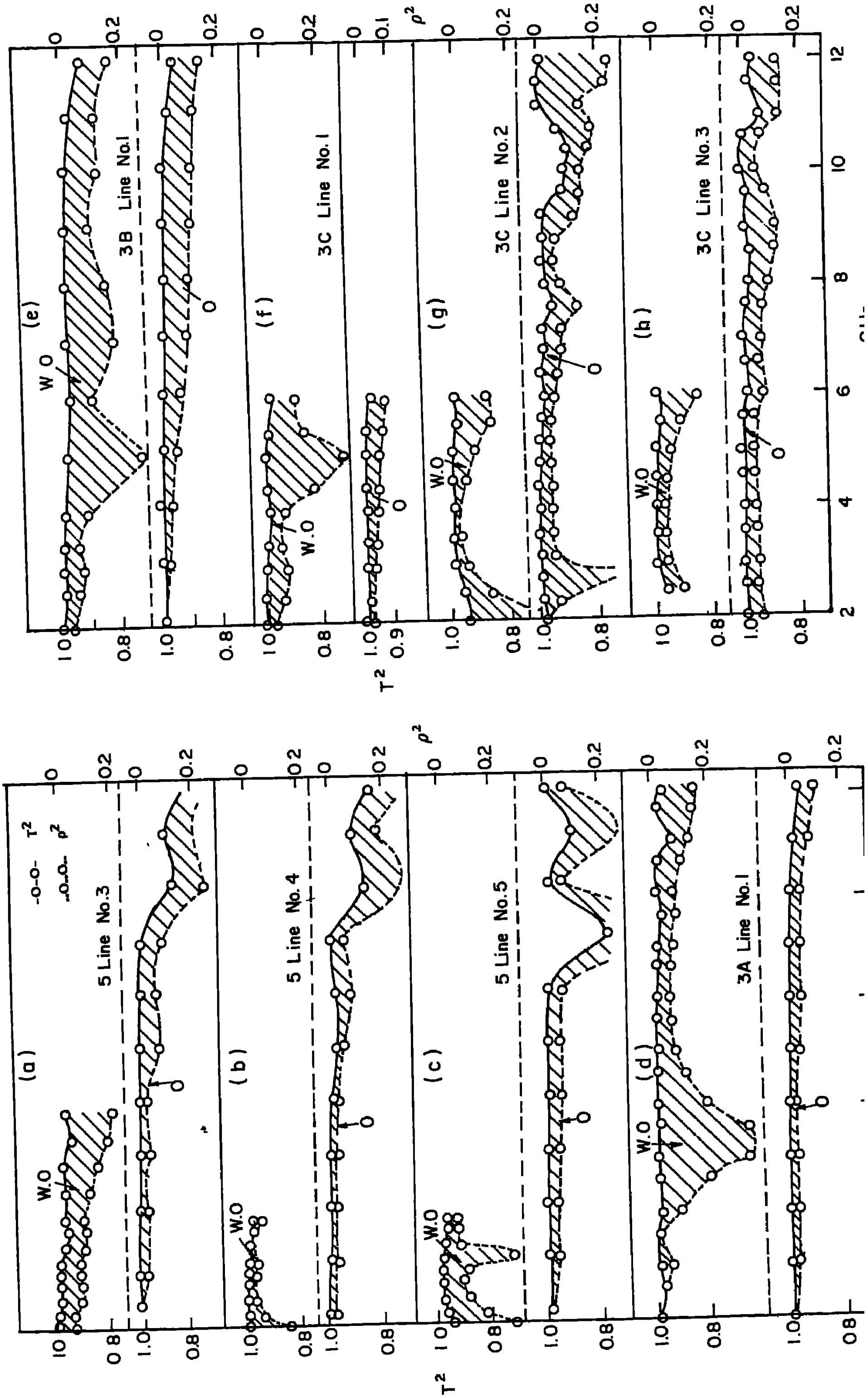
(a)
5 Line No.3
-o-o- T²
-o-o- ρ²
(b)
5 Line No.4
(c)
5 Line No.5
(d)
3A Line No.1
(e)
3B Line No.1
(f)
3C Line No.1
(g)
3C Line No.2
(h)
3C Line No.3
W.O
O
T²
ρ²
1.0
0.8
0.9
0
0.1
0.2
2
4
6
8
10
12

The variation of transmission and RL with frequency show resonant dips at harmonic frequencies. Though the coupling effects are not analyzed in detail, the amplitudes of dips decrease with overlay. The complete data of eight different microstrip widths for ρ^2 and T^2 with and without overlay are given in figure 2, where the shaded portion shows the relative power loss $(1\text{-}\rho^2\text{-}T^2)$. Table 1 gives the corresponding average decrease in the loss due to Al_2O_3 overlay but no specific relationship between percentage loss and strip width is observable. Further the decrease, which is present at all frequencies between 2 and 10 GHz, is more prominent at higher frequencies (in some cases where the readings are available). On an average the decrease is 1·7% at 4 GHz and 8·8% at 6 GHz indicating better wide band operations. The results are sometimes over shadowed due to the coupling between neighbouring parallel lines.

The decrease in total loss of power from microstrip leads to increased transmission of power, whereas increase in the return loss (i.e. reflection coefficient) indicates change in Z_0. Characteristic impedance given by $1/V_pC$ is therefore affected by change in effective permittivity. Our observations show increase in transmitted power (T^2) by about 5% and decrease in the reflected power by about 0·8% at 3 GHz. These figures indicate that the increase in transmission is mainly due to the decrease in microstrip losses. If the change in ρ^2 is comparable to the change in transmission (T^2) then it can be attributed to the improvement in matching, which is not the case. Thus the decrease in total loss is attributed to the following phenomenon.

When a homogeneous overlay is placed on a microstrip substrate a layer of air is replaced by the Al_2O_3 thin film. Thus the propagation mode will tend to move from quasi-TEM towards TEM propagation, reducing the surface mode or other highe order modes, due to increased homogeneity of the medium. Secondly, the fringin field otherwise dispersing in air will be compressed, to some extent, into the overla region because of its high permittivity. Hence the radiating fields will be confine more to the overlay dielectric region which may have manifested in the observe reduction of radiation loss (particularly because the dielectric and conductor losse cannot be expected to decrease with overlay (Pucel *et al* 1968)). Denlinger (196 predicted a similar decrease in the radiation loss with increase in the effecti permittivity. The reported change in ε_{eff} for Bi_2O_3 overlay is 0·9 for the thickness

Table 1. Actual line widths and average percentage loss for the samples at 4 and 6 GHz.

Width W (cm)	Decrease in percentage loss $(1\text{-}\rho^2\text{-}T^2) \times 100\%$ 4 GHz	6 GHz
0·057	4·5	15·0
0·050	−2·0	9·0
0·052	1·0	4·0
0·054	5·0	2·0
0·062	0·0	8·0
0·064	3·5	15·0
0·066	1·0	–
0·069	0·5	–

1·3 μ (Pande 1976). The change in percentage radiation loss is about 1–2% for th change in ε_{eff}, which can be considered as the maximum limit of change percentage radiation in our study. Hence the rest of the average decrease in los especially at a higher frequency, may be attributed to the change in the propagatic mode.

Acknowledgements

One of the authors (KKJ) is thankful to Prof. S Mahapatra and Prof. S M Shrivasta of IIT Bombay for making available fabrication and measurement facilities for tl work.

References

Dhanavantri C, Karekar R N and Rao V J 1985 *Thin Solid Films* **127** 85
Denlinger E J 1969 *IEEE Trans. Microwave Theory Tech.* **17** 235
Haupt G and Delysh H 1974 *Electron. Lett.* **10** 142
Karekar R N and Pande M K 1976 *IEEE Trans. Microwave Theory Tech.* **24** 262
Lee Y S 1974 *IEEE Trans. Microwave Theory Tech.* **22** 66
Pande M K 1976 *Studies on microstrip circuits with special reference to thin film Bi_2O_3 overlay* Pł Thesis, University of Poona, 142
Pucel R A, Masse D J and Hertwig C P 1968 *IEEE Trans. Microwave Theory Tech.* **16** 6
Spielman B 1974 *Analysis of Electrical characteristics of edge-coupled microstriplines with a dielec overlay* NRL Report 7810
Weirather R R 1974 *IEEE Trans. Microwave Theory Tech.* **22** 71
Young L and Sobol H (eds) 1974 *Advances in microwaves* (New York: Academic Press) Vol. 8, p 121

Bull. Mater. Sci., Vol. 8, No. 4, October 1986, pp. 541–542.
© Printed in India.

Thermoluminescence of alkali halides doped with alkaline earth impurities

A R LAKSHMANAN and S V MOHARIL*
Division of Radiological Protection, Bhabha Atomic Research Centre, Bombay 400 085, India
*Department of Physics, Nagpur University, Nagpur 400 010, India

MS received 31 March 1986; revised 12 May 1986

In this note we elaborate some points on LiF mentioned in the review article on "Thermoluminescence of alkali halides doped with alkaline earth impurities" by Deshmukh and Moharil (1985), hereafter referred to as paper I.

(1) The last sentence in § 3·1 of paper I states "In recent years, the 285°C peak has been correlated with the 310 nm band (Lakshmanan *et al* 1982)". This should read as "In recent years, the 285°C peak (peak No. 7 according to the notation of Sunta *et al* 1971) has been correlated by Lakshmanan *et al* (1982) with two-electron centres". Lakshmanan *et al*'s (1982) studies have shown that there is a trap conversion between peak 7 and 450°C (peak 10) centres just as one would expect from $Z_2 \rightleftarrows Z_3$ trap conversion. This has prompted them to suggest that peak 7 correlates with Z_2 centres; not to be confused with 310 nm band as assigned by Nink and Kos (1976). Peak 7 optical absorption (OA) is not yet identified unambiguously because of the presence of intense F(250 nm) band.

Mayhugh (1970) established that the 200°C TL peak (peak No. 5) corresponds to the 310 nm OA band. It is now generally agreed that Nink and Kos's (1976 identification of 310 nm OA with Z_2 centres in LiF : Mg, Ti is not correct (Jain and Kathuria 1978; Nepomnyashchikh and Radzhabov 1980; Horowitz 1982; Caldas *et al* 1983; Mckeever 1984; Lakshmanan 1984).

(2) Mort (1966) and Mort and Zimmerman (1966) empirically predicted the Z centre absorption maximum at 225 nm in LiF : Mg. Nepomnyashchikh and Radzhabov (1980) again predicted the absorption of Mg^0 type centres from semi empirical relation at 225 nm. Lopez and Lopez (1981) predict that Mg should act a an electron trap. On the contrary, Bosi and Nimis (1985) in a recent analysis predic that Mg should form Z centres in LiF. All these diverse predictions show that suc an analysis is premature.

(3) The arguments concerning 310 nm→225 nm conversion during low temperatur optical bleaching and the correlation of 310 nm and 225 nm OA bands with Mg and Mg^0 centres by Nepomnyashchikh and Radzhabov (1980) (refer § 4·1) have bee questioned recently by Lakshmanan *et al* (1985). If the argument that all Mg centres change to Mg^0 centres when peak 5 readout is correct, then one should n have observed peak 5 at all. Even if one assumes that only some Mg^+ centres chang to Mg^0 centres, then the peak 10 (correlated with 225 nm OA) TL in virgin Li TLD-100 should have been considerably greater than that for the 140°C pr irradiation annealed sample, because peak 5 (correlated with 310 nm OA) TL tra

and hence the electrons released from them are a factor of 20 to 30 times higher in the former sample than in the latter one. But experiments show no appreciable difference in peak 10 TL between the two samples (Lakshmanan *et al* 1985).

(4) In § 4·1 of paper I, it is also mentioned that ESR measurements by Watterich *et al* (1980) show that in LiF : Mg, the g value is 2·006 for the F band and 2·029 for the 225 nm band suggesting that the latter is not a Z_3 band. Nevertheless, this band seems to be definitely related to the presence of Mg. Subsequently Watterich *et al* (1984) stated that the presence of OH in LiF : Mg made the ESR investigation of any Mg^+ ions impossible upto now.

Landreth and Mckeever (1985) have recently reported that from their optical absorption data on LiF : Mg, Ti, they find no compelling evidence to relate either the 4·4 eV or the 5·3 eV bands to Z-type centres. The 5·7 eV may be a Z-type defect but of unknown structure. Hence more detailed experimental studies including optical absorption, ESR, ENDOR, Faraday rotation etc are needed to identify the TL trap centres bearing in mind that the behaviour of LiF could be different from other alkali halides.

As mentioned in paper I, the ultimate photon emission step is not satisfactorily elaborated in any of the models in literature. The mobile electron and mobile interstitial models have led to two groups of researchers, each proceeding almost independently and ignoring the work of the other. The recent article by Lakshmanan *et al* (1985) attempts to answer these questions in LiF TLD-100 and suggests that both the processes may be operating at the same time.

References

Bosi L and Nimis M 1985 *Phys. Status Solidi* **B131** K111

Caldas L V E, Mayhugh M R and Stoebe T G 1983 *J. Appl. Phys.* **54** 3431

Deshmukh B T and Moharil S V 1985 *Bull. Mater. Sci.* **7** 427

Horowitz Y S 1982 *Phys. Status Solidi* **A69** K29

Jain V K and Kathuria S P 1978 *Phys. Status Solidi* **A50** 329

Lakshmanan A R, Chandra B and Bhatt R C 1982 *J. Phys.* **D14** 1683

Lakshmanan A R 1984 *Radiat. Prot. Dosim.* **6** 52

Lakshmanan A R, Bhuwan Chandra, Bhatt R C, Hoffmann W and Spallek R 1985 *J. Phys.* **D18** 1673

Landreth J L and Mckeever S W S 1985 *J. Phys.* **D18** 1919

Lopez F and Lopez F A 1981 *Cryst. Lattice Defects* **9** 131

Mckeever S W S 1984 *Radiat. Prot. Dosim.* **8** 3

Mayhugh M R 1970 *J. Appl. Phys.* **41** 4776

Mort J and Zimmerman D W 1966 *Phys. Lett.* **21** 273

Mort J 1966 *Phys. Lett.* **21** 124

Nepomnyashchikh and Radzhabov E A 1980 *Opt. Spectrosc.* (*USSR*) **48** 154

Nink R and Kos H J 1976 *Phys. Status Solidi* **A35** 121

Sunta C M, Bapat V N and Kathuria S P 1971 *Proc. Third Int. Conf. on Lum. Dosimetry*, Riso Report No. 249, Danish AEC and IAEA p 146

Watterich A, Foldvari I, Corradi G and Opyrchal H 1984 *Phys. Status Solidi* **B121** 117

Watterich A, Foldvari I and Voszka R 1980 *J. Phys.* (*Paris*) **41** C6-159

Bull. Mater. Sci., Vol. 8, No. 5, December 1986, pp. 543–546. © Printed in India.

A simple hydrothermal cell for synthesis at moderate temperatures an pressures

J A K TAREEN, B BASAVALINGU, M A SHANKARA and AL
REZA FAZELI
Mineralogical Institute, Manasagangotri, Mysore 570 006, India

MS received 27 February 1986; revised 7 April 1986

Abstract. A simple hydrothermal cell without threaded parts has been developed f routine synthesis of materials at moderate temperatures (upto 500°C) and pressures (up 5 kb). The sealing of the fluid pressure in the cell has been achieved with a cone-se arrangement, but the sealing pressure has been through a hydraulic ram instead of threaded cap. Experience showed that this cell is more convenient for rapid and routi experimentation.

Keywords. Hydrothermal cell; material synthesis.

1. Introduction

The hydrothermal method has increasingly been recognised as a potential techniq for synthesis of inorganic materials, crystal growth (Laudise 1973) and even for t large scale preparation of pure ultrafine oxides (Stambaugh 1982). To mineralogis hydrothermal investigation of the mineral reactions is of immense value to unde stand their paragenesis and the conditions of their formation. Hydrotherm reactors employing different kind of sealing systems (Morey and Ingerson 19 Walker and Buchler 1950; Bridgman 1914; Roy and Tuttle 1956) have been in use f the past few decades. The authors have also designed and fabricated such reactors this laboratory for hydrothermal studies. All these reactors invariably conta threaded parts and call for an extremely precise machining. Except for the Tutt type cold seal reactors, other systems such as Bridgman type etc also need the use deformable gaskets and such gaskets are to be replaced after every experime Further, all these hydrothermal reactors which employ threaded caps for seal need frequent machining for cleaning and dressing the threads.

The high cost for precision machining and the considerable loss of time due to frequently required machining of these reactors was a disadvantage for the rout experimentation. This prompted the authors to develop a more simpler and low c cell which was found to be extremely convenient for routine exploratory runs un moderate temperatures and pressures. This paper is a report of this cell.

2. The new hydrothermal cell

As shown in figure 1*, the cell consists of two parts:

(a) the lower part is the furnace assembly with supporting shell made from mild s

---

*Engineering drawing can be obtained from the author on request.

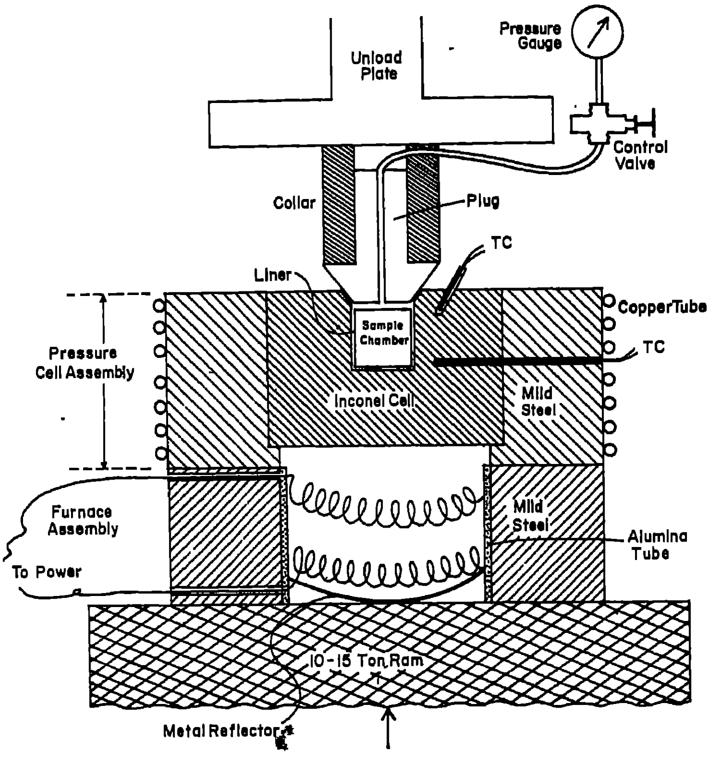

Figure 1. The new hydrothermal cell (scale 1 : 1).

18 series. The resistance heating coil is wound from kanthal AI placed spirally the ceramic sleeve tightly fitted into the supporting shell. The coil power be limited to 30 amp and 50 V to raise the temperature of the sample er to a maximum of 500°C. The power supply is through a voltage stabilizer 50 A variac.

upper part of the system consists of the pressure cell made from inconel. This ressure cell has been tightly heat-fitted into another concentric shell of mild r EN-18 series. The pressure cell (10 cc capacity) has been provided with a eating closure. The seating cone is made from stainless steel 316, preferably ied by heating upto 400°C and quenching in water.

ater or any non-corrosive fluid is used as mineralizer, the cell can be used it a protective liner in the sample chamber. But, with corrosive fluid, the has to be encapsulated in a noble metal ampoule. A small silver liner can also d in which case the pressure generated inside the liner has to be balanced by ting equal pressure outside the liner by using appropriate percent fill of water. essure generated in the cell depends on the initial fluid filled into the cell. For le, if 80% of free volume of the cell is filled with H_2O at 500°C, it generates 3200 bars fluid pressure. The P-V-T diagrams for some fluids such as H_2O edy 1950), CO_2 (Kennedy 1954), HCl (Rau and Kutty 1972), etc are reported make the pressure reading straightforward. Alternatively the fluid pressure could also be read on Bourden gauge connected to the sample chamber through stainless steel high pressure tubing. This is possible only when the charge encapsulated and the pressurising fluid is water or gas.

The quenching of the vessel to arrest the reaction in equilibrium can be achieve by flushing compressed chilled air or water through the copper tubing on the oute shell. The quenching time to cool from 500°C to ambient by this process is abo 10 minutes.

The cell, after being charged with the sample is placed between the two rams hand operated hydraulic press of 15 ton capacity (figure 2) and pressed with abo 5–6 tons of load. The sealing thus achieved will be effective to retain upto 5 k pressure inside the chamber. The use of hydraulic press eliminates the threaded par in the system which makes the sealing as well as opening of the cell considerab simple and rapid, thus reducing the changing time to about 15–20 minutes from o experiment to another. Further, the concentric shell arrangement ensures safe against any rupture. The expected life of the cell is about 10,000 hr. However, owi to the reasonably low cost of the cell (Rs. 500 to 600) it enables any laboratory afford a few spare cells and change them after about 2000 hr of running use. T authors, in fact, have been using a cell for over 2000 hr which still does not call f replacement or re-machining.

Finally, the authors would like to emphasize that the new sealing device suggeste in this report is not a total substitute to the other type of reactors but it is extremely convenient and low cost device for rapid experimentation at modera hydrothermal conditions.

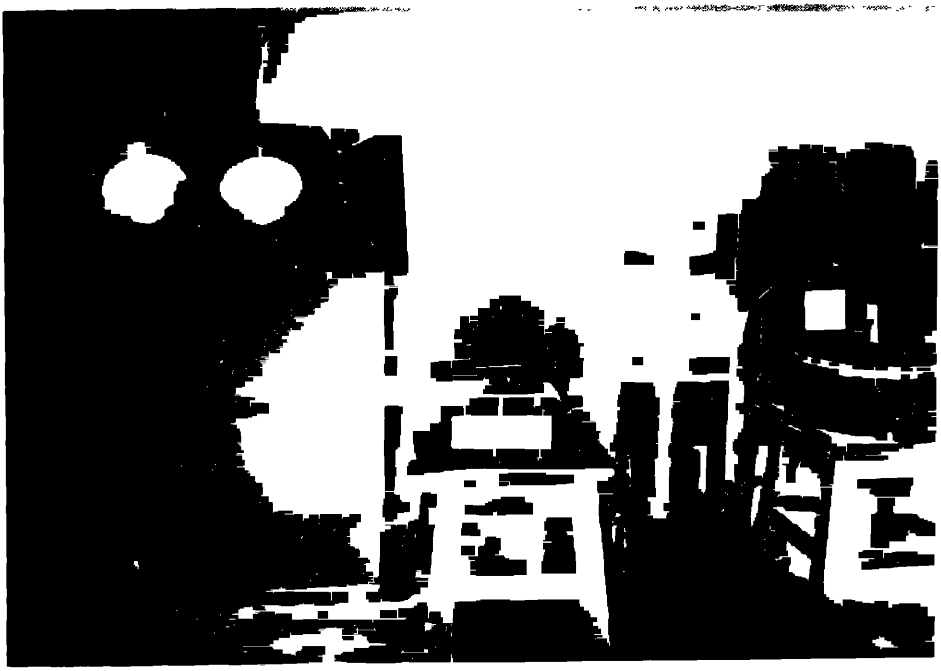

Figure 2. Positioning of the cell between the rams of the hydraulic press.

Acknowledgements

The authors thank Prof. V Venkatachalapathy for encouragement. The skilful machining work of Mr Nadeem-ur-Rehman-Khan is acknowledged.

References

Bridgman P W 1914 *Proc. Am. Acad. Arts Sci.* **49** 625
Kennedy G C 1950 *Am. J. Sci.* **248** 540
Kennedy G C 1954 *Am. J. Sci.* **252** 225
Laudise R A 1973 *Crystal growth: An introduction* (The Netherlands: North Holland Publishing Co.) p 162
Morey G W and Ingerson E 1937 *Am. Mineral.* **22** 1121
Rau H and Kutty T R N 1972 *Ber. Bun. Ges. Phys. Chem.* **76** 645
Roy R and Tuttle O F 1956 *Phys. Chem. Earth* **1** 138
Stambaugh E P 1982 *Proc. First Int. Symp. Hydrothermal Reaction* (Japan: Gakujutsu Bunken Fukyu-Kai) p 859
Walker A C and Buehler E 1950 *Ind. Eng. Chem.* **42** 1369

ıll. Mater. Sci., Vol. 8, No. 5, December 1986, pp. 547–555. © Printed in India.

haracterization and thermal behaviour of lanthanum tartrate crystals rown from silica gels

P N KOTRU, N K GUPTA, K K RAINA and M L KOUL†
Department of Physics, †Department of Chemistry, University of Jammu, Jammu 180 001, India

MS received 15 February 1986; revised 7 May 1986

Abstract. Results obtained on characterization of lanthanum tartrate crystals, grown by the gel method, using chemical analysis, x-ray and electron diffraction, infra-red and mass spectroscopy are reported. The thermal behaviour is studied using DTA, TGA and DTG. The decomposition pattern is reported to be typical of a hydrated metal tartrate. Kinetic parameters like order of reaction, frequency factor and activation energy are evaluated. Contracting cylinder kinetic model is found to be the best fit for the decomposition processes involved. Magnetic susceptibility measurements indicate the material to be diamagnetic.

Keywords. Lanthanum tartrate crystal; thermal behaviour; silica gels.

. Introduction

are-earth materials have attracted considerable attention on account of their uminescent and magnetic properties (Eyring 1964). The present efforts have been nitiated to obtain rare-earth tartrates for various investigations. However, it is ecessary to establish the exact chemical composition and other characteristics of the naterial. In the present work the crystals of $La_2(C_4H_4O_6)_3 \cdot 7H_2O$ were grown by sing the controlled diffusion system of silica gels (Kotru *et al* 1985). Crystals of aried morphologies grown in the gel media are shown in figure 1. A literature urvey showed that no studies have been carried out on the growth or the x-ray liffraction data on lanthanum tartrate crystals. The present characterization of anthanum tartrate crystals is therefore studied and the results obtained from hemical analysis, infra-red and mass spectroscopy, x-ray and electron diffraction nd thermal analysis are discussed.

. Experimental details

To determine the contents of lanthanum (metal), carbon and hydrogen, the material vas subjected to conventional physical and chemical methods. Carbon-hydrogen nalysis was performed and x-ray diffraction pattern recorded on the powdered amples using x-ray powder diffractometer (Phillips model PW1350) with nickelltered CuKα radiations (30 kV, 15 mA). Electron diffraction was obtained by using ransmission electron microscope (AEI TEM-802, UK). Mass spectrum was recorled using JMS-300 at 70 eV. The IR spectrum (range: 300 to 4000 cm^{-1}) was ecorded by employing Spektromom 2000, using KBr pellet technique. Thermal nalysis, involving DTA, TGA and DTG techniques was carried out using a MOM lerivatograph (Paulik-Paulik-Eredey Hungary) at the heating rate of 10°C/min. The

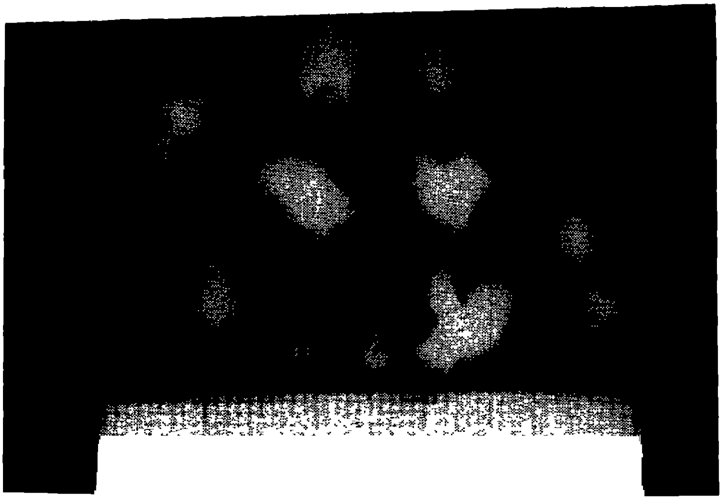

Figure 1. Gel grown crystals of $La_2(C_4H_4O_6)_3 \cdot 7H_2O$ of different morphologies.

weight of the sample used was 200 mg. To identify the final product in TG analysis, x-ray powder pattern was recorded after heating the original compound to 850°C in an electronically controlled muffle furnace working within an accuracy of ± 10°C. Kinetic parameters of solid state reactions from the thermal analysis such as activation energy, order of reaction and frequency factor were determined by using different thermo-analytical kinetic equations and Gouy's balance was used for magnetic susceptibility measurements.

3. Results and discussion

3.1 *Chemical analysis*

To establish the chemical composition of crystals grown, the metal and carbon-hydrogen analysis was made use of. The chemical composition of the material was $La_2(C_4H_4O_6)_3 \cdot 7H_2O$. These results are further supported by TGA in which after the mass loss of 63% La_2O_3 is formed. The TGA results also agree with those obtained from chemical analysis.

3.2 *X-ray analysis*

The x-ray diffractogram recorded (figure 2) indicates the crystallinity of the sample. Table 1 shows the x-ray diffraction data for $La_2(C_4H_4O_6)_3 \cdot 7H_2O$.

3.3 *TEM results*

TEM was used to establish the crystallinity of the sample. It is seen that there is a decomposition resulting in the change of the diffraction pattern. Figures 3(a) and 3(b)

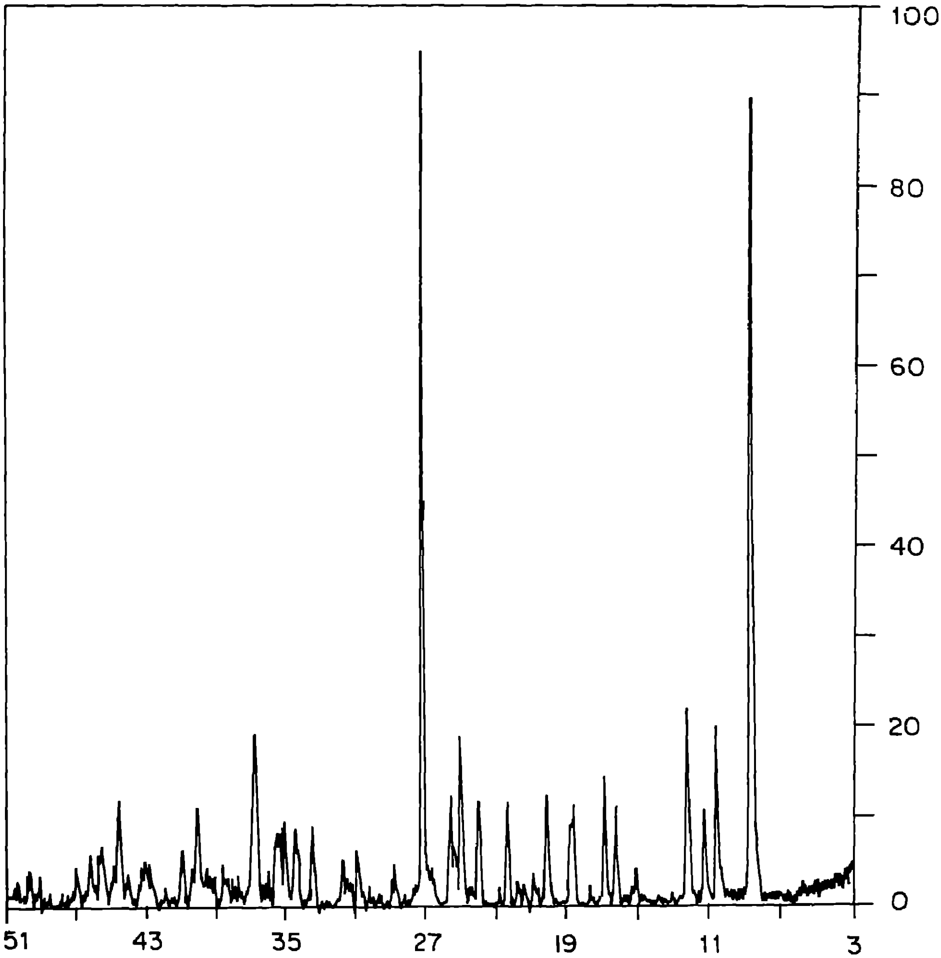

Figure 2. X-ray diffraction trace.

Table 1. X-ray powder data.

d values	Intensity values
10·0480	89·5
8·2678	20·0
7·0810	22·0
5·3402	9·0
5·1257	12·0
4·6707	9·0
4·3532	10·0
3·9342	11·5
3·5339	19·0
3·2433	95·0
2·4332	19·0
2·2378	11·0
2·0273	12·0

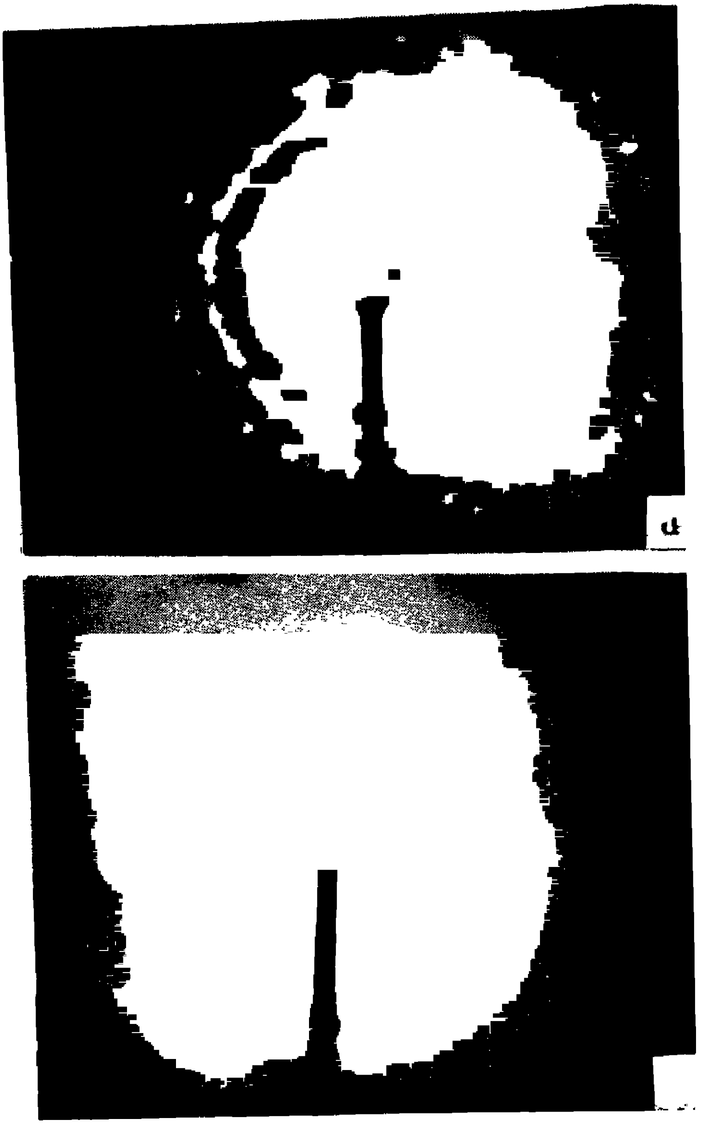

Figure 3. (a) Electron diffraction pattern recorded immediately on loading and (b) electron diffraction pattern recorded after some time of loading.

are electron diffraction patterns of the material recorded immediately or after some time of loading. The pattern shown in figure 3(a) indicates the crystallinity of the material. A comparison between figures 3(a) and 3(b) shows that the diffraction pattern changed from polycrystalline to nearly amorphous pattern (Kotru and Gupta 1983). This could be due to the presence of water in the original material.

3.4 *Mass spectroscopy*

Mass spectrum of the crystal sample was recorded using 70 eV electron bombardment for ionization. Figure 4 shows the mass spectrum of $La_2(C_4H_4O_6)_3 \cdot 7H_2O$.

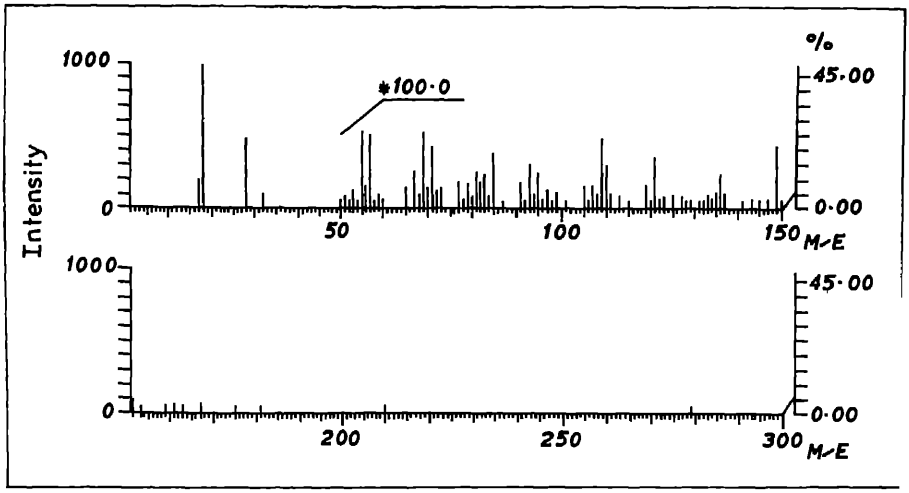

Figure 4. Mass spectrum of $La_2(C_4H_4O_6)_3{\cdot}7H_2O$ crystals.

Table 2. Mass spectrum data corresponding to significant peaks of $La_2\ (C_4H_4O_6)_3{\cdot}7H_2O$.

M/E	Raw int.	Relative intensity	Sigma (%)
16·0	11·1	13·9	0·68
17·0	169·9	212·0	10·40
18·0	801·2	1000·0	49·04
28·0	388·8	485·2	23·79
32·0	87·0	108·5	5·32
43·0	10·3	12·9	0·63
44·0	16·9	21·0	1·03
149·0	3·4	4·3	0·21

The mass fragmentography corresponding to prominent peaks is indicated in tabl The base peak of M/E 18 suggests the possible presence of water of crystallizati The M/E peak at 149 may be due to the tartrate constituent of the parent mater

The mass spectrum suggests the decomposition of the material and furt supports the presence of water, carbon and oxygen as constituents of the cry sample which is expected on fragmentation of the tartrate and water crystallization in the parent material. To find out if there was any volatility, repea experiments were performed to capture the molecular ion along with the metal, they failed to yield the desired results indicating that the molecule got decompo before it was captured.

3.5 *IR spectrum results*

Figure 5 shows the infra-red spectra of $La_2(C_4H_4O_6)_3{\cdot}7H_2O$. The peak 3400 cr is due to water and strongly stretching modes of OH group. The bands near 1

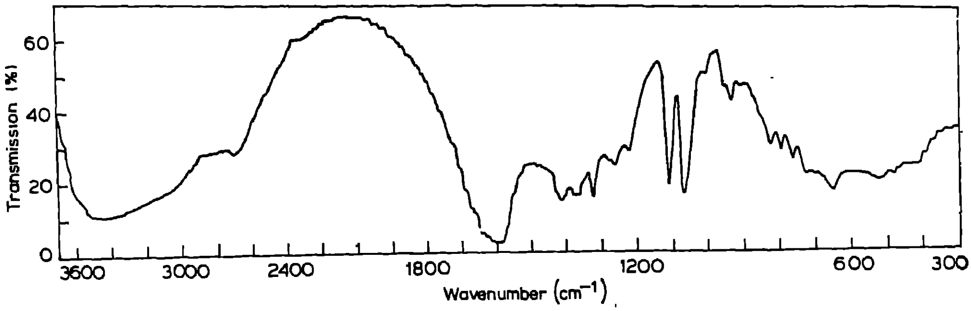

Figure 5. Infra-red spectrum of $La_2(C_4H_4O_6)_3 \cdot 7H_2O$ crystals.

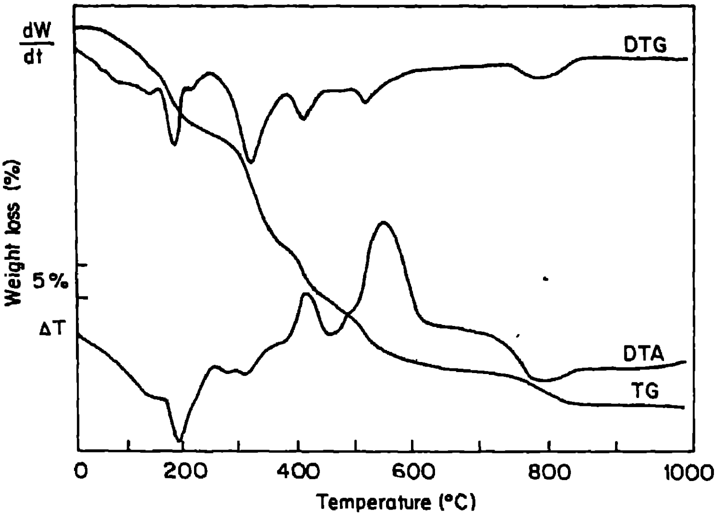

Figure 6. Thermogram showing TGA, DTA and DTG curves for $La_2(C_4H_4O_6)_3 \cdot 7H_2O$ crystals.

and 1370 cm^{-1} may be attributed to OH in plane bending. While the band at 1590 cm^{-1} is due to C=O stretch, those at 1415 and 1325 cm^{-1} are due to CO sym + δ O–C=O modes. The modes of δ C–H and π C–H are indicated by bands at 1115 and 1070 cm^{-1}. A significant band is observed at 650 cm^{-1} which is attributed to the presence of crystal water (Niekerk and Schoening 1951). Besides, there are some peaks below 500 cm^{-1} indicating metal oxygen bond.

3.6 *Thermal analysis*

Figure 6 shows the thermogram for TGA, DTA and DTG for $La_2(C_4H_4O_6)_3 \cdot 7H_2O$. It is seen from TGA that the material starts decomposing around 60°C and the process is completed after the mass loss attains saturation. Some of the decomposition steps in the TG show considerable overlapping but are very much distinct in

Table 3. Results of decomposition process of $La_2(C_4H_4O_6)_3\cdot 7H_2O$.

Temperature range (°C)	Observed mass loss (%)	Calculated mass loss (%)	Loss of molecules in the step
60–200	14·51	14·85	$7H_2O$
200–370	35·00	36·08	$6H_2O+6C$
370–470	45·00	45·99	$3CO$
470–610	55·50	56·36	$2CO_2$
610–835	62·00	61·55	CO_2

G curve. A combined study of TG and DTG indicates a decomposition pattern n in table 3.

DTA curve also indicates peaks corresponding to the DTG peaks. The first ages in DTA are endothermic and hence the involvement of oxidation accom-g the decomposition process is ruled out. However, the subsequent exothermic n DTA suggest that decomposition is accompanied by oxidation which may e atmospheric oxygen.

owing is the stoichiometry of the different intermediates involved in the position process of lanthanum tartrate.

$La_2(C_4H_4O_6)_3\cdot 7H_2O$ [lanthanum tartrate crystals]	$\xrightarrow{-7H_2O}$	$La_2(C_4H_4O_6)_3$ [lanthanum tartrate anhydrous]
$La_2(C_4H_4O_6)_3$ [lanthanum tartrate anhydrous]	$\xrightarrow{-(6H_2O+6C)}$	$La_2(C_2O_4)_3$ [lanthanum oxalate]
$La_2(C_2O_4)_3$ [lanthanum oxalate]	$\xrightarrow{-3CO}$	$La_2(CO_3)_3$ [lanthanum carbonate]
$La_2(CO_3)_3$ [lanthanum carbonate]	$\xrightarrow{-2CO_2}$	$2LaO\,(CO_3)_{\frac{1}{2}}$ [basic carbonate]
$2LaO\,(CO_3)_{\frac{1}{2}}$ [basic carbonate]	$\xrightarrow{-CO_2}$	La_2O_3 [lanthanum oxide]

ecomposition pattern is typical of a hydrated metal tartrate (Alfred *et al* 1970). ch thermal decomposition study leaves no doubt about the stoichiometry of the rial.

study the reaction kinetics of solid state reactions involved, three equations used for calculating the activation energy, the order of reaction and the ency factor for the first stage of decomposition only, as in subsequent stages the le characteristics cannot be controlled. The equations of Horowitz-Metzger), Piloyan-Novikova (1966) and Coats-Redfern (1964) were used for this ose.

plication of H-M equation leads to a good linear fit in the case of $f(\alpha)=(1-\alpha)^{\frac{1}{2}}$

Table 4. Energy of activation, order of reaction and frequency factor calculated from first stage of decomposition.

Relation used	Order of reaction (n)	Frequency factor (Z)	Energy of activation (E_a) (Kcal/mol)
Horowitz-Metzger	$\frac{1}{2}$	—	9·426
Piloyan-Novikova	—	$5{\cdot}49 \times 10^6$	6·669
Coats-Redfern	—	$3{\cdot}653 \times 10^4$	7·254

which indicates a contracting cylindrical mechanism of decomposition. The Coats-Redfern method also gives a linear fit for $g(\alpha) = 2[1-(1-\alpha)^{\frac{1}{2}}]$, thereby suggesting the same mechanism of decomposition. Table 6 gives the activation energy, order of reaction and frequency factor as calculated from the first stage of decomposition. As is evident from table 4, the values of kinetic parameters like activation energy and frequency factor obtained by the application of three kinetic equations (viz. H–M, P–N and C–R for E_a and P–N and C–R for frequency factor as well) are in reasonably good agreement. An agreement on the reaction mechanism leading to decomposition as suggested by the application of Coats-Redfern and Horowitz-Metzger relation is noteworthy: both indicating contracting cylinder-kinetic model as the appropriate one to explain the results obtained in the present case.

3.7 *Magnetic characteristics*

Magnetic characteristic of the material grown was studied using Gouy's balance at room temperature (34°C). The magnetic susceptibility measurements indicated the material to be diamagnetic.

4. Conclusion

(i) The gel-grown system involving the use of lanthanum nitrate or lanthanum chloride as the upper reactant and sodium metasilicate gel impregnated with tartaric acid leads to crystallization of lanthanum tartrate.

(ii) Chemical analysis supplemented by the results of infra-red spectroscopy and TGA establish the crystals to be hydrated; the chemical composition being $La_2(C_4H_4O_6)_3 \cdot 7H_2O$.

(iii) The x-ray and electron diffraction results reveal crystallinity of the gel-grown lanthanum tartrate crystals.

(iv) The results of thermal analysis (DTA, TGA and DTG) suggest the material to be thermally unstable beyond 60°C. The decomposition of the material at 70 eV of energy is suggested by the fragmentography in the mass spectrum. Changes in the electron diffraction pattern recorded immediately or after some time of loading also reveal changes in the crystalline character of the material due to electron beam heating and the presence of waters of hydration (Lorento 1975); the diffraction patterns revealing transition from poly-crystalline to nearly amorphous pattern.

(v) Application of Horowitz-Metzger and Coats-Redfern relations in understanding the reaction kinetics of solid state reactions leading to decomposition of the crystalline material suggests the contracting cylinder-kinetic model to explain the decomposition.

(vi) Magnetic susceptibility measurements indicate the material to be diamagnetic.

Acknowledgements

The authors (NKG and KKR) are thankful to UGC and to the university authorities for research fellowships. The research work has been partially supported by the UGC. We are thankful to Prof. Y Prakash for his interest.

References

Alferd C, Latz G, Litant I and Rubin B 1970 *Analytical calorimetry* (New York & London: Plenum) **2** 25
Coats A W and Redfern J P 1964 *Nature* (*London*) **201** 68
Eyring L 1964 *Progress in science and technology of rare earths* (New York: Pergamon Press) **1&2** 416
Horowitz H H and Metzger G 1963 *Anal. Chem.* **35** 1464
Kotru P N and Gupta N K 1983 *Bull. Elect. Microsc. Soc. India* **7** 119
Kotru P N, Gupta N K and Raina K K 1985 *J. Mater. Sci.* **21** 90
Lorento M H 1975 *Physicochemical methods of mineral analysis* (ed) A W Nicol (New York: Plenum Press
Niekerk J V and Schoening F R L 1951 *Acta. Crystallogr.* **4** 35 381
Piloyan G O and Novikova O S 1966 *Russ. J. Inorg. Chem.* **12** 313

Bull. Mater. Sci., Vol. 8, No. 5, December 1986, pp. 557–565. © Printed in India.

Glass ceramics containing ferroelectric phases

OM PARKASH, DEVENDRA KUMAR* and LAKSHMAN PANDEY
School of Materials Science and Technology, *Department of Ceramic Engineering, Institute of Technology, Banaras Hindu University, Varanasi 221 005, India

MS received 31 March 1986

Abstract. Glass ceramics prepared by controlled crystallization of glasses produce fine dispersion of crystallites in a glassy matrix. Glasses containing a major portion of constituents of a ferroelectric phase produce crystallites of ferroelectric phase in glass through a suitable heat treatment. The amount of network former in the initial glass has a profound influence on its crystallization behaviour and microstructure of the resulting ferroelectric glass ceramics. The value of dielectric constant and the nature of ferroelectric to paraelectric transition depend on the crystallite size and volume fraction of the ferroelectric phase. These glass ceramics are transparent for crystallite size less than 0·1 μm and exhibit large quadratic-electro-optic effect.

Keywords. Glass ceramics; ferroelectric; crystallization; heat treatment.

1. Introduction

Stookey (1959) discovered the method of controlled nucleation and crystallization of glass to produce ceramic bodies. Such materials are referred to as glass ceramics (McMillan 1979) in which crystallites of a particular phase are dispersed in a continuous glassy matrix. Their preparation consists of making a homogeneous glass, its shaping in the desired form and finally heat-treating it to produce microcrystalline glass ceramic body. These glass ceramic bodies are free from pores in contrast to conventionally sintered ceramics. Absence of pores imparts them higher mechanical and dielectric breakdown strengths. Glass ceramic bodies having intricate shapes and close tolerance in dimensions can be produced using commercial methods of glass production. This is because the conversion of glass into glass ceramic is rarely accompanied by more than 3–5% change in volume.

Soon after the discovery of the glass ceramic process, attempts were made to produce glass ceramics having high permittivity, low dielectric loss, high electrical resistance and dielectric breakdown strength by precipitating ferroelectric phases in the glassy matrix (Bergeron 1961; Herczog 1964; Borrelli *et al* 1965). These materials find applications as capacitor dielectrics (Herczog 1967), as electronic components (Herczog 1973) and as infrared detectors (Takahashi *et al* 1975) etc. The ferroelectric phases are generally ABO_3 perovskite type where A ion is from first, second and third group and B ion is from second to fifth group of the periodic table.

The ferroelectric perovskites can be produced in the glassy form in the pure state without addition of a network former (Ulrich and Smoke 1966; Glass *et al* 1978; Nassau *et al* 1979a, b, 1981). The viscosity of the melt without network former is low. This requires rapid quenching of the melt of the order of 10^6 degrees/sec or more producing only very small thin platelets. On the other hand crystallization of bodies made of glass powder may produce undesirable porous structure. The addition of network formers, such as SiO_2, B_2O_3, Al_2O_3 etc increases the viscosity of the melt.

This helps in producing a few millimeter thick discs or plates by cooling of the mel at a moderate rate of a few hundred degrees/sec. The devitrification of a glass to crystalline phase of the same composition produces crystals of varying sizes which difficult to control. The glasses containing network formers yield two or more phas during crystallization. The minor phase acts as grain growth inhibitor of the maj phase. With this, an exact control of grain size in glass ceramics is possible. Due these various factors, the glasses prepared from the melts of pure perovskites and t crystalline product obtained therefrom are not yet usable and have academ interest only. In this review, we attempt to present the processing, crystallization a electrical properties of various glass ceramic systems containing ferroelectric phas studied so far. These glass ceramics are prepared from glasses containing netwo formers.

2. Processing

The glasses are prepared by melting batches containing a major amount of con tuents of desired ferroelectric phase and an optimum amount of network formers inert crucibles. The use of inert crucibles is recommended because any contaminati during melting may adversely affect the crystallization behaviour of the glass and dielectric properties of the resulting glass ceramic product (Grossman and Is 1969a). The melt is quenched by pouring it into a suitably designed mould provi with an arrangement of pressing. The pressing time and temperature are adjuste avoid the devitrification and development of thermal cracks in the quenched g body. Fully or semi-automatic arrangements are used for this purpose (Herc 1964, 1984). The glass melt is transferred to a mechanized glass delivery sys designed to ensure reproducible glass forming conditions. It consists of a plati crucible which discharges molten glass droplets through a platinum tube. The fal droplets sensed by a photocell are caught in a horizontal mould and transferred miniatured water cooled press. The pressed pieces are annealed to relieve the stre The annealed glasses are subjected to differential thermal analysis (DTA) determine the nucleation T_N and growth T_G temperatures of various crystal phases which would precipitate during ceramization of the glass (Herczog 1 Bergeron and Russel 1965; Layton and Herczog 1967). A typical DTA plot glass (21 PbO–21 BaO–42 TiO_2–6 SiO_2–10 B_2O_3 mole%) is shown in figure 1.

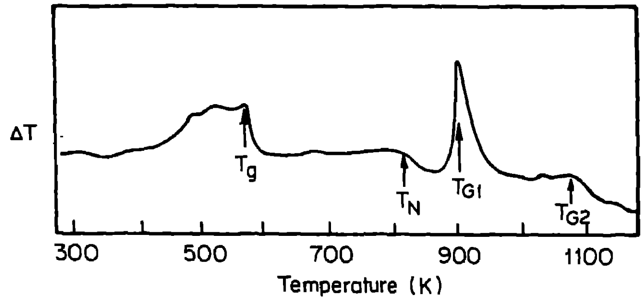

Figure 1. DTA curve for the glass in the system BaO–PbO–TiO_2–B_2O_3–SiO_2 (Om P *et al* 1986).

first endotherm at 575 K represents the glass transition. The second endotherm 810 K corresponds to nucleation of crystalline phases. The exothermic peaks 900 K and 1075 K represent the growth temperatures T_G of two phases respectivel which are developed during heat treatment of this glass (Om Parkash *et al* 1986).

The glasses are then subjected to various heat treatment schedules based on DT results. The crystalline phases precipitated during ceramization are identified by x-r diffraction (XRD) and their respective nucleation and growth temperatures are th identified. In figure 1, 900 K corresponds to the growth of $BaTiO_3$, while 1075 represents the growth of second crystalline phase. An optimum heat treatme schedule is determined based on the measurements of optical and electron micr scopy and dielectric properties of the glass ceramics obtained by different he treatment schedules.

When crystallization of glasses in the system $BaO–TiO_2–Al_2O_3–SiO_2$ is carri out in reducing atmosphere, interconnected dispersion of semiconducting $BaTiO_3$ glassy matrix is obtained. Oxidation of this semiconductor leads to surface lay with very high dielectric strength and resistivity about 100 times higher than t resistivity obtained by direct crystallization of the glass in air (Herczog 1984).

3. Systems

As mentioned in §1, the ferroelectric phases which are precipitated during controll crystallization of glasses in these glass ceramics are of ABO_3 perovskite ty Ferroelectric glass ceramics studied can be put into two categories depending on crystallite size and resulting properties: (1) those glass ceramics with crystalli having size $>0{\cdot}1\ \mu m$. They are opaque and have potential applications as h permittivity materials, and (2) those with crystallites having size $<0{\cdot}1\ \mu m$. Th glass ceramics are transparent and exhibit interesting electro-optic properties.

The different systems investigated are given in table 1. $BaTiO_3$ and $PbTiO_3$ c stals have been precipitated in different glass ceramic systems (Herczog 1 Bergeron and Russell 1965). Solid solution ferroelectric ceramics possess m desirable properties than pure ferroelectric materials. Various attempts have b made to precipitate similar solid solution crystallites in the glass ceram Formation of pure lead titanate has been reported during ceramization of vari glasses in the system $PbO–BaO–TiO_2–B_2O_3–SiO_2$ (Grossman and Isard 1969 Lynch and Shelby 1984). However, $BaTiO_3$ was obtained in the same sys (Rajgopalan 1985). From these studies it is concluded that the ratio of PbO to and ($PbO+BaO$) to TiO_2 determines whether $PbTiO_3$ or $BaTiO_3$ would precip out during heat treatment. Other substitutions such as Sr for Ba and Zr for Ti r in precipitation of different phase rather than solid solutions. Formation of cr llites of various ferroelectric niobates and tantalates in the pure and the solution form over wide ranges of composition has been reported in glass cer systems (Borrelli 1967; Borrelli and Layton 1971) as shown in table 1. Most of glass ceramics can be obtained with crystallite size $<0{\cdot}1\ \mu m$ and are opti transparent. Thin crystals having large surface area have been obtained by ceramic processing in the system $Pb_5Ge_{3-x}Si_xO_{11}$ (Takahashi 1975).

Table 1. Glass ceramic systems containing ferroelectric phases.

Glass system	Ferroelectric phase	Reference
BaO-TiO_2-SiO_2-B_2O_3	$BaTiO_3$	Herczog (1964)
BaO-TiO_2-SiO_2-Al_2O_3	$BaTiO_3$	Herczog (1984)
PbO-TiO_2-B_2O_3	$PbTiO_3$	Bergeron and Russell (1965)
PbO-TiO_2-Al_2O_3-SiO_2	$PbTiO_3$	Kokubo and Tashiro (1973/74)
PbO-BaO-TiO_2-B_2O_3	$PbTiO_3$	Lynch and Shelby (1984)
PbO-BaO-TiO_2-B_2O_3-SiO_2-Al_2O_3	$PbTiO_3$	Grossman and Isard (1969a, b)
PbO-BaO-TiO_2-B_2O_3-SiO_2	$BaTiO_3$	Om Parkash *et al* (1986)
Na_2O-Nb_2O_5-SiO_2	$NaNbO_3$	Layton and Herczog (1967)
CdO-Na_2O-Nb_2O_5-SiO_2	$Na_{1-x}Cd_{x/2}NbO_3$	Layton and Smith (1975); Borrelli and Layton (1971)
PbO-Na_2O-Nb_2O_5-SiO_2	$Na_{1-x}Pb_{x/2}NbO_3$	Borrelli and Layton (1971)
Na_2O-K_2O-Nb_2O_5-SiO_2	$Na_{1-x}K_xNbO_3$	-do-
SrO-Na_2O-Nb_2O_5-SiO_2	$Na_{1-x}Sr_{x/2}NbO_3$	-do-
PbO-MgO-Nb_2O_5-SiO_2	$Pb_3MgNb_5O_9$	-do-
SrO-K_2O-Nb_2O_5-SiO_2	Sr_2KNbO_5	-do-
Li_2O-Na_2O-K_2O-Nb_2O_5-SiO_2	$Li_xNa_yK_zNbO_3$	-do-
BaO-CaO-PbO-Nb_2O_5-SiO_2	$Ba_xCa_yPb_2Nb_2O_6$	-do-
BaO-SrO-PbO-Nb_2O_5-SiO_2	$Ba_xSr_yPb_2Nb_2O_6$	-do-
Li_2O-Na_2O-K_2O-Ta_2O_5-SiO_2	$Li_xNa_yK_zTa_2O_6$	-do-
PbO-GeO_2-SiO_2	$Pb_5Si_xGe_{3-x}O$	Takahashi *et al* 1975

4. Nucleation and crystallization

An understanding of the mechanism of nucleation and crystallization in these glasses helps in better control of properties of resulting glass ceramics. Bergeron and Russell (1965) investigated the rate of growth of $PbTiO_3$ crystals from a PbO–TiO_2–B_2O_3 glass at different temperatures. The Brown-Ginell equation satisfactorily explained the growth rate data. It was also observed that temperature of maximum growth rate was 100–150°C above the exotherm associated with the growth of lead titanate crystals in DTA plots of solid and powdered glass samples. It was ascribed to the large surface area of the powdered sample. The large number of nuclei present in such samples may result in a large heat effect even at low growth rate at the temperature of the exotherm. Most of the total quantity of the crystals which can be in equilibrium at the higher temperatures were precipitated below the temperature of maximum growth rate.

The crystallization behaviour of glasses in the system Na_2O–Nb_2O_5–SiO_2 has been investigated by measuring the viscosity, grain size and crystalline content as a function of temperature at different constant heating rates (Layton and Herczog 1967). The crystallization was very rapid and exothermic, making the measurements at constant temperatures very difficult. From electron microscopic observations at various stages of heat treatments it was observed that in the beginning of crystallization, particles of 500–1000 Å in diameter appear in the glass. These particles were agglomerates of very fine crystallites of diameter 100 Å or less. These fine crystallites constituting a particle, formed a star-like configuration indicating a growth from central nucleus. Slightly crystallized specimens also showed the presence of a large number of phase separated regions of 20–50 Å in diameter. On further heating, these regions subsequently coalesced until a critical size was reached forming a stable nucleus. At low SiO_2 content, uniform and very large concentration of these nuclei are formed indicating a high rate of nucleation. The transformation of the glass to the crystalline phase is complete with minimum of grain growth and sintering. Thus the final glass ceramic product is transparent due to crystallite size being less than 0·1 μm. At high SiO_2 content, the nucleation rate is slower resulting in growth of crystals upto 1 μm or more in diameter making the glass ceramic opaque.

Phase separation occurring during heat treatment may be due to the microheterogeneities in the structure of glass having the same size and composition as the phase separated regions. This can be understood in terms of the ratio of number *B* of multivalent cations (such as Ti^{4+} and Nb^{5+}) and network forming cations N (such as Si^{4+}, B^{3+}, Al^{3+} etc) present in the initial glass composition (Layton and Herczog 1969). The randomness of the glass network is attributed to flexibility of Si-O-S bond angle or to that of angle formed by other network formers. Ti^{4+} and Nb^{5+} are normally octahedrally coördinated to oxygen in oxide lattices and they can replace the network forming ions upto a certain limit in oxide glasses. These ions lack flexibility of bond angles. When these cations are not associated with a true network former as their nearest neighbours, they become structurally ordered with respect to each other. These structurally ordered regions represent microheterogeneities in the glass structure. It is reasonable to assume that the ratio $B/N = 1$ represents the limi of substitution of network forming cations by these ions without causing majo structural inhomogeneities in the glass. As the ratio exceeds 1, microheterogeneitie are formed and on heating, phase-separated regions are produced in sufficient concentration, approaching the size of a stable nucleus allowing rapid interaction between them. This explains high rate of nucleation and rapid completion of crystallization without substantial grain growth in glasses with low network forming conten

The DTA curve in figure 1 shows the presence of second exothermic peak representing the growth of another crystalline phase beside barium titanate. Therefor when the glass or the glass ceramic samples are heated at higher temperature (growt temperature of second phase) the second phase separates out along with BaTiO This is shown in the scanning electron micrograph (figure 2) of the glass ceram sample obtained by heat treatment at this temperature (Om Parkash *et al* 1986). I order to obtain the maximum recovery of a ferroelectric phase during ceramizatio it is recommended to start with a glass composition corresponding to stoichiometr composition of two crystal phases; the ferroelectric phase and a secondary pha containing all network forming additions. Presence of any residual glass reduces t yield of ferroelectric phase either by keeping it in solution or by secondary hi temperature reaction with it (Herczog 1984).

5. Electrical properties

Uniform fine-grained microstructure is very desirable in ferroelectric ceramics as imparts mechanical and dielectric stability suitable for various device applicatio

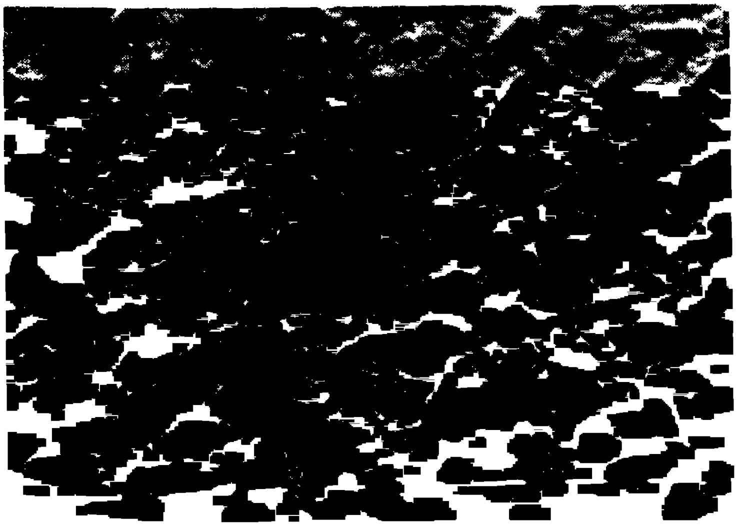

Figure 2. Microstructure of the glass ceramics in the system $PbO–BaO–TiO_2–B_2O_3–SiO_2–P_2O_5$, heat treated at 975 K for 12 hours, — 10μm (Om Parkash *et al* 1986).

This type of microstructure can be easily produced in ferroelectric glass ceramics by controlled heat treatment. The dielectric constant depends on the particle size and content of crystalline phase in these materials. A high percentage (75–80 volume%) of a ferroelectric phase can be obtained starting with a suitable composition.

Variation of dielectric constant and loss tangent with temperature at 1 kHz with $BaTiO_3$ content and particle size is shown in figure 3 (Herczog 1964). The curves on the left side show the characteristics of the materials containing different percentages of $BaTiO_3$ but having the same particle size. The right side curves are for materials of different particle size and of same barium titanate content. Dielectric anomaly was distinctly seen in samples having particle size $\geqslant$ 0·8 μm (curves (a), (b) and (c)) becoming diffuse with decreasing particle size (curves (d) and (e)) and disappear completely below 0·1 μm. A maxima in dielectric constant as a function of grain size at 0·8 μm was observed. A similar maxima in dielectric constant of microcrystalline $PbTiO_3$ crystallized from $PbO–TiO_2–Al_2O_3–SiO_2$ glass was observed at a grain size of 0·15 μm (Kokubo and Tashiro 1973/74). Similar dielectric behaviour has been reported in glass ceramics containing $NaNbO_3$ (Borrelli and Layton 1971).

This dielectric behaviour as a function of crystallite size has been explained in terms of internal stresses generated in these submicrometer range crystallites and suppression of ferroelectric-to-paraelectric transition due to crystal clamping in the rigid surrounding glass matrix. This model was proposed by Buessem *et al* (1966) to explain the high permittivity in fine-grained $BaTiO_3$. Kokubo and Tashiro (1973/74) through careful experimentation using XRD showed that the maximum dielectric constant was obtained at the same grain size at which the two-dimensional stress was maximum. The decrease in dielectric constant at higher grain size was ascribed to 90° twinning within the grain as proposed by Buessem *et al* (1966), which leads to reduction in two-dimensional stresses. Similarly, temperature-independent behaviour for submicron range can be understood due to the absence of domain walls in these

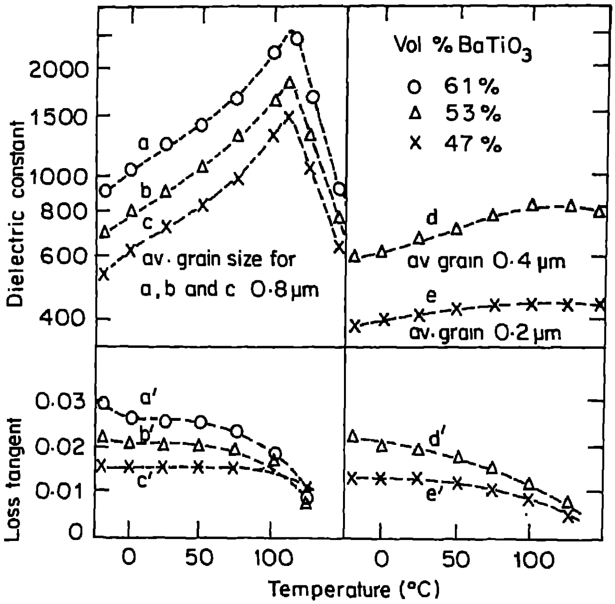

Figure 3. Variation of dielectric constant and loss tangent with temperature at 1 kHz for glass ceramics containing different contents and size of $BaTiO_3$ crystallites (Herczog 1964).

crystallites. For particles $\geqslant 1\ \mu m$ or so, 90° twinning of domain wall becomes possible and hence glass ceramics containing particles in this range show a normal dielectric anomaly at the Curie point.

These glass ceramics show a higher dielectric breakdown strength and resistivity as compared to normally-sintered ferroelectric ceramics due to absence of porosity.

When the crystallite size in these glass ceramics is $\leqslant 0{\cdot}1\ \mu m$, they become transparent and exhibit interesting electro-optic properties. A quadro-electro optic effect is observed when an electric field E is applied on the as crystallized glass ceramics. The induced birefringence Δn_2 is expressed by the equation

$$\Delta n_2 = \tfrac{1}{2} n^3\, g\, \varepsilon^2\, E^2, \qquad (1)$$

where n, g and ε are the refractive index, electro-optic coefficient and dielectric constant of the glass ceramic. When an electric field is applied on the prepoled glass ceramic, however, a linear electro-optic effect is observed and the induced birefringence Δn_1 is expressed by

$$\Delta n_1 = \tfrac{1}{2} n^3\, g\, P_1\, \varepsilon\, E, \qquad (2$$

where P_1 is the remanent polarization of the glass ceramic. The ferroelectric-para electric transition is suppressed below the crystallite size of 0·1 μm. This als represents the upper limit upto which these materials are transparent. Therefore, linear electro-optic effect cannot be observed in these transparent material However, they have a large value of dielectric constant even when the particle size i $<0{\cdot}1\ \mu m$. Therefore, a large quadro-electro-optic effect is observed (Borrelli 196 Borrelli and Layton 1971).

Observation of a hysteresis loop between polarization and applied electric field the true test of the presence of ferroelectricity in a given material. Fully developed hysteresis loops have been observed for glass ceramics containing crystallites having size $>1\ \mu m$ while some hysteresis effects have been observed down to $0{\cdot}2\ \mu m$ (Herczog 1964). For transparent glass ceramics containing particles having size $<0{\cdot}1\ \mu m$, no hysteresis loops were observed and it can be understood by the absence of domain walls in these small crystallites (Borrelli and Layton 1971). However, the pyroelectric measurements on these glass ceramics show that the sign of the pyroelectric signal reversed on the reversal of the maximum bias field, a positive proof of reversible spontaneous polarization, establishing ferroelectricity in transparent glass ceramics (Layton and Smith 1975).

6. Conclusions

Glass ceramics containing a variety of ferroelectric phases can be produced with a precise control of microstructure. The value of dielectric constant can be varied by controlling the crystal content and its size. A high and an almost temperature-independent value of dielectric constant is obtained for crystallite size in the submicron range. If the crystallite size is $<0{\cdot}1\ \mu m$, these are optically transparent and exhibit a large quadratic electro-optic effect. These characteristics make them potentially useful in various electronic components and devices in different forms (Kokubo *et al* 1968; Herczog 1973; Devendra Kumar and Om Parkash 1985).

Various attempts to precipitate ferroelectric crystallites in the solid solution form to obtain improved properties have not yielded any encouraging results in the case of titanates. Though the formation of extensive solid solution in niobates and tantalates in glass ceramics have been reported, yet no conclusive evidence is given in its support. Therefore problems associated with precipitation of solid solution ferroelectric crystallites in the glass ceramics require detailed investigations. This problem, if solved, will enhance the utilization of ferroelectric glass ceramics.

References

Bergeron C G 1961 *Crystallization of perovskite lead titanate from glass*, Ph.D. Thesis, University of Illinois

Bergeron C G and Russell C K 1965 *J. Am. Ceram. Soc.* **48** 115

Borrelli N F 1967 *J. Appl. Phys.* **38** 4243

Borrelli N F, Herczog A and Maurer R D 1965 *Appl. Phys. Lett.* **7** 117

Borrelli N F and Layton M M 1971 *J. Non-Cryst. Solids* **6** 197

Buessem W A, Cross L E and Goswami A K 1966 *J. Am. Ceram. Soc.* **49** 33

Devendra Kumar and Om Parkash 1985 Ferroelectric glass ceramics, Symposium on Emerging Frontiers in Ceramic Engineering, Banaras Hindu University, Varanasi

Glass A M, Nassau K and Negram T J 1978 *J. Appl. Phys.* **49** 4808

Grossman D G and Isard J O 1969a *J. Am. Ceram. Soc.* **52** 230

Grossman D G and Isard J O 1969b *J. Mater. Sci.* **4** 1059

Herczog A 1964 *J. Am. Ceram. Soc.* **47** 107

Herczog A 1967 *Glass Ind.* **48** 455

Herczog A 1973 *IEEE Trans PHP* **9** 247

Herczog A 1984 *J. Am. Ceram. Soc.* **67** 484

Kokubo T, Kung C T and Tashiro M 1968 *J. Ceram. Assn. Jpn.* **76** 89

Kokubo T and Tashiro M 1973/74 *J. Non-Cryst. Solids* **13** 328

Layton M M and Herczog A 1967 *J. Am. Ceram. Soc.* **50** 369

Layton M M and Herczog A 1969 *Glass Technol.* **10** 50

Layton M M and Smith J W 1975 *J. Am. Ceram. Soc.* **58** 435
Lynch S M and Shelby J E 1984 *J. Am. Ceram. Soc.* **67** 424
McMillan P W 1979 *Glass ceramics* (2nd ed) (London: Academic Press)
Nassau K, Wang C A and Grasso M 1979a *J. Am. Ceram. Soc.* **62** 74
Nassau K, Wang C A and Grasso M 1979b *J. Am. Ceram. Soc.* **62** 503
Nassau K, Cava R J and Glass A M 1981 *Solid State Ionics* **2** 163
Om Parkash, Devendra Kumar and Rajgopalan R 1986 *Bull. Mater. Sci.* **8** 13
Rajgopalan R 1985 *Preparation and characterization of glass ceramic containing ferroelectric pha* M.Tech. Thesis, Institute of Technology, Banaras Hindu University
Stookey S D 1959 *Glasstech. Ber. 32K* (Fifth International congress on glass, Verlag der Deutsch Glastechnischen Gesellschaft, Frankfurt am Main) p 574
Takahashi K, Cross L E and Newnham R E 1975 *Mater. Res. Bull.* **10** 599
Ulrich D R and Smoke E J 1966 *J. Am. Ceram. Soc.* **49** 210

Bull. Mater. Sci., Vol. 8, No. 5, December 1986, pp. 567–575. © Printed in India.

Magnetic hysteresis and crystallization studies on metallic glass all $Fe_{67}Co_{18}B_{14}Si_1$

A M VARAPRASAD and C RADHAKRISHNAMURTHY*
Naval Chemical and Metallurgical Laboratory, Naval Dockyard, Bombay 400 023, Ind
*Tata Institute of Fundamental Research, Bombay 400 005, India

MS received 10 February 1986; revised 21 May 1986

Abstract. Magnetic hysteresis studies were carried out on Metglas 2605 Co ($Fe_{67}Co_{18}B_{14}$ samples, cut parallel and perpendicular to the ribbon axis and annealed at different t peratures. The samples annealed at 450°C for 2 hr show a coercive force of 8·75 Oe 0·60 Oe in the parallel and perpendicular directions respectively. Electron probe mi analysis studies revealed the onset of primary crystallization at 400°C and a grad displacement of B and Si from the lattice as the annealing temperature was increased 450°C. The observed large coercive force is due to an increase in anisotropy resulting fr an intergrowth pattern of the type Fe_xCo_{1-x}, $0{\cdot}3 < x < 1{\cdot}0$, including boron contain phases such as (EeCo) B, $(FeCo)_2B$, $(FeCo)_3B$, developed by the displacement of and Si fr the original amorphous lattice.

Keywords. Amorphous alloys; anisotropy; crystallization; magnetic hysteresis.

1. Introduction

Recently, amorphous alloys have emerged as a new class of materials for constitut high performance transducers and sensors. Both isotropic and anisotropic proper of amorphous alloys find applications in device construction (Mohri 1984; Sasad *al* 1984). The material under study, commercially known as Metglas 2604 Co w the composition $Fe_{67}Co_{18}B_{14}Si_1$, has a high magnetostriction constant ($\lambda = 35 \times 10$ (Allied 1981) coupled with a higher saturation induction and is suitable for unc water transducer applications (Mohri 1984). The magnetic properties of this mate could be conveniently modified by adopting suitable annealing procedures. magnetic hysteresis properties, crystallization aspects and its relation to magn anisotropy of this material annealed to different temperatures have been reporte this paper.

2. Experimental

Metglas 2605 Co ribbon, 50 mm wide, 27 μ thick (supplied by Allied Corporat USA) was cut into strips of dimensions 50 mm × 4 mm and of equal weight, t parallel and perpendicular to the ribbon axis. These were annealed at 100, 200, 400 and 450°C for a constant period of 2 hr.

Hysteresis studies were carried out on the strip samples using a hysteresis tracer (Radhakrishnamurthy *et al* 1978) suitably modified to minimize the magnetization effects. The coercive force H_c measured on the original samp 0·08 Oe, which corresponds well with the value given in the specification of material. The crystallization and composition analysis were carried out usin electron probe micro analyser (model: Camebax, Chemica, France) (Beaman and Isasi 1972). Phase analysis, if any, was carried out using a Siemens Kristalloflux x-ray diffractometer. The statistical data on the crystallite dimensions were obtained using a TAS plus image analyser.

3. Results and discussion

Figures 1(a) to (f) depict the hysteresis of the Metglas samples taken parallel to the ribbon axis and annealed for 2 hr at temperatures (a) as obtained, (b) 100°C, (c) 200°C, (d) 300°C, (e) 400°C and (f) 450°C. The hysteresis loops for samples taken perpendicular to ribbon axis are shown in figures 2(a) to (f). The H_c data are presented in table 1.

From figures 1(a) and 2(a) a slight difference is seen in the H_c of the original sample in either direction. It can be inferred, therefore, that the starting samples possess little anisotropy due to magnetostriction and/or magnetoelastic effects (Haregawa 1976; Suja *et al* 1975; Takahashi *et al* 1976). Samples annealed at 400°C have shown clusters of tiny crystallites (figure 3a), without a significant change in the magnetic hysteresis (figures 1e and 2e). The crystallite dimensions range from a few hundred to about a thousand Angstroms. Due to their small size such small crystallites formed with the onset of crystallization may be considered as single domain regions (Chaughule *et al* 1983). At 450°C these crystallites coalesce to form into narrow regions of nearly 50–100 μ length and about 10 μ width (figure 3b). The hillock type crystallization products show a regular pattern elongated perpendicular to the ribbon axis. Texture Analysis System (TAS) image analysis revealed that the form factor of the regions is about 0·528 with an equivalent diameter of about 107 μ.

3.1 *X-ray diffraction studies*

X-ray diffraction analysis revealed a consistent amorphous structure with the samples annealed at 100, 200, 300 and 400°C. The sample annealed at 450°C shows a distinct crystalline diffraction pattern with *d*-values at 2·03, 1·43 and 1·17 Å. A variety of phases such as α-Fe, Fe_xCo_{1-x}, (FeCo)B, $(FeCo)_2B$, $(FeCo)_3B$ are expected (Baburaj *et al* 1985; Harold and Kosten 1978; Takacs *et al* 1975). Thus the observed XRD lines possibly belong to some of these phases. Further, distinct regions of α-Fe or (FeCo) type phases were not identified in the electron probe analysis (see table 2), suggesting that these could be intergrowth regions of submicron dimensions.

3.2 *Electron probe micro analysis*

Electron probe micro analysis was carried out at nearly 20, 40, 60 and 80 μ distance from one end to the other for several crystallites. The percentage composition of

Figure 1. Hysteresis loops of Metglas 2605 Co parallel to the ribbon axis. Annealing temperatures (a) As obtained, (b) 100°C, (c) 200°C, (d) 300°C, (e) 400°C, (f) 450°C. Scale: X-axis (a) to (e) one big division = 2·5 Oe and for (f) it is 3·5 Oe.

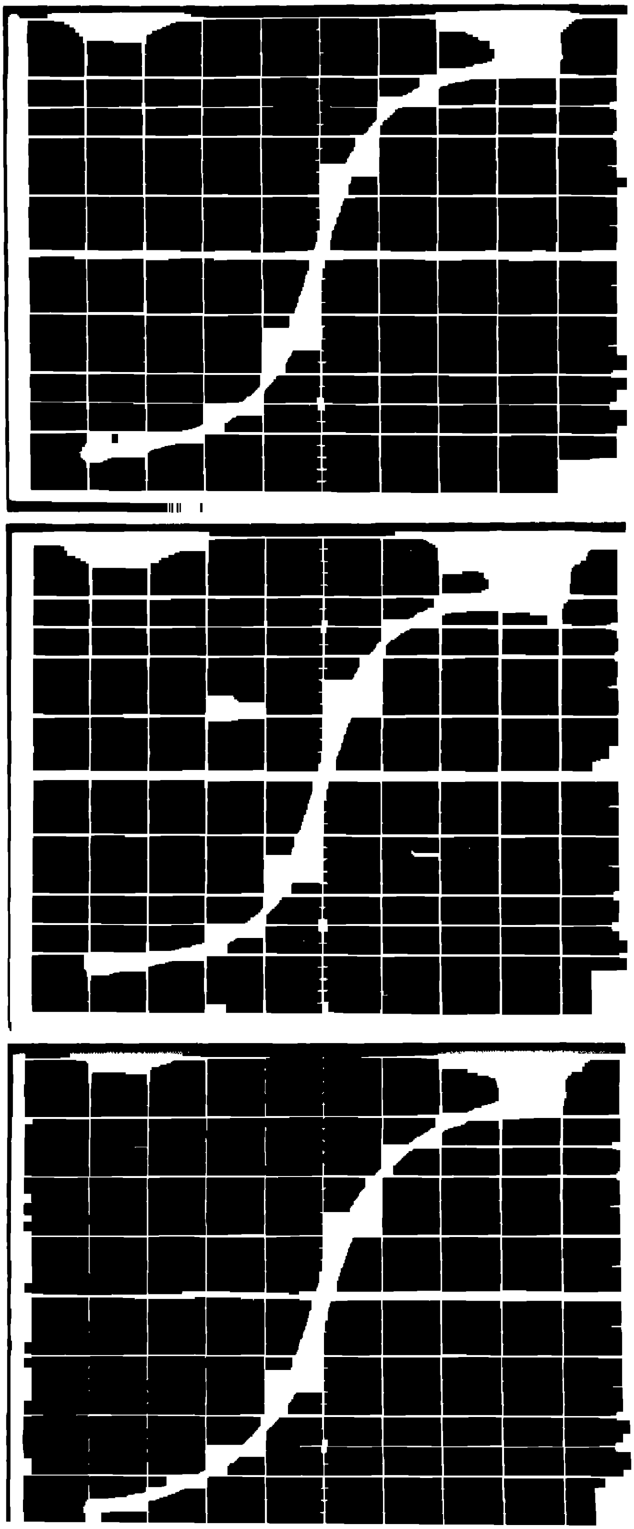

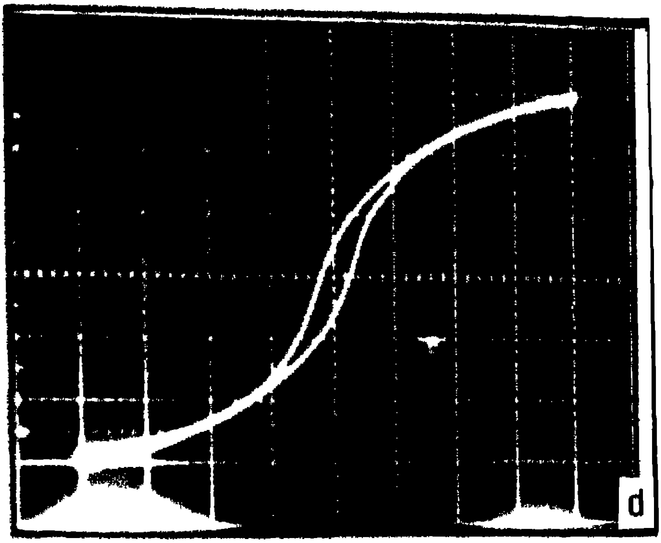
d

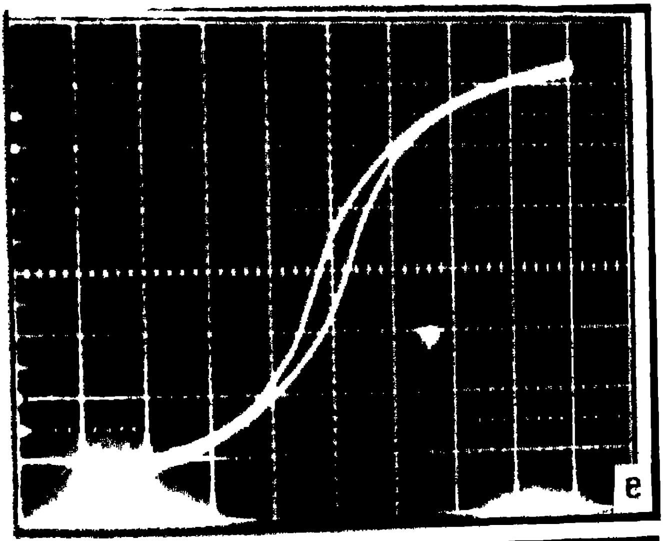
e

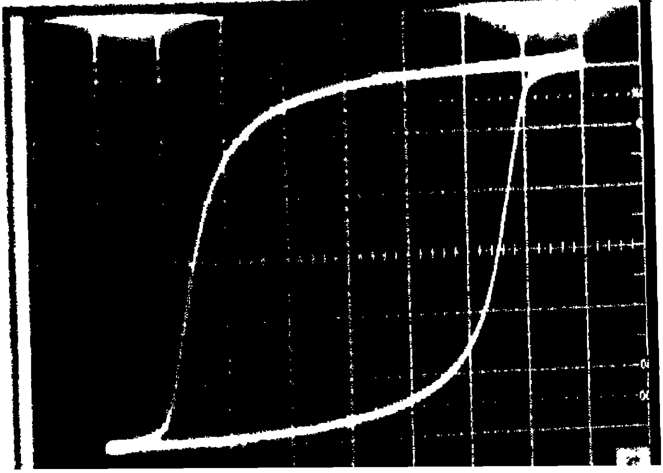

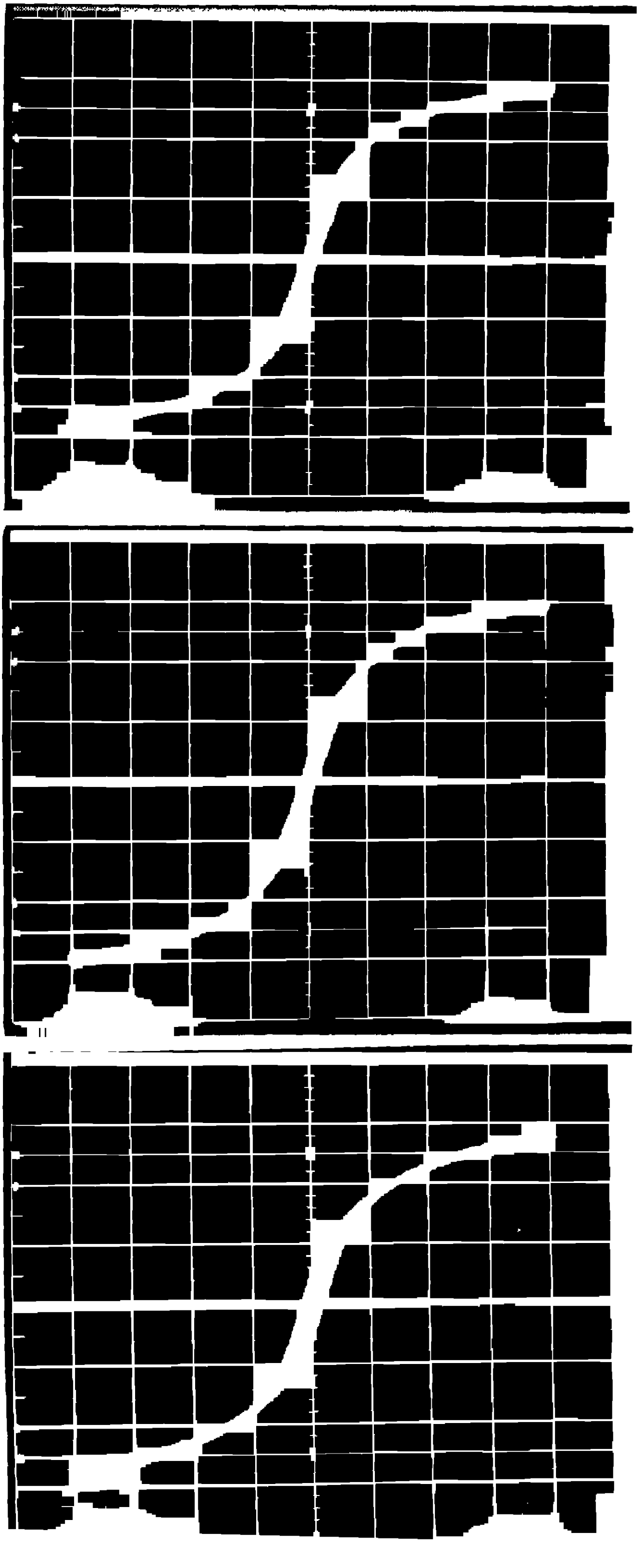

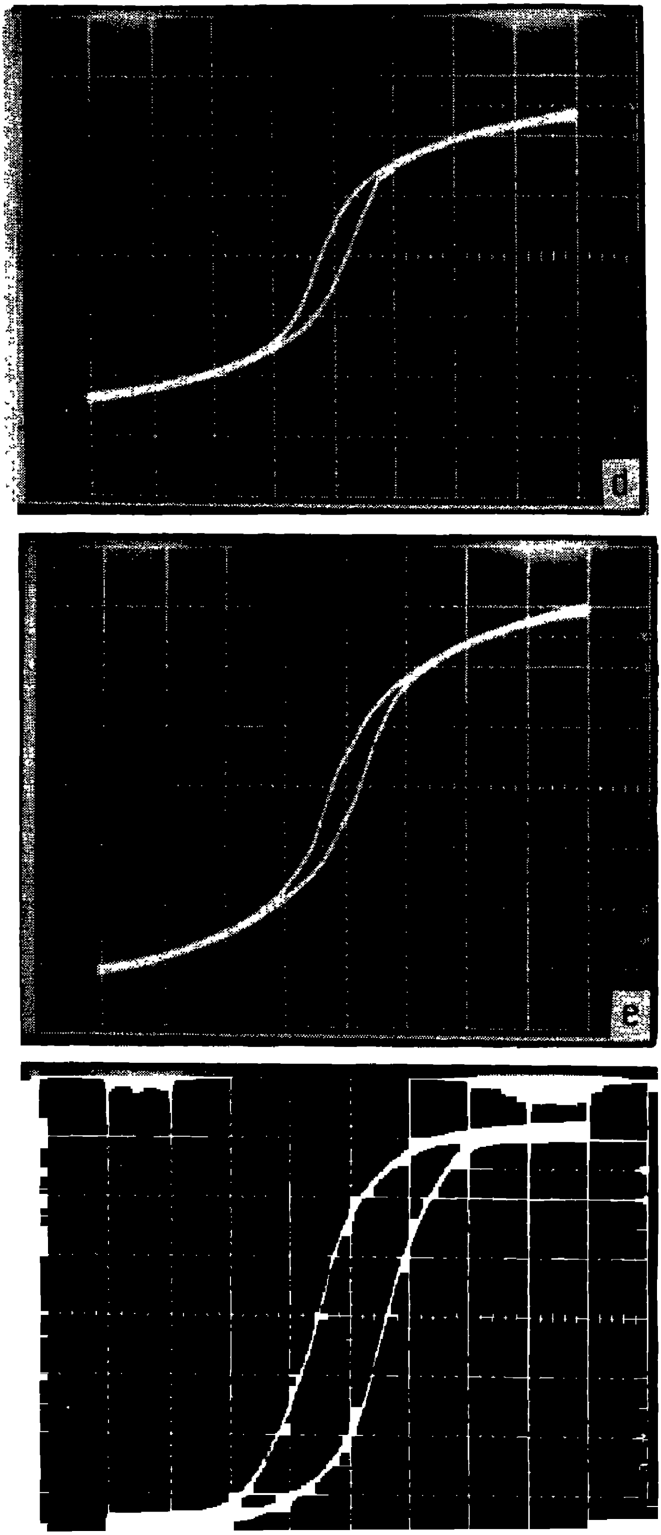
d
e

Table 1. Coercive force H_c of Metglas 2605 in the directions parallel and perpendicular to ribbon axis.

Annealing temperature (°C)	Coercive force (Oe)	
	Parallel	Perpendicular
30	0·08	0·15
100	0·08	0·15
200	0·15	0·20
300	0·30	0·30
400	0·35	0·35
450	8·75	0·60

Fe, Co, Si was obtained against calibrated standards with a statistical accurac 0·5% of the measured value and B concentration was obtained by calculating difference. The error estimated is about +1% of the measured concentra (Beaman and Isasi 1972; Heinrich 1981). The results show a significant sp variation in composition as given in table 2. These results indicate that the cry are boron-deficient at its centre. When there is a gradual increase in boron con away from the centre the composition around the periphery of the crystal enriched in boron and silicon. Also, there seems to be a preferential rejectio boron at the first instance when compared to that of silicon as inferred from th enrichment at 20 and 80 μ (see table 2). The crystallization process could there be categorized as the primary crystallization (Baburaj *et al* 1985; Harold and K 1978; Takacs *et al* 1975) which involved preferential displacement of boron follo by silicon into the amorphous matrix. Distinct regions of iron have not observed suggesting that the α-Fe phase identified in x-ray diffraction study coul possibly present as intergrowth regions of submicron dimensions during the pri crystallization process.

3.3 *Magnetic anisotropy*

The hysteresis loops for the samples annealed at 450°C (figures 1f and 2f) enhanced anisotropic effects. H_c increased to a value of 0·60 Oe perpendicular t ribbon axis, while it is 8·75 Oe in the parallel direction. However, the sa annealed at 400°C showed an H_c value of 0·35 Oe in either direction (figures 1 2e), despite the fact that microcrystalline regions appeared due to the onset o stallization (figure 3a). The composition of such crystallites is, therefore, expect be nearly the same as that of the bulk. The crystallization may proceed throug formation of intergrowth structures with complex repeat sequences (Rao 1985 are possible with the evolution of textures based on Bernal polyhedra (Finne Wallace 1981). Further, as seen in figure 3b the hillock regions are elongate pendicular to the long axis of the ribbon. The hysteresis loops in figures 1f reveal that the hard axis of the 450°C annealed ribbon lies in a direction para the ribbon axis. These results suggest that the intergrowth pattern is likely to in a direction perpendicular to the long axis of the hillock structure which, i indicates that the intergrowth patterns are parallel to the ribbon axis.

Figure 2. Hysteresis loops of Metglas 2605 Co perpendicular to the ribbon axis. A (a) As obtained (b) 100°C, (c) 200°C, (d) 300°C, (e) 400°C, (f

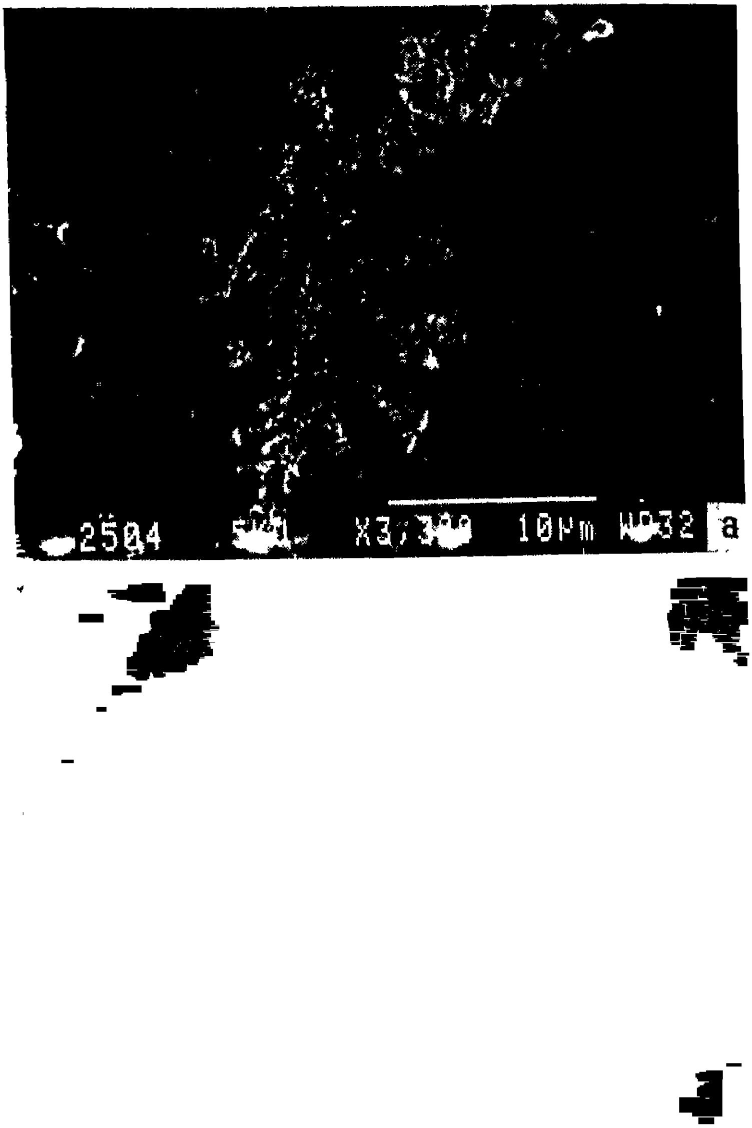

Figure 3. (**a**) Microcrystallites formed at 400°C. Scale: the bar represents 10 μ. (**b**) Hillock type crystallization formed at 450°C. Scale: the larger rectangle represents 100 μ. Arrow indicates the direction of the ribbon axis.

In accordance with the recent Mössbauer investigations (Bhatnagar *et al* 1985) nd in the wake of preferential rejection of boron and silicon, we propose that the ntergrowth regions may comprise of compositions of the form Fe_xCo_{1-x}, $0{\cdot}3 < x < 1{\cdot}0$), α-Fe including the boron-containing phases (FeCo)B, $(FeCo)_2B$, FeCo)$_3$B preferentially grown parallel to the ribbon axis. The compositions Fe_xCo_{1-x}, with $0{\cdot}3 < x < 1{\cdot}0$ were known to be strongly anisotropic with anisoropic constant K for α-Fe, $Fe_{0{\cdot}7}Co_{0{\cdot}3}$ and $Fe_{0{\cdot}3}Co_{0{\cdot}7}$ being 460, −430 and 102 [illegible] 10^{-3} [illegible] (Gray 1963). Thus the observed anisotropy

Table 2. Typical composition of a crystallite from end to end—EPMA data.

Element	Composition from one end at (μ) 20	40	60	80
Fe	73·37	75·99	75·49	70·10
Co	20·16	20·56	20·36	19·22
Si	1·01	0·92	0·67	1·14
B By difference	5·46	2·53	3·47	9·54

Note: Fe, Co and Si were estimated against calibrated standards and B concentration was obtained by difference. Estimated error is of the order of ±1% of the measured value.

$Fe_{0\cdot3}Co_{0\cdot7}$ and FeCo among the various compositions that appear as intergrowth regions preferentially formed parallel to the ribbon axis.

4. Conclusions

(i) Thermal annealing of Metglas 2605 Co at 450°C leads to pronounced magneti anisotropy with respect to ribbon axis. (ii) The thermally-induced anisotropy o Metglas 2605 Co samples could be explained on the basis of the intergrowth pattern formed preferentially parallel to the ribbon axis leading to local compositions of th type α-Fe, Fe_xCo_{1-x}, $(0{\cdot}3 \leqslant x \leqslant 1{\cdot}0)$, FeCo, (FeCo)B, $(FeCo)_2B$, $(FeCo)_3B$ etc.

Acknowledgements

Sincere thanks are due to Mr V V Modak and Mr K K Karmakar for EPMA an SEM studies. We gratefully acknowledge the useful discussions with Dr S Banerje BARC, Bombay. AMV acknowledges his sincere regards to Dr R Krishnan, Directo NCML, for initiation, guidance and encouragement.

References

Allied Corporation 1981 Bulletin No. 15M-10/81 on Metglas electromagnetic alloys p 16

Baburaj E C, Dey G K, Patni M J and Krishnan R 1985 *Scr. Metall.* **19** 305

Beaman D R and Isasi J A 1972 Electron probe micro analysis: The fundamentals and applications, AST STP 506, Am. Soc. Test Mater. pp 23–28

Bhatnagar A K, Bhanuprasad B and Jagannathan R 1985 *J. Appl. Phys.* **57** 3514

Chaughule R S, Radhakrishnamurthy C, Sampathkumaran E V, Mallik S K and Vijayaraghavan R 19 *Mater. Res. Bull.* **18** 817

Finney J L and Wallace J 1981 *Proc. Fourth Int. Conf. Rapidly Quenched Metals*, (ed) T Masumoto a K Suzuki Sendai Japan p 253

Gray D E (ed.) 1963 *AIP Handbook* (2nd edition) (New York: McGraw-Hill) Chapter 5 p 190

Haregawa R 1976 *AIP Conf. Proc.* **29** 216

Harold V and Koster U 1978 *Proc. Third Int. Conf. Rapidly Quenched Metals Brighton* (ed) B Cantor 1

Heinrich K F J 1981 *Electron beam micro analysis* (New York: Van Nostrand) p 355

Mohri K 1984 *IEEE Trans. Mag.* **20** 942

Radhakrishnamurthy C, Lkhite S D and Sahasrabudhe P W 1978 *Proc. Indian Acad. Sci.* (*Earth Pla. Sci.*) **87A** 245

Rao C N R 1985 *Bull. Mater. Sci.* 7 155

Sasada I, Hiroike A and Harada K 1984 *IEEE Trans. Mag.* **20** 951

Suja N T, Arai K I, Shiirija Y and Masumoto T 1975 *Phys. Lett.* **A51** 121

[illegible] 1975 *J. Phys.* **F5** 800

Mater. Sci., Vol. 8, No. 5, December 1986, pp. 577–580. © Printed in India.

luence of eutectic addition on the electrical conductivity of $_2O:B_2O_3$ system

V K DESHPANDE and K SINGH
Department of Physics, Nagpur University, Nagpur 440 010, India

MS received 4 July 1986; revised 13 November 1986

Abstract. Addition of three eutectics, $Li_2SO_4:Li_2CO_3$, $3Li_2O{\cdot}Nb_2O_5:LiNbO_3$ and $AgI:Ag_2SO_4$ has been tried in the $Li_2O:B_2O_3$ glass system. The electrical conductivity increases with the addition of eutectic. The amount of lithium fraction and the melting point of the eutectic govern the conductivity.

Keywords. Eutectic; lithium fraction; electrical conductivity.

Introduction

recent years, considerable research has been devoted to electrolytes based on Li n conducting glasses suitable for solid state batteries. Non-crystalline solid electrotes have definite advantages over their crystalline counterparts, like isotropic roperties, ease of thin film formation, flexibility of size and shape (at satisfactory ost) etc. One of the important features of glass as a solid electrolyte is the possibility f continuous change of the composition over a wide range. A major characteritic of oxide glasses concerns the large variation in the conductivity with alkali oxide ontent. Recently, more complex glasses have been synthesized by dissolving salts in n oxide based glass (Smedley and Angell 1978; Levasseur *et al* 1979a).

A number of workers have reported fast ion conduction in lithium borate glasses Otto 1966; Charls 1966; Levasseur *et al* 1979b; Biefeld *et al* 1978; Audier *et al* 1976; Malugani and Robert 1979; Glass *et al* 1978). As reported by Singh and Rokade 1984), conventionally quenched $Li_2O:B_2O_3$ (40:60 m%) is the best homogeneous glass-forming composition with maximum conductivity. Tuller and Button (1985) ave suggested that an enhancement in the conductivity of $Li_2O:B_2O_3$ system can e obtained by increasing the alkali ion concentration. According to Øye (1963) the mobility of Li ion increases in the presence of silver ions. Low melting point is one of the important criteria responsible for high ionic conductivity (Reau *et al* 1978). In a binary system, an eutectic is the lowest melting point composition.

By considering the above factors, an attempt has been made to study the influence on the electrical conductivity of $Li_2O:B_2O_3$ (40:60) system by the addition of $Li_2SO_4:Li_2CO_3$, $3Li_2O.Nb_2O_5:LiNbO_3$ and $AgI:Ag_2SO_4$ eutectics. It is expected that the presence of these eutectics in the glass system under study will provide an enhancement in the conductivity.

2. Experimental details

In the present work, the starting materials, Li_2SO_4, Li_2CO_3, B_2O_3, AgI, Ag_2SO_4 and Nb_2O_5 of 99·9% purity were used for the synthesis of the glasses. For preparing

$Li_2SO_4:Li_2CO_3$ eutectic, about 10 g of raw material in eutectic ratio (60:40) m% was weighed to an accuracy of 0·0001 g and mixed under acetone. The mixture was then heated in an electric furnace. It was maintained at a temperature of 20 K above the melting point for 2 hr to homogenize the melt. Then the melt was quenched in an aluminium mould at room temperature. This eutectic was then crushed to a fine powder and added in the host $Li_2O:B_2O_3$ system.

Similarly, other eutectics of $3Li_2O.Nb_2O_5:LiNbO_3$ and $AgI:Ag_2SO_4$ were prepared. Later, these eutectics were added in different concentrations to the lithium borate glass. In all these compositions, the ratio of $Li_2O:B_2O_3$ was maintained to be 40:60 m%. After quenching the glasses in aluminium mould, they were immediately transferred to an annealing furnace maintained at 473 K. After 4 hr of annealing, the samples were subjected to furnace cooling.

The glasses thus obtained were polished flat. Silver paint was used to ensure the ohmic contact before loading the sample in the sample holder which has been described elsewhere (Deshpande and Singh 1982). The conductivity of these samples was measured at 1 kHz as a function of temperature.

3. Results and discussion

Figure 1 shows the variation of log σT vs $10^3/T$ for $Li_2O:B_2O_3$ glass system with addition of three eutectics; $Li_2SO_4:Li_2CO_3$, $3Li_2O.Nb_2O_5:LiNbO_3$ and $AgI:Ag_2SO_4$ In general, the conductivity increases with increase in temperature. Typical conductivity values at two different temperatures, lithium fraction and the melting point o the dopant eutectic, are given in table 1 and it is evident that the addition of all the

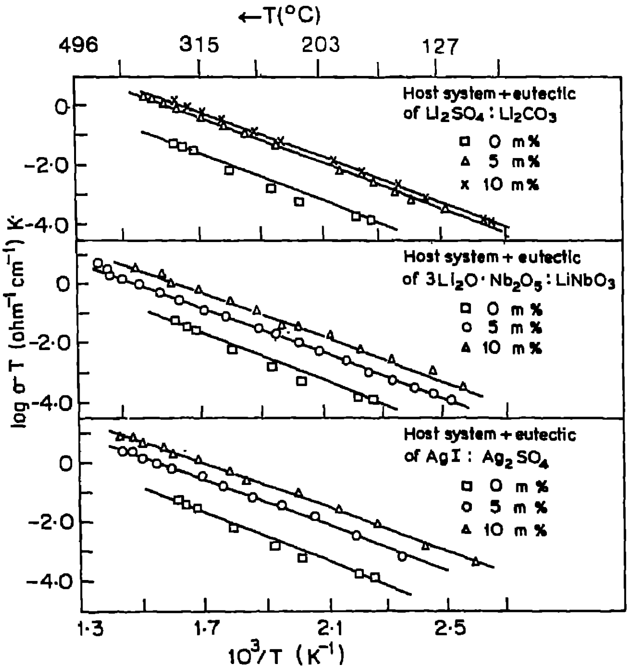

Figure 1. Variation of log σT vs $10^3/T$ for $Li_2O:B_2O_3$ host system with the addition three different eutectic.

Table 1. Conductivity values at 623 and 523 K, lithium fraction and melting point of the dopant eutectic.

$Li_2O:B_2O_3$ (40:60) + 10 m% of eutectic	σ in ohm^{-1} cm^{-1} at 623 K	523 K	$^{*}f_{Li^+}$	Melting point of the eutectic
$Li_2SO_4:Li_2CO_3$	$1{\cdot}15\times10^{-4}$ $2{\cdot}02\times10^{-3}$	$5{\cdot}70\times10^{-5}$ $1{\cdot}51\times10^{-4}$	0·80 0·92	530°C (Amadon 1912)
$3Li_2O{\cdot}Nb_2O_5:LiNbO_3$	$1{\cdot}60\times10^{-3}$	$1{\cdot}35\times10^{-4}$	0·84	1160°C (Reismen 1958)
$AgI:Ag_2SO_4$	$4{\cdot}03\times10^{-3}$	$5{\cdot}3\times10^{-4}$	0·72	158°C (Takahashi *et al* 197

$$^{*}f_{Li^+}=\frac{^{2n}Li_2O+{}^{2n}Li_2SO_4+{}^{2n}Li_2CO_3}{^{n}Li_2O+{}^{n}B_2O_3+{}^{n}Li_2SO_4+{}^{n}Li_2CO_3}$$

where n_i is the number of moles of constituent i in the mixture.

three eutectics enhances the conductivity of the host system by more than an order magnitude. The enhanced conductivity for higher concentration of the first t eutectics is due to increased Li^+ fraction. Similar enhancement in the conductiv with increasing Li^+ fraction has been reported earlier (Deshpande *et al* 1985).

Among the three eutectic samples, the conductivity for $3Li_2O.Nb_2O_5:LiNbO$ minimum. This is because of its higher melting point and lower lithium fraction th that for $Li_2SO_4:Li_2CO_3$. The lithium fraction for 10 m% $Li_2SO_4:Li_2CO_3$ contain sample (0·92) is higher than that observed for 7 m% Li_2SO_4 containing $Li_2O{:}B$ glass (0·88) (Deshpande *et al* 1985). Also the conductivity in this case is higher th what was reported earlier for 7 m% Li_2SO_4 added sample. Thus, the melting poin the eutectic and the lithium fraction governs the conductivity for eutectic of lith salts.

For 10 m% $AgI:Ag_2SO_4$ eutectic, maximum conductivity is observed. Th because of the lowest melting point of this sample over all the others studied in present investigation. This sample was a homogeneous glass without any cr llization in it suggesting that, upto 10 m%, $AgI:Ag_2SO_4$ gets adjusted in amorphous matrix of the host system. The SO_4, being tetrahedra might exten BO_3/BO_4 glass network. Due to the larger size of the iodine, it expands the l which enhances the mobility of the mobile ion. In this case, silver ions might contribute to the conduction. However, due to non-availability of the experim facilities, it was not possible to separate out the contribution of silver and lit ions. The study of AgX(X = I, Br) containing borate glasses suggests tha containing glasses give more conductivity (Minami *et al* 1982). According to M (1983), those Ag ions surrounded by halide ions in the glass contribute t conduction. In B_2O_3 containing glasses, Ag ions interacting with BO_4 grou contribute to the conduction as well as the Ag ions surrounded by halide i

4. Conclusion

From the present investigation it can be concluded that, lower the melting p the eutectic, higher is the conductivity of the system. The maximum v conductivity, $\sigma\simeq4{\cdot}03\times10^{-3}$ ohm^{-1} cm^{-1} at 623 K obtained for sampl 10 m% $AgI:Ag_2SO_4$ eutectic can be used for technical applications.

References

Amadori M 1912 *Atti Relea Acad.* Lincel Sex II **21** 68

Audier M, Ravaine D and Souquet J C 1976 *C R Acad. Sci.* **C282** 499

Biefeld R M, Johnson R T and Baughman R J 1978 *J. Electrochem. Soc.* **125** 179

Charls R J 1966 *J. Am. Ceram. Soc.* **49** 55

Deshpande V K and Singh K 1982 *Solid State Ionics* **6** 18

Deshpande V K, Rokade S and Singh K 1985 *Proc. Sixth Riso Int. Symp. on Transport-structure Relations in fast ion and Mixed Conductor,* (eds) F W Poulsen, N Hessel Andersen, K Clausen, S Skaarup and O Toft Sorensen (Denmark: RISØ National Laboratory) 227

Glass A M, Nassau K and Negran T J 1978 *J. Appl. Phys.* **49** 4808

Levasseur A, Kbala M, Brethous J C, Reau J M and Hagenmuller P 1979a *Solid State Commun.* **32** 839

Levasseur A, Brethous J C, Reau J M and Hagenmuller P 1979b *Mater. Res. Bull.* **14** 921

Malugani J P and Robert G 1979 *Mater. Res. Bull.* **14** 1075

Minami T, Ikeda Y and Tanaka M 1982 *J. Non-Cryst. Solids* **52** 159

Minami T 1983 *J. Non-Cryst. Solids* **56** 15

Otto K 1966 *Phys. Chem. Glasses* **7** 29

Øye H A 1963 Thesis, Trondheim, Norway

Reau J M, Portier J, Levasseur A, Villenuve and Pouchard M 1978 *Mater. Res. Bull.* **13** 1415

Reismen A and Holtzberg F 1958 *J. Am. Chem. Soc.* **18** 6503

Singh K and Deshpande V K 1982 *Proc. DAE Symp. on Interactions at electrode Electrolyte Interfaces* Indian Inst. Technol., Madras, p 167

Singh K and Rokade S 1984 *J. Power Sources* **13** 151

Smedley S I and Angell C A 1978 *Solid State Commun.* **27** 21

Takahashi T, Nomura E and Yamamoto O 1972 *J. Appl. Electrochem.* **2** 51

Tuller H L and Button D P 1985 *Proc. Sixth Risø Int. Symp. on Transport-structure Relation in fast ion and Mixed conductors, Denmark,* 119

Bull. Mater. Sci., Vol. 8, No. 5, December 1986, pp. 581–586. © Printed in India.

Optical black coatings for space applications

K RAMASESHAN, M VISWANATHAN and G K M THUTUPALLI
ISRO Satellite Centre, Bangalore 560 017, India

MS received 19 October 1985; revised 2 January 1986

Abstract. The durability properties of PTX-205 optical black coatings deposited on metallic and non-metallic substrates are studied. The coatings are stable against adverse environmental requirements for space applications. Typically, coatings with 8–11 μ thickness are opaque and have an average reflectance loss ($<5\%$) in the spectral range of 200–1500 nm. The absorption to emission ratio is 1·01.

Keywords. Black coatings; opaque coatings.

1. Introduction

Electrically conducting optical black coatings are extensively used in various terrestrial and space-oriented optical, thermal and electrical appliances (Birnbaum *et al* 1982). A few important applications among these are: (i) in high absorbing and low scattering of optical devices in far infrared cryogenic systems; (ii) as special masks in satellite-based electro-optical sensors; (iii) in thermal detectors and solar absorbers to increase their efficiency; and (iv) in space-borne systems to keep the differential charging of spacecraft external surfaces and equipment to a minimum to prevent problems due to electrostatic fields, arc etc.

For these, a variety of optical black coatings ranging from simple carbon soot layers of burning camphor, wax, kerosene etc., to vacuum-evaporated metallic and non-metallic blacks are available (Harris *et al* 1948; Okanto and Hatanaka 1981). However, when these coatings are used for defence and space applications, they should not only meet the basic optical and electrical properties needed for terrestrial systems, but also should functionally be stable against the adverse environmental conditions (table 1) to which they are exposed to, over an extended period of time. But, our experience shows that the majority of these black coatings cannot meet these requirements.

Even among the limited black paints available, there are hardly any studies available on their durability properties although their optical and electrical properties are known. In many cases, the details of the process technology are kept as guarded trade secrets.

Keeping these in view, a systematic study of the functional and durabilit properties of various organic and inorganic blacks has been carried out and in thi paper, the coating process technology, the functional and durable properties o PTX-205 of Polytronix brand are reported (Back 1982).

2. Process technology

The various performance requirements and specifications to be met for a usef space/terrestrial borne black paint are summarized in tables 1 and 2. While some

Table 1. Performance specifications.

Adhesion	Cellotape peel test (MIL-F-48616)
Abrasion	Eraser abrasion for 50 strokes with 0·5 kg continuously applied.
Humidity	Steady state (48° ± 2°C) and 95–100% relative humidity for 24 hr (MIL-C-675A)
Temperature	
(a) Soaking	at high temp. +85°C for 24 hr at low temp. −85°C for 24 hr
(b) Thermal shock	100 cycles, each cycle consisting of a dwell time of 10 min each, at +85°C, ambient, −85°C, ambient and then back at +85°C with a transfer time from one temperature to another in less than 15 sec
Vacuum baking	At 85°C and 10^{-5} torr for 24 hr
Salt solubility	Immersed in a salt solution of 4%, (common salt in water) at room temperature for 24 hr (MIL-C-675A)

Table 2. Performance specifications.

Parameter	Desired value
Substrate for coating	Metallic/non-metallic
Outgassing (total mass loss)	Less than 1%
Pinholes on the coated area	Class-A (number of pinholes of size 0·05 mm per square cm will be less than 1).
Transmittance	1% in the visible and near IR
Total reflectance	<5%
Emissivity	>0·8

the applications such as thermal control of devices require only deposition of blac coatings on suitable metallic/non-metallic substrates, some other applications suc as (space borne sensor masks etc) also require a suitable pattern generation on th black paints. Therefore, its optimized process technology is presented in this pape The functional and durability properties of the black paint so deposited on metalli non-metallic substrates with and without pattern are also reported.

2.1 *Substrate preparation*

For non-metallic substrates, optically plane glass and quartz (25 mm × 25 mm si and 1·5 mm thick) are taken and their surface quality is better than 60:40 in t optical standards. Aluminium and copper foils (25 mm × 25 mm square and 100 thick) and free from sleeks, scratches and wrinkles etc., are used for metall substrates.

Substrate cleaning prior to deposition of coating plays a vital role and t following cleaning procedure is adopted. The glass and quartz substrates are vapo degreased to remove grease, oil etc in reagent grade trichloroethylene, followed b sequential ultrasonic cleaning in alkaline solution, distilled water and chromic ac These are then rinsed in distilled water and finally, ultrasonically, cleaned in reag grade isopropyl alcohol. The aluminium and copper foils are vapour-degreased and cleaned in dilute hydrochloric acid, distilled water and dried. The substrates are baked at 200°C for 30 min.

2.2 *Coating process and generation of pattern*

The cleaned dry surface on which the black coating has to be deposited is treated with silane type adhesion promoter (Polytronix) and spin-dried at 4000 rpm. The black paint is then spread uniformly, spin-coated and baked at 90°C for 45 min. The photoresist (Waycoat HPR-204 positive photoresist) is similarly spin-coated on the dried black surface and pre-baked at 90° for 45 min. The photoresist is exposed under the desired photomask, developed and post-baked at 90°C for 45 min. The unprotected black is etched in a warm dilute alkaline solution at 50°C to realize the final pattern. The treated surface is rinsed in distilled water and dried. The undeveloped photoresist is stripped and the sample is baked at 200°C for 60 min.

2.3 *Thickness measurement*

Thickness of black coatings is maintained in the range of 8–12 μ. Films with thickness lower than 8 μ on the non-metallic substrates cannot meet the required opacity level. On the other hand, for films, thicker than 12 μ on both metallic and non-metallic substrates, although the functional properties remain unaltered the adhesion is poor. The thickness is measured at various points randomly on the coatings using vertical metroscope (Carl Zeiss, Jena ABBE P 01) having a resolution of 0·1 μ.

It has been observed that due to variations in the speed of the spinning system used in this Laboratory, a non-uniformity upto ±0·5 μ is noticed in the coatings. But as it can be seen later, these variations do not have adverse effect on the required properties of the coatings when subjected to environmental test conditions.

3. Test results

3.1 *Functional properties*

3.1a *Thermo-optical properties*: The transmission spectra of the coated samples are measured in the range of 400–1000 nm and 2–15 μ on spectrometers (Schimatzu Model VV-120-02 and Perkin Elmer Model 783). The reflection spectra are measured in the same ranges on the photospectrometer (Beckmann Model AC 7A MIV and Perkin Elmer Model 783). For non-metallic substrates, the average reflectance is <5% in the entire spectral range and transmittance is <0·1% in the range 400–1500 nm and zero in the range 2–15 μ. For metallic substrates, while the transmittance is zero, the reflectance values are less than 5% in the entire spectral range. Typical reflectance spectra on metallic/non-metallic substrates are shown in figures 1a and 1b. The noise spectrum in the range 6 to 7 μ seen in figure 1b is due to the ambient water vapour and is not the intrinsic property of the coatings.
values are measured using an emissometer (Devices and Services

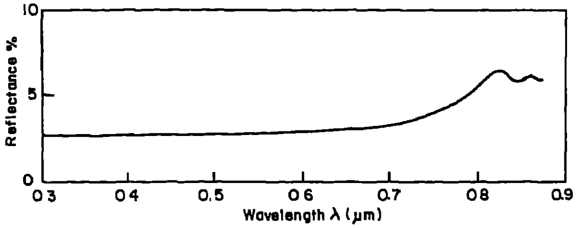

Figure 1a. Reflection spectra of PTX-205.

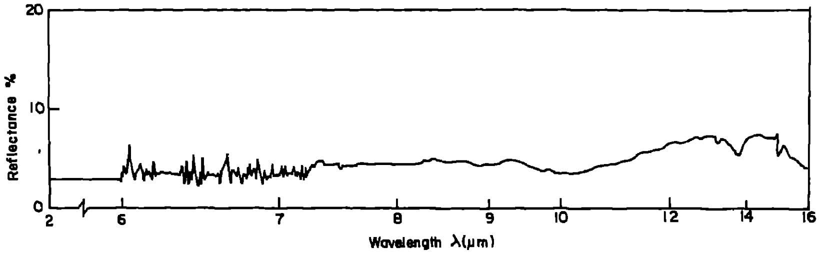

Figure 1b. Reflection spectra of PTX-205.

Company Model 4, E.S.No. 175) and the values range from 0·83 to 0·86 depending upon the surface finish. However, the results are reproducible to an accuracy of ±1%. The corresponding absorption to emission (a/e) ratio is calculated to be 1·01.

3.1b *Electrical properties*: To estimate the volume and surface resistivities, the following simple method is adopted.

A conducting foil is cut and placed exactly over the painted area of a metallic substrate and compressed firmly against the paint surface. Resistance is measured from the top surface of the conducting foil to the bottom of the substrate. From this the volume resistivity is calculated. The measurements on different samples show that the volume resistivity is in the range of 18·14 ohm metre to 6·1 ohm metre for the coating thickness corresponding to the range of 10 to 8 μ. The surface resistivity is deduced from this and the corresponding values range from 1·814 ohms per square to 0·76 ohms per square.

3.1c *Mechanical properties*: Five samples are selected at random in a batch of 30 samples and the adhesion test is conducted according to military standards (MIL-F-48616). A scotch tape (peel strength 0·5 kg/cm) is uniformly adhered to the coating surface by pressing it against the surface. The tape is peeled rapidly at an angle between 45° and 90° to the surface. The coating is evaluated for peel-off and other surface defects such as pin holes, scratches etc. Also, the optical properties are measured as post-adhesion test. The bonding is extremely good in all the samples and no deterioration in the optical properties and no defects in the coating surface quality are found

A moderate abrasion test is conducted on the same set of samples. The coatec surface is abraded with a standard eraser mounted in an eraser abrasion countin tester. The rubbing is done across the surface from one point to another over th same path for 50 strokes with a load of 0·5 kg continuously applied. The length of th stroke is approximately 3 times the diameter of the eraser piece. The surface i evaluated for cosmetic defects and the optical properties measured as post-abrasio tests. No deterioration is observed suggesting the good abrasion resistance of th black paint system.

3.2 *Durability properties*

Stability of the functional properties of the samples, when subjected to th accelerated environmental conditions (table 1), is evaluated to ascertain th usefulness of the black coatings for various other applications in space. A batch of samples are divided at random into sets, each consisting of 5 numbers, and tests a conducted on the set of samples in the sequence given in figure 2. Commercial available environmental test chambers are used and the standard procedures a adopted (MIL-C-675A). The results are summarised in table 3.

4. Conclusion

The PTX-black coatings are stable functionally against adverse environmen conditions such as humidity, thermal shock cyclings, etc. These coatings can

Table 3. Summary of test results under accelerated environmental conditions.

Type of test	Inference	
Adhesion	Surface quality Optical properties	—Good —Good
Abrasion	–do–	
Humidity	–do–	
Thermal shock	–do–	
Thermal soaking		
(i) Hot soaking	*Pinholes (5–10 number) appear randomly in samples. But their sizes are <0·05 mm The integrated optical transmission is less than 0·1 the visible and near IR	
(ii) Cold soaking	No change in the surface quality or pinhole size number	
Vacuum baking	*Pinholes appear randomly. But their size is <0·05 The integrated optical transmission is not affected a <0·1%. Total mass loss <1%	
Salt solubility	Surface quality Optical properties	—Good —Good

*(In hot soaking and vacuum baking, except for the vacuum environment, the tempe and duration of heating are the same. Therefore, with extended heating, the pinholes appear due to the release of entrapped air lockets during coating)

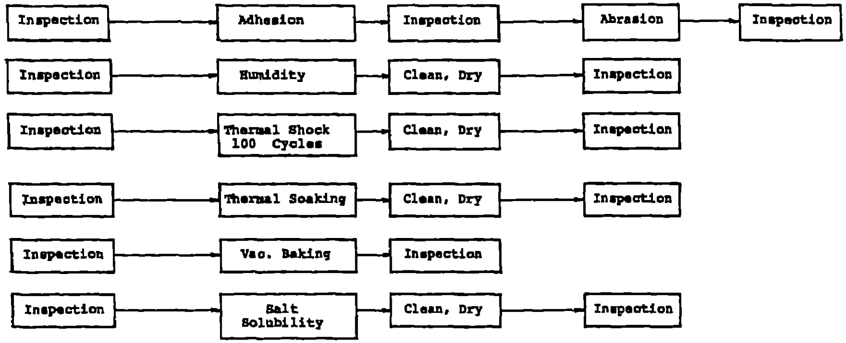

(Inspection is done for surface quality and optical properties.)

Figure 2. Test sequence.

applied on metallic/non-metallic substrates, either as a uniform layer or as layer with required pattern generation and these can find immense applications in various terrestrial and space-borne systems.

References

Birnbaum M, Mettler E C and Cieland E L 1982 *Proceedings of SPIE* **362** 60
Harris L, McGinnies R T and Siegel B M 1948 *J. Opt. Soc. Am.* **38** 582
Lineback R J 1982 *Electronics* April **21** 42
Okanto S and Hatanaka Y 1981 *Bull. Bismuth Inst.* **33** 8
Polytronix data sheet P O Box 3024 Richardson Texas 75081
US Military Specification MIL-C-675A 1976 Coating of glass optical elements
US Military Specification MIL-F-48616 1977 Federal Specification L-T-90 Tape pressure sensitive adhesive cellophane and cellulose acetate

Bull. Mater. Sci., Vol. 8, No. 5, December 1986, pp. 587–590. © Printed in India.

Dislocation density in electrolytically-coloured KCl crystals

N L BHOLE* and B T DESHMUKH
Department of Physics, Nagpur University, Nagpur 440 010, India
*Department of Physics, Vidarbha Mahavidyalaya, Amravati 444 604, India

MS received 5 May 1986; revised 6 August 1986

Abstract. Dislocation densities have been investigated in potassium chloride crystals, electrolytically coloured in the temperature range of 550–710°C. The results show an increase in the dislocation density with coloration temperature upto 650°C and decrease thereafter. This is attributed to the movement of dislocations and interactions between them during electrolytic coloration of the crystals.

Keywords. Dislocation density; electrolytic coloration; coloration temperature; dislocation annihilation.

1. Introduction

It is well known that dislocations play an important role in the coloration of alkali halide crystals (Seitz 1954; Belyeav *et al* 1968; Koikov *et al* 1967). Dislocation densities in electrolytically-coloured alkali halides have been studied earlier (Deshmukh and Soman 1976; Kolomiitsev *et al* 1978). However, there is no work on the temperature variation of dislocation density in electrolytically-coloured crystals. An attempt is therefore made in this paper to study the effect of variation of coloration temperature on dislocation density in electrolytically-coloured KCl crystals.

2. Experimental procedure

Single crystals of KCl used in the present work were grown from melt by the Czochralski technique. Two crystals (each of size $10 \times 5 \times 5$ mm^3) obtained from the as-grown block were used in the experiments. One of them (to be electrolytically-coloured) was mounted between two platinum electrodes (one pointed electrode and the other flat) and the other was placed beside it in the coloration furnace. The temperature of the crystals was measured with an accuracy of ± 5°C by chromel-alumel thermocouple. The crystals were kept at the required temperature for nearly an hour. The crystal clamped between the electrodes was coloured with a pointed cathode by applying a DC electric field of 120 V. After coloration, both the coloured and uncoloured crystals were quenched by rapidly removing them from the furnace and placing them on the metal plate. In this manner the crystals were coloured at desired temperatures ranging from 550°C to 710°C.

The coloured and uncoloured crystals were cleaved from the central part of the crystals and etched with an etchant consisting of an ethanol (99%) saturated at 50°C with $PbCl_2$. This etchant is found to attack at dislocation sites on (100) faces of KCl crystals. The dislocation density was measured with a NU_2 research microscope on a number of crystal specimens and the average dislocation density was obtained at each temperature.

Results and discussion

s observed that electrolytic coloration proceeds at a faster rate with increase of oration temperature i.e. the efficiency of formation of colour centres increases with rease of coloration temperature. For example, the coloration over the entire stal takes 4 min at 550°C and about 30 sec at 710°C.

̄igures 1a and 1b respectively show the variation of dislocation density with iperature in KCl crystals for uncoloured and coloured crystals. The dislocation isity varies linearly with temperature in uncoloured crystals and nonlinearly in oured crystals. Dislocation density in coloured crystals reaches a maximum at)°C and decreases on either side of 650°C. Figures 2a, b and c show the otomicrographs of dislocation patterns in KCl crystals electrolytically-coloured 550°C, 650°C and 710°C respectively. Figure 2b shows the maximum dislocation isity at 650°C.

Γhe observed increase of dislocation density linearly with quenching temperature uncoloured crystals can be attributed to severe surface stresses developed in the 'stals with increasing quenching temperature (Rao and Hari Babu 1976; Chawre *al* 1978).

For coloured crystals the coloration temperature range can be divided into two rts (i) coloration temperature from 550°C to 650°C in which the dislocation isity increases with temperature and (ii) coloration temperature above 650°C in iich dislocation density decreases with temperature. In the range 550–650°C, as the location density increases linearly with coloration temperature the behaviour of ; coloured crystal is similar to that of the uncoloured one and the increase in location density can again be attributed to surface stresses. In other words, the ctrolytic coloration has only a little effect on the increase of dislocation density to coloration temperature 650°C. Its effects in decreasing the dislocation density in Cl crystals are, however, seen above the coloration temperature of 650°C.

Electrolytic coloration occurs at high temperature with large electric field gradient. nder these conditions, dislocations move inside the crystals. In the range of loration temperature 550–650°C, the dislocations during their motion may take icancies (possibly anion vacancies) with them thereby forming positive jogs in them.

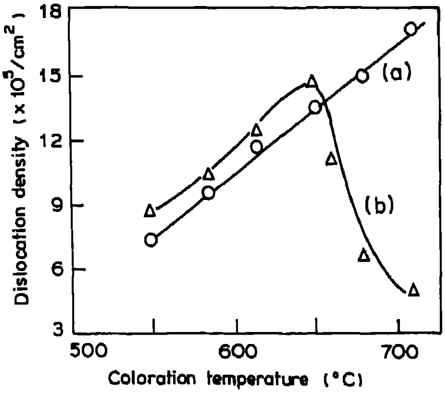

Figure 1. Variation of dislocation density with temperature in KCl crystals (a) uncoloured, (b) electrolytically coloured.

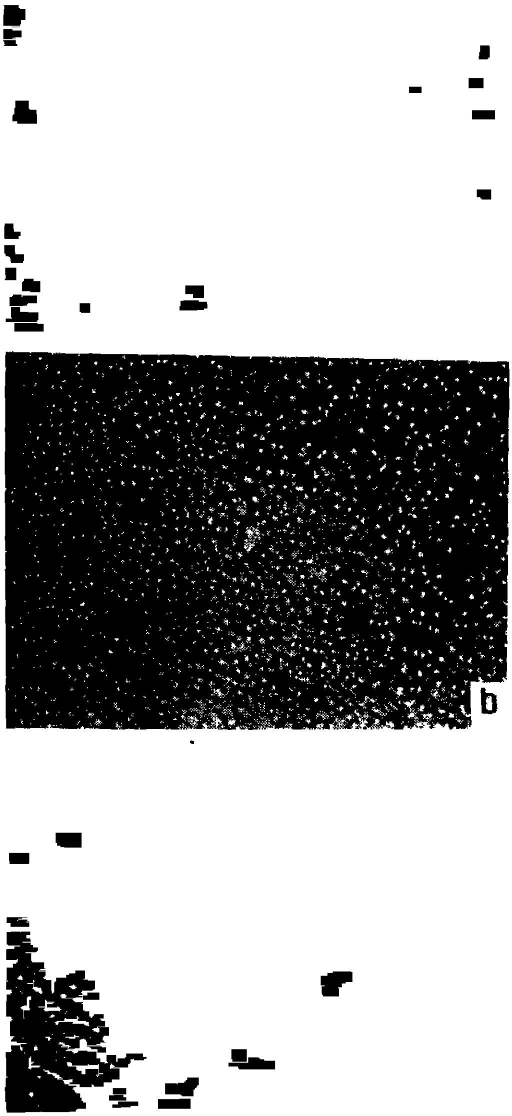

Figure 2. Photomicrographs of electrolytically coloured KCl crystals. **a.** Coloured at 550°C; **b.** Coloured at 650°C; **c.** Coloured at 710°C.

These anion vacancies may be formed due to the dissociation of *F*-centres by dislocations (Sierra and Cabrera 1975). This presence of jogs in the dislocation impedes its motion. The dislocations will thus move comparatively slowly which will lead to an increase in the dislocation density. The jogs in the dislocation may increase with increase of coloration temperature which will provide greater resistance to the motion of dislocation. As a result, dislocations will move slowly with increasing coloration temperatures thereby giving rise to an increase in dislocation density with increasing coloration temperatures.

In the range of coloration temperature 650–710°C the decrease of dislocation density can be attributed to the mutual annihilation of opposite edge dislocations. This might occur because, in this temperature range the dislocations become sufficiently mobile to cause their annihilation. The annihilation of opposite dislocations may result from the following two processes: (i) when two opposite dislocations glide on the same plane, their mutual interaction results in a perfect lattice; (ii) when two opposite edge dislocations glide on neighbouring planes, their interaction will leave a row of vacancies or interstitials. This row of vacancies or interstitials diffuse away under the conditions of high temperature and high electric field gradient of electrolytic coloration leaving a perfect lattice. This process of diffusion of vacancies or interstitials is energetically costly and thus occurs at high temperatures only. The above two processes contribute to the decrease in dislocation density above 650°C. Deshmukh and Soman (1976) observed such a decrease in dislocation density in alkali halides on electrolytic coloration. The process of annihilation of dislocations increases at increasingly high temperatures which results in decrease in dislocation density at temperatures beyond 650°C. At temperatures upto 650°C the energy supplied is insufficient for the diffusion of vacancies produced during the interaction of opposite dislocations. Hence the process of annihilation of opposite dislocations does not occur before 650°C.

4. Conclusions

Our results show that the dislocation density in the electrolytically coloured KCl crystals increases with coloration temperature upto 650°C and decreases thereafter. The following conclusions can be drawn: (i) The efficiency of electrolytic coloration increases with coloration temperature in KCl crystals, (ii) dislocation density in electrolytically coloured KCl crystals varies nonlinearly with coloration temperature, (iii) dislocations in electrolytically coloured KCl crystals are generated in the temperature range 550–650°C whereas they are annihilated in the temperature range 650–710°C.

Acknowledgement

NLB is thankful to the UGC, New Delhi for financial assistance.

References

Belyeav V D, Semuskin G B and Tsikın A N 1968 *Sov. Phys. Solid State* **9** 2564
Chawre R S, Jain S K and Shrivastava R N 1976 *Indian J. Pure Appl. Phys.* **16** 434
Deshmukh B T and Soman S T 1978 *Pramana* (*J. Phys.*) **7** 423
Koikov S N, Semuskin G B and Tsikin A N 1967 *The Physics of dielectrics and semiconductors* (Leningrad)
Kolomiitsev A I, Svetashov A A and Tyapunina N A 1978 *Sov. Phys. Crystallogr.* **23** 138
Rao M L and Hari Babu V 1976 *Indian J. Pure Appl. Phys.* **14** 769
Seitz F 1954 *Rev. Mod. Phys.* **26** 64
Sierra J and Cabrera J M 1975 *Phys. Status. Sol.* **A27** K43

ter. Sci., Vol. 8, No. 5, December 1986, pp. 591–595. © Printed in India.

-temperature attachment for a four-circle neutron diffractometer

A SEQUEIRA, SANDHYA BHAKAY-TAMHANE and S R SAWANT*
Neutron Physics Division, *Physics Group Workshop, Bhabha Atomic Research Centre, Trombay, Bombay 400 085, India

MS received 29 September 1986

Abstract. A single-stage closed-cycle helium gas cryogenerator, capable of cooling between 77 K and 300 K, has been installed on the 4-circle neutron diffractometer at CIRUS. The cryo-tip assembly has been incorporated directly on the φ-circle of the full-circle crystal orienter in place of the goniometer head used in room temperature experiments. The salient features of this low-temperature attachment and its performance are discussed.

Keywords. Low temperature diffraction; diffractometer cryo-assembly; helium gas cryo-tip; closed-cycle cryogenerator.

ntroduction

cryostat mounted on a conventional four-circle diffractometer (with an Eulerian le) must be capable of tilting atleast 90° off the vertical and work for long ods without interruption. This places severe limitations on the type of cryotips on these diffractometers. A number of different cryo-systems for use on x- neutron single-crystal diffractometers have been reported; the various methods table 1) can be broadly classified (Rudman 1976) into: (a) gas stream i.e. a stream old gas (He, N_2 or air) is directed over the sample, (b) conduction i.e. the sample ooled by means of a good thermal conductor (cold finger) in contact with a ling unit; the cooling unit may be a cold bath, mechanical refrigerator, rmoelectric cooler, Joule–Thomson expansion device or a closed-cycle cryo- igerator and (c) immersion, where the entire camera is immersed in cold liquid cold liquid is dripped over sample.

The immersion method does not allow a fine temperature control. The gas stream thod (Lippman and Rudman 1976; Burbank 1973), though easily adaptable to any trument, is not so convenient due to the cumbersome nature of cryogen handling quid N_2 or compressed gas), temperature instability during cryogen refilling and sting problems, which persist even with proper insulations during the actual rking of a cryo-system over prolonged periods of time as in neutron diffraction.

The conduction cooling apparatus with liquefied gasses (Coppens *et al* 1974) was t favoured as the levels of performance of these systems seem to be directly oportional to their cost and complexity. Thermoelectric coolers (working on the ebeck–Peltier thermoeffect), though very clean and simple to operate, are capable f cooling to only −45°C with a single-stage (Agron *et al* 1972) and to −80°C with ulti-stages (Khan and Erickson 1970) and hence are of limited use. Alternately, self- gulating Joule–Thomson coolers are also not convenient to use, due to the ringent requirements on the purity and dryness of gas, the cleanliness of gas lines nd the open cycle nature of the operation.

The introduction of closed-cycle cryo-refrigerators has made available a new range f cryogenic devices inexpensive in use and simple to operate, as against the earlier

Table 1. Different cryo-systems in use.

Type of apparatus	Manufacturers
Gas stream cooling apparatus	Enraf-Nonius, Netherlands; Philips X-ray Instruments, Netherlands; Rich Seifert, West Germany; Syntex Analytical Instruments, USA; Techsnabexport, USSR.
Conduction cooling with liquid N_2 or liquid He continuous-flow cryostats.	Air-Products and Chemicals USA; Cryogenic Associates, USA; Oxford Instruments, UK.
Thermoelectric coolers	Borg-Warner Corp., USA; Jepson Thermoelectrics, USA; Cambion Thermoelectrics, USA.
Self-regulating J-T coolers	Hymatic Engineering, UK; Air-Products and Chemicals, USA.
Closed-cycle cryo-refrigerators.	Air-Products and Chemicals. USA; Custom-built according to specified requirements.

cryo-systems which have liquids as refrigerants or are somewhat uneconomical in prolonged operations. Further, the cold-tip is so compact that its adaptation on a full-circle diffractometer is not a problem; with minor modifications the same design can be used on a x-ray diffractometer. The cryo-tip opted for was a compact single-stage Air-Products DISPLEX (model CS–1003) closed-cycle cryo-system capable of cooling in the range 45–300 K. The DISPLEX system is a closed-cycle cryogenerator, consisting of a single-stage displacer/expander cooler, a compact air-cooled, oil-lubricated compressor module with integral oil clean-up package and electrical controls. The compressor is connected to the valve assembly with flexible metal lines, the valve assembly in turn is connected to the displacer/expander cold end with more flexible nylon tubings. M/s Air-Products have modified the cold head, embedding a standard 30 Watt heater and chromel/gold (0·07 atomic% iron) thermocouple according to our requirements and supplied a compatible temperature controller. The refrigeration capacity of the cooler is 1 W at 77 K. A two-stage DISPLEX cooler was not favoured as the system is not as compact as a single stage one and could not be incorporated on our diffractometer.

2. General description

The neutron diffractometer (Sequeira *et al* 1978) has a 45 cm-dia full-circle crystal orienter which is sturdy enough to carry a cryostat. The single-stage displacer-expander is mounted directly on the φ-circle of the Eulerian cradle. A schematic drawing of the displex-cryo-tip assembly (similar to the ILL, Grenoble assembly (Allibon *et al* 1981)) as incorporated on the φ-circle of the full-circle Eulerian cradle is shown in figure 1. The total height of the cryo-tip is $\sim$10·1 cm while the space available on the χ-circle is $\sim$10·6 cm. Thus no vertical adjustment has been provided for the cold tip. The crystal is mounted directly on the cryo-tip using OFHC copper mounting studs of $\sim$2–3 mm height; the exact height of the stud is matched so that the centre of the sample crystal comes to the centre of the full circle. The crystal orientation is determined directly (without goniometer head) using optimized χ and φ angles for a few reflections. The φ-motion entails the rotation of the cryo-tip on

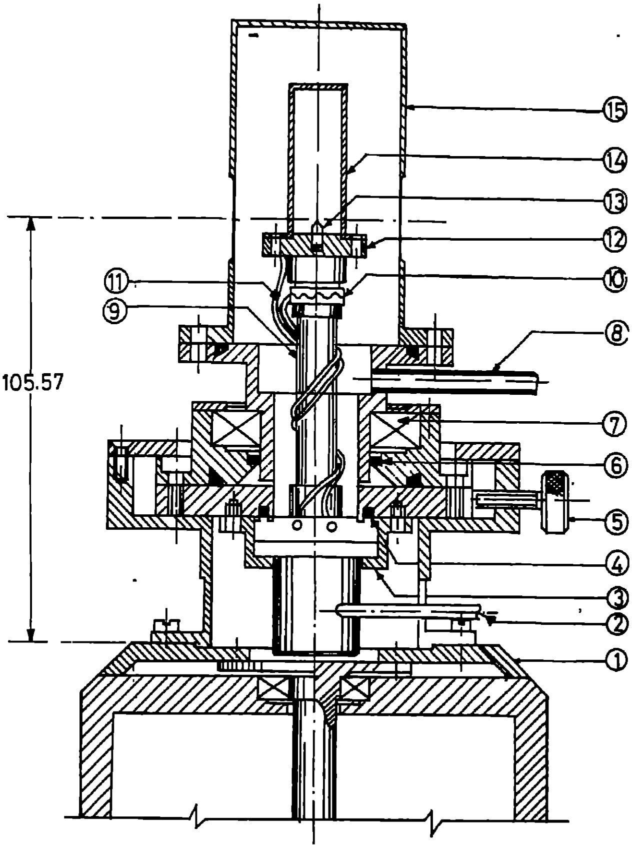

Figure 1. A schematic drawing of the displex cryo-tip assembly as incorporated on the φ-circle of the neutron full circle crystal orientor. The parts indicated are the φ-drive box (1), helium lines to/from cold head (2), split-cup which provides rigid support to cryo-tip and isolates the vacuum chamber from the lower half of the assembly (3), teflon O-ring (4), lateral translation screws (5), rotary vacuum seal (6) and ball-bearings (7) for decoupling the φ-rotation from vacuum pumping port (8) and vacuum shroud (15). The DISPLEX CS-1003 cryo-tip (9) has a heater (10) and a thermocouple (11) embedded in the cold head flange (12). The centre of the diffractometer (13), the inner (14) and outer (15) aluminium vacuum shrouds are also indicated. The cold finger is of OFHC copper; all adapter parts are fabricated using anti-magnetic SS-304.

which the crystal has been mounted. The φ-rotation is decoupled from the vacuum port and vacuum shroud by use of a rotating vacuum seal and ball-bearing to avoid mechanical instabilities arising from a rotating vacuum port. This places limitations on the ultimate vacuum reached ($> 10^{-4}$ torr). A simple rotary pump does the task within half an hour.

Figure 2 shows the various components (valve-motor, cables, gas lines and vacuum inlet) placed to avoid excessive twisting of the lines, fouling up of the moving parts of the diffractometer by cables or lines or obstructing the incident and diffracted beams of neutrons. The rotation of φ has to be limited to 300° both by hardware as well as software to avoid twisting of the nylon tubing connecting the cold head to the valve motor assembly. The vacuum port and the external vacuum shroud is held in place by using two clamps which hold on to the χ-ring.

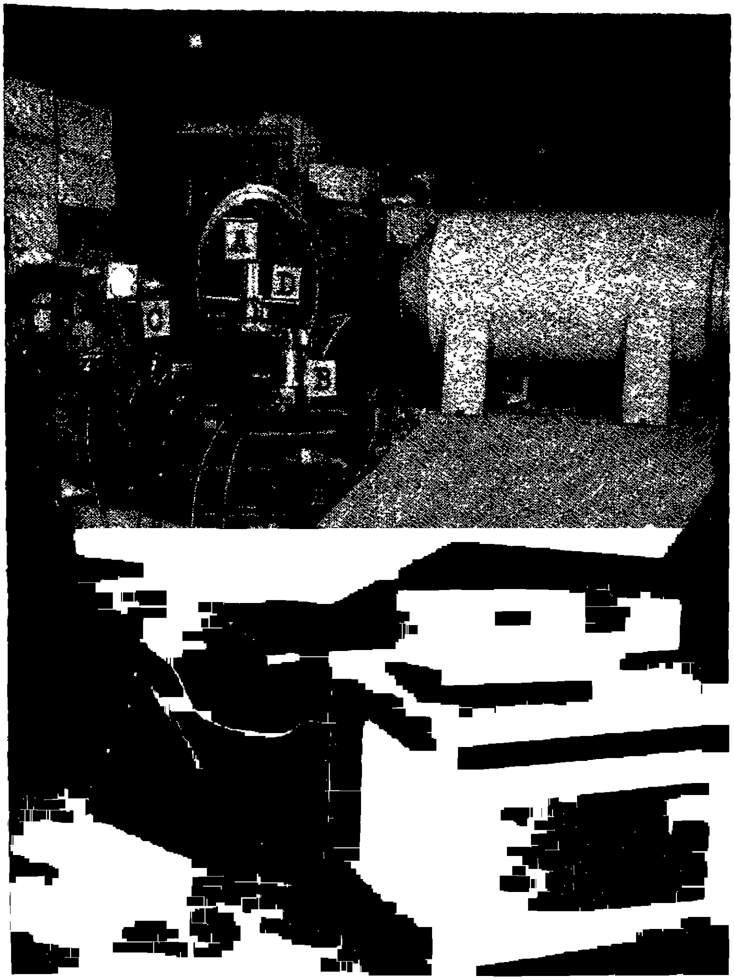

Figure 2. Photograph of the low-temperature assembly after installation on the four-circle diffractometer. (A) is the vacuum shroud over the cryo-tip, (B) is the valve assembly held onto the ω-plate of the diffractometer, (C) is the vacuum port and (D) are the clamps which hold onto the χ-circle. The compressor and temperature controller are placed on a trolley visible in the foreground. The positions of all the components are optimized to minimize the twists/strains on the tubes and possible entangling with the diffractometer moving parts.

The heat and vacuum shields are made of Al; both shields are designed in the forn of cylinders ~0·5 mm thick. The external heat shroud has been ground to ~0·3 mn to provide a window in the region where the beam is incident. In x-ray diffracto meter the vacuum shields will have to be preferably of Be so as to be 'invisible' to x ray radiation.

3. Use and performance

As the positions of all the components have been determined, the mounting of th low-temperature device onto the diffractometer can be accomplished within 10 mi The sample is mounted directly on the cryo-tip using a mounting stud of suitabl the vacuum shields. The Cu cold tip which falls within the beam area has to be covered with Cd to minimize the contamination and background scattering.

The space between the inner and outer vacuum shields is pumped till a vacuum of better than 10^{-3} torr is obtained and cooling is then started. The system cools to 130 K in about 1 hr and to ~ 80 K in approximately 2 hr. The cooling curve is nearly exponential. Temperature control is achieved by using the resistance heater embedded in the cold head along with the chromel/gold (iron) thermocouple and the temperature controller unit. The temperature indicator displays temperature on a 4-digit readout, the resolution is 0·1 K and the stability $\pm 0{\cdot}5$ K. The calibration was done using the room temperature, liquid nitrogen and dry ice temperatures. Though the low temperatures match perfectly well (within $\pm 1°$), the room temperature display is off by 10° and remains so even with all the zero and span adjustments. The low temperature calibration points, however, reproduce themselves.

The assembly is extremely simple to use and can be used without interruption for long periods. The charging of the system with commercial-grade helium gas has to be done once in approximately six months (nominal He-gas pressure 115 psi). Long-term measurements (as required in neutron diffraction experiments) are not possible at temperatures below 90 K as accurate temperature control becomes a problem. Also, if the compressor is used continuously for very long periods (exceeding a month or so), the temperature starts wandering. Further, continuous long usage of the compressor increases the risk of oil cross-over from the compressor; hence regular servicing of the cold head assembly is necessary. The filters installed in the compressor module must also be changed periodically.

The installation of the device introduces limits on the χ and φ angles in addition to the intrinsic blind areas of the diffractometer. The χ accessibility has been nominally restricted to the range $-10° < \chi < 100°$ and φ accessibility to the range 45–300°. Even with these restrictions on the diffractometer angles, half the reciprocal space is accessible for crystals of all space groups other than the triclinic. The facility has so far been used to record over 1500 reflections in five low-temperature data sets to investigate the low-temperature structural phase transitions in $LiKSO_4$ (Bhakay-Tamhane and Sequeira 1986).

Acknowledgement

We are grateful to Dr R Chidambaram for useful suggestions and encouragement.

References

Agron P A, Levy H A and Bogardus B J 1972 *J. Appl. Crystallogr.* **5** 432

Allibon J R, Filhol A, Lehmann M S, Mason S A and Simms P 1981 *J. Appl. Crystallogr.* **14** 326

Bhakay-Tamhane S and Sequeira A 1986 *Ferroelectrics* **69** 241

Burbank R D 1973 *J. Appl. Crystallogr.* **6** 437

Coppens P, Ross F K, Blessing R H, Cooper W F, Larsen F K, Leipoldt J G, Rees B and Leonard R 1974 *J. Appl. Crystallogr.* **7** 315

Khan D C and Erickson R A 1970 *Rev. Sci. Instrum.* **41** 107

Lippman R and Rudman R 1976 *J. Appl. Crystallogr.* **9** 220

Rudman R 1976 '*Low temperature x-ray diffraction*': *Monographs in low-temperature physics* (New York: Plenum)

[illegible] Momin S N, Rajagopal H. Soni J N, Chidambaram R, Dilip Kumar, Ramana Rao A and

Bulletin of Materials Science

Volume 8, January–December 1986

SUBJECT INDEX

Absorptance
  Cobalt oxide-iron oxide selective coatings for high temperature applications 385
Absorption coefficient
  Optical constants in the ultraviolet region of evaporated high index thin films 347
Aluminium oxide
  Microstrip losses with Al_2O_3 overlay 535
Amorphous alloys
  Magnetic hysteresis and crystallization studies on metallic glass alloy $Fe_{67}Co_{18}B_{14}Si_1$ 567
Amorphous
  Electron microscopy study of chemically deposited Ni-P films 433
Amorphous silicon
  Electrical and optical properties of μc-SiH films 267
Anisotropy
  Magnetic hysteresis and crystallization studies on metallic glass alloy $Fe_{67}Co_{18}B_{14}Si_1$ 567
Anodic chemical film
  Electrochemical bath deposition technique: Deposition of CdS thin films 419
Anti-reflection coatings
  Quality and reliability of optical coatings 351
Apex angle
  Computer-aided roll pass design for continuous billet mill 183
Asbestos
  Thermal transformation in a chrysotile asbestos 497
a-Si:H
  a-Si:H/$CuInS_2$ heterojunctions for photovoltaic conversion 285
As-Sb-Se glasses
  Thermal expansion studies on As-Sb-Se glasses 53
Atmospheric pressure chemical vapour deposition
  Growth of polysilicon and silicide films for MOS-VLSI application 297
Attenuation
  Microstrip losses with Al_2O_3 overlay 535
Auxiliary crate controller
  Personal computer-based CAMAC system for data acquisition 225

Barium oxalate
  Periodic crystallization of barium oxalate in silica hydrogel 511
Barium oxalate dihydrate
  Studies on etching of gel-grown barium oxalate dihydrate crystals 519
Beam combiner
  Design and development of a thin film dielectric beam combiner 343
Beta alumina
  Kinetics of electrophoretic deposition of β-alumina 1
$Bi_{2-x}As_xS_3$ films
  Preparation and properties of $Bi_{2-x}As_xS_3$ thin films by solution-gas interface technique 427
Binary diagrams
  Computer calculations of phase diagrams 107
Bit quad
  Image analysis system for quantitative metallography 231
Black coatings
  Optical black coatings for space applications 581

Cadmium films
  X-ray diffraction study of epitaxial zinc and cadmium films prepared by hot-wall technique 449
Calcium molybdate
  Kinetics of calcium molybdate crystallization 489
CAMAC
  Personal computer-based CAMAC system for data acquisition 225
CAMAC trainer software
  Personal computer-based CAMAC system for data acquisition 225
Carrier concentration
  Liquid phase epitaxy growth of GaAs:Si by temperature difference method 439
Carrier injection
  Space charge limited currents in chlorazole black E dye 531
Cathodic chemical film
  Electrochemical bath deposition technique Deposition of CdS thin films 419
$CdZnS/CuInSe_2$
  Thin film $CdZnS/CuInSe_2$ solar cells by spray pyrolysis 279
Ceramics
  Dielectric properties of the system $Pb_{2-x}Nd_xLi_{0\cdot}$ $Nb_{1\cdot 5}O_{6+\delta}$ 2

characterization of flash-
$_2$ thin films 319
osition
vith Al_2O_3 overlay 535
thesized by chemical vapour
ue using hydrofluoric acid as
315
ical properties of SnO_2 films
ical vapour deposition 357
dye
ed currents in chlorazole black
531

nation in a chrysotile asbestos
497
nerator
re attachment for a four-circle
meter 591

rs for high power laser appli-
339

n oxide selective coatings for
e applications 385
s
and activities in the Co-Ni-O
K 71
el oxide solid solution
and activities in the Co-Ni-O
K 71

uel performance code PROFESS
tion for predicting the behaviour
ents of D-Com blind problem
253
e
file analysis of silver base Ag-Cd-
61
erature
ensity in electrolytically coloured
587
design
ed design of rolling mills 123
model
ed roll pass design for continuous
183

r fuel performance code PROFESS
ation for predicting the behaviour
ments of D-Com blind problem
253

ing
ded design of rolling mills 123
lling
ded composition-treatment-struc-
correlation studies in steels 193

Computer model
  Computer modelling application in life prediction of high temperature components 133
Computer modelling
  Computer models for fuel element behaviour 93
  Water reactor fuel performance code PROFESS and its application for predicting the behaviour of the fuel elements of D-Com blind problem 253
Computer simulation
  Computer-aided design of rolling mills 123
  Computer simulation of defects and radiation damage 155
  Computer simulation of pressure sintering 199
  Computer simulation of dislocation-carbon interaction in nickel 247
Concentration
  Kinetics of electrophoretic deposition of β-alumina 1
Condensed phase
  Concept of thermodynamic capacity 453
Copper
  Flash-evaporated thin films of $CuInSe_2$ 291
Copper phthalocyanines
  Thermoelectroluminescence in thin films of zinc and copper phthalocyanines 407
Correlation
  Computer-aided composition-treatment-structure-property correlation studies in steels 193
Crack growth model
  Computer modelling application in life prediction of high temperature components 133
Creep modulus
  Computer simulation of pressure sintering 199
Crystallization
  Glass ceramics containing ferroelectric phases 557
  Magnetic hysteresis and crystallization studies on metallic glass alloy $Fe_{67}Co_{18}B_{14}Si_1$ 567
Crystallization kinetics
  Kinetics of calcium molybdate crystallization 489
$CuInS_2$
  a-Si:H/$CuInS_2$ heterojunctions for photovoltaic conversion 285
$CuInSe_2$ solar cells
  Thin film CdZnS/$CuInSe_2$ solar cells by spray pyrolysis 279
Czochralski technique
  Growth of low dislocation density single crystals of nickel 467

Deformation
  Computer models for fuel element behaviour 93
Dehydration
  Thermal transformation in a chrysotile asbestos 497

Development of ductile permanent magnet
  Magnetic and Mössbauer studies on ductile Fe-Cr-Co permanent alloys 39
Dielectric behaviour
  Microstructural and dielectric behaviour of glass ceramics in the system PbO-BaO-TiO$_2$-B$_2$O$_3$-SiO$_2$ 13
Dielectric films
  Deposition and assessment of thin dielectric films on photocathode substrate made of Kodial glass 325
Dielectric overlay
  Effect of bulk and thin film dielectric overlay on the characteristics of microstrip rejection filter and simple microstriplines 397
Dielectric properties
  Dielectric properties of the system Pb$_{2-x}$Nd$_x$ Li$_{0.5}$Nb$_{1.5}$O$_{6+\delta}$ 23
Differential thermal analysis
  Microstructural and dielectric behaviour of glass ceramics in the system PbO-BaO-TiO$_2$-B$_2$O$_3$-SiO$_2$ 13
Diffractometer cryo-assembly
  A low-temperature attachment for a four-circle neutron diffractometer 591
Dilation
  Image analysis system for quantitative metallography 231
Dislocation
  Computer simulation of dislocation-carbon interaction in nickel 247
Dislocation annihilation
  Dislocation density in electrolytically coloured KCl crystals 587
Dislocation density
  Dislocation density in electrolytically coloured KCl crystals 587
Dislocations
  Computer simulation of defects and radiation damage 155
Displacement damage
  Computer simulation of defects and radiation damage 155
Drop profiles
  An absolute method for the determination of surface tension of liquids using pendent drop profiles 217
Dynamic method
  Computer simulation of defects and radiation damage 155

Edge filter
  Design and development of a thin film dielectric beam combiner 343
Electrical conductivity
  Preparation and characterization of flash-evaporated CuInSe$_2$ thin films 319
  Influence of eutectic addition on the electrical conductivity of Li$_2$O:B$_2$O$_3$ system 577
Electrochemical photovoltaic cells
  Electrochemical bath deposition technique: Deposition of CdS thin films 419
Electrochemistry
  Characterization of Pb$_3$O$_4$ films by electrochemical techniques 415
Electrode separation
  Kinetics of electrophoretic deposition of β-alumina 1
Electroless
  Electron microscopy study of chemically deposited Ni-P films 433
Electrolytic coloration
  Dislocation density in electrolytically coloured KCl crystals 587
Electromotive force
  Phase relations and activities in the Co-Ni-O system at 1373 K 71
Electronic analog
  Computer simulation of serrated yielding 209
Electron microscopy
  Electron microscopy study of chemically deposited Ni-P films 433
Electron-optics
  Development of high resolution thin film patterns on curved photocathode substrates of image tubes 333
Electron tunnelling
  Tunnelling of electrons from deep traps of MgO 49

Electrophoretic deposition
  Kinetics of electrophoretic deposition of β-alumina 1
Electrophoretic kinetics
  Kinetics of electrophoretic deposition of β-alumina 1
Emission spectrography
  Emission spectrographic technique for the quantitative determination of trace elements in granitic rocks 471
Emittance
  Cobalt oxide-iron oxide selective coatings for high temperature applications 385
Epitaxial growth
  X-ray diffraction study of epitaxial zinc and cadmium films prepared by hot-wall technique 449
Erosion
  Some fundamental considerations to precede image analysis 169
  Image analysis system for quantitative metallography 231
Etching
  Studies on etching of gel-grown barium oxalate dihydrate crystals 519

Eutectic
  Influence of eutectic addition on the electrical conductivity of $Li_2O:B_2O_3$ system 577
Extinction coefficient
  Optical constants in the ultraviolet region of evaporated high index thin films 347

Failure
  Computer models for fuel element behaviour 93
Fatigue life
  Computer modelling application in life prediction of high temperature components 133
Feature extraction
  Image analysis system for quantitative metallography 231
Ferroelectric
  Glass ceramics containing ferroelectric phases 557
Figure of merit
  Optical and electrical properties of SnO_2 films prepared by chemical vapour deposition 357
Finite element analysis
  Computer simulation of pressure sintering 199
Fission gases
  Computer models for fuel element behaviour 93
Fission products
  Computer models for fuel element behaviour 93
Flash evaporation
  Flash-evaporated thin films of $CuInSe_2$ 291
Fracture
  Effect of texture and grain size on the mechanical properties of warm-worked cadmium, zinc and zinc-0·35% aluminium alloys 81
Free energy of mixing
  Phase relations and activities in the Co-Ni-O system at 1373 K 71
Fuel performance
  Water reactor fuel performance code PROFESS and its application for predicting the behaviour of the fuel elements of D-Com blind problem 253
Furnace design
  Computer applications in the field of furnace design 147

GaAs:Si doping
  Liquid phase epitaxy growth of GaAs:Si by temperature difference method 439
GaAs thin films
  Surface morphology and properties of GaAs epilayers controlled by temperature difference method of liquid phase epitaxy 29
Gel growth
  Studies on etching of gel-grown barium oxalate dihydrate crystals 519
Gel permeation chromatography
  Determination of molecular weight distribution of polyethylene terephthalate by gelpermeation
Geometrical dimensions
  Computer-aided roll pass design for continuous billet mill 183
Germanium
  Quality and reliability of optical coatings 351
Glass ceramic
  Microstructural and dielectric behaviour of glass ceramics in the system $PbO\text{-}BaO\text{-}TiO_2\text{-}B_2O_3\text{-}SiO_2$ 13
Glass ceramics
  Glass ceramics containing ferroelectric phases 557
Glass transition region
  Thermal expansion studies on As-Sb-Se glasses 53
Global parameters
  Image analysis system for quantitative metallography 231
Grain size
  Effect of texture and grain size on the mechanical properties of warm-worked cadmium, zinc and zinc-0·35% aluminium alloy 81
Granitic rocks
  Emission spectrographic technique for the quantitative determination of trace elements in granitic rocks 471
Growth rate
  Liquid phase epitaxy growth of GaAs:Si by temperature difference method 439

Hall mobility
  Liquid phase epitaxy growth of GaAs:Si by temperature difference method 439
Heating furnaces
  Computer applications in the field of furnace design 147
Heat transfer
  Computer models for fuel element behaviour 93
Heat treatment
  Glass ceramics containing ferroelectric phases 557
Heat treatments
  Magnetic and Mössbauer studies on ductile Fe-Cr-Co permanent magnet alloys 39
Helium gas cryo-tip
  A low-temperature attachment for a four-circle neutron diffractometer 591
Heterojunction
  a-Si:H/$CuInS_2$ heterojunction for photovoltaic conversion 285
High pressure growth
  Growth of low dislocation density single crystals of nickel 467
High temperature components
  Computer modelling application in life prediction of high temperature components 133
Hill climbing technique

- H^+ ion irradiation
  - Effect of H^+ ion irradiation on surface morphology of $Fe_{40}Ni_{40}B_{20}$ metallic glass 505
- Hot-wall technique
  - X-ray diffraction study of epitaxial zinc and cadmium films prepared by hot-wall technique 449
- Hydrothermal cell
  - A simple hydrothermal cell for synthesis at moderate temperature and pressure 543

- Ideal gas mixture
  - Concept of thermodynamic capacity 453
- Image analysis
  - Some fundamental considerations to precede image analysis 169
  - Image analysis system for quantitative metallography 231
- Image tube
  - Development of high resolution thin film patterns on curved photocathode substrates of image tubes 333
- Impurity defects
  - Computer simulation of dislocation-carbon interaction in nickel 247
- Inclusion grade
  - Modern computer assisted methods in metallurgy 239
- Inclusion type
  - Modern computer assisted methods in metallurgy 239
- Indium
  - Flash-evaporated thin films of $CuInSe_2$ 291
- Infrared detection
  - Pyroelectric polymer films for infrared detection 365
- Infrared detector
  - Photoresponsive measurements on $InAs_{0.3}Sb_{0.7}$ infrared detector 373
- Integrated circuits
  - Development of high resolution thin film patterns on curved photocathode substrates of image tubes 333
- Interaction
  - Computer simulation of dislocation-carbon interaction in nickel 247
- Interatomic potential
  - Computer simulation of defects and radiation damage 155
- Interference photoemission
  - Deposition and assessment of thin dielectric films on photocathode substrate made of Kodial glass 325
- Inter level insulator
  - Electrical and structural characteristics of oxides grown from polycrystalline silicon 307
- Iron-chromium-cobalt alloys
  - Magnetic and Mössbauer studies on ductile Fe-Cr-Co permanent magnet alloys 39
- Irradiation behaviour
  - Water reactor fuel performance code PROFESS and its application for predicting the behaviour of the fuel elements of D-Com blind problem 253
- Irradiation effects
  - Water reactor fuel performance code PROFESS and its application for predicting the behaviour of the fuel elements of D-Com blind problem 253
- Isothermal decay
  - Tunnelling of electrons from deep traps of MgO 49

- Lanthanum tartrate crystals
  - Characterization and thermal behaviour of lanthanum tartrate crystals grown from silica gels 547
- Laser
  - Transistors made in laser recrystallized polysilicon on insulator films 391
- Lasers
  - Dielectric mirrors for high power laser applications 339
- Lattice stability
  - Computer calculations of phase diagrams 107
- Lattice statics
  - Computer simulation of dislocation-carbon interaction in nickel 247
- Life prediction
  - Computer modelling application in life prediction of high temperature components 133
- Line profile analysis
  - X-ray line profile analysis of silver base Ag-Cd-In alloys 61
- Liquid phase epitaxy
  - Surface morphology and properties of GaAs epilayers controlled by temperature difference method of liquid phase epitaxy 29
  - Liquid phase epitaxy growth of GaAs:Si by temperature difference method 439
- Lithium fraction
  - Influence of eutectic addition on the electrical conductivity of $Li_2O:B_2O_3$ system 577
- Low temperature diffraction
  - A low-temperature attachment for a four-circle neutron diffractometer 591

- Machine equations
  - Computer simulation of serrated yielding 209
- Magnetic hysteresis
  - Magnetic hysteresis and crystallization studies on metallic glass alloy $Fe_{67}Co_{18}B_{14}Si_1$ 567
- Magnetic properties
  - Magnetic and Mössbauer studies on ductile Fe-Cr-Co permanent magnet alloys 39
- Magnetron sputtering
  - R.F. magnetron sputtered tungsten carbide thin films 379

l synthesis
ıple hydrothermal cell for synthesis at
rate temperature and pressure 543
ıatical models
ıuter applications in the field of furnace
ı 147
: glass
of H^+ ion irradiation on surface
hology of $Fe_{40}Ni_{40}B_{20}$ metallic glass 505
graphy
e analysis system for quantitative metallo-
ıy 231
ıxide semiconductor
vth of polysilicon and silicide films for
ʒ-VLSI application 297
rystalline
ron microscopy study of chemically depo-
Ni-P films 433
trip
'ostrip losses with Al_2O_3 overlay 535
.trip rejection filter
:t of bulk and thin film dielectric overlay on
characteristics of microstrip rejection filter
simple microstriplines 397
ıtructure
rostructural and dielectric behaviour of glass
mics in the system $PbO\text{-}BaO\text{-}TiO_2\text{-}B_2O_3$-
ı 13
y line profile analysis of silver base Ag-Cd-
lloys 61
wave power
rostrip losses with Al_2O_3 overlay 535
rs
lectric mirrors for high power laser appli-
ons 339
oility gap
nputer calculations of phase diagrams 107
l fields
·dern computer assisted methods in metal-
ʒy 239
FET
ınsistors made in laser recrystallized poly-
con on insulator films 391
bauer studies
ıgnetic and Mössbauer studies on ductile Fe-
-Co permanent magnet alloys 39
ilayers
electric mirrors for high power laser appli-
.ions 339

lymium doping
electric properties of the system $Pb_{2-x}Nd_x$
$_{0.5}Nb_{1.5}O_{6+\delta}$ 23
el crystals
'owth of low dislocation density single crystals
nickel 467
el-phosphorous
ectron microscopy study of chemically depo-

sited Ni-P films 433

Noise
  Computer simulation of serrated yielding 209

Nuclear fuel element
  Water reactor fuel performance code PROFESS and its application for predicting the behaviour of the fuel elements of D-Com blind problem 253

Nuclear fuels
  Computer models for fuel element behaviour 93

Opaque coatings
  Optical black coatings for space applications 581

Optical absorption
  Preparation and characterization of flash-evaporated $CuInSe_2$ thin films 319

Optical coating
  Quality and reliability of optical coatings 351

Optical constants
  Optical constants in the ultraviolet region of evaporated high index thin films 347

Optics
  Dielectric mirrors for high power laser applications 339
  Design and development of a thin film dielectric beam combiner 343

Overlay
  Microstrip losses with Al_2O_3 overlay 535

Overture
  Some fundamental considerations to precede image analysis 169

Oxide fuels
  Computer models for fuel element behaviour 93

Oxygen-metal ratio
  Determination of oxygen to metal ratio of U-Pu mixed oxides by x-ray diffraction 479

Oxygen potential
  Phase relations and activities in the Co-Ni-O system at 1373 K 71

Pass sequence
  Computer-aided roll pass design for continuous billet mill 183

Periodic crystallization
  Periodic crystallization of barium oxalate in silica hydrogel 511

Personal computer
  Personal computer-based CAMAC system for data acquisition 225

Phase diagram
  Phase relations and activities in the Co-Ni-O system at 1373 K 71

Phase diagrams
  Computer calculations of phase diagrams 107

Phase identification
  Magnetic and Mössbauer studies on ductile Fe-Cr-Co permanent magnet alloys 39
Photoelectrochemical
  Characterization of Pb_3O_4 films by electrochemical techniques 415
Photoemission
  Development of high resolution thin film patterns on curved photocathode substrates of image tubes 333
Photolithography
  Development of high resolution thin film patterns on curved photocathode substrates of image tubes 333
Photoresponsivity
  Photoresponsive measurements on $InAs_{0.3}Sb_{0.7}$ infrared detector 373
Photovoltage
  Characterization of Pb_3O_4 films by electrochemical techniques 415
Photovoltaics
  a-Si:H/$CuInS_2$ heterojunctions for photovoltaic conversion 285
Pixel
  Image analysis system for quantitative metallography 231
Plasma deposition
  Electrical and optical properties of μc-SiH films 267
Point defects
  Computer simulation of defects and radiation damage 155
Polycrystalline silicon films
  Growth of polysilicon and silicide films for MOS-VLSI application 297
Polycrystalline silicon
  Electrical and structural characteristics of oxides grown from polycrystalline silicon 307
Polyethylene terephthalate
  Determination of molecular weight distribution of polyethylene terephthalate by gelpermeation chromatography 527
Polymer films
  Pyroelectric polymer films for infrared detection 365
Polyoxide
  Electrical and structural characteristics of oxides grown from polycrystalline silicon 307
Pressure sintering
  Computer simulation of pressure sintering 199
Pressure vessel
  Computer modelling application in life prediction of high temperature components 133
Process parameters
  Computer applications in the field of furnace design 147
Property
  Computer-aided composition-treatment-structure-property correlation studies in steels 193
Pyrochlore-structured system
  Dielectric properties of the system $Pb_{2-x}Nd_x Li_{0.5}Nb_{1.5}O_{6+\delta}$ 23
Pyroelectricity
  Pyroelectric polymer films for infrared detection 365

Reactive gas mixture
  Concept of thermodynamic capacity 453
Recrystallisation
  Transistors made in laser recrystallized polysilicon on insulator films 391
Refractive index
  Deposition and assessment of thin dielectric films on photocathode substrate made of Kodial glass 325
  Optical constants in the ultraviolet region of evaporated high index thin films 347
Regression analysis
  An absolute method for the determination of surface tension of liquids using pendent drop profiles 217
Resistivity
  Preparation and properties of $Bi_{2-x}As_xS_3$ thin films by solution-gas interface technique 427
Resolution
  Development of high resolution thin film patterns on curved photocathode substrates of image tubes 333
Rolling force
  Computer-aided roll pass design for continuous billet mill 183
Rolling mills
  Computer-aided design of rolling mills 123
Runge-Kutta method
  An absolute method for the determination of surface tension of liquids using pendent drop profiles 217

Selective coatings
  Cobalt oxide-iron oxide selective coatings for high temperature applications 385
Selenium
  Flash-evaporated thin films of $CuInSe_2$ 291
Semiconductor
  Photoresponsive measurements on $InAs_{0.3}Sb_{0.7}$ infrared detector 373
  Transistors made in laser recrystallized polysilicon on insulator films 391
Serrated yielding
  Computer simulation of serrated yielding 209
Silica gels
  Characterization and thermal behaviour of lanthanum tartrate crystals grown from silica gels 549
Silica hydrogel
  Periodic crystallization of barium oxalate in silica hydrogel 511

Index

n-gate process
  ınsistors made in laser recrystallized polycon on insulator films 391
·n
  ınsistors made in laser recrystallized polycon on insulator films 391
r base ternary alloys
  ray line profile analysis of silver base Ag-Cd-alloys 61
ıle microstriplines
  fect of bulk and thin film dielectric overlay on ɜ characteristics of microstrip rejection filter d simple microstriplines 397
$_2$:F
  ıO$_2$:F films synthesized by chemical vapour ·position technique using hydrofluoric acid as ›ping material 315
$_2$ film
  ptical and electrical properties of SnO_2 films ·epared by chemical vapour deposition 357
ware
  omputer-aided composition-treatment-strucıre-property correlation studies in steels 193
ır cells
  lectrical and optical properties of μc-SiH films 267
d state cell
  'hase relations and activities in the Co-Ni-O ystem at 1373 K 71
ution-gas interface technique
  'reparation and properties of $Bi_{2-x}As_xS_3$ thin lms by solution-gas interface technique 427
ution models
  Computer calculations of phase diagrams 107
ıce-charge-limited-current
  Space charge limited currents in chlorazole black Ǝ dye 531
ray pyrolysis
  Thin film CdZnS/$CuInSe_2$ solar cells by spray pyrolysis 279
ray pyrolysis technique
  Spray pyrolytic deposition of $CuBiS_2$ thin films 423
ray rate
  Spray pyrolytic deposition of $CuBiS_2$ thin films 423
ıuare-diamond pass
  Computer-aided roll pass design for continuous billet mill 183
acking fault probabilities
  X-ray line profile analysis of silver base Ag-Cd-In alloys 61
atic method
  Computer simulation of defects and radiation damage 155
eel
  Computer-aided composition-treatment-structure-property correlation studies in steels 193
Structure
  Computer-aided composition-treatment-structure-property correlation studies in steels 193
Styragel
  Determination of molecular weight distribution of polyethylene terephthalate by gelpermeation chromatography 527
Surface morphology
  Surface morphology and properties of GaAs epilayers controlled by temperature difference method of liquid phase epitaxy 29
  Liquid phase epitaxy growth of GaAs:Si by temperature difference method 439
  Effect of H^+ ion irradiation on surface morphology of $Fe_{40}Ni_{40}B_{20}$ metallic glass 505
Surface tension
  An absolute method for the determination of surface tension of liquids using pendent drop profiles 217
System operation
  Modern computer assisted methods in metallurgy 239

Temperature
  Kinetics of electrophoretic deposition of β-alumina 1
Temperature difference method
  Liquid phase epitaxy growth of GaAs:Si by temperature difference method 439
Template matching
  Some fundamental considerations to precede image analysis 169
Ternary chalcogenide films
  Spray pyrolytic deposition of $CuBiS_2$ thin films 423
Ternary diagrams
  Computer calculations of phase diagrams 107
Texture
  Effect of texture and grain size on the mechanical properties of warm-worked cadmium, zinc and zinc-0·35% aluminium alloy 81
Thermal expansion coefficient
  Thermal expansion studies on As-Sb-Se glasses 53
Thermodynamic capacity
  Concept of thermodynamic capacity 453
Thermodynamic properties
  Phase relations and activities in the Co-Ni-O system at 1373 K 71
Thermoelectroluminescence
  Thermoelectroluminescence in thin films of zinc and copper phthalocyanines 407
Thermoluminescence
  Tunnelling of electrons from deep traps of MgO 49
Thin films
  Electrical and optical properties of μc-SiH films 267

SnO_2:F films synthesized by chemical vapour deposition technique using hydrofluoric acid as doping material 315
Preparation and characterization of flash-evaporated $CuInSe_2$ thin films 319
Dielectric mirrors for high power laser applications 339
Design and development of a thin film dielectric beam combiner 343
Optical constants in the ultraviolet region of evaporated high index thin films 347
Photoresponsive measurements on $InAs_{0.3}Sb_{0.7}$ infrared detector 373
Effect of bulk and thin film dielectric overlay on the characteristics of microstrip rejection filter and simple microstriplines 397

Thin film solar cells
Thin film $CdZnS/CuInSe_2$ solar cells by spray pyrolysis 279

Torque
Computer-aided roll pass design for continuous billet mill 183

Trace elements
Emission spectrographic technique for the quantitative determination of trace elements in granitic rocks 471

Transformation
Thermal transformation in a chrysotile asbestos 497

Transparent conducting film
Optical and electrical properties of SnO_2 films prepared by chemical vapour deposition 357

Transparent conductors
SnO_2:F films synthesized by chemical vapour deposition technique using hydrofluoric acid as doping material 315

Trapping groups
Tunnelling of electrons from deep traps of MgO 49

Traps
Space charge limited currents in chlorazole black E dye 531

Tungsten carbide
R.F. magnetron sputtered tungsten carbide thin films 379

Uranium plutonium oxides
Determination of oxygen to metal ratio of U-Pu mixed oxides by x-ray diffraction 479

Very large scale integration
Growth of polysilicon and silicide films for MOS-VLSI application 297

Warm working
Effect of texture and grain size on the mechanical properties of warm-worked cadmium, zinc and zinc-0·35% aluminium alloy 81

Water reactor
Water reactor fuel performance code PROFESS and its application for predicting the behaviour of the fuel elements of D-Com blind problem 253

Worst fields
Modern computer assisted methods in metallurgy 239

X-ray diffraction
X-ray diffraction study of epitaxial zinc and cadmium films prepared by hot-wall technique 449
Determination of oxygen to metal ratio of U-Pu mixed oxides by x-ray diffraction 479
Thermal transformation in a chrysotile asbestos 497

Yield stress
Effect of texture and grain size on the mechanical properties of warm-worked cadmium, zinc and zinc-0·35% aluminium alloy 81

Z 80-A CPU
Personal computer-based CAMAC system for data acquisition 225

Zinc films
X-ray diffraction study of epitaxial zinc and cadmium films prepared by hot-wall technique 449

Zinc phthalocyanines
Thermoelectroluminescence in thin films of zinc and copper phthalocyanines 407

AUTHOR INDEX

arya H N
e Dixit B B 307
rwal S K
rowth of polysilicon and silicide films for
OS-VLSI application 297
hotri O P
e Ram P Raja 279
ee Saxena A K 315
la R
oncept of thermodynamic capacity 453
parao K V S R
ielectric mirrors for high power laser appli-
ations 339
esign and development of a thin film dielectric
eam combiner 343
ptical constants in the ultraviolet region of
vaporated high index thin films 347
te P R
ee Chandrasekhar S 391
ora S K
see Batra N M 489
unachalam V S
see Ramakrishnan N 199

burao C
see Chadda V K 231
bu S Ramesh
An absolute method for the determination of surface tension of liquids using pendent drop profiles 217
gchi T C
see Apparao K V S R 347
al M
see Agarwal S K 297
anerjee A
see Pachori R D 291
apat M N
Tunnelling of electrons from deep traps of MgO 49
aral D
see Rao D U Krishna 1
asavalingu B
see Tareen J A K 543
atra N M
Kinetics of calcium molybdate crystallization 489

hattacharya D K
see Chadda V K 231
hattacherjee S
see Datta A K 497
hat T Balakrishna
see Ramakrishnan N 199
hole N L
Dislocation density in electrolytically coloured KCl crystals 587

Bhosale C H
see Pawar S H 419
Bhosale P N
see Pawar S H 423
see Pawar S H 427
Bialy A El
Emission spectrographic technique for the quantitative determination of trace elements in granitic rocks 471

Chadda V K
Image analysis system for quantitative metallography 231
Chandrasekaran V
Magnetic and Mössbauer studies on ductile Fe-Cr-Co permanent magnet alloys 39
Chandrasekhar S
Transistors made in laser recrystallized polysilicon on insulator films 391
Chang C C
see Su Y K 29
see Wei C C 439
Chauhan J P S
Space charge limited currents in chlorazole black E dye 531
Chopra K L
see Kumar Satyendra 285
see Pachori R D 291
see Srivastava P K 379
see Uma C S 385

Datta A K
Thermal transformation in a chrysotile asbestos 497
Deshmukh B T
see Bhole N L 587
Deshmukh L P
see Pawar S H 419
Deshpande V K
Influence of eutectic addition on the electrical conductivity of $Li_2O:B_2O_3$ system 577
Dhanavantri C
see Joshi K K 535
Dharmaprakash S M
Studies on etching of gel-grown barium oxalate dihydrate crystals 519
Dixit B B
Electrical and structural characteristics of oxides grown from polycrystalline silicon 307
Dube D C
see Chauhan J P S 531
Dubey G C
Electrical and optical properties of μc-SiH films 267
Dwarakadasa E S
see Vijayaraju K 193

Fazeli Ali Reza
  see Tareen J A K 543

Gangal S A
  see Vijaya K 397
  see Joshi K K 535
Gaonkar V G
  see Kataria S K 225
Giridhar A
  Thermal expansion studies on As-Sb-Se glasses 53
Guirguis L A
  see Bialy A El 471
Gupta N K
  see Kotru P N 547

Iyengar G N K
  see Jacob K T 71

Jacob K T
  Phase relations and activities in the Co-Ni-O system at 1373 K 71
  see Akila R 453
Jadhav M L
  see Vijaya K 397
Jawalekar S R
  see Reddy S Raghunath 357
  see Sharon M 415
Jenkinson G W
  Modern computer assisted methods in metallurgy 239
Jha Sudhakar
  see Kumar Ashok 183
Joshi D G
  see Chadda V K 231
Joshi K K
  Microstrip losses with Al_2O_3 overlay 535

Karekar R N
  see Vijaya K 397
  see Joshi K K 535
Kataria S K
  Personal computer-based CAMAC system for data acquisition 225
Katti V R
  Deposition and assessment of thin dielectric films on photocathode substrate made of Kodial glass 325
  see Rangarajan L M 333
Kelly T
  see Jenkinson G W 239
Khanna S K
  Growth of low dislocation density single crystals of nickel 467
Khokle W S
  see Dixit B B 307
Kotru P N
  Characterization and thermal behaviour of lanthanum tartrate crystals grown from silica gels 547
Koul M L
  see Kotru P N 547
Krishan K
  Computer simulation of defects and radiation damage 155
Kulgod S V
  see Chadda V K 231
Kulkarni A V
  X-ray diffraction study of epitaxial zinc and cadmium films prepared by hot-wall technique 449
Kumar Ashok
  Computer-aided rool pass design for continuous billet mill 183
Kumar Devendra
  see Parkash Om 13
  see Parkash Om 557
Kumar Satyendra
  a-Si:H/$CuInS_2$ heterojunctions for photovoltaic conversion 285
Kumar Sudhir
  see Sharon M 415
Kumar Surendra
  see Kataria S K 225

Lakshmanan A R
  Thermoluminescence of alkali halides doped with alkaline earth impurities 541
Laroia K K
  see Agarwal S K 297
Lu S C
  see Su Y K 29
  see Wei C C 439

Mahadevan K
  see Dixit B B 307
Malage A B
  see Rao D U Krishna 1
Malhotra L K
  see Uma C S 385
Mallik A K
  Computer calculations of phase diagrams 107
  see Reddy S Raghunath 357
Mathur S C
  see Chauhan J P S 531
Matthews J R
  Computer models for fuel element behaviour 93
Misra Y
  see Tripathi L N 407
Moharil S V
  see Lakshmanan A R 541
Moussa W
  see Bialy A El 471
Mukherjee S N
  see Dubey G C 267
Murthy C H Sreerama
  see Chandrasekaran V 39

Murthy S N
  see Chadda V K 231

Nagendra C L
  Quality and reliability of optical coatings 351
Naidu B Srinivasulu
  see Reddy M Raja 373
Nair D Prabha
  see Sreenivasan K 527
Neelakantan K
  Computer simulation of serrated yielding 209

Pachori R D
  Flash-evaporated thin films of $CuInSe_2$ 291
Pakala V S
  Computer applications in the field of furnace design 147
Pal Surendra
  see Dubey G C 267
Pandey K G
  Computer-aided design of rolling mills 123
Pandey Lakshman
  see Parkash Om 557
Pandya D K
  see Kumar Satyendra 285
Parkash Om
  Microstructural and dielectric behaviour of glass ceramics in the system PbO-BaO-TiO_2-B_2O_3-SiO_2 13
  Glass ceramics containing ferroelectric phases 557
Pawar A J
  see Pawar S H 423
Pawar S H
  Electrochemical bath deposition technique: Deposition of CdS thin films 419
  Spray pyrolytic deposition of $CuBiS_2$ thin films 423
  Preparation and properties of $Bi_{2-x}As_xS_3$ thin films by solution-gas interface technique 427
Phadnis S G
  Dielectric properties of the system $Pb_{2-x}Nd_xLi_{0.5}Nb_{1.5}O_{6+\delta}$ 23
Prakash S M Dharma
  Periodic crystallization of barium oxalate in silica hydrogel 511
Prasad A J K
  Effect of H^+ ion irradiation on surface morphology of $Fe_{40}Ni_{40}B_{20}$ metallic glass 505
Prasad J J B
  see Sridevi D 319
Pratap R
  see Kulkarni A V 449
Purniah B
  see Krishan K 155
  Computer simulation of dislocation-carbon interaction in nickel 247

Radhakrishnamurthy C
  see Varaprasad A M 567
Radhakrishnan V M
  Computer modelling application in life prediction of high temperature components 133
Raina K K
  see Kotru P N 547
Rajagopalan R
  see Prakash Om 13
Rajan K Govinda
  see Khanna S K 467
Rajan R
  see Phadnis S G 23
Raj Baldev
  see Chadda V K 231
Ramadasan E
  see Sah D N 253
Ramakrishnan N
  Computer simulation of pressure sintering 199
Ramamurthy V S
  see Kataria S K 225
Ramaseshan K
  Optical black coatings for space applications 581
Ramaswamy V
  see Kumar Ashok 183
Ram P Raja
  Thin film $CdZnS/CuInSe_2$ solar cells by spray pyrolysis 279
Ranganathan S
  see Rao K Ratnaji 81
Rangarajan L M
  see Katti V R 325
  Development of high resolution thin film patterns on curved photocathode substrates of image tubes 333
Rao D U Krishna
  Kinetics of electrophoretic deposition of β-alumina 1
Rao K Ratnaji
  Effect of texture and grain size on the mechanical properties of warm-worked cadmium, zinc and zinc-0·35% aluminium alloy 81
Rao M G
  see Dubey G C 267
Rao P Mohan
  see Prakash S M Dharma 511
  see Dharmaprakash S M 519
Rasmy M
  see Bialy A El 471
Ray S
  see Tyagi S V S 433
Reddy K V
  see Sridevi D 319
Reddy M Raja
  Photoresponsive measurements on $InAs_{0.3}Sb_{0.7}$ infrared detector 373

Reddy P Jayarama
Pyroelectric polymer films for infrared detection 365
see Reddy M Raja 373
Reddy S Raghunath
Optical and electrical properties of SnO_2 films prepared by chemical vapour deposition 357
Reddy S Venkat
X-ray line profile analysis of silver base Ag-Cd-In alloys 61
Roy P R
see Verma Ravi 479
Roy S K
see Chandrasekhar S 391

Sah D N
Water reactor fuel performance code PROFESS and its application for predicting the behaviour of the fuel elements of D-Com blind problem 253
Sahoo N K
see Apparao K V S R 343
Samantaray B K
see Datta A K 497
Sandhya Bhakay-Tamhane
see Sequeira A 591
Sastry D H
see Rao K Ratnaji 81
Sastry O S
see Kumar Satyendra 285
Sawant S R
see Sequeira A 591
Saxena A K
SnO_2 : F films synthesized by chemical vapour deposition technique using hydrofluoric acid as doping material 315
Sequeira A
A low-temperature attachment for a four-circle neutron diffractometer 591
Shankara M A
see Tareen J A K 543
Sharda G D
see Agarwal S K 297
Sharon M
Characterization of Pb_3O_4 films by electrochemical techniques 415
Shukla A K
see Akila R 453
Singh A K
see Giridhar A 53
Singh K
see Deshpande V K 577
Singh Mahavir
see Agarwal S K 297
Singh R A
see Dubey G C 267
Singh S P
see Saxena A K 315
Singh Vakil
see Prasad A J K 505
Sirajuddin M
see Reddy P Jayarama 365
Sivaraman S
see Bapat M N 49
Sreenivasan K
Determination of molecular weight distribution of polyethylene terephthalate by gelpermeation chromatography 527
Sridevi D
Preparation and characterization of flash-evaporated $CuInSe_2$ thin films 319
Srikanth S
see Jacob K T 71
Srinivasan S
see Krishan K 155
see Purniah B 247
Srivastava P K
R.F. magnetron sputtered tungsten carbide thin films 379
Subbarao E C
see Rao D U Krishna 1
Subramaniam P
see Chandrasekaran V 39
Subramanian M
see Phadnis S G 23
Sudha Mahadevan
see Giridhar A 53
Suryanarayana S V
see Reddy S Venkat 61
Su Y K
Surface morphology and properties of GaAs epilayers controlled by temperature difference method of liquid phase epitaxy 29
see Wei C C 439

Tandon V K
see Tyagi S V S 433
Tareen J A K
A simple hydrothermal cell for synthesis at moderate temperatures and pressures 543
Thangaraj R
see Ram P Raja 279
see Saxena A K 315
Thutupalli G K M
see Nagendra C L 351
see Ramaseshan K 581
Tiwari A N
see Kumar Satyendra 285
Tripathi L N
Thermoelectroluminescence in thin films of zinc and copper phthalocyanines 407
Tyagi S V S
Electron microscopy study of chemically deposited Ni-P films 433

Uma C S
Cobalt oxide-iron oxide selective coatings for high temperature applications 385

Vankar V D
see Srivastava P K 379
Varaprasad A M
Magnetic hysteresis and crystallization studies on metallic glass alloy $Fe_{67}Co_{18}B_{14}Si_1$ 567
Venkatesh D
see Sah D N 253
Venkateswarlu G
see Chandrasekaran V 39
Verma Ravi
Determination of oxygen to metal ratio of U-Pu mixed oxides by x-ray diffraction 479
Vijaya K
Effect of bulk and thin film dielectric overl the characteristics of microstrip rejection and simple microstriplines
Vijayaraju K
Computer-aided composition-treatment- ture-property correlation studies in steels
Viswanathan M
see Ramaseshan K
Vollath Dieter
Some fundamental considerations to pr image analysis
Vyas P D
see Dixit B B
Wei C C
see Su Y K
Liquid phase epitaxy growth of GaAs: temperature difference method

3. Results

For the sake of better comparison, the same accelerating voltage has been maintained (60 kV) throughout the experiment, which gives the wavelength of the incident radiation as 0.0487 Å. Since the same camera constant is used, it is possible to compare the spots/rings of one figure with that of the other.

Figures 1a,b show the electron micrograph and the electron diffraction pattern respectively of the film deposited at room temperature. The electron micrograph shows formation of small granular structures indicating formation of crystalline state. The electron diffraction pattern had a number of rings. The diameter of these rings given in table 1 shows that the ratios of d^2 for the outer ring to the next ring in order is a constant

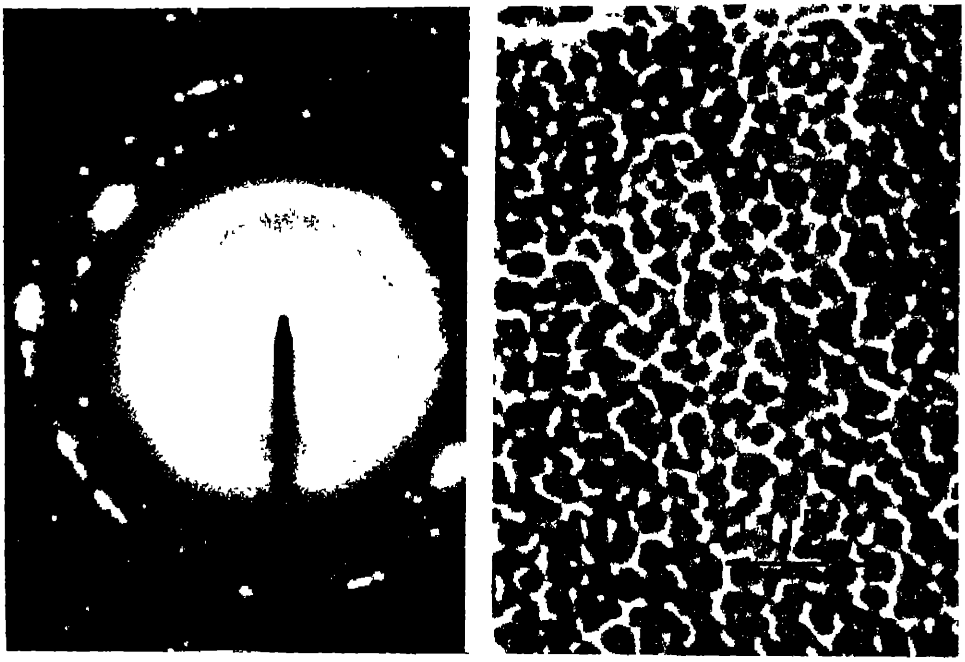

(a) (b)

Figure 1. a. Electron diffraction pattern **b.** Electron micrograph of the antimony film deposited at room temperature

Table 1. Diameter of electron diffraction rings and the ratio of their squares, substrate being at room temperature.

Ring No.	d_n = diameter of the ring n	d_n^2	$\sum = (d_n/d_{n-1})^2$
1	3.07	9.43	—
2	3.92	15.37	1.63
3	4.94	24.40	1.59
4	6.22	38.69	1.59
5	7.83	61.31	1.59

1·59. Reference to the camera geometry and Bunn charts reveals that the structure is hcp and the distance corresponds to $(10\bar{1}0)$ plane. The constants of the hcp crystal were according to the previous literature, *i.e.* $a = 3{\cdot}33$ Å and $c/a = 1{\cdot}58$ (Dilshad Akhter *et al* 1979).

Figures 2a,b show the diffraction patterns and the electron micrograph respectively of the films deposited at 323 K. It has been observed that the grain size has become larger and the crystal structure has started changing. The electron diffraction pattern corresponds to a spot pattern showing (110) planes of a cubic structure and some traces of the previous ring pattern are also seen.

At further elevated temperatures i.e. at 373 K, the cubic pattern becomes predominant and large crystals are formed. The previous ring pattern is faintly visible (figures 3a,b).

At 423 K the pattern becomes more complicated and absolutely polycrystalline (figures 4a,b). We get a number of rings in the diffraction pattern. Nine rings which were predominantly seen were taken for comparison. Starting from the outermost ring, squares of the ratios of the diameters of the inner ones were taken and are shown in table 2.

A close look at the table shows that the ratios 9/7, 8/6, and 6/4 are around 1·59. Since the magnification, incident radiation and camera constant have remained the same, it can be concluded that these rings resemble the previous hcp structure with $a = 3{\cdot}33$ Å and $c/a = 1{\cdot}58$. The second commonly occurring ratio is between 6/5, 5/4, 4/3 and 9/8 and is 1·12.

Excepting these two ratios there are no more ratios which are repeating. We can

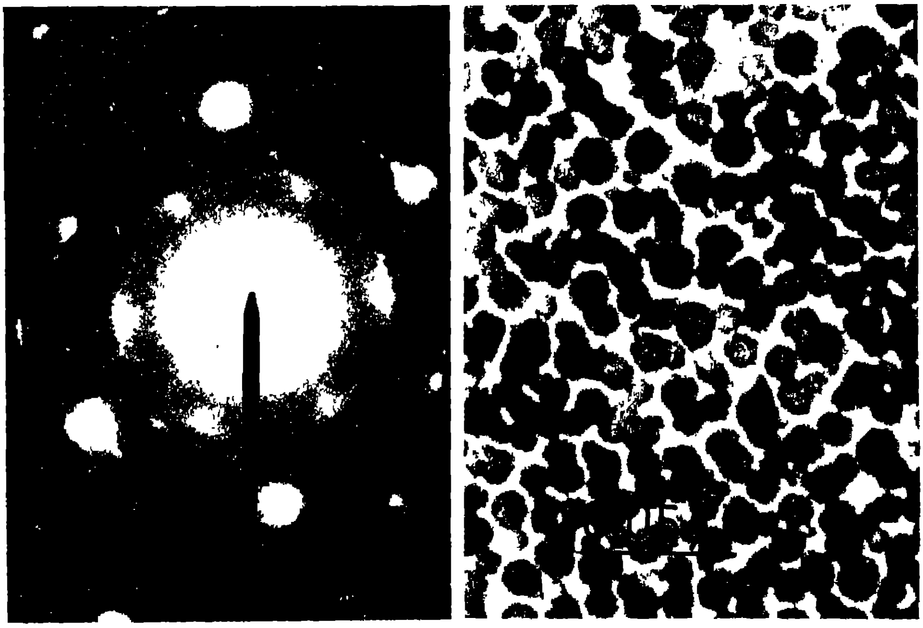
(a) (b)

Figure 2. a. Electron diffraction pattern **b.** (×44000) Electron micrograph deposited at 323K.

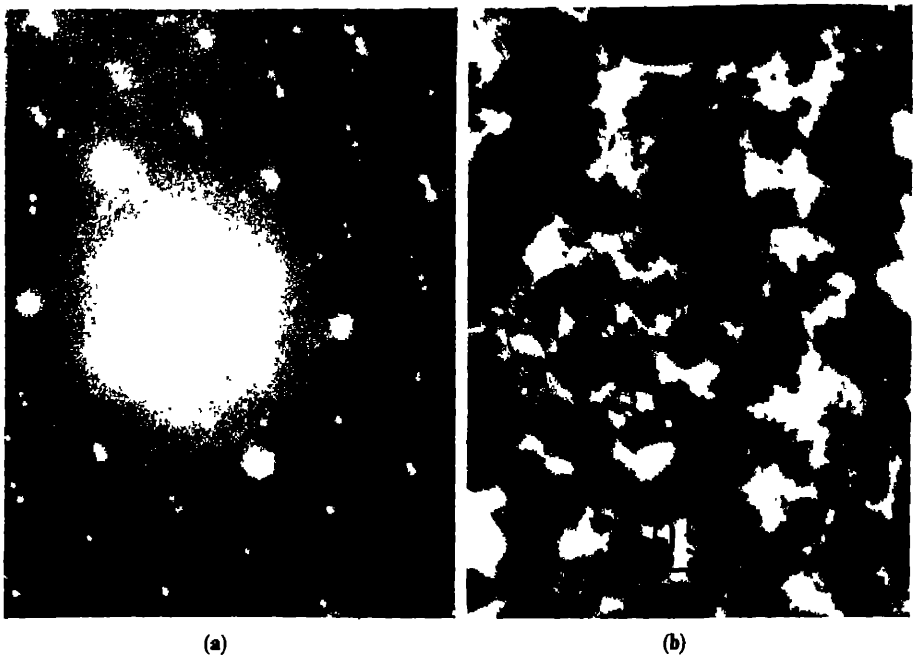
(a) (b)

Figure 3. a. Electron diffraction pattern **b.** (×44000) Electron micrograph of the film deposited at 373K.

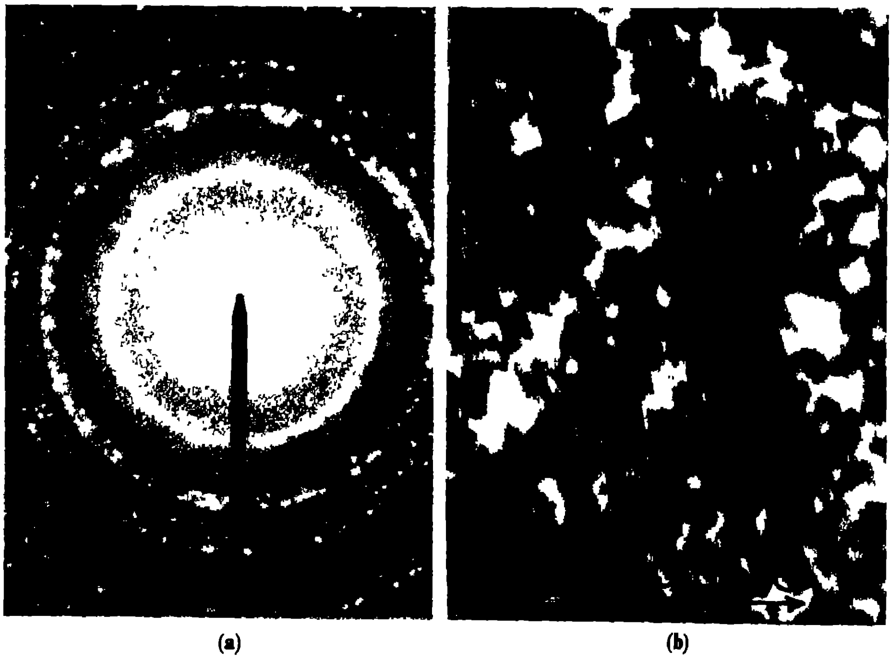
(a) (b)

Figure 4. a. Electron diffraction pattern **b.** (×44000) Electron micrograph of the film deposited at 423K.

Table 2. Squares of the ratios of the outer diameter to the inner one.

Ring No.	Value for various ratios $\sum = (d_{ni}/d_{Nj})^2$							
	$N = 98$	7	6	5	4	3	2	1
9	−1·14	1·57	2·25	2·48	3·11	3·93	6·90	13·08
8	—	1·43	1·67	1·84	2·33	2·92	5·14	9·73
7	— —	—	1·57	1·98	2·50	3·10	4·39	8·31
6	— —	—	—	1·12	1·59	1·75	2·78	5·27
5	— —	—	—	—	1·12	1·45	2·80	5·30
4	— —	—	—	—	—	1·12	1·76	3·32
3	— —	—	—	—	—	—	1·76	3·32
2	— —	—	—	—	—	—	—	1.89

attribute this second ratio to the cubic phase seen in the previous figures. Other ratios may be due to the metastable phases of other crystals in the process of formation or might be some other reflections of the existing crystals. They were not considered as they were not significant in number.

Since the photographs were taken under the same magnification and since we know that the cubic plane is (110), and the hexagonal one is $(10\bar{1}0)$, the interatomic distance of the cubic phase is estimated to be 3·4 Å.

4. Discussion

The present study shows that because of the variation of the substrate temperature a number of additional phases are developed in the vapour-deposited antimony film. If the series of the diffraction patterns are observed carefully, it is found that the sample gradually changes from a polycrystalline hcp to crystalline cubic and then back to polycrystalline hcp and cubic mixture. In figure 3 the hcp structure has almost vanished. Similarly it is also expected that at some temperature between 373 and 423 K this hcp structure may reappear again. The study of this point is worth undertaking; however it would need a better control of substrate temperature. The cubic phase observed has a larger interatomic distance *i.e.* 3.4 Å. In previous studies by splat cooling (Dilshad Akhter *et al* 1979), such a structure with $a = 3.16$ was observed.

5. Conclusions

(i) hcp phase of antimony is observed by vapour deposition also. (ii) By increasing the substrate temperature, the cubic phase is also observed. (iii) The cubic phase has larger interatomic distances than usual. (iv) At intermediate substrate temperature hcp phase vanished and reappeared at higher temperatures. (v) At the substrate temperature of 423 K both hexagonal and cubic phases become polycrystalline.

Acknowledgments

Thanks are due to Dr C S Harendranath for making the TEM facility available. The authors also thank Mr Nageshwar Rao and Miss Mruga H Joshi for help in the use of TEM.

References

Boyer A, Des B, Chacht and Groubert 1981 *Thin Solid Films* **76** 119
Dilshad Akhtar Venkar V D and Chopra K L 1979 *Thin Solid films* **58** 327
Kabalkina S S and Mylov V P 1964 *Sov. Phys-Dokl* **8** 917

Bull. Mater. Sci., Vol. 6, No. 3, July 1984, pp. 617–623. © Printed in India.

Formation of lamellar $M_{23}C_6$ on and near twin boundaries in austenitic stainless steels

B SASMAL

Department of Metallurgical Engineering, Indian Institute of Technology, Kharagpur 721 302, India

Abstract. Thin foil electron microscopy studies were made on the precipitation of lamellar $M_{23}C_6$ during aging at 973 K and 1073 K in water-quenched specimens of two austenitic stainless steels. After the precipitation on incoherent twin boundaries $M_{23}C_6$ formed on coherent twin boundaries and in the regions adjacent to incoherent twin boundaries. These precipitates showed lamellar morphology and were aligned in a specific manner with respect to the twin boundaries. Such lamellar precipitates were absent in the specimens which were isothermally treated at 1073 K after being transferred from the solution treatment temperature. The lamellar morphology of $M_{23}C_6$ is suggested to be developed by the influence of residual specific stress field around twin boundaries resulted from quenching.

Keywords. Electron diffraction; lamellar $M_{23}C_6$; precipitation morphology; twin boundaries.

1. Introduction

Precipitation of $M_{23}C_6$ in austenitic stainless steels was studied by many investigators. In quenched and aged conditions $M_{23}C_6$ precipitates (Lewis and Hattersley 1965; Wolff 1966; Beckitt and Clark 1967; Singhal and Martin 1967; Wilson 1971; Weiss and Stickler 1972) on incoherent twin boundaries after the precipitation on grain boundaries. During the later stages of aging, precipitation occurs on coherent twin boundaries and within the grains. The precipitates adjacent to an incoherent twin boundary grow as plates on both sides of the boundary, which are parallel to the coherent twin boundaries (Lewis and Hattersley 1965; Beckitt and Clark 1967; Singhal and Martin 1967; Hattersley 1964 and Lewis 1964).

Two models have been put forward to explain the formation of .these lamellar precipitates. Beckitt and Clark (1967) suggested that the stress generated due to growth of precipitates nucleated on an incoherent twin boundary drives the twinning dislocations out of the boundary. These dislocations have been attributed to act as sites for nucleation continuously as they move out into the matrix and thus to form the plates of $M_{23}C_6$ on the $\{111\}$ (twinning) planes. Singhal and Martin (1967) however observed the stacking faults formed possibly by bowing of the twinning dislocation out of the incoherent twin boundary after the precipitation on the boundary. They have suggested that $M_{23}C_6$ precipitation occurs by nucleation along the bounding Shockley dislocation and by growth across the stacking fault to form a sheet of carbide. Shockley partial might again be repelled by the precipitate and the repetition of the precipitation process might cause further growth of the plate.

In order to examine these models a detailed electron microscopy study was made on the formation of lamellar $M_{23}C_6$ adjacent to incoherent twin boundaries and on the precipitation at coherent twin boundaries.

2. Experimental

The chemical composition of two austenitic stainless steels (AISI 316L and DIN 4981, hereafter referred to as A and B respectively) studied are given in table 1. The cold-rolled sheet specimens (about 150 μm thick) were solution-treated (5·4 Ksec (1 hr 30 min) at 1433 K for steel A and 1·8 Ksec (30 min) at 1550 K for steel B) inside sealed silica tubes in argon atmosphere and quenched in water. The quenched specimens were then aged at 973 K and 1073 K inside evacuated silica tubes for various durations from 3·6 Ksec (1 hr) to 14·4 Msec (4000 hr). A few bulk specimens (10 × 5 × 3 mm) of A after being solution-treated were transferred to 1073 K, held for 360 Ksec and 1·8 Msec and then cooled in air. Thin foils for electron microscopy examination were prepared by twin-jet electrolytic polishing with a mixture of 10% perchloric acid and 90% acetic acid.

3. Results and discussion

Steel A was fully austenitic in the as-quenched condition, while B contained a considerable amount of undissolved NbC particles. $M_{23}C_6$ was the only carbide to be precipitated in A during aging at 973 K and 1073 K. In B both NbC and $M_{23}C_6$ formed. Because of the precipitation of NbC in very fine form on grain boundaries, on dislocations, in association with stacking faults and as dot-like particles, the precipitation of $M_{23}C_6$, in general, was appreciably low and was delayed in B (Sasmal 1980). $M_{23}C_6$ first precipitated on grain boundaries and later on incoherent twin boundaries followed by intragranular precipitation on continued aging. After the precipitation on incoherent twin boundaries a preferential precipitation of $M_{23}C_6$ was noted in the regions adjacent to these boundaries (figure 1). Precipitation on coherent twin boundaries also occurred simultaneously. In B, though the intragranular precipitation was rarely observed, a new mode of precipitation of $M_{23}C_6$ around undissolved NbC particles was noted. This is reported earlier (Terao and Sasmal 1978, 1981).

Electron diffraction analysis showed that the $M_{23}C_6$ precipitates were face-centred cubic and had almost the same lattice parameter in both the steels: $a = 10.7$ Å. They were found to grow at all the sites with the cube orientation relationship with austenite matrix, *i.e.*

$$\{100\}_{M_{23}C_6} \parallel \{100\}_\gamma,$$
$$\langle 100\rangle_{M_{23}C_6} \parallel \langle 100\rangle_\gamma.$$

Table 1. Chemical analysis of steels.

Steel	Composition, wt.%								
	C	Ni	Cr	Mn	Mo	Si	Nb	B	Fe
A	0·014	11·5	17·3	1·15	2·2	0·56	—	—	Balance
B	0·057	15·8	16·2	1·12	1·84	0·41	0·77	0·0003	"

1

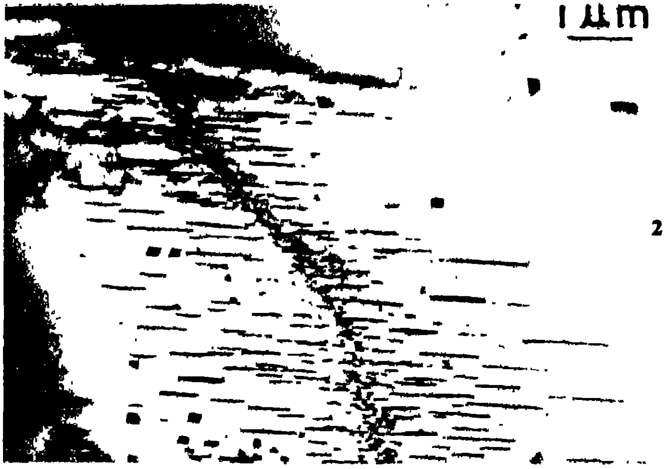

2

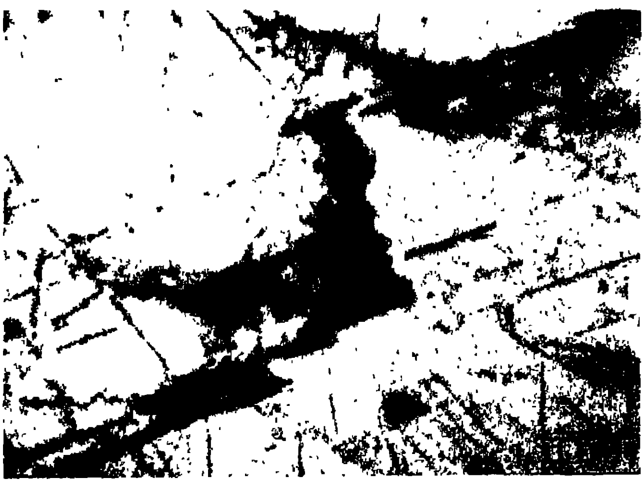

3

Figures 1–3. Steel A, aged for 28·8 Ksec (8 hr) at 1073 K. Lamellar $M_{23}C_6$ formed close to incoherent twin boundaries and on coherent twin boundaries. **2.** Steel A, aged for 1·80 Ksec (50 hr) at 1073 K. $M_{23}C_6$ plates increased in number on both sides of the incoherent twin boundary. The specimen foil is nearly parallel to the (110) of the matrix and the twin axis is $[\bar{1}11]$. **3.** Steel B, aged for 14·4 Msec (4000 hr) at 1073 K. $M_{23}C_6$ plates formed on coherent twin boundaries and adjacent to incoherent twin boundaries, but considerably less in number.

The results agree with those reported earlier (Lewis and Hattersley 1965; Weiss and Stickler 1972; Singhal and Martin 1968). The morphology of these precipitates after a long aging period, however, depends on the precipitating sites (Sasmal 1980). Whatever may be the morphology of these particles, their interfaces always consist of {111} and {110} types of planes. This result confirms the suggestion made by Beckitt and Clark (1967).

In the adjacent regions of an incoherent twin boundary $M_{23}C_6$ grew as plates into the austenite matrix on both sides of the boundary (figure 1). The plates grew in a direction parallel to the coherent twin boundaries. On longer aging, more and more lamellar $M_{23}C_6$ formed in a similar fashion and gradually grew away from the incoherent twin boundaries (figure 2). The number of lamellae however decreased progressively with increase in distance. On the coherent twin boundaries also, $M_{23}C_6$ grew as similar plates which on longer aging joined one another making almost a continuous layer of precipitates. In B, $M_{23}C_6$ plates also formed on coherent twin boundaries and in the vicinity of incoherent twin boundaries, but to a lesser extent, (figure 3). A few examples of morphology of the lamellar precipitates in the vicinity of an incoherent twin boundary are shown schematically in figure 4. The large planes of these plates are parallel to the twinning planes. A detailed study of the characteristics of these lamellar precipitation has been reported elsewhere (Terao and Sasmal 1980). The

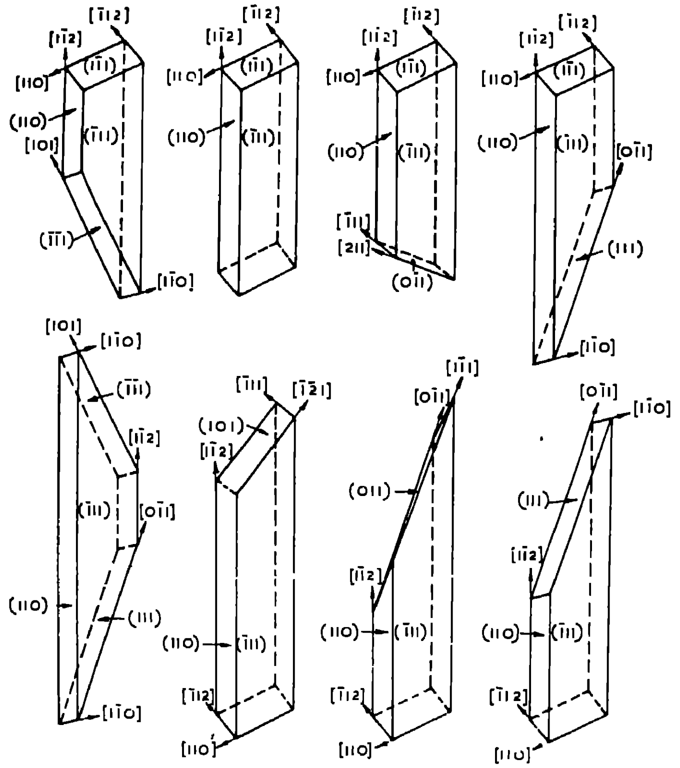

Figure 4. Several examples of morphology of $M_{23}C_6$ lamellae formed adjacent to an incoherent twin boundary, the twinning plane being ($\bar{1}11$).

specific features of the formation of these $M_{23}C_6$ lamellae were observed to vary from one twin to another.

The lamellar $M_{23}C_6$ precipitates, as reported by the previous investigators (Beckitt and Clark 1967; Singhal and Martin 1967) were assumed to result from emanation into the grains of the precipitates nucleated earlier, on incoherent twin boundaries. On the basis of this assumption in the mechanisms suggested for their formation the glide of the twinning dislocations possibly repelled from the incoherent twin boundaries by the stress field of growing particles at the boundaries has been proposed to play the most important role. The plate morphology has been attributed to result by a repeated nucleation (Beckitt and Clark 1967) on these gliding Shockley particles, or by the formation of stacking faults, nucleation on the outer particals and subsequent growth across the stacking faults (Singhal and Martin 1967). A close examination (by tilting the thin foils about different axes) of these lamellae, however revealed that most of them stood separate from the precipitates formed on incoherent twin interfaces, having no contact whatsoever. On the other hand, if any one of these mechanisms were operative, the lamellar $M_{23}C_6$ might not form in B since dislocations are more preferable sites for precipitation of NbC. Further, none of these mechanisms is able to explain the lamellar precipitation on coherent twin boundaries.

To examine further the validity of these models another experiment was made. A few bulk specimens of A were held at 173 K for sufficiently long periods, after being transferred directly from the solution-treatment temperature. As shown in figure 5, $M_{23}C_6$ precipitated in these specimens only on incoherent twin boundaries. No lamellar precipitation occurred either on coherent twin boundaries or in the regions adjacent to the incoherent twin boundaries. These observations indicated that quenching from the solution-treatment temperature is essential to induce lamellar precipitation during aging, and the existing models have no provisions to accommodate this fact.

Due to differential contraction between cooler and hotter parts of a metallic body, quenching from a high temperature induces pronounced stress. The state of stress inside a specimen becomes complicated in the vicinity of a barrier such as grain boundaries, twin boundaries and undissolved particles. The effect of the quenching stress near twin boundaries would, however, be different from that near a grain boundary owing to the inherent difference in characteristics of these two types of boundaries. In this respect coherent twin boundaries would once again behave differently from incoherent twin boundaries. Quenching stress produces residual stresses in the specimens, the maximum value of which has been calculated (Lang 1965) to be

$$\sigma_{\max} = \frac{E\alpha\Delta T}{1-\nu} \cdot \frac{S^2}{3a\,t_0},$$

where E = Young's modulus; α = coefficient of thermal expansion; ΔT = temperature range $(T_q - T_{\text{room}})$; ν = Poisson's ratio $(= 0.3)$; $2S$ = thickness of the plate; a = thermal diffusivity in cm^2/sec; t_0 = total transient time.

The change of orientation of a crystal in a specific manner across twin boundaries is expected to induce a specific stress field around the boundaries since the elastic constants of a material are different along different directions. In these regions, $M_{23}C_6$ which always nucleates on $\{111\}$ austenite planes, because of least misfit (Beckitt and Clark 1967) across these interfaces has to choose one of the possible habits in order to

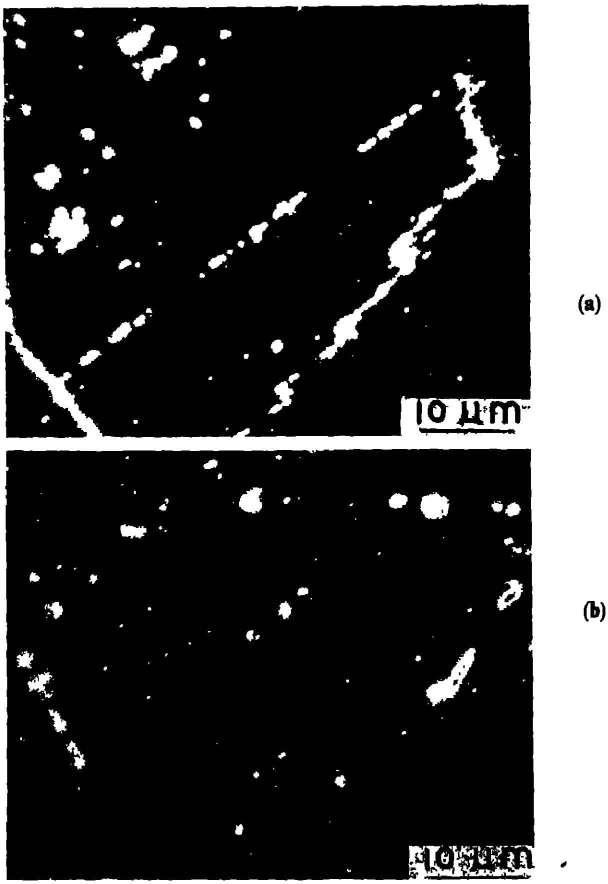

Figure 5. Dark-field optical micrographs of steel A. **a.** Water quenched and aged at 1073 K for 1·8 Msec (500 hr). $M_{23}C_6$ precipitated on incoherent and coherent twin boundaries and also in the regions adjacent to incoherent twin boundary. **b.** Quenched to 1073 K and held for 1·8 Msec (500 hr). Coherent twin boundaries and regions close to the incoherent twin boundaries are free from lamellar $M_{23}C_6$.

minimise the coherency strain. This is in conformity with the observations made. It is therefore, proposed that the presence of a residual specific stress field around twin boundaries in the quenched specimens is responsible for the formation of lamellar $M_{23}C_6$ precipitates on coherent twin boundaries and in the regions close to incoherent twin boundaries. Possibly vacancies play an important role in the process of their nucleation.

4. Conclusions

The lamellar $M_{23}C_6$ precipitates on coherent twin boundaries and near incoherent twin boundaries form during aging in the quenched samples only. The morphology and the specific orientation of these precipitates are influenced by the residual stress developed around twin boundaries due to quenching. The nucleation of these precipitates is aided by vacancies.

References

Beckitt F R and Clark B R 1967 *Acta Metall.* **15** 113
Hattersley B and Lewis M H 1964 *Philos. Mag.* **10** 1075
Lang W 1965 *Keruforschungzentrom Karlsruhe Report No* 274
Lewis M H and Hallersley B 1965 *Acta Metall.* **13** 1159
Sasmal B 1980 Ph.D. Thesis, Indian Institute of Technology, Kharagpur
Singhal L K and Martin J W 1967 *Acta Metall.* **15** 1603
Singhal L K and Martin J W 1968 *Acta Metall.* **16** 1159
Terao N and Sasmal B 1978 *C. R. Acad. Sci. (Paris)* **C287** 487
Terao N and Sasmal B 1980 *Metallography* **13** 117
Terao N and Sasmal B 1981 *Trans. Jpn. Inst. Metals* **22** 379
Weiss B and Stickler R 1972 *Met. Trans.* **3** 851
Wilson F G 1971 *J. Iron Steel Inst.* **209** 126
Wolff V E 1966 *Trans. MS-AIME* **236** 19

FOREWORD

The mechanical behaviour of materials is of vital interest to many branches of engineering and technology. Although at one time physicists were interested in this subject, at present its study is pursued mainly by metallurgists and mechanical engineers. However, the recent focus on topological defects etc., made some of us wonder whether the time was ripe for physicists to renew their interest in mechanical properties. In order to explore this, a Discussion Meeting was held at the Reactor Research Centre, Kalpakkam on February 7, 8 and 9, 1983. The Meeting was sponsored by the Indian Academy of Sciences, the Department of Science and Technology, the Defence Metallurgical Research Laboratory and the Department of Atomic Energy. About 70 scientists belonging to various disciplines took part.

We present in this volume the written version of the talks given at the Meeting, the record of the discussions that followed the oral presentations, and of the Panel Discussion that took place in the concluding session. Owing to restrictions of space, and in the interests of reasonable uniformity of style and notation, we have been forced to make (generally minor) editorial changes in the manuscripts submitted by the speakers, and on occasion, prune the material in places. While great care and pains have been taken to preserve the essential spirit of every point the authors have intended to make, we do accept the responsibility for the changes necessitated by the reasons stated.

The Meeting itself was quite lively and absorbing, with a variety of views expressed by people with varying specializations. In offering the Proceedings we hope that the excitement of the Meeting would be shared by a wider audience, and enthuse at least some physicists to enter this area.

The task of preparing the Proceedings for publication has been quite strenuous and could not have been accomplished but for the unstinted help and cooperation we have received from many. Particular mention should be made of G Ananthakrishna, B Purniah, Radha Ranganathan, V Sridhar, P Subba Rao and T D Sundarakshan. We also would like to express our personal indebtedness to Prof. S Ramaseshan for support and encouragement in organising the Discussion Meeting.

February, 1984
C N R Rao
Editor of Publications,
Indian Academy of Sciences

Guest Editors
V BALAKRISHNAN
G VENKATARAMAN

Bull. Mater. Sci., Vol. 6, No. 4, September 1984, pp. 627–631. © Printed in India.

Observations on the physical basis of mechanical behaviour

S RAMASESHAN
Indian Institute of Science, Bangalore 560 012, India

1. General remarks

It gives me great pleasure to participate in this Discussion Meeting. This is perhaps the first time that physicists, materials scientists and metallurgists in India have planned a meeting to understand each other and to see whether phenomena not completely comprehended by one group can be looked into by another or jointly. The motivations are so praiseworthy that I am sure something will come out of such meetings. If these meetings are to be successful many obstacles have to be surmounted. The first, of course, is that of language. Each person here must understand the jargon of the other. The second is to make a conscious attempt to change one's attitudes.

The metallurgists and physicists today appear to be two different animals. The purpose of this meeting is to see that the barriers that have been artificially raised are removed. One has only to read the fascinating books by Cyril Stanley Smith, *From Art to Science* and *A Search for Structure* to realise that metallurgy which has been an empirical science for a long time has been eminently successful; and yet what is common to the village blacksmith is very mysterious to the physicist. Science was injected into metallurgy only recently. Most metallurgists, like chemists, are pragmatists. They reduce many sophisticated theories to thumb rules which work and which have advanced the fields most spectacularly. However, there is a tendency among many of them not to go too deeply into the fundamentals of the phenomena they observe. The physicist, on the other hand, choose rather simple ideal systems and model them. As this approach has been rather successful in physics he feels that by using a similar one he can "clean" up many of the problems which the metallurgist does not understand. In this connection, I must recall what Prof. Andrew Huxley—a physicist himself who entered biology and distinguished himself—said when he lectured at the Indian Institute of Science, Bangalore on Physical Sciences and Biology. Biology, according to him, is inherently complex. Simplistic models sometimes hinder rather than advance the subject. It is the complexity and the basis of this complexity that one must try to understand and describe. The physicist, if he is to be useful at all, must enter biology with great humility, with a genuine intent to understand the subject and its spirit. What Huxley said of biology is, in my view, applicable to metallurgy and materials science.

In each field of science when sufficient knowledge accumulates, a great step is usually taken which throws new light and opens up new vistas. This happened to biology about 25 years ago when biologists and crystallographers combined to unravel the structure of DNA and caused a revolution which biology is still experiencing.

For metallurgy there was one such great flash in 1934 when the theory of dislocation was put forward by physicists which opened the gates for the understanding of the mechanism of strengthening, crystal growth etc. Fifty years have now passed and one feels that a coming together of scientists in related fields may possibly help is taking another important step even if it is not as revolutionary as the dislocation theory. Being an experimenter myself I must stress the importance of experiments. Unfortunately the experimental approach is sometimes neglected by physicists in India. Experiment forms the backbone of progress is any field. I am told that Prof. Mott often stressed that every theoretical paper or idea must suggest a clean interesting experiment which can be *performed*. I do hope that at the end of this meeting crucial experiments will be suggested which will help to bring about the proper understanding of some of the puzzling phenomena in this field.

If such meetings are held often they would create a community of scientists interested in mechanical behaviour of materials. They may also provoke individuals or groups with complementary competences to collaborate. One hopes that the theorists and experimenters would join hands to look into some of the exciting problems in this field. Following the spirit advocated by the organisers of this Meeting, in this inaugural talk I shall mention a few experiments which I and my group have performed (many of which are unpublished) and others which are not so well-known, that have come my way. I shall also raise some questions which have troubled me particularly those connected with crack generation, hardness and its variation, friction, wear, surface states and the nature of grain boundaries.*

2. Welding of surfaces and generation of cracks

In some experiments done in 1944 I noticed that diamond surfaces freshly cleaved in vacuum (10^{-5} torr) do not rejoin when brought together almost immediately after cleaving. It was also possible to show by studying the Jamin effect (*i.e.* by ellipsometric methods) that a thin film is formed on the cleaved surface. In 1948 Gwathemay showed that cleaved copper single crystal welded together in vacuum (10^{-8} torr) a phenomenon now common in space.**

At the surface of a metal due to discontinuity there would be a spill-over of electrons and the consequent charge imbalance is prevented by the electrons collectively conspiring to set themselves into oscillations. When two clean metal surfaces are brought close to each other these oscillations in each piece (which are independent) can become coupled and they go backwards and forwards from one piece to the other, bonding the two surfaces. Another crucial question is: Can stress concentration in a metal cause an instability in the electron oscillations so that decoupling can take place causing the formation of two surfaces (i.e. a crack?) These are topics of great interest worthy of some thought and discussion.***

---

*No attempt is made to pad it up to make it more intelligible!

** I am not aware of any experiments done in space attempting to join or weld diamonds. It is not clear to me why diamond surfaces should not also weld as copper surfaces do. The dangling bonds in diamond may help to *chemisorb* atoms to form a thin film. In metals also thin films are formed by physical adsorption. One wonders whether the difference in the magnitude of the energies of chemisorption and physisorption is the real cause of the two types of behaviour.

*** Some may disagree with the conjecture that two metal surfaces weld together in vacuum because the surface plasmons go backwards and forwards from one piece to another. It is strange that the magnitude of the surface energy is very close to the contribution of the correlation part of the electron energy. Does this imply that for some reason there is a cancellation of some of the very large terms like the lattice contribution, the kinetic energy of the electron etc? Similarly, when one considers the cohesive energy (next section) is there also a cancellation of the Madelung term, corresponding to the kinetic energy of the electron so that the electrons are mostly responsible for the cohesive energy.

Crude measurements (by us) of the stress optic coefficients of metals indicate that stress has considerable effect on the electrons. Stress distorts the lattice and due to this there are two optical effects. Firstly, the anisotropic distribution of the polarisable atoms in the strained lattice alters the index (n) and absorption (k) tensors. Secondly, electrons moving in the strained lattice can also alter the n and k tensors. The latter effect appears to be quite large and is opposite to that of the former.

3. Do electrons contribute to the hardness of metals?

Since electrons do contribute so much to the cohesive energy of a solid, it seems very probable (at least to me) they contribute to the hardness of a metal.[†]

Some compounds like rare earth chalcogenides (example SmS which has the NaCl structure) are semiconductors and become metals under pressure, undergoing isostructural semiconductor-to-metal transformation. There is a volume change and the resistance drops by five to six orders of magnitudes. These are peculiar metals which have positive and negative ions inside with 'free electrons" in them. By measuring the hardness of the two phases one can get an idea as to whether electrons do contribute to hardness or not. To make measurements at high pressures is not easy although the method mentioned in the next section could be adopted for this purpose. The effect of the density change on hardness must also be taken into account.

A similar isostructural semiconductor-metal-transition can be effected by adding adequate amounts of rare earth metal which simulates the effects of pressure (*e.g.* SmS is a semiconductor while $Sm_{0.85}$, $Gd_{0.15}S$ is a metal). The hardness of the metal is much higher than that of the semiconductor. But one cannot be certain whether this increase is due to the electrons, the change of density or the additional Gd atoms in the substance.

4. The hardness pendulum—The measurement of the variations of hardness

The hardness pendulum, devised by experimentors in USSR, in which a loaded cylinder oscillates on the surface under study can be used to measure hardness of the metal under a variety of conditions. The hardness is estimated from the rate of damping of the oscillations. Liquids can be placed between the surface and the cylinder to study the effects of adsorption and hardness. With an electrolyte, variation of hardness can be studied with varying potentials applied on the system. The hardness of the material increases with increasing potential and becomes maximum when the charge on the surface is zero and it decreases as the surface becomes progressively negatively charged. In fact, this curve is very similar to the variation of the interfacial tension of Hg solution interface with applied voltage indicating clearly that the surface energy (which changes with the application of potential) is involved in the phenomenon of hardness. By analogy with the Hg solution interface the effect of atoms absorbed on the surface was studied. Many patents on additives to increase the machining rates have resulted from this work.

[†] I am not at all happy using the word 'electron' in this loose manner as I am aware that there are several contributions to the energy from electrons themselves and they even have opposite signs.

[‡] To my mind the question "do electrons" contribute to the hardness of metals is an important one and deserves further theoretical and experimental investigation.

It is also found that the effect of absorption of neutral atoms decreases the hardness. It is also a known fact that the work function $W(\phi)$ of a refractory transition metal is lowered by as much as 4 eV by a monolayer of Cs. This is possibly the reason why adsorption can decrease hardness. Theoretical calculations of the electron distribution on the surface have also been done. When a tin crystal is coated with liquid gallium the crystal becomes brittle. Laue photographs show that a single crystal becomes polycrystalline. It is thought that the grains are held together by surface tension forces of the liquid. The strength of the solid decreases considerably although its ductility is not affected.

5. Friction, surface roughness and surface states

The second law of friction discovered by the great Leonardo da Vinci (which states that the coefficient of friction (μ) is independent of the surface area) appears mysterious to many when they first come to know of it. To explain this experimental law one must seek a phenomenon by which a true area of contact is proportional to load (the first law states that the $\mu \propto$ load). The real surface of any material consists of microscopic hills and valleys (asperities). When two surfaces touch, the area of contact being small the stress is very large. An elastic deformation takes place first and this is followed by a plastic one till the total area of contact increases to a value which can support the load. This phenomenon can be elegantly demonstrated by observing intensively the total internal reflection in a right angle prism. When the surface (with its asperities) is laid on the hypotenuse of the prism wherever there is a real contact there is no total internal reflection, and where there is no contact, evanescent wave returns into the medium of the prism. The intensity of the totally reflected beam decreases with load.

The existence of the asperities has also been demonstrated by measurements of the AC surface resistance (at very high frequencies 24000 MHz when the skin depth is as low as 0·4 μ) and this surface resistance is much greater than the DC resistance. If the surface is bathed in carbon monoxide, the AC resistance increases considerably indicating that the electrons are trapped in the surface states created by CO.

6. Electrons and metals

There are many other questions which require consideration. What is the submicroscopic beilby layer which forms when one metal is rubbed against another? And which spalls off during wear producing hard particles? Why is it harder and more brittle than the parent metal—although it is said to have the same composition? Has the metal turned amorphous due to the high temperatures and pressures produced during wear? Does the contribution of the electron to cohesive energy increase in amorphous metals, making them harder and corrosive resistant? Electron micrographs definitely indicate that the boundaries in large angle polycrystalline metals and alloys are extremely thin (about 3 to 5 atomic layers). Are these really "amorphous" regions with coordination polyhydra postulated by Bernal for "liquids"? Are polycrystals stronger than the monocrystals because dislocation cannot wander across the grain boundaries or is it because electron "lattice" interactions at the grain boundaries contribute to the cohesive energy?

We know that the dislocation theory has been very successful but are we leaning a bit too heavily on it, relegating the effect of free electrons on the mechanical properties, to the background?

Soon after the discovery of the quantum theory, it was appreciated that the physical basis for the optical and magnetic properties of solids must be found at the microscopic level. Unfortunately, the physical basis of mechanical behaviour was relegated as engineering. Only some outstanding scientists like Mott and Pierls appreciated that one must look at microscopic phenomena to understand mechanical behaviour also. Soon after the advent of the dislocation theory, their interest shifted to other problems and physicists have been very reluctant to contribute to this complex but important field. It is a bit ironical because the most dramatic and obvious property of a solid is, of course, its mechanical strength. This meeting clearly shows that we in India have a unique opportunity to make some important contributions before the rest of the world wakes up, so to say.

Bull. Mater. Sci., Vol. 6, No. 4, September 1984, pp. 633–641. © Printed in India.

Shocks and high velocity deformation

R CHIDAMBARAM

Physics Group, Bhabha Atomic Research Centre, Bombay 400085, India

Abstract. The shock Hugoniot curves of a large number of materials up to a few Mbar have been obtained experimentally. Metallurgical examination and physical measurements on metallic and other samples recovered after shock loading up to several 100 kbar indicate the existence of large concentrations of point, line and planar defects. Dislocation mechanisms have been invoked to explain shock wave propagation and the phenomena related to the quick homogenisation of stress and strain behind the shock front. Computer simulation models using molecular dynamics calculations have also been used to understand some aspects of shock wave propagation at an atomistic level. For very strong shocks, the material is expected to melt under shock heating, but the experimental evidence regarding this is inconclusive. A combination of shock temperature measurement and theory may be able to answer this question.

Keywords. Shock propagation; shock deformation; shock melting.

1. Introduction

During the last decade or two, our understanding of the mechanical effects of shock waves on materials has advanced considerably. There is now a wealth of metallurgical information on samples recovered after being subjected to shock loading. Active measurements of physical parameters such as the electrical resistivity have also been attempted in a few cases. Physical phenomena like shock deformation, phase transformations under shock loading and shock melting have been understood to a somewhat smaller extent at the microscopic level. We shall discuss some of these aspects in this paper.

If the shock wave propagating in a material is considered to be a sharp discontinuity in stress, then, using the laws of conservation of mass, momentum and energy, it can be shown that the undisturbed state is related to the shocked state at the shock front as follows:

$$U_s\rho_0 = \rho_1(U_s - U_p), \tag{1}$$

$$P_1 - P_0 = \rho_0 U_s U_p, \tag{2}$$

$$E_1 - E_0 = \tfrac{1}{2}(P_1 + P_0)(V_0 - V_1), \tag{3}$$

where U_s is the shock front velocity, U_p is the particle velocity in the compressed region; P, E, ρ and $V(=1/\rho)$ are respectively the pressure, specific internal energy, density and specific volume: the suffixes 1 and 0 represent quantities in the shocked and the unshocked regions respectively.

If the equation of state $E = E(P, V)$ of the material is also known, we can use (3) to write P as a function of V (for all practical purposes, $P_0 \simeq 0$). The locus of all states (P, V) which can be obtained by a single shock from an initial state (P_0, V_0) is known as the Rankine-Hugoniot curve or simply the Hugoniot curve (figure 1).

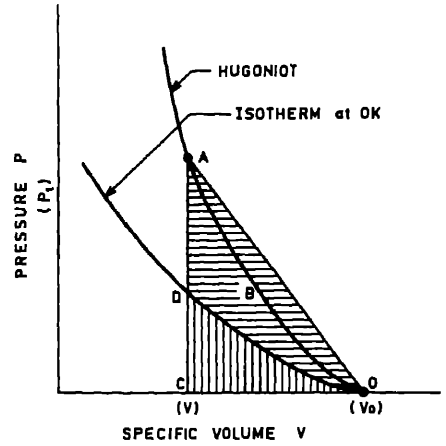

Figure 1. The Hugoniot curve. The vertically-hatched area is a measure of the cold compressive energy. The horizontally-hatched area is a measure of the heat energy in the shocked sample.

It is evident from (3) that the internal energy deposited in the compressed body is the area of the triangle *OAC*. If the compression is carried out isothermally at 0°K to the same final volume *V*, the material will be at the point *D*. The area of the curved triangle *ODC* therefore represents the "cold" elastic energy. The difference between the areas of *OAC* and *ODC* is a measure of the heat energy deposited by the shock in the compressed sample; the contribution from defects created by the shock, such as vacancies and dislocations, is relatively negligible. To give some numbers, a shock pressure of 1 Mbar* will compress a sample of aluminium from a density of 2·78 to 4·30 g/cm^3 and heat it to 3540 K. The corresponding shock velocity is 10·1 mm/μsec and the particle velocity is 3·6 mm/μsec.

After the shock wave has passed, the sample will unload along the curved path *ABO* doing work on the surroundings represented by the area of the curved triangle *OBAC*. (For simplicity we assume that the terminal specific volume $\simeq$ the initial value V_0, which would be true in the absence of porosity in the initial sample, etc.) The difference in the areas *OAC* and *OBAC* represents the (waste) heat deposited in the terminal sample. In aluminium, the residual temperature is 1440 K. If the amount of waste heat exceeds the enthalpy of vaporization (or melting), the terminal sample will be in the vaporised (or molten) state. In peaceful nuclear explosions (*e.g.*, see Chidambaram and Ramanna 1975), when a nuclear explosive is detonated underground in a rock medium, about 20% of the explosive energy is utilised in vaporising approximately 70 tons of rock, and another 20% in melting approximately 300 tons of rock for every kton of yield.

2. Range of shock pressures achieved experimentally

By keeping chemical explosives (usually in the form of lenses and pads) in contact, shock pressures of a few 100 kbar can be transmitted into materials. Alternately, a metal plate (flyer plate) can be accelerated by a contact explosive or a gas gun, and can subsequently be made to deliver its momentum to a target plate by impact. Pressures up to several Mbars can be achieved in this manner, though the pressure pulse widths are smaller (typically a few mm in space); still higher pressures can be obtained using curved rather than plane geometries. Exploding foils and rail guns can also be used to accelerate flyer plates. The highest shock pressures achieved to date have been through laser—or nuclear explosive-driven shocks and are in the range of tens of Mbars (for a more detailed discussion see Godwal *et al* 1983a). The metallurgical and physical observations to be discussed below have generally been on samples shocked to pressures less than about 1 Mbar.

---

* 1 Mpa = 10 bar, 1 Gpa = 10 kbar, 1 Tpa = 10 Mbar.

3. Finite elastic-plastic deformation by shock waves

When a plane shock wave propagates through a material, the change in density occurs—from a macroscopic point of view—through uniaxial compression. Consider a volume element of cross-sectional area A (perpendicular to the direction of shock propagation) and length L. During shock compression, A remains unchanged while L decreases in direct proportion to the decrease in the specific volume (see figure 2). If the element were allowed to expand from the final compressed state without lateral constraints it would reach normal density at the boundaries shown by the broken lines, provided it had been in a state of hydrostatic strain and stress in the compressed state. This gives us the elastic and plastic strain components in the direction of shock propagation and in the lateral directions, as indicated in the figure.

The time scales involved in shock propagation are typically in the μsec region, while the rise times are well below a nsec. Are conditions of hydrostatic stress and strain achieved behind the shock front, and, if so, how quickly? The answer to this question comes from the beautiful flash x-ray diffraction experiments of Johnson and Mitchell (1980) with single crystals of LiF, Al and graphite. Specific Bragg reflections were recorded using a Mo x-ray pulse synchronised with the duration of the shock compression of the crystal. These authors concluded that: (a) single crystals transform to the hydrostatically-compressed state within less than 20 nsec—there is no immediate conversion to a polycrystalline state; (b) the unit cell volume compression is in agreement with the conventional macroscopic volume compression data to within 1 %, independent of crystal orientation (shocks of strengths between 400 kbar and 1·1 Mbar were propagated along [100] and [111] in LiF). In related experiments at Trombay (Gupta 1980) we shocked polycrystalline samples of zirconium (hexagonal crystal

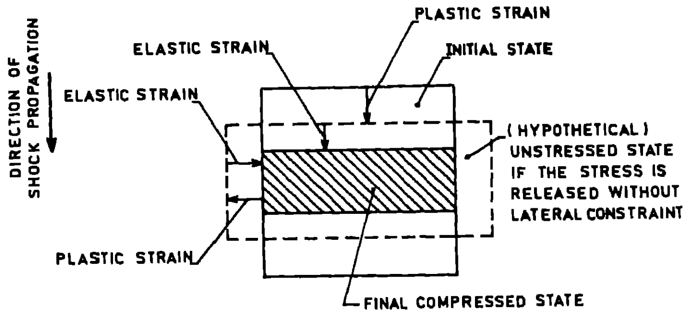
DIRECTION OF SHOCK PROPAGATION
ELASTIC STRAIN
ELASTIC STRAIN
PLASTIC STRAIN
PLASTIC STRAIN
INITIAL STATE
(HYPOTHETICAL) UNSTRESSED STATE IF THE STRESS IS RELEASED WITHOUT LATERAL CONSTRAINT
FINAL COMPRESSED STATE

Figure 2. Finite elastic-plastic deformation created by a shock wave.

system) which showed a prominent texture ({100} planes preferentially normal to the axis of the cylindrical sample). The texture was retained to a substantial extent in the terminal sample, after shock loading to about 150 kbar.

At very low pressures, the unit cell of the crystal may be expected to respond by one-dimensional compression. Correspondingly, in the Hugoniot curve, there is a pressure value known as the Hugoniot elastic limit (HEL) below which the response of the material to the shock pressure is nearly linear; the Hugoniot really begins to curve (concave upwards) from this point. The HEL is related to the shear strength of the material; one may expect that, for shock pressures lower than this limit, no rearrangement of the crystal lattice occurs (unlike in strong shocks discussed below). However, Jamet (1980) found, in some recent flash x-ray experiments with NaCl single crystals (HEL = 280 bar), that the one-dimensional deformation must be taken into account even for shock pressures above 10 kbar. Some experiments on the measurement of triaxial stress components using piezo-resistive gauges for shock pressures below, around and above the HEL are now being carried out for several materials (see, *e.g.* Chartagnac 1982).

Computer simulation of shock propagation in crystal lattices has also been attempted (Tsai and Macdonald 1976). Shock compression is initiated in a semi-infinite lattice by moving the lattice along the x-axis towards the origin with (mass) average velocity corresponding to the particle velocity U_p defined in (1)–(3), and making it collide with its image at $x = 0$. Many effects are correctly predicted by these molecular dynamics calculations including the achievement of thermal equilibrium and a state of hydrostatic stress, and also the right temperature. However, the strain in the compressed state turns out to be far from hydrostatic! This is related, we believe, to the computer limitation that necessitates a small-sized crystal lattice without scope for the generation of dislocations. As we shall see, the introduction of mobile-dislocation mechanisms is unavoidable in the description of shock propagation in solids.

4. Defect-generation during shock propagation

A variety of point, line and planar defects can be induced by shocks. Solid samples are usually examined after recovery following shock loading, and there is always the question of the relation of the residual defects to those present during the different stages of shock loading. On the one hand, shock heating may anneal out defects; on the other, the shock unloading process may lead to further plastic deformation. The former may be prevented to some extent by doing the experiment at liquid nitrogen temperatures, and then ejecting and storing the sample also at the same low T; electrical resistivity annealing measurements in copper shock-loaded (70–380 kbars) in this manner yield typical vacancy concentrations $\sim 10^{-4}$ (Mogilevskii 1970). The vacancy concentrations estimated from active resistance measurements in shock-loaded silver foils are perhaps ten times higher (Dick and Styris 1975; Graham 1981). Similarly, the density of dislocations in metals increases with shock pressure-approximately as $P^{1/2}$, according to Murr and Kuhlmann-Wilsdorf (1978). This density is about 10^{10}–10^{11} cm^{-2} in recovered samples shock-loaded up to 100–200 kbar, although once again the dislocation density could be much higher *during* shock propagation (Graham 1981; Svensson 1981).

In the original model of Smith (1958) for shock wave propagation, an interface of dislocations was postulated between the shocked and unshocked regions so that the deviatoric stresses arising from the shock could be relieved. The dislocation interface separates two lattices with different parameters. This interface of dislocations would, according to Smith, move with the shock front. If the dislocations move on a slip plane making an angle ϕ with the shock-front plane, the velocity of the dislocations becomes $U_s \operatorname{cosec} \phi$ which produces the necessary plastic strain. Such supersonic dislocations are, however, unacceptable for several reasons (Meyers and Murr 1981). This had led Meyers to postulate a new model whose essential features are as follows: (a) Dislocations are homogeneously at (or close to) the shock front by the deviatoric stresses set up by the state of uniaxial strain; the generation of these dislocations relaxes the deviatoric stresses. Adjacent dislocation layers are made up of dislocations with Burgers vectors of opposite signs; (b) The dislocations move short distances at subsonic speeds; (c) New dislocation interfaces are generated as the shock wave propagates through the material.

This model qualitatively explains many experimental results. Meyers and Murr also believe that the rarefaction part of the wave (corresponding to shock unloading) plays only a minor role in dislocation generation.

The shock front has a width W extended over a few lattice spacings, *i.e.*, $W \sim 10^{-6}$ cm. The strain rate $\dot{\varepsilon}$ can be written as (Gilman 1979)

$$\dot{\varepsilon} \simeq \frac{U_s}{2W} \frac{(\rho_1 - \rho_0)}{\rho_0}. \tag{4}$$

If the shock velocity is taken to be 1 cm/μsec and a density compression of 2 is achieved by the shock, $\dot{\varepsilon} \approx 10^{12}\ \mathrm{sec}^{-1}$, which is enormous. What is the mechanism of the transport of momentum down the steep velocity gradient? It is through atoms and dislocations, and the dislocation velocity may be expected to be proportional to U_s. The drag pressure D, which acts in opposition to the driving pressure P and equals it under steady motion conditions, can be written as a product of an effective viscosity η and the strain rate $\dot{\varepsilon}$. Gilman finds that the value of the viscosity that arises from the dislocations is of the order of 1 poise. As both η and $\dot{\varepsilon}$ are proportional to U_s, $D \sim U_s^2$, and hence can be very large for strong shocks. I have discussed this aspect in detail to emphasize the complexity that a first-principle calculation of shock wave structure, shock width, etc., would entail. The heating of the material by the shock wave can, however, be calculated using (1)–(3) and condensed matter theory, because the contribution of the various defects produced by the shock wave propagation to the free energy of the material is small.

What about shock propagation in liquids? One has to re-interpret the mobile-dislocation mechanisms in this case, taking into account the short-range order in liquids on the one hand, and the narrow width of the shock front on the other. To the best of my knowledge, no work has been done along these lines.

5. Phase transformations and melting under shock

Most phase transitions observed under static pressures are also observed under shock pressures. In fact, many sluggish phase transitions are readily observed under shock conditions because the deviatoric shear stress provides a driving force to overcome any activation barrier. The phase transformation is best examined in terms of U_s and U_p, rather than the conventional variables P, V. The plot of U_s vs U_p is (surprisingly) linear for a given phase (up to pressures of several megabars), and shows a discontinuity and change of slope upon the occurrence of a phase transformation. There is one important point which must be kept in mind when discussing shock-induced phase transformations: unlike static pressures, shock pressures also induce heating, and the rise in temperature may influence or inhibit the transformation. For example, in the alpha (hcp) to omega (simple hexagonal) phase transformation in Ti, the amount of ω-phase formed increases continually with pressure in the 'static' case; in contrast, under shock this amount first increases and then decreases as the shock pressure is increased. The reason for this behaviour is the change in temperature (Sikka *et al* 1982).

As one keeps on increasing the shock pressure, does the shock heating lead to melting in the compressed state, and, if so, what is the melting temperature? There is still considerable controversy with regard to this point. This is because the slope changes in the $U_s - U_p$ curves are either small or else have an alternative interpretation in terms of certain electronic changes. The shock-Hugoniot measurements show, for example, the existence of a relatively less-compressible high-pressure phase (beyond 300 kbar) in all members of the rare-earth series. This 'stiffening' of the Hugoniot curves has been identified with melting by Carter *et al* (1975), but Gust and Royce (1973) attribute it to the onset of a repulsive interaction between the noble-gas atomic cores. McMahan *et al* (1981), on the other hand, have analysed this phenomenon in terms of the completion of $s-d$ transfer in La. Again, in Pb, the various estimates of shock melting pressures range from 220 kbar to 1·24 Mbar (Duvall and Graham 1977).

The melting temperature under shock compression increases as indicated schematically in figure 3. We feel that the onset of shock melting may be established by a combination of shock temperature measurement and theoretical considerations (Godwal *et al* 1983b). The Hugoniot curves obtained by equation-of-state calculations in the solid and liquid states are quite distinct in the $T-P$ plane, as shown schematically in figure 3. There is a mixed solid-liquid region in the middle. (We have done these calculations for Al and Pb by the pseudopotential method. At $\rho_1/\rho_0 = 1{\cdot}8$ in Al, for example, the temperatures predicted are 12500 K and 8100 K respectively using the corresponding solid and liquid state theories.) Thus, a measurement of shock temperatures over a range of shock pressures will presumably yield information of the type shown in figure 3, so that the onset of melting may be discerned clearly.

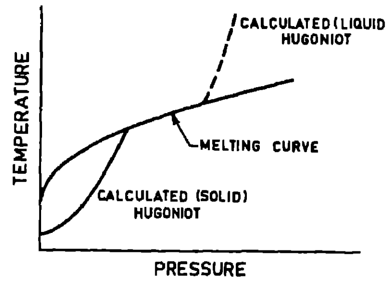

Figure 3. Schematic phase diagram for melting by shock heating.

6. Conclusions

There are many problems in the shock deformation of metals which are not yet fully understood. Most of the metallurgical studies have been on terminal samples shock-loaded to a few 100 kbar or less. Large concentrations of a variety of defects are found in these samples. These concentrations are presumably even greater during the various stages of shock propagation, since shock heating is supposed to anneal out many of the defects. The generation and motion of dislocations are essential in explaining shock front propagation which leaves behind a shocked region in a state of essentially hydrostatic strain (at least for strong shocks). Some computer simulation studies on atomistic models have also been attempted, but they do not account for all the experimental facts. Evidence for the melting of materials under very strong shocks is still in some doubt and may need a combination of theory and shock temperature measurement in order to be established conclusively. Much theoretical and experimental work still remains to be done in the field of shock deformation and related effects in materials.

Acknowledgements

The author thanks Dr S K Sikka and Dr B K Godwal for many helpful discussions.

References

Carter W J, Fritz J, Marsh S P and McQueen R G 1975 *J. Phys. Chem. Solids* **36** 741

Chartagnac P F 1982 *J. Appl. Phys.* **53** 948

Chidambaram R and Ramanna R 1975 *Proc. Tech. Commun. PNE IV* (Vienna: International Atomic Energy Agency) p 421

Dick J J and Styris D L 1975 *J. Appl. Phys.* **46** 1602

Duvall G E and Graham R A 1977 *Rev. Mod. Phys.* **49** 523

Gilman J J 1979 *J. Appl. Phys.* **50** 4059

Godwal B K, Sikka S K and Chidambaram R 1983a *J. Phys. Rep.* (under publication)

Godwal B K, Sikka S K and Chidambaram R 1983b (unpublished)

Graham R A 1981 in *Shock waves and high-strain-rate phenomena in metals* (eds) M A Meyers and L E Murr (New York: Plenum Press) p 375

Gupta S C 1980 Ph.D Thesis, University of Bombay (unpublished)

Gust W H and Royce E B 1973 *Phys. Rev.* **B8** 3595

Jamet F 1980 in *High pressure science and technology* (eds) B Vodar and Ph Marteau (Oxford: Pergamon Press) Vol 2 p 974

Johnson Q and Mitchell A C 1980 in *High pressure science and technology* (eds) B Vodar and Ph Marteau (Oxford: Pergamon Press) Vol 1 p 977

McMahan A K, Skriver H L and Johanseen B 1981 *Phys. Rev.* **B23** 5016

Meyers M A and Murr L E 1981 *Shock waves and high strain-rate phenomena in metals* (eds) M A Meyers and L E Murr (New York: Plenum Press) p 487

Mogilevskii M A 1970 *Combustion, explosion and shock waves* Vol 6 p 197

Murr L E and Kuhlmann-Wilsdorf D 1978 *Acta Met.* **26** 847

Sikka S K, Vohra Y K and Chidambaram R 1982 *Prog. Mater. Sci.* **27** 245

Smith C S 1958 *Trans. AIME* **212** 574

Svensson T 1981 *Shock waves and high strain rate phenomena in metals* (eds) M A Meyers and L E Murr (New York: Plenum Press) p 547

Tsai D H and Macdonald R A 1976 *High Temp. High Pressures* **8** 403

Discussion

C K Majumdar: Entropy production is not taken into account satisfactorily in any essentially hydrodynamics-based formalism. Eckart's work (1945) may perhaps indicate how this aspect should be incorporated into the description of shocks.

K Srinivasa Raghavan: There is nothing unusual about nonhydrostatic strain due to hydrostatic stress, because one is dealing with nonhomogeneous structures.

R Chidambaram: The question here is whether, in Tsai's molecular dynamics calculation on a bcc crystal, unit cells can be strained nonhydrostatically under hydrostatic stress. This has been achieved here by 'buckling' of neighbouring cells—akin to twinning. This picture appears to be somewhat artificial to me, the problem arising from the neglect of mechanisms of plastic deformation.

K A Padmanabhan: Can the amount of explosive charge be estimated, when, say, a hollow cylinder of Al is cald on to a hollow inner cylinder of steel?

Chidambaram: The attenuation behind the shock front is related to the ratio of the mass of the metal to the mass of the explosive. In the problem of explosive welding one has to strike a balance between having too little explosive (the attenuation is then too high) and having too much explosive (the metal cylinder is then damaged).

A P Pathak: Can channeling by charged particles be used to extract information about the defects while experiments on mechanical properties (including shock wave propagation) are in progress?

Chidambaram: I think the penetration of charged particles into the specimen could pose problems, as the diameter of the metal plates under study $\gtrsim 1$ cm

R Krishnan: In uniaxial tensile testing, an increased strain rate is equivalent to a reduction in test temperature. Is this so also for hydrostatic stress?

Chidambaram: For shock induced deformation, a higher strain rate implies a higher shock pressure which would lead to increased shock heating.

S Ramaseshan: How long does the rise in T due to the shock wave take to cool down?

Chidambaram: The fall from the high temperature in the compressed state to the residual temperature after shock unloading usually occurs in μsec. The cooling beyond that is by normal mechanisms.

Ramaseshan: How are boundary conditions specified in the molecular dynamics study of the shock front? How does this method differ from the finite element approach?

Chidambaram: As in usual solid state theory, cyclic boundary conditions were used by Tsai and Macdonald. The finite element method is a more general mathematical technique that is useful even in problems where there are no periodic lattices.

P Rodriguez: What is an ideal powder?

Chidambaram: In the context of diffraction, it is one in which there is no preferred orientation of the grains.

Rodriguez: For melting to occur, the dislocation density must be of the order

$10^{13}/\mathrm{cm}^2$, but experimentally it is $10^{11}/\mathrm{cm}^2$. How is this discrepancy explained?

Chidambaram: The high temperatures prevailing probably cause annealing of some of the dislocations, reducing their density.

Rodriguez: The high strain rates used in shock experiments are also used in metallurgical techniques like explosive forming and welding. The physical basis of these methods needs to be understood.

Rodriguez: In the flyer plate method used for welding and forming the interface is wavy. Could you comment on this?

Chidambaram: The uniformity with which one can produce a plane wave or shock wave by any of these methods is about 100 nsec. Within this time a non-uniformity of the order of 0·1–1 mm sets in. This has to be carried through.

D Kumar: In the energy diagram, a part of the triangle is the recoverable elastic energy and a part is the dissipated heat energy. Does the rest go into the formation of dislocations?

Chidambaram: The energy required to create dislocations is small and is generally ignored in the book-keeping.

S N Bandopadhyay: What is the evidence that the *strain* is hydrostatic?

Chidambaram: Flash x-ray diffraction experiments on cubic crystals indicate that the crystal behind the shock front reaches a state of hydrostatic strain within 20 nsec.

Bull. Mater. Sci., Vol. 6, No. 4, September 1984, p. 643. © Printed in India.

Computer simulation of tensile testing*

V SRIDHAR

Materials Science Laboratory, Reactor Research Centre, Kalpakkam 603 102, India

Abstract. A brief overview of the molecular dynamics method, with emphasis on the work of Parrinello and Rahman, is presented. Molecular dynamics is a method for studying classical statistical mechanics of well-defined systems through a numerical solution of Newton's equations. A set of N particles with coordinates r_i ($i = 1, \ldots, N$) and confined in a cell are allowed to interact through a potential. The bulk is usually simulated by periodically repeating the cell in space. Newton's equations are then solved numerically and the statistical averages of dynamical properties are calculated as temporal averages over the trajectory of the phase space. This method has already been used to simulate a liquid. Now, based on a Lagrangian formulation, it is possible to study systems under the most general conditions of externally applied stress. Unlike the earlier calculations, in this procedure, shape and size are governed by equations of motion obtained from the Lagrangian. Thus it allows us to study structural transformations which may be brought about by an interplay of external and internal stresses. By applying this technique to a single crystal of Ni, Parrinello and Rahman observe that the stress-strain relations obtained confirm with reported results. Under compressive loading it is found that Ni shows a bifurcation in its stress-strain relation and the system changes from cubic to hexagonal close packing. Such a transformation could perhaps be observed under extreme conditions of shock. Finally the scope of computer simulation is highlighted and the limitations of employing such a method are pointed out.

---

*only summary of the talk

Bull. Mater. Sci., Vol. 6, No. 4, September 1984, pp. 645–651. © Printed in India.

Instabilities in yielding

G VENKATARAMAN

Reactor Research Centre, Kalpakkam 603 102, India

Abstract. This paper addresses itself to instabilities observed during tensile testing, and complements the papers of Rodriguez and Ananthakrishna presented at this Meeting. The work of Caglioti *et al* on the elastic to plastic transformation is first reviewed. The work of Kubin *et al* on the serrated (repeated) yielding observed at liquid helium temperatures is then discussed in brief. Finally, our own work relying on electronic simulation is described. We conclude with some brief remarks on a few important questions that merit attention in the future.

Keywords. Tensile testing; yielding; instabilities; electronic simulation.

1. Introduction

Yielding observed during a tensile test is being discussed by several speakers at this Meeting. While metallurgists are by and large interested in the deformation mechanisms, for physicists the nonlinearities and the instabilities arising thereof are perhaps attractive avenues for investigation. Dr Rodriguez will present the metallurgist's point of view while Dr Ananthakrishna will discuss how he views the phenomena as a physicist. My talk will deal with some work on the subject that is pertinent to the present Meeting but not touched upon by them.

2. Elastic to plastic transition

The work done by Prof. Caglioti and coworkers (Boffi *et al* 1980) who address themselves to the instability associated with the elastic to plastic transition is first reviewed. They adopt a hydrodynamic approach, and their basic idea is as follows. One starts with the Helmholtz free energy F expressed as a function of the temperature T and strain ε, since these are quantities which can be measured in real time during an experiment. $F(T, \varepsilon)$ is expanded in a series in ε and $\theta = (T - T_0)/T_0$, $F(T_0, 0)$ being the free energy of the undeformed solid at temperature T_0, assuming that a uniaxial tension is applied. By differentiating $F(T, \varepsilon)$ appropriately with respect to the state variables, expressions are deduced for the entropy S and the equilibrium stress σ_e. These are substituted in the space- and time-dependent partial differential equations representing entropy and momentum balance. This is the starting-point for the subsequent stability analysis, the procedure up to this point being identical to what is normally done in hydrodynamics.

We are interested in the question of stability as the material deforms through the elastic region. Let us suppose that the applied (constant) strain rate is $\dot{\varepsilon}_a$. To investigate the stability of a particular state $\varepsilon_a (= \dot{\varepsilon}_a t$, t being the elapsed time) and temperature θ,

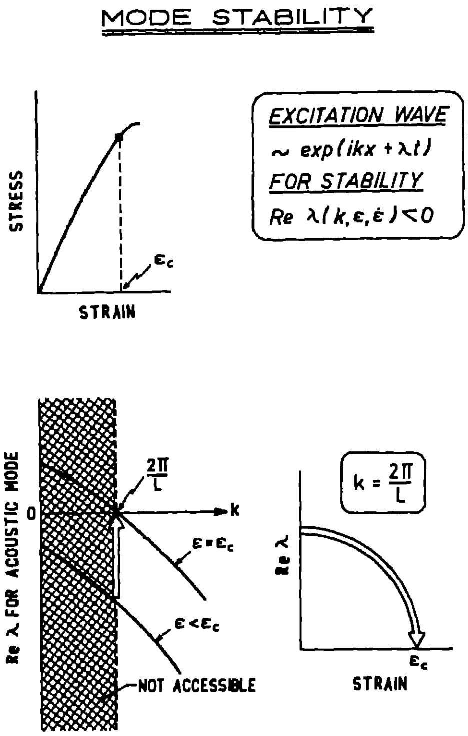

Figure 1. Instability of acoustic mode as $\varepsilon \to \varepsilon_c$. Owing to finite size of the specimen, the shaded region is not accessible.

one imposes small fluctuations $\delta\varepsilon$ and $\delta\theta$ around the reference state. Linearization yields a set of three coupled first-order equations for the quantities $\delta\theta$, $(\delta\dot{\varepsilon}/\varepsilon_a)$ and $\delta\varepsilon$, on which the standard normal-mode analysis may be performed. (In fluid dynamics, one would obtain the Rayleigh and Brillouin modes in this manner.) For a given mode to be stable, it is necessary that $\mathrm{Re}\,\lambda(k) < 0$, where λ is the corresponding eigenfrequency and k is the wavevector. It turns out that all the modes are stable as long as ε_a is smaller than a critical strain ε_c. At the critical strain, the acoustic mode with the longest wavelength (*i.e.*, $k \approx 2\pi/L$ where L is the length of the sample) becomes unstable (figure 1). There is an obvious analogy with phase transitions; Boffi *et al* (1980) have indeed drawn a parallel with the nonequilibrium transition in the laser. As yet there is only partial experimental confirmation of these ideas, but I understand (Bottani, private communication) that efforts are in progress to monitor the transition more completely by measuring the associated temperature fluctuations.

3. Repeated yielding

Let us consider next the instability aspects of serrated yielding. Dr Rodriguez in his presentation offers a comprehensive survey of the various mechanisms responsible for repeated yield drop. Dr Ananthakrishna considers one of these models, namely, that due to Cottrell, and analyzes how instabilities can arise. I shall complete the picture by discussing the work of Kubin *et al* and some of our own work.

3.1 *Low-temperature yielding*

Kubin and coworkers (Estrin and Kubin 1981; Kubin *et al* 1982, 1983) are concerned with repeated yield drops observed at liquid helium temperatures. These arise due to thermomechanical instabilities for which a model is proposed. The stability analysis is rather similar to that carried out by Boffi *et al* (1980) (the applied stress and the temperature are now chosen as the state variables characterizing the material undergoing deformation). These two variables are coupled through two nonlinear differential equations, the mechanical equation and the equation describing heat removal, in which the experimental conditions are suitably introduced. Linearization, stability analysis, etc., are then performed as usual, and contact is made with elementary bifurcation theory (Haken 1977).

The parameters that enter into the thermomechanical model of Kubin and coworkers (Estrin and Kubin 1981; Kubin *et al* 1982, 1983) are: the specimen dimensions, the applied strain rate, the combined elastic modulus of the specimen and the machine, the specific heat of the specimen and the coefficient of heat transfer. These parameters are combined into three dimensionless quantities $\dot{\Sigma}_a$ (the reduced elastic slope of the straining curve), α (the reduced activation volume) and ν (representing, apart from a factor, the ratio of the elastic and thermal energies). These are the control parameters. Figure 2 shows the $(\nu/\alpha, \dot{\Sigma}_a\alpha)$ plane in control parameter space. The different regions represent qualitatively different kinds of mechanical behaviour, the nature of which is amplified in figure 3. The types of trajectories in the phase space (σ, θ) associated with the various regions in figure 2 are sketched in figure 3a, and the corresponding yield curves are shown in figure 3b. While one has an asymptotic steady state in region II, one obtains serrations in region III. The crossing of the II-III boundary corresponds to a hard-mode instability. (A similar instability is discussed by Ananthakrishna with reference to his model.) To sum up, the work of Kubin *et al* demonstrates that it is possible to predict whether plastic deformation at low (cryogenic) temperatures will be smooth or jerky, depending on the values of a specified set of mechanical, geometric and thermal parameters, by using bifurcation theory and stability analysis.

3.2 *Electronic simulation*

I now turn to the work on serrated yielding which Neelakantan and myself (1983) have been engaged in recently. Our work was triggered by a fascinating paper by Franck

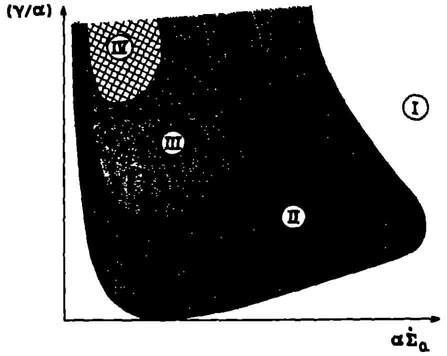

Figure 2. Regions of different types of mechanical behaviour in the parameter plane $(\dot{\Sigma}_a\alpha, \nu/\alpha)$ (Kubin *et al* 1983).

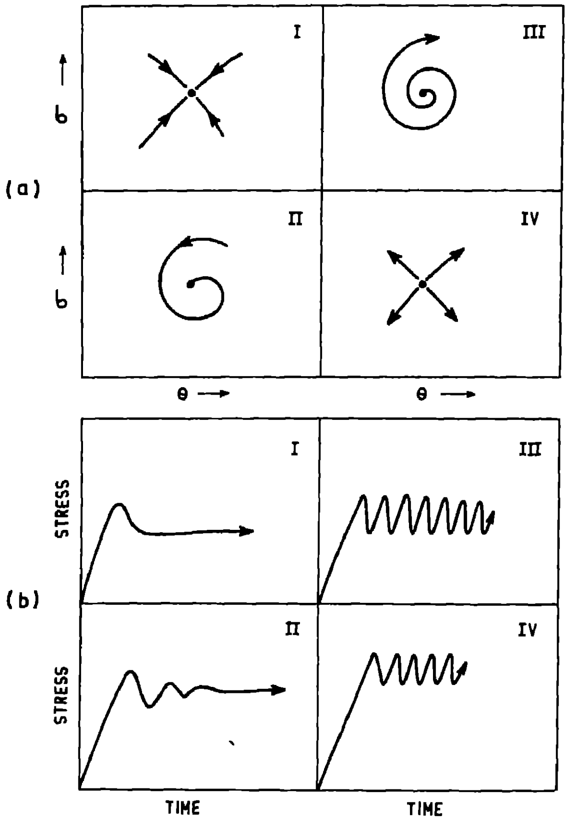

Figure 3. **a.** Phase space plots corresponding to the different regions shown in figure 2. **b.** Stress *vs* time curves corresponding to the different regions of figure 2 (Kubin *et al* 1983).

(1974) which gives an overview of feedback oscillations occurring in widely different chemical and biological systems. According to Franck, these diverse systems exhibit very similar behaviour because they share an underlying "negative resistance" feature. In serrated yielding, it is well known that at least for one class of models, *viz.*, the Cottrell-Bilby model (1949) (see also the paper by Rodriguez at this Meeting), there *is* such a negative resistance feature. We (Neelakantan and Venkataraman 1983) therefore explored how some of the observed features of repeated yielding could be understood along the lines indicated by Franck. It was most convenient to map the problem onto an equivalent electronic problem, and essentially carry out an analog simulation.

Skipping the details, the essential idea underlying our work may be understood by referring to figure 4. Shown here is a typical negative resistance characteristic, the detailed nature of which is dependent (in the physical problem under consideration) on parameters such as the dislocation density, temperature, etc. The applied strain rate prescribes the *load line*; the behaviour of the specimen during the test depends on where the load line cuts the characteristic curve. If the intersection is in the negative resistance region, then there is instability and oscillations (in stress) ensue.

Now, in contrast to the situation obtained usually in an electronic device, the characteristic curve itself evolves during the test for a specimen undergoing plastic

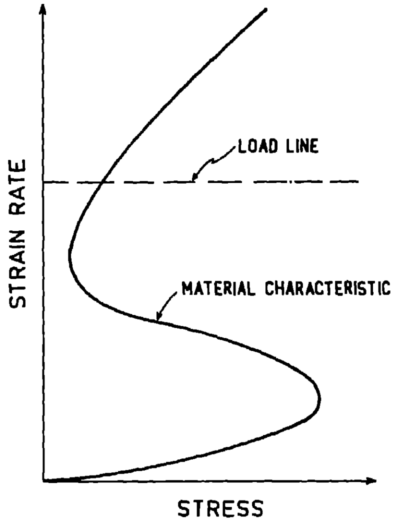

Figure 4. Schematic plot of the strain rate *vs* stress curve for a material exhibiting serrated yielding. (For examples of such curves in the Fe-C system, see Neelakantan and Venkataraman 1983). The negative resistance feature arises due to dislocations breaking away from their atmospheres.

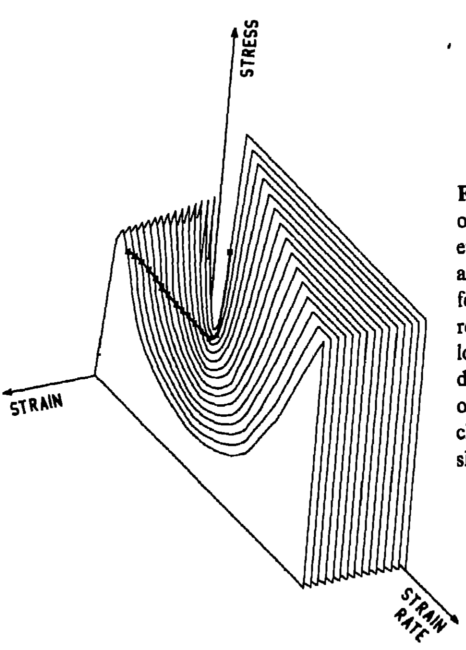

Figure 5. Perspective plot of a family of characteristic curves, simulating the evolution during an actual test. The valley associated with the negative resistance feature is seen to widen as the test progresses. The trajectory obtained by the load line method is also partially indicated. Serrations occur during the test only when the load line intercepts the characteristic in a region of negative slope.

yields. Thus, at a fixed temperature, and for the *same* material, the intersection of the load line and the characteristic may occur in a region of positive slope at one instant and in a region of negative slope at the next. The general form of the characteristic also suggests why serrations occur only in a certain region of the test curve. Figure 5 shows a schematic plot of a family of evolving characteristic curves for a material at a particular temperature. The trajectory resulting from the load line is also indicated, and one can see that instability can occur in certain ranges of the strain and not in others.

Our approach demonstrates that numerous aspects of tensile test curves observed in practice are readily reproduced and studied under convenient, controlled conditions in a suitably constructed analog device. One can begin to understand some of the observed trends in depth. For example, it is known that at a given temperature, serrations are absent both at very high and low strain rates; likewise, at a given strain rate, serrations appear only in a certain temperature band. There is therefore a well-defined region in the $\dot{\varepsilon}-T$ plane within which serrations occur. Our study shows that such a bounded region is indeed to be expected.

4. Conclusions

One common feature of all the models cited is that they tacitly assume the medium to respond homogeneously during repeated yielding. There are, however, reasons to believe that the deformation is in fact spatially inhomogeneous. This aspect has not received the attention it deserves in theoretical studies of the phenomenon, and one hopes that in the years to come this will be set right.

Another relatively neglected aspect is the important role played by noise: a considerable amount of irregularity exists in the observed serrations. Ananthakrishna discusses the effects of fluctuations to some extent in his paper. In our work, too, some thought has been given to the matter. Our preliminary finding is that when noise is included, the simulated tensile test curves begin to resemble real-life curves such as, *e.g.*, those found in Hall (1970). This work is still in progress. One's experience with the study of fluctuations in other areas of physics suggests that here, too, such an analysis would be a fruitful avenue of investigation.

References

Boffi S, Bottani C E, Caglioti G and Ossi P M 1980 *Z. Phys.* **B39** 135

Cottrell A H and Bilby B A 1949 *Proc. Phys. Soc.* **A62** 49

Estrin Y and Kubin L P 1981 in *Deformation of polycrystals Proc. 2nd Risø Int. Symp. Metal. Mat. Sci.*, (eds) N Hansen, A Horserrell, T Leffers and H Lilholt p. 179

Franck U C 1974 in *Physical chemistry of oscillatory phenomena Symp. Faraday Soc.* No. 9, p. 137

Haken H 1977 *Synergetics* (Berlin: Springer)

Hall E O 1970 *Yield point phenomena in metals and alloys* (New York: Plenum)

Kubin L P, Spiesser Ph and Estrin Y 1982 *Acta Metall.* **30** 385

Kubin L P, Estrin Y and Spiesser Ph 1983 preprint, Low temperature plastic deformation of metals and bifurcation theory (to appear in *Res. Mechanica*)

Neelakantan K and Venkataraman G 1983 *Acta Metall.* **31** 77

Discussion

G Srinivasan: The introduction of noise seems to produce bands. Is it that you are seeing some kind of a beat phenomenon?

G Venkataraman: We have not explored all the possibilities to say something at this stage.

R Ramaswamy: The kind of bunching phenomenon that occurs does have a practical analogue. This is the phenomenon of intermittency—shortly before the onset of a truly turbulent phase, long range periodicity appears in bursts.

K R Rao: Referring to Caglioti *et al*'s work, in the yield instability region, the soft mode may go to zero giving rise to an incommensurate phase reciprocal lattice point. Has this been experimentally observed?

Venkataraman: It has not been observed. This is only a model.

Bull. Mater. Sci., Vol. 6, No. 4, September 1984, pp. 653–663. © Printed in India.

Serrated plastic flow

P RODRIGUEZ

Metallurgy Programme, Reactor Research Centre, Kalpakkam 603 102, India

Abstract. This paper attempts an assessment of the current understanding of the phenomenon of "serrated plastic flow", which manifests itself as serrations, load drops, jerkiness or other discontinuities in the stress-strain curves obtained in constant extension rate tensile tests, and as sudden bursts of strain in constant loading rate tests and in constant load (stress) creep tests (the so called staircase creep). Though one can identify at least seven physical processes that can cause serrations, the discussion here is restricted mainly to serrated yielding in tension tests originating from dynamic strain ageing (DSA). The characteristics of the five types of serrations that have been identified so far and the experimental conditions under which they occur are discussed. The various models of serrated flow that have been put forward are reviewed critically. Some recent results on 316 stainless steel are presented to illustrate the effects of grain size, temperature and strain rate on serrated flow. Manifestations of DSA other than serrations such as a negative strain rate sensitivity, positive temperature dependence for flow stress and work hardening, and the ductility minimum are also discussed. Finally the various issues to be resolved are enumerated.

Keywords. Serrated flow; dynamic strain ageing; continual mechanical twinning; flow stress; work hardening peaks; ductility minimum.

1. Introduction

The organisers of this discussion meeting in their invitation requested that I should present here the metallurgist's viewpoint of 'serrated plastic flow'. At the outset let me state that whatever I say in the following should be considered as my own understanding of the phenomenon. There will be many materials scientists and engineers (including those with both physics and metallurgy backgrounds) who may not agree with all the views propounded here; there must also be an equally large number of physicists and metallurgists who may find common ground with the interpretations offered. It is interesting to note that in a recent international conference on deformation, two different treatments of the phenomenon, both by metallurgists have been given. One is based on a strain ageing mechanism involving the diffusion of solute atoms to temporarily arrested dislocations (McCormick 1983) and the other interprets it as an example of catastrophe theory in physical metallurgy (Strudel 1983).

The objective of the present paper is an assessment of the current understanding of the phenomenon of serrated plastic flow. We start with a brief description of the methodology of the tensile test. The physical processes that can cause serrated flow are then identified. Subsequent discussions are restricted to serrations due to dynamic strain ageing (DSA) or the Portevin-Le Chatelier (PL) effect (Portevin and Le Chatelier 1923) arising from interactions between diffusing solute atoms and mobile dislocations. The characteristics of five types of serrations observed under conditions of DSA are then discussed. The various quantitative models for serrated flow that have been put forward are then critically reviewed. Some recent results on 316 stainless steel are presented to illustrate the effects of grain size, temperature and strain rate on the DSA behaviour. This is followed by a discussion of the various manifestations of DSA in tensile test results. Finally, the various issues to be resolved are considered and catalogued.

2. Phenomenology

In a tension test, (the specimen suitably gripped between two crossheads, one moving and the other fixed) is deformed at a constant nominal strain rate determined by the velocity of the moving crosshead. At any instant of time, the total strain ε, the plastic strain ε_p in the specimen, and the elastic strain ε_e of the specimen-machine system are related by

$$\varepsilon = \varepsilon_p + \varepsilon_e, \tag{1}$$

$$\dot{\varepsilon} = \dot{\varepsilon}_p + \dot{\varepsilon}_e. \tag{2}$$

Equation (2) can be rewritten as

$$\dot{\varepsilon} = \dot{\varepsilon}_p + \frac{1}{E_s}\dot{\sigma}, \tag{3}$$

where σ is the stress and E_s the elastic modulus of the specimen-machine system. The condition for serrations or load drops is that the plastic strain rate $\dot{\varepsilon}_p$ exceeds the imposed strain rate $\dot{\varepsilon}$, *i.e.* whenever there is a sudden increase in $\dot{\varepsilon}_p$, a load drop occurs.

The phenomenon can also occur in creep tests in which strain in a specimen under a constant stress is measured as a function of time. Sudden bursts of plastic strain occur periodically, with the result that the creep curve has the shape of a staircase (hence the name 'staircase creep'). This manifestation of DSA in creep tests is discussed in another paper (Ananthakrishna 1983) presented at this Meeting.

3. Physical processes that can cause serrated flow

A survey of the literature shows that we can identify at least seven physical processes that can lead to serrations in the flow curve:

(i) The plastic strain rate under dislocation glide is given by

$$\dot{\varepsilon}_p = \rho_m b \bar{v}, \tag{4}$$

where ρ_m is the mobile dislocation density, $\bar{v}$ the average velocity of dislocations and b the Burgers vector. Serrations will therefore occur whenever there is an instantaneous increase in ρ_m or in $\bar{v}$ or in both.

(ii) Interaction of moving dislocations with DSA can lead to sudden increases in ρ_m and/or $\bar{v}$ and we shall be mainly examining this particular phenomenon.

(iii) In alloys undergoing order-disorder transformations, gradients or modulations in order encountered by moving dislocations can cause serrated flow (Mannan and Rodriguez 1972; Samuel and Rodriguez 1975, 1980).

(iv) Another phenomenon that can cause serrations is continual mechanical twinning as has been reported for an Fe-25 at % Be alloy (Bolling and Richman 1965). Twinning is characterised by a positive temperature dependence and a negative strain rate sensitivity for the flow stress which are also obtained under conditions of DSA.

(v) A sudden increase in the specimen temperature due to adiabatic heating is another possibility (Ramachandran 1983; Ramachandran *et al* 1970; Kubin *et al* 1982). This has been found to occur in tests at cryogenic temperatures. Dissipiation of the heat of deformation becomes difficult since the specimen surface is covered by a layer of gas molecules of the cryogenic liquid. The resultant increase in specimen temperature satisfies the condition for a load drop since a higher plastic strain rate can now occur at the applied stress level.

(vi) Phase transformations induced by stress and strain can also cause serrated flow. This aspect is covered in another paper presented at this Meeting (Seetharaman 1983).

(vii) Weertman (1967) has pointed out that yielding across fracture surfaces in brittle materials when tested under both hydrostatic pressure and triaxial non-hydrostatic stresses can cause serrations.

4. Types of serrations

Five types of serrations due to DSA termed A, B, C, D and E have so far been identified (figure 1). Types A, B and C are well-known and their characteristics are also well documented (Russel 1963; Macherauch and Munz 1966; Solar-Gomez and McG-Tegart 1969; Brindley and Worthington 1970; Cuddy and Leslie 1972) whereas serrations of types D and E have been referred to only relatively recently (Pink and Grinberg 1981; Wijler *et al* 1972). The characteristics of the different types of serrations and the experimental conditions that produce them are as follows.

(i) Type A serrations are periodic serrations from repeated deformation bands initiating at the same end of the specimen and propagating in the same direction along the gauge length. These are considered as locking serrations, characterised by an abrupt rise followed by a drop to below the general level of the stress-strain curve. They occur in the low temperature (high strain rate) part of the DSA regime.

(ii) Type B serrations are oscillations about the general level of the stress-strain curve that occur in quick succession due to discontinuous band propagation arising from the DSA of the moving dislocations within the band. (This contrasts with the smooth propagation of the band that occurs after initiation with a type A load drop). Type B

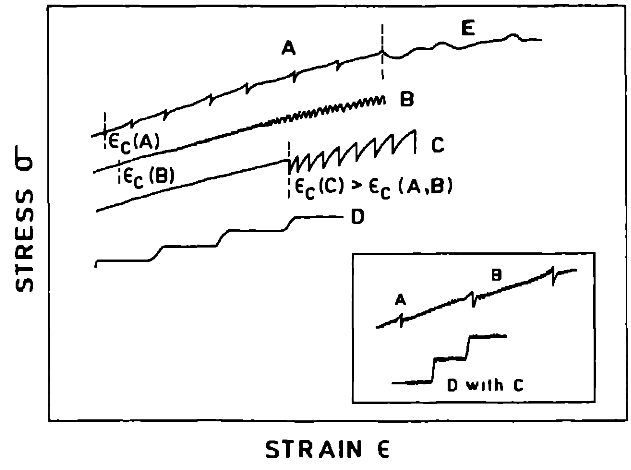

Figure 1. Types of serrations.

serrations often develop from those of type A with increasing strain (figure 1 inset) or occur at the onset of serrated yielding at high temperatures and low strain rates.

(iii) Type C serrations are yield drops that occur below the general level of the flow curve and are therefore considered to be due to dislocation unlocking. They occur at higher temperatures and lower strain rates than in the case of types A and B serrations.

(iv) Type D serrations are plateaus in the σ-ε curve due to band propagation similar to Luders band with no work hardening or strain gradient ahead of the moving band front. Like type A serrations, they can occur alone or with type B serrations during the band propagation (figure 1 inset). In Au-Cu 14 wt $\%$ alloy, Wijler *et al* (1972) produced type D serrations by homogeneous prestraining at high temperatures.

(v) Type A serrations change over to type E serrations at high strains. The latter are similar to type A serrations, but with little or no work hardening during band propagation.

5. Models for serrated flow from DSA

Any theory or model for serrated flow should account for the different types of serrations that appear in different alloys and for the influence of temperature, strain and strain rate on these various types. For the onset of serrations in substitutional alloys, a critical strain ε_c is required. The ε_c value is dependent on both $\dot{\varepsilon}$ and the temperature T (figure 2). At high strain rates and low temperatures where the first serrations are of type A or B, ε_c increases with increasing strain rate and decreasing temperature. At high temperatures and low strain rates, where serrations of type C are observed, ε_c increases with increasing temperature and decreasing strain rate. While current theoretical models are unable to account for this latter behaviour, the variation of ε_c with T and $\dot{\varepsilon}$ in the low temperature (high strain rate) regime has been rationalized by a number of theoretical models based on the interaction of diffusing solute atoms and mobile dislocations.

5.1 *Interpretations of* ε_c

The oldest quantitative model for serrated yielding is due to Cottrell (1953) in which the mobile solutes are assumed to interact with quasi-viscously moving dislocations; serrations are attributed to repeated locking and unlocking of dislocations in solute atmospheres, which occurs when $\bar{v}$ equals the drift velocity of the solutes in the stress field of the dislocations. In subsequent modifications of this model that integrate it with the theory of thermally activated deformation processes, it was recognised (Sleeswyk

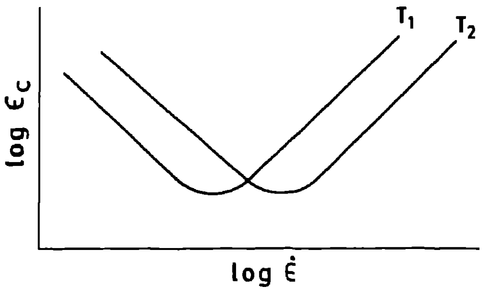

Figure 2. Effect of strain rate and temperature on critical strain; $T_2 > T_1$.

1958; McCormick 1972) that the "ageing" of the dislocations would take place during the waiting time of the dislocations at discrete obstacles rather than during their actual motion. When the diffusion coefficient is high enough to saturate the dislocation with a solute atmosphere during the waiting time, serrated yielding will start. In the model of van den Beukel (1975) though the same picture of solute-dislocation interaction was adopted, ε_c was chosen (following the ideas of Sleeswyk 1958; Penning 1972) to be the strain at which the strain rate sensitivity $\gamma = \partial\sigma/\partial \ln \dot{\varepsilon}$ became negative. In all the three approaches, the final result is that at ε_c

$$\rho_m^{(c)} C_v^{(c)} = K_1 \dot{\varepsilon} \exp(E_m/kT), \tag{5}$$

where C_v is the vacancy concentration E_m is the vacancy migration energy and T the absolute temperature. The three models yield widely different values for the constant K_1 (the value in the original Cottrell model does not account for the experimental values of ε_c). The vacancy concentration is enhanced due to the strain (Van Bueren 1955) according to

$$C_v = A\varepsilon^m. \tag{6}$$

Similarly, the strain dependence of ρ_m can be expressed as

$$\rho_m = B\varepsilon^\beta. \tag{7}$$

From (5), (6) and (7) we get

$$\varepsilon_c^{m+\beta} = K_2 \dot{\varepsilon} \exp(E_m/kT). \tag{8}$$

DSA due to interstitial solutes (8) reduces to

$$\varepsilon_c^\beta = K_2' \dot{\varepsilon} \exp(E_m/kT). \tag{9}$$

Experimental results in the low temperature-high strain rate region have given reasonable values for m, β and E_m. Typical $(m+\beta)$ values are between 2 and 3 for substitutional alloys; for interstitial alloys (Van den Beukel 1980), β lies between 0·5 and 1.

It has generally been observed that the critical strain ε_c increases with increasing grain size (Brindley and Worthington 1970; Charnock 1968, 1969; Mannan 1981; Mannan *et al* 1983). Relating this increase to the grain size dependence of ρ_m, Charnock (1968, 1969) has shown that (8) can be modified to include the grain size dependence of ε_c according to

$$\varepsilon_c = K_3 d^p \dot{\varepsilon}^q \exp[E_m/kT(m+\beta)] \tag{10}$$

where $p = n''/(m+\beta)$, $q = 1/(m+\beta)$ and the parameter n'' arises from the $\rho_m - d$ relationship of Conrad and Christ (1963): $\rho_m = N\varepsilon^\beta/d^{n''}$.

5.2 *Some results on* 316 *stainless steel*

The flow curves obtained in the temperature range 523–923 K at a strain rate of 3 × 10^{-4} sec^{-1} for 316 stainless steel of two different grain sizes (0·04 and 0·125 mm) are shown in figures 3 and 4 (Mannan 1981; Mannan *et al* 1982, 1983). (The serration types are labelled as in §4). The observed effects of the grain size on DSA are the following: (a) The DSA temperature region gets shifted to higher temperatures with increasing grain size; (b) For all grain sizes (8) is valid with $(m+\beta) = 2{\cdot}3$, β was estimated to be $\simeq$ 0·9, in

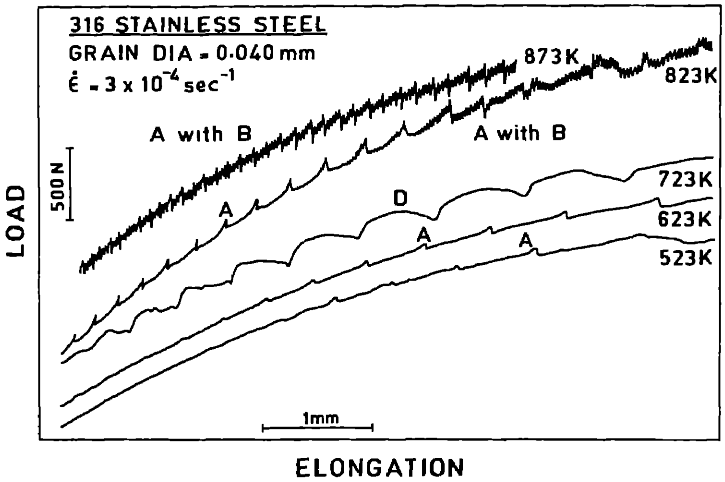

Figure 3. Serrated plastic flow in 316 stainless steel with grain size $d = 0{\cdot}04$ mm.

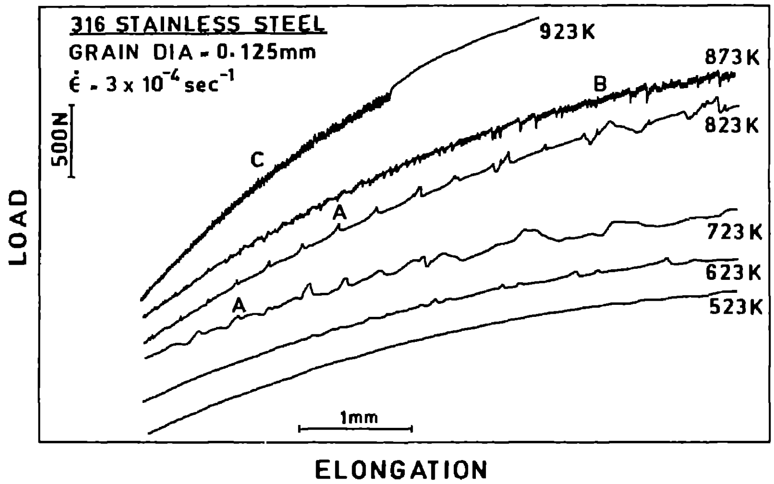

Figure 4. Serrated plastic flow in 316 stainless steel with grain size $d = 0{\cdot}125$ mm.

good agreement with the prediction of $\beta = 1$ for a linear increase in dislocation density with strain; (c) The relationship between ε_c and d follows (10) with $p = 0{\cdot}6$; (d) An apparent activation energy for DSA of 255 kJ/mol is obtained for all grain sizes from the variation of ε_c with T, (8); (e) A fit to the Hall-Petch equation for the variation of the flow stress σ_ε with grain size d, namely, $\sigma_\varepsilon = \sigma_{0\varepsilon} + K_\varepsilon d^{-1/2}$ where K_ε and $\sigma_{0\varepsilon}$ are constants (called the Hall-Petch slope and intercept respectively), yields a monotonic decrease of $\sigma_{0\varepsilon}$ with temperature; whereas K_ε though it generally decreases with temperature, shows a peak in the temperature region 523–723 K. This indicates that grain boundary regions are preferred sites for dynamic strain ageing (Armstrong 1968); (f) A peak in the variation of work hardening with temperature is also obtained but towards the upper

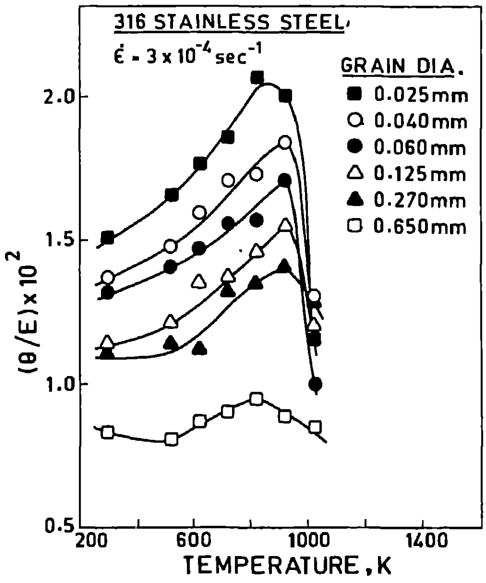

Figure 5. Variation in work hardening with temperature for 316 stainless steel with different grain sizes. E is the Young's modulus. $\theta = \Delta\sigma/\Delta\varepsilon$, $\Delta\sigma$ is the flow stress increment over the strain interval $\Delta\varepsilon$ from $\varepsilon = 0{\cdot}005$ to $\varepsilon = 0{\cdot}05$.

end of the DSA temperature range (figure 5). Consistent with the fact that this temperature range represents conditions for strong pinning and accordingly the most rapid and strongest dislocation immobilisation, leading to an increased rate of dislocation accumulation (Reed-Hill 1974), the DSA peak for work hardening also becomes more pronounced with decreasing grain size.

5.3 *Other interpretations of serrated flow*

Equation (4) allows serrations to occur for sudden increases in ρ_m or in $\bar{v}$ or in both of them. The models discussed in §5·1 assume that the average velocity is unchanged, and that serrations occur due to changes in ρ_m owing to the locking and unlocking of dislocations during deformation. It has also been pointed out that the solute atmospheres formed could be dragged along with the moving dislocations, and that such atmospheres would exert a drag stress on the dislocation which varies with dislocation velocity as schematically illustrated in figure 6(a) (Hirth and Lothe 1968; Schmidt and Miller 1982). With this drag stress contribution included, the normal stress-velocity variation for dislocations shown in figure 6(b) assumes the shape shown in figure 6(c). Nabarro (1967) has suggested that serrations will occur in the strain rate (dislocation velocity) region between the points B and D in this figure since the dislocation velocity is a multivalued function of stress in this region; for a given value of the applied stress it is possible for the velocity to increase suddenly to a higher value. The region between C and D where the moving dislocation requires a lower stress for a higher velocity (negative strain rate sensitivity) is more commonly identified with the dynamic instability of plasticity leading to the PL effect (Sleeswyk 1958; Sleeswyk and Verel 1972; Wilcox and Rosenfield 1966; Yoshinaga and Morozumi 1971; Penning 1972; Malygin 1973). Suggestions have also been made that serrated yielding could be considered as a manifestation of 'chaotic' behaviour (Neelakantan and Venkataraman 1982) or as an example of a 'catastrophe' in plastic deformation (Strudel 1983) arising from the negative-resistance feature between C and D.

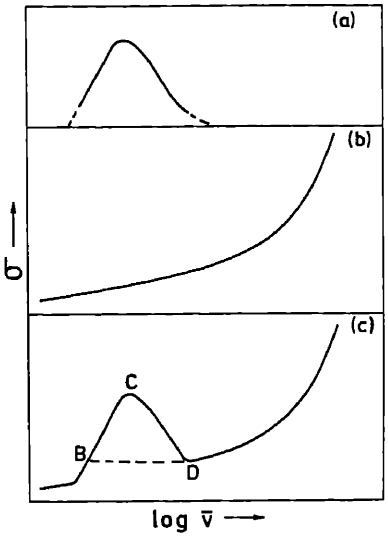

Figure 6. (**a**) The solute drag stress on a dislocation as a function of dislocation velocity. (**b**) Normal stress-velocity relation for dislocation in the absence of the drag stress. (**c**) Actual stress-velocity variation due to the presence of a drag stress at intermediate velocities.

That negative strain rate sensitivity is a crucial factor for the PL effect is now recognised in all the models. The treatment of McCormick (1983), for example, points out that the critical strain for the onset of serrated flow can be rationalised by matching the critical velocity (for negative resistance) with the solute diffusion coefficient. In the models of Van den Beukel (1975, 1980) and of Mulford and Kocks (1979) it is held that any solute mobility makes a negative contribution to the total strain rate sensitivity and that this contribution increases with strain; when the total strain rate sensitivity becomes negative plastic flow becomes unstable. In arriving at the strain dependence of the strain rate sensitivity, Van den Beukel retains the notions of a strain-dependent solute diffusion coefficient and strain-dependent mobile dislocation density from the older models. Mulford and Kocks (1979), on the other hand, describe the strain rate sensitivity in terms of the flow stress σ which is the sum of two components—the friction stress σ_f and the dislocation flow stress σ_d; solute mobility affects σ_d, the strain-hardening component of the flow stress. More recently, Van den Beukel and Kocks (1982) have arrived at a unified approach which enables the negative strain rate sensitivity to arise as a consequence of the influence of solute mobility on both the friction stress (by decreasing the obstacle spacing along the dislocation) and forest hardening (by increasing the strength of dislocation junctions).

In a paper that has not received the attention that it deserves, Weertman (1967) has suggested that the PL effect occurs as a result of an instability of the dislocations in going back and forth between a slow moving state and a fast moving state due to dynamic frictional stress drops. The effect occurs because of the inherent instability of the position that separates the fast slip region from the slow slip region in the slipped zone. The similarity between earthquakes and the behaviour of groups of dislocations in a slip band when the frictional force is reduced for any reason has also been pointed out: "Earthquakes are merely, the PL effect exhibited in a sample whose dimensions happen to have a grand scale".

Mention should also be made of attempts to understand serrated yielding through mechanical and electronic models. Dry friction models that simulate the strain bursts in staircase creep (Bodner and Rosen 1967) and the load drops in tensile tests (Rosen and Bodner 1969) have been devised which consider some of the features of DSA such as the negative strain rate sensitivity, work hardening and deformation by band propagation. Similar electronic analogs for the tensile test situation have also been demonstrated (Neelakantan and Venkataraman 1983).

6. Other manifestations of DSA

As we have mentioned earlier, serrations represent only one of the manifestations of dynamic strain ageing. In figure 7 the various other anomalies associated with DSA are illustrated schematically. These are (i) a peak in the variation of σ with T (ii) a peak in the variation of the work hardening $\theta = \Delta\sigma/\Delta\varepsilon$ with T, (iii) a peak in the variation of the Hall-Petch slope K_ε with T, (iv) a minimum in the variation of the ductility with T and (v) a minimum in the strain rate sensitivity $\gamma = \Delta\sigma/\Delta \ln \dot{\varepsilon}$ with γ going negative in the temperature region of serrated flow. The variations in γ with stress and strain at different temperatures are also shown in figure 7. The types of serrations normally observed in the different temperature regions are also indicated.

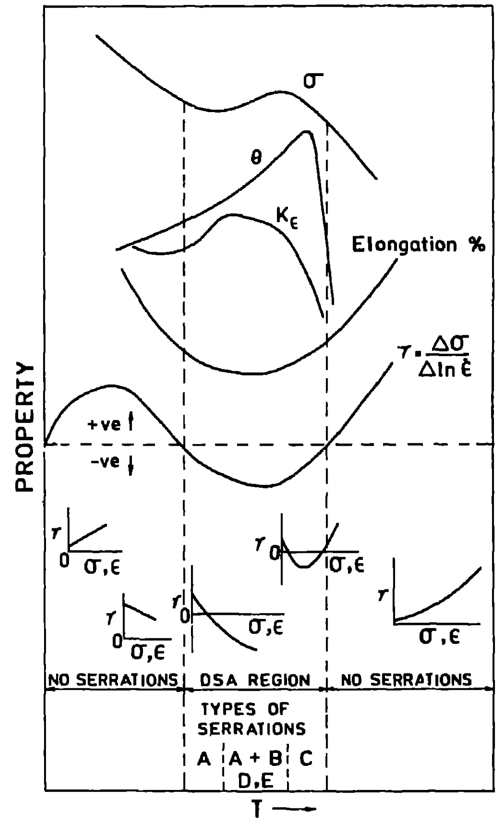

Figure 7. Schematic illustration of the various manifestations of dynamic strain ageing.

7. Issues to be resolved

(i) The main issue to be resolved unambiguously is whether the load drops are caused by a sudden increase in ρ_m or in $\bar{v}$ or in both. We are handicapped by the fact that we do not so far have an experimental technique to measure ρ_m or $\bar{v}$ during deformation. Acoustic emission measurements hold out promise as a potential method of attack on this problem.

(ii) Deformation during serrated flow is inhomogeneous and localised in bands. The actual strain rate in the deformation band is much higher than the imposed or assumed strain rate. Measurements and analysis of deformation band parameters such as the band velocity, band strain, band width and the average strain rate in the band should therefore receive greater attention than they have hitherto (McCormick 1983).

(iii) Current theoretical models are unable to account for the inverse effects (ε_c increasing with increasing temperature and decreasing strain rate) observed in the high temperature-low strain rate region in which type C serrations are observed.

(iv) Most of the models are incomplete in that they make *ad hoc* assumptions or use empirical relationships; there is no detailed understanding either experimentally or theoretically of the effect of strain on diffusion, of the dependence of mobile dislocation density on strain or of the effect of a solute atmosphere on dislocation–dislocation interactions.

(v) Though it is often recognised that only short range diffusion in dislocation core (pipe diffusion) is involved in many manifestations of DSA, we are handicapped by the lack of an adequate knowledge of the appropriate diffusion coefficients.

(vi) In analysing the dependence of σ on $\dot{\varepsilon}$ and T, is the splitting of the flow stress into additive contributions from forest interactions, solutes, lattice friction, justified? How is such an approach reconciled with the idea that the obstacle with the highest energy barrier will be rate-controlling?

This list is evidently not an exhaustive one, but it does highlight some of the aspects of DSA that deserve greater attention from both experiment and theory in future.

References

Ananthakrishna G 1984 *Bull. Mater. Sci.*

Armstrong R W 1968 in *Dislocation dynamics* (eds) A R Rosenfield, G T Hahn, A L Bement and R I Jaffee (New York: McGraw Hill) p. 293

Bodner S R and Rosen A 1967 *J. Mech. Phys. Solids* **15** 63

Brindley B J and Worthington P J 1970 *Met. Rev.* **15** 101

Bolling G F and Richman R H 1965 *Acta Metall.* **13** 709, 723, 745

Charnock W 1968 *Philos. Mag.* **18** 89

Charnock W 1969 *Philos. Mag* **20** 209

Conrad H and Christ B 1963 in *Recovery and recrystallization of metals* (ed) L Himmel (New York: Interscience) p. 124

Cottrell A H 1953 *Philos. Mag* **44** 829

Cuddy L J and Leslie W C 1972 *Acta Metall.* **20** 1157

Hirth J P and Lothe J 1968 *Theory of crystal dislocations* (New York: McGraw-Hill)

Kubin L P, Spiesser Ph and Estrin Y 1982 *Acta Metall.* **30** 385

Macherauch E and Munz D 1966 *Z. Metall.* **57** 552

Malygin G A 1973 *Phys Status Solidi* **A15** 51

Mannan S L 1981 *Influence of grain size on the flow and fracture in AISI type* 316 *stainless steel at elevated temperatures* Ph.D. Thesis, Indian Institute of Science, Bangalore

Mannan S L and Rodriguez P 1972 *Philos. Mag.* **25** 673

Mannan S L, Samuel K G and Rodriguez P 1982 in *Proc. 6th Int. Conf. Strength of Metals and Alloys,* Melbourne, Aug. 1982 (ed) R C Giffkins (New York: Pergamon Press) Vol 2 pp. 637–642

Mannan S L, Samuel K G and Rodriguez P 1983 *Trans. Indian Inst. Metals* **36** 313

McCormick P G 1972 *Acta Metall.* **20** 351

McCormick P G 1983 in *Deformation—All aspects, Int. Conf. on Metal Sci., ICMS,* Ranchi (Calcutta: Indian Institute of Metals)

Mulford R A and Kocks U F 1979 *Acta Metall.* **27** 1125

Nabarro F R N 1967 *Theory of crystal dislocation* (Oxford: University Press) p. 431

Neelakantan K and Venkataraman G 1983 *Acta Metall.* **31** 77

Penning P 1972 *Acta Metall.* **20** 1169

Pink E and Grinberg A 1981 *Mater. Sci. Eng.* **51** 1

Portevin A and LeChatelier F 1923 *CR Acad. Sci.* **176** 507

Ramachandran V 1983 in *Deformation—All aspects, Int. Conf. on Metal Sci., ICMS,* Ranchi (Calcutta: Indian Institute of Metals)

Ramachandran V, Baldwin D H and Reed-Hill R E 1970 *Metall. Trans.* **1** 3011

Reed-Hill R E 1974 *Rev. High Temp. Mater.* **2** 214

Rosen A and Bodner S R 1969 *Mater. Sci. Eng.* **4** 115

Russel B 1963 *Philos. Mag.* **8** 615

Samuel K G and Rodriguez P 1975 *Trans. Indian Inst. Metals* **28** 323

Samuel K G and Rodriguez P 1980 *Trans Indian Inst. Metals* **33** 285

Schmidt C G and Miller A K 1982 *Acta Metall.* **30** 615

Seetharaman V 1984 *Bull Mater. Sci.* **6**

Sleeswyk A W 1958 *Acta Metall.* **6** 598

Sleeswyk A W and Verel D J 1972 *Scr. Metall.* **6** 1972

Solar-Gomez A J R and McG Tegart W J 1969 *Philos. Mag.* **20** 507

Strudel J L 1983 in *Deformation—All Aspects, Int. Conf. on Metal Sci., ICMS,* Ranchi, (Calcutta: Indian Institute of Metals)

Van Bueren H G 1955 *Acta Metall.* **3** 519

Van den Beukel A 1975 *Phys Status Solidi* **A30** 197

Van den Beukel A 1980 *Acta Metall.* **28** 965

Van den Beukel A and Kocks U F 1982 *Acta Metall.* **30** 1027

Weertman J 1967 *Can. J. Phys.* **45** 797

Wijler A, Schade Van Westrum J and Van den Beukel A 1972 *Acta Metall.* **20** 355

Wilcox B A and Rosenfield A R 1966 *Mater. Sci. Eng.* **1** 201

Yoshinaga H and Morozumi S 1971 *Philos. Mag.* **23** 1351, 1367

Bull. Mater. Sci., Vol. 6, No. 4, September 1984, pp. 665–676. © Printed in India.

Repeated yield drop phenomena as a cooperative effect

G ANANTHAKRISHNA

Materials Science Laboratory, Reactor Research Centre, Kalpakkam 603 102, India

Abstract. We present a theoretical model of repeated yielding (RY) which reproduces many experimentally observed features, apart from showing how the temporal behaviour of the phenomenon emerges as a consequence of the cooperative behaviour of defects. We first consider the case of step-like creep curves. Our model leads to a coupled set of nonlinear differential equations which admit limit cycle solutions, and thence jumps on the creep curve. Approximate closed form solutions for the limit cycles and the steps on the creep curve are obtained. The model is then extended to the constant strain rate experiment by including the machine equation. The temporal ordering of RY is shown to follow, as well as several other features characteristic of RY. Chaotic flow is also exhibited: the model has a sequence of period-doubling bifurcations with an exponent equal to that of the quadratic map. Finally, we have analysed the fluctuations during the onset of RY using nonlinear Langevin equations. Fluctuations in the periodic (RY) phase are also investigated. We conclude that RY is another example of a dissipative structure.

Keywords. Repeated yield drop; defects; cooperative behaviour; limit cycle solutions; nonlinear Langevin equations.

1. Introduction

There have been numerous phenomenological treatments of repeated yielding (RY) in the metallurgical literature (Bell 1973; Bodner and Rosen 1967; Cottrell 1953; McCormic 1972; Penning 1972; van den Beukel 1975, 1980). The best known model is Cottrell's dynamic strain-ageing model and its extensions (McCormic 1972; van den Beukel 1975, 1980). In these models, expressions are derived for such quantities as the critical strain, the critical strain rate, the dependence of the flow-stress on the strain rate, etc. Little attention has been paid to relating these quantities to the basic dislocation mechanisms such as cross glide, the Frank-Read mechanism, the formation of dislocation locks, etc. Also, there has been no attempt to investigate how the temporal behaviour of repeated yielding could arise naturally as a consequence of the basic dislocation mechanisms. From this point of view Cottrell's model is essentially static in character.

The transition from a single yield drop to a situation where RY occurs when certain 'drive' parameters (*e.g.*, the strain rate, temperature, etc.), are varied has the physical features of a nonequilibrium phase transition. (For examples of such transitions which arise only when the system is driven away from equilibrium, see Nicolis and Prigogine 1977; Haken 1978). We have constructed dislocation-dynamical model (Ananthakrishna and Sahoo 1981; Ananthakrishna and Valsakumar 1982; Valsakumar and Ananthakrishna 1983) which exhibits most of the experimentally observed features of RY and demonstrates that RY is a nonequilibrium phase transition. Needless to say, we consider somewhat idealized conditions, and further do not attempt to fit any actual data. In § 2, we start with the simplest case, namely, steps on the creep curve. Based on well-known dislocation mechanisms, we introduce a model which transforms one type of dislocation into another, giving rise to a set of coupled nonlinear differential equations for the corresponding densities. For a range of values of the rate constants, these equations are shown to admit *limit cycle* solutions. These lead immediately to jumps on creep curves. The model predicts a temperature range in which these jumps appear. In §3, we outline how approximate closed form solutions for the limit cycles and the steps on the creep curve are obtained. The results are shown to agree with experiments on zinc (Zagorukuyko *et al* 1977). Section 4 contains the extension of the model to the constant strain rate case by coupling the equations of §2 to the machine equations. The temporal ordering of RY is shown to follow (Ananthakrishna and Valsakumar 1982). Also demonstrated are several important features typical of RY such as bounds on the strain rate, bounds on the concentration of solute atoms, the negative strain rate dependence of the flow stress, the dependence of the amplitude on the strain rate and strain, etc.

Our model also exhibits chaotic flow, which finds some support from experiments. We find a sequence of period doubling bifurcations (Ananthakrishna and Valsakumar 1983) with an exponent identical to that for a quadratic map. This is presented in §5. Section 6 is devoted to the study of fluctuations during the onset of RY using nonlinear Langevin equations. We have used the Monte-Carlo and Gaussian decoupling methods (Valsakumar *et al* 1983). As the strain rate approaches its critical value, the variance not only diverges, but also shows the periodic nature of the fluctuations. Fluctuations within the periodic phase (RY) are also investigated. Our entire analysis shows that RY is another example of a dissipative structure (Nicolis and Prigogine 1977). In the final section, some unresolved problems are discussed.

2. Steps on the creep curve

2.1 *The model*

Perhaps the simplest manifestation of instability in plastic flow, from a conceptual point of view, is a creep curve with steps. However, there are not many instances of measurements where stepped response has been observed (Ardley and Cottrell 1953; Navratil *et al* 1974; Stejskalova *et al* 1981; Zagorukuyko *et al* 1977; Da Silveira and Monteiro 1979; Lubahn and Felgar 1961). There appears to be no detailed theory for the phenomenon. The model we propose (Ananthakrishna and Sahoo 1981; Valsakumar and Ananthakrishna 1983) is a natural extension of our earlier work (Sahoo and Ananthakrishna 1982) where a theory of creep was developed under the assumption that mobile dislocations (denoted by g) and immobile dislocations (denoted by s) transform into each other and are in dynamical balance. In the present case, we introduce a third species of dislocations (denoted by i) which are surrounded by clouds of solute atoms. These are dislocations moving much slower than the mobile species, ultimately becoming immobile. The introduction of this species is reminiscent of the basic feature of Cottrell's (1953) theory, so that the model is in keeping with the essential spirit of Cottrell's theory.

Let N_g, N_s and N_i denote the densities of the g, s and i species respectively. The rate equations for these quantities are (a dot denotes the time derivative):

$$\dot{N}_g = \theta V_g N_g - \mu N_g^2 - \mu' N_g N_s + \lambda N_s - \alpha N_g, \qquad (1)$$

$$\dot{N}_s = k\mu N_g^2 - \mu' N_g N_s - \lambda N_s + \alpha' N_i, \tag{2}$$

$$\dot{N}_i = \alpha N_g - \alpha' N_i. \tag{3}$$

Here V denotes the dislocation velocity. We assume that θ, $\bar{\mu}$, μ', α, α', and λ are constants for a given stress at a given temperature. The first term in (1) corresponds to the production of dislocation by the cross glide mechanism; the second corresponds to the immobilization of two mobile dislocations and the annihilation of pairs of dislocations at a rate $(l-k)\mu$; the third corresponds to the annihilation of a mobile dislocation with an immobile one; and the last arises from solute atoms gathering around dislocations. Once a certain number of solute atoms gather around a moving dislocation, its mobility is reduced, and it becomes a type i dislocation (hence the source term αN_g in (3)). As the size of the solute atom cloud increases, the dislocation eventually becomes immobile (hence the source term $\alpha' N_i$ in (2)). The term λN_s comes from the (thermal or athermal) activation of immobile dislocations. The parameter α is expected to depend on the diffusion constant of the solute atoms, their concentration and the velocity of dislocations of type i. The parameter α' is the rate of immobilization, and hence should be expected to depend on the critical velocity (k is a parameter close to unity).

It is convenient to make equations (1)–(3) dimensionless by setting

$$x = (\mu/\lambda)N_g, \quad y = (\mu/\theta V_g)N_s, \quad z = (\mu\alpha'/\lambda\alpha)N_i. \tag{4}$$

Then

$$\mathrm{d}x/\mathrm{d}\tau = (l-a)x - bx^2 - xy + y, \tag{5}$$

$$\mathrm{d}y/\mathrm{d}\tau = b(kbx^2 - xy - y + az), \tag{6}$$

$$\mathrm{d}z/\mathrm{d}\tau = c(x-z), \tag{7}$$

where

$$\lambda = \theta V_g t, \quad a = \alpha/\theta V_g, \quad b = \lambda/\theta V_g, \quad c = \alpha'/\theta V_g. \tag{8}$$

(We have set $\mu = \mu'$ in order to reduce the number of parameters.)

2.2 *Stability analysis and existence of limit cycles*

Equations (5)–(7) form a nonlinear system. Under well-known conditions (Minorsky 1962), these admit periodic solutions called limit cycles for a certain range of values of the parameters a, b, c and k. Although the method of investigation is well known, for the sake of completeness we briefly outline the procedure used. Limit cycles are special classes of solutions which are isolated closed trajectories in the phase space (x, y, z) such that any trajectory which is sufficiently close to it either approaches it or recedes from it. Such closed trajectories can arise only in nonlinear systems. The search for limit cycles is generally preceded and aided by an investigation of the properties of the system around the steady state values x_a, y_a, and z_a. The stability of the system is decided by the nature of its singular points—node, focus, saddle point or centre. Linearising the set of equations around (x_a, y_a, z_a), one obtains an equation of the form

$$\mathrm{d}\boldsymbol{\psi}/\mathrm{d}\tau = \boldsymbol{W}\boldsymbol{\psi}, \tag{9}$$

where $\boldsymbol{\psi}$ is the column vector with components $(x-x_a)$, $(y-y_a)$, $(z-z_a)$, and $\boldsymbol{W}$ is a 3×3 matrix. A node arises when all three eigenvalues of $\boldsymbol{W}$ are of the same sign, and a saddle point when only two of these are of the same sign; a focus occurs when there are two complex conjugate eigenvalues, and a centre when one eigenvalue is identically zero and the other two are pure imaginary. (In the last case the nature of the singular point may have to be analysed more carefully; see Minorsky 1962).

An attractive limit cycle exists if there is a surface surrounding an unstable focus into which all trajectories enter: in the present case, we first look for a domain in the parameter space (a, b, c, k) when two of the eigenvalues are complex with at least one of them having a positive real part, and then show that such a surface exists (Ananthakrishna and Sahoo 1981). The only constraints that we have on the values of the parameters are $a < 1$ (which arises because the total rate of production of dislocations is positive); $k < 1$; and $a, b, c > 0$. (N_g, N_s and N_i are obviously positive).

2.3 *Staircase creep*

An analytical solution of (5)–(7) for arbitrary values of the parameters, and valid for all times, is difficult. To obtain numerical solutions, V_g must be known as a function of $N = N_i + N_s + N_g$ and $\sigma^*(N)$, where σ^* is the effective stress. For simplicity we assume V_g to be constant. Although this assumption is not physical, it can be argued that it will not alter the qualitative features of staircase creep (Ananthakrishna and Sahoo 1981). The creep curve obtained by integrating the Orowan equation is shown in figure 1. The steps on the creep curve appear only in the secondary region, which is consistent with the existing experimental results (Zagorukuyko *et al* 1977; Da Silveira and Monteiro 1979).

Our model also predicts a feature which is in agreement with experiment, namely, that there are upper and lower bounds for the asymptotic creep rates for which staircase creep occurs. These arise because the frequency of oscillation $\sim V_g \operatorname{Im} \omega_1$, where ω_1 is one of the two complex conjugate eigenvalues of $\boldsymbol{W}$. Bounds can be put on $\operatorname{Im} \omega_1$,

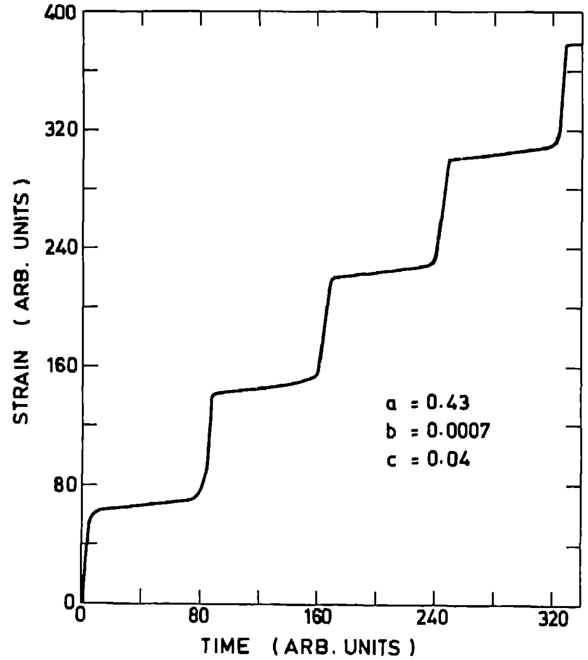

Figure 1. Staircase creep for typical values of the parameters *a*, *b* and *c*.

depending on the basic mechanism prevailing in the system. This implies corresponding bounds on V_g in order to have *observable* steps on the creep curve. This in turn implies that the phenomenon can only be observed over a finite range of $\dot{\varepsilon}$ (in practice, somewhat less than three orders of magnitude). Moreover, since V_g is temperature dependent (for a fixed stress), this phenomenon can only occur over a fixed range of temperature, as corroborated by the experimental results of Zagorukuyko *et al* (1977).

3. Approximate solutions

We outline an analytic procedure for obtaining asymptotic solutions to our equations. This is essential if one wants to relate the theoretical rate constants to accessible parameters such as the applied stress σ_a, temperature T, concentration of solute atoms C, etc. Our method follows that of Tyson (1977) for the Belousov-Zhabotinski oscillating chemical reaction. The main point is to identify a fast mode and adiabatically eliminate it to obtain a reduced set of two coupled equations from the original set of three equations (5)–(7). Approximate solutions are then obtained by using the method of relaxation oscillations (Minorsky 1962; Tyson 1977). Defining $X = x - X_a$, $Y = y - y_a$, $Z = z - z_a$, and $\tau' = b\tau$, (5)–(7) may be re-written in the form

$$b\dot{X} = -[\alpha X + \beta Y + bX^2 + XY], \tag{10}$$

$$\dot{Y} = -[\gamma X + \delta Y - bX^2 + XY - aZ], \tag{11}$$

$$\dot{Z} = \frac{c}{b}[X - Y], \tag{12}$$

where the dot now refers to differentiation with respect to τ'. Further, the constants $\alpha, \ldots, \delta$ are

$$\alpha = a + 2bx_a + y_a - 1,\ \beta = x_a - 1,\ \gamma = y_a - 2bx_a,\ \delta = x_a + 1 \tag{13}$$

(The constant α used here is distinct from that appearing in (1) of §2.) Since $b \ll a, c$, we see that $|\dot{X}| \to \infty$ as $b \to 0$ unless the right side in (10) vanishes identically. This amounts to saying that X must change with a characteristic time $\sim b$ to maintain the condition

$$\alpha X + \beta Y + bX^2 + XY = 0 \tag{14}$$

Thus X is a fast variable that can be adiabatically eliminated from (10)–(12), and the resulting pair of independent equations used for further analysis.

We use the results of stability analysis and further express α, β, γ, δ, x_a, y_a and z_a as power series in b. We then determine the 'null clines'

$$\dot{Y} = 0 \leftrightarrow Z_1 = Z(Y) = X(Y) + \frac{2}{a}[x_a + X(Y)]Y, \tag{15}$$

and

$$\dot{Z} = 0 \leftrightarrow Z_2 = X(Y), \tag{16}$$

and again express $Z(Y)$ in powers of b. To find the limit cycles, we look for the intersection of the null clines in the region of negative slope. From the expressions for the null clines Z_1 and Z_2 we obtain a reasonable idea of the phase portrait. For $a < 1/3$ and for $1/\sqrt{2} < a < 1$, the steady state is stable. For $1/3 < a < 1/\sqrt{2}$, the null clines intersect in the negative slope region, which means that a limit cycle exists. Figure 2

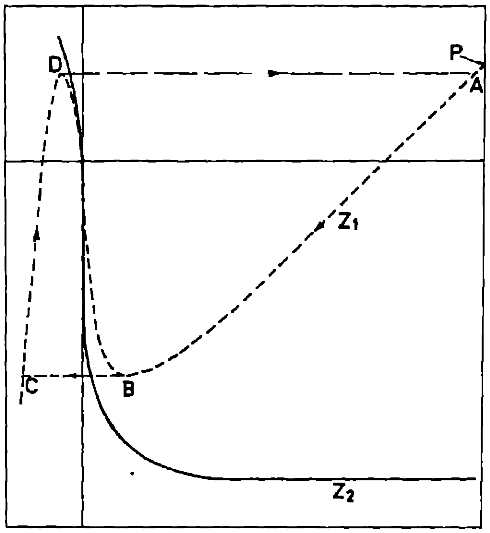

Figure 2. Phase plane portrait (the null clines Z_1 and Z_2 plotted as a function of Y) in the case $1/3 < a < 1/2$. The limit cycle is ABCDA.

shows a typical phase portrait for $1/3 < a < 1/2$. Starting from an arbitrary point, the trajectory moves along the null cline $\dot{Y} = 0$ until it reaches the turning point D, from where it almost instantaneously jumps to A. Thereafter it moves along the branch $\dot{Y} = 0$ (slowly) until it reaches the second turning point B from where it jumps to C, and the process continues. Thus the trajectory is a closed one and the limit cycle is $A \rightarrow B \rightarrow C \rightarrow D \rightarrow A$. From the expressions for Z_1 and Z_2, it is possible to calculate also the period, the amplitude and the wave form of the limit cycle solution. Finally, as already stated, we can integrate the Orowan equation to obtain the steady state creep curve which exhibits steps (Valsakumar and Ananthakrishna 1983).

Although the results of the model (in its present form) are not directly applicable to the detailed results on zinc (Zagorukuyko *et al* 1977), they still permit qualitative comparison. That the steps are seen only in the secondary creep region is obviously consistent with our theory, since the latter predicts a bifurcation from the steady state solution to a periodic one. Zagorukuyko *et al* (1977) report a rapid monotonic increase of the magnitude of the step in the strain as a function of σ_a; a weak, decreasing dependence of the period of the jump on σ_a; and a decrease of the magnitude of the jump in strain with increasing T. All these features are consistent with our work.

4. Repeated yield drop

Our model can be extended to a constant strain rate experiment by augmenting equations (1)–(3) with the machine equation representing the load sensed by the load cell, namely

$$\dot{\sigma}_a = K[\dot{\varepsilon} - b_0(N_g + \gamma N_i)V_g(\sigma^*)], \tag{17}$$

where a dot denotes the time derivative. Here $\dot{\varepsilon}$ is the imposed strain rate, K is the effective compliance, b_0 is the Burgers vector and σ^* is the effective stress. The second term on the right in (17) is the plastic strain rate $\dot{\varepsilon}_p$. We assume the power law $V_g = V_0(\sigma^*/\sigma_0)^m$, with $\sigma^* = \sigma_a - HN^{1/2}$, where H is a constant characteristic of hardening and m is a velocity exponent. Following a procedure similar to that of § 2, it can be shown that there is a domain in the space of the relevant parameters for which limit cycle solutions exist. Choosing values of the parameters in the domain of instability so as to be consistent with the expected values of the dislocation densities and the yield drops, numerical solutions of the system of equations may be obtained, and various characteristic features of the RY exhibited may be studied. These appear to be generally consistent with the experimental results. (Note that the latter are in the nature of averages over the sample dimensions.) We list these salient features: (a) There is a range of $\dot{\varepsilon}$ over which serrations are seen. (b) The model exhibits the negative strain rate behaviour of the flow stress at a fixed value of the plastic strain. The inset in figure 3 shows a typical plot of σ_a *vs* $\dot{\varepsilon}_p$, with a minimum in σ_a at a point $\dot{\varepsilon}_p = \dot{\varepsilon}_{\text{min}}$. Curves corresponding to larger ε_p are displaced successively upwards. This feature has been both theoretically (Penning 1972; van den Beukel 1975) and experimentally verified (Bodner and Rosen 1967). (c) Figure 3 shows a typical plot of serrated yielding. The serrations are asymptotically periodic. Since it is not possible to identify them (from the plot itself) as serrations of type A or type B, a strain rate change test (Wijler and van Westrum 1971) must be carried out, from which it is found that beyond $\dot{\varepsilon}_{\text{min}}$ the serrations are of type B. (d) The amplitude of the serration increases up to $\dot{\varepsilon}_{\text{min}}$ and decreases thereafter. (e) The amplitude increases and saturates as a function of ε, consistent with experiments (McCormic 1971). (f) There are upper and lower bounds on the parameter α of (1) within which serrated yielding occurs. Since α depends on the concentration of solute atoms, this implies that there is a range of the solute atom concentration in which the phenomenon occurs. (g) ε_c (the critical strain), as a function of $\dot{\varepsilon}$, first decreases and then increases (McCormic 1971). (h) Beyond the range of $\dot{\varepsilon}$ where serrated yielding occurs, the 'normal' behaviour of $\sigma_a(\varepsilon)$ is resumed.

It should be pointed out that there has so far been no attempt to derive the negative strain rate behaviour of flow stress (which is crucial for any meaningful description of the phenomenon) starting from dislocation *interactions*. In the existing theories this is either assumed (Penning 1972) or derived (van den Beukel 1975) through a phenomenological treatment of waiting times involving in any case only individual dislocations. In contrast, this property emerges naturally in the present model from a consideration of dislocation interactions.

We have shown that the new temporal order represented by serrated yielding is the consequence of a bifurcation from a temporally homogeneous steady state plastic flow

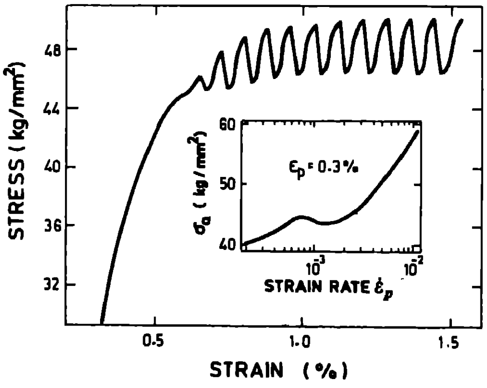

Figure 3. Calculated stress-strain curve showing repeated yielding. The inset is a graph σ_a *vs* $\dot{\varepsilon}_p$ for the same values of the parameters.

beyond some critical values of the parameters. This order is a result of a balance between the energy input (in the form of dislocation multiplication) and dissipation (annihilation, immobilisation and other processes). The phenomenon is obviously a far-from-equilibrium situation and is an example of a dissipative structure (Nicolis and Prigogine 1977).

5. Chaotic flow

We now turn to the chaotic flow exhibited by our model over a certain range of a drive parameter, the applied strain rate. (There is also some experimental evidence for such a flow, which will be discussed subsequently in brief). This adds to the growing list of models and physical situations exhibiting chaos (Ott 1981; Eckmann 1981; Lauterborn and Kramer 1981; Jefferies 1982). The model has an infinite sequence of period-doubling bifurcation eventually leading to chaos. The region over which chaos is exhibited is very small compared to the range of $\dot{\varepsilon}$ over which RY is seen (RY is considered to be periodic). We have calculated the value of the associated exponent and found it to be the same as the exponent for the quadratic map. We have also obtained the associated one-dimensional map. As the parameter of interest is the applied strain rate $\dot{\varepsilon}$, we fix the values of all the other parameters within the instability region and study the bifurcation sequence with respect to the parameter $e = \dot{\varepsilon}(\mu/\lambda V_0 b_0)$. The region where the period doubling bifurcation occurs is small, and is located near the upper end of the range of e (the dimensionless strain rate) over which RY is observed. For the chosen values of the parameters, the first bifurcation from the periodic state with period T to a state with a period $2T$ occurs at $e_1 = 159{\cdot}98444$, while the successive bifurcation to states with period 2^2T, $2^3T, \ldots$, occur at $e_2 = 173{\cdot}7178$, $e_3 = 175{\cdot}8974$, ... The exponents $\delta = \lim(e_n - e_{n-1})/(e_{n+1} - e_n)$ appears to be very close to that obtained by for the quadratic map (Grossman and Tnomae (1977), Feigenbaum (1978)). The estimated value of e_∞ is 176·4669, beyond which we find chaotic motion. Figures 4 and 5 show the variation of the stress σ_a with time (equivalently, the strain) for $e = 174{\cdot}679$ (motion with period $4T$) and $e = 178{\cdot}205$ (chaotic motion) respectively. A log-log plot of the projection of the strange attractor in the $N_g - \sigma_a$ plane is shown in figure 6. The associated one-dimensional map is shown in figure 7. Unlike the corresponding map for the Lorenz model (Ott 1981), our map has a smooth rounded maximum similar to the quadratic map except that it is very much skewed.

The fact that our model can exhibit chaotic flow has prompted us to look for experimental evidence for the plots of repeated yield drops. (Of course, the value of the parameter which controls the magnitude of the variation in σ_a, *i.e.*, the magnitude of the yield drop, has to be appropriately chosen). Even though we are constrained by the fact that the *average* stress level remains constant in our model, we have found evidence (Hall 1970) in support of such flows. Experimentally, too, this occurs towards the end of the $\dot{\varepsilon}$ range for which RY is seen. If we subtract the normally observed slow increase in the base level of the stress, there appear to be many more situations which perhaps correspond to chaos (Rosen and Bodner 1969).

6. Fluctuations during the onset of repeated yielding

We have discussed so far the possibility of a new temporal phase arising as a drive parameter (here, $\dot{\varepsilon}$) is varied. The situation corresponds to a *hard mode instability* in

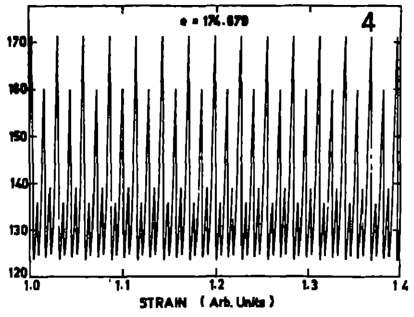

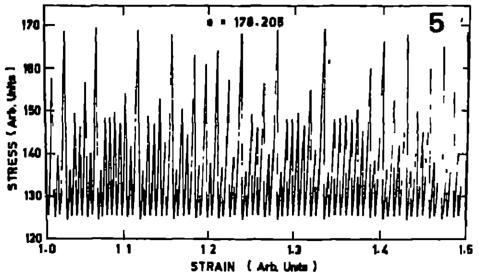

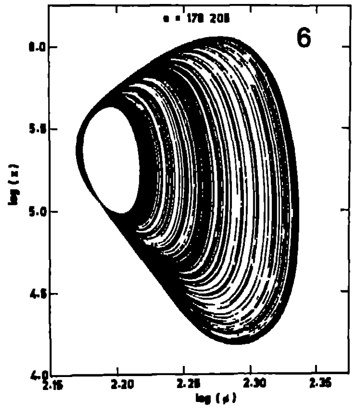

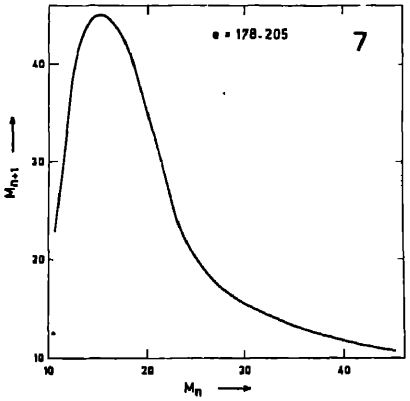

Figure 4. Stress-strain curve for $e = 174{\cdot}679$ with period 4T.

Figure 5. Stress-strain curve for $e = 178{\cdot}205$, *i.e.*, in the chaotic region.

Figure 6. A log-log plot of the projection of the strange attractor for $e = 178{\cdot}205$ in the $x-\phi$ plane. Here $x = (\mu/\lambda)\, N_g$ and $\phi = \sigma_a/\sigma_0$.

Figure 7. The one-dimensional map associated with chaotic flow in the model.

which the real part of complex conjugate modes changes sign (from negative to positive) in the frequency plane, as the drive parameter crosses its critical value. The foregoing analysis is completely deterministic. We now analyse the nature of the fluctuations when the parameter is in the neighbourhood of its critical value.

Our analysis begins with the nonlinear Langevin equations obtained by adding Gaussian white noise terms to the deterministic equations. We have used both the Monte Carlo technique and a Gaussian decoupling method (Valsakumar *et al* 1983) to study the fluctuations. (However, in the present context the second method can be applied only in the special case $H = 0$; otherwise powers of $N^{1/2}$ are present, which cannot be handled without further approximations). It is convenient to discuss the general features of the fluctuations with the help of the equivalent Fokker-Planck equation. The standard form of the Fokker-Planck equation is

$$\frac{\partial \pi}{\partial t}(\xi,t) = \frac{\partial}{\partial \xi}[(K(t)\cdot \xi\pi(\xi,t))] + \frac{1}{2}\frac{\partial^2}{\partial \xi^2}[D(t)\pi(\xi,\, t)], \tag{18}$$

where

$$K(t) = \frac{\partial C_1(y)}{\partial y},\ D(t) = C_2(y), \tag{19}$$

and

$$\frac{dy}{dt} = C_1(y) \text{ and } \xi = \varepsilon^{-1/2}[x - y]. \tag{20}$$

Here, x is the random variable, y its mean, $C_1(y)$ the first jump moment and $C_2(y)$ the second moment. (K is the regression matrix.) ε is the (system-size) expansion parameter. To identify the onset of the periodic state beyond the critical value of the drive parameter, it is convenient to use the concept of the 'irreversible circulation of fluctuation' defined by (Tomita and Tomita 1974; Tomita *et al* 1974)

$$\alpha = \tfrac{1}{2}[(K\sigma)^T - K\sigma] \tag{21}$$

where σ is the variance (T represents the transpose). K and σ are related by

$$\tfrac{1}{2}\sigma = \alpha + K\sigma + \tfrac{1}{2}D. \tag{22}$$

If a periodic state occurs as a result of the hard mode instability both α and σ diverge; the instability is incurred through α, which becomes increasingly large as the transition point is approached from below.

Our preliminary investigations reveal that as $\dot{\varepsilon} \to \dot{\varepsilon}_c$ from below, the fluctuations show an overall growth which is indicative of the divergence of the variance, in addition to exhibiting a near periodic modulation which is indicative of the approach to a periodic state. For $\dot{\varepsilon} > \dot{\varepsilon}_c$, the fluctuations have the normal characteristics expected when limit cycle solutions are supported. The details of this study will be reported elsewhere.

7. Concluding remarks

We have shown that the state of temporal order represented by steps on the creep curve or by repeated yield drops is a consequence of a bifurcation from a temporally homogeneous, steady-state plastic flow. (A similar approach has been used by Kubin *et al* (1984) for low temperature RY.) A major criticism that can be raised is that the theory does not take into account the inhomogeneous deformation that normally accompanies the phenomenon. (Although, to the best of the author's knowledge, experiments do not show which is the cause and which is the effect, *i.e.*, whether an inhomogeneous deformation is the cause and a yield drop is the effect, or *vice versa*. We believe that it is not possible to disentangle the two. Nor is there any theory that takes the inhomogeneous deformation into proper account. The closest is that of Penning (1972) in which the feature is simply assumed). However, we argue (Ananthakrishna and Valsakumar 1982) that if the space dependence is properly taken into account, the inhomogeneity of the deformation should follow automatically. The point is that such an extended model would still exhibit the negative strain rate behaviour of the flow stress (which has been assumed by Penning (1972) to show that hopping and propagating band type solutions are supported). Attempts are underway to demonstrate explicitly that such solutions indeed occur when appropriate space dependence is included.

Another possible criticism could be that the model merely 'mimics' the effects of the waiting of dislocations at obstacles which van den Beukel (1975) has used to derive $\sigma(\dot{\varepsilon}_p)$. However, this work deals with individual dislocations whereas what is observed in an actual experiment is an ensemble average over participating dislocations. Therefore, for such a theory to hold good, there must be a 'phase coherence' between the dislocations, if the effects are to manifest themselves at a gross level. Further, it is known that the negative strain rate behaviour is essential for RY. (For a detailed analysis of various tensile test conditions using the negative strain rate behaviour, see Neelakantan and Venkataraman 1983). Our analysis shows that this behaviour is a consequence of the competition between different dislocation interaction mechanisms. We have also checked (Ananthakrishna and Sahoo 1981) that the incorporation of certain other basic dislocation mechanisms (pile up, pinning and depinning of dislocations from obstacles) leads to similar results.

Finally, it should be pointed out that several materials like nylon (Schultz 1974), metallic glasses (Takayama 1979), wood, etc. are known to show RY. The present work suggests that the *mathematical mechanism in all these cases must be the emergence of limit cycle solutions which are characteristic of non-linear systems. As plastic flow is basically nonlinear, such solutions are an intrinsic possibility.* The basic microscopic physical mechanisms of course are bound to be different in different materials.

Acknowledgement

The author thanks Dr G Venkataraman for arousing his interest in this problem.

References

Ananthakrishna G and Sahoo D 1981 *J. Phys.* **D14** 2081

Ananthakrishna G and Valsakumar M C 1982 *J. Phys.* **D15** L171

Ananthakrishna G and Valsakumar M C 1983 *Phys. Lett.* **A95** 69

Ardley G W and Cottrell A H 1953 *Proc. R. Soc.* **A219** 328

Bell J F 1973 *Handbuch der Physik Band* VIa/I (Berlin: Springer-Verlag)

Bodner S R and Rosen A 1967 *J. Mech. Phys. Solids* **15** 63

Cottrell A H 1953 *Philos. Mag.* **44** 829

Da Silveira T L and Monteiro S N 1979 *Met. Trans.* **A10** 1795

Eckmann J P 1981 *Rev. Mod. Phys.* **53** 643

Feigenbaum M J 1978 *J. Stat. Phys.* **19** 25

Grossman S and Tnomae S 1977 *Z. Naturforsch.* **32a** 1353

Haken H 1978 *Synergetics* (Berlin: Springer-Verlag)

Hall E O 1970 *Yield point phenomena in metals and alloys* (Macmillan: London)

Jefferies D J 1982 *Phys. Lett.* **A90** 317

Kubin L P, Estrin Y and Spiesser Ph 1984 *Res. Mechanica* **10** 25

Lauterborn W and Kramer E 1981 *Phys. Rev. Lett.* **47** 1445

Lubahn J D and Felgar R P 1961 *Plasticity and creep of metals* (New York: John Wiley)

McCormic P G 1971 *Acta Metall.* **19** 463

McCormic P G 1972 *Acta Metall.* **20** 351

Minorsky N 1962 *Nonlinear oscillations* (New Jersey: Van Nostrand)

Navratil V, Hammersky M and Blazkova 1974 *Czech. J. Phys.* **B24** 907

Neelakantan K and Venkataraman G 1983 *Acta Met.* **31** 77

Nicolis G and Prigogine I 1977 *Self organization in non-equilibrium systems* (New York: Wiley)

Ott E 1981 *Rev. Mod. Phys.* **53** 643

Penning P 1972 *Acta Metall.* **20** 1169

Rosen A and Bodner S R 1969 *Mater. Sci. Eng.* **4** 115
Sahoo D and Ananthakrishna G 1982 *J. Phys.* **D15** 1439
Schultz J 1974 *Polymer materials science* (New Jersey: Princeton-Hall)
Stejskalova V, Hammersky M, Luckac P, Vostry P and Sprusil B 1981 *Czech J. Phys.* **B31** 195
Takayama 1979 *Scr. Met.* **13** 463
Tomita K, Ohta T and Ohta H 1974 *Prog. Theor. Phys.* **52** 1744
Tomita K and Tomita H 1974 *Prog. Theor. Phys.* **51** 1731
Tyson J J 1977 *J. Chem. Phys.* **66** 905
Valsakumar M C and Ananthakrishna G 1983 *J. Phys.* **D16** 1055
Valsakumar M C, Murthy K P N and Ananthakrishna G 1983 *J. Stat. Phys.* **30** 637
van den Beukel A 1975 *Phys. Status Solidi* **A30** 197
van den Beukel A 1980 *Acta Metall.* **20** 965
Wijler A and van Westrum S 1971 *Scr. Metall.* **5** 531
Zagarukuyko L N, Ostasky A L and Soldatov V P 1977 *Phys. Met. Metallogr.* **43** 156

Discussion

P Rodriguez: You cited some results on zinc. In your model, the Cottrell type of solute locking is envisaged. What was the solute species?

G Ananthakrishna: Zinc is a poor example (the dislocations are actually produced due to inhomogeneities at the surface).

Rodriguez: Many of the conclusions with respect to the critical strain, the magnitude of the strain burst, the delay time for the strain burst to occur, etc., follow automatically once Cottrell locking is introduced. It is therefore not surprising that the model gets these right.

Ananthakrishna: Cottrell locking is not manifest in the equations of the model.

N Kumar: You get period doubling bifurcations even though your maps are not discrete. Is this because of the higher dimensionality of the system of equations?

Ananthakrishna: One-D are the simplest of systems which exhibit chaos. Coupled system of differential equations also exhibit such a behaviour. The associated 1-D map can be obtained.

C K Majumdar: It would be interesting to examine the structure of your set of equations from the point of view of catastrophe theory.

Bull. Mater. Sci., Vol. 6, No. 4, September 1984, pp. 677–687. © Printed in India.

Mechanisms and empirical equations for deformation and some principles of alloy design

T BALAKRISHNA BHAT

Defence Metallurgical Research Laboratory, Kanchanbagh, Hyderabad 500 258, India

Abstract. Some aspects of the deformation behaviour of solids at very high, moderately high and low strain rates are discussed. In the very high strain rate region, deformation equations and the physics of the shock front are analysed to propose a route to lower energy dissipation at the shock front. In the moderately high strain rate region, alloy design principles for maximizing the deformation resistance are outlined. In the low strain rate region, an analysis of the physical basis for the power law creep equation is presented. Some physical arguments are presented as a rationale for the high stress exponents and activation energies often observed in particle-strengthened alloys. The additivity of strain rates by various mechanisms is also briefly discussed.

Keywords. Deformation mechanisms; empirical equations; dislocation dynamics; shock front; impact resistance; alloy design.

1. Introduction

The behaviour of solids under deformation depends on the operating stress level, the temperature, and many material properties such as the elastic modulus, the microstructure and the properties of the individual constituents. The behaviour is indeed complex and can be described only by semiquantitative and quasi-empirical relations. In the very high strain rate region where shock waves predominate in the flow process, the microstructure and initial temperature are relatively unimportant. The crystalline state and basic material properties such as the modulus and density are important in this region. In the lower strain rate region such as that observed in the ballistic testing of materials, the stress-strain diagrams, the glide resistances, the phonon drag and the temperature play important roles. In the low strain rate region as in creep, the operating temperature and stress are most important. A smaller but significant role is also played by the microstructure. The regimes of deformation rates and stresses of interest in the present discussion are shown in figure 1.

2. Deformation at very high pressures and strain rate

Pressure impulses injected into materials generate shock waves. At low pressures the shock front consists of purely elastic strains and the wave propagates over large distances with relatively little attenuation. A typical example of such a wave is that of sound waves generated by gentle knocks on any solid. More intense waves such as those generated during hollow charge collisions or in implosions intended for thermonuclear fusion generate high nonelastic strains at the wave-fronts. Such waves suffer large drags and tend to get dissipated. This drag is in some cases undesirable, for example in

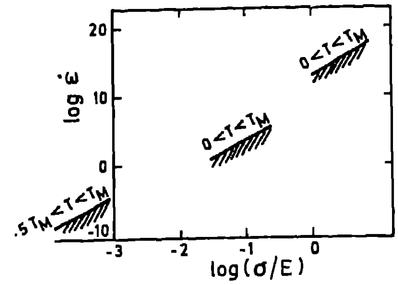

Figure 1. Stress-strain rate regimes considered in this paper.

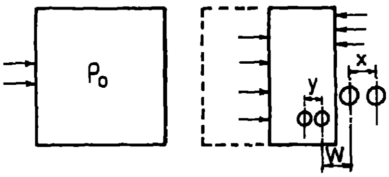

Figure 2. Schematic diagram illustrating the strain at a shock front: $\varepsilon = (x-y)/x$.

thermonuclear experiments. We may therefore analyse the drag mechanisms in terms of a specific question, namely, how to reduce the drag.

At the shock front a low density phase is transformed to a high density phase. This transition induces both bulk and shear strains at the front (Gilman 1979). Figure 2 illustrates the situation at the shock front. The strain there may be written as

$$\varepsilon = (\rho - \rho_0)/\rho_0, \tag{1}$$

where ρ_0 is the initial density and ρ is the shocked density. The power dissipated at the moving front is

$$G = B\dot{\varepsilon} = Bv_{\mathrm{sh}}/W, \tag{2}$$

where B is the drag coefficient, v_{sh} is the speed of the shock front, and W is the width of the transition region between the shocked and the unshocked state. The power dissipated at the shock front is thus controlled by the parameters B and W.

In crystalline solids the shock front moves *via* the coordinated motion of atoms. The interface between the shocked and the unshocked regions is thought to consist of a set of interface dislocations and a compressed zone (figure 3). The areal density of dislocations, ρ_{dis}, depends on the compression ratio according to

$$\rho_{\mathrm{dis}} = \frac{1}{\sqrt{2}b}[1 - (\rho_0/\rho)^{1/3}], \tag{3}$$

where b is the Burgers vector. Figure 4 is a plot of this dependence. The dislocation spacing approaches b at high compression ratios. The shear strain rate at those dislocations (which travel with the shock front) becomes $\dot{\varepsilon} = v_{\mathrm{sh}}/b$. Typical values are $v_{\mathrm{sh}} \simeq 10^7$ cm/sec and $b = 2{\cdot}5 \times 10^{-8}$ cm, so that $\dot{\varepsilon} \simeq 4 \times 10^{14}\,\mathrm{sec}^{-1}$. At such a high strain rate, even in a material as fluid as water (viscosity $\sim 10^{-2}$ poise) the drag becomes 4×10^4 kg/mm^2! Shock pulses therefore attenuate extremely rapidly. One way to reduce this drag pressure would be the use of metallic glasses which have a liquid-like structure on either side of the shock front. The intense localisation of strains arising from the smallness of the Burgers vector of the dislocations is then avoided.

3. Deformation at moderately high strain rates

At lower stress levels (the middle shaded region in figure 1), the deformation front advances at subsonic speeds. A typical example in this range of strain rates is the

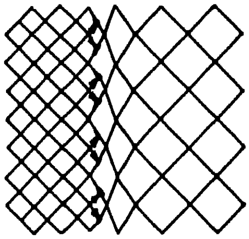

Figure 3. Schematic illustration of the interface structure at shock fronts in crystalline materials.

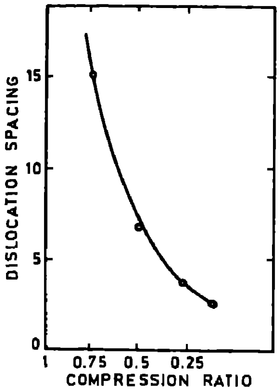

Figure 4. Variation of dislocation spacing (in units of b) at the shock front as a function of the compression ratio.

deformation armour under ballistic attack. Strain in this regime normally occurs by dislocation movement. The flow is governed by high-velocity dislocation dynamics. The equation of motion for a dislocation line is of the form (Kocks *et al* 1973)

$$M\ddot{y}+B\dot{y}=b(\sigma-\tau), \tag{4}$$

where M is the 'mass' of the dislocation, B is the viscous drag coefficient, σ is the applied stress, and τ is the lineglide resistance of the dislocation element against slow glide. Clearly, M, B and τ must be maximised for increasing the strength of the material. The 'mass' M of the dislocation can be shown to be

$$M=U/v_s^2=1/2\,b^2\rho, \tag{5}$$

where U is the line energy per unit length of the dislocation, v_s is the velocity of sound, and ρ is the material density of the material. Hence high density materials (*e.g.*, steel) and materials with large Burgers vectors (*e.g.*, intermetallics) offer greater resistance to dynamic flow. The drag coefficient B is controlled by the Peierls potential and the phonon-dislocation interaction. Dissipation of energy occurs when dislocations interact with phonons. In addition, shear-stress fluctuations due to phonons cause dislocations to flutter. Nonlinear elastic strains near dislocations also scatter phonons because of local changes of modulus and density (and hence of the speed of elastic waves). These mechanisms retard moving dislocations. Further, a moving dislocation has to build up and relax elastic strains, and this process is also retarded by the interaction with phonons. All these factors lead to a drag coefficient of the form (Kocks *et al* 1973)

$$B=k_BT/\Omega\omega, \tag{6}$$

where Ω is the atomic volume and ω is the atomic frequency. In contrast to the other mechanisms resisting flow, the drag B increases with temperature. Moreover, there is also a rapid increase of B when the speed of the dislocation $\gtrsim 0{\cdot}5\,v_s$. This is because the strain field of the dislocation begins to be compressed into smaller volumes (for lack of time!) at any given location. However, the discrete nature of the atoms and the low compressibility of atomic cores puts an upper limit to this contraction and allows 'supersonic' speeds to be reached at high stress levels, as in the shock waves discussed earlier.

Turning to the parameter τ (the line glide resistance) in (4), we observe first that this resistance normally varies with the location on the glide plane. The Peierls resistance, for instance, varies periodically with a wavelength b. Solute atoms provide small discrete obstacles. Precipitates, interphase interfaces and cell or grain boundaries provide a coarser but stronger set of obstacles. Some of these obstacles are repulsive to dislocations, some are attractive and some are energy-storing. A schematic glide-resistance diagram is shown in figure 5. The spatial variation of the effective driving force on the dislocation results in an oscillatory motion superposed on its steady state motion. This induces radiation of elastic energy from the moving dislocation into the crystal. As this energy must also be supplied by the applied stress, the hills and valleys in the glide-resistance diagram contribute to the drag. The varying effective driving force also causes rapid acceleration or deceleration of the dislocation as it moves in the glide plane. The dislocation may then be able to overcome an obstacle on its path at least in part through its inertia. Attractive obstacles are specially prone to this phenomenon, for the energy picked up in the 'downhill' motion of the dislocation can facilitate its subsequent travel 'uphill'. Similarly, many small obstacles met with after passage through a large repulsive obstacle can be overcome dynamically. It is also possible for a moving dislocation to interact with near-by dislocations and transfer energy to them. Thus, under dynamic conditions obstacles incorporated in the matrix begin to lose their individuality and efficacy and the macroscopic concepts of flow stress may no longer be valid.

The onset of this dynamic behaviour is influenced by many factors. Higher values of the viscosity and larger obstacles sizes or spacing postpone the onset to higher dislocation velocities. Larger values of M and b favour an early transition. For obstacles of width smaller than a few Burgers vectors, dynamic effects emerge when (Kocks *et al* 1973)

$$(\sigma/G) > (k_B T/\Omega G)^2, \tag{7}$$

where σ is the stress level and G is the shear modulus. A rationale for specifying low-T impact properties for armour materials is hidden in this above equation, because low temperatures bring out the dynamic effects at lower stresses and strain rates. This also suggests that the results of low-T tensile tests may correlate better with ballistic performance when the highest suitable test temperature is chosen by the onset of simultaneous decrease in strength and ductility.

Certain alloy design criteria (for good ballistic performance) also emerge from this discussion. A material that must resist flow at the strain rates, presently under

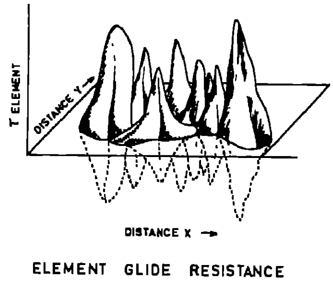

Figure 5. Schematic glide-resistance diagram in multiphase materials.

consideration, should not exhibit significant dynamic weakening. Thus, a high Peierls stress is particularly detrimental. Also undesirable are microstructures with precipitates that almost touch each other, as are attractive precipitates, even when they are strong. Long range barriers such as subgrains, martensite lath boundaries, strong and large (>2000 Å) repulsive precipitates, or repulsive-type solute elements would be the ideal candidates for the purpose at hand.

4. Deformation at low stresses and strain rate

Even at low stresses materials can deform provided the temperature is sufficiently high to permit thermal activation of certain microscopic processes. This deformation mode, called creep, has been extensively studied over the years and a variety of equations, mechanisms and explanations have been proposed by various workers.

One particular widely-used semi-empirical equation is the 'power law', according to which the creep rate $\dot{\varepsilon}$ can be expressed as the product of a (small) power of the stress and an exponential function of T:

$$\dot{\varepsilon} = A(Gb/KT)\,(\sigma/G)^n D_0 \exp(-Q/RT). \tag{8}$$

Here A is a constant, D_0 is the preexponential in the diffusion coefficient, R is the gas constant and Q is the activation energy for diffusion. This equation has been shown to work for simple metals and ionic solids (Bird *et al* 1969). Nevertheless, many difficulties and unexplained modes of behaviour persist. The magnitude of the creep rate predicted by (8) is often incorrect (Evans and Knowles 1981). The index n lies anywhere between 1 and 6 and sometimes can be as high as 40 (Benjamin and Cairns 1971). The observed activation energy for creep often deviates significantly from that for diffusion, and in addition varies with T and σ (Poirier 1978). Moreover, even if there is a correlation between the activation volumes for self-diffusion and creep, one cannot unequivocally conclude that the creep is diffusion-controlled, because it can be shown that any process that depends on the pressure through the modulus will also have the same activation volume (Beyeler 1969). In spite of the large literature extant on the subject, a generally-agreed upon theory is lacking as yet.

4.1 *The stress exponents and the creep deformation mechanisms*

The index n is unity for viscous flow in solids, as in fluids. This is a characteristic of microscopically homogeneous or structureless flow. Diffusional flow as in polycrystalline materials at elevated temperatures also exhibits a linear stress dependence. Basically, the applied stress serves only to generate higher point defect concentrations on grain boundaries under tensile stress relative to boundaries under no stress. The concentrations are exponential functions of $(\sigma\Omega/k_B T)$ which approximate to linear functions of σ at low stress levels (Nabarro 1948; Coble 1963).

Several anomalies exist in the dislocation creep region. Stocker and Ashby (1973) have used a heuristic statistical analysis to prove that $n = 3$ is the most probable value for dislocation creep. A simple way to see this is as follows: The dislocation density $\propto \sigma^2$, while the dislocation velocity $\propto \sigma$, in a viscous flow picture. Orowan's equation then directly leads to $\dot{\varepsilon} \propto \sigma^3$. The same conclusion can also be reached if we treat the creep as being controlled by the coarsening of dislocation networks (Evans and Knowles 1981).

Dislocation creep that is controlled by recovery processes generally has a larger stress exponent. One such process is the mutual annihilation of dislocations with opposite Burgers vectors (or their segments) when they meet each other. If ρ_+ and ρ_- denote the densities of dislocations with Burgers vectors of opposite signs, the annihilation can be considered as a second order reaction with a rate given by $\dot{\rho} = K_1 v \rho_+ \rho_-$ where ρ is the total dislocation density and K_1 is a reaction constant. The rate of reaction, and hence of recovery, is evidently greater the higher the dislocation velocity. The strain rate associated with the recovery can be written as $\dot{\varepsilon} = \dot{\rho} b s$ where s is the average distance travelled by a dislocation before annihilation. Substituting a quadratic dependence of the dislocation density on σ and a linear dependence of v on σ, we get

$$\dot{\varepsilon} \sim \sigma^4. \tag{9}$$

This recovery strain rate leads to a proportional but larger glide strain rate, which is the observed strain rate. Thus, recovery-controlled creep is expected to have a stress exponent equal to four.

One may be tempted to combine such power laws into a general functional form

$$\dot{\varepsilon} = \sum_n a_n (\sigma/G)^n, \tag{10}$$

where the a_n are independent of σ, a particular mechanism being associated with each distinct n value. Equation (10) implies that the control of the creep rate shifts to the mechanisms corresponding to higher n values with increasing stress. Often, however, this is not the case. One plausible conclusion from this is that the index n has no specific connection with any mechanism. Alternatively, one may invoke a back stress concept, such that the effective stress for creep is given by

$$\sigma_{\text{eff}} = \sigma - \sigma_b = \sigma - f_n(\sigma),$$

where σ is the applied stress and the function f_n depends on the specific mechanism concerned. The back stress can be considered as a measure of the energy spent on athermal steps that are essential for creep but do not directly lead to any significant creep strain. A specific illustration of the use of back stress concept is in the creep behaviour of particle-strengthened systems. Unusually large n values are often observed in both diffusional creep and dislocation creep regions (Benjamin and Cairns 1971). Recently, we have shown how the anomalous stress exponents in TD Nichrome and Mar M·200 superalloys fall in line with that for nickel once the back stress arising from strong dislocation-particle interactions is taken into account (Balakrishna Bhat and Arunachalam 1980; Balakrishna Bhat 1981). When the particles are attractive, the back stress appears as a threshold stress; when they are repulsive, the back stress increases with applied stress, reaching a limiting value as shown in figure 6. The back stress for diffusion creep is believed to be associated with the interaction of grain boundary dislocations with particles at the grain boundaries. It must be mentioned that the term 'back stress' has also been used in several different contexts. For example, it has been identified with the internal stress which includes the average stress field of the dislocation structure together with the cell boundaries (Pahutova and Cadek 1973; Argon *et al* 1981). In reality, the power law discussed earlier is the result of the interaction of defects among themselves and with the background stress field; the average stress field of the other defects is therefore already taken into account, and it is incorrect to include it once again in the back stress.

4.2 *Activation energy for deformation*

4.2a *Activation energy and the bulk modulus*: The activation energy can be considered as the work a solid under load has to perform on itself in temporarily expanding against its own bulk modulus to accommodate the moving unit of flow. Figure 7 is a plot of $Q/[\Omega(1-P_f)]$ *vs* the bulk modulus for various metals. (P_f is the packing factor for the crystal). The approximately linear fit is noteworthy. It is interesting to note also that the activation energy is the energy that gets stored in the empty space $\Omega(1-P_f)$ as the solid momentarily dilates or contracts!

4.2b *Activation energy for dislocation creep and the creep mechanism*: A power law for creep presupposes that the activation energy for creep is equal to that for diffusion. However, the observed value of the activation energy is not constant. It increases with T

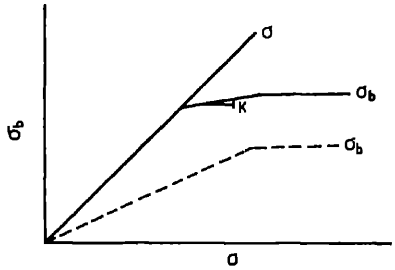

Figure 6. Schematic variation of back stress σ_b with applied stress σ in particle-strengthened alloy systems.

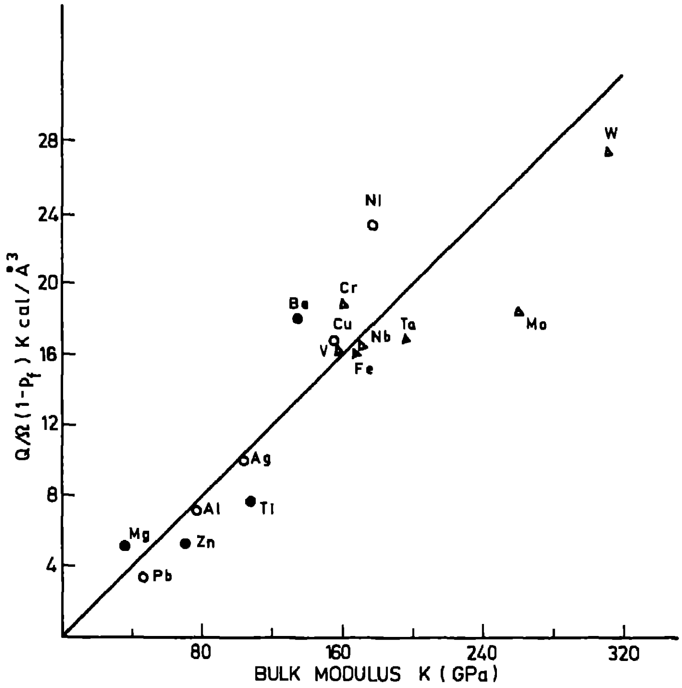

Figure 7. Dependence of $Q/[\Omega(1-P_f)]$ on bulk modulus for metals.

to match the activation energy for diffusion only in some small range of homologous temperature which, moreover, is different for each material (Poirier 1978). In particle-strengthened systems anomalously high and variable activation energies have often been reported.

It has often been suggested that the variation of the elastic modulus with temperature should account for the anomaly (Shewfelt and Brown 1974). However, this is not very convincing. Consider a force-displacement diagram between the atoms in a crystal as shown in figure 8. The elastic modulus reflects the rate of energy storage for infinitesimal displacements from the equilibrium value whereas the activation energy reflects the energy needed for a displacement equal to a lattice parameter which is more like the *area* under the curve. The inadequacy of the effect of T on E as a measure of its effect on Q is obvious.

The apparent activation energy for creep in particle-strengthened systems also depends on the back stress and its variation with temperature. This contribution to the apparent activation energy is given by (Balakrishna Bhat 1981)

$$\Delta Q = [nRT^2/(\sigma - \sigma_b)]\,[\partial \sigma_b/\partial T]. \tag{11}$$

For diffusion creep with low n and σ_b, the contribution is relatively small. For dislocation creep with large n and σ_b (as in TD nichrome), the contribution can be large. Further, σ_b varies an order of magnitude more rapidly with T than is predicted by the variation of the elastic modulus alone. The reason for this difference is not clear at the moment. Perhaps, with increasing T dislocation climb increases exponentially, facilitating the selection of easier flow paths by a sampling of the field of glide resistance along all three axes. The effective glide resistance (which one may call the 'volume glide resistance') or the back stress for creep will be different from the 'plane glide resistance' derived for a planar distribution of obstacles and a largely in-plane overcoming of obstacles by the dislocations. During creep, dislocations accumulate in difficult-to-glide locations and direct the other dislocations to climb over to easier regions of flow. When once climb has become possible, the back stress changes only slowly with temperature (figure 9).

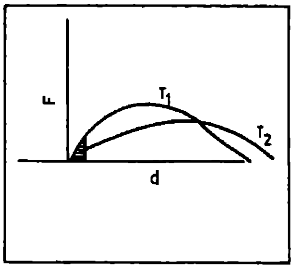

Figure 8. Atomic force-displacement diagram for two different temperatures.

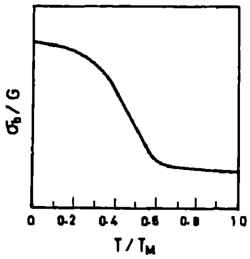

Figure 9. Temperature dependence of the back stress in particle-strengthened alloys.

A consequence of the volume-sampling hypothesis is that high n and high Q are not necessarily coupled. Even at high temperatures, σ_b in ODS alloys can be relatively large, giving a large effective n. The volume-sampling process reaches saturation above a particular temperature and the back stress then drops slowly with further increase of T. The apparent activation energy would then be small in spite of a large n value. Indeed, the results of Benjamin and Cairns (1971) on ODS alloys show a modulus-compensated activation energy close to that for self-diffusion in spite of a high apparent stress exponent of 32·8 at $T = 1350$°C. At a lower temperature, a lower n value is obtained, but Q is still twice the activation energy for self-diffusion. Another consequence of volume-sampling is that there will be no influence of particle shape on the T-dependence of σ_b for a random distribution of obstacles, since the T-dependence arises primarily from the climb-controlled volume-sampling of weaker regions from the same random distribution of obstacles, and not from climb around individual particles. This observation is substantiated by the experiments of Shewfelt and Brown (1974). It would be of interest to perform a computer simulation of this volume-sampling glide process during the creep of particle-strengthened systems, in order to optimize the particle size and distribution for effective resistance to creep flow.

5. Additivity of creep rates

An unsolved problem in creep relates to the additivity of creep rates through various mechanisms. The expansion of (10) presupposes such additivity. All theoretical treatments to date have also made this assumption. However, the basic physical processes involved cast a doubt on the validity of this assumption.

Consider for instance diffusion creep and grain boundary sliding. Diffusion creep elongates the grains; when added over all the grains, this leads to directional elongation. However, grain sliding events as in superplastic flow introduce new directions for diffusional creep, with the net result of eliminating diffusion creep on the average.

Then again, dislocation creep pre-empts diffusion creep by consuming vacancies en route as they move from one grain boundary to the other. Dislocation creep also generates ledges on grain boundaries and hinders both diffusion creep and grain boundary sliding. On the other hand, diffusion creep tends to retard the onset of grain boundary sliding by generating nonequiaxed grains. It also retards dislocation creep by not allowing large stress concentrations to build up at the grain boundaries. Thus, each mechanism appears to possess an intrinsic inhibiting effect on the others, which may explain why one obtains well-delineated deformation mechanisms in creep experiments. The opposite can also happen in some cases. For example, dislocation glide and climb favour each other. Dislocation activity at the grain boundary zone can enhance grain boundary diffusivity and hence superplastic strain rates. Computer simulation of the deformation process should be of help in understanding these coupled processes.

6. Summary

Our discussion above may be summarized in the form of the following specific questions:

(a) Will metallic glasses exhibit low damping of shock waves? (b) Can low temperature tensile and compressive tests be used to design alloys for good ballistic performance?

(c) Will attractive precipitates prove inferior to repulsive precipitates in the context of ballistic resistance? (d) Can the Arrhenius term in the creep rate be rewritten as a combination of the bulk modulus, the atomic volume and the packing factor? (e) Is the back stress concept relevant, and is it correct to subtract internal stresses due to defects which move to cause strain? (f) Can a microstructure suitable for optimal creep resistance be designed using the concept of volume glide resistance? (g) Can the strain rates arising from different mechanisms be considered to be additive, even though some of them appear to be mutually inhibiting?

Acknowledgements

The author acknowledges many useful and inspiring discussions with Dr V S Arunachalam and Prof. K Srinivasa Raghavan during the course of this work. He is also grateful to Dr P Rama Rao for inspiring him to write this article. The curves in figure 9 are a result of discussions with Shri A K Gogia.

References

Argon A S, Print F and Moffatt W C 1981 in *Creep and fracture of engineering materials and structures* Proc. Int. Conf., Swansea, U.K.
Balakrishna Bhat T and Arunachalam V S 1980 *J. Mat. Sci.* **15** 1614
Balakrishna Bhat T 1981 *Effect of second phase on microstructural development and engineering properties* Ph.D. Thesis, Indian Institute of Technology, Madras
Balakrishna Bhat T 1983 *Principles for protection* Trans. I.I.M. (to be published)
Benjamin J S and Cairns R L 1971 in *Modern developments in powder metallurgy* (ed) H Hausner (New York: Plenum) **5** 47
Beyeler M 1969 Report CEAR 3715
Bird J E, Mukherjee A K and Dorn J E 1969 in *Quantitative relations between properties and microstructure* (eds) D G Brandon and A Rosen, (Jerusalem: Israel University Press) p 255
Coble R L 1963 *J. Appl. Phys.* **34** 1679
Evans H E and Knowles G 1981 in *Creep and fracture of engineering materials and structure* Proc. Int. Conf. at Swansea, U.K. (eds) B Wilshire and D R Owen J. p 169
Gilman J J 1979 *J. Appl. Phys.* **50** 4059
Kocks U F, Argon A S and Ashby M F 1973 *Thermodynamics and kinetics of slip* (Illinois: Argonne National Laboratory)
Malu M and Tien J K 1975 *Scr. Met.* **9** 1117
Nabarro F R N 1948 Report of a Conference on the strength of solids 1963 The Physical Society, London 1.
Pahutova M and Cadek 1973 *J. Mater. Sci. Eng.* **11** 151
Poirier J P 1978 *Acta Metall.* **26** 629
Shewfelt A S W and Brown L M 1974 *Philos. Mag.* **30** 1125
Stocker R L and Ashby M F 1973 *Scr. Met.* **7** 115

Discussion

K A Padmanabhan: Your statement that dislocations could move as fast as the shock front does not appear to tally with the detailed analysis of J D Eshelby on dynamical effects on dislocations. Moreover, as in special relativity, the mass of a dislocation increases with its velocity. Incidentally, Dr Chidambaram's observation that the density of dislocations at the shock wave front is $\sim 10^{11}$ cm^2 also indicates that the total strain arises from a larger *number* of dislocations rather than a few moving at extremely high speeds.

N Kumar: In his book, Frank describes what led him to the theory of the Frank-Read mechanism: the realization that the velocity of a dislocation could never exceed the velocity of sound.

Bhat: When the width and amplitude of the incident impulse are large, shock waves travelling at speeds higher than the speed of sound develop. The strain gradients at the front have to be established in the short duration of the passage of the front, so that the strain rate becomes high. This strain rate can be achieved by either or both the terms in the classical equation $\dot{\varepsilon} = \rho b v + \dot{\rho} b s$ where the symbols are as explained in the text. Clearly, movement of the dislocations is required, v being associated with ρ and s with $\dot{\rho}$. If quasistatic dislocations alone account for the shock front, the shocked stress state would acquire permanence in the material. When shock waves can travel faster than the speed of sound, dislocations too can do the same. Physically both share the same important characteristics—strains and strain gradients in their vicinity.

S N Bandhopadhyay: The basic equations of plasticity like those for the velocity field, strain field, localized modes of deformation etc., do not appear to be taken care of properly in the finite element modelling of deformation.

Bhat: I think that the finite element method specialises in taking care of localized modes of deformation *without* sacrificing the basic equations of plasticity.

K A Padmanabhan: Did you measure the back stress in your experiment by either the stress reduction or stress relaxation method? Otherwise you are just introducing an adjustable variable.

Bhat: The existence of the back stress has not been experimentally established, and it cannot be measured directly. It is felt only by the dislocation that is moving in a structure. Even though the back stress is an adjustable empirical variable it has a certain consistency associated with it. When we introduce this parameter in order to bring the stress exponents to normal values, the anomalous activation energies in such materials automatically come down to normal values for diffusion. This certainly suggests that back stress is a parameter that has some fundamental significance associated with it.

V Balakrishnan: Regarding the computer simulation results on deformation, if you begin with empty spaces between grains, should you not expect further cavitation to occur? Or do you have hydrostatic stress, and the cavities just get filled in?

Bhat: We apply hydrostatic or uniaxial compressive loading in order to simulate hot pressing conditions.

V Balakrishnan: Within a single grain or element, what sort of compatibility conditions do you put in to ensure that no holes are formed?

Bhat: Strain compatibility conditions are put in to ensure that any particular mode has a unique displacement. Regarding your observations on the additivity *vs* interdependency of various creep mechanisms, another interesting example is provided by grain boundary sliding and diffusion creep. Grain boundary sliding occurs via the climb as well as glide of dislocations at the boundary. Climb generates vacancies which can in turn lead to vacancy creep.

Bull. Mater. Sci., Vol. 6, No. 4, September 1984, pp. 689–698. © Printed in India.

Superplasticity

K SRINIVASA RAGHAVAN

Department of Metallurgical Engineering and Department of Physics, Indian Institute of Technology, Madras 600 036, India

Abstract. Superplasticity is the phenomenon of extraordinary ductility exhibited by some alloys with extremely fine grain size, when deformed at elevated temperatures and in certain ranges of strain rate. To put the phenomenology on a proper basis, careful mechanical tests are necessary. These are divided into (i) primary creep tests, (ii) steady state deformation tests, and (iii) instability and fracture tests, all of which lead to identification of macroscopic parameters. At the same time, microstructural observations establish those characteristics that are prerequisites for superplastic behaviour. Among the macroscopic characteristics to be explained by any theory is a proper form of the equation for the strain rate as a function of stress, grain size and temperature. It is commonly observed that the relationship between stress and strain rate at any temperature is a continuous one that has three distinct regions. The second region covers superplastic behaviour, and therefore receives maximum attention. Any satisfactory theory must also arrive at the dependence of the superplastic behaviour on the various microstructural characteristics. Theories presented so far for microstructural characteristics may be divided into two classes: (i) those that attempt to describe the macroscopic behaviour, and (ii) those that give atomic mechanisms for the processes leading to observable parameters. The former sometimes incorporate micromechanisms. The latter are broadly divided into those making use of dislocation creep, diffusional flow, grain boundary deformation and multimechanisms. The theories agree on the correct values of several parameters, but in matters that are of vital importance such as interphase grain boundary sliding or dislocation activity, there is violent disagreement. The various models are outlined bringing out their merits and faults. Work that must be done in the future is indicated.

Keywords. Superplasticity; ductility; stress and strain rate; grain boundary; dislocation creep; diffusional flow.

1. Introduction

Structural superplasticity is a high-homologous-temperature phenomenon exhibited by some metals and alloys which suffer extended or anomalous ductility under restricted circumstances. Elongations amounting to a few thousands per cent have been reported. When the conditions of deformation are changed, the same material does not possess the same ductility, and this has led to serious inquiries into the fundamental reasons for this behaviour. The technological off-shoot of this research, *viz.*, the development of many commercial alloys as well as forming processes, has not lagged behind. The aim of this paper is to summarize the observations made on superplastic materials and to identify their characteristics, to list the most important mechanisms identified as responsible for this behaviour, and to outline the more important models/theories presented so far. For recent reviews, see Edington *et al* (1976), Gifkins (1982), Hazzledine and Newbury (1976) and Padmanabhan and Davies (1980). Some points of controversy, which needs to be eliminated, are indicated.

2. Observations

The first systematic study on low-melting eutectics displaying superplasticity (Pearson 1934) is by now familiar. Observations on superplastic materials may be divided broadly into two classes: (i) those involving macroscopic aspects, from mechanical deformation studies; and (ii) those involving microscopic aspects, from microstructural observations.

2.1 *Macroscopic observations*

The variables are stress, strain, strain rate and temperature. However, a curve as shown in figure 1 is most common, showing the relationship between the flow stress σ and the strain rate $\dot{\varepsilon}$. This relationship can be mathematically written as

$$\sigma = A\dot{\varepsilon}^m, \tag{1}$$

where A is a constant and m is the strain rate sensitivity index (on a log-log plot, the slope of the curve). Three regions can be recognized which may conveniently be labelled I, II and III. Region II is the one of interest, where superplasticity is displayed. The peak values of m in this region coincide with maximum elongation, indicating a direct, if not linear, relation between them. In the superplastic region, m has values from 0·3 to 0·9. It may be mentioned here that all the three regions of figure 1 may not be found with a single experimental set-up.

The steady state strain rate in region II may be expressed in the familiar form of a diffusion-controlled process according to

$$\dot{\varepsilon} \propto \frac{Gb}{k_B T}(b/d)^p\ (\sigma/G)^n\ \mathrm{D}_0 \exp(-Q/RT), \tag{2}$$

where G is the shear modulus, b is the magnitude of the Burgers vector, and d the grain size. D_0 and Q denote a pre-factor and activation energy, respectively, while p and n are indices to be determined. Alternative equations to describe the behaviour of $\dot{\varepsilon}$ are also available in the literature. Their relative merits will be discussed in a later section.

The (thermal) activation energy in (2) may be determined by three different methods (Langdon 1982): (i) changing the temperature very rapidly during a test on a single

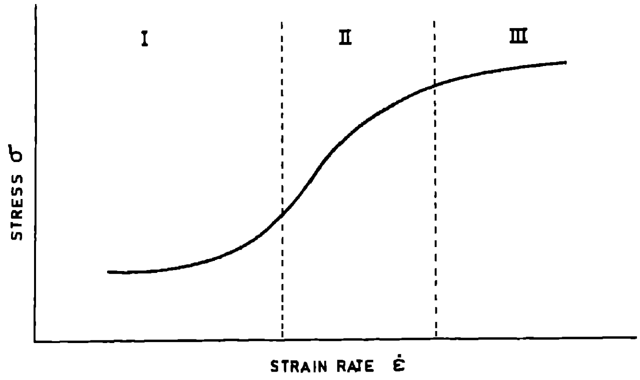

Figure 1. Flow stress plotted against strain rate.

specimen at constant stress; one finds

$$Q = \frac{R \ln (\dot{\varepsilon}_2 G_2^{n-1} T_2)(\dot{\varepsilon}_1 G_1^{n-1} T_1)}{[(T_2 - T_1)/(T_1 T_2)]}, \tag{3}$$

where $\dot{\varepsilon}_1$ and $\dot{\varepsilon}_2$ are the strain rates before and after the increase in temperature, and G_1 and G_2 the values of the shear modulus at the respective temperatures. (ii, iii) data from different specimens tested to steady state flow yield either

$$Q_\sigma = -R\left(\frac{\partial \ln \dot{\varepsilon} G^{n-1} T}{\partial (1/T)}\right)_{d,\sigma}, \tag{4}$$

or, in another version,

$$Q_{\dot{\varepsilon}} = R\left(\frac{\partial \ln (\sigma^n / G^{n-1} T}{\partial (1/T)}\right)_{d,\varepsilon}. \tag{5}$$

We shall assume the equality of these two versions. Typical values of Q for the three regions suggest an activation energy for self-diffusion, Q_{SD}, in region I, an activation energy for grain boundary diffusion in region II, and an activation energy equal to or lower than Q_{SD} in region III.

The different activation energy values led to the belief that several mechanisms were operative. It must be noted here that $m (= 1/n)$ varies with strain rate at different temperatures. The index m itself can be measured in several ways (Edington *et al* 1976). With the experimental values of n and Q, the grain size index p can be obtained by plotting $\dot{\varepsilon}$ *vs* the grain size at constant stress and temperature. A p value between 2 and 3 is typical of a number of superplastic materials in region II.

2.2 *Metallographic observations*

The microstructural study of superplastic materials includes surface observation through optical microscopy, replica electron microscopy and scanning electron microscopy, and internal structure determination through transmission electron microscopy. On a few specimens, fracture and cavitation have also been studied. Of great importance is the relative contribution of grain boundary sliding to the total strain. Microstructural observations made on specimens undergoing superplastic deformation show that: (i) there is no massive recrystallisation, (ii) there is grain rotation (both ways), (iii) a new surface is created, (iv) texture is generally reduced: (a) texture weakens continuously with strain; (b) texture weakens to a steady distinct lower level; (c) texture generally weakens, while retaining some components. (In some cases, new texture is introduced). (v) there is little dislocation activity, (vi) there is deformation near grain boundaries, (vii) grain boundary sliding takes place, (viii) there is diffusional flow in region I.

It is clear that any model proposed to explain superplastic behaviour must satisfactorily account for these observations. It must also lead to the proper constitutive equations to give the activation energy, strain rate sensitivity index and the grain size index. The general conclusions that may be drawn from the results of metallographic observations are listed in the next section.

3. Characteristics of superplastic materials

From the various observations made, the following general conclusions may be drawn (Sherby and Ruano 1982): (i) The superplastic material must have a fine grain size ($\leqslant 10\ \mu$m), which must remain so, (ii) the presence of a second phase is necessary to inhibit grain growth, (iii) the mechanical strength of the second phase must generally be of the same order as that of the matrix, (iv) the second phase, if harder, should be finely distributed within the matrix, (v) the grain boundaries between the matrix grains should be of the high angle kind, (vi) the grain boundaries should be mobile so as to reduce stress concentration at triple points, (vii) the grains should be equiaxed in order to enable a grain boundary to experience a shear stress, allowing grain boundary sliding to occur, (viii) the grain boundaries must resist tensile separation.

4. The role of grains

Noting that superplasticity is confined to materials with fine grains which remain fine-grained and equiaxed, one can conclude that the grain centres must move as if the material were deforming homogeneously (Hazzledine and Newbury 1976). Thus it is necessary that the grains slide past one another during deformation. Sherby and Ruano (1982) have considered two phenomenological equations

$$\dot{\varepsilon} = 10^9 \frac{D_{\mathrm{GB}} b}{d^3} (\sigma/E)^2 \tag{6}$$

when grain boundary diffusion is thought to be the rate-controlling step, and

$$\dot{\varepsilon} = 10^8 \frac{D_{\mathrm{latt}}}{d^2} (\sigma/E)^2, \tag{7}$$

when lattice diffusion is considered to be the rate-controlling step. Experimentally a plot of $(\dot{\varepsilon} d^3 / b D_{\mathrm{GB}})$ *vs* (σ/E) gives the correct exponent, namely, 2. Grain boundary sliding is therefore conceded to be the dominant mechanism.

Grain boundary sliding has been sought to be explained as brought about either by the motion of dislocations or by diffusion. In the dislocation model, crystal dislocations gliding to a grain boundary confine their subsequent motion to its vicinity. Special grain boundary dislocations whose Burgers vector is different and is related to a particular boundary may also move conservatively with the grain boundary. In this model, the strain-rate sensitivity m could be manipulated to be less than one, but then the grains would have to be elongated, which is not observed. On the other hand, the diffusion model considers the easy sliding of grains on smooth portions. If further sliding is opposed by irregularities, the rate of sliding is controlled by the movement or elimination of irregularities by diffusion. Such sliding could take place also at interphase boundaries. (These are classical notions and have been questioned by Padmanabhan and Davies 1980). However, since the strain rate is directly proportional to the applied stress, m will have a value of 1, which is at variance with experimental values. It would therefore appear that changes in the grain shape must also be taken into account.

4.1 *Grain strain*

Since structural continuity must be preserved, the grains must undergo some strain. This can be thought of in two different ways. Vacancy diffusion in the bulk can result in a change of shape, when the path of diffusion is fully across the grain. This Herring-Nabarro creep is given by the expression

$$\dot{\varepsilon} = (20\,D_{\text{latt}}\Omega)/(k_B T d^2), \tag{8}$$

where Ω is the atomic volume. When the diffusion path is confined to the grain boundary region, one has Coble creep, given by

$$\dot{\varepsilon} = 50\,D_{\text{GB}}\Omega\delta/(k_B T d^3). \tag{9}$$

Here δ is the width of the diffusion path. It may be noted that in both the above expressions, $m = 1$.

On the other hand, matter can be moved by conservative and non-conservative motion of dislocations. Nabarro (1967) has given two expressions, the first being a power dependence $\dot{\varepsilon} \propto \sigma^3$; the second for pipe-diffusion along the cores of dislocations, leads to $\dot{\varepsilon} \propto \sigma^5$. It may be mentioned that the grain size does not figure in these expressions. Friedel creep envisages a pile-up of dislocations against a grain boundary, from which the leading dislocation climbs into the grain boundary. The process is controlled by the climb rate of dislocations. This has been utilized to yield a relation $\dot{\varepsilon} \propto \sigma^2$. However, it is clear that grain elongation is unavoidable, and that as the grains elongate, the process must be exhausted. There is nothing in this picture to indicate the rotation of the grains. Moreover, no dislocation pile-ups have been observed in superplastic alloys.

4.2 *Interaction between grain strain and grain boundary sliding*

It is commonly believed that neither of the above can take place without the other, as they must together produce strain rates compatible with one another. The amount of strain produced by grain sliding is usually measured by surface markers, even though there is considerable controversy about the measurement. However experimentally the value $(\varepsilon_{\text{GBS}}/\varepsilon_{\text{tot}})$ varies between wide limits. It may be pointed out here that such measurements have been made at a strain of about 0·2, which is not typical of superplastic deformation. Stevens (1971) puts an upper limit of 0·62 to this ratio. Hazzledine and Newbury (1976) point out that at any instant the strain *rate* due to sliding is of the same order as the *rate* of strain of the grain.

Nevertheless, the idea has persisted that the strain due to grain boundary sliding must necessarily be less than the total strain. Consequently, an overwhelming majority of the mechanisms suggested invoke some process or the other to accommodate grain boundary sliding. It is against this background that different mechanisms are outlined in the next section. It is instructive to reproduce the figure from Edward and Ashby (1979) illustrating the different accommodation processes (figure 2).

5. Atomic mechanisms for superplasticity

It has been pointed out earlier that mechanisms employing diffusion creep or slip are unable to account for many of the observations satisfactorily, in particular for the large

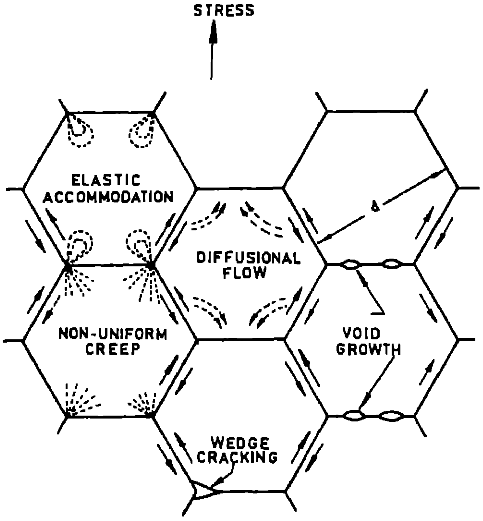

Figure 2. Consequences of grain boundary sliding (After Edward and Ashby 1974).

amount of grain boundary sliding. In this section, some more mechanisms will be listed where grain boundary sliding (GBS) is considered along with some accommodating processes.

5.1 *GBS accommodated by dislocation motion*

Ball and Hutchison (1968) put forward the idea that several groups of grains slide at once. When there is an unfavourably oriented grain, a stress concentration results which can be relieved by dislocation motion. The dislocations, which are necessarily in a pile-up, prevent further sliding until the lead dislocation climbs. Mukherjee (1971) contended that the grains move individually. Again a pile-up is invoked because dislocations are produced by irregularities in the grain boundaries. This itself is a major difficulty since, as mentioned earlier, no pile-ups have been seen. Moreover, the same dislocation motion will be rate controlling in region III too, and it would be impossible to distinguish between the two.

5.2 *GBS and diffusion creep*

Ashby and Verral (1973) proposed a grain switching event as central to their model. A group of four grains reacts to a tensile stress, sliding past each other and changing their shape to maintain continuity. These switching events occur randomly throughout the specimen with various clusters in different stages of the process. The accommodation strain is accounted for by bulk and boundary diffusion. While the model, which considers the topological aspects of the sliding process, satisfactorily explains most of the observations, there are large variations in the predicted values of parameters.

Hazzledine and Newbury (1976) have used the concept of grain emergence: as a group of adjacent grains slide, a grain from the layer below emerges at a location where a fissure would otherwise open up. Grain boundary migration occurs at the same time to restore the dihedral angles, resulting in the rounding off of the emergent grain and the curvature of all other grain boundaries. Having conceded that the phenomenon is too complicated for analysis, Hazzledine and Newbury proceed to give a viscoelastic model of superplasticity with several dashpot elements representing Nabarro, Coble and Friedel creep, as well as grain boundary and interphase sliding. The general conclusion is that a single comprehensive mechanism is not possible.

5.3 *GBS and core-mantle theory*

Gifkins (1976) proposed for each grain a non-deforming core surrounded by a mantle in which flow occurs. While the core contains statistically stored dislocations, the mantle, which is a few per cent of the grain diameter, contains geometrically necessary dislocations. The grain boundary dislocations piled-up against a triple edge are responsible by their movement for grain boundary sliding. The stress concentration of the pile-up is regarded as that of a freely slipping crack. By climb and glide the lead dislocations accommodate grain boundary sliding. Gifkins arrived at an appropriate equation to account for the observed parameters. Since the widths of the core and mantle are adjustable parameters, the experimental verification has been criticised as "an exercise in curve fitting". Further, no single mechanism has been identified as responsible for superplasticity.

Arieli and Mukherjee (1980) have also criticised this model on the ground that the deformation will slow down in time and eventually come to a stop, since many dislocations will be lost by annihilation. Also the stress concentration has been calculated by the Eshelby, Frank and Nabarro method, which does not apply to climb or any other deformation process.

Arieli and Mukherjee themselves employed a modified mantle behaviour. The small number of pre-existing dislocations are attracted to the boundary under the action of the applied stress and their own line-tension. The individual dislocations climb the short distance to the boundary and, in the process, create new dislocations by the Bardeen-Herring mechanism. At the boundary, the dislocations are annihilated. The eventual stress concentration created by the dislocations climbing into the boundary are relaxed by grain boundary diffusion. It may be noted here that there has been no experimental evidence for the Bardeen-Herring mechanism.

5.4 *Micromultiplicity*

As the grain boundary network has alternate sets of shear paths, the deformation continues even if grain boundary sliding is obstructed locally. In other words, the local stress conditions would alternatively enhance or decrease the importance of the obstacles. A number of processes, mentioned above, could be appropriately combined to give the total strain rate. It is obvious that this is also merely a curve-fitting exercise since the arbitrary constants of the constitutive equations can be adjusted appropriately.

5.5 *Unaccommodated GBS*

There has been considerable controversy as to whether grain boundary sliding is independent of diffusional strain. The work of Raj and Ashby (1972), Speight (1975) and Beere (1976) has shown that specimen strain can only develop when both sliding and diffusion can operate simultaneously. Therefore the deformation can be attributed to either sliding or diffusion, and can be described as diffusion-accommodated sliding or sliding-accommodated diffusion; in no sense can they contribute independently (Burton 1977).

Accordingly, Padmanabhan (1977) regards the upper limit of 60–65 % placed on the contribution from sliding to be a consequence of the assumption that both diffusion and sliding are present as separate steps. It is also held that the ideas concerning sliding in coarse-grained materials were not necessarily relevant to sliding in ultrafine-grained alloys, and that superplastic deformation is a result of pure grain boundary sliding of non-deformation grains that require no accommodation. Starting from the fundamental rate equation one arrives at a constitute equation

$$\dot{\varepsilon} = C\frac{\delta}{d^2}\sigma^n \exp(-Q_0/RT), \tag{10}$$

where C is a constant and δ is the jump distance in the grain boundary region. The stress exponent n may be recognized as the inverse of the strain-rate sensitivity index, m, and is shown to be a function of stress, grain size and temperature. Excellent agreement with experimental results is achieved, as is a demonstration of the transition to the region III in which climb-controlled motion of dislocations occurs.

6. The activation energy for superplasticity

The activation energy Q has been introduced in (2). It was mentioned there that different values are obtained for Q in the three regions of figure 1. This is done by treating the sigmoidal curve as a combination of three linear curves. The assumption of the equality of Q_σ and $Q_{\dot{\varepsilon}}$ ((4) and (5)) has also been mentioned. Padmanabhan (1981) has objected to the procedure on the grounds that (2) is empirical, that for each range a constant but different n value is assumed, and that within each range the activation energy is assumed to be independent of the temperature and the stress level of its evaluation. He has pointed out that the evaluation of the activation energy from an equation that has no physical basis is bound to lead to erroneous results, and that since n is continuously variable, there is no justification for treating this as a constant. At the junctions of region II with regions I and III the n value becomes ambiguous. Topologically and microstructurally regions I and II are not different. Only region III indicates a change of mechanism. Another serious objection is the treatment of an expression containing a T-dependent pre-factor as a true Arrhenius form. Padmanabhan (1981) has derived expressions for Q_σ and $Q_{\dot{\varepsilon}}$ (the values corresponding to the shear mode) and has pointed out that the best estimates of the real activation energy are only attained when data pertaining to the range in which m is large ($\sim$ 1) are used. It is regrettable that many of the leading workers in the field have not recognized the force of these arguments.

7. The role of dislocations in superplasticity

Even though many of the models invoke dislocations to explain superplasticity, there has been no direct experimental evidence to support dislocation activity. However, Edington *et al* (1976) have argued, taking Nicholson's (1972) experiments as an example, that dislocations might have been active or that they might have been obstructed by precipitates. Padmanabhan (1980) has argued that this was unlikely. He has further held that any dislocation seen was the residue of the initial configuration or the existence of local stress concentrations or a favourable strain rate at which dislocation motion commences. *In situ* experiments have also failed to reveal substantial quantities of dislocation.

Melton and Edington (1973) have maintained that since (i) statistically significant differences in the angular distance of the dislocations from their nearest possible glide planes were found as a function of the deformation rate; (ii) the Burgers vector distribution changed as a function of strain rate; (iii) increasing the initial density by cold working prior to superplastic deformation did not produce any detectable differences in the Burgers vectors and densities after superplastic deformation; (iv) there is an equilibrium dislocation density typical of superplastic flow and (v) dislocations are also observed at strain rates an order of magnitude less than that corresponding to $m_{\max}$, one must conclude that crystallographic slip plays a small but significant role in superplasticity. Padmanabhan (1980) has countered these arguments by citing experimental results accepted by Melton and Edington themselves. It therefore appears that the available experimental evidence could support either point of view. Lücke (1974) has pointed out that any sequence of deformation processes leading to a given strain tensor will give the same texture. Hence the operating mechanisms cannot be deduced solely from texture results. TEM has provided no evidence for dislocation activity.

8. Future work

To set at rest the controversy regarding the mechanism of superplasticity, work is required along the lines indicated below: (i) a better understanding of the structure of grain boundaries and interphase boundaries, (ii) a correct analytical form for the flow stress as a function of strain rate, temperature and grain size, (iii) unequivocal experimental evidence to support or discount dislocation activity, (iv) an understanding of the role of the stacking fault energy, (v) an unambiguous interpretation of experimental curves such as the double sigmoidal plot of figure 1.

It is to be hoped that there will be a happier conclusion to superplasticity than in the case of work hardening, in which field the workers have apparently agreed not to agree.

Acknowledgements

The author is indebted to Prof. K A Padmanabhan of IIT, Madras for many valuable clarifications.

References

Arieli A and Mukherjee A K 1980 *Mater. Sci. Eng.* **45** 61
Ashby M F and Verral R A 1973 *Acta Metal.* **21** 149
Ball A and Hutchison M M 1968 *Met. Sci. J.* **3** 1
Beere W B 1976 *Met. Sci. J.* **10** 133
Burton B 1977 *Diffusional creep in polycrystalline materials* (Ohio: Trans Tech Publications)

Edington J W, Melton K N and Cutler C P 1976 *Prog. Mater. Sci.* (eds) B Chalmers, J W Christian and T B Massalski (Oxford: Pergamon Press) Vol. 21 p. 61

Edward G and Ashby M F 1979 *Acta Metal.* **27** 1505

Gifkins R C 1976 *Met. Trans.* **A7** 1225

Gifkins R C 1982 in *Superplastic forming of structural alloys* (eds) N E Paton and C H Hamilton, The Metallurgical Society of AIME 3–26

Hazzledine P M and Newbury D E 1976 in *Grain boundary structure and properties* (eds) G A Chadwick and D A Smith (New York: Academic Press) Chap. 7

Langdon T E 1982 in *Superplastic forming of structural alloys* (eds) N E Patson and C H Hamilton, The Metallurgical Society of AIME 27–40

Lücke K 1974 *Can. Metall. Q.* **13** 261

Melton K N and Edington J W 1973 *Met. Sci. J.* **7** 172

Mukherjee A K 1980 *Mater. Sci. Eng.* **8** 83

Nabarro F R N 1967 *Philos. Mag.* **16** 231

Nicholson R B 1972 in *Electron microscopy and structure of materials* (ed) G Thomas (University of California) 682

Padmanabhan K A 1977 *Mater. Sci. Eng.* **29** 1

Padmanabhan K A 1980 *Met. Sci.* **14** 506

Padmanabhan K A and Davies G J 1980 *Superplasticity* (Berlin: Springer Verlag)

Padmanabhan K A 1981 *J. Mater. Sci. Lett.* **16** 531

Pearson C E 1934 *J. Inst. Met.* **54** 111

Raj R and Ashby M F 1972 *Met. Trans.* **3** 1937

Sherby O D and Ruano O A 1982 in *Superplasticity forming of structural alloys* (eds) C E Paton and C H Hamilton, The Metallurgical Society of AIME 241–256

Speight M V 1975 *Acta Metall.* **23** 779

Stevens R N 1971 *Philos. Mag.* **23** 265

Bull. Mater. Sci., Vol. 6, No. 4, September 1984, pp. 699–700. © Printed in India.

Grain boundary-dislocation interactions*

S RANGANATHAN

Department of Metallurgy, Indian Institute of Science, Bangalore 560012, India

Abstract. Our current understanding of the structure of grain boundaries will be described first. The structure of low angle boundaries can be rigorously described in terms of arrays of dislocations. The structure of high angle boundaries continues to defy a complete and rigorous description. A model has been developed based on coincidence site lattices. This model postulates the presence of grain boundary dislocations even at high angles of misorientation to accommodate the deviation from exact coincidence conditions. The Burgers vectors of such grain boundary dislocations can be found by the translation vectors of the DSC lattice. An interesting point is that the Burgers vectors are not lattice translations. Hence the dislocations are confined to the surface of the boundary and cannot move into the grain. Alternative descriptions of the structure of grain boundaries make appeal to the Bernal type of polyhedral voids that occur in metallic glasses. A brief discussion of the strength of this approach will be outlined. Dislocations at grain boundaries can affect both grain boundary migration and sliding. The possible mechanisms for these phenomena will be described. The importance of understanding these mechanisms to explain deformation of metals at high temperatures will be stressed.

Discussion

M Youssuff: Is it possible to include vacancies in the approach you have described?

S Ranganathan: This is an important question; the answer is not known.

P Rodriguez: How do you explain migration with the help of imprisoned grain boundary dislocations?

Ranganathan: It is easy to explain this migration in a framework similar to Aronson's theory of the growth of precipitates. For example, in cases where the ledge mechanism operates, the ledges move along the plane in which the precipitate is growing.

Rodriguez: If we provide energy in the form of stress, is it possible that the smaller grain boundary dislocations combine to form larger mobile lattice dislocations?

Ranganathan: It should be possible, but no clear evidence is available.

S Ray: Can only certain lattice vectors be split into DSC vectors?

Ranganathan: Any lattice vector can be broken into DSC vectors, since the DSC lattice consists of both the lattice positions.

Ray: Are ledges inherited from the energetics of growth? Are these a common feature?

Ranganathan: They need not be inherited from the growth. Yes, they are a reasonably common feature.

---

* Only a summary is presented.

S Ramaseshan: Why is a polycrystalline material stronger than a real single crystal?

Ranganathan: In a polycrystalline material, the dislocations are stopped at the grain boundaries, thereby impeding their movement.

Ramaseshan: In the Bernal picture, could a polycrystalline material be considered as a composite of grains and grain boundaries?

Ranganathan: One could think of the polycrystalline material as a two phase material—the grain boundaries and the grains. The idea, though found in the literature, has no validity. We have to consider the boundary as a whole.

T V Ramakrishnan: Is there any evidence for the existence of dislocations and their movement?

Ranganathan: We can actually see dislocations by etch, pit techniques, field-ion microscopy, electron microscopy, etc.! There is no doubt about the movement of the boundary of a bicrystal when it is loaded in the form of a cantilever.

G Srinivasan: Should not the energetics contain all sorts of things, including contributions from the electrons?

Ranganathan: I am tempted to agree with this since all existing theories seem to be succeeding only up to a point. There seems to be something basic that is missing.

Srinivasan: Could the unique microscopic properties shown by a metallic glass (*e.g.*, the electronic properties and ductility) be translated to a microscopic description of grain boundary sliding?

Ranganathan: One would indeed like to do that. However we are rather ignorant about both these areas and hence not much progress has been made.

Srinivasan: Is this analogy being used only with reference to structure?

Ranganathan: Right now, for the structure and the geometry.

K R Rao: As the dislocation structure can change owing to a variety of factors, it appears that the structure of the specimen is really transient—how does one ensure reproducible conditions in this sense?

Ranganathan: The underlying structures are not as transient as appears at first sight, but careful investigation of this point is certainly in order.

A P Pathak: Is there a study of the variation of the strength with respect to the orientation of the boundaries?

Ranganathan: I think this has been done for bicrystals, but not for polycrystals.

Bull. Mater. Sci., Vol. 6, No. 4, September 1984, p. 701. © Printed in India.

Instabilities in first order phase transitions*

S BANERJEE

Metallurgy Programme, Bhabha Atomic Research Centre, Bombay 400085, India

Abstract. Majority of the metallurgical phase transformations are first-order transitions which occur by the nucleation and growth process near equilibrium conditions. In recent years, homogeneous transformation has been reported in some of these cases at conditions significantly away from those of equilibrium. In this paper some of these transformations will be discussed. In the first part of the presentation the thermodynamic and the mechanistic distinctions between first and higher order phase transformations will be discussed and a comparison made between homogeneous and heterogeneous modes of phase transformations and those of deformation. Based on Landau's free energy *vs* generalised order parameter plots, an instability temperature is defined for first order phase transformations below which the transformation can occur by a continuous amplification of a concentration or a strain fluctuation. In the second part experimental evidence in support of the continuous mode of transformations in two ordering reactions are presented. These are: (i) a transition from the short range to the long range chemical order in Ni_4Mo (D1a structure) and (ii) a hybrid displacive-replacive ordering in Zr_2Al ($B8_2$ structure). In order to make the continuous mode operative in these first order transformations (which is possible at a high "supercooling"), radiation in the former and rapid quenching in the latter were employed. In the last part, the martensitic transformation and the shape memory effect is described in terms of Landau's plots and the mechanical and thermodynamical consequences of the model are discussed.

Discussion

M Youssuff: What is the criterion by which we can distinguish whether the development of long-range order is by nucleation and growth or by a continuous mechanism?

S Banerjee: The only criterion is whether we are below T_0 or not. Also, not all ordering can be described in terms of compositional modulations.

V K Wadhawan: What is order parameter in Ni_4Mo?

Banerjee: The population density of Mo atoms on a given lattice site.

V C Sahni: Is there any example where there is a formation volume and the transformation is homogeneous?

Banerjee: It is possible that the volume change is very small like in Ni_4Mo.

Sahni: How is the expansion of free energy in terms of the order parameter justified in a first order phase transition (since the OPM is discontinuous)?

Banerjee: It cannot be justified.

---

* Only a summary is presented.

Bull. Mater. Sci., Vol. 6, No. 4, September 1984, pp. 703–716. © Printed in India.

Deformation and martensitic transformation

V SEETHARAMAN

Metallurgy Programme, Reactor Research Centre, Kalpakkam 603 102, India

Abstract. The influence of applied stresses and imposed plastic deformation on the martensitic transformation of a parent phase is described. Changes in mechanical properties such as flow stress, work hardening rate, fracture toughness, etc brought about by strain-induced martensitic transformation are briefly examined. In the absence of appreciable dislocation glide, atomic displacements associated with glissile boundaries are highly ordered and reversible modes of (plastic or nonlinear pseudoelastic) deformation. Such processes lead to large strains and are encountered in deformation twinning, martensitic transformations and in the reorientation of martensite units. The reversibility leads to phenomena such as elastic twinning, thermoelastic martensites, superelasticity, shape memory and two-way shape memory effects, and rubber-like behaviour. These are discussed using a unified approach based on thermoelastic equilibrium. The shape memory effect suggests several potential applications of the martensitic transformations in non-ferrous alloys in which the effect is most commonly observed. Recent developments in this area are reviewed with special reference to the prerequisites for the effect and the influence of metallurgical processing on the extent of shape recovery.

Keywords. Plastic deformation; pseudoelasticity; shape memory effect; martensitic transformation.

1. Introduction

A martensitic transformation is a first-order solid-state structural transformation that is diffusionless, involves relative atomic motion by amounts smaller than the interatomic spacing, and exhibits a lattice correspondence between the parent and product structures. The transformation is generally adiabatic, athermal and exhibits hysteresis. It proceeds by a shear mechanism, and the net macroscopic distortion of the crystal can be regarded as an invariant plane strain. This implies that the interface between the parent phase and the growing martensite crystal is a plane of zero average macroscopic distortion. This feature has been verified in several experiments on the surface relief effect produced by the transformation. According to the phenomenological theories proposed by Wechsler *et al* (1953) and by Bowles and Mackenzie (1954) it is possible to consider the invariant plane strain as a superposition of the following components: a lattice strain (Bain strain), a lattice-invariant shear, a rotation and a dilation. The lattice-invariant shear required can manifest itself as slip, twinning or faulting of the martensite units. Besides, the different variants of martensite units formed from a parent phase crystal are generally arranged as three dimensional self-accommodating groups such that the total macroscopic strains are minimised.

Martensitic transformations can be induced by the application of external stress or by lowering the temperature. The former possibility arises because the free enthalpies of the parent phase and the martensite, and their equilibria, depend not only on the temperature and the composition but also on the stress; moreover, the nucleation and growth processes are associated with shear strains and these couple to the internally or externally applied stresses. This paper deals with the relationship between martensitic transformations and deformation (both recoverable and nonrecoverable). We first consider the thermodynamic and kinetic aspects of stress-assisted and strain-induced martensitic transformations. This is followed by an account of an experimental study of the influence of plastic deformation at cryogenic temperatures on the martensitic transformation in an austenitic stainless steel. Next, we deal with the phenomenon of transformation-induced plasticity and its applications. Finally, a series of related phenomena including thermoelasticity, pseudoelasticity and the shape memory effect are discussed from a unified point of view based on the reversibility of the deformation caused by the migration of glissile interfaces.

2. Stress-assisted and strain-induced martensitic transformations

The driving force for the spontaneous martensitic transformation is the difference ΔG^c in the chemical free energy between the parent and the martensite phases. It is known that the transformation does not set in at the equilibrium temperature T_0 ($\Delta G^c(T = T_0) = 0$). Instead, it requires substantial undercooling, and commences at a temperature $M_s < T_0$. If the parent phase is stressed at a temperature T ($T_0 > T > M_s$), a mechanical driving force, U, is added to the chemical driving force; stress-assisted martensitic transformation occurs at T if

$$|\Delta G^c(T)| + U \geqslant |\Delta G^c(M_c)|. \tag{1}$$

U is a function of the stress and the orientation of the martensite crystal with respect to the parent phase. Patel and Cohen (1953) have shown that

$$U = \tau\gamma_0 + \sigma\varepsilon_0, \tag{2}$$

where τ is the shear stress resolved along the transformation shear direction on the habit plane, γ_0 is the transformation shear strain, σ is the dilatational stress resolved normal to the habit plane, and ε_0 is the normal component of the transformation strain. If a single crystal of the parent phase is stressed according to the geometry shown in

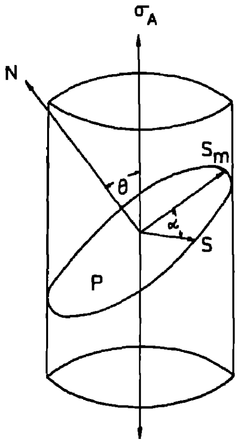

Figure 1. Geometry of stressing in a single crystal. P is the habit plane having N as its normal. S is the shear direction and S_m is the maximum shear direction of the applied stress on the habit plane. (The other symbols are explained in the text).

figure 1, τ and σ can be expressed for any given orientation of the martensite plate as

$$\left.\begin{aligned} \tau &= 0{\cdot}5\,\sigma_A \ \sin 2\theta \cos\alpha \\ \sigma &= \pm 0{\cdot}5\,\sigma_A (1+\cos 2\theta) \end{aligned}\right\} \tag{3}$$

where σ_A is the absolute value of the applied stress, θ is the angle between the axis of the applied stress and the normal to the habit plane, and α is the angle between the shear direction of the transformation and the maximum shear direction of the applied stress on the habit plane (the sign of σ specifies whether the stress is tensile or compressive). If the chemical driving force (ΔG^c) decreases linearly with an increase in temperature above M_s, it is logical to expect that the critical applied stress for martensite formation should increase linearly with temperature. In practice, it is observed that the critical stress shows a linear dependence only between M_s and M_s^σ (figure 2). Beyond M_s^σ the stress required would exceed the flow stress of the parent phase and thus cause plastic deformation of this phase. Olson and Cohen (1972) have postulated that in the temperature range $M_s^\sigma < T < M_d$ the nucleation of martensite is aided by the large number of defects caused by the plastic deformation, and hence the transformation is considered to be strain-induced (M_d is the highest temperature at which the

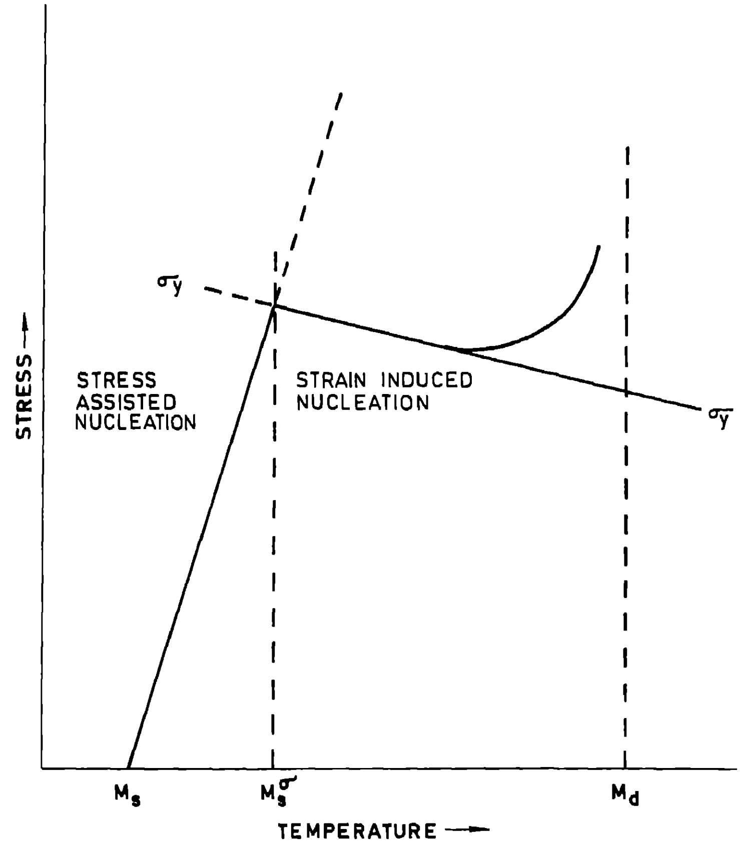

Figure 2. Variation of the critical stress required for the onset of the transformation at different temperatures. (The regimes of stress-assisted and strain induced transformation are indicated.)

transformation can be induced; $M_d < T_0$). There is thus a fundamental difference between stress-assisted and strain induced transformations.

The volume fraction f of the martensite formed at any given level of plastic strain ε_p is given by (Olson and Cohen 1975; Murr *et al* 1982)

$$f = 1 - \exp\{-\beta[1 - \exp(-\alpha\varepsilon_p)]^n\} \tag{4}$$

where α, β and n are temperature dependent parameters. Recently, Tamura (1982) has suggested that the transformation kinetics should be based on the stress rather than the strain, and has proposed a different expression for f that depends on σ_A, γ_0 and ε_0. The role of plastic deformation in the strain-induced nucleation of martensite has been a subject of controversy. Olson and Cohen (1972, 1976) firmly believe that the intersection of slip bands produced as a result of plastic deformation acts as a nucleation site for martensite. In contrast, Suzuki *et al* (1977) and Onodera and Tamura (1979) have expressed the view that the local stress concentration near the grain boundaries due to the pile-up of dislocations would raise the applied stress to values obtained by the extrapolation of the straight line in figure 2 well beyond M_s^σ.

3. Strain-induced martensitic transformation in a type 316 austenitic stainless steel

Type 316 austenitic stainless steel does not transform to martensite spontaneously even when it is cooled down to 77 K. In contrast, plastic deformation at low temperatures leads to the formation of two different types of martensites: ε martensite with an hcp structure and α martensite with a bcc structure. Figure 3 illustrates the variations in the volume fractions of these phases with plastic strain at 77 K. The main conclusions that can be drawn from this plot are: (i) With increasing plastic strain, the amount of ε phase present increases to a maximum and then decreases gradually, (ii) Detectable amounts of the α phase are formed only beyond a certain minimum value of the plastic strain, beyond which its volume fraction increases continuously with the plastic strain. These results imply that the α martensite forms at the expense of the ε martensite.

Plastic deformation of the austenite (γ) at temperatures below 220 K leads to the progressive formation of wide stacking faults, clusters of overlapping stacking faults, and finally, thin sheets the ε martensite. Transmission electron microscopy of the deformed samples reveals a large number of shear bands on $\{111\}_\gamma$ planes. These bands

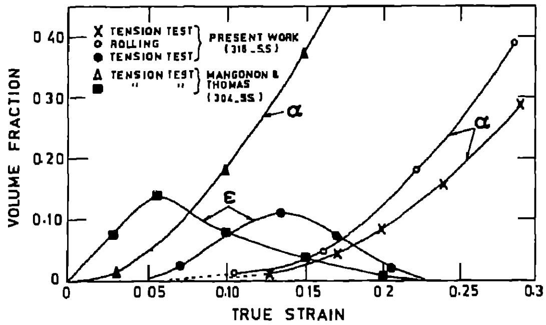

Figure 3. Variation of the volume fraction of the ε and α martensites in a type 316 stainless steel as a function of the true strain at 77 K. The results of Mangonon and Thomas (1970) in a type 304 stainless steel are shown for comparison.

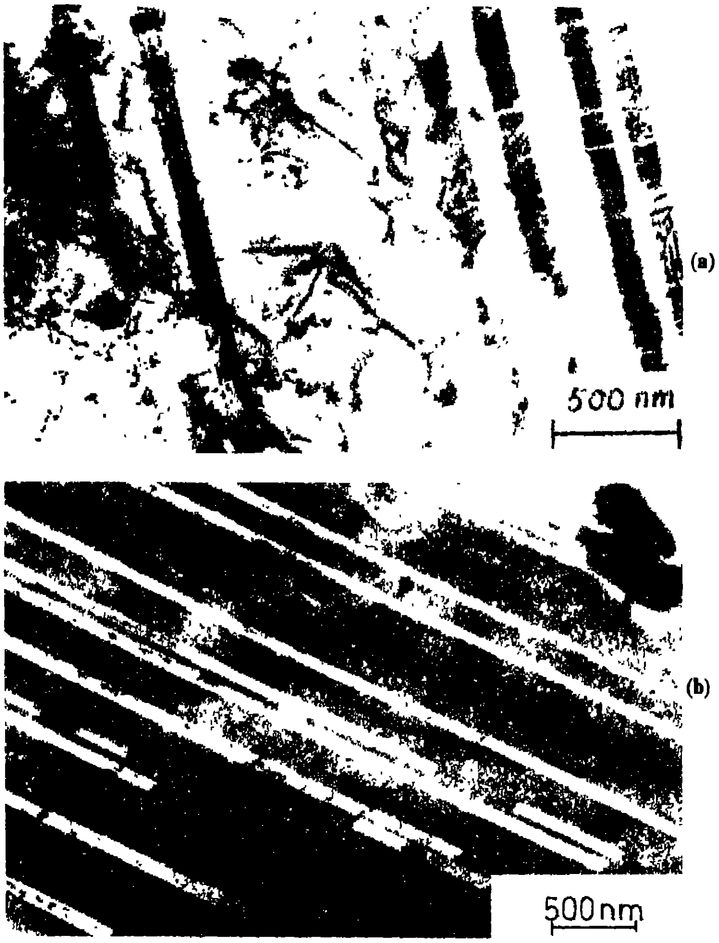

Figure 4. Transmission electron micrographs of type 316 stainless steel deformed at 77 K up to 5 % strain. (**a**) wide stacking faults forming on the $\{111\}_\gamma$ planes, (**b**) dark field micrograph showing one of the variants of the deformation bands.

consist of overlapping faults, deformation twins and the ε martensite, the relative proportions of which vary with the temperature, strain rate and the extent of deformation. Typical examples of the microstructure obtained after tensile deformation at 77 K up to 5 % strain are shown in figure 4. When the austenite is subjected to strains larger than 15 % at 77 K, tiny crystals of α are observed at the intersections of two different variants of the shear bands. On continuing the deformation, the α nuclei grow along the cylinderical axes of the rod-shaped volumes comprising the intersections of these bands. The above experimental evidence obtained by x-ray diffraction and electron microscopy techniques proves conclusively that the ε martensite forms as an intermediate phase in the $\gamma \rightarrow \alpha$ transformation, the sequence being representable as $\gamma \rightarrow \varepsilon \rightarrow \alpha$ (Seetharaman 1976; Seetharaman and Krishnan 1981).

4. Transformation-induced plasticity (TRIP)

As already mentioned, martensitic transformation can be considered as a mode of plastic deformation of the parent phase that competes with other modes such as slip and twinning. Therefore, if martensite forms dynamically during the mechanical testing of any alloy, the mechanical properties of the alloy would inevitably be altered considerably. Figure 5 shows the stress-strain curves of the Fe-29 Ni-0·26 C austenitic alloy deformed in tension at different temperatures (Tamura *et al* 1970a). The values of M_s and M_d for this alloy are 213 K and 298 K, respectively. The large serrations observed in the curves at 223 K and 203 K are due to the formation of stress-assisted martensite. On the other hand, the curves corresponding to 243 K or 263 K exhibit very fine serrations and also substantial tensile elongation: the samples corresponding to these curves show evidence of the presence of strain-induced martensite. Such an enhancement in the ductility of an alloy owing to the onset of strain-induced martensitic transformation is known as 'transformation-induced plasticity (TRIP).

The tensile properties of three different austenitic steels in the temperature range $M_s^\sigma < T < M_d$ are shown in figure 6 (Tamura *et al* 1970b). The inverse temperature dependence of the 0·2 % proof stress observed between M_s^σ and M_s (figure 6a) is due to the transformation strain caused by the stress-assisted martensite formed before the yielding of the parent austenite phase. The total elongation exhibits a maximum at temperatures just above M_s^σ. Such an enhancement in elongation has been attributed to the suppression of the necking phenomenon. This, in turn, is due to the increase in the work-hardening rate caused by the strain-induced martensitic transformation. Similar increases in the work-hardening rates have also been encountered in austenitic stainless steels (Angel 1954; Ludwigson and Berger 1969; Seetharaman 1976). The hardness of the martensite increases with increase in the carbon content of the steel. It follows that, for a given volume fraction of martensite, the increase in the work-hardening rates will be high for high carbon steels. Thus the TRIP phenomenon will be dominant in austenitic steels containing high levels of carbon.

Although ductility can be enhanced markedly by TRIP, strengthening must be achieved by other methods. Zackay *et al* (1967) developed an ultra-high-strength steel called TRIP steel in which the ductility is enhanced by the TRIP of the retained austenite

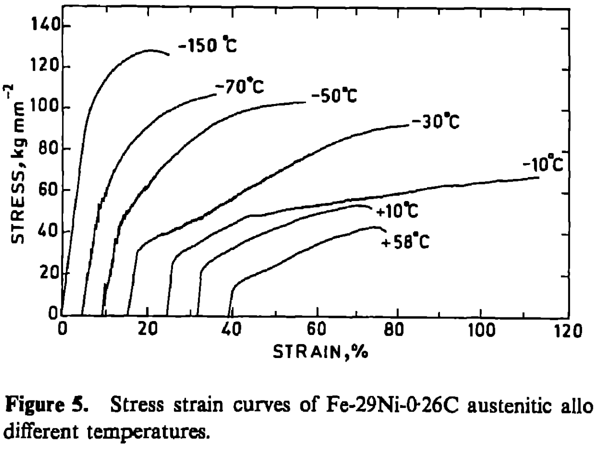

Figure 5. Stress strain curves of Fe-29Ni-0·26C austenitic alloy deformed in tension at different temperatures.

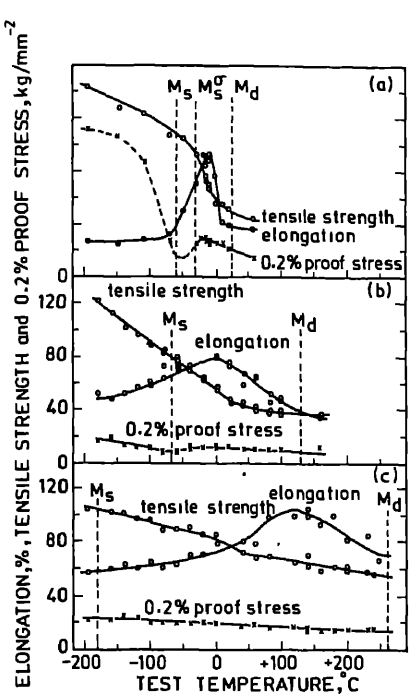

Figure 6. Effect of test temperature on tensile properties in three different types of metastable austenitic steels (a) Fe-29Ni-0·26C, (b) Fe-19-Cr-11Ni, (c) Fe-24Mn-0·26C.

while the strength is increased by the ausformed martensite. TRIP steels exhibit good properties at low temperatures because of the retained austenite, and are therefore suitable structural materials for chemical plants, containers for liquified gases, armour plates and earthquake dampers. Furthermore, the TRIP phenomenon is very effective in improving the formability, particularly the deep drawability, of austenitic stainless steels (Divers 1964).

5. Thermoelasticity, pseudoelasticity and shape memory effect

The thermodynamics of the growth of the martensite plate can be represented by the following energy balance:

$$G_T^c + U \lesseqgtr \tau_0\gamma_0 + \sigma_0\varepsilon_0 + S_M A + \xi\gamma_0, \qquad (5)$$

where τ_0 is the intrinsic shear resistance of the parent phase against the shear strain γ_0, σ_0 is the intrinsic tensile resistance of the parent phase against ε_0, S_M is the specific surface energy of the parent-martensite interface, A is the shape factor of the martensite, and is a dissipation factor. Let us exclude the trivial case of the stoppage of a growing plate by a grain boundary or some equivalent obstacle. Then an equality in (5) implies that any small change in the thermal or mechanical components of the driving force will cause growth or shrinkage of the martensite plate. This equilibrium condition forms the basis of the thermoelastic martensitic transformation. A thermoelastic martensite forms and grows continuously as the temperature is lowered, and shrinks and vanishes as the temperature is raised. Figure 7(a) gives a schematic representation of this transformation indicating the increase in the internal stress σ_i and the volume fraction f of the martensite, these being measures of the progress of the transformation.

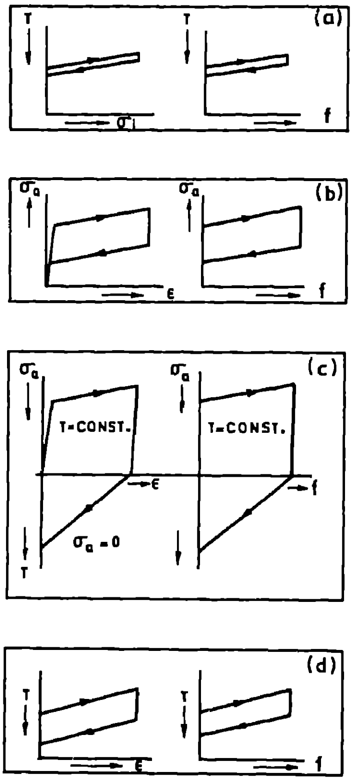

Figure 7. Schematic representation of (a) thermoelasticity (b) pseudoelasticity (c) shape memory effect and (d) two-way shape memory effect.

There is no sudden appearance or disappearance of large groups of martensite plates (the burst phenomenon).

Pseudoelastic behaviour (figure 7b) is a complete mechanical analogue of the thermoelastic transformation. In this case, the transformation proceeds continuously with increased applied stress. The 'plastic' strain is caused by the shape strain accompanying the formation of martensite. Recovery of the shape strain therefore occurs when the transformation is reversed. This type of pseudoelastic behaviour is obtained when the material is stressed at temperatures higher than the finish temperature A_f for the reverse transformation. Pseudoelasticity can also occur by the reorientation of the existing martensite variants (Krishnan *et al* 1974). Other terms such as superelasticity, ferroelasticity, rubber-like behaviour etc. have sometimes been used to describe pseudoelastic behaviour.

The shape memory effect arises if a macroscopic deformation is accompanied, as before, by a martensitic transformation which is not reversed on removal of the applied stress; in a second step the reverse transformation and a concomitant reversal of the macroscopic deformation are induced by heating. Figure 7(c) shows this behaviour schematically. The upper half represents the response of the specimen to the isothermal variation of the applied stress, while the lower half pertains to the effect of subsequent heating. The idealised curves shown in figure 7(a–c) suggest close interrelations between these processes. If the stress hysteresis in a pseudoelastic transformation is so large that the reverse transformation is incomplete at $\sigma_a = 0$, then the residual martensite can be reverted by heating, *i.e.*, by employing the shape memory effect. This clearly demonstrates the interchangeability of stress and temperature as state variables.

A two-way shape memory effect occurs when the specimen deforms spontaneously during the cooling half-cycle and recovers during the heating half-cycle (figure 7d). An alloy which exhibits the one-way or normal shape memory effect can often be converted into a reversible memory alloy by "training" with a few cycles of the one-way type, or (more effectively), a few pseudoelastic cycles above M_s (Christian 1982). The maximum strains of the reversible effect are normally much smaller than those of the simple shape memory effect for a given alloy.

6. Common characteristics of materials exhibiting the memory effect

On the basis of extensive investigations conducted on Au-Cd, In-Tl, Ni-Ti, Cu-Zn, Fe-Pt and Cu-Al-Ni alloys, Wayman and Shimizu (1972) have concluded that the following conditions are necessary for an alloy to exhibit the shape memory effect: (i) The martensitic transformation should be a thermoelastic one; (ii) the parent phase and the martensite should be ordered; (iii) the lattice-invariant shear must occur by twinning rather than by slip.

While the first two conditions hold good for all the alloys investigated so far, the last condition, namely, the internal twinning of martensite does not appear to be very general. In fact, there is ample evidence in the literature to show that martensites in silver- and copper-based ordered alloys contain extensive and periodic faulting in the stacking sequence of the close packed planes, and these alloys do exhibit the shape memory effect to a significant extent.

6.1 *Thermoelastic martensites*

A thermoelastic martensite is generally characterised by (i) a small driving force, (ii) a small shear component of the shape strain, (iii) a small volume change, and (iv) a matrix with a high elastic limit (Dunne and Wayman 1973; Tong and Wayman 1975). It is clear that a thermoelastic martensite crystal must have a perfectly coherent interface with the surrounding matrix and that the coherence must be maintained during the whole process of growth or shrinkage. This is possible only if the volume change associated with the transformation is small. Furthermore, the small value of the thermal hysteresis is a direct consequence of the smallness of the driving force.

6.2 *Effect of ordering*

It is found that some degree of ordering (usually, long range ordering) is present in all parent phases which are known to transform thermoelastically. As a case in point, the ordered Fe_3Pt alloy undergoes a thermoelastic martensitic transformation and also exhibits the shape memory effect, while disordered specimens of the same composition display neither.

According to the phenomenological theory of martensitic transformation (Wayman 1964), the habit plane is a plane of zero average distortion. However, localised distortions still persist at the interface though they are macroscopically arranged out by the lattice-invariant shear. This fine-scale distortion is not expected to exceed the elastic limit of the matrix in ordered alloys (because of the order-hardening effects), but in

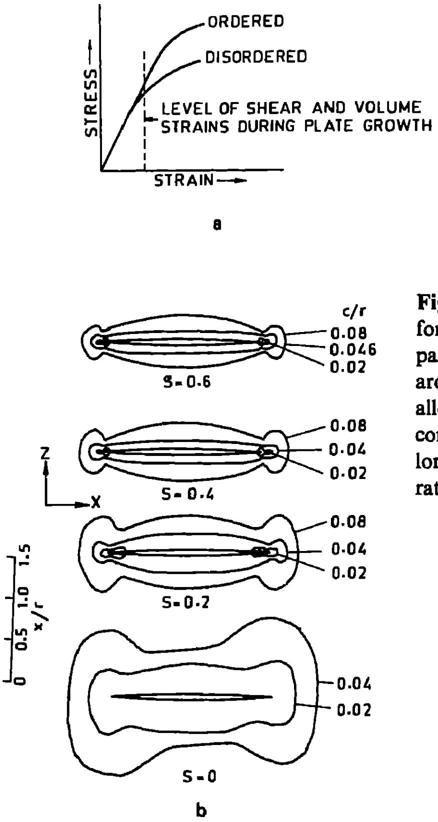

Figure 8. (a) Schematic stress-strain curves for the disordered and ordered states of the parent phase. (b) Matrix yield stress contours around an oblate spheroidal plate of an Fe-Pt alloy. The plate is in the x-y plane and the contours are drawn for varying values of the long range order parameter, S and the aspect ratio, c/r.

disordered alloys the elastic limit is evidently exceeded and the interface eventually becomes incoherent. This is explained with the help of the hypothetical stress-strain curves shown in figure 8(a). Ling and Owen (1979) have re-examined the plastic deformation around a growing thermoelastic plate, and have predicted the size of the plastic zone around plates of various shapes and in materials with varying long-range order (figure 8b). In the disordered alloy (longrange order parameter $S = 0$), general yielding has occurred all around the isolated plate with an aspect ratio $c/r = 0{\cdot}02$. However, when $S > 0{\cdot}4$, such yielding is confined to a small volume near the radial edge. It is therefore clear that the primary role of ordering is to strengthen the parent and the martensite phases without affecting significantly the value of the shear modulus, μ, thereby increasing the ratio σ_y/μ of the yield strength to μ.

The ordered arrangement of atoms is also important when one considers the reverse transformation upon heating. If a material is to exhibit the shape memory effect, it is essential that all the martensite plates formed in a single crystal of the parent phase should revert as a unit to the original orientation of the parent phase. When an ordered parent phase transforms to an ordered martensite, the arrangement of atoms, though ordered, exhibits a lower symmetry in the latter phase (following the deformation of the lattice). Considering that another lattice distortion must be operative during the inverse transformation, it follows that the number of reverse lattice correspondences is more limited than in cooling transformation, one imposes the restriction that the original ordered arrangement in the parent phase be recovered. In fact, in Cu-Al-Ni alloys it has been shown that there is only one lattice correspondence between the parent and the martensite phases which maintains the original order (Wayman and Shimizu 1972). Accordingly, the ordered martensite is obliged to revert to the original orientation of the parent phase in this case.

6.3 *Lattice softening*

Shape memory alloys exhibit interesting and anomalous behaviour with respect to the temperature dependence (near M_s) of the electrical resistivity, elastic constants, etc. Moreover, 'extra' reflections appear in the x-ray and electron diffraction patterns taken at temperatures just above M_s. The damping capacity of these alloys increases anomalously to reach a maximum near M_s. Among all these pre-martensitic phenomena, the most important and striking feature is that the temperature derivative of the elastic shear constant $\mathrm{d}C'/\mathrm{d}T$ (where $C' = (C_{11} - C_{12})/2$) is large and positive. Zener (1947) has explained the low values of $C_{11} - C_{12}$ observed in β-brass for $T \approx M_s$ on the basis of the instability of the bcc lattice with respect to a (110) $[1\bar{1}0]$ shear. Thus it is suggested that the very low value of the thermodynamic driving force required at M_s is due to the assistance by long wavelength phonon instabilities of the nucleation of martensite in a soft lattice. As with ordering, it is probable that the major, and certainly the most direct consequence, of lattice softening in the nature of martensite growth would be with regard to the ratio σ_y/μ. A decrease in μ increases the magnitude of the shear strain which can be accommodated elastically.

6.4 *Mechanisms for the shape memory and related effects*

The most remarkable consequence of deformation by interface migration is that the substantial strains produced this way are often completely recoverable when the chemical or mechanical driving force is removed. This 'shape recovery' is a consequence of the highly ordered nature of the atomic displacements during thermoelastic interface deformation. It contrasts with the irreversibility of the plastic deformation produced by dislocation glide or by the formation of martensite plates or deformation twins with an accompanying dislocation deformation. The most important mechanisms based on interface migration which have been put-forward for the effects under consideration include (i) the stress-assisted reversible growth of martensite; (ii) the reorientation of the martensite plates under an applied stress; (iii) inter-twin growth; and (iv) martensite-to-martensite transformation under stress. We now discuss these mechanisms in brief.

6.4a *Stress-induced reversible growth of martensite:* The essential feature of this mechanism is that those plates of martensite grow which have orientation and shear directions favoured by the dominant shear due to the imposed macroscopic change in shape; while other less favourably oriented variants shrink. The growth must be mechanically reversible (and hence thermoelastic) if the shape is to be completely recoverable. The martensite plates which participate in this mechanism may be nucleated under the action of the applied stress, in which case only the favourably-oriented variants will be produced; or they may be plates which may have been formed athermally before the external stress is applied.

6.4b *Reorientation of martensite plates:* Macroscopic shape deformation can be achieved by an externally applied stress through the growth of martensite plates favourably oriented in the stress field at the expense of less suitably oriented plates. It is to be noted that when the martensite interface moves, the habit plane itself remains unchanged, suggesting that ratio of the thickness of alternate segments of transformation twins within the plates remains unchanged. A special and specific mechanism whereby martensite plates can be reoriented under stress has been proposed by Wasilewski (1975). It is described as a 'stress-assisted double transformation'. When a stress is applied at a temperature between A_d and M_f, the martensite transforms to the β'-phase by the stress-assisted reverse transformation; (M_f is the martensite finish temperature during cooling and A_d is the lowest temperature at which martensite reverts to austenite under deformation) and then, because it is both thermally unstable and subject to an external stress, it transforms instantaneously to a martensite variant more favourably oriented with respect to the applied stress field than the original plate. However, there is no experimental evidence as yet for the transitory existence of an intermediate β'-phase.

If the specimen is fully martensitic and consists of self-accommodating groups of martensite, then on the application of external stress, movements of the existing plate boundaries or creation of new ones together with changes in internal structure will occur. Because no untransformed parent phase is present, no invariant plane strain conditions need to be satisfied; only a three-dimensional strain minimisation is necessary.

6.4c *Inter-twin growth:* Macroscopic deformation by change in the thickness of two twin variants under an applied stress was first reported by Olander (1932) and studied in detail in Au-Cd and In-Tl alloys by Chang and Read (1951). This mechanism does not involve any movement of the martensite-martensite interfaces. On applying a stress the twin boundaries move so as to thicken those twins which are favourably oriented with respect to the applied stress. On removal of the stress, the twin boundaries return (relatively slowly) to their original positions, and the specimen recovers its original shape. The strains thus recoverable may be as large as 0·08 in Au-Cd.

6.4d *Martensite-to-martensite transformation under stress:* In Cu-Ni-Al alloys two different martensites β'_1 and γ'_1 form from the parent β_1. It is reported that the β' martensite can be transformed partially to γ'_1 by applying a stress below M_s. Similarly, athermally formed β'_1 martensite in Cu-Al alloys can transform either to an fcc or hcp structure by deformation. Delaey and Warlimont (1975) have demonstrated a similar martensite-to-martensite-transformation in a Cu-Zn-Al alloy.

The different possible routes in a pseudoelastic cycle and a shape memory cycle are illustrated in figure 9 (Cook 1981). This diagram compares the changes involved in a shape memory cycle (VABCDEZ) with those in a pseudoelastic cycle (VWXYZ). If the same martensite phase is produced in the two cycles, the structure at X is identical with that at C and D, and the state X may be converted into D by cooling at a constant strain.

7. Applications of the shape memory effect

One of the earliest applications of the shape effect was the introduction of tubing or pipe couplings that shrink during heating. Ni-Ti alloy couplings are used for connecting aircraft hydraulic lines. These are expanded by 4% in the martensitic

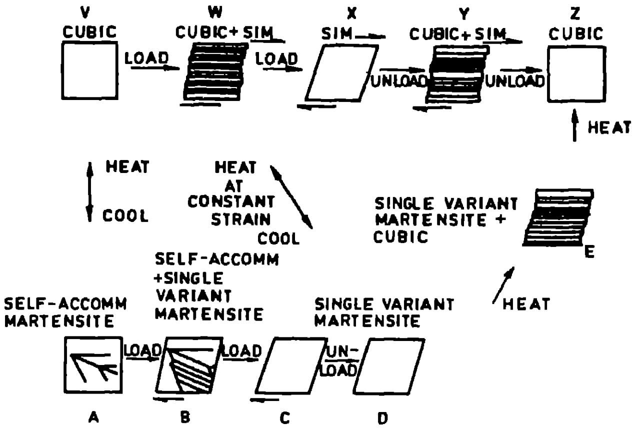

Figure 9. Schematic structural changes during a pseudoelastic cycle VWXYZ and a shape memory cycle VABCDEZ.

condition at liquid nitrogen temperatures, and placed around the tubes to be joined. Warming at room temperature produces a tight seal. Substantial developments have taken place in the field of copper-based shape memory alloys, particularly the Cu-Zn-Al alloys, with emphasis on their applications as thermostats, automotive control devices and actuators. Applications in the field of medicine include the use of such materials for orthodontic dental arch wires, blood clot filters and orthopaedic devices.

References

Angel T 1954 *J. Iron Steel Inst.* **177** 165

Bowles J S and Mackenzie J D 1954 *Acta Metall.* **2** 129

Chang L C and Read T A 1951 *Trans. Met. Soc. AIME* **191** 47

Cook J M 1981 Ph.D. Thesis, Cambridge University (unpublished)

Christian J W 1982 *Met. Trans.* **A13** 509

Delaey L, Krishnan R V, Tas H and Warlimont H 1974 *J. Mater. Sci.* **9** 1521

Delaey L and Warlimont H 1975 *Proc. conf. shape memory effects in alloys*, (eds) J Perkins (New York: Plenum Press) p. 59

Divers C K 1964 *Met. Prog.* **86** 115

Dunne D P and Wayman C M 1973 *Met. Trans.* **4** 137

Krishnan R V, Delaey L, Tas H and Warlimont H 1974 *J. Mater. Sci.* **9** 1536

Ling H S and Owen W S 1979 *Proc. int. conf martensitic transformation* (ICOMAT 1979), (Cambridge: MA) p. 368

Ludwigson D C and Berger J A 1969 *J. Iron Steel Inst.* **207** 63

Mangonon Jr P L and Thomas G 1970 *Met. Trans.* **1** 1587

Murr L E, Staudhammer K P and Hecker S S 1982 *Met. Trans.* **A13** 627

Olsen G B and Cohen M 1972 *J. Less Common Metals* **28** 107

Olsen G B and Cohen M 1975 *Met. Trans.* **A6** 791

Olsen G B and Cohen M 1976 *Met. Trans.* **A7** 1905

Olander A 1932 *J. Am. Chem. Soc.* **54** 3819

Onodera H and Tamura I 1979 US-Japan seminar on *Mechanical behaviour of metals and alloys associated with displacive transformation*, (Troy, NY) p. 24

Patel J R and Cohen M 1953 *Acta Metall.* **1** 531

Seetharaman V 1976 *Effect of thermomechanical treatments in stainless steels* M.Sc. (Tech) Thesis, University of Bombay

Seetharaman V and Krishnan R 1981 *J. Mater. Sci.* **16** 523
Suzuki T, Kojima H, Suzuki K, Hashimoto T and Ichihara H 1977 *Acta Metall.* **25** 1162
Tamura I 1982 *Met. Sci.* **16** 245
Tamura I, Maki T and Hato H 1970a *Trans. Iron Steel Inst. Jpn* **10** 163
Tamura I, Maki K, Hato H, Tomoto Y and Okada M 1970b *Proc. ICSMA* 3, (ASM, Metals Park Ohio) p. 900
Tong H C and Wayman C M 1975 *Acta Metall.* **23** 209
Wasilewski R J 1975 *Met. Trans.* **A6** 1405
Wayman C M 1964 *Introduction to the crystallography of martensitic transformation* (London: Macmillan)
Wayman C M and Shimizu K 1972 *Met. Sci. J.* **6** 175
Wechsler M S, Lieberman D S and Read T A 1953 *Trans. AIME* **197** 1503
Zaekay V F, Parker E R, Fahr D and Busch R 1967 *Trans. ASM* **60** 252
Zener C 1947 *Phys. Rev.* **71** 846

Discussion

V K Wadhawan: What is the role of the superlattice structure in the shape memory effect?

V Seetharaman: Ordering of the parent and martensite phases has two consequences. (i) It increases the yield strength of the parent and product phases by the 'Fisher's order hardening mechanism' (ii) It reduces the number of variants available for the reverse transformation so that strain recovery can occur efficiently.

S Ray: Does the shape memory effect occur only in isothermal martensite systems (through mode softening) or is it possible in athermal martensites also?

Seetharaman: It is seen in athermal martensites though the mode may not soften completely.

R Krishnan: Are there examples of transformation induced plasticity in ceramic materials?

Seetharaman: I know only a few examples of these. The material must have a residual plasticity before we can introduce TRIP.

Bull. Mater Sci., Vol 6, No. 4, September 1984, pp. 717–732. © Printed in India.

Strength and electronic structure

K GOVINDA RAJAN

Materials Science Laboratory, Reactor Research Centre, Kalpakkam 603 102, India

Abstract. The main attribute of a solid is its resistance to deformation, or its 'strength'. We discuss first the interpretation of the strength parameter. The current situation with regard to the central problem of providing a microscopic description of the strength parameter is briefly reviewed. Electrons in metals provide the cohesion, so that an understanding of the role played by electronic structure in the strength attribute should lead to practical hints for building stronger materials. The useful 'aircraft alloy' (Ti + Al + V) illustrates one such important relationship, *viz.*, that the addition of a non *d*-character metal to a *d*-electron host strengthens the latter. Again, metals are distinguished from non-metals by the Fermi surface they possess, and it is interesting to examine any possible relationship between the anisotropy of the Fermi surface with the observed anisotropy in hardness (or yield strength). Next, we turn to cleavage, and point out that the assumption that it is the exact opposite of cohesion faces objections. Cohesion is an average property, whereas cleavage is a crack-tip phenomenon. Finally, among the processes familiar to the metallurgist wherein a metal is hardened, electron-moderated mechanisms have been identified in at least two cases, and we conclude with a brief account of these.

Keywords. Strength; cohesive energy; electronic energy; electron-mediated interactions; strengthening mechanisms.

> "... merely corroborative details to lend an aspect of verisimilitude to what would otherwise be a bald and unconvincing narrative ..."
>
> Gilbert and Sullivan—The Mikado

1. Introduction

A solid is characterized by its resistance to deformation, or its strength. In particular, the ability of a solid to resist shearing forces is used to distinguish it from a fluid. Three broad characteristics can be recognized when the meaning of 'strength' is considered. Resilience or elasticity, when subjected to transient forces—that is, how strongly does the solid attempt to regain its original shape if a force is applied to it for a time and then removed? The Young's modulus, which is a measure of such resistance, varies over three orders of magnitude (10^{10}–10^{13} dyn/cm^2). Resistance to flow is the next characteristic and it concerns the question: how much applied force is required to obtain a particular rate of flow? Flow resistance varies even more—from 10^5 to 10^{12} dyn/cm^2—and the measured rates of flow vary over 12 orders of magnitude. Third, by applying sufficient tension, solids can be pulled apart into two pieces. How much applied force is required to fracture a solid? Fracture resistance is the resistance of a material to crack propagation. It is measured in terms of the fracture surface energy, which may be as little as 10 dyn/cm or as high as 10^8 dyn/cm, *i.e.*, varies over 7 orders of magnitude.

Owing to these diverse and variable aspects, the problem of strength is one of great complexity. Strength depends on the collective response of a crystal to applied stress, so that its description is quite involved. That is, strength depends on the behaviour of aggregates of particles, and the central problem in the science of strength has been to learn how to describe mechanical behaviour in terms of the fundamental properties of matter, so that the shapes of stress-strain or strain-time curves and their dependence on loading conditions can be predicted from a small number of experimental relationships (Gilman 1969).

Turning to metals, we know that the properties of metals arise from the behaviour of the free electrons, and their interaction with the metallic ions. Much attention has therefore been directed to the properties of electrons (in particular, the free electrons) in metals, and features such as electrical conduction, magnetic properties and structure in metals have been understood. This success provides the motivation to look into the question of whether progress with regard to the strength attribute too can be made using this approach.

2. Perfect cleavage

We begin by discussing how the strength of a solid is calculated in order to understand the role of electronic structure.

The separation of a crystal into two or more parts by the propagation of a geometrically plane crack through the solid is called cleavage. Perfect cleavage is portrayed in figure 1. A crystal is stressed in tension vertically to the point of theoretical cohesive strength (figure 1a), and then this stress is exceeded simultaneously at every one of the atomic bonds across the cleavage plane extending interminably and mathematically all the way across the stressed crystal (figure 1b), with no intermediate stages. The crystal goes directly from cohesion to cleavage with no crack propagation direction. The more recent, and present, concept of perfect cleavage is that the elastic bonds connecting the atoms are individually overcome one by one in chronological order, as shown in figure 1c. In this visualization, perfect cleavage is the propagation of an atomically sharp crack with the applied stress overcoming the elastic stresses in a purely elastic manner, and with the atoms separating in geometrically opposite directions, along the direction of the tensile stress.

2.1 *Ideal strength of a crystalline solid*

The maximum stress required to produce, in an ideal crystal, a perfect cleavage of the form imagined above is called the ideal strength or the theoretical strength of a solid

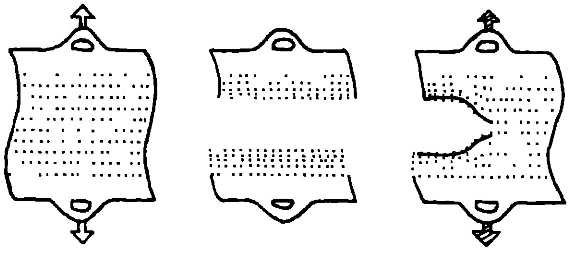
(a) (b) (c)

Figure 1. Perfect cleavage: (a) and (b) Original picture; (c) present concept of perfect cleavage.

(TS). Before the development of the dislocation theory of solids, this problem was of considerable interest because calculated values of the strength were typically greater than experimental values by a factor of 100 or more. Even at the present time, this problem is of theoretical and practical importance, as a knowledge of the TS is useful in determining the stress distribution and other properties in the region at the tip of a crack; in determining the dislocation core radii; in defining the point at which coherency breakdown occurs at a particle-matrix interface; and in providing insight into the phenomenon of melting. The reviews by Milstein (1982) and Macmillan (1972) exemplify these points. Macmillan also reviews the practical approach to the measurement of TS. The measurements are carried out either on specially grown whiskers or on single crystals of materials in which the dislocation density is very small ($\sim 10^1$–10^2 cm^2). Table 1 provides a comparison between the calculated and measured strength for a few solids.

A simple way of estimating the cleavage stress of a perfect crystal is as follows (Kelly 1973). It is assumed that the crystal is pulled at $T = 0$, and the restoring force per unit area between two adjacent atomic planes is assumed to vary with distance according to $\sigma = K \sin \pi/a\,(x - a_0)$, where a_0 is the equilibrium separation between the atomic planes, and a is the range of the interatomic force. The latter is evaluated by setting

$$2\gamma = \int_{a_0}^{a_0+a} \sigma\, \mathrm{d}x$$

at cleavage, γ being the surface energy of the solid; the factor 2 appears because a pair of surfaces is created when cleavage occurs. Thus $a = \pi\gamma/K$. The maximum value of σ is identified as the TS of the solid, so that we have simply $\sigma_{\max} = K$. K is evaluated from the definition of the Young's modulus Υ for the appropriate direction in the solid, namely, $\Upsilon = a_0\, \mathrm{d}\sigma/\mathrm{d}x$. For $x \simeq a$, this gives

$$\Upsilon = K\pi \frac{a_0}{a} \cos \frac{\pi}{a}(a - a_0) \simeq \frac{K\pi a_0}{a},$$

Table 1. Comparison of calculated and measured values of the strength of a few solids.

Calculated values of TS				Experimental data		
Material	Tensile direction	Theoretical strength (calculated) × 10^{-11} dyn/cm^2: equation (1)*	Theoretical strength (calculated) × 10^{-11} dyn/cm^2: equation (2)	Material	Max. tensile stress $\sigma_{\max} \times 10^{-10}$ dyn/cm^2	$\frac{\sigma_{\max}}{\Upsilon} \approx$ strain
Ag	⟨111⟩	2·4 (0·20)	—	Whiskers		
Ag	⟨111⟩	2·7 (0·25)	—	Ag	1·73 ⟨100⟩ tension	0·040
Cu	⟨111⟩	3·9 (0·20)	3·796	Cu	2·94 ⟨111⟩ tension	0·028
Cu	⟨100⟩	2·5 (0·51)	3·60	Fe	13·10 ⟨111⟩ tension	0·049
W	⟨100⟩	6·1 (0·22)		Cd	2·80 ⟨1120⟩ tension	0·040
α-Fe	⟨100⟩	3.0 (0·34)				
α-Fe	⟨111⟩	4·6		Crystal		
C(dia)	⟨111⟩	20·5		Ge	7-12	0·05–
Si	⟨111⟩	3·2				0·08
Ni	⟨100⟩		2·3			

* Values indicated in parentheses are the calculated strains.

so that we have, finally,

$$\sigma_{\max} = (\Upsilon\gamma/a_0)^{1/2}. \tag{1}$$

This simple treatment indicates that the strength goes as $\sqrt{\Upsilon}$ and $\sqrt{\gamma}$. The values of strengths obtained from this approach are indicated in table 1.

2.2 *More exact calculations of* TS

After Born's work on the necessary conditions for the thermodynamic stability of a crystal lattice with respect to arbitrary (but small) homogeneous deformations, many attempts have been made to refine the calculations of the theoretical strength (Esposito *et al* 1980; Milstein 1982). The current approach is to proceed along the following lines: (a) The solid under consideration is defined by specifying its crystal structure, parameters of the unit cell, etc. (b) The interaction between the ions and electrons is specified next. For simplicity, pair potentials (Lennard-Jones, Morse, etc.) are used. However, for metals where there is a clear deviation from the Cauchy relation $C_{12} = C_{44}$, the pair potential approximation is not applicable. Recently, the so-called "*ab-initio* potential" method for the calculation of the TS has been developed to overcome the limitations of the pair-potential approximation (Carlsson *et al* 1980). (c) The Born stability criteria are applied, and the suitability of the potential is checked. (d) The cohesive energy per atom (or unit cell) is calculated as a function of the parameters of the potential and other geometric parameters. (e) The unit cell is stretched, and the energy is calculated as a function of the strain. (f) Considering for the moment a cubic crystal with lattice parameter a_0 (thus $a_1 = a_2 = a_2 = a_0$), it is clear that a stretch, for example along [100], will impart a tetragonal distortion. For computational ease the deformation is imagined to increase a_1 and decrease a_2 and a_3 in such a manner as to keep $a_2 = a_3$ and the transverse stress $\sigma_2 = \sigma_3 = 0$. In practice, this is achieved by an iterative technique. The relevant stress σ_1 is calculated from the expression

$$\sigma_1 = \frac{4}{a_0^3}\frac{\partial U}{\partial(a_1/a_0)}. \tag{2}$$

where U is the cohesive energy. The theoretical strength is identified as

$$\mathrm{TS} = (\sigma_1)_{\max}. \tag{3}$$

Figure 2 gives an idea of the way σ_1 varies with extension along [100] in nickel. The maximum σ_1 value is the TS, and the corresponding a_1 value gives the strain at fracture. Obviously, the cleavage process is imagined to be the exact opposite of cohesion, with all bonds snapping simultaneously when σ_1 reaches $(\sigma_1)_{\max}$.

Further details may be found in the references listed at the end (*e.g.*, Milstein 1982). Table 1 also contains the TS values calculated by these more exact methods. It is interesting to note that even the naive calculations outlined in § 2.1 are already in reasonably good agreement with the observed values. The more exact calculations, in addition to improving this agreement, also help us in understanding the correlation between the electronic structure and strength of metals.

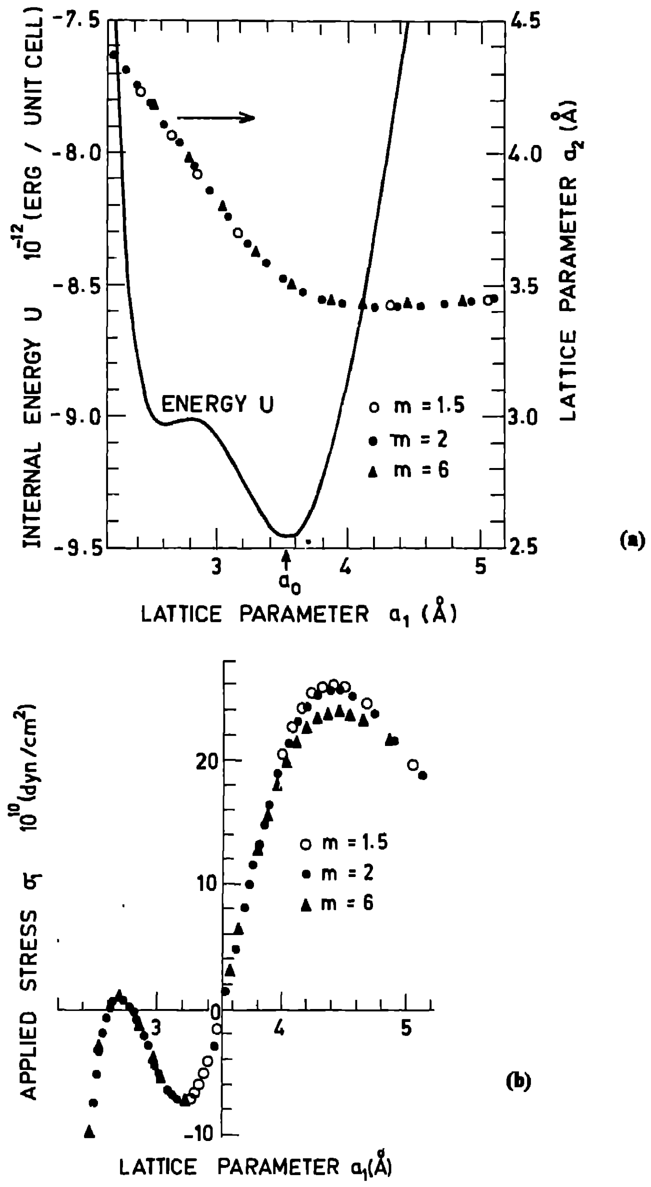

Figure 2. (a) The internal energy (cohesive energy) as a function of the axial lattice parameter a_1 for [100] uniaxial loading in fcc Ni. (b) Computation of the true axial stress σ_1 as a function of a_1 for [100] loading. The maximum value of σ_1 is the theoretical strength. The calculations were performed using a Morse potential $\phi(r) = D[\exp\{-2m\alpha(r-r_0)\} - 2\exp\{-m\alpha(r-r_0)\}]$. Results for a few values of m are shown (after Milstein 1982).

3. Cohesion and electronic structure

We have seen that in strength calculations, the cohesive energy of the solid has to be first determined. It therefore becomes necessary to see how the electronic structure enters the calculation of cohesive energy, for a better understanding of the relationship between strength and electronic structure (especially in metals).

The calculations of the total energy of a metallic structure is formulated as the determination of the energy of an assembly of N ions (each with volume Ω) at sites $\mathbf{r}_n$ arranged on a crystal lattice, and NZ valence electrons. The total energy U is first separated into the energy of the ions, which is purely potential and comes from their mutual repulsion, and that of the electrons, which contains both kinetic and potential terms. The energy of an electron with momentum k is given (to a second order of approximation) by

$$E(k) = \frac{\hbar^2 k^2}{2m} + V_0 + \sum_q{}' \frac{V_q^2}{E_k - E_{k+q}}, \tag{4}$$

in standard notation. To obtain the total energy of the electrons, we must sum $E(k)$ over all occupied states, *i.e.*, over all $k \leqslant k_F$, the Fermi momentum of the electrons. The first two terms on the right in (3) are free-electron terms, this being the zeroth approximation for the perturbation theory. All such terms are *structure-independent*. The first term is the kinetic energy of the free electron gas, and the second is the average value of the lattice potential. Both terms depend upon the total volume. All the structure dependence of $E(k)$ resides in the third term, which contains the strengths of atomic potentials expressed in some suitable form. If the potentials are weak, a second-order correction is adequate and this leaves $E(k)$ only slightly structure-dependent. The corresponding mechanical characteristic is softness; *e.g.*: Na, K, etc. As the strength of the atomic potentials in a sequence of metals increases more terms have to be added to $E(k)$, making it more and more structure-dependent. As a result, these metals fall into a sequence of increasing hardness (or strength). It has been suggested that the parameter E_g/Δ can also be used as a measure of atomic potential strength, where E_g is the width of a low-lying band gap at the zone boundary and Δ is the width of the energy band itself.

The cohesive energy of a metal can be written as a sum

$$U = U_0 + U_s \tag{5}$$

of a structure-independent part U_0, and a structure-dependent term U_s. The former is given by

$$\begin{aligned} U_0 &= U_e + ZV_0 + W_E \\ &= \frac{3}{5} ZE_F + ZV_0 - 0{\cdot}9 \frac{Z^2 e^2}{R}. \end{aligned} \tag{6}$$

The first two terms represent the free electron energy averaged over all the occupied states. (E_F is the free electron Fermi energy.) ZV_0 is the mean value of the pseudopotential in a sphere of Ω, *i.e.* the mean potential energy per electron multiplied by the number of electron per ion. W_E is the electrostatic energy of the ions in the uniform free electron gas. In determining its value, the ions are imagined to be spheres immersed in the electron gas. When crystal structures are taken into account, the geometric factor 0·9 is modified to other values very close to 0·9. Correction terms like

Table 2. Comparison between the observed values of the cohesive energy U with the calculated values of the structure independent part of U.

Element	$-U_0$ (in ry) calculated	Measured cohesive energy (ry)
Li	0·513	0·512
Na	0·457	0·460
K	0·369	0·388
Be	0·995	1·13
Mg	0·852	0·892
Zn	0·991	1·05
Cd	0·937	0·993
Al	1·32	1·38
Sn	1·69	1·77
Pb	1·73	1·81

the electrostatic self-energy, that is, the interaction of the electron gas with itself, also have to be considered. The structure-independent energy U_0 is thus

$$U_0 = \frac{3}{5} ZE_F + ZV_0 - 0{\cdot}9\frac{Z^2e^2}{R} - \frac{e^2}{2Z}\int \frac{\rho(\mathbf{r})(r)}{|\mathbf{r}-\mathbf{r}'|}\,\mathrm{d}\mathbf{r}\,\mathrm{d}\mathbf{r}'. \tag{7}$$

Further correction terms to allow for correlation and exchange effects among the conduction electrons and for the exclusion of conduction electrons from the core, enable U_0 to be determined more accurately.

A comparison (table 2) between the observed and calculated cohesive energies for a number of metals shows that the structure-independent energy dominates the volume dependence of the total energy; so that, by choosing a particular pseudopotential form, U_0 can be evaluated as a function of Ω. From this, the structure, compressibility and strength follow readily.

The structure-dependent energy U_s has the following terms:

$$U_S = U_{\mathrm{BS}} + \Delta W_E. \tag{8}$$

The band structure energy U_{BS} is the change in energy in going from the free electron model to one containing a periodic potential. ΔW_E is a structure-dependent correction to W_E. In one dimension, if the Fermi level lies just below a band gap, the effect of the band structure is a lowering of the energy below the free electron level. If the Fermi level were far above a band gap, the net effect would leave the free electron energy unaltered. However, the actual Fermi surfaces in metals and other crystals always lie close to the first few reciprocal lattice vectors so that the effect of the band gaps always decreases the total energy, *i.e.* U_{BS} is always negative. Figure 3 shows this schematically. This structure-dependent part of the electron energy can be expressed as

$$U_{\mathrm{BS}} = \sum_{k<k_F} \sum_{g}{}' \frac{V_g V_g^*}{E_k - E_{k+g}}. \tag{9}$$

This is a perturbation-theoretic result, and is not accurate close to the Brillouin zone boundary—it diverges when the Bragg condition is exactly satisfied. The way the structure controls U_{BS} can be seen by writing the final form of U_{BS} as

$$U_{BS} = \sum_{\substack{g \\ g \neq 0}}' [S(g)]^2[V(q)]^2\chi(q)\varepsilon(q), \tag{10}$$

where $S(g)$ is zero except at reciprocal lattice vector points and is thus the sole repository for the influence of the structure. The remaining factors are characteristic only of the nature of the atoms in question, and they are usually collectively termed the energy-wavenumber characteristic $F(q)$:

$$F(q) = V(q)^2\chi(q)\varepsilon(q), \tag{11}$$

$F(q)$ has the form as shown in figure 4 for various metals.

The theory described so far has been used by metal physicists to understand the crystal structure of metals, to provide the basis for the Hume-Rothery rules, and to explain the stability of alloy phases at the absolute zero of temperature (Harrison 1966; Wilkes 1973). Calculation of the theoretical strength has been attempted only for copper and fcc iron. Once U is calculated the calculation of the strength proceeds on the lines explained in § 2.2. Table 3 indicates the values of theoretical strengths obtained for copper using three different potentials. Obviously, this approach of treating the

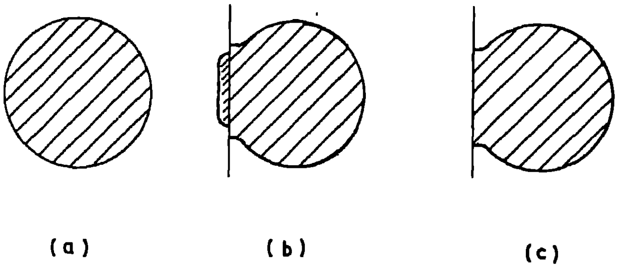

Figure 3. (a) Free electron Fermi surface—a sphere. (b) The Fermi sphere intersected by a Brillouin zone. This gives rise to little energy change. (c) Sphere touching plane—energy gain.

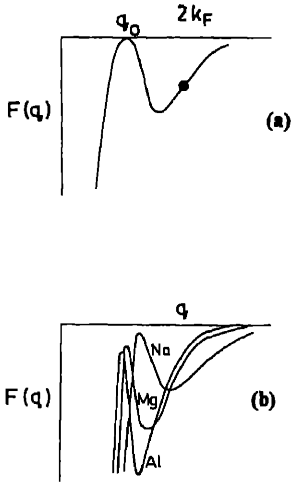

Figure 4. (a) Schematic diagram of energy-wavenumber characteristic. (b) Energy-wavenumber characteristic for some metals.

Table 3. The theoretical strength of copper calculated using three different model potentials.

Potential	Theoretical strength, σ_t (dyn/cm^2)	Strain $\varepsilon_t = \sigma_t/\Upsilon$
Nonself-consistent KKR	$5{\cdot}5 \times 10^{11}$ ($\Upsilon/2{\cdot}3$)	0·5
Self-consistent ASW with Ewald correction	3·6 ($\Upsilon/4{\cdot}0$)	0·3
Pair potential	3·6 ($\Upsilon/4{\cdot}0$)	0·5

electrons as nearly free cannot be used when dealing with transition and rare-earth metals, as these possess narrow *d* and *f* bands respectively.

It may be observed from tables 1 and 3 that while there is satisfactory agreement between the computed and observed σ_t values, the calculated values of the *strains* ε_t at failure are nearly an order of magnitude greater than those found experimentally. Brenner's (1956) early experiments on single crystal copper whiskers indicated for [111] tension, a maximum stress $\sim \Upsilon/40$, where Υ is the measured Young's modulus for polycrystalline copper, and a strain of only 0·03 (3 %). Brenner noticed that in his experiments, all the specimens did not cleave, but sheared apart. It might also be of interest to note that in another study (McQueen and Marsh 1962), flat single crystal samples of Cu were subjected to shock waves of sufficient intensity to cause fracture. Because of the geometry of the experiment, the transverse dimensions of the sample remain essentially fixed. For the [100] orientation, the yield strength obtained was $\Upsilon/7{\cdot}5$. However, the derivation of this value from the known shock-wave intensity involved the use of hydrodynamic equations and equations of state whose validity is difficult to assess.

The substantial difference between the calculated and the observed strains prompts us to examine closely how good the foregoing picture of cleavage is. It is true that in some experiments a shear yield rather than no clean cleavage was observed. Yet, this alone cannot account for the entire difference. It must be that, after all, fracture is not as simple as pure cleavage, which is just the antithesis of cohesion. Finally, it should be mentioned that the strength calculations have so far been performed for a simple cubic unit cell; it is not known at present just how complicated these calculations are for other lower symmetries.

4. Cohesion *vs* cleavage

Cohesion may be described as a process holding the atoms together and cleavage as a process parting the atoms, and it is tempting to imagine these processes being exactly opposite in character. In tensile tests crystals are held together by cohesion until a load is reached where cleavage (or other fracture) occurs. From the measured load and the cross-sectional area one can compute the average force per unit area which existed at the time of fracture. This is the fracture, or cleavage, stress. It is not the cohesive strength; up to the point of fracture, the crystal had cohesion, and every atomic bond across the future cleavage plane was certainly strained in something close to perfectly-elastic tension. The moment a crack formed, however, be it 10 Å or 2000 Å, a new condition came into being—the crack tip. In short, cleavage is a crack-tip phenomenon, whereas cohesion is an average property of a crystal. It is appropriate to quote Beachem (1978) here: "Cohesive energies, or cohesive forces, do account for the loads to which tensile or bend specimens can be subjected before they break. Once fracture starts, however, events become localized and average properties become less important than local stresses, general microstructures become less important than local crack-tip microstructures, and bulk environments become less important than local crack-tip environments. Those average macroscopic bulk properties which were used in predicting the forces to which the whisker (or other specimen) could be loaded, before fracture, no longer apply. Local properties and events become decisive. Once fracture starts, it is a whole new ball game."

5. Yield strength, hardness and related parameters

The hardness of materials is a very useful quantity from the practical viewpoint. It is an empirical parameter; depending on the material, and is measured on a suitable scale. Figure 5 shows how the Vicker's hardness varies across the periodic table for the various elements. The hardness of a crystalline material and its yield strength are proportional to each other (Gilman 1973; Havner 1979). Thus the same trend in variation is expected for the strength attribute. The first prominent peak at around $e/a \sim 7$ lies among the transition metals possessing narrow d-bands. The second, higher peak is found among the group IV metalloid elements. This latter peak in the

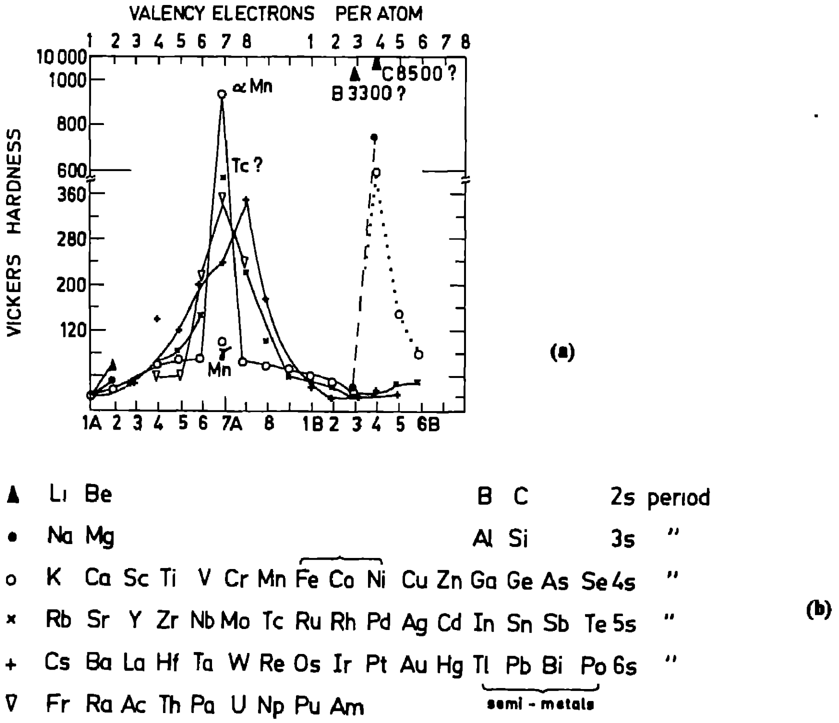

Figure 5. Vickers hardness at room temperature for various metals (after O'Neill 1967).

strength is interpreted in terms of the progressive changeover from metallic to covalent bonding. The second peak will *still* be there, even if one questions the validity of inclusion of diamond (metastable phase) in the figure.

Extensive data on the hardness of metals and alloys are available in the literature. In recent years, the microhardness parameter of metals and alloys has come to be regarded as the 'strength' microprobe (Westbrook and Conrad 1973). Two recent results concerning the behaviour of microhardness are relevant here and serve to illustrate the subtle interplay between the electronic structure and the strength. The first is the rather surprising correlation found between the microhardness and the semiconductor-to-metal transition pressure in group IV elements (Gerk and Tabor 1978). The hardness values of Ge, Si and C (diamond) were found to be 800, 1200 and 10^4 kg/mm^2 respectively. These values are remarkably close to the hydrostatic pressure values necessary to initiate semiconductor-to-metal transition in these elements (1000, 1550 and $\sim 10^4$ kg/mm^2). This indicates that plastic flow has been sustained (ductility indicates the presence of the metallic phase) in these brittle materials, and is probably because the indentation process involves a large component of hydrostatic stress inhibiting brittle failure. The second point concerns the now-established anisotropy with respect to crystallographic direction of the hardness of crystals. The elegant experiments of Tabor and his school, especially those of Brookes, have established the scratch hardness technique on an analytical basis, and data on the hardness along different crystallographic directions is available (Brookes 1981; O'Neill 1967; Westbrook and Conrad 1973). Results for copper appear in figure 6. One interprets the anisotropy in terms of the variation in the resolved shear stress for a specified indentor orientation, and therefore with the relevant active slip system. Since hardness and yield strength can be imagined to be directly related in metals, the question arises whether the

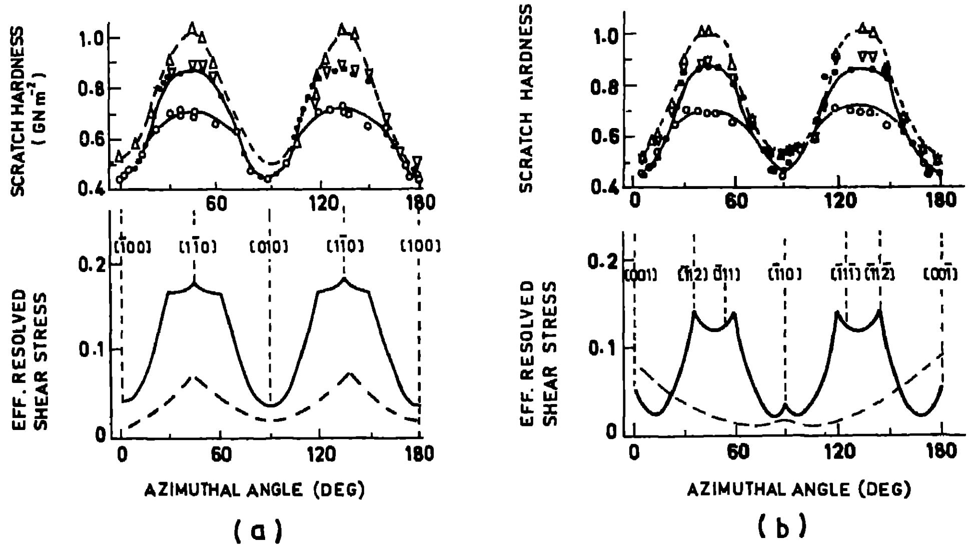

Figure 6. The measured scratch hardness results for copper. The indentor used was diamond with a 120° cone and an edge-leading 136° pyramid, and with a normal load of 500 g. (**a**) (001) surface and (**b**) (110) surface. The bottom curves represent the calculated stress values along various directions, all lying in the plane on which measurements are made (Brookes 1981).

above anisotropy can emerge from the calculation of the cohesive energy. The structure-dependent term U_{BS} in the total energy (equation (9)) must therefore be subjected to a closer examination. This involves analysing the band structure and Fermi surface in the presence of an applied stress. A beginning has been made in Watts (1979). It appears that by calculating the electron density from these Fermi surface results, one can discuss the influence of external stress on the elastic constants and, consequently the hardness. It is suggested that this line of approach might help in the endeavour to correlate the anisotropy in hardness with the anisotropy in the Fermi surface.

6. Strengthening mechanisms: role of electron mediated processes

There are a number of processes, well-known to metallurgists, available for enhancing the strength of elemental metals. The chief methods are (Peckner 1967): (a) dislocation strengthening, (b) strain hardening, (c) solid-solution hardening, (d) precipitation hardening, (e) dispersed-phase strengthening, (f) diffusionless (martensitic) transformation strengthening, (g) superlattice strengthening, and (h) radiation hardening. If we ask whether a definite electron-mediated effect has been identified with the strengthening mechanism in any of the above processes, the answer is a tentative 'yes' for mechanisms (c) and (g). We therefore start with the discussion of solid-solution strengthening.

6.1 *Solid-solution strengthening*

The simplest method of strengthening or hardening is by alloying the host element with other suitable elements/impurities. According to Conrad (1981), the solubility of the impurities will have a different value in the vicinity of dislocations than in other regions, and that the solute distribution will be such as to minimize the energy of the alloy. As the dislocations move under external stress this minimum energy configuration of the impurities is disturbed, raising the energy; the impurities thus tend to act as pinning centres for dislocations. The actual detailed mechanism could either be elastic or electronic in origin. (Ultimately, of course, elastic energy can be traced to an electronic origin). The problem of solution hardening in alloy physics can be related to that of calculating the change in energy of an impurity as its nearest neighbours vary their relative positions. The impurities are assumed to be arranged such that the distortion around the impurity is part of a macroscopic and uniform distortion of the surrounding host. The distortion is produced by first considering a single impurity in the host, undistorted except for the elastic distortion produced by a possible size mismatch. Thus a macroscopic and uniform distortion ΔS is applied to the host so as to produce the desired distortion around the impurity. Changes in the energy of the system as a function of the distortion are calculated and ΔE_i, the part due to the presence of the impurity, is isolated. The interaction between the impurities is neglected (assuming the impurity to be sufficiently dilute). The magnitude of $\Delta E_i/\Delta S$ is a measure of the solution strengthening; the larger it is, the greater is the solution strengthening. Figure 7 shows the strengthening coefficient for a few Ti-based alloys (Collings and Gegel 1975). It can be deduced from these figures that the solid solution strengthening increases roughly in proportion to the distance between the columns in the periodic table of the solvent and solute. In Ti, when such an impurity is added, its lack of d-character causes a larger perturbation in the wave function of the system in its vicinity.

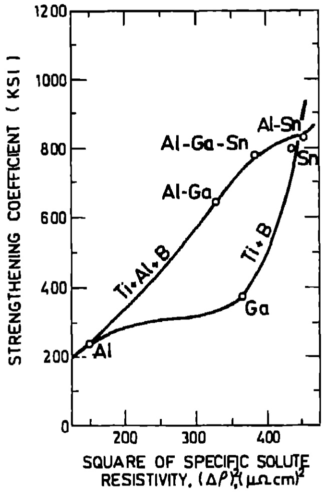

Figure 7. Correlation between the strengthening coefficient ($\mathrm{d}\sigma/\mathrm{d}C$) (equivalently, $\mathrm{d}E_i/\mathrm{d}a$) and the electrical resistivity for a set of Ti + *B* alloys and a set of Ti + Al + *B* alloys (*B* = Ga, Sn, etc.) (Collings and Gegel 1975).

Assuming that the wavefunction in the vicinity of an atom is the same as it is in the atomic configuration, the problem is simplified by imagining the perturbation introduced by the impurity to be spherically symmetric and highly localized. This then permits the definition of phase shifts introduced by the presence of the impurity. The phase shift (for a general *l*-character: $l = s, p, \ldots$) has the form

$$\delta_l = \pi Z_l/(4l+2), \tag{12}$$

where Z_l is the difference in the number of valence electrons between the impurity and the host. The introduction of the impurity and the corresponding phase shifts disturbs the wave function in the vicinity of the impurity. The distortion is appreciable and causes a given Bloch state to scatter into other states and decay with time. This leads to electrical resistivity; and indeed, a significant correlation has been found in experimental studies between the increase in electrical resistivity $\Delta\rho$ and the solution hardening. It is of interest to look at the form of the final expression for the strengthening coefficient $\mathrm{d}E_i/\mathrm{d}a$ (Stern 1975)

$$\frac{\mathrm{d}E_i}{\mathrm{d}a} = \frac{1}{6\pi}\frac{\mathrm{d}W}{\mathrm{d}a}\left[E_i + \frac{2}{\pi}\int_{-\infty}^{0}\frac{\varepsilon_0 I(\varepsilon)\,\mathrm{d}\varepsilon}{\{1-\varepsilon_0 R(\varepsilon)\}^2 + \{\varepsilon_0 I(\varepsilon)\}^2}\right]. \tag{13}$$

This is entirely equivalent to $\mathrm{d}\sigma/\mathrm{d}C$, the variation of the conductivity with the impurity concentration. In (13), W is the band width and a is the lattice parameter. (ε is the reduced energy parameter, E/W.) ε_0 is six times the ground state energy of the impurity in units of W. R and I are certain functions that involve the phase shifts. As $\mathrm{d}W/\mathrm{d}a$ in (13) is independent of the impurity, the variation of interest is the expression in square brackets. If the impurity forms a bound state level below the bottom of the band ($U_0 \ll -1$), then ($\mathrm{d}E_i/\mathrm{d}a$) is proportional to U_0; thus larger the magnitude of U_0, greater is the $\mathrm{d}E_i/\mathrm{d}a$, and greater the solid solution strengthening.

Thus, it seems that an impurity with an electronic structure very different from that of the host causes a large perturbation of the wavefunction of the latter, leading to large phase shifts and consequently to high solution hardening. It would be worthwhile to measure the changes in the various elastic constants of the alloy with impurity concentration, in particular to confirm the expected increase in elastic constants with the addition of impurities of the above type (Conrad 1981).

6.2 *Superlattice strengthening*

In a solid solution, the atoms of the different components of the alloy form a common crystal lattice, generally that of the solvent. The metallic type of bond is found in all metal-based solid solutions regardless of the type of bond peculiar to the solute in the solid state. Nonmetallic atoms (C, N, Si, etc.) do not change the metallic bond of metallic solid solutions. In a number of metallic systems (Cu + Au, Fe + Al, Fe + Si, Ni + Mn, etc.) the atoms of both components occupy entirely definite positions in the solid solution lattice if the alloy has been slowly cooled or has been heated for a long time at a definite temperature. Such ordered solid solutions are distinct from those in which the components assume statistically random positions in the lattice. This new order superimposed on the solvent lattice results in a structure called a 'superlattice'. Ordered solid solutions occur when the ratios of the alloyed components (in atomic %) are equal to whole numbers, and are designated Cu_3Au, Fe_3Al etc. The formation of an ordered solid solution is accompanied by a sharp fall in electrical resistivity and a sharp increase in hardness and strength.

The 'order-disorder' compounds are regarded as intermediate phase between solid solutions and chemical compounds. Much work has been done on these alloys (Warlimont 1974), including the correlation between their mechanical properties (in particular, the strength) and their electronic structure. Experimentally, correlations are found between a typical strength attribute, namely, hardness, and the so-called short-range-order (SRO) parameter, which is related to the ordering energy $V(k)$. The SRO parameter can be determined from diffuse x-ray scattering measurements, as in these measurements one really probes the chemical nature of the nearest neighbours of an atom, and thus the SRO. Interesting Fermi surface effects giving rise to satellites in the diffuse x-ray scattering have been seen (Scattergood *et al* 1970), and thus the SRO and the Fermi surface effects in these compounds can be imagined to be related. If only the connection between any elastic constant (or any other suitable strength attribute) and the SRO parameter, can be established, the correlation between the strength and electronic structure in this mode of strengthening can be understood. This last step constitutes the lacuna in this area of investigation.

7. Summary

Elucidating the physical basis of one of the important mechanical attributes of a solid, namely, its strength, continues to be a challenging problem. Much success has, no doubt been achieved using the dislocation idea. We have examined the problem of understanding the strength of a crystalline solid on the basis of its electronic properties. The attempts that have been made so far adopted the view that cleavage can be regarded as the exact opposite of cohesion. This enables one to use in full the electronic theory of the cohesion of solids. The strength values calculated on this assumption agree by and large with the limited experimental values available. However, as pointed out in §3, there is an order of magnitude difference between the calculated and measured strains at failure. Also, it is true that the way the unit cell is assumed to deform in calculating the strength is not realistic. There is scope for refinements here, both in terms of allowing for more realistic deformations as well as extending the calculation to non-cubic symmetries of the unit cell. Nevertheless, it appears that as far as the problem of cleavage is concerned, well-known dislocation mechanisms and dislocation-crack-tip interactions are adequate to account for the strength of materials. The electronic theory (in the form of a phase shift analysis) meets with reasonable success when applied to the solution-strengthening problem. Systematic measurements of the elastic constants of sequences of alloys with, say, titanium as the host metal will be valuable. In the case of order-disorder compounds, an analysis of the relationship between the short-range-order parameter and the elastic constants (and thus the strength) would be very desirable. We have not commented in this article on the possible correlations that may exist between the electronic structure and the other strengthening mechanisms listed in §6.

Acknowledgement

The author thanks Dr G Venkataraman for suggesting this problem.

References

Beachem C D 1978 in *Proceedings of the Second International Conference on Mechanical Behaviour of Materials* (Ohio, Metals Park, ASM) 322ff
Brenner S S 1956 *J. Appl. Phys.* **27** 1484
Brookes C A 1981 *Philos. Mag.* **A43** 529
Carlson A E, Gelatt C D and Ehrenreich H 1980 *Philos. Mag.* **A41** 241
Collings E W and Gegel H L 1975 *Physics of solid solution strengthening* (New York: Plenum Press)
Conrad H 1981 *Prog. Mater. Sci.* **26** 2
Esposito E, Carlsson D D, Ehrenreich H and Gelatt C D (Jr) 1980 *Philos. Mag.* **A41** 251
Gerk A P and Tabor D 1978 *Nature (London)* **271** 732
Gilman J J 1969 *Micromechanics of flow in solids* (New York: McGraw Hill)
Gilman J J 1973 *J. Appl. Phys.* **44** 982
Hall E O 1970 *Yield phenomena in metals and alloys* (London: Macmillan and Co.)
Harrison W 1966 *Pseudopotentials in the theory of metals* (Massachussetts: Benjamin Inc.)
Havner K S 1979 *J. Mech. Phys. Solids* **27** 393
Kelly A 1973 *Strong solids* (Oxford: Clarendon Press)
Macmillan N H 1972 *J. Mater. Sci.* **7** 239
McQueen R G and Marsh S P 1962 *J. Appl. Phys.* **33** 654
Milstein F 1982 in *Mechanics of solids* (eds) H G Hopkins and M J Sewell (Oxford: Pergamon Press) 417ff
O'Neill H 1967 *Hardness measurement of metals and alloys* (London: Chapman and Hall)
Peckner D 1967 *The strengthening of metals* (New York: Reinhold Publishing Co.)
Scattergood R O, Moss S C and Bever M B 1970 *Acta Metall.* **18** 1087
Stern E A 1975 in Collings and Gegel (1975)
Warlimont H 1974 *Order-disorder transformations in alloys* (Berlin: Springer-Verlag)
Watts B K 1979 *J. Phys.* **F9** 1565
Westbrook J H and Conrad H 1973 *The science of hardness testing and its research applications* (Ohio, Metals Park, ASM)
Wilkes P 1973 *Solid state theory in metallurgy* (London: Cambridge University Press)

Discussion

K R Rao: Could you comment on the nature of the electronic systems you are considering and their relation to the strength of materials?

K Govinda Rajan: The kind of electrons being considered will be specified once the potential is specified. It may also be useful to think in terms of electron charge densities around ion cores and their distortion during loading to understand strength phenomena.

A P Pathak: Instead of talking about the "effects of electronic structure on strength", it appears to be preferable to consider the *correlation* of electronic and mechanical properties. After all, all cohesion in solids is due to electronic structure (either orbital core electrons or conduction/valence electrons), and strength must necessarily be due entirely to electronic structure. Evidently the strength does not depend simply or directly upon, say, the band gap or the conduction electron density (as do the electrical properties), but on combinations of these properties, the core electrons, and of course the structure of the solid. Would you like to comment on this?

Govinda Rajan: In the exhaustive review by K A Gschneider (Solid State Physics, Vol. 16), one finds graphs of electronic properties (resistivity, valence electrons per atom, etc.) *vs* mechanical properties (yield strength hardness) for elemental metals. No significant microscopic picture, however, has emerged. What I have attempted instead is to identify—from the plethora of mechanical properties—the "strength" attribute, and to discuss the role of electronic structure in this context. This is because the strength parameter is, in a sense, the final stage of the mechanical response of a solid, and thus should be amenable to simple calculations. Even this view in which, for instance, cleavage is imagined to be the exact opposite of cohesion has met with serious objection from the metallurgists, as I have taken care to point out

G Venkataraman: It might be interesting to measure the hardness of a semiconductor after pumping electrons into the conduction band by, say, using a laser. This would also have practical relevance to devices like GaAs diode lasers.

Bull. Mater. Sci., Vol. 6, No. 4, September 1984, pp. 733–753. © Printed in India.

Ferroelasticity

V K WADHAWAN

Neutron Physics Division, Bhabha Atomic Research Centre, Trombay, Bombay 400 085, India

Abstract. This paper surveys the present-day description of ferroelasticity in terms of the notion of symmetry descent. Based on the work of earlier authors, a symmetry classification of phase transitions is presented. A general classification of twinning in crystals is also attempted on the basis of this scheme. Most kinds of twinning fall into two broad categories: nonferroelastic and ferroelastic. The shape-memory effect associated with martensitic transitions is discussed briefly. The interesting possibilities of this effect in the case of ferroelectric ferroelastics, for which the electric field provides an additional control parameter, are also mentioned.

Keywords. Ferroelasticity; symmetry; phase transitions; twinning; ferroelectric ferroelastics.

1. Introduction

The elastic (or recoverable) response of a material to a small external stress can be nonlinear in general, although it is predominantly linear in a large number of crystalline substances, glass, and many cross-linked polymers. The elastic response is markedly nonlinear in cellular structures like wood and in "elastomers" like rubber, which consist of long, spaghetti-like, entwined molecules. The recoverable strain in materials of either the linear or the nonlinear type is usually a *single-valued* function of the small applied stress. There is, however, a technologically important class of materials for which the elastic response is neither linear nor single-valued. Ferroelastic materials belong to this class.

A good deal of our present understanding of ferroelastics has been obtained by considering them as the mechanical analogues of ferroelectric and ferromagnetic materials. In fact, the concept of ferroelasticity itself was introduced by direct analogy with ferroelectricity and ferromagnetism. In particular, one associates stress-strain hysteresis with a ferroelastic, which implies that the spontaneous strain is a double-valued function of stress, even for vanishingly small values of the stress (figure 1). The key to such mechanical behaviour lies in the domain structure of the ferroelastic. As we shall see, the most elegant and rational description of the domain structure of a crystal comes from considerations of broken symmetry at a real or hypothetical phase transition. A proper understanding of ferroelastic behaviour is hardly possible unless one pays attention to the ferroelastic phase transition.

The most significant factor contributing to this understanding has been the approach, initiated by Aizu (1970) and developed by a number of other workers, (Janovec *et al* 1975; Tolédano and Tolédano 1976, 1977, 1980, 1982), according to which ferroelastic phase transitions form part of the larger class of *ferroic phase transitions*: these are transitions which result in a change of the point-group symmetry of the crystal. A *ferroelastic* phase transition, by definition, entails not only a change of the

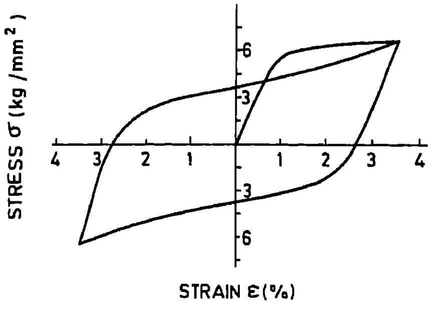

Figure 1. Stress-strain hysteresis curve for the ferroelastic $\beta' - Au_{26}Cu_{30}Zn_{44}$ martensite at 298 K (Nakanishi *et al* 1971).

point symmetry, but also a change of the crystal system (if we regard the hexagonal and trigonal crystal systems as a single system) (Tolédano and Tolédano 1980).

Ferroic behaviour of crystals encompasses not only ferroelasticity but also other, more subtle, types of mechanical properties like ferrobielasticity. Here I shall describe the salient features of the formalism of ferroicity, developed over the last decade and a half. It will be further argued that the notion of ferrocity also provides a very rational and fairly comprehensive description of the occurrence of twinning in crystals. Twinning, in its general sense, is a far more common feature of crystals than has been realized so far. Ferroelasticity itself is a type of mechanical twinning "with change in form" (Klassen-Neklyudova 1964).

2. Ferroelasticity

The term "ferroelasticity" has had a number of connotations, all similar, and yet not quite the same. It was first used in physical metallurgy by Frank in the early 1950's to describe the "rubber-like" memory effect in the gold-cadmium alloy (see Lieberman *et al* 1975). A piece of $Au_{1.05}Cd_{0.95}$ or InTl, when deformed severely (with up to 10% strain) at room temperature, exhibits almost complete crystallographic and morphological recovery when the external stress is removed. As has been pointed out by Lieberman *et al* (1975), there is a tendency in the literature to use the term "ferroelasticity" somewhat indiscriminately in this context. It is important to distinguish clearly between two situations for describing this pseudoelastic behaviour, depending on whether the deforming stress is applied just above the phase transition temperature T_c, or at temperatures below T_c. Figure 2 depicts the two cases schematically. The first case represents "pseudoelasticity by transformation", and the second "pseudoelasticity by reorientation" (Warlimont 1976). In the first case the crystal is initially in the parent phase and the application of a deforming stress causes a reversible stress-induced phase transition. When the stress is removed, all parts of the specimen revert to the parent phase. This behaviour is also described as *superelasticity* (Wasilewski 1975; Barrett and Massalski 1980), or *martensitic thermoelasticity* (Lieberman *et al* 1975). But it must not be called ferroelasticity. Ferroelastic response does not involve any phase transition. Pseudoelastic recovery by reorientation, depicted on the right in figure 2, does correspond to ferroelasticity (Liberman *et al* 1975). The material is already in the lower-temperature, or ferroelastic phase. It is also capable of existing in more than one twin state or domain. The rubber-like pseudoelastic behaviour results from the reversible migration of the twin boundaries or

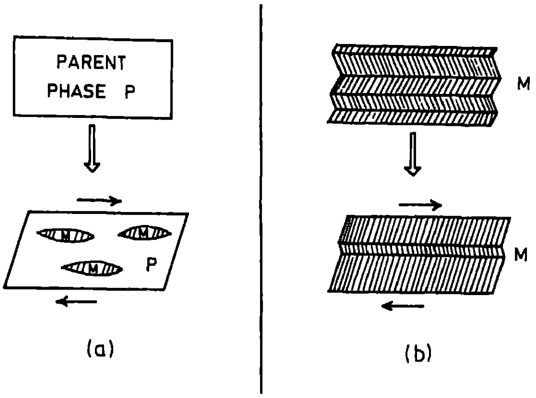

Figure 2. (**a**) Pseudoelasticity by transformation (or superelasticity), and (**b**) pseudoelasticity by reorientation (or ferroelasticity).

domain walls. This property is also referred to as *piezomorphic memory* by Lieberman *et al* (1975). As we shall see presently, shape recovery or memory is not regarded by physicists as an essential feature of ferroelasticity; the shape recovery at temperatures below T_c results from a volume-dependent restoring force, which may not always be present in a ferroelastic crystal.

The stress-assisted double phase transition in TiNi also leads to a mechanical response which resembles ferroelasticity (Wasilewski 1975). However, in keeping with the usage in the rest of physics, the term "ferroelastic" should not be used for those switching phenomena which involve a stress-assisted or any other kind of *phase transition.*

The term "ferroelasticity" was introduced in 1969 (Alefeld *et al* 1969; Aizu 1969) and was used in quite different contexts. Alefeld and coworkers (see Alefeld 1971) were dealing with the problem of hydrogen and other point defects in metals like Nb and Pd, whereas Aizu viewed ferroelastic behaviour as resulting from the occurrence of domain structure (or "orientation states"), taking no note of the presence of any defects in the crystal. We first consider the question of hydrogen or other interstitial impurities in crystals in brief, followed by an exposition of Aizu's approach and its subsequent development by other workers.

Hydrogen occupies interstitial sites in metals and causes a displacement of the surrounding metal atoms, thus creating local strain fields, as well as a net macroscopic strain. Point defects like hydrogen which distort the host lattice are called *elastic dipoles* (see, *e.g.* Peisl 1978). In general the distortion may be anisotropic and one needs a second-rank polar tensor, (ε_{ij}^{d}), to describe the strain field around a defect. If a uniaxial stress is applied to such a system, a stress-induced diffusion of the interstitial defects to neighbouring sites occurs, resulting in a reorientation of the anisotropic elastic dipoles (figure 3). This time-dependent or anelastic relaxation is known as the *Snoek effect.* Obviously, a stress-strain hysteresis loop looking like the ferroelastic curve of figure 1, will result from such a process. If the defects are highly mobile, one observes the so-called *Gorsky relaxation*, in which the directed diffusion of the defects over many lattice distances occurs under a stress *gradient.* The strain field created by an elastic dipole is long-ranged and is felt by the other elastic dipoles in the metal. This "elastic interaction" is believed to be largely responsible for the $\alpha \rightarrow \alpha'$ phase transition in the H-Nb and H-Pd systems (see Wagner 1978). The reason is that Landau's mean field theory works well for this phase transition and it is known that this theory is good for transitions driven by long-range interactions.

Clearly, ferroelastic behaviour resulting from the presence of point defects will disappear in the absence of these defects. This is where Aizu's concept of ferroelasticity differs from that of Alefeld *et al.* In the former, ferroelastic properties arise from the pseudosymmetry resulting from a (real or hypothetical) structural phase transition, and not from the presence of defects. The concept of a *prototype symmetry* plays a central role here. The prototype is the highest supergroup symmetry attainable by, or conceivable for, a given crystal without requiring a rupture or reconstructive rearrangement of chemical bonds. A ferroelastic phase (more generally, a ferroic phase) emerges from the prototype symmetry owing to a small, spontaneous, symmetry-breaking "distortion" when some control parameter such as the temperature is varied. Figure 4 provides an illustration of this, where an orthorhombic symmetry *mmm* (D_{2h}) is assumed for the prototype. A phase transition to monoclinic symmetry can lead to two possible *orientation states*, S_1 and S_2, both of which are equally stable in the absence of an external force. Although the actual symmetry of the ferroelastic phase is monoclinic, it is also pseudo-orthorhombic because it differs only slightly from the prototype configuration. Since the two states S_1 and S_2 also differ only slightly from each other, it should be possible to switch S_1 to S_2 and *vice versa* by applying a small, suitably oriented, uniaxial stress, as shown in the lower part of figure 4. This possibility of the occurrence of more than one orientation state, (*i.e.*, the presence of domain structure), is what is responsible for ferroelastic behaviour, in particular the stress-strain hysteresis. Aizu (1969) defined a ferroelastic as a crystal which has two or more equally stable

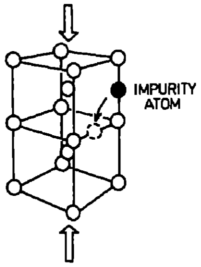

Figure 3. Stress-induced diffusion of an interstitial impurity (Snoek effect).

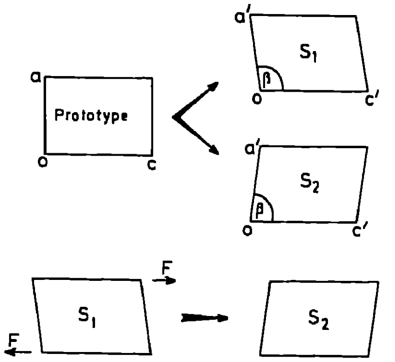

Figure 4. Schematic of an orthorhombic-to-monoclinic ferroelastic phase transition, giving two equivalent orientation states S_1 and S_2 in the lower-symmetry phase.

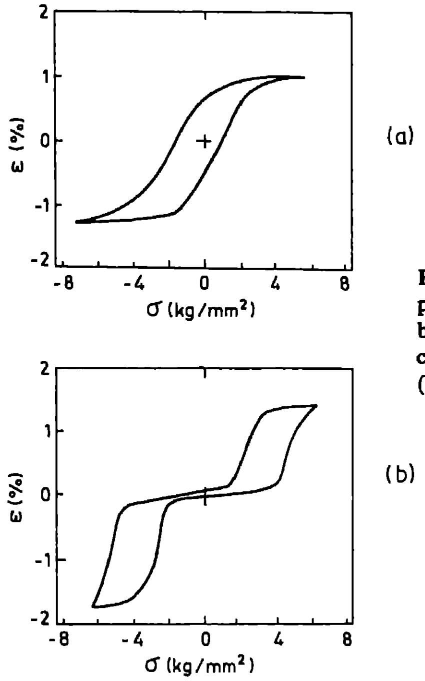

Figure 5. Illustrating the distinction made in physical metallurgy between (a) ferroplastic behaviour and (b) ferroelastic behaviour. The curves shown are for the alloy $Au_{1.05}Cd_{0.95}$ (Lieberman *et al* 1975).

orientation states, and which can be switched from one such state to another by the application of a suitable uniaxial stress. Since all the orientation states are equally stable, the system may not bounce back to the initial state when the stress is removed. It is clear from the above definition that what is called ferroelasticity by Aizu would be described as *ferroplasticity* by physical metallurgists (see Lieberman *et al* 1975). The distinction between ferroelastic and ferroplastic behaviour is illustrated in figure 5 for a gold-cadmium alloy. Very often this distinction is not made in physics, because the term "ferroelastic" is used to imply "ferromechanical", in the sense that the driving force conjugate to the 'order parameter' (strain) is mechanical or elastic in nature (and not electric or magnetic).

Aizu's definition of ferroelasticity also supersedes the earlier usage of this word in physics for describing magnetostrictive and electrostrictive distortions in ferromagnetic and ferroelectric crystals. It is possible for a crystal to be ferroelastic without also being ferroelectric or ferromagnetic. The present concept of ferroelasticity has led to the development of an elegant, symmetry-based, classification of a very large class of phase transitions, and we turn now to an outline of this scheme.

3. A symmetry classification of phase transitions in crystals

Figure 6 presents a symmetry classification of phase transitions in crystals based on the work of various authors (Tolédano and Tolédano 1982 and references therein). We exclude from this scheme reconstructive phase transitions like the graphite-to-diamond transition. We also exclude those martensitic and other phase transitions where the lattice distortion is so drastic that it results in a change of coordination number. An example of this is the transition occurring in CsCl, where the structure changes from

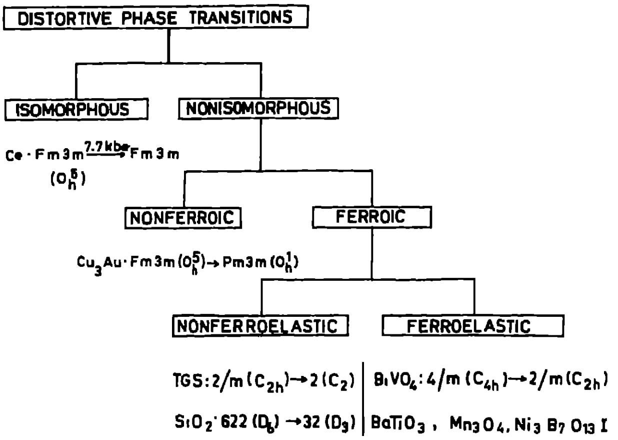
DISTORTIVE PHASE TRANSITIONS
ISOMORPHOUS
NONISOMORPHOUS
Ce · Fm3m $\xrightarrow{7.7\,\text{kbar}}$ Fm3m
(O_h^5)
NONFERROIC
FERROIC
Cu_3Au · Fm3m (O_h^5) → Pm3m (O_h^1)
NONFERROELASTIC
FERROELASTIC
TGS: 2/m (C_{2h}) → 2 (C_2)
SiO_2 · 622 (D_6) → 32 (D_3)
$BiVO_4$: 4/m (C_{4h}) → 2/m (C_{2h})
$BaTiO_3$, Mn_3O_4, $Ni_3B_7O_{13}I$

Figure 6. A classification of phase transitions based on considerations of symmetry descent from a prototype symmetry.

simple cubic to fcc on heating through the phase transition at 733 K, resulting in a change of the coordination number from 8 to 6.

We use the term *distortive* for the phase transitions considered in figure 6, although even this term is not entirely adequate. It is intended to cover both displacive and order-disorder phase transitions (Muller 1981). The term "group-subgroup type phase transitions" would be perhaps more appropriate if we remember that a group permits the trivial possibility of being its own subgroup or supergroup. In this scheme, all phases of a crystal are regarded as derived from a certain supergroup symmetry called the *prototype* (Aizu 1981). The prototype is the highest conceivable crystallographic symmetry from which a given phase can result by a small distortion. Phase transitions in this classification are therefore not always between two consecutive phases, but between the prototype and the phase under consideration. All phase transitions in crystals can be divided into two categories: *isomorphous phase transitions and nonisomorphous phase transitions*. In the former, there is no change in the space-group symmetry of the crystal. A well-known example is the transition occurring in Ce at a pressure of 7·7 kbar (0·77 GPa), involving a volume collapse of about 14 %, but leaving the space-group symmetry unchanged as *Fm*3*m* (O_h^5). The change of space-group symmetry at a nonisomorphous phase transition can be of two types: *nonferroic* and *ferroic*. In a nonferroic phase transition there is a change in only the translational symmetry, but no change in the point-group symmetry (Tolédano and Tolédano 1982). Perhaps the best known example of this type is the order-disorder transition occurring in the alloy Cu_3Au at 667 K, where the symmetry changes from *Fm*3*m* (O_h^5) to *Pm*3*m* (O_h^1). The high pressure transition occurring in EuS at 215 kbar (21·5 GPa) is another example, involving the same symmetry change as Cu_3Au. Ferroic phase transitions involve a change of the point-group symmetry with or without a change of the translational symmetry. If there is a change of the point-group symmetry but no change of the crystal system (provided we do not regard the hexagonal and trigonal crystal systems as distinct for the purposes of this definition), the phase transition is defined as *nonferroelastic* (Tolédano and Tolédano 1976). Examples of nonferroelastic transitions include the ferroelectric transition in triglycine sulphate (symmetry changing from

$2/m(C_{2h})$ to $2(C_2)$), and the $\beta \to \alpha$ transition in quartz (symmetry changing from $622(D_6)$ to $32(D_3)$). With the above proviso about hexagonal and trigonal crystal systems, a change of crystal system becomes a necessary as well as a sufficient condition for a phase transition to be called *ferroelastic* (Tolédano and Tolédano 1980). A ferroelastic phase transition may be either purely ferroelastic, as in $BiVO_4$, or it may be simultaneously ferroelectric as in $BaTiO_3$, or simultaneously ferromagnetic as in Mn_3O_4. The Ni-I boracite undergoes a phase transition which is simultaneously ferroelastic, ferroelectric and ferromagnetic.

I have recently come across a statement by Fleury and Lyons (1981) according to which a centre of symmetry is always preserved across a ferroelastic phase transition. The rationale behind this statement is not entirely clear; in the cubic-to-tetragonal phase transition in $BaTiO_3$, for example, the centre of symmetry is not preserved even though the phase transition is ferroelastic; the fact that the order parameter of this transition does not have the symmetry of a strain component does not preclude the occurrence of ferroelasticity in the tetragonal and the other lower-symmetry phases of $BaTiO_3$ (see also Aizu 1972a).

4. Ferroic crystals

A ferroic crystal is one which can undergo a ferroic phase transition. The definition of a ferroic transition in terms of a change in the point-group symmetry has a deep significance. Among other things, it enables us to classify ferroic crystals in terms of their macroscopic physical properties like polarization, strain, etc. The reason for this is that these properties are described by the point group symmetry of the crystal, and a ferroic phase is derived, by definition, by deleting certain point-group operations of the prototype. The lowering of the point symmetry at a ferroic phase transition must necessarily be accompanied by the emergence of at least one new macroscopic tensor property component. If this component also has the symmetry of the order parameter, the corresponding response function becomes anomalously large in the vicinity of the transition. This is important in many of the device applications of ferroic crystals.

Let us imagine a crystal in a particular orientation state S_1, under the influence of an external electric field (E_i), a magnetic field (H_i) and a stress (σ_{ij}). The free energy density for this orientation state can be written as

$$d\Phi = S dT - P_i dE_i - M_i dH_i - \varepsilon_{ij}\, d\sigma_{ij}, \tag{1}$$

where S denotes the entropy, P_i the polarization, M_i the magnetization, and ε_{ij} the strain. P_i, M_i and ε_{ij} consist of a spontaneous part (if any) and an induced part owing to the presence of the external fields. One can integrate (1) to obtain the free-energy density Φ_1 for state S_1. Similarly, the free-energy density Φ_2 can be obtained for another orientation state S_2. The difference $\Delta\Phi = \Phi_2 - \Phi_1$ determines whether the crystal makes a state shift from S_1 to S_2, or vice versa under the action of the external forces. The final expression for $\Delta\Phi$ can be written as follows (see Wadhawan 1982 for details):

$$\begin{aligned} -\Delta\Phi = {} & \Delta P_i^0 E_i + \Delta M_i^0 H_i + \Delta\varepsilon_{ij}^0 \sigma_{ij} + \tfrac{1}{2}\Delta\kappa_{ij} E_i E_j + \tfrac{1}{2}\Delta\chi_{ij} H_i H_j \\ & + \tfrac{1}{2}\Delta s_{ijkl}\, \sigma_{ij}\sigma_{kl} + \Delta\alpha_{ij} E_i H_j + \Delta d_{ijk} E_i \sigma_{jk} + \Delta Q_{ijk} H_i \sigma_{jk} \\ & + \tfrac{1}{6}\Delta e_{ijk} E_i E_j E_k + \ \ldots \end{aligned} \tag{2}$$

Here $\Delta P_i^0 = P_{2i}^0 - P_{1i}^0$ is the difference between the values of the *i*th component of the spontaneous polarization in the states S_2 and S_1. The other difference terms are defined similarly. κ_{ij}, χ_{ij} and s_{ijkl} are, respectively, the elements of the electric susceptibility tensor, the magnetic susceptibility tensor, and the compliance tensor. α_{ij}, d_{ijk} and Q_{ijk} are elements of the magnetoelectric, piezoelectric and piezomagnetic tensors respectively, and e_{ijk} stands for the components of the third-order electric susceptibility tensor. Equation (2) serves to define the various types of ferroic crystals. A ferroelectric crystal is defined as one for which at least one pair of orientation states exists such that $\Delta P_i^0 \neq 0$ for one or more values of *i*. Similarly, a ferroelastic crystal is one for which $\Delta \varepsilon_{ij}^0 \neq 0$ for at least one pair of orientation states. A ferromagnetic crystal is defined similarly. Ferroelectric, ferroelastic and ferromagnetic crystals are collectively called *primary ferroics*.

It is clear from (2) that other types of ferroicity are also possible. For example, if $\Delta s_{ijkl} \neq 0$ for one or more pairs of orientation states, the crystal is said to be a *ferrobielastic*. Quartz is a well-known example of a ferrobielastic crystal. The Dauphiné twins of α-quartz differ in the sign of the elastic compliance coefficient s_{1123} (as well as in the signs of other symmetry-related coefficients). Consequently, although the two twin states do not differ in spontaneous strain (and therefore quartz is not a ferroelastic), a difference in *induced* strain can be established between them under the action of a common uniaxial stress. A suitable stress can then act on this difference to cause switching from one twin state to the other. Lead germanate, $Pb_5Ge_3O_{11}$, is another crystal which can be expected to exhibit ferrobielastic and ferroelectric switching concomitantly. Hence, for applied stresses smaller than the elastic limit, crystals may exhibit elastic, ferroelastic and ferrobielastic (figure 7) mechanical response, or any combination of these.

Still other types of ferroic behaviour can be anticipated from (2). Differences in the piezoelectric tensor between two orientation states can result in *ferroelastoelectric* switching under the *combined* action of an electric field and a uniaxial stress. In an analogous manner, *ferromagnetoelastic* switching becomes possible through differences in the piezomagnetic tensor, and so on. Ferrobielasticity ($\Delta\Phi \sim \sigma^2$), ferrobielectricity ($\Delta\Phi \sim E^2$), ferrobimagnetism ($\Delta\Phi \sim H^2$), ferroelastoelectricity ($\Delta\Phi \sim \sigma E$), ferromagnetoelasticity ($\Delta\Phi \sim \sigma H$) and ferromagnetoelectricity ($\Delta\Phi \sim HE$) are the six types of *secondary ferrocity* possible in crystals (Aizu 1972a, 1973). Aizu (1970) has derived 773 possible "species" of ferroic crystals (a species is characterized by the point symmetry of the prototype and the point symmetry of the ferroic phase in question) by assuming that: (a) every time-symmetric point group can become the prototypic point group in some species of ferroic crystal; (b) when a prototypic point group is specified, every one of its proper subgroups can become the ferroic point group in some species with this prototypic point group; and (c) when a

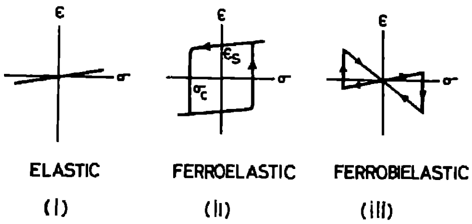

Figure 7. Typical curves illustrating the distinction between elastic, ferroelastic, and ferrobielastic response of crystals to external stress.

prototypic and a ferroic point group are specified, as many species are possible as the number of different ways in which the elements of the ferroic point group can be put in correspondence with the elements of the prototypic point group.

5. Domain structure

The mechanical behaviour of a ferroelastic is influenced in a crucial way by its domain structure. In fact, many of the applications of ferroelastics and other ferroic crystals depend on our ability to control the nucleation and mobility of their domain walls. The fracture-toughness achieved in zirconia by exploiting the ferroelastic phase transition is a case in point. A surprisingly large amount of information about the expected domain structure of a crystal can be obtained from symmetry considerations alone. Two or more domains or twin configurations become possible in a crystal because of the lowering of the prototype symmetry at a real or hypothetical phase transition. Regions of the crystal which were completely equivalent under the operations of the prototype symmetry group become nonequivalent either with respect to orientation, or with respect to mutual disposition, or both; this is what gives a crystal its domain structure.

In the spirit of the Landau theory, one holds the emergence of an order parameter responsible for the lowering of the prototype symmetry. The symmetry G of the daughter phase is determined by the symmetry G_0 of the prototype and the symmetry Γ of the order parameter. G can be obtained by the principle of superposition of symmetries, commonly known as the *Curie principle* (see Kopstik 1968). Shubnikov and Kopstik (1974) have stated a more updated version of it and called it the Neumann-Minnigerode-Curie principle, (NMC) principle. According to the Curie principle: "When several different natural phenomena are superimposed on one another, forming a single system, their *dissymetries* add up. As a result, only those elements of symmetry common to all the phenomena remain". If, for example, G_1 and G_2 denote the symmetry groups corresponding to two physical properties of a crystal, the symmetry G of the crystal cannot be higher than the intersection of G_1 and G_2. If we consider the symmetry groups G_i, $i = 1, 2, 3, \ldots$, of all possible physical properties of the crystal, the symmetry G of the crystal is given by the intersection of all these groups:

$$G = G_1 \cap G_2 \cap G_3 \ldots = \overset{i}{\cap} G_i \tag{3}$$

The more familiar Neumann's principle follows from the above as an inclusion relation:

$$G_i \supseteq G. \tag{4}$$

In other words, the symmetry element (G_i) of any physical property of a crystal include all the symmetry elements (G) of the crystal. G is contained in every G_i; in fact, it is a subgroup of every G_i. Equations (3) and (4) can be combined (Shubnikov and Kopstik 1974) to read

$$G_i \supseteq G = \overset{i}{\cap} G_i \tag{5}$$

In the context of a phase transition accompanied by the emergence of an order parameter having the symmetry group Γ, it follows that the symmetry group G of the resultant phase is given by

$$G = G_0 \cap \Gamma, \tag{6}$$

where G_0 is the symmetry group of the disordered phase. G is that maximal subgroup of G_0 which leaves the order parameter invariant (Janovec 1972).

The Curie principle can be applied not only to determine the compatibility or incompatibility of G, G_0 and Γ, but also to understand inter-domain relationships. Suppose a crystal undergoes a phase transition from symmetry G_0 to G on cooling, (that is, under the influence of a scalar control parameter, T); it follows that, in the lower-temperature phase, the macroscopic symmetry of the sample crystal *as a whole* would be the intersection of G_0 and the symmetry group of a scalar. The intersection of these two is G_0 itself. Thus, macroscopically speaking, the crystal *as a whole* has an average symmetry G_0 even in the daughter phase. But the microscopic symmetry has actually been reduced from G_0 to G. The two statements, taken together, imply that the crystal must split into domains in the lower phase. It also follows that, since the symmetry group of each domain is G, transformation operations which can map one domain to another are those which are *lost* at the phase transitions (Janovec 1976). These are called *Φ-operations* (Aizu 1974). In particular, mirror planes of symmetry lost at a phase transition can become domain walls separating two contiguous domains of the lower phase (Mallard's law). To quote Shubnikov and Kopstik (1974): "The whole process of a phase transition obeys the astonishing law discovered by philosophers—*the symmetry compensation law*: If symmetry is reduced at one structural level, it arises and is preserved at another!"

Let G_0' and G' denote the point groups of the space groups G_0 and G respectively. If n_p and n_f are the orders of the groups G_0' and G', the maximum possible number of orientation states or rotational domains possible in the ferroic phase is given by (Aizu 1970; Janovec 1972) $q' = n_p/n_f$. Any operation which is a symmetry operation of G_0', but not that of G', is called an *F-operation*. An F-operation maps one orientation state to another. Choosing a common reference frame for all the orientation states, if G' is the point group for a particular orientation state S_1 and f is any F-operation from S_1 to another orientation state S_1', the set of all F-operations from S_1 to S_1' is equal to fG' (Aizu 1970; Janovec 1972). The point group G_0' can be split into a sum of q' left cosets of the subgroup G':

$$G_0' = f_1G' + f_2G' + \dots + f_{q'}G'. \tag{7}$$

Here a coset f_rG' comprises all operations mapping the domain S_1 to the domain S_r. There is a one-to-one correspondence between domains and left cosets. Extending the above considerations from point groups to space groups, if G is a subgroup of G_0 of index q, G_0 can be written as a sum of left cosets as follows

$$G_0 = \phi_1G + \phi_2G + \dots + \phi_qG. \tag{8}$$

Once again, there is a one-to-one correspondence between a left coset and a possible structural configuration called a *situation* or a *terrain* (Aizu 1974). The ϕ's are a representative set of Φ-operations from a particular situation to each of the q situations.

A single domain may consist of one or more terrains, but a uniterrain sample is necessarily unidomain also. The possible occurrence of more than one terrain in a domain is referred to as *domain degeneracy* (Janovec 1976). It can be determined with the help of *Hermann's theorem* (Hermann 1929), according to which, if G is a subgroup of a space group G_0, then one can always find a space group Z which contains G as a klassengleiche or equipoint-group subgroup, and which is also a maximal equitranslational subgroup of G_0 ($G \subseteq Z \subseteq G_0$). The index of Z in G_0 is also equal to $q' (= n_p/n_f)$. The number of terrains (also called translational domains or antiphase domains) possible in each (rotational) domain is given by the index m of G in Z. The domain degeneracy is m. It is also equal to the number of times by which the volume of the primitive unit cell of the daughter phase is nominally larger than that of the primitive cell of the prototype. The total number of situations, q, is related to the number of orientation states, q', through m:

$$q = q'm. \tag{9}$$

The fact that q is a finite number is a consequence of the discrete nature of crystallographic space groups. If the prototype symmetry G_0 is described only by a continuous symmetry group, the symmetry group G of the ordered phase may have an infinite index q. In such a case the domain structure is replaced by its dynamical counterpart, namely the occurrence of *Goldstone modes*, which are gapless excitations that tend to restore the prototype symmetry (Janovec 1976).

6. An unsolved problem of ferroelasticity

The elegant and powerful group-theoretical formalism developed by physicists for describing ferroelastic and other forms of ferroic switching in crystals in a unified way is not without a flaw. This was first pointed out by Laves (1975) by citing the example of mechanical twinning in hcp metals like Mg. Such metals have a point-group symmetry $6/mmm$ (D_{6h}), and apparently undergo ferroelastic switching by shearing along the planes $\{1\ 0\ \bar{1}\ 2\}$ in the directions $\langle\bar{1}\ 0\ 1\ 1\rangle$. This type of mechanical twinning results in a large reorientation (by 84°) of the slip plane (0001), and has a drastic influence on the plastic behaviour of these metals (Klassen–Neklyudova 1964). But this apparently ferroelastic twinning does not come within Aizu's formalism because it is not possible to conceive a *crystallographic* prototype symmetry, of which the symmetry $6/mmm$ of the ferroelastic phase is a subgroup.

Aizu (1970) gave a precise definition of prototype symmetry by demanding that the following two conditions be satisfied: (a) The point-group symmetry of the prototype should contain all the F-operations from each of the orientation states of the ferroic to all orientation states. (b) If any symmetry operation of the prototype point group is performed on any orientation state, the result must only be one of the possible orientation states, and none other.

The prototype group is also a proper supergroup of the ferroic point group. The example of Mg seems to indicate that ferroelasticity can also occur in materials with a symmetry such that only a subgroup of this symmetry is a subgroup of the prototype symmetry (Laves 1975). If a relaxing of the definition of a prototype is allowed so as to accommodate such a possibility, the prototype would not always contain *all* the symmetry elements of the point group of the ferroelastic phase. Such a modification of the theory does not look very appealing, particularly because it negates a good deal of the elegant description of domain structure of ferroelastic and other ferroic crystals (§ 5). It also goes against the spirit of the Landau theory of phase transitions. No really good solution of this problem is available at present.

7. Twinning

Before the development of x-ray crystallography, the classification of twinning in crystals was based mainly on morphological studies made by contact goniometry and optical goniometry (Friedel 1926). X-ray diffraction patterns, particularly those obtained with Buerger's precession camera, give us directly a picture of the reciprocal lattice of a twinned crystal. This has led to what may be called the second stage in the classification of twinning (Donnay and Donnay 1974). All twinned crystals are divided into two categories, depending on whether the diffraction pattern reveals a single orientation of the reciprocal lattice for the twins ("obliquity" $\omega = 0$), or two or more orientations with a common origin ($\omega \neq 0$). In the first case one talks of *twinning by twin-lattice symmetry* (TLS), and in the second case *twinning by twin-lattice quasi-symmetry* (TLQS). A further subdivision of each of these main categories is made in terms of the *twin index n*, defined as the ratio of the volume per node in twin lattice to the volume per node in crystal lattice. The twin lattice is the lattice with the smallest cell that is common to both members of the pair. The twin lattice is perfectly continuous across the twin wall for $\omega = 0$, but has a small deviation at the wall when $\omega \neq 0$. Twinning by TLS and by TLQS is also called, respectively, "twinning without change of form" and "twinning with change of form" (Klassen-Neklyudova 1964).

This description of twinning concerns itself mainly with geometrical features like orientational relationships of the lattices. Although many crystallographers have indeed dealt with twinning at the structural level, the descriptive terminology available at present does not make evident certain features such as electrical twinning in a ferroelectric crystal, or more subtle effects like differences in the piezoelectric tensor in the twin structure of a crystal like NH_4Cl. I think a stage has now been reached where a more comprehensive and informative classification of twinning can be made in terms of the ideas of symmetry descent discussed in §§3 and 5. We shall use the word "twinning" in a very general sense here, covering all electric, magnetic, elastic or other forms of domain structure possible in a crystal.

Twinning in a crystal implies that the structure can exist in two or more configurations that are energetically equivalent, but differ in mutual orientation, or mutual disposition, or both. The enthalpy barrier for changing one configuration to the other across a twin wall may be either reasonably low (as in Dauphine twins in α-quartz), or it may be extremely high, even exceeding the breakdown field or the fracture strength (as in Brazil twins in quartz, and also many growth twins). In the former case, barring exceptions like magnesium (§6), an F- or Φ-operation derived from an appropriately assigned prototype symmetry should always be definable. In the latter case, there are two possibilities:

(a) The twins across the interface are lawfully related by an F- or Φ-operation, and the enthalpy barrier just happens to be high; (b) a proper F- or Φ-operation is not definable for mapping one twin into the other; this may happen when, for example, the crystal is in a prototypic phase, and not a ferroic phase (see Aizu 1981).

Thus all twinning can be divided into two types (I and II, say). Type I twins are related by an F- or Φ-operation, whereas type II twins are not. For type I twins a prototype symmetry is always conceivable. In many cases of this type, even if switching from one twin to the other is not possible at room temperature, it may become possible at temperatures sufficiently close to the transition temperature. In any case, demonstration of switching is neither a necessary nor a sufficient condition for assigning a twin to type I; It is necessary and sufficient that an F- or Φ-operation, derived from an appropriate prototype symmetry, is definable. In this scheme, twinning in magnesium will be classified as type II (§6). A better example of type II twinning is provided by Brazil twins in quartz. They are related by a mirror operation, which is not a part of the nmetry 622 (D_6) of β-quartz. The symmetry 622 is prototypic for the symmetry 32 $_3$) of α-quartz, which can consequently exist in two orientation states related by an operation that is a two-fold rotation about the optic axis (Wadhawan 1982). These two entation states are just the Dauphiné twins. Unless a prototypic symmetry higher n 622 can be conceived for this crystal (which is not possible because that would olve a drastic breaking and reassembling of the structure), Brazil twins do not nstitute domains or terrains in the sense discussed in §5. (The concept of the ototype has been discussed with great clarity by Aizu 1978, 1981.) .

For type I twins, a nonisomorphous phase transition to the prototypic phase either ually exists, or can be imagined. In $BaTiO_3$, for example, the cubic phase is ototypic to the tetragonal, trigonal and orthorhombic phases, whereas in $H_4)_2SO_4$ the hexagonal prototypic phase is hypothetical (Sawada *et al* 1976; also Dvorak 1978). A nonisomorphous phase transition can be either nonferroic or roic (figure 6). If it is nonferroic, twinning comprises antiphase domains only. About crystals undergoing nonferroic transitions have been listed by Tolédano and lédano (1982). This twinning is obviously of the TLS type, and the superlattice ections resulting from it lead to a smaller primitive unit cell in the reciprocal lattice. r ferroic crystals, twinning can occur either by TLS or by TLQS, depending on whether phase transition is nonferroelastic or ferroelastic (figure 6).

Nonferroelastic twinning

hough all nonferroelastic twinning will be dubbed as just twinning by TLS in the er scheme of classification, the advantage of the new scheme suggested here can be n from the fact that many further subdivisions are possible: We can have oelectric twinning (as in TGS, SbSI and $LiNbO_3$), ferrobielastic twinning (as in uartz), ferroelectric-ferrobielastic twinning (as in $Pb_5Ge_3O_{11}$), ferroelastoelectric nning (as in NH_4Cl, $CuCsCl_3$ and α-quartz), ferromagnetoelastic twinning (as in F_2, MNF_2 and $FeCO_3$), ferromagnetoelectric twinning (as in Cr_2O_3), and otrielastic twinning (as in $Cr_5(PO_4)_3Cl$ and the mineral elapsolite (K_2NaAlF_6)). ersion domains observed in $Fe_{36}Cr_{22-x}(Ti, Mo)_x$, γ-brass, δ-NiMo, lithium ferrite l Al_4Mo (Amelinckx 1976) also constitute a subclass of nonferroelastic twinning.

Nonferroelastic twinning may indeed occur in ferroelastic crystals, in the so-called *tial* ferroelastics, in which some twins are ferroelastically related and some are nferroelastically related. Examples of the latter are the antiparallel (180°) domains in and $BaTiO_3$. A partial ferroelastic is that for which $\Delta\varepsilon^0_{ij} = 0$ in (2) for at least one r (but not all pairs) of orientation states.

n extremely useful tabulation of the "orders" of state shifts in ferroic crystals has n given by Aizu (1972a). The same tabulation can provide a very informative basis defining the "order" of twinning in a ferroic crystal. For example, ferroelectric nning can be described as "first-order electrical twinning", and ferrobielastic nning as "second-order mechanical twinning".

LS twinning or zero-obliquity twinning has two subclasses: (i) *twinning by merohedry*, which the twin index $n = 1$, and (ii) *twinning by reticular merohedry*, for which $n > 1$. the second case n is usually equal to 3, and very rarely equal to 5 (Donnay and nnay 1974). For purposes of crystal structure determination, twinning by merohy presents some special problems. Various procedures have been suggested to dle these (Catti and Ferraris 1976; Rees 1982; Jameson 1982). Both Dauphiné and

Brazil twinning in α-quartz is described as twinning by merohedry in the old scheme of classification (Donnay and Donnay 1974), whereas, in the present scheme, Brazil twins are type II twins, while Dauphiné twins are type I ferrobielastic-ferroelastoelectric twins.

7.2 *Ferroelastic twinning*

This corresponds to twinning by TLQS in the old scheme. Only one further subdivision is made in the old classification: The twinning is said to be by *pseudomerohedry* if $n = 1$, and by *reticular pseudomerohedry* if $n > 1$ (Cahn 1954; Donnay and Donnay 1974). In the new scheme, the twinning is characterized as purely ferroelastic in $Pb_3(PO_4)_2$ and $BiVO_4$, ferroelectric-ferroelastic in $BaTiO_3$, ferromagnetic-ferroelastic in Mn_3O_4, and ferromagnetic-ferroelectric-ferroelastic in $Ni_3B_7O_{13}I$. The presence of any antiphase domains can also be adequately rationalized in terms of reduction of the translational symmetry of the prototype.

8. Ferroelastic phase transitions

Ferroelastic phase transitions are characterized by a change of the crystal system, subject to the proviso that hexagonal and trigonal crystal systems are not regarded as distinct for the purpose of defining ferroelastic transitions (§ 3). The lattice distortion responsible for the change of crystal system is embodied in the spontaneous strain accompanying such transitions.

8.1 *Proper ferroelastic transitions*

A further subdivision of these is sometimes made between *true-proper* and *pseudo-proper* ferroelastic transitions. For the former, the strain itself is the primary order parameter. For the latter, though the strain ε has the same symmetry as the order parameter Q, the order parameter is some other primary instability. In LaP_5O_{14}, for example, the driving force of the transition is an instability with respect to a Raman-active optical mode (Errandonea 1980). The strain arises because of a bilinear coupling term of the form $K_1 Q\varepsilon$. A typical Landau expansion of the free energy density in this case can be written as follows (Wadhawan 1982):

$$\Phi = \Phi_0 + \frac{a}{2}(T-T')Q^2 + \frac{b}{4}Q^4 + \frac{C_0}{2}\varepsilon^2 + \frac{B}{4}\varepsilon^4 + K_1 Q\varepsilon. \qquad (10)$$

The elastic stiffness coefficient goes to zero (that is, the response function corresponding to ε diverges) at the phase transition temperature T_c given by the equation

$$T_c - T' = K_1^2/aC_0. \qquad (11)$$

Here T' is the temperature at which the optical soft mode frequency *would* have gone to zero on cooling if the phase transition had not actually occurred at the higher temperature T_c. The distinction between true-proper and pseudoproper transitions disappears as $K_1 \to 0$. In any case most, if not all, proper ferroelastic transitions are of the pseudoproper type. Luthi and Rehwald (1981), who have listed a large number of them, make no distinction between the two types. Many other authors follow the same practice. The temperature shift ($T_c - T'$) can be as large as 160 K in LaP_5O_{14}, and 230 K in $BiVO_4$.

The Landau theory of phase transitions works well for systems for which the range of the interaction driving the phase transition is longer than the correlation length characterizing the critical fluctuations of the order parameter. The theory therefore provides a good description of proper ferroelastic transitions for which the critical fluctuations are the acoustic modes (Cowley 1976). (As already stated in § 2, the theory holds exactly also for the "ferroelastic" phase transitions in hydrogen-metal systems (Alefeld and Volkl 1978; Wagner 1978), the elastic interaction mediated via the distortion fields around interstitial hydrogen atoms being a long-ranged attractive interaction.)

8.2 *Improper ferroelastic transitions*

In these transitions, the spontaneous strain arises only as a secondary effect, through a nonlinear coupling with the order parameter. The Landau expansion therefore contains a coupling term proportional to $\varepsilon\eta^n$, where η is the order parameter modulus, and n is a finite integer called the *faintness index* (Aizu 1972b, c; Dvorak 1974). The spontaneous strain varies as the nth power of the order-parameter modulus, $\varepsilon_0 \sim \eta^n$. The higher the value of n, the smaller is the spontaneous strain. Since strain is no longer the order parameter, the elastic response function does not show very large anomalies at the phase transition. Barring a few exceptions, the Landau theory does not, in general, provide a good description of this class of ferroelastic phase transitions (Wadhawan 1982).

8.3 *Incommensurate phase transitions*

This fundamentally new class of phase transitions (new, that is, for nonmagnetic systems) is currently attracting a good deal of attention (Pynn 1979; Bak 1982). In the usual "commensurate" phase transitions, the pattern of static displacements of atoms in the lower-symmetry phase can be described by a frozen-in wave of wavevector **k**, which is a *rational* fraction of a prototype reciprocal-lattice vector **r*** along the same direction:

$$\mathbf{k} = (n_1/n_2)\mathbf{r}^*, \qquad (12)$$

where $n_1 = 0, \pm 1, \pm 2, \ldots$ and $n_2 = \pm 1, \pm 2, \ldots$. For example, for a "zone-centre" phase transition $n_1/n_2 = 0$, and for a "zone-boundary" phase transition it is equal to 1/2. In an incommensurate transition, **k** is an *irrational* fraction of **r***, so that no two atoms have the same static displacement. In other words, in the incommensurate phase no translational symmetry exists in the direction of **k**. Therefore, the notion of antiphase domains or translational domains discussed in §5 does not apply any more for this direction. However, the incommensurate phase still has a well-defined point-group symmetry and the concepts of rotational domains or orientation states and of F-operations between them are still relevant.

In incommensurate transitions no finite-order coupling between the order parameter and any macroscopic property such as the strain or polarization is possible in the Landau expansion (Riste 1978). Consequently, no spontaneous strain or polarization can appear in the incommensurate phase. Such a polarization or strain gets averaged out to zero because of the zero-energy phase modulation of the displacement pattern.

However, as the temperature of the incommensurate phase is lowered, a point is reached where a "lock-in" transition occurs, at which the fraction connecting **k** to **r*** becomes rational, and a finite-order nonlinear coupling between the order parameter and one or more macroscopic properties (each with a definite faintness index) can occur. The lock-in transition has been observed to be first-order in all the cases studied so far. The mechanical behaviour of a crystal near an incommensurate transition is influenced by the effect of the transition on its elastic constants. A number of studies of this have already been made, notably by ultrasonic techniques and include the following crystals listed by Luthi and Rehwald (1981): K_2SeO_4, Rb_2ZnCl_4, $(N(CH_3)_4)_2ZnCl_4$, $(NH_4)_2BeF_4$ and $K_2PbCu(NO_2)_6$.

It is pertinent to mention here a relatively new experimental technique, namely, γ-ray diffractometry (Schneider 1981) which is particularly well suited for studying ferroelastic phase transitions, and especially the critical behaviour of the order parameter. Because of the small wavelength involved ($\lambda = 0{\cdot}03$ Å usually), γ-ray diffractometry is a forward-scattering experiment (with scattering angles seldom exceeding 2°). The change $\Delta\theta$ in the Bragg angle is related to the change Δd in the interplanar d-spacing by equation

$$\Delta\theta = -(\Delta d/d)\tan\theta. \tag{13}$$

As θ is very small, it follows that changes in the d-spacings have a vanishingly small effect on the Bragg peak position, θ. Therefore, any significant shifts of the peak position in the "ω-scan" normally employed for recording the diffraction pattern can be attributed almost entirely to a tilting (reorientation) of the concerned lattice planes, with a negligible contribution from changes in their d-spacing. This is in marked contrast to the situation in conventional x-ray or neutron crystallography where in the back-scattering region ($\theta \simeq 90°$) normally preferred for lattice-parameter determination, $\Delta\theta$ is extremely sensitive to changes in the d-spacing. γ-ray diffractometry is therefore ideally suited for studying those phase transitions which entail spontaneous deformation of the crystal lattice, and the consequent tilting of the lattice planes. This is just what happens in ferroelastic phase transitions. The spectral width of the nuclear γ-rays used is extremely small ($\Delta\lambda/\lambda = 10^{-6}$ for the ^{198}Au source); this results in excellent angular resolution. A resolution of 1″ of arc can be achieved. Further, since the γ-rays are extremely penetrative, the presence of massive high-pressure cells, or elaborate arrangements for achieving a high degree of sample temperature control, do not present any serious problems. The technique looks very promising. Its applications in this direction have begun only recently (see Bastie and Bornarel 1979; Alkire and Yelon 1981).

9. The shape-memory effect

The shape-memory effect (SME) in alloys is associated with martensitic phase transitions, which are first order, diffusionless, structural phase transitions involving a distortion of the crystal lattice. Their closeness to ferroelastic phase transitions is obvious. The SME pertains to the shape recovery of a material on heating to a certain temperature, after it has been subjected to a deforming strain of as much as 10% at a lower temperature. As in pseudoelastic recovery (§ 2), two situations are possible for the "one-way" SME: by transformation or by reorientation (Warlimont 1976). In the former case, the deforming stress induces a phase transition to the martensitic phase, whereas in the latter case the material is already in the martensitic phase and the applied stress makes some domains grow at the cost of others. The shape recovery on heating in both cases involves a phase transition to the parent phase.

In a martensitic transition the parent and the martensitic phase coexist over a certain range of temperatures. For good shape recovery in the SME, it is necessary that the interface between the parent and the martensitic phases be created, annihilated or moved in a reversible manner. A number of conditions should be met for this (Nakanishi 1975; Wasilewski 1975). For example, plastic flow should not occur during deformation. Thus a high yield strength of the initial matrix is required. Also, the driving force required for the nucleation and/or growth of martensite plates should be low. The dominant term in the free energy barrier opposing the nucleation of martensite in the matrix can be written as $C\varepsilon_m^2$, where C is the relevant shear elastic constant of the matrix and ε_m is the effective martensitic strain. A low value of C would be favourable for the stress-induced nucleation of martensite, but it would also imply a lower yield strength. The optimization of these two requirements indicates that one should apply the deforming stress at a temperature close to M_f, the martensite finish temperature (Wasilewski 1975).

In a proper ferroelastic phase transition, some stiffness constant, or a combination of stiffness constants, necessarily tends to zero (§ 8). The presence of such a transition should therefore indicate the possibility of SME in the material (Nakanishi 1975).

Over the last few years, the Landau theory has been increasingly applied to martensitic transitions. The Landau theory was initially formulated for dealing with second-order phase transitions. Further, a Landau expansion like that of (10) presupposes that the order parameter is a slowly varying quantity. Martensitic transitions are first-order phase transitions. One has therefore to employ Devonshire's (1954) generalization of the Landau theory to deal with them. Further, a first-order transition normally exhibits thermal hysteresis. In the temperature range of the thermal hysteresis, the two phases coexist. In addition to this, there also are domain walls associated with the domain structure of the daughter phase. At the domain walls and in the coexistence range of T, the order parameter changes rapidly. This makes the usual Landau expansion of the free energy inadequate, and one must include terms involving the derivatives of the order parameter, in the spirit of Ginzburg's (1955, 1960) extension of the Landau theory.

For understanding the SME, one has to deal not only with the effect of temperature on the martensitic transition, but also that of stress. In fact, many workers believe that the SME is merely one of the manifestations of the effect of stress on a martensitic phase transition, the martensitic transition for systems exhibiting the SME being taken as just a first-order proper ferroelastic transition (Wasilewski 1975; Falk 1980). In other words, some suitably defined spontaneous strain can be taken as the order parameter of the transition. A very simple but fairly universal model Landau expansion of the free energy has been proposed by Falk (1980), which explains a large number of features in a whole group of alloys exhibiting the SME. Falk's calculation is the mechanical counterpart of Devonshire's (1954) treatment of first-order proper ferroelectric phase transitions driven by the temperature and the electric field. The martensitic alloys CuZn, CuAlNi, AgCd, $CuAuZn_2$, NiTi and NiAl are treated together in this phenomenological theory, ignoring their superlattice structure and the differences in the stacking sequence of their close-packed layers. After a suitable rescaling, the following ansatz is made for the free-energy:

$$f(e, t) = f_0(t) + (t + 1/4)e^2 - e^4 + e^6, \tag{14}$$

where f, e and t respectively denote the scaled values of the free-energy density, the shear strain (the order parameter), and the temperature. Equation (14) is a universal one for a large number of shape-memory alloys. The properties of specific materials enter through the scaling constants. All mechanical and thermodynamic properties are derived from (14). It is remarkable that this simplest of possible models leads to qualitative agreement with numerous experiments on shape-memory alloys; the stress-strain curves exhibiting elasticity, ferroelasticity and superelasticity in the appropriate temperature regions, the mode softening, the shape-memory effect, the occurrence of the stress-induced and temperature-induced phase transition, and the latent heat of the transition.

At the next level of complication, the electric field must also be brought in. From the point of view of theory, this is naturally a more difficult problem, but it also promises to present a richer variety of physical behaviour. One does not normally think of studying the effect of the electric field in alloys because of their high electrical conductivity. Especially interesting in this regard are materials such as PLZT and $BaTiO_3$ which are simultaneously ferroelastic and ferroelectric. The presence of ferroelectricity ensures that the spontaneous strain can be manipulated both by a mechanical stress and by an electric field. This is also important in applications of the SME because, by and large, electric fields are easier to apply in practice than mechanical stresses of appropriate magnitude and frequency. Experimental results on the effect of electric fields on the SME are just beginning to come in. Perhaps the first experiment of this type was that on PLZT ceramics (Wadhawan *et al* 1981). The composition of PLZT, that is (Pb, La) (Zr, Ti)O_3, is conveniently specified by the $x/y/z$ notation, where y/z indicates the Zr/Ti ratio, and x denotes the atomic percentage of La ions substituted for Pb. The composition $x/65/35$ has received a great deal of attention because of its closeness to the morphotropic phase boundary (Haertling and Land 1971; Haertling 1971). Its ferroelastic nature was first demonstrated by Meitzler and O'Bryan (1971). For $x > 4{\cdot}5$, this material possesses a property known as *penferroelectricity* (Meitzler and O'Bryan 1973), or *quasiferroelectricity* (Carl and Geisen 1973). There is a very interesting phase transition, called the $\alpha \rightarrow \beta$ transition by Keve and Annis (1973), which is similar in many ways to a martensitic phase transition. Whereas above a temperature T_c the material behaves like a normal paraelectric, the dielectric behaviour immediately below T_c, *i.e.*, in the α-phase, is not that of a normal ferroelectric. The α-phase is "quasiferroelectric" in which there are polar distorted microregions shorter than the wavelength of light. Application of an electric field between T_c and a lower temperature T_p changes the microdomains to macrodomains, which, however, revert back to randomly distributed microdomains (giving a macroscopically nonferroelectric state) when the electric field is switched off. The experimentally observed "slim" hysteresis loops constitute evidence in favour of this model (Carl and Geisen 1973). When the electric field is applied at a temperature below T_p, stable macrodomains indicative of long-range order are induced and the material behaves like a normal ferroelectric (as well as a ferroelastic), exhibiting "fat" hysteresis loops. Materials showing this type of diffuse phase transition are called "relaxor" ferroelectrics (Smolensky 1970). In the temperature range between T_c and T_p, microdomains of polar short-range order coexist with the paraelectric matrix, just as martensite coexists with the parent matrix over a certain temperature range.

The SME in PLZT ceramic of composition $x/65/35$, with $4 \leqslant x \leqslant 8$, was investigated in some detail by Kimura *et al* (1981), and the effect of an electric field on the SME in 6·5/65/35 PLZT was studied by Wadhawan *et al* (1981) by performing very simple bending experiments on thin bars of the ceramic. The modification introduced by the electric field on the SME could be interpreted in terms of the above microdomain model. In the temperature region in which the microdomains exist, the system is "electrically soft", but not "mechanically soft", and the load does not produce a large bending. However, when the electric field is switched on, it changes the microdomains to macrodomains, the material also becomes mechanically soft, and the load produces an additional bending. This was only a preliminary experiment. Much more work is needed to understand the phenomena involved in detail. Since ferroelectricity and ferroelasticity are coupled properties in the case of PLZT, it should be possible to produce changes in strain, including shape-memory bending, purely by electrical means, without the need for any mechanically-produced deformation. Electrically-produced SME would present challenging possibilities for both theory and experiment, as well as for device applications.

10. Concluding remarks

The subject of ferroelasticity has gained maturity being viewed as a part of the much larger subject of ferroicity. Much has been learnt or predicted about ferroelasticity by analogy with ferroelectricity. It appears that we can improve, considerably, our understanding of the physical basis of mechanical behaviour by drawing analogies with electrical phenomena (Alefeld 1971).

Based on the symmetry classification of phase transitions, a more rational-looking classification of twinning in crystals has been attempted. Two broad categories of twinning emerge: nonferroelastic and ferroelastic. Although this appears to run parallel to the existing division into twinning by merohedry and twinning by pseudo-merohedry, the advantage of the new scheme is that many finer features like piezoelectric twinning can also be distinguished.

As was brought out repeatedly, our present description of ferroelasticity is based on the concept of symmetry descent and the principle of superposition of symmetries (the Curie principle). In fact the Landau theory of phase transitions, which is so effective in explaining a large body of experimental facts, is itself based on the Curie principle. The Landau theory is being increasingly applied to martensitic phase transitions which have a substantial overlap with ferroelastic phase transitions. Although this is a promising development, a certain amount of caution is warranted because we are dealing with *first-order* phase transitions, many of them of so drastic a nature that a change of coordination number and "internal topology" is involved. In some of these transitions there is no group-subgroup relationship between the symmetries of the parent and the daughter phases. While the theoretical apparatus for dealing with second-order phase transitions is very well-developed, in first-order phase transitions only a beginning has been made in some respects (Aizu 1981).

References

Aizu K 1969 *J. Phys. Soc. Jpn* **27** 387
Aizu K 1970 *Phys. Rev.* **B2** 754

Aizu K 1972a *J. Phys. Soc. Jpn* **32** 1287

Aizu K 1972b *J. Phys. Soc. Jpn* **33** 629

Aizu K 1972c *J. Phys. Soc. Jpn* **33** 1390

Aizu K 1973 *J. Phys. Soc. Jpn* **34** 121

Aizu K 1974 *J. Phys. Soc. Jpn* **36** 1273

Aizu K 1978 *J. Phys. Soc. Jpn* **44** 683

Aizu K 1981 *Phys. Rev.* **B23** 1292

Alefeld G, Schaumann J, Tretkowski J and Volkl J 1969 *Phys. Rev. Lett.* **22** 697

Alefeld G 1971 in *Critical phenomena in alloys, magnets and superconductors* (ed) R E Mills (New York: McGraw-Hill) p 339

Alefeld G and Volkl J 1978 in *Hydrogen in metals, I: Basic properties* (eds) G Alefeld and J Volkl (Berlin: Springer-Verlag) p 1

Alkire R W and Yelon W B 1981 *J. Appl. Cryst.* **14** 362

Amelinckx S 1976 in *Developments in electron microscopy and analysis* (ed) J A Venables (London: Academic Press) p 417

Bak P 1982 *Rep. Prog. Phys.* **45** 587

Bastie P and Bornarel J 1979 *J. Phys.* **C12** 1785

Cahn R W 1954 *Adv. Phys.* **3** 363

Carl K and Geisen K 1973 *Proc. IEEE* **61** 967

Catti M and Ferraris G 1976 *Acta Cryst.* **A32** 163

Cowley R A 1976 *Phys. Rev.* **B13** 4877

Devonshire A F 1954 *Adv. Phys.* **3** 85

Donnay G and Donnay J D F 1974 *Can. Miner.* **12** 422

Dvorak V 1974 *Ferroelectrics* **7** 1

Dvorak V 1978 *Czech. J. Phys.* **B28** 989

Errandonea G 1980 *Phys. Rev.* **B21** 5221

Falk F 1980 *Acta Metall.* **28** 1773

Fleury P A and Lyons K 1981 in *Structural phase transitions I* (eds) K A Muller and H Thomas (Berlin: Springer-Verlag) p 9

Friedel G 1926 *Lecons de Cristallographie* (Paris: Berger-Levrault)

Ginzburg V L 1955 *Nuovo Cimento* **2** 1234

Ginzburg V L 1960 *Sov. Phys. Solid State* **2** 1824

Haertling G H and Land C E 1971 *J. Am. Ceram. Soc.* **54** 1

Haertling G H 1971 *J. Am. Ceram. Soc.* **54** 303

Hermann C 1929 *Z. Kristall.* **69** 533

Jameson G B 1982 *Acta Crystallogr.* **A38** 817

Janovec V 1972 *Czech. J. Phys.* **B22** 974

Janovec V, Dvorak V and Petzelt J 1975 *Czech. J. Phys.* **B25** 1362

Janovec V 1976 *Ferroelectrics* **12** 43

Keve E T and Annis A D 1973 *Ferroelectrics* **5** 77

Kimura T, Newnham R E and Cross L E 1981 *Phase Transitions* **2** 113

Klassen-Neklyudova M V 1964 *Mechanical twinning of crystals* (New York: Consultants Bureau)

Kopstik V A 1968 *Sov. Phys. Cryst.* **12** 667

Laves F 1975 *Acta Crystallogr.* **A31** S9

Lieberman D S, Schmerling M A and Karz R S 1975 in *Shape memory effects in alloys* (ed) J Perkins (New York: Plenum Press)

Luthi B and Rehwald W 1981 in *Structural phase transitions I* (eds) K A Muller and H Thomas (Berlin: Springer-Verlag) p 131

Meitzler A H and O'Bryan Jr H M 1971 *Appl. Phys. Lett.* **19** 106

Meitzler A H and O'Bryan Jr. H M 1973 *Proc. IEEE* **61** 959

Muller K A 1981 in *Structural phase transitions* I (eds) K A Muller and H Thomas (Berlin: Springer-Verlag) p 1

Nakanishi N, Murakami Y, Kanchi S, Mori T and Miura S 1971 *Phys. Lett.* **A37** 61

Nakanishi N 1975 in *Shape memory effects in alloys* (ed) J Perkins (New York: Plenum Press) p 147

Olson G B and Cohen M 1982 *Proc. Conf. Solid–Solid Transf.* 1981 ICOMAT 1982

Peisl H 1978 in *Hydrogen in metals I. Basic properties* (eds) G Alefeld and J Volkl (Berlin: Springer-Verlag) p 53

Pynn R 1979 *Nature (London)* **281** 433
Rees D C 1982 *Acta Crystallogr.* **A38** 201
Riste T (ed) 1978 *Electron-phonon interactions and phase transitions* (New York: Plenum Press)
Sawada A, Makita Y and Takagi Y 1976 *J. Phys. Soc. Jpn* **41** 174
Schneider J R 1981 *Nucl. Sci. Appl.* 1 227
Shubnikov A V and Kopstık V A 1974 *Symmetry in science and art* (New York: Plenum Press)
Smolensky G A 1970 *J. Phys. Soc. Jpn* **28** Suppl 26
Suzuki T 1978 *J. Phys. Soc. Jpn* **45** 860
Tolédano P and Tolédano J C 1976 *Phys. Rev.* **B14** 3097
Tolédano P and Tolédano J C 1977 *Phys. Rev.* **B16** 386
Tolédano J C and Tolédano P 1980 *Phys. Rev.* **B21** 1139
Tolédano P and Tolédano J C 1982 *Phys. Rev.* **B25** 1946
Wadhawan V K, Kernion M C, Kimura T and Newnham R E 1981 *Ferroelectrics* **37** 575
Wadhawan V K 1982 *Phase Transitions* **3** 3
Wagner H 1978 in *Hydrogen in metals I: Basic properties* (eds) G Alefeld and J Volkl (Berlin: Springer-Verlag) p 5
Warlimont H 1976 *Mater. Sci. Eng.* **25** 139
Wasilewski R J 1975 in *Shape memory effects in alloys* (ed) J Perkins (New York: Plenum Press) p 245

Discussion

G Venkataraman: It is observed that to understand the domain structure, one has to use not only the symmetry of the ferroelastic phase, but also that of the parent phase. This is similar to what Mermin does when he classifies defects using G, the symmetry of the disordered phase, and H, the symmetry of the ordered phase.

N Kumar: Is ferroelasticity a noncentrosymmetric phenomenon?

V K Wadhawan: The spontaneous-strain is a second-rank polar tensor. Thus the presence or absence of a centre of symmetry does not effect the occurrence of ferroelasticity in a crystal.

N Kumar: Since there was no prototype group for magnesium, can it be ferroic?

Wadhawan: The D_{6h} symmetry of magneisum does not admit of a crystallographic prototype group. Therefore we are not able to assign this crystal a place in the existing classification of ferroic crystals.

N Kumar: In order to have one-to-one correspondence is it necessary to have distortion connected with displacement vectors which are not some multiples of lattice spacing?

Wadhawan: We are talking here about the *one-way* SME and I think the question of one-to-one correspondence is more relevant for the two-way SME.

Bull. Mater. Sci., Vol. 6, No. 4, September 1984, pp. 755–772. © Printed in India.

Effects of mechanical deformation: Exoemission

G MUKHOPADHYAY

Department of Physics, Indian Institute of Technology, Bombay 400 076, India

Abstract. An introduction to some of the physical effects (*e.g.* exoemission, acoustic emission and mechanoluminescence) associated with the mechanical deformation of solids is presented. Greater emphasis has been given to exoelectron emissions. Experimental information and plausible mechanisms for exoemission have been described briefly. In particular, exoelectron emission from metals and oxide-coated metals has been discussed at some length, with the hope of generating a common interest among physicists and metallurgists.

Keywords. Mechanical deformation; stress; defects; dislocations; electron emission.

1. Introduction

There exist a number of effects associated with the mechanical deformation of solids. One class of effects is the emission of particles (charged and/or neutral), light and sound, when a material is undergoing deformation or is subjected to a constant strain rate. The emission of particles (in particular, electrons) is called exoelectron emission. The emission of light usually occurs in the form of luminescence from those materials which contain luminescent sources, and such an effect when induced by mechanical deformation is called mechanoluminescence. The emission of sound or stress waves is known to occur from a variety of materials, and is usually called acoustic emission. We shall describe here these effects and their understanding at the present time, with particular emphasis on exoemission, especially from metals and metal oxides during mechanical deformation. We shall see that these effects have some common features, require a great deal of future study and promise to be excellent tools for applied research (especially for metallurgists) in the field of nondestructive testing.

2. Exoemission

The phenomenon of exoemission (EE) was reported quite a long time ago (McLennan 1902). However, it was mainly after the introduction of the Geiger tube in the 1920's that the effect was truly recognised. Freshly-prepared Geiger tubes gave high and irregular counting rates for the first few hours or days, before functioning normally, and this led to the discovery that freshly machined metal surfaces emit electrons. This phenomenon was first carefully investigated by Kramer (1950) and sometimes referred to as the Kramer effect. Kramer himself found that all freshly prepared metal surfaces gave off electrons and suggested that the electrons gained the required energy for coming out of a metal by acquiring some of the energy released in the exothermal processes occurring on the surface. The prefix 'exo-' originates from this explanation. Although our present understanding indicates that the actual explanation of the phenomenon is not as simple as this, the name has survived. It now appears that EE occurs for almost all materials in varying degree.

2.1 *Main features of EE*

The main features of EE occurring in various materials can be summarized as follows:

(i) The material exhibiting EE must be 'excited' externally to produce a perturbation in the form of a structural change. The external excitation may be in the form of cold working, irradiation by electromagnetic radiation (UV or higher frequencies), particle bombardment (α, β-rays, neutrons, protons, slow electrons, ions), exposure to gases, abrasion, mechanical deformation, etc.

(ii) The effect is strongly correlated with relaxation processes in the material, both causally and temporally, and it appears only after the generation of the perturbation. The observed time dependence can often be fitted by one or more decaying exponentials. The corresponding time constants reflect the presence of one or more relaxation processes, which normally depend strongly on the amount and nature of the defects in the system. It is this aspect of the EE process that makes it an attractive nondestructive technique of characterizing a material for its defect contents.

(iii) Unlike stationary effects, such as photoemission (PE) and thermionic emission (TE), EE is a nonstationary process, *i.e.* the EE flux is of transient character. Further, the effect is rather weak compared to PE or TE, with a EE flux typically in the range of 10^{-13} A/m^2.

(iv) The emission may be spontaneous or may require external stimulation, in addition to the external excitation. The stimulation may be in the form of increased temperature (thermally-stimulated exoemission (TSEE)) or electro-magnetic radiation (photo-stimulated exoemission (PSEE)), usually in the optical range. The EE observed without any photostimulation is usually referred to as 'dark emission'. Normally TSEE is observed non-isothermally, although it can also be observed isothermally. For PSEE, it is necessary that the photon energy is less than the work function of the material under study. Otherwise normal PE will accompany EE making data analysis rather difficult. PSEE can enhance a normal 'dark EE' intensity by a factor as large as 10^4 or more. Both TSEE and PSEE have been correlated with several other effects, such as thermally stimulated luminescence (TSL), electron-stimulated desorption (ESD), thermally stimulated conductivity (TSC), thermally stimulated depolarization currents (TSDC), and thermally stimulated desorption (TSD), depending on the material studied. Observations of these effects enhance the understanding of the EE process and are therefore generally desirable. There does not appear to have been any attempt as yet to correlate EE with acoustic emission or mechanoluminescence.

(v) The EE rate is strongly correlated with the work function ϕ of the system. This correlation is of major relevance for PSEE as well as TSEE, and it is necessary to measure the work function simultaneously by an independent method during an EE observation, to facilitate understanding of the EE process.

(vi) The EE effect has two components, one of which is volume dependent and the other, surface dependent. For a particular system one or both may occur depending on the material and its surface condition as well as its surrounding gas medium. The surface effect is strongly related to the surface condition, and in a controlled EE experiment it is often desirable to have an ultra-high vacuum ($\sim 10^{-10}$ Torr) to separate the surface effect from the volume effect. It is also desirable to have an experimental arrangement for characterizing the surface condition of the sample.

(vii) EE emission can occur continuously, or in large bursts, or with the latter superimposed over the former. It is usually believed that the continuous emission is related to the motion of defects in the sample, whereas the emission in bursts is related to the propagation of cracks (or micro-cracks). Thus the nature of the EE may reveal the nature of its source.

2.2 *Experimental arrangement*

The apparatus for measuring EE consists of an excitation unit, a stimulation unit and a detection unit, attached to an ultrahigh vacuum (UHV) chamber containing the sample. It should be equipped with an Auger spectrometer and a quadrupole mass analyzer for structural and chemical analysis of the surface of the sample and for the identification of the chemical composition of the residual gases in the chamber. A facility for measuring the work function (*eg.*, by the Kelvin or Fowler method) is desirable. In addition, a LEED facility may be used for characterization of the surface structure. A quartz window on the chamber will facilitate optical measurements (*e.g.* luminescence, optical absorption, etc.), which often prove valuable for understanding EE.

An apparatus and the technique for observing TSEE has been described by Glaefeke (1979). We describe here an apparatus for observing EE or PSEE (figure 1). This is perhaps one of the most sophisticated versions of this type, developed and used by Rosenblum *et al* (1977) for studying EE during the mechanical deformation of a dogbone shaped sample (marked S in figure 1) of Al, Ni or Ti, with and without oxidised layers. The details of their experimental arrangement are described briefly here. The excitation unit consists of an arrangement for producing uniaxial tensile strain at a constant rate. The sample placed inside an UHV chamber (part of a LEED apparatus) is clamped at both ends, with the fixed end attached to a load cell (LC) and the other end attached to a pulling rod coupled to a linear variable differential transformer (LVDT) for measuring the displacement and thereby the strain rate. Strain at a constant rate is applied at intervals, causing EE in bursts. The vacuum chamber (UHVC) is equipped with a ion-gun (IG) for *in-situ* cleaning of the sample surface. No stimulation unit was used by Rosenblum *et al* (1977), although a LiF window (W) is provided for the purpose of photostimulation. In such experiments the EE flux is usually weak $(10^4-10^6$ particles/sec/m$^2)$ and it is desirable to have a single-event charged particle and photon

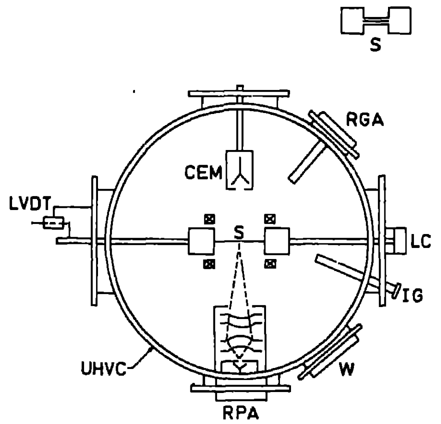

Figure 1. Schematic diagram for EE apparatus. (Rosenblum *et al* 1977).

detector as part of the detection unit. Rosenblum *et al* used a channel electron multiplier (CEM in figure 1) with an input cone (for focussing and accelerating the emitted particles into CEM) with an appropriate shielding and magnetic-discrimination scheme (for identifying the charged particles as electrons, or negative or positive ions). The shield ensured that the electrostatic field developed between the emitting surface and the cone was due to the CEM's biasing potential relative to the specimen rather than to the potential across the CEM. A retarding potential analyser (RPA) was used for Auger and photoelectron spectrometry for studying and characterizing the surface condition of the sample. For the detection of photons (presumably arising from the mechanoluminescence effect), a miniature single-photon counter tube (Bendix BX 754) was used in place of the (removable) RPA unit. For measuring the energy distribution, an electron spectrometer of high resolution (retarding grid potential analyser-RGA in figure 1) was specially designed to suit the way the strain was applied and the EE observed. However, the energy in the energy distribution could be measured only with respect to the Fermi level of the retarding grid, since the work functions of the oxides were uncertain, especially under mechanical strain. Figures 2–5 show the results of EE from Al with an oxide (Al_2O_3) layer, observed by Rosenblum *et al* (1977, 1977a). In figure 2, curves 1–3 correspond to electron emission intensity plotted against strain for samples with oxide thickness of 2000 Å, 250 Å and 50 Å respectively; the oxides for 2000 Å and 250 Å were grown anodically while the 50 Å thick oxide was grown naturally (*i.e.*, natural air-formed oxide). Curve-4 corresponds to negative ion emission from the 2000 Å thick oxide sample. Curve 5 is the stress-strain curve for the sample. In all cases a constant strain rate of $\dot{\varepsilon} = 2{\cdot}2 \times 10^{-4}\ \mathrm{sec}^{-1}$ was used at an ambient pressure of 10^{-10} Torr. In figure 3, curve 1 corresponds to photon emission from the 2000 Å thick oxide sample

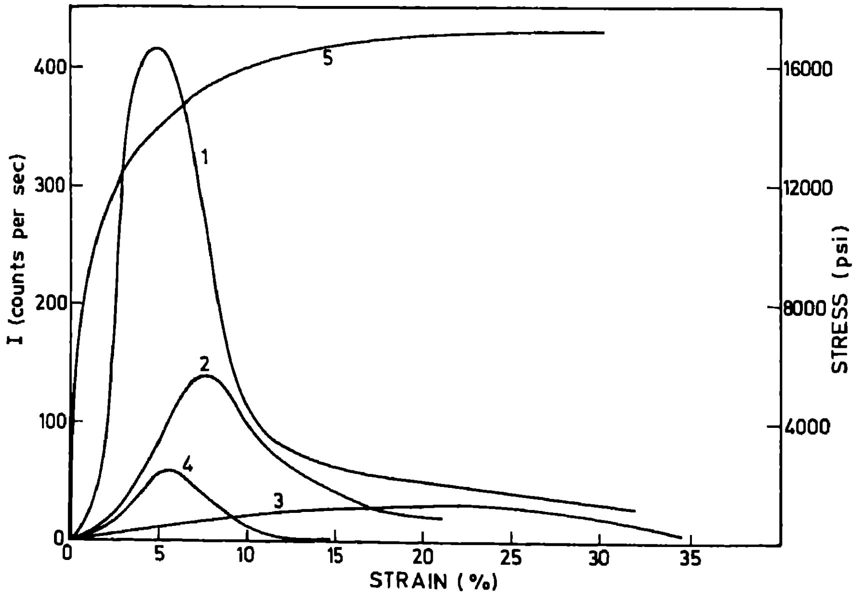

Figure 2. Electron emission intensity *vs* strain: **1.** *d* (oxide thickness) = 2000 Å; **2.** *d* = 250 Å; **3.** *d* = 50 Å; Negative ion emission: **4.** *d* = 2000 Å; stress-strain relation: **5.** Strain rate $\dot{\varepsilon} = 2{\cdot}2 \times 10^{-4}\ \mathrm{sec}^{-1}$ (Rosenblum *et al* 1977, 1977a).

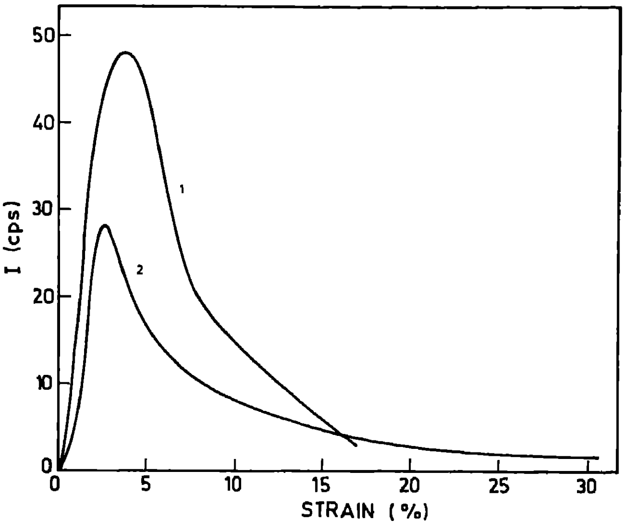

Figure 3. Photon emission intensity *vs* strain: 1. $\dot{\varepsilon} = 2·2 \times 10^{-4}$ sec^{-1}. Positive ion emission: 2. $\dot{\varepsilon} = 5·3 \times 10^{-4}$ sec^{-1} $d = 2000$ Å (Rosenblum *et al* 1977, 1977a).

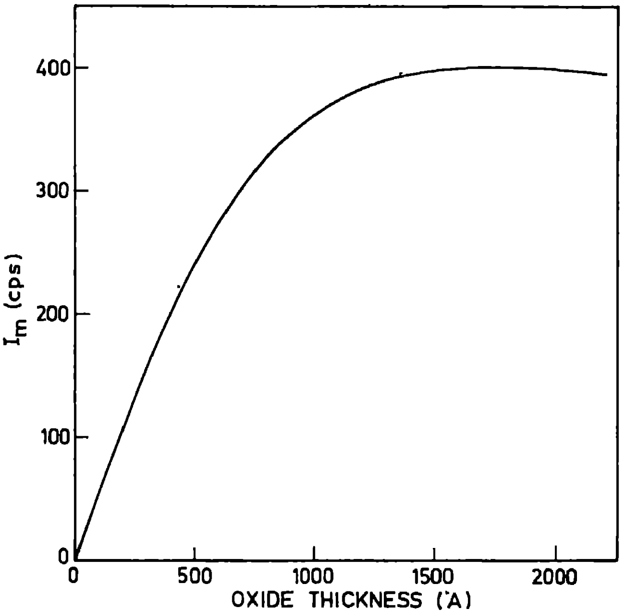

Figure 4. Maximum electron emission intensity *vs* oxide thickness: $\dot{\varepsilon} = 2·2 \times 10^{-4}$ sec^{-1} (Rosenblum 1977a).

for the same strain rate as above, while curve 2 corresponds to positively charged ion emission for the same sample at a strain rate of $5·3 \times 10^{-4}$ sec^{-1}. The general features of the intensity as a function of strain are the same for the emission of electrons, positively or negatively charged ions, or photons. Figure 4 shows the peak electron

2.3 *Mechanism and general understanding*

The mechanisms for EE have always been a subject of controversy, partly because each worker or group of workers has tried to explain the experimental results through phenomenology suitable for that particular experimental situation (which is not easily reproduced), and mainly because of the very complex nature of the EE phenomenon. We now describe briefly some of the mechanisms based on observations under specific situations (see Glaefeke 1979 for further details).

2.3a *Excitations induced chemically:* Spontaneous EE can occur when chemically reactive gases interact with initially clean metal surfaces (Bohun 1961; Bohun *et al* 1965; Delchar 1967; McCarrol 1969; Gesell *et al* 1970; Brus and Comas 1971; Born and Linke 1976). The process involved here is adsorption, the subsequent emission occurring from the surface. An adsorption process can be either physical (physisorption) or chemical (chemisorption) in nature. In physisorption, the adsorption-desorption equilibrium (at constant T) is reached without activation. The heat of physisorption is typically of the order of 0·1 eV per species, which is too small to trigger EE. In contrast, chemisorption requires an activation energy and is preceded by physisorption. The heat of chemisorption is of the order of several eV per species, sufficient for EE. Compared to physisorption which is reversible and forms multilayers, chemisorption is partially irreversible and ceases at monolayer coverage unless the adsorbed species diffuses into the bulk of the substrate. Such diffusion does occur in the case of oxidation and growth of the oxide layer. The rate of chemisorption may be determined from the chemical kinetic rate equation when the chemical reaction velocity is rate-determining, or from Fick's law of diffusion when the diffusion process is rate-limiting. The EE rate is then assumed to be proportional to the rate of chemisorption. Analysis along these lines then indicates a maximum in the EE current as a function of time. When more than one species is chemisorbed, one would expect a maximum corresponding to each species. Thus, the two observed maxima in the EE from clean Mg surfaces exposed (by abrasion) to O_2 and H_2O in the dark have been attributed to the two different adsorbing species (Gesell *et al* 1970). It has also been found from a simultaneous measurement of the work function that the maximum in the EE corresponds to a minimum in the work function ϕ. Thus, the EE has been attributed to (a) the lowering of the work function due to adsorption with a dipole moment of the adsorbed complex favouring emission, and (b) transfer of the released heat of chemisorption to generate surface plasmons which in turn transfer their energy to electrons causing EE. For Al, a substantial decrease in the work function ϕ (with the minimum in ϕ coinciding with the maximum in dark EE) during adsorption of water has been reported (Born and Linke 1976, from 4·5 eV to 1·3 eV; Wortmann 1978).

Spontaneous EE can also occur during thermally stimulated desorption (TSD) without any preliminary excitation, and such TSEE is sometimes referred to as self-excited EE (Bohun 1961; Krylova 1976; Krylova *et al* 1976). For *e.g.*, highly hydrated oxides (Al_2O_3, MgO etc.) and alkali halides (NaCl etc.) show a strong gas desorption accompanied by EE (Krylova 1976). It is believed that the active species at the surface recombine with the sites which have become vacant through desorption due to thermal stimulation. The released recombination energy is then responsible for this TSEE (Krylova *et al* 1976).

TSEE has been observed during heterogeneous catalytic reaction, for example during catalytic oxidation of hydrogen and carbon monoxide on NiO, ZnO and platinum black (Krylova 1976). Since both TSEE and catalysis depend on chemical thermodynamics, a relationship between the two is to be expected. Indeed, a reproducible linear relation between the two has been demonstrated for catalytic oxidation (Krylova 1976).

2.3b *Excitation by UV and x-rays:* Some alkali halides (especially those with small electron affinity at the surface, *e.g.*, chlorides and fluorides), during exposure to UV light, exhibit PSEE when photostimulated with an additional UV light source. TSEE may be observed during thermal annealing. The mechanism for EE is believed to be a two-step photothermal process involving colour centres generated by the exciting UV light. The first step is the optical transition from the colour centre to the conduction band, and the second step is the thermionic emission from the conduction band to vacuum. The stimulation spectra (*i.e.*, PSEE as a function of the stimulating wavelength) have been studied extensively and found to give information about the colour centres similar to that yielded by their optical absorption spectra (Ford *et al* 1970; Bichevin *et al* 1971; Nink and Holzapfel 1973; Maiste *et al* 1973; Kortov *et al* 1982; Tale *et al* 1982).

TSEE has been reported after excitation with x-rays, and a correlation between TSL and TSEE established (Holzapfel and Krystek 1976). TSEE from oxides irradiated with x-rays has also been investigated (Rudolf and Glaefeke 1982). In most cases, a direct liberation of electrons from traps (produced by irradiation) is assumed to explain the EE.

2.3c *Excitation by electrons:* EE has been observed from materials during exposure to electron beams. However, this occurs only for insulators. So far, atomically clean metal surfaces have not exhibited EE on irradiation, and the presence of oxide or adsorbed species seems to be absolutely essential for EE observation here. This seems to be true also for semiconductors. The EE behaviour is strongly dependent on the energy of the exciting electron beam. For low energy electrons (0.2 to 30 eV) the adsorbed species on the surface and the surface states are affected and here EE is essentially a surface phenomenon. These EE spectra are similar to the UV-excited spectra, and electron-stimulated desorption (ESD) can occur. ESD can influence TSEE spectra appreciably. Concepts involving chemical reactions at the surface are utilized to correlate the two (Jakowski and Glaefeke 1976; Euler and Scharmann 1976; Brunsmann and Scharmann 1977; Kirihata and Akutsu 1979). For moderate energy electrons (several hundred to several thousand eV), volume states are excited, generating a complicated space charge inside the insulator. This in turn produces a positive-negative double layer whose electric field (as large as 10^6 V cm^{-1}) causes EE (Fitting *et al* 1979; Fitting 1981). Systems studied, among others, are Al_2O_3 (Krylova 1971; Schlenk 1976; Chrysson and Holzapfel 1980). ZnO (Krylova 1971; Hiernaut *et al* 1972; Kriegseis and Scharmann 1975), NiO (Krylova 1971; Hiernaut *et al* 1972), SiO_2 (Krylova 1971; Jakowski and Glaefeke 1976), BeO (Euler and Scharmann 1976; Scharmann and Wiessler 1980) and NaF (Brunsmann and Scharmann 1977).

2.3d *Excitation by nuclear radiation:* Reproducible EE has been observed from a number of substances using nuclear radiation as the source of excitation. Among the substances studied are alkali halides, alkaline-earth halides, sulphates, sulphides and a number of metal oxides. TSEE from BeO and LiF have been studied extensively because of their dosimetric applications (see Glaefeke 1979 for details). Simultaneous measurement of TSL and TSEE from the same emitter can discriminate between those types of radiation which cause bulk effects (TSL) and those causing surface effects (TSEE).

For example, both α- and soft β-irradiation yield high TSEE intensity (since the total energy is absorbed near the surface) but rather weak TSL, in BeO. On the other hand, γ irradiation causes very weak TSEE but a very strong TSL. Thus, TSEE and TSL from BeO can distinguish between α (or soft β) and γ doses. Fast neutrons can cause EE via recoil protons or α radiation, and the corresponding TSEE may be separated from the γ-ray TSEE by a subtraction procedure to determine the fast neutron dosage. BeO dosimeters based on these properties may have a dose response range from as low as 10^{-6} rad to 10^2 rad. Compared to conventional dosimeters, however, a TSEE-based dosimeter has some technical shortcomings, such as a strong dependence of the TSEE on the mechanical treatment and the ambient atmosphere of the detecting material. This may be responsible for its lack of commercial usage.

2.3e *Excitations through direct structural change:* EE has been observed from a number of materials in which excitation is brought about by direct structural changes. Such changes can be induced by external application of stress, or by generating stress internally through heat treatment of the material.

EE has been observed from metals with atomically clean surfaces in ultrahigh vacuum. Kortov *et al* (1971) observed EE during plastic deformation of Al. Mints *et al* (1973) tried to correlate EE with the process of recovery and recrystallization of metals. Mechanical deformation generates a high concentration of defects (vacancies and dislocations). The relaxation of the stress is accompanied by the diffusion of vacancies towards the surface and the recovery of dislocations. These defects can rearrange themselves exothermally, and the localized release of thermal energy may be taken up by electrons. However, emission of these electrons would require a substantial lowering of the work function ϕ, which is believed to be due to high roughness on a clean metal surface (Lewis 1954; Rhead 1977). Pardee and Buck (1977) and Buck *et al* (1977) considered the roughness-enhanced coupling of incident light with surface plasmons (which can transfer their energy to electrons) to explain PSEE.

EE from oxide covered metals has been observed both in the dark as well as with photostimulation during mechanical deformation. Since most metals in practical situations are oxidised at the surface, these EE observations are of considerable applied interest. The dark emission under UHV has been observed only during mechanical deformation or abrasion of oxide covered metals (Gieroszynski and Sujak 1965; Sujak *et al* 1965; Brotzen 1967; Sujak and Gieroszynski 1970; Linke 1970; Kortov *et al* 1970; Arnott and Ramsey 1971; Kortov and Myasnikov 1972; Kelly and Himmel 1976; Rosenblum *et al* 1977, 1977a). Photostimulated emission during abrasion or plastic deformation of oxide-coated metals can be very large as compared to the dark emission (by a factor of 10^4 or more) and a number of oxidised metals have been investigated exploiting this fact (Grunberg 1958; Von Voss and Brotzen 1959; Pimbley and Francis 1961; Mueller and Pontinen 1964; Claytor and Brotzen 1965; Gieroszynski and Sujak 1965; Sujak *et al* 1965; Sujak and Gieroszynski 1970; Baxter 1973; Shorshorov *et al* 1976; Baxter and Rouze 1978; Wortmann 1978; Dickinson *et al* 1978; Komai 1978). Among various oxide coated materials (*eg*., Al, Ni, Steel, Ti, Mo, etc.), the most widely studied one is Al_2O_3-coated Al. Qualitatively the same emission behaviour has been observed when the oxide covered metal is mechanically abraded or plastically deformed under tension. In the case of tensile strain, dark emission occurs only during a change in the strain and ceases abruptly when the deformation stops. Similarly, when photostimulated, considerable enhancement in electron emission occurs only during constant strain rate, the emission being regarded as burst emission, even though a continuous component (much smaller in magnitude) may be present. In case of burst emission, typically, for a constant strain rate, the emission increases to a maximum followed by a monotonic decrease with increasing deformation or strain (see figure 2). The emission depends on the strain rate as well as the oxide thickness (see figure 4). The burst emission has been associated with the propagation of cracks or micro-cracks. PSEE from thick oxide layers has been attributed to the propagation of cracks perpendicular to the stress direction, independently of the underlying micro-structure of the metal. In thin oxide layers, it has been attributed to fracture at slip steps (Baxter and Rouze 1978).

The continuous EE is believed to arise from two components, one controlled by the diffusion of point defects (generated by strain) towards the surface, and the other controlled by the relaxation of dislocations. One may dominate over the other, or both may be present. For example, Pimbley and Francis (1961) could explain EE from abraded oxidised Al through a model based on the diffusion of vacancies, while Claytor and Brotzen (1965) explained EE from mechanically deformed oxidised Al in terms of the diffusion of other point defects. On the other hand, Mueller and Pontinen (1964) studied EE from freshly abraded as well as from abraded and aged samples of oxidised Al and concluded against the defect diffusion mechanism. However, Shorshorov *et al* (1976) could correlate PSEE during plastic deformation with the generation of dislocations as well as vacancies by simultaneously studying the behaviour of these defects (using metallographic methods). They found no diffusion of vacancies but found relaxation of dislocations in molybdenum, while both phenomena occurred in α-iron.

The burst emission, especially in dark, is supposed to originate from cracks or microcracks which develop in the oxide as soon as the local surface strain in the underlying metal substrate exceeds the ultimate tensile strain of the oxide layer (Sujak 1964). Originally it was believed that the opposing surfaces of a propagating fissure (microcrack) become charged, providing a strong electric field that causes field emission (Gieroszynski and Sujak 1965). This so-called electrified-fissure model for EE was reinvestigated by Arnott and Ramsey (1971) who restricted its applicability to polar substances. For non-polar substances, they proposed to interpret EE in terms of rearrangement of dangling bonds created during the propagation of cracks. Rabinowicz (1977) has elucidated this model, but also questioned its feasibility. Rosenblum *et al* (1977a) believe that the release of strain energy in the vicinity (*e.g.* the tip) of a propagating crack results in local heating to a temperature (estimated to be ~ 3000 K for Al) sufficient to cause thermionic emission from the walls. However, they also observed emission of positive and negative ions, which indicates that field-assisted emission of electrons cannot be ruled out.

EE during heat treatment of materials (without external excitation) arises from the internal mechanical stress generated thermally due to the process of phase transformation. Thus EE has been observed during changes of the state of aggregation or modification (first order phase changes, *e.g.*, transition from the hexagonal to the cubic form in thallium, change or modification of hexagonal chromium and selenium, melting of ice, lead, tin, etc.) and during changes of orientation (second order phase changes, *e.g.*, the antiferromagnetic-paramagnetic transition in $Ni + NiO$ and $Cr + Cr_2O_3$). The EE intensity is regarded as proportional to the defect content and a measure of the degree of completion of the phase change. The mechanism is believed to be the same as that for stress-induced EE. The emission has also been observed during second-order phase changes in crystalline pyroelectrics (*e.g.*, lithium niobate, BeO), where the mechanism is regarded as a thermally stimulated field effect (see Glaefeke 1979 for further details).

2.4 *Theoretical models for* EE

It is clear from the preceding description that EE is a rather complex phenomenon involving several intermediate steps, depending on the type of material and the actual experimental condition. However, there appear to be three broad steps in the electron emission mechanism: (i) External excitation generates defects and the relaxation of the response to the excitation is associated with the motion or relaxation of these defects. (ii) The defects transfer their energy either directly or via some other agent (*e.g.*, surface plasmons in metals, and possibly phonons) to the electrons by the process of annihilation, or rearrangement, or by chemical reactions (at the surface). (iii) Electrons gaining this energy escape the material in the form of EE when their energy exceeds the work function or the electron affinity, or when an electric field (in electrified fissures) assists the emission. The controlling factors here (*e.g.* work function, etc.) may themselves depend on the nature of the excitation and on the experimental conditions.

Glaefeke (1979) has discussed various theoretical models for the last two steps, especially for dielectrics. Following Kelly (1972), he has described the thermionic emission model, in which the electron concentration is determined by reaction kinetics controlled by the concentration of defects (electron traps) and the retrapping-recombination processes for electrons. The theory has been applied to TSEE with some success. A field-assisted emission model has been developed for space-charge-controlled EE from highly insulating materials (excitation induced by electron bombardment) with the transport and escape of electrons determined by a Monte-Carlo process. The model can explain the intensity, energy and angular distribution of EE, for example in BeO (Kortov and Zolnikov 1975; Fitting *et al* 1979).

In EE from metals with or without an oxide layer, most of the theoretical work has been devoted to step one. Early studies on EE were on the diffusion of vacancies or point defects towards the surface. The rate of arrival of the defects at the surface was determined by Fick's law. This was then assumed to be proportional to the rate at which the electron emitting centres were activated and thereby to the electron emission rate (Grunberg and Wright 1955; von Voss and Brotzen 1959; Pimbley and Francis 1961; Claytor and Brotzen 1965). More recently Nagornykh and Demin (1978) have incorporated into the diffusion equation the generation of vacancies during the straining of oxide coated metals. The diffusion of point defects from the metal into the oxide was matched by the diffusion of oxygen in the opposite direction. The formation of a filled electron trap (F-centre type) at the oxygen vacancy in the oxide was assumed. The electron emission rate was determined from the reaction kinetics involving thermal ionization of traps and recapture of electrons by the traps. The model was applied to EE from oxidised Al with some success.

The model for EE in bursts is based on crack propagation, and is more phenomenological than the model described above (Arnott and Ramsey 1971; Rosenblum *et al* 1977a). These however apply specifically to oxide coated metals. For surface-controlled EE, models based on chemisorption and Auger transitions have been evolved (Kasemo *et al* 1979). Models based on the stress dependence of thermionic emission have also been considered (Tinder 1968).

3. Acoustic emission

By acoustic emission (AE) one means the generation of stress waves during structural changes in a material. These may be generated internally (*eg*., during phase transitions) or by an externally applied stress. The phenomenon is known to occur for almost all kinds of materials, and has been called by different names in different fields of research; for example, it is referred to as 'seismoacoustic activity' when observed in rocks under stress. AE usually refers to all kinds of stress waves even though the emitted frequencies may be far above the audible range. Extensive work has been done in this field, although to a somewhat applied nature (especially in relation to seismic studies of rocks), and some excellent review articles are available (Green 1969; Liptai *et al* 1971; Dunegan and Tatro 1971; Lord 1975). A brief description of the relevant parts of the subject follows:

The first systematic study of AE was by Kaiser in the 1950's, on polycrystalline zinc, steel, aluminium, copper and lead. He observed that AE was irreversible, *i.e*., emission did not occur during reloading of a material until the stress exceeded its previous value—a phenomenon usually known as the 'Kaiser effect'. This memory effect applies to most metals but generally not to other materials. In 1961 Schofield reported AE from aluminium and zinc single crystals, commercial copper, aluminium, lead and 70–30 brass, and established correlation with dislocations, slips and grain boundary motion. Tatro and Liptai (1962) studied AE from polycrystalline aluminium and steel for various strain values, and from the observed dependence on the surface condition of the specimen, concluded that AE was a surface phenomenon. Later Schofield studied AE from aluminium single crystals, with and without the oxide layer, and found the surface condition to be of secondary importance except for influencing the strain locally at the point where AE commenced in a burst. It was found that the oxide coating was not a source of AE. Further work by Schofield has established AE as primarily a volume effect. The general features of AE derived from the work of several persons can be summarized as follows (Lord 1975).

AE occurs in two forms: continuously, and in bursts. Continuous emissions of rather high frequency ($\gtrsim 10^2$ kHz) and very low intensity usually occur in metals and metallic systems, and supposedly arise from mobile dislocations and possibly slip movements. Burst emissions occur with much higher intensity and are supposedly associated with failures such as twinning, microcracks, unpinning of dislocations from obstacles, and growth of already existing cracks; they occur at relatively large values of the plastic strain.

Figure 7 shows a typical experimental AE rate as a function of the tensile strain (Dunegan and Harris 1969). This particular result is remarkable in that it fits beautifully with Gilman's mobile dislocation model (Gilman 1966) which gives the mobile dislocation density N_m as a function of the plastic strain ε_p through the relation $N_m = m\varepsilon_p \exp(-\phi\varepsilon_p)$, where m is the dislocation breeding factor, and $\phi = H/\sigma$, where H is the hardening coefficient, and σ is the rms stress. The fit is shown in the dashed curve in figure 7 with $m = 1{\cdot}44 \times 10^7$ and $\phi = 70$ (Lord 1975). This shows that the AE rate is directly related to the mobile dislocation density, so that one may contemplate determining H, an important mechanical parameter, using the AE technique. Unfortunately such a fit of Gilman's formula does not work for many materials. This has been attributed to the inhomogeneity in the strain caused by the occurrence of Lüder's bands.

At present there does not seem to be any rigorous microscopic theory for the actual

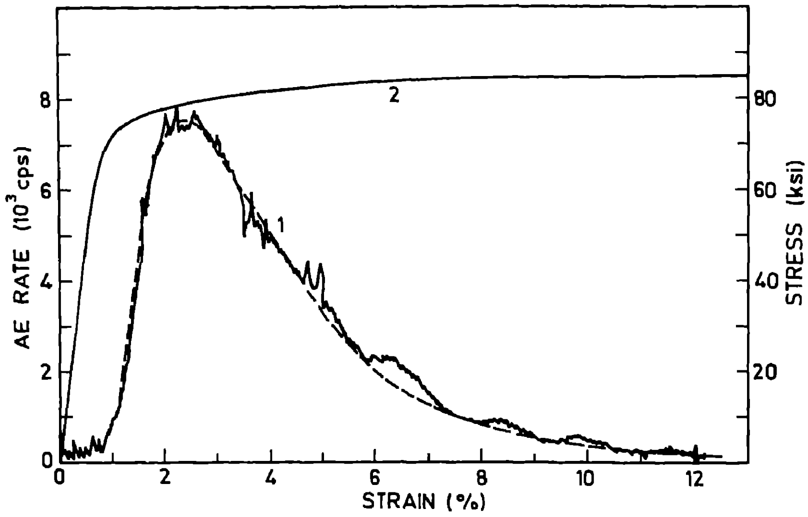

Figure 7. Acoustic emission intensity *vs* strain: 1. experimental: dashed curve. Gilman's relation. Stress *vs* strain: 2. (see Lord Jr 1975).

internal mechanism of AE. The major thrust in this area is in the direction of applied research, of establishing empirical relationships between AE and mechanical parameters (Lord 1975). Further, there has been no attempt to correlate AE with EE, although the typical emission intensity vs strain curves for Al are remarkably similar (compare figures 2 and 7).

4. Mechanoluminescence

Some materials emit light when subject to stress beyond a particular level. This phenomenon is broadly called mechanoluminescence (ML) or triboluminescence. (ML is preferred, to avoid confusion with thermoluminescence which is customarily denoted by TL). Extensive research has been done in this field on a very large number of materials, and the subject has been reviewed by a number of authors (Meyer *et al* 1970; Walton 1977; Zink 1978). Only a brief account of the relevant aspects is given here.

The most widely-studied materials are the alkali halides where the electron traps are the source of luminescence. ML spectra are similar to the TL spectra of a given material. Belyaev *et al* (1963) observed ML spectra during the growth of cracks in alkali halides under uniaxial strain, with photon emission in bursts, indicating that ML is associated with crack propagation. ML during fracture can be a hundred times more intense than TL, the concept of electrified fissures has been used to explain this (Belyaev *et al* 1966; Belyaev and Martyshev 1969). Observations on ML during abrasion or scratching of alkali halides have been correlated with the propagation of cracks and TL (estimated temperatures as high as 10^4 K) at the crack-tip (Meyer *et al* 1970). ML emission has been found to have a memory (analogous to the Kaiser effect) in activated alkali halides and ZnS. In experiments where the strain is repeated, no emission is observed in the elastic or plastic regions; and for a second application of strain, not until its magnitude exceeds that of the previously applied strain. This indicates that the ML intensity depends on the depinning of dislocations under stress (Alzetta *et al* 1970; Scarmozzino 1971). Simultaneous ML and AE have been observed during mechanical deformation of organic glasses, steel and copper plates, indicating a common origin (Sodomka *et al* 1980). ML during the deformation and fracture of metallic alloys has also been reported (Borisova *et al* 1975). Molotskii (1978) observed ML during the plastic deformation and fracture of copper. Zink and his coworkers have observed ML in many organic and inorganic crystals (Zink 1978; Chandra and Zink 1980). In many cases, explanations on the basis of piezo-electrification, cleavage electrification and triboelectrification, have been given (Meyer *et al* 1970; Walton 1977; Chandra 1981).

Intense ML has been observed from coloured alkali halides (coloured by x- or γ-ray irradiation) by a number of workers. The emission is thought to be a result of the interaction of dislocations with colour centres (Butler 1966; Shmurak 1969; Alzetta *et al* 1970; Guerrero and Alvarez-Rivas 1978; Chandra and Zink 1980). Recently ML emission during the application as well as the release of uniaxial compression in x-ray irradiated alkali halides have been reported by Chandra and Elyas (1978). They have also studied γ-irradiated alkali halides and ML emission from coloured alkali halides under repeated stress, and established a linear relationship between the ML intensity and the measured density of newly-created dislocations at the end of repeated-stress cycles (Elyas 1981). At present a proper theoretical understanding of ML emission, particularly from materials containing active luminescence centres, is still lacking, although some theoretical attempts have been made to understand ML in terms of electric field and pressure effects (Lin *et al* 1980). Studies correlating ML with EE or AE also seem to be inadequate.

5. Conclusions

We have tried to present an introduction to the subject of some special physical effects, especially exoelectron emission, in the context of the mechanical deformation of solids. For a better understanding of the exoelectron process, we have also discussed possible mechanisms for EE and two other related phenomena, AE and ML. While a number of possibly important references may have been inadvertently omitted, it is hoped that this article is sufficiently self-contained to generate interest in studying EE in a systematic manner. It can be safely said that, at present, a concrete theory of EE is lacking. Further, extensive, experimental study is required for understanding and correlating EE with AE and ML. For example, one should study more carefully the role of the work function, dislocations (the applicability of Gilman's theory or modification thereof), the mechanism of energy transfer to electrons, and the escape of electrons from metals and oxide-coated metals. On the applications side, one ought to study more extensively the growth of microcracks using spot scanners (PSEE, as in Baxter 1973) and establish empirical relationships with mechanical parameters in the same manner as has been done for acoustic emission studies.

Further references on EE are: Scharmann (1967), Becker (1972), Ramsey (1976), Krylova (1976) and Glaefeke (1979).

Acknowledgements

The author thanks Dr G Srinivasan and Prof. S Ramaseshan for bringing this subject to

his attention. Thanks are also extended to Mr C V Krishna Murthy for providing some of the material presented here.

References

Alzetta G, Chudacek I and Scarmozzino R 1970 *Phys. Status Solidi* **a1** 775

Arnott D R and Ramsey J A 1971 *Surf. Sci.* **28** 1

Baxter W J 1973 *J. Appl. Phys.* **44** 608

Baxter W J and Rouze S R 1978 *J. Appl. Phys.* **49** 4233

Becker K 1972 CRC *Crit. Rev. Solid State Sci.* **3** 74

Belyaev L M, Nabatov V V and Martyshev Yu N 1963 *Sov. Phys. Crystallogr.* **7** 464

Belyaev L M and Martyshev Yu N 1969 *Phys. Status Solidi* **34** 57

Belyaev L M, Nabatov V V, Pisarevskii Yu V and Shaldin Yu V 1966 *Sov. Phys. Crystallogr.* **10** 647

Bichevin V, Käämbre H and Lushchik Ch. 1971 *Phys. Status Solidi* **a5** 525

Bohun A 1961 *Czech. J. Phys.* **11** 819

Bohun A, Sak J and Psenickova M 1965 *Czech-Z-Phys.* **15** 667

Borisova E A, Glebova R D, Platonov A A and Skyarov N M 1975 *Sov. Phys. Dokl.* **20** 435

Born D and Linke E 1976 *Proc. 5th Int. Symp. on EE and Dosimetry* (eds) A Bohun and A Scharmann (Prague: Inst. Solid St. Phys. Acad. Sci.) p 265

Brotzen F R 1967 *Phys. Status Solidi* **22** 9

Brunsmann U and Scharmann A 1977 *Phys. Status Solidi* **a43** 519

Brus L E and Comas J 1971 *J. Chem. Phys.* **54** 2771

Buck O, Pardee W J, Szalkowski F J and Thompson D O 1977 *Appl. Phys.* **12** 301

Butler C G 1966 *Phys. Rev.* **141** 750

Chandra B P 1981 *Phys. Status Solidi* **a64** 395

Chandra B P and Elyas M 1978 *Kristall. U. Tech.* **13** 1341

Chandra B P and Zink J I 1980 *Phys. Rev.* **B21** 816

Chrysson E and Holzapfel G 1980 *Phys. Status Solidi* **a59** K49

Claytor R N and Brotzen F R 1965 *J. Appl. Phys.* **36** 3549

Delchar T A 1967 *J. Appl. Phys.* **38** 2403

Dickinson J T, Braunlich P, Larson L A and Marceau A 1978 *Appl. Surf. Sci.* **1** 515

Dunegan H L and Harris D O 1969 *Ultrasonics* **7** 160

Dunegan H L and Tatro C A 1971 *Techniques of metals research* (ed) R F Bunshah (New York: Wiley Interscience) Vol V p 273

Elyas M 1981 *Studies of mechanoluminescence produced during application and release of a uniaxial pressure in x-irradiated KBr, KCl, KI, LiF and NaCl crystals*, Ph.D. Thesis, The Ravishanker University, Raipur, India

Euler M and Scharmann A 1976 *Phys. Status Solidi* **a34** 297

Fitting H J 1981 *Phys. Status Solidi* **a63** K47

Fitting H J, Glaefeke H, Wild W and Lange J 1977 *Phys. Status Solidi* **a42** K75

Fitting H J, Glaefeke H, Wild W, Franke M and Müller W 1979 *Exp. Tech. Phys.* **27** 13

Ford L H, Holzapfel G and Kaul W 1970 *Z. Angew Phys.* **30** 259

Gesell T F, Arakawa E T and Calcott T A 1970 *Surf. Sci.* **20** 174

Gieroszynski A and Sujak B 1965 *Acta Phys. Pol.* **28** 311

Giimann J J 1966 *Proc. 5th U.S. Nat. Congr. Appl. Mech.* 385

Glaefeke H 1979 *Topics in applied physics* (ed) P Bräunlich (Berlin: Springer-Verlag) Vol 37 p 224

Green A T 1969 *Nucl. Safety* **10** 4

Grunberg L 1958 *Br. J. Appl. Phys.* **9** 85

Grunberg L and Wright K H R 1955 *Proc. Roy. Soc. London* **A232** 403

Guerrero E and Alvarez-Rivas J L 1978 *Solid State Commun.* **28** 199

Hiernaut J P, Forier R P and Van Cakenberghe J 1972 *Vacuum* **22** 471

Holzapfel G and Krystek M 1976 *J. Phys. (Paris)* **37** C-7-238

Jakowski N and Glaefeke H 1976 *Thin-Solid Films* **36** 195

Kasemo B, Tornqvist E, Nørskov J K and Lundqvist B T 1979 *Surf. Sci.* **89** 554

Kelly P 1972 *Phys. Rev.* **B5** 749

Kelley P and Himmel L 1976 *Comm. Solid State Phys.* **7** 81

Kirihata H and Akutsu J 1979 *Phys. Status Solidi* **a51** K 109

Komai K 1978 *Trans. Jap. Inst. Met.* **19** 119

Kortov V S and Myasnikov I E 1972 *Phys. Status Solidi* **a9** 119

Kortov V S and Zolnikov P P 1975 *Phys. Status Solidi* **a31** 331

Kortov V S, Mints R I, Myasnikov I E and Gaprindoshvily A Y 1970 *Phys. Status Solidi* **a3** 13

Kortov V S, Mints R I and Teplov V G 1971 *Phys. Status Solidi* **a7** K89

Kortov V, Isakov V, Glaefeke H and Fitting H J 1982 *Phys. Status Solidi* **a73** K275

Kramer J 1950 *Der metallische zustand* (Gottingen: Vanderhoeck Ruprecht)

Kriegseis W and Scharmann A 1975 *Phys. Status Solidi* **a29** 407

Krishna Murthy C V 1982 *Exoelectron emission*, M.Sc. Thesis, Indian Institute of Technology, Bombay, India

Krylova I V 1971 *Phys. Status Solidi* **a7** 359

Krylova I V 1976 *Usp. Biol. Khimii* **45** 2138 (English Transl.: 1976, *Russ. Chem. Rev.* **45** 1101)

Krylova I V, Svitov V I and Konyushkina N I 1976 *Zh. Fiz. Khimii* **50** 933 (English Transl.: 1976 *J. Phys. Chem.* **50** 555)

Lewis T J 1954 *Proc. Phys. Soc.* **B67** 187

Lin S H, Wutz D, Ho Z Z and Eyring H 1980 *Proc. Natl Acad. Sci.* (*USA*) **77** 1245

Linke E 1970 *Z. Angew Phys.* **29** 241

Liptai R G, Harris D O, Engle R B and Tatro C A 1971 *Int. J. Nondestruct. Test.* **3** 215

Lord A E Jr. 1975 *Physical acoustics* (eds) W P Mason and R N Thurston (Academic Press: New York) Vol. XI 289

McCarrol B 1969 *J. Chem. Phys.* **50** 4758

McLennan J C, 1902 *Philos. Mag.* **3** 195,

Maiste A, Sorkin B, Elango M and Käämbre H 1973 *Phys. Status Solidi* **a20** K83

Meyer K, Obrikat D and Rossberg M 1970 *Kristall. Tech.* **5** 5, 181

Mints R I, Melekin V P, Segal V M and Icolev I Yu 1973 *Sov. Phys. Solid State* **14** 2153

Molotskii M I 1978 *Sov. Phys. Solid State* **20** 956

Mueller R K and Pontinen K 1964 *J. Appl. Phys.* **35** 1500

Nagornykh S N and Demin Yu A 1978 *Phys. Met. Metall.* **46** 170

Nink R and Holzapfel G 1973 *J. Phys.* (*Paris*) **34** C-9-491

Pardee W J and Buck O 1977 *Appl. Phys.* **14** 367

Pimbley W T and Francis E E 1961 *J. Appl. Phys.* **32** 1729

Rabinowicz E 1977 *Sci. Am.* **236** 74

Ramsey J A 1976 *Progr. surface and membrane Sci.* (New York: Academic Press) Vol 11 p 117

Rhead G E 1977 *Surf. Sci.* **68** 20

Rosenblum B, Carrico J P, Bräunlich P and Himmel L 1977 *J. Phys.* **E10** 1056

Rosenblum B, Braunlich P and Himmel L 1977a *J. Appl. Phys.* **48** 5262

Rudolf G and Glaefeke H 1982 *Phys. Status Solidi* **a73** K253

Scarmozzino R 1971 *Solid State Commun.* **9** 1159

Scharmann A 1967 *Festkorperprobleme* (Berlin: Akad.-Verl.) Vol 6 p. 106

Scharmann A and Wiessler U 1980 *Phys. Status Solidi* **a60** 117

Schlenk W 1976 *Phys. Status Solidi* **a33** 217

Shmurak S Z 1969 *Sov. Phys. Solid State* **10** 1526

Shorshorov M Kh., Zhebynev D A and Alekhin V P 1976 *Proc. 5th Inter. Symp. on EE and Dosimetry* (ed) A Bohun and A Scharmann (Prague: Inst. Solid St. Phys. Acad. Sci.) p. 229

Sodomka L, Leistner M, Tessmar H and Karel F 1980 *Kristall. U. Tech.* **15** 1101

Sujak B 1964 *Acta Phys. Pol.* **26** 1033

Sujak B and Gieroszynski A 1970 *Acta Phys. Pol.* **A37** 733

Sujak B, Gieroszynski A and Pega E 1965 *Acta Phys. Pol.* **28** 61

Sujak B, Gieroszynska K and Gieroszynski A 1982 *Phys. Status Solidi* **a72** K177

Tale I, Kortov V and Popov V 1982 *Phys. Status Solidi* **a74** 395

Tatro C A and Liptai R G 1962 *Proc. Symp. on Physics and Non Destructive Testing* (Southwest Research Inst., San Antonio, Texas) p. 145

Tinder R F 1968 *J. Appl. Phys.* **39** 355

Von Voss W D and Brotzen F R 1959 *J. Appl. Phys.* **30** 1639

Walton A J 1977 *Adv. Phys.* **26** 887

Wortmann J 1978 *Phys. Status Solidi* **a50** 509

Zink J I 1978 *Acc. Chem. Res.* **11** 289

Discussion

M Yussouff: Has the velocity distribution of the emitted electrons been measured?

G Mukhopadhyay: Yes, it has, in some cases.

R Chidambaram: How does thermoluminiscence dosimetry compare with exoemission?

Mukhopadhyay: I am sorry, I can't give you a precise answer.

R Krishnan: If there are two or more processes of exoemission occurring simultaneously, can one separate one from the other?

Mukhopadhyay: Only by doing additional experiments.

G Venkataraman: Would the exoemission rate depend on the type of defect migrating to the surface?

Mukhopadhyay: Yes, it would—particularly the temperature dependence, because activation is involved.

C K Majumdar: How long before the actual crack occurs can one detect anything by the techniques you have described?

Mukhopadhyay: This depends on the material. In fatigue cycling with a large stress amplitude, very early detection is possible (at 0·7% of failure).

P Rodríguez: Is the exoemission phenomenon more amenable to measurement in fatigue cycling than in a uniaxial tensile test?

Mukhopadhyay: Not necessarily, but I think this depends on the experimentalist.

M Yussouff: Is exoemission a field emission process?

Mukhopadhyay: No, because the actual explanation depends on the type of sample and environment involved.

Bull. Mater. Sci., Vol. 6, No. 4, September 1984, pp. 773–774. © Printed in India.

Relevance of liquid state to solid state properties*

H R KRISHNA MURTHY and T V RAMAKRISHNAN

Department of Physics, Indian Institute of Science, Bangalore 560 012, India

Abstract. We outline in this talk the beginning of a new programme to study physical properties of crystalline solids. It is based on considering the latter, a broken symmetry phase, in terms of the higher symmetry liquid phase. The solid is a calculable perturbation on the fluid. This is exactly opposite to the standard approach which relates mechanical properties to the behaviour of defects (mainly dislocations) etc., in an otherwise perfect crystalline solid. However, most other broken symmetry phases (*e.g.* ferromagnets) are discussed starting from a symmetric Hamiltonian or a free energy functional, and earlier work by one of the authors shows that the liquid-solid transition is well described, qualitatively and quantitatively, by this approach. On the other hand, defect theories of melting have a long record of nonsuccess. In the first part of the talk, the density wave theory of freezing will be outlined, and it will be shown how properties such as Debye Waller factor, entropy change of freezing etc. can be calculated with no or one free parameter. The problem of calculating shear elastic constants and dislocation core structures as well as energies in terms only of observable liquid state properties will be set up, and results presented. The method will be contrasted with zero temperature 'atomistic' models which obscure the essential dependence on structure and flounder in a mass of detail. The concluding part will describe further proposed applications, some suggestive experimental results extant in the literature, and some speculations.

Discussion

G Venkataraman: Is something like the Josephson effect possible in this case of change of phase associated with ballistic motion or diffusion?

T V Ramakrishnan: This is a hard question to answer.

V Balakrishnan: What stabilizes the system against other possible μ_G's? How does the system choose, say, between the fcc and bcc structures?

Ramakrishnan: We examine the stability of the fluid with respect to a *given* structure.

V Balakrishnan: What is it in the system that kills fluctuations with other wavevectors?

Ramakrishnan: The correlation function $S(q)$ is strongly peaked at a particular q. Thus the energy to excite this mode is far less than that for any other mode.

G Ananthakrishna: How does one measure the three-point correlation?

Ramakrishnan: This can be estimated either by computer simulation or by doing light scattering experiments on colloidal crystals.

G Srinivasan: Could one find the pressure dependence of the two-point correlation?

Ramakrishnan: This does not give the quantity required here.

---

* Only a summary is presented.

K R Rao: Is it necessary that the three-point correlation measurement be done in solid state?

Ramakrishnan: No. A "combination" scattering experiment has to be done in the liquid state for information in the short-range region.

K R Rao: What is the difficulty in predicting the melting temperature?

Ramakrishnan: The difficulty is that μ_G and C_G are dimensionless quantities.

S Ranganathan: Can your theory take into account the liquid-glass transition?

Ramakrishnan: No. We are very far from it.

D Dhar: How is the effective potential you use related to the effective potential used in cell theories of melting?

Ramakrishnan: The two are not related to each other.

S R Shenoy: Can one use your theory to handle a crystal with frozen-in defects?

Ramakrishnan: Perhaps one could, depending on how perfect these crystallites are and also on how rapidly the phase changes.

R Chidambaram: Where is the entropy of melting in this model?

Ramakrishnan: We calculate the entropy of melting from the known thermodynamic functions.

G Ananthakrishna: How do you describe dislocations and vacancies in your model?

Ramakrishnan: I don't know how to describe vacancies, but dislocations can be described in a manner similar to vortices in a superconductor.

Bull. Mater. Sci., Vol. 6, No. 4, September 1984, pp. 775–798. © Printed in India.

Elastic continuum theories of lattice defects: a review

DEBENDRANATH SAHOO

Materials Science Laboratory, Reactor Research Centre, Kalpakkam 603 102, India

Abstract. The presently available elastic continuum theories of lattice defects are reviewed. After introducing a few elementary concepts and the basic equations of elasticity the Eshelby's theory of misfitting inclusions and inhomogeneities is outlined. Kovács' result that any lattice defect can be described by a surface distribution of elastic dipoles is described. The generalization of the isotropic continuum approach to anisotropic models and to Eringen's isotropic but non-local model is discussed. Kröner's theroy (where a defect is viewed as a lack of strain compatibility in the medium) and the elastic field equations (formulated in a way analogous to Maxwell's field equations of magnetostatics) are described. The concept of the dislocation density tensor is introduced and the utility of higher-order dislocation density correlation tensors is discussed. The beautiful theory of the affine differential geometry of stationary lattice defects developed by Kondo and Kröner is outlined. Kosevich's attempt to include dynamics in the elastic field equations is described. Wadati's quantum field theory of extended objects is mentioned qualitatively. Some potential areas of research are identified.

Keywords. Elastic continuum theory; lattice defects; inhomogeneities; dislocations; disclinations; dislocation density tensor; torsion tensor; curvature tensor; dislocation density correlations; elastic field equations; nonlocal elasticity.

1. Introduction

This paper is intended to survey the elastic continuum theories of lattice defects. The understanding of the behaviour of crystal defects is essential for studying such processes as anelasticity, plastic flow, rupture, fatigue and radiation damage, which play a crucial role in materials science. The lattice distortion produced by a defect can be calculated by using elastic models at sufficiently large distances from the defect. In many applications, a continuum theory offers precise analytic expressions for the stress fields of defects, their interaction energies, etc., and hence is of immense practical value. In contrast to this, a discrete atomistic approach (which is unavoidable at short distances from the defects) does not offer analytically convenient working relations, although it yields reliable numerical data.

At present there is no unified theory of defects in continuous media. Most theories are developed with a particular type of defect in view. Thus the methods applicable to point defects are different from those applicable to line defects—for dislocations, see *e.g.*, de Wit (1960), Nabarro (1967), Mura (1968); for volume defects (inclusions), see Eshelby (1957). Moreover, almost all theories are restricted to static defect problems. The dynamical theory of defects in continua is still in its infancy. This review presents a bird's eyeview of the various approaches to defects in a continuous medium.

2. Continuum modelling of defects

In the elastic continuum theory, defects are modelled following the procedure given by (See e.g. Eshelby 1956). In order to construct a defect, one marks out in the medium an appropriate surface S_C bounded by a curve C and makes a cut coinciding with C. Then a relative displacement $\delta\mathbf{u}$ is given to each pair of points on either side of S_C, scraping away material where there would be interpenetration and filling in the remaining gaps with additional material. In general, $\delta\mathbf{u}$ can be written as

$$\delta u_i = b_i + \Omega_{ij} x_j \quad (i, j = 1, 2, 3),$$

where x_j denotes the coordinates of the point, b_i the relative translation of this point, and $\Omega_{ij} (= -\Omega_{ji})$ describes the relative rotation of S_C. A general dislocation is thus described by six constants—in other words, it consists of six elementary (Volterra) dislocations. Each of the latter can be characterized by a single constant, the other five being set equal to zero. A rotational dislocation with $b_i = 0$ is actually a disclination. When $\Omega_{ij} = 0$, one has the usual (translational) dislocation with a Burgers vector $\mathbf{b}$. Some examples of defects created in this manner are shown in figure 1. Figure 1(a) shows an edge dislocation produced by cutting a ring-shaped cylinder across the surface S_C, choosing the axis of the cylinder as the curve C, and displacing the upper side of the surface S_C over the lower by an amount $\mathbf{b}$ perpendicular to the axis. In figure 1(b), a sector of the cylinder is cut defining the surface S_C and the axis as C, and both sides of the surface are pulled apart widening the angle of the sector so as to accommodate a larger sized sector. This produces a wedge disclination, $\mathbf{\Omega}$ being a rotation around the axis. Figure 1(c) shows the Somigliana prescription for creating a substitutional or an interstitial atom. A sphere is cut out of the matrix, its radius altered by adding or removing material, and the sphere is then reinserted in the matrix. This is the familiar misfitting sphere model. Note that there is no boundary curve C in this case. It can be shown that a knowledge of $\delta\mathbf{u}$ as a function of position x_i on the surface S_C, together with the boundary conditions at the surface of the body, completely determines the resulting state of internal stress.

3. Basic equations of elasticity theory

In the linear theory of elasticity, the condition of equilibrium is given by

$$\sigma_{il,l} + f_i = 0, \tag{1}$$

where σ_{il} is the stress tensor, f_i is the body force and the usual comma notation for derivatives and the convention of summation over repeated indices are used. σ_{ij} is related to the strain tensor e_{ij} by Hooke's law:

$$\sigma_{il} = C_{ilmn} e_{mn}, \tag{2}$$

where

$$e_{mn} = \tfrac{1}{2}(u_{m,n} + u_{n,m}), \tag{3}$$

is the symmetric part (sym) of the gradient (grad) of the displacement field $\mathbf{u}$: thus $e = \text{sym grad } \mathbf{u} \equiv \text{def}\,\mathbf{u}$. For an isotropic homogeneous medium

$$C_{ilmn} = \lambda\delta_{il}\delta_{mn} + \mu(\delta_{im}\delta_{ln} + \delta_{in}\delta_{lm}), \tag{4}$$

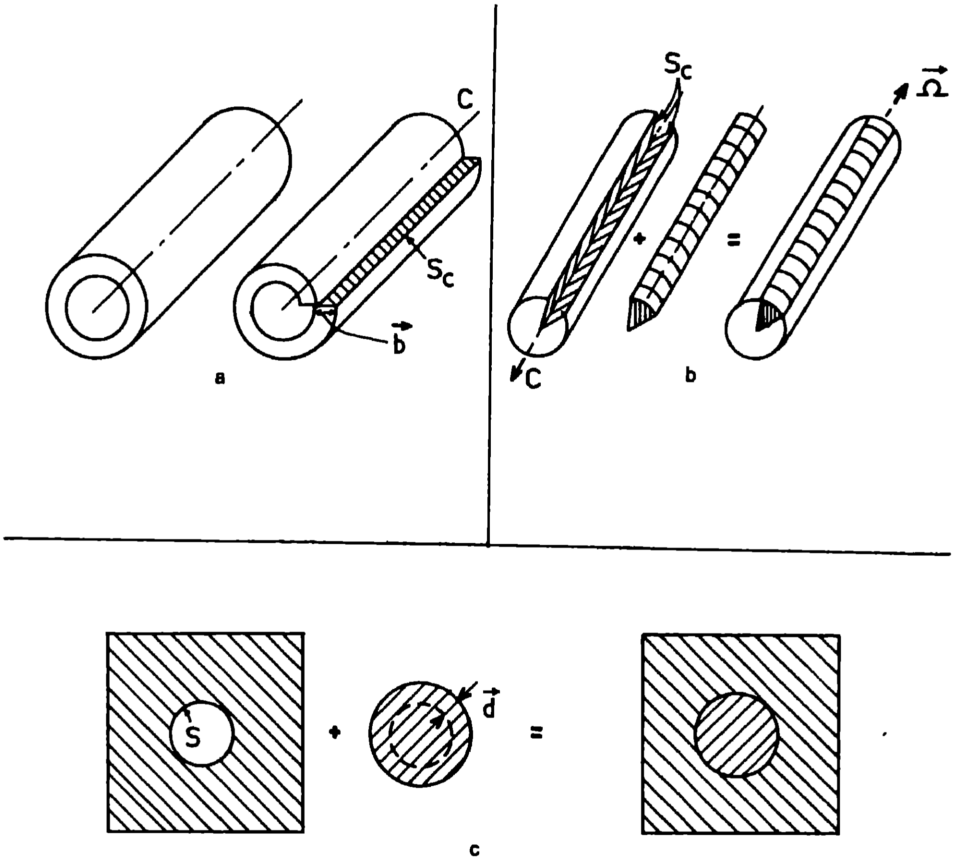

Figure 1. (a) Continuum model of an edge dislocation. (b) Continuum model of a wedge disclination. (c) Misfitting sphere model for a substitutional atom.

where λ is Lame's constant and μ is the shear modulus. Equations (1)–(3) imply the differential equations

$$C_{ilmn}u_{m,nl}+f_l=0 \tag{5}$$

for $\mathbf{u}$. Let G_{li} be the Green function tensor defined by the equation

$$C_{ijkl}G_{km,lj}(|\mathbf{r}|)+\delta_{im}\delta(|\mathbf{r}|)=0 \tag{6}$$

and the boundary condition $G_{km}(r\rightarrow\infty)=0$. Then

$$G_{km}(r)=\frac{1}{8\pi\mu}\left[\delta_{km}r_{,pp}-\frac{\lambda+\mu}{\lambda+2\mu}r_{,km}\right]. \tag{7}$$

The elastic field due to the body force $\mathbf{f}$ is given by

$$u_l(\mathbf{r})=\int f_i(\mathbf{r}')G_{li}(|\mathbf{r}-\mathbf{r}'|)\mathrm{d}^3r'. \tag{8}$$

The existence of a continuous single-valued displacement field u_l requires the incompatibility (inc) of the strain tensor to vanish, *i.e.*,

$$\operatorname{inc} \boldsymbol{e} = 0, \tag{9}$$

where, in component form,

$$(\operatorname{inc} \boldsymbol{e})_{ij} = -\varepsilon_{ikl}\varepsilon_{jmn}e_{ln,km} = [\operatorname{curl}(\operatorname{curl} \boldsymbol{e})]_{ij}, \tag{10}$$

ε_{ikl} denoting the completely antisymmetric Levi-Civita tensor or the alternator.

There are two broad ways of introducing defects into this picture. One is to start with (1) and assign an effective f_i, as is usually done in a point defect (Eshelby 1957). In line defects, one puts $f_i = 0$, but generalises (8) to include the contribution from the cut surface S_C (Mura 1968). In the second approach, one must recognise that when defects are present in the medium, the displacement field **u** is no longer a continuous single-valued function on S_C, and therefore the compatibility condition ought to be modified. This is achieved by generalizing (9) to include a source term η characterising the incompatibility distribution of the defect, *i.e.*, (9) is replaced by

$$\operatorname{inc} \boldsymbol{e} = \eta. \tag{11}$$

In the next section we describe briefly the first approach which is due largely to Eshelby (1957).

4. The Eshelby approach

Volume defects such as precipitates, solute atoms, self-interstitials, etc contribute to the change in the elastic state of the medium. A self-interstitial is modelled as a misfitting homogeneous inclusion (MHI). It corresponds to matter of volume $V + \Delta V$ being forced into a cavity of volume V in the medium (see figure 2a). Both the inclusion (I) and the matrix (M) have the same elastic moduli. An MHI is created in a body because of internal stress, *i.e.*, some region I of volume V develops internal stress and is transformed to a different shape and size with a volume $V + \Delta V^C$ while remaining inside the matrix M (see figure 2b). Thus a constrained stress (σ^C_{ij}) or a constrained strain (e^C_{ij}) is developed both in I and M.

Now suppose M was absent and I alone were to undergo a transformation (see figure 2c). It would acquire a different shape and size, with volume $V + \Delta V^T$. Let σ^T_{ij} and e^T_{ij} be the stress and strain associated with the transformation. These *need not* be of elastic origin (they may arise from metallurgical transformations, for example). Thus, symbolically, $I \xrightarrow{T} I^T$, and $M \xrightarrow{T} M$. Eshelby has posed and answered the following questions:

(i) How can one relate σ^C_{ij} and e^C_{ij} to σ^T_{ij} and e^T_{ij}? (ii) What can one deduce about the behaviour of $\mathbf{u}^C$, σ^C and e^C, the dilation and the self-energy of an MHI of arbitrary shape? (iii) What is the interaction energy of an MHI with an applied stress field σ^A_{ij}?

After answering these questions Eshelby asks the same questions for an "inhomogeneity" (see figure 2d). The inhomogeneity is an inclusion having elastic constants (λ^*, μ^*) different from those of the matrix (λ, μ). Note that a perfectly-fitting inhomogeneity (PFI) does not perturb the stress field in the matrix. However, a misfitting inhomogeneity (MFI) would alter the stress field in M.

An MFI is an appropriate model for a foreign interstitial in a crystal. Eshelby shows how to reduce the problem of an MFI to an equivalent MHI problem. The problem of an MFI in the presence of an external stress σ^A_{ij} is of interest in many practical situations such as SIPA creep (Heald and Speight 1974), voids in strained metals, etc. In the presence of σ^A_{ij}, a PFI can undergo an induced transformation strain e^T_{ij} 'proportional' to the applied strain e^A_{ij}. To illustrate the Eshelby approach, consider an MHI for which the displacement field u^C_i is given by

$$u^C_i(r) = \int \mathrm{d}S'_l C_{jlmn} e^T_{mn}(\mathbf{r}') G_{ij}(|\mathbf{r}-\mathbf{r}'|). \tag{12}$$

Eshelby considers a spherical and an ellipsoidal MHI for which e^T_{mn} is constant, and, using (7) for the Green function, arrives at the familiar relations (for the spherical MHI):

$$\left.\begin{aligned} e^C_{ij} &= {}'e^C_{ij} + \tfrac{1}{3} e^C \delta_{ij} \\ &= \beta\, {}'e^T_{ij} + \tfrac{1}{3} \alpha e^T \delta_{ij}, \\ e^C &\equiv e^C_{ii},\ {}'e^C_{ij} \equiv e^C_{ij} - \tfrac{1}{3} e^C \delta_{ij}, \\ \alpha &= \frac{1}{3}\left(\frac{1+\nu}{1-\nu}\right),\ \beta = \frac{2}{15}\left(\frac{4-5\nu}{1-\nu}\right). \end{aligned}\right\} \tag{13}$$

Here ${}'e_{ij}$ is the deviatioric part of e_{ij} and e is the scalar part. The general results for a PFI and an MFI under an applied load are given in Eshelby (1957).

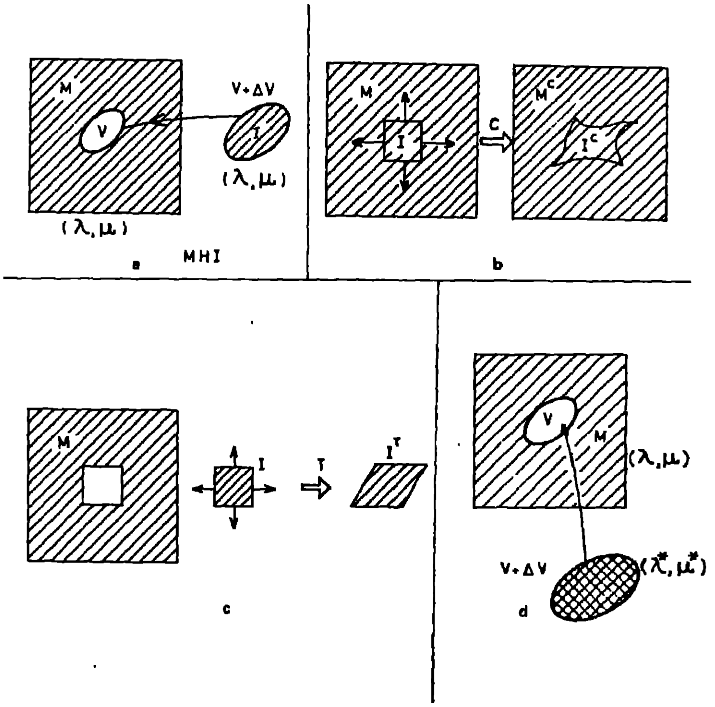

Figure 2. (a) A misfitting homogeneous inclusion (MHI). (b) The rectangular region *I* undergoing a constrained transformation in the matrix resulting in a curved shape. (c) The region *I*, detached from the matrix, undergoing a *T* transformation. (d) A misfitting inhomogeneity (MFI).

A significant feature of Eshelby's theory is the recognition of the important role of surfaces in defect problems. Eshelby was the first to show that the surface contribution to the change in volume of the medium, when defects are present, is quite significant. When defects (internal stresses) are present in a bounded medium, one must invoke image forces such that the boundary of the medium is kept free of stresses (the equilibrium condition), analogous to the method of images in electrostatics. As in the latter case, the image stress in the defect problem should have no internal sources in the medium. A well-known result derived by this method is that the volume change of a finite medium when a single spherical point defect is present is γ times the corresponding volume change in the infinite medium, where $\gamma = 3(1-\nu)/(1+\nu)$ is the famous Eshelby factor and ν is Poisson's ratio. If ν is taken as 1/3, then γ is as large as 3/2.

5. The elastic dipole tensor

Of central importance in the study of defects is the concept of the elastic dipole. Let a point force f_j be acting at a point $\mathbf{r}'$ in an elastic medium. The displacement u_j at a point $\mathbf{r}$ caused by the force is

$$u_j(\mathbf{r}) = f_l(\mathbf{r}')G_{lj}(|\mathbf{r}-\mathbf{r}'|). \tag{14}$$

Now suppose that in a small volume centred at $\mathbf{r}'$, N point forces $f_k^\alpha(\mathbf{r}'+\mathbf{s}^\alpha)$ are acting at the points $\mathbf{r}'+\mathbf{s}^\alpha$ ($\alpha = 1, \ldots, N$). Then (14) must be generalised to

$$\begin{aligned} u_l(\mathbf{r}) &= \sum_{\alpha=1}^{N} f_k^\alpha(\mathbf{r}'+\mathbf{s}^\alpha)G_{lk}(|\mathbf{r}-\mathbf{r}'-\mathbf{s}^\alpha|) \\ &= \left[\sum_{\alpha=1}^{N} f_k^\alpha\right] G_{lk}(|\mathbf{r}-\mathbf{r}'|) + \left[\sum_{\alpha=1}^{N} s_j^\alpha f_k^\alpha\right] G_{lk,j'}(|\mathbf{r}-\mathbf{r}'|) \\ &\quad + \frac{1}{2}\left[\sum_{\alpha=1}^{N} s_j^\alpha s_m^\alpha f_k^\alpha\right] G_{lk,j'm'}(|\mathbf{r}-\mathbf{r}'|). \end{aligned} \tag{15}$$

Here the second equality is obtained by expanding the Green function in a Taylor series about ($|\mathbf{r}-\mathbf{r}'|$). (Note that $G_{lk,j'}$ stands for $\partial G_{lk}/\partial x_j'$). The first term in the expansion vanishes, because for physically realizable defects the invariance of the entire system under a rigid infinitesimal translation implies that

$$\sum_\alpha f_k^\alpha(\mathbf{r}'+\mathbf{s}^\alpha) = 0. \tag{16}$$

The elastic dipole (P_{jk}), tripole (P_{jkl}), etc are then defined as the quantities in parentheses in the successive terms that remain:

$$\begin{aligned} P_{jk} &= \sum_{\alpha=1}^{N} s_j^\alpha f_k^\alpha, \\ P_{jmk} &= \sum_{\alpha=1}^{N} s_j^\alpha s_m^\alpha f_k^\alpha, \text{ etc.} \end{aligned} \tag{17}$$

The displacement field due to a dipole is thus

$$u_l(\mathbf{r}) = P_{jk}G_{lk,j'}(|\mathbf{r}-\mathbf{r}'|) \text{ and } P_{jk} = P_{kj}. \tag{18}$$

It can be shown easily that a dipole is simulated by a body force according to

$$f_i(r) = P_{ik}\delta_{,k'}(r-r'). \tag{19}$$

The importance of the elastic dipole can be judged from the following result due to Kovács (1978): *Any lattice defect can be described by a surface distribution of elastic dipoles.* To establish this fact, consider a surface S in a medium, and let it undergo a transformation such that the surface element dS'_m at a position $\mathbf{r}'$ on the surface has a displacement $a_l(\mathbf{r}')$. Due to this transformation, the surface element dS'_m becomes a source of an elastic singularity with a dipole strength which can be defined by the expression

$$\mathrm{d}P_{lk} = C_{iklm}a_l\mathrm{d}S'_m. \tag{20}$$

The total strength of the defect is given by

$$P_{lk} = \int_S C_{iklm}a_l\,\mathrm{d}S'_m. \tag{21}$$

The displacement field of the defect is obtained by applying (18) and integrating over the dipole distribution

$$\begin{aligned} u_n(\mathbf{r}) &= \int G_{nl,k'}(\mathbf{r}-\mathbf{r}')\,\mathrm{d}P_l(\mathbf{r}') \\ &= C_{iklm}\int_S G_{nl,k'}(\mathbf{r}-\mathbf{r}')a_l(\mathbf{r}')\,\mathrm{d}S'_m. \end{aligned} \tag{22}$$

To apply this result to a dislocation, consider a cut in the medium over the surface S_C bounded by a closed curve C. The positive direction of the normal to S_C is related to C by the right hand rule. Now let each point on S_C be given a displacement $a_l(\mathbf{r}') = b_l$, $\mathbf{b}$ being a constant vector. Then we obtain the familiar Burgers (1939) result

$$u_n(r) = C_{iklm}b_i\int_{S_C} G_{ln,m}(r-r')\mathrm{d}S'_k, \tag{23}$$

which is the displacement field of a dislocation loop C of Burgers vector $\mathbf{b}$.

The displacement field of an MHI can be obtained by choosing for S a closed surface enclosing a volume $V \neq 0$ and considering the displacement $a_l(r')$ inside and outside S:

$$a_l(\mathbf{r}') = \begin{cases} u_l^T(r'), & \text{if } \mathbf{r}' \in V \\ 0, & \text{otherwise.} \end{cases} \tag{24}$$

Using (18) and applying Gauss's theorem, one obtains

$$u_n(\mathbf{r}) = \int_V C_{iklm}u^T_{l,m}G_{nl,k'}\,\mathrm{d}V' + \int_V C_{iklm}u^T_l G_{nl,k'm'}\,\mathrm{d}V'. \tag{25}$$

As the Green tensor is symmetric and satisfied the equation

$$C_{iklm}G_{nl,k'm'} = -\delta_{nl}\delta(\mathbf{r}-\mathbf{r}'), \tag{26}$$

we obtain

$$u_n(\mathbf{r}) = \begin{cases} \displaystyle\int_V \sigma^T_{ik} G_{ni,k'}\,\mathrm{d}V' - u^T_n, & \text{if } r \in V, \\ \displaystyle\int_V \sigma^T_{ik} G_{ni,k'}\,\mathrm{d}V', & \text{if } r \notin V, \end{cases} \tag{27}$$

where $\sigma^T_{ik} = C_{iklm} u^T_{l,m}$. This result is essentially the same as that obtained by Eshelby (1961) if we identify $\frac{1}{2}(u^T_{l,m} + u^T_{m,l})$ with the transformation strain e^T_{ml}. The total strength of this defect is

$$\begin{aligned} P_{ik} &= \oint_S C_{iklm} u^T_l\,\mathrm{d}S'_m \\ &= \int_V C_{iklm} u^T_{l,m} \quad \mathrm{d}V' = \int_V \sigma^T_{ik}\,\mathrm{d}V'. \end{aligned} \tag{28}$$

Thus an MHI can be interpreted as a space distribution of dipoles with a volume density σ^T_{ik}. A PFI can be treated similarly (Kovàcs 1978), and the results of Eshelby (1957) rederived.

The interaction energy U between the defect, a strain field e^A_{ik} and the associated force F^t_n acting on the defect are expressed by the following general relations:

$$\begin{aligned} U &= -\int e^A_{ik}(\mathbf{r}')\,\mathrm{d}P_{ik}(\mathbf{r}') \\ &= -\int_S C_{iklm} e'_{ik}(\mathbf{r}') a_l(\mathbf{r}')\,\mathrm{d}S'_m. \end{aligned} \tag{29}$$

$$\begin{aligned} F^t_n &= \int e^A_{ik,n}\,\mathrm{d}P_{ik} \\ &= C_{iklm} \int_S e^A_{ik,n}(\mathbf{r}') a_l(\mathbf{r}')\,\mathrm{d}S'_m. \end{aligned} \tag{30}$$

These equations are applicable to any type of defect. Thus, substituting in (30) the displacement appropriate for a dislocation and using Stokes' theorem, one recovers the Peach-Koehler (1950) expression for the force

$$F^{\mathrm{disl}}_n = \oint_C \varepsilon_{mnk} \sigma^A_{lm} b_l\,\mathrm{d}l'_k, \tag{31}$$

where σ'_{lm} is the stress field associated with the strain e'_{lm} and $\mathrm{d}l'_k$ is a line element along C.

6. Generalizations of elastic continuum models

An important step towards bridging the gap between the elastic continuum approach outlined in the previous sections and the more detailed atomistic calculations has been achieved on two different fronts: the anisotropic continuum approach and the nonlocal continuum approach.

6.1 *The anisotropic continuum models*

These models are well described in the recent book by Teodosiu (1982) which also contains an exhaustive set of relevant references. A point defect in a crystal lattice is better represented by an elastic dipole tensor which is *anisotropic*, conforming to the symmetry of the actual defect site in the lattice, whereas the host lattice may be modelled as an elastically isotropic medium. We mention as an example the calculation of the interaction energy between two point defects with cubic symmetry O_h by Siems (1968). He showed that two elastic dipoles do not interact, and that the principal singularity of the elastic interaction energy between two such defects is the dipole-octupole interaction. Models along these lines have been proposed for faceted voids in irradiated crystals (Evans *et al* 1972; Malen and Bullough 1971).

Another approach is to consider spherically symmetric point defects in a host medium that is elastically anisotropic. The major drawback of this approach is the nonavailability of a closed form analytic expression for the Green tensor. For symmetries other than hexagonal symmetry (Kröner 1953), the solutions are in the form of series, thus necessitating perturbation-type calculations. For these reasons of mathematical inconvenience, not much work has been done along these lines. (For point defects, see Eshelby 1956; for line defects in an anisotropic host medium, Teodosiu 1982; Steeds and Willis 1979).

6.2 *The nonlocal elastic continuum models*

Eringen and Edelen (1972) and Eringen (1972, 1976) have developed a new theory of elasticity called nonlocal elasticity. This theory makes use of nonlocal elastic constants (a closer approximation to the force constants of the atomistic theories). The basic equations of linear isotropic elastic solids, for the static case and vanishing body forces are:

$$\left.\begin{aligned} \bar{\sigma}_{ik,k} &= 0, \\ \bar{\sigma}_{ik} &= \int_V \sigma_{ik}^{NL}(\mathbf{r},\mathbf{r}')\,\mathrm{d}^3r', \\ \sigma_{ik}^{NL} &= \alpha(|\mathbf{r}-\mathbf{r}'|)C_{iklm}e'_{lm}, \\ e'_{lm} &= \tfrac{1}{2}(u_{l,m'}+u_{m,l'}). \end{aligned}\right\} \tag{32}$$

Here $\alpha(|\mathbf{R}|)$ attenuates rapidly as $R \to 0$, it is a continuous function which depends on a parameter a such that when $a \to 0$, $\alpha(R) \to \delta(R)$ and the classical equations of elasticity are recovered. Here $e'_{lm} \equiv e_{lm}(\mathbf{r}')$ and $u_{l,m'} = \partial u_l/\partial x'_m$. The stress $\sigma^{NL}(\mathbf{r})$ is the nonlocal stress in the sense that its value at $\mathbf{r}$ depends on the strain at all $\mathbf{r}' \in V$. Eringen has shown that the first equation in (32) is satisfied if and only if $(C_{iklm}e_{lm})_{,k} \equiv \sigma_{ik,k} = 0$ in V. This means that the *displacement* field remains the same in the nonlocal theory as in the classical theory. The *stresses* differ in the two theories.

Kovàcs and Vörös (1979) showed that the appropriate body force F_i to be included in the generalization of (32) is

$$F_i(\mathbf{r}) = \int \alpha(\mathbf{r}-\mathbf{r}')f_i(\mathbf{r}')\,\mathrm{d}V', \tag{33}$$

where $f_j(\mathbf{r})$ is the body force in the classical theory (see (1)). The force acting on an elastic dipole is then

$$F_j(\mathbf{r}) = \mathbf{P}_{jk}(\mathbf{r}')\alpha_{,k'}(\mathbf{r}-\mathbf{r}') \tag{34}$$

and the interaction energy U between the elastic dipole and a displacement field u_i^A is

$$U(r) = -\int P_{jk}(\mathbf{r})\alpha(\mathbf{r}'-\mathbf{r})\mathbf{e}_{jk}^A(\mathbf{r}')\,\mathrm{d}V'. \tag{35}$$

Note that the interaction depends on the strain field at *all* points in the medium. The force acting on the dipole is

$$f_n = \int P_{jk}(\mathbf{r})\alpha(\mathbf{r}'-\mathbf{r})e_{jk,n}^A(\mathbf{r}')\,\mathrm{d}V'. \tag{36}$$

Note that (34)–(36) reduce to the corresponding equations of the classical theory, *i.e.* to (19), (29) and (30) when $\alpha(\mathbf{r}'-\mathbf{r}) \to \delta(\mathbf{r}'-\mathbf{r})$.

Since any defect can be described as a surface distribution of dipoles (discussed in § 5), it is interesting to generalise the results of the local theory for a surface distribution of dipoles. Kovács and Vörös (1979) have shown that (29) then generalises to the form

$$U = -\int_S \bar{\sigma}_{lm}^A(\mathbf{r}')a_l(\mathbf{r}')\,\mathrm{d}S'_m, \tag{37}$$

where

$$\bar{\sigma}_{ik}^A(\mathbf{r}) = \int_V \sigma_{ik}^{NL,A}(\mathbf{r},\mathbf{r}')\,\mathrm{d}V' = \int_V \alpha(|\mathbf{r}-\mathbf{r}'|)C_{iklm}e_{lm}'^A\,\mathrm{d}V' \tag{38}$$

and $a_l(\mathbf{r})$ and S are as defined in § 5. Similarly, (30) generalises to

$$f_n = \int_S \bar{\sigma}_{lm}^A(\mathbf{r}')a_l(\mathbf{r}')\,\mathrm{d}S'_m. \tag{39}$$

It is easy to show that the self-energy of the defect is

$$U_s = -\frac{1}{2}\int_S \bar{\sigma}_{lm}^s(\mathbf{r}')a_l(\mathbf{r}')\,\mathrm{d}S'_m, \tag{40}$$

where $\bar{\sigma}_{lm}^s$ is the stress field due to the defect alone.

As expected, the stress singularities and the embarassing infinite self-energies in the usual defect calculations are replaced by well-defined, finite quantities in the nonlocal theory. This is closer to physical reality, and the advantage of obtaining realistic defect properties without performing tedious atomistic calculations makes this approach very attractive. For lack of space, we quote a single result to substantiate this remark. The interaction energy U between two dilation centres of volume increments ΔV_1 and ΔV_2 is given by

$$U = 2\mu\frac{(1-\nu)}{(1-2\nu)}\Delta V_1 \Delta V_2 \alpha(R), \tag{41}$$

where R is the distance between the two defects. (Note that when $\alpha(R)$ is replaced by $\delta(R)$, $U \to 0$, since $R \neq 0$.) The self-energy U_s of a dilation centre of volume increment ΔV is

$$U_s = \tfrac{1}{2}P\Delta V\alpha(0) \tag{42}$$

A convenient representation of the kernel $\alpha(r)$ is the Gaussian

$$\alpha(R) = \frac{\pi^{3/2}k^3}{a^3}\exp(-k^2R^2/a^2). \tag{43}$$

It is natural to interpret the parameter a as the lattice parameter. The other parameter k is estimated by Eringen (1977a, b) from a consideration of the critical shear stress needed to create a dislocation. This leads to $k = 0{\cdot}94$ for fcc metals. In fcc metals $\Delta V = a^3\varepsilon/4$ where $\varepsilon = (V - V_0)/V_0$, the relative volume difference between the host and the alloying atoms. Then, using $\nu = 1/3$ and $k = 0{\cdot}94$, one obtains $U_s = 0{\cdot}56\mu a^3\varepsilon^2$. This is to be compared with the atomistic model calculation of Flinn and Maradudin (1962) which yields $U_s \approx 0{\cdot}54\mu a^3\varepsilon^2$.

Other examples of the application of the nonlocal theory include expressions for the stress field, strain energy, etc. of screw and edge dislocations (Eringen 1977a, b; Eringen and Balta 1979), as well as a nonsingular expression (Eringen *et al* 1977) for the stress-concentration function in the problem of an elastic plate with a sharp crack and subjected to a uniform tension (at infinity) perpendicular to the crack (the Griffith problem). These results show the potential utility of the nonlocal elastic models of defects which certainly needs to be explored much more elaborately. Moreover, calculations in nonlocal elastic theory are much simpler than the corresponding ones in the anisotropic elasticity approach briefly described in § 6.1.

7. The linear continuum theory of dislocations

Electron microscopic observations show that deformed crystals have numerous dislocation lines which are very often randomly tangled. A convenient way to describe these dislocations is via the *dislocation density tensor* $\alpha_{ij}(\mathbf{r})$ (Nye 1953). Consider an arbitrary point P in the material. In the neighbourhood of P, within a small area element dS, there are several dislocation lines with Burgers vector $\mathbf{b}^{(a)}$ $(a = 1, 2 \ldots n)$ in the directions $\hat{\nu}^{(a)}$, as shown in figure 3. The effective Burgers vector d**b** of n dislocations threading the surface dS is then given by

$$\mathrm{d}S_i\alpha_{ij} = \sum_{a=1}^{n} (\hat{\nu}^{(a)}.\hat{\nu})b_j^{(a)} \equiv \mathrm{d}b_j, \tag{44}$$

where $\hat{\nu}$ is the unit vector at P defining the element dS. The scalar product $(\hat{\nu}^a, \hat{\nu})$ measures the threading of the surface dS by the ath dislocation. In integral form, (44) is written as

$$\int_S \mathrm{d}S_i\alpha_{ij} = b_j = \oint_C \mathrm{d}u_j, \tag{45}$$

where C is the closed curve bounding the surface S. (Kröner 1964 and Noll 1967 have

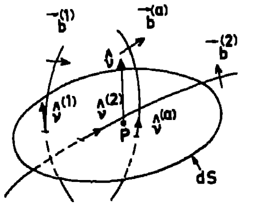

Figure 3. The area element dS showing the threading of dislocation lines.

defined α_{ij} somewhat differently; see Teodosiu (1982)). Now

$$\alpha_{ij} = \varepsilon_{ikl}\partial_k \beta_{lj} \quad (\text{or } \boldsymbol{\alpha} = \operatorname{curl} \boldsymbol{\beta}), \tag{46}$$

where $\beta_{ij}(\mathbf{r}) = u_{j,i}(\mathbf{r})$ is the gradient of the elastic displacement. Using (46) in (45) and invoking Stokes theorem, we find

$$\partial_i \alpha_{ij} = \alpha_{ij,i} = 0, \ (\text{or div } \boldsymbol{\alpha} = 0), \tag{47}$$

because the divergence of a curl vanishes. Physically this relation means that dislocations cannot end inside the medium. Another feature of the α-tensor is worth noting. The first index i of α_{ij} denotes the average direction of the dislocation lines whereas the second index j denotes the direction of the Burgers vector. Thus the diagonal components of $\boldsymbol{\alpha}$ correspond to screw dislocations and the off-diagonal elements to edge dislocations. Since the diagonal and nondiagonal components of a tensor are not invariant notions, *the classification of dislocations into edge and screw types is not to be taken too seriously.*

The introduction of the $\boldsymbol{\alpha}$-tensor has given impetus to the development of the beautiful differential-geometric theory (see § 9). The connection with geometry arises from the physical fact that dislocations involve a certain curvature or bending of the lattice network, thus imparting a curvature to the continuum (Nye 1953). To be more precise, the rotation tensor ω_{ij} defined as the antisymmetric part of β leads to an axial rotation vector $\omega_k = \frac{1}{2}\varepsilon_{ijk}\omega_{ij}$. The difference in ω between two points separated by an infinitesimal distance $d\mathbf{r}$ is given by

$$\mathrm{d}\omega_j = (\varepsilon_{jkl}\partial_k e_{li} + \kappa_{ij})\mathrm{d}x_i,$$

where

$$\kappa_{ij} = \alpha_{ij} - \tfrac{1}{2}\alpha_{kk}\delta_{ij} \tag{48}$$

is the Nye's curvature tensor (see also Kröner 1981). Thus, in the absence of elastic strains, the presence of a continuous distribution of dislocations alone leads to a rotation $d\theta$ between two points separated by a distance $d\mathbf{r}$ given by $d\theta_j = \kappa_{ij}\mathrm{d}x_i$. It is also straightforward to calculate the incompatibility tensor η associated with the presence of the dislocation distribution. We quote the final result (Kröner 1981):

$$\eta_{ij} = -\varepsilon_{ikm}\varepsilon_{jln}\partial_{kl}e_{mn} = \varepsilon_{ikm}\partial_k\kappa_{mj} = -\tfrac{1}{2}(\varepsilon_{iln}\partial_n\alpha_{jl})_{(ij)}, \tag{49}$$

$$\bar{\boldsymbol{\eta}} = \operatorname{inc} \boldsymbol{e} = \operatorname{curl} \boldsymbol{\kappa} = (\boldsymbol{\alpha} \times \nabla)_{\text{sym}} = -\operatorname{curl} \boldsymbol{\alpha}^T.$$

It is evident that the divergence of η vanishes.

8. The internal stress problem and Kröner's theory

Defects are characterized by the incompatibility tensor η associated with them. For a continuous distribution of dislocations it is given by (49). A single dislocation is described as a limiting case of the continuous distribution with the help of delta functions:

$$\alpha_{ij} = t_i b_j \delta(p)\delta(q), \tag{50}$$

where t_i is the tangent to the dislocation line and p, q are suitable coordinates perpendicular to the dislocation line. For a spherical interstitial atom occupying a volume ΔV and located at $\mathbf{r}_0$, the incompatibility tensor is

$$\eta = \Delta V(\vec{\nabla} \times I \times \overleftarrow{\nabla})\delta(\mathbf{r} - \mathbf{r}_0), \tag{51}$$

where I is the unit tensor (δ_{ij}).

The main problem in defect theory is: given the tensor η as a function of $\mathbf{r}$, to calculate the internal stress and strain in the body. This is a boundary value problem for the equations $\partial_i \sigma_{ij} = 0$ (force equilibrium condition in the bulk) and $\sigma_{ij} n_j = 0$ on the surface S of the body (the traction boundary condition) together with the incompatibility equation $\operatorname{inc} e = \eta$. There are three ways of calculation of e.

(i) *The Eshelby-Eddington method*: Eshelby (1956) uses the fact that, because of the tensor identities

$$\operatorname{inc}(\operatorname{def} u) = 0 \text{ and } \operatorname{div}(\operatorname{inc} A) = 0, \tag{52}$$

any solution of the incompatibility equation can be written as

$$e = \operatorname{def} \mathbf{u} + \tilde{e}, \tag{53}$$

where $\tilde{e}$ is a particular solution of the equation and $\mathbf{u}$ is an arbitrary vector field. If we put $\eta = 0$ on the boundary S, then following the method of Eddington in the general theory of relativity, one can write

$$\tilde{e}(\mathbf{r}) = \frac{1}{4\pi} \int_V d^3\mathbf{r}' \frac{\eta(\mathbf{r}') - (\operatorname{Tr}\eta) I}{|\mathbf{r} - \mathbf{r}'|}. \tag{54}$$

Next, by substituting (53) into the other field equation and the boundary conditions, one obtains a traction boundary-value problem of classical elasticity theory where $\mathbf{u}$ plays the role of a displacement field, while the body forces and the surface forces are given by

$$f_k = C_{klmn} \tilde{e}_{mn,l}, \tag{55}$$

$$t_k = -C_{klmn} \tilde{e}_{mn} n_l. \tag{56}$$

(ii) *Mura's method*: This method make use of the elegant Green function technique. The working relation (derived in Mura 1968; Teodosiu 1982) for the calculation of the elastic deformation tensor is

$$\beta_{mr}(\mathbf{r}) = \int \mathrm{d}^3 r' C_{plqn} \varepsilon_{nrt} \alpha_{qt,l'}(\mathbf{r}') G_{mp}(|\mathbf{r} - \mathbf{r}'|). \tag{57}$$

(iii) *Kröner's method*: Kröner (1981) exploited the analogy of the elastic field with the magnetostatic field. The following is the correspondence between quantities and relations in both theories. (See Seeger 1961 for an excellent review where reference to Kröner's earlier work are given.)

Elasticity	*Magnetism*
vector quantity	scalar quantity
rank two tensor	vector
rank four tensor	rank two tensor
div	div
inc	curl

Elasticity	*Magnetism*
div inc $\equiv 0$	div curl $\equiv 0$
def	grad
inc def $\equiv 0$	curl grad $\equiv 0$
Burgers vector **b**	current **I**
incompatibility tensor η	current density **J**
strain tensor e	magnetic intensity **H**
stress tensor σ	magnetic induction **B**
elastic constant C	permeability μ
$\sigma = C\!:\!e$	$\mathbf{B} = \mu\mathbf{H}$
div $\sigma = 0$	div $\mathbf{B} = 0$
inc $e = \eta$	curl $\mathbf{H} = \dfrac{4\pi}{c}\,\mathbf{J}$
tensor potential χ	vector potential **A**
$\sigma =$ inc χ	$\mathbf{B} =$ curl **A**

Another auxiliary tensor potential χ' is introduced ingeniously by Kröner. This is given by

$$\chi'_{ij} = \frac{1}{2\mu}\left(\chi_{ij} - \frac{\nu}{1+2\nu}\,\chi_{kk}\delta_{ij}\right), \tag{58}$$

the inverse relation being

$$\chi_{ij} = 2\mu\left(\chi'_{ij} + \frac{\nu}{1-\nu}\,\chi'_{kk}\delta_{ij}\right). \tag{59}$$

χ' satisfies the equations

$$\nabla^4\chi' = \eta \text{ and div } \chi' = 0. \tag{60}$$

Assuming that $\eta \to 0$ at the boundary of the infinite medium one calculates χ' from the relation

$$\chi'_{ij}(\mathbf{r}) = -\frac{1}{8\pi}\int d^3\mathbf{r}'\,|\mathbf{r}-\mathbf{r}'|\,\eta_{ij}(\mathbf{r}'). \tag{61}$$

In principle this solves the internal stress problem, since σ can now be calculated using $\sigma = \text{inc}\,\chi$.

Kröner has also put the elastic theory of point defects in a broader perspective. According to him, the elastostatics of a continuum with extrinsic point defects (foreign interstitials) is analogous to electrostatics, whereas in intrinsic defects (vacancies, self-interstitials) the elasticity theory is analogous to magnetostatics:

Electrostatics	Elastostatics with extrinsic defects
div $\mathbf{D} = \rho$	div $\sigma = -\mathbf{f}$
curl $\mathbf{E} = 0$	inc $e = 0$
$\mathbf{D} = \varepsilon\cdot\mathbf{E}$	$\sigma = C\!:\!e$
$U = \frac{1}{2}\mathbf{D}\cdot\mathbf{E}$	$U = \frac{1}{2}\sigma\cdot e$

Magnetostatics	Elastostatics with intrinsic defects (internal sources)
$\operatorname{div} \mathbf{B} = 0$	$\operatorname{div} \sigma = 0$
$\operatorname{curl} \mathbf{H} = \mathbf{J}$	$\operatorname{inc} e = \eta$
$\mathbf{B} = \mu \cdot \mathbf{H}$	$\sigma = C : e$
$U = \frac{1}{2}\mathbf{B} \cdot \mathbf{H}$	$U = \frac{1}{2}\sigma : e$

The distinction between extrinsic and intrinsic defects is considered to be a most fundamental one, since this has deeper implications in terms of differential geometry. The terms 'diaelasticity' and 'paraelasticity' now acquire meanings by analogy with electro- and magnetostatics. Carbon atoms in iron are permanent elastic dipoles giving rise to paraelasticity; whereas, in diaelasticity, the induced elastic dipoles p_{ij}^{ind} arise only in the presence of an applied elastic strain e_{kl}, according to $p^{\mathrm{ind}} = \alpha : e$. The PFI leads to diaelasticity, while MFI leads to both para- and diaelastic effects. A quantitative measure of the para- or diaelasticity associated with a point defect is the corresponding polarizability. The calculation of this quantity is an important problem in the study of point defect relaxation as in the Snoek effect (see, *e.g.*, Leibfried and Breur 1978). There are also ferroelastic solids possessing permanent macroscopic elastic dipole moment along favoured directions (see, *e.g.* Wadhawan 1982).

9. Differential geometry of defects

The description of defects in the foregoing was confined to linearalized theories. When finite deformations are included, the language of differential geometry and tensor calculus becomes indispensable. A summary of these theories is given by Kröner (1981) and we follow his presentation. The nature of the differential geometry is decided by the degrees of freedom associated with the atoms or molecules of the crystal. For constituent particles of the same kind, each having only three translational degrees of freedom (a Bravais lattice), affine geometry seems to be appropriate; whereas for a non-Bravais lattice of molecules possessing rotational degrees of freedom in addition to translational ones, Finsler's geometry (Amari 1962) is required.

Consider for simplicity a cubic primitive Bravais lattice and choose the lattice lines as the Cartesian coordinate lines. The Cartesian coordinates of this defect-free, reference crystal are denoted by x^k. Let the crystal be deformed and let this configuration have coordinates z^k. The connection between infinitesimal increments in the coordinates in the two configurations is given by

$$\mathrm{d}z^k = B_m{}^k \mathrm{d}x^m, \quad B_m{}^k = \partial z^k / \partial x^m. \tag{62}$$

Now $\mathrm{d}x^m$ being the corresponding change in the undeformed configuration, the relative displacement is given by

$$\mathrm{d}u^k = (B_m{}^k - \delta_m{}^k)\mathrm{d}x^m = \beta_m{}^k \mathrm{d}x^m. \tag{63}$$

With the coordinates x^k we associate an 'external observer' (also called the Eulerian frame of reference). Consider another observer, the 'internal observer' (the Lagrangian frame of reference) whose reference coordinates are 'dragged along' in the process of deformation. As long as the crystal is defect-free and the deformation is compatible, the internal observer feels no deformation. Let the coordinates of this frame of reference be

$y^{k'}$. Then the square of the distance between two infinitesimally separated points

$$ds^2 = \delta_{k'l'}\, dy^{k'} dy^{l'} \tag{64}$$

is an invariant for this observer. In contrast, for the external observer, there is a change in ds^2 after a deformation takes place, given by

$$ds^2 - ds_0^2 = (g_{kl} - \delta_{kl})\, dx^k dx^l \equiv 2e_{kl}\, dx^k dx^l. \tag{65}$$

Here ds_0^2 is the value of ds^2 before deformation, and

$$g_{kl} = \delta_{mn} B_k{}^m B_l{}^n. \tag{66}$$

The strain tensor can be easily shown to be

$$e_{kl} = \tfrac{1}{2}(\beta_{kl} + \beta_{lk}) + \tfrac{1}{2}\beta_k{}^m \beta_l{}^n \delta_{mn}. \tag{67}$$

Next, let us establish a connection between dislocations and torsion. Cartan (1928) introduced the concept of 'torsion' in a purely mathematical context. Later, Frank (1951) constructed the Burgers circuit to define a dislocation. That there is a remarkable similarity between Cartan's procedure for introducing torsion in differential geometry and Frank's construction for a dislocation was noted by Kondo (1952, 1955), Bilby *et al* (1955) and Bilby (1960). Frank considers the nonclosed path $A'B'C'D'E'$ (see figure 4) around a dislocation in a crystal counting the steps (each step consists of one atomic spacing). The closer failure A′E′ is the Burgers vector. Cartan transports a vector **CD** along the path **CB** from C to B and then a vector **CB** along the path from C to D. The vectors $\mathbf{CD} = \mathbf{d}_1\mathbf{x}(C)$, $\mathbf{BA} = \mathbf{d}_1\mathbf{x}(B)$, $\mathbf{CB} = \mathbf{d}_2\mathbf{x}(C)$ and $\mathbf{DE} = \mathbf{d}_2\mathbf{x}(D)$ are all of infinitesimal length. The law of parallel transport of $\mathbf{d}_1\mathbf{x}(C)$ along $\mathbf{d}_2\mathbf{x}(C)$ can be written as

$$d_1x^h(B) = d_1x^h(C) - \Gamma_{ml}{}^h d_1x^l(C) d_2x^m(C), \tag{68}$$

where $\Gamma_{ml}{}^h$ is the affine connection. Similar transport of $\mathbf{d}_2\mathbf{x}(C)$ along $\mathbf{d}_1\mathbf{x}(C)$ gives

$$d_2x^h(D) = d_2x^h(C) - \Gamma_{ml}{}^h d_2x^l(C) d_1x^m(C). \tag{69}$$

The closure failure is thus

$$\begin{aligned}(\mathrm{AE})^h &= d_1x^h(C) + d_2x^h(D) - d_2x^h(C) - d_1x^h(B)\\ &= \Gamma_{ml}{}^h(d_1x^l d_2x^m - d_2x^l d_1x^m)\\ &= -\Gamma_{ml}{}^h dS^{ml},\end{aligned} \tag{70}$$

where $dS^{ml} = (d_1x^m d_2x^l - d_1x^l d_2x^m)$ is the area element enclosed by the four infinitesimal vectors. The tensor dS^{ml} is related to the area vector dS_n by the relation

$$dS^{ml} = \bar{\varepsilon}^{nml} dS_n, \quad dS_n = \tfrac{1}{2}\bar{\varepsilon}_{nml}\, dS^{ml}, \tag{71}$$

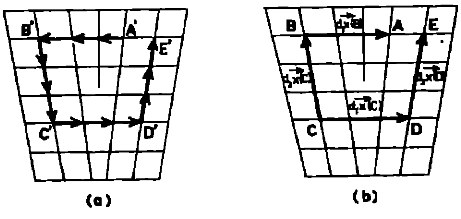

Figure 4. (a) Frank's circuit, (b) Cartan's circuit.

where $\bar{\varepsilon}^{nml} = g\bar{\varepsilon}^{nml}$, with $g = (\det(g_{lm}))^{1/2}$ (i.e., $\bar{\varepsilon}^{nml}$ is the contravariant Levi-Civita tensor, etc.). Note that only the antisymmetric part of the connection contributes to the vector $(\mathbf{AE})^h$ in (70). This is Cartan's torsion tensor,

$$T_{ml}{}^h = \tfrac{1}{2}(\Gamma_{ml}{}^h - \Gamma_{lm}{}^h). \tag{72}$$

Now, to establish contact with the dislocation density tensor α_{ij} defined in § 7, note that by definition the Burgers elemental vector is

$$\mathrm{d}b^k = \alpha^{nk}\mathrm{d}S_n \equiv \alpha_{ml}{}^k\mathrm{d}S^{ml}, \tag{73}$$

where

$$\alpha_{ml}{}^k = \tfrac{1}{2}\bar{\varepsilon}_{nml}\alpha^{nk}, \quad \alpha^{nk} = \bar{\varepsilon}^{nml}\alpha_{ml}{}^k. \tag{74}$$

On comparing $\mathrm{d}b^k$ with $(\mathbf{AE})^k$ we get

$$T_{ml}{}^k = -\alpha_{ml}{}^k. \tag{75}$$

This basic identification of the dislocation density tensor with the torsion tensor is the starting point of the differential geometric approach.

The presence of torsion leads to a non-Riemannian geometry. It is known (Schouten 1954) that if the metric is to satisfy the relation $\nabla_m g_{lk} = 0$ where ∇_m is the symbol for covariant derivative, then the most general form of the affine connection possible is related to the torsion as follows: writing $\Gamma_{ml}{}^h = g^{hk}\Gamma_{mlk}$, it turns out that

$$\Gamma_{mlk} = g_{mlk} + h_{mlk}, \tag{76}$$

where

$$g_{mlk} \equiv \tfrac{1}{2}(\partial_m g_{kl} + \partial_l g_{mk} - \partial_k g_{lm}) \tag{77}$$

and

$$h_{mlk} \equiv T_{mlk} + T_{kml} - T_{lkm}. \tag{78}$$

Here g_{mlk} is the Christoffel symbol of the second kind, and h_{mlk} is the *contortion tensor*. The earlier definitions of the distortion tensor β_{lk}, the strain tensor e_{lk} and the rotation tensor ω_{lk} are generalised to read

$$\left.\begin{aligned} \mathrm{d}\beta_{lk} &= \Gamma_{mlk}\mathrm{d}x^m, \\ \mathrm{d}e_{lk} &= \Gamma_{m(lk)}\mathrm{d}x^m, \\ \mathrm{d}\omega_{lk} &= \Gamma_{m[lk]}\mathrm{d}x^m, \end{aligned}\right\} \tag{79}$$

where (lk) and $[lk]$ respectively stand for symmetric and antisymmetric combinations of these indices. Equation (9) of the linearized theory, which can also be written as

$$\vec{\nabla} \times e \times \overleftarrow{\nabla} - \mathrm{sym}\{\boldsymbol{\alpha} \times \overleftarrow{\nabla}\} = 0 \tag{80}$$

is generalised in the nonlinear theory to the vanishing of the curvature tensor, *i.e.*,

$$R_{nmlk} = 0, \tag{81}$$

where $R_{nmlk} = g_{kh}R_{nml}{}^h$ and

$$R_{nml}{}^h = 2(\partial_n\Gamma_{ml}{}^h - \Gamma_{mp}{}^h\Gamma_{nl}{}^p)[nm]. \tag{82}$$

Equation (81) is the *second basic law* of the differential geometric theory of lattice defects. Physically, this means that if a crystal has dislocations as the only defects in it during deformation, and if it does not develop cracks, then the dislocation distribution must be accompanied by elastic strains such that the curvature tensor vanishes.

The second basic identification states that elementary *extrinsic* defects (extra matter on interstitial sites, fission fragments, α-particles stuck in the medium, etc) cause a *rotation-like* curvature ($R_{nm[lk]} \neq 0$, $R_{nm(lk)} = 0$). According to the third basic identification, *intrinsic* point defects like self-interstitials and vacancies lead to a *non-metric* curvature ($R_{nm[lk]} = 0$, $R_{nm(lk)} \neq 0$). The non-metric situation is not as well understood in differential geometry as the metric connection. When extrinsic defects are present in addition to dislocations, a beautiful analogy emerges between the field equations of defects and Einstein's equations in the general theory of relativity. To see this, we note that the curvature tensor R_{nmlk} is antisymmetric in l and k for the metric geometry, and, by definition, it is also antisymmetric in n and m. Thus, without any loss of information, it can be replaced by a second rank tensor E^{ij} (called the Einstein tensor) given by

$$E^{ij} = \tfrac{1}{4}\bar{\varepsilon}^{inm}\bar{\varepsilon}^{jlk} R_{nmlk}. \tag{83}$$

It can be shown that, in the linear approximation, (83) reduces to

$$\boldsymbol{E} = -\operatorname{inc} \boldsymbol{e} + \operatorname{curl} \boldsymbol{\kappa}. \tag{84}$$

Note that when $R_{nmlk} = 0$, $E^{ij} = 0$. When extra matter is present, the Einstein tensor does not vanish and becomes equal to the matter tensor M^{ij} or $\boldsymbol{E} = \boldsymbol{M}$. This is analogous to the Einstein's field equation. Thus the defects in a crystal are analogous to matter in the universe. "Without matter, the universe is not interesting; without defects, a crystal is dead—" (Kröner 1981).

The approach to defect theories *via* differential geometry is undoubtedly an elegant one. There is a related approach by Wang (1967) and Noll (1967) which starts with the philosophy that the constitutive law of the continuum being fundamental, it must determine the geometry. There are attempts at constructing a Yang-Mills type of minimal coupling theory for materials with dislocations and disclinations (Kadić and Edelen 1982; Edelen 1980). The work of Julia and Toulouse (1979) and that of Dzyaloshinskii and Volovik (1978) are efforts in the same direction. There are further treatments of the differential geometry of defects by Gairola (1979), Zorawski (1967) and Marcinkowski (1979). Marcinkowski in several publications has applied differential geometric techniques extensively to dislocations on surfaces, grain boundaries, cracks, etc.

In spite of its mathematical elegance, the differential-geometric approach to defect problems has not helped much in the development of the phenomenological theory of plasticity. The reason is that, in contrast to the case of electric or magnetic lines of force in electromagnetic theory, dislocation lines almost always form very irregular interconnected networks. This is the main reason why the continuum theory of dislocations and the differential-geometric approach as such can never constitute a good macroscopic theory of plasticity. Dislocations piercing through an area element in the crystal usually appear with positive as well as negative signs so that their resultant Burgers vector is often zero or has a very small value. This results in a very small magnitude for the dislocation density $\boldsymbol{\alpha}$. To understand this, consider for example the configuration of dislocations shown in figure 5. All the dislocation lines are in the z direction; positive (⊥) and negative (T) dislocations have Burgers vectors $+b$ and $-b$, respectively. Let the domain be divided by a mesh as shown in the figure and let a^2 be the area of each small square. If we consider as the area ΔS_3 the rectangle AA′B′B, $\alpha_{31} = -b/a^2$; if ΔS_3 is the rectangle BB′C′C, $\alpha_{31} = +b/a^2$; whereas if area ΔS_3 = AA′C′C, $\alpha_{31} = 0$. Note that if we let $\Delta S_3 \to 0$ around the point P_1, then $\alpha_{31}(P) = \pm b_1 \delta(P - P_1)$, where the + sign is applicable if there is a positive dislocation at P_1, and

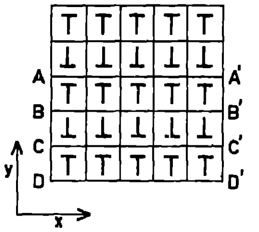

Figure 5. Positive and negative edge dislocations arrays piercing through a rectangular region.

the − sign if there is a negative dislocation. This means that the microscopic theory of dislocations is built into the formalism, but that in the process of coarse-graining over the distribution of dislocations, too much information seems to be lost.

Kröner (1970) has suggested the following way to rectify this deficiency. According to him, the random distribution of dislocations calls for the use of statistical mechanics. Information about the actual dislocation distribution may be given by n-point correlation tensor functions $\langle \alpha(\mathbf{r}_1)\alpha(\mathbf{r}_2)\ldots\alpha(\mathbf{r}_n)\rangle$ which give the probability of finding dislocation elements at $\mathbf{r}_1, \mathbf{r}_2 \ldots \mathbf{r}_n$. Thus one considers, instead of a single real specimen, a whole ensemble of crystals all filled with dislocation line elements in such a way that the ensemble represents all possible realizations of a given macroscopic dislocation state. One may impose extra conditions by prescribing the total energy, the total dislocation length, etc. These would correspond to various types of ensembles (analogous to the well-known microcanonical, canonical and grand canonical ensembles). Kröner (1970) shows that the information contained in the two-point correlation $\langle \alpha_{ij}(\mathbf{r})\alpha_{kl}(r')\rangle$ is quite extensive. For example, it gives information about the total dislocation length in a given volume element, the density of dislocation dipoles, etc. It is (obviously) suitable for describing planar dislocation networks, and, to some extent, dislocation pileups as well. Kröner and Teodosiu (1974) have made the important observation that the internal mechanical state, instead of being represented by the dislocation density tensor and its higher-order correlations, can also be specified by means of the fluctuations of the stress and elastic strain produced by the dislocations. This is of interest because it is the fluctuating stresses and strains that determine the deformation behaviour of materials. This line of approach is very attractive, but much work needs to be done. For example, if the dislocation elements are the basic entities of the system which we want to describe by statistical mechanics, what is the counterpart of Liouville's theorem that would guarantee that the known equations of motion of the dislocation line elements are satisfied? It is worth mentioning here that in another attempt to rectify the shortcomings of the dislocation density tensor, Kroupa (1962) has introduced the dislocation loop density as an additional variable. This approach too has not yet had any practical application.

10. Continuum mechanics of moving dislocations

Kosevich (1979) has generalised the basic equations of continuum mechanics taking into account the motion of dislocations during deformation. He has given a very simplified treatment under the (rather drastic) assumption that the energy conservation equation remains unchanged. (This is equivalent to assuming that no heat is generated in the process of dislocation motion). Thus, only the equations of continuity expressing the (local) conservation of mass and (linear) momentum are considered. One begins with the fundamental equation which introduces dislocations into elasticity theory, namely, (46). If dislocations remain static during the deformaton, then the velocity field $V_k(\mathbf{r})$ is related to the elastic distortion field $\beta_{ik}(\mathbf{r})$ by $\partial_i V_k = \partial_t \beta_{ik}$. However, when dislocations move, this equation must be generalized to

$$\partial_i V_k = \partial_t \beta_{ik} - j_{ik}. \tag{85}$$

Here $j_{ik}(\mathbf{r})$ is the dislocation flux tensor which must be so chosen that (85) is consistent with (46). Taking the curl of (85) and using (46), one obtains the (local) law of conservation for the Burgers vector

$$\partial_t \alpha_{ik} + \varepsilon_{ilm} \partial_l j_{mk} = 0. \tag{86}$$

If C is a closed curve bounding a surface S, then (86) can be expressed in the alternate form

$$\mathrm{d}b_k/\mathrm{d}t = -\oint_C j_{ik}\, \mathrm{d}x_i. \tag{87}$$

The total distortion β^T_{ik} is the sum of the elastic distortion β_{ik} and the plastic distortion β^P_{ik}. Since $\partial_i V_k = \partial_t \beta^T_{ik}$ by definition, we have evidently $\partial_t \beta_{ik} = -j_{ik}$. Hence

$$\partial_t e^P_{ik} = -j_{(ik)}, \tag{88}$$

which is the Orowan equation. For a continuous distribution of dislocations,

$$j_{ik} = \varepsilon_{ilm} \sum_a b_k V_m(\mathbf{r}, \hat{\nu}^{(a)}) \nu_l^{(a)}. \tag{89}$$

(compare with (46) which defines α_{ik}). The trace j_{kk} of the flux tensor j_{ik} is of special interest in connection with the continuity equation for mass. Noting that the relative change in density $\delta\rho$ is given by $e_{kk} = -\delta\rho/\rho$ (where ρ is the density of the medium) and using (85), one obtains

$$\partial_t \rho + \operatorname{div}(\rho \mathbf{V}) = -\rho j_{kk}. \tag{90}$$

The 'complete system' of dynamical equations can then be presented in the form

$$\left.\begin{aligned} &\partial_i \sigma_{ik} = \rho \partial_t V_k \quad \text{(Newton's Law)},\\ &\sigma_{ik} = C_{iklm} \beta_{lm} \quad \text{(elastic constitutive Law)},\\ &\varepsilon_{ilm} \partial_l \beta_{mk} = -\alpha_{ik},\\ &\partial_i V_k = \partial_t \beta_{ik} - j_{ik}, \end{aligned}\right\} \tag{91}$$

where the tensors α_{ik} and j_{ik} must be specified. Note that α_{ik} and j_{ik} must satisfy (47) and (86).

We mention here that a lattice defect approach to plasticity and viscoplasticity has been proposed by Kröner and Teodosiu (1974), in which particular emphasis is laid on dislocations. These authors propose a complete set of equations which consist of the continuity equations including the law of conservation of energy, and the thermoelastic constitutive equations for the stress and the heat flux. However, the theory is rather formal and has not yet been tested on any practical problem.

11. The quantum field theory approach

Field theorists have recently been interested in defects in crystals. Defects (termed 'extended objects' to stress the generality of the formalism) are viewed as classical macroscopic objects in a quantum ordered state (a perfect crystal). They are a macroscopic manifestation of the local condensation of bosons associated with a quantum mechanical collective mode (the phonons). There is an efficient tool called the boson transformation technique which describes the condensation process mathematically. In high energy physics, the topological structure of extended objects has been of great interest, being connected with the problems of quark confinement and particle structure. The boson transformation approach to defects was motivated by the success of the theory of solitons. A soliton is a localized wave solution of a classical nonlinear equation which behaves like a particle. The search for soliton solutions in three space dimensions is a challenging problem in itself. Their localized nature suggests that dislocations, point defects, grain boundaries, etc. are somehow related to soliton-like objects in three-dimensions. As it would require a rather lengthy presentation of the field-theoretic background and the boson transformation formalism, we do not describe this approach here. It is best described in the review article of this theory by Wadati (1979). (See also: Umezawa *et al* 1982.) We mention also that Holz (1979, 1980) has given a microscopic Hamiltonian theory of dislocations in crystals.

12. Conclusion

The present review was intended to bring out the fact that there is as yet no single unified theory of all defects in crystals. The merits and drawbacks of the various theories available have been pointed out. To the reviewer the following areas seem to need urgent attention. The idea of Kröner (1970) that the loss of information in the coarse-graining process needed to define the dislocation-density tensor can be remedied with the help of higher-order correlation functions, needs to be pursued further. The alternate idea of Kröner and Teodosiu (1974) that it must be possible to describe the deformation behaviour of materials in terms of the fluctuations of the stress and strain (produced by dislocations) clearly suggests a stochastic approach to plastic flow. The difficulty here is the fact that even the deterministic equations needed to completely describe plastic flow are yet to be developed. In fact this was the spirit of the work of Kröner and Teodosiu (1974). Perhaps some extremely simple situations (like steady state creep) must be modelled first in terms of a stochastic description, and the relevant correlation tensors explicitly computed. Both Kosevich (1979) and Kröner and Teodosiu (1974) have proposed hydrodynamic equations for matter undergoing deformation. One testing ground for such hydrodynamic equations could be the work-hardening behaviour of materials. Cottrell (1953) has given a beautiful analogy between stage I of work-hardening and the laminar flow of a fluid, and between stage II and turbulent flow. However, one does not yet know what the 'Reynold number' is which would characterize the transition to 'turbulence' in the case of plastic flow. In the spirit of this analogy, it may be possible to introduce different types of dislocation density tensors to describe the transition from stage I to stage II of the work-hardening curve. It seems that much work remains to be done in developing a hydrodynamic theory of a continuous medium containing dislocations.

References

Amari S 1962 in *RAAG memoirs of the unifying study of the basic problems in engineering and physical sciences by means of geometry* (ed) K Kondo (Tokyo: Gakujutsu Bunken Fukyu-kai), Vol 3, p 193

Bilby B A 1960 in *Progress in solid mechanics* (eds) I N Sneddon and R Hill (Amsterdam: North-Holland), Vol 1, p 329

Bilby B A, Bullough R and Smith E 1955 *Proc. R. Soc. (London)* **A231** 263

Burgers J M 1939 *Proc. Acad. Sci. Amsterdam* **42** 378

Cartan E 1928 *Lecons sur la Géomètrie des espaces de Riemann* (Paris: Gauthier-Villars)

Cottrell A H 1953 *Dislocations and plastic flow in crystals* (Oxford: Clarendon Press)

de Wit R 1960 in *Solid state physics* (eds) F Seitz and D Turnbull (New York: Academic) Vol 10, p 249

Dzyaloshinskii I and Volovik G 1978 *J. Phys.* **39** 693

Edelen D G B 1980 *Int. J. Eng. Sci.* **18** 1095

Eringen A C 1972 *Int. J. Eng. Sci.* **10** 425

Eringen A C 1973 *Lett. Appl. Eng. Sci.* **1** 11

Eringen A C 1976 *Continuum Physics*, Vol IV, (New York: Academic)

Eringen A C 1977a *J. Phys.* **D10** 671

Eringen A C 1977b *Int. J. Eng. Sci.* **15** 177

Eringen A C and Balta F 1979 *Crystal Lattice Defects* **8** 73

Eringen A C and Edelen D G 1972 *Int. J. Eng. Sci.* **10** 233

Eringen A C, Speziale C G and Kim B S 1977 *J. Mech. Phys. Solids* **25** 339

Eshelby J D 1956 in *Solid state physics* (eds) F Seitz and D Turnbull (New York: Academic) Vol 3, p. 79

Eshelby J D 1957 *Proc. R. Soc. (London)* **A241** 376

Eshelby J D 1961 in *Progress in solid mechanics* (eds) I N Sneddon and R Hill (Amsterdam: North-Holland) Vol 2, p 89

Evans J H, Bullough R and Stoneham A M 1972 in *Radiation induced voids in metals* (eds) J W Corbett and L C Ianiello USAEC-CONF-71061

Flinn P A and Maradudin A A 1962 *Ann. Phys.* **18** 81

Frank F C 1951 *Philos. Mag.* **42** 809

Gairola B K D 1979 in *Dislocations in solids* (ed) F R N Nabarro (Amsterdam: North-Holland) Vol 1, p 223

Heald P T and Speight M V 1974 *Philos. Mag.* **29** 1075

Holz A 1979 *Phys. Rev.* **A20** 2521

Holz A 1980 *Phys. Rev.* **B22** 3678

Julia B and Toulouse G 1979 *J. Phys.* **40** L-395

Kadić A and Edelen D G B 1982 *Int. J. Eng. Sci.* **20** 49, 433, 747, (see also Kadić A and Edelen D G B 1983 *A gauge theory of dislocations and disclinations* (Berlin: Springer-Verlag))

Kondo K 1952 On the geometrical and physical foundations of theory of yielding in *Proc. 2nd Japan Nat. Congr. Applied Mechanics*, Tokyo

Kondo K 1955 Non-Riemannian geometry of imperfect crystals from a macroscopic viewpoint, in *RAGG memoirs of the unified study of basic problems in engineering and physical sciences by means of geometry* (ed) K Kondo (Tokyo: Gakujutsu Bunken Fukyu-kai)

Kosevich A M 1979 in *Dislocations in solids* (ed) F R N Nabarro (Amsterdam: North-Holland) Vol 1, p 33

Kovács I 1978 *Physica* **B94** 177

Kovács I and Vörös G 1979 *Physica* **B96** 111

Kröner E 1953 *Z. Phys.* **136** 402

Kröner E 1964 *Phys. Kondens. Materie* **2** 262

Kröner E 1970 in *Inelastic behaviour of solids* (eds) M F Kanninen, W F Adler, A R Rosenfeld and R I Jaffee (New York: McGraw-Hill) p 135

Kröner E 1981 in Les Houches Session XXXV, 1980 – *Physics of defects* (eds) R Balian *et al* (Amsterdam: North-Holland)

Kröner and Teodosiu C 1974 in *Problems of plasticity*, Int. Symp. on Foundations of Plasticity, Warsaw 1972, (ed) A Sawczuk (Leyden: Noordhoff Intl Publishing) p 45

Kroupa F 1962 *Czech. J. Phys.* **B12** 191

Leibfried G and Breur N 1978 *Point defects in metals* (Berlin: Springer-Verlag) Vol I

Malen K and Bullough R 1971 in BNES European Conf, Reading, England, March 1971

Marcinkowski M J 1979 *Unified theory of the mechanical behaviour of matter* (New York: Wiley)

Mura T 1968 *Adv. Mater. Res.* **3** 1

Nabarro F R N 1967 *Theory of crystal dislocations* (Oxford: Clarendon)

Noll W 1967 *Arch. Rational Mech. Anal.* **27** 1

Nye J F 1953 *Acta Metall.* **1** 153

Peach M and Koehler J S 1950 *Phys. Rev.* **80** 436

Schouten J A 1954 *Ricci-Calculus* (Berlin: Springer-Verlag)
Seeger A 1961 *Phys. Status Solidi* **1** 669
Siems R 1968 *Phys. Status Solidi* **30** 645
Steeds J W and Willis J R 1979 in *Dislocations in solids* (ed) F R N Nabarro (Amsterdam: North-Holland) Vol 1 p 33
Teodosiu C 1982 *Elastic models of crystal defects* (Berlin: Springer-Verlag)
Umezawa H Matsumoto H and Tachiki M 1982 *Thermo field dynamics and condensed systems* (Amsterdam: North-Holland)
Wadati M 1979 *Phys. Rep.* **50** 87
Wadhawan V K 1982 *Phase Transitions* **3** 3
Wang C C 1967 *Arch. Rational Mech. Anal.* **27** 33
Zorawski M 1967 *Théorie mathématique des dislocations* (Paris: Dunod)

Discussion

T V Ramakrishnan: What is the continuum local theory value for the self-energy of a point defect?

D Sahoo: For a mathematical point defect, it is infinity, but for a rigid 'point' defect occupying a volume ΔV, it is $\frac{2}{3}\mu\Delta V$, where μ is the shear modulus of the medium.

N Kumar: What is P in the nonlocal theory? Can you go to the local limit through some approximation?

Sahoo: P is the elastic dipole tensor, as in the local theory. It is the interaction between a dipole and a strain field which is nonlocal. Yes, one can go to the local limit by the replacement $\alpha(R) \rightarrow \delta(R)$.

H R Krishna Murthy: Is the nonlocal theory supposed to simulate the lattice?

Sahoo: Yes, it is intermediate between the local continuum theory and the discrete atomistic theory. The lattice appears through the parameter a occurring in the kernel $\alpha(R)$. This a is essentially the lattice constant.

Ramakrishnan: In that case, where is the dispersion?

Sahoo: Eringen (1972, 1973) has explicitly calculated the dispersion for a one-dimensional lattice. He has also calculated the dispersion curve for Rayleigh surface waves.

A S Parasnis: What exactly is it in the nonlocal theory that removes the infinities in the stress and strain at the core of a (screw) dislocation—a divergence which seems to be almost a necessity in a continuum theory?

Sahoo: It is essentially the replacement of all the δ functions by the finite kernel $\alpha(R)$. Being a smooth function like a Gaussian, this removes the infinities in the calculation of the integrals involved.

Parasnis: I have two comments: (i) I wonder if mere analogies, such as are implied in the attempt to have a 'unified' theory of defects, are likely to give physically significant theories and results. For example, two decades ago some mathematically-minded people drew an analogy between the closure failure *a la* the Burgers/Frank circuit and Ampere's law and built up a fair edifice. But this could *not* explain the simple fact that like-currents attract whereas like-dislocations repel. What is needed is a *physical* theory going beyond such analogies. (ii) The difference between a Burgers circuit and a Frank circuit is that since the latter closes in the dislocated crystal/medium, it refers to the Burgers vector in the undislocated reference crystal/medium. You called the circuit a 'Frank circuit' but opened it in the dislocated crystal!

G Srinivasan: I wonder whether in the multiple glide region, the analogy may be with a cross-linked polymer rather than with turbulence. The problem in the polymer case has been made tractable by de Gennes, Edwards and others. The analogy may be worth pursuing.

C K Majumdar: Dr Srinivasan is apparently referring to the calculation of the elastic property of rubber by Prof. S F Edwards. There is a linear part, a plateau and a nonlinear rising part—somewhat similar to the regions I and II you refer to. It is quite possible that this analogy is better than that with laminar and turbulent flow. Now, the rubber and the polymer problems are dominated by entropy. Entropy is always difficult to handle in a mechanistic or hydrodynamic model. This difficulty appears also in the treatment of shocks or grain boundaries discussed earlier. The entropy equation, if written down from the second law, is somewhat different in nature from the hydrodynamic equations or the electrodynamic or the elastic equations (compare for example, the entropy generation equation of Sommerfeld). Edward's calculation of rubber elasticity is statistical mechanical in character, because entropy is involved. (Hydrodynamic equations or electrodynamic equations in continuous media are also statistical in character, but entropy is not so easily expressed in mechanical terms—entropy has an integral character in phase space and is not easily expressed in a differential equation.) If the entropy equation could be written down, or rather, if the entropy could be woven into the framework, the analogy could be exploited—the insight of de Gennes and Edwards in random network problems may perhaps be useful here.

Bull. Mater. Sci., Vol. 6, No. 4, September 1984, pp. 799–804. © Printed in India.

Fracture of particulate composites

S RAY

Department of Metallurgical Engineering, University of Roorkee, Roorkee 247 672, India

Abstract. A thermodynamic analysis of the process of fracture in elastically deformable composites is formulated. The critical dimensions leading either to particle fracture or to matrix-particle decohesion are identified. Fracture in plastically deformable composites is discussed in the light of the experimental evidence regarding void or cavity nucleation. Models of void growth under the application of stress and the role of void growth in causing failure are described in brief.

Keywords. Fracture; composite; void nucleation; void growth; cavity.

1. Introduction

Particulate composites are materials containing one or more discontinuous phases dispersed in a matrix of a distinctly different phase, such that the length to diameter ratio of each dispersoid is of the order of unity. If the extent of the discontinuous phase (or phases) is small and the load shared by it is insignificant, the material is not effectively regarded as a composite because the mechanical property of the material does not reflect the characteristics of the discontinuous phase. However, many materials that are not originally designed as particulate composites may pick up discontinuous phases during processing in the form of particles of insoluble impurities or inclusions which subsequently exert an important influence on the fracture behaviour of these materials. Particulate composites can be divided into four basic classes depending on the mechanical properties of the continuous phase (the matrix) and the discontinuous phase (the particle). (a) brittle matrix-brittle particle, (b) brittle matrix-ductile particle, (c) ductile matrix-brittle particle, and (d) ductile matrix-ductile particle. The fracture behaviour of the first two classes will be analysed under the broad heading of elastically deformable composites in § 2, and fracture in the other two classes will be examined in § 3.

The first systematic approach to the process of fracture was developed by Griffith (1920) to explain the discrepancy between the ideal strength and the observed strength in a brittle material. The thermodynamics of the process of extension of an atomically sharp pre-existing crack of length $2c$ under an applied stress of σ was examined. When a crack extends, elastic energy is released due to relaxation of stress around the extended part of the crack; some energy is also expended by the system in creating a fresh crack surface. The extension of the crack becomes feasible only when the former energy exceeds the latter, thereby reducing the total free energy. The fracture stress, σ_0, calculated on the above basis is as given below.

$$\sigma_0 = (2\alpha E/\pi c)^{1/2}, \quad (1)$$

where α is the specific energy of the crack surface and E is the Young's modulus.

Orowan (1949) provided a similar analysis for the extension of a crack under the plane stress condition. Sack (1946) and Sneddon (1946) modified the estimate of σ_0 in (1) by including the stress concentration effect around the crack. However, the original approach is based on the very general principles of thermodynamics and so provides a *necessary* criterion for the propagation of a crack leading to fracture. Here, we use this simple approach to examine the different possible fracture processes in the problem at hand, to gain an insight into the underlying essentials. Detailed stress calculations will not be of help in this regard because crack propagation is controlled by the local stress and strain which are inhomogeneous and dependent on the exact particle shape and distribution. These material parameters vary considerably from sample to sample, even for the same engineering material.

2. Elastically deformable composites

Any composite with a brittle matrix can be deformed only elastically irrespective of the nature of the reinforcing particle. To determine the fracture behaviour it is necessary to analyse the local stress distribution around the particles. When a particulate composite is deformed, the force is not directly applied to the particles but is transferred through the matrix. We consider the simple model of a particle embedded in a brittle matrix as given in figure 1. To simplify the mathematical treatment the following assumptions are made: (i) Poisson's effect is negligible; (ii) both the particle and the matrix have the same shear modulus. The elastic matrix is subjected to a tensile stress of σ_m. The forces acting on an element extending an angle $d\theta$ at the centre are shown in figure 1(b). If τ_θ is the shear stress acting at the particle-matrix interface, the elemental force balance in the direction of the applied stress gives

$$d\sigma/d\theta = 2\tau_\theta. \tag{2}$$

A special case (*i.e.*, equal elastic moduli for particle and matrix) of the general result derived by Sezawa and Miyazaki (1928) then yields, for the magnitude of the stress distribution τ_θ at the particle-matrix interface, the expression

$$\tau_\theta = (1/2)\sigma_m \sin 2\theta. \tag{3}$$

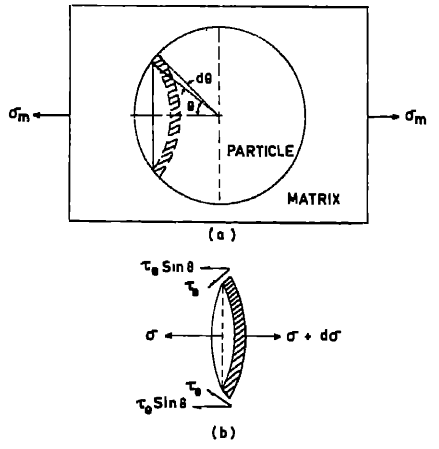

Figure 1. (**a**) Schematic representation of a single particle composite model. (**b**) Elemental force balance at a section of the particle.

Inserting this in (2) and integrating, the magnitude of the stress in the particle at a plane labelled by the angle θ is

$$\sigma_p = \sigma_m \sin^2\theta. \tag{4}$$

Let $\bar{\sigma}_m$, $\bar{\sigma}_p$ and $\bar{\tau}$ be the fracture strengths of the matrix, particle and interface. Then the matrix, or the particle, or the interface fractures first, if $\bar{\sigma}_m$, or $\bar{\sigma}_p$, or $2\bar{\tau}$ is the smallest of the three quantities $\bar{\sigma}_m$, $\bar{\sigma}_p$, $2\bar{\tau}$. In the first case, the original analysis of Griffith and its subsequent modifications are applicable, after the inhomogeneous stress distribution is determined. In the second and third cases, a similar analysis brings out certain additional parameters of interest.

2.1 *Particle fracture*

When the particle has fractured at a plane whose angle of extension is 2θ at the centre, this crack will be able to propagate in the matrix provided it is thermodynamically feasible. If the particle has a radius r, the change in energy ΔE for an infinitesimal extension $\mathrm{d}r$ of the crack is given by

$$\Delta E = -4\pi r^2 \,\mathrm{d}r\, \sigma_m^2 (1-\nu_m)^2 \sin^2\theta / E_m + 2\pi r \,\mathrm{d}r\, \gamma_m \sin\theta, \tag{5}$$

where ν_m and E_m are Poisson's ratio and the elastic constant respectively of the matrix and γ_m is the surface energy of the matrix. For the crack to propagate spontaneously, ΔE should be negative, which implies that

$$r > r_c = E_m \gamma_m / [2(1-\nu_m)^2 \sigma_m^2 \sin^2\theta]. \tag{6}$$

Since the particle has fractured when $\sigma_p = \bar{\sigma}_p = \sigma_m \sin^2\theta$ the composite will at once satisfy the necessary condition for failure if

$$r > E_m \gamma_m \sin^3\theta / [2(1-\nu_m)^2 \bar{\sigma}_p^2]. \tag{7}$$

Otherwise, the load can be increased till it attains the value

$$\sigma_m = [E_m \gamma_m / 2r(1-\nu_m)^2 \sin^2\theta]^{1/2}. \tag{8}$$

The matrix will fail at a load different from that causing the fracture of the particles. As a *range* of particle size is involved in real-life composites, the estimate of σ_m given by (8) must be calculated using the largest value of the particle radius r that is involved.

2.2 *Interface fracture*

When the interface is weak, let a crack be initiated there at an angle θ. The crack will extend along the interface from an angle θ to $\theta + \mathrm{d}\theta$ if the corresponding change in energy is negative. This change is given by

$$\Delta E = -\pi r^3 \sigma_m (1-\nu_p)^2 \sin^4\theta \,\mathrm{d}\theta / E_p + 2\pi r^2 (\gamma_p + \gamma_m - \gamma_{pm}) \sin\theta \,\mathrm{d}\theta, \tag{9}$$

where ν_p and E_p are Poisson's ratio and the elastic constant, respectively, of the particle; γ_p is the surface energy of the particle and γ_{pm} is the particle-matrix interfacial energy. The debonding between the matrix and the particle will take place as long as $\Delta E < 0$, and will extend up to

$$\theta_c = \sin^{-1}\left[\frac{2(\gamma_p + \gamma_m - \gamma_{pm})E_p}{r(1-\nu_p)^2 \sigma_m}\right]^{1/2}. \tag{10}$$

Clearly, this crack can propagate into the matrix if the size of the particle is such that

$$r \geqslant E_m \gamma_m / [2(1-\nu_m)^2 \sigma_m^2 \sin\theta_c]. \qquad (11)$$

If r is smaller than the quantity on the right, the load must be increased to the level given by (8) in order to fracture the matrix.

The surface energy of the particle, that of the matrix, and the particle-matrix interfacial energy play a vital role in determining the mode of fracture. The experimental determination of these energies is difficult and sometimes unreliable because of the segregation of impurities. The predictions of the above analysis may also become unreliable due to kinetic factors.

3. Plastically deformable composites

The phenomenon of fracture in a composite with a ductile matrix is commonly encountered in metals and alloys with inclusions. As composites contain a combination of phases, it is instructive to explore first the mechanism of fracture in a ductile single-phase material.

It is observed that cavities form in front of propagating cracks. It has therefore been assumed that vacancies in the highly strained region condense into voids. Under appropriate conditions of stress, these voids give rise to propagating cracks leading to the failure of the material. However, Balluffi and Siegel (1955) contend that the excess concentration of vacancies produced due to strain is not sufficient to lead to the homogeneous nucleation of voids, and that nuclei for void formation must pre-exist in the specimen. It is well known that cavities may also nucleate through a host of other mechanisms. For example, grain boundary sliding at low strain rates and intermediate temperatures gives rise to voids; and under such circumstances any factors preventing grain boundary sliding would also suppress the nucleation of cavities. Smith and Barnby (1967) have observed the nucleation of cavities at dislocation pile-ups, while Davies and Williams (1969) have observed this process taking place at twin-grain boundary intersections. All these mechanisms are operative at sites with large stress concentrations.

Such stress concentrations exist in the neighbourhood of the particles in a composite, and cavities form there either by cavity nucleation as in pure materials, or by mechanical decohesion of the matrix-particle interface as explained in § 2. Thermodynamic analysis (Greenwood and Harris 1965) shows that if $\gamma_{pm} < 10^{-3}\ \gamma_m$, mechanical decohesion is the most likely mode for cavity formation. Brown and Stobbs (1971) have estimated the critical strain for mechanical decohesion. A comparison of this estimate with the experimental value observed in a composite of silica particles dispersed in copper (Palmer and Smith 1968) indicates that the theoretical value is highly overestimated. This poses a problem, because a thermodynamic analysis provides *necessary* conditions and therefore *minimal* estimates in general. The discrepancy here may be attributed to the relaxation of stress observed around the smaller particles by the formation of prismatic loops. However, no such stress relaxation occurs around large particles and voids are readily formed there. Given a detailed understanding of the mechanisms of void creation, no quantitative theory of the fracture process under consideration is available, because the process is ultimately controlled by local stresses and strains, which in turn are governed by the shape and distribution of the particles in the matrix. Moreover, once voids are formed, the stress induces further growth and both the volume and the shape of the voids change, with the actual strain history exerting a significant influence.

Mcclintock (1968) proposed the first model for the growth of a cylindrical hole in a hardening plastic matrix. Subsequently, Rice and Tracey (1969) investigated another model for the growth of a spherical hole in a non-hardening plastic matrix and proposed a nonlinear relation between the radial velocity of the void surface and the applied strain field. Jalinier (1981) applied the linear version of the model to the damage observed in sheet metal. For a void caused by the decohesion of the particle-matrix interface as well as for a void generated by the cracking of the particle, $\varepsilon_i = B_i \varepsilon_i^{\infty}$, where ε_i is the relative extension of the void in the i-direction and ε_i^{∞} is the applied strain field far from the void. For decohesion, B_i is a function of the ratio $\varepsilon_2/\varepsilon_1$ of the principal strains, which for fragmentation is a constant ≈ 4. These theoretical results agree well with experimental observations.

The growth of the voids leads to failure by two possible mechanisms. The material between growing voids starts getting thinner till a necking instability sets in, resulting in the coalescence of the voids and eventual fracture. It is also possible that at some stage in the growth of the voids, conditions become ripe for cracks to originate from the voids, as explained in § 2.

4. Conclusions

Fracture in particulate composites is an important area in need of viable theories. The difficulties arise from the complexity of the stress distribution in an inhomogeneous material and the dependence of the fracture process on highly local stress and strain conditions. Estimates based on energy considerations have led to some understanding of the phenomena involved, but much remains to be done.

References

Balluffi R W and Siegel L L 1955 *Acta Metall.* **3** 170
Brown L M and Stobbs W M 1971 *Philos. Mag.* **23** 1201
Davies P W and Williams K R 1969 *J. Metal Sci.* **3** 48
Greenwood G W and Harris J E 1965 *Acta Metall.* **13** 936
Griffith A A 1920 *Philos. Trans. R. Soc.* **A221** 163
Jalinier J M 1981 Thesis, Univ. of Metz, France (unpublished)
Mcclintock F A 1968 *J. Appl. Mech.* **35** 363
Orowan E 1949 *Rep. Prog. Phys.* **12** 185
Palmer I G and Smith G C 1968 *Oxide dispersion strengthening* (New York: Gordon and Breach) p 253
Rice J R and Tracey D M 1969 *J. Med. Phys. Solids* **17** 201
Sack R A 1946 *Proc. Phys. Soc.* **58** 729
Sezawa K and Miyazaki B 1928 *Proc. Jpn Soc. Mech. Eng.* **31** 625
Smith E and Barnby J T 1967 *J. Metal Sci.* **1** 1
Sneddon I N 1946 *Proc. R. Soc.* **A187** 229

Discussion

P Rodriguez: Why has the dislocation pile-up at the interface not been taken into account?

S Ray: Dislocation pile-up treatments are suspect. All these effects have been put into an experimental parameter ε_m.

V C Sahni: What is the implication if you have an interface of finite thickness?

Ray: I do not know the answer at present.

G Srinivasan: Is there an essential difference between the way a crack propagates in metals and insulators on the one hand, and in crystalline and amorphous materials on the other?

Ray: There is no appreciable difference.

K Srinivasa Raghavan: What about the possibility that the crack nucleates at the interface and goes into the matrix or the particle as decided by the relative moduli?
Ray: It is possible to treat this case along the same lines, but my interest has been in the problem of incipient cracking of the particle.

Bull. Mater. Sci., Vol. 6, No 4, September 1984, p. 805–806. © Printed in India.

Experimental study of fluctuations in materials*

K R RAO

Nuclear Physics Division, Bhabha Atomic Research Centre, Bombay 400085, India.

Abstract. Mechanical behaviour is decided by the structure and kinetics of defects in materials. External forces play an important role in determining the growth, decay and motion of defects. In addition there is an inherent fluctuation in the various microscopic characteristics of the system as the latter acts as a 'heat bath'. A disturbance that is set up in the system is affected by these fluctuations. The response of the system to external forces can be related to the behaviour of the system due to intrinsic fluctuations in the absence of impressed forces. This is the basis of relation between study of fluctuations in the system and various relaxation phenomena observed. It is proposed to discuss certain features of this subject in relation to various material properties.

Discussion

A P Pathak: What kind of information does one get about defects and defect structures from small angle neutron (or x-ray) scattering? For thin specimens charged particle scattering (channeling as well as backscattering) gives detailed information about all kinds of defects and defect structures. How do the two techniques compare as regards defect studies?

K R Rao: As I have explained in my talk, small angle scattering (x-ray or neutron) can give information on the *average* size, number and distribution of defects present in a solid (x-rays and neutrons give essentially similar information). Electron microscopy and charged particle scattering give useful information on point defects. Charged ionic particles in channeling experiments, for example, have helped one to decide whether certain impurities are substitutional or interstitial. However, such experiments generally require single crystals, and such studies have mostly been confined to 'ideal' defect studies. Small angle neutron scattering has the advantage that it can be used with bulk systems with large beam diameters, but the intensities are limited at present.

G Venkataraman: It seems to be of interest to consider, say, a creep experiment set up in a neutron beam. By studying the small angle scattering, one could perhaps learn something about the kinematics of defects during the course of deformation.

G Ananthakrishna: How do you measure the two-time correlation function in nonlinear systems?

Rao: I believe that *non-stationary* situations are the ones being investigated currently.

G Ananthakrishna: Binder remarks that coarse graining leads to fuzziness of the spinoidal boundary. How would one measure such an effect?

---

*Only a summary is presented.

Rao: My *guess* would be that perhaps one ought to start with compositions corresponding to the fuzzy boundary, and then carry out experiments quite similar to the ones I have already described.

Bull. Mater. Sci., Vol. 6, No. 4, September 1984, pp. 807–815. © Printed in India.

Elementary concepts in chaos and turbulence

RAMAKRISHNA RAMASWAMY

Tata Institute of Fundamental Research, Homi Bhabha Road, Colaba, Bombay 400 005, India

Abstract. The phenomenology of aperiodic or chaotic behaviour is described with reference to simple theoretical models and experiments. A brief description is given of the current understanding of how irregular dynamical motions can arise.

Keywords. Chaos; nonlinear dynamics; turbulence.

1. Introduction

In the past few years, an intense effort has been devoted towards the detailed study of intrinsically random phenomena. Random phenomena are plentiful; in this talk, I will attempt to give a brief introduction to the rather simple concepts that at present underlie a basic understanding of chaos or irregularity, and the onset of turbulence. Many of the ideas are novel and interesting; whether or not these concepts are directly applicable in the context of mechanical behaviour as discussed in this Meeting is not entirely clear, but that is more a problem of application. This talk will be primarily phenomenological and qualitative without much emphasis on the mathematics (although much of the insight in this field really comes from the mathematics). Rather than give explicit references through the text, I prefer to list in the bibliography several articles that discuss these concepts in greater detail.

It is of interest to examine families of (nonlinear) systems rather than particular cases, as this type of study is apt to reveal more of the general behaviour. Typically, such systems can be parametrized by some physical variable such as temperature, pressure, applied voltage, etc. In many situations, the following general pattern has been seen to occur as a function of the relevant control parameter:

Smooth behaviour → transitional range → erratic behaviour

periodic → ? → aperiodic

A few examples are given below.

(1) *Heart beats* are possibly the most familiar instance of regular, periodic behaviour. As a function of applied stress (for example during physical exertion), we can easily observe the period changing as the heart beats faster. When this exertion is now coupled with oxygen availability, when one is climbing a mountain, say, the period can change drastically, and in fact may become quite erratic. This has unfortunate physiological effects (death is likely), and emphasises the importance of a transition from regular to irregular behaviour under the variation of a control parameter.

(2) A less familiar example occurs in the study of *animal populations*. This assumes

importance in livestock farming or fishery management, where it is necessary to know the behaviour of the population as a function of time, typically from generation to generation. One can in fact write fairly simple equations (of the difference, differential, or differential-delay type) to describe the population, where the control parameters are the food supply and the reproductive ability. These simple equations can give rise to totally chaotic behaviour for some values of these parameters.

(3) An example that I will discuss later on has to do with the *onset of turbulence*. In the classic Rayléigh-Benard experiment, when a liquid is heated, convective motion is established within the liquid. As the rate of heating is increased, the motion can become quite irregular, leading eventually to the full scale turbulence which is seen in the boiling liquid.

(4) It is possible that in a material under stress, this kind of behaviour is present as well, as may be deduced from the equations that model *serrated yielding*, for some values of the applied strain.

There are several more examples that one could cite. What is important, however, is that chaos is a *dynamical* phenomenon, and is abundant, in that it occurs frequently in nonlinear situations. (Nonlinearity of the dynamical system is a necessary condition for chaos, but is not a sufficient one.)

2. Dynamics

We define a dynamical system in terms of one independent variable, such as time, t, one or more dependent variables, $x_i(t)$, and an external (control) parameter, μ. One requires a prescription to determine the evolution of the dependent variables. This is done via a system of differential equations,

$$\frac{\mathrm{d}}{\mathrm{d}t}x_i(t) = F_\mu(\mathbf{x}(t)), \tag{1}$$

or difference equations,

$$x_i(j+1) = F_\mu(\mathbf{x}(j)). \tag{2}$$

The index j plays the role of a discrete time in the latter case. The parametric dependence is contained in F_μ. Given these and a set of initial conditions, it is straightforward to obtain the time evolution of the dependent variables. This defines an *orbit*, and it is the behaviour of these orbits as a function of time that describes the dynamics. It is customary to examine the dynamics in the phase space of the variables $x_i(t)$, $i = 1, 2 \ldots$

We can simply define *regular* behaviour as motion, $x_i(t)$, which is predictable. That is, the dynamical variables are periodic functions of time, or combinations of periodic functions, *i.e.*, quasiperiodic functions. Irregular or chaotic motion is, in contrast, unpredictable, and therefore is given by an aperiodic function (equivalently, of infinite period). It is important to emphasize that these motions are discussed entirely in terms of deterministic evolution via (1) or (2). Chaotic motions arise independent of random noise or fluctuations. In fact, it is customary to label such intrinsic erratic behaviour as *self-generated chaos.*

The notions of regular and chaotic motion can be quantified in several ways. A direct and rather obvious means is through the spectral or Fourier analysis of the orbits.

Regular motion leads naturally to a discrete Fourier spectrum, since the motion is either periodic or quasiperiodic. The spectrum for chaotic motion must necessarily be continuous owing to the aperiodicity (*i.e.*, any and all frequencies—in particular, zero-frequency). Another means of distinction is based on the Liapunov instability of orbits. The euclidean distance between regular orbits can grow linearly; whereas, between chaotic orbits, it grows exponentially. It is also possible to examine the orbits themselves, to get an idea of how they develop in phase space. When there are n dependent variables, corresponding to m degrees of freedom, the phase space is of dimension n ($x_i(t)$; $i = 1, 2, \ldots, n$). Examining the motion in this n-dimensional space is a difficult task. One can, however, essentially accomplish this by examining the Poincare surface-of-section. This works best when the number of degrees of freedom is small, $m = 2$ or 3. To construct a surface of section, one chooses a particular plane in the phase space, and locates the point of intersection each time the orbit passes through this plane. If a given orbit is examined for a sufficiently long time, there are several points of intersection, and these give an idea of the geometry of the orbit. For regular motions, the points of the Poincare section lie on smooth curves, whereas for chaotic motions, these points are scattered apparently randomly in the plane (independent of which particular plane is chosen).

In discussing dynamical systems, it is useful to distinguish between conservative systems (where the volume of phase space is constant in time) and non conservative systems (where this volume changes with time). The behaviour is somewhat different in the two cases. In most physical situations one encounters dissipative, nonconservative systems, owing to the presence of frictional forces, and in that sense these systems are more important. It is however necessary for completeness to describe in brief the behaviour of conservative systems.

2.1 *Conservative (Hamiltonian) systems*

The most common examples of conservative systems are Hamiltonian systems, wherein one can define a Hamiltonian function, $H(\mathrm{x})$. As general dynamical systems, these have $n = 2m$ dependent variables for m degrees of freedom. Thus, the phase space is of dimension $2m$; m of these variables are 'coordinates', and m are their conjugate 'momenta'. Evolution is governed by Hamilton's equations. (In the discrete case, the requirement of constant phase space volume is replaced by the condition that the Jacobian of the transformation in (2) have the value ± 1). One can further separate such systems into two classes: integral systems and nonintegral systems. In the former class, it is possible to make a canonical transformation such that $H(x)$ is given in terms of m (in general, new) 'momentum' variables alone. These are constants of the motion, which is then constrained to lie on well-defined geometrical objects, namely, m-dimensional tori in the phase space of dimension $2m$. Thus the motion is *always* regular. We can regard nonintegrable Hamiltonians as arising from integrable ones by the addition of perturbation terms (depending on μ), such that H can no longer be expressed as a function of m momentum-like variables alone. There is then no guarantee that the motion will lie on m-dimensional tori. The powerful KAM theorem applies in such cases. Loosely speaking, this theorem states that, depending on the magnitude of the perturbation, some of the tori that exist in the integrable case get distorted, and some of them are destroyed. When the tori are merely distorted, the motion still remains regular; but when they are destroyed, the orbits are free to wander over all of phase space, and can therefore become highly irregular and chaotic. The phenomenology of Hamiltonian chaos is in fact extremely bizzare and involved; this erratic behaviour basically arises from the complicated interactions between internal resonances. The foregoing is a cursory description of the bare essentials of the matter. As a simple example, consider the discrete map

$$x_{i+1} = \mu x_i - (y_i - x_i^2)(1-\mu)^{1/2}, \tag{3}$$

$$y_{i+1} = x_i(1-\mu)^{1/2} + (y_i - x_i^2)\mu. \tag{4}$$

This roughly models the Poincaré surface of section of an $m = 2$ degree of freedom Hamiltonian system. Orbits are constructed by iterating points in the xy plane under the above transformations. Depending on where one starts, successive points in figure 1 can lie on a smooth curve (A) or on a set of smooth curves (B)—these correspond to regular motion on tori; or else the points can be scattered all over the plane (C)—this is a chaotic orbit and is not confined to any simple geometrical object. In general, the motion can be extremely complicated. This is both typical, in the sense that most nonlinear Hamiltonian systems are likely to be nonintegrable, and pathological, in the sense that for any nonzero value of μ, a nonintegrable Hamiltonian will exhibit *some* chaotic motions.

2.2 *Dissipative systems*

As already mentioned, dissipative systems are more common, and thus more pertinent. A typical example is provided by the forced-beam problem. A beam of length b is

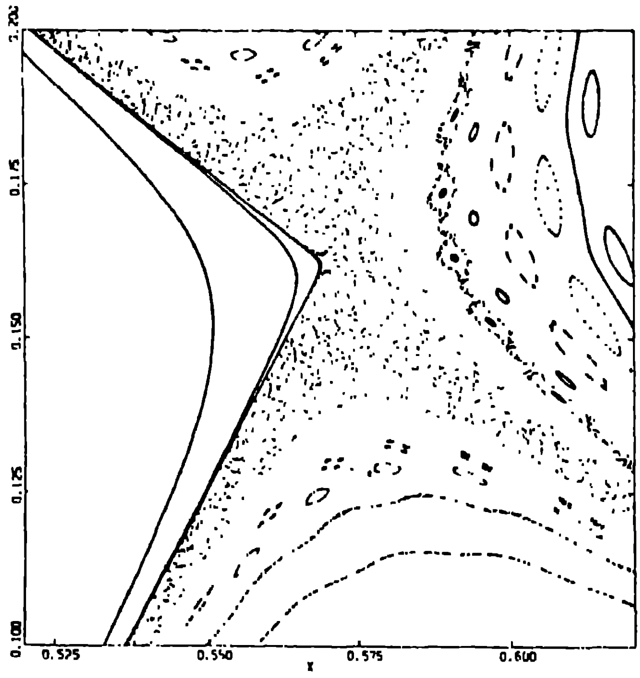

Figure 1. Orbits in the xy plane induced by the discrete transformation of equations (3)–(4). A and B are examples of regular motion, while the set of points C is typical of the Poincaré section of a chaotic orbit.

pinned at two ends, separated by distance l. When l is less than the beam length, the beam settles into one of the two symmetric equilibrium configurations. A sinusoidal force is applied at the ends, and the beam oscillates about the equilibrium position. As the excitation increases, however, the rod begins to snap back and forth between the two equilibria. If $w(x, t)$ is the lateral displacement,

$$w(x, t) = \xi(t) \sin(\pi x). \tag{5}$$

For small forcing amplitudes, $\xi(t)$ is a periodic function; but as the forcing amplitude increases, $\xi(t)$ can become quite chaotic. The problem can be properly formulated mathematically, and simplified to a more familiar problem, the Duffing equation. The latter describes a simple nonlinear forced oscillator with frictional damping,

$$\ddot{x} + \alpha\dot{x} + x + \beta x^3 = f \cos(\omega t). \tag{6}$$

This example is sufficient to illustrate much of the phenomenology. When $\alpha = \beta = f = 0$, (6) corresponds to the equation of motion of a simple harmonic oscillator of unit mass and frequency. The motion in phase space is extremely simple: a circle in the $x\dot{x}$ plane, given by the parametric equations,

$$x(t) = A \cos(\omega t + \phi);\ \dot{x}(t) = -A \sin(\omega t + \phi). \tag{7}$$

The motion is trivially regular. If damping is now introduced, keeping $\beta = f = 0$, one has damped harmonic oscillations; the motion now consists of orbits that spiral exponentially into a *sink* at $\dot{x} = x = 0$. When forcing is also included, one has a *limit cycle* behaviour, *i.e.*, orbits converge asymptotically onto a limiting structure in the phase plane, and the motion is periodic on this limit cycle.

The sink and the limit cycle are examples of simple *attractors*. When nonlinearity is included in the equation of motion, it is possible to have more complicated attractors—in particular, *strange*, or chaotic, aperiodic attractors. One early example of such an attractor was found by Lorenz in a 3-mode truncation of the Navier-Stokes equation

$$\begin{aligned}\dot{x} &= 10(y - x),\\ \dot{y} &= \mu x - y - xz,\\ \dot{z} &= xy - 8z/3.\end{aligned}$$

The strange attractor (SA) that occurs in this system is shown in perspective in figure 2. The orbit spends random amounts of time on the two distinct portions of the attractor.

SA's are crucial in one picture of the onset of chaos and turbulence, the Ruelle-Takens model. Here chaos is presumed to occur by the creation of SA's, and the mechanism is as follows. Solutions to (1) are studied. For small μ, some simple periodic motion is present; as μ increases, (Hopf) bifurcations occur; the motion is still regular, but now on m-dimensional tori, where $m > 1$. When two such bifurcations have occurred, then it can be (mathematically) proven that any small perturbation suffices to create a SA, and hence chaos.

Currently, there exist several such scenarios for the onset of chaos and turbulence, each applicable in different circumstances. In the so-called Feigenbaum picture, we consider systems described by (1) or (2). As a function of the parameter μ, the following behaviour pattern occurs. For $\mu < \mu_0$, there is some kind of a simple sink. At μ_0, a bifurcation takes place and an orbit of period τ becomes stable and attracting. (Technically, this is through a "pitchfork" bifurcation). As μ is increased beyond a certain

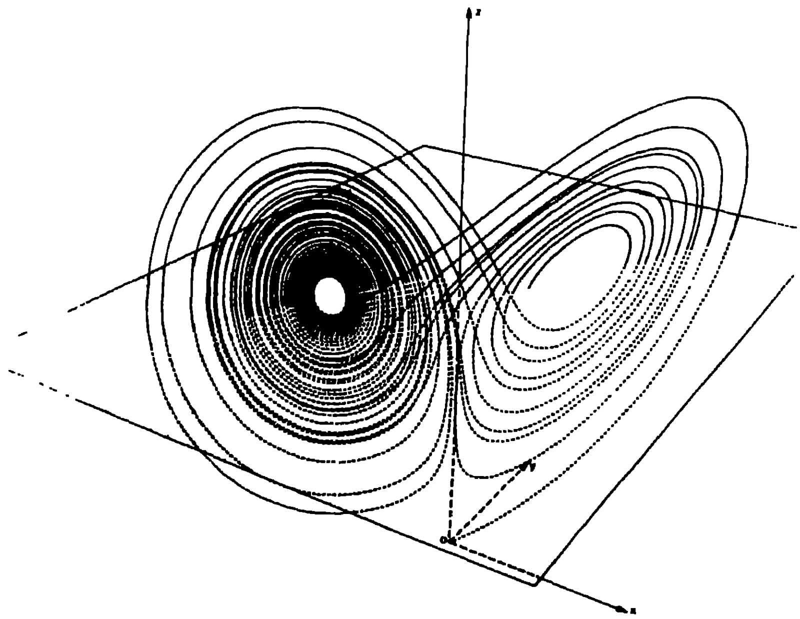

Figure 2. The strange attractor in the Lorenz system, equation (8), for $\mu = 28$. The attractor consists of two almost planar portions, and the orbit wanders chaotically from one side to the other.

value μ_1, the period $-\tau$ orbit loses stability, but one of period 2τ is born which is now stable and attracting. At a higher value μ_2 another bifurcation takes place, with the period-2τ orbit losing stability while a period-4τ orbit becomes stable. This process repeats itself: at μ_n, a period-$2^n\tau$ orbit becomes stable and attracting while the period-$2^{n-1}\tau$ orbit loses stability. In the limit, one has a $2^\infty\tau$-period orbit, *i.e.*, an orbit of infinite period, or chaos. The interesting thing is that μ_∞ is finite—the *period-doubling cascade* occurs quite rapidly, and furthermore, the rate of convergence of the bifurcation points,

$$\delta_n = \frac{\mu_n - \mu_{n-1}}{\mu_{n+1} - \mu_n} . \tag{9}$$

logarithmically approaches $\delta = 4{\cdot}669201609 \ldots$ as $n \to \infty$. The most surprising fact is that the number δ is universal for a large general class of F_μ. The precise form of F_μ does not matter (within certain restrictions). Wherever the period-doubling route to chaos is found, the number δ that one computes from measurement is identical to that found by Feigenbaum (i.e., 4·669 . . .). Historically, this number was discovered in a study of the discrete one-humped map of the unit interval known as the logistic equation, namely,

$$\begin{gathered} x(j+1) = \mu x(j)[1 - x(j)], \\ 0 \leqslant x \leqslant 1,\ 0 \leqslant \mu \leqslant 4. \end{gathered} \tag{10}$$

(In fact, there are several other universal constants that can be found within such a picture.) The period-doubling route to chaos has been seen to occur in a wide variety of cases—in abstract maps such as (10), in differential equations such as (8), in a variety of theoretical experiments modelling chemical reaction kinetics, in forced oscillator problems, in a seven-mode truncation of the Navier-Stokes equation, and even in the equations that model repeated yielding in mechanical behaviour. Most crucially, though, a number of physical experiments have also confirmed this picture. The Rayleigh-Bénard flow problem mentioned earlier is one such. In this experiment, liquid helium is heated at around 4 K, and the temperature at a point within the cell is monitored as a function of time. The Rayleigh number, R, plays the role of the parameter μ. For low R, convective rolls are formed in the experimental cell; the motion is periodic. As the temperature is raised, the motion begins to become turbulent. The Fourier transform of the temperature as a function of the time clearly shows the existence of a basic frequency, f, and the subharmonic bifurcations, which give rise to peaks at $f/2$, $f/4$, $f/8$, $f/16$, etc. (see figure 3). The Feigenbaum constant computed from this experiment turns out to be about 4·8, amply confirming the general theory.

It must also be mentioned that the Rayleigh-Bénard experiment prepared differently displays the Ruelle-Takens behaviour as well. There is yet another common mechanism, *intermittency*, through which chaos can occur, *via* "tangent" bifurcations. Prior to the onset of full-scale chaotic behaviour, there are long periods of time when the motion is perfectly regular, interspersed with short bursts of erraticity. This route too can be observed experimentally.

In dissipative systems, chaos comes about in a manner different from that in conservative systems. Essential ingredients are bifurcations and attractors. One can have either period-doubling bifurcations and a periodic attractor in the Feigenbaum scenario (thus only one independent frequency), or bifurcations from a period orbit to tori, followed by a strange attractor in the Ruelle-Takens picture (thus at most three independent frequencies).

3. Summary

This talk has only briefly touched upon the basic phenomenology of irregular motion. Much of the interest in nonlinear dynamics arises from the existence of a large component of the unexpected and the counterintuitive. I have tried to outline the

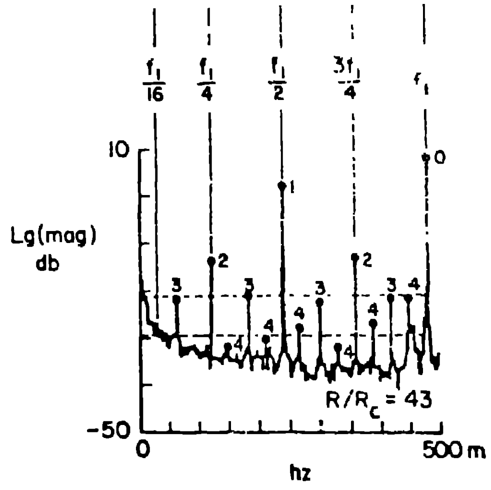

Figure 3. Period doubling subharmonics in the temperature power-spectrum of liquid helium in a Rayleigh-Benard experiment (from Maurer and Libchaber, *loc. cit.*).

various paths or routes to chaos; unavoidably, there are gaps in this short presentation.

Although much progress has been made, there are still several open questions. For example, there is no minimal (or maximal) degree of complexity necessary to ensure chaos—very nonlinear systems can be integrable, while even the simplest (cubic) nonlinearity can induce chaos. And at the microscopic level, which may or may not be of interest here, quantum effects occur, and there is no clear understanding of how this can modify classical chaos.

When it does occur, chaos can have important consequences. For one thing, it becomes possible to apply statistical methods to advantage, if the behaviour is sufficiently random-like. On the other hand, chaos may be an undesirable feature if one wishes to remain in the region of the precisely predictable—this situation is common, for example, in particle storage rings where particle losses occur via erratic orbits: It is then essential to minimise or totally avoid chaos. The very ubiquity of chaos makes it necessary to examine dynamical processes in greater detail, whatever the context—this can well include mechanical behaviour.

References

1. General references on chaos

1980 *Proc. Int. Conf. on Nonlinear Dynamics* (ed) R H G Helleman (Ann. N.Y. Acad. Sci. No. 603)
Jorna S (ed) 1978 *Topics in nonlinear dynamics* (Am. Inst. Phys. Conf. Proc., Vol. 46)
Helleman R H G 1970 in *Fundamental problems in statistical mechanics* (ed) E D G Cohen (New York: North-Holland Publ) Vol 5, p 165
Moser J 1978 *Math. Intell.* **1** 65
Ruelle D 1980 *Math. Intell.* **2** 126
May R M 1976 *Nature (London)* **261** 459
Hofstadter D 1981 *Sci. Am.* **245** 16

2. Conservative systems

Berry M V 1978 in *Topics in nonlinear dynamics* (ed) S Jorna Vol 46 (*Am. Inst. Phys. Conf. Proc.*)
Ramaswamy R 1981 *Phys. News* **12** 60

3. Dissipative systems

Eckmann J P 1981 *Rev. Mod. Phys.* **53** 665
Kumar D 1982 *Phys. News* **13** 109
Tomita K 1982 *Phys. Rep.* **86** 113
Crutchfield J, Farmer J and Humberman B 1982 *Fluctuations and simple chaotic dynamics Phys. Rep.* **92** 45

4. Some experimental references

Maurer J and Libchaber A 1979 *J. Phys. Lett.* **40** 419
Maurer J and Libchaber A 1980 *J. Phys.* **41** C3
Feigenbaum M 1979 *Phys. Lett.* **A74** 375
Gollub J P, Besons S V and Steinmann J 1980 *Proc. Int. Conf. nonlinear dynamics* (ed) R H G Helleman (Ann. N.Y. Acad. Sci. No. 203)

5. Other references

Lorenz E N 1963 *J. Atmos. Sci.* **20** 130
Ruelle D and Takens F 1971 *Commun. Math. Phys.* **20** 167
Feigenbaum M 1978 *J. Stat. Phys.* **19** 25
Feigenbaum M 1979 *J. Stat. Phys.* **21** 669

Discussion

G Ananthakrishna: Why is it often said that Landau's theory does not give a correct description of turbulence?

R Ramaswamy: The trouble with the Landau picture of turbulence is that as you vary a particular parameter, you have a series of bifurcations to the wrong geometrical object. These are in a certain sense bifurcations from a periodic orbit to a toroid, and thence a sequence of toroids. A limiting strange attractor does not appear.

G Ananthakrishna: Which route to the turbulent state is followed in the Rayleigh-Benard case?

Ramaswamy: It has been shown that all 3 routes may be followed.

G Ananthakrishna: Is there any algorithm to get the Poincare map for multidimensional systems?

Ramaswamy: It is a difficult process.

S R Shenoy: Can one make a statement about the minimum order of the differential equations and of the nonlinearity in them in order to get chaos?

Ramaswamy: This is difficult. We do not even have a clear way of predicting whether a system is going to be integrable or not. A minimum requirement for chaos is of course nonlinearity, but it is not easy to make a more exact statement of general applicability.

K R Rao: Does the central peak in a second order phase transition have anything to do with chaos?

Ramaswamy: There is no analogy at all between the onset of chaos/turbulence with any kind of phase transition.

M Youssuff: How does one develop a probabilistic description of the chaotic state?

Ramaswamy: One of the reasons for studying chaos is to determine when ergodic theory is valid. Clearly, at the very least, chaos is needed for ergodicity to occur.

Bull. Mater. Sci., Vol. 6, No. 4, September 1984, pp. 817–822. © Printed in India.

Fractals

D DHAR

Tata Institute of Fundamental Research, Bombay 400005, India

Abstract. An elementary introduction to the concept of fractals is given. Some examples of fractals drawn from nature are briefly discussed. It is suggested that fractal geometry may be useful in characterizing the grain size and shape distributions in polycrystalline solids.

Keywords. Fractals; non-integral dimensions; grains.

1. Introduction

This talk is intended as an elementary introduction to the concept of fractals for non-experts. I shall try to concentrate on some of the qualitative geometrical features, and will not discuss more technical topics such as phase transitions on fractals.

The organization of the talk is as follows: In § 2 I shall briefly discuss the motivation for studying these unconventional geometrical objects. The intuitive notion of dimension is generalized in § 3 to include non-integral values of the dimension. Some illustrative examples are given in § 4. Section 5 contains some concluding remarks.

2. Motivation

Fractals are geometrical objects having an effective dimensionality which is non-integral. They are useful in modelling several quite different physical situations. It may not be unreasonable to hope that they would also be useful in describing certain aspects of the mechanical behaviour of matter.

This situation is not entirely like that of a biochemist who tries to sell a 'wonder drug' without quite knowing which ailment it cures. In our case, the drug is acknowledged to be 'neurosensitive'. Whether the effects are desirable or undesirable in a specific proposed application is not known beforehand. In some cases, for example in the understanding of the influence of dimensionality on critical phenomena near phase transitions, fractals have been found to be very useful.

The mechanical specification of a system involves the listing of the variables in terms of which the state of the system is described (kinematics), and of the laws of mutual interaction and time-evolution of these variables (dynamics). The choice of variables in terms of which we characterize the state is important: unnatural choices lead to convoluted descriptions. An example of a bad choice of variables is the Ptolemaic insistence on describing planetary motion in terms of a superposition of uniform circular motions. A comparatively more recent example is the phrase 'temperature-dependence of the Debye temperature' used by some physicists around 1910 to describe the non-agreement of the measured temperature-dependence of the specific heat of materials with Debye's theoretical predictions.

The introduction of fractals to describe the mechanical behaviour of matter has, first, a kinematical aspect. It has not yet been established that our difficulties in understanding the mechanical properties of solids are sufficiently acute to necessitate a substantial change from the conventional picture involving an ideal solid plus defects. However, the general trend of the discussions at this Meeting would seem to indicate that, near the plastic limit, the formalism is under stress. It may be useful to explore the possibility of alternative modes of description.

Most text books on the mechanics of solids start out by classifying the defects in solids as point-, line-, surface-, or volume-defects. It is not surprising that the classification scheme is geometrical, and is almost universally preferred over other possible schemes (alphabetical, historical, mobile/immobile defects, annealed/quenched defects, etc.). The geometrical characterization of defects captures some of their most important features. It cannot be the whole story, but it is a useful place from which to begin.

3. A definition of non-integer dimensionality

It is well-known that the strength of solids is a strong function of the grain size and grain shape. Earlier it has been emphasized by Ranganathan that grains in metals are quite irregular in shape (Ranganathan 1984). A schematic representation of possible grain shapes on a two-dimensional lattice is shown in figure 1. Clearly, a material with compact hexagonal grains (as in figure 1a) would be different, mechanically, from a material with very ramified grains (figure 1d). It would be useful to have a numerical characterization of these grain shapes to be able to specify whether the grains are compact objects with a few holes, or are ramified and stringy. Roughly speaking, a compact volume, a disc-like shape, and a string-like shape respectively would behave like three-, two- and one-dimensional objects. A numerical characterization of attributes such as 'stringiness' often gives rise to nonintegral answers, when applied to objects of complex geometrical shapes. Such objects may be said to have a non-integral dimension and are called fractals (Mandelbrot 1977, 1982).

What is meant by saying that an object has dimension 1·5? For that matter, what is meant by saying that an object is three-dimensional? Before giving a definition of dimension, which is generalizable to non-integral values, it is useful to remember that the dimension we assign to an object depends very much on our choice of its representation. A ball of wool may be represented as a point, or a sphere, or as a tangled line (having dimensions 0, 3, and 1 respectively) depending on our scale of description (Mandelbrot 1977). The dimension we assign actually pertains to the mathematical representation of the object, and not to the object itself.

In order to be useful, a definition of dimension must be simple, robust (insensitive to small changes in geometry), and should agree with our intuitive notion of dimension

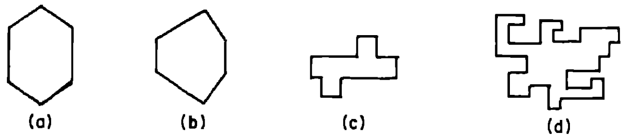

Figure 1. A sequence of increasingly complex grain shapes (schematic).

when applied to conventional spaces (like manifolds). Several such definitions may be found in the literature (Mandelbrot 1977, 1982; Dhar 1977; Engelking 1978). In the following, we consider only the simplest of these.

Consider a space in which the distance between two points, and a volume measure, are defined. Let $V(R)$ be the volume of the set of points whose distance from an arbitrarily chosen origin is less than R. If $V(R)$ varies as R^D for large R, for all choices of the origin, we define D to be the fractal dimensionality of the space. Formally,

$$D = \lim_{R \to \infty} [\log V(R)/\log R].$$

Clearly, using this definition, a straight line has dimension 1 and a plane has dimension 2. Now consider the triangular gasket shown in figure 2. It consists of an equilateral triangle, the mid-points of the sides of which are joined together and divide the triangle into four smaller, equal triangles (three upright, and the central one inverted). Each of the three upright second-generation triangles is divided similarly into four third-order triangles. The 3^2 upright triangles of the third generation are further divided to give 3^3 fourth order triangles, and so on, *ad infinitum*. The gasket consists of all the points in the plane which belong to at least one of the line segments used in this division procedure.

It is easy to see that the points belonging to the gasket have zero area, but that the total length of the line segments which constitute the gasket is infinite. It would thus seem reasonable to assign this set of points a dimensionality between 1 and 2. To determine the fractal dimensionality of the gasket we have to define the metric and a volume-measure for this case. The distance between two points is most simply defined as the Euclidean distance between them (alternatively, as the length of the shortest line joining them and lying completely on the gasket). The volume of an rth generation triangle with all inside points included is defined to be 3. Using these definitions, it is easy to see that

$$V(2R) = 3V(R).$$

Using the definition of D given earlier, this gives $D = \log_2 3 \approx 1{\cdot}54$. The triangular gasket is thus an example of a fractal.

4. Other examples

In the following we give some additional illustrative examples of fractals. For additional examples, and some very beautiful pictures, see Mandelbrot (1977, 1982).

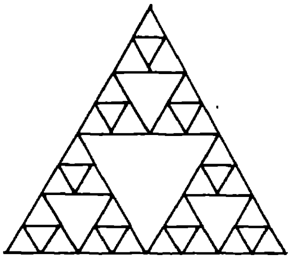

Figure 2. The triangular gasket. Only the edges belonging to the first, second, and third order triangles are shown here for clarity.

4.1 *Lattice animals*

Lattice animals are defined as connected clusters of sites embedded on a lattice (figure 3). The problem of the determination of the mean values of the properties of animals containing a given number of sites, given that all distinct shapes of such animals have equal statistical weights, is called the random animal problem. This assumption is not true for crystal grains, as compact grains have lower surface energy, and are favoured thermodynamically.

If a typical animal on a d-dimensional hypercubical lattice (d is an integer here) were compact, its maximum lateral extent R would vary as $n^{1/d}$, where n is the number of sites in the animal. It is found that random animals are typically stringy, and R varies as a *larger* power of n. In 3-dimensions, the dependence is $r \sim n^{1/2}$. Thus a random animal in 3-dimensions has a fractal dimension equal to 2 because $n \sim R^2$.

4.2 *Percolation clusters*

Consider a d-dimensional hypercubical lattice (d integral) in which each nearest-neighbour bond is, independent of others, unbroken (*i.e.*, connects the sites at its ends) with a probability p (figure 4). For small p values (p less than a critical value p_c), a site chosen at random is connected to only a finite number of other sites through occupied bonds. In this case, the effective dimension of the clusters may be defined to be zero. For $p > p_c$, the mutually connected sites constitute a finite fraction of the total number of sites of the lattice, and form a d-dimensional network (with some holes). When p is equal to the critical probability p_c, the incipient infinite cluster has zero fractional volume, and is very tenuous. However, if we construct a sphere of radius R about a point, the expected number of sites connected to the origin varies as R^D where $D \approx 1{\cdot}6$ for $d = 2$. The infinite cluster at the percolation threshold is an easily-realizable example of a fractal.

4.3 *Soap powder*

If we look at soap powder under a microscope, it is seen to consist of a large number of particles of varying sizes. As in the case of crystallites in metals, the average linear extent

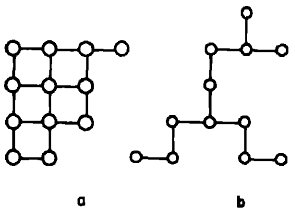

Figure 3. Animals on a square lattice. (a) is a compact cluster, while (b) is stringy.

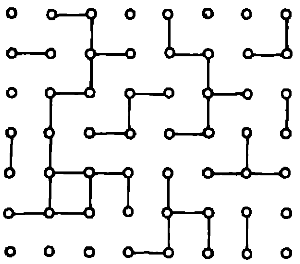

Figure 4. A random configuration of unbroken bonds on a square lattice.

of these powder particles grows faster than the cube root of their mass, and can be used to define an effective dimension of the powder. We should expect the fractal dimension of soap powder to be between 2 and 3. The precise numerical value may perhaps depend upon its chemical structure.

4.4 *The distribution of galaxies*

The precise nature of the large-scale structure of the distribution of matter in the universe is not very well-known. According to one view, the distribution of galaxies in the universe is essentially uniform. However, a different picture, in which the universe shows clustering at all scales of length, is also consistent with experimental data. According to this picture, galaxies typically reside in clusters of galaxies, which themselves are part of clusters of galaxies and so on. Each cluster contains about 3 subclusters on the average. The size of the cluster is appreciably smaller than inter-cluster distance, which implies that the number of galaxies in a sphere of radius R, centred at any particular galaxy, grows as R^D with $D < 3$. Thus the distribution of the galaxies in the universe shows a fractal structure.

4.5 *Coastlines*

The coastline of an island is typically a very zigzag line (figure 5), and its measured length depends very much on the size of the divider spacing (or calliper length) used to measure it (say, from a very detailed map). If we use a smaller divider spacing, we measure more of the small detours and turns that the line makes, and the measured length is larger. If the line is smooth at very short distances, then, as the divider spacing is decreased, the length will tend to a limiting finite value (which is defined to be the 'length of the line'). If, however, the line is rough at all length scales, we may find that $L(s)$, the length measured when the divider spacing is s, varies as s^{1-D}, where $D > 1$. This D may be called the fractal dimension of the coastline. For several actual coastlines $D = 1{\cdot}2$. For a Brownian motion path $D = 2$.

5. Concluding remarks

It should be clear from the preceding examples that fractals are not exotic, pathological objects dreamt up by mathematicians, but are very much a part of the world around us. They provide a natural description of the non-classical geometrical forms encountered in nature. It is this common geometrical character, and not the occurrence of fractional powers, which is the characteristic feature of fractals. Fractional power laws are, of course, encountered quite frequently in Nature. For two observables X and Y, if X varies as an integral power of Y (not equal to ± 1), then Y varies as a non-integral power of X. It is preferable not to use the term 'fractal' in the absence of a geometrical structure in the problem (as in, say, of stock-market prices). Fractals may also show up in the discussion of mechanical properties of matter in the context of dynamical response and the onset of chaos. A discussion of these aspects may be found elsewhere (Ramaswamy 1984). Additional references on fractals may be found in Dhar (1981).

Figure 5. A schematic representation of a coastline. The line will show further wrinkles and detours, if observed on an expanded scale.

References

Dhar D 1977 *J. Math. Phys.* **18** 577
Dhar D 1981 in *Current trends in magnetism* (Bombay: Indian Physics Association) p. 207
Engelking R 1978 *Dimension theory* (Amsterdam: North-Holland)
Mandelbrot B B 1977 *Fractals: form, chance and dimension* (San Francisco: Freeman)
Mandelbrot B B 1982 *The fractal geometry of Nature* (San Francisco: Freeman)
Ramaswamy R 1984 *Bull. Mater. Sci.* **6**
Ranganathan S 1984 *Bull. Mater. Sci.* **6**

Discussion

N Kumar: Are fractal dimensions and similar apparently geometrical concepts applicable to *dynamics*?

D Dhar: Yes, there are connections. An example is magnetisation creep.

G Venkataraman: These concepts have also been employed in describing turbulence.

R Ramaswamy: Strange attractors have been shown to have well-defined fractal dimensions.

S Ranganathan: Fractals may have some bearing on the shapes of second phase particles which influence mechanical properties.

Bull. Mater. Sci., Vol. 6, No. 4, September 1984, pp. 823–825. © Printed in India.

Summary and outlook

V BALAKRISHNAN

As we are running short of time, I will be brief. I would like to begin by repeating the platitude (or self-evident truth!) that, just as approaches to a certain problem can be different, so can the motivations. A person may be motivated to study a problem for purely aesthetic reasons, and not out of any practical considerations at all; but the person should have the freedom to do so. To paraphrase what has been said by many eminent scientists: If a fraction of time spent in a subjective argument over different approaches to a problem was spent in actual computation using any of the techniques under contention, there would perhaps be no need for the argument because the problem would be considerably closer to resolution! Similarly, I feel that there is no need here to debate the respective motivations of physicists and metallurgists, including the question of what constitutes a problem and what is meant by a solution to one. All techniques, however mathematical or however empirical, are acceptable and indeed essential to make any headway in a subject as complicated as the one we have been discussing.

I would now like to make two general comments, one taken from Prof. N Kumar and the other based on Dr K R Rao's talk. In any given subject, theorists generally like to have the broad paradigms brought out so as to have a framework for further development. The general paradigm that is used in the area of mechanical deformation is of course that of dislocations. Given a paradigm, the theoretical physicist then faces the interesting question of the adequacy or otherwise of the paradigm in the light of subsequent experimental information. A well-known example is that of the soliton which is the "paradigm of the 80's" in several branches of physics. When certain regimes of essential nonlinearity are reached, the traditional plane wave-cum-superposition principle is no longer adequate, and new basic entities like solitons (or more generally 'lumps') have to be introduced. So, in this sense, it is very relevant to ask whether, when we look at a practical problem like a large-angle grain boundary, the paradigm of the dislocation is still meaningful—notwithstanding the fact that in the limit of small angles, the boundary is describable in terms of an array of dislocations. Thus, a radical approach which gives up the idea of dislocations altogether would be worth examining further. Equally welcome are other approaches which bring out geometrical coincidences like the DSC lattice together with the idea of dislocations on *this* lattice.

My second general comment concerns the experimental side. A large number of possibilites were catalogued systematically this morning by Dr Rao. Some techniques like acoustic emission, which perhaps have not been emphasized sufficiently for lack of time, should be explored more systematically. Turning to questions for theoreticians arising out of experiment, consider, for example, spinoidal decomposition and the various nonlinear theories of diffusion associated with it. What light does experiment shed on the cut-off and truncation procedures employed in Cahn's theory and its various modifications to include 'higher order' nonlinearities? What are the experimental inputs needed for a critical discrimination between the various theories—in the manner, for example, critical experimental inputs to the theory of freezing were spelt out by Prof. Ramakrishnan in his lecture? You may recall that he pointed out how the shape of the structure factor really determines how good the approximation is and also serves as a self-consistency check. Something like that would be worth attempting for theories of spinoidal decomposition too. Perhaps this has already been done. I am tempted to recall a remark I came across once—I think it was made by Frauenfelder in the early days when many nuclear physicists were getting into solid state physics *via* the Mössbauer effect—that it is always a big surprise to a person getting into another field to realize that the "natives were not as stupid as they seemed from outside", and that all the obvious things had been done! I am sure all the physicists here have this realization about metallurgy.

There are some other points of interest which I should like to mention, although my list will surely reflect my personal bias as a theoretical physicist. Consider for example the general question of nucleation and discontinuous transitions. The diversity and richness of the phenomena encountered here were well brought out in the talk by Dr Wadhawan. It seemed to me that considerable work remained to be done to get the 'theory' here to the same stage of development as has been reached for continuous transitions. Another point which struck me relates to describing things in terms of disorder rather than order. For example, when one considers systems with quenched disorder, one starts with simple models, but pretty soon when the defect density becomes high, one introduces things like disorder variables. Starting from the high-temperature phase, one can then use duality properties, for instance, and get information on the ordered phase as well as on the defects in the ordered phase. This is more fruitful than attempting to start at the ground state and work one's way upwards. Perhaps when the dislocation density is very high, this kind of approach may be useful—indeed, I should think that recent ideas on 'solid-state turbulence' are preliminary steps in this direction. But a great deal of work remains to be done to 'quantify' the properties of random tangles of dislocations, etc. Starting from the theory of liquids is of course carrying the idea of coming in from the disordered phase to its ultimate, but this may be *too* basic for the purpose I have in mind here. The theory of *freezing* we heard about was aptly named, for it did not deal with the question of how to go from the solid to the liquid phase, *i.e.*, how to restore the broken symmetry. A complete picture of the transition should of course give us an idea of this obverse side of the coin, too.

I would also like to emphasize a point that Dr Ramaswamy made during his presentation. When one tries to apply ideas like chaos to mechanical behaviour (as has been initiated by Dr Ananthakrishna), it would be good to try and obtain first a *model-independent characterization of* the *basic* variables in the mechanical behaviour problem. It is very interesting to demonstrate that chaos appears in specific models of dislocation dynamics. Presumably the phenomenon is much more general. So one would like to know what the minimal set of relevant variables is, and so on, in order to extract model-independent information to the extent possible. This is all the more important in an area like chaos because we know that 'neighbouring' dynamical systems can have widely different behaviour. We should at least be able to put various models of dislocation dynamics into their appropriate 'universality' classes. Only then can one undertake a critical examination of the role of various physical parameters in inducing bifurcations, chaotic behaviour, etc.

Having mentioned chaos, I should also like to make a remark on the slightly older paradigm of solitons, nonlinearities, etc. It may be relevant to ask whether nonlinearities of the kind that arise in the continuum elasticity theory Dr Sahoo talked about, can help to stabilize nondissipative structures like solitons—and if so, what are these? Are they the analogues of dislocations in discrete models? This is no doubt an entirely theoretical kind of question, but I am sure that it would aid progress if we understood the basic reason why these objects get stabilized.

I realize I have essentially been conveying the prejudices of a theorist but that is because I am not really competent to say much about the experimental possibilities. However, I will emphasize that this is a field in which observation is prime. We want facts. However, I should like to heartily endorse a point made by Prof. Kumar. Given the plethora of facts and the very large number of variables involved in the field of mechanical behaviour, physicists generally find the going difficult since they like things to be presented in terms of basic features, or very general arguments and reasons. To snow a physicist with a mass of metallurgical details sounds a bit like French grammar where you list all the irregular verbs and exceptions *ad nauseum.* So, if I may make an appeal—it would be nice for the metallurgists to *intentionally oversimplify* the problems that they face when presenting them to a physicist. *After* he gets interested and starts answering questions, you can 'bring him down to earth', as Prof. Srinivasaraghavan said, by gradually including the complications; otherwise there is a tendency for him to get turned off right in the beginning. This approach will also help sift and place all the facts in order of importance and relevance, in itself a worthwhile and by no means trivial task. Fortunately, in the talks we have had during these three days, this has, by and large, been achieved. Many of us physicists have noted down at least some things that are general features, notwithstanding exceptions, and I am sure some of us will actually explore at least the simplified cases. In that sense, I think, this Meeting has worked out well.

Bull Mater Sci., Vol. 6, No. 4, September 1984, pp. 827–835. © Printed in India

Panel discussion

Moderator: Prof. S K Joshi, Department of Physics, Roorkee University

Panelists: Dr R Krishnan, Metallurgy Division, Bhabha Atomic Research Centre

Dr V C Sahni, Nuclear Physics Division, Bhabha Atomic Research Centre

Dr S Ray, Metallurgy Department, Roorkee University

Prof. N Kumar, Department of Physics, Indian Institute of Science

Prof. Joshi: We have had a busy and very fruitful Discussion Meeting. This is the last session, and we are gathered to hear the reactions of the panelists, as well as their suggestions. There are no restrictions or guidelines, and the panelists are completely free to express what they feel. I shall alternate between metallurgists and physicists, and will start with Dr Krishnan.

Dr Krishnan: During the past three days I have informally talked to many of the participants, and I have come to the conclusion that this Meeting has been a unique experience. I suggest it should continue as an annual feature—if not on the same subject, at least on topics of an allied nature.

A general remark I would like to make is that many of the theoretical papers have shown that it is necessary to take the theoretical aspects more seriously and also utilize mathematical and physical concepts in explaining some of the behaviour of materials. On the other hand, I also felt that perhaps it is not necessary to explain some of the well-accepted observations the metallurgists have made. It would be more useful to complement the metallurgists in a suitable manner.

One topic not fully discussed at this Meeting is fracture. Why are we interested in obtaining a better understanding of the physical basis of mechanical behaviour? Essentially it is so that one can design better materials which will withstand service conditions. For instance, one might be interested in designing a material with good fatigue resistance or good creep resistance. We know that materials can fracture in widely different ways—ductile, brittle, cleavage etc. On the opening day, Prof. Ramaseshan has already pointed out how important it is to know the stress corrosion cracking behaviour of materials under service environments.

Take the nuclear field as an example. The iodine produced as a fission product can interact with the zircaloy clad and make the clad susceptible to stress corrosion cracking. The basic question here is: What does iodine do under stress to the grain boundary? Is there a decohesion caused by a lowering of the cohesive energy of the grain boundary which is locally under stress? Is it possible to predict which atomic species (like iodine) are efficient in lowering the cohesive energy? Theoretical studies of this problem coupled with suitable experiments will go a long way in establishing interplay between physical concepts and metallurgical interests.

Another example, again from the nuclear industry, relates to the irradiation creep behaviour of zircaloy coolant tubes. While the reactor itself has a life span of about 30 years, one is forced at present to change these tubes once in every 12 yrs or so because of irradiation creep. To develop a material that will be good for the entire life span of the reactor, we must perhaps introduce new ideas. One should examine how the texture (*i.e.* the preferred orientation) and grain shape influence irradiation growth of the material. Perhaps, as Prof. Ranganathan suggested, one could use the concept of fractals to characterize grain shape topology— and thus have a better measure for studying and characterizing irradiation growth.

These are some examples of practical problems where there can be a meaningful dialogue between physicists and metallurgists. They involve finding real-time solutions to real-life problems based on an understanding of the basic behaviour of materials.

Prof Joshi: Thank you, Dr Krishnan, for pointing out some problems where physicists and metallurgists could come together. We now turn to Dr Sahni.

Dr V C Sahni: I would like to go back to the remark which Dr Venkataraman made on the opening day. He was looking at a certain matrix element and trying to find out whether it would be zero or non-zero at the end of the Meeting. Now metallurgists are essentially practitioners. In fact, you would have noticed this from Dr Krishnan's remarks. On the other hand, physicists are a different kind of people. They tend to look behind a phenomenon, try to understand it from an atomistic basis and so on.

An analogy comes to my mind at this point. Consider the automobile engine. Obviously there are (automobile) engineers who design such objects. But there are also people trying to understand the basics of the combustion process *via* tools like Raman scattering. The hope is that such basic studies can lead to the improvement of the efficiency of the engine.

Physicists cannot from the word go come up with solutions to the practical problems of metallurgists. The important thing is they try to analyze the microscopic basis for a particular type of behaviour. In turn, the metallurgist can build on this instead of relying on a phenomenological understanding of the situation. Of course this is the way science progresses.

So, coming back to the point Dr Venkataraman made about whether there is an overlap matrix element or not, I think we really have to look at the interface between the two disciplines. As Prof. Ranganathan's talk clearly brought out, a topic like the large-angle grain boundary is something which physicists can examine from an atomistic point. If some light is shed, then perhaps it will enable the metallurgists to come up with better materials. In short, physicists can *via* tools of their own (like fluctuation spectroscopy) explore microscopic processes which in turn can form inputs to the metallurgical aspects. So my own view is that the matrix element might not be as large as one would hope for, but it is not zero either. I am in agreement with Dr Krishnan that exercises like this Meeting should continue. Hopefully, if we repeat it a couple of times, we may converge on something significant and improve the matrix element in the future.

Prof. Joshi: Thank you, Dr Sahni. I think the value of the matrix element depends on the "frame" of reference just as Deepak Dhar pointed out that the length of a coastline depends on the length scale used for measurement. Locally the matrix element is sometimes positive and sometimes negative. What we must all do is to go to a scale where it becomes *globally* positive! I now request Dr Ray to give his views.

Dr Ray: Before we try to explain the mechanical behaviour of a material, we must first define the mechanical *state* of the material. Important in this context is a proper description of the grain boundary concerning which Prof. Ranganathan described a beautiful model. However, from the questions that were raised after that talk, I can see that there are limitations to that model. One wonders what the correct description of the situation at the grain boundary should be. May be something will emerge in the future.

One topic on which we did not focus is vacancies, especially their role in defining the mechanical state of matter. Vacancies play an important role as we know from annealing experiments on cold-worked samples. They are also pertinent to certain aspects of plastic deformation.

Next comes the grain shape. We all know that the grain shape is probably important but we do not yet know how to describe it quantitatively. Probably, the fractal concept might help us.

Let us now consider the transition from the elastic to the plastic regime. We used to think of this in terms of dislocations becoming mobile and multiplying. Now they are being described in terms of fluctuations, bifurcations, chaos and what not! Incidentally, I would like to point out that for bcc metals, there is a temperature below which this transition does not take place; for fcc metals however, this does not hold. All facts taken together, the picture to my mind is a bit puzzling. Is the elastic to plastic changeover really a transition or the emergence of a stable fluctuation of a particular kind?

Prof. Joshi: Thank you, Dr Ray. I now invite Prof. Kumar who has all along been making illuminating remarks from the floor, to give us his views as a panelist.

Prof. Kumar: I believe it is a part of conventional wisdom (which goes back to the Greek philosopher Lucretius) which says that a thing is explained only if it is done in terms of underlying microscopic objects (which, one presumes, exist). This may be a mental bias but no one seriously questions such an approach now. Certainly it is a part of our training as physicists. The question therefore is: What is the appropriate level of microscopy at which we want to discuss the present problems? Certainly you don't start with quantum mechanics if you want to build a house! There must be an "efficient" relationship between the microscopic world and the phenomenon we wish to understand. Of course all phenomena are not easily reducible to microscopic pictures. That we shall bear in mind. Now I shall get down to something specific.

Physicists often work with paradigms. For instance, if we are talking about a solid, we immediately imagine a perfect crystalline lattice and invoke Bloch's theorem. Everything is fine. Any departure from this idealization is a bit unfortunate but we take care of it in terms of a small perturbation. This is an example of an ideal picture that a physicist uses as a paradigm. On the other hand, a metallurgist, confronted as he is with *actual* metals, has his own paradigms. As I understand it now having come here, they mostly have to do with dislocations (which, I believe, live, multiply, climb, pile up and even die!). This is very nice. It is not necessary that dislocations exist; it is enough if they exist as paradigms! For example, quarks most probably do not exist but it is quite convenient to explain all matter in terms of quarks; it is a good mental picture. On the other hand, if we are going to discuss heavily deformed materials, is this paradigm based on dislocation as an elementary object convenient? True there are pictures showing dislocation— they are real objects and they certainly exist. We can even work out the mathematics of a single dislocation— no problem. I am told the two-body problem also can be done. But what if we have more than two, say 10, 20 or 10^{11}? That is where the problem lies. Near a large-angle grain boundary, do they retain their imitable integrity or not? If they don't, then we may have to look for something else in terms of which to describe these structures. Prof. Ranganathan did this by resolving the large deformation at the grain boundaries into a big part (DSC) plus a small part (described in terms of dislocation with Burger's vector taken from the DSC). I am happy with this picture. However, a doubt remains in my mind. In a metal, the large deformations at the grain boundaries must surely be sensed and felt by the electrons. If so, are we justified in ignoring the reactions of the electrons to such a heavy distortion? Even geometrically speaking, one wonders whether the dislocation concept is appropriate at a large angle grain boundary where there is such a pile up. Perhaps things are too amorphous-like in that region, and some alternate description should be tried (if not already done). So, the large-angle grain boundary appears to be a problem which physicists would be interested in because this is a case where one paradigm might give way to another.

Aside from this, there is a nontechnical matter that I raise on behalf of Prof. Ramakrishnan, which is: Where do we go from here? We obviously cannot meet time and again just to review work already available in books and journals. The important question is: Are we sure that there are sufficiently important, interesting, nontrivial open problems which physicists would be interested in? As of now, most of us physicists are *not* working on problems of mechanical behaviour. We are looking for the possibility of Discussion Meeting induced transitions. For something worthwhile to emerge, physicists must be willing to give more than 10% of their time. This is a practical issue if we mean business, and I suppose we do!

Prof. Joshi: Thank you Prof. Kumar. I now invite comments from the floor. Comments may please be restricted to broad issues or questions rather than matters of specific detail.

Dr G Venkataraman: As mentioned by you Prof. Joshi, I would like to make a few broad suggestions. The first of these arises out of a conversation I had with Prof. Ramaseshan at the time when the idea for the present Meeting took shape. Prof. Ramaseshan pointed out that while holding a meeting of this type was fine, everyone would go back and continue working on the same problems as before, instead of exploring the new grounds revealed at the Meeting. He emphasized that if fresh ground is to be broken, it would essentially have to be by young people who have not yet committed themselves to working in an already established area. I have been discussing this question informally during the last three days with several people, and the consensus appears to be that we must organize a regular, pedagogic school wherein young people can be given a systematic introduction that will orient them for research in this area.

Next I would like to point out that the Department of Science and Technology (DST) has identified this subject as a Thrust Area. If good proposals concerning experimental or theoretical research are made to DST, I am sure funds would be forthcoming.

Lastly, as regards future Meetings of this type, my sampling seemed to reveal that: (i) Future Meetings are necessary, (ii) they should not be large, and (iii) the topic of the Meeting should be more specific say like fracture, physics of large deformations etc.

Prof. Joshi: If we look at the growth of the interaction between physicists and metallurgists (in this country), we notice that some of it originated right here at RRC. In this Meeting, we heard on the first day a description of some experiments on serrated yielding performed by Dr Rodriguez's group. A theory of serrated yielding was also presented by a physicist from RRC. Maybe the theory was not explicitly motivated by those experiments but the interactions between the Materials Science group and the Metallurgy group must have had some influence. Some catalytic agent is definitely needed to promote such interdisciplinary interaction, may be in the form of an official directive!

I was having a conversation with Prof. Kumar wherein he remarked that when we return from this Meeting, most of us will go back to doing what we were doing earlier! What we do is, I suppose, decided by many factors but the value system is a key one. If one wants to encourage such interaction, then one must attach a value to it. I suggest that physicists and metallurgists in multidisciplinary Institutes like, for example BARC, should experiment in investing some percentage of their time to interdisciplinary activity of this kind. The outcome of such experiments could perhaps be reported at the next Meeting whenever we have it.

Anyway, as far as this Meeting is concerned, it has been a very fruitful one though, as some comments both from the panel and the floor indicate, a few aspects could have been better. But this Meeting has certainly had its utility, and we shall take advantage of whatever we have learnt to augment this interaction.

Prof. Kumar: I just want to add something. When I came here, I had a little misgiving in the sense that the subject obviously is an old one. I was aware that eminent physicists like Sir Charles Frank had worked on the subject. The point is that I had a feeling that around the World there must be many physicists working on metallurgy. Now as a physicist, I am not directly involved in this type of work and therefore I just don't know what has already been done. Unfortunately, no one here explicitly pointed that out, and also what has *not* been done. As someone remarked, the natives are not quite stupid! If we are not properly informed about what has already been done, we might end up reinventing the wheel!! Would someone like to comment?

Dr R Ramaswamy: I want to say a few things—probably in repetition, and some of them platitudinous perhaps! When a person like me comes to a Meeting like this, he does not necessarily come looking for problems. One comes, one listens to the problems aired, one says what one can, and one contributes. In that sense, I don't think it is valuable for us to seek where we are going *vis-a-vis* conferences of this type because such a conference serves precisely the purpose for which it was arranged *i.e.* to bring together people of different disciplines and see what each one can get out of it. *Of course* we will go back to doing whatever we were doing before. The hope is that the little one might have heard might make *the* difference. Undoubtedly there will be more conferences of this type in the future but whether they should be held or not are spontaneous questions. When Deepak and I go back to TIFR we might well say, "Why are we doing abstract problems? Let us get together with chemists etc". In that case we are the ones who would have benefited. One cannot induce such things; they happen reasonably spontaneously.

Prof. C K Majumdar: When I came here, I certainly did so with the purpose of hearing metallurgists because we physicists do not often hear people of other disciplines. It was certainly educative. The things learnt should not be viewed in terms of immediate return alone because they also broaden your outlook. Even if you go back to doing what you were doing before, your view point would have changed a little and that is a good thing.

Turning to specific suggestions, I think we should have another such Meeting, perhaps in three years. Time scales are a bit long in this country, and probably, it will be at least three years before we can really talk anything new— by new I mean results obtained in *our* laboratories.

Now there are not many places where interdisciplinary work of this type is being done. I for one do not even know where metallurgical work goes on, apart from organizations like RRC, BARC, HAL and the IIT's. Obviously there must be other organizations using at least some metallurgical skills, the State Transport Corporations for example. Judging from the conditions of the buses they ply, there is clearly scope for some technological improvement (!) which could perhaps be done by metallurgists. At the same time, the wayside auto shops seem to manage alright, and they appear to be having a way of accumulating empirical knowledge that is beneficial to their work. In all the training we talk about, we should not forget such people. Somehow they have to be exposed to modern developments. In other countries this is taken care of, and phenomena like exoemission are actually put to practical use by high-technology companies like Lockheed. Details of such applications are often not discussed in the open literature and we have to learn them on our own. History in fact shows that advanced civilizations often keep technology to themselves and do not allow it to percolate to other civilizations. In such cases therefore, we have to learn the hard way.

Not everything in science should be done just for publication or priority. Certain things, even if it means repetition, *have* to be done to make Society run better. Repetition may not actually be a bad thing for in the process one might actually improve on what is already known. I can give you an example. The Chinese apparently had ice cream long before the Europeans knew about it. Marco Polo brought ice cream knowhow from China to Europe, and later the Americans improved it! In short, there are aspects of technology which we have to develop on our own. In that sense, we should find a way of inducing some technologists also to attend such Meetings in the future.

The other thing I would like to comment on is the School that Dr. Venkataraman mentioned. The School should not just involve lectures alone; the students must also get exposed to some experiments. In that case, I think the School should be organized in places like this (RRC) or at the Indian Institute of Science, where there are appropriate facilities.

Dr K R Rao: My comments relate to the remarks made earlier by Prof. Kumar. I think many of us would like to go back and actually do something different instead of continuing to do the same thing we have been doing for the last 25 years or so. In this context, I think the identification of unsolved problems is very important. One example comes to mind and that relates to Atomic Data for Fusion Research prepared by the IAEA about four years ago. A huge report has been written identifying hundreds of problems. IAEA has followed up this effort with some funding, and has also been evaluating the data coming out of the various research Centres. Although we are not trying anything on that scale, I feel that if problems are identified and made known say through the Proceedings of this Meeting, it might lead to various people (including those not present here) picking up the strands. Particularly in the experimental field, there is no reason why some of us cannot try something new, provided new experiments or problems are identified by specialists.

Prof. V Balakrishnan: I wish to comment briefly on a point raised yesterday by Prof. Ramakrishnan. In his characteristic fashion, Prof. Ramakrishnan pointed out that it would be useful for solid state physicists to learn the basics of physical and mechanical metallurgy. This is being done in some places but perhaps the exercise could be made more systematic. It is certainly being done with respect to courses on materials science but not so much in the case of solid state physics. As far as the latter is concerned, if one can spend a lot of time on electronic properties then surely a chapter of mechanical properties is reasonable, especially as it will at least get the jargon straightened out for condensed matter physicists. This chapter need not be very long. I noticed that right here on the first day, many physicists expressed to me their concern about the jargon. They could not understand it, but repeated use of the term dislocation seems to have made it familiar enough to most people (rather like the way theorems are established in high energy physics, namely you repeat it often enough and it becomes a theorem)!

In a slightly more serious vein, I think that some simple experiments on mechanical behaviour should also be introduced in the undergraduate curriculum. And there are very dramatic experiments, like the one on work-hardening demonstrated by Bragg in his Royal Institution lectures. A similar one, perhaps already known to some of you, involves closing one end of an open cylinder with a tissue paper, filling it with sand, after which you put a metal rod and apply enormous load on it. We got this set up at IIT recently and I personally along with several other people put my full weight on the rod and the tissue paper did not break because the stress was distributed by those fine grains of sand. Experiments like this bring out beautifully the effect of interfaces, grain boundaries and so on. Perhaps we should spend some time generating ideas for such elementary but very effective demonstrations which will convey to physicists the basic concepts of metallurgy.

Dr R Chidambaram: I think what was unique about this Meeting was that it brought a small group of metallurgists and physicists together. Also, unlike other meetings where people come and either give invited talks or present contributed papers, I got the impression that one was expected in this Meeting to talk about problems one had not completely finished or one did not know enough about. Thus, for example, I did not talk about our work on the equation of state— something we know how to handle. Instead, I talked on something in which we had some doubts and in which some metallurgical concepts were involved. If you look at the matrix element which Dr Sahni was talking about, the value of that matrix element must be obtained, I think, by integrating over the personal responses from all the individual participants, as is being done here during the present Panel Discussion. With this in mind, I will tell you what I personally gained from this Meeting. Honestly, I did not expect that the metallurgists would ask the kind of questions they actually asked after my talk. Of course Dr Majumdar raised a point about the entropy equation which I had not written down. If one knew how to write it down, the problem of the structure of the shock front would be solved substantially, but the current state of the art is such that one does not know how to discuss entropy production in the case of shock propagation in solids. On the other hand, after listening to the large number of talks we had on dislocations and grain boundaries, I think I now have a better perspective on how to think about these physically, in relation to the propagation of a shock front. That way I think this Meeting has been very successful.

As regards the periodicity of such Meetings, I think a Meeting once in three years as Dr Majumdar suggested would be appropriate. And that should be interspersed with a School in which there are lectures both by physicists (theoretical as well as experimental) and metallurgists.

Prof. Joshi: Would a metallurgist from the floor like to react? Yes Dr Rodriguez.

Dr P Rodriguez: I would like to make a few observations and the first of these relates to Prof. Ramakrishnan's remark that before physicists deal with the real physical nature of problems in complex materials like alloys, they need to develop a better understanding of the basics of physical and mechanical metallurgy. As history shows, metallurgy has been enriched considerably by the work of the physicists, and in fact many physicists have contributed to the study of plastic deformation and the fracture of metals. For example there is the monumental work of Schmidt and Bose on the deformation behaviour of single crystals of fcc metals. Prof. Ramakrishnan showed a picture of such deformation behaviour, and quoting from Bell's work said that metallurgists ignore it but that is really first-year text book material for metallurgist! We start with the deformation behaviour of a fcc single crystal and then extend it to the polycrystal. That is my first point.

People have quoted many things, the old testaments, their heroes, etc!. I will quote George Santayana who said that those who do not learn history will be condemned to repeat it. So let us be careful about not repeating history! Particularly from some theoretical physicists, I got the impression that they would like to apply some newly discovered mathematical formalisms to explain already explained phenomena. I am not stating this as a criticism but it is important that before going ahead with applying a theory or a model one should take stock of the state of the art. This point was made by Prof. Kumar and it is important. One way of achieving this is to organize a course or even write a text book. We have beautiful books on physics for engineers, physics for metallurgists etc. May be it is time to write a book on metallurgy for physicists!

Another aspect that I would like to point out is that in the important area of deformation and fracture behaviour of materials, we have reached a stage of understanding wherein we can now *a priori* design an alloy. This topic, *i.e.* the relationship between microstructure and mechanical properties of alloys has been completely left out from this Discussion Meeting. By microstructure I mean the substructure for example, the distribution of second phases, their morphology, the dislocation density etc. We find that the total dislocation density *per se* is not always the controlling factor, rather the way the dislocations are arranged, *i.e.* whether they are tangled or have a cell-structure. This topic has been completely overlooked. Of course it is obvious that all topics could not have been covered in a Discussion Meeting like this. But this argument shows that there is enough scope to have more frequent Meetings, focussing attention on such specific topics.

Prof. Joshi: Since there is a time restriction, I am afraid I have to interrupt and cut short this interesting Discussion!

I will sum up by saying that there is a need for future Discussion Meetings as well as a tutorial School. The duration, the periodicity, the organization, the themes—all these could be left open at the moment.

Being the last speaker permit me to express our grateful thanks to the Organizers of this unique Meeting. I would also like to express our special thanks to our hosts who have taken such good care of us. Finally, I wish to thank the panelists, those who participated from the floor, and the audience in general for making this discussion lively. Thank you all once again!

Bull. Mater. Sci., Vol. 6, No. 5, September 1984, pp. 837–899. © Printed in India.

Phase transformations—a physicist's perception

G VENKATARAMAN
Reactor Research Centre, Kalpakkam 603 102, India

Abstract. Echoing a recent remark by Prof. Ramaseshan, a perspective review is made of the field of phase transformation, highlighting areas that might appeal to physicists. Prominent in this category are the study of ground state structures, the study of phase diagrams and the study of kinetic phenomena.

Enumeration of ground state structures calls for inputs from group theory as well as reliable potentials, and physicists are therefore well equipped to make significant contributions. The theoretical analysis of phase diagrams (concerning which much experimental information already exists) raises challenging questions in equilibrium statistical mechanics. Since the problems map to Ising models of varying complexity and their generalizations, there are also very interesting connections to magnetism. Lately, computer simulation has added a new dimension, opening up fresh vistas both for theory and experiments. The study of kinetics belongs to the newly emerging area of non-equilibrium statistical mechanics. The focus being on *temporal* phenomena, physicists can play a key role, particularly through the application of various types of relaxation spectroscopy. On the theoretical side too there are challenging problems, especially on account of the dominance of nonlinearities. Indeed if one is bold enough, one could even speculate on possible universalities underlying the complex microstructures invariably seen in late-stage evolution. In short, though the subject of phase transformations has thus far been nursed predominantly by metallurgists, there is enough room for physicists to make an independent entry and to make distinctive contributions.

Keywords. Phase transformations; phase diagrams; spinodal decomposition; ordering kinetics.

1. Introduction

The theme of this paper relates to a remark made by Prof. Ramaseshan at the Baroda Seminar on Thrust Areas in Physics, and it is perhaps relevant to begin by outlining the background.

Around 1980, the Department of Science and Technology (DST) initiated an intensive exercise to identify Thrust Areas in various scientific disciplines. As a part of this, a Seminar was organized in Baroda during November 1981 to which were invited a cross-section of active physicists in the country. Although the ostensible purpose of the Seminar was to aid the DST in identifying areas which it could fund selectively, Dr. Ramanna who presided made the suggestion that since there was a rare gathering of physicists with diverse interests, the occasion should in fact be utilized to draw up something like a National Plan for Physics. A part of this Plan could then be funded by the DST, and the balance by other appropriate agencies. This suggestion was greeted with enthusiasm, and several exciting proposals were unveiled by those present. Intervening in the discussion, Prof. Ramaseshan remarked that while large projects in areas like gamma-ray astronomy or high-energy physics were no doubt to be commended and also needed, some thought should also be given to researchers in small

---

This paper was originally prepared for the 60th birthday volume of Prof. S Ramaseshan.

universities, most of whom remained outside the orbit of "big science". He went on to emphasize that in drawing up a list of Thrust Areas, consideration must also be given to subjects like phase transformations which not only offered challenge but also did not require massive funding and could therefore be pursued by those with modest resources. I was quite delighted by this suggestion and the specific reference to Phase Transformations since I had just then begun to gravitate towards the subject myself.

Now the subject of phase transformations is well established amongst metallurgists. Physicists, on the other hand, have generally stayed away possibly because it appeared messy to them. However, in the light of many recent developments in physics (*e.g.* advances in the understanding of nonlinear phenomena), some of these so-called messier aspects have acquired an attraction of their own. The main purpose of this article therefore is to draw the attention of physicists to such aspects, and hopefully induce at least some of them to enter this area. The paper is thus essentially a perspective review addressed to physicists, keeping in mind the needs of those who may be totally unfamiliar with the subject. However, in the spirit of Prof. Ramaseshan's remarks, interspersed are several suggestions for further work for those adventurous enough to enter the area.

2. Preliminaries

2.1 *Some elementary facts*

To most physicists, a phase transition usually calls to mind a change of state like solid to liquid etc. Metallurgists on the other hand, are interested mainly in transformations *within* the solid state. Of the many variations possible even in this category, we restrict attention to order-disorder transformations associated with compositional fluctuations. In the interest of simplicity, we shall further confine ourselves to binary alloys $A_{1-x}B_x$ $0 \leqslant x \leqslant 1$ (*e.g.* Al-Zn or Cu-Au).

To fix our ideas, let us consider a Cu-Zn alloy (β-brass) with equiatomic composition *i.e.* $x = 0{\cdot}5$. Both at high as well as at low temperatures, there is a well-defined lattice (*viz* bcc) associated with this alloy. However, there is a difference in the way the atoms are distributed amongst the lattice sites. Above 468°C, the occupancy of the lattice sites by Cu and Zn atoms is statistical whereas below that temperature, there is a well-defined order in the arrangement (see figure 1). One can intuitively see that entropy considerations must dominate at high temperatures leading to disorder. On the other hand, interatomic forces assert themselves at low temperatures leading to an ordered structure as in figure 1b. The temperature 468°C represents a transition point for the order-disorder process.

In the example just discussed, every atom has an atom of the other species as a nearest neighbour in the ordered state, implying that the potential v_{AB} dominates over v_{AA} and v_{BB}. It could also happen that v_{AB} is not strong enough to achieve this in which case a different type of ordering ensues wherein, the material organizes itself into large crystalline domains rich in either A or B type atoms. Essentially, "birds of a feather flock together", and the phenomenon is often called *phase separation* or clustering.

Superficially, phase separation and an order-disorder transition (like the one in β-brass) appear different but if we associate a wavelength scale with the two processes as is schematically done for a 1-D example in figure 2, then we can discuss the two in the same framework, as is done for ferro- and antiferromagnetism. Phase separation being

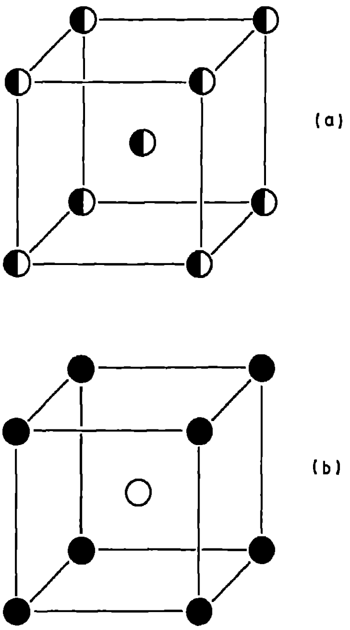

Figure 1. Schematic illustration of order-disorder in β-brass. The structure is bcc in both phases but in the disordered phase, the occupation of the lattice sites by the two species of atoms (shaded and full) is strictly statistical as in (a).

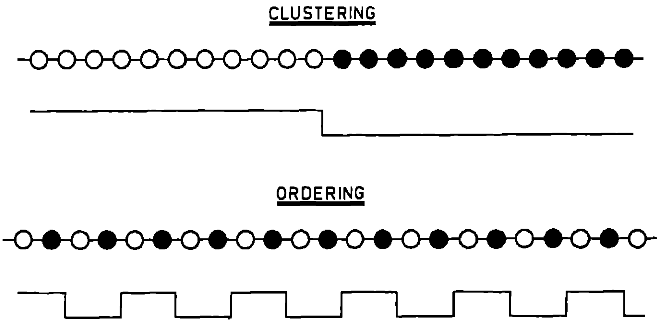

Figure 2. One-dimensional example to illustrate the different wavelength scales for clustering and ordering.

similar to ferromagnetic ordering will be associated with a wavevector $k \sim 0$ while order-disorder transition being similar to antiferromagnetism will be associated with a wavevector $k \sim$ zone boundary.

2.2 *Phase diagrams—a primer*

A study of phase transformations without some knowledge of phase diagrams is hardly possible. Most physicists are no doubt familiar with phase diagrams for monatomic systems but once one enters the world of multicomponent systems, phase diagrams can become quite complex, indeed even for binaries such as we shall be considering. A brief primer on phase diagrams is therefore useful.

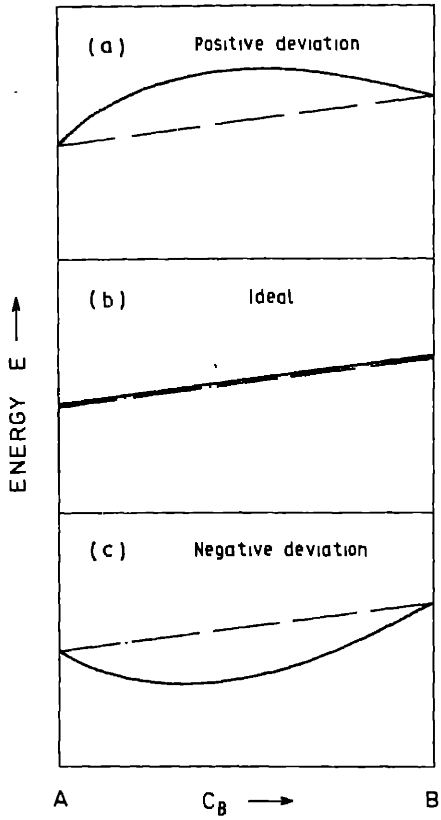

Figure 3. Schematic plot of energy as a function of composition for the three situations discussed in the text.

Broadly speaking, a phase is a state of aggregation. Our interest is in the various phases possible when two atomic species A and B are mixed together to form a solid at different temperatures and at different compositions. A phase diagram is therefore essentially a map of the various possible states of aggregation in the temperature-composition plane. From thermodynamics we know that the equilibrium state of a system is determined by the minimum of the free energy (FE) with respect to the appropriate thermodynamic variables. Accordingly, we direct attention now to the minimum of the FE at various temperatures and compositions. To start with we note that the free energy is given by

$$F = E - TS$$

where E is the internal energy*, T the temperature and S the entropy. In figure 3, E is plotted schematically as a function of composition (Wulff 1971). Here the dashed lines denote the energy before mixing and the solid lines that after the mixing. The 'ideal' situation is that shown in figure 3b where the energy does not change on mixing. More usually, one has either a positive or negative deviation from ideality as in figure 3a or c.

We next consider entropy, for which the situation prior to and after mixing will be as schematically depicted in figure 4. The results of the last two figures may now be

---

* Strictly speaking, we should have enthalpy $H (= E + pV)$ instead of E. However, most material processing is done around atmospheric pressure. From a practical point of view therefore H is well approximated by E.

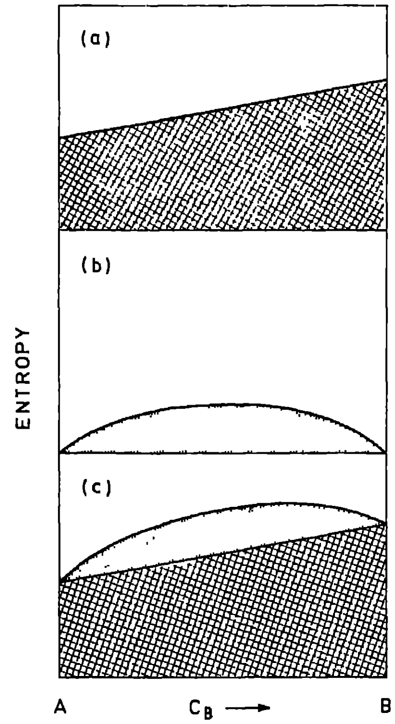

Figure 4. (**a**). entropy of the $A_{1-x}B_x$ system before mixing. (**b**). sketch of entropy of mixing. The total will then be as in (c).

combined to visualize how F varies with composition at a given T. Of the several possibilities, that corresponding to negative deviation from ideality is of particular interest to us and the free energy curve for this situation is sketched in figure 5. To find the most stable arrangement that results after mixing at the chosen temperature T we must obviously look for the minima in F. Using this criterion, it is clear from the figure that if we prepare a mixture of composition c_B, then this mixture will be unstable. It will seek stability by splitting into a mixture of two solutions of compositions c_B^1 and c_B^2. Observe that after such a separation, the F value diminishes from F_u to F_s.

The above scenario applies to all mixtures with composition in the range c_B^1 to c_B^2, and we conclude that for all compositions in this range, a *mixture of two phases* is the most stable state. This is the phase separation briefly mentioned earlier. When T is increased slightly, essentially a similar situation is obtained, with c_B^1 moving slightly away from the A end and c_B^2 moving slightly away from B. As T increases, c_B^1 and c_B^2 approach each other continuously, eventually merging at some temperature T_c. For $T > T_c$, segregation into two phases of different compositions no longer occurs; instead the solid solution itself is stable, and we have a one-phase region. Thus, the locus of c_B^1 and c_B^2 in the temperature-composition plane provides a boundary separating the one-phase and two-phase regions of the solid. Figure 6 shows a portion of the phase diagram of Al-Zn where such a two-phase region exists.

It is of course not necessary that when two atomic species are mixed, one should always get phase separation at low temperatures. Instead one could also obtain ordering, as *e.g.* in Cu-Au systems. We shall have more to say later about these two

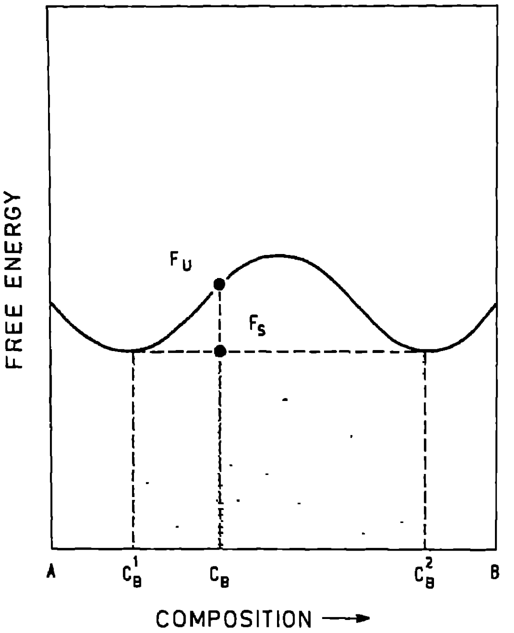

Figure 5. Free energy curve corresponding to a particular temperature for negative deviation from ideality. F_u is the value corresponding to the unstable state created immediately after mixing, while F_s is the value corresponding to the stable state. For every composition in the shaded region, the terminal state is a mixture of two phases of compositions c_B^1 and c_B^2.

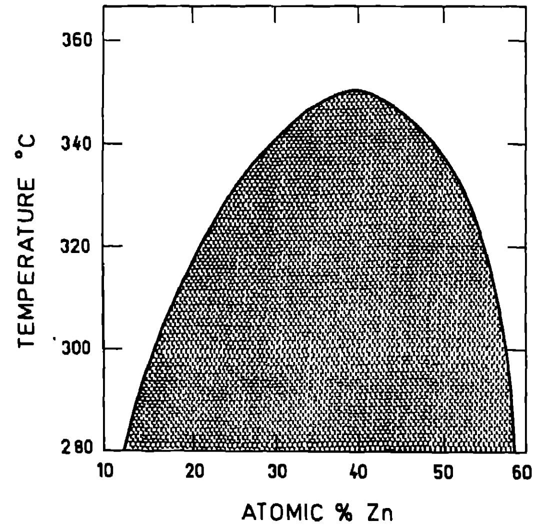

Figure 6. Portion of the Al-Zn phase diagram showing the two-phase region.

representative cases of phase separation and ordering.* For the nonce let us note that the solid mixtures we are considering are restricted to the substitutional type *i.e.* if we take a perfect *A* type solid and add *B* type atoms, the latter replace *A* at the lattice sites. For this to be possible, the following criteria must be broadly satisfied:

---

* Phase separation is *also* a type of ordering! Only the wavelength scale is different.

(i) The atomic radii of the two elements must be within 15 % of each other. (ii) The crystal structures of A and B must be the same. (iii) The valence of A and B must not differ by more than unity. (iv) The electronegativity must be nearly equal.

While we have sketched the concept of the phase diagram from (elementary) theoretical considerations, we should remember that metallurgists often actually map phase diagrams by doing experiments. Indeed there is a wealth of such data (Hansen 1958), and, as we shall see later, a theoretical analysis of such diagrams is a possible avenue of interest for physicists.

2.3 *Areas of interest*

Given the fact that metallurgists have already contributed much to the subject, especially on the experimental side, it is natural to wonder whether there is any room for physicists (*e.g.* Chen *et al* (1979) point out that prior to the late sixties, there were at least 36 books and reviews on the subject. Also, there have been several major conferences held on the subject during the last decade). However, a careful appraisal does show that there are certain areas in this vast domain where physicists could bring to bear tools that are their specialities. Prominent among these areas are:

(i) The elucidation of ground state structures, (ii) Calculation of phase diagrams, and (iii) The study of kinetic phenomena.

Of the above, the calculation of phase diagrams belongs to the realm of equilibrium statistical mechanics, and, as we shall see in § 3, raises problems in the traditions of Onsager since one mainly deals with Ising models of various complexity. The study of kinetic phenomena on the other hand, takes one to the newly emerging area of nonequilibrium statistical mechanics. The presence of nonlinearities is an added attraction.

In terms of tools, apart from neutron and x-ray scattering which are already familiar, physicists could also exploit various types of relaxation spectroscopy. No doubt the scattering techniques have already been used to some extent in the past but there is considerable scope for enhancing their applications. Particularly in the case of x-rays, the recent availability of synchrotron radiation opens up many new exciting possibilities. Also, there are many technical innovations like position-sensitive detectors that have hardly been used for such studies. As far as relaxation spectroscopic studies are concerned, the field is literally wide open. Complementing all these is the powerful technique of computer simulation, used already to some extent, but admitting of considerably more exploitation. In short, there is plenty of scope for physicists to make a distinctive contribution of their own to the field, although they may be latecomers.

3. Equilibrium structures

3.1 *Ground state structures*

Given a disordered structure (say belonging to the fcc lattice), there arises the general question of the type of ordering that will occur at lower temperatures. In a simple situation as in β-brass (see figure 1), one could perhaps have made a good guess of the ordered structure purely from inspection. However, such guesses are not always easy, requiring, as they do, considerable crystallographic insight. A systematic approach to enumerating the possible ordered structures has been evolved by Soviet scientists, inspired largely by Landau's theory of phase transitions.

Before sketching the work of the Soviet School, we note first that the ground state structure is the atomic arrangement assumed by the solid at absolute zero of temperature. While it is the onus of theory to predict this structure from first principles, a considerable body of information about the structures actually occurring in Nature has already been accumulated through diffraction experiments. Next we remark that ordering is essentially characterized by the appearance of a superlattice. The superlattice structure that emerges depends on (i) the structure of the parent lattice, (ii) the interatomic forces, and (iii) the atomic composition of the system. If, for example, we consider the fcc lattice, then several ordered structures based on it are possible some of which are illustrated in figure 7. The distribution of the various superlattices possible amongst the alloys realizable by combining various elements in the periodic table have been painstakingly compiled by Kozlov *et al* (1974) and the data is worth glancing through.

Returning to the enumeration of possible superlattice structures, the basic idea is the following: Let us first describe the atomic distribution by means of a function $n(\mathbf{r})$ which gives the probability of finding an atom of some definite kind at site $\mathbf{r}$ of the lattice. In a disordered alloy $n(\mathbf{r})$ is a constant c. On the other hand, when the system orders, $n(\mathbf{r})$ assumes m (say) different values $n_1, n_2, \ldots, n_m$ at the m sublattices are associated with the structure. In brass, *e.g.*, $m = 2$. Of course, $n(\mathbf{r})$ corresponding to a particular sublattice position has the same value in all the unit cells. The problem now is to determine the possible distribution $n(\mathbf{r})$ can have when ordering occurs. Khachaturyan (1974) approaches this by regarding $n(\mathbf{r})$ as being built up of *static* composition waves as follows:

$$n(\mathbf{r}) = C + \frac{1}{2} \sum_{\mathbf{k}} \{Q(\mathbf{k}) \exp(i\mathbf{k} \cdot \mathbf{r}) + \mathrm{C.C}\}. \tag{1}$$

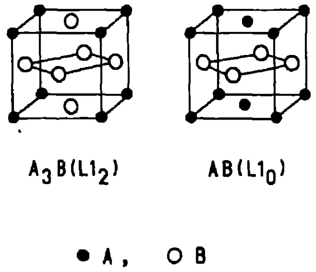

Figure 7. Some of the ordered structures observed in fcc lattices.

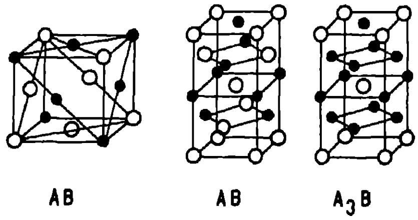

Here the summation over **k** runs over the first Brillouin zone of the disordered alloy. $Q(\mathbf{k})$ is the (complex) amplitude of the concentration wave of wavevector **k**. Following Landau, one now writes the sum over **k** as sums over various possible stars one can form in the Brillouin zone (see figure 8). With this regrouping,

$$n(\mathbf{r}) = C + \sum_s \eta_s \varepsilon_s(\mathbf{r}), \tag{2}$$

where

$$\varepsilon_s(\mathbf{r}) = \frac{1}{2}\sum_i \{\gamma_s(\mathbf{k}_i(\star s)) \exp i\, \mathbf{k}_i(\star s)\cdot \mathbf{r} + \text{C.C.}\}. \tag{3}$$

In (3), the summation runs over all the members i of the star s whereas in (2) the sum is over all the possible stars. Together, all the wavevectors in the Brillouin zone are accounted for. Comparing with (1)

$$Q(\mathbf{k}_i) = \eta_s \gamma_s(\mathbf{k}_i). \tag{4}$$

The quantities η_s are the long-range parameters which assume the value 0 in the disordered state, and the value 1 at 0°K. Since composition is conserved, the number of order parameters required to describe the ordered structure will be $(m-1)$. Later (in § 3.3) we shall see that the order parameters η_s are essentially the analogues of sublattice magnetizations.

Although formally the summation in (2) ranges over all the stars in the Brillouin zone, in practice (—and this is in the spirit of Landau's theory of phase transition) one

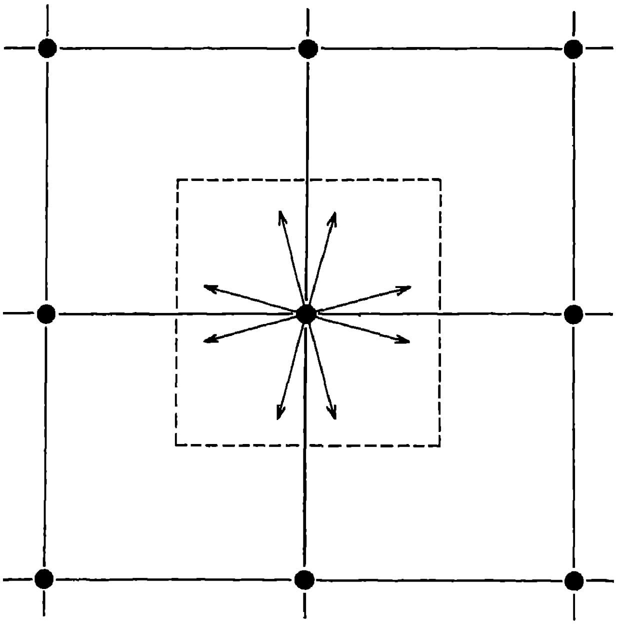

Figure 8. Illustration of the concept of star of the wavevector for a square lattice. The dots indicate the reciprocal lattice points, and the dashed line the central Brillouin Zone. The cluster of eight arrows represents a star. Starting from any one of these arrows, one can generate the entire cluster by a systematic application of the point group operations of the lattice.

supposes that a given ordering is associated uniquely with composition waves corresponding to a particular star. For illustration, let us consider ordering in Cu-Au alloys. X-ray experiments have revealed that ordering is linked to the appearance of superlattice {100} reflections (which, of course, are forbidden in the disordered state). It is reasonable therefore to suppose that the ordering is governed by the star of the wavevector [100] which comprises of the wavevectors [100], [010] and [001]. Thus (2) can be written as

$$n(\mathbf{r}) = C+\eta\{\gamma_1 \exp(i\mathbf{k}_1\cdot\mathbf{r})+\gamma_2 \exp(i\mathbf{k}_2\cdot\mathbf{r})+\gamma_3 \exp(i\mathbf{k}_3\cdot\mathbf{r})\}. \tag{5}$$

where $\mathbf{k}_1$, $\mathbf{k}_2$ and $\mathbf{k}_3$ are the three wavevectors of the star. The lattice vector $\mathbf{r}$ can be expressed in terms of the (cubic) unit cell vectors $\mathbf{a}_1$, $\mathbf{a}_2$, $\mathbf{a}_3$ as

$$\mathbf{r} = x\mathbf{a}_1+y\mathbf{a}_2+z\mathbf{a}_3 \tag{6}$$

with $(x+y+z) = $ constant. By letting $\mathbf{r}$ vary in (5), it is easily seen that $n(\mathbf{r})$ can take the following values

$$n_1 = C+\eta(\gamma_1+\gamma_2+\gamma_3); \qquad n_2 = C+\eta(\gamma_1-\gamma_2-\gamma_3);$$

$$n_3 = C+\eta(-\gamma_1+\gamma_2-\gamma_3); \qquad n_4 = C+\eta(-\gamma_1-\gamma_2+\gamma_3). \tag{7}$$

If now we invoke the fact that $(m-1)$ equals the number of distinct order parameters and remember that in this case there is only one order parameter, namely η, we are led to the fact that $m = 2$ for Cu-Au. Hence n can take only two values at the set of all sites (xyz) of the fcc lattice, leading to the two possibilities

$$\text{(i) } n_1 = n_4,\ n_2 = n_3; \quad \text{(ii) } n_2 = n_3 = (n_1+n_4). \tag{8}$$

The first alternative arises if $\gamma_1 = \gamma_2 = 0$ whence

$$n(xyz) = C+\eta\gamma_3 \exp(2\pi iz) = C\pm\eta\gamma \tag{9}$$

in alternate (001) planes. This is the so-called CuAu I structure. On the other hand, if alternative (ii) is to be realized, then we must have all the γ_i's equal whence

$$n(xyz) = C+\eta\gamma\{\exp(2\pi ix)+\exp(2\pi iy)+\exp(2\pi iz)\}$$

$$= \begin{cases} C+3\eta\gamma & \text{at the corners of the unit cell cube} \\ C-3\eta\gamma & \text{at the face centres.} \end{cases} \tag{10}$$

This is the Cu_3Au structure.

The above example shows how symmetry considerations may be applied a la Landau's theory to obtain some idea of the superlattice structures possible. Merely enumerating possible superlattice structures alone is not enough. This is somewhat similar to the exercise often done for ferroelectrics, where one uses group theory to enumerate the type of ordered structures that can arise. Symmetry thus picks out the various possibilities; which of these is actually favoured depends of course on the interatomic forces. To illustrate, we once again consider the fcc lattice, and direct attention now to the internal energy. The three potentials to be considered are, $v_{AA}(r)$, $v_{BB}(r)$ and $v_{AB}(r)$. In terms of these pair potentials, the internal energy E may be expressed as

$$\mathscr{E} = \frac{1}{2}\sum_{ij}\sum_{l\neq m} v_{ij}(l-m)\langle\sigma_i(l)\sigma_j(m)\rangle. \tag{11}$$

Here i, j refer to the species A, B while l and m denote lattice sites. The quantity σ is an occupation operator defined by

$$\begin{aligned} \sigma_A(l) &= 1 \quad \text{if site } l \text{ is occupied by an A-type atom} \\ &= 0 \quad \text{if site } l \text{ is not occupied by an A-type atom.} \end{aligned} \tag{12}$$

$\sigma_B(l)$ is defined similarly. The bracket denotes an average (here over the ground state). The lattice energy will evidently be determined by the correlations of the σ's at the various sites, and the system will choose that atomic configuration for which $\mathscr{E}$ is a minimum.

It is convenient to introduce an operator $\gamma_i(l)$ which describes deviations from mean occupation by

$$\gamma_A(l) = \sigma_A(l) - c_A = \begin{cases} 1 - c_A \\ -c_A \end{cases}; \tag{13}$$

where c_A is the concentration of A. Since $c_A + c_B = 1$, one has

$$\gamma_B(l) = -\gamma_A(l). \tag{14}$$

Using the γ's, the part of the internal energy that relates to occupation deviations can be written as

$$E = \frac{1}{2}\sum_{ij}\sum_{l \neq m} v_{ij}(l-m)\langle \gamma_i(l)\gamma_j(m)\rangle. \tag{15}$$

By elementary manipulation, this can be written as

$$E = \frac{1}{2}\sum_{lm} V(l-m)\langle \gamma(l)\gamma(m)\rangle, \tag{16}$$

where we have written γ for γ_A, and V is an effective potential defined by

$$V(\mathbf{r}) = 2v_{AB}(\mathbf{r}) - v_{AA}(\mathbf{r}) - v_{BB}(\mathbf{r}). \tag{17}$$

In terms of Fourier transforms

$$E = \frac{N}{2}\sum_{\mathbf{k}} V(\mathbf{k})|\Gamma(\mathbf{k})|^2 \tag{18}$$

where $\Gamma(\mathbf{k})$ is the transform of $\gamma(\mathbf{r})$.

The quantity $V(\mathbf{k})$ is periodic in reciprocal space reminiscent of, say, phonon dispersion curves, and will therefore have maxima, minima and saddle points (—the well-known van Hove (1953) singularities). The expectation now is that the state of order is governed primarily by where minima in $V(\mathbf{k})$ occur. One knows that barring unusual circumstances, minima of lattice periodic functions occur at points of high symmetry in the Brillouin zone (van Hove 1953). Thus, ordering is mainly associated with the build up of a compositional wave (also sometimes called concentration wave) with a wavevector corresponding to the special point where $V(\mathbf{k})$ has a minimum. This therefore is also the wavevector at which a superlattice reflection is seen in the diffraction pattern when ordering occurs. As may be expected, around the transition temperature there are critical fluctuations of the composition in this region of $\mathbf{k}$-space and consequently there is an enhancement of the scattering in the superlattice reflection region just prior to ordering. We shall say more about critical scattering later.

The potential $V(\mathbf{r})$ depends on the details of the electronic structure, and is often not known with sufficient accuracy for present purposes. It is therefore customary to parametrize pair interactions in terms of interactions up to a specified set of neighbours. One now examines minima in $V(\mathbf{k})$ as the ratio (V_2/V_1) is varied (where V_1 and V_2 denote the first and second neighbour interactions). The results can be succinctly paraphrased as in figure 9 due to Clapp and Moss (1968) who followed Villain (1959) who had earlier made such plots for magnetic structures. Incidentally, we see from figure 9 that in a certain range of ratios, ordering occurs for $k = 0$ leading to clustering of like atoms.

Mention should also be made of the work of Richards and Cahn (1971) and various Japanese workers (Katsura and Narita 1973; Kudo and Katsura 1976; Kanamori and Kakehashi 1977) who have studied ground-state structures using a real-space analysis. Recently some rigorous methods for describing low temperature structures of very general lattice systems have also been developed (Progov and Sinai 1975, 1976; Holsztynski and Slawny 1978; Slawny 1979).

Although some territory has no doubt been covered in the work of the various above mentioned authors, there is considerable scope for further work. One might wonder whether ground-state structures are not encompassed in a study of the phase diagram as a whole (§ 3.2). Indeed they are; however an independent knowledge of ground state structures does help phase diagram calculations and in that sense is a worthwhile, stand-alone activity.

Before leaving the subject, a brief reference must be made to off-stoichiometric structures. Suppose, for instance, we consider an alloy where, say, the concentration of A species is slightly less than 0·5. The question now is what happens in the ordered state. One's first guess would be that small deviations from stoichiometry would be absorbed as defects. However, when the deviations are substantial, the situation may not be that

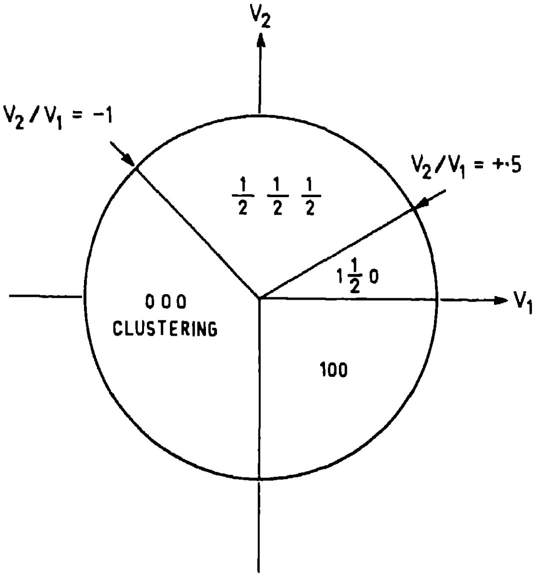

Figure 9. Location of minima of $V(k)$ as a function of the ratio V_2/V_1 for the fcc lattice. (After Clapp and Moss 1968).

simple. Krivoglaz and Smirnov (1965) suggested that at 0°K, an off-stoichiometric alloy decomposes into alloy of stoichiometric composition and a pure metal. It is not clear whether there is any experimental evidence in support of this suggestion. Kozlov *et al* (1974) have advanced the alternate idea that the excess atoms may undergo further ordering at suitable sites, leading to a new complex structure which they refer to as 'super-superstructure'. The experimental situation if assessed from the literature, can be quite bewildering to a physicist! When an alloy is prepared at high temperatures and cooled below the transition, it not only orders but develops a lot of microstructure; one has therefore to be quite careful in drawing the right conclusions.

One case worth mentioning explicitly is CuAu (nominal equiatomic composition). When this alloy is cooled from high temperatures, it transforms below 385°C into what is called the CuAu II structure illustrated in figure 10 (Ogawa 1974). There is an alternation every five cells, and the overall structure can be thought of as composed of antiphase domains of size $5b$. The oscillations are also referred to as long period oscillations (LPO). Such oscillations are reported for many ground state structures, and, in view of the extensive interest amongst physicists on charge density waves etc. are worth a close look (see also § 4.5). Returning to LPO's in Cu-Au alloys, there is evidence that the period $2M$ is not always an integral number (see figure 11) (Ogawa 1974). Noteworthy here is the fact that M varies with composition (which effectively alters the electron/atom ratio). There is also a lattice modulation of density related to the LPO. This, as well as the nonintegral values observed for M are interesting questions (Sato and Toth 1961) but unfortunately we cannot pursue them further here.

Another comment that needs to be made concerns the effective potential $V(r)$ in (17). Now an implicit assumption underlying (15) is that all ions always exactly occupy the lattice sites. In practice this is not so, and ions could deviate, *e.g.* on account of size. One must therefore allow for such 'positional relaxation', and evaluate the energy of the relaxed system. In effect, it amounts to modifying $V(k)$ as

$$V(k) \rightarrow V^{(1)}(k) = V(k) - \text{relaxation energy}. \tag{19}$$

Of course if the potential is parametrised, then the parameters refer actually to the effective potential $V^{(1)}$. For further details concerning the relaxation energy, a recent article by de Fontaine (1979) may be consulted.

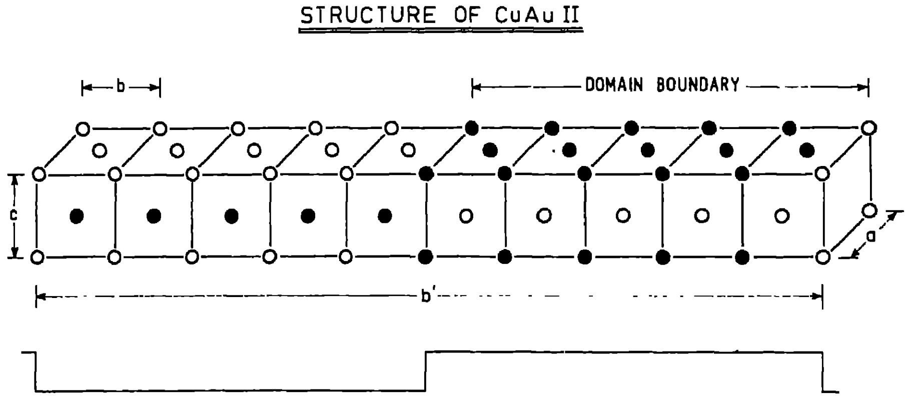

Figure 10. Illustration of the long-period oscillation in CuAu II. After every five cells, there is an alternation in the occupancy pattern (after Ogawa 1974).

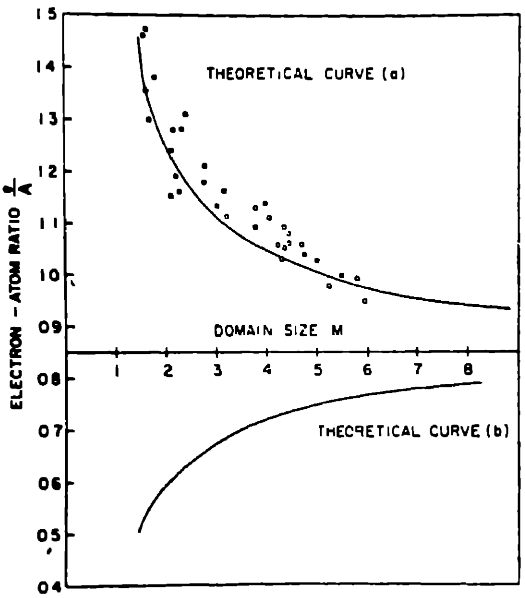

Figure 11. Variation of M with electron to atom ratio. The solid lines are theoretical curves (due to Sato and Toth 1961) corresponding to two assumptions (after Ogawa 1974).

3.2 *Calculation of phase diagrams*

The phase diagram problem is a logical extension of the ground state problem in that one now studies when order disappears.

It is convenient to discuss the problem in the language of Ising spins rather than in terms of the occupation operators σ introduced earlier. The Ising spin operator S_l associated to lattice site l is defined in terms of $\sigma_B(l)$ as

$$S_l = 1 - 2\sigma_B(l) = \begin{cases} +1 & \text{if site } l \text{ is occupied by an } A \text{ atom} \\ -1 & \text{if site } l \text{ is occupied by a } B \text{ atom.} \end{cases} \tag{20}$$

Observe that in terms of $\sigma_A(l)$,

$$S_l = 1 + 2\sigma_A(l). \tag{21}$$

Using the Ising spins to describe the Hamiltonian, the statistical mechanics of order-disorder can now be mapped into an appropriate Ising problem, establishing links with the rich traditions that already exist in this area.

Now at absolute zero of temperature, the spin system will be perfectly ordered. As the temperature is raised, some spins will flip (meaning A and B atoms will exchange places). Such flips no doubt cost energy but the entropy term $-\tau s$ in the expression for free energy provides the required compensation. However, the disorder cannot be increased indefinitely, and at every temperature there is an optimum disorder. If the disorder exceeds the optimum, then F increases due to increase of E whereas if it is less, then it again increases but due to inadequate cancellation from the entropy term. Equilibrium is thus dictated by the minimum of the free energy, and in the calculation of the phase boundaries, the computation of this minimum is an important step.

Given the range of interaction of the Ising spins, the calculation of E is straightforward (and is discussed further in § 3.3). Far more problematical is the entropy term, and to appreciate the difficulty let us consider a 1-D Ising chain. We assume first that the chain is fully ordered (!) with all spins up (say). The entropy is then zero. At the other extreme where each spin is completely free to flip, there are 2^N configurations possible (N is the number of spins), and the corresponding entropy is $S = k_B \log 2^N = Nk_B \log 2$. The question is how does one calculate the entropy for situations in between where there is intermediate order. If, for example, we *definitely* know two spins alone are down and all the rest up then the number of configurations possible is a simple matter to work out. But unfortunately, we cannot make definitive statements about exactly how many spins are up and how many are down. We can at best have only statistical information about the state of order embodied in the correlation functions

$$\xi_1 = \langle S_l \rangle; \quad \xi_2 = \langle S_l S_m \rangle; \quad \xi_3 = \langle S_l S_m S_n \rangle \ldots \tag{22}$$

The set $\{\xi_l\}$ must first be known and using it the entropy and indeed F itself must then be computed. Calculation of S in terms of the ξ's is precisely where problems enter, for one must in principle know and use all correlation functions up to ξ_N. This evidently is also the place for approximations to make their entry!

Before discussing the approximations, we call attention to Onsager's (1944) famous paper on the 2-D square lattice Ising problem where he calculated the partition function exactly. This is not only a *tour de force* but also a touchstone for evaluating various approximation schemes (as we shall soon see).

The approximation schemes alluded to, reduce in effect to using a suitable subset of the full set $\{\xi_l\}$ of the correlation functions. The subset is so chosen that the group of spins involved form a cluster which is consistent both with the geometry of the lattice and the range of interactions (usually restricted to near neighbours (*nn*) and next nearest neighbours (*nnn*)).

Figure 12 gives samples of some clusters used in the study of ordering in fcc Ising lattices. In figure 12a the cluster is a regular tetrahedron made up of *nn* spins. In figure 12b one has a *nn* regular tetrahedron and an octahedron consisting of *nn* and *nnn* spins. Within a cluster itself one can identify subclusters *e.g.* the triangle (123) in figure 12b, which is in the overlap of the tetrahedron and the octahedron. Likewise, the triangle (126) in figure 12c is a subcluster shared by two irregular tetrahedra.

The entire computational scheme based on cluster approximation is known as the cluster variation method (CVM). As formally developed by Morita (1972), it is based on the exact variational principle of equilibrium statistical mechanics. In any given implementation of the CVM, one first chooses the largest cluster L one is going to work with. One then considers all the subclusters l consistent with L. Corresponding to each subcluster l, one now considers the various possible arrangement of spins/atoms. For instance, the arrangement in the triangle (123) could be (AAA), (ABA), (BAB) etc. If J_l denotes a configuration such as above, then we next need to know $x_{J_l}(l)$ the concentration of this configuration in the cluster l. It is in the calculation of the cluster configuration that the correlation functions enter. To illustrate, we again consider the triangular subcluster (123). Let p_1, p_2 and p_3 denote the lattice sites. The correlation functions we then need are the single spin, two spin and three spin functions ξ_1, ξ_2, ξ_3

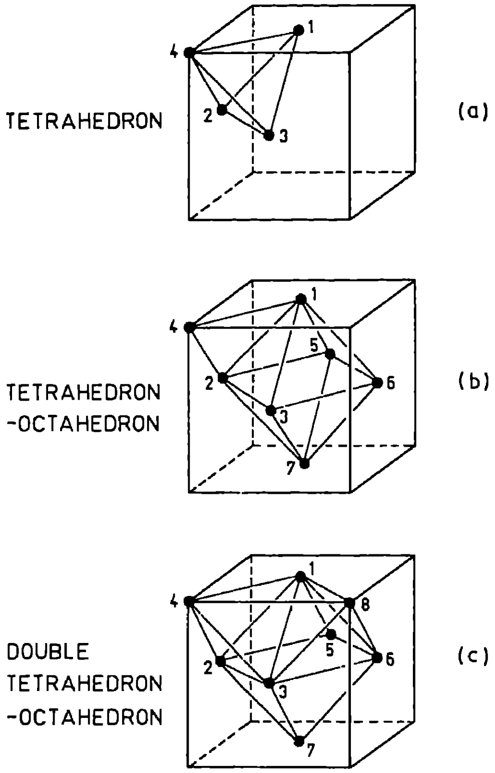

Figure 12. Some of the clusters used in CVM calculations for fcc lattices (a). tetrahedron used by Kikuchi *et al* 1980 (b) and (c) are larger clusters used by Sanchez and de Fontaine (1978, 1980, 1982).

respectively. In terms of these correlation functions, x_{AAB}, for example will be

$$x_{AAB} = \tfrac{1}{8}\{1 + (+1+1-1)\xi_1 + [(1\times 1) + (1\times -1) + (-1\times 1)]\xi_2 + (1\times 1\times -1)\xi_3\}. \tag{23}$$

The formal expressions for the cluster probabilities are:

$$\begin{aligned} x_i(p_1) &= \langle \sigma_i(p_1)\rangle = \tfrac{1}{2}\langle 1 + iS_{p_1}\rangle, \\ x_{ij}(p_1p_2) &= \langle \sigma_i(p_1)\sigma_j(p_2)\rangle \\ &= \frac{1}{2^2}[1 + i\langle S_{p_1}\rangle + j\langle S_{p_2}\rangle + ij\langle S_{p_1}S_{p_2}\rangle], \\ x_{ijk}(p_1p_2p_3) &= \langle \sigma_i(p_1)\sigma_j(p_2)\sigma_k(p_3)\rangle \\ &= \frac{1}{2^3}[1 + i\langle S_{p_1}\rangle + j\langle S_{p_2}\rangle + k\langle S_{p_3}\rangle + ij\langle S_{p_1}S_{p_2}\rangle \\ &\quad + jk\langle S_{p_2}S_{p_3}\rangle \\ &\quad + ki\langle S_{p_3}S_{p_1}\rangle + ijk\langle S_{p_1}S_{p_2}S_{p_3}\rangle]\text{etc.} \end{aligned} \tag{24}$$

Here $i, j, k \ldots$ take on values ± 1 for each of the two components in the system. (Result (23) thus readily follows from above).

The entropy can now be expressed as a series in cluster probabilities as

$$S \approx Nk_B \sum_{l=1}^{L} \gamma_l \sum_{J_l} x_{J_l}(l) \log x_{J_l}(l) \tag{25}$$

where γ_l is an appropriate coefficient (Barker 1953). Once the clusters have been identified and their concentrations or probabilities evaluated, the rest is largely numerical, and will be described shortly.

Historically, one of the early attempts at explaining the order-disorder transformations is due to Bragg and Williams (1934, 1935). Domb (1981) narrates an interesting story concerning these famous papers. Apparently, Bragg gave a seminar in 1933 in Manchester during which he qualitatively described his thoughts on how ordering occurred in binary alloys. Williams, a member of the audience, presented Bragg with a mathematical outline of Bragg's theory at the end of the lecture. (The story of the Rushbrook inequalities is similar! See Stanley 1971). Bragg was impressed but felt that the calculation was so simple, it surely must have been published earlier. However, no such paper had yet appeared and so Bragg and Williams proceeded to publish their ideas!

In the CVM language, the Bragg-Williams theory retains only ξ_1 or point clusters. Next comes the Bethe approximation (1935) which includes pairs *i.e.* also ξ_2. From these early beginnings, the push has always been towards larger clusters. Modern applications of the CVM have been promoted largely by de Fontaine and coworkers, building upon schemes originally developed by Kikuchi (1951), Barker (1953) and van Baal (1973). Before describing some of these recent results, we refer to figure 13 which gives a feel for the improvements available in going to larger clusters in 2-D square lattice, where Onsager's exact result is available as a bench mark.

Turning now to phase diagrams calculations for real alloys, the main steps in the calculational schemes as implemented at present are as follows (de Fontaine 1982):

(i) Choose the basic lattice system, the range of interactions and the largest cluster to be used. Form then the ξ's.

(ii) Construct the thermodynamic potential Ω (also called the grand potential) defined by

$$\Omega = F - \tfrac{1}{2}(\mu_A - \mu_B)\sum_l S_l \tag{26}$$

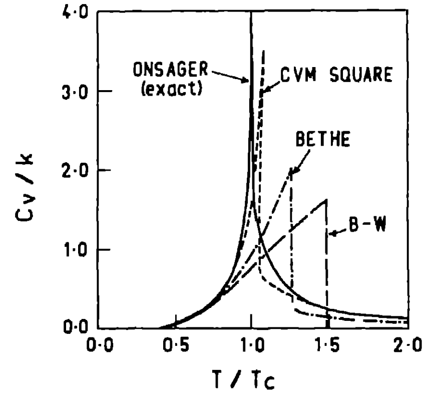

Figure 13. Specific heat variation for the square-Ising lattice. Onsager's result is the exact one. Observe the improvement in going from the Bragg-Williams approximation to the CVM square cluster approximation.

where the μ's are the chemical potentials of the two atomic species. The chemical potential term is required since we would like to permit concentration C_B to vary (while the total number of atoms is fixed).

(iii) For a fixed $(T, \mu \equiv 1/2(\mu_A - \mu_B))$, minimize Ω with respect to the ξ's considered *i.e.* the set of ξ's consistent with the largest cluster L chosen.

(iv) When Ω is minimized, it leads to a set of (nonlinear algebraic) equations for the ξ's. Solve these equations.

(v) Use the ξ's obtained in step (iv) to compute the equilibrium potential Ω_{eqbr}.

(vi) Plot Ω_{eqbr} *vs* T for fixed values of μ for the different phases. The point (T, μ) at which two curves cross is a point of phase coexistence. An example is given in figure 14.

(vii) Vary T and μ and establish the locus of phase coexistence *i.e.* the phase boundaries.

(viii) Every intersection between the Ω curves for two phases, α and β, say, gives two values of the point correlation function ξ_1. From these, determine the average concentrations c_B^α and c_B^β.

(ix) Assemble the results into phase diagrams in the (T, μ) and (T, c) planes.

Following Iliopoulos (1980), one might also add:

(x) Publish your result,

(xi) Choose another alloy system and GO TO (i)!

The CVM has been extensively applied by Kikuchi, de Fontaine and coworkers, from whose contributions we will now cite a few examples. Firstly in table 1 (de Fontaine 1979) we summarize some results obtained for Ising ferromagnets (which, incidentally, are isomorphous to AB binary solutions; recall earlier remarks about the correspondence between magnetic systems and alloy systems).

Next we consider results for ordering. Kikuchi *et al* (1980) have obtained the phase diagram for the Cu-Au system using *nn* interactions for the Ising spins, and a tetrahedron cluster. The calculated phase diagram is shown in figure 15b which is to be

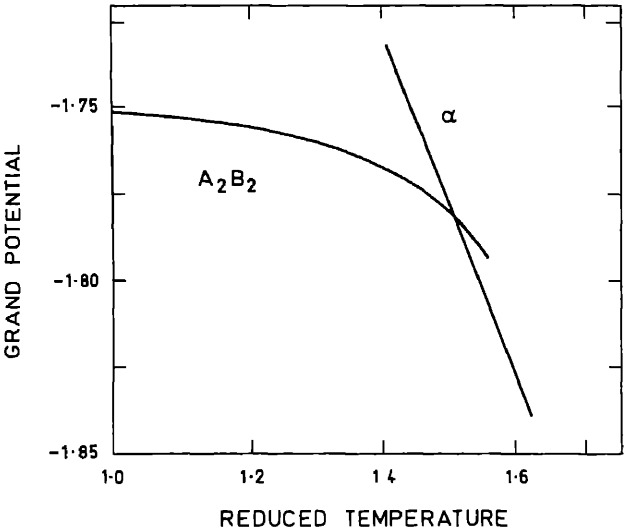

Figure 14. Variation of the grand potential with temperature for the A_2B_2 and disordered (α) phases, for zero chemical potential ($c_B = 0.5$). The intersection gives the temperature value at which the two phases coexist. (after de Fontaine 1982).
]

Table 1. Calculated normalized transition temperature in units of $k_B T/zJ$ where J is the strength of the nearest neighbour interactions and z the number of nearest neighbours (after de Fontaine 1979).

	2D Square lattice	2D Triangular lattice	3D Simple cubic	Remarks
z	4	6	6	
Bragg-Williams (point)	1·0	1·0	1·0	all refer to transition temperatures
CV Bethe (pair)	0·7212	0·8222	0·8222	
CV square or triangle	0·6057	0·62525	0·7683	
CV cube or tetrahedron	—	—	0·7628	
Exact (or best known)	0·567	0·6062	0·7522	

compared with the experimentally determined one (figure 15c) and that calculated by Shockley (1938) using the Bragg-Williams approximation (figure 15a). While those not used to phase diagrams may regard the agreement between CVM and experiment fair, the comparison is actually quite impressive given the approximations involved.

Sanchez and de Fontaine (1978) have gone beyond the tetrahedral approximation to the clusters illustrated in figure 12b and c, and investigated (Sanchez and de Fontaine 1980, 1982) the phase diagram for the $\langle 1\tfrac{1}{2}0 \rangle$ family of ordered superstructure *i.e.* lattices where ordering is associated with a $\langle 1\ \tfrac{1}{2}\ 0\rangle$ compositional wave. In addition to the usually considered *nn* interactions, the *nnn* interactions were also included. Results have been obtained for a range of values of the ratio of second-to-first-neighbour pair interactions in the range 0 to 0·5. The results are relevant for ordering in diverse systems like Ni-Mo, Ni-V etc. Incidentally, a knowledge of the ground state structure is very helpful in testing out a particular ordered state as in figure 14.

These calculations by de Fontaine and coworkers have shown the distinct superiority of the CVM over earlier models in yielding realistic results. For instance, in Cu-Au systems, the Bragg-Williams approximation predicts a first-order transition for Cu_3Au ($L1_2$ ordering) and a second-order transition for CuAuI ($L1_0$ ordering), whereas experimentally the transition is of first order for both the stoichiometric compositions. The Bethe approximation is even worse, and predicts no transition at all. The CVM does much better and predicts correctly a first order transition for both. The main advantage of the CVM is that reasonably accurate results are obtained without too much computational effort (—much of this has no doubt been due to the exercise of ingenuity in arriving at the practical computational scheme). In the results reported thus far, about 30 to 70 nonlinear algebraic equations had to be solved but it was not taxing. However, numerical difficulties were found at low temperatures where some of the cluster probabilities tended exponentially to zero. Where transition temperatures are concerned, the CVM does a respectable job, judging from the 3-D cubic Ising ferromagnet for which independent, reliable results are available from high-temperature expansion methods (table 1). But where exponents are concerned, CVM predicts only classical ones for higher-order transitions. This is not unexpected since the method is built around equilibrium correlation functions and does not include fluctuations. It is perhaps not out of place here to mention that Mahan and Claro (1977) have used the real-space renormalization-group approach to calculate a CuAu-type

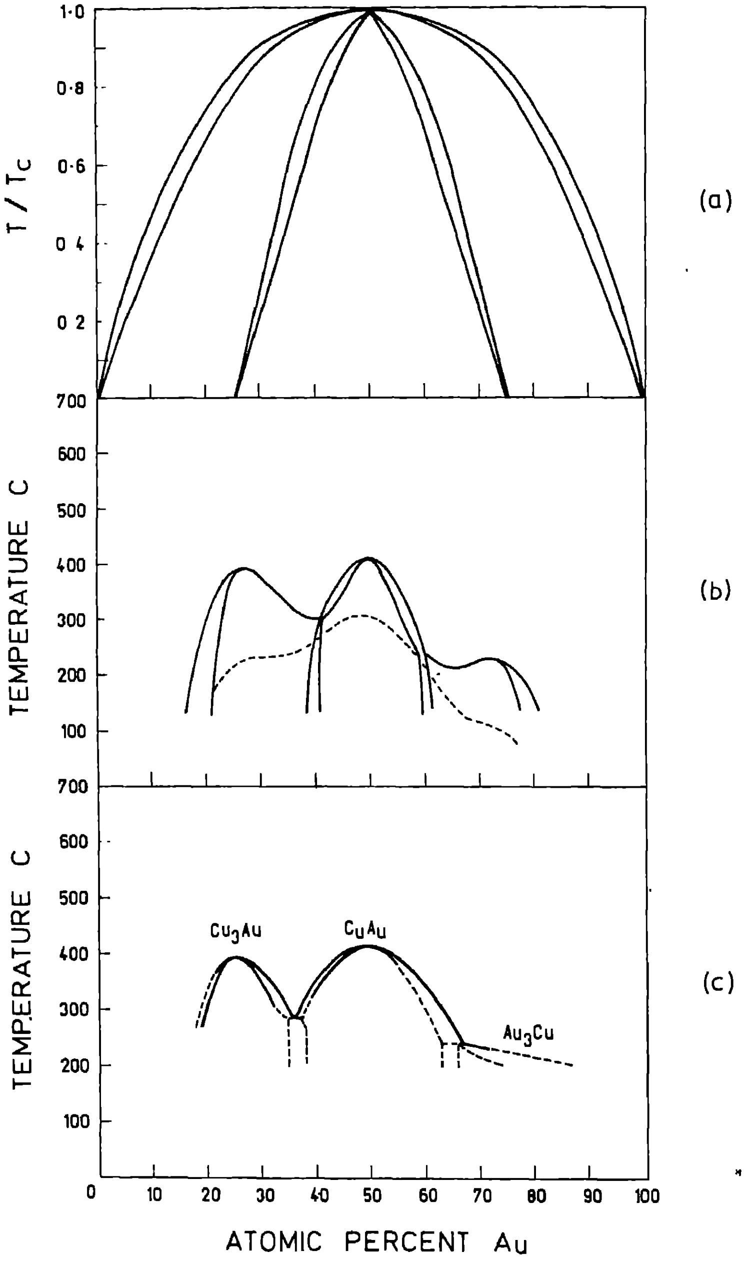

Figure 15. Phase diagram for the Cu-Au system (a). results obtained by Shockley (1938). (b). shows the CVM results of Kikuchi *et al* (1980). For comparison, the experimental results are given in (c) (Hansen 1958).

phase diagram. The results are however poor in that the ordering of CuAu ($L1_0$ ordering) is not predicted and the ordering of Cu_3Au ($L1_2$ ordering) is predicted to be of second order.

The stage is now set to consider a totally different approach to the calculation of phase diagrams *viz.*, that of computer simulation.

3.3 *Phase diagrams and computer simulation*

As in several other branches of physics, computer simulation has proved extremely useful in unveiling various subtle aspects relating to phase transformations. In this subsection, we review the work done in relation to phase diagrams while in a later section, we shall touch upon studies in kinetics.

The basic idea is to start with a representative Hamiltonian that describes configuration interactions, and then use a Monte Carlo technique to deduce the structure appropriate to specific thermodynamic conditions. Since the problem is formulated in the Ising-spin language, there are understandable links with many magnetic problems.

To obtain the desired Hamiltonian, we go back to (11), the expression for internal energy. Adding to it a chemical potential term $(\mu_A-\mu_B)\sum_l \sigma_B(l)$ as earlier, we have

$$\mathscr{H} = \frac{1}{2}\sum_{ij}\sum_{l\neq m} v_{ij}(l-m)\langle\sigma_i(l)\sigma_j(m)\rangle + (\mu_A-\mu_B)\sum_l \sigma_B(l). \qquad (27)$$

Introducing Ising spins as in (20), the Hamiltonian in (27) can now be transformed (barring a constant term) as

$$\mathscr{H} = \sum_{l\neq m} J_{lm} S_l S_m - H\sum_l S_l, \qquad (28)$$

where

$$J_{lm} = -\{v_{AA}(l-m)+v_{BB}(l-m)-2v_{AB}(l-m)\}/4, \qquad (29)$$

is the exchange integral for Ising spins, and

$$H = \frac{1}{2}\sum_{m(\neq l)}\{v_{AA}(l-m)-v_{BB}(l-m)\} + \frac{1}{2}(\mu_A-\mu_B), \qquad (30)$$

is an 'external' field acting on the Ising spins.

As it stands, the spin at site l interacts with spins at all other sites m in the lattice. To make the problem tractable, one restricts, as earlier, the range to the nearest and next nearest neighbours so that $\mathscr{H}$ now is given by

$$\mathscr{H} = -J\sum_{(nn)} S_l S_j + \alpha J\sum_{(nnn)} S_i S_j - H\sum_i S_i. \qquad (31)$$

The parameter $(-\alpha)$ is a measure of the relative strength of the *nnn* interaction.

One now takes a system of $N = 4L^3$ spins on a fcc lattice with periodic boundary conditions. In the actual simulation, N was ~ 15000. Next one specifies an initial configuration $X_0 = \{S_1, S_2, \ldots, S_N\}$, the choice of which will be discussed shortly. Using pseudo random numbers, one then generates a random change of configuration $X_0 \rightarrow X_1$. There are two ways of achieving this, depending on what ensemble one works with. If one is using a canonical ensemble, then the total 'up' spin as well as the total 'down' spin must be individually conserved. Hence $X_0 \rightarrow X_1$ is achieved by choosing at random a nearest neighbour AB pair and exchanging spins. This 'Kawasaki dynamics' (Kawasaki 1972) conserves the concentration c_B of the system. In the case of the grand canonical ensemble, the magnetic field is held constant and $X_0 \rightarrow X_1$ is implemented *via* the flip $S_i \rightarrow -S_i$ of a randomly chosen spin. These spin fluctuations are equivalent to fluctuations of c_B. As is well-known, both ensembles should yield results equivalent to each other in the thermodynamic limit $N \to \infty$. Working with finite N as in simulation experiments, it is important to verify that the results do not depend on the ensemble chosen. Having produced a change $X_0 \to X_1$, one now computes (in both cases) the energy change $\delta U = \mathscr{H}(X_1) - \mathscr{H}(X_0)$ resulting from the configurational change. The transition probability for such a change is

$$W = \exp(-\delta U/k_B T)/\{1 + \exp(-\delta U/k_B T)\}, \tag{32}$$

which is compared to a random number η chosen uniformly from the interval (0, 1). If $W > \eta$, the transition is performed; otherwise the old configuration is counted once more for the averaging, the attempted X_1 is rejected, and another transition is tried. The Monte Carlo steps (MCS) are repeated till an equilibrium distribution is obtained. To achieve convergence within a few thousand MCS, it is necessary to choose the initial state X_0 appropriately.

Two groups, namely that of Lebowitz and of Binder have been active in studying phase diagrams by simulation. Recently they merged their efforts to make a detailed study of a system that is a prototype for Cu-Au alloys (Binder *et al* 1981). Since this is the most comprehensive study to date, we shall present some results from it.

In this work, nearest neighbour interactions alone were considered *i.e.* α was set equal to zero. The initial state was variously chosen as ferromagnetically ordered state, a disordered state or an antiferromagnetic state, as appropriate. Runs using the canonical ensemble were done at various fixed compositions c_B, and for each composition, runs were taken at several temperatures (actually at several values of $k_B T/|J|$). The grand canonical ensemble runs were done for various fields corresponding to a fixed temperature, and the temperature was subsequently varied. The quantities monitored were, (i) the internal energy, (ii) the net magnetization m and (iii) the order parameter $\tilde{m}$. In terms of the sublattice magnetization m_ν ($\nu = 1,2,3,4$) defined by

$$m_\nu = (1/N)\sum_{i} \langle S_{i,\nu} \rangle, \tag{33}$$

over νth sublattice

m is given by

$$m = m_1 + m_2 + m_3 + m_4, \tag{34}$$

while $\tilde{m}$ is given by

$$\begin{aligned} \tilde{m} &= m_1 + m_2 - m_3 - m_4 \qquad (AB \text{ structure}) \\ &= m_1 + m_2 + m_3 - m_4 \qquad (A_3B \text{ structure}). \end{aligned} \tag{35}$$

Figure 16 shows a plot of magnetization as a function of the applied field. When H is zero, there is no magnetization. As H is increased, m also increases, and the increase would have been linear (dashed line) if the system were disordered. Instead, the m value stays below the dashed line indicative of order until a field H'_{C_1} is reached when it jumps. H'_{C_1} is thus a critical field required to derive the system to disorder. Order sets in again at H_{C_2}'' and disappears at H_{C_2}. The order parameter variations are also shown in figure 16, from which the field-induced transitions (at a fixed temperature) are clearly evident.

Figure 16 is what is termed 'raw data' by Binder *et al* (1981). For several such data, the phase diagram of the Ising antiferromagnet was constructed as in figure 17. Noting that $\sigma_B(l) = (1 - S_l)/2$, the average concentration C_B of B atoms in the alloy is related to m by $C_B = (1 - m)/2$. Therefore, the diagram of figure 17b which is the phase diagram

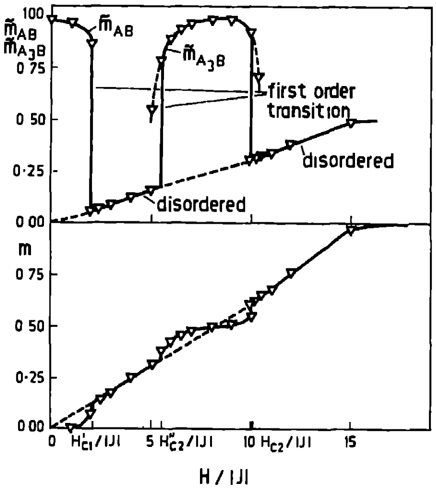

Figure 16. Order parameter (top) and magnetization (bottom) for the nearest neighbour Ising antiferromagnet plotted as a function of the field for the temperature $T_{k_B}/|J| = 1{\cdot}5$. Estimates for the three critical fields H'_{C_1} H''_{C_2} and H_{C_2} are also indicated. (after Binder *et al* 1981).

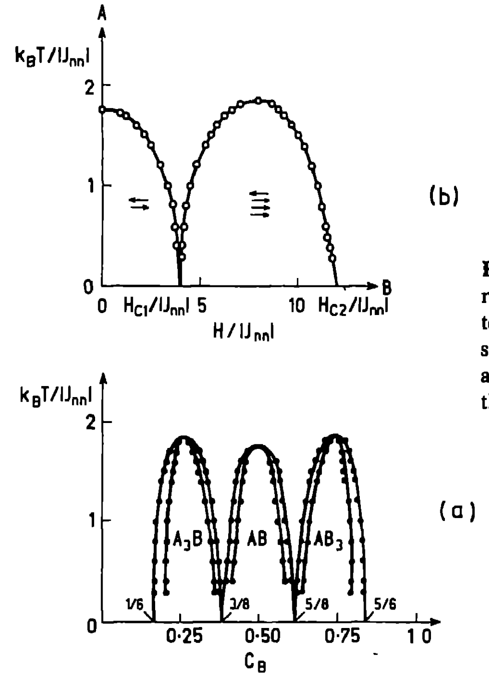

Figure 17. (**a**) Phase diagram of the nearest neighbour fcc lattice in the temperature-composition plane. Ordered structures are indicated. All transitions are of first order. (**b**) Phase diagram in the temperature-field plane.

for an Ising antiferromagnet in a magnetic field can be mapped to the temperature-composition plane as in figure 17a to yield a phase diagram appropriate to the alloy *AB*. The two-phase regions shown here arise from the fact that for certain values of the field, *m* is multivalued.

Recently, Binder (1981) has extended the above work to include *nnn* interactions also. The phase diagram is now considerably altered (see figure 18), a noteworthy feature being the occurrence of a multicritical point at $H = 0$. This is an interesting finding in view of a recent theoretical prediction that such a point arises out of a meeting of lines of 3- and 4-state Potts model-like transitions.

Returning to the implications for the alloy problem, the broad finding is that simulation corroborates CVM results as is explicitly brought out in figure 19. At stoichiometric compositions, the two methods come fairly close to each other. This has also been noted from limited simulations done for $\alpha = 0{\cdot}25$. The feeling therefore is that stoichiometric alloys are rather insensitive to the parameters of the model as well as the accuracy of the approximations used. Study of off-stoichiometric systems (both experimentally and theoretically) may be more worthwhile. In this context, Binder (1980a) has proposed that one could, for example, explore short-range order as a function of composition (see figure 20). Measurements of this type would provide a valuable test of whether a model faithfully represents a real system. Another useful hint to emerge from these studies is that the interaction parameters are probably composition dependent. In other words, the same exchange integral $J(r)$ cannot be used over the entire composition range. The possibility of 'frustration' is yet another interesting finding. To understand this, we refer to figure 21 which shows two neighbouring cells of the A_3B structure. Focussing attention on the spin at the centre of the common plane, it is found that four of its bonds to *nn* are energetically favourable while the other eight are unfavourable. Therefore at the critical field H'_{c_1}, this spin can be overturned at no cost. One has essentially a 'frustration-type' of situation here since the central spin is under conflicting orders. Binder *et al* (1981) therefore advocate improvements to theoretical methods so as to handle frustration.

As of now, the computer simulation method has some limitations. Being time consuming, it cannot be applied for wide ranging explorations as, for example, the CVM. Also the treatment of the configurational entropy is crude. However, there is no doubt that valuable insight has been gained from whatever has been done so far. And it is also

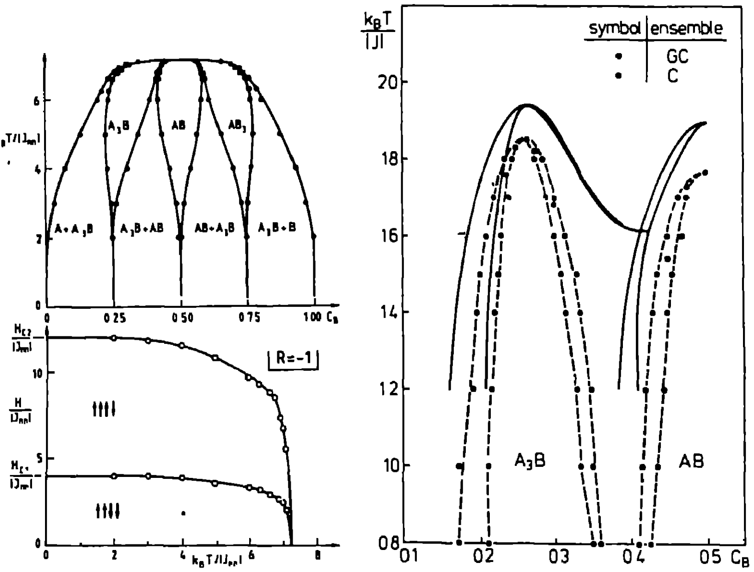

Figures 18–19. **18.** (Left) Phase diagram of the next nearest neighbour Ising antiferromagnet in the T-field and T-composition planes. Observe that the simulated diagram is still far from experiment. (after Binder 1981). **19.** (Right) Comparison of the phase diagram for the fcc binary alloy as obtained by simulation and the CVM results (after Binder *et al* 1981).

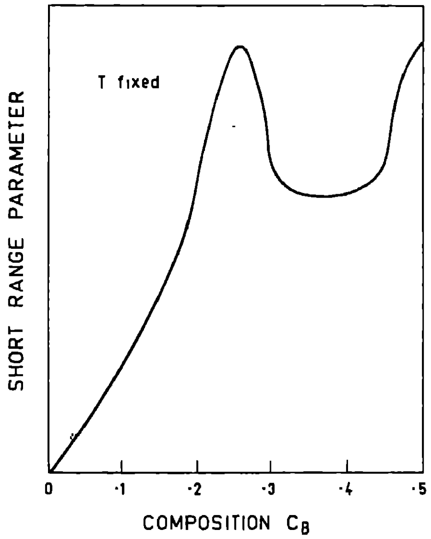

Figure 20. Schematic plot of the variation of the (Cowley) short-range order parameter as a function of concentration. The temperature is fixed, and below T_c. The sharp variations are related to the crossings of the phase boundaries. See also figure 45 (after Binder 1980a).

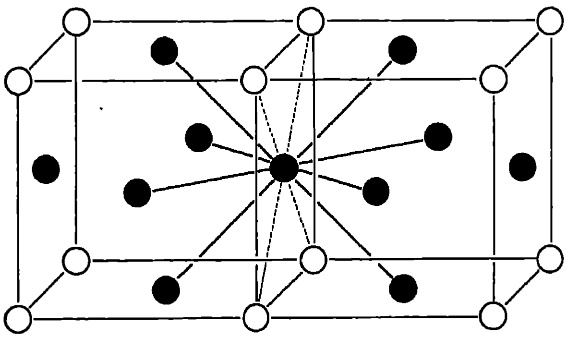

Figure 21. Illustration of the concept of a 'spin' under conflicting orders and thereby becoming 'loose' at the critical field. For explanations, see text. According to Binder *et al* (1981) such a 'conflict' leads to a frustration-type of situation as in spin glass (after Binder *et al* 1981).

clear that simulation will always be required both to complement as well as to continually spur experiment and theory.

4. Kinetic phenomena

We turn our attention now to phenomena that occur when one either approaches a phase boundary or crosses it. As is to be expected, there will be manifestations of critical phenomena in the neighbourhood of a transition across the boundary, and such critical effects have indeed been observed even in the twenties. For instance, Johansson and Linde (1928) found that the electrical resistivity of Cu_3Au rose sharply with increasing temperature around 390°C, the transformation temperature. One could therefore envisage extensive studies on critical exponents related to the vast variety of transformations possible. It is however unlikely that such studies while *very useful* will reveal anything fundamentally *new* concerning the *basic universalities* under lying critical phenomena since the cream has in a sense already been skimmed off. Far more interesting is the study of dynamic phenomena following a quench as it raises questions in nonequilibrium statistical mechanics, currently an active area.

In systems such as we are interested in, quenching (notionally) causes a step function change of temperature. However, although the phonons have readjusted, the atoms are unable to follow suit and occupy their new equilibrium positions with such rapidity. Positional readjustments involve large scale migration of atoms through diffusive processes, necessarily requiring some time. Thus, immediately after a quench, the system is left in a highly non-equilibrium state. It then coasts down (with the atoms readjusting their positions), eventually attaining equilibrium. Studies made during the coastdown can shed valuable light on the behaviour of systems far from equilibrium. The attendant nonlinearities make such investigations even more interesting.

In this Section, we shall review progress in the understanding of such kinetic phenomena and also indicate questions that still await solutions.

4.1 *Linear kinetics*

The broad question one faces is: What exactly happens after a quench? There is no simple universal answer to such a question for much depends on whether one is considering the early- or the late-stage behaviour, whether it is a clustering or an ordering system, etc. We shall deal with some of these complications as we go along. For the present we will offer a qualitative picture assuming the system responds linearly to the forces set up following the quench (—a bad assumption!).

Let c_B be the average concentration of the B species and $c(r,t)$ the distribution (of the B species) in the quenched alloy. It is convenient to consider $c(k,t)$ the Fourier transform of the composition fluctuation $[c(r,t)-c_B]$. $c(k,t)$ thus represents a compositional wave of wavevector k. If the system behaves linearly, then each Fourier component has an evolution history that is completely delinked from those of the others. The task now reduces to formulating an equation of motion for $c(k,t)$ and solving it. Thanks to the linearity assumption, one has (Cahn 1961, 1968)

$$c(k,t) \sim \exp[\alpha(k)t], \tag{36}$$

where $\alpha(k)$ depends on the forces acting in the quenched system. If α is negative, the fluctuations decay but if α is positive the fluctuations grow, in fact indefinitely, indicative of an instability in the system. The question therefore is: How does $\alpha(k)$ behave as a function of k, and, in particular, is it positive for certain values of k? The latter would depend of course on the instabilities.

Figure 22 shows some schematic plots of α both above and below the transition temperature for a clustering as well as an ordering system (Cook *et al* 1969). We notice that α becomes positive only below the transition temperature. Only then do certain fluctuations grow to giant proportions, driving the system to a totally new state altogether. For a clustering system α becomes positive near the zone centre, whereas for an ordering system it becomes positive in the neighbourhood of the superlattice position associated with the ordering process.

Now fluctuations cannot really grow in an unbounded manner, and such growth is in fact arrested by nonlinearities. Another way of saying this is that the different Fourier

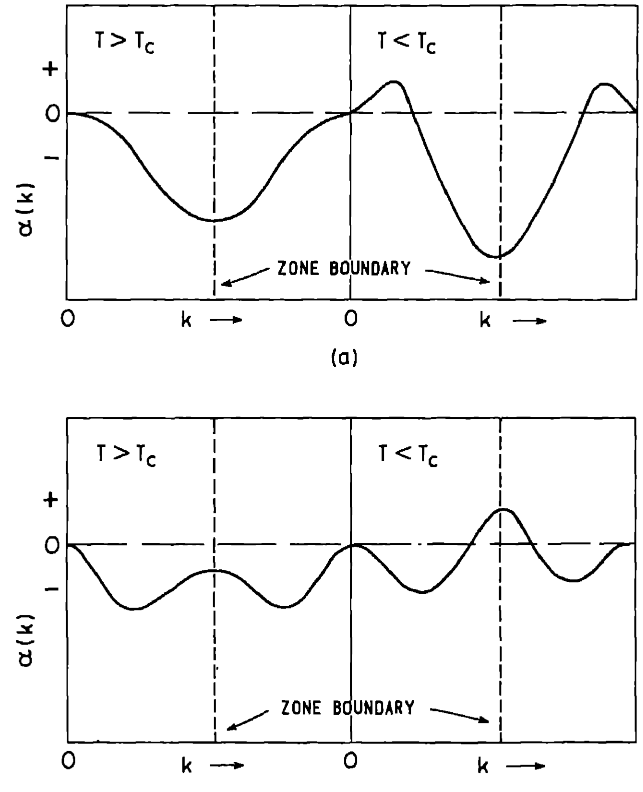

(a)

(b)

Figure 22. Schematic plot of α above and below the transition temperature T_c (a). situation for a clustering reaction, where α becomes positive below T_c around $k = 0$. In an ordering reaction on the other hand, α becomes positive in the region of the superlattice reflection. The region where α becomes positive is related to the region where $V(k)$ has a minimum (after Cook *et al* 1969).

components start interacting with each other, checking runaway growth. While the concept of a 'linear' amplification factor $\alpha(k)$ does become blurred to some extent in the presence of non-linearities, it certainly is meaningful in the disordered region at least.

Some interesting experiments on 'disordering kinetics' have been performed to obtain plots of $\alpha(k)$ and they are worth a brief mention (Paulson and Hilliard 1977). In these experiments, a multilayer film several thousand Angstroms thick was prepared by alternately depositing two elements (*e.g* Cu and Au) in the desired proportions. The as-deposited composition modulation produces satellite peaks in an x-ray diffraction pattern. One now upquenches the specimen, taking it into the one-phase region. The modulation then progressively disappears due to the interdiffusion of the atomic species. By monitoring the time-dependence of the intensity of the satellite peak, $\alpha(k)$ can be obtained. The wavelength of the modulation can be varied by controlling the deposition, and in this way $\alpha(k)$ can be studied as a function of k. A typical plot so obtained is shown in figure 23. We shall return again to the amplification factor for clustering systems in § 4.3.

Linear theories essentially provide first-order answers. They are reasonably adequate

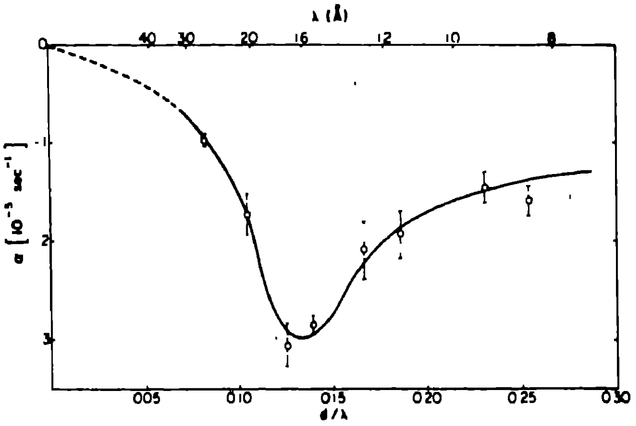

Figure 23. Amplification rates α *vs* λ observed at 225°C in thin films of Cu-16 at % Au (after Paulson and Hilliard 1977).

in the disordered region where *all* fluctuations decay, and one does not encounter runaway situations. However, such theories are inadequate as one approaches the critical region; and in the ordered region, they totally fail to describe the kinetics.

4.2 *Beyond linear theories*

For answers beyond linear theories one should look to nonequilibrium statistical mechanics, and presently we shall consider some general aspects. To provide a framework for the discussion, we shall suppose the free energy density f to be given by

$$f(x; a, b) = \tfrac{1}{2} a x^2 + \tfrac{1}{4} x^4 + b x. \tag{37}$$

This is the Ginzburg-Landau form, together with a magnetic field term bx. The quantities a and b are the control parameters while x is the order parameter. Our f here is equivalent to the grand potential discussed in § 3.

Our first interest is in the minima of f, and the locus traced by them as a and b are varied. In the language of catastrophe theory (Gilmore 1981), the minima are the critical points of f. The various critical points of f are obtained as follows:

$$\begin{array}{lll} \text{nondegenerate crit. pt.} & (\mathrm{d}f/\mathrm{d}x) = 0 \ \textit{i.e.}\ x^3 + ax + b & = 0 \\ \text{two-fold degenerate} & & \\ \text{crit. pt.} & (\mathrm{d}^2 f/\mathrm{d}x^2) = 0 \ \textit{i.e}\ 3x^2 + a & = 0 \\ \text{three-fold degenerate} & & \\ \text{crit. pt.} & (\mathrm{d}^3 f/\mathrm{d}x^3) = 0 \ \textit{i.e}\ 6x & = 0. \end{array} \tag{38}$$

It is easily seen from above that the locus of the doubly degenerate critical points is given by (Gilmore 1981)

$$(a/3)^3 + (b/2)^2 = 0. \tag{39}$$

This 'fold curve' also called the separatrix is sketched in figure 24, and it divides the parameter space into two regions representing functions with one critical point and functions with three critical points. This feature is made explicit with representative

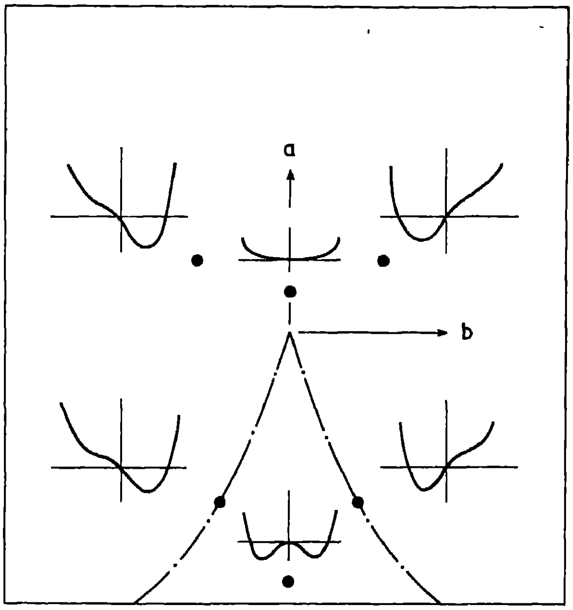

Figure 24. Sketch of the fold curve for f given by (37). Also shown are representative plots of f *vs* x for the various points in the (a, b) plane indicated by dots (after Gilmore 1981).

plots for f corresponding to various points in the a-b plane. The origin represents the function $f = (x^4/4)$, and corresponds to a three-fold degenerate critical point.

It is helpful also to have some idea of certain surfaces associated with f (Gilmore 1981; Kikuchi and de Fontaine 1976). These are (i) the critical manifold defined by $(\mathrm{d}f/\mathrm{d}x) = 0$, (ii) the critical value surface f_c made up by the values assumed by f when $\nabla f = 0$ and (iii) the critical curvature surface defined by $(\mathrm{d}^2f/\mathrm{d}x^2) = 0$. Sketches of these surfaces are given in figure 25, and they aid the analysis of system behaviour following a disturbance to the system. Thus, for instance, the critical curvature surface is useful while discussing the stability of the system.

In nonequilibrium phenomena, the state of the system is governed by f which often changes for one reason or the other. In this changing situation, the system attempts to find a minimum appropriate to the prevailing conditions but when several minima are available, the question naturally arises regarding which minimum the system jumps to. Two extremes are possible as illustrated in figure 26. In figure 26a the system remains in a stable or metastable equilibrium state until that state disappears whereas in figure 26b the system always chooses the global minimum. Between these two limiting conventions, many other possibilities exist. Which of these conventions operate in a given situation depends on the relative values of the barrier height ΔE and the noise level N. If $N/\Delta E \ll 1$, then the delay convention is observed while if $N/\Delta E \gg 1$ the Maxwell convention operates (figure 27).

Another way of looking at a system evolution is *via* the probability distribution function $P(x, t)$. Figure 28a shows a schematic plot of $f(x)$ at some instant of time while figure 28b depicts $P(x, t)$ for that same instant. Notice P peaks away from the minimum, typical of a nonequilibrium situation. As time evolves, $P(x, t)$ will seek to attain a form appropriate to equilibrium. There are two characteristic times T_1 and T_2 associated with

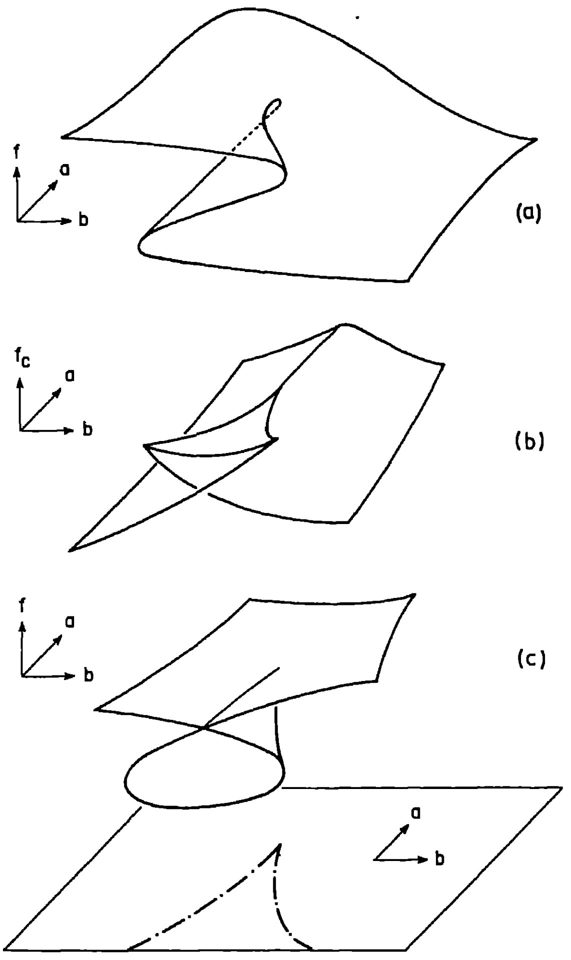

Figure 25. Schematic plots of various critical surfaces associated with the f of (37) (a). surface defined by $\nabla f = 0$. (b). critical value surface f_c which, for a given (a, b) gives the f value corresponding to the condition $\nabla f = 0$. The critical curvature surface $f'' = 0$ is sketched in (c). This is useful for discussing instabilities. At the bottom is projected the fold curve. The relationship of the latter to the various surfaces sketched above it should be clear (after Gilmore 1981).

this approach to equilibrium. Of these, T_1 is the time for relaxation to a local minimum and T_2 from a metastable minimum to a global minimum (see figure 28d). In transiting from a local minimum to a global minimum the system essentially drifts (in x space). Relaxation to a local minimum on the other hand is like a diffusive process.

The regime of the two conventions can also be spelt out in terms of T_1 and T_2. If $C = \{a, b, \dots\}$ denotes the set of control parameters, then the delay convention operates if (Gilmore 1981)

$$T_1^{-1} \gg (\mathrm{d}C/\mathrm{d}t) \gg T_2^{-1}, \tag{40a}$$

while the Maxwell convention operates if

$$T_2^{-1} \gg (\mathrm{d}C/\mathrm{d}t). \tag{40b}$$

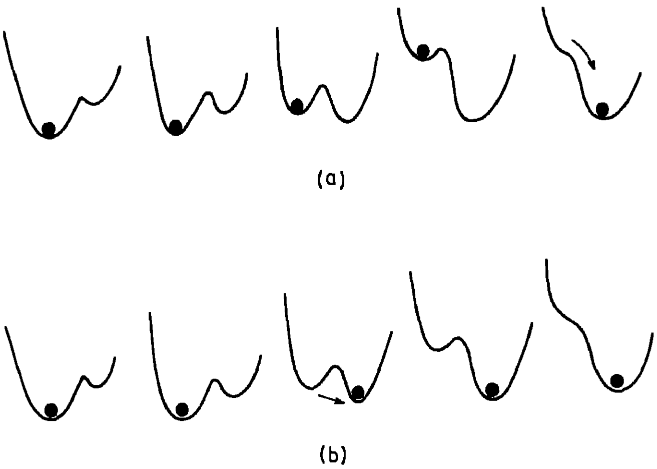

Figure 26. Illustration of the two conventions adopted for discussing change of state under nonequilibrium conditions. (**a**). Delay convention—the system remains in a stable or metastable state until that state disappears, (**b**). Maxwell convention—the system always chooses the global minimum (after Gilmore 1981).

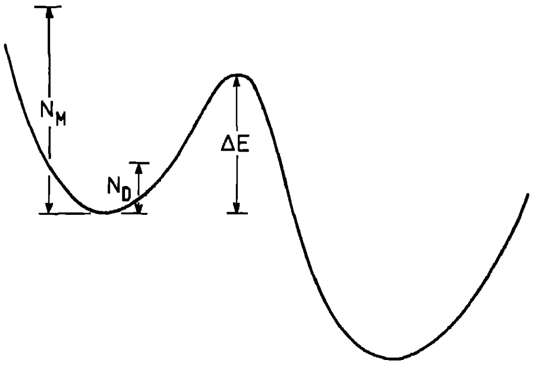

Figure 27. Illustration of the conditions under which the delay and Maxwell conventions are applicable.

To see the link between these two conventions and the topography of the critical manifold, we present in figure 29 the projections of the critical manifold on the (a, b) as well as the (a, x) plane. When the Maxwell convention is adopted, the critical manifold is a "soldered manifold" because the portions of the manifold $\nabla f = 0$ describing unstable critical points and metastable minima have been removed and replaced by a flat piece which interpolates between the two mimima. Later in § 4.3 when we consider phase separation, we will recognize the projections of the two manifolds on the (a, x) plane as the coexistence line and the spinodal respectively. The projections on the (a, b) plane are of special interest in a ferromagnet where one has the practical possibility of varying the magnetic field and inducing a phase transition. It is illuminating to follow the transitions (especially under nonequilibrium conditions), as trajectories on the critical manifold (see Gilmore (1981) for examples and details).

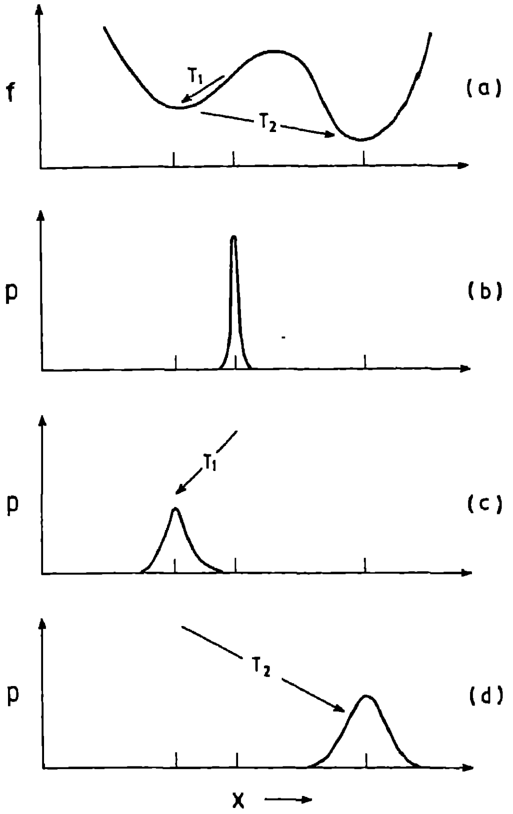

Figure 28. Description of the system evolution in terms of the probability distribution function $P(x;t)$. (a) and (b) depict $f(x)$ and $P(x,t)$ at some instant t, say (after Gilmore 1981).

The quantitative aspects of the approach to equilibrium revolve almost entirely around the probability distribution function $P(x,t)$. A quench, for example, creates a certain $P(x,0)$. The system not being in equilibrium, P will naturally evolve approaching that appropriate to equilibrium. The questions in this context are: What is the equation that governs the evolution of P, how does one solve this question, and how does one use this knowledge of P to make predictions pertinent to specific experiments?

The evolution of P is governed by the well-known Fokker-Planck equation

$$\frac{\partial P}{\partial t} = -\frac{\mathrm{d}}{\mathrm{d}x}[K(x)P] + \frac{1}{2}D\frac{\mathrm{d}^2 P}{\mathrm{d}x^2}, \tag{41}$$

here D is the diffusion coefficient and $K(x)$ a drift force. In many problems, this drift force can be expressed as the gradient of a potential *i.e.*

$$K(x) = -[\mathrm{d}V(x)/\mathrm{d}x]. \tag{42}$$

In our problems, $K(x)$ will be related to the free energy.

The derivation of the Fokker-Planck equation from the more fundamental Master equation is too involved a question to be discussed here but fortunately good treatments are available in literature (—see, for example, Haken 1978; for a discussion

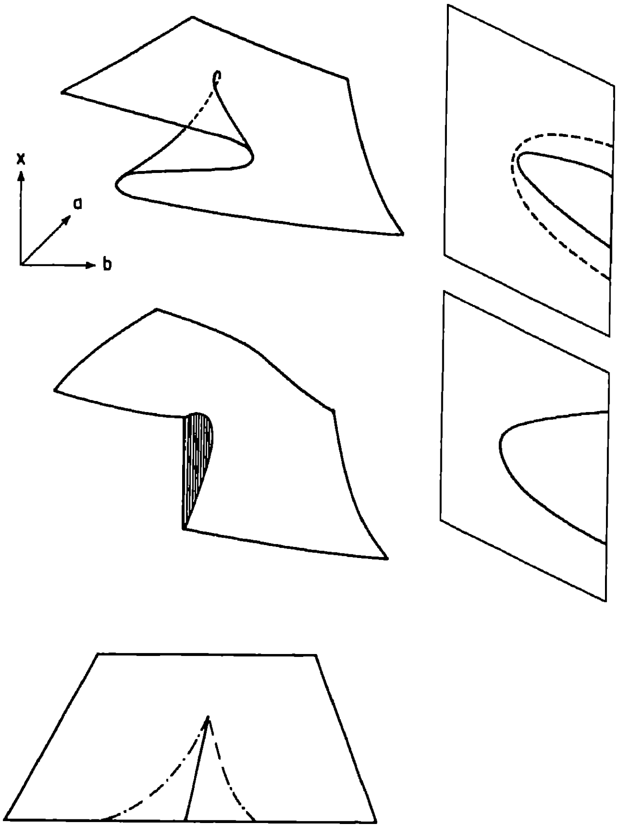

Figure 29. Projections of the critical manifold ($\nabla f = 0$) on the (a, b) and (a, x) planes.

vis-a-vis problems of materials science, see Venkataraman and Balakrishnan 1977; Venkataraman 1982).

The Fokker-Planck equation is sometimes written as a continuity equation i.e. as

$$\overset{\circ}{P} + \frac{\mathrm{d}}{\mathrm{d}x} j = 0, \tag{43}$$

where j the probability current is given by

$$j = \left[K(x)\, P - \frac{1}{2} D \frac{\mathrm{d}P}{\mathrm{d}x} \right]. \tag{44}$$

In equilibrium statistical mechanics, one is interested in the stationary solutions of the Fokker-Planck equation; but in our kind of situations, it is the time-dependent solution that is of interest. In general, finding exact solutions is not possible, and one must resort to a suitable approximation scheme. A very readable account of these problems is available in the book of Haken (1978). Figure 30 shows a schematic plot of the evolution of P in a typical problem. Starting off as a δ-function, P drifts (which gives rise to the dotted line trajectory) and it also broadens (due to diffusion).

The probability density function we need for discussing clustering etc is somewhat

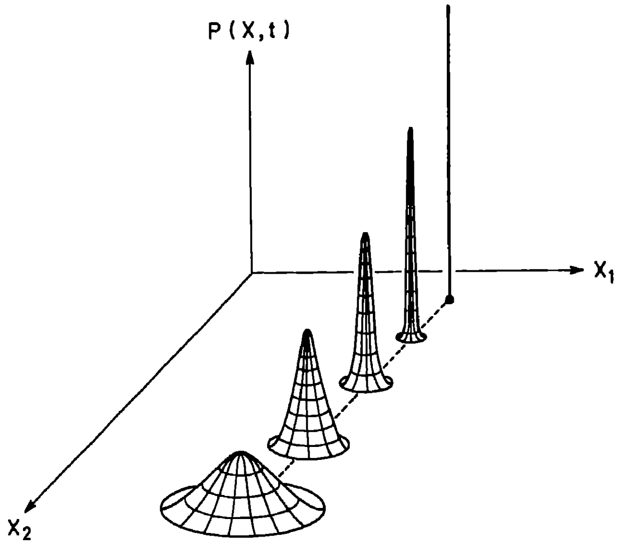

Figure 30. The concept of time evolution of $P(x,t)$ is discussed in this figure. For convenience x is assumed to be two dimensional and it is supposed that at $t = 0$, P starts off as a δ-function. With the passage of time, the state of the system *drifts* in x-space as indicated by the dotted trajectory. Simultaneously, due to fluctuations, the distribution function also broadens.

more general, being a functional of the form $P(\{\psi\},t)$. Here

$$\{\psi\} = (\psi_1, \psi_2, \ldots, \psi_n), \tag{45}$$

with ψ_r being the coarse-grained value of the order parameter ψ in the rth cell. *i.e*

$$\psi_r = \frac{1}{n_r}\sum_{l\in\text{cell}\,r} \psi(l) \tag{46}$$

There are n_r lattice sites l in cell r and there are n cells in all. $\{\psi\}$ comprehensively describes the state of the system.

Like $P(x,t)$ which we considered earlier, $P(\{\psi\},t)$ is also conserved. In the continuum limit (where sums over coarse-grained cells are replaced by integrals), the continuity equation is given by

$$\frac{\partial}{\partial t}P(\{\psi\},t) = -\int \mathrm{d}\mathbf{r}\,\frac{\delta J_r}{\delta\psi(\mathbf{r})}, \tag{47}$$

where J_r is the probability current, and δ signifies a functional differentiation.

The expression for J_r depends on whether the order parameter is conserved or not. The latter quantity is said to be conserved if the change $\psi_r \to \psi_r + \varepsilon$ in the cell r is accompanied by a compensating change $\psi_s \to \psi_s - \varepsilon$ in a neighbouring cell s. In clustering reactions, the order parameter is composition which obviously is conserved. On the other hand, in ordering reactions the order parameter is *not* conserved (—recall the examples of ferro- and antiferro magnets). Bearing these two possibilities in mind, the expression for J_r can be written as (Billotet and Binder 1979)

$$J_r(\{\psi\},t) = -C\left[\frac{\delta F\{\psi\}}{\delta\psi(\mathbf{r})}P(\{\psi\},t) + k_B T\frac{\delta P(\{\psi\},t)}{\delta\psi(\mathbf{r})}\right], \tag{48}$$

where $F\{\psi\}$ is the (coarse-grained) free energy functional. If the order parameter is conserved, then $C = -M\nabla_r^2$ where M is the mobility*, whereas if the order parameter is not conserved then C is simply a rate factor fixing the time scale.

Equations (47) and (48) are too formal and complex for practical use, and watered down versions are necessary. A common practice is to use the above equations to construct equations of motion for various moments of P. A few illustrative examples follow.

Consider the clustering problem, and let $c(\mathbf{r})$ denote the local concentration of B atoms. This is the order parameter, and being conserved

$$J_r(\{c(\mathbf{r})\}, t) = -M\nabla^2\left[\frac{\delta F\{c(\mathbf{r})\}}{\delta c(\mathbf{r})}P + k_BT\frac{\delta P(\{c(\mathbf{r})\}, t)}{\delta c(\mathbf{r})}\right]. \tag{49}$$

Multiplying both sides of (47) by $c(\mathbf{r})$ and integrating we get

$$\int \delta\{c(\mathbf{r})\}\, c(\mathbf{r})\frac{\partial}{\partial t}P(\{c(\mathbf{r})\}, t) = -\int \delta\{c(\mathbf{r})\}\int \mathrm{d}\mathbf{r}' \times \frac{\delta J}{\delta c(\mathbf{r}')}c(\mathbf{r}). \tag{50}$$

After simplifications, this gives the *average* equation

$$\frac{\partial}{\partial t}\langle c(\mathbf{r})\rangle = -M\nabla^2\left\langle\frac{\delta F}{\delta c(\mathbf{r})}\right\rangle. \tag{51}$$

(M is assumed to be a constant *i.e* independent of $c(\mathbf{r})$). At this stage one makes the convenient assumption that P is *always* sharply peaked around $\langle c(\mathbf{r})\rangle$ *i.e*

$$P(\{c(\mathbf{r})\}, t) = \pi\delta(c(\mathbf{r}) - \langle c(\mathbf{r})\rangle) \tag{52}$$

This then leads to

$$\frac{\partial}{\partial t}\langle c(\mathbf{r})\rangle = -M\nabla^2\frac{\delta F\{\langle c(\mathbf{r})\rangle\}}{\delta c(\mathbf{r})}. \tag{53}$$

Being an average equation, the bracket $\langle\ \rangle$ can be dropped. The assumption (52) is crucial, for it implies that there are no fluctuations. In terms of figure 30 what it implies is a drift of a δ-function with no broadening. In § 4.3 we shall discuss an application of (53).

Our next example relates to ordering where, we must remember, the order parameter is *not* conserved. Binder (1973) has used the same steps as above for this problem. He starts with (47) which, after manipulations, takes the form

$$\frac{\partial P(\{\psi\}, t)}{\partial t} = -C\int \mathrm{d}\mathbf{r}\frac{\delta}{\delta\psi(\mathbf{r})}[K(\psi(\mathbf{r}))P] + C\int \mathrm{d}\mathbf{r}\frac{\delta^2 P}{\delta\psi(\mathbf{r})^2}, \tag{54}$$

where the drift force $K(\psi(\mathbf{r}))$ is given by

$$K(\psi(\mathbf{r})) = -\frac{\delta F\{\psi\}}{\delta\psi(\mathbf{r})}. \tag{55}$$

Equation (54) is the Fokker-Planck equation generalized to deal with a situation where P is a functional rather than a function; compare with equation (41). For F, Binder assumes the Ginzburg-Landau form. He then calculates the first moment as in (50), making an assumption similar to (52). The resulting equation for $(\partial\psi(\mathbf{r})/\partial t)$ is the time-dependent Ginzburg-Landau equation as applied to the alloy problem. Once again, because of the approximation (52), fluctuations are not included in the treatment.

---

*The mobility is related to the diffusion coefficient by the Einstein relation $D = Mk_BT$.

For comparison with experiment, one needs correlation functions involving the order parameter like

$$\langle\psi(\mathbf{r},t)\psi(\mathbf{r}',t)\rangle = \int \delta\{\psi\}\,\psi(\mathbf{r},t)\psi(\mathbf{r}',t)P(\{\psi\},t). \tag{56}$$

Multiplying both sides of (47) by $\psi(\mathbf{r},t)\,\psi(\mathbf{r}'t)$ and integrating, one obtains an equation of motion for the correlation function. This was essentially the starting point for Langer's theory (Langer 1969; Langer and Turski 1973; Langer *et al* 1975) of spinodal decomposition. Billotet and Binder (1979) also used a similar approach in their theory of ordering reactions. Suitable approximations were then introduced by the above authors to make the solution of the equation of motion tractable, for subsequent comparison with experiment. As we shall note in the following subsections such theories while including in some measure the nonlinearities (which the time-dependent Ginzburg-Landau equation does) and fluctuations (which the Ginzburg-Landau equation does not) do not yet give perfect agreement, signalling the need for improved approximations.

In brief, the usual starting point for problems involving nonequilibrium systems is the ('generalized') Fokker-Planck equation. From here, one must make one's way through suitable approximations to an equation which can form the basis for comparison with experiments. The latter aspects will be dealt with shortly.

For historical completeness we must mention that, Dienes (1955) and Vineyard (1956) wrote down by analogy with chemical reactions, a *rate* equation for the (long-range) order parameter $S \equiv \langle\psi\rangle$. Dienes (1955) calculated $\dot{S}$ numerically for both first order and second order transitions, and the trends obtained by him are sketched in figure 31. If $\dot{S}$ is positive for a certain value of S, then a fluctuation in the system corresponding to that particular S value will be unstable. Figure 31 will now show that in a second-order phase transition, the system is unstable to infinitesimal fluctuations whereas in a first-order transition, a large fluctuation (in S) is necessary. Qualitatively, this is often identified with a nucleation and growth mechanism (Yamauchi and de Fontaine 1974).

The Dienes-Vineyard approach to ordering kinetics has now been superseded by the more formal treatment based on the Fokker-Planck equation.

4.3 *Spinodal decomposition*

It was at one time believed that phase separation occurred only through a nucleation and growth process *i.e.* small pockets of A-rich and B-rich regions first formed scattered throughout the specimen which subsequently grew and coalesced, transforming the entire specimen to the ordered state. Experiments however revealed that under certain conditions of quenching, the approach to ordering was quite different being akin to "continuous" ordering that one usually associates with a second-order phase transition. This mode of decomposition is referred to as spinodal decomposition.

One picture being worth a thousand words (!) it is perhaps desirable at this stage to refer to figure 32 (Oki *et al* 1974) which, incidentally, gives some idea of the diversity of microstructure one can observe in such experiments.

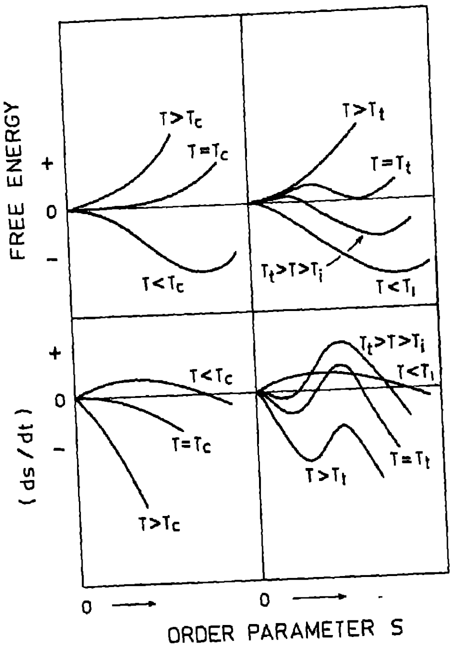

Figure 31. Schematic plots of $\dot{S}$ *vs* S based on the calculations reported by Dienes (1955). The top half of the figure shows sketches of the free energy as a function of the long-range order parameter S for a first- as well as a second-order phase transition. Sketched below are the variations of $\dot{S}$ at different temperatures.

The fact that ordering occurred (under certain conditions) simultaneously over large distances indicated that a large scale migration of atoms was involved; and yet when a diffusion model was tried, it failed. The first nontrivial insight into the processes actually occurring came from the work of Cahn (1961, 1962, 1968). To obtain his model, we go back to (53) and put

$$F\{c(\mathbf{r})\} = \int \mathrm{d}\mathbf{r}(\tfrac{1}{2}K|\nabla c|^2 + f(c)), \tag{57}$$

with

$$f(c) = f_0 + \frac{A}{2}(c - c_B^{\text{crit}})^2 + \frac{B}{4}(c - c_B^{\text{crit}})^4, \tag{58}$$

thus obtaining

$$\frac{\partial c(r,t)}{\partial t} = M\nabla^2[-K\nabla^2 c + (\partial f/\partial c)_T]. \tag{59}$$

Writing $c(r,t) = c_B + \delta c(r,t)$ and linearizing,

$$\frac{\partial \delta c}{\partial t} = M\nabla^2[-K\nabla^2 + (\partial^2 f/\partial c^2)_{T,c_B}]\delta c. \tag{60}$$

Solving by Fourier transform,

$$\begin{aligned} c(k,t) &= F\cdot T \text{ of } \delta c(r,t),\\ &= c(k,0)\exp[\alpha(k)t], \end{aligned}$$

where

$$\begin{aligned} \alpha(k) &= -Mk^2(Kk^2 + f''),\\ &= -MKk^2(k^2 - k_c^2), f'' \equiv (\partial^2 f/\partial c^2)_{c_B T}, k_c^2 = K^{-1}|f''| \text{ for } f'' < 0. \end{aligned} \tag{61}$$

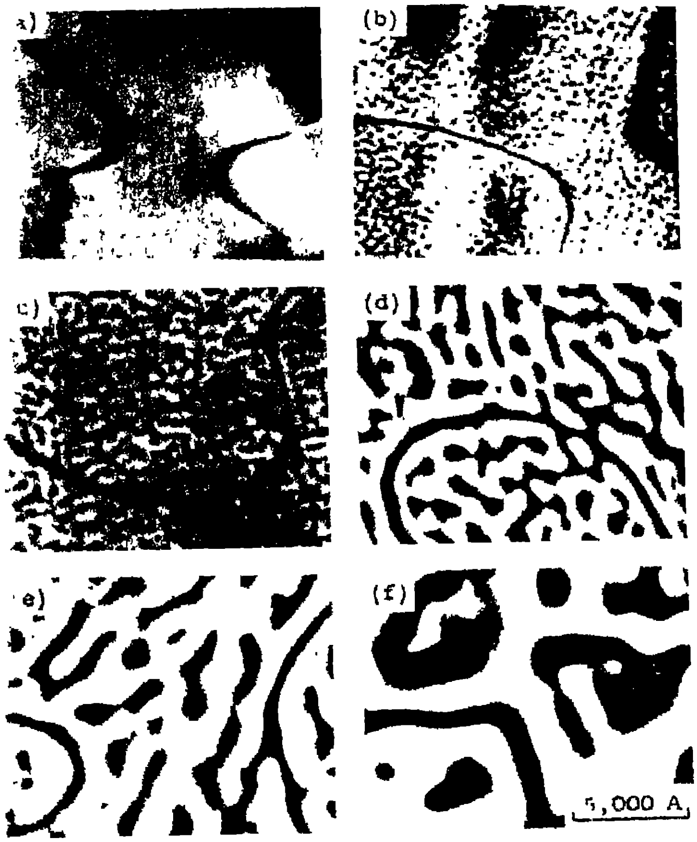

Figure 32. Domain structures of Fe-24·7 at % Al alloy quenched from 630°C and annealed at 570°C. Shown here are the dark field micrographs with 200 reflection. (**a**). quenched. (**b**). annealed for 10 min (c). (d). (e). (f). annealed for 100, 1000, 3000 and 10000 min respectively (after Oki *et al* 1974).

This is the gift of Cahn's theory.

At this stage, it is worth emphasizing the contributions made by Cahn. Firstly he noted that instead of writing the diffusion current as

$$j(r) = -M\nabla(\partial f/\partial c) \tag{62}$$

as one usually does, one must allow for the possibility of the chemical potential varying from point to point in the medium and rewrite the current as

$$j(r) = -M\nabla\frac{\delta F\{c(r)\}}{\delta c(r)} \tag{63}$$

with F as in (57) and (58). (It is interesting that Cahn was not aware of the Ginzburg-Landau theory at that time!).

Another question addressed by Cahn is that of coherency strain (figure 33). Sketched in figure 33 are two different scenarios for the coformation of the two phases α and β

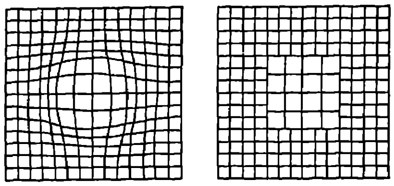
COHERENT INCOHERENT

(a) (b)

Figure 33. Illustration of the concept of the coherency strain. (**a**). A cluster that is coherent with the matrix. The lattice spacing changes gradually from the grain to the surrounding region through a distortion zone. The strain associated with this distortion is the coherency strain, and makes a contribution to the energy. In the sketch in (**b**) there is atomic mismatch at the boundary, and no coherency strain. The cluster in this case is said to be incoherent.

(say) after the quench*. In figure 33b there is complete atomic mismatch at the boundaries separating the α and β regions. With such a discontinuity, the clusters are said to be *incoherent*. By contrast, in figure 33a there is a gradual accommodation of the lattice parameter change through a distortion zone; the corresponding clusters are called *coherent*. While incoherency is the terminal state, the phases initially formed are coherent whence the free energy has a contribution associated with coherency strain. Assuming the medium to be elastically isotropic, an energy density $\eta^2 Y (c - c_B^{\mathrm{crit}})^2$ must then be added to $f(c)$. Here $\eta = (\mathrm{d} \ln a/\mathrm{d}a)$, a being the lattice constant, and Y is given in terms of the Young's modulus E and Poisson's ratio ν as $Y = E/(1-\nu)$. Consequent to this addition, $\alpha(k)$ gets modified as

$$\alpha(k) = -Mk^2(Kk^2 + f'' + 2\eta^2 Y). \tag{64}$$

It is now seen from (61) and (64) that the sign of α depends on a balance of various factors. If coherency strain is absent and if f'' is negative, then α (in (61)) can assume a positive value in the range $0 \leqslant k \leqslant k_c$ as illustrated in figure 34. Thus compositional fluctuations with wavevectors in this region will grow, the component corresponding to k_m dominating. All other fluctuations will decay. Simple diffusion theory on the other hand predicts $\alpha(k) = -Mk^2 f''$ whence *all* fluctuations will grow, the short wavelength ones preferentially.

Referring now to figure 35 we see that f'' is negative only for a certain range of compositions. One could therefore plot within the two-phase region, the locus of points where $f'' = 0$. This is the spinodal and, as may be seen from figure 35 it divides the two-phase region into two zones (—see also figure 29).† If a quench is made into the region within the spinodal, an *instability* occurs causing the system to evolve to equilibrium through the growth of long wavelength compositional waves. Ordering thus sets in on a macroscopic scale, and increases gradually in amplitude (—hence the reference to

---

[*] It must be mentioned that spinodal decomposition is also possible in certain binary fluid mixtures. However, there, one does not have coherency strain. For a comprehensive review of both alloys and liquid mixtures, see Gunton (1982).

[†] The Chamber's dictionary defines spinode as a cusp, the root being the Latin word *spina* meaning thorn. From figure 29 we see the relationship of the cusp to the critical manifold, although one is more used to the projection on the (a, x) plane rather than the projection on the (a, b) plane. See also Kikuchi and de Fontaine (1976).

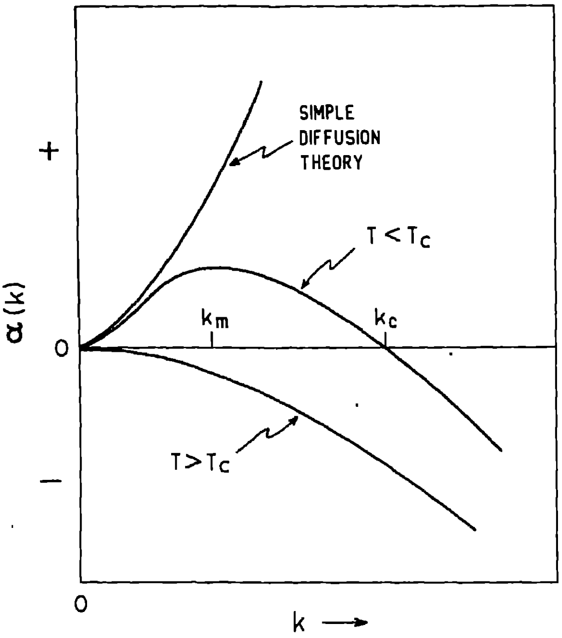

Figure 34. Plots of α *vs* k as given by linear theories.

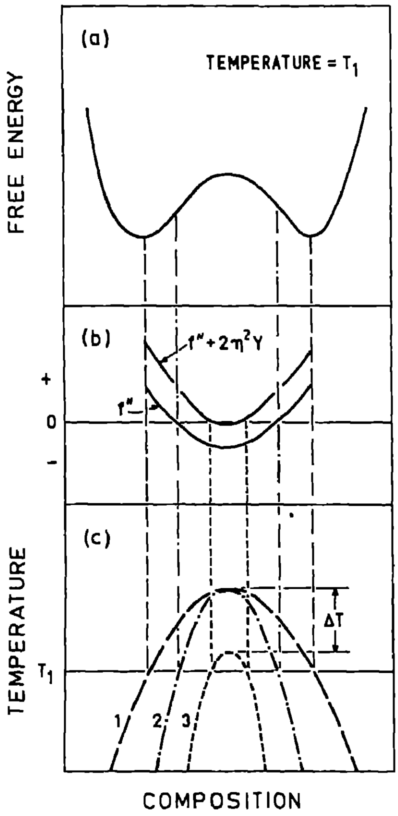

Figure 35. At the top is sketched the usual double well form of the free-energy *vs* composition. (See also figure 5 and (58)). The second derivative f'' is sketched in the middle. Instability is connected with f'' being negative. If coherency strain is included then $(f'' + 2\eta^2 Y)$ must be negative. At the bottom are shown the coexistence curve 1 and the spinodals 2 and 3.

"continuous" ordering). Outside the spinodal but within the coexistence line, there is *metastability* instead of instability. If a quench is made into the metastable region, the system evolves through the nucleation of order in several localized regions. These pockets grow in size and eventually link up so that order percolates everywhere. It appears that after equilibrium is finally reached, it is immaterial what route exactly was taken towards its attainment *i.e.* whether it was quenched into the metastable or the unstable region. However, immediately after nonequilibrium conditions are established, the scenario does depend on whether one is in the region of metastability or of instability. It is in this context one wishes to know where f'' vanishes, and this is precisely where a plot as in figure 25c is useful.

If coherency strain is included, then

$$k_c^2 = K^{-1}|f''+2\eta^2 Y|, \tag{65}$$

and for instability one must have $(f''+2\eta^2 Y)$ negative rather than f''. As a result, the spinodal is depressed with respect to the (incoherent) coexistence curve (see figure 35c). In liquids, such a depression is absent for obvious reasons. In passing, it should also be pointed out that the phase diagrams deduced from theory as in § 3.2 refer to the *coherent* phase diagrams whereas those determined by experiment (Hansen 1958) refer to *incoherent* phase diagrams.

While Cahn's theory gave some clue as to the origin of spinodal decomposition, quantitatively it was inadequate as it assumed linearity. Now one of the stringent tests for a theory is to compare the structure factor $S(k, t)$ predicted by it in the small k region with that observed experimentally. In Cahn's theory

$$S(k,t) \equiv \langle c(k,t)c(-k,t)\rangle = S(k,0)\exp[2\alpha(k)t]. \tag{66}$$

Based on figure 34, one would expect $S(k, t)$ to peak at k_m for all t whereas experiment showed that $k_m \to 0$ as $t \to \infty$. Another failing of Cahn's theory is that it predicts the decay of $S(k, t)$ to zero for $k > k_c$ whereas it must actually approach that appropriate to the fluctuations at temperature T (to which the sample has been quenched). Cook (1970) traced this deficiency to the absence of fluctuations in Cahn's theory (recall remarks circa equation (53)) and therefore modified Cahn's diffusion equation into a Langevin equation, *i.e.* he wrote

$$\frac{\partial c}{\partial t} = -\nabla j+\zeta j = -M\nabla(\delta F/\delta c), \tag{67a}$$

with

$$\langle\zeta(r,t)\zeta(r',t')\rangle = 2M\delta(r-r')\delta(t-t'). \tag{67b}$$

Cook's model produced only marginal improvements to that of Cahn's since it too relied on linearity. The real breakthrough came with the work of Langer and coworkers (Langer 1969, 1980; Langer and Turski 1973; Langer *et al* 1975) who not only included fluctuations (as Cook did), but also the nonlinearities (though only approximately).

To understand Langer's work we start with the formal equation of motion for $S(\mathbf{k}, t)$ which is obtained as described in § 4.2 circa equation (56). Ignoring elastic effects, the equation for $S(\mathbf{k}, t)$ is:

$$\frac{\partial S(k,t)}{\partial t} = -2Mk^2[(Kk^2+f'')S(k,t)+\tfrac{1}{2}(\partial^3 f/\partial c^3)_{c_B}S_3(k,t) + \tfrac{1}{6}(\partial^4 f/\partial c^4)_{c_B}S_4(k,t)+\ldots]+2Mk_BTk^2. \tag{68}$$

Here

$$S_n(r_1 - r_2, t) = \langle \delta c^{n-1}(r_1, t)\delta c(r_2, t)\rangle \tag{69}$$

and $S_n(k, t)$ is the Fourier transform of $S_n(r, t)$. From (68) we see that Cahn had only the first term of the series and that Cook added the noise term.

A major difficulty with (68) is that it involves the higher-order correlation function $S_n(k, t)$ to know which we need additional equations of motion! One thus ends up with a hierarchy of coupled equations, a familiar malaise of many-body theory. Langer and coworkers argued that no matter what n is, S_n always involves only two spatial positions $\mathbf{r}_1$ and $\mathbf{r}_2$. It should therefore be possible to compute S_n for any n (albeit-approximately), given a knowledge of the two-point distribution function $P_2[c(\mathbf{r}_1), c(\mathbf{r}_2)]$. The latter was approximated by

$$P_2[c(\mathbf{r}_1), c(\mathbf{r}_2)] = P_1[c(\mathbf{r}_1)]P_1[c(\mathbf{r}_2)] \times \left\{1 + \frac{\langle \delta c(\mathbf{r}_1)\, \delta c(\mathbf{r}_2)\rangle}{\langle (\delta c)^2\rangle} \frac{\delta c(\mathbf{r}_1)\, \delta c(\mathbf{r}_2)}{\langle (\delta c)^2\rangle}\right\}. \tag{70}$$

If there were no correlations between the concentrations at $\mathbf{r}_1$ and $\mathbf{r}_2$, then P_2 would just be a simple product of the one-point probabilities. In Langer's scheme, the correction is proportional to $\langle \delta c(\mathbf{r}_1)\, \delta c(\mathbf{r}_2)\rangle$. The equation of motion now simplifies to

$$\frac{\mathrm{d}S(k, t)}{\mathrm{d}t} = -2Mk^2[Kk^2 + A(t)] + 2Mk_BTk^2, \tag{71}$$

where $A(t)$ itself depends on $S(k, t)$ and must therefore be calculated by a self-consistent scheme. For comparison, Cahn's theory gives

$$\frac{\mathrm{d}S(k, t)}{\mathrm{d}t} = -2Mk^2[Kk^2 + f''], \tag{72}$$

while Cook's theory gives

$$\frac{\mathrm{d}S(k, t)}{\mathrm{d}t} = -2Mk^2[Kk^2 + f''] + 2Mk_BTk^2. \tag{73}$$

The major success of the Langer theory is the prediction that k_m shifts towards the origin as time increases, in accord with experiment. Another important finding is that the structure factor satisfies dynamic scaling *i.e*

$$S_T(k, t; c_B) = \varepsilon^{-\gamma}\tilde{S}[k\varepsilon^{-\nu}, t\varepsilon^{\gamma}, (c - c_B^{\text{crit}})] \tag{74}$$

where $\varepsilon = (1 - T/T_c)$, and β, ν, γ have their usual meanings (Stanley 1971). Equation (74) is significant because it shows that dynamic scaling can apply to relaxation *far from equilibrium.*

The theory of Langer also is not without blemishes. One shortcoming is that it exhibits metastable states of infinite life-time. A related defect is the inability to describe properly the late stages of the separation. According to Binder (1977) these failings can be cured by explicitly building in features related to nucleation and growth. The late stage behaviour will be briefly touched upon again in a subsequent section.

To counter the impression one might get that it is all theory (!), we now present some representative but important experimental results. Figure 36 shows small-angle

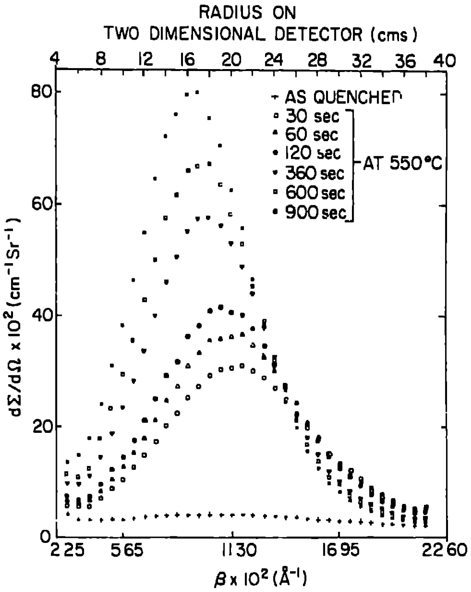

Figure 36. Differential scattering cross-section ($d\Sigma/d\Omega$) *vs* scattering vector β (k in our notation) for Au-60 at % Pt alloy quenched from 1270°C and aged at 550°C. In making the measurements, an "arresting technique" as illustrated in figure 44 was used (after Singhal *et al* 1978).

neutron scattering results for a Au-60 at % Pt alloy obtained by Singhal *et al* (1978). The sample was quenched from 1270 ($\pm$ 5)°C into iced brine and subsequently aged at 550°C. After aging for a certain time, the sample was quenched into water to prepare for measurements (which were done at room temperature). The sample was then successively subjected to additional aging treatment, followed in each case by a measurement to monitor the state of ordering. The data clearly indicates the shift of k_m towards zero with increasing time.

The next result we discuss is that of Schwahn and Schmatz (1978) for Al-40 at % Zn alloy. This was a clever experiment designed to check the fact that due to coherency strain, T_c the critical temperature associated with the spinodal is depressed below the (incoherent) phase boundary (see figure 35). Starting from the one-phase region, the sample was quenched to a temperature T just *above* T_c. Holding the sample at T, small-angle neutron scattering measurements were carried out. In contrast to what one observes in a usual second-order phase transition while approaching T_c from above, it was noticed that $S(k)$ changed with time. The reason is that though $T > T_c$, the sample was actually below the equilibrium (*i.e* incoherent) phase boundary. Thus, with passage of time, ordering occurred slowly *via* nucleation and growth and $S(k)$ probably went over to a form appropriate to that process. Under the circumstances, the spectrum measured just after quench is the one representative of critical scattering *i.e.* the excess scattering arising out of the proximity of T to T_c (coherent). A rapid increase of scattered intensity (so isolated) was indeed observed as $T \rightarrow T_c^+$, and it was firmly established that T_c (coherent) was 28°C below the incoherent critical point of 351·5°C (see figure 37). Further, $S(k)$ immediately after quench had the well-known Ornstein-Zernike (1914) form usually found while approaching a second-order phase transition. Only, in this case the Ornstein-Zernike form was transient, giving way to a fluctuation spectrum appropriate to other processes.

Spinodal decomposition has no doubt been explored by a variety of tools but of these, small-angle neutron scattering is perhaps the most useful for checking out aspects we are interested in presently. The spectrometers currently available at the various high-flux reactors are quite powerful, being placed in cold-neutron beams and equipped with 2-D detectors and online computers. The possibility of rapid, real-time measurements (as in the Schwahn and Schmatz experiment) is a very attractive feature. At the new DHRUVA reactor at Trombay, a cold neutron source is being planned, and a small-angle measurement facility is also being contemplated. Such a spectrometer would give a great impetus to the above type of experiments in the country. While neutron scattering has an edge at the moment, x-rays have a strong possibility of staging a comeback, especially with the advent of synchrotron-radiation sources.

Computer simulation is another important technique employed to test theoretical predictions. Lebowitz *et al* (1982) for example, have used the Monte Carlo method to study quenching under various conditions (see figure 38). In each case $S(k, t)$ was determined, with time measured in units of α^{-1} where α^{-1} is the average time interval

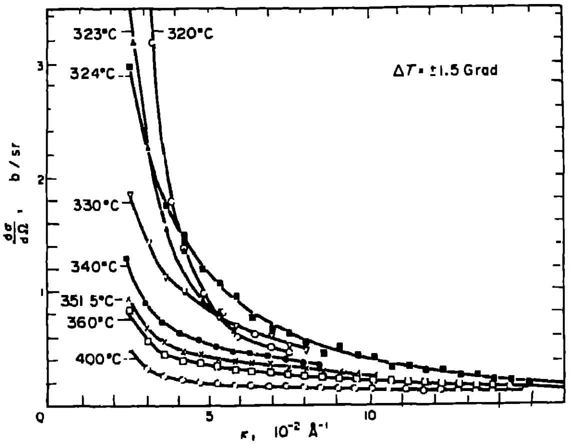

Figure 37. Differential scattering cross-section *vs* wavevector observed at various temperatures in the neighbourhood of the (coherent) critical temperature (~ 324°C). The sharp rise at small k is characteristic of critical behaviour. No critical scattering was found at 351°C the incoherent critical temperature. The k-dependence near 324°C follows the Ornstein-Zernike form (after Schwan and Schmatz 1978).

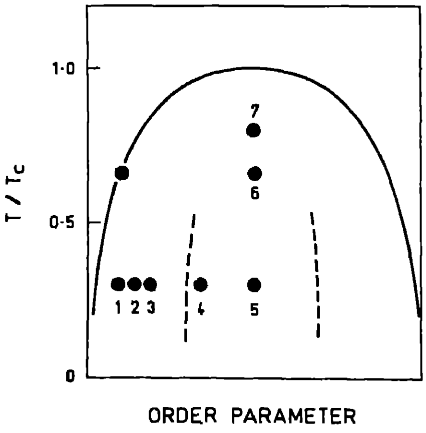

Figure 38. Phase diagram of the Ising model used by Lebowitz *et al* (1982) in their computer simulation studies. The broken lines are spinodals. The dots correspond to the various quenches made. In each case, the system is started from an infinite temperature (after Lebowitz *et al* 1982).

between two attempts at exchanging a specific site. A time range up to $10^4\alpha^{-1}$ was scanned, and, as expected, phase separation occurred with varying speeds depending on the nature of the quench. The relaxation was fastest for quench 5 and slowest for quench 1. A problem arises in making comparisons with experimental data since time in the latter is measured in real physical units *i.e.* seconds. However a link is possible since the unit of time in the simulations appropriate to a temperature T can be taken as $a^2/6D(T)$ where a is the lattice constant and D is the diffusion coefficient of A atoms in a crystal of B atoms. Using such a scaling, Lebowitz *et al* (1982) made comparisons with data obtained by Singhal *et al* (1978). The comparison is reproduced in figure 39 and the notable feature is that one could make the data from the actual and computer experiment lie on the same curve by only rescaling the vertical axis. Further comments on the scaling behaviour will be made when we consider long-term behaviour.

4.4 *Late stages of phase separation kinetics*

Subsequent to quenching, the system will after sometime, segregate locally into regions of A-rich and B-rich phases (referred to as grains or droplets or domains). With further passage of time, two things happen. Firstly, within individual grains itself, the atoms continue to approach an organization characteristic of the equilibrium configuration. In addition, the droplets themselves grow, coarsen or ripen, whichever way one wants to describe it. A proper theory for $S(k, t)$ must reflect both these aspects (see figure 40, Binder 1980b), but such a theory does not exist. Present theories have only one length scale whereas what figure 40 shows is the need for two.

Quantitatively, the above ideas may be expressed as

$$S(k, t) \approx S_{\mathrm{DW}}(k, t) + S_{\mathrm{ID}}(k, t) \tag{75}$$

where DW refers to domain wall and ID to intradomain. As $t \to \infty$, $S_{\mathrm{DW}} \to \text{const} \times \delta(k)$ while $S_{\mathrm{ID}} \to S_{\mathrm{ID}}(k, eq)$. Immediately after quench, DW's are not important and $S \sim S_{\mathrm{ID}}$. However, during late stages, it is S_{DW} that is more interesting as it gives an insight into the coarsening processes.

One interesting discovery concerning late-stage behaviour is the existence of scaling. Since there is a characteristic length (~ domain size), associated with the process, it has

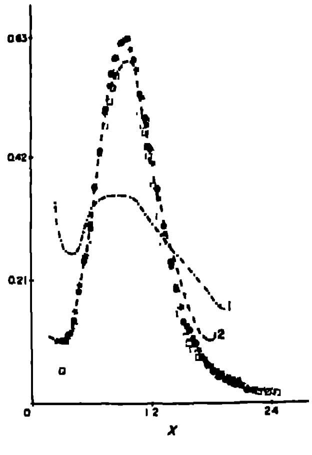

Figure 39. Comparison of the computer simulation results (empty symbols) with experimental data (Singhal *et al* 1978) for Au-60 at % Pt alloy quenched to $T \sim 0{\cdot}6\,T_c$. The broken line is for $t = 0$ (the initial sample was already decomposed to some extent) (after Lebowitz *et al* 1982).

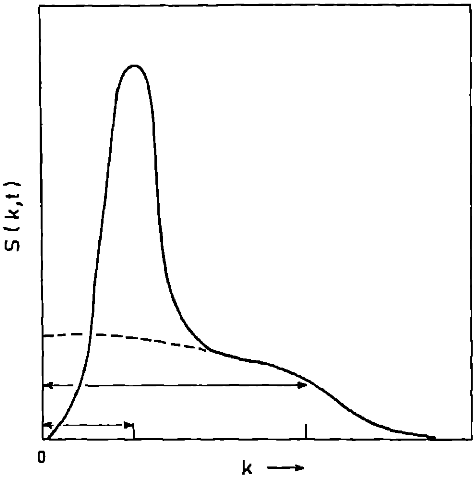

Figure 40. Sketch of $S(k, t)$ *vs* k at long time. The two arrows show the two wavevectors corresponding to the two length scales (intra domain correlations and domain size). (After Binder 1980b).

been conjectured (Binder 1977; Lebowitz *et al* 1982) that

$$S_{\mathrm{DW}}(k, t) \sim b(t)\mathscr{F}(k/K(t)) \tag{76}$$

where $K(t)$ is the characteristic wavevector associated with the characteristic length, and $b(t)$ is a normalizing function. Lebowitz *et al* (1982) have analyzed the data of Singhal *et al* (1978) for Au-Pt alloy and found good confirmation of this hypothesis (see figure 39).

The question of coarsening has been considered even earlier in the context of nucleation theories. Lifshitz and Slyozov (1961) and independently Wagner (1961) have discussed the growth of droplets of B-rich phase immersed in an A-rich matrix. This theory was really derived for small supersaturation such as one obtains in the late stages of a nucleation and growth process (*e.g.* in clouds). It is however often assumed that the LSW theory can also be applied to the late stage coarsening of a spinodally decomposing system. The basic idea is that larger droplets grow at the expense of smaller droplets *via* the diffusion of B atoms between different droplets. An important conclusion of the theory is that the average droplet size $\bar{R}(t)$ (which is the characteristic length of the system) satisfies a $t^{1/3}$ power law. Lebowitz *et al* (1982) found that $K^{-1}(t)$ derived from simulation studies appeared to show such a behaviour. Attention must here be drawn to the fact that existing studies on grain growth neglect the possible influence of coherency strain, a factor that is pertinent in alloys, though not in liquids (Binder 1977).

There is one aspect of late stage behaviour we now wish to comment on that does not appear to have received attention thus far. It was noticed many years ago by de Fontaine (1967) during a simulation of spinodal decomposition (in one dimension) that whereas a compositional wave of well-defined wavelength develops immediately after instability is established, pretty soon a period doubling occurs. At that time, the possibility of period doubling as a route to chaos was not known (Feigenbaum 1978, 1979, 1980). The question of whether the formation of irregular domains is due to chaos appears worth a fresh examination. It is pertinent here to point out that de Fontaine (1975a) has mapped the problem of concentration evolution into a Hamiltonian problem and examined system evolution in terms of trajectories in a $(c, \mathrm{d}c/\mathrm{d}x)$ phase space. More recently, Aubry (1981, 1983) has in the study of certain defect structures, carried out a similar trajectory analysis and, what is more interesting, discovered the possibility of chaos under certain conditions. One wonders whether it would not be worthwhile to go back to the de Fontaine problem and reexamine it from this new perspective. In support of such a suggestion, we call attention to figure 41 which shows a computer simulated spinodal structure and that for a real binary glass (Hopper 1982): The simulated structure was obtained by superposing twenty 3-D waves of a *single* wavelength but of random orientation and phases. Notwithstanding this, there appears to be a regularity of sorts in the simulated pattern as compared to the real micrograph. Perhaps features related to stochasticity arising out of period doubling do play a role.

4.5 *Ordering reactions*

The extensive theoretical work on spinodal decomposition reviewed in § 4.3 has been extended to some extent (Binder 1973; Billotet and Binder 1979) to ordering reactions, although there has not been matching experimental work on the kinetic aspects. However, some attention has been paid to critical phenomena one expects near phase boundaries.

We have already called attention to the early work of Johansson and Linde (1928). A more recent example is provided by the work of Hashimoto *et al* (1976) who studied ordering in Cu_3Au. Starting from the one-phase region, the sample was quenched to and held at various temperatures T below the (first-order) transition temperature T_t of 391°C. At each temperature, the electrical resistivity was monitored as a function of time, and the relaxation time τ for approach to equilibrium was deduced. A plot of τ *vs* T showed a sharp increase as $T \rightarrow T_t^-$. Other probes have also been used to study critical phenomena *e.g.* Zener relaxation (Radelaar and Ritzen 1969) and isothermal release of energy (d'Heurle and Gordon 1961).

X-rays have always been popular (see, for example the review by Cohen 1970), a recent example being the study of Hashimoto *et al* (1978). Cu_3Au the work horse, was the material investigated. The specimen was first annealed at a temperature $T > T_t$ and later quenched to a temperature below T_t and annealed at the latter temperature for various spells. After each spell, the sample was quenched into water and the x-ray intensity in the superlattice region (110) was scanned. Initially, only a broad and diffuse

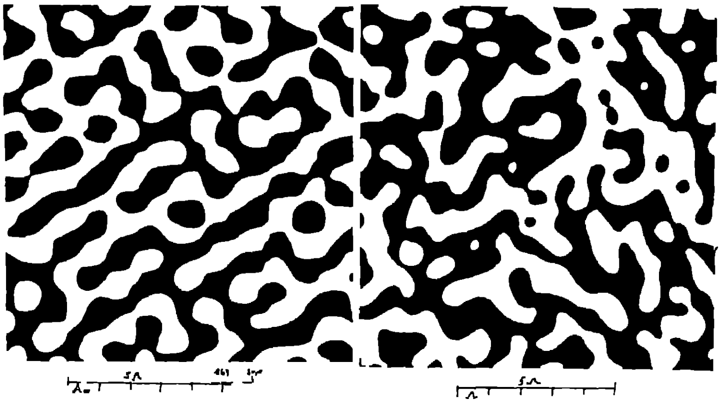

Figure 41. On the right is an electron microscope picture of a real binary glass, showing the phase-separated structure. On the left is the simulated structure obtained using a *single* wavelength (after Hopper 1982).

peak was observed but on increasing annealing time the peak narrowed and intensified, signalling the onset of order. From a plot of linewidth as a function of annealing duration, the relaxation time τ could be extracted. A slowing down of relaxation was markedly evident as $T \to T_t^-$. Another investigation meriting particular mention is that of Chen and Cohen (1977). The unique feature was that by employing single crystals, Chen and Cohen were able to study τ as a function of k. Figure 42 shows their results for $Cu_{81.5}Au_{18.5}$ obtained after a temperature change 355° and 330°C. As expected, τ peaks near the superlattice position.

Earlier (in § 4.3) we noted that under certain conditions, phase separation takes on the character of a continuous transition. Is such a scenario possible in *ordering* systems? Indeed it is, as has been emphasized by de Fontaine (1981). The basic concept is easily understood with a reference to figure 43. In figure 43a is shown a family of free energy curves appropriate to a system undergoing a first-order phase transition. If the temperature is gradually lowered from above, order will set in at $T = T_t$ (figure 43b) *via* a nucleation and growth process. On the other hand, a sudden quench to a temperature below T_t can produce the situation depicted in figure 43c. The system responds to the instability through the generation of an ordering wave of wavevector corresponding to the minimum of $V(k)$. The wave swells in amplitude gradually, spreading order everywhere. Therefore, vis-a-vis nonequilibrium situations, one can think of an instability temperature T_{instab} ($< T_t$) below which *continuous ordering* occurs.

While the concept seems possible, there is as yet no direct evidence for the existence of the instability temperature, although in an experiment due to Bardhan *et al* (1977) on Cu_3Au there is a strong suggestion. The analogue of the Schwahn-Schmatz experiment (§ 4.3) would be desirable. Incidentally, the dashed line in figure 15b is the variation of T_{instab} with composition, as deduced from CVM.

In some situations, continuous ordering is possible with an interesting twist. Following the creation of an instability, the system responds with a compositional wave whose wave vector does *not* coincide with that corresponding to the superlattice reflection.

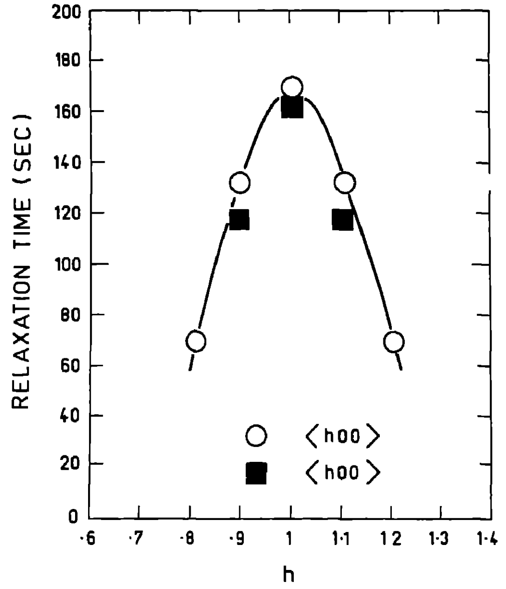

Figure 42. Wavevector-dependent relaxation time τ (k). Shown here are data obtained along ⟨h00⟩ and ⟨hh0⟩ lines. The continuous line is a guide to the eye (after Chen and Cohen 1977).

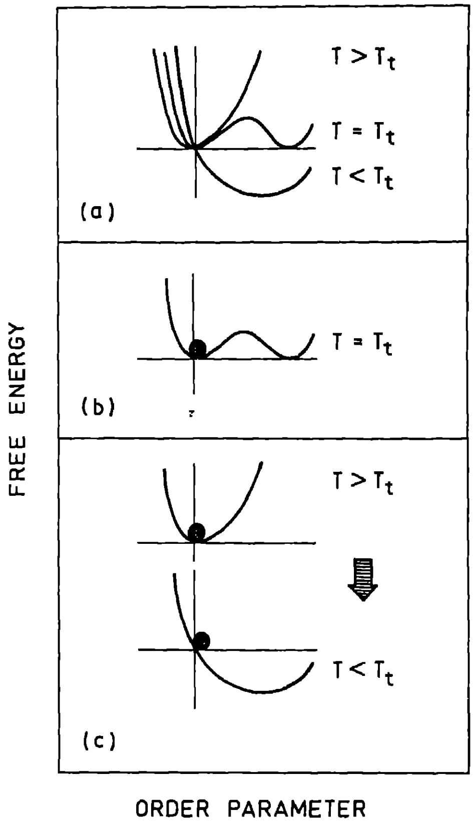

Figure 43. System response to different temperature treatments (a). free energy curves for a first order transition, with transition temperature T_t. When slowly cooled from above, the system experiences metastability on reaching T_t, and orders by a nucleation and growth process. If suddenly cooled to a temperature well below T_t as schematically illustrated in (c), it experiences an instability.

However, the system somehow seems to realize this during its evolution, and comes up with a suitable mid-course correction (rooted in nonlinearities?) so that the correct ordered structure results on attainment of equilibrium. Apparently, the point of maximum instability in reciprocal space need not always coincide with the wavevector corresponding to the ordering wave. de Fontaine (1975b) has suggested that Ni-Mo is a good candidate system for exhibiting such a schizophrenic behaviour! Here the instability is associated with a $\langle 1\ \frac{1}{2}\ 0\rangle$ wave whereas the ordering is based on a $\langle 100 \rangle$ wave. There is some evidence from x-ray diffraction (Chakravarti *et al* 1974) and electron microscopy (Das *et al* 1973) in support of the idea but a convincing test would be through a suitably designed real-time experiment.

On the theoretical side, Cook *et al* (1969) extended the Cahn-type analysis (which was essentially applied to a continuum) to discrete lattice systems and demonstrated that under suitable conditions, ordering with the formation of a superlattice was possible. In fact, the curves of figure 22 are the products of such a *linear* theory. In an effort to incorporate nonlinearities, Billotet and Binder (1979) have followed the footsteps of Langer with, however, due allowance for the fact that the order parameter is *not* conserved. (Recall remarks made in § 4.2 regarding conserved and nonconserved order parameters). Earlier, Binder (1973) had tried a time-dependent Ginzburg-Landau type approach, with as much success as may be expected of a mean field theory.

Billotet and Binder (1979) report many numerical calculations but unfortunately, barring some simulation results, they do not have much experimental data to compare with. In fact Binder and Stauffer (1976) attempted to stimulate experimenters by explicitly calling attention to various aspects of the behaviour of electrical resistivity of binary alloys at phase transitions but the response of the experimental community does not seem to be adequate.

A few remarks now about late stage behaviour in ordering systems. It has been noted (Binder 1980b) that as in clustering reactions, one has to recognize the existence of two length scales (see figure 40), one of which is related to intradomain ordering and the other to domain size. Since one is dealing with an ordering reaction, the intradomain part can be conveniently explored near superlattice positions in a diffraction experiment. The domain-wall effects on the other hand, are best picked up in a small-angle scattering experiment.

There is another aspect of domain walls that has occasionally been mentioned in the literature (*e.g.* Gunton 1982) but does not appear to have been examined in depth. Now the formation of different domains is usually thought of in terms of nucleation of ordering in different regions and the subsequent growth of the latter, leading to the formation of interfaces. In the symmetry-breaking language on the other hand, each ordered region corresponds to a manifestation of one of the possible ground states. The macroscopic physical system is thus trapped in different ground states in different physical regions. The resulting configuration/defect (*i.e.* DW) is therefore a topological entity. The topological aspects of DWs have barely been investigated and are probably worth a closer scrutiny.

Finally, a brief hark back to long-period oscillations (see § 3.1) (Aubry 1981, 1983). One wonders whether some of the considerations in Aubry's analysis of incommensurate structures do not have relevance to LPO seen in some ordered systems. This also appears worth looking into.

We close this section by calling attention to an authoritative review by Freidel (1974) on the electronic aspects of order-disorder transformations (which we have skipped!). Physicists wishing to study order-disorder transformations, should not miss this paper!

5. What can experimenters do?

The title of this section is not intended to suggest that experimenters have been slack but merely that there is a dearth of certain types of information *e.g.* relaxation data.

Now each probe has its own characteristic sensitivity, and it is necessary to integrate for a certain time τ_M during the experiment to obtain a signal above the background. When exploring nonequilibrium phenomena this poses a problem if the relaxation time τ_R is less than τ_M. One then has to use an "arresting" technique as illustrated in figure 44, wherein the system is periodically "frozen" in its coast down and then monitored. For example, the data of figure 36 was obtained in this fashion. However, if the signal is strong, one may be able to follow temporal changes directly in realtime. Improvements are therefore necessary for many techniques, if realtime measurements are to become feasible. In some cases like electrical resistivity, the required sensitivities are already there but nevertheless, the capabilities do not appear to have been fully exploited. Where neutron and x-ray scattering are concerned, increase in the primary source strength is an important factor. The availability of synchrotron radiation sources is therefore a welcome development in respect of x-ray scattering. Hardly any results pertaining to phase transformations have been reported using synchrotron sources, and there is much room for innovation and ingenuity.

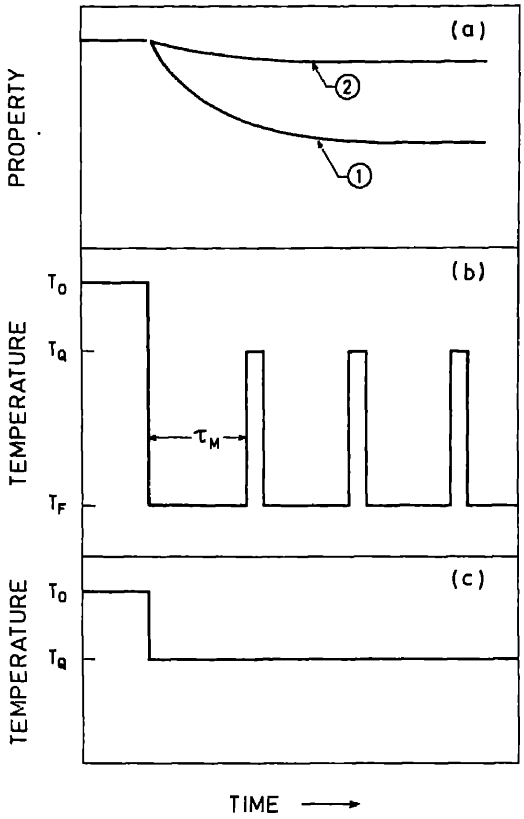

Figure 44. (a) Time variations of some property when a system is quenched as in (c). If the decay is rapid as in case (1), then the system must be periodically arrested in its coast down as illustrated in (b). This gives convenient measurement slots whose width τ_M can be chosen suitably to optimize (signal/noise) ratio. However, if the measurement time is small, then one can follow the decay in realtime i.e. the time-temperature profile will be as in (c). In the examples shown, this could be applied to case (2).

While discussing realtime measurements, it must be remembered that depending on the temperature, composition etc., the relaxation times can vary over several orders of magnitude. Attention is drawn in this context to the various quenches attempted by Lebowitz *et al* (1982) in their simulation experiments (see figure 38) and the wide spread in relaxation times observed by them. Thus, many techniques can in fact be used on an as-available basis without waiting for improvements, provided one chooses the conditions of experiment properly. In passing, it is worth noting that computer simulation is an expensive way of obtaining relaxation times. It is therefore very desirable to back it up with more extensive studies using a convenient probe (like resistivity).

The types of probes one could think of are many. Some, like resistivity, have already been mentioned. Others include internal friction, ultrasonic attenuation etc. Binder and Stauffer (1976) have discussed in detail how resistivity measurements can be linked to order parameter dynamics. They have also called attention to the need for conventional studies of scaling behaviour as one crosses the phase boundaries. For instance, it would

M → 5

be very interesting to follow the variation of resistivity with concentration at various temperatures as sketched in figure 45. The sharp rise and fall in the indicated regions are closely related to critical dynamics of the order parameter.

In contrast to "macroscopic" probes like resistivity, the Mössbauer effect provides a probe that is nucleus sensitive. Oki *et al* (1977) have, for example, exploited this method to examine aspects of transformations in Fe-Al alloys. There is clearly more scope for work of this kind. Indeed, one could also consider NMR. With high-power pulsed NMR systems now commercially available, relaxation studies of the type considered here are no longer a mere theoretical possibility. The neutron is yet another nucleus-sensitive probe. In addition, it can also undergo magnetic scattering. Both these factors can be skilfully exploited, particularly where magnetic alloys are concerned. As of now, there appear to be very few examples of ordering kinetics studied using neutrons. One investigation I am aware of is the experiment of Collins and Teh (1973) on Ni_3Mn. These authors upquenched in the ordered state, and for each step change ΔT of temperature, they measured the time required for the order parameter to stabilize to its new value. The kinetics of the order parameter were monitored *via* Bragg intensity of an appropriate reflection. Of course, a sophisticated technique like neutron scattering is not always required. Nowick and Weisenberg (1958) for example, simply followed the time variation of the Young's modulus in their upquench experiments on ordered Cu_3Au. In general, there is a paucity of information about system dynamics following a quench. One needs both upquench and downquench experiments, within a given phase (Binder 1977) as well as across a boundary.

While it is natural to think of relaxation time studies in the time domain, we should not forget traditional spectroscopy which also can give information about relaxation time, though of smaller magnitude. An experiment one could think of would be the analogue of the soft-mode studies made in connection with structural phase transitions (—for a review of this area, see Venkataraman 1979). There one has a lattice dynamical

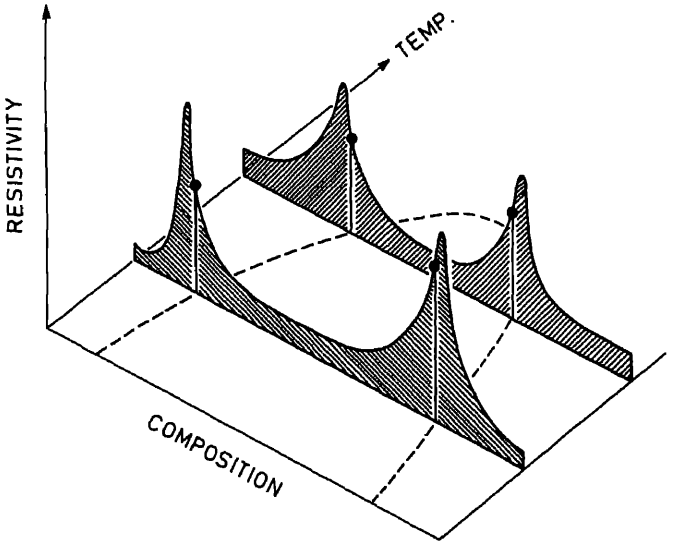

Figure 45. Schematic plot of resistivity *vs* composition at various temperatures. The dots show the regions where there is a sharp rise or fall. (after Binder and Stauffer 1976).

mode whose frequency diminishes as $T \rightarrow T_c^+$. In ordering reactions, we have a compositional wave but of zero frequency. The scattering of radiation from this wave gives rise to intensity in the superlattice region. If an energy scan is made of the scattered intensity (—and this is possible with neutrons), then one will observe a certain frequency spread around $\omega = 0$, the spread being related to the relaxation time of the concerned compositional fluctuation. As $T \rightarrow T_c^+$, the line width must decrease, indicative of critical slowing down of the compositional fluctuations. A systematic, quasi-elastic scattering investigation of the 'softening' of compositional fluctuations does not appear to have been made so far.

Our preoccupation with long-range order should not blind us to short-range order which too is an important quantity! As the name itself indicates, the focus is on ordering on a localized scale. The key quantity is the (Ising) spin correlation $\langle S_l S_m \rangle$. By suitable definitions (de Fontaine 1979), this spin correlation function can be related to the pair correlation function g ($\mathbf{R} = \mathbf{m} - \mathbf{l}$) well-known in theory of liquids, and to experimentally measured quantities like the Warren-Cowley parameters. Clearly, short-range order would be of particular interest in the early stages after a quench, and in the disordered phase close to T_c. With synchrotron sources now available, it may be possible to follow the evolution of short-range order in realtime, at least in select cases. The results can then be linked to models for spin dynamics. Other possible studies concerning short-range order have been mentioned in § 3.3.

At a recent Discussion Meeting on the Physical Basis of Mechanical Behaviour organized under the auspices of the Academy (where, incidentally, Prof. Ramaseshan delivered the keynote address), Dr G Srinivasan raised the interesting question of heat liberated following a quench. In the discussion that followed, Prof. C K Majumdar drew attention to the pioneering work of Bragg and Williams (1935) wherein the approach to order had been discussed in terms of a fictious temperature. Today, with our knowledge of magnetic resonance etc., we would identify this as the Ising spin temperature and the approach to equilibrium as a spin-lattice relaxation problem. This digression in the Discussion Meeting served to focus attention on the paucity of thermal measurements. Subsequently, I have come across one paper (d'Heurle and Gordon 1961) wherein calorimetry experiments on Au_3Cu during ordering are reported. By and large, studies on the energetics of ordering appear to be rare.

While comparing relaxation times obtained *via* different techniques, we should note that the coupling of the various probes to the order parameter is not the same. Moreover, some like resistivity, integrate the fluctuations of the order parameter over the wavevectors. Two such "integral" probes may not weight the different k's in the same manner. In this sense, x-rays and neutrons enjoy the advantage that one can select a specific wavevector for study. All the same, other probes have their own utility in that they are usually faster and also less expensive!

Thus far, we have confined attention to *equal-time* correlation functions of the form $\langle \psi(r, t)\ \psi(r', t) \rangle$. This function continually changes with time till equilibrium is attained at $t = \infty$. Probes like x-rays sample equal-time correlation function because they essentially produce an "instantaneous snapshot" of the system. We now extend consideration to *unequal* time correlation functions *i.e.*, functions of the form $\langle \psi(r, t)\ \psi(r', t') \rangle$. The relevance of such functions to experiment will be discussed shortly.

Billotet and Binder (1980) were the first to consider such functions in the context of phase transformations. The kinetics of such functions were modelled closely after Langer's and their own earlier work on equal-time correlation function. They start with the conditional probability $P^{\text{cond}}(\{\psi^1\}, t_1; \{\psi^2\}, t_2)$ which is the probability that the system is in the state $\{\psi^2\}$ at time t_2, given that it was in state $\{\psi^1\}$ at t_1. The continuity equation for P^{cond} is:

$$\frac{\partial}{\partial t_2} P^{\text{cond}}(\{\psi^1\}, t_1; \{\psi^2\}, t_2) = -\int \mathrm{d}\mathbf{r} \frac{\delta J_{\mathbf{r}}^{\text{cond}}(\{\psi^1\}, t_1; \{\psi^2\}, t_2)}{\delta \psi_{\mathbf{r}}^{(2)}}, \tag{77}$$

the expression for $J_{\mathbf{r}}^{\text{cond}}$ being an obvious extension of (48). The sequence of steps thereafter is essentially the same as before, and, as earlier, a decoupling approximation is made for $P(\psi_{r_1}^{(1)}, t_1; \psi_{r_2}^{(2)}, t_2)$ which is the probability that we have a state $\psi_{r_1}^{(1)}$ at $\mathbf{r}_1$ at time t_1 and a state $\psi_{r_2}^{(2)}$at $\mathbf{r}_2$ at time t_2. In this way, they finally arrive at the following expression for $S(\mathbf{k}, t_2, t_1)$:

$$S(\mathbf{k}, t_2 t_1) = S(\mathbf{k}, t_1) \exp\left[-C \int_{t_1}^{t_2} \mathrm{d}t \{Kk^2 + A(t)\}\right], \; t_2 > t_1. \tag{78}$$

with $C = Mk^2$ if the order parameter is conserved.

The need for unequal-time correlation functions arises from the fact that some techniques probe the system not instantaneously, but over a certain period of time. For example, in an ultrasonic attenuation experiment, a time ~ (1/frequency) is involved. Similarly, in a neutron inelastic scattering experiment, fluctuations on a time scale $t \sim (\hbar/\Delta E)$ are explored where ΔE is the energy transfer (Brockhouse 1958). Now in a system in thermodynamic equilibrium, one can exploit the fact that the system is stationary and express a correlation function of the form

$$\langle \psi(t)\, \psi(t') \rangle \text{ as } \langle \psi(0)\, \psi(t'-t) \rangle.$$

Stationarity however does not obtain in our kind of situations. At best, one can divide the whole time range into suitable slots, and hope for stationarity within each slot (Stratanovich 1963).

Figure 46 offers a schematic comparison of the measurement of equal-time and unequal-time correlation functions. The total time span from $t = 0$ (instant of quench) to $t = \infty$ (when terminal equilibrium is attained) is imagined to be divided into convenient (not necessarily equal!) intervals such that there is local stationarity in each time slot in the Stratanovich sense. An experiment like x-ray diffraction if done in real time, would give the "average" structure for each time slot. Fluctuations *within* each slot will not be explored. For that, it is necessary to either use a "frequency sensitive" probe or directly a correlation technique. Owing to the overall nonstationary nature of the process, the correlation function $C(k, \tau; n)$ will depend on the index n of the time slot.

As just indicated, one method of exploring fluctuations is to employ a frequency-dependent probe like slow neutron inelastic scattering. Billotet and Binder (1980) have used their model for fluctuations to compute $S(k, \omega; n)$. Their spectra show pronounced deviations from the usually expected Lorentzian line shapes; also there are oscillations. However, they obtain negative cross-sections which, as they themselves note, is unphysical. Billotet and Binder attribute this to the inadequacy of their approximations. If earlier experience in the theory of liquids is any guide (de Gennes 1959), then I suspect that the trouble probably lies in the fact that the decoupling approximation for P has failed to respect the relevant sum rules.

While as of now theory is in a somewhat poor shape, there is nothing to prevent experimenters from studying fluctuations under nonequilibrium conditions using the various probes at their disposal. In particular, slow neutron scattering, ultrasonic

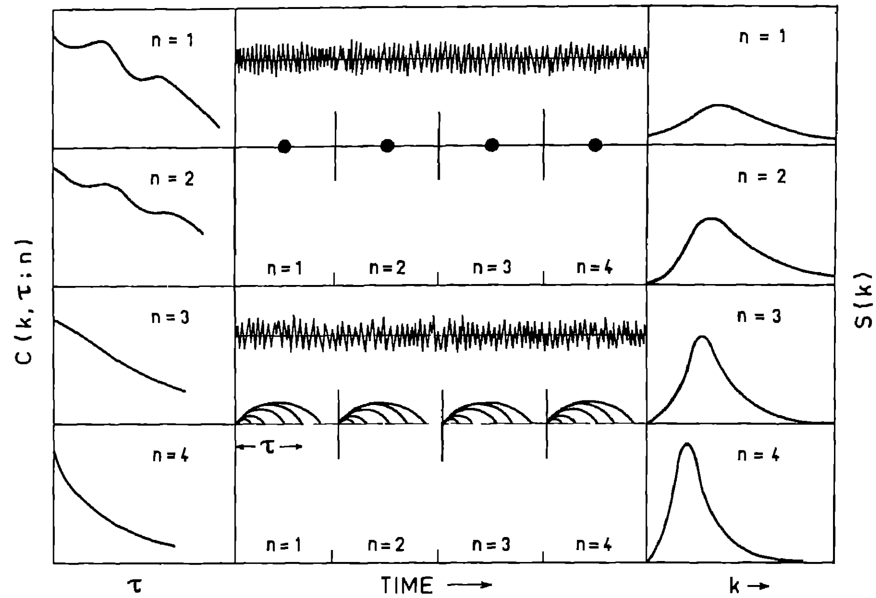

Figure 46. Shown in the middle are signals and their compartmentalization into slots indexed by n. In each slot, there is assumed to be stationarity. A conventional x-ray experiment measures equal-time correlation function for each slot, and the results finally appear as on the right. By performing an intensity correlation experiment in each slot, one can obtain information related to $\langle \psi(k, t)\psi(k, t+\tau) \rangle_n$ for each slot. Sketches of $C(k, \tau; n)$ are given on the left. For each n, one will have different $C(\tau)$ plots for the different k's.

attenuation, internal friction are some of the tools which could be tried. Vigorous experimentation could in fact act as a spur to theory!

An alternative method of exploring unequal-time correlation functions is to resort to the newly emerging technique of fluctuation spectroscopy (Magde 1977; Venkataraman 1982). Here one observes a suitable quantity Q (which couples to the order parameter) over a time span corresponding to one of our slots, and records all its fluctuations. One then processes the data to obtain $\langle Q(t)Q(t') \rangle_n$. One example of fluctuations observed by neutron scattering is given in figure 47 (Pederson and Riste 1980). Of course in this particular example the system was in a stationary state but that is not necessarily a requirement. In fact, Kim *et al* (1978) have carried out a similar experiment but using light, and have actually studied phase separation kinetics in a fluid binary mixture. Intensity fluctuation spectroscopy (Berne and Pecora 1976) is being regularly used for exploring biophysical problems but its use in condensed matter physics is still rare. Where alloys are concerned light scattering is not possible but one could resort to a study of resistivity fluctuations (*e.g.* Venkataraman and Balakrishnan 1979). No such experiment relating to kinetics of phase separation in solids has been reported so far. However, Kim *et al* (1980) have used precisely this technique to study fluctuations in a binary fluid mixture near its critical point. If sufficient intensity is available, even x-ray and neutron experiments to explore fluctuations in the time domain can be attempted. In brief, the entire subject of fluctuations during decay to equilibrium is largely unexplored both theoretically and experimentally.

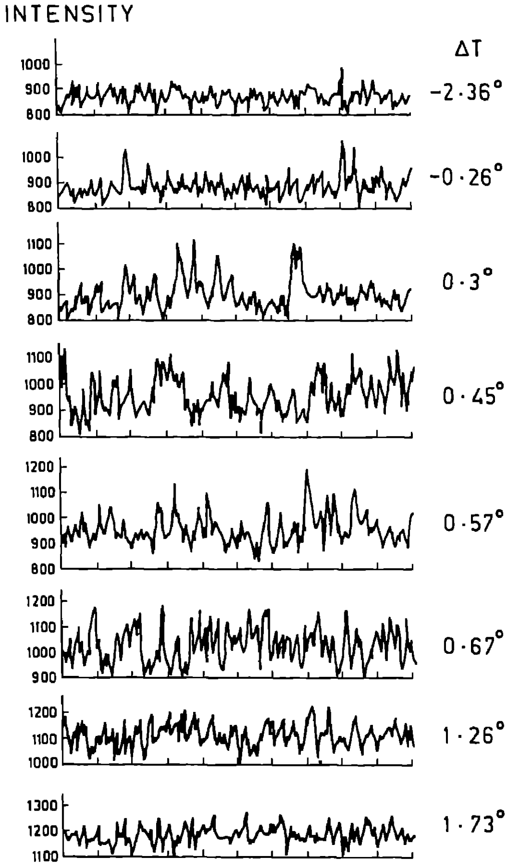

Figure 47. Fluctuations of the scattered neutron intensity from a liquid crystal with a temperature gradient across. The system is in a stationary but nonequilibrium state. Observe that as the temperature gradient is varied, the fluctuation amplitude becomes large at a certain stage. This is associated with the onset of turbulence in the material (after Pedersen and Riste 1980).

6. Lamellar eutectic growth

In addition to the solid-to-solid transformations so far considered, certain liquid-to-solid transformations are also interesting, besides being important technologically. To understand such transformations, we refer to figure 48 which shows a binary phase diagram of the type we are currently interested in. For example, Ag-Cu and Pb-Sn systems exhibit such diagrams. Consider an alloy of composition C_0 and at a temperature such that its state is represented by the point *a* in the figure. On cooling and crossing the liquidus curve, one enters the region marked $(\alpha + L)$ which is a two-phase region where a liquid and a solid both coexist, the solid with composition C and the liquid with composition C_L. The relative proportions of the solid and the liquid vary continuously as one moves down the line *abc* until at the temperature T_E called the eutectic temperature, the liquid (of composition C_e) freezes. Of course one could come down along *df*; then one would have a pure liquid phase until T_E at which point freezing occurs. This phase transformation *i.e.*, the freezing of the eutectic liquid is often called a eutectic reaction.

The solid state microstructure of the material having the composition C_e will be an intimate mixture of two phases α and β which are often present in the form of thin (around a few microns) platelets or rods. The lamellar microstructure of a typical

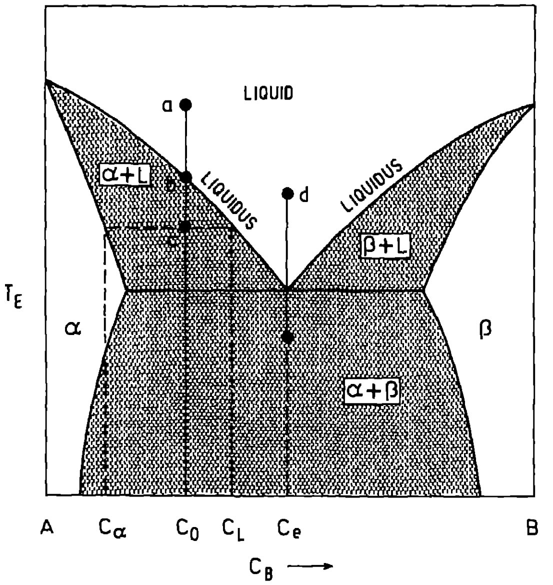

Figure 48. Illustration of the eutectic reaction.

eutectic is shown in figure 49 (Lyman 1972). The pattern is quite striking, undoubtedly reminding physicists of the patterns associated with hydrodynamic instabilities, for example. Indeed Langer has recently noted such similarities and has pointed out that as in the well-known Benard patterns associated with convective instability, the relevant steady state equations are incapable of predicting the unique behaviour observed experimentally. Specifically, the steady state theory of lamellar eutectic permits a wide range of lamellar spacings at any growth velocity whereas experiments seem to indicate a unique spacing. Accordingly, Datye and Langer (1981) have performed (as in hydrodynamics) a stability analysis for a model thinfilm eutectic. A major conclusion to emerge is that for off-eutectic compositions, there occurs a short wavelength instability. Figure 50 taken from the work of these authors shows a sketch of the oscillatory mode at its point of marginal instability. There is apparently some evidence from experiment for the existence of such a mode. As Langer notes, there is scope for much more work in this area both experimental and theoretical (especially in relation to kinetics). It certainly would be interesting to attempt experiments which are the analogue of those discussed in figure 47.

7. Summary

In this article, a broad overview of phase transformations has been attempted, essentially from a physicist's angle. While there are many aspects that might appeal to physicists, three areas have been highlighted since overlap with physics is manifestly evident. They are: The study of ground structures, the study of phase diagrams and the study of kinetics. In each area there are no doubt specifics and important details such as metallurgists are usually interested in, but there are also general features amenable to a basic analysis which physicists are likely to be attracted to.

In the area of ground state structures, the emphasis thus far appears to have been mainly on structures derived from bcc and fcc lattices. There is an obvious need to

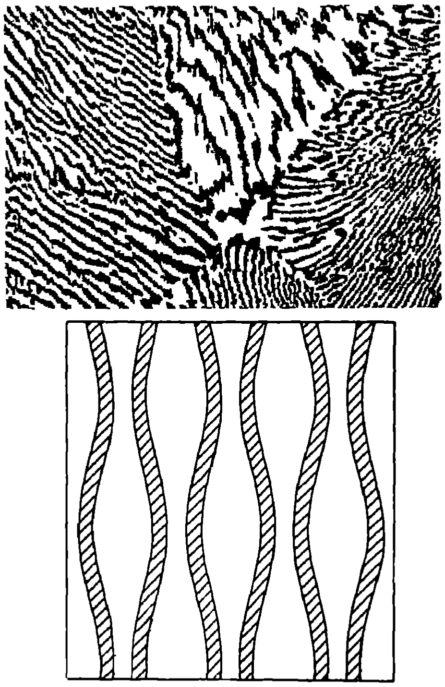

Figure 49–50. **49.** Picture of a 63 Sn-37 Pb eutectic (softsolder). The lead-rich solution appears dark in a matrix of tin lamellae (light) (after Lyman 1972). **50.** Oscillatory mode at its point of marginal instability (after Datye and Langer 1981).

extend this to other systems like hcp etc. We call attention also to formal papers (Progov and Sinai 1975, 1976; Slawny 1979) on the subject lest such activity be dismissed as pedestrian! Inputting potential derived from first principles has thus far been largely avoided but given the vast progress made in pseudopotentials in recent years and the prospects for bigger and faster computers, one could envisage a new thrust. No doubt there is the additional complication of relaxation energy (see equation (19)) but one now knows how to handle this, at least in principle.

Study of phase diagrams *via* simulation has made impressive progress but there is still a vast territory ahead. The viability of the CVM has been well established although there is room for improvement both in terms of going to larger clusters (which, incidentally, will call for fresh computational ingenuity) as well as allowing the exchange integral to vary with composition. The possibility of frustration is a stimulating discovery and so far, theory has not addressed itself to this question. Given the vigorous study made of this concept in spin glass, one could envisage exciting new vistas in the study of ordered systems also. The mappings that phase diagram investigations have achieved vis-a-vis models popular in the study of magnetism should act as an extra stimulant to physicists. Indeed one could probably now hunt around for suitable systems which are proving grounds for various kinds of Potts model etc.

As regards kinetics, there is a pressing need for real-time measurements. This therefore is an area where physicists can make important contributions, given their vast experience with the study of relaxations. Of course the experiments may not be always easy, and ingenuity may be required in many cases! Correlation techniques have a bright future if one is bold enough to apply them (although theoretical support for interpretation is at present not available). Neutron scattering and x-ray scattering (especially using synchrotron radiation sources) are the preferred tools but others like

Mössbauer spectroscopy, ultrasonic attenuation and even resistivity can provide useful complements, being less expensive and also less time-consuming. Thus, while neutron scattering could be reserved for select measurements, back-up wide ranging scans can come from the other probes mentioned. Where theory is concerned, the area of kinetics is a veritable jackpot in as much as one is faced with fascinating questions about phase changes far from equilibrium.

To keep the discussion relatively simple we have confined ourselves to substitutional systems (usually, metals with metals give such systems). If we extend consideration to systems where the B atoms enter interstitially in A (*e.g.* 0 in Ti), then it opens up a new world altogether. And then there are ternaries. No doubt they complicate matters, but who knows what surprises they have in store? In addition, there are the mixed oxides and mixed glasses which too, under certain circumstances, show phase separation. The interesting point about these systems is that they are amenable to study by light scattering (Schroder 1977), a technique we have barely mentioned. In respect of light scattering, the new wave of interest on colloidal crystals (Pieranski 1983) is also noteworthy. It is quite conceivable that various kinetic studies of colloidal crystals can be performed using laser light the way one usually investigates alloys using x-rays.

We have stayed away from defects, for example vacancies. One knows vacancies affect diffusion and therefore the role of vacancies may require examination. Perhaps for the present, these questions are best left to the metallurgists!

We have also not dwelt much on microstructure. Metallurgists relish them! Certainly the patterns are fascinating but one tends to dismiss any underlying universality on the grounds that microstructure is probably controlled by local factors like dislocation density etc. This may be true to some extent but at the same time it is difficult to believe that Nature has no basic rules governing domain formation etc. Now that some links between defects and symmetry have been established (Mermin 1979), it is worth searching for possible universalities governing microstructure formation and evolution. Such deep insight can come only from physics but it requires a really bold venture!

8. Concluding remarks

The story goes that towards the end of the twenties when the Golden Age of quantum mechanics was drawing to a close, Dirac remarked that, 'the rest is all chemistry'. Such an extreme view of physics has continued to prevail, and as late as 1970, van Hove (who has himself made notable contributions to condensed matter physics) observed during an after-dinner address at the Batelle Colloquium on Critical Phenomena that, "We should constantly recall and reassert that the elucidation of the fundamental laws remain the most essential task of physics". Referring to critical phenomena and topics of a similar kind he said, "It seems to me that physics now looks more like chemistry in the sense that in percentage, a much larger portion of the total research activity deals with complex systems, structure and processes, as against a smaller fraction concerned with the fundamental laws of motion and interaction. This Colloquium is a good example. Surely we all believe that the fundamental laws of classical mechanics, of the electromagnetic interaction and of statistical mechanics dominate the multivarious transitions and critical phenomena you discuss this week, and I presume that none of you expects his work on such problems to lead to the modification of these laws. You know the basic equations better than the phenomena. You are after the missing link between them *i.e.* the intermediate concepts ". . . . which should allow a quantitative understanding and prediction of the phenomena . . . ". Domb (1981) from whose essay on Critical Phenomena these quotes have been extracted, strongly disputes such a narrow interpretation of the goals of physics and points out that the goal is not restricted to the discovery of fundamental laws alone but encompasses the understanding of natural phenomena in general. Asserting that the giants of the past followed such an approach Domb observes, "Clerk Maxwell tried to construct a mechanical model to illustrate Faraday's laws of induction. He drew heavily on the theory of vortices in a perfect fluid and classical elasticity and was thereby led to introduce his famous displacement current. It was only later that he removed the 'scaffolding' to reveal the beautifully symmetric pattern of Maxwell's equations".

It is ironic that just around the time van Hove expressed his misgivings, Wilson did his celebrated work on critical phenomena which later earned for him the highest accolade of Science— the Nobel Prize. More significant, this paved the way for important feedback from statistical mechanics to particle physics (— *e.g.* there have been Monte Carlo simulations in connection with lattice gauge theories (Callaway and Rahman 1982), not dissimilar to the simulations discussed in §3.3).

In a different context, Anderson (1972) too has taken exception to the excessive importance attached to the study of fundamental laws. He observes, "The ability to reduce everything to simple fundamental laws does not imply the ability to start from those laws and reconstruct the Universe. In fact, the more the elementary particle physicists tell us about the nature of the fundamental laws, the less relevance they seem to have to the very real problems of the rest of science, . . .". Illustrating his point with examples from many-body physics, he questions whether a cooperative phenomenon like symmetry breaking (which lies at the heart of a phase transition) can be predicted starting purely from a knowledge of the basic interaction between the constituent elementary objects. As he succinctly puts it, more is different! Incidentally, symmetry breaking is another area where there has been a profitable feedback from condensed matter physics to particle physics.

The purpose of the above remarks and quotes is not merely to reinforce the point that condensed matter physics can as much be a frontier area, as, say, particle physics but also to remind condensed matter physicists that they in turn should avoid a snooty attitude towards materials science. As we have tried to argue in this article, there are many fascinating questions in materials science also, buried in the 'complexities' that traditional physicists shun. For those who dare to delve into these complexities and isolate the basic questions, the rewards could be great.

Beauty, it is said, is in the eyes of the beholder. Where physics is concerned, something similar appears to be true. The physics, turned out, often depends more on the investigator than on the phenomenon (at least the usual perception one has of it). We merely have to remind ourselves of the magical touch that Einstein gave to the observations of the botanist Robert Brown on the dancing pollen grain. What if he had dismissed it as 'not physics'?

In this country, Prof. Ramaseshan was perhaps the first person to establish a bridge between physics and materials science in a big way. Reared in the traditions of the Raman School, where the emphasis always was on natural phenomena in their totality, he was not averse to taking on the problems of materials when the challenge came. On the other hand, he invariably put to use his rich experience in physics and demonstrated that by doing so, one could introduce novel approaches to familiar problems. Not surprisingly, he made the plea at Baroda for a larger perspective while defining Thrust Areas. It has been a pleasant task for me to amplify and illustrate that theme through this article. I only hope it does full justice to his remarks.

Acknowledgements

My interest in this area was aroused by the lectures I heard a few years ago at Varenna given by Prof. de Fontaine. I am grateful to him for subsequently sending me several of his reprints and preprints which helped me dig deeper into the subject. I would also like to express my thanks to Dr D Sahoo for several discussions, to Radha Ranganathan for assistance with the preparation of the manuscript, to P Subba Rao for efficient and skilful typing and to P Harikumar and R Kannan for taking care of the graphics. Finally, I would like to acknowledge my indebtedness to the many authors whose work I have freely drawn upon in preparing this review.

References

Allen S M and Cahn J W 1972 *Acta Metall.* **20** 423
Anderson P W 1972 *Science* **177** 393
Aubrey S 1981 in *Physics of defects* (ed) R Balian et al (Amsterdam: North Holland) p 431
Aubrey S 1983 *J. Phys.* **44** 147
Bardhan P, Chen H and Cohen J B 1977 *Philos. Mag.* **35** 653
Barker J A 1953 *Proc. R. Soc.* (*London*) **A216** 45
Berne B J and Pecora R 1976 *Dynamic light scattering* (New York: Wiley)
Bethe H A 1935 *Proc. R. Soc.* (*London*) **A150** 552
Billotet C and Binder K 1979 *Z. Phys.* **B32** 195
Billotet C and Binder K 1980 *Physica* **A103** 99
Binder K 1973 *Phys. Rev.* **B8** 3423
Binder K 1977 *Phys. Rev.* **B15** 4425
Binder K 1980a *Phys. Rev. Lett.* **45** 811
Binder K 1980b in *Systems far from equilibrium*, Lecture Notes in Physics 132 (ed) L. Garrido (Berlin: Springer)
Binder K 1981 *Z. Phys.* **B45** 61
Binder K, Lebowitz J L, Phani M K and Kalos M H 1981 *Acta Metall.* **29** 1655
Binder K and Stauffer D 1976 *Z. Phys.* **B24** 407
Bragg W L and Williams E J 1934 *Proc. R. Soc.* (*London*) **A145** 699
Bragg W L and Williams E J 1935 *Proc. R. Soc.* (*London*) **A151** 540
Brockhouse B N 1958 *Nuovo Cimento* **9** (Suppl.) 45
Cahn J W 1961 *Acta Metall.* **9** 795
Cahn J W 1962 *Acta Metall.* **10** 179
Cahn J W 1968 *Trans. AIME* **242** 166
Cahn J W and Hilliard J E 1958 *J. Chem. Phys.* **28** 258
Callaway D and Rahman A 1982 *Phys. Rev. Lett.* **49** 613
Chakravarti B, Starke E A, Sparks C J and Williams R O 1974 *J. Phys. Chem. Solids* **35** 1317
Chen H and Cohen J B 1977 *J. Phys.* **C7** 314
Chen H, Comstock R J and Cohen J B 1979 *Annu. Rev. Mater. Sci.* **9** 51
Cohen J B 1970 in *Phase transformations* (ed) H I Aaronson (Metals Park Ohio: Am. Soc. Metals) p 561
Collins M F and Teh H C 1973 *Phys. Rev. Lett.* **30** 781
Cook H E 1970 *Acta Metall.* **18** 297
Cook H E, de Fontaine D and Hilliard J E 1969 *Acta Metall.* **17** 765
Clapp P C and Moss S C 1968 *Phys. Rev.* **171** 751

Das S K, Okamoto P R, Fisher P M J and Thomas G 1973 *Acta Metall.* **21** 913

Datye V and Langer J S 1981 *Phys. Rev.* **B24** 4155

de Fontaine D 1967 Ph.D Thesis (Evanston Ill: Northwestern University)

de Fontaine D 1975a in *Treatise on solid state chemistry* (ed) N B Hannay (New York: Plenum) p 129

de Fontaine D 1975b *Acta Metall.* **23** 553

de Fontaine D 1979 in *Solid state physics* (eds) H Ehrenreich, F Seitz and D Turnbull (New York: Academic) Vol. 34 p 73

de Fontaine D 1981 *Met. Trans* **A12** 559

de Fontaine D 1982 in *Mechanical and thermal behaviour of materials* (eds) C Caglioti and A Ferro Milone (Amsterdam: North Holland) p 449

de Gennes P G 1959 *Physica* **25** 825

d'Heurle F M and Gordon P 1961 *Acta Metall.* **9** 304

Dienes G J 1955 *Acta Metall.* **3** 549

Domb C 1981 in *Perspectives in statistical physics* (ed) H J Raveche (Amsterdam: North Holland) p 173

Feigenbaum M J 1978 *J. Stat. Phys.* **19** 25

Feigenbaum M J 1979 *J. Stat. Phys.* **21** 665

Feigenbaum M J 1980 *Commun. Math. Phys.* **77** 65

Freidel J 1974 in *Order-disorder transformations in alloys* (ed) H Warlimont (Berlin: Springer) p 1

Gilmore R 1981 *Catastrophe theory for scientists and engineers* (New York: Wiley)

Gunton J D 1982 *First order transitions, metastability and spinodal decomposition* (Temple: University Report)

Haken H 1978 *Synergetics, An introduction* (Berlin: Springer)

Hansen M 1958 *Constitution of binary alloys* (New York: McGraw Hill)

Hashimoto T, Miyoshi T and Ohtsuka T 1976 *Phys. Rev.* **B13** 1119

Hashimoto T, Nishimura K and Takeuchi Y 1978 *Phys. Lett.* **A65** 250

Holsztynski W and Slawny J 1978 *Commun. Math. Phys.* **61** 177

Hopper R W 1982 *J. Non. Crystall. Solids* **49** 263

Iliopoulos J 1980 *Contemp. Phys.* **21** 159

Johansson C M and Linde J O 1928 *Ann. Phys.* **86** 291

Kanamori J and Kakehashi Y 1977 *J. Phys.* **38** C7 274

Katsura S and Narita A 1973 *Prog. Theor. Phys.* **50** 1426, 1750

Kawasaki K 1972 in *Phase transitions and critical phenomena* (eds) C Domb and M S Green (New York: Academic) Vol 2 p 443

Khachturyan A G 1974 in *Order-disorder transformations in alloys* (ed) H Warlimont (Berlin: Springer)

Kikuchi R 1951 *Phys. Rev.* **81** 988

Kikuchi R and de Fontaine D 1976 *Scr. Metall.* **10** 995

Kikuchi R, Sanchey J M, de Fontaine D and Yamauchi H 1980 *Acta Metall.* **28** 651

Kim M W, Chou Y C, Goldburg W I and Kumar A 1980 *Phys. Rev.* **A22** 2138

Kim M W, Schwartz A J and Goldburg W I 1978 *Phys. Rev. Lett.* **41** 651

Kozlov E V, Demetryev V M, Emelyanov V N, Kormin N M, Taylashev A S and Stern D'M 1974 in *Order-disorder transformations in alloys* (ed) H Warlimont (Berlin: Springer) p 58

Krivoglaz M A and Smirnov A A 1965 *Theory of order-disorder in alloys* (Amsterdam: Elsevier)

Kudo T and Katsura S 1976 *Prog. Theor. Phys.* **56** 435

Langer J S 1969 *Ann. Phys.* **54** 258

Langer J S 1980 in *Systems far from equilibrium* Lecture notes in Physics 132 (ed) L Garrido (Berlin: Springer) p 12

Langer J S, Bar-on and Miller H 1975 *Phys. Rev.* **A11** 1417

Langer J S and Turski L A 1973 *Phys. Rev.* **A8** 3230

Lebowitz J L, Marro J and Kalos M H 1982 *Acta Metall.* **30** 297

Lifshitz I M and Slyozov V V 1961 *J. Phys. Chem. Solids* **19** 35

Lyman T (ed) 1972 *Atlas of microstructures of industrial alloys* (Metals Park, Ohio: Am. Soc. Metals) Vol 6, p 318 (picture no: 2628)

Magde D 1977 in *Molecular biology, biochemistry and biophysics* (eds) J Pecht and R Rigler (Berlin: Springer-Verlag) p 43

Mahan G D and Claro F H 1977 *Phys. Rev.* **B16** 1168

Mermin N 1979 *Rev. Mod. Phys.* **51** 591

Morita T 1972 *J. Math. Phys.* **13** 115

Nowick A S and Weisenberg L R 1958 *Acta Metall.* **6** 260

Ogawa S 1974 in *Order-disorder transformations in alloys* (ed) H Warlimont (Berlin: Springer) p 240

Oki K, Sagane H and Eguchi T 1974 *Jpn J. Appl. Phys.* **13** 753

Oki K, Yamamura A, Masaka M and Eguchi T 1977 *Trans. Jpn Inst. Metals* **18** 520

Onsager L 1944 *Phys. Rev.* **65** 117

Ornstein L S and Zernike F 1914 *Proc. Acad. Sci. (Amsterdam)* **17** 793

Paulson W M and Hilliard J E 1977 *J. Appl. Phys.* **48** 2117

Pedersen A M and Riste T 1980 *Z. Phys.* **B37** 171

Pieranski P 1983 *Contemp. Phys.* **24** 25

Progov S A and Sinai Y 1975 *Theor. Math. Fizika* **25** 358

Progov S A and Sinai Y 1976 *Theor. Math. Fizika* **26** 61

Radelaar S and Ritzen J M J 1969 *Phys. Status Solidi* **B31** 277

Richards M J and Cahn J W 1971 *Acta Metall.* **19** 1263

Sanchez J M and de Fontaine D 1978 *Phys. Rev.* **B17** 2926

Sanchez J M and de Fontaine D 1980 *Phys. Rev.* **B21** 216

Sanchez J M and de Fontaine D 1982 *Phys. Rev.* **B25** 1759

Sato H and Toth R S 1961 *Phys. Rev.* **124** 1833

Schwahn D and Schmatz W 1978 *Acta Metall.* **26** 1571

Shockley W 1938 *J. Chem. Phys.* **6** 130

Shroder J 1977 in *Treatise on materials science and technology* (eds) M Tomozowa and R H Doremus (New York: Academic Press) Vol 12 p 158

Singhal S P, Herman H and Koztorz G 1978 *J. Appl. Crystall.* **11** 572

Slawny J 1979 *J. Stat. Phys.* **20** 711

Stanley H E 1971 *Introduction to phase transitions and critical phenomena* (Oxford: Clarendon)

Stratanovich R L 1963 *Topics in the theory of random noise* Vol 1 (New York: Gordon and Breach)

van Baal C M 1973 *Physica* **64** 571

van Hove L 1953 *Phys. Rev.* **89** 1189

Venkataraman G 1979 *Bull. Mater. Sci.* **1** 129

Venkataraman G 1982 in *Mechanical and thermal behaviour of materials* (eds) C Caglioti and A Ferro Milone (Amsterdam: North Holland) p 278

Venkataraman G and Balakrishnan V 1977 in *Proceedings of the Indo-German Seminar on Radiation Damage* (Kalpakkam: RRC) p 273

Venkataraman G and Balakrishnan V 1979 *Mater. Sci. Bull. (India)* **1** 59

Villain J 1959 *J. Phys. Chem. Solids* **11** 303

Vineyard G H 1956 *Phys. Rev.* **102** 981

Wagner C 1961 *Z. Electrochem.* **65** 243

Wulff J 1971 (ed) Structure and properties of materials (Bombay: Wiley-Eastern) Vol II

Yamauchi H and de Fontaine D 1974 in *Order-disorder transformations in alloys* (ed) H Warlimont (Berlin: Springer) p 148

Bull. Mater. Sci., Vol. 6, No. 5, September 1984, pp. 901–922. © Printed in India.

Growth of research and development in rare metals extraction in India

C V SUNDARAM and C K GUPTA*

Reactor Research Centre, Kalpakkam 603 102, India

* Extractive Metallurgy Section, Bhabha Atomic Research Centre, Trombay, Bombay 400 085, India

Abstract. The ushering in of the era of high technology in our country witnessed the emergence and growth of several new technologies which are either totally unconventional or less common in otherwise well known and established areas of industrial practice. A vivid example of the second category of advances is found in the development of extractive processes for obtaining the less common metals particularly required for service in nuclear, aerospace and electronics industries. In this paper, the growth of research and development in rare metals extraction in India is surveyed from its infancy in the fifties to the present stature of a firm footed technology accredited with several directed achievements and well-developed maturity.

Keywords. Rare metal extraction; physical beneficiation; chemical beneficiation; breakdown process; separation process; halide metallurgy; electrolytic reduction.

1. Introduction

One of the greatest technological upheavals in the history of human civilization was triggered by the second world war. During the post war period a large spectrum of high technology industries flourished. The frontiers of established technologies expanded and new highways opened up in the hitherto unexplored regions. The march of human progress entered into what is variously referred to as the nuclear age, the space age and the electronics age.

If one looks at the mainstream technologies which defined the direction and sustained the momentum of such a total technological advance, achievements in metals and materials development stand out, having played a vital role. The development of appropriate metals and materials has always been crucial to transform scientific ideas into practical realities.

We witness today, in our country, wide-ranging activities in the fields of science and technology. Since independence, we have come a long way in securing such an expansion. It is a matter of pride that we observe in the national scene massive development programmes in a number of advancing technological areas, as for instance, in nuclear energy, aeronautics and aerospace, electronics and oceanography—thanks to the efforts made and the support given to usher in this new era.

Tracing back the sequence of science and technology development, it would seem to have started with the launching of the atomic energy programme in the country. Following the institution of the Atomic Energy Commission (AEC) and the modest beginnings made in the early fifties, many disciplines of science and engineering—of relevance to this programme—have evolved and flourished. The wide variety and scope in these disciplines have enabled the progressive transfer of the experience to other areas of science and technology. Developments in space, aeronautics and electronics have gradually entered the national scene.

Any discussion on technological growth has to lead a discussion on materials development which constitutes the supporting structure like a back bone. As indicated in figure 1, while many of the ferrous and non-ferrous metals that are in every day use, are also required for peripheral structural applications in modern technology, they are not adequate for the critical core component applications in these technologies. Several members of the rare metals group *viz* beryllium, titanium, zirconium, hafnium, vanadium, niobium, tantalum, thorium, uranium, plutonium and the rare earths, possess the unique combination of physicomechanical, nuclear, electronic, and chemical properties. Taken together, these characteristics have qualified many of the above mentioned metals for core component applications.

The extractive processes to obtain this specific family of metals indigenously at sufficient purity levels and in adequate quantities were not initially available. The development programme of AEC, however, proceeded on the basic assumption that as it progresses, an adequate, dependable and continuing supply of appropriate metals and materials will be assured. To relieve the dependence on overseas sources for the strategic materials and to keep scientific and technological progress from being impeded or slowed down by materials shortages, pursuits on metals and materials development received close attention. It is needless to mention here that without a strong and sound materials base, it is difficult to attain, in the long run, technological self-sufficiency, particularly in the frontier areas.

India is fortunately blessed with significant raw material reserves with respect to many of the strategic metals. Complete and proper utilization of our natural rare metal resources presupposes the availability of a comprehensive body of scientific knowledge and engineering experience in the field of metal processing. An organization with multidisciplinary resources and skill to support a large spectrum of research projects in virtually all phases of metallurgy (figure 2) could accomplish this feat. This responsibility was thus taken over by the various laboratory and industrial units of the Department of Atomic Energy and, in particular, by the Bhabha Atomic Research Centre (BARC). "Growth of R & D in rare metal extraction in India" then predominantly

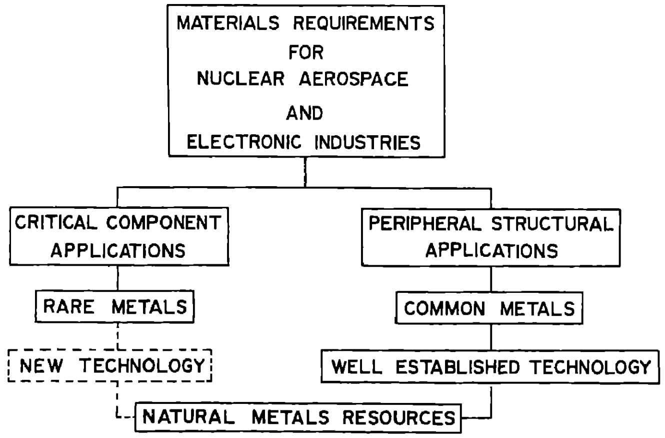
MATERIALS REQUIREMENTS FOR NUCLEAR AEROSPACE AND ELECTRONIC INDUSTRIES
CRITICAL COMPONENT APPLICATIONS
PERIPHERAL STRUCTURAL APPLICATIONS
RARE METALS
COMMON METALS
NEW TECHNOLOGY
WELL ESTABLISHED TECHNOLOGY
NATURAL METALS RESOURCES

Figure 1. Status of materials requirement in high technologies.

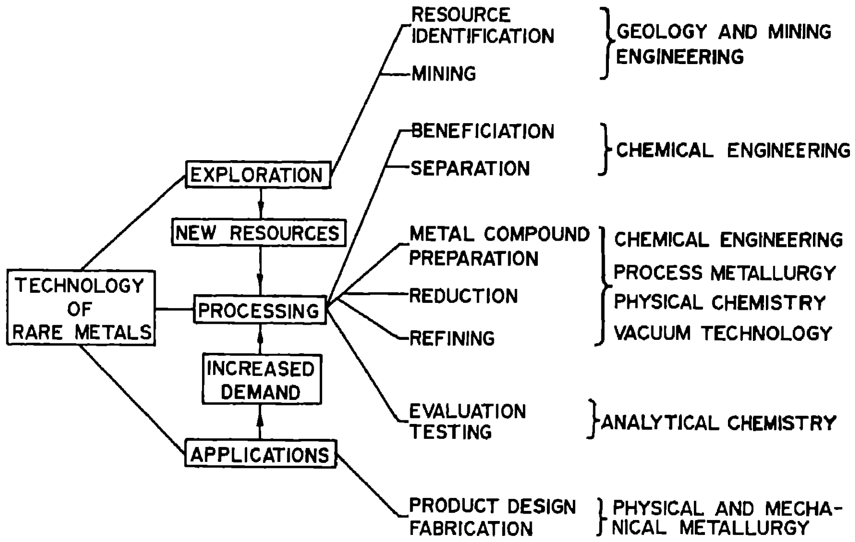

Figure 2. Multidisciplinary content of rare metal extraction.

pertains to tracing the process metallurgy activities of the DAE family during the past three decades.

2. Definition of rare metals extraction

Extractive metallurgy consists of the science and art of winning metals from the mined ore. For most common metals, the extractive metallurgy means the sequence of roasting, smelting and refining operations as indicated in figure 3. This scheme has characteristically failed to work in the extraction of many of the rare metals with which this presentation is concerned. Rare metals occur in nature in very complex forms, often in very low concentration. The procedures involved for recovering metal values are very elaborate, complex and require special equipment, processes and skill. Further, these metals show a high degree of sensitivity to impurities, which influence pronouncedly their physical, chemical and metallurgical properties. This dictates that the rare metals be properly protected at every stage of their production and use.

Broadly, the process sequence for rare metals, as indicated in figure 3 consists of the all important separation step followed by specialised reduction and refining operations. As a further elaboration, figure 4 presents a generalised scheme for rare metal extraction. For an appreciation of such a sequence, a brief reference may be drawn to the extractive metallurgy of niobium, the flow sheet for which appears in figure 5.

The joint occurrence of niobium and tantalum in nature conditioned by their close chemical similarities and the difficulties in separating them from each other halted their industrial development. In the past three decades, with substantial growth in demand and also in technology, complete flowsheets have been developed to get the pure metals in sufficient quantities.

The beneficiated columbite-tantalite ore is fed to the separation step. A pyrovacuum method was first attempted to separate the metals by chlorination but a hydro-

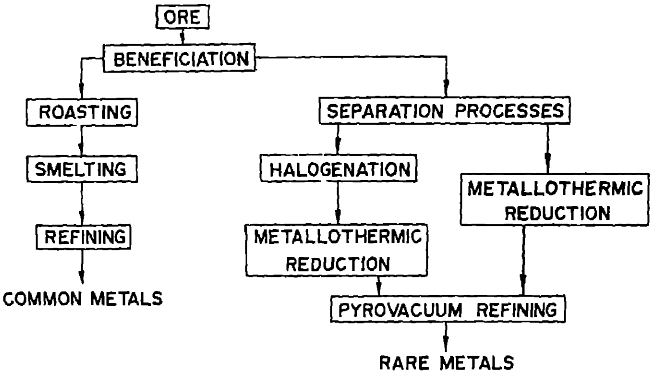

Figure 3. Extraction sequences for common and uncommon metals.

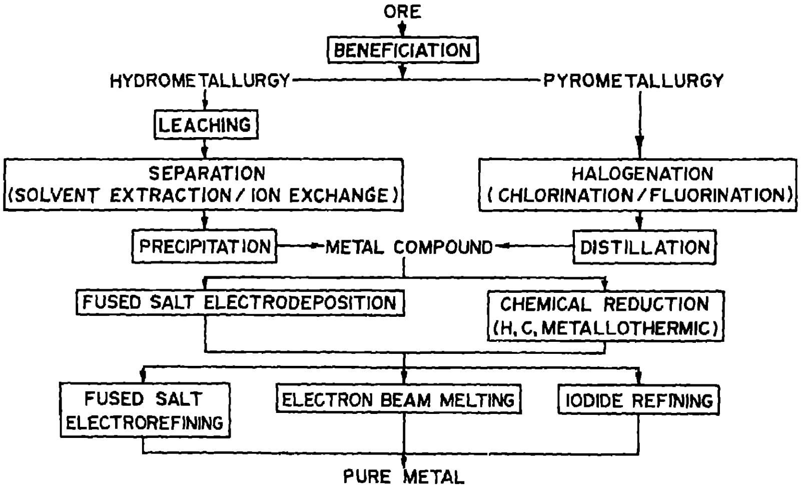
ORE
BENEFICIATION
HYDROMETALLURGY
PYROMETALLURGY
LEACHING
SEPARATION (SOLVENT EXTRACTION/ ION EXCHANGE)
HALOGENATION (CHLORINATION/FLUORINATION)
PRECIPITATION
METAL COMPOUND
DISTILLATION
FUSED SALT ELECTRODEPOSITION
CHEMICAL REDUCTION (H, C, METALLOTHERMIC)
FUSED SALT ELECTROREFINING
ELECTRON BEAM MELTING
IODIDE REFINING
PURE METAL

Figure 4. Generalised scheme for rare metal extraction.

metallurgical route involving solvent extraction of the fluoride leach liquor of the beneficiated columbite-tantalite found industrial acceptance sooner. Pure niobium pentoxide obtained after the separation step is converted to the metal by either carbothermic reduction at high temperatures under vacuum or aluminothermic reduction and pyrovacuum refining. Depending on the purity desired, primary niobium is subjected to electron beam melt refining/electron beam floating zone refining to obtain the final product.

Now one can see the path niobium ore travels before it becomes metal. It may be added here that niobium is a well-behaved member of the rare metal family, and in many cases we may have to encounter tougher reactive rare metals.

3. Indian experience in rare metal extraction

The Indian experience in rare metal extraction has been founded on a commitment to provide means by which the current and emerging demands for special metals and

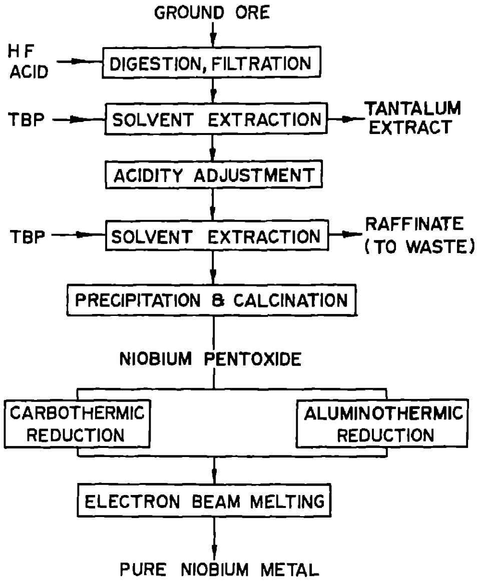

Figure 5. Flow sheet for niobium extraction.

materials in our country could be met. The emphasis has been on developing techniques effective on our indigenous resources. It is needless to say that this development of technology being totally indigenous, we encountered several teething troubles with respect to some processing steps due to scale up which were successfully overcome by persistent efforts. Every effort was made to introduce indigenous equipment which posed considerable problems and cost considerable time. Based on the research and development work at BARC administered mainly under the metallurgy, chemical engineering and chemistry groups, techniques and processes have been successfully evolved and developed to levels conducive to setting up of production plants. By way of some typical examples, mention may be made of:

—uranium oxide and metal production, involving ore leaching, ion exchange, solvent extraction, calcination, hydrofluorination and chemical reduction, induction melting, high temperature sintering and further fabrication;

—zirconium metal production by alkali fusion of zircon, solvent extraction, calcination, chlorination, magnesium reduction and vacuum distillation, vacuum arc melting, extrusion and pilgering;

—tantalum metal production by hydrofluoric acid dissolution of columbite-tantalite, solvent extraction, sodium reduction, powder metallurgy and electron beam melting;

—beryllium metal production by silicofluoride sintering of beryl, leaching, purification, fluoride decomposition, magnesium reduction, vacuum melting and vacuum hot pressing.

The experience has led to the setting up of the Nuclear Fuel Complex (NFC) at Hyderabad which for the past ten years has been engaged in the production of a range of nucler and special materials. Based on the parallel investigation on titanium sponge production and pilot plant demonstration at NFC, a larger production plant for the metal is under establishment at the Defence Metallurgical Research Laboratory (DMRL), Hyderabad. The pilot plant for beryllium, set up at Vashi, New Bombay has commenced operation.

Starting off from this introductory indication of the scope and level of directed R & D efforts that have gone into the emergence and rise of India in the rare metals field in the world, it is now appropriate to proceed a coverage of the Indian experience in more representative detail by looking at each of the unit operations in turn.

4. Physical beneficiation

It is a characteristic of all the rare metal resources that they occur as dilute, multicomponent complex minerals widely dispersed and distributed in various geological formations. Development of beneficiating techniques for these ores has, in fact, grown into a technology of lean ore beneficiation. This technology has also aided in many instances in the beneficiation of lean and complex common metal resources also.

In table 1 are listed the main rare metals minerals occurring in our country. Besides there are at least twice as many secondary minerals for each of these metals. There are then the second line reserves to be prospected. The principal beneficiating methods which are at our disposal are indicated in figure 6. One or more of these methods in combination have been employed for beneficiation. It is instructive to briefly review the processes applied to the important resources of many rare metals, beach sands.

Table 1. Important rare metal resources

Metal	Mineral	Composition	Location
Th	Monazite	(Ce, Y, Ca, Th) PO_4	Beach sands of Kerala, Orissa, Andhra Pradesh, Tamil Nadu
Zr	Zircon	$ZrSiO_4$	Beach sands
Ti	Ilmenite Rutile	$FeTiO_3$ TiO_2	Beach sands
Nb	Columbite	(Fe, Mn) Nb_2O_6	Hazaribagh, Monghyr (Bihar)
	Pyrochlore	$(Na, Ca)_2$ Nb_2O_6 (OH, F)	Dharmapuri Dist (TN), Khammam (AP), Gujarat, Bhilwada Dist (Rajasthan)
	Samarskite	$(Fe, Y, U)_2(Nb, Ti, Ta)_2O_7$	Pegmatites of Hazaribagh, Nellore, Jaipur and Tonk Dist of Rajasthan
Ta	Tantalite	(Fe, Mn) $(Ta, Nb)_2O_6$	Hazaribagh, Monghyr (Bihar)
	Microlite	$(Ca, Na)_2$ Ta_2O_6 (O, OH, F)	Hazaribagh, Monghyr (Bihar)
Be	Beryl (aquamarine, emerald, heliodro, morganite)	Al_2Be_3 (Si_6O_{18})	Bihar, Rajasthan, AP, MP.,
U	Uraninite	$(U_{1-x}^{+4}\, U_x^{+6})O_{2+x}$	Jaduguda, Singhbhum (Bihar)
	Pitchblende	Variety of uraninite	South Kanara (Karnataka)

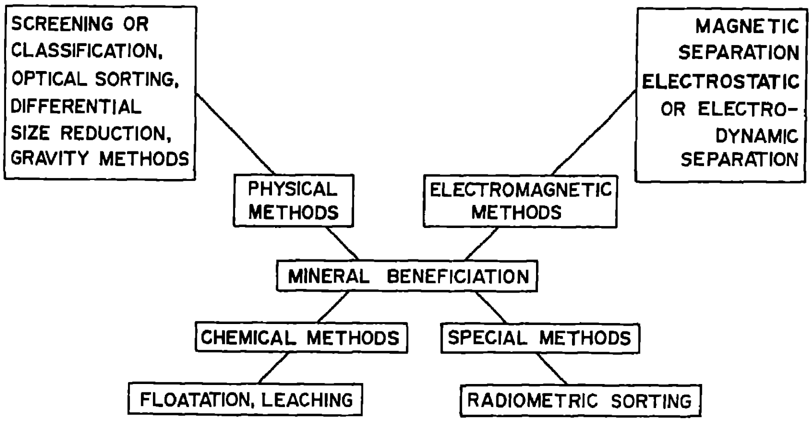
SCREENING OR CLASSIFICATION, OPTICAL SORTING, DIFFERENTIAL SIZE REDUCTION, GRAVITY METHODS
MAGNETIC SEPARATION ELECTROSTATIC OR ELECTRO-DYNAMIC SEPARATION
PHYSICAL METHODS
ELECTROMAGNETIC METHODS
MINERAL BENEFICIATION
CHEMICAL METHODS
SPECIAL METHODS
FLOATATION, LEACHING
RADIOMETRIC SORTING

Figure 6. Beneficiation techniques for rare metals resources.

Table 2. Typical mineral composition of monazite sands

Constituent	Percent
Monazite	0·5–1
Ilmenite	65–80
Rutile	3–6
Zircon	4–6
Sillimanite	2–5
Garnet	1–5

The commonly occurring minerals in beach sand deposits are ilmenite, rutile, zircon, monazite, sillimanite and garnet. Table 2 gives the typical mineral composition of the beach sands. The beach sand minerals occur extensively but in small concentrations in the alluvial deposits. The sand is mined by suction dredging and subjected to preconcentration with a view to obtain a bulk gravity concentrate comprising the heavy minerals. The lean sand deposit containing 2–5% heavy minerals is subjected to concentration using pinched sluices, cone concentrators, spirals and wet tables to obtain a concentrate with more than 80% heavy minerals. The separation of individual minerals is carried out by dry methods. Almost all the principal mineral dressing methods *viz* screening, gravity separation, magnetic separation, electrostatic separation, froth flotation etc are employed in the recovery of economic minerals from beach sand deposits.

Monozite, ilmenite, rutile and zircon are classified as scheduled minerals according to the Atomic Energy Act of 1962. Indian Rare Earths Limited operates three beneficiating plants—two at Manavala Kurichi in Tamil Nadu and one at Chavara, Kerala. Another plant is operated by Kerala Minerals and Metals Limited. At present the country's entire need of beach sand minerals is being met by IRE and KMM. Extensive dense sand deposits along the south Orissa coast over a stretch of 150 km has been located by Atomic Minerals Division and unlike the existing dry mill beneficiating operations, the Chatrapur operation would include a wet plant also for exploiting the Orissa deposit.

5. Chemical beneficiation and breakdown processes

The tenor of the uranium ores—uraninite, pitch blends, brannerite, uranothorite and carnotite—exploited for metal production assays usually around 0·05–0·2% U_3O_8. These low grade ores are directly leached to extract the uranium values since most of the physical beneficiation techniques have not been found economically feasible. There are many methods and techniques in leaching. Ore characteristics, material handling problems, methods employed for metal recovery from the pregnant solution, tailings disposal and many other factors determine the leaching technique.

Except in the case of high grade uranium ores or ores with a high concentration of acid consuming minerals which will necessitate alkali leaching with sodium carbonate, acid leaching with sulphuric acid is particularly suited to the dissolution of uranium values from the ore. As only hexavalent uranium is soluble in aqueous solution, the leaching is performed in the presence of an oxidising agent such as MnO_2, $NaClO_3$ and $Fe_2(SO_4)_3$. Acid concentration and pH are the two important process parameters. In the case of ores containing uraninite and pitchblende, such as the one at Jaduguda, acid concentration is normally controlled by maintaining pH of 1·5 to 2. This type of leaching, under controlled pH conditions helps in preventing the dissolution of acid consuming minerals like spatite. It has been found that high concentration of phosphate in the solution influences the oxidation potentials and complicates the uranium recovery process.

Besides aqueous leaching, chemical breakdown processes involve digestion with acid or alkali solution or more drastic fusion with alkali and alkali fluorides. The major breakdown processes commonly employed in our country to solubilize the metal values are schematically outlined in figure 7. It is understood that, as broadly presented for uranium, several parameters require control for accomplishing successful breakdown operation. The beryl ore is opened up to yield water soluble Na_2BeF_4 by fusing it with sodium silicofluoride and sodium carbonate at 700°C.

Having seen so far the established and commercially operating breakdown processes, we can briefly digress to see the direction for new developments.

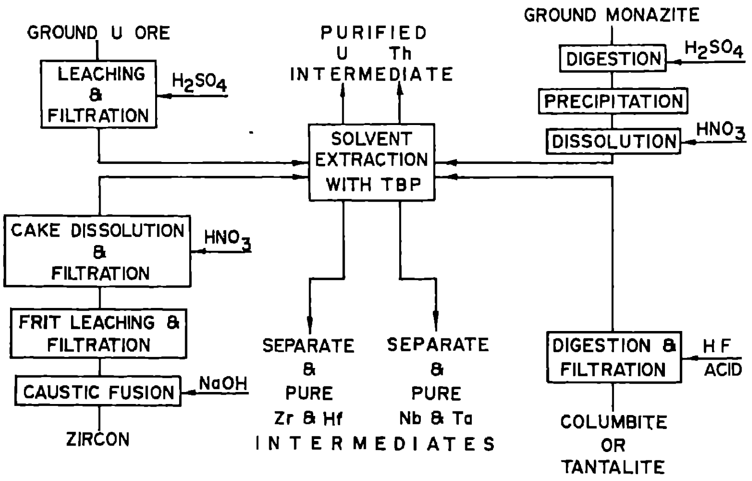

Figure 7. Schematics of ore treatment processes prior to solvent extraction separation.

A powerful new leaching technique is pressure leaching. Complex minerals like ilmenite and pyrochlore can be transformed into relatively pure oxides in a single step by treatment with hydrochloric acid at high temperature and pressure in an autoclave. References abound evidencing application of pressure leaching to many other minerals including those of uranium. A new approach to leaching low grade uranium ores is provided by the so-called bacterial or microbial leaching. Certain types of autotropic bacteria of the thiobacillus-ferrobacillus group act on the sulphate minerals like pyrite and lead to generation of ferric sulphate and sulphuric acid to leach out uranium.

Other breakdown methods developed to various levels of advancement include soda ash sintering of zircon, electrothermal smelting of ilmenite, beneficiation of ilmenite and zircon in plasma furnaces and chlorination breakdown of ores.

6. Separation processes

The leach solution obtained by chemical breakdown of the beneficiated ore is passsd through some unique sequence of "purification" operations peculiar to rare metal extraction. This purification of the pregnant rare metal solution is essentially to separate the co-occurring elements from the desired metal before it is put through subsequent reduction and refining operations. It must be emphasised that the elements co-occurring with the rare metals if allowed to proceed through the reduction step normally cannot be removed from the reduced primary metal by any of the common post reduction refining. This situation may be thought of as arising due to the great reactivity of the rare metals in general. A great deal of effort has gone into the development of separation processes for the purification of uranium and thorium to nuclear grades of purity, separation of rare earth metals from one another, niobium from tantalum and zirconium from hafnium. Of the many alternatives explored and studied at Trombay, two major processes have emerged for effective plant level utilization—solvent extraction and ion exchange.

In solvent extraction, the purification is achieved by selective extraction of compounds of a given element or impurities from aqueous solutions into an organic solvent which is immiscible with water. This is possible when the distribution coefficients of the components in the mixture differ from each other sufficiently. The distribution coefficient which is the crucial parameter in solvent extraction depends on the properties of the solvent, the concentration of the extracted species in the aqueous phase, the presence of other species in the solution, the acidity of the aqueous phase and the temperature. The studies conducted at Trombay were directed not only at optimising these conditions but also obtaining the engineering details such as selection of suitable solvent, collection of equilibrium data, determination of stages, mass transfer rates, choice of contacting equipment and scale-up.

A typical extraction flowsheet is given in figure 8. Starting from its application for recovering uranium from ore leach liquors, solvent extraction has grown in diversity and some of the important systems are presented in table 3. Solvent extraction is practised on a plant scale in our department for the extraction of uranium, thorium, plutonium and for the separation of zirconium from hafnium and niobium from tantalum starting from a variety of aqueous feed solutions using TBP as the organic phase and mixer settlers for contacting equipment.

Ion exchange has been the specialist separation process for use with very dilute feed

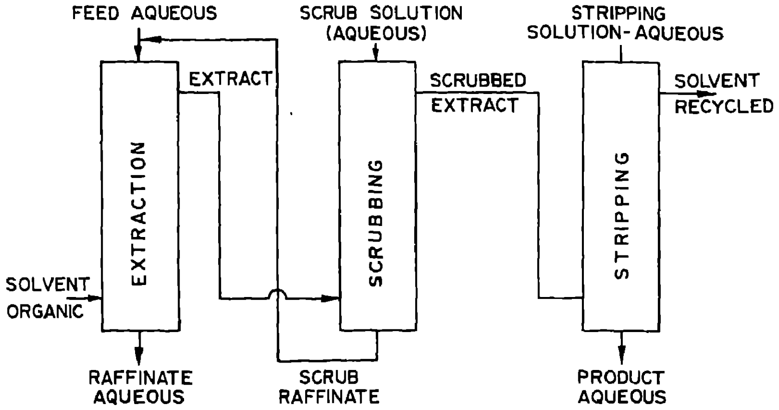

Figure 8. Typical solvent extraction flowsheet.

Table 3. Solvent extraction for separation for purification of rare metals

Metal	Organic phase	Aqueous solution	Remarks
U	TBP	Nitrate	Purification of U to nuclear grade
Th	TBP	Nitrate	Purification of Th to nuclear grade
Zr	TBP	Nitrate	Separation from Hf
Ta	TBP	Fluoride	Separation from Nb
Lanthanides	DEHPA	Chloride	Separation of individual lanthanides

solutions. The most spectacular application of ion exchange has been in the recovery of uranium from low grade ore leach liquors. It is especially better than solvent extraction in such cases.

Ion exchangers are sparingly soluble solids (organic or inorganic) with active functional groups which can be exchanged for ions present in the solution. The schematics of the ion exchange operation is given in figure 9. As the affinity of the ion exchange resin depends on the charge and size of the ionic species involved in the exchange and the distribution coefficient varies with the conditions of the aqueous phase like acidity etc, selective separation and purification can be achieved. Ion exchange separations are generally slow and operate on much less throughputs compared to solvent extraction processes. However as indicated already, for dilute solutions, in cases where separation factors are close and in some cases for processing unclarified solutions ion exchange is particularly sought after. Some important systems processed by ion exchange are given in table 4.

7. Halide metallurgy

The separation steps generally give the pure products in the form of either oxides or halides. These metal compound intermediates are converted to the metal by various reduction processes. Here again, peculiar for rare metals, one encounters a unique

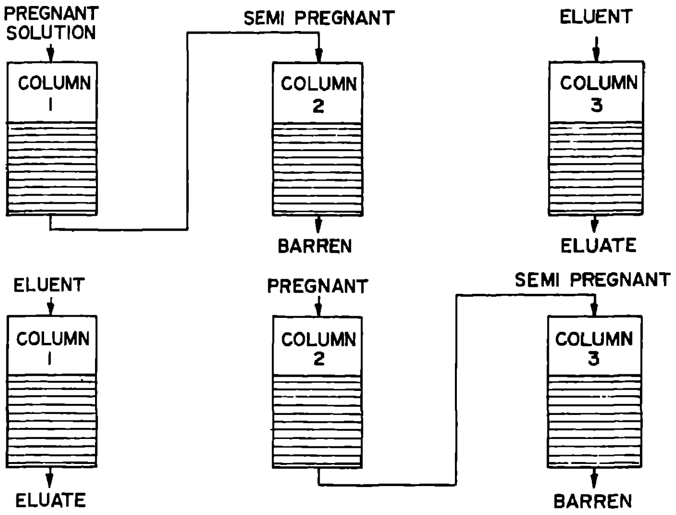

Figure 9. Ion exchange—adsorption, elution flow-sheet.

Table 4. Ion exchange separation for purification of rare metals

Metal	Ion Exchanger	Aqueous feed	Remarks
U	Deacidite FF(530)	Sulphate	Uranium separated from elements co-occurring in the ore
Zr	Cation exchanger ZK-225	Nitrate	Zr is separated from Hf
Ta	Anion exchanger EDE-10P	Fluoride	Ta is separated from Nb
Rare earths	Cation exchanger Dowex 50, ZK 225	Chloride	Rare earth metals are separated from each other

system of metal production. The intermediate which is reduced to obtain the metal is invariably a halide. The involvement of halides in rare metals extraction is certainly not restricted to the reduction step. Its omnipresent close involvement at many other stages of metal extraction also shall be looked into in what follows.

Halogens and halides find application in almost all stages of rare metal extraction from ore beneficiation to metal purification as given in figure 10. The diversity of halide metallurgy can be gauged from the following examples. (i) Ore breakdown: chlorination of zircon, ilmenite, rutile, silicofluoride treatment of beryl, zircon; (ii) Halogenation of crude intermediate: chlorination of zirconium carbide; (iii) Halogenation of pure intermediate: chlorination of zirconium dioxide, titanium dioxide; hydrofluorination of uranium dioxide; (iv) Reduction of metal halides: sodium reduction of K_2TaF_7, calcium reduction of UF_4 magnesium reduction of $TiCl_4$, $ZrCl_4$, BeF_2, electrolysis of RE chlorides; (v) Reclamation of scrap: by chlorination and fused salt electrorefining; (vi) Ultrapurification of commercial grade metal: iodide process for crystal bar titanium, zirconium and hafnium.

Starting with the gas-solid reactions, to carry out the entire range of processes as

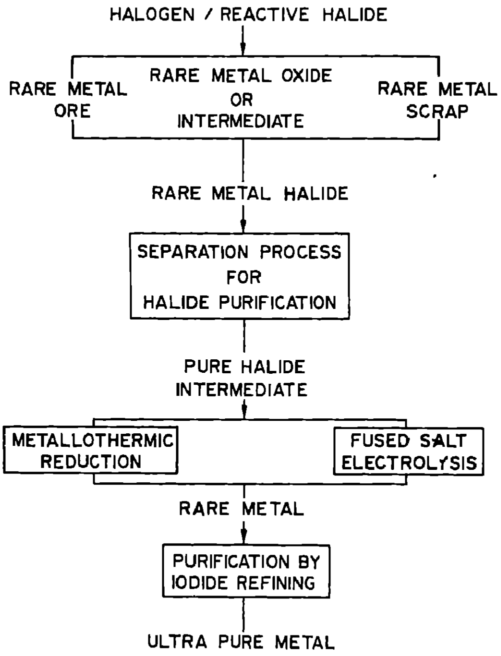

Figure 10. Halogenation in rare metal extraction.

indicated above, a large variety of reactors have been developed and process optimised at Trombay and later transferred to the industrial units of the Department.

The high temperature of these reactions and the corrosive nature of the halogen and the halide vapours, restrict the choice of the material of construction and the type of equipment for large scale operation. While nickel is compatible with fluorine and fluoride vapours upto 800°C, nickel and inconel alloys can withstand chlorine upto 600°C. In the production of $ZrCl_4$ or $TiCl_4$ that involves temperatures of 700–900°C, one has to use quartz or silica in the reaction zone.

Further, a halogenation plant will also include provision for safe metering of the corrosive halogens and the safe disposal of the unreacted halogens by neutralising with alkali or otherwise, due to high toxicity.

At Trombay, a rotating magnesium-tube lined reactor is employed for the production of UF_4 by the hydrofluorination of UO_2 powder. A special constructional feature of the reactor is that it has two concentric tubes with the annular space filled with an inert seal gas. The inside tube is made of magnesium to withstand the corrosive action of hydrofluoric acid, while steel is chosen for the outer tube for ease of fabrication and strength. The leak tightness of the seals between the rotating tube and the stationary end parts of the furnace is obtained by adopting the principle of positive gas pressure seal between teflon inner sealing rings and outer rubber sealing rings. The reactor is held in a slightly inclined position to facilitate smooth flow of UO_2 powder fed through a screw conveyor.

As a further example, one can look at the chlorinator used for the production of zirconium and titanium chloride.

The feed for static bed chlorinators consists of a mixture of oxide and carbon preformed into briquettes. The green briquettes are dried and coked at 800°C in inert nitrogen atmosphere to obtain highly porous briquettes for efficient chlorination. The large scale chlorination is carried out in a high purity silica brick lined furnace. The briquettes are heated by impressing three phase voltage across three graphite electrodes embedded in the charge. The carbonised briquettes possess sufficient electrical conductivity which improves with temperature, and with appropriate voltage and current control, the charge is slowly heated to the reaction temperature of 700–900°C. $ZrCl_4$ vapours evolving from the chlorinator furnace are condensed in a double walled inconel condenser at 150–200°C as dense crystals suitable for metal production. Blocking is a common problem in chlorinators. Hence pressure monitoring gauges, pressure release discs, and clearance ports have to be provided at critical locations.

Most of the chlorination reactions are exothermic in nature and require close control of temperature which is better achieved in fluidised bed reactors. These reactors also offer advantages like excellent gas-solid contact, good heat transfer, relatively inexpensive reactors and easier start-up and shutdown operations. Systems for the multistage fluidised bed hydrofluorination of UO_2 and the fluidised bed chlorination of zircaloy scrap in an inert bed have been developed at this Department.

The volatility of halides, the facility for purifying these by distillation and possibility of reducing these halides with metals like magnesium, sodium, and calcium have provided a powerful means for the production of reactive metals.

8. Metal reduction processes

The reduction of rare metal starts either from a halide or an oxide and follows the route as given in figures 11 and 12.

A majority of the rare metals have been produced by reducing their halides. The reason may either be that it is not possible to reduce the oxide directly at all (*e.g.* Ti, U, Be) or that it is more convenient to reduce the halide (*e.g.* Zr, Hf, Ta, Th).

9. Reduction of halides

The reduction of halides is accomplished by using the metals, sodium, magnesium or calcium as the reducing agent. Depending upon the physical properties of the reactants

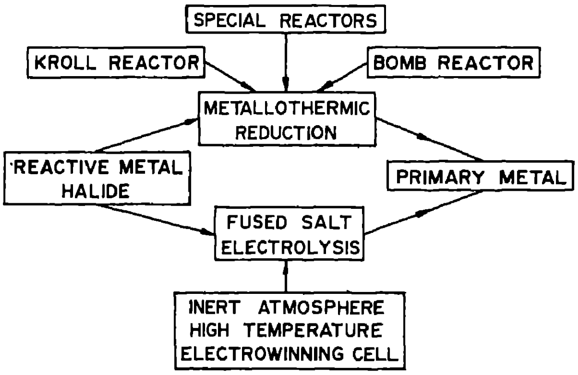

Figure 11. Reduction of rare metals—halide route.

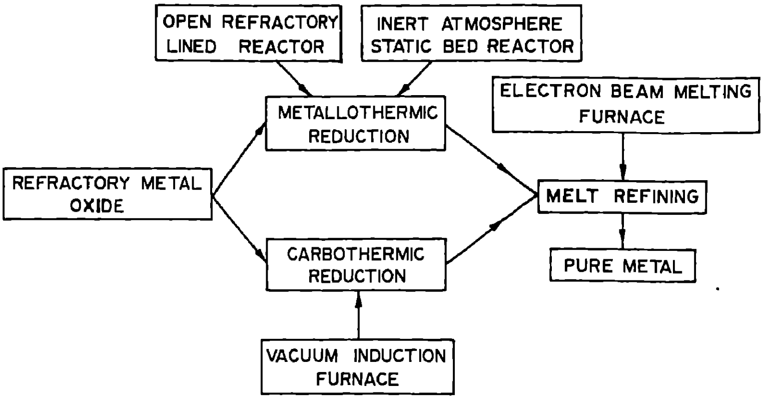

Figure 12. Reduction of rare metals—oxide route.

and products and the heat of reaction, the product metal is recovered as an ingot (U, Th), sponge (Zr, Ti) or powder (Ta). The reduction processes developed for U, Th, Zr, Ti, Ta and Be in fact provide fine examples of process metallurgy of fluorides and chlorides realised on an industrial scale for the production purposes. The exothermic metal reduction processes fall under two major categories—adiabatic (thermit type) and isothermal (Kroll type). Calciothermic reduction of uranium tetrafluoride is a fine example of the thermit type reaction. The uranium metal plant at Trombay has been producing consistently and efficiently uranium metal by the calciothermic reduction route.

In the Trombay practice, high purity UF_4 powder is intimately mixed with calcium granules and the mixture is charged into a leak tight tapered S.S. bomb reactor, which is initially lined with dry CaF_2 powder by vibratory packing. The CaF_2 lining serves for heat insulation and containment of the molten uranium. The calciothermic reduction is triggered—in an argon atmosphere—by electrically igniting a magnesium ribbon embedded at the top of the charge. The reaction is instantaneous, spreads rapidly through the mass, and the resulting liquid uranium droplets coalesce and collect at the bottom, forming a massive solid ingot on cooling.

A reduction route employing indigenous magnesium in place of imported calcium has been developed on a pilot plant scale is due to be adopted in the plant's expansion.

The calciothermic route described for uranium is applicable to the production of thorium and plutonium metals also.

The production of metals by the isothermal Kroll type reduction is exemplified by the magnesium reduction of zirconium tetrachloride. The process that has been tested on pilot plant scale at Trombay and adopted for tonnage production at the Nuclear Fuel Complex, Hyderabad is described below.

The reactor employs a specially designed S.S. retort and a three-zone furnace system for carrying out the reduction reaction. Zirconium tetrachloride and clean magnesium pigs are loaded in separate containers in the retort. After *in situ* purification of the chloride by pumping out the voltalite impurities at 300°C, the magnesium temperature is raised to above its melting point (to 850°C) and the chloride distilled in a controlled manner to react at the surface of molten magnesium. At the end of the reduction the excess magnesium and $MgCl_2$ are separated from the resulting zirconium sponge by pyrovacuum distillation in another heavy-walled retort capable of evacuation down to

< 1 micron at 900°C, the inconel retort is heated to 900°C using an evacuated bell-type furnace.

Similar reduction and pyrovacuum distillation equipment are suitable for production of titanium, thorium and hafnium metals.

For the production of tantalum powder from K_2TaF_7, a liquid-liquid reactor technique was developed at Trombay. Filtered high purity liquid sodium is continuously metered under argon cover on to the stirred mass of molten K_2TaF_7 and NaCl kept at 800–900°C in an inconel alloy 600 reactor. The tantalum metal powder is recovered from the reduced mass after leaching out the by-product fluorides with a series of aqueous reagents. This effort has extended to setting up of a production plant at NFC.

Calcium metal is unsuitable for the reduction of beryllium fluoride due to the formation of highly stable $CaBe_{13}$. Beryllium metal is produced in the form of pebbles by the magnesium reduction of BeF_2 in a graphite crucible in an induction furnace at 1100–1400°C. The metal pebbles owing to their lightness float to the surface of the slag. The beryllium pilot plant at Vashi, New Bombay is designed for the production of the metal and its alloys to meet indigenous requirement.

10. Reduction of oxides

The area of oxide reduction processes has been extensively investigated for producing a number of rare metals. The oxides are characterised by their good stability, they are easily prepared and are often the economically attractive intermediates in metal production processes. As specific examples of the advances at Trombay, reference may be made of fairly large scale production processes operated for preparation of zirconium, hafnium and thorium metal powders through calciothermic reduction of their respective oxides. Another notable advance has been in the aluminothermic reduction technology applied with great ingenuity in the preparation of niobium, tantalum, vanadium and molybdenum.

A metallothermic reduction process that does not generate excess heat and thereby avoids the growth or sintering of reduced metal particles is highly conductive to metal powder preparation. Calcium reduction of zirconium dioxide at 900°C generates only around 43 kcals per g mole of oxide. Further, the reduction is carried out in the presence of a heat sink like $CaCl_2$, very fine metal powder (predominantly 3 micron size) results dispersed in a matrix of CaO and $CaCl_2$. The metal powder is recovered from the reduced mass by careful aqueous leaching and drying. This technique has led to the establishment of a production facility for 1 ton Zr powder per annum at NFC.

Calciothermic reduction has also been investigated in detail for the preparation of hafnium, thorium, niobium and tantalum metal powders from their oxides. The process essentially consists of mixing the charge of calcium metal granules, metal oxide and calcium chloride heat sink in proper proportions and soaking it at the reduction temperature (950–1000°C) in flowing argon atmosphere, for sufficient time; the reduced mass is subsequently leached with dilute acids.

Unlike the static bed reduction described above, in a bomb process, highly exothermic reactions are conducted to prepare high melting metals in their consolidated form. To achieve this objective in reactions releasing inadequate heat, there are various means.

These include: (i) preheating to ignition, (ii) additives acting as thermal boosters, and (iii) combination of both.

The best reductant for the purposes just outlined is aluminium. The aluminothermic reduction may be described as combustion of aluminium to its oxide—the oxygen being released from the metal oxide. The reactions are carried out in an open vessel lined with refractory. The reactants at room temperature are mixed and charged and the charge is primed locally by means of an electric fuse embedded in the charge. In preheating to ignition, the entire charge is set to fire and the reaction is under near adiabatic conditions. The aluminothermic reduction, essentially a non-furnace process, proceeds rapidly to completion, but several hours of cooling is allowed before the contents are taken out. The metal if showing some slag adherence is cleaned by manual chipping.

A flowsheet, based on the aluminothermic reduction, for the production of niobium metal has been chosen for setting up of a plant at NFC.

Carbothermic reduction to produce refractory metals has become a reality only with the advancement in the regime of vacuum technology. The reactions are performed in a high temperature-high vacuum induction furnace where the pelletised oxide-carbon or carbide-oxide charge is reacted in the solid state to yield carbide or metal. A precise control of charge composition and the reaction conditions is very essential for obtaining pure metals having low residual carbon and oxygen contents. Adopting this process, complete flowsheets have been developed at the Metallurgy Division, BARC for the production of reactor grade niobium and capacitor grade tantalum metals.

11. Electrolytic reduction

For electrowinning of the reactive metals, only fused salt systems operating in an inert atmosphere have been found suitable.

Molten salt electrowinning processes for the preparation of refractory metals, particularly tantalum and titanium and rare earths like misch metal and cesium have been extensively investigated at Trombay. The metal compound (chloride, fluoride or oxide) is dissolved in a low melting eutectic salt mixture composed of two or more alkali or alkaline earth chlorides or fluorides. During electrolysis, the high melting rare metals are obtained as adherent dendrite deposits on the cathode (which is kept suspended in the fused salt) or alternatively if the adherence characteristics are poor, the metal is generated in the form of powder, in which case the cell itself is used as the cathode (and the anode is kept suspended).

Tantalum and titanium have been electrodeposited in the dendritic and sponge form by electrolysing KCl-NaCl melt containing respectively potassium tantalum fluoride and titanium chloride as functional salt. While for tantalum a centrally suspended metallic rod has been used as cathode, for titanium a perforated metallic basket served as the cathode. Such electrode arrangement for multivalent titanium has been found essential to separate the catholyte and anolyte.

In the pilot plant work on electrowinning of titanium, a 1000 amp internally heated inert atmosphere electrolytic cell has been used to standardise the parameters. The metals belonging to the rare earth group have been electrodeposited from all-chloride electrolytes.

12. Consolidation and purification of rare metals

The primary sponge metals and metal powders are required to be consolidated by melting or sintering prior to conversion to mill products. In some cases the melting or sintering operation refines the metal to an extent.

The tolerable limits of impurities in rare metals are quite low. All the properties which make these metals unique in comparison with other common metals are drastically impaired even by low levels of metallic and interstitial impurities. Therefore, great care and special techniques are employed in the refining operation as summarised in figure 13.

Most of the purification methods for rare metals involve high temperature and vacuum. The purification methods available for the rare metals include (i) vacuum melting, (ii) iodide refining, (iii) zone melting, and (iv) molten salt electrorefining.

Except the metals uranium and beryllium which are consolidated and to some extent refined by vacuum induction melting and casting, majority of the rare metals are consolidated and refined by arc and electron beam melting procedures. In both these methods, crucible contamination is eliminated by carrying out the meltings in watercooled copper crucibles.

In vacuum arc melting, the heat is generated on the surface of the molten metal by the application of a low voltage high current electric arc from an electrode which may be either consumable or nonconsumable. While nonconsumable method is suitable for consolidation of metals, no appreciable purification is achievable on account of the low vacuum involved. On the other hand, in the consumable arc melting, the material to be melted is preformed into an electrode which is progressively consumed during melting. The process has the advantage of operating under higher vacuum (10^{-2} to 10^{-3} torr) without contamination from electrode material and finds widespread use in the consolidation of rare metals. Facilities available at Trombay allow melting of 4 to 6 in. dia ingots of zirconium and titanium and at NFC metal ingots upto 12 in. dia can be cast.

Electron beam melting furnaces operate in high vacuum and provide high degree of super heat in the melt region and thus enable much greater refining than that possible with arc furnaces. In electron beam melting, the specimen is heated by subjecting it to

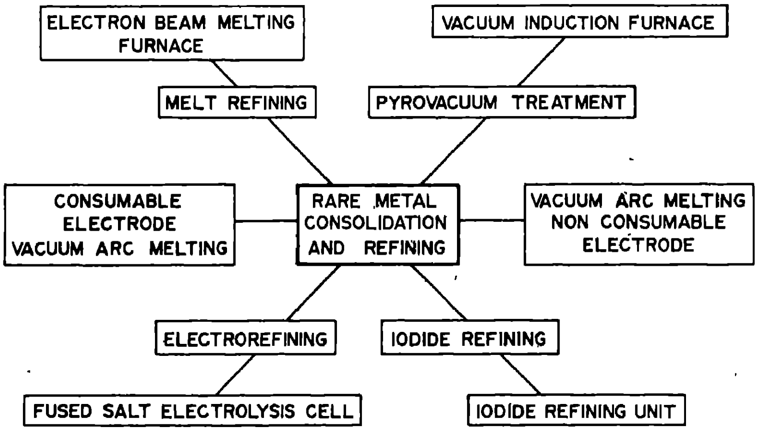
ELECTRON BEAM MELTING FURNACE
VACUUM INDUCTION FURNACE
MELT REFINING
PYROVACUUM TREATMENT
CONSUMABLE ELECTRODE VACUUM ARC MELTING
RARE METAL CONSOLIDATION AND REFINING
VACUUM ARC MELTING NON CONSUMABLE ELECTRODE
ELECTROREFINING
IODIDE REFINING
FUSED SALT ELECTROLYSIS CELL
IODIDE REFINING UNIT

Figure 13. Techniques for consolidation and refining of rare metals.

bombardment by a beam of high energy electrons under a vacuum better than 10^{-4} torr. Electron beam melting has, in fact, played a prominent role in its application to consolidation and purification of primary metals with widely different production history, and to preparation of metals with their finished purities meeting specific application requirements. Electron beam melting is effective and extensively used particularly in the production flowsheets of niobium and tantalum metals.

The reactions and processes that take place during vacuum melting and result in purification include (i) distillation of volatile impurities, (ii) vaporization of suboxides, (iii) carbon deoxidation, and (iv) vacuum degassing.

While vacuum melting is very effective in the purification of refractory metals it is not so with reactive rare metals like titanium, zirconium and hafnium. The so-called iodide refining has been found to be very effective in the refining of these metals.

Iodide refining, also known as the Van Arkel de Boer process, is based on the reversibility of a reaction between a metal and iodine. Purification of zirconium by this process has been studied extensively in the Metallurgy Division, BARC. The process is carried out in an evacuated inconel 600 vessel along the axis of which a high purity zirconium wire is aligned and electrically heated to 1300°C. The crude zirconium sponge is stacked inside the vessel in the annular space between the vessel wall and a concentric screen. Iodine required for the process is sublimed into the evacuated vessel. The vessel is externally heated to 250–400°C to form volatile ZrI_4 by reaction between zirconium sponge and iodine. The iodide vapours decompose on the surface of the high temperature zirconium filament resulting in a deposit of pure metal on it. The iodine vapours simultaneously liberated travel back for further reaction with the crude sponge.

A decomposition assembly developed at Metallurgy Division, BARC has been growing kilogram quantities of high purity crystal bars of zirconium, titanium and hafnium.

Zone melting is essentially a purification process by repeated crystallization from the melt. In practice two liquid-solid interfaces are produced for distribution of impurities by causing a relatively small molten zone to transverse the length of the bar of the charge. Many repetitions of the process lead to considerable purification even in cases where the distribution coefficient is close to unity. The impurities more soluble in the solid concentrate in the starting end.

It has been possible to produce kg quantities of metals such as Bi, Sb, Sn and Cd in their ultra-pure form for use in the semiconductor industry with zone refiners designed and fabricated at Trombay. A larger semi-automatic zone refiner is turning out ultrapure materials at NFC.

Zone refining in vacuum combines the benefits of conventional zone refining in a protective atmosphere, vacuum degassing and selective distribution of impurities. For refining of refractory metals an electron beam floating zone melting unit has been fabricated and used at the Metallurgy Division.

Electrorefining, next to electrowinning of metals is the most important aspect of fused salt electrolysis. While in electrowinning graphite has been found to be the most popular and inexpensive anode material, electrorefining cells essentially employ impure metal as the anode. The metal is crushed to suitable size and spread over the crucible bottom or packed in the annular space between the crucible and a perforated graphite screen to expose a large anode area. Molybdenum is the best reported cathode material in electrorefining. Iron has been used for vanadium electrorefining.

Molten salt electrorefining technique has been perfected for the preparation of high purity metals like niobium, tantalum, vanadium, molybdenum and chromium from their aluminothermically reduced alloy form. More recently electrorefining technique has been proved to be an effective mode for purification of calcium reduced hafnium. It has been possible to apply electrorefining for metal values of zircaloy scrap, and off-grade titanium sponge. Such purification technique has been found suitable not only for clean scrap but also for scraps contaminated with other metals and alloys which cannot be directly re-used in conventional remelting. Thus of all the refining methods applicable to rare metals, electrorefining stands out to be the most powerful technique with a wide range of refining capabilities.

13. Thermodynamics in rare metals extraction

In the development of process metallurgy of rare metals, the role of basic research particularly thermodynamic investigations has been very significant. Thermodynamic data have come to the rescue in many situations either during the choice of process parameters or in explaining many of the system behaviours. Though the involvement of thermodynamic analysis is very extensive and pervades almost all stages of rare metals reduction, refining and service, investigations concerning the vapour pressure and vaporization behaviours at elevated temperatures; solid solubility and phase diagram data have particularly been the main thrust areas for data collection and utilization. Investigations on metal-crucible interaction behaviours and decomposition processes can be cited for some of the direct application areas for thermodynamic data.

At the Extractive Metallurgy Section, several actual processes have been developed based solely on the available thermodynamic data of the system concerned. While it is impossible to carbothermically reduce zirconium and hafnium oxides, the important master alloys zirconium-niobium and hafnium-tantalum have been obtained by a carbothermic reduction process consisting of reduction of niobium pentoxide with zirconium carbide or tantalum pentoxide with hafnium carbide respectively. This scheme of reduction was worked out from the theoretical considerations of the thermodynamic stabilities of carbides and oxides and the stabilities and vaporization behaviours of the suboxides of zirconium, hafnium, niobium and tantalum. Another example of major flow sheet development that was visualised from the thermodynamic properties of the concerned compounds, is found in a recently concluded investigation on the preparation of pure niobium and tantalum through their nitride intermediates. The comparative stability of niobium and tantalum nitrides with respect to the niobium and tantalum carbides at moderate temperatures and the complete instability of these nitrides (in contrast to the persistent stability of the carbides) at higher temperatures and vacuum conditions has made it possible to obtain the pure metals starting from the oxides by a single sequential step consisting of (i) carbothermic reduction of niobium or tantalum pentoxide under a nitrogen atmosphere at 1500–1600°C to obtain the corresponding nitride and (ii) pyrovacuum decomposition of the nitride, at 2000–2100°C under 10^{-4} torr, to pure metal.

In addition to the above mentioned types of applications, thermodynamic analyses have extensively been employed in various pyrovacuum refining operations, leading to successful process operation, improved yield, reduction in number of processing steps and similar improvements.

14. Evaluation of rare metals

The development of flow sheets for the extraction of high pure rare metals has depended to a great extent on the parallel development and availability of powerful analytical techniques which enabled the evaluation of products at various stages. Special efforts are required particularly when the impurity concentrations are vanishingly low. The important analysis techniques applied in the rare metals evaluation are diagramatically presented in figure 14.

15. Concluding remarks

In the evolution and developments of flowsheets for rare metal extraction, the R&D effort has had many facets as summarised in figure 15.

As compared with the historical development of the process metallurgy of common metals, there has been a much more systematic and scientific approach to the chemical metallurgy of rare metals. This has been possible through many advances in analytical chemistry, physical chemistry, instrument and equipment development, physical and chemical engineering which have provided new technologies, and also through entirely

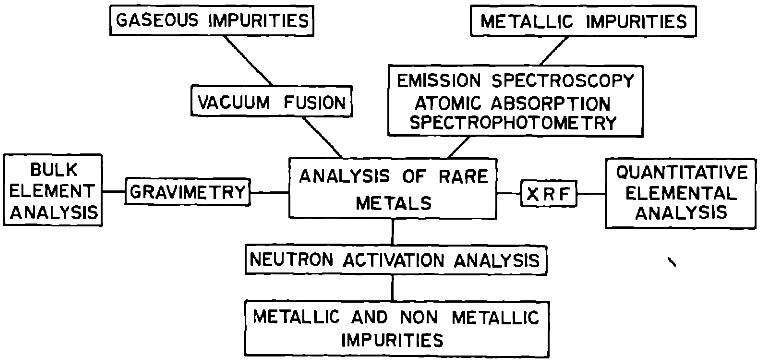
GASEOUS IMPURITIES
METALLIC IMPURITIES
VACUUM FUSION
EMISSION SPECTROSCOPY
ATOMIC ABSORPTION SPECTROPHOTOMETRY
BULK ELEMENT ANALYSIS
GRAVIMETRY
ANALYSIS OF RARE METALS
XRF
QUANTITATIVE ELEMENTAL ANALYSIS
NEUTRON ACTIVATION ANALYSIS
METALLIC AND NON METALLIC IMPURITIES

Figure 14. Evaluation of rare metals.

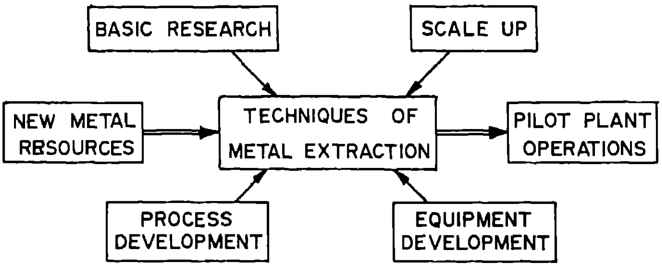

Figure 15. Development of extractive processes for rare metals.

novel metallurgical engineering designs. Our basic understanding of chemical and metallurgical systems, phenomena and reactions has also vastly improved through progress in theory and experiment in rare metals extraction.

Although process metallurgy of rare metals has grown into a powerful, mature and composite discipline, a good deal of scope for further R&D efforts still remains. Specifically one can mention fertile areas like pyrochemical counter current fused salt reactors for achieving separation of zirconium from hafnium, adoption of fluidised bed reactor for gas solid reactions, employment of plasma processing techniques for mineral beneficiation and refractory metal reduction—all of which deserve detailed study.

An interesting aspect of development of processes for rare metals extraction has been that many of these new techniques have important relevance to the common metals processing also. Special mention may be made of the prospects of solvent extraction processes in the copper and nickel industries and ion exchange in certain by-product metal recovery processes from effluent solutions, chlorination processing of complex sulphide ores, and vacuum melt refining.

Growth, development and maturity in operating practice have marked the evolution of various process options taken for investigations at BARC. Whenever possible and desirable, the process development was pursued through the various stages and led to its logical conclusion—setting up of operating production facilities. An important aspect that has marked this style of evolution is that the person or persons who have conceived, tested and developed the idea and the process have also been given the opportunity of setting up the plant and running it. This has made further growth and expansion of the plant feasible and easier. In certain cases, the nature of the project is more suited for effecting a transfer of technology to organizations outside the department. In this context, it is well worth noting that the technology of aluminothermic reduction of ferroalloys viz., ferrovanadium, ferroniobium, ferromolybdenum and ferrotungsten—so well mastered at the Extractive Metallurgy Section has been transferred to industries in Madhya Pradesh. In another instance, based on the flowsheet and technology developed at the Extractive Metallurgy Section, a demonstration plant for the processing of casseterite concentrates is being set up at Raipur by Metallurgy Division jointly with the Madhya Pradesh State Mining Corporation. One would appreciate that such instances are tantamount to bringing the advanced research facilities and expertise within the reach of a wider section of industries and to the greater service for our country's mainstream industrial activity.

The foresight and imagination in the organisation, of the successive stages of the programme, has paid good dividends; strong and comprehensive base that we now have in rare metals processing industry should inspire confidence for further growth and diversification of this technology in our country.

Acknowledgement

The authors appreciate the manysided help rendered by Shri N Krishnamurthy, Metallurgy Division, BARC in the preparation of this paper. Contributions from the various research groups, particularly from the Metallurgy, Chemistry, Chemical Engineering and Ore Extraction Divisions of BARC, Bombay and the Nuclear Fuel Complex, Hyderabad have actually provided the basic theme of this present article.

Representative bibliography

Damodaran A D, Deshpande S G, Majumdar A A, Sastri M S, Jena P K, Bose D K, Chandra S, Gupta C K and Taneja A K 1970 *Proc. Indian Nat. Sci. Acad.* **A36** 306

Gupta C K 1972 in *Recent developments in metallurgical science and technology, Proc. IIM Symp. on Process Metallurgy*, New Delhi p. 515

Gupta C K 1984 Extractive metallurgy of niobium, tantalum and vanadium *Int. Metals Rev.* (Under Publication)

Gupta C K and Sundaram C V 1973 *The Banaras Metall.* **5** 190

Krishnamurthy N, Venkataramani R, Garg S P and Sundaram C V 1981 in *Trends in refractory metals, hard metals, and special materials and their technology, Proc. Tenth Plansee Seminar Metallwerk* Plansee, Reutte, Vol. 1, p 263

Mukherjee T K, Bose D K and Gupta C K 1972 in *DAE Symp. High. Temp. Mat.* Hyderabad, p. 221

Mukherjee T K and Gupta C K 1976 *Trans. SAEST* **11** 127

Mukherjee T K, Garg S P, Gupta C K, Sundaram C V, Taneja A K and Damodaran A D 1978 in *Electron beam melting and welding, Proc. Int. Conf.*, Avignon

Proc. INSA-BARC Winter School on Chemistry and Metallurgy of Rare Metal Extraction, BARC (Jan 1975)

Saratchandran N and Sundaram C V 1970 in *DAE Materials Science Symp.* NAL, Bangalore, p. 251

Subramanyam R B, Saratchandran N and Sundaram C V 1973 *J. Sci. Ind. Res.* **32** 672

Subba Rao K S, Sharma B P, Paul C M and Sundaram C V 1977 *Beryllium development programme in India*, Conf. Preprints: Beryllium, *Fourth Int. Conf.* on Beryllium, The Metals Society, London

Sundaram C V, Garg S P and Sehra J C 1979 in *Metal sciences–The emerging frontiers, Proc. Int. Conf.*, The Indian Institute of Metals

Sundaram C V and Sharma B P 1972 in *Recent developments in metallurgical science and technology, Proc. IIM Symp. on Process Metallurgy*, New Delhi, p. 479

Sundaram C V and Suri A K 1976 in *High temperature reactions and processes Proc. KREC*, Suratkal p. 27

Bull. Mater. Sci., Vol. 6, No. 5, September 1984, pp. 923–958. © Printed in India.

Plutonium metallurgy in India

P R ROY and C GANGULY

Radiometallurgy Division, Bhabha Atomic Research Centre, Bombay 400085, India

Abstract. The embryo of plutonium metallurgy in India, as well as in Asia, was formed nearly 25 years back in Trombay. Thereafter, in the intervening 25 years, significant amount of research and development work have been carried out at BARC on this man-made fissile element and indigenisation has been achieved in the fabrication, characterisation and property evaluation of plutonium metal, delta-stabilised alloys, Al-Pu fuels, Pu-Be neutron sources, $(UPu)O_2$ fuels for thermal and fast reactors and (UPu)C and (UPu)N advanced fuels for liquid metal-cooled fast breeder reactors (LMFBR).

This paper summarises the development of plutonium metallurgy in India highlighting the safety aspects, our achievements and potential of plutonium for generation of nuclear electricity in the coming decades.

Keywords. Plutonium; fissile; delta-stabilised alloys; Al-Pu fuels; Pu-Be neutron sources; Mixed oxide and carbide fuels; fast breeder-test reactor; liquid metal-cooled fast breeder reactors; nuclear electricity.

1. Introduction

The metallurgy of plutonium, the man-made unique and most unusual metal, was introduced in India in 1960 when a team consisting of a chemist, a chemical engineer and a metallurgist successfully isolated mg quantities of plutonium metal beads in the Trombay laboratory by calciothermic reduction of plutonium tetrafluoride. Thereafter, in the intervening 25 years, there has been an enormous scale-up of production and extensive investigation of plutonium metal, its alloys and compounds. A sophisticated plutonium metallurgy laboratory for safe and secured fabrication and characterisation of plutonium fuels has come up in Trombay and today we are on the threshold of intensive utilisation of plutonium for generation of nuclear electricity and breeding of fissile materials simultaneously.

Plutonium does not occur in nature but is synthetically formed by the transmutation of the naturally occurring $^{238}_{92}U$. Soon after its discovery by Seaborg, Wahl and Kennedy in February 1941, in the Berkeley laboratory in USA, plutonium served as a major ingredient of the Manhattan nuclear weapon project during the second world war (Seaborg 1958). However, today it is most significant because of its peaceful potential as a nuclear reactor fuel offering energy thousand times greater than all available fossil fuels.

From the very inception of nuclear energy programme in India in the mid 1950s, the tremendous potential of plutonium for unlocking the huge energy reserves of our limited uranium (Rao 1982) (~ 60000 tons) and abundant thorium (~ 320000 tons) resources was recognised. Accordingly, laboratory separation and analytical procedures for plutonium started in Trombay in 1958 and by 1964 our spent uranium fuel reprocessing plant for recovery of plutonium was commissioned, for the first time in Asia.

The present dissertation summarises the milestones of plutonium metallurgy in India, highlighting our achievements in development and fabrication of plutonium metal and plutonium bearing metallic and ceramic fuels and our future programme for utilisation of plutonium for generation of nuclear electricity.

2. Formation and separation

As is known, uranium occurring in nature contains mainly two isotopes, *viz.* ^{238}U (99·3 %) and ^{235}U (0·7 %). The present generation of nuclear reactors derive energy from the fission of ^{235}U by slow or thermal neutrons and use natural uranium or 2 to 4 % ^{235}U enriched uranium in the form of metal or oxide as fuels. The fission reaction is as follows:

$$^{235}_{92}U + ^{1}_{0}n \rightarrow ^{236}_{92}U \rightarrow \text{fission fragments} + 2 \text{ to } 3\ ^{1}_{0}n + 200\ \text{MeV}.$$

One of these released fission neutrons is needed for maintaining the chain reaction and out of the remaining neutrons some are captured by the fertile ^{238}U to form ^{239}U which undergoes two successive beta decays, as shown below, leading to the formation of ^{239}Pu, which is an excellent fissile material:

$$^{238}_{92}U + ^{1}_{0}n \rightarrow ^{239}_{92}U \xrightarrow[23\cdot5\,\text{m}]{\beta^-} ^{239}_{93}Np \xrightarrow[2\cdot3\,\text{d}]{\beta^-} ^{239}_{94}Pu$$

Thus, the nuclear reactors, apart from generating power also produce fissile ^{239}Pu as a byproduct, through neutron capture by the fertile ^{238}U. Other prominent isotopes of plutonium namely ^{240}Pu, ^{241}Pu and ^{242}Pu are formed from ^{239}Pu by successive neutron captures. The isotopic content of plutonium in a thermal reactor and the formation of plutonium radionuclides and daughters depend on such factors as discharge burn-up of the fuels, neutron flux and energy spectrum, fuel enrichment, moderator to fuel volume ratio, fuel diameter, cladding materials etc., and are shown in figures 1 and 2 respectively. Typical isotopic composition of plutonium[(3)] from the spent fuel elements of the 40 MW (th) CIRUS test reactor in Trombay, the 200 MW(e) boiling water reactors (BWR) at the Tarapur Atomic Power Station (TAPS) and the pressurised heavy water reactors (PHWR) at the Rajasthan Atomic Power Station (RAPS) are given in table 1.

The irradiated or the spent uranium fuel elements are a mixture of depleted uranium ($^{238}U + < 0{\cdot}7\,\%\ ^{235}U$), highly radioactive fission fragments and plutonium. The major

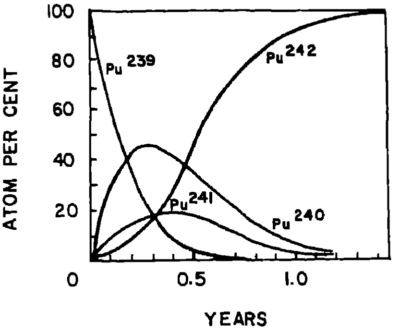

Figure 1. Plutonium isotopic composition as a function of exposure to thermal neutrons.

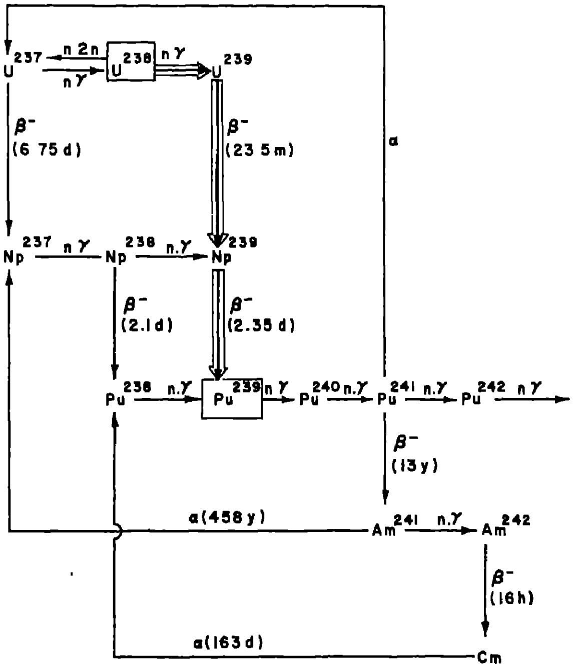

Figure 2. Plutonium radionuclides and daughters.

Table 1. Isotopic composition of plutonium from different reactors.

Reactor	Burn-up (MWD/ton)	^{238}Pu (w/o)	^{239}Pu (w/o)	^{240}Pu (w/o)	^{241}Pu (w/o)	^{242}Pu (w/o)
BWR	6100	0·125	82·7	13·94	2·89	0·339
(TAPS)	9500	0·203	73·54	20·31	4·81	1·080
	13750	0·393	65·77	25.17	6·45	2·21
	29000	0·500	53·40	29·60	10·48	6·01
PHWR	2960	0·02	82.52	15·01	2·2	0·22
(RAPS)	5700	0·05	67·7	26·0	4·8	1·2
	6200	0·06	66·07	26·87	5·52	1·48
CIRUS (Trombay)	1000	0·01	93·32	6·27	0·38	0·02

process steps (Roy 1978) in the separation of plutonium from spent fuels are shown in figure 3. After appropriate cooling for the shortlived radioactivity to die down, the spent fuel elements are transferred to a reprocessing plant where the fuel is first mechanically or chemically dejacketed from the cladding material. Next, the fuel is dissolved in nitric acid and the solution is subjected to solvent extraction for removal of fission products in the first stage and uranium in the second stage. The separated plutonium is further purified by ion-exchange process and obtained as plutonium nitrate.

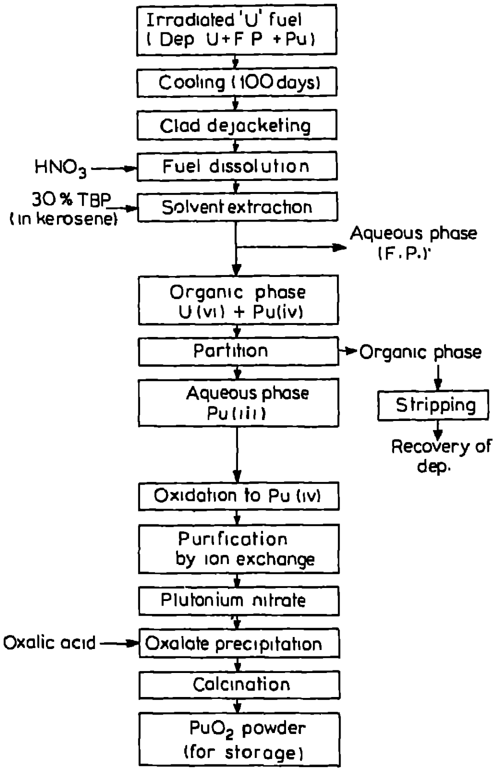

Figure 3. Flowsheet for recovery of plutonium from irradiated fuel.

The nitrate solution is converted to the oxide, mainly by the oxalate precipitation route followed by calcination in air at temperatures ranging from 400–700°C to get PuO_2 powder suitable for subsequent use. The oxalate process has low filtrate losses, good filterability and relatively high decontamination, particularly for iron. Direct calcination of the nitrate to oxide could dispense with the intermediate precipitation process and thus achieve considerable simplification. The process has been performed satisfactorily on laboratory scale, but suffers from the drawback of complete lack of purification and decontamination which is achieved during precipitation step and thus requires a very pure feed solution.

PuO_2 powder is usually the end product of a spent fuel reprocessing plant because it is most convenient to store plutonium in the form of the oxide from the point of chemical stability and ease of subsequent transportation.

3. Safety considerations

The high radiotoxicity, biological behaviour and fissile properties of plutonium present radiological and criticality hazards necessitating special safety considerations in handling of plutonium. In fact, this handling problem makes plutonium metallurgical operations a distinctively different and much more formidable task when compared with that of other conventional metals including uranium. Thus we had to first master the technique of safe handling of plutonium, either as fine powders or as bulk material, before any significant development of its metallurgy.

The decay characteristics of plutonium isotopes and their daughters are given in table 2 (Janardhanan *et al* 1973). ^{239}Pu, the major constituent, and other isotopes of plutonium except ^{241}Pu are predominantly powerful emitters of alpha radiation. Alpha particles emitted by plutonium isotopes do not constitute an external hazard because of its short range in air and body tissue (for ^{239}Pu alphas the range in air and body tissues

Table 2. Radioactive decay characteristics of plutonium isotopes and daughters.

Isotope	Radiation	Yield %	Energy (MeV)	Half-life	Specific activity (Ci/g)
Pu-238	Alpha	100	5·49	86·4 yr	17·4
	Gamma	10^{-3}	0·15		
	Gamma	8×10^{-3}	0·10		
	Gamma	$3·8 \times 10^{-2}$	0·044		
	L-X-ray	13	0·017		
Pu-239	Alpha	100	5·14	$2·436 \times 10^{4}$ yr	0·052
	Gamma	2×10^{-3}	0·038		
	Gamma	7×10^{-3}	0·052		
	Gamma	2×10^{-3}	0·12–0·20		
	Gamma	3×10^{-3}	0·38		
	L-X-rays	1·4	0·0136		
		2·2	0·0174		
		0·2	0·0205		
Pu-240	Alpha	76	5·162	$6·58 \times 10^{3}$ yr	0·23
	Alpha	24	5·118		
	Gamma	10^{-2}	0·044		
	L-X-rays	10	0·017		
	K-X-rays	40	0·102–0·125		
Pu-241	Alpha	3×10^{-3}	4·9	13·0 yr	111·5
	Beta	99·997	0.02		
	Gamma	2×10^{-4}	0·145		
	Gamma	10^{-3}	0·10		
Pu-242	Alpha	76	4·89	$3·79 \times 10^{5}$ yr	0·004
	Alpha	24	4·86		
	Gamma	10^{-2}	0·045		
	L-X-rays	10	0·017		
U-237	Beta	100	0·245	6·75 day	$6·74 \times 10^{-4}$
	Gamma	61	0·059		
	Gamma	35	0·207		
	Gamma	4	0·334		
Am-241	Alpha	84	5.48	458 yr	3·13
	Alpha	13·6	5.43		
	Gamma	37	0·017		
	Gamma	2·7	0·026		
	Gamma	0·05	0·043		
	Gamma	37	0·059		
	Gamma	0·02	0·099		

Table 3. Maximum permissible concentrations for plutonium radionuclides in body, air and water.

Radionuclide	MPBB		MPC (40 hr exposure/week) (*uc/cc*)	
	uc	*ug*	Air	Water
Pu-238	0·04	$2{\cdot}4 \times 10^{-3}$	2×10^{-12}	10^{-4}
Pu-239	0·04	0·65	2×10^{-12}	10^{-4}
Pu-240	0·04	0·18	2×10^{-12}	10^{-4}
Pu-241	0·9	$8{\cdot}2 \times 10^{-3}$	9×10^{-11}	7×10^{-3}
Pu-242	0·05	12·8	2×10^{-12}	10^{-4}
Am-241	0·05	$1{\cdot}6 \times 10^{-2}$	6×10^{-12}	10^{-4}
U-237	0·06	89	4×10^{-12}	9×10^{-5}

are 3·68 cm and 40 μm respectively). The primary concern in plutonium handling is to prevent particulate matter containing plutonium from entering the body of the operator through inhalation, ingestion or injection because plutonium poses the highest biological hazard when taken into the body. The long biological half-life, the high energy of the emitted alpha particles and the body's selective localisation of plutonium in the bone and lung lead to very low maximum permissible body burdens (MPBB) and maximum permissible concentrations (MPC) in air and water (table 3) (ICRP 1955). Any plutonium-bearing material is, therefore, handled in a well-ventilated laboratory within the confines of hermetically-sealed glove boxes through alpha-tight neoprene gloves. The glove box is maintained under a slightly negative pressure (− 0·2 to − 2″ WG) under a dynamic flow of air or high purity inert gas (N_2, A or He) in order to have 3–10 box volume changes per hour. Figure 4 gives the view of a glove box train

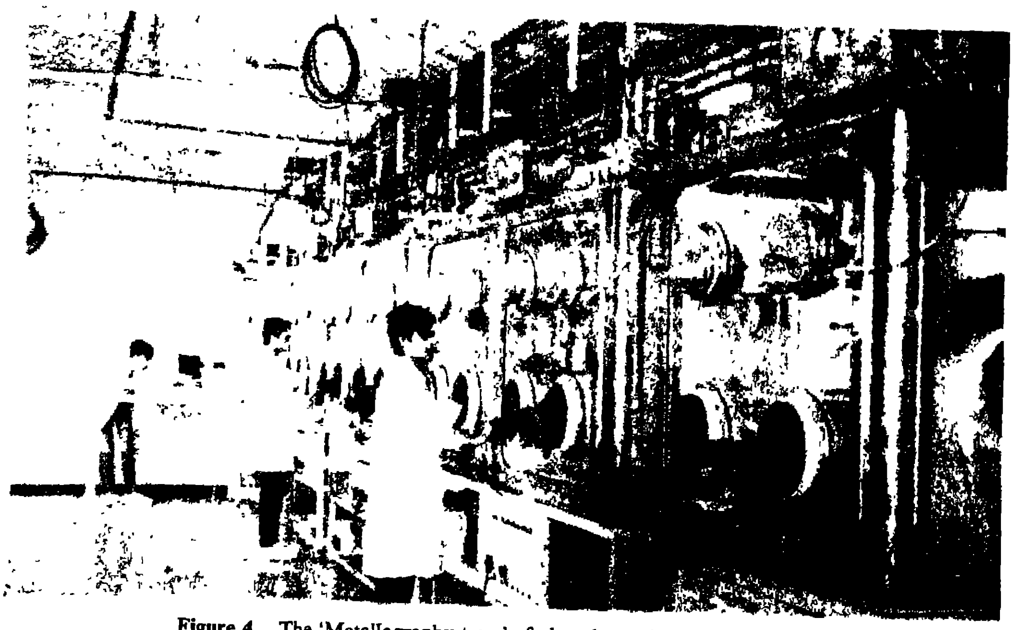

Figure 4. The 'Metallography train' of glove boxes in RMD, BARC.

set up in the Radiometallurgy Division at Trombay for safe handling of plutonium (Ghosh *et al* 1973). Inert atmosphere glove boxes are used for handling plutonium metal, carbide and nitrides which are highly susceptible to oxidation and hydrolysis and are pyrophoric in powder form.

The external hazard of plutonium is mainly from gamma and neutron radiations emitted by higher isotopes of plutonium which are present in significant amounts in high burnup plutonium. The surface dose rate of plutonium since its purification increases with time because of build up of ^{241}Am and ^{237}U, which are the daughter products of the beta emitting ^{241}Pu. Appreciable neutron dose rates are also associated with plutonium mainly from the spontaneous fission neutrons emitted by the even-numbered plutonium isotopes, e.g. ^{238}Pu, ^{240}Pu etc., and to some extent due to (α, n) reactions from plutonium in contact with light elements.

In order to keep the radiation exposure of operators below the permissible limits specified by the International Commission of Radiation Protection (ICRP) the following guidelines are usually followed:

(a) restrictions are imposed on the mass of plutonium that is handled at a time, to minimise mainly the neutron dose;

(b) great emphasis is given towards automation and remotisation during handling of plutonium;

(c) close containment of plutonium bearing powder and dust such that radioactive dust does not build up on equipment and glove box surfaces;

(d) use of external or localised composite lead glass and lucite shield for gamma and neutron radiation and the use of lead-loaded neoprene gauntlets, particularly while handling high burn-up plutonium.

Unlike other metallurgical industries, in a plutonium facility a maximum of a few kg

Table 4. Critical masses of some plutonium compounds.

Compound	Density (g/cc)	Critical mass (kg)	
		Bare	Water reflected
Pu-solution	—	—	0·51
Pu			5·6 α phase 7·6 δ phase
PuO_2	11·46	24·5	12·2
PuN	14·25	18·4	9·23
PuC	13·6	17·93	9·07
PuH_2	10·4	15·64	7·49
PuH_3	9·61	12·69	6·32
Pu_2C_3	12·7	19·72	9·96
Pu_2O_3	11·47	24·95	12·05
$PuCl_3$	5·7	167·05	61·59
PuF_3	9·32	32·59	16·0
PuF_4	7·0	56·29	25·29
$Pu(C_2O_4)_2$	4·5	152·0	66·87
$Pu(NO_3)_4$	6·2	103·96	54·94

of fissile material is handled at a time to avoid spontaneous self-sustaining nuclear chain reaction or what is known as the criticality accident which can be catastrophic to the personnel and its surroundings. The critical mass of plutonium and its compounds depend on the geometry and the environment. Table 4 gives the critical mass of plutonium and some of its important compounds (Hansen and Clayton 1967). The upper safe limit during handling is usually kept at 50% of the critical mass.

In the plutonium metallurgy laboratory at Trombay safety has always been given priority over cost, convenience and even production capacity. As a result, there has not been a single radiation incident till todate.

4. Nuclear parameters

The important nuclear parameters of the three principal fissile nuclides ^{235}U, ^{239}Pu and ^{233}U are listed in table 5 (Hanna *et al* 1969). η, the average number of neutrons produced per neutron absorbed by the fissile nucleus is the most important parameter as it influences the conversion or breeding ratio (CR), *i.e.* the average number of fissile atoms produced in a reactor per fissile atom consumed by fission or capture. The conversion ratio is quantitatively expressed as:

$$\text{CR} = \eta - 1 - L$$

where one neutron is needed to continue the chain reaction and L represents the non-productive absorption and leakage per neutron absorbed by fissile atom.

Since ^{239}Pu and ^{233}U have the highest η values in the fast and thermal neutron range respectively, plutonium breeds best in a fast reactor and ^{233}U is best suited for thermal converter reactors. In fact, in a fast reactor operating on a ^{238}U-^{239}Pu fuel cycle, it is possible to have a breeding ratio in the range of 1·2 to 1·4.

The other advantages of plutonium as a fissile material in fast reactors compared to ^{235}U are the higher fast fission cross-section (Pu : 1·77 barns; U : 1·44 barns), 5% higher

Table 5. Nuclear properties of the principal fissile nuclides.

	Property	^{233}U	^{235}U	^{239}Pu
σ_a =	Neutron absorption cross-section	578 ± 2	578 ± 2	1013 ± 4
σ_f =	Fission cross-section	531 ± 2	580 ± 2	742 ± 3
σ_c =	Neutron capture cross-section	47 ± 1	98 ± 1	271 ± 3
α =	Ratio of captures to fissions	0·089 ± 0·002	0·169 ± 0·002	0·366 ± 0·004
ν =	The number of neutrons produced per fission	2·487 ± 0·007	2·423 ± 0·007	2·880 ± 0·009
η =	The number of neutrons created per neutron absorbed by the nuclide			
	(a) Thermal neutrons	2·284 ± 0·006	2·072 ± 0·006	2·109 ± 0·007
	(b) Fast neutrons	2·31	1·93	2·49

The cross-sections σ_a, σ_f, and σ_c are in barns and α, ν and η are ratios.

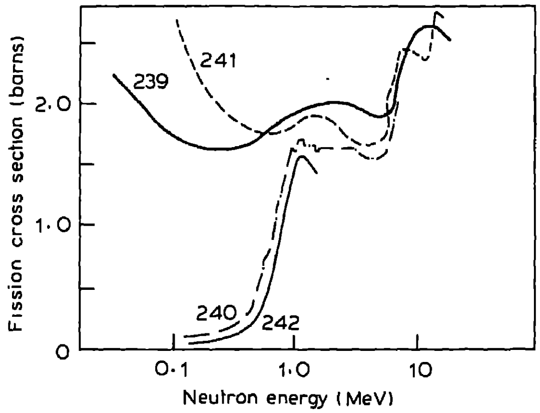

Figure 5. Fast fission cross-section (barns) of Pu isotopes

fission energy release and lower xenon poisoning. Further, ^{241}Pu is fissile in both thermal and fast neuton range and ^{240}Pu and ^{242}Pu, though parasitic, neutron absorber for thermal neutrons, contribute significantly to fast fission. The fission cross-section of important plutonium isotopes in the fast neutron range is shown in figure 5 (Wick 1980).

From reactor physics consideration it may, therefore, be summarised that plutonium is the best fuel for fast reactors but is slightly inferior to ^{233}U and ^{235}U in the thermal neutron range.

5. Plutonium metal

5.1 *Preparation*

While starting plutonium metallurgical work at Trombay, we had already selected uranium metal as the fuel for our CIRUS Research reactor. It was, therefore, logical for us to first direct all the efforts towards manufacture of high purity nuclear grade plutonium metal.

Much of the metallurgical knowledge for preparation of plutonium metal was acquired during the Manhattan Project in the 1940s. The free energy diagrams of oxide and fluoride of plutonium (Coffinberry and Miner 1961) and other metals are shown in figure 6 and table 6 gives the various thermodynamic data of the reduction reaction (Stoller and Richards 1961). Reduction of plutonium halides, in particular, fluoride and chloride remains the only method by which virtually all the metal is produced till today.

The need to obtain plutonium in massive form with a high yield dictates the choice of a reducing reaction. The reduction reaction should be accompanied by evolution of large quantity of heat which should not only melt the reaction products but also keep them molten long enough for good slag-metal separation. The reducing agent should not dissolve in plutonium or form any intermetallic compound with it. Low melting point of the slag and high boiling point of the reducing agent are additional requirements. Considering all these factors it is found that the reduction of plutonium tetrafluoride with calcium is sufficiently exothermic and the slag in this case melts at a

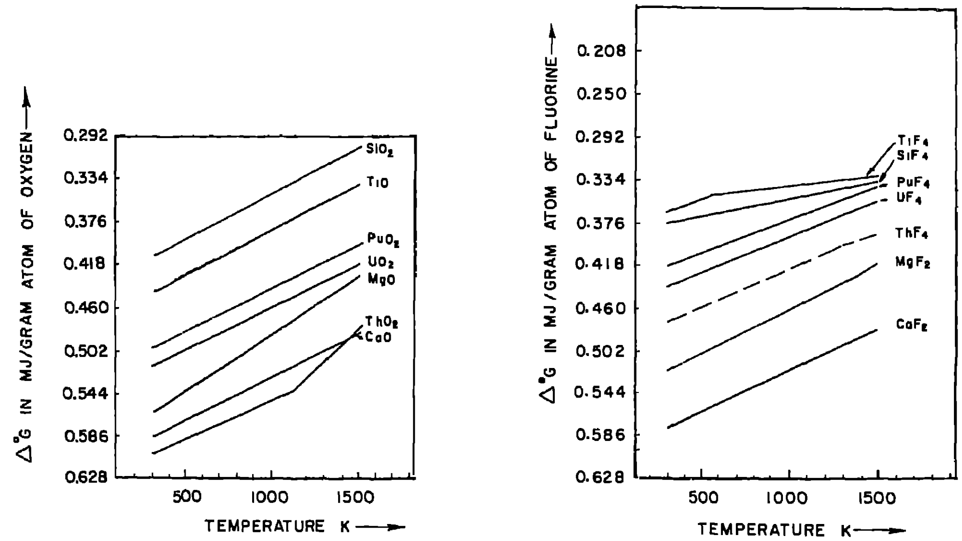

Figure 6. Standard free energy of formation (ΔG°) for important oxides and fluorides of U and Pu.

Table 6. Thermodynamic data of the possible reduction reactions for preparation of plutonium metal

Reaction	ΔH at 291 K, kcal/mol. plutonium	Melting Point of Slag (°C)
$PuO_2 + Ca \rightarrow Pu + 2CaO$	−52·4	2572
$PuO_2 + 2Mg \rightarrow Pu + 2MgO$	−40·5	2500–2800
$PuO_2 + \frac{4}{3}Al \rightarrow Pu + \frac{2}{3}Al_2O_3$	−9	2050
$PuF_4 + 2Ca \rightarrow Pu + 2CaF_2$	−149·5	1414
$PuF_4 + 0{\cdot}3I_2 + 2{\cdot}3Ca \rightarrow$		
$Pu + 0{\cdot}3CaI_2 + 2CaF_2$	−196	1320
$PuF_4 + 2Mg \rightarrow Pu + 2MgF_2$	−104·6	1225
$PuF_4 + \frac{4}{3}Al \rightarrow Pu + \frac{4}{3}AlF_3$	+15	1040
$PuCl_3 + \frac{3}{2}Ca \rightarrow Pu + \frac{3}{2}CaCl_2$	−56·0	772
$PuCl_3 + \frac{3}{2}Mg \rightarrow Pu + \frac{3}{2}MgCl_2$	+0·2	708

reasonably low temperature. It can be further seen that the addition of 0·3 mole of iodine makes the reaction more exothermic and also lowers the melting point of the slag by about 100°C.

Figure 7 shows the flowsheet followed at BARC (Roy and Mahajan 1975) for the reduction of tetrafluoride with calcium. Plutonium tetrafluoride and calcium metal in amount equal to stoichiometric plus 30 to 50% excess are mixed thoroughly and charged into a steel bomb which is capable of withstanding pressures of 0·5–3 MPa and temperature upto 1600°C. The bomb is first purged with argon to exclude any air present. The sealed bomb is subjected to resistance or induction heating to about 600°C when the reduction reaction takes place and the products are melted by the heat

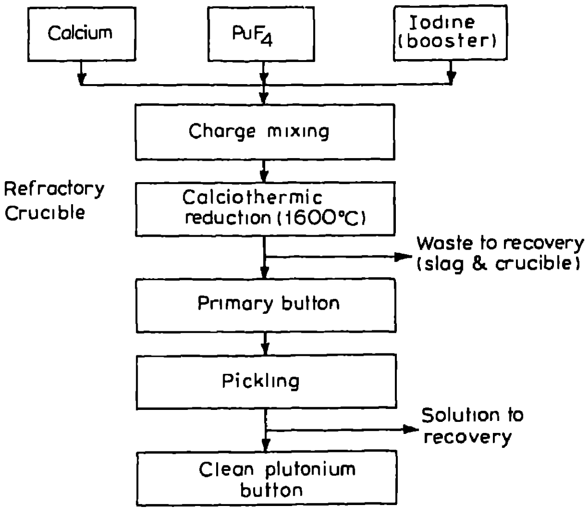

Figure 7. Flowsheet for preparation of plutonium metal.

generated. It is very essential to control the heating rate. If the heating is too rapid, the reaction takes place only at the surface and thus the slag solidifies too rapidly. On the other hand, if preheating period is too long, the calcium particles get coated with CaI_2 retarding the rate of reaction. The start of the reduction reaction is indicated by a sudden rise in the temperature monitored by a thermocouple or by a drop in the neutron emission from the reaction chamber. The yield in this process is generally 97–99 % and the purity normally exceeds 99·8 %. Alternatively PuF_4 and finely divided calcium (50 % excess) are mixed and pressed into pellets. The pellets are loaded into a calcium fluoride crucible and then in a quartz tube. On heating a bright flash shows the initiation of the reaction.

Direct reduction of dioxide would overcome the drawbacks of the fluoride and chloride processes namely high neutron emission and hygroscopicity respectively. It would also simplify the process by the elimination of the costly halogenation step. Recent studies (Wade and Wolf 1969) have shown that by proper modification of the reduction apparatus and by using a suitable flux, it is possible to obtain plutonium in massive form by calciothermic reduction of the oxide. Reduction of dioxide by carbon becomes feasible only at temperatures of the order of 3000°C and requires high vacuum system. It also suffers from the formation of plutonium carbide.

5.2 *Melting and casting*

The fabrication of plutonium involves many of the techniques commonly utilised for working of the common metals. However, all operations are directly affected by the extreme toxicity of plutonium in any form, the tendency of the metal to oxidise rapidly, the pyrophoricity and by the obvious necessity of avoiding conditions of criticality.

The low melting point of plutonium offers a considerable amount of freedom in the selection of melting equipment. Although resistance, arc and electron beam furnace have been used for melting plutonium, inductive heating is most advantageous.

Extremely high reactive nature of molten plutonium poses a big problem in the choice of crucible material. Different types of crucible materials have been used. Of the metallic crucibles, tantalum has been extensively used but its use is limited to a maximum temperature of 1000°C after which it is rapidly dissolved by plutonium. Ceramic materials like CaO, Y_2O_3 and CaF_2 are good but not used because of their fragile nature. Al_2O_3, BeO, ThO_2 lead to contamination of the melt. MgO has been widely used but it also leads to slight contamination of the melt. Graphite has been found to be an excellent crucible material. It is inexpensive, can be easily fabricated and is not subject to thermal shock. However, a suitable coating must be applied to the graphite surface to prevent carbon pick up in the melt. Crucibles may be either tilt-pouring or bottom-pouring type depending upon the type of work to be carried out.

Graphite also serves as the most commonly employed mould material. Metal moulds made of gray cast iron, mild steel, copper and for special purposes tantalum have been used.

Unalloyed plutonium has the general characteristics of a very castable material. The low melting point, high fluidity, high density and extremely small volume change on freezing are all favourable characteristics for casting. Piping and shrinkage porosity observed in most other metals are not encountered when casting plutonium. However, during cooling to room temperature a number of phase transformations take place in pure plutonium metal some of which are accompanied by large volume changes. Accordingly extreme care is exercised in the design of the mould such that the casting does not adhere firmly to the mould and cause cracking. The mould is usually heated to avoid cold shuts in the casting.

6. Aluminium-plutonium alloys

As early as in 1961, side by side with the production of plutonium metal, we had also taken up the preparation of Al-Pu alloys by employing similar metallothermic reduction technique (Roy 1962). This technique is particularly advantageous for plutonium alloy preparation because it eliminates costly steps of plutonium metal production, its handling in inert atmosphere and also avoids the problem of gravity segregation which is a common occurrence when a light metal like aluminium is alloyed with plutonium.

Around 500 mg of Al-6·27% Pu were prepared by aluminothermic reduction of PuO_2 in the presence of excess aluminium and cryolite in a graphite crucible around 1100°C. The reaction involved is as follows:

$$3PuO_2 + 4Al = 3Pu + 2Al_2O_3$$
$$\Delta G_{1500K} = -42\ \text{kcal/mol.}$$

The reduced plutonium immediately alloys with the excess aluminium and the cryolite fluxes the Al_2O_3. The reaction thus proceeds in the forward direction with proper slag metal separation and high yield. The alloy thus made was recovered by breaking the graphite crucible, remelted for proper homogenisation and cast in another graphite crucible. In the very first preparation itself we could get a yield as high as 96%.

No plutonium metallography facility was available in Trombay at that time. A make-shift arrangement was made for sample preparation, *e.g.* cutting, mounting, grinding, polishing and etching of alloy samples inside a glove box. The microscope, however, was kept outside the glove box and the sample was examined through a transparent plastic bag attached to the glove box. The as-cast microstructure of the alloy ingot (figure 8) clearly shows lamellar $PuAl_4$ particles in an Al matrix.

Al-Pu alloys containing 3–20 w/o plutonium have found widespread application in many research reactors. Aluminium because of its low parasitic thermal neutron absorption cross-section (0·22b) and high thermal conductivity is considered as an excellent inert carrier for the fissile plutonium. Since plutonium has negligible solid solubility (Roy 1964; Ellinger *et al* 1962) with aluminium (figure 9) these alloys essentially comprise of a dispersion of the intermetallic $PuAl_4$ in an aluminium matrix.

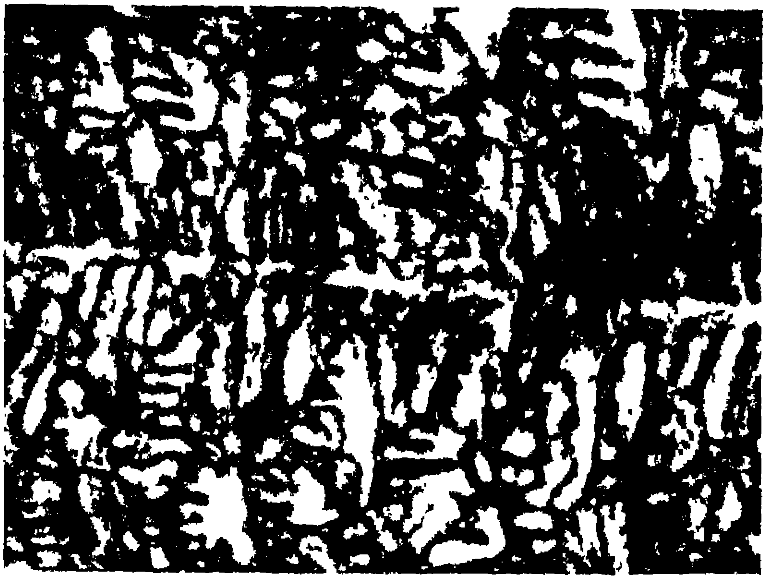

Figure 8. Microstructure of cast aluminium-plutonium alloy (prepared in 1961, × 100).

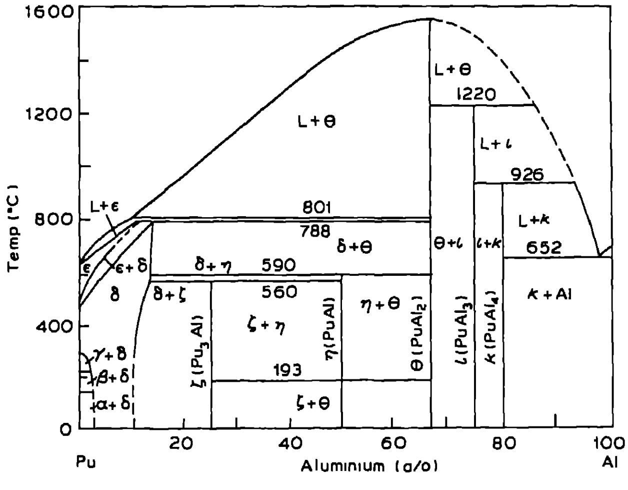

Figure 9. Plutonium aluminium phase diagram.

Such dispersion fuel has the advantage of minimum radiation damage by restricting the fission recoil damage to the area immediately adjacent to the fissile dispersoid particles, namely $PuAl_4$, which are relatively small in size leaving a large area of undamaged non-fissile matrix metal aluminium, which is predominant in volume and in the form of a continuous network surrounding the $PuAl_4$ phase.

Towards the end of 1960s, 60 g of Al-13 w/o Pu in the form of sheets (40 × 40 × 0·5–2 mm) was prepared for nuclear physics experiments (Roy *et al* 1969). Experience in cold rolling of Al-Pu alloys was obtained during this campaign.

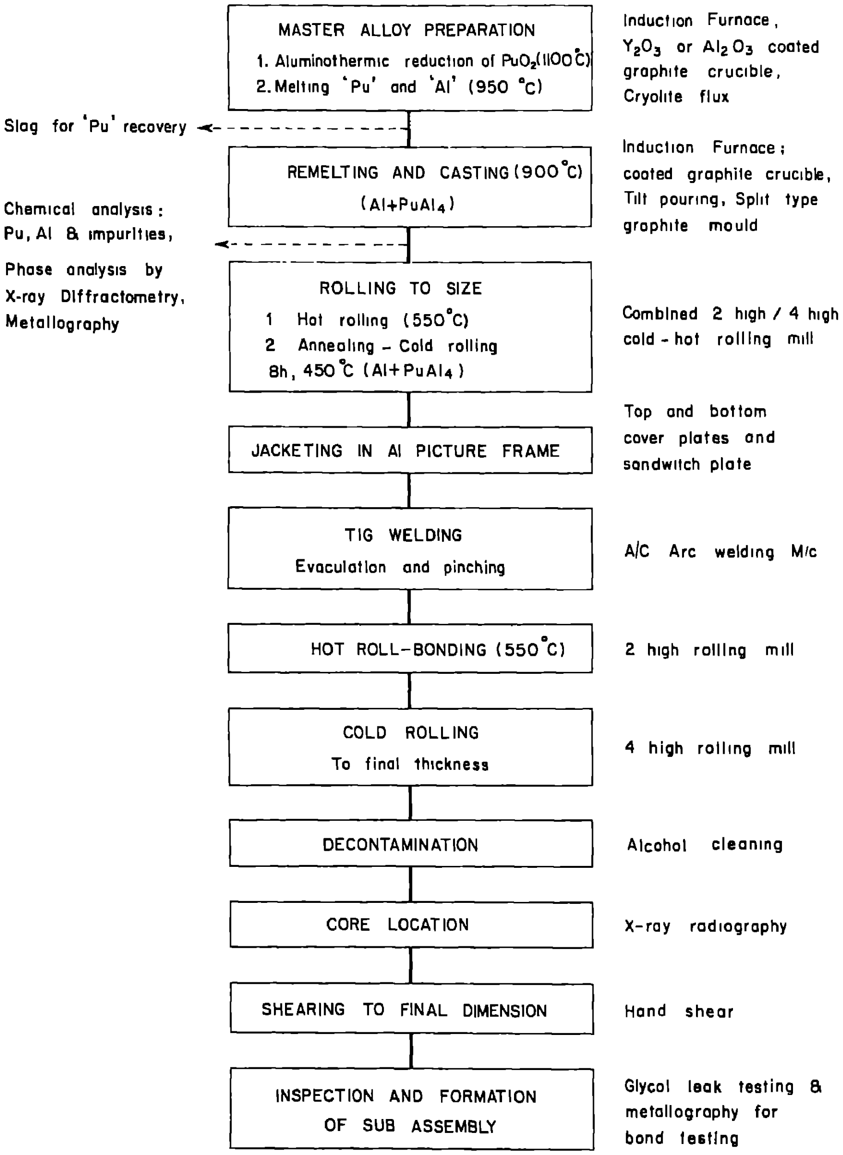
MASTER ALLOY PREPARATION
1. Aluminothermic reduction of PuO₂(1100°C)
2. Melting 'Pu' and 'Al' (950 °C)
Induction Furnace, Y₂O₃ or Al₂O₃ coated graphite crucible, Cryolite flux
Slag for 'Pu' recovery
REMELTING AND CASTING (900°C) (Al+PuAl₄)
Induction Furnace; coated graphite crucible, Tilt pouring, Split type graphite mould
Chemical analysis: Pu, Al & impurities,
Phase analysis by X-ray Diffractometry, Metallography
ROLLING TO SIZE
1 Hot rolling (550°C)
2 Annealing - Cold rolling 8h, 450 °C (Al+PuAl₄)
Combined 2 high / 4 high cold - hot rolling mill
JACKETING IN Al PICTURE FRAME
Top and bottom cover plates and sandwich plate
TIG WELDING
Evaculation and pinching
A/C Arc welding M/c
HOT ROLL-BONDING (550°C)
2 high rolling mill
COLD ROLLING
To final thickness
4 high rolling mill
DECONTAMINATION
Alcohol cleaning
CORE LOCATION
X-ray radiography
SHEARING TO FINAL DIMENSION
Hand shear
INSPECTION AND FORMATION OF SUB ASSEMBLY
Glycol leak testing & metallography for bond testing

Figure 10. Flow sheet followed in BARC for fabrication of Al clad Al-Pu plate fuel element.

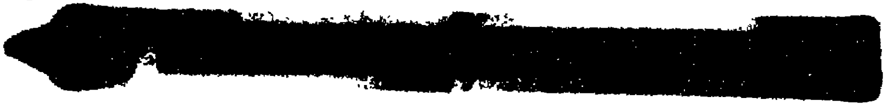

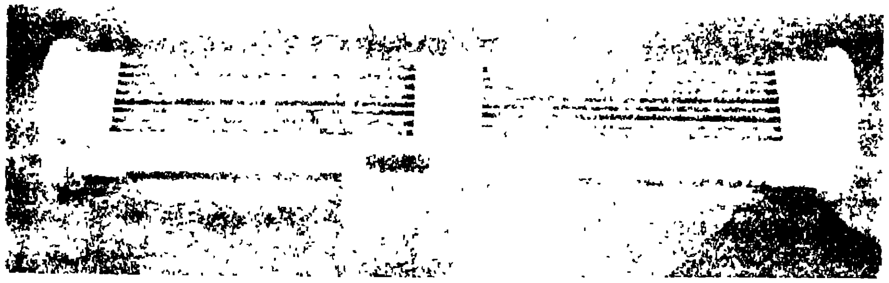

Figures 11, 12. **11.** X-ray radiograph of Al clad Al-Pu alloy plate fabricated in radiometallurgy division, BARC. Dark areas show the alloy meat. **12.** 9 plate fuel subassembly of Al clad Al-Pu alloy. After irradiation testing in Zerlina reactor in BARC.

With the commissioning of the new Plutonium Metallurgy Laboratory in 1970, a new pilot scale facility was set up for fabrication of Al-Pu alloy fuel elements at BARC. The main equipment consisted of a high vacuum induction melting-casting unit, a 2 high/4 high cold/hot rolling mill and an annealing furnace.

This facility was utilised in 1973 to fabricate 2 nine plate sub-assemblies of Al-10 w/o Pu and Al-18 w/o Pu plate fuel elements (445 × 51·75 × 1·78 mm) by the "picture-frame technique" according to the flowsheet shown in figure 10 (Prasad *et al* 1976) for nuclear physics experiments in the ZERLINA reactor at BARC. The Al-Pu alloy meat was hot roll-bonded to the aluminium cover plates at 450°C. The radiograph of a roll-bonded Al clad Al-Pu alloy fuel plate and the photograph of a 9-plate sub-assembly fabricated at BARC are shown respectively in figures 11 and 12.

Such Al-Pu plate fuel elements could be utilised as a substitute for the imported aluminium clad Al-13 w/o U(85% enriched ^{235}U) plate fuels used in the Apsara Swimming Pool type test reactor at BARC. It also can be used as boosters in our pressurised heavy water reactors (PHWR) to overcome xenon poisoning following post shut-down start-ups.

7. Plutonium-beryllium alloys

Pu-Be alloys are used as low flux neutron sources utilising the interaction of alpha particles from plutonium with beryllium atoms to generate neutrons according to the reaction $\mathrm{Be}^9\,(\alpha, n)\mathrm{C}^{12}$. The principal advantages of Pu-Be alloys over Ra-Be and Po-Be neutron sources is the stability of the neutron yield with respect to time due to the long half-life of ^{239}Pu (24360 yr) and the relatively small amount of low energy gamma radiation. Moreover, plutonium is relatively non-volatile as compared with radium or polonium and since it readily alloys with beryllium, it is possible to prepare the Pu-Be neutron source as an alloy rather than pressed mechanical mixtures. The alloying further leads to mechanically strong, non-friable body and reproducibility in neutron yield. The neutron yield of Pu-Be alloys, as shown in figure 13 depends on the beryllium to plutonium atom ratio N according to the relation:

$$\frac{n}{n_{\max}} = \frac{N \times S_{\mathrm{Be}}}{(N \times S_{\mathrm{Be}} + S_{\mathrm{Pu}})}$$

where, $n/n_{\max}$ is the fraction of maximum neutron yield, S_{Pu} is the stopping power of Pu $= 4{\cdot}5$ and S_{Be} is the stopping power of Be $= 0{\cdot}63$. The neutron yield for a beryllium and plutonium ratio of 13, at which the alloy consists of the intermetallic PuBe_{13} (figure 14) is only 36·7 per 10^6 alphas compared to 54·9 per 10^6 alphas for an atom ratio of 200. An atom ratio of 30 leads to good compromise between the physical size of the source and

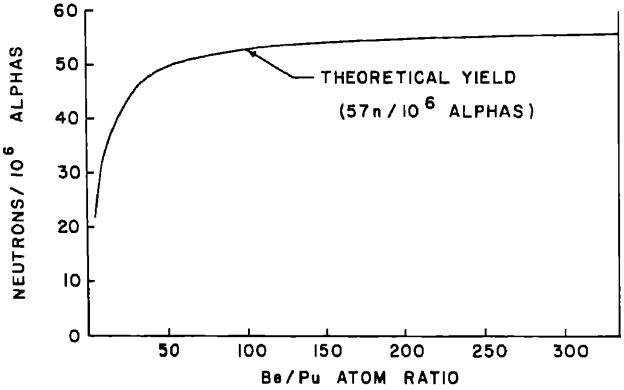

Figure 13. The variation of neutron yield with Be:Pu atom ratio.

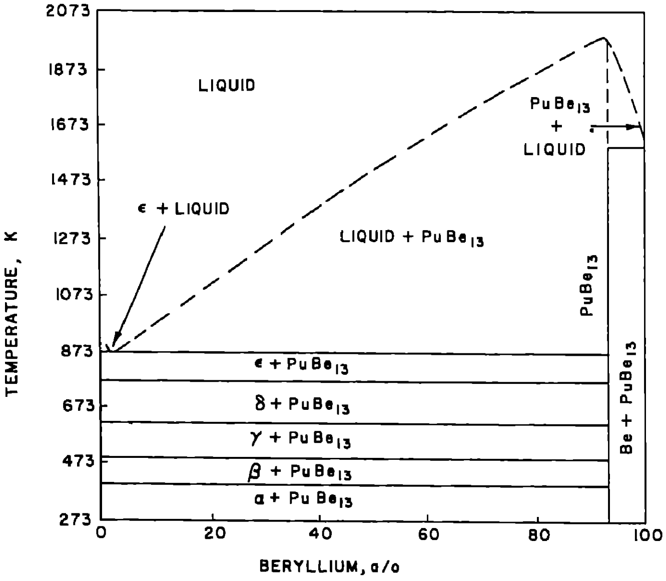

Figure 14. Pu-Be phase diagram.

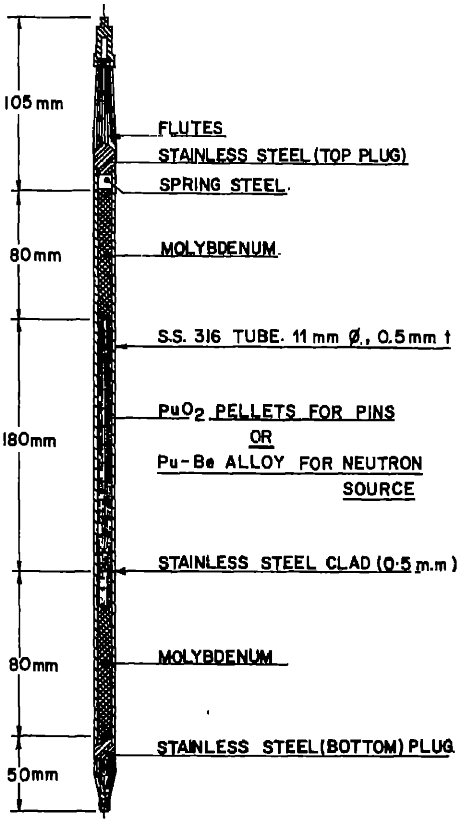
105mm
80mm
180mm
80mm
50mm
FLUTES
STAINLESS STEEL (TOP PLUG)
SPRING STEEL
MOLYBDENUM
S.S. 316 TUBE. 11 mm Ø, 0.5mm t
PuO2 PELLETS FOR PINS
OR
Pu-Be ALLOY FOR NEUTRON SOURCE
STAINLESS STEEL CLAD (0·5 m.m)
MOLYBDENUM
STAINLESS STEEL (BOTTOM) PLUG

Figure 15. Fuel pin and pencil neutron source for Purnima.

its neutron yield of 46 per 10^6 alphas. Further, alloys with $N \geqslant 30$ are easily sintered at a relative low temperature of 1250°C but for N lower than 30 a minimum sintering temperature of 1400°C is required.

The first Pu-Be neutron source of nearly 1 Curie strength was prepared at BARC (Roy *et al* 1967) in 1967 by berylothermic reduction of pellets prepared from a powder mixture of around 18 g each of PuO_2 and Be in vacuum at 1250°C (Be:Pu atom = 30). The reaction is as follows:

$$PuO_2 + 2\,Be = Pu + 2\,BeO \qquad \Delta G_{1000K} = -29{\cdot}4\ \text{kcal/mol.}$$

The presence of BeO in the reaction product does not alter the neutron emission. The alloys thus prepared undergo reaction sintering and consist of a fine dispersion of $PuBe_{13}$ and BeO in a matrix of Be. Subsequently in 1972, the same technique was followed for the preparation of several point and pencil neutron sources of strength between 50 mCi and 5 Ci (Mahajan *et al* 1972).

The Pu-Be neutron sources are encapsulated in metallic cans. For the point source the Pu-Be alloy tablet is first loaded in a one end closed aluminium or stainless steel container with a screwed cap. This sealed inner container is next loaded in an outer container of stainless steel and encapsulated by TIG welding. These point sources have been delivered to several agencies within and outside BARC for calibration of neutron counters, physics experiments and devices for measuring moisture and hydrocarbons in soil. The 900 mCi pencil sources (figure 15) were used for start-up of the PURNIMA reactor at BARC.

8. Delta-stabilised plutonium alloys

Unalloyed plutonium, unlike uranium has never been tried as a nuclear fuel because of its unfavourable metallurgical properties. First, plutonium has a low melting point (640°C). Secondly, there are as many as 6 allotropic transformations of plutonium between 20 and 640°C as shown in table 7 (Zachariasen and Ellinger 1959). No other metal shows as many phase changes within such a narrow temperature range. Particularly undesirable is the large volume change, of the order of 10%, which accompanies the alpha to beta transformation at 122°C. It was, therefore, natural to look for a high temperature phase which could be stabilised down to the room temperature by a proper combination of alloying and heat treatment.

Delta plutonium which is stable between 315 and 456°C has a fcc structure and exhibits the highest ductility and best formability amongst all the plutonium allotropes. The delta phase can be retained at room temperature by small additions of Al, Sn, Zn, Ga, Zr, In, Hf, Tl, Ce, Dy, Er, Tn, La or Th. The delta-stabilised plutonium has many desirable mechanical and metallurgical properties. It is ductile and soft, has a hardness value of 40–45 kg/mm^2 (Vicker's DPH) which is comparable to annealed copper and can be conveniently machined, worked and turned. Further, these alloys have negligible volume change during working, produce good quality casting and are more resistant to oxidation compared to unalloyed plutonium. However, the density of delta-stabilised plutonium is less than unalloyed plutonium.

Delta-stabilised plutonium alloys have been used as fuels in the first fast reactor Clementine of LASL in the late 1940s and subsequently in core IV of EBR I of ANL, ZEPHYR of Harwell and BR-1 and 2 of USSR in the early 1950s.

Delta-stabilised plutonium alloys have been prepared at BARC in the 1970s by vacuum induction melting in coated graphite crucibles and casting in graphite moulds. The principal difficulties faced in melting, and casting these alloys are gravity segregation due to large density difference between plutonium and the alloying elements and adherence of the cast alloy with the mould because of negligible solidification shrinkages of delta plutonium.

Table 7. Allotropes of plutonium and their properties.

Phase	Structure	Stability range (°C)	Density (g/CC)	Coeff. of expansion (micro in./in. °C)	$\Delta V\%$
α	Simple monoclinic	Up to 117	19·84	48·4	10·10
β	Body centred monoclinic	117–213	17·8	38.0	2·58
γ	Face centred orthorhombic	213–315	17·14	34·7	6·75
δ	fcc	315–456	15·92	−8·8	−0·25
δ'	bct	456–475	16·01	−116·0	−3·0
ε	bcc	475–640	16·48	36·5	

9. Plutonium dioxide

In the field of ceramic fuel too the trend developed in the uranium system had set the pattern in the plutonium field. In the 1960s uranium dioxide was universally used in most of the commercial thermal power reactors, including ours, and the technology for the production of zircaloy clad UO_2 fuels by the "pellet-in-tube" process was available in Trombay (Fareeduddin *et al* 1975). This know-how was conveniently extended for the initial development of stainless steel clad PuO_2 fuels in the new plutonium metallurgy laboratory at Trombay in 1970 (Roy 1975).

Subsequently, the first major plutonium fuel fabrication job was executed in 1972 when the complete core for the zero energy fast reactor PURNIMA in BARC consisting of 186 fuel pins containing around 25 kg, of sintered PuO_2 fuel pellets was fabricated. The fuel pin (495 mm long × 11 mm OD) (figure 15) with a cladding thickness of 0·5 mm and consists of a stack of sintered PuO_2 fuel pellets of average density of 90 % theoretical, held tight by a spring between a pair of axial molybdenum reflectors in a 316 stainless steel cladding tube which is sealed leak tight by TIG welded end plugs.

PuO_2 pellets were prepared from oxalate derived sinterable PuO_2 powder by the powder metallurgy route of cold compaction at around 25 TSI followed by sintering at 1600°C in $A + 8\,\%H_2$ atmosphere. The finished fuel pins were subjected to rigorous inspections for dimensional checks, x-ray radiographic examinations, mass spectrometric helium leak detection and surface contamination.

10. Mixed oxide fuels

Pure PuO_2 as such is not suitable for use as fuel in power generating reactors as it fails to satisfy the reactor engineering and safety requirements of bigger reactors. Further, for breeding additional fissile material simultaneously with power generation it is essential to dilute PuO_2 by mixing with fertile materials like UO_2 or ThO_2.

The following mixed oxide fuel compositions have been studied and developed in the last ten years as a part of our fuel development programme for water-cooled thermal and liquid metal cooled fast breeder reactors (LMFBR):

(a) 76 % PuO_2–24 % natural UO_2 or 70 % UO_2–30 % PuO_2 (assuming availability of 85 % enriched ^{235}U for actual use) fuels for our fast breeder test reactor (FBTR).
(b) UO_2–PuO_2 (up to a maximum of 5 w/o PuO_2), popularly known as the MOX fuel, as substitute for the 2–4 % enriched UO_2 fuels for the BWRs at TAPS.

Since UO_2 and PuO_2 are isostructural (fcc, CaF_2 type), mutually solid soluble and have similar physical and chemical properties (table 8), the fabrication flowsheets (figure 16) of the mixed oxides are essentially the same and involves three major steps, namely, (i) simultaneous mixing grinding of the two oxide powders in the desired proportion, (ii) cold compaction of the powder mixture into pellets with or without binder addition, and (iii) sintering the pellets in a controlled atmosphere. The process control steps in pellet fabrication should ensure homogeneous solid solution formation, uniform distribution of plutonium, an oxygen to metal ratio slightly in the hypostoichiometric range and a controlled density.

In addition to the above route, in Trombay we are also working on the "vibrosol" process as an alternative method of preparation of mixed oxide fuel pins (Sood and

Table 8. Selected properties of U, Pu and Th compounds.

Property	Oxide			Carbide		Nitride	
	UO_2	PuO_2	ThO_2	UC	PuC	UN	PuN
Theoretical density (g/cm^3)	10·96	11·46	10·00	13·63	13·60	14·32	14·25
Metal density (g/cm^3)	9·66	10·10	8·79	12·97	12·95	13·52	13·46
Metal fraction (w/o)	88·15	88·19	87·89	95·20	95·20	94·44	94·46
Melting point (K)	3000	2675	3640	2780	1875	3125	2840
Thermal conductivity (W/cm K) for 100% TD material							
1000 K	0·052	0·034	0·062	0·199	0·108	0·185	0·146
1500 K	0·035	0·023	0·024	0·213	0·142	0·248	0·167
2000 K	0·022	0·018	—	0·225	0·159	0·270	0·184

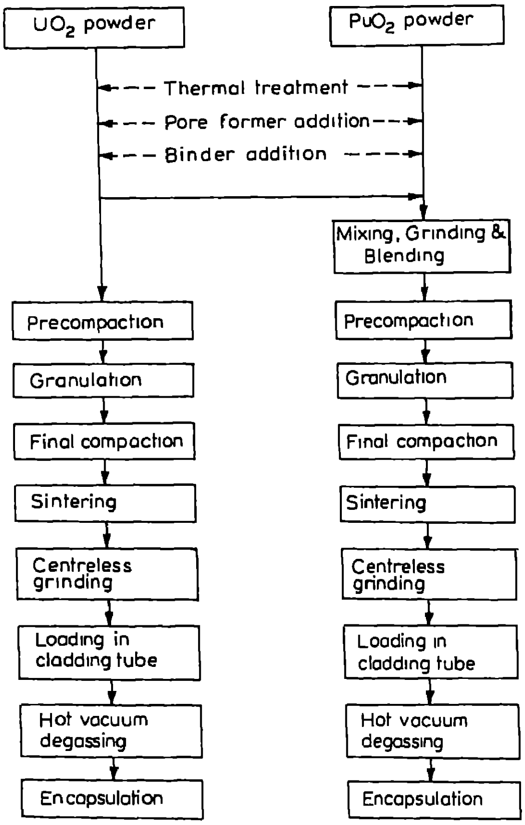

Figure 16. Process flow sheet for UO_2 and UO_2-PuO_2 pellet fuel pin.

Vaidya 1979). This method consists of preparing mixed oxide gels by a "wet chemical route" starting from uranyl and plutonium nitrate solutions followed by calcination of the gels to get mixed oxide microspheres of high density ($\sim$ 98% TD). By blending microspheres of different size fractions in the range of 10–100 μm and packing them in the fuel pin by "vibratory compaction", smear density of the fuel pin can be controlled between 60 and 90% TD. An "internal gelation" (Kanij *et al* 1974) process has been followed for preparing mixed oxide microspheres according to the flowsheet shown in figure 17. The nitrate solutions of the actinides are mixed and cooled. To this, concentrated hexamethylene tetra amine (HMTA) and urea solutions are added which act as internal gelation agents. Droplets of this solution are gelled by contact with hot (~90°C) silicone or paraffin oil.

The vibro-sol method offers the following advantages over the cold pressing sintering process:

(a) There are less number of fabrication steps and maximum flexibility of operation.

(b) A high degree of microhomogeneity is obtained in the microsphere since the blending is effected in the liquid stage and steps like prolonged ball milling of oxide powders for achieving good homogenisation are avoided.

(c) The build-up of radioactive dust on equipment and glove box surfaces which is rather common in the powder metallurgy route is also avoided since no fine powder handling is involved.

(d) The method is more suitable for remote operation and automation.

The main drawback of the vibro-sol route is that in the event of an accidental breach of the cladding tube, there could be more expulsion of fuel particles to the coolant circuit as compared to pellet fuel, thereby causing a gross contamination of the primary coolant.

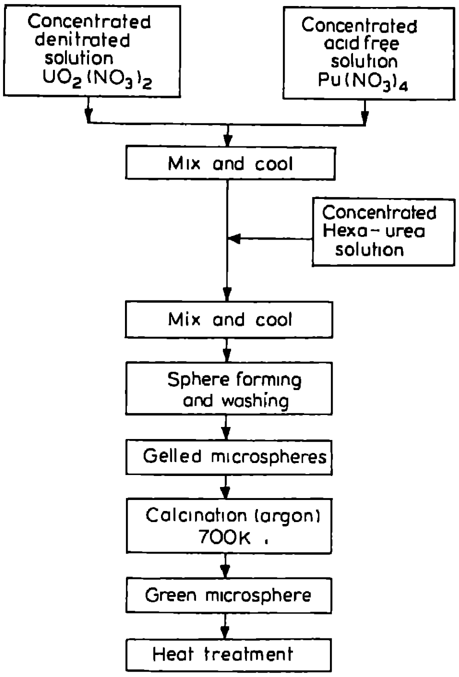
Concentrated denitrated solution $UO_2(NO_3)_2$
Concentrated acid free solution $Pu(NO_3)_4$
Mix and cool
Concentrated Hexa-urea solution
Mix and cool
Sphere forming and washing
Gelled microspheres
Calcination (argon) 700K
Green microsphere
Heat treatment

Figure 17. The kema internal gelation process.

10.1 UO_2–PuO_2 *for* LMFBRS

As a first step of our venture in the LMFBR technology a decision was taken in the 1970s to set up a small 42·5 MW(th) fast breeder test reactor (FBTR), similar to the Rapsodie-Fortissimo reactor of France, at the Reactor Research Centre, Kalpakkam. It was also decided to fabricate the fuel for this reactor in Trombay from our available natural uranium resources and plutonium. Normally, in such small test reactors the fissile requirement of the core, as shown in figure 18, is met by enriched uranium along with plutonium in order to have a high neutron flux level and to compensate for the neutron leakage loss in the small core. However, we preferred to replace the ^{235}U completely by plutonium and consequently looked into the possibility of using 76 % PuO_2–24 % UO_2 in place of already proven 70 % UO_2 (enriched to 85 % ^{235}U)–30 % PuO_2 fuel of Rapsodie.

Unfortunately, preliminary metallurgical investigations revealed that $(U_{0\cdot24}Pu_{0\cdot76})O_2$ was not compatible with the sodium coolant and led to the formation of $Na_3(U, Pu)O_4$ with accompanying high swelling as shown in figure 19(a) (Internal Report 1970; Housseau 1974). The sodium-fuel interaction and in turn the swelling could be significantly reduced if the O/M ratio of the fuel was kept around 1·8 (figures 19b, c) but then the already low thermal conductivity of the plutonium rich oxide fuel further reduces by nearly 30 % (figure 20) (Internal report 1974). Moreover, the mixed oxide fuel of this composition with an optimum O/M ratio of 1·98 and pellet density of 92 % TD always had a two-phase microstructure at room temperature as shown in the x-ray diffraction pattern (figure 21) and photomicrograph (figure 22) (Ramachandran *et al* 1981).

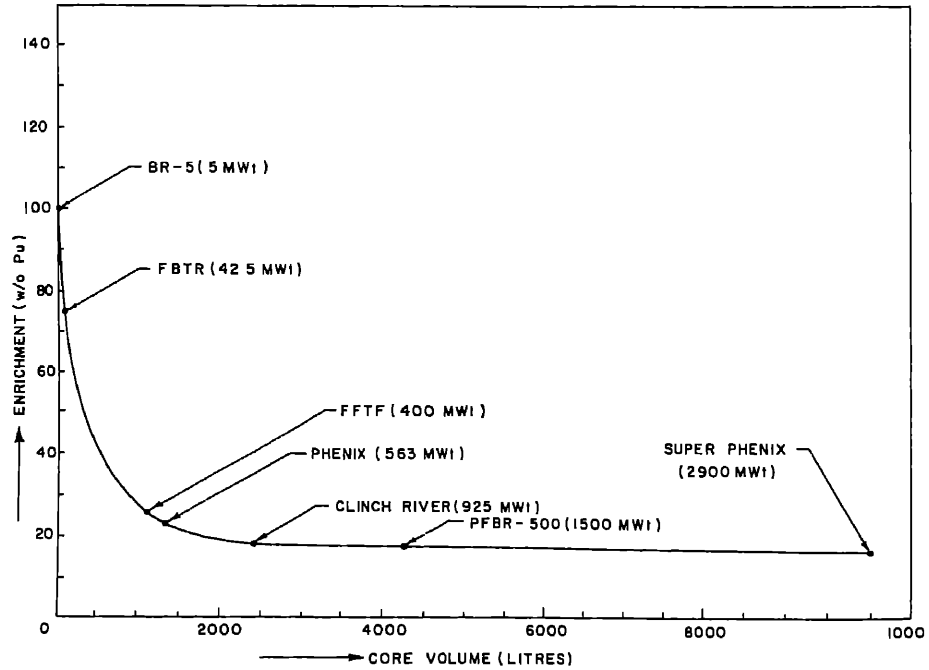

Figure 18. Enrichment—core volume.

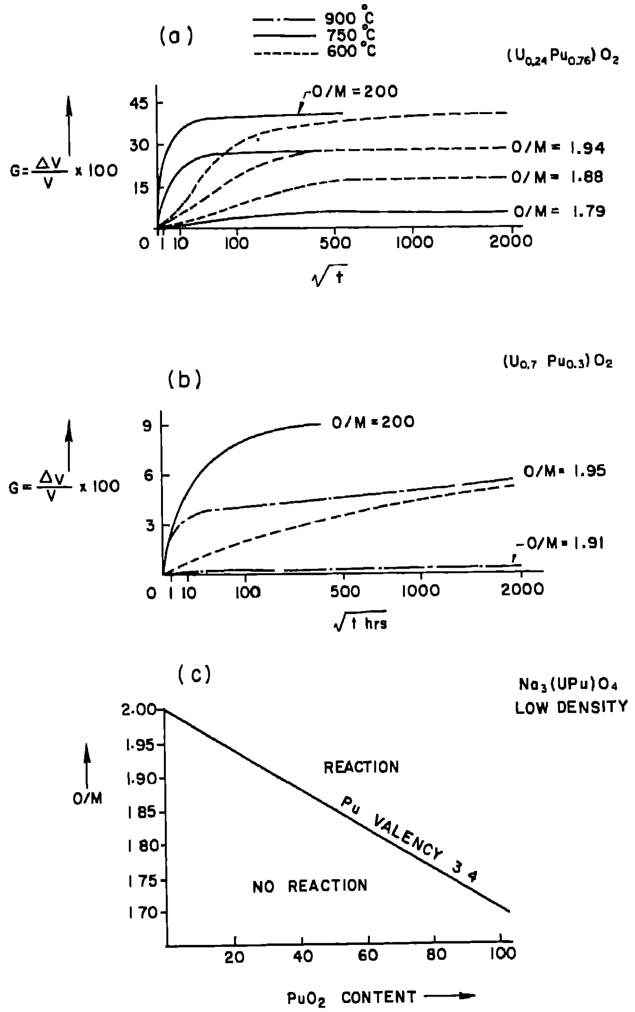

Figure 19. Swelling of uranium and plutonium rich mixed oxide after interaction with sodium.

In view of the above deficiencies, investigation of plutonium rich $(U, Pu)O_2$ was not pursued further. The next logical step was to revert back to the development of fabrication flowsheet of 70 % UO_2–30 % PuO_2. Single-phase mixed oxide pellets of this composition with density 92% TD and O/M ratio 1·98 could be reproducibly fabricated in our laboratory (Majumdar *et al* 1984). A typical microstructure of single phase mixed oxide pellet is shown in figure 23.

10.2 *MOX fuel for TAPS*

Zircaloy-2 clad 2–4 % enriched UO_2 is the fuel for the two BWR at TAPS. The enriched uranium for these reactors was imported ever since the reactors were commissioned in 1967. However, with changing political conditions great difficulties were experienced in

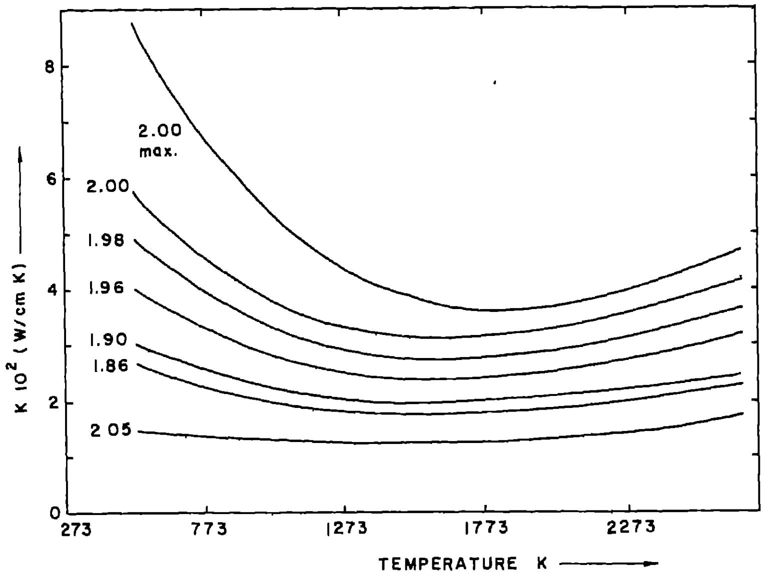

Figure 20. Thermal conductivity *vs.* temperature of 76 % PuO_2-24 %UO_2 pellets of different stoichiometry.

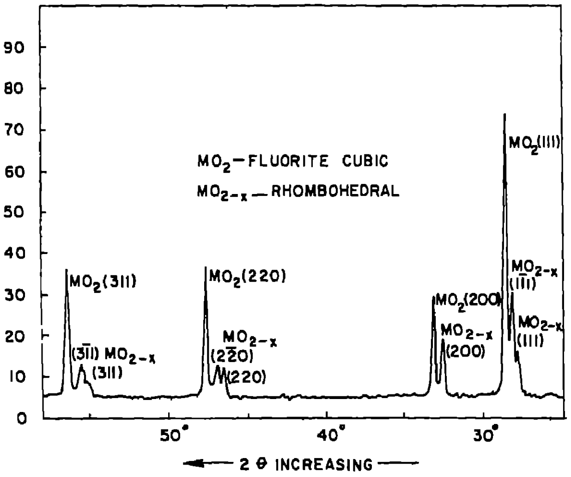

Figure 21. XRD pattern of $(U_{0.24}\ Pu_{0.76})O_{2-x}$ sintered pellet.

importing enriched uranium and a decision was taken in 1978 to explore the possibility of fabricating indigenously MOX fuel containing 2–5 w/o PuO_2 as a substitute for the enriched UO_2 fuel. Accordingly, a crash programme was launched to augment the existing plutonium fuel fabrication laboratory with a capacity of 1 kg fuel per day to 50 kg per day to meet the interim requirement of TAPS.

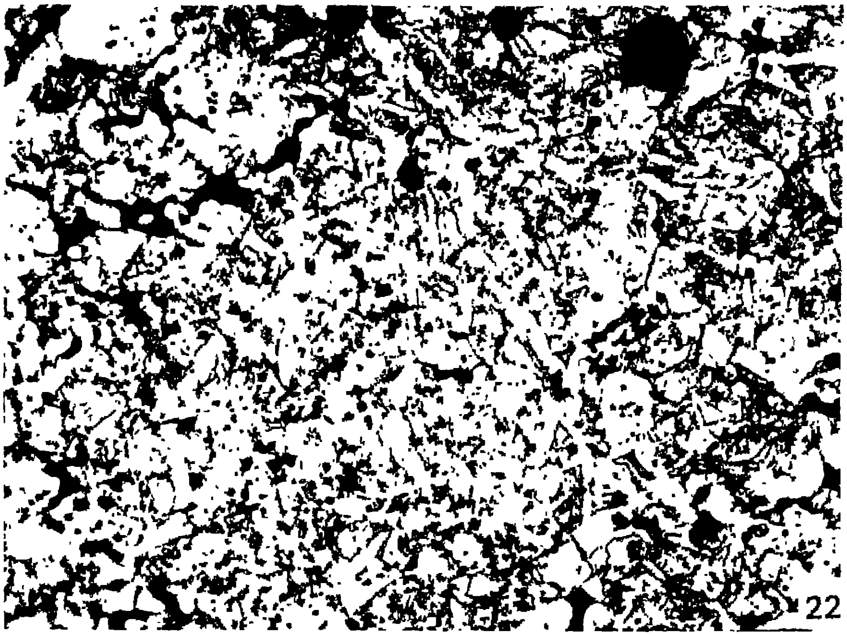

22

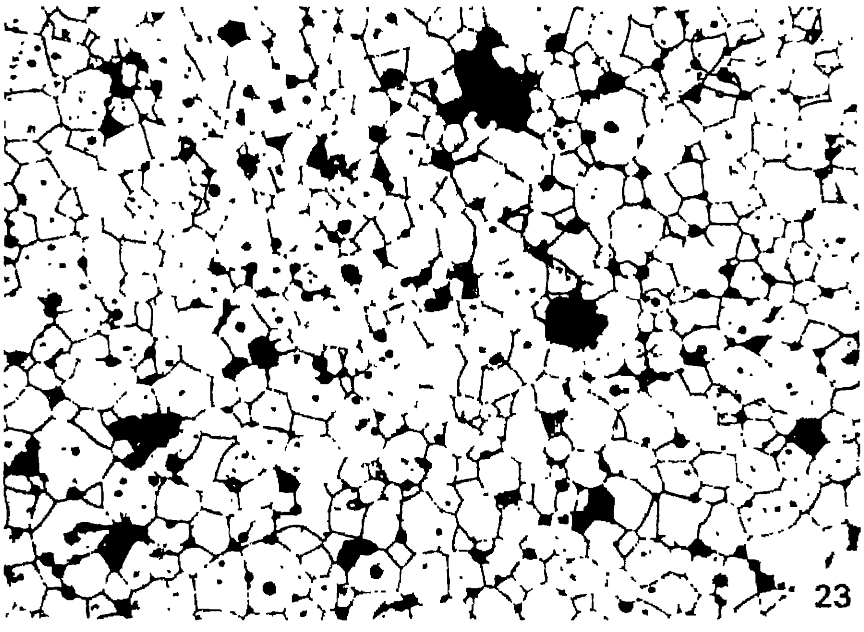

23

Figures 22, 23. 22. Microstructure of $(U_{0\cdot24}\ Pu_{0\cdot76})O_2$ showing two phases (× 400). **23.** Microstructure of single phase $(U_{0\cdot70}\ Pu_{0\cdot30})O_2$ (× 320).

Though the first MOX fuel experience (Sah *et al* 1977) was acquired in Trombay in 1972 when a test pin of UO_2–1·5 w/o PuO_2 of specifications similar to our PHWR fuel element was fabricated for irradiation testing in the pressurised water loop (PWL) of our CIRUS reactor, the MOX substitute fuel for TAPS was a real challenge to the metallurgists as this was a time bound project involving plant scale handling and fabrication of plutonium fuels in a laboratory originally designed for R and D work only.

After extensive investigation, fabrication flowsheet with optimum process parameters was developed to get MOX fuel pellets according to specification (Roy *et al* 1984). There is a stringent requirement of uniformity of plutonium distribution in the fuel pellets from the view point of in-reactor performance. This has been confirmed from the alpha-autoradiography of the MOX pellets shown in figure 24.

The pilot scale MOX fuel fabrication facility of capacity 50 kg sintered MOX pellets per day has been commissioned in BARC and production trials with a few tons of UO_2 pellets have been successfully completed. The facility essentially consists of:

(a) a train of interconnected glove boxes for preparation of MOX granules starting from UO_2 and PuO_2 powders by milling, blending, precompaction and granulation;
(b) a compaction-sintering train consisting of a 30 ton automatic double action hydraulic press, dewaxing furnaces and a continuous sintering furnace (Sengupta *et al* 1982) (figure 25);
(c) a centreless grinder for grinding pellet to final diameter;
(d) a welding train for vacuum degassing of sintered pellets, followed by loading of pellets in a one end welded preautoclaved 4m long zircaloy-2 tubes and encapsulation by TIG welding under a helium pressure of around 0·3 MPa;
(e) a train of glove boxes for refabrication of sintered MOX pellets from rejected oxide; and
(f) facilities for nondestructive testing (NDT) of zircaloy hardwares and fuel pins by airgauging, ultrasonic testing, radiography, helium leak detection mass spectrometry and other quality control facilities like metallography, x-ray diffractometry and x-ray fluorescence spectrometry.

The mechanical and thermal properties of UO_2 are not significantly affected by addition of up to 5 w/o of PuO_2. With 5 % PuO_2 addition, the thermal conductivity is reduced by around 5 %, the melting point decreases by 26°C, the thermal expansion and density increase marginally by 1 %, the fission gas release and swelling are unaffected and the creep and nuclear self-shielding properties are improved.

Irradiation-testing of a prototype MOX fuel cluster of 6 pins (figure 26) in the PWL, CIRUS was started in December 1979 simulating the operating conditions at TAPS. This MOX fuel cluster has performed very satisfactorily without failure up to the target burn-up of 18000 MWD/ton. A second similar cluster has already been fabricated and is under testing in the reactor.

11. Mixed carbide and nitride fuels

The mixed oxide fuels are not, however, the ultimate in the field of development of plutonium fuels for LMFBR. The oxide fuel has the inherent drawback of relatively low heavy atom density, high light atom fraction and poor thermal conductivity. These factors are responsible for its low breeding ratio and low power ratings. On the other hand the potential of (UPu)C and (UPu)N have all along been recognised as better and advanced LMFBR fuels on the basis of their higher breeding ratio and higher linear and specific power ratings which results in much shorter doubling time. An added advantage is the relatively good compatibility of (UPu)C and (UPu)N with sodium (Sengupta *et al* 1982).

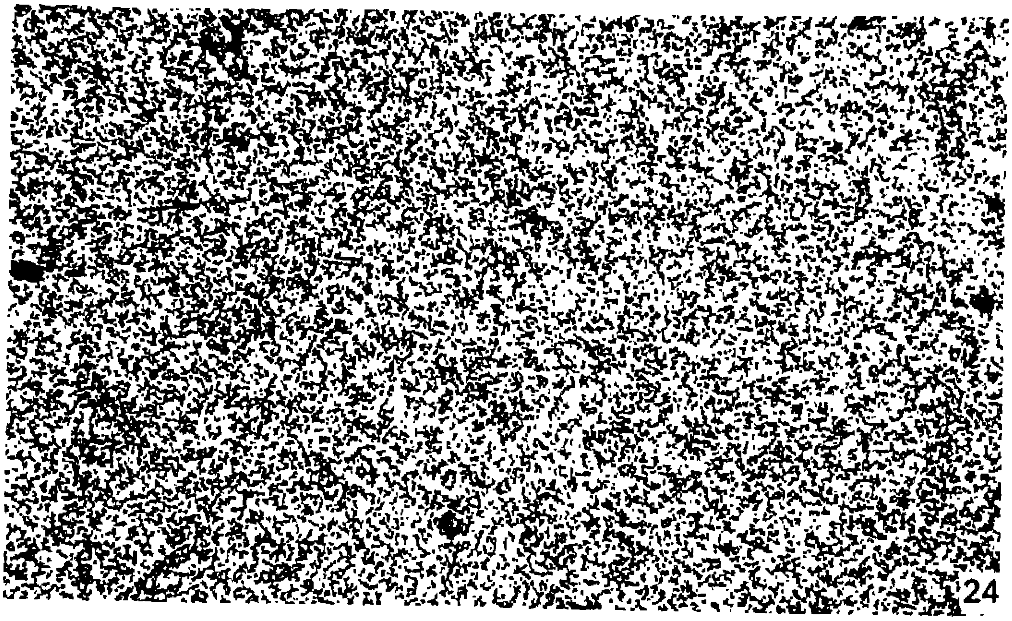
24

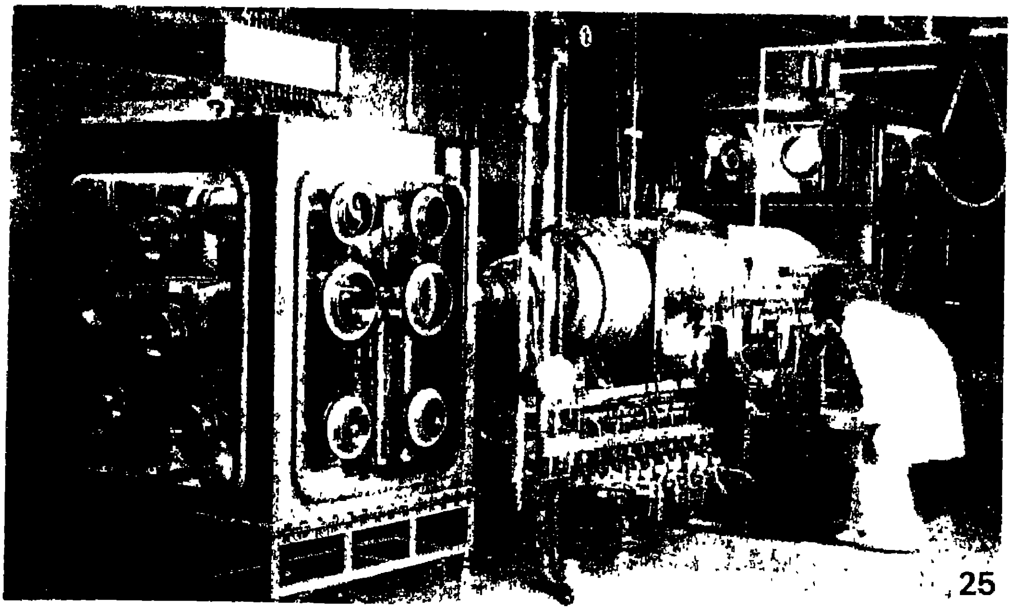
25

Figures 24, 25. **24.** Alpha auto radiograph of MOX pellets (× 80). **25.** Continuous sintering furnace for MOX pellets.

Since plutonium-rich mixed oxide fuels were not suitable for FBTR, efforts were directed to develop the fabrication flowsheet for plutonium rich (UPu)C and (UPu)N fuels. Towards the end of 1970s $(U_{0\cdot3}Pu_{0\cdot7})C$ and $(U_{0\cdot3}Pu_{0\cdot7})N$ pellets of controlled density and phase content were successfully produced in the plutonium metallurgy laboratory at Trombay as per the flowsheet shown in figure 27 (Ganguly 1980).

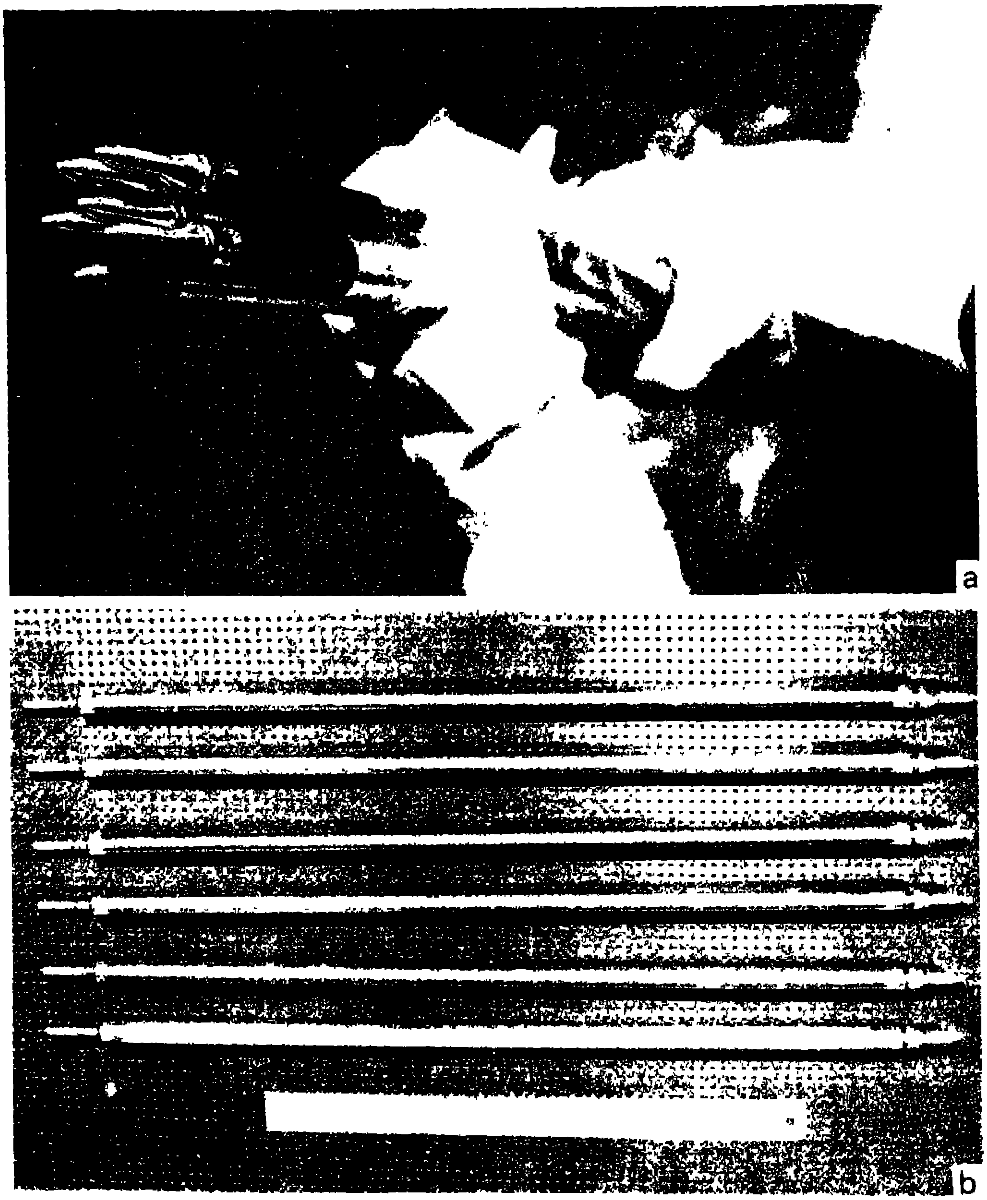

Figure 26. MOX fuel pin cluster for irradiation in PWL, CIRUS (**a**). MOX cluster (**b**). Individual MOX pins.

The two main stages in the fabrication are: (a) synthesis of (UPu)C and (UPu)N by carbothermic reduction of mechanically mixed UO_2, PuO_2 and graphite powders compacted in the form of tablets in vacuum or flowing argon for the carbide and flowing nitrogen or nitrogen + 8 % hydrogen mixture for the nitride; (b) crushing and milling of carbide and nitride clinkers followed by cold pressing and sintering in argon, argon + 8 % hydrogen or vacuum.

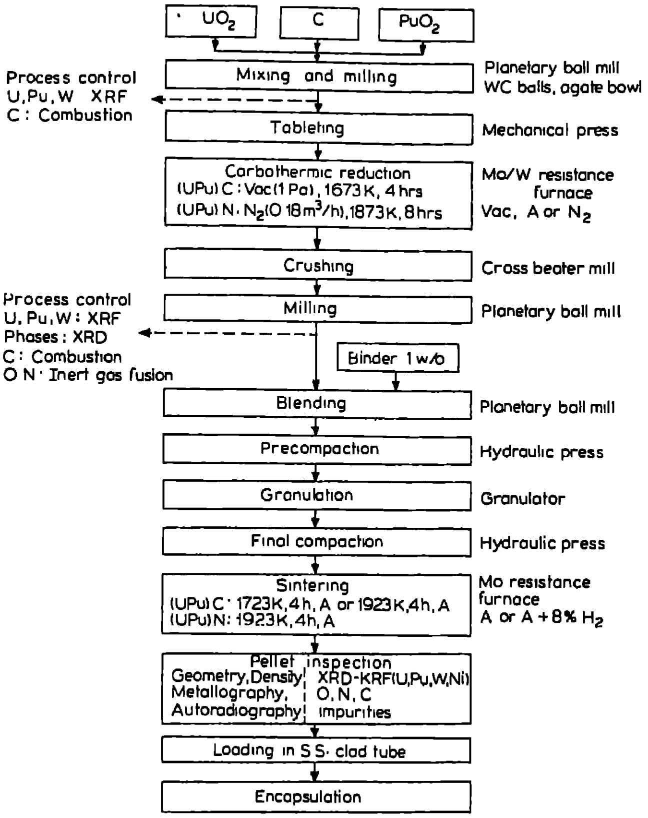

Figure 27. Flow sheet for preparation of $(U_{0.3}\ Pu_{0.7})C$ and $(U_{0.3}\ Pu_{0.7})N$ fuel pellets for LMFBR at BARC.

Equilibrium thermodynamic calculations confirmed by experimental results show that (UPu)C prepared by carbothermic reduction of oxides contain substantial amount of oxygen because of the formation of a mixed uranium plutonium monoxy-carbide solid solution in the final stage of the carbothermic reduction process which above 1625°C remove essentially all the oxygen from the monocarbide but might result in the formation of the undesirable liquid phase PuC_{1-x} by peritectic decomposition and lead to high plutonium volatilisation losses.

In the synthesis of (UPu)N by solid state carbothermic reduction of a powder mixture of UO_2, PuO_2 and graphite, nitrogen plays the dual role of the reactant and the carrier for the removal of CO. The (UPu)N produced by this method has high oxygen and carbon contents.

11.1 *Advantages of plutonium rich (UPu)C and (UPu)N*

Initial theoretical studies on plutonium rich (UPu)C and (UPu)N unfolded the following advantages of this fuel over the uranium rich composition: (a) UC and uranium rich (UPu)C have no carbon solubility range but there is a limited carbon homogeneity range in the PuC and plutonium rich (UPu)C as shown in the U-Pu-C phase diagram (figure 28) (Storms and Ackermann 1974). It is, therefore, relatively simple to prepare $(U_{0\cdot3}Pu_{0\cdot7})C$ as a nearly single phase material.

(b) With nitrogen, plutonium forms only one compound namely PuN whereas uranium has three nitrogen compounds, namely UN, U_2N_3 and UN_2 (Potter 1975). The higher nitrides of uranium, however, are easily decomposed to the mononitride by a high temperature treatment in vacuum or inert gas. Single phase PuN and plutonium rich (UPu)N are therefore relatively easy to prepare.

(c) Pu_2C_3 and $(U_{0\cdot3}Pu_{0\cdot7})C_{1\cdot02}$ have lower carbon potentials compared to U_2C_3 at all temperatures and a lower carbon potential than stainless steel 316 up to 725°C as shown in figure 29 (Gotzmann and Hofmann 1974; Internal report 1980). The chances of carbon transfer from plutonium rich mixed carbide to stainless steel is therefore lower and there will be no clad carburisation if the temperature inside the clad is kept below 725°C.

(d) The melting points of (Sheth and Leibonitz 1974) of PuC and PuN are less than that of UC and UN respectively for which the optimum carbothermic and sintering temperatures of plutonium rich (UPu)C and (UPu)N are 150–200°C lower than their uranium rich counterparts (Ganguly *et al* 1980, 1982). Hence, the plutonium volatilisation losses are relatively less (within 1–2%).

11.2 *Mixed carbide facility for* FBTR

The small scale (60 g) laboratory experiments established the overall feasibility of the fabrication of controlled density (UPu)C and (UPu)N pellets as nearly single phase material as shown in the x-ray diffraction patterns (figure 30) and the microstructures (figure 31). On the basis of this experience a production laboratory was set up during 1981–82 for the fabrication and quality control of 1·5 kg/day of finished mixed carbide fuel pellets from UO_2 and PuO_2 feed materials (Ganguly and Roy 1981). This laboratory has two main facilities, namely (a) pellet production facility, and (b) process control facility.

The pellet production facility consists of a train of 12 interconnected glove boxes housing conventional powder metallurgy equipment. In addition, for rapid process control at different stages in the preparation and sintering of MC and MN

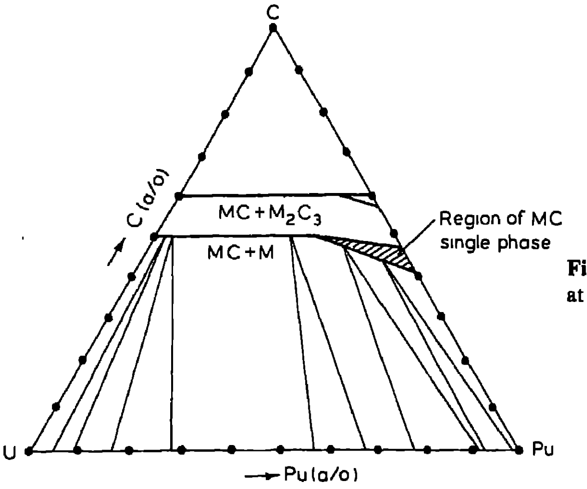

Figure 28. U-Pu-C system at 600°C (M = U, Pu).

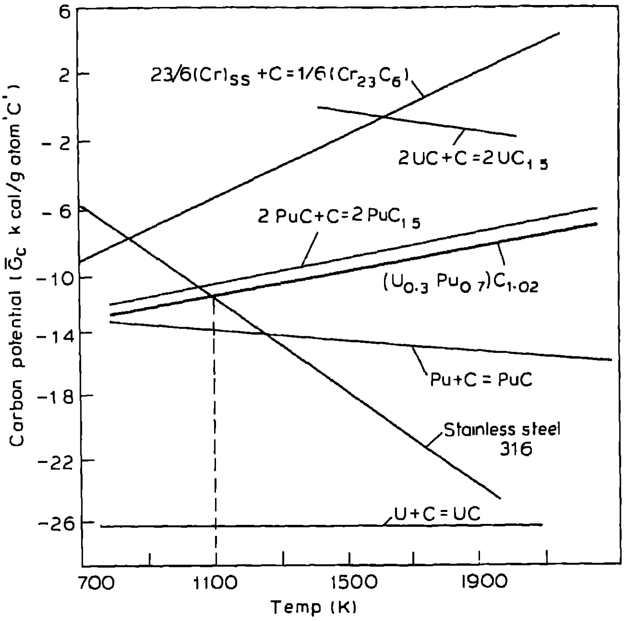

Figure 29. Carbon potentials of carbides.

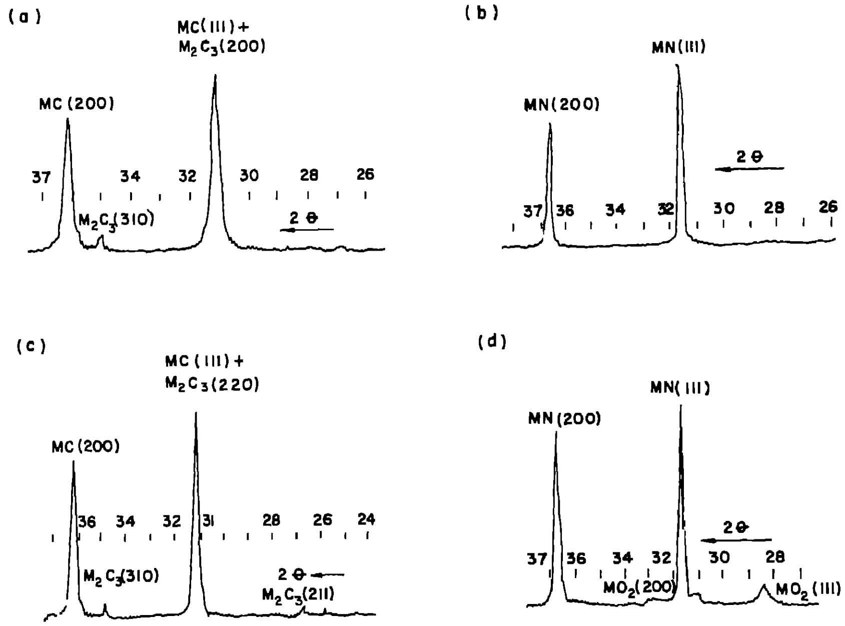

Figure 30. X-ray diffraction pattern of MC and MN; M = ($U_{0.3}$ $Pu_{0.7}$) after carbothermic reduction of $UO_2 + PuO_2 + C$ for (**a**). carbide (**b**). nitride; after sintering of (**c**). carbide (without -Ni) and (**d**). nitride.

powders the following equipment have also been installed (Ganguly *et al* 1981): (a) a combined and sequential oxygen and nitrogen inert gas fusion analyser for rapid analysis of oxygen and nitrogen in powders and pellets; (b) a rapid carbon analyser for powder and pellet based on the method of combustion and determination by thermal conductivity meter; (c) an automatic, combined and sequential x-ray fluorescence spectrometer and x-ray diffractometer for rapid analysis of U, Pu, tungsten, nickel and different phases present in powder and pellets (figure 32).

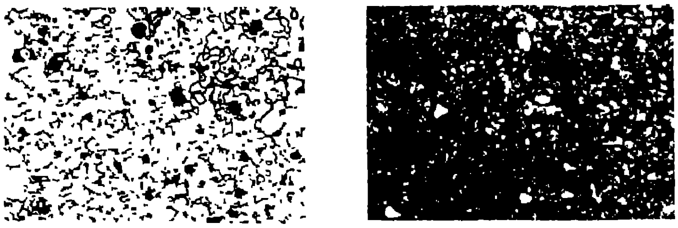

MC (WITHOUT 'NI') (x 600)
Ar + 8 v/o H_2, 1923 K/4 HRS

MC (WITH 0.4 w/o 'Ni') (x600)
Ar, 1773 K /4 HRS

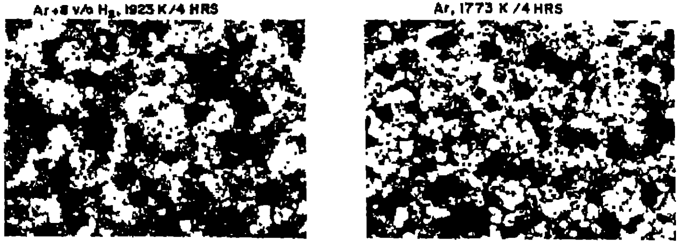

MN (x 600)
Ar + 8 v/o H_2, 1923 K/4HRS

MN (x 600)
Ar + 8 v/o H_2, 1823K /4 HRS

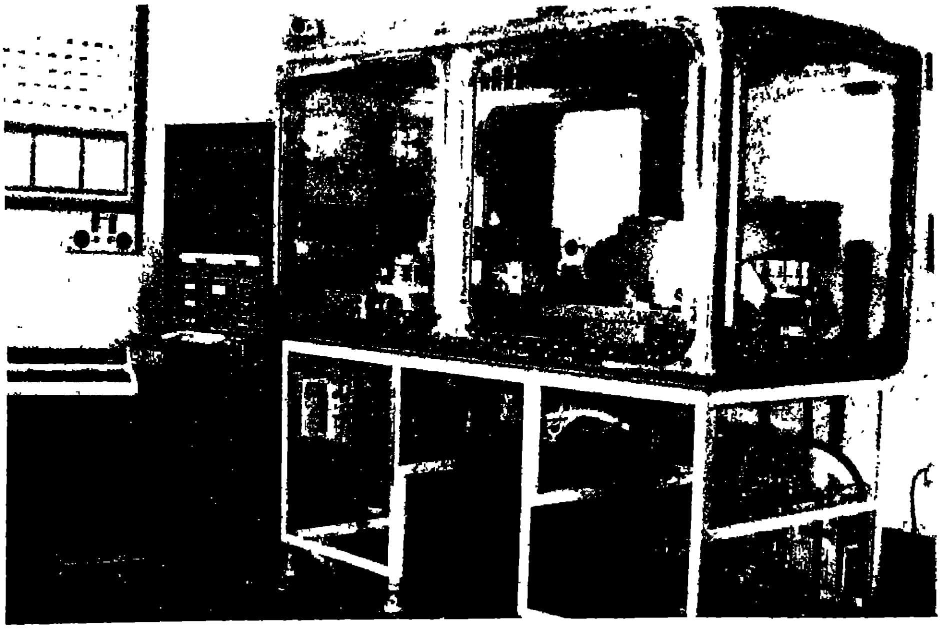

Figures 31, 32. 31. Microstructure of plutonium rich (U Pu)C and (U Pu)N pellets. 32. Combined XRD-XRF unit in RMD, BARC under commissioning inside a glove box.

12. Looking forward

In our travels into the plutonium age over the past quarter of a century, we have passed many milestones, meeting new challenges, probing new frontiers, indigenising all aspects of plutonium metallurgy and fuels and have reached today a stage of commercial exploitation of plutonium in nuclear power reactors.

Our well-known three stage nuclear power strategy projects the pivotal role of plutonium in the coming decades for a viable and rapidly expanding electricity generation programme. The first stage based on our operating and forthcoming natural UO_2 fuelled PHWRS will be limited to only 10–15 GW(e) for 30 yr but will produce between 100–150 tons of fissile plutonium as by-product along with depleted uranium. The second stage, which is likely to start towards the turn of this century, will make most effective utilisation of these large quantities of plutonium by recycling it several times with depleted uranium in LMFBR. Around 350 GW(e) would be possible for 65 yr with ^{238}U–^{239}Pu fuel cycle and simultaneously ^{232}Th could be converted to ^{233}U. Finally, in the third stage, the self sustaining ^{232}Th–^{233}U thermal breeder fuel cycle could be used in PHWR to unlock 1000 GW(e) for 240 yr, thus establishing that nuclear power is the only long term answer to our energy crisis.

A plutonium-fuelled prototype fast breeder reactor of 500 MW(e) capacity (PFBR-500) has been already planned for the 1990s (Singh *et al* 1981). This reactor will essentially act as a "lead station" to demonstrate the basic safety, reliability and economics of plutonium fuel reprocessing, refabrication and irradiation on a commercial scale and will generate data on which "series ordered LMFBR stations" can be commissioned with confidence after 2010.

A larger capacity plutonium fuel fabrication plant is coming up at Tarapur to meet our future requirement of plutonium fuels in PFBR-500 and thermal reactors. This plant is being designed and constructed in the philosophy of "secured automated fabrication (SAF)" through a carefully staged development from present glove box operations to semi-remote or remote operations placing emphasis on radiotoxic dust reduction and its containment. This development should ultimately result in systems that maximise personnel radiation protection, restrict and control access to plutonium, provide near real time accountability and improve the uniformity and quality of plutonium fuels.

New fabrication flowsheets for plutonium bearing fuels amenable to automation and remotisation are being developed in Trombay. One of the promising process is the 'gel-pelletisation route' (Gilissen *et al* 1982) which uses gel derived microspheres rather than powder as feed material for pellet pressing. Because of the free flowing and dust-free nature of microspheres, the gel-pelletisation process is ideally suited for remote fabrication of the fuel pellets. In our preliminary experiments with gelled microspheres of $(UPu)O_2$, high density sintered pellets have been prepared. Figure 33 shows the microstructure of such a pellet and figure 34 shows the alpha autoradiograph.

The ThO_2-PuO_2 (up to maximum of 5 % PuO_2) is a promising fuel for our thorium based PHWR (Ganguly and Roy 1982). If due to technological or political reasons recycling of plutonium is delayed in our LMFBR, such fuels could be conveniently used in our existing PHWR without involving major resource investment and engineering modifications.

In conclusion it may be stated that plutonium technology is mostly classified in nature and detailed informations are not available in open literature. In spite of that we have succeeded in the harnessing of plutonium entirely with indigenous resources and

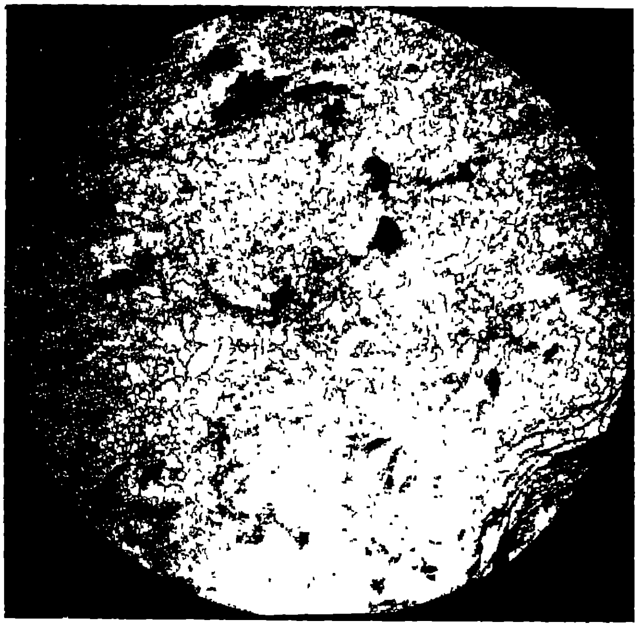

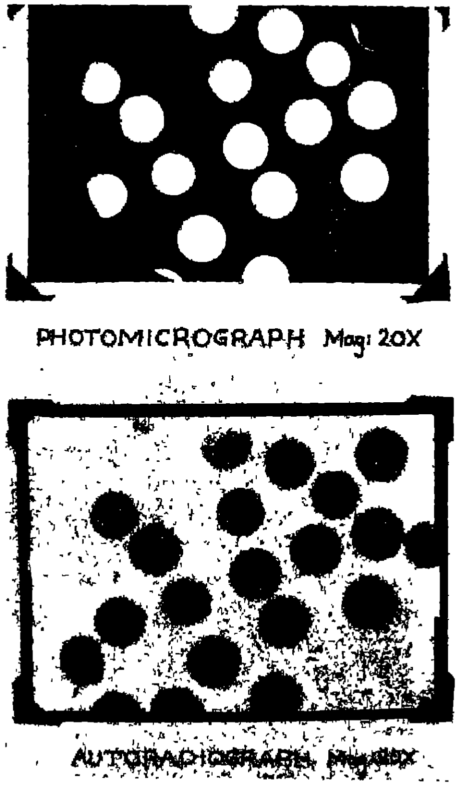

Figures 33, 34. **33.** Microstructure of UO_2 pellet prepared by the gel pelletisation route (× 90). **34.** Microstructure and alpha-autoradiograph of MOX structures.

without any foreign assistance. Only a vertical take off is needed and a few obstacles are to be overcome before this great gift of nature and our control over it bears the fruit of its present promise.

Acknowledgement

Thanks are due to the Radiometallurgy Division as a whole, including the staff members of Post Irradiation Examination, Engineering Services, Oxide Fuels, Advanced Fuels, Quality Control and Inspection and Cladding and Welding Sections. In addition, the support from Fuel Reprocessing Division and Radiochemistry Division is acknowledged. The continuous encouragement received from the higher authorities is also gratefully acknowledged.

References

Coffinberry A S and Miner W N 1961 *The metal plutonium* (Chicago: University Press)

Ellinger F G, Land C C and Miner W N 1962 *J. Nucl. Mater.* 5 165

Fareeduddin S, Garg R K, Gupta U C, Kantan S K, Rajendran R and Rao N K 1964 *3rd Int. Conf. Peaceful use of atomic energy*, IAEA, Vol. II p 345

Ganguly C 1980 *Studies on preparation and sintering of mixed uranium plutonium monocarbide, mononitride and monocarbonitride*; Ph.D. Thesis, University of Calcutta

Ganguly C, Jain G C and Roy P R 1981 *Proc. of DAE Sym. on Nucl. Chemistry and Radiochemistry*

Ganguly C and Roy P R 1981 *Proc. BNES Conf. on Fast Reactor Fuel Cycles*, London

Ganguly C and Roy P R 1982 *Proc. Int. Sym. in Ceramics*, BHEL Bangalore

Ganguly C, Roy P R and Seal A K 1980 *Trans. PMAI* 7 40

Ganguly C, Roy P R and Seal A K 1982 *Trans. IIM* Vol. 35 No. 2 p 148

Ghosh J K, Roy P R and Moorthy V K 1973 BARC/I-254

Gilissen R, Panwels H, Sleurs J and Smolders A 1982 *Trans. Am. Nucl. Soc.* 40 26

Gotzmann O and Hofmann P 1974 *Proc. of Int. Sym. on Fuel and Fuel Elements for Fast Reactor* IAEA p 233

Hanna G C, Westcott C H, Lemmel H D, Leonard B R Jr., Story J S and Altree P M 1969 *Atomic Energy Rev.* 7 p. 3

Hansen L P and Clayton R D 1967 *Nucl. Appl.* 3 484

Housseau M 1974 *Proc. Sym. on fuel and fuel element for fast reactors*, IAEA p 277

Internal Report prepared on FBTR mixed oxide fuel by DAE, India and CEA, France (Sept. 1970)

Internal Report of DAE working group on mixed uranium plutonium carbide fuels for FBTR (1980)

Janardhanan S, Krishnamurthi T N, Dabhadkar S B and Soman S D 1973 BARC/I-259

Kanij J B W, Noothont A J and Votock I 1974 IAEA-161 p 185, Vienna

Mahajan V K, Ganguly C, Ramakumar M S, Roy P R and Moorthy V K 1972 BARC-629

Majumdar S, Arunkumar, Kamath H S, Ramachandran R, Purushotham D S C and Roy P R 1984 BARC-1182

Majumdar S, Purushotham D S C and Roy P R 1982 BARC/I-730

Potter P E 1975 *Plutonium and other actinides* p 211

Prasad G J, Ganguly C and Roy P R 1976 BARC/I-423

Recommendation of the ICRP-Suppl. 6, 1955 *Br. J. Radiol.*

Ramachandran R, Arunkumar, Purushotham D S C and Roy P R 1981 *Trans. PMAI* 8 277

Rao N K 1982 *Proc. Sym. Int. Conf. on Nucl. Power Experience* IAEA, Vienna

Roy P R 1962 *AEET/Radiochem.* 22

Roy P R 1964 *J. Nucl. Mater.* 11 59

Roy P R 1975 *Proc. IAEA group meeting on facilities and techniques for* $(UPu)O_2$ *fuel fabrication, Mol,* Belgium

Roy P R 1978 *Proc. Seminar on Nucl. Metallurgy*, IIM Bombay

Roy P R, Deshpande R G and Laxminarayanan T S 1967 BARC-294

Roy P R, Laxminarayanan T S, Singh R K and Haraprakash A 1969 BARC/I-37

Roy P R and Mahajan V K 1975 *Proc. IWSA-BARC Winter School*, Bombay
Roy P R, Purushotham D S C, Majumdar S, Ramachandran R, Kamath H S, Ghosh J K and Goswami G L *et al* 1984 BARC-1203
Sah D N, Sahoo K C, Chatterjee S, Majumdar S, Kamath H S, Ramachandran R, Bahl J K, Purushotham D S C, Ramakumar M S, Sivaramakrishnan K S and Roy P R 1977 BARC-918
Seaborg G T 1958 *The transuranium elements* (Massachusetts, USA: Addison-Wesley Publishing Co.)
Sengupta A K, Ganguly C and Roy P R 1982 BARC/I-740
Sheth A and Leibonitz L 1974 ANL-AFP-3
Singh B, Bhoje S B, John T M, Lee S M, Singh R S and Paranjpe S R 1981 *Proc. BNES Conf. on Fast Reactor Fuel Cycles*, London
Sood D D and Vaidya V N 1979 *Proc. Sym. on Sintering and Sintered Products*, BARC, Bombay
Stoller S M and Richards R B 1961 *Reactor Handbook* (New York: Interscience Publishers) 2 454
Storms E K and Ackermann R J 1974 *Proc. of IAEA Panel Meeting on U-Pu-C System*, Grenoble, France
Wade W Z and Wolf T 1969 *J. Nucl. Sci. Technol.* 6 402
Wick O J 1980 *Plutonium handbook* (La-Crange Park, Illinois: American Nuclear Society)
Zachariasen W H and Ellinger F H 1959 *Acta Crystallogr.* **12** 175

Bull. Mater. Sci., Vol. 6, No. 5, September 1984, pp. 959–969. © Printed in India.

Internal friction in hexagonal metals

M K ASUNDI and C N RAO

Physical Metallurgy Division, Bhabha Atomic Research Centre, Trombay, Bombay 400 085, India

Abstract. An overview of the studies of internal friction in hexagonal metals and alloys is presented. An outline of the experimental techniques of measurement and the atomistic mechanisms causing internal friction is also given.

Keywords. Anelasticity; internal friction; hexagonal metals.

1. Introduction

All materials possess the intrinsic ability to dissipate mechanical energy by some internal atomistic or microscopic processes. This property is called *internal friction* or damping capacity. Internal friction is mainly observed in systems undergoing periodic vibrations and its magnitude can be determined by the decay of free vibrations or of travelling waves in a test piece. In recent times, internal friction has become an important tool for investigating the atomistic processes in solids. One of the best known examples is the internal relaxation due to the diffusion of interstitial solutes in a bcc solid which can be conveniently studied by low cycle torsion pendulum measurements.

This paper gives a brief account of the various measures of internal friction, the experimental techniques of measurement and the mechanisms for internal friction followed by an overview of the studies on hexagonal materials. The results on zirconium and titanium alloys are given in greater detail due to the extensive studies made on these materials.

2. Relaxation and internal friction

A measure of the damping capacity is the quantity $\Delta W/W$ where ΔW is the energy loss per cycle and W is the total vibrational energy. It is given by the integral $\int \sigma \, d\varepsilon$ over one cycle where σ is the applied stress and ε is the resulting strain. For an ideal elastic body, there will be no dissipation of energy and the integral vanishes. When there is internal dissipation, stress and strain are no longer in phase with each other and the dissipation can be due to static or dynamic hysteresis (figure 1). For static hysteresis (figure 1a) part of the strain is irreversible and the internal friction will generally be independent of the frequency of vibrations, but will be strongly dependent on the amplitude of vibrations.

For dynamic hysteresis (figure 1b) relaxation occurs over a finite time by internal rearrangements in the material and depends on the rate of change of σ and ε. Such a behaviour is called *anelastic*, a term introduced by Zener (1948). For small amplitude of

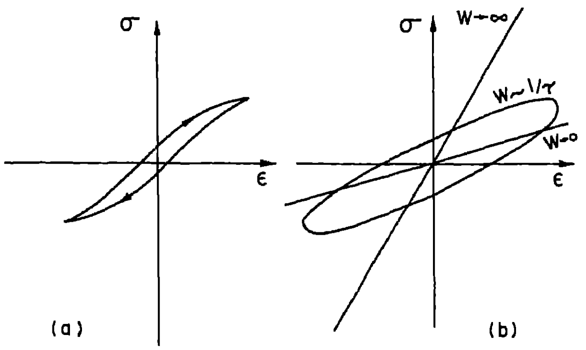

Figure 1. Schematic representation of mechanical hysteresis (a) static hysteresis (b) dynamic hysteresis.

the vibrations, the relation between σ, ε and their time derivatives is linear and the damping will be independent of amplitude but strongly dependent on the frequency of vibration. At very high frequencies, there is little time for the relaxations to take place and no energy loss will be obtained. At very low frequencies, complete relaxation occurs and the behaviour of the system is purely elastic with a smaller relaxed value of the elastic modulus. At some intermediate frequency ω (of the order of $1/\tau$ where τ is the relaxation time for the internal rearrangement) a maximum in internal friction will occur.

The various parameters used for quantitative specification of damping are dimensionless ratios which are independent of the size of the sample and the nature of the experimental system when the damping is independent of the amplitude of vibration.

2.1 *The logarithmic decrement δ*

The damping of a system freely vibrating in a single mode can be expressed in terms of the rate of decay of the vibration amplitude. The logarithmic decrement is given by

$$\delta = \frac{1}{n} \ln (A_0/A_n), \tag{1}$$

where A_0 and A_n are the amplitudes before and after n cycles of vibration.

2.2 *Q^{-1} value*

For a system undergoing forced vibrations, the amplitude magnification factor Q at resonance and the relative width $\Delta\omega/\omega_r$ of the resonance (where ω_r is the resonance frequency) depend solely on the damping of the system. For the resonance width at half maximum they are related as

$$Q^{-1} = \Delta\omega/\omega_r, \tag{2}$$

and provide a direct measure of the damping.

2.3 *Specific damping capacity, P*

If W is the total energy of the oscillating system at the commencement of a cycle and ΔW the energy dissipated in the cycle, the specific damping capacity is defined as

$$P = \Delta W/W. \tag{3}$$

2.4 *Tangent of the phase angle*

In the case of linear damping, an applied sinusoidal force $f_0 \sin \omega t$ produces a displacement $x_0 \sin(\omega t - \phi)$, where ϕ is the phase lag between the applied force and displacement. The ratio of the components of strain out-of-phase and in-phase with the stress given by $\tan \phi$ can be used as a measure of the damping.

For small damping values, the different quantities defined above are approximately related to each other as

$$\delta/\pi = Q^{-1} = P/2\pi = \tan \phi. \tag{4}$$

3. Experimental methods of measurement

When considering a relaxation effect, four quantities are of interest; (i) the relaxation strength, which determines the peak height; (ii) the relaxation time which determines the peak position on the temperature scale; (iii) the shape of the peak which can be characterized in terms of the width at half maximum; and (iv) the modulus defect which causes a variation of the resonance frequency of the specimen in the temperature range of the damping peak.

Over the years, a variety of equipment have been built in various laboratories to measure internal friction. According to the method by which stresses are generated in the specimen, the techniques can be divided into resonance methods, pulse-echo methods and mechanical after-effect methods. Whereas the pulse-echo technique is restricted to high frequencies (over 1 MHz) and the after-effect method to very long relaxation times (over 10 sec), the resonance methods are useful in the range of low to medium frequencies (0·01 Hz to 100 kHz). In a given type of experimental system one is usually restricted to a limited number of operating frequencies and hence to observe a relaxation process one has to vary the temperature. Thus, practically all the instruments described in the literature provide for measurements over a range of temperature.

A comprehensive description of the experimental methods can be found in the books by Nowick and Berry (1972) and De Batist (1972).

4. Mechanisms of internal friction

A number of atomistic and microscopic mechanisms can contribute to energy dissipation in solids. Some of these are: (a) stress-induced ordering of interstitial and substitutional atoms, commonly known as Snoek and Zener relaxations (Snoek 1941; Zener 1947), (b) grain boundary viscosity (Kê 1949), (c) thermoelastic damping (Waterman 1958), (d) dislocation damping (Read 1940), (e) magnetic damping in ferromagnetic materials (Cochardt 1959) and (f) electronic damping at low temperatures (Bommel 1954).

Covering the various aspects of relaxation processes and experimental results, extensive reviews have been published by Zener (1948), Nowick and Berry (1972), Nowick (1953), Entwistle (1962), De Batist (1972), Berry (1962), Mason (1966), Niblet and Wilks (1960), Wilks (1965), Burdett and Queen (1970), Fantozzi and Ritchie (1981) and Lucke and Granato (1957).

A brief account of the relaxations ascribed to point defects, dislocations and grain boundaries is given below:

4.1 *Internal friction due to point defects*

Point defects produce anelastic behaviour through a process known as stress-induced ordering, in which the equilibrium configuration of a collection of defects in the crystal changes with time to a new state under applied stress. When the stress is removed, the change is reversed and with time the original state of order is restored. The occurrence of stress-induced ordering for point defects depends mainly on the ability of an applied sress to change the free energy associated with the presence of a defect in the crystal. If defects are present in several crystallographically equivalent positions whose free energies can be split by an external stress, a redistribution of the defects among these states will re-establish equilibrium. Only those defects which produce local strains having a lower symmetry than that of the lattice are capable of producing relaxation under shear. Such defects are called *asymmetric defects* or *elastic dipoles.*

An outstanding example of anelasticity produced by an elementary point defect acting as an elastic dipole is provided by the Snoek relaxation, first observed in α-Fe containing small amounts of C or N (Snoek 1941, 1942). The Snoek effect has since been observed in a number of other bcc transition metals containing impurity atoms (like C, N, O, H) in interstitial positions of the lattice. The Snoek peaks due to O, C and N in niobium are shown in figure 2 (Hoffman and Wert 1966).

In α-Fe, the carbon atoms occupy the octahedral sites of the type [1/2, 0, 0] (figure 3). The interstitial atom is an elastic dipole of ⟨100⟩ tetragonal symmetry, which will cause stress induced ordering. The direction of the tetragonal dipole axis may lie along any one of the crystal cube axes X, Y, Z depending on the particular site which the interstitial atom occupies. Sites which produce the tetragonal axis along the X direction have been labelled X in the figure (Similarly Y and Z sites). When an interstitial impurity makes thermally-activated jumps between neighbouring sites, which are $a/2$ apart, the dipole axis re-orients by 90° with each jump. Thus, the relaxation rate is related in a simple way to the mean jump rate of the interstitial atoms.

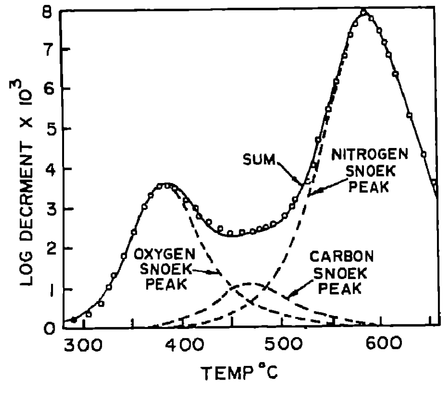

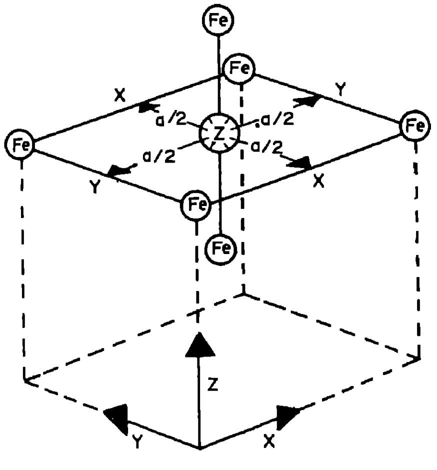

Figure 2. Snoek peaks in a ⟨100⟩ crystal of niobium tested in longitudinal vibration at 80 kHz.

Figure 3. Solute atom (shaded) in an interstitial octahedral site of bcc Fe.

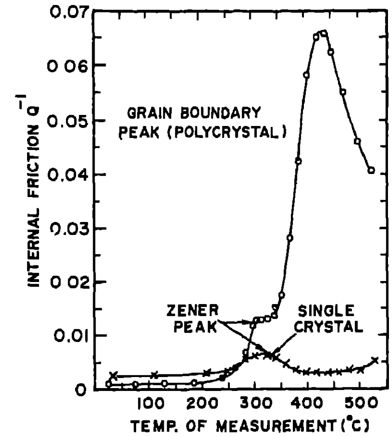

Figure 4. Zener peak in polycrystalline and single crystal specimens of α-brass (torsional vibration at 0·5 Hz).

Another important kind of point defect process, ascribed to stress-induced reorientation of solute pairs, is the Zener relaxation, first observed by Zener (1943) in a single crystal of 70–30 α-brass. Since then, similar relaxation peaks have been found in a number of binary (and other complex) alloys with fcc, bcc and hcp crystal structures. According to the pair reorientation theory of Zener (1947) asymmetric distortions can be expected around two adjacent solute atoms *i.e.* around a nearest neighbour pair. This enables splitting of free energies of differently oriented pairs by an applied stress. Figure 4 gives the Zener peak observed in α-brass.

In addition to the solute-solute (*S-S*) defect pair, interaction of substitutional-interstitial (*S-I*) pairs, and *I-I* pairs may lead to internal friction peaks (see for example Nowick and Berry 1972).

4.2 *Relaxation involving dislocations*

A variety of relaxation peaks occur at temperatures, usually below room temperature, after plastic deformation. They are considered to be caused by the movement and interaction of dislocations with point defects.

In the vibrating-string model (Granato and Lucke 1956) the dislocation line is considered to behave like an elastic string fixed at two points in the lattice, restricted to move in two dimensions in the glide plane. A number of anelastic effects can be deduced from the model. One important result is that the anelastic properties of dislocations should be strongly frequency dependent. Changing the resonance frequency of dislocations by decreasing the free length of the vibrating string (introducing additional pinning centres by irradiation) affords an effective method of checking the results of the dislocation damping theory and to study the production and recovery of defects.

By considering the movement of the dislocation string in a periodic lattice potential—the Peierls potential—additional relaxation effects due to anelastic motion of segments of the dislocation line are predicted.

Dislocation motion described by means of kink diffusion (Brailsford 1961) along dislocation lines can also be used to explain dislocation damping caused by resonance effects as well as relaxation effects.

The trapping of point defects in the stress field of a dislocation will have a profound effect on dislocation damping through variation in free dislocation length. A number of relaxation peaks observed in plastically deformed metals have been attributed to the interaction and motion of point defects and dislocations. The amplitude dependence of dislocation damping can be explained qualitatively in terms of dislocations anchored by point defects.

The Bordoni peak, first observed at low temperatures for deformed copper, has been studied in a number of metals. A second (Niblett–Wilks) peak associated with the Bordoni peak occurs at a lower temperature and is usually much smaller than the main peak (Niblett and Wilks 1956). A series of three peaks has been observed in deformed metals in the range between room temperature and the low temperature Bordoni peaks (Hasiguti *et al* 1962).

4.3 *Boundary relaxation processes*

Grain boundaries, domain boundaries and semi-coherent and incoherent interface boundaries between phases can result in relaxation effects giving an internal friction maximum when the boundary movement corresponds to the frequency of the applied stress field. Such effects will be observed at low frequencies and relatively high temperatures. The grain boundary peak in aluminium is shown in figure 5.

5. Internal friction studies in hexagonal metals

5.1 *Relaxation effects in hcp metals*

In the hexagonal close-packed structure, there are two possible locations for an interstitial (figure 6). The volume associated with the octahedral site is larger than that of the tetrahedral site and hence larger atoms like O, C and N are expected to occupy the octahedral sites. Both the sites have trigonal symmetry, the same as that of the host lattice, and hence single interstitials are not expected to cause anelastic effects, unless there is an interaction between the two kinds of interstitials forming an *I-I* pair (Povolo

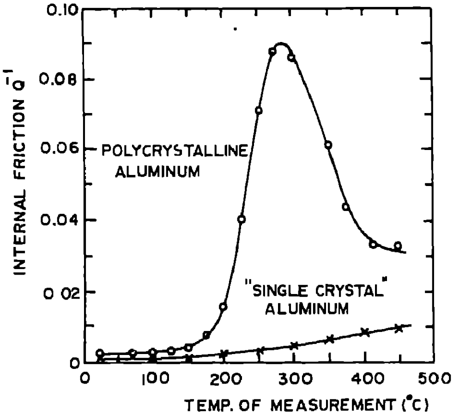

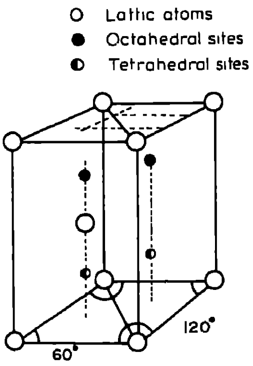

Figure 5. Grain boundary peak in polycrystalline aluminium (Torsional vibration at 0·8 Hz).

Figure 6. Interstitial positions in the hexagonal close packed lattice.

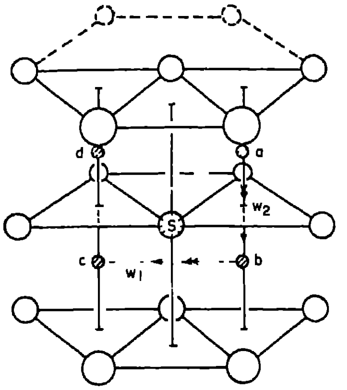

Figure 7. The two types of interstitial jumps producing reorientation of a nearest neighbour *I-S* pair in the hcp structure. W_1 is the jump rate parallel to the basal plane and W_2 is perpendicular to the basal plane.

and Bisogni 1967). This will be possible for small atoms like H which may occupy octahedral as well as tetrahedral sites. In terms of the jump probabilities W_1 for the transition from tetrahedral to octahedral site and W_2 for the reverse jump, the relaxation time τ is given by

$$\tau^{-1} = W_1 + W_2. \tag{5}$$

Relaxation due to interstitial-substitutional (*I-S*) pair in hexagonal crystals has been discussed by Nowick (1967). The nearest neighbour pairs lie in (100) type planes and the (*I-S*) defect is of the ⟨100⟩ monoclinic type and two kinds of jumps are possible during the relaxation (figure 7). In terms of the probability W_1 for a jump normal to the basal plane and W_2 for a jump within the basal plane, the two relaxation times are given by

$$\begin{aligned} \tau_1^{-1} &= 3W_2 + 2W_1, \\ \tau_2^{-1} &= 3W_2. \end{aligned} \tag{2}$$

In addition to the relaxations due to point defect interactions, relaxation effects can also occur due to dislocations and semi-coherent or incoherent interface boundaries.

5.2 *Relaxations associated with interstitials*

5.2a *I-I interactions*: Relaxation peaks due to hydrogen interstitial pair have been observed by Koster *et al* (1956) in Ti, by Bungardt and Preisendanz (1960) in Zr and by Hasiguti *et al* (1965) in zircaloy-2. Miller and Browne (1970) and Browne (1972) reported a relaxation peak due to oxygen interstitial pair in Ti, Zr and Hf. For *I-I* interaction the relaxation strength should be proportional to the number of such pairs and hence to the square of the interstitial content. Miller and Browne (1970) reported such behaviour for both Ti-O and Ti-C alloys. However, investigations by others (Misra and Asundi 1972a, b; Povolo and Bisogni 1967) failed to identify the *I-I* peak in zirconium and titanium. Interstitials were observed to give rise to relaxation only in conjunction with a substitutional atom.

5.2b *I-S pair relaxations*: Interstitial relaxation in hcp metals involving *I-S* pairs was first reported by Pratt *et al* (1954) for Ti containing oxygen. Similar results were reported by Gupta and Weinig (1962) and Bratina (1962). The height of the *I-S* peak was a linear function of the oxygen content, and was related to the size of the substitutional atom.

Bisogni *et al* (1964) measured the relaxation of oxygen and nitrogen in polycrystalline hafnium containing zirconium as substitutional element. Miller (1962) reported an oxygen peak in 'iodide pure' titanium, but the result could be due to the presence of traces of substitutional atoms. Misra and Asundi (1970, 1972) made extensive study of the internal friction due to oxygen and nitrogen in Ti and Zr with a variety of substitutional atoms having different size factors. In zirconium for all the alloying elements, oxygen gave two peaks, the relaxation strength depending on the concentration of oxygen. At low oxygen concentrations, the high temperature peak was more prominent and was ascribed due to three oxygen atom jumps. At high oxygen concentrations, the low temperature peak was more prominent and was due to a single oxygen jump. In nitrogen, only those substitutional elements with atomic size larger than that of zirconium gave internal friction peaks similar to those for oxygen. In titanium, *S-I* relaxation peaks were studied for various interstitials like C, O and N.

Using the torsion pendulum technique in the frequency range 0·5 to 1·5 Hz and the temperature range −190°C to 800°C, Misra (1976) presented extensive results on a series of Zr and Ti base dilute alloys.

5.2c *I-V pair interactions*: In materials with low temperature irradiation damage interstitial-vacancy pairs may cause relaxation effects. Moser *et al* (1973) have studied *I-V* pair interaction in neutron irradiated bcc, hcp and fcc metals. The influence of oxygen and γ-irradiation on the elastic modulus and internal friction of iodide pure zirconium has been reported by Federov *et al* (1971). It has been shown that stable oxygen-vacancy aggregates of various complexities may exist even after annealing. Three relaxation processes associated with oxygen-vacancy complexes are reported in quenched or irradiated zirconium samples.

5.3 *Boundary relaxations*

There are a number of results in the literature pertaining to twin boundary and grain boundary relaxations. Reed-Hill and Dahlberg (1966) studied the elastic after-effect in iodide pure zirconium prestrained at 77°K. At a prestrain of less than 1%, the microstructure indicated $\{11\bar{2}1\}$ twins. It is very likely that the twin boundaries move easily under load. The activation energy obtained in their study (22·7 kcal/mol) has been interpreted as that for slip ahead of the twin interface.

Studies of internal friction associated with grain boundaries in Ti and Zr were reported by Pratt *et al* (1954), Bratina and Winegard (1956), Bungardt *et al* (1962) and Misra and Asundi (1972a). Bungardt *et al* (1962) observed well-developed peaks around 600°C at 1 Hz, whose magnitude changes with grain size.

Bedford *et al* (1972) in their studies on zirconium having different cell structures found an increase in the damping for finer cell structure similar to that observed for grain boundary relaxations for fine grain structure. The high background damping in deformed zirconium is attributed to relaxation of dislocation cell walls. On recovery, dislocation rearrangement results in polygonized sub boundaries and lowering of the damping at higher temperatures.

5.4 *Dislocation relaxations*

The behaviour of dislocations in hexagonal crystals is highly anisotropic because of the limited number of slip systems that can operate in the structure. Consequently, strong orientation dependence of dislocation damping effects is to be expected in single crystal experiments.

The Bordoni peak in Zr and Ti is generally much smaller than the corresponding peak for fcc metals, probably due to the presence of interstitial impurities. Gruzin and Semenikhin (1963) studied the low temperature damping (Bordoni peak) in high purity zirconium which had been deformed to various amounts using a flextural vibration technique. The effect of alloying as well as fast neutron irradiation on the stability of the peak was studied. Doherty and Gibbons (1971) studied the Bordoni peaks in zirconium using a composite resonator technique in the frequency range of 100 to 150 kHz and found an additional peak towards the low temperature range for a sample cold worked by 38 % reduction in cross-section. Under the application of hydrostatic pressure, both the peaks were observed to increase in height. Fonquet *et al* (1970) studied Zr and Zr base alloys at a frequency of 13 kHz.

Hasiguti (1953) found that there exists an internal friction peak above the temperature of the Bordoni peak in cold worked metals. This type of peak known as the Hasiguti peak has been reported in Ti, Zr, Mg (Hasiguti *et al* 1962) and beryllium (Abrams *et al* 1966). The Hasiguti peak is usually small and has higher activation energy than the Bordoni peak and is caused by dislocation relaxation. Yukiti and Hasiguti (1972) reviewed the basic mechanism of thermally-activated unpinning of dislocations resulting in the Hasiguti peak and deduced that the peak temperature shifts with stress amplitude.

The most extensive study on single crystals was carried out by Tusi and Sack (1967). Internal friction studies and electron microscopic observations were carried out on Mg single crystals. Figure 8 shows the results for magnesium single crystals after 0·5 % compression. (θ is the angle between the crystal axis and the hexagonal axis). A broad peak at around 200°K was observed in 2–40 kHz range. From the orientation dependence, it is inferred that dislocation motion in the basal plane is involved in the relaxation process. The peak height increased with deformation and attained a maximum by 2.5 % deformation by compression. The peak height was quite sensitive to the presence of impurities. About 1 % Li completely suppress it, whereas Fe and Ni prevent the peak from disappearing even in annealed samples. A small peak at about 20°K was noticed in cold worked polycrystals and highly deformed single crystals, presumably due to grain boundary or twin boundary relaxations.

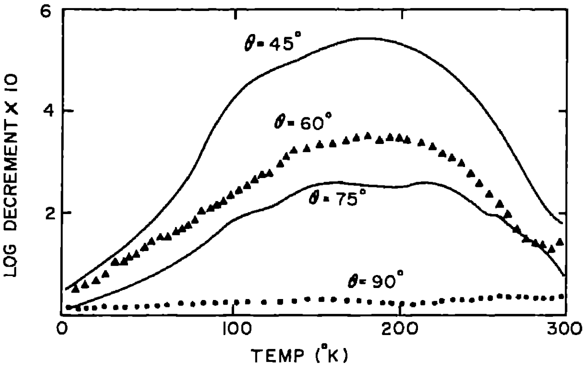

Figure 8. Internal friction of single crystals of magnesium of different orientations after 0·5 % compression.

Amplitude-dependent internal friction in Mg single crystals has been studied by Roberts (1968) in the temperature range of 80–320°K at frequencies 0·015 to 0·75 Hz. Very broad peaks were observed indicating the possibility of a large number of relaxation processes occurring together. The results are interpreted in terms of thermally activated dislocation-dislocation interactions. (Roberts and Hartman 1963; Alefeld 1962).

Esnouf and Fantozzi (1981) observed a strong internal friction peak at about half the melting temperature in high purity polycrystalline Mg. The position of the peak was dependent on strain amplitude. The results are explained in terms of dislocation glide controlled by jog climbing and diffusion of vacancies along dislocations. Atrens (1974) studied the interaction of oxygen as pinning points for dislocations in zirconium. In deformed and annealed zirconium, Ritchie and Sprungmann (1981) observed three internal friction peaks in the temperature range of 480 to 600°C and interpreted them in terms of dislocation core diffusion and unpinning of dislocations.

6. Conclusion

Compared to bcc and fcc metals, the experimental studies on hexagonal metals are fewer and various aspects are to be investigated in detail for a better understanding of the relaxation processes in hexagonal metals. Many of the results were obtained on polycrystalline materials in the form of wires or rods and hence subject to pronounced texture effects. Single crystal studies are desirable for elucidating the orientation effects on dislocation interactions. Such results would be of considerable value in understanding the point defect and dislocation interactions in hcp metals.

References

Abrams E H, Kamber K T and Ang C Y 1966 *Acta. Metall.* **14** 729

Alefeld G 1962 *Z. Phys.* **170** 249

Atrens A 1974 *Scr. Metall.* **8** 401

Bedford A J, Fuller P G and Miller D R 1972 *J. Nucl. Mater.* **43** 164

Berry B S 1962 *Acta Metall.* **10** 271

Bisogni E, Mat G and Wert C 1964 *J. Less Common Metals* **7** 197

Brailsford A D 1961 *Phys. Rev.* **122** 778

Bratina W J 1962 *Acta Metall.* **10** 332

Bratina W J and Winegard W C 1956 *Trans. AIME* **206** 186

Bommel H E 1954 *Phys. Rev.* **96** 220

Browne K M 1972 *Acta Metall.* **20** 507

Bungardt K and Preisendanz H 1960 *Z. Metall.* **51** 280

Bungardt, Preisendanz H and Horn E 1956 *Z. Metall.* **53** 495

Burdett C F and Queen T J 1970 *Metall. Rev.* **143** 47

Cochardt A 1959 in *Magnetic properties of metals and alloys* (ed) R M Bozorth, (Cleveland, Ohio: Am., Soc. Metals) 251

De Batist R 1972 *Internal friction of structural defects in crystalline solids* (Amsterdam: North-Holland Publishing Company)

De Fouquet J, Boch P, Petit J and Hisu G 1970 *J. Phys. Chem. Solids* **31** 1901

Doherty J E and Gibbons D F 1971 *J. Appl. Phys.* **42**

Entwistle K M 1962 *Metall. Rev.* **7** 175

Esnouf C and Fantozzi G 1981 *J. Phys. Colloq (France)* **42** C-5 445

Fantozzi G and Ritchie I G 1981 *J. Phys. Colloq. (France)* **42** C-5 3

Fedorov G B, Kissil A Ye and Festisov G V 1971 *Fiz. Met. Metalloved* **32** 621

Granato A V and Lucke K 1956 *J. Appl. Phys.* **27** 583, 789

Gruzin P L and Semenikhin A N 1963 *Fiz. Met. Metalloved* **15** 791

Gupta D and Weinig S 1962 *Acta Metall.* **10** 292

Hasiguti R R 1953 *Proc. Int. Conf. Theor. Phys.*, Kyoto and Tokyo 577

Hasiguti R R, Igata N and Kamoshita G 1962 *Acta Metall.* **10** 442

Hasiguti R R, Igata N, Tonomae R, Nakumara Y, Saso S and Domato K 1965 *Symp. Nondestructive testing in nuclear technology*, Bucharest

Hoffman R A and Wert C 1966 *J. Appl. Phys.* **37** 237

Ke T S 1949 *J. Appl. Phys.* **20** 274

Koster W, Bangert L and Evers M 1956 *Z. Metall.* **47** 567

Lucke K and Granato A V 1957 in *Dislocations and mechanical properties of metals* (ed) J Fischer, (New York: Wiley)

Mason W P (ed) 1966 *Physical acoustics* (New York: Academic Press) Vol III

Miller D 1962 *Trans. Met. Soc. AIME* **224** 275

Miller D and Browne K M 1970 *The science technology and applications of titanium* (London: Pergamon) 401

Misra S 1976 *Anelastic and internal friction behaviour of zirconium and titanium and their alloys* Ph.D Thesis, The Banaras Hindu University.

Misra S and Asundi M K 1970 *Trans. Indian Inst. Metals* **23** 73 1972a *Can. Met. Q.* **11** 69

Misra S and Asundi M K 1972b *Titanium science and technology* (ed) R I Jaffe and H M Burte (New York: Plenum Press)

Moser P, Verdone J, Chambron W, Nivert V and Pichon R 1973 *5th Int. Conf. Internal Friction and Ultrasonic Attenuation in Crystalline Solids*, Achen

Niblet D H and Wilks J 1956 *Philos Mag* **1** 415

Niblet D H and Wilks J 1960 *Adv. Phys.* **9** 1

Nowick A S 1953 *Prog. Metal Phys.* **4** 1

Nowick A S 1967 *Adv. Phys.* **16** 1

Nowick A S and Berry B S 1972 *Anelastic relaxation in crystalline solids* (New York: Academic Press)

Povolo F and Bisogni E A 1967 *Acta Metall.* **15** 701

Pratt J N, Bratina W J and Chalmers B 1954 *Acta Metall.* **2** 203

Read T A 1940 *Phys. Rev.* **58** 371

Reed-Hill R E and Dahlberg K P 1966 *J. Elec. Chem. Technol* **4** 303

Ritchie I G and Sprungmann K W 1981 *J. Phys. Colloq (France)* **42** C-5 427

Roberts J M 1968 *Trans. Jpn Inst. Metals* **9** 69

Roberts J M and Hartmann D E 1963 *J. Phys. Soc. Jpn* **18** 119

Snoek J L 1941 *Physica* **8** 711

Snoek J L 1942 *Physica* **9** 862

Tusi R T C and Sack H S 1967 *Acta Metall.* **15** 1715

Waterman P C 1958 *J. Appl. Phys.* **29** 1190

Wilks J 1965 *Brit. J. Appl. Phys.* **16** 587

Yukuti R and Hasiguti R R 1972 *J. Less Common Metals* **28** 249

Zener C 1943 *Trans. AIME* **152** 122

Zener C 1947 *Phys. Rev.* **71** 34

Zener C 1948 *Elasticity and anelasticity of metals* (Chicago: University Press)

Bull. Mater. Sci., Vol. 6, No. 6, December 1984, pp. 971–977. © Printed in India.

A novel method of RF powder sputtering

K SOLOMON HARSHAVARDHAN and K N KRISHNA
Materials Research Laboratory, Indian Institute of Science, Bangalore 560012, India

MS received 12 June 1984

Abstract. A new method of RF sputtering by which thin films of metals, semiconductors and insulators can be sputtered from their respective powders, has been successfully demonstrated. The films have been characterized for their surface and crystal structure using conventional methods of SEM and TEM. All the films are amorphous with a relatively smooth surface topography. The relative merits and demerits of the technique have been briefly discussed.

Keywords. RF sputtering; target; shield; Crookes dark space; amorphous films; scanning electron microscopy; transmission electron microscopy.

1. Introduction

Owing to their remarkable performance RF sputtering techniques have evolved as indispensable tools for vapour deposition of materials (Holland 1956; Chopra 1969; Jackson 1970; Maissel and Glang 1970). The technique offers manifold advantages over the other conventional methods such as thermal (resistive heating) and electron beam evaporation when a precise control over the film composition, thickness and adhesion is desired (Chopra 1969).

By definition, sputtering is the physical removal of the surface atoms of a solid target by the energetic particle bombardment and is caused by the momentum transfer of the incoming particles to the atoms near the surface layers of the solid. The ejected atoms can be deposited onto suitably placed substrates. Sputtering can be categorized into DC and RF sputtering. The former method is used effectively for sputtering of metal targets (Maissel and Glang 1970) but fails in insulating (dielectric) and semiconducting targets because of the build-up of a surface charge of positive ions on the insulator (or semiconductor) which prevents any further ion bombardment (Holland 1956; Chopra 1969). Applications of an RF field, in such cases, removes the inherent problems by providing swarms of secondary electrons from the plasma, which neutralize the positive space charge.

Targets used in conventional or commercial systems are fabricated in the form of discs and are secured to the target holders which are often water cooled. The targets are generally supported or suspended horizontally, fastened to the chamber top plate and electrically insulated from it. The substrates are kept below the target on a plate at a distance of ~ 8 cm and can be maintained either at ground potential or at a negative bias. Fabrication of such targets involves long and cumbersome procedures primarily because of the geometrical constraints of the existing set-up in commercial instruments. Further, the amount of material and the cost involved in making such targets can be enormous, particularly when large area targets are desired. Hence, there is a definite need to improve the geometrical set-up, so that the efficiency of the technique can be considerably enhanced. We have successfully solved this problem by redesigning the apparatus. The present paper reports this simple and versatile technique by which practically all types of materials can be sputtered as thin films, the material being taken in the form of compressed powders.

2. Conventional and redesigned RF sputtering

Block diagrams of a conventional RF sputtering system with its important accessories and the redesigned (modified) apparatus are shown in figures 1a and b respectively. The sputtering system used (Materials Research Corporation, USA, Model SEM-8622) is provided with a 13·56 MHz RF generator capable of producing a maximum output power level of 1·5 kW. A capacitatively coupled tuning network is used for impedance matching between the generator and the load. Before each sputtering run, the system is evacuated ($\sim 10^{-7}$ Torr) using standard high speed oil diffusion pumps (Varian Associates, USA). Sputtering was performed in an argon plasma at a constant pressure of 2×10^{-3} Torr. The pressure was controlled using a micrometer leak valve. High purity argon gas (99·999 %, Indian Oxygen Limited) was used. During sputtering, liquid nitrogen was circulated in the cryo-trap to reduce contamination either from the backstreaming of vapours of diffusion pump oil or from the adsorbed gases inside the chamber.

Unlike in the conventional system (figure 1a), the cathode in the modified set-up (figure 1b) is at the bottom of the chamber and the substrates are kept on the top at a distance of ~ 8 cm. The powdered form of the material to be sputtered is uniformly spread into a circular trough (0·5 mm depth and 50 mm dia.) machined out from a stainless steel plate. The target and the target holder are thus integrated into one single element. The powder is first compressed into the trough using a hydraulic press at loads of ~ 5000–10000 kg and the holder is then secured to the cathode which is watercooled.

The circular area surrounding the target (usually < 6 mm in thickness) which does not glow during the sputtering process is called the Crookes dark space (Maissel and Glang 1970; Chopra 1969). When electrons leave the target and move under the influence of an RF field, they travel some distance before picking up energy from the field and making ionizing collisions with inert gas atoms. This distance is determined by the pressure of the gas. As a result there is no ionization in this region and hence no discharge in the immediate vicinity of the target. This fact has been exploited by us for placing a shield over the cathode (figure 1b). The shield has a central aperture, the area of the aperture being determined by the area from which sputtering from the target is desired. The crucial feature of the design is that, the shield is at the ground potential and the shield to target distance is less than the Crookes dark space. Further, the annulus in the shield must follow all the contours of the cathode-target combination such that at no point the distance between them exceeds the length of the Crookes dark space, at the working pressure of the sputtering gas. The target-to-shield distance should not be made very small so as to avoid loss of power to the target. The typical distance used was 4 mm at a working pressure of $\sim 2 \times 10^{-3}$ Torr and the aperture diameter was ~ 50 mm. It may be worthwhile to note that the plasma is confined in space in the shape of a truncated cone, with its smaller end fitting into the annulus in the shield (figure 1b). Further, for a fixed area of the aperture, the cone diameter at the minimum can be made

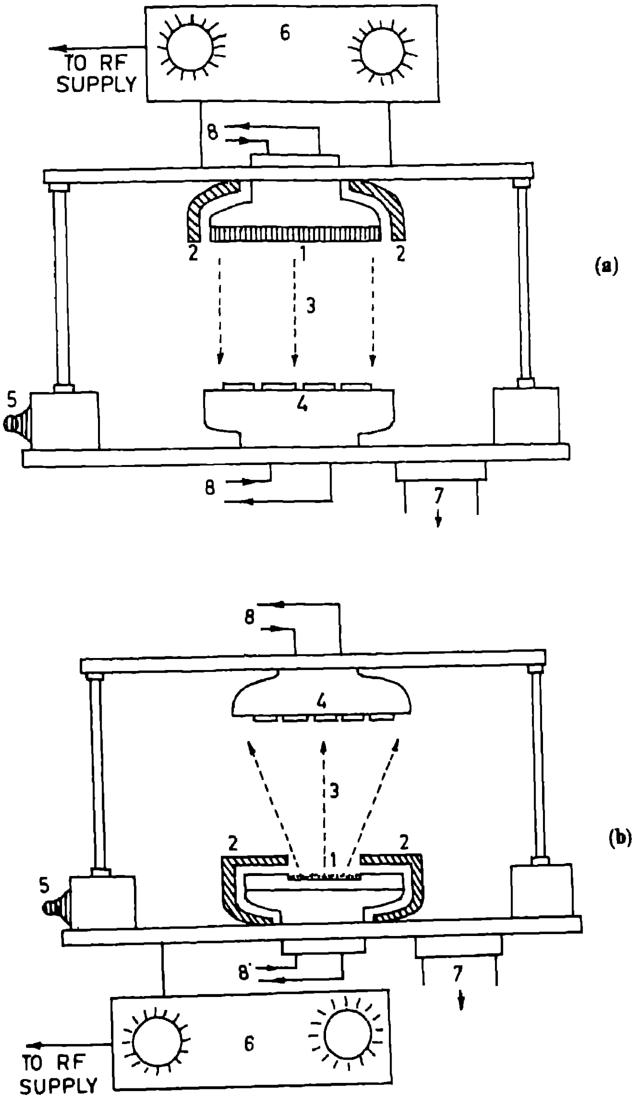

Figure 1. Block diagrams of the RF sputtering system with the important accessories **a.** Conventional and **b.** Modified (1-target, 2-cathode shield, 3-plasma region, 4-anode (substrate holder), 5-argon gas inlet, 6-RF tuning network, 7-gasoutlet, 8-coolant water).

smaller by reducing the argon gas pressure. However, this flexibility is limited and beams approximately 20 mm less than the aperture diameter can be obtained.

3. Sputtering and characterization of films

This method which is essentially a powder sputtering method has been successfully used by us for depositing thin films of metals such as Cu and Al, semiconductors such as Ge, Se, As_2Se_3 and insulators such as SiC. Typical RF power levels and other sputtering parameters used are listed in table 1.

Table 1. Deposition parameters of various materials.

Material sputtered	RF power (W)	Target potential (V)	Sputtering pressure ($\times 10^{-3}$) (Torr)	Nature of the films	
				Present work	Earlier Reports (References)
Cu	200	1000	2	Amorphous	Polycrystalline (Buckel 1959; Patten *et al* 1971; Segmuller 1973)
Al	325	700	2	Amorphous	Polycrystalline (Barna *et al* 1970; Bosnel and Thomas 1972; Tellier and Tosser 1977; Sherman 1977)
Ge	175	1200	2	Amorphous	Amorphous (de Neufville 1972; Kolomiets *et al* 1976; Tauc 1970)
Se	100	1200	2	Amorphous	Amorphous (Grigorovici 1969; Kolomiets *et al* 1976, Lucovsky 1967)
As_2Se_3	75	60	2	Amorphous	Amorphous (de Neufville 1972; Kolomiets *et al* 1976; Tauc 1970)
SiC	325	1800	10	Amorphous	Amorphous (Fritzsche 1973), Polycrystalline (Nishino *et al* 1977)

The powder sputtered films of various materials were characterized for their surface morphology and structures. The surface morphology, surface roughness and the topology of the gross microstructure were investigated (Cambridge Stereoscan-150 SEM). Prior to the analysis, the films were coated with a thin layer of sputtered gold (when non-conducting specimens were studied), to reduce the charging and blurring effects which lead to the loss of definition and resolution of the image particularly at higher magnifications. The surface of most of the films had no distinguishing features. The SEM for a typical case of As_2Se_3 (figure 2) depicts a fairly smooth surface. Since

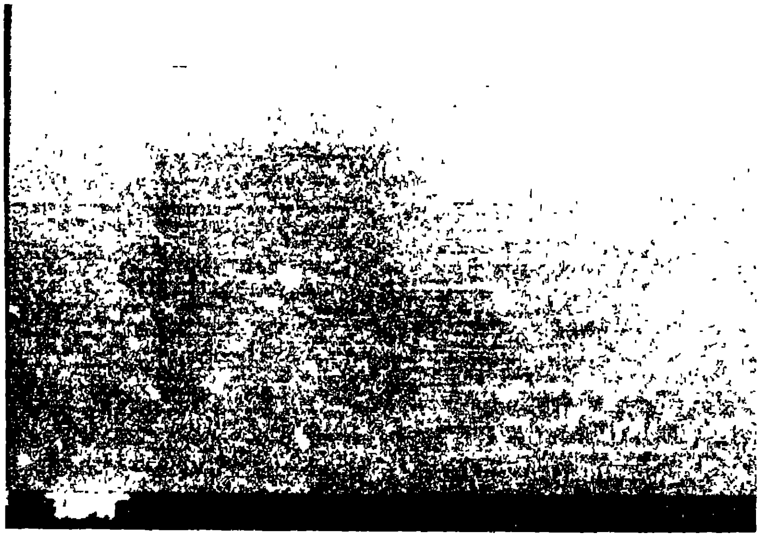

Figure 2. Scanning electron micrograph of As_2Se_3 film ($\times$ 1200).

Figure 3. Laue photographs of amorphous films of **a.** Al **b.** Cu **c.** Ge **d.** Se **e.** As_2Se_3 **f.** SiC.

⟶

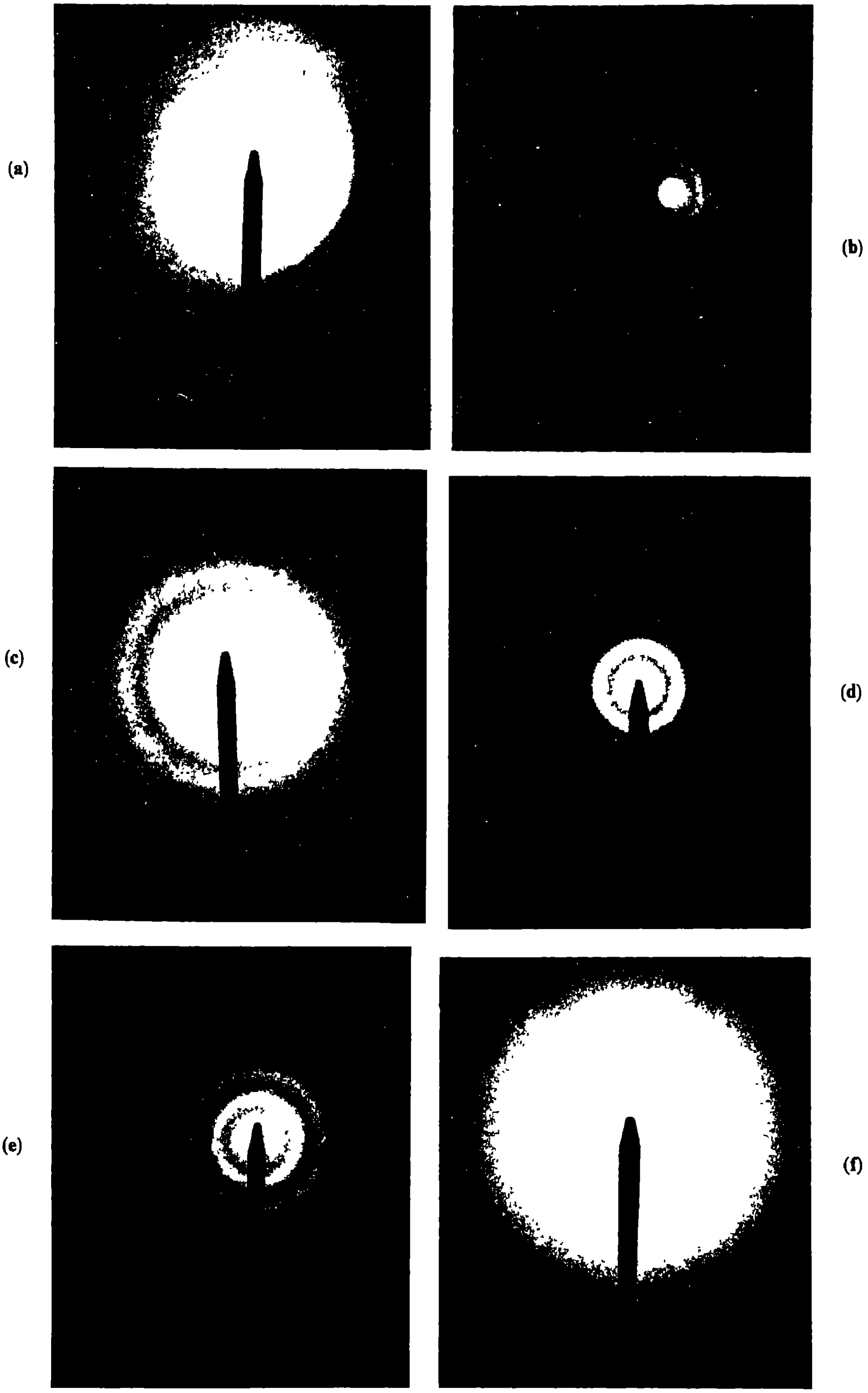
(a)
(b)
(c)
(d)
(e)
(f)

sputtering is a high temperature deposition process, the smooth surface structure can be attributed to high adatom mobility of the sputtered species, which agrees with earlier reports (Holland 1956; Chopra 1969; Maissel and Glang 1970).

Structures of these films were investigated using electron diffraction technique. Films of thickness 500–1000 Å were deposited onto freshly cleaved NaCl single crystals and floated in distilled water. Films were lifted onto 400 mesh copper grids. The grids were then transferred to the specimen holder of a Philips EM 301 electron microscope and examined. The diffraction patterns as well as the micrographs were recorded for all the films studied. Low beam conditions ($\sim 10^{-6}$ A/cm^2) were used for the semiconducting films to minimize the heating effects as well as the electron beam-induced structural changes. A striking feature of all the films studied has been that their diffraction patterns were featureless halos indicating that the films were all amorphous. Though our results for semiconducting films agree with similar results (Lucovsky *et al* 1967; Grigorovici 1969; Tauc 1970; de Neufville 1972; Kolomiets *et al* 1976), there are surprising differences in the case of sputtered metal films of Al and Cu, which were reported to give polycrystalline sputtered films (Buckel 1959; Patten *et al* 1971; Segmuller 1973; Barna *et al* 1970; Bosnel and Thomas 1972; Tellier and Tosser 1977; Sherman 1977) but were found to be amorphous in our studies. RF sputtered films of SiC have been reported to be both amorphous (Fritzsche 1973) like in the present case, and polycrystalline (Nishino *et al* 1977) depending on the sputtering conditions. Laue photographs of various films are shown in figures 3(a–f).

4. Limitations and possible improvements of the set-up

We have noted that the present set-up offers several advantages over the conventional sputtering methods. However, there are a few disadvantages associated with the present design. (i) By employing the cathode shield with a central aperture, the area of sputtering has been controlled but the thickness uniformity has been adversely affected. This can be minimized by a proper choice of target to substrate distance and redesigning of the substrate holder. (ii) It may be reasonably argued that undesirable gases and impurities are entrapped in the target in the present design. But such effects have not been well understood and some of these aspects are being presently investigated.

5. Conclusions

In the present study a simple and versatile technique for RF sputtering of thin films of metals, semiconductors and dielectrics has been described and its use has been successfully demonstrated. The method offers a cost effective means of sputtering of various materials particularly when commercial targets are not available.

Acknowledgements

The authors would like to thank Prof. C N R Rao for encouragement and Prof. K J Rao for helpful discussions.

References

Barna A, Barna P B, Pocza J F and Pozsgai I 1970 *Thin Solid Films* **5** 201

Bosnell J and Thomas C B 1972 *Solid State Electron.* **15** 1261

Buckel W 1959 *Proc. Int. Conf. on Structure and Properties of thin films* (eds) C A Neugebauer, J B Newkirk and D A Vermilyea (New York: John Wiley) p. 53

Chopra K L 1969 *Thin Film Phenomena* (New York: McGraw Hill)

de Neufville J P 1972 *J. Non-Cryst. Solids* **8–10** 85

Fritzsche H 1973 *Electronic and structural properties of amorphous semiconductors* (eds) P G LeComber and J Mort (New York: Academic Press) p. 106

Grigorovici R 1969 *J. Non-Cryst. Solids* **1** 303

Holland L 1956 *Vacuum deposition of thin films* (Chapman and Hall) Chap. 14

Jackson G N 1970 *Thin Solid Films* **5** 209

Kolomiets B T, Lantrotova S S, Lyubin V M, Pukh V P and Tagirdzhanov M A 1976 *Sov. Phys. Solid State* **18** 866

Lucovsky G, Mooradian A, Taylor W, Wright G B and Keezer R C 1967 *Solid State Commun.* **5** 133

Maissel L I and Glang R 1970 *Handbook of thin film technology* (New York: McGraw Hill) Chap. 4

Nishino S, Matsunami H, Odaka M and Tanaka T 1977 *Thin Solid Films* **40** L27

Patten J W, McClanahan E D and Johnston J W 1971 *J. Appl. Phys.* **42** 4371

Segmuller A 1973 *Thin Solid Films* **18** 287

Sherman D 1977 *Thin Solid Films* **45** 537

Tauc J 1970 *Optical properties of solids* (ed) F Abeles (Amsterdam: North Holland)

Tellier C R and Tosser A J 1977 *Thin Solid Films* **43** 261

Bull. Mater. Sci., Vol. 6, No. 6, December 1984, pp. 979–989. © Printed in India.

Preparation and characterisation of β''-Al_2O_3

H S KALSI, R P TANDON, BALBIR SINGH, R C GOEL and B K DAS
National Physical Laboratory, New Delhi 110012, India

MS received 6 August 1983; revised 6 April 1984

Abstract. Beta alumina solid electrolyte is a potential candidate in the fabrication of Na-S batteries. In the present study, it has been prepared in the form of discs by uniaxially as well as isostatically pressing and sintering in the temperature range 1585–1630°C, the highest sintered density of $3{\cdot}25\ g/cm^3$ has been achieved in the samples isostatically pressed and sintered at 1630°C. X-ray analysis of the samples shows formation of β''-phase. Microstructure of the sintered samples reveals some darker regions which are attributed to low soda content. Resistivity at 300°C measured by the two-probe method at a frequency of 1 MHz on samples having vacuum-deposited silver electrodes is 15 ohm-cm, which is slightly higher than the value of 5–13 ohm-cm reported in literature using molten sodium electrodes. The activation energy of conductivity is 0·24 eV which is comparable to the literature value of 0·24–0·35 eV.

Keywords. Conducting ceramic; ionic conductor; sodium beta alumina; solid electrolyte.

1. Introduction

Beta-alumina ceramics have potential application in a variety of devices such as (a) electrolyte in the Na-S battery (Kummer and Weber 1968) for automotive propulsion or electric utility load levelling (b) thermoelectric devices (Weber 1974) and electrochemical devices for measuring sodium and oxygen activities. Amongst these, the sodium sulphur battery system based on beta alumina is the most advanced one.

The general formula for beta alumina is $Na_2O \cdot x$-Al_2O_3, where x varies from 5–11. Two structural forms of beta type alumina exist (Kummer 1972). At $x = 11$ the composition yields β-alumina which starts converting in β''-alumina as the sodium content increases and at $x = 5$, the β-phase is completely converted into the β''-phase. β''-alumina has higher ionic conductivity than β-alumina but is unstable at a temperature greater than 1500°C. As the sintering temperature of β''-alumina is > 1500°C, some stabilizing agent like lithium oxide or magnesium oxide or both are added (Gordon *et al* 1977).

Lithium-stabilised β''-alumina was synthesised from reactive α-alumina which was prepared at NPL, India (Das *et al* 1982). To compare the results, reactive α-alumina of M/s Reynolds, USA was also used to synthesise β''-alumina.

2. Experimental procedure

β''-Al_2O_3 was synthesised using two varieties of reactive α-Al_2O_3 (NPL, India; M/s Reynolds USA (which has particle size $\leq 0{\cdot}7\ \mu m$ and purity $> 99{\cdot}6\%$)). The other two raw materials, sodium carbonate and lithium carbonate were of AR grade. The material was processed by using zeta process (Youngblood *et al* 1977) in which sodium-alumina composition and a lithium alumina composition known as zeta alumina were processed and calcined separately and the two were then mixed in proper proportions to yield the desired composition.

The composition chosen for this experiment was 84·09 % Al_2O_3, 13·54 % Na_2O and 2·37 % Li_2O all taken in mole percent. $Na_2O5{\cdot}25\,Al_2O_3$ and $Li_2O5{\cdot}5Al_2O_3$ prepared for making the above composition were separately calcined at 1340°C for 2 hr and the compositions dry-ball milled to a particle size of $< 1\ \mu m$. The powder was then mixed with polyvinyl butyral and benzene, which acts as a binder for about 2 hr and the slurry dried in air. The material was granulated using a nylon sieve and pressed uniaxially and isostatically into discs (15 mm dia and 2·5 mm thickness). A flow chart of the zeta process is shown in figure 1. To study the effect of particle size on the density, the

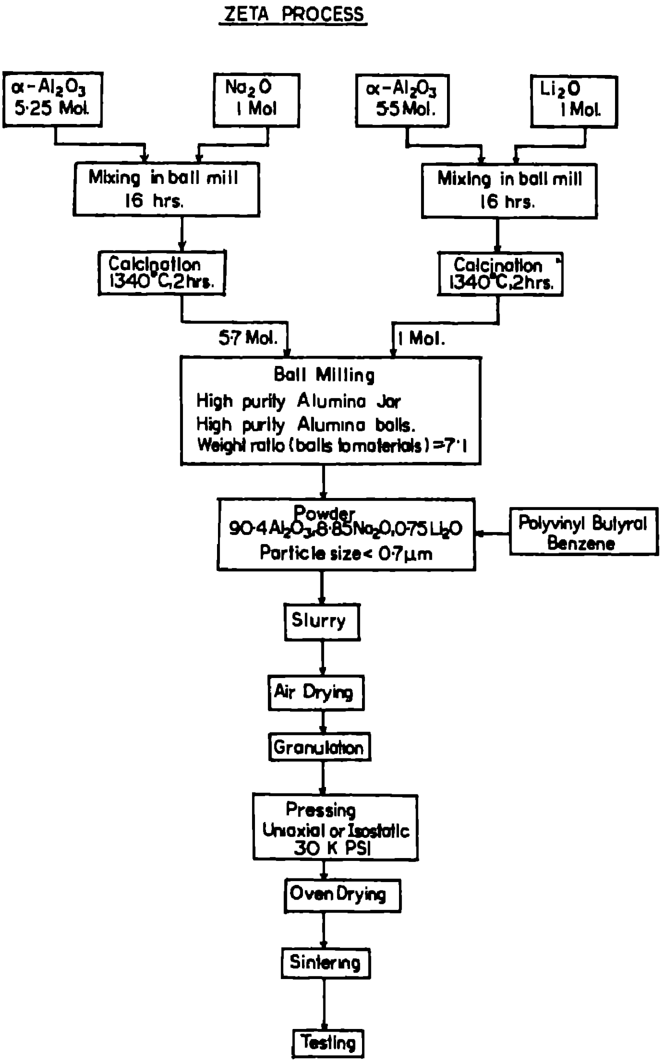

Figure. 1. Flow chart of zeta process for the synthesis of β''-Al_2O_3.

Table 1. Particle size analysis of powders A–E.

Particle size (μm)	Materials (comm %)				
	A	B	C	D	E
+1·8	0·4	0·2	0·1	0	0
+1.15	4·2	3·4	2·3	1·2	1·2
+0·8	14·0	12·1	10·7	9·5	9·2
+0·65	26·3	22·6	21·3	19·9	20·2
+0·57	38·2	33·2	32·5	31·1	31.3
+0·5	49·2	43·2	43·0	42·3	42·3
+0·46	59·0	52·3	52·6	51·3	51·5
+0·43	67·5	60·5	61·0	59·3	59·5
+0·36	86·3	83·2	83·8	77·8	77·4
+0·33	94·0	90·3	89·9	85·6	86·4
+0·30	98·4	95·5	95·9	92·4	92·9
+0·28	100·0	98·8	99·2	97·6	97·5
+0·26	100·0	100·0	100·0	100·0	100·0
Mean Particle size	0·56	0·54	0·52	0·5	0·5

material was ground for various durations of time to yield different particle size distributions. Five such powders (table 1) having different particle size distribution were processed by pressing uniaxially and isostatically at different pressures. The pressed tablets were dried overnight in an oven (160°C) and then covered with coarse beta alumina powder and sintered in super kanthal furnace at a temperature ranging from 1585–1630°C for various time intervals (2–32 min). The temperature schedule of the sintering is shown in figure 2. The material was annealed at 1480°C for 4 hr for complete conversion into the β''-phase. An almost similar two-step sintering schedule was adopted by Kvachkov *et al* (1981, 1982).

Rectangular samples (33 × 32·7 × 2·7 mm) for x-ray analysis were prepared by uniaxially pressing and sintering at a temperature ranging from 1585–1630°C. Tables 2a and 2b give the x-ray analysis and it is evident that mostly the β''-phase is present (Ray and Subbarao 1975; ASTM 1967). The density of the sintered discs was measured by Archemedes principle by immersion in xylene.

For microstructural evaluation the discs were broken into small pieces and the broken faces examined under a scanning electron microscope (JEOL JSM-35 CF). Energy dispersive spectroscopy (EDS) mode was employed for the elemental analysis of aluminium and sodium.

The electrical resistivity was measured by employing evaporated silver full face electrodes and by using Siemen's Bridge at 1 MHz to avoid interface polarisation (Yao and Kummer 1967) in a temperature range of 20–300°C.

3. Results and discussions

3.1 *Effect of compacting pressure on green density*

Figure 3 depicts the effect of uniaxial as well as isostatic pressure on the green density of the materials (Kalsi *et al* 1983). The green density increases with pressure. The highest

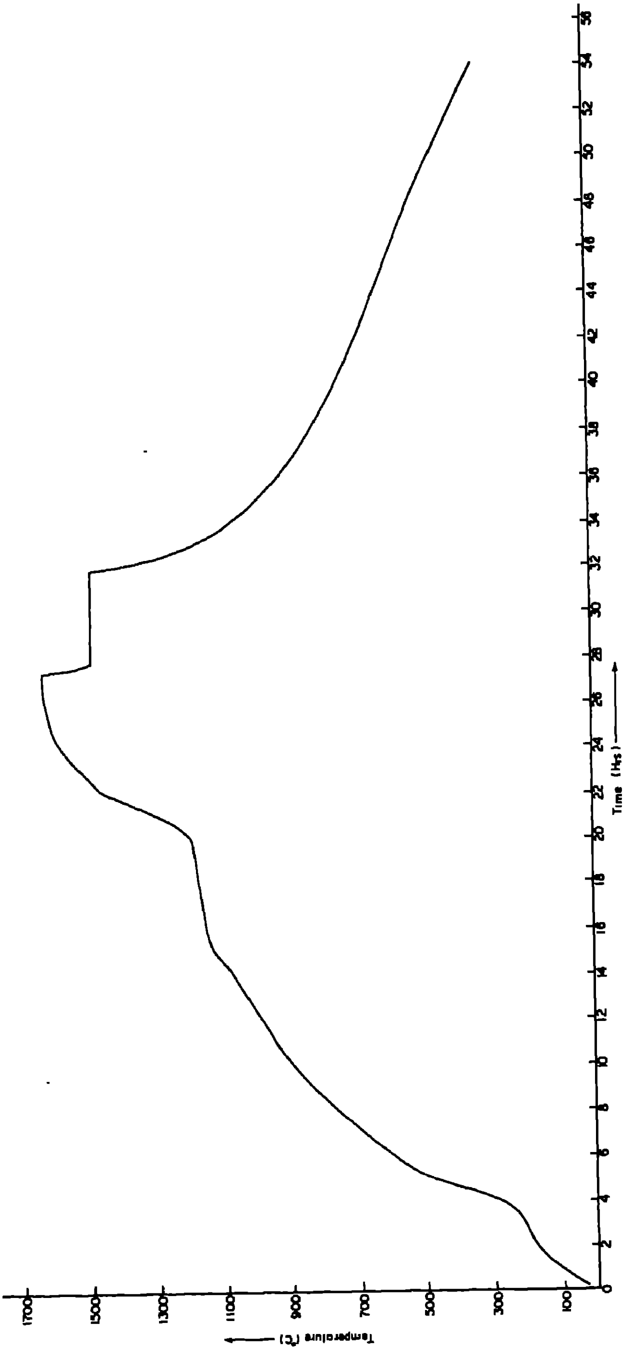

Figure 2. Temperature profile of sintering cycle.

Table 2(a). X-ray diffraction data for β''-Al_2O_3 prepared from powder D.

dA°	I/I_1	*hkl*
11·632	100	003
5·644	47	006
4·495	5	100
4·086	3	001
2·818	12	110
2·683	24	114
2·515	16	116
2·429	9	0014 200
2·380	3	204 118
2·254	13	110
2·132	9	1014 207
2·040	9	209
1·973	5	2010
1·943	7	1016
1·596	6	2014
1·559	6	306
1·406	17	220

Table 2(b). X-ray diffraction data for β'' Al_2O_3 prepared from powder E.

dA°	I/I_1	*hkl*
11·632	100	003
5·717	56	006
4·484	7	100
4·086	6	001
2·818	16	110
2·691	28	114
2·600	5	101 0013
2·515	22	116
2·417	12	0014 200
2·383	3	203
2·254	18	110
2·139	12	1014 207
2·045	16	200
1·973	5	2010
1·943	8	1016
1·596	8	2010
1·559	8	306
1·486	4	309
1·404	25	220

green density of 2·27 g/cm^3 was obtained in powder A (table 1) at a uniaxial compacting pressure of 3600 kg/cm^2 whereas at an isostatic pressure of 2600 kg/cm^2 a highest green density of 2·3 g/cm^3 was obtained for the same powder.

The variation of green density with particle size presented in figure 3 shows that the density decreases with particle size.

3.2 *Effect of compacting pressure on the sintered density*

Variation of the sintered density with uniaxial and isostatic pressure is shown in figure 4. The highest sintered density of 3·22 g/cm^3 was obtained for powder D (table 1) compacted at uniaxial pressure of 1800 kg/cm^2 and sintered at 1630°C, whereas for the isostatically pressed samples sintered at 1630°C, the sintered density is independent of the isostatic pressure in the range of 700–2600 kg/cm^2. The highest sintered density of 3·25 g/cm^3 for powder D was obtained.

The variation of sintered density with particle size is also shown in figure 4 and it is clear that as the particle size decreases the sintered density increases.

3.3 *Shrinkage studies*

The shrinkage was measured as a function of uniaxial compacting pressure for all the five powders by sintering at 1630°C. The results are shown in figure 5. Shrinkage is higher at lower pressures with no significant change beyond 3000 kg/cm^2. Powder D exhibits the highest shrinkage followed by powder E (table 1).

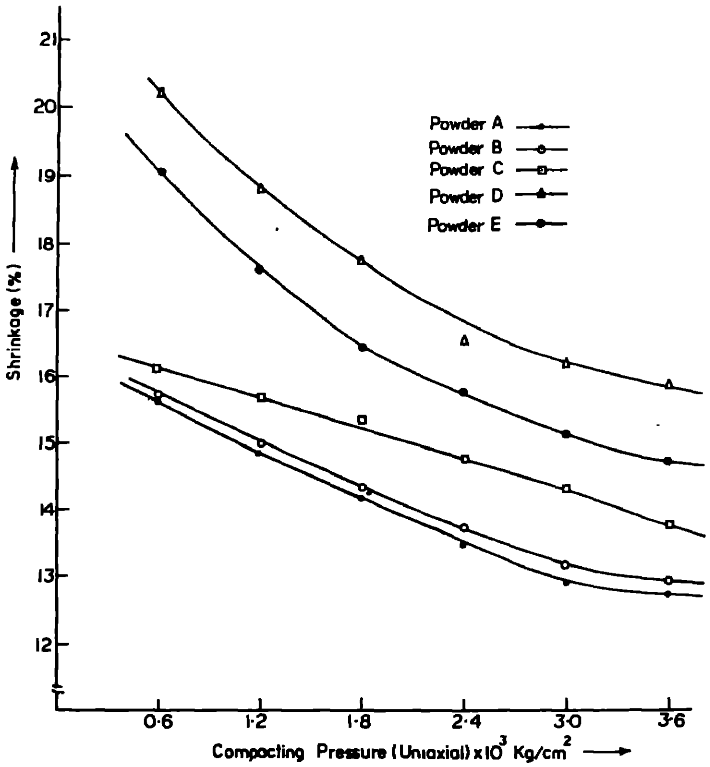

Figure 5. Variation of shrinkage with uniaxial compacting pressure for samples of different initial particle sizes and sintered at 1630° C for 20 min.

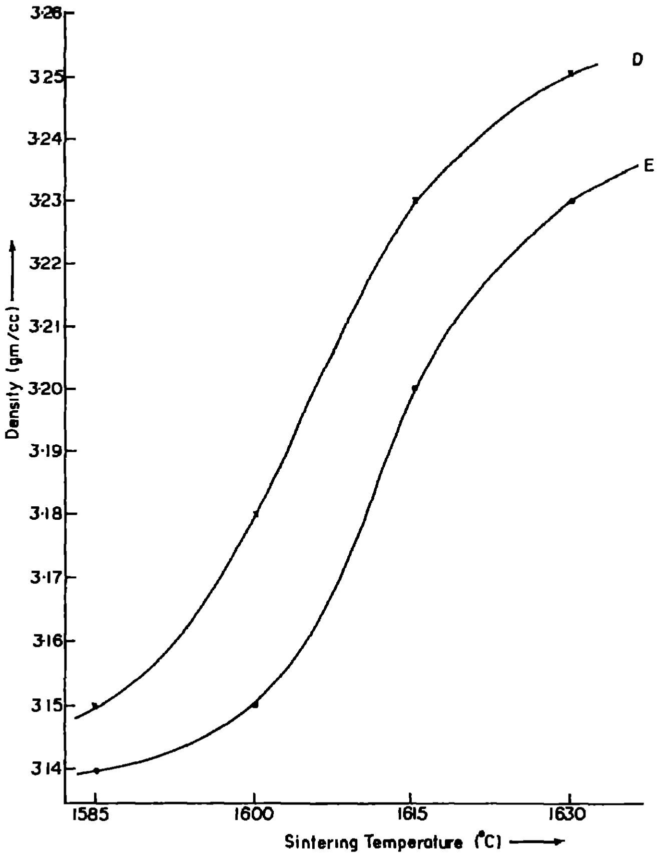

Figure 6. Variation of sintered density of powders D and E as a function of sintering temperature.

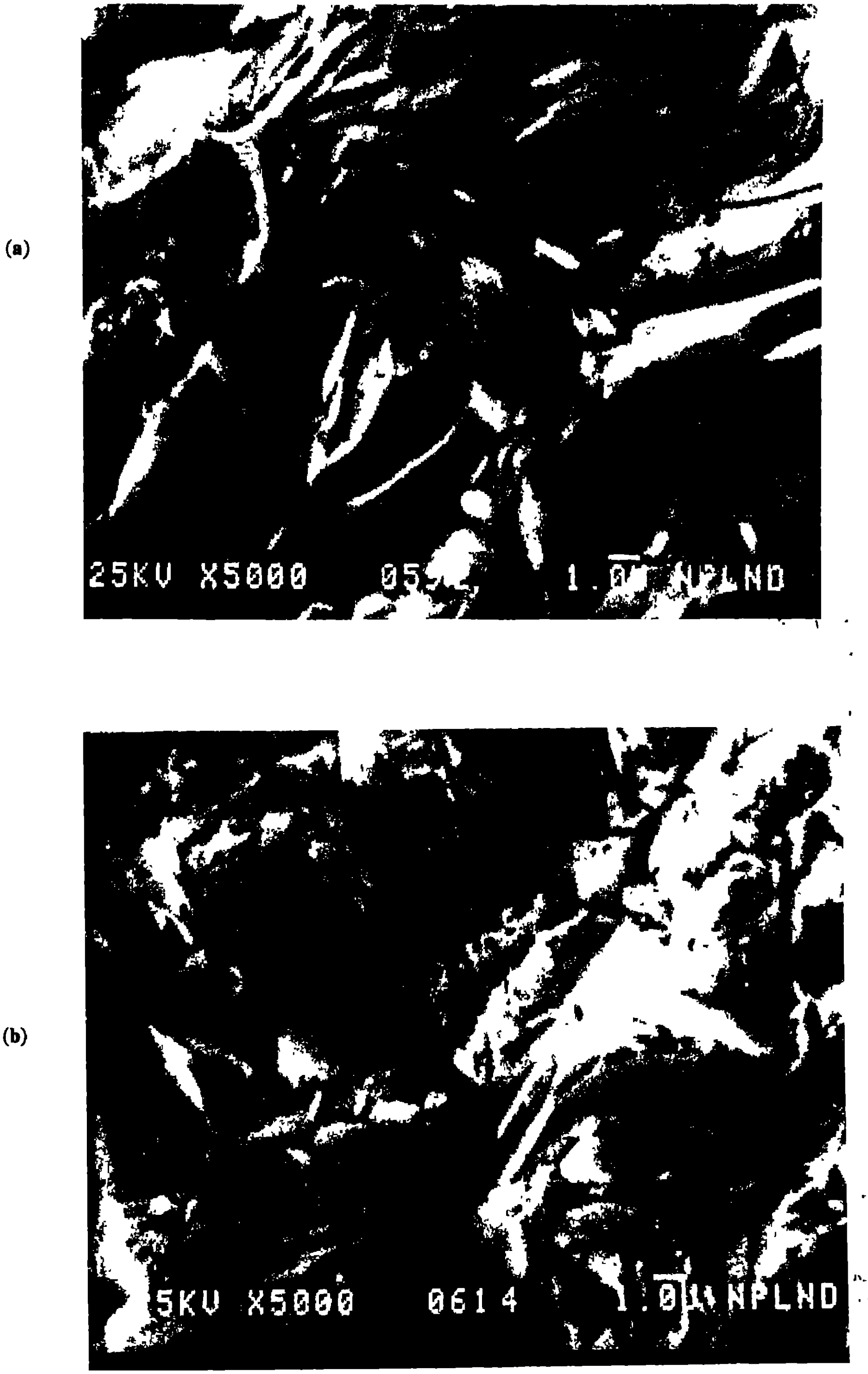

Figure 7. Microstructure of β''-Al_2O_3 prepared from a. powder D and b. the powder E and sintered at 1630°C for 20 min.

4. Conductivity measurements

Ionic conductivity of beta alumina type superionic conducting material has been studied by several investigators (Wynn and Miles 1971; Demontt and Hancock 1971; Kummer 1972; Whittingham and Huggins 1971). Such measurements need either reversible electrodes *i.e.* molten sodium (Demontt and Hancock 1971) or $NaNO_2/NaNO_3$ (Sudworth *et al* 1973) eutectic mixture, in which case conductivity is independent of the frequency. For measurements made using platinum or silver blocking electrodes the conductivity becomes frequency dependent below 1 MHz. At 1 MHz and above, it is independent of the frequency. In this study the measurements were made at 1 MHz using evaporated silver blocking electrodes; and resistivity of the order of 15 ohm-cm at 300°C was obtained.

The activation energy of conductivity was 0·24 eV which is close to the value reported (Kalsi *et al* 1983) for Li_2O doped compositions of β''-Al_2O_3. It may be pointed out here that this is slightly higher (Kalsi *et al* 1983) than those for the corresponding MgO-doped compositions. This difference could be due to the difference in structure or atomic jump mechanism which controls the ionic conductivity.

5. Conclusion

In β''-Al_2O_3 samples isostatically pressed and sintered at 1630°C a density of 3·25 g/cm^3 has been obtained. A maximum shrinkage of 20% was observed in samples uniaxially pressed at 600 kg/cm^2 and sintered at 1630°C. X-ray analysis reveals the formation of β''-phase. The microstructure reveals randomly oriented elongated crystals of β''-Al_2O_3 having some darker portions; which are regions of low soda content. The resistivity of the order of 15 ohm-cm at 300°C has been obtained. An activation energy of 0·24 eV was obtained which is close to the value reported in literature.

Acknowledgement

The authors thank the Director, NPL, New Delhi for facilities. Thanks are due to Mr S U M Rao and Shri D K Suri for scanning electron microscopy and x-ray diffraction analysis work respectively. This work is supported financially by the Department of Nonconventional Energy Sources, New Delhi.

References

ASTM 1967 19–1173

Das B K, Kalsi H S, Khullar S M, Kumar Rahul, Goel R C and Misra S C K *Int. Symp. on Ceramics* 27–30 Nov. 1982 Bangalore (India) Vol. I Part II

Demont D S and Hancock P 1971 *Proc. Br. Ceram. Soc.*

Fielder W L, Kantz H E, Fordyce J S and Singer J 1975 *J. Electrochem. Soc.* **122** 528

Gordon R S, McEntire B J, Miller M L and Virkar A V 1977 *Mater. Sci. Res.* Vol. 11, p. 1405

Hodge J D 1983 *J. Am..Ceram. Soc.* **66** 166

Kalsi H S, Tandon R P and Das B K 1983 *Symp. on Adv. in electrochemical Energy Storage and Conversion* 21-1-1983, CECRI, Karaikudi (India)

Kummer J T 1972 *Prog. Solid State Chem.* 7 141

Kummer J T 1972 *Prog. Solid State Chem.* (ed.) H Reiss and J O McCaldin (New York: Pergamon Press) Vol. 7

Kummer J T and Weber N 1968 *Soc. Automotive Eng. Trans.* **76** 1003

Kvachkov R, Yanakiev A, Poulieff C N, Bakanor I, Yankulov P D and Budevski E 1981 *J. Mater. Sci.* **16** 2710

Kvachkov R, Yanakiev A, Poulieff C N, Yankulov P D, Rashkov S and Budevski E 1982 *Solid State Ionics* **7** 151

Ray A K and Subbarao E C 1975 *Mater. Res. Bull.* Vol. **10** 583

Sudworth J L, Tilley A R and South K D 1973 *East ion transport in solids* (ed.) W Van Gool (Amsterdam: North Holland) p. 581

Weber N 1974 *Energy Convers.* **14** 1

Whittingham M S and Huggins R A 1971 *J. Electrochem. Soc.* **118** 1

Wynn Jones I and Miles L T 1971 *Proc. Br. Ceram. Soc.* 161

Yao Y F V and Kummer J T 1967 *J. Inorg. Nucl. Chem.* **29** 2453

Youngblood C E, Virkar A V, Canon W R and Gordon R S 1977 *Am. Ceram. Soc. Bull.* **56** 206

Bull. Mater. Sci., Vol. 6, No. 6, December 1984, pp. 991–996. © Printed in India.

Evidence of screw dislocations on (002) cleavages of lithium carbonate single crystals

K S RAJU*, M PALANISWAMY, P RAMASAMY and G S LADDHA
Crystal Growth Centre, AC College of Technology, Anna University, Madras 600 025, India
*Department of Crystallography and Biophysics, University of Madras, Guindy Campus, Madras 600 025, India

MS received 2 April 1983; revised 8 December 1983

Abstract. Well-defined triangular etch pits are produced on etching (002) cleavages of lithium carbonate single crystals with 2% citric acid. On etching of cleavage face and matched face these pits nucleate at the intersection sites of dislocations with the cleavage face. On successive etching of a cleavage face, shallow irregular arrays of pits do not enlarge in size as compared to other isolated pits on the same face. These irregular arrays of pits have reasonable correspondence on an etched match face, suggesting they form at dislocation sites.

Keywords. Chemical etching; tilt boundaries; twist boundaries; spiral etch pits; lithium carbonate single crystal.

1. Introduction

Etch methods have been applied to understand the history of growth of crystals and their dislocation content (Gilman and Johnston 1956; Patel and Tolansky 1957; Patel and Goswami 1964; Patel and Raju 1966, 1967; Raju 1981). It was established that the geometric shape of the etch pits on a crystal face is strictly related to the symmetry of the crystal face and the nature of the etchant (Patel and Singh 1968; Hari Babu and Bansigir 1968; Buckley 1958; Borle and Bagai 1976; Connick and May 1969; Wehner 1958 etc). Irregular arrays comprising of edge and screw dislocations on (0001) and $(10\bar{1}1)$ faces of hematite (Sunagawa 1968) as well as on (010) faces of gypsum (Raju 1980) have been reported.

In the present paper spiral etch pits observed along the irregular arrays on (002) cleavage faces of Li_2CO_3 single crystals are reported.

2. Experimental

In the present work, transparent single crystals (Palaniswamy *et al* 1982) of lithium carbonate were cleaved parallel to the (002) plane and etched in 2% citric acid for the required time. The etch patterns were studied by optical methods. Silver coating on the etched cleavages was avoided as it would spoil the surface for further etching. For examining the cleavage surfaces at higher resolution and magnification, scanning electron microscope (Cambridge Stereoscan model S-150 and operating voltage 20 kV) was used after sputtering the crystal surface with gold.

3. Observations

3.1 *Successive etching of an isolated cleavage*

Figures 1 and 2 reveal the etch patterns produced on etching a (002) basal cleavage face of lithium carbonate crystal with 2% citric acid for 2·5 and 4 min respectively. It is clear that on successive etching, some isolated etch pits enlarge in size and shape whereas the array (marked XY in figure 1) remains almost the same (marked X′Y′ in figure 2). The

(1)

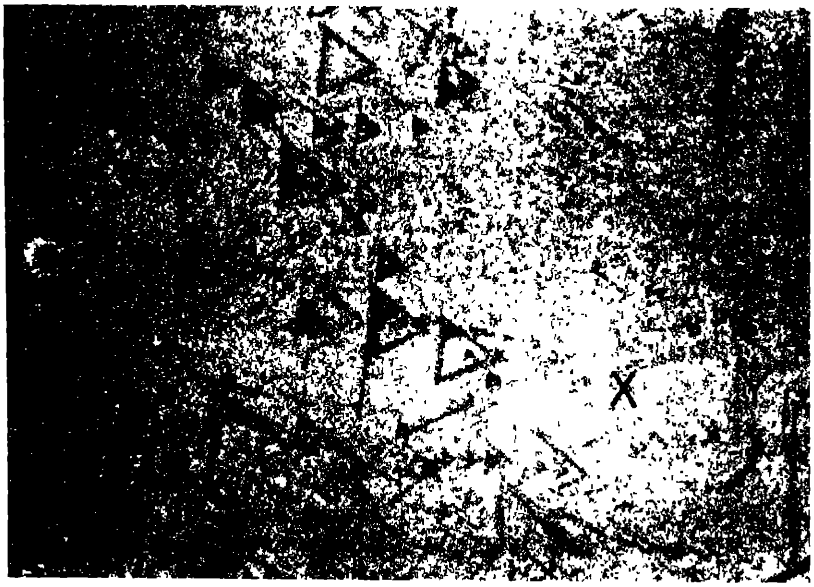

(2)

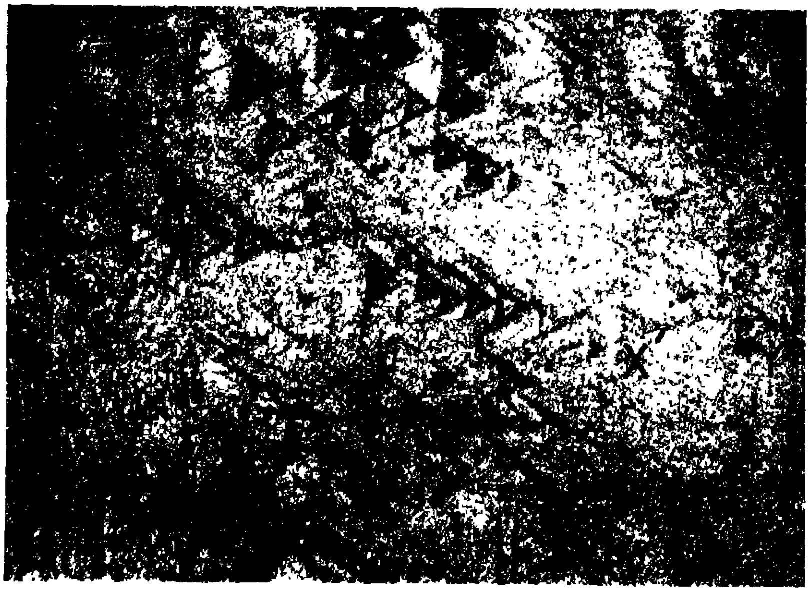

Figures 1 and 2. (× 200) Etch pattern **1.** on (002) cleavage etched 2% citric acid for 2½ min. **2.** of the region of figure 1 etched for a total of 4 min pit marked Y in figure 1 on successive etching appears like a clockwise spiral as seen in the pit marked Y′ in figure 2.

3.2 *Etching of a matched pair*

In order to investigate the irregular arrays of etch pits, a matched face is etched identically for $2\frac{1}{2}$ min in 2% citric acid. Figures 3 and 4 clearly show a reasonable

(3)

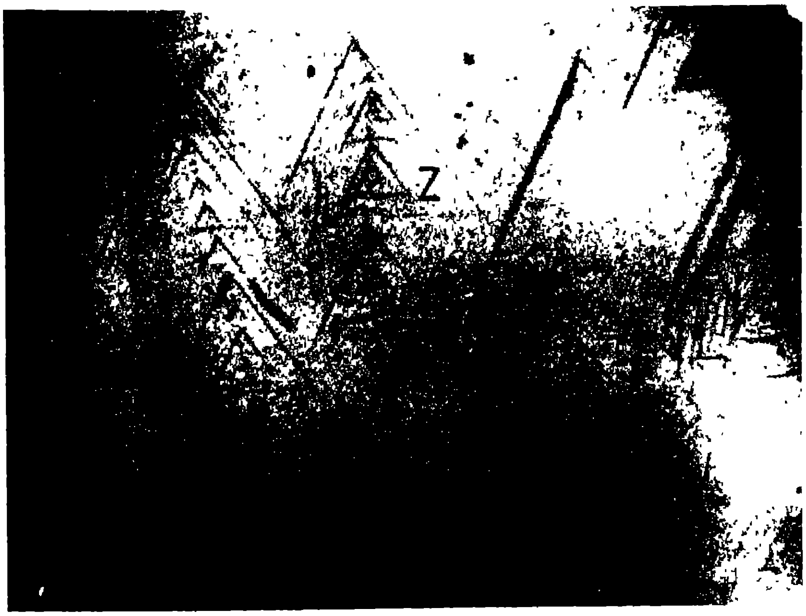

(4)

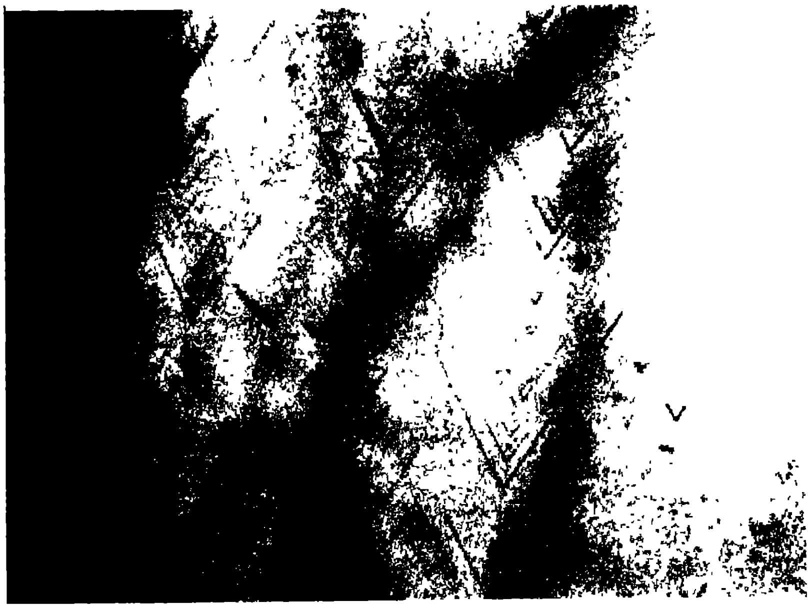

Figures 3 and 4. (× 325) Etch patterns of a matched cleavage etched in 2% citric acid for $2\frac{1}{2}$ min.

amount of correlation in the three dominant irregular arrays of etch pits. The pit marked Z in the central array of figure 3 resembles an anticlockwise spiral.

3.3 SEM *studies*

One of the arrays in figure 3 is scanned in the electron microscope (figure 5). The pit marked M clearly looks like a clockwise spiral of single turn, while the pit marked N is

(5)

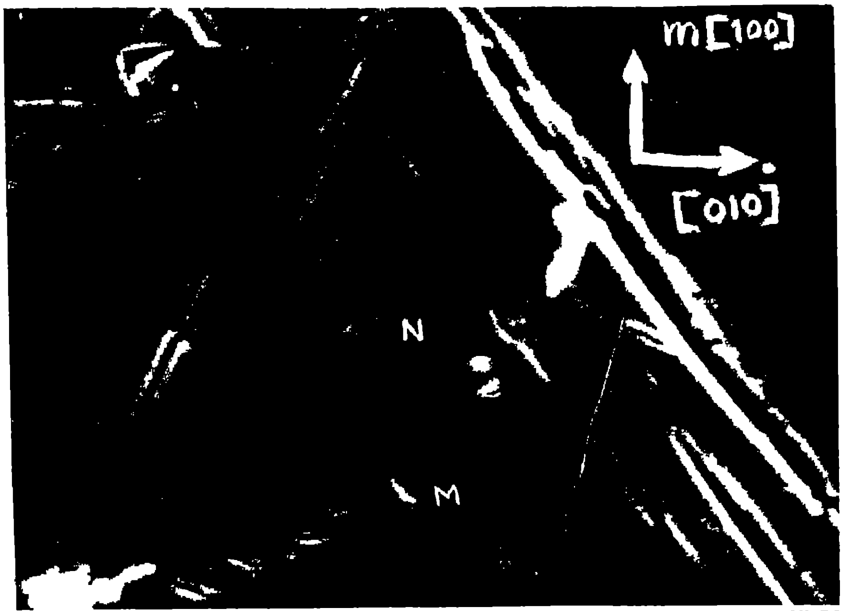

(6)

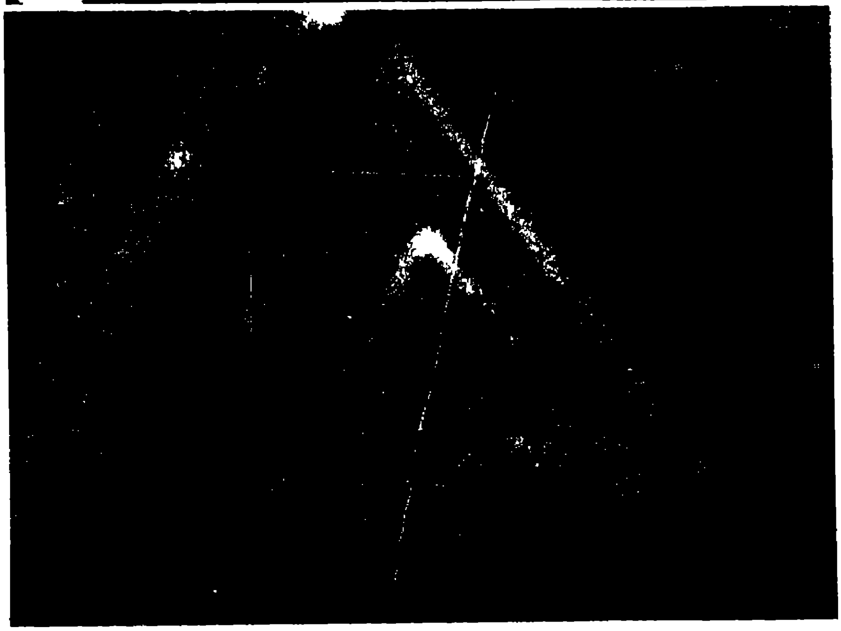

Figures 5 and 6. SEM photograph **5.** revealing an irregular array of etch pits (× 2000) **6.** of the magnified region of figure 5 (× 7500).

not clear. Hence the pit N is observed at higher magnification as shown in figure 6. It is interesting to note that pit N also resembles a clockwise spiral having a white contour.

4. Discussion

The shape of the etch pits on (002) cleavage face of Li_2CO_3 single crystal has been observed to be triangular, irrespective of the etchants used (Palaniswamy *et al* 1982). Li_2CO_3 is monoclinic and has the space group $C2/c$ which is a part of class $2/m$. The (002) cleavage in $2/m$ is mono-symmetrical, which means it contains one mirror plane. Etch pits on (002) plane must show mirror symmetry. The mirror symmetry axis m [100] is perpendicular to the base of the etch pits, which happens to be the two-fold axis [010] as shown in figure 5.

On successive etching, the isolated pits enlarge in size retaining their shape, suggesting dislocation of etch pits. This has been supported by the exact correspondence of isolated etch pits on matched faces. That the irregular arrays remain shallow without enlarging reasonably in depth on successive etching and reveal correspondence on etched match faces suggest that these are also dislocation arrays of a different nature than those of isolated dislocation pits. One of the pits marked Z in the irregular array in figure 3 indicates that this dislocation may be of screw type, anticlockwise. That the pits forming the irregular array etch differently than those of isolated pits enlarging in size, may be attributed to the association of screw dislocations in the array of pits.

That the pits (marked M and N in figure 5) constituting the irregular array resemble spirals support the conjecture that they reveal screw dislocations in the crystal (Patel and Raju 1966).

These irregular arrays of etch pits may represent general grain boundaries having both edge and screw dislocations, which might have been formed due to the impingement of misoriented guest crystals causing stresses in the growing crystal. This agrees with the findings of Sunagawa (1968) on hematite and Raju (1980) on gypsum.

5. Conclusions

That the spiral etch pits observed are along irregular arrays and these irregular arrays (of etch pits) have correspondence on match faces indicate that they may reveal tilt or twist boundaries consisting of edge and screw dislocations in the crystal. Therefore it is concluded that the spiral etch pits forming the components of irregular arrays represent the sites of screw dislocations on (002) basal cleavages of lithium carbonate single crystal.

Acknowledgements

The authors thank Dr N Ramanathan, Director, Central Leather Research Institute, Adyar, Madras for permission to use the scanning electron microscope and to Dr A Rajaram for the assistance in SEM studies. One of the authors (KSR) thanks Dr E Pippel and Dr W Neumann for valuable discussions. MP thanks Anna University for the award of a fellowship.

References

Buckley H E 1958 *Crystal growth* (New York: John Wiley) 4 edn p. 321
Borle W N and Bagai R K 1976 *J. Cryst. Growth* **36** 259
Connick W and May F G J 1969 *J. Cryst. Growth* **5** 65
Gilman J J and Johnston W G 1956 *J. Appl. Phys.* **27** 1018
Hari Babu V and Bansigir K G 1968 *J. Cryst. Growth* **2** 9
Patel A R and Tolansky S 1957 *Proc. Roy. Soc.* (*London*) **A243** 41
Patel A R and Goswami K N 1964 *Acta Crystallogr.* **17** 569
Patel A R and Raju K S 1966 *Acta Crystallogr.* **21** 190
Patel A R and Raju K S 1967 *Acta Crystallogr.* **23** 217
Patel A R and Singh R P 1968 *J. Cryst. Growth* **2** 373
Palaniswamy M, Gnanam F D, Ramasamy P and Laddha G S 1982 *Cryst. Res. Technol.* **17** 911
Raju K S 1980 *Bull. Mater. Sci.* **2** 139
Raju K S 1981 *J. Mater. Sci.* **16** 2512
Sunagawa I 1968 *Mineral Mag.* **36** 625
Wehner G K 1958 *J. Appl. Phys.* **29** 217

Bull. Mater. Sci., Vol. 6, No. 6, December 1984, pp. 997–1000. © Printed in India.

Etch pit observations on the habit faces of gel grown nickel molybdate crystals

K V KURIEN* and M A ITTYACHEN

Department of Physics, University of Kerala, Kariavattom 695 581, Trivandrum, India
*Department of Physics, Mar Thoma College, Tiruvalla 689 105, India

MS received 30 April 1983; revised 30 April 1984

Abstract. The results obtained from etching experiments on the habit faces of $NiMoO_4 \cdot xH_2O$ are described. Dilute solutions of chemical reagents such as HNO_3, CH_3COOH, NaOH, KOH are found to be the best etchants for revealing dislocation etch pits. The shape and nature of the etch pits are also described.

Keywords. Etch pits; dislocation; habit faces; gel grown; $NiMoO_4 \cdot xH_2O$ crystals

1. Introduction

Etching is a well-known technique for dislocation studies in crystals. It is the result of variation in surface reaction or dissolution rates influenced by crystallographic orientation effects, lattice imperfection and chemical combination. Etch patterns observed on crystal faces play an important role in obtaining information on the history of growth of crystals, as their etch patterns are intimately related to the growth phenomena. The first attempt to provide an explanation for the process of etching is due to Goldschmidt (1904). A satisfactory explanation regarding the origin of etch pits and their development has been given on the concept of lattice defect known as dislocation. A dislocation etch is an attractive means of studying the early stages of deformation in crystalline solids. This has led to the discovery of a number of etchants.

In the present work, an attempt has been made to investigate the nature and shape of etch pits by etching the (001) and (011) surfaces of gel-grown nickel molybdate crystals (Kurien and Ittyachen 1980). Well-shaped square and octagonal platelets (average size $3 \times 2 \times 0.3$ mm^3) have been selected for this purpose.

2. Experimental and results

As there is no previous study of etching behaviour of these crystals, a number of prospective etchants were tried to reveal the dislocation sites and dislocation density. Water and quite a few acids were found to etch the cleavage faces of their flakes of nickel molybdate crystals. Nitric acid, acetic acid, sodium hydroxide, potassium hydroxide and a mixture of nitric acid and hydrochloric acid are suitable etchants for their action on the (001) face. Water has some polishing action on the surface. Sulphuric and hydroflouric acids were unsuitable for etching the faces of gel-grown nickel molybdate

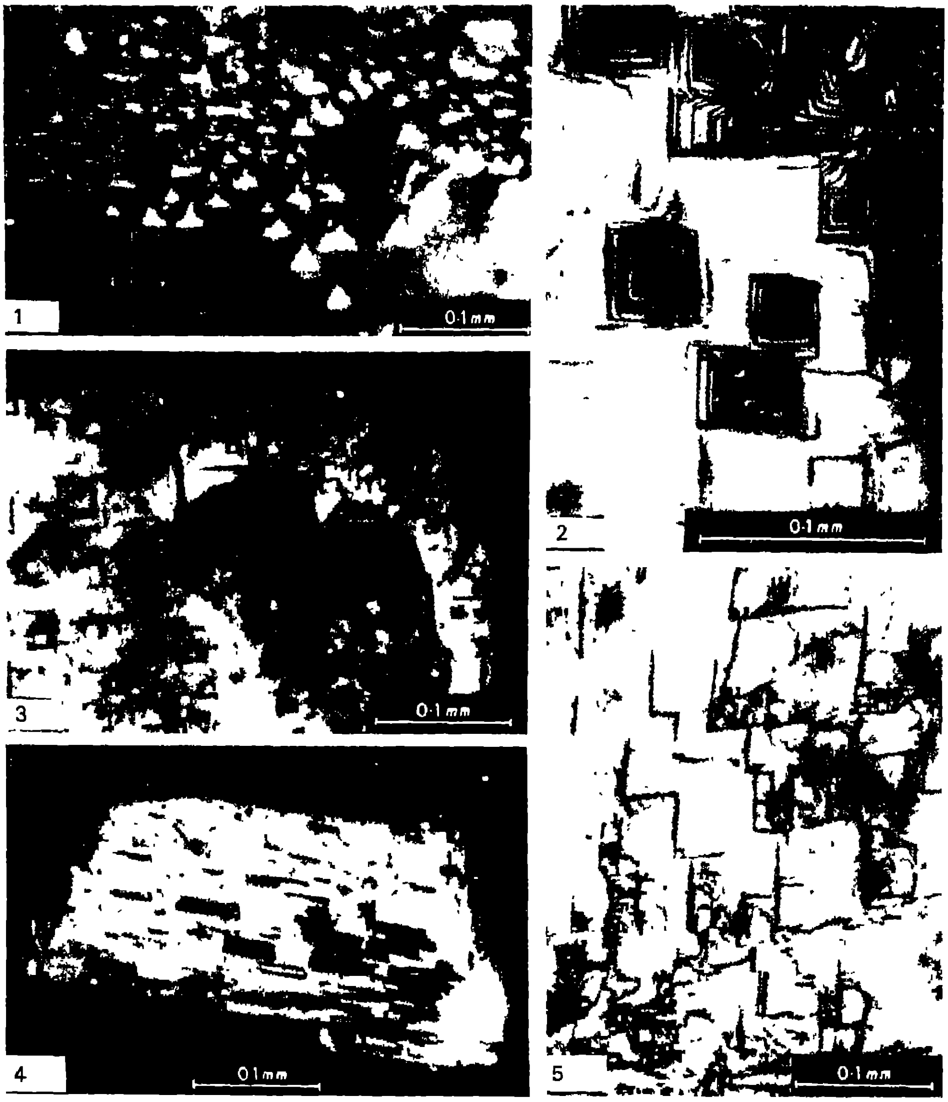

Figures 1–5. **1.** Square type etch pits on the (001) face when etched in nitric acid. **2.** Well-defined square and rectangular etch pits with terrace when etched in acetic acid. **3.** Square-shaped pits with two sides well developed when etched in sodium hydroxide. **4.** Rectangular pits on the (001) face when etched in nitric acid. **5.** Square-shaped pits with two sides well-developed when etched in potassium hydroxide.

crystals. Increase in concentration or temperature resulted in the increase of surface dissolution without forming the visible pits tabulated in table 1. A large number of clusters of pits were formed first on the surfaces of thin flake-like crystals in the initial stages of etching. However, on repeated etching most of the pits became flat-bottomed, enlarged and eventually vanished. But some of the pits remained nearly constant during successive etching. A large number of pits were symmetrical pits, composed of closed rectangular and square terraces. Both nitric and acetic acids could yield identical etch

Table 1. Experimental conditions for etch pit formation on the (001) and (011) faces of gel grown nickel molybdate crystals

Etchant	Concentration	Time (min)	Observation
HCl	1:100	1	Rapid attack
	1:150		
	1:200	1	Few perfect pits were observed on the (001) and (011) faces
HF	1:150	1	Rapid attack
	1:200		
	1:400		
HNO_3	1:200	1–2	Well-defined square and rectangular pits were obtained on the (001) (figure 1) and (011) (figure 4) faces
	1:300		
	1:400		
CH_3COOH	1:200	1	Clustered etch pits of smaller size
	1:100	2	Well-defined square and rectangular pits with terrace (figure 2)
	1:150		
NaOH	0·05–0·1 N	2	Square-shaped pits with two sides well developed (figure 5)
HF + HNO_3	1:300	1	Destructive reaction: no etch pit formation

The experiment was conducted at room temperature.

pits. But in the case of sodium and potassium hydroxides only two sides of the square pits were well-developed. The sides of the square pits in all cases were parallel to the ⟨100⟩ direction. The average etch pit density was of the order of 10^4–10^5 cm^{-2}. In isolated crystals, the dislocation density was between 10^2 and 10^3 cm^{-2}.

3. Discussion

Studies on different types of etch pits and their densities give useful information regarding the nature of the defects, impurity content and the history of growth of crystals. Etch pits may be produced due to several reasons. In the present case, initially a clustering of etch pits is formed. They are well-defined, very small point-bottomed, rectangular square pits. However, on repeated etching most of the pits became flat-bottomed and eventually vanished. The origin of flat-bottomed pits is due to the localised defects such as microprecipitates, vacancies etc. (Michael *et al* 1970). Evidently in this case etch pits are not being formed at the dislocation sites but at the impurity sites. The large flat-bottomed pits were assumed to be due to edge dislocations produced during the later stages of crystal growth (Johnston 1962). The edge and screw dislocations give rise to two distinct types of pits. The etch pits due to edge dislocations were generally small compared to those due to screw dislocation (Amelinckx 1976). The terrace nature of pits is a common phenomenon in the case of calcite, mica, etc. (Patel *et al* 1963). The terrace nature of pits obtained in this study can be explained by postulating the precipitation of some sort of impurities along the dislocation line which inhibits the action of the etchant depending on the nature, density and location of the impurities. The impurities might be evenly spaced along the dislocation line which result into pits having various types of terraces. The number of times the inhibition action is operated can be judged by the number of terraces—obtained when the inhibition action lasts longer, widely terraced pits are produced.

4. Conclusion

The high density etch pits obtained in the initial stages of etching suggests that the crystals have a high density of impurities adsorbed on the surfaces in the later stages of growth.

References

Amelinckx S and Dekeyser N 1952 *Naturwissenschaften* 39 448
Amelinckx S 1976 *J. Appl. Phys.* **31** 1359
Goldschmidt V 1904 *Z. Kristallogr.* **38** 273
Gilman J J and Johnston W G 1956 *J. Appl. Phys.* **27** 1018
Horn F H and Gevers W 1952 *Philos. Mag.* **43** 1210
Johnston W G 1962 *Progress in ceramic science* (ed.) J E Burke (New York: Pergamon) Vol 2
Kurien K V and Ittyachen M A 1980 *Krist. Tech.* **15** 7, 763
Michael F, Ehman G R, Jindal J W, Faust Jr and William B White 1970 *J. Appl. Phys.* **41** 7
Patel A R and Goswami S 1963 *Physica* **29** 33
Patel A R and Ramanathan S 1963 *Amer. Miner.* **48** 691

Bull. Mater. Sci., Vol. 6, No. 6, December 1984, pp. 1001–1007. © Printed in India.

Elastic properties of As-Sb-Se glasses

A GIRIDHAR, SUDHA MAHADEVAN and A K SINGH
Materials Science Division, National Aeronautical Laboratory, Bangalore 560017, India

MS received 27 June 1983; revised 23 August 1983

Abstract. Results of measurement of elastic modulii on As-Sb-Se glasses are reported and their composition dependence discussed. The Young's and the shear modulii lie in the range of 170–210 and 65–80 kb respectively. These values are typical of chalcogenide glasses. For (As, Sb)$_{40}$Se$_{60}$ glasses, the modulii increase monotonically with increasing Sb$_2$Se$_3$ content. The observed composition dependence of the modulii for the As$_x$Sb$_{15}$Se$_{85-x}$ glasses is examined in terms of the chemically ordered structural units in the glasses.

Keywords. As-Sb-Se glasses; elastic properties; CONM model.

1. Introduction

The results of measurement of glass transition temperature (T_g), electrical conductivity and density (d) on glasses of the As-Sb-Se system were reported earlier (Giridhar and Sudha Mahadevan 1982). The study covered two groups of glasses: (i) those whose composition could be represented by (As, Sb)$_{40}$Se$_{60}$ and (ii) those whose composition could be represented by As$_x$Sb$_{15}$Se$_{85-x}$. The (As, Sb)$_{40}$Se$_{60}$ glasses fall along the (As$_2$Se$_3$) (Sb$_2$Se$_3$) pseudobinary section and represent the so-called 'stoichiometric' compositions of the As-Sb-Se system. The T_g, electrical conductivity and d of these glasses showed a monotonic increase with increasing Sb$_2$Se$_3$ content. In the As$_x$Sb$_{15}$Se$_{85-x}$ glasses, with the stoichiometric As$_{25}$Sb$_{15}$Se$_{60}$ composition as reference, glasses with more than 60 at. % of Se were referred to as Se-rich glasses and those with less than 60 at. % of Se as As-rich glasses of this family. The As$_x$Se$_{100-x}$ and Ge$_x$Sb$_{15}$Se$_{85-x}$ glasses show an extremum in T_g and d at the respective stoichiometric compositions (Myers and Felty 1967; Mohan *et al* 1981; Narasimham *et al* 1981; Giridhar *et al* 1981). The composition dependence of T_g and d of the As$_x$ Sb$_{15}$ Se$_{85-x}$ glasses exhibit an interesting feature, namely, that the T_g and d of the As-rich glasses of this family are higher than those of the As$_{25}$Sb$_{15}$Se$_{60}$ composition (Giridhar and Sudha Mahadevan 1982).

The results of measurements of elastic properties on eight glass compositions are reported in this paper. Four of these compositions can be represented by (As, Sb)$_{40}$Se$_{60}$, while the other four belong to the As$_x$Sb$_{15}$Se$_{85-x}$ family.

2. Experimental

The cylindrical samples (about 12 mm in diameter and 6 mm in length) suitable for ultrasonic sound velocity measurements were obtained by the following procedure.

The elemental components (5N purity, from Koch Light Co.) in appropriate proportions were sealed in a quartz ampoule (12 mm in diameter) under a vacuum of 10^{-3} torr. The contents of the ampoule were melted in a rotary furnace at about 950°C for 24 hr. The melt was then cooled to 800°C and quenched in water at 90°C. Care was taken to see that the ampoule stayed in a vertical position during the quenching operation. Quenching in hot water rather than in cold water was found essential to prevent any cracking or shattering of the cylindrical sample during further processing. The ampoule was then introduced into a tubular furnace where the glass was annealed at a temperature of about 5° higher than T_g for 1 hr and then brought to room temperature by slow cooling. Just before breaking open, the ampoule was chilled in an ice bath for 15 min to facilitate retrieval of the specimen from the ampoule. The faces of the cylindrical samples thus obtained were rendered flat and parallel (the wedge angle being better than 0·2 sec) using a lapping-polishing jig specially designed and fabricated for this purpose. Using Salol (phenyl salicilate) as the bonding material the longitudinal and transverse velocities in the samples were measured (at 25°C) by using 10 MHz X-cut and Y-cut transducers, by McSkimin's pulse superposition technique (McSkimin 1961; McSkimin and Andreatch 1962). As already indicated (Sudha Mahadevan *et al* 1983), an ultrasonic pulse echo interferometer (supplied by Systems Dimensions, Bangalore, model SDUI-003) in conjunction with a 50 MHz Philips oscilloscope and frequency/time interval counter (accuracy of one nsec) was used for this purpose. The accuracy of velocity measurements limited mainly by thickness measurements (for which a Mitutoyo height master transfer stand combination was used), was 0·03 %; A spread of about 1·5% was observed in the velocities in different specimens of the same composition. The typical quality of the echo pattern obtained in our set up is shown in figures 1–3. A train of 10–12 echoes could be obtained in most cases (figure 1); this is because of the high parallelism of the faces. The measurement of the delay time was facilitated by the good resolution obtained in the amplitude of the expanded echoes (figures 2 and 3).

3. Results and discussion

3.1 *(As, Sb)$_{40}$Se$_{60}$ glasses*

The results for these glasses are summarised in figure 4 and table 1. The shear (*G*), the Young's (*E*), the bulk (*K*) modulii and the Poisson's ratio (σ) of $(As, Sb)_{40}Se_{60}$ glasses increase monotonically with increasing Sb_2Se_3 content (figure 4). Extrapolation of *G*, *E*, *K* and σ values (figure 4) of these glasses to zero Sb_2Se_3 content, which corresponds to As_2Se_3, gives the values of modulii which agree well with one set of reported values for As_2Se_3 (Thompson and Bailey 1978). The other values (Hilton and Hayes 1975; Soga and Kunugi 1973) fall slightly away from the extrapolated data. Also shown in figure 4 is the variation of the mean atomic volume with composition. For isostructural crystalline compounds, the bulk modulus increases with decrease in volume (Anderson and Nafe 1965). However, in our discussion (Sudha Mahadevan *et al* 1983) of the variation of *K* with mean atomic volume of several chalcogenide glass systems, namely Ge-Sb-Se, Ge-As-Se, Ge-Sb-S and Ge-Se, it was seen that the mean atomic volume is not the only factor determining the bulk modulus of these glasses. Besides volume, other factors such as the nature of the type of bonding could also be effective in

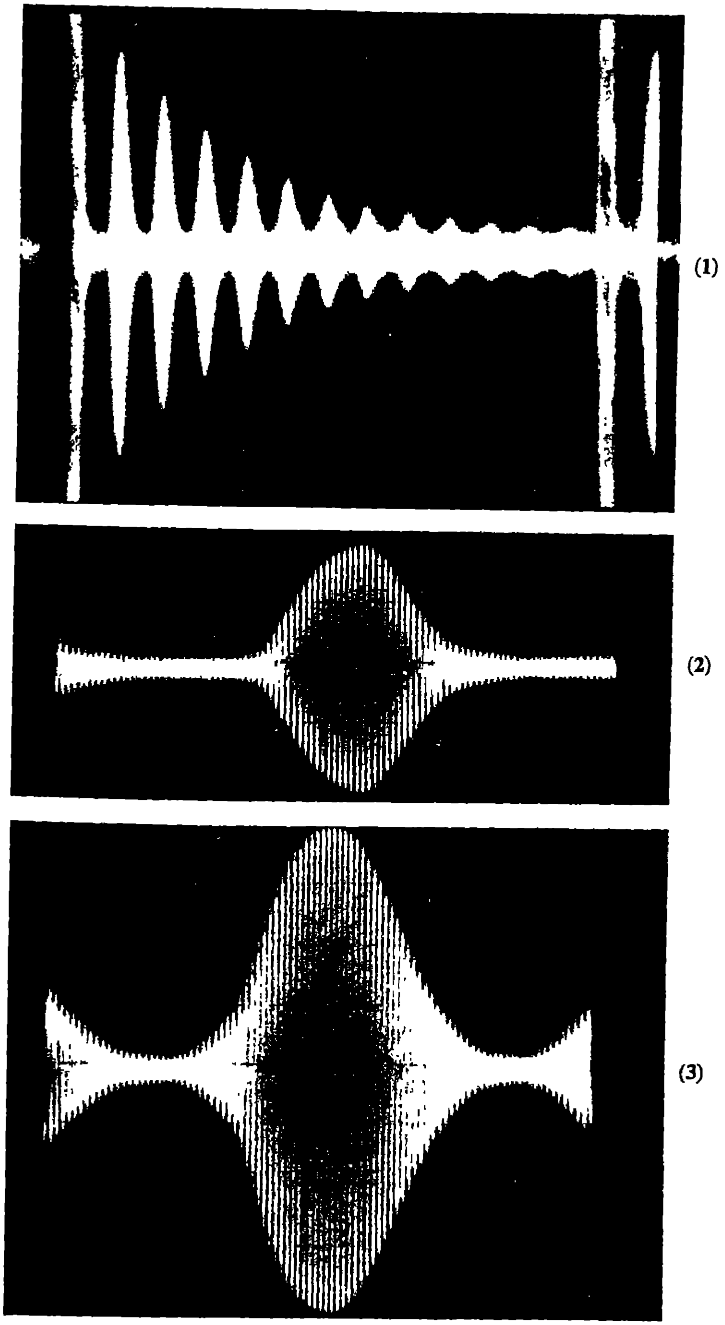

Figures 1–3 1. Typical exponential echo train for a $\mathrm{As_{10}Sb_{15}Se_{75}}$ sample for longitudinal waves. 2. Expanded echo wave form for pulse superposition for $p = 2$, minimum amplitude. 3. Expanded echo wave form for pulse superposition for $p = 2$, maximum amplitude.

determining the bulk modulus. In $(As, Sb)_{40}Se_{60}$ glasses, (figure 4) the bulk modulus increases with increasing Sb_2Se_3 content while the corresponding volume has also increased. Therefore, the type of bonding, rather than the volume has greater influence in determining the bulk modulus of these glasses.

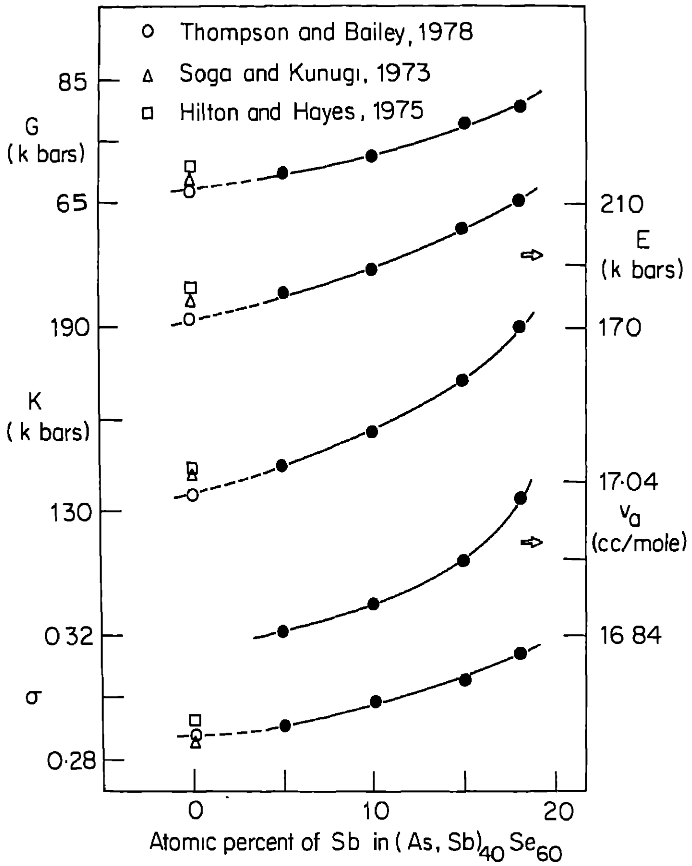

Figure 4. Variation of elastic modulii and mean atomic volume for $(As, Sb)_{40}Se_{60}$ glasses shown as a function of Sb content. Data for As_2Se_3 are from literature.

Table 1. Elastic data for As-Sb-Se glasses

Composition (As : Sb : Se)	d(g/cc)	Long. vel. C_l (m/sec)	Trans. vel. C_t (m/sec.)	Shear mod. G (kbars)	Young's mod. E (kbars)	Bulk mod. K (kbars)	Poisson's ratio σ
35:15:50	4·990	2302	1253	78·34	202·05	159·97	0·2895
30:15:55	4·983	2294	1245	77·24	199·46	159·21	0·2912
25:15:60	4·980	2358	1248	77·56	202·30	173·26	0·3054
20:15:65	4·920	2243	1208	71·80	186·05	151·78	0·2957
10:15:75	4·850	2121	1170	66·39	170·14	129·66	0·2813
35: 5:60	4·730	2245	1218	70·17	181·24	144·80	0·2914
30:10:60	4·860	2281	1222	72·57	188·50	156·07	0·2987
22:18:60	5·040	2429	1263	80·40	211·40	190·14	0·3147

3.2 $As_xSb_{15}Se_{85-x}$ glasses

The data for $As_xSb_{15}Se_{85-x}$ glasses are shown in figure 5 and table 1. With the stoichiometric composition $As_{25}Sb_{15}Se_{60}$ as reference, the G and E of As-rich glasses are seen to be essentially constant while those of the Se-rich glasses show a decrease with increasing Se-content. The bulk modulus exhibits a maximum for the stoichiometric composition (figure 5). Also shown in figure 5 is the variation of the mean atomic volume with composition. Based on the decrease of the mean atomic volume with increasing As content in the As-rich glasses, an increase of bulk modulus is expected, while it is seen that the bulk modulii of these glasses have decreased (figure 5).

In Ge-Sb-S and Ge-Sb-Se systems (Hayes *et al* 1974; Hilton and Hayes 1975; Sudha Mahadevan *et al* 1983) the Poisson's ratio (σ) increases with increasing chalcogen content. As σ denotes the ratio of transverse to longitudinal strains which arise from a single tensile stress, its increase with increasing chalcogen content has been attributed to a change in glass structure from an essentially network to a chain-like form (Hilton and Hayes 1975). However, in the $As_xSb_{15}Se_{85-x}$ glasses studied presently, σ exhibits a maximum for the stoichiometric composition and there is a decrease of σ for the Se-rich glasses in contrast to the expected increase.

The chemically-ordered network model (CONM) wherein the maximum number of

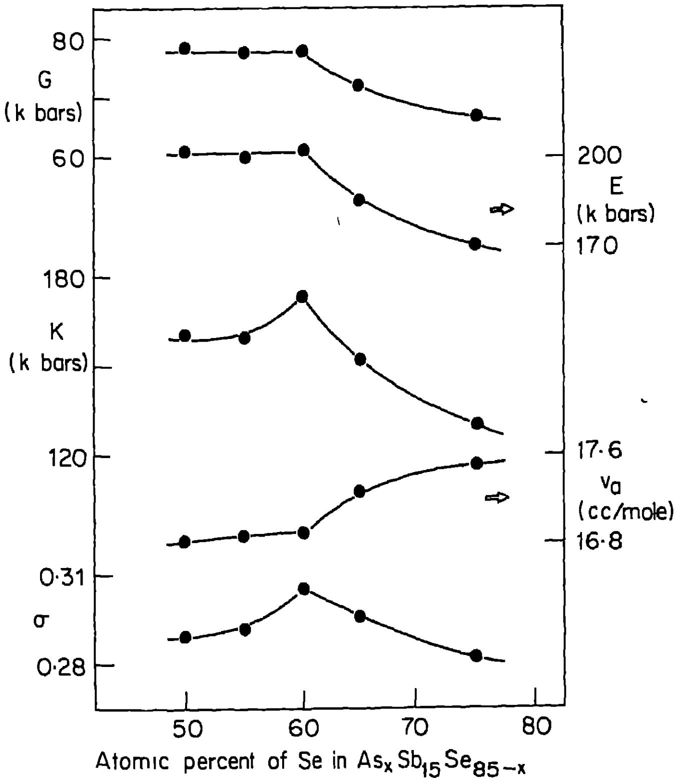

Figure 5. Variation of elastic modulii and mean atomic volume with composition for $As_xSb_{15}Se_{85-x}$ glasses.

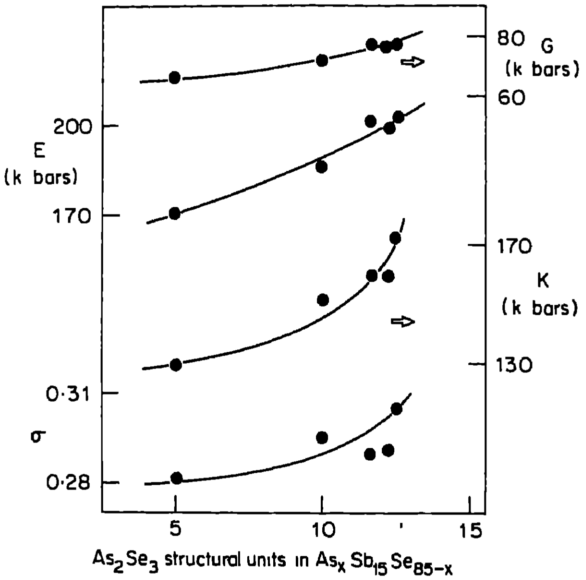

Figure 6. Dependence of elastic modulii on the As_2Se_3 structural units in As_x $Sb_{15}Se_{85-}$ glasses.

heteropolar bonds are formed first and the remaining part of the valence requirement is met with by homopolar bonding at random accounted satisfactorily for the composition dependence of the density of these glasses (Giridhar and Sudha Mahadevan 1982). For a correlation of the elastic properties with composition, the results were examined using the CONM model. A close study of the glass compositions in view of the results of figure 5 indicates the importance of As_2Se_3 content (*i.e.* As-Se bonds) in determining the elastic properties of these glasses, as the observed features in the composition dependence of K and σ can be linked to the As_2Se_3 content in these glasses. It can be seen (figure 6) that the moduli do show in general an increase with increasing As_2Se_3 content in the glasses. Though scatter in the points is seen in the dependence of the modulii on the As_2Se_3 content (figure 6), the increase in these quantities is obvious.

4. Conclusions

Elastic modulii of $(As, Sb)_{40}Se_{60}$ glasses decrease monotonically with decreasing As_2 Se_3 content in the glasses.

In the $As_xSb_{15}Se_{85-x}$ glasses, with the $As_{25}Sb_{15}Se_{60}$ glass as reference, the shear and Young's modulus of As-rich glasses do not vary much with the composition, while those of the Se-rich glasses decrease with increasing Se content. The bulk modulus and the Poisson's ratio of these glasses exhibit a maximum at the stoichiometric composition. An examination of the results indicates that the elastic properties of these glasses are sensitive to the As_2Se_3 content in these glasses.

References

Anderson O L and Nafe J E 1965 *J. Geophys. Res.* **70** 3951

Giridhar A, Narasimham P S L and Sudha Mahadevan 1981 *J. Non-Cryst. Solids* **43** 29

Giridhar A and Sudha Mahadevan 1982 *J. Non-Cryst. Solids* **51** 305

Hayes D J, Rechtin M D and Hilton A R 1974 *Ultrasonics Symp. Proc.* p. 502 (ed.) De Klerk, Institution of Electrical and Electronics Engineers, New York

Hilton A R and Hayes D J 1975 *J. Non-Cryst. Solids* **17** 339

McSkimin H J 1961 *J. Acoust. Soc. Am.* **33** 12

McSkimin H J and Andreatch P 1962 *J. Acoust. Soc. Am.* **34** 609

Mohan R, Panchapakesan T S and Rao K J 1981 *Bull. Mater. Sci.* **3** 29

Myers M B and Felty E J 1967 *Mater. Res. Bull.* **2** 535

Narasimham P S L, Giridhar A and Sudha Mahadevan 1981 *J. Non-Cryst. Solids* **43** 365

Soga N and Kunugi M 1973 *J. Phys. Chem. Solids* **34** 2143

Sudha Mahadevan, Giridhar A and Singh A K 1983 *J. Non-Cryst. Solids* **57** 423

Thompson J C and Bailey K E 1978 *J. Non-Cryst. Solids* **27** 161

Bull. Mater. Sci., Vol. 6, No. 6, December 1984, pp. 1009–1012. © Printed in India.

DC electrical conductivity of Na_2O-ZnO-B_2O_3 glass system

R V ANAVEKAR, N DEVARAJ and J RAMAKRISHNA*

Department of Physics, Bangalore University, Bangalore 560001, India
*Department of Physics, Indian Institute of Science, Bangalore 560012, India

MS received 12 December 1983

Abstract. The d.c. electrical conductivity of Na_2O-ZnO-B_2O_3 glass system has been measured as a function of temperature in the range of 350–600°K. The conductivity data show that the activation energy of Na^+ ions is dependent on ZnO concentration. The results have been discussed in the light of the cluster model of glasses.

Keywords. Na_2O-ZnO-B_2O_3 glass; electrical conductivity; density; activation energy.

1. Introduction

It is well known that glasses containing alkali ions are essentially solid cationic electrolytes, the current being carried by relatively mobile alkali ions. The motion of alkali ions in glasses is important, not only because of its relation to electrical conductivity, but also to chemical durability and to ion exchange kinetics. Similar work has been earlier reported on binary silicate and binary borate glasses. Some studies on borate glasses containing two different alkali oxides and alkali-alkaline earth oxides have also been reported (Israd 1969; Erzukyan 1969; Day 1976; Sakka *et al* 1979; Mutusita *et al* 1980). In the present work we report the d.c. electrical conductivity of sodium borate glasses with different concentrations of ZnO. The behaviour of activation energy of Na^+ ions has been discussed on the basis of the cluster model of glasses (Rao and Rao 1982).

2. Experimental

Analytical grade chemicals were used to prepare glasses corresponding to their glass-forming region (Rawson 1967). Appropriate quantities of boric acid (H_3BO_3), sodium carbonate (Na_2CO_3) and zinc oxide (ZnO) were taken and melted in a crucible at 1100°C for about 2 hr. The melt was then poured on a brass-block and it was quickly pressed with a polished copper-block. The glasses formed were annealed at about 400°C for 2 hr. X-ray studies showed that the glasses were amorphous. Samples of dimensions ($\sim 20 \times 20 \times 2$ mm) suitable for the measurement of electrical conductivity were prepared by grinding and polishing (using rough powder) the two flat surfaces. Silver paint was applied to these flat surfaces to serve as electrodes.

Measurements were made with glasses of the compositions listed in table 1. To measure the resistance of the samples, a special sample holder was designed following Mahadevan *et al* (1977). The resistance of the samples was determined by measuring the

Table 1. Glass composition, density and activation energy (E_a).

Mol % composition			Density (gm/cm^3)	Activation energy (eV)	
Na_2O	ZnO	B_2O_5		(600–500) °K	(500–400) °K
10	5	85	2·04	0·77	—
10	10	80	2·49	0·97	0·15
10	15	75	2·60	0·95	0·17

current through the sample for an applied voltage (25 V); the voltage was briefly applied to avoid polarization. The temperature was measured with a chromel-alumel thermocouple placed very close to the sample. The d.c. electrical conductivity was measured as a function of temperature over the range 350–600°K. Density was also measured by the Archimedes method using benzene and the values are given in table 1.

3. Results and discussion

The variation of the d.c. electrical conductivity as a function of $1/T$ for three different compositions is shown in figure 1. The activation energies are calculated from the Arrhenius equation;

$$\sigma = \sigma_0 \exp\left(\frac{-E_a}{kT}\right)$$

where σ_0 is the pre-exponential factor, E_a is the activation energy for conduction and k is the Boltzmann constant. The variation of E_a as a function of ZnO concentration is shown in figure 2. The values of activation energy obtained are shown in table 1. The conductivity behaviour in figure 1 shows that the glass with 5 mol % ZnO has a single activation barrier and also has a higher conductivity, while the glass with 10 and 15 mol % ZnO has two conductivity regions and lower overall conductivity. In order to understand the behaviour of $\ln \sigma$ in figure 1, we note the following features about borate glasses.

In borate glasses the principal structural elements present are boroxol, tetraborate and diborate groups. The diborate groups get converted into triborate and pentaborate units. In the glasses investigated here the extent of any such borate grouping which consist of tetrahedral borons depends upon the total quantity of added oxides ($Na_2O + ZnO$). In order to investigate the role of Zn^{2+} ion in these glasses, we note that the e/r^+ ratio (2·7) is quite high. It is likely that it acts as a network former, particularly in low Zn^{2+} concentration. Such Zn^{2+} positions in the network also help in cross-linking the borate chains. Zn^{2+} ions in such situations can modify the diborate groups into more open rings without affecting the extent of tetrahedral borons (Selvaraj and Rao 1983). However at higher concentrations Zn^{2+} ions act as network modifiers and may ultimately lead to phase separation. In glasses containing 5 mol % ZnO, therefore, $\ln \sigma$ variation as a function of $1/T$ is linear. Addition of 5 mol % ZnO is unlikely to cause any phase separation. The activation energy of Na^+ ions (0·77 eV) may be compared with that of (0·60 eV) 10 mol % Na_2O-90 mol % B_2O_3 glass (Chakravorty and Chakraborti 1980). This may perhaps reflect the fact that incorporation of Zn^{2+}

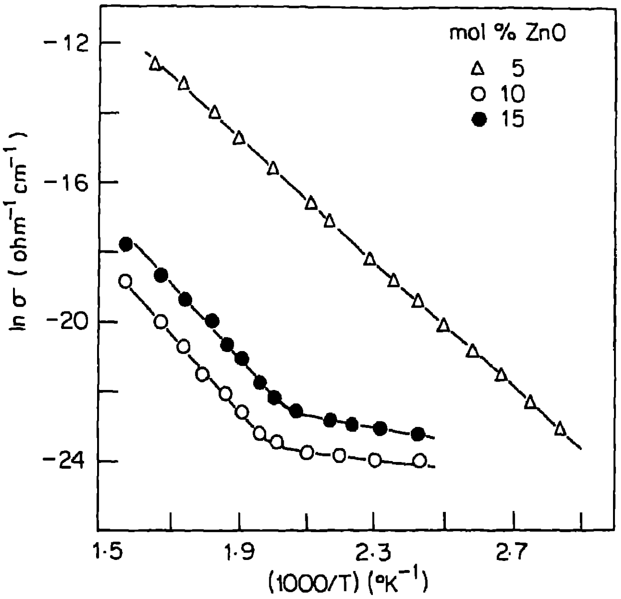

Figure 1. Variation of d.c. conductivity with temperature.

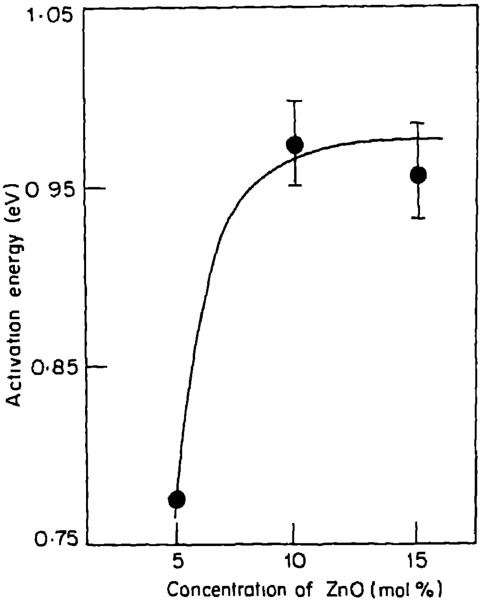

Figure 2. Variation of activation energy with concentration of ZnO.

into cross-linking positions increases the cohesion and density, thereby increasing the activation barrier for migration of Na^+ ions. In samples with 10 mol% ZnO and 15 mol% ZnO there appears to be two regions of conductivity (figure 1) characterized by two values of activation energy (E_a). This possibly indicates the presence of two distinct regions which act as precursors to phase separations. We feel that the two phases correspond to oxide-poor and oxide-rich regions (oxide representing the total quantity of Na_2O and ZnO). The oxide-poor region can be expected to be less dense with lower E_a and lower conductivity (low concentration of charge carriers and perhaps even low mobility). The oxide-rich region corresponds to high E_a and high conductivity. The charge carriers being primarily Na^+ ions, one can see that the conductivity is slightly lower for lower effective concentration of Na^+ ions. The activation barriers for both glasses (10 mol% and 15 mol% ZnO) are virtually constant (figure 2) which should be the case if conduction is mainly by the oxide-rich region and hence we find that the results support a two-region model for these glasses.

The two-region model is essentially a cluster model recently described by Rao and Rao (1982). The more ordered cluster region is likely to be an oxide-rich region while the oxide-poor region corresponds to the tissue (less order) region. Indeed AgI-Ag_2O-MoO_3 glasses (Senapati *et al*, private communication) also exhibit such two-region conductivity behaviour in accordance with the cluster model of glasses. In 5 mol% ZnO glass, the regions are not sufficiently differentiated to exhibit two-region conductivity at high temperatures; it is likely to be seen in low temperature measurements.

Acknowledgements

The authors (RVA and ND) express their thanks to Prof. P Paramasivaiah for his interest and encouragement and to Prof. K J Rao of IISc., Bangalore for many useful discussions.

References

Chakravorty D and Chakraborti S 1980 *J. Non-Cryst. Solids* **38 and 39** 295
Day D E 1976 *J. Non-Cryst. Solids* **21** 343
Erzukyan E 1969 *Arm. Khim. Zh.* **22** 109
Israd J O 1969 *J. Non-Cryst. Solids* **1** 235
Mahadevan S, Giridhar A and Rao K J 1977 *J. Phys.* **C10** 4499
Mutusita K, Takayama S and Sakka S 1980 *J. Non-Cryst. Solids* **40** 149
Rao K J and Rao C N R 1982 *Mater. Res. Bull.* **17** 1337
Rawson H 1967 *Inorganic glass-forming system* (New York: Academic Press) pp. 97
Sakka S, Mutusita K and Kimiya K 1979 *Phys. Chem. Glasses* **20** 25
Selvaraj U and Rao K J 1983 *Spectra. Chim. Acta.* (communicated)
Senapati H, Parthasarathi G and Rao K J (Private communication)

Bull. Mater. Sci., Vol. 6, No. 6, December 1984, pp. 1013–1018. © Printed in India.

Photon, electron and ion beam induced physical and optical densification in chalcogenide films

K L CHOPRA, L K MALHOTRA, K SOLOMON HARSHAVARDHAN and S RAJAGOPALAN

Department of Physics, Indian Institute of Technology, New Delhi 110016, India

MS received 10 October 1983

Abstract. Irradiation of 80° deposited Se-Ge films with band gap photons, 8 keV electrons and 50 keV He^+ ions produces, primarily irreversible red shift of the absorption edge and major changes in doping and electrochemical adsorption processes. These changes have been attributed predominantly to the radiation-induced thickness and hence volume contraction resulting due to the physical collapse of the low density columnar microstructure of the obliquely deposited films. The far IR and Urbach tail studies reveal an enhanced strength of electron-phonon coupling, in obliquely deposited films having a very porous columnar microstructure, compared to normally deposited films. It has been shown that this enhanced electron phonon coupling is conducive to large thickness contraction and associated changes. These changes have been used in reprographic and lithographic applications. A correlation has been established between the thickness contraction and lithographic parameters. The possibility of generating both positive and negative relief patterns on the same film by controlling the etching time has been demonstrated.

Keywords. Chalcogenide films; optical densification.

1. Introduction

Thin films of amorphous Se-Ge have been shown to behave as inorganic resists for visible, UV and deep UV light as well as electron beam and ion beam exposures and possess many advantages over the conventional organic resists currently in use (Yoshikawa *et al* 1976, 1977, 1980; Tai *et al* 1979; Balasubramanyam *et al* 1981; Venkatesan 1981). Using the light, electron beam or ion beam induced doping, or the darkening effects, both negative and positive type resists can be realized. Extensive studies carried out in our laboratory have shown that very large thickness and hence volume contraction (physical densification) takes place in $Se_{75}Ge_{25}$ films deposited at 80° incidence and exposed to photons, electrons or ions (Singh *et al* 1979, 1980a; Chopra *et al* 1981, 1982). The thickness contraction results in a much larger darkening in these films, compared to that obtained on exposure of films deposited at normal incidence. Thickness contraction occurs also when $Se_{75}Ge_{25}$ films overcoated with a very thin (100–200 Å) layer of a metal, such as Ag, are irradiated. This affects the doping of Ag into the chalcogenide film. Both the positive and negative resist behaviour of the obliquely deposited films are expected to be different from that of the normal incidence films and to be correlated with the thickness contraction resulting in these films on irradiation. In the present study, we have examined this correlation and utilized it to (a) yield a better lithographic sensitivity and contrast, both for the negative and positive resist behaviour, and (b) obtain both positive and negative resist characteristics in the same film.

2. Experimental

The experimental details for vacuum deposition of amorphous Se-Ge films are the same as reported earlier (Singh *et al* 1979; Rajagopalan *et al* 1979). The films were masked with a sharp edge and exposed to photons and ions. A 250 W mercury vapour lamp with an intensity of 30 mW/cm^2 was used for band gap photon illumination. Ion (He$^+$) irradiation was carried out with a 50 keV ion beam, using an ion accelerator (Sames J-15) in a vacuum of 10^{-7} torr, at room temperature. No ion sputtering or deformation of the film occurred during irradiation. The films were irradiated with an 8 keV, 0·2 μm diameter electron beam (PHI 590-A Super SAM instrument) for electron beam exposures. The thickness contraction was determined by measuring the thickness difference between the exposed/irradiated and the unexposed/unirradiated regions with the help of Talystep and then normalized against the original starting thickness of the as-deposited film.

For studying the negative resist behaviour, thin layers of Ag and Cu, (about 200 Å thick), were deposited on the as-prepared Se-Ge films by electrochemical adsorption (dipping in 0·025 M $AgNO_3$ 1 M $CuSO_4$ respectively) as well as by thermal evaporation. The resulting metal-Se-Ge films were then irradiated with photons, electrons and ions in the same way as described above and the thickness contraction was determined. The chemical dissolution rates of the films, with and without the metal overlayer, were determined by developing the films in 0·25 M NH_4OH solution.

3. Results and discussion

A comparison of the thickness contraction brought about by the irradiation of the 80°-deposited $Se_{75}Ge_{25}$ films by photons, electrons and ions is shown in figure 1. A

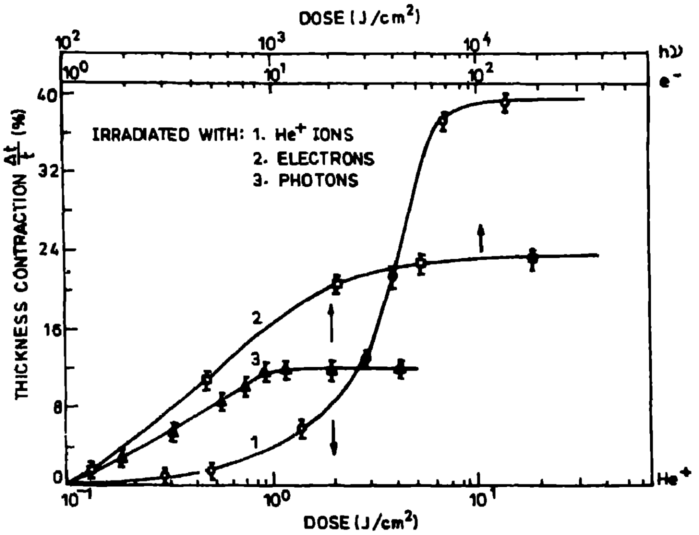

Figure 1. Thickness contraction as a function of incident flux for photon, electron and ion beam-irradiated 80°-$Se_{75}Ge_{25}$ films.

comparison of the incident energy reveals that ions are more effective in bringing about contraction followed by electrons and then photons. It may be pointed out that calculations of projected range and range straggling for He^+ ions in $Se_{75}Ge_{25}$ film show that there is no ion implantation in the film since the film thickness is smaller than the projected range.

The as-deposited Se-Ge films dissolve readily in an alkaline solution. The solubility is increased on irradiation. For $Se_{75}Ge_{25}$ films deposited at normal incidence, the increase in the solubility is rather small and hence not a very useful effect. The large thickness contraction occurring in 80° films leads to large microstructural changes which in turn increases the solubility difference between the irradiated (contracted) and unirradiated regions (Singh *et al* 1980b). The dissolution rates can be obtained from figure 2 which shows the normalized remaining thickness *vs* normalized etching time (*i.e.* the time taken to remove a certain thickness of an irradiated or a virgin film divided by the total time taken for the complete removal of the irradiated or the virgin film) for an as-deposited and irradiated (with ions, electrons and photons) $Se_{75}Ge_{25}$ film. Two kinds of etching selectivity are obtained as a function of the etching time. In the initial stages of etching, the unexposed regions etch faster than the exposed regions, *i.e.*, a negative resist behaviour is obtained even without the use of an overlayer metal. The etching behaviour changes to a positive resist type (exposed portion dissolving faster than the unexposed portion) after a certain etching time which is higher for photons and comparatively much lower for electrons and ions. If the etching is stopped when the exposed or irradiated portion has been completely etched off, the fractional final thickness remaining in the unirradiated or unexposed portion is about 88 % for the ion irradiated, 78 % for electron irradiated and 33 % for photon irradiated films. A comparison of this data with that reported by earlier workers reveals that a much higher remaining thickness is obtained by us (Yoshikawa *et al* 1976, 1977; Tai *et al* 1979;

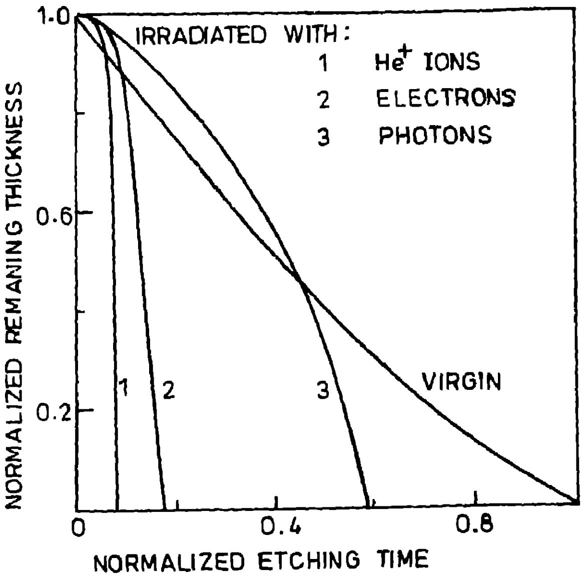

Figure 2. Normalized remaining thickness *vs* normalized etching time for a virgin and irradiated (with ions, electrons and photons) 80°-$Se_{75}Ge_{25}$ films.

Balasubramanyam *et al* 1981; Venkatesan 1981). Thus the value of 33% obtained in photon-irradiated films in the present case is much higher than 13% reported by Yoshikawa *et al* (1976), in normal incidence $Se_{75}Ge_{25}$ films obtained by sputtering. The difference can be attributed to the large thickness contraction obtained in the 80° films and absent in normal incidence films. Similarly, the large value of 88% in the ion-irradiated case obtained in the present study is much higher than 58% reported by Balasubramanyam *et al* (1981), on obliquely deposited films of the same material possibly due to the larger thickness contraction in our films resulting from the use of heavier He^+ ions. Thus, a control of etching time can permit both positive and negative relief patterns to be generated on the same film.

Figure 3 shows the normalized remaining thickness *vs* ion dosage corresponding to an etching time just sufficient for the complete removal of the exposed portion. As mentioned above; a very large selective etching of 88% has been obtained. A contrast (γ) of 4·5 and sensitivity (S) $\sim 10^{-4}$ C/cm^2 have been obtained. Though the sensitivity is lower than the conventional organic resists, the large selective etching and a reasonably good value of contrast make the films suitable for positive resist applications. Typical values of the lithographic parameters for positive resist applications for different radiations are listed in table 1.

Negative resist characteristics are obtained when the films with an overlayer of Ag or Cu are irradiated with ions, electrons or photons. Figure 3 shows our results on the negative resist characteristics for He^+ irradiated Se-Ge films with an overlayer of Ag. A sensitivity $\sim 1{\cdot}4 \times 10^{-5}$ C/cm^2 and a contrast of 8·3 have been obtained. The negative resist characteristics for different radiations obtained by this process are also listed in table 1. The high value of contrast should produce a high intrinsic resolution in these films for ion beam lithographic applications. Submicron lithographic patterns have been generated by us and other workers routinely (Balasubramanyam *et al* 1981; Venkatesan 1981; Chopra *et al* 1982).

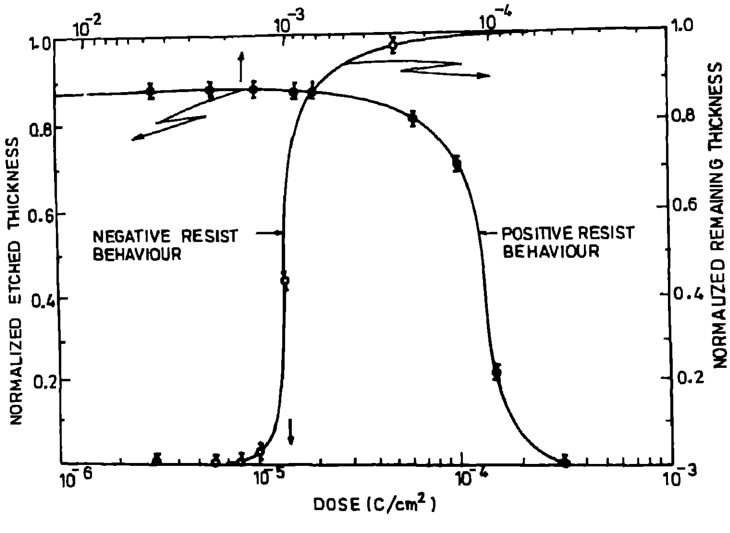

Figure 3. Positive and negative resist characteristics of 80°-$Se_{75}Ge_{25}$ films subjected to He^+ irradiation.

Table 1. Lithographic parameters (sensitivity, S, and contrast, γ) for different radiations for 80°-$\mathrm{Se}_{75}\mathrm{Ge}_{25}$ films.

Radiation	As-positive resist		As-negative resist	
	S	γ	S	γ
He$^+$ ions	$\sim 1{\cdot}2 \times 10^{-4}$ C/cm^2	4·5	$\sim 1{\cdot}6 \times 10^{-5}$ C/cm^2	8·3
Electrons	$\sim 8 \times 10^{-4}$ C/cm^2	4	$\sim 1 \times 10^{-4}$ C/cm^2	7·6
Band gap photons	$\sim 10^{20}$ photons/cm^2	1·7	$\sim 10^{19}$ photons/cm^2	3·5

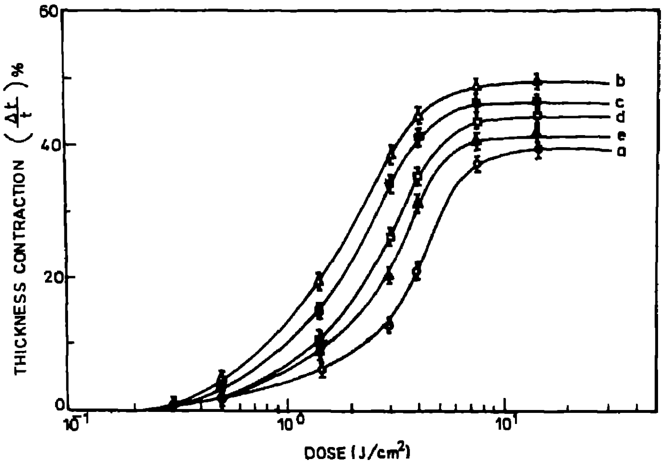

Figure 4. Thickness contraction as a function of ion dosage for: **a.** as-deposited, **b.** as-deposited with an overlayer of electrochemically adsorbed Ag, **c.** as-deposited with an overlayer of evaporated Ag, **d.** as-deposited with an overlayer of electrochemically adsorbed Cu, and **e.** as-deposited with an overlayer of evaporated Cu.

Our studies show that the thickness contraction plays an important rolè in the negative resist action in the obliquely deposited films. Figure 4 shows the thickness contraction as a function of ion dosage for: (a) as-deposited, (b) as-deposited with an overlayer of electrochemically adsorbed Ag, (c) as-deposited with an overlayer of evaporated Ag, (d) as-deposited with an overlayer of electrochemically adsorbed Cu, and (e) as-deposited with an overlayer of evaporated Cu. It is noteworthy that the thickness contraction is larger in a film having an overlayer of a metal than in one without an overlayer. The improved negative resist characteristics in obliquely deposited films is therefore a direct consequence of enhanced thickness contraction.

Acknowledgements

The authors are grateful to Mr A K Tyagi of RRC Kalpakkam, for ion irradiation and Miss M Rajeswari for assistance. The financial aid from the Electronics Commission, Government of India, is gratefully acknowledged.

References

Balasubramanyam K, Karapiperis L K, Lee C A and Ruoff A L 1981 *J. Vac. Sci. Technol.* **19** 1
Chopra K L, Harshavardhan K S, Rajagopalan S and Malhotra L K 1981 *Solid State Commun.* **40** 387
Chopra K L, Harshavardhan K S, Rajagopalan S and Malhotra L K 1982 *Appl. Phys. Lett.* **40** 428
Rajagopalan S, Singh B, Bhat P K, Pandya D K and Chopra K L 1979 *J. Appl. Phys.* **50** 1
Singh B, Rajagopalan S, Bhat P K, Pandya D K and Chopra K L 1979 *Solid State Commun.* **29** 167
Singh B, Rajagopalan S, Bhat P K, Pandya D K and Chopra K L 1980a *J. Non-Cryst. Solids* **35–36** 1053
Singh B, Rajagopalan S and Chopra K L 1980b *J. Appl. Phys.* **51** 1768
Tai K L, Sinclair W R, Vadimsky R G, Moran J M and Rand M J 1979 *J. Vac. Sci. Technol.* **16** 1977
Venkatesan T 1981 *J. Vac. Sci. Technol.* **19** 1368.
Yoshikawa A, Ochi O, Nagai H and Mizushima Y 1976 *Appl. Phys. Lett.* **29** 10
Yoshikawa A, Ochi O, Nagai H and Mizushima Y 1977 *Appl. Phys. Lett.* **31** 3
Yoshikawa A, Ochi O and Mizushima Y 1980 *Appl. Phys. Lett.* **36** 107

Bull. Mater. Sci., Vol. 6, No. 6, December 1984, pp. 1019–1027. © Printed in India.

Oxidation of thin films of tin at room temperature in hydrogen sulphide atmosphere

C I MUNEERA and V UNNIKRISHNAN NAYAR

Department of Physics, University of Kerala, Kariavattom, Trivandrum 695 581, India

Abstract. The oxidation of thin films of tin at room temperature in an atmosphere containing 10% H_2S and 90% air has been studied by measuring the changes in resistance of thin films. Morphological studies have also been carried out using optical and scanning electron microscopes. Reaction kinetics change from logarithmic law at ordinary atmospheres to a power law in the presence of H_2S. The basis of formation of sulphide along with the oxide is explained, the former growing on a lower layer and the latter on an upper layer.

Keywords. Oxidation; tin; hydrogen sulphide; thin films; resistance change.

1. Introduction

Hydrogen sulphide is a naturally occurring gas forming part of the sulphur-cycle (Minster 1963). Owing to its highly corrosive nature, H_2S testing on metals and alloys is of industrial importance. Tin is a metal of widespread use in external atmosphere mainly as a sacrificial coating on metals. Extensive studies on the oxidation of tin have been carried out by Boggs and coworkers (Boggs *et al* 1961a, b, 1963, 1964a; Boggs 1961c, 1964b). Chan duc Thiep *et al* 1977a, b employed the selective Mössbauer spectroscopy method to study the oxidation mechanism of thin films of tin deposited on glass. The formation of sulphur containing mixed films on tin was discussed by Gabe (1977). The present paper contains investigations about the effect of H_2S on the oxidation of thin films of tin at constant relative humidities ($\approx 85\%$) and at room temperature (≈ 303 K).

2. Experimental

The oxidation rate was followed by measuring the rate of increase of resistance of thin films (900 A) of tin (99·999%) which had been evaporated on to optically plane glass substrates at room temperature. Thick electrode films of tin were previously deposited at the ends of the glass substrates, which were cleaned by chemical and ion-bombardment methods. All evaporations were carried out in a conventional vacuum line at pressures greater than 10^{-5} torr. The films and electrodes were evaporated from a molybdenum boat.

After measuring the resistances, the films coated in the same pump-down were quickly transferred to an enclosed glass chamber (Muneera *et al* 1983) evacuated to a pressure of 10^{-2} Torr. The required amount of air was then admitted into the chamber followed by 10% by volume of dry H_2S stored in a reservoir. The relative humidity inside the chamber was assessed using a dry and wet thermometer assembly. Resistances of the films were measured at regular intervals for several hours using a vernier potentiometer of accuracy 10^{-6} v. div^{-1}. After about ten days, the films were taken out and photographed. Both optical and scanning electron microscopes were used to study the structure of the oxide films formed. Resistance could not be measured for longer periods due to the failure of metal contacts used for external connections. Studies with higher percentage of H_2S were also not possible because of the vigorous attack by the highly corrosive gas on the metal contacts used.

3. Results and discussion

The change in resistance of the thin film can be related to the oxide thickness (Hunt and Ritchie 1972). If the evaporated thin film is regarded as a thin isotropic metal sheet which oxidises on one surface only and obeys Ohm's law, then it follows that the film resistance R and the oxide thickness X are related by the equation

$$x = \frac{\phi \rho l}{\omega}\left(\frac{1}{R_0} - \frac{1}{R}\right), \tag{1}$$

where ϕ is the thickness of the oxide, derived from unit thickness of metal, ρ is the resistivity of the metal film, l is the length of the film between contacts, ω is the width of the film and R_0 is the resistance of the film prior to oxidation. In deriving this equation it has been assumed that the resistivity of oxide formed is very much larger than that of the metal. This condition is satisfied in the present studies as the oxide and sulphide formed on the thin film of tin at room temperature are amorphous (Bound and Richards 1939; Hart 1952; Britton and Bright 1957; Boggs *et al* 1961b; Raymond and Donald 1955). From (1) it is clear that the oxide thickness x is proportional to $-1/R$.

The oxidation of tin at room temperature obeys a direct logarithmic rate law (Tamman and Köster 1922; Katz 1956; Britton and Bright 1957; Gabe 1977). With the introduction of 10% H_2S, the oxidation rate changed from a direct logarithmic law to a power law of the form

$$x^n = kt, \tag{2}$$

where x is the oxide thickness and k and n are constants. This is evident from the plot of $\log 1/R$ vs $\log t$ in figure 1.

The surface structures developed on the film after about ten days of exposure to H_2S + air atmosphere are shown in figures 2–8. There are two types of nucleation centres: the slightly large bright centres and the more distributed form of fine grains or powdery nuclei (figure 2). Some of the former grow into larger growth centres near the edges of the films (figures 3–5). They are different from the wheel-shaped or dendritic growth centres (Boggs *et al* 1961b; Muneera *et al* 1983) observed on films exposed to normal atmospheres (figures 9–10). Figure 6 shows the larger growth centre along with the other nucleation centres. Growth centres under different stages of growth are observed on the same specimen.

The various chemical reactions which can take place when the film is kept in an atmosphere containing 10% H_2S and 90% air are as given below (Boggs *et al*

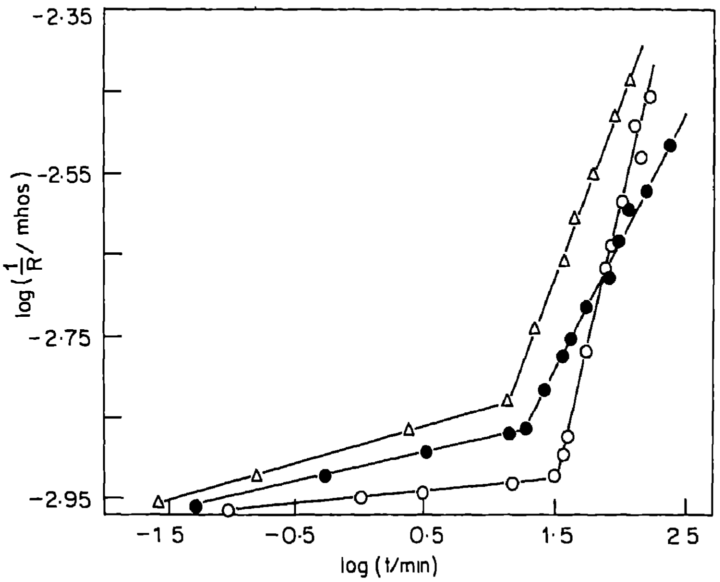

Figure 1. Plot of log $1/R$ vs log t. The oxidation rate for the initial period is different as observed usually.

Figure 2. The two types of nucleation centres observed on a film kept in 10% H_2S + air atmosphere for about ten days (×220).

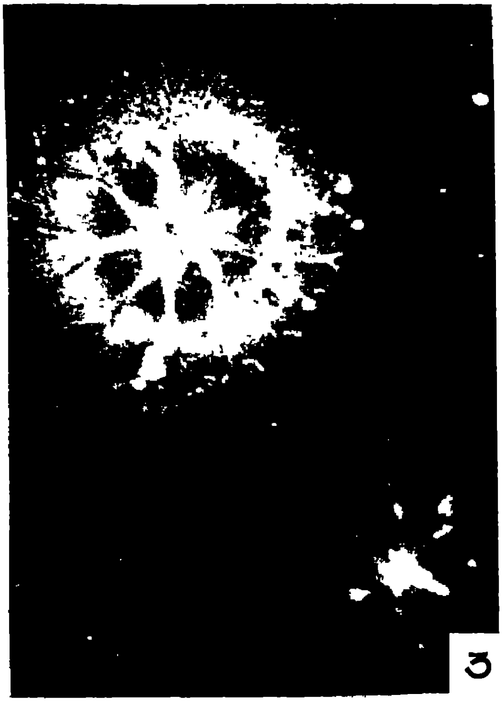

Figure 3. Optical micrograph of the wheel-shaped dendrites seen at the edges of the film (×480).

1961 a, b, c; Gabe 1977). The relevant thermodynamical data are obtained from Kubaschewski *et al* (1967)

$$\mathrm{Sn} + 1/2\ \mathrm{O_2} \rightleftharpoons \mathrm{SnO};\ \Delta G_T = -68400 + 23.3\ T\ \mathrm{cal.}$$
$$\approx -61{\cdot}46\ \mathrm{kcal}\ (T = 303\ \mathrm{K}), \qquad (3)$$

$$\mathrm{Sn} + \mathrm{H_2S} \rightleftharpoons \mathrm{SnS} + \mathrm{H_2};\ \Delta G_T = -22100 + 14{\cdot}96\ T$$
$$\approx -17{\cdot}64\ \mathrm{kcal.}\ (T = 303\ \mathrm{K}) \qquad (4)$$

Thermodynamically the greater possibility of reaction is the one in which there is maximum decrease in free energy change. Thermodynamic equilibrium will not be attained for short periods of oxidation and at room temperature, the conditions under which the present studies are made. In such cases the reaction kinetics determine the possibility of occurrence of a particular chemical reaction. It has been reported that the oxide formed on tin at room temperature is SnO (Boggs *et al* 1961 a, b, 1963; Gabe 1977). Therefore considering the higher partial pressure of O_2 (143·64 mm of Hg) and greater electron affinity of sulphur, both SnO and SnS are expected to form, although the free energy change associated with reaction (4) is less than that with reaction (3).

The oxidation of tin at room temperature takes place by the outward migration of cations (Boggs *et al* 1961). In the presence of 10% H_2S and 90% air, both hydrogen sulphide and oxygen are expected to be adsorbed on the surface. Because of the higher partial pressure of oxygen, it seems reasonable that SnO is formed first and grows by

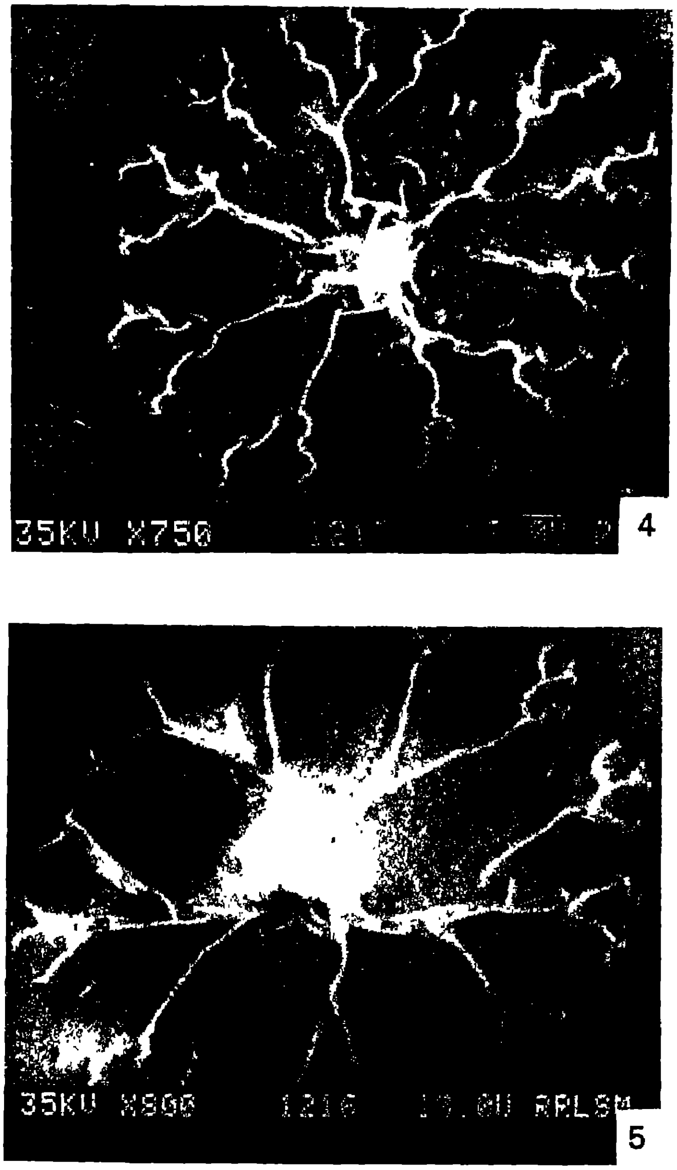

Figures 4–5. SEM of the rosette-shaped dendrite in which the lower sulphide layer **4.** also grows into branches following the upper oxide dendrites and **5.** forms a circular bed for the radiating oxide dendrites.

outward migration of cations. From SEM and optical microscopic studies, it can be concluded that at sites where SnO grows into 'radially symmetric dendrites', the sulphide forms a layer beneath the oxide layer (figures 3–5). The oxide and sulphide together forms 'wheel-shaped' (figure 3) or 'rosette shaped' (figures 4–5) dendrites at these sites. Even at other sites where SnO forms comparatively smaller growth centres the powdery or fine-grain like SnS is observed on a lower layer (figures 2, 6). Therefore

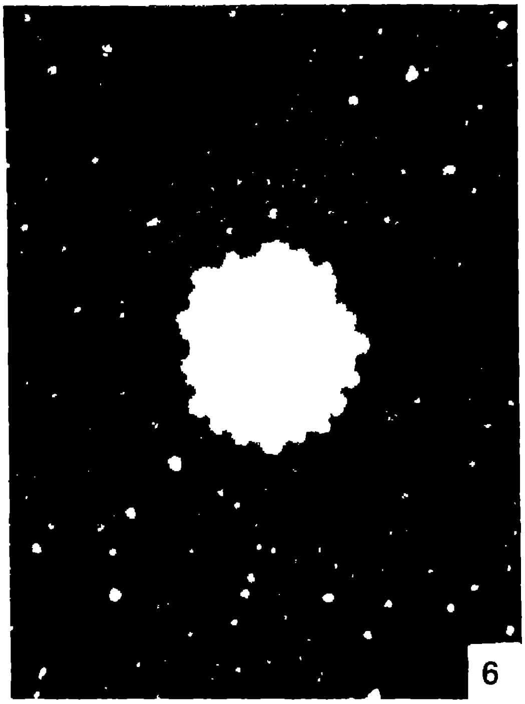

Figure 6. The larger growth centre along with the two types of nucleation centres (× 220).

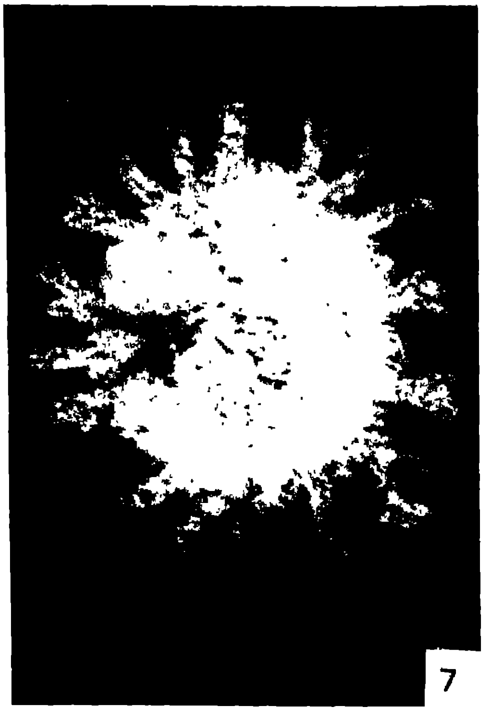

Figure 7. Optical micrograph of figure 4 under transmitted light showing podia-like extensions at the boundary (× 540).

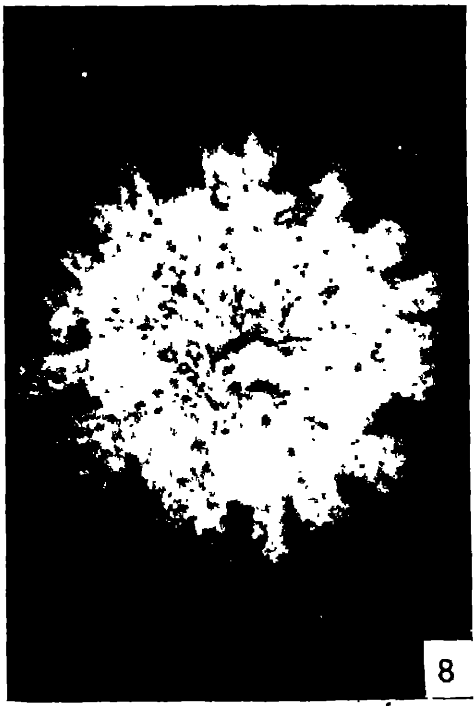

Figure 8. Later growth stage of a pattern similar to that shown in figure 7 (×500).

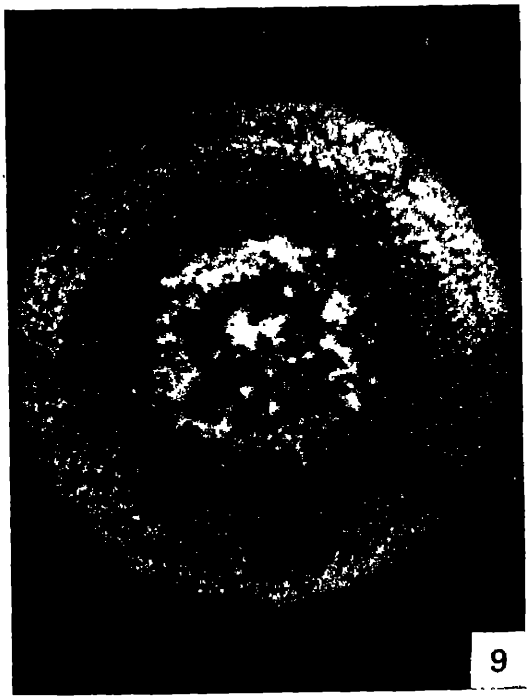

Figure 9. Wheel-shaped growth centre observed on a film kept in normal atmosphere (×1440).

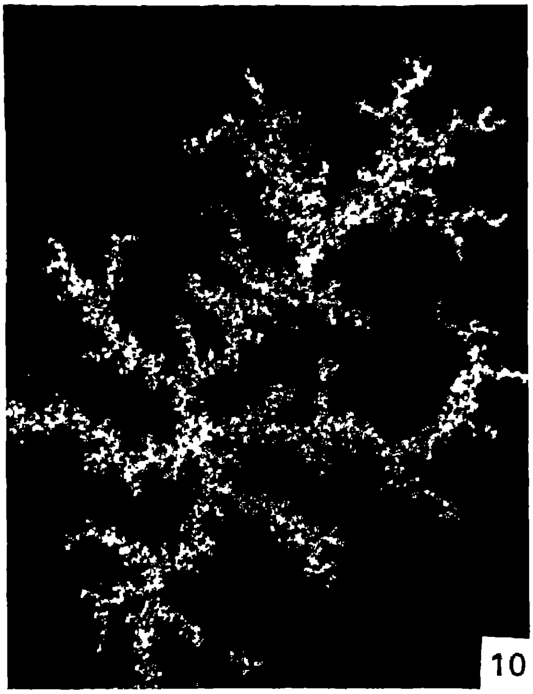

Figure 10. The dendritic growth of oxide observed on the film kept in normal atmosphere (× 200).

SnS is presumed to form between the metal and the oxide layer, *i.e.*, at the oxide-metal interface. It must grow by the inward migration of sulphur through the oxide layer reacting with cations and electrons at the sulphide-oxide interface. The presence of sulphur in the oxide remarkably enhances the cation diffusivity (Wooten and Birks 1972; Lawless 1974). The oxidation rate is therefore increased to that of a power law when 10% H_2S is introduced.

The radially symmetric dendrites may be formed in a way similar to that of the dendrites found at low oxygen pressures (Boggs *et al* 1961b). These structures are commonly observed near the edges of the films where the chance of finding high density of grain-boundaries is greater. Although the partial pressure of oxygen is considerably high, the presence of H_2S and the higher electron affinity of sulphur leads to an initial adsorbed layer of variable oxygen concentration. The 'wheel-shaped' or 'rosette shaped' dendrites grow laterally in radial directions (see the small growth centre in figure 3). The areas between adjacent primary branches become depleted in oxygen as oxygen in the adsorbed layer is consumed during the formation of radiating branches. These branches grow outward into areas richer in oxygen uniformly forming secondary and tertiary branches and a well-defined radially symmetric circular pattern is obtained. The sulphide layer also grows laterally forming a circular bed for the radiating dendrites (figure 5). In figure 3 the sulphide layer formed below the radially symmetric dendrite forms a rim at its boundary. In certain cases (figure 4) the sulphide layer also grows into branches following the oxide dendrites. When viewed under transmitted light using an optical microscope, figure 4 appears as shown in figure 7. The distinction between oxide and sulphide layer is less clear in figure 7. At the boundary of the growth centre, the oxide and sulphide together form 'podia'-like extensions (figures 7, 8). The tips of the branches seem to have thickened. With further oxidation, the area between podia-like extensions get filled up gradually (figure 8).

4. Conclusion

With the presence of 10 % H_2S, the rate equation changes from a logarithmic law to a power law, indicating an increase in oxidation rate. This is explained on the basis of formation of sulphide along with the oxide, the former growing on a lower layer and the latter on the upper layer. The oxide and sulphide together forms 'wheel-shaped' or 'rosette-shaped' dendrites at the edges of the film.

References

Boggs W E, Kachik R H and Pellissier G E 1961a *J. Electrochem. Soc.* **108** 6
Boggs W E, Trosso P S and Pellissier G E 1961b *J. Electrochem. Soc.* **108** 13
Boggs W E 1961c *J. Electrochem. Soc.* **108** 124
Boggs W E, Kachik R H and Pellissier G E 1963 *J. Electrochem. Soc.* **110** 4
Boggs W E, Kachik R H and Pellissier G E 1964a *J. Electrochem. Soc.* **111** 636
Boggs W E 1964b *Br. Pat.* **963** 763
Bound M and Richards D A 1939 *Proc. Phys. Soc. London* **51** 256
Britton S C and Bright K 1957 *Metallurgia* **56** 163
Chan duc Thiep, Ts. Bonchev, Mitrikov M, St. Peneva, Topalova K and Zukeva E 1977a *Bulg. J. Phys.* **4** 130
Chan duc Thiep, Ts. Bonchev, Nguyen Chi Toa and St. Peneva 1977b *Bulg. J. Phys.* **4** 399
Gabe D R 1977 *Surf. Technol.* **5** 463
Hart R K 1952 *Proc. R. Soc.* (*London*) **B65** 955
Hunt G L and Richie I M 1972 *J. Chem. Soc., Faraday Trans. I*, **68** 1413
Katz W 1956 *Stahl Eisen* **76** 1672
Kubaschewski O, LL Evas E and Alock C B (eds) 1967 *Metallurgical thermochemistry* (New York: Pergamon Press)
Lawless K R 1974 *Rep. Prog. Phys.* **37** 231
Minster J T 1963 *Nature* (*London*) **199** 474
Muneera C I, Varghese S and Unnikrishnan Nayar V 1983 *Oxid. Met.* **19** 187
Raymond E K and Donald F O (eds) 1955 *Kirk-Othmer encyclopedia of chemical technology* (New York: Interscience) vol. 14
Tamman G and Köster W 1922 *Z. Anorg. U. Allegm. Chem.* **123** 196
Wooten M R and Birks N 1972 *Corrosion Sci.* **12** 829

Bull. Mater. Sci., Vol. 6, No. 6, December 1984, pp. 1029–1033. © Printed in India.

Annealing behaviour of electron-beam deposited tin dioxide films

ARJEESH GUPTA, POONAM GUPTA and V K SRIVASTAVA
Department of Physics, University of Roorkee, Roorkee 247 672, India

MS received 23 November 1983; revised 31 March 1984

Abstract. The sheet resistivity of tin dioxide films deposited by electron-beam evaporation has been studied during annealing, both as a function of time and temperature. The annealing behaviour of SnO_2 films under the above two different conditions is consistent. A qualitative interpretation has been given for the decrease and the minimum observed in the resistivity. The increase in resistivity has been confirmed by scanning-electron micrographs. The films were also characterized by x-ray diffractometry.

Keywords. Tin dioxide films; electron beam evaporation; annealing behaviour; sheet resistivity.

1. Introduction

Thin transparent conducting films of SnO_2, because of their wide application in solar cells, have currently become a subject of intense investigation. The SnO_2 film is a transparent conductor which is sometimes known as Nesa glass (Ishiguro *et al* 1958). The optical and electrical properties of SnO_2 films were studied by Arai (1960) who found them to be polycrystalline *n*-type degenerate semiconductor with a free carrier density of 7×10^{18}–$1{\cdot}7 \times 10^{19}\ \mathrm{cm}^{-3}$ and an energy band gap of about 3·5 eV. The change in the conductivity of the material (SnO_2) in thin films as compared to that in bulk arises due to anion oxygen defects.

It is known (Raccanelli and Madalena 1976; Viscrian and Georgescu 1969; Shanthi *et al* 1980) that post-annealing treatment of SnO_2 films can result in change of electrical properties. It has recently been reported (Ghosh *et al* 1978; Nagatoma *et al* 1979) that the annealing of SnO_2 films plays an important role in the improvement of the performance characteristics of SnO_2/Si solar cells. It has been found that on annealing the resistivity of pure SnO_2 single crystals reduces and that of the SnO_2 films deposited by hydrolysis of an ether-alcohol solution of Sn $(OC_2H_5)_4$ first decreases and then increases drastically on annealing at temperatures higher than 500°K (Jarzebeski 1976). But no satisfactory explanation is available for the phenomenon.

As far as the authors are aware, investigations on the annealing behaviour of electron beam deposited SnO_2 film, which are important in solar cells, have not been reported. The present work was therefore undertaken.

2. Experimental

2.1 *Sample preparation*

SnO_2 films were prepared by electron-beam evaporation at a pressure $\sim 10^{-6}$ torr. Undoped SnO_2 (99·90 %) was evaporated by an electron-beam gun onto chemically cleaned glass substrates at room temperature (300°K). An evaporation rate of 4 Å sec^{-1} was maintained to produce films of SnO_2 with approximately uniform thickness of about 1300 Å. The thickness of the films was measured during evaporation by a quartz crystal thickness monitor and also by the interferometry method.

2.2 *Resistivity measurement*

The resistivity of the films was measured in a furnace during annealing as a function of time. The temperature of the furnace was maintained constant ($\pm 5°C$). The sheet resistivity of SnO_2 films was also measured during annealing as a function of temperature in the range (623–808 K). The temperature of the furnace was regulated at approximately 3°C/min. The temperature was measured with a chromel-alumel thermocouple. X-ray diffraction measurements of the films were made (Philips x-ray diffractometer, model No. PW-1140/90) and scanning electron micrographs taken (SEM-501, Philips make).

3. Results and discussion

The sheet resistivity of the as-deposited SnO_2 films was very high ($> 20\ M\Omega$) and decreased with annealing in air. The variation of sheet resistivity as a function of time during isothermal annealing at different temperatures is shown in figure 1. The as-deposited or unannealed SnO_2 films (evaporation temperature above 1800°C) are expected to be amorphous in character as shown by its high resistivity. This amorphous character is confirmed by x-ray diffractometric characterisation (figure 2a). The peaks of the x-ray diffraction pattern show crystallization with time during annealing at 717, 701 and 688 K respectively (figure 2) as also indicated by decrease in resistivity. As expected, the general shape of the isothermal annealing curves (figure 1), at different temperatures is very similar.

It was observed that the time at which the films became conducting increases as the annealing temperature decreases. This is expected because the thermally activated process of transformation from the amorphous to the polycrystalline phase will slow down with decrease of annealing temperature. This also explains the broadening of the minima with decreasing annealing temperature. The decrease in sheet resistivity with time (figure 1) may be attributed to the reduction in defect density as shown by the x-ray diffraction results, and in addition chemisorption of oxygen also takes place which further reduces the resistivity of the films (Shanthi *et al* 1980). The sheet resistivity attains a minimum when the defect distribution may be assumed to be in equilibrium (Chopra 1969). The increase in the observed resistivity after the minimum is dominated by the formation of pores and further increase in size of the pores. The SEM photographs (figures 3a, b) corresponding to 37 and 60 min annealing give only pores with their size increasing.

The variation in sheet resistivity with temperature on annealing the SnO_2 film in air is plotted in figure 4. The film showed irreversible decrease in sheet resistivity, perhaps due to the reduction of defect density with increasing temperature. This mechanism governing the resistivity of films is well known (Maissel and Glang 1970). The minimum nearly corresponds to the Debye temperature of SnO_2 [$\sim 500°$ K], so that the largest

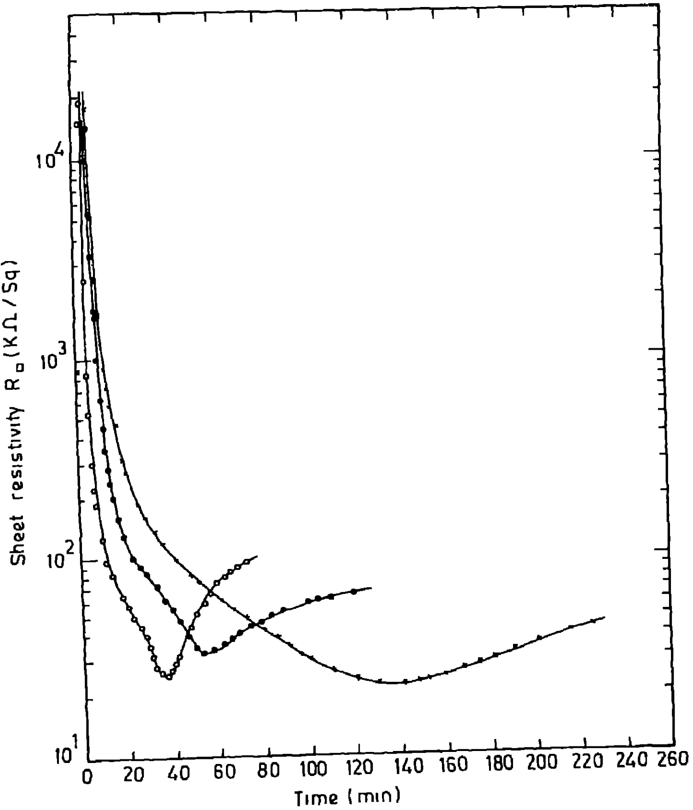

Figure 1. Sheet resistivity *vs* time for SnO_2 films deposited on glass substrate during isothermal annealing (o)-701 K; (●)-688 K; (×)-660 K.

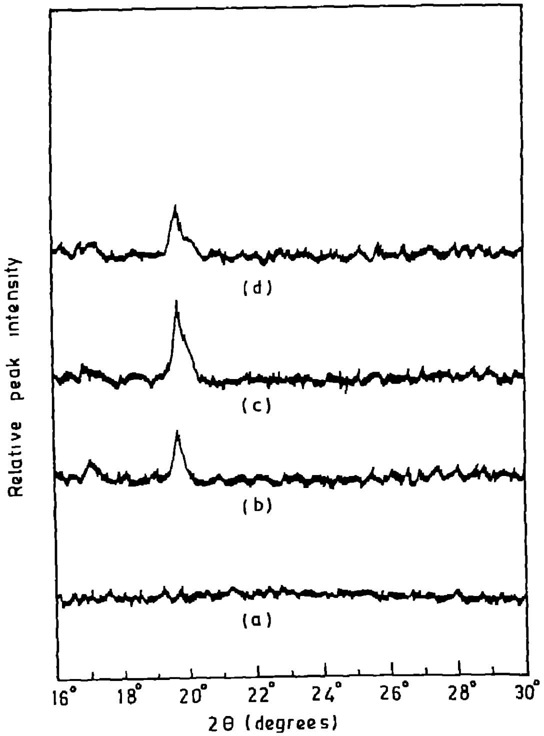

Figure 2. X-ray diffraction pattern for SnO_2 films deposited on glass substrate. **a.** Unannealed films, **b.** $t = 4$ min annealed at 717 K, **c.** $t = 37$ min annealed at 701 K, **d.** $t = 1$ hr annealed at 688 K.

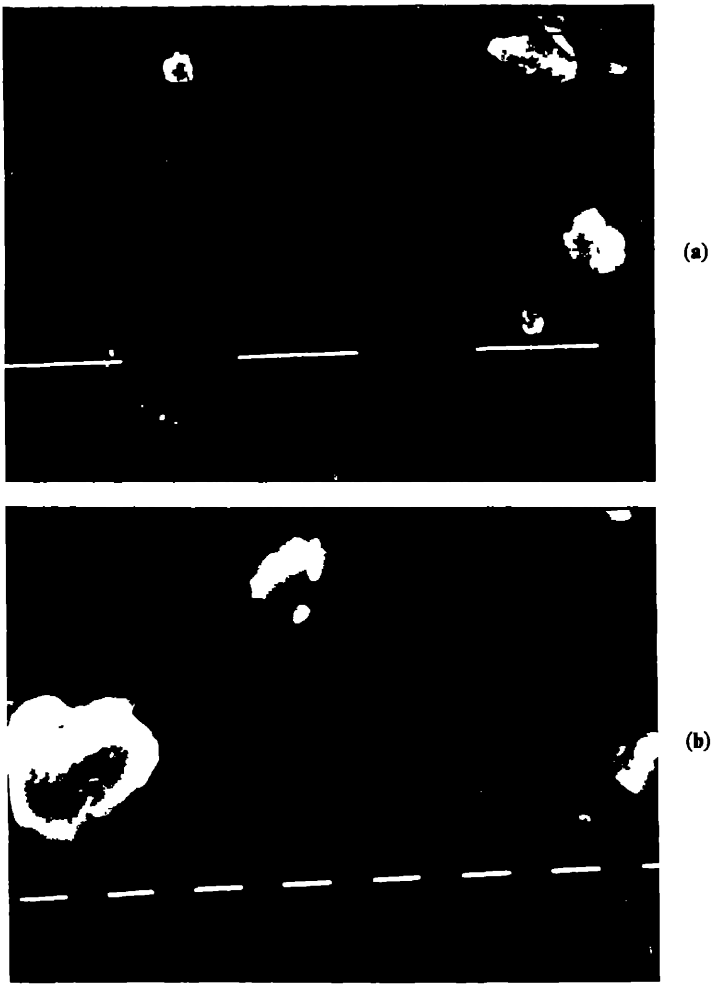

Figure 3. Scanning electron micrograph of SnO_2 films deposited on a glass substrate annealed at 701 K, **a.** annealed for 37 min (magnification: 160 × 1·1). **b.** annealed for 1 hr (magnification 640 × 1).

part of the lattice defects is removed because of the maximum frequency of the lattice vibrations (Chopra 1969). Therefore, beyond this point the resistivity increases.

We have attempted here to give a qualitative interpretation of the results obtained on the annealing behaviour of tin dioxide films. A quantitative study is in progress.

Acknowledgement

AG and PG are thankful to CSIR (India) for financial support. The authors express their sincere thanks to Mr N K Saini for help in carrying out SEM experiments.

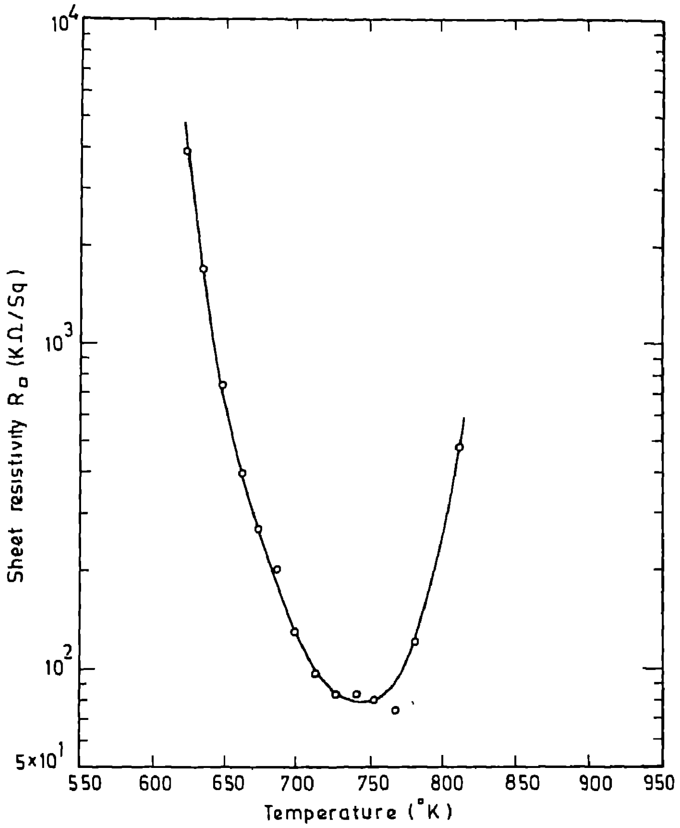

Figure 4. Sheet resistivity *vs* temperature for SnO_2 film deposited on a glass substrate.

References

Arai T 1960 *J. Phys. Soc. Jpn* **15** 916
Chopra K L 1969 *Thin film phenomenon* (New York: McGraw Hill) 381–387
Ghosh A K, Fishman C and Feng T 1978 *J. Appl. Phys.* **49** 3490
Ishiguro K, Sasaki T, Arai T and Imai I 1958 *J. Phys. Soc. Jpn* **13** 296
Jarzebeski Z M 1976 *J. Electrochemical Soc.* **123** 299C
Maissel L I and Glang R 1970 *Handbook of thin films technology* (New York: McGraw Hill) 13–26
Nagatoma T, Endo M and Omoto O 1979 *Jpn J. Appl. Phys.* **18** 1103
Raccanelli A and Madalena A 1976 *J. Am. Ceram. Soc.* **59** 425
Shanthi E, Banerjee A, Dutta V and Chopra K L 1980 *Thin Solid Films* **71** 237
Viscrian I and Georgescu V 1969 *Thin Solid Films* **3** R17

Bull. Mater. Sci., Vol. 6, No. 6, December 1984, pp. 1035–1039. © Printed in India.

Temperature dependence of microhardness in mixed crystals

SANKAR P SANYAL and R K SINGH

Department of Physics, Rani Durgawati University, Jabalpur 482 001, India

MS received 7 October 1983

Abstract. The temperature dependence of microhardness of mixed KCl-KBr crystals has been studied using the Kataoka and Yamada theory which considers plastic deformation and internal stress field due to elastic interactions in mixed crystals. The microhardness showed systematic variation with temperature in both the components and the mixed crystals and the probable reasons for this variation are indicated.

Keywords. Mixed crystals; microhardness; temperature dependence; Kataoka-Yamada theory.

1. Introduction

In recent years, considerable attention has been paid to the study of mixed crystal properties as they are useful in many technological applications (*e.g.* mixed crystals of alkali halides are used for laser windows). One well-known property is microhardness, which for mixed crystals always exceeds its value for the component crystals (Armington *et al* 1973; Hari Babu *et al* 1975). A number of theories (Gilman 1973; Shukla and Bansigir 1976; Boser 1972; Ridhagani and Asimow 1968) have been proposed to explain this extra hardness of mixed crystals. Earlier theories of Gilman (1973) and Shukla and Bansigir (1976) could not explain the microhardness of mixed crystals as indicated by Bhimshankaran (1974), and Srivastava (1980). Kataoka and Yamada (1977) have given a theory according to which the random distribution of doped ions can produce an internal stress field interaction that increases the microhardness of the mixed crystals. This theory has been applied to mixed alkali halides (Srivastava 1980) and mixed silver halides (Sanyal and Singh 1982).

Motivated by the success of the theory of Kataoka and Yamada theory, we have applied it to study the temperature dependence of microhardness of KCl_xBr_{1-x} system from 300–1000 K. It is known (Subba Rao and Hari Babu 1978) that the excess of microhardness in mixed crystals results from the increased value of dislocation density. However, this dislocation density in mixed crystals decreases with increase in temperature. Thus, it seems worthwhile to investigate the exact nature of change of microhardness with temperature in mixed crystals. Srivastava (1980) used the Kataoka-Yamada theory to explain the microhardness of KCl_xBr_{1-x}, measured by Subba Rao and Hari Babu (1978) at 300 K only. In doing so, he used the measured microhardness values of KCl, KBr and $KCl_{0.48}Br_{0.52}$ as the input data. Thus, the predictions made by Srivastava are more or less borne out. In the present analysis, however, the results of microhardness of $KCl_{0.48}Br_{0.52}$ have only been used at 300 K to determine a parameter. The values of microhardness of component crystals (KCl and KBr) have been obtained in terms of Debye temperatures (Bollmann 1980).

2. Theory

The microhardness (H_v) of binary ionic solids is related to the Schotky defect formation energy (w_s) as (Shukla and Bansigir 1976)

$$H_v = 205{\cdot}8\ W_s/r^3, \tag{1}$$

where r is the interionic separation. According to Sastry and Mulimani (1969), W_s is also related to the Debye temperature (Θ_D), such that

$$W_s = (\Theta_D/32.37)^2\ MV^{2/3}. \tag{2}$$

Here, M and V are the molar mass and volume. Now, H_v can be written in terms of the Debye temperature as:

$$H_v = 6{\cdot}833\ (MV^{2/3}/r^3)\ \Theta_D^2 \times 10^{-5}\ (\mathrm{kg/mm^2}), \tag{3}$$

from (1) and (2). This equation is, however, valid only for the component crystals and not for mixed crystals, as it fails to account for the extra hardness in them. We have therefore considered the extra hardness using the Kataoka-Yamada theory in which the doped ions are assumed to behave as a source of constriction and expansion in the lattice in order to maintain the crystal symmetry. The random distribution of these ions produces a fluctuating stress in the mixed crystals and is responsible for the increase in their hardness. The mean expectation value of the internal stress, τ_0, arising from the random distribution of anions is given by (Kataoka and Yamada 1977)

$$\tau_0 = \frac{4\sqrt{2}}{\pi}\,\alpha\left(\frac{\alpha}{\alpha'}\right)^{1/2}\frac{\sigma^2 r^2}{\lambda}\left(\frac{\Delta V}{r^3}\right)\beta_1\beta_2, \tag{4}$$

where α and α' are the lattice sums. ΔV is the difference in anion volume of the two components and β_1 and β_2 are fractional molar concentrations of the two components in the mixed crystals. The symbols σ and λ are related to the second order elastic constants by

$$\sigma = \tfrac{1}{2}\,(C_{11} - C_{12}) \tag{5}$$

and

$$\lambda = \tfrac{1}{2}\,(C_{11} + C_{12})\left[\frac{C_{44}(C_{11} - C_{12})}{C_{11}(C_{11} + C_{12} + C_{44})}\right]^{1/2} r^2. \tag{6}$$

In terms of τ_0 the hardness due to internal stress field can be expressed as

$$H_{\mathrm{isf}} = F\tau_0 \tag{7}$$

with F as a constant. Thus, the microhardness of mixed crystals is ultimately given by

$$H_m = \beta_1 H_1 + \beta_2 H_2 + H_{\mathrm{isf}}, \tag{8}$$

where H_1 and H_2 are the hardness of the component crystals.

3. Results and discussion

The microhardness (H_v) values of the component crystals, KCl and KBr at different temperatures (300–1000 K) were calculated from (3) using the values of Debye temperature (Θ_D) and interionic separation (r_0) reported by Tolpadi (1977) and

Subramaniam (1979). Their values for KCl and KBr at different temperatures are listed in table 1 and are compared with their measured data at 300 K (Bollman 1980; Subba Rao and Hari Babu 1978). The microhardness (H_m) values for the mixed crystals at different temperatures have been calculated from (8) using the required values of elastic constants reported by Subramaniam (1978). The variations of microhardness with temperature for the component crystals and mixed KCl-KBr are presented in figure 1 and those with mole percentage of KBr are presented in figure 2.

Table 1. Microhardness (H_v) of KCl and KBr at different temperatures.

Temperature (K)	H_v (kg/mm^2)	
	KCl	KBr
300	10·306	8·468
	9·9[a]	7·9[b]
400	9·464	8·231
500	8·906	7·785
600	8·317	7·329
700	7·706	6·847
800	7·020	6·331
900	6·236	5·784
1000	5·293	5·133

[a] Bolmann (1980); [b] Subba Rao and Hari Babu (1978).

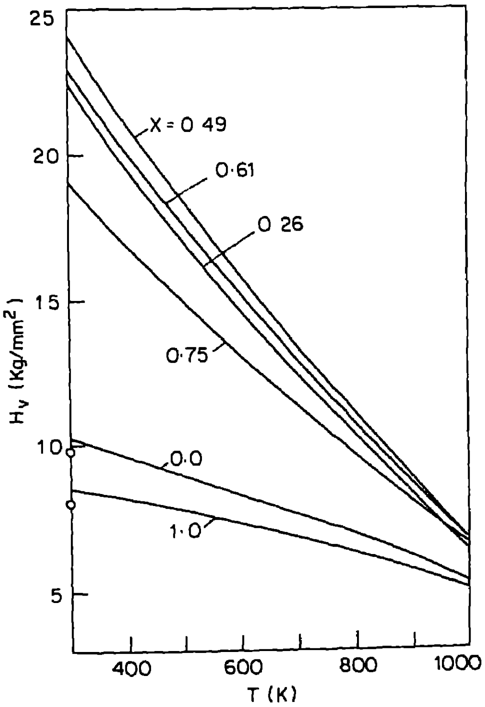

Figure 1. Variation of microhardness of KCl_xBr_{1-x} system with temperature. Experimental points (o) at 300 K have been taken from Subba Rao and Hari Babu (1978).

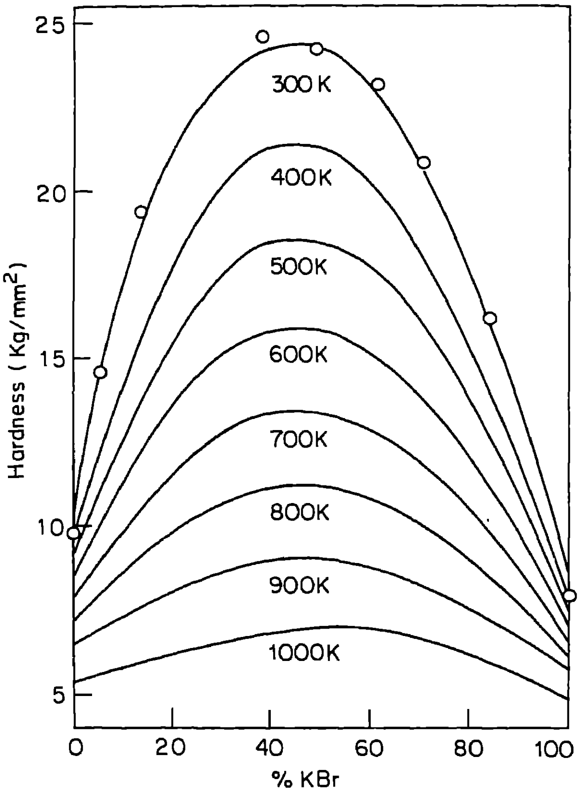

Figure 2. Variation of microhardness of KCl_xBr_{1-x} system with % of KBr in KCl at different temperatures. Experimental points are taken from Subba Rao and Hari Babu (1978).

Table 1 shows that the microhardness of the component crystals can be satisfactorily predicted by using (3). These values decrease almost linearly with temperature as shown in figure 1. This might be so because the microhardness is a measure of the resistance offered by dislocation motion which becomes easier when the temperature is raised. The variation of H_v with temperature in mixed crystals is, however, not linear, perhaps due to the elastic effects arising from the size misfit of cations.

Figure 2 shows that the extra hardness in mixed crystals (Hari Babu and Subba Rao 1978) at 300 K has been adequately explained even without using the H_v values of the component crystals. This prediction is better than that achieved by Subba Rao and Hari Babu (1978) where they neglected the effects due to elastic interactions (Kataoka and Yamada 1977). Our results on H_v at higher temperatures could not be compared due to lack of measured data. Their variation with temperature is, however, systematic and consistent with the measured results in other solids (Bhatt and Desai 1982).

References

Armington A F, Posen H and Lipson H 1973 *J. Electron. Mater.* **2** 127
Bhatt V P and Desai C F 1982 *Bull. Mater. Sci.* **4** 23

Bhimasankaran T 1974 Ph.D. Thesis, Osmania University, AP
Bollman W 1980 *Phys. Status Solidi* **A6** 395
Boser O 1972 *Metall. Trans.* **3** 843
Gilman J J 1973 *J. Appl. Phys.* **44** 983
Hari Babu V, Subba Rao U V and Venkata Ramaiah K 1975 *Phys. Status Solidi* **A28** 269
Kataoka T and Yamada T 1977 *Jpn J. Appl. Phys.* **16** 1119
Riddhagni B R and Asimow R M 1968 *J. Appl. Phys.* **39** 4164
Sanyal S P and Singh R K 1982 *J. Phys.* **D15** 1083
Sastry P V and Mulimani P G 1969 *Philos. Mag.* **20** 859
Shukla M and Bansigir K G 1976 *J. Phys.* **D9** L49
Srivastava U C 1980 *J. Appl. Phys.* **51** 1510
Subba Rao U V and Hari Babu V 1978 *Pramana* **11** 149
Subramaniam B 1979 *Indian J. Phys.* **A54** 109
Tolpadi S 1977 *Indian J. Phys.* **A51** 181

Bull. Mater. Sci., Vol. 6, No. 6, December 1984, pp. 1041–1046. © Printed in India.

Some aspects of dislocation-precipitate interaction in under-aged aluminium-germanium alloy

KISHORE

Department of Metallurgy, Indian Institute of Science, Bangalore 560 012, India

MS received 6 September 1982; revised 13 December 1983

Abstract. The glide dislocation-precipitate interaction in under-aged alloy is investigated by microscopy and low-temperature deformation techniques. Slip-line features of room temperature deformed samples were observed by optical microscopy. From tensile tests at various temperatures the variation of flow stress with $T^{2/3}$ was established. Comparing the present results with those obtained on the peak-hardened condition of the same alloy it is concluded that moving dislocation shear through the small rod-shaped germanium precipitates.

Keywords. Under-aged; dislocation-precipitate interaction; slip lines; flow stress.

1. Introduction

The interaction between glide dislocations and precipitate particles has been studied in detail in many age-hardenable alloy systems (Nicholson and Nutting 1961; Kelly 1963; Lutzering and Weissman 1970; Raynor and Silcock 1970; Nourbakhsh and Nutting 1980). From mechanical property studies coupled with microscopy, it is possible to arrive at the likely interaction between moving dislocations and precipitate particles. While efforts are not wanting in understanding the dislocation precipitate interaction in peak-aged and over-aged states, the partially-aged condition has received hardly any attention. The purpose of the present work is to study the dislocation-precipitate interaction in under-aged aluminium-2% germanium alloy using microscopy and mechanical deformation techniques.

2. Experimental

Weighed quantities of super-pure aluminium and germanium were melted together in an argon atmosphere in a resistance furnace and cast in a graphite-lined metal mould. The Ge content was 1·98% by weight. The cast ingot was lightly worked by hammering before annealing at 400°C for 48 hr. The homogenised rod was reduced to a 1 mm thick strip by cold-rolling coupled with intermediate annealing treatment. Tensile and hardness samples were cut from the rolled strip and electropolished after mechanical polishing. They were solutionised at 450°C for 2 hr and quenched into ice-water mixture maintained close to 0°C. Thermostatically-controlled paraffin oil bath, maintained at 165°C, was used for ageing the samples. Hardness variation with ageing time was determined using a Vicker's unit. From such a data it was possible to establish the peak-hardened condition. In the present experiment as the peak hardness occurred at around 70 hr, the tensile test specimens were aged for 18 hr to have the microstructure corresponding to the under-aged condition.

The partially-aged test specimens with a gauge length of 20 mm were pulled in a modified Hounsfield tensometer (Prasad *et al* 1969) at a strain rate of about 10^{-3} $\sec^{-1}$ at temperatures varying between 77 and 420°K. From the load-elongation plot, the flow stress was determined. The tensile-deformed samples were viewed under a light microscope for slip-line features. Using the window technique and an electrolyte of 90/10 acetic acid/perchloric acid mixture maintained at -15°C, electron transparent thin specimen in aged condition was prepared for viewing under a Philips 301 microscope. Electrolytic thinning was achieved by applying a voltage of 18 V between the electrode and the specimen.

3. Results and discussion

Figure 1 shows the variation in Vickers hardness number as a function of time of ageing at 165°C. The data points follow the typical trend seen in any age-hardenable alloy system, namely, an increase of hardness as ageing occurs, a peak followed by a decrease. The peak corresponding to an optimum dispersion of precipitates (Mott and Nabarro 1940) occurs around 70 hr as mentioned earlier. Figure 2, a TE micrograph, depicts the appearance and distribution of precipitates in the under-aged condition. Small and dense rod-shaped Ge precipitates can be clearly seen in the photomicrograph. The inter-particle spacing and the size of the rods in the under-aged sample are smaller (figure 2) compared to the peak-aged condition (figure 3).

The slip-line pattern of partially-aged and room temperature-deformed sample is shown in figure 4. They are straight running, continuous and thin. Slip-line features resemble the pattern obtained for peak-aged state (Kishore and Vasu 1978). It is known that slip bands give reliable information about the mechanism of plastic deformation of the materials (Seeger 1963). The slip-line appearance could change with a change in the type of obstacle present in the matrix. When small coherent particles are present, the dislocation can easily shear the particle aggregates and the appearances of the line in such cases are only slightly different from those obtained for the pure metal or solid

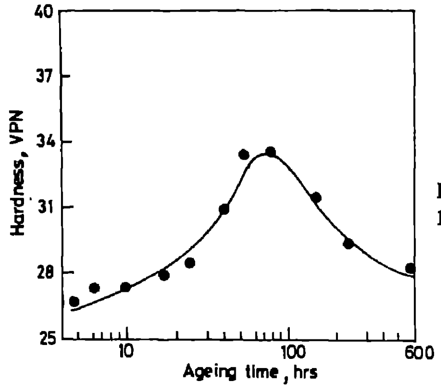

Figure 1. Hardness variation with time during ageing at 165°C (T_q = 450°C).

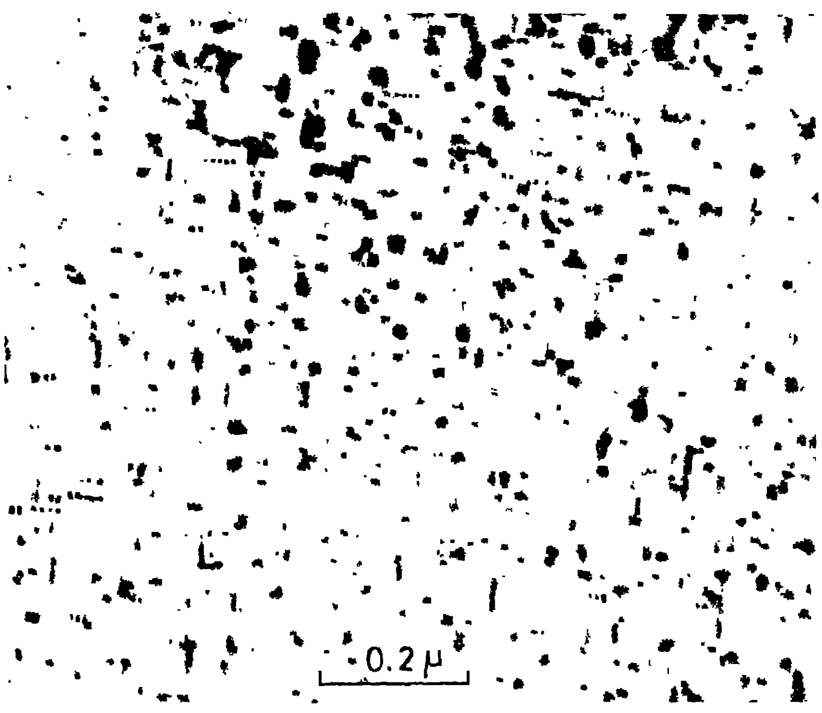

Figure 2. Electron micrograph of partially-aged sample showing small and dense rod-shaped precipitates ($T_q = 450°\text{C}$, $T_a = 165°\text{C}$, $t_a = 18$ hr).

solution (Greetham and Honeycombe 1960–61; Silcock 1960; Thomas and Nutting 1956–57, 1957–58). Wavy, fragmented slip lines are seen when incoherent, large nondeforming particles are encountered during the movement of glide dislocations (Wilcox and Gilbert 1967; Greetham and Honeycombe 1960–61; Price and Kelly 1962). Starke *et al* (1973) have shown that small germanium clusters can be sheared. As the slip traces in partially-aged condition used in this work are similar to those obtained on peak-hardened condition (Kishore and Vasu 1978) and the longer and somewhat widely spaced rods of peak-aged state have been shown to be sheared by moving dislocation using TEM (Kishore *et al* 1976), it may be inferred that in the present under-aged condition also the precipitate particles are cut through by the glide dislocations. Further evidence to this deduction comes from an examination of $\tau - T^{2/3}$ relation following the report of Chun and Byrne (1969). They examined the strengthening in a Mg-5% Zn alloy by determining the temperature dependence of CRSS for the as quenched, fully-hardened and overaged conditions. The shearing of the precipitates in the peak aged state, and the linear variation of flow stress, τ with $T^{2/3}$ were noticed by them. Lipsitt (1971) also showed that yield strength in the Al-Zn alloy varies linearly with $T^{2/3}$. In figure 5 are plotted the data showing variation of flow stress with $T^{2/3}$ for the under-aged Al-Ge alloy. For the sake of comparison the results obtained in the peak-aged state are also included. It is noteworthy that the points lie on a straight line in both the cases suggesting the existence of similar interaction between the glide dislocations and the precipitate particles. Hence, it may be inferred that as in the peak-hardened

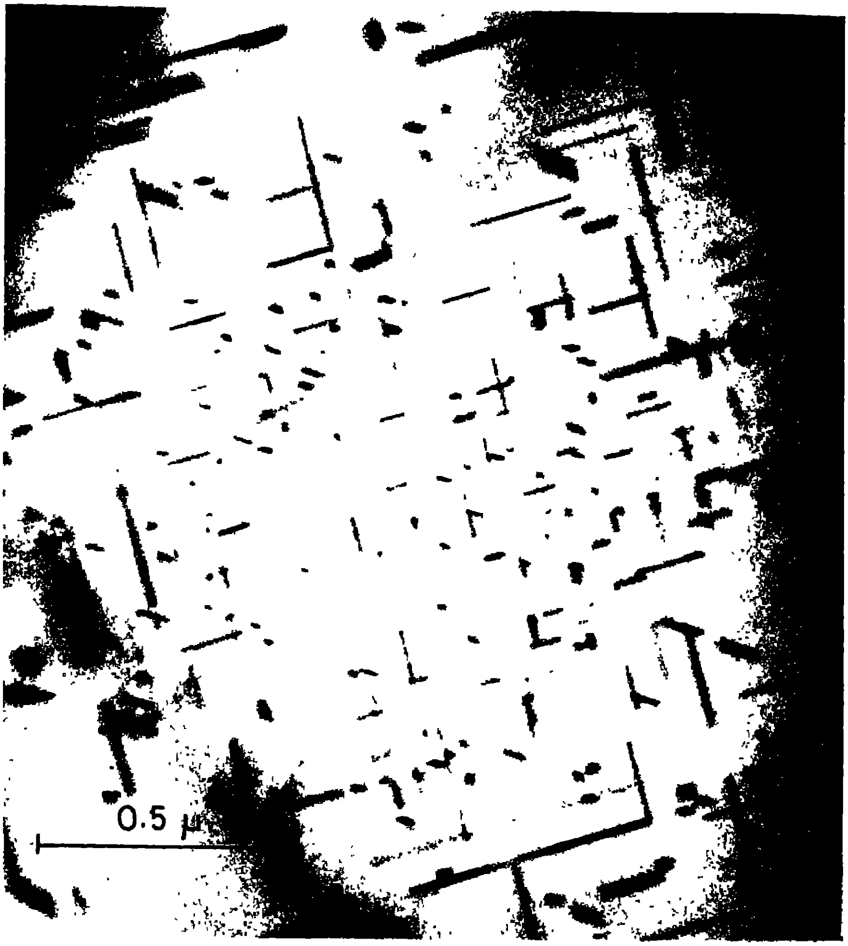

Figure 3. A TEM photograph of the peak-hardened alloy (70 hr at 165°C) showing rod-, triangular-, and rectangular-shaped precipitates.

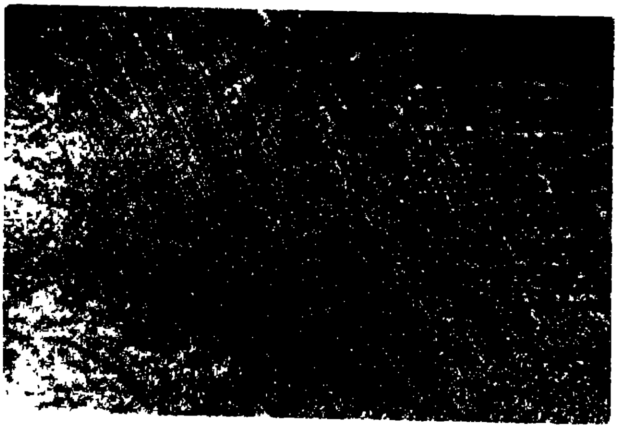

Figure 4. Slip traces in under-aged sample deformed at room temperature ($\varepsilon = 25\%$; 200×).

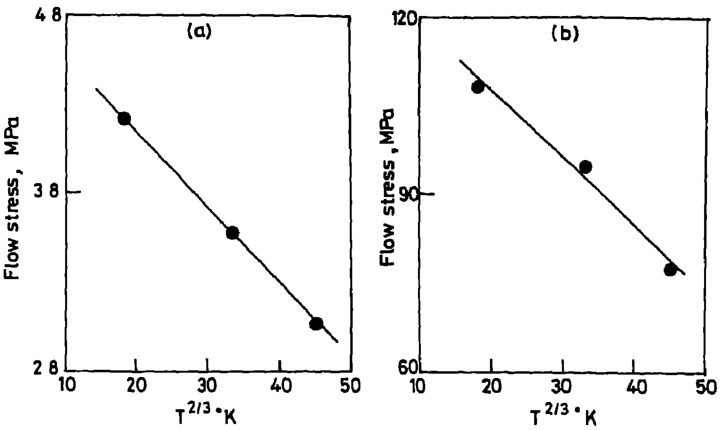

Figure 5. Flow stress-(temperature)$^{2/3}$ relation for (a). under-aged (b). peak-aged conditions ($\dot{\varepsilon} = 9{\cdot}8 \times 10^{-4}$ sec^{-1}).

state, in the under-aged state too, the dislocations penetrate the germanium precipitates.

In view of the similarity of behaviour of flow stress variation with temperature as well as nature of slip traces in the under-aged condition with peak-aged alloy reported earlier (Kishore and Vasu 1978) it can be said that in the partially-aged condition also the Ge precipitates are sheared by the glide dislocations.

4. Conclusions

Partially-aged alloy exhibit straight slip traces. The flow stress of the dilute alloy varies linearly with $T^{2/3}$ and the moving dislocations cut through the germanium precipitates.

Acknowledgements

The author thanks Prof. K I Vasu for his interest in the work. The assistance received from colleagues in the Department is gratefully acknowledged.

References

Chun J C and Byrne J G 1969 *J. Mater. Sci.* **4** 861
Greetham G and Honeycombe R W K 1960–61 *J. Inst. Metals* **89** 13
Kelly A 1963 in *Electron microscopy and strength of crystals* (eds) G Thomas and J Washburn (New York: Interscience) p. 947
Kishore, Sastry D H and Vasu K I 1976 *Proc. Second Int. Conf. on Mechanical Behaviour of Materials*, Boston, USA 1851
Kishore and Vasu K I 1978 *Metallography* **11** 51
Lipsitt H A 1971 *Metall. Trans.* **2** 1739
Lutzering G and Weissman S 1970 *Acta Metall.* **18** 785
Mott N F and Nabarro F R N 1940 *Proc. Phys. Soc.* **52** 86
Nicholson R B and Nutting J 1961 *Acta Metall.* **9** 332
Nourbakhsh S and Nutting J 1980 *Acta Metall.* **28** 357

Prasad Y V R K, Sastry D H and Vasu K I 1969 *J. Indian Inst. Sci.* **51** 377

Price R J and Kelly A 1962 *Acta Metall.* **10** 980

Raynor D and Silcock J M 1970 *Metal Sci.* **J.4** 121

Seeger A 1963a *J. Phys. Soc. Jpn* **18** p. 59

Seeger A 1963b *Proc. at NPL*, Vol I Symp. No. 15 The relation between structure and mechanical properties of metals 4

Silcock J M 1960 *Acta Metall.* **8** 589

Starke E A, Kralik G and Gerold V 1973 *Mater. Sci. Eng.* **11** 319

Thomas G and Nutting J 1956–57 *J. Inst. Metals* **85** 1

Thomas G and Nutting J 1957–58 *J. Inst. Metals* **86** 8

Wilcox B A and Gilbert A 1967 *Acta Metall.* **15** 601

Bull. Mater. Sci., Vol. 6, No. 6, December 1984, pp. 1047–1052. © Printed in India.

Evaluation of magnetic hyperfine field distributions from Mössbauer spectra of disordered alloys and metallic glasses

C BANSAL

School of Physics, University of Hyderabad, Hyderabad 500 134, India

MS received 15 March 1983

Abstract. A simple computer program is described to evaluate magnetic field distributions from complex Mössbauer spectra of magnetic alloys. The use of this program for test cases of Vitrovac 4040 amorphous sample and a simulated spectrum of two gaussian peaks is discussed.

Keywords. Mössbauer spectra; metallic glasses; magnetic hyperfine field distributions.

1. Introduction

The Mössbauer spectra for disordered magnetic alloys and metallic glasses are generally complex because of the overlap of the component lines due to a wide variety of environments in which the Mössbauer atom is situated. In some cases when the overlap is not too large the average hyperfine field can still be evaluated if the field is distributed around an average value (Bansal *et al* 1975). In other cases when the broadening is large this may not be possible. When two or more types of magnetic behaviour are present *i.e.* magnetic splitting due to magnetically ordered regions and a single line due to a paramagnetic contributions it is again very difficult to extract useful information from Mössbauer spectra (Bansal and Chandra 1979).

Several methods have been proposed to obtain the distribution of magnetic fields which generate the complex spectra (Window 1971; Hesse and Rübartsch 1974; Logan and Sun 1976) and improvements on them also given (LaCaer and Dubois 1979; Wivel and Morup 1981).

2. Window's method

Amongst these, the method due to Window is a model-independent field distribution analysis which assumes an arbitrary probability distribution of the magnetic hyperfine fields $P(H)$ and expands it in a Fourier series of trignometric functions.

$$P(H) = \sum_{n=1}^{N} a_n [\cos(n\pi H/H_{\max}) - \cos n\pi]. \tag{1}$$

The field distribution in this form satisfies the boundary conditions: (i) $P(-H) = P(H)$, since in the absence of an external field the lines produced due to a field H are in the same positions as those produced by a field $-H$. The series therefore contains only cosine terms. (ii) There is an upper cut-off point beyond which $P(H)$ goes to zero smoothly *i.e.*

$$\left.\frac{\mathrm{d}P(H)}{\mathrm{d}H}\right]_{H=H_{\max}} = 0.$$

If now the coefficients a_n of the series can be determined so as to fit the experimental spectrum, the required field distribution is known.

The Mössbauer spectrum generated at velocity v due to this distribution is given by

$$S(v) = \int_0^{H_{\max}} P(H)\, L_6(v, H)\, \mathrm{d}H, \tag{2}$$

where

$$L_6(v, H) = \sum_{i=1}^{6} \frac{1}{\pi} \frac{\Gamma_i/2}{(\Gamma_i/2)^2 + (v - \alpha_i H)^2}, \tag{3}$$

is the normalised Lorentzian shape function of the lines of a component spectrum for field H. Γ_i are the linewidths of the six lines of the component spectrum and $\alpha_i H$ are their positions. Equation (2) can be rewritten as

$$S(v) = \sum a_n \int_0^{H_{\max}} f_n(H)\, L_6(v, H)\, \mathrm{d}H,$$

$$= \sum_n a_n S_n(v), \tag{4}$$

where $$S_n(v) = \int_0^{H_{\max}} f_n(H)\, L_6(v, H)\, \mathrm{d}H$$

is the spectrum created by the term $f_n(H)$. If the experimental spectrum at velocity v is denoted by $W(v)$, the coefficients a_n of the field distribution can be found by minimizing the function

$$\phi = \sum_v [S(v) - W(v)], \tag{5}$$

with respect to the parameters a_n or other parameters like isomer shift if necessary. A χ^2 nonlinear least square fitting procedure is normally used to obtain the required coefficient a_n. This procedure is iterative and therefore time-consuming. If the isomer shift is also required to be obtained from a fit to the spectrum this procedure is justified. However in most systems when one is not concerned with relatively small isomer shift values exactly one can safely assume a constant isomer shift for all the elementary fields H. A good guess for this can usually be obtained from the centroid of the spectrum or from a spectrum above the Curie temperature. This then can be given as a fixed parameter.

3. Procedure

We get N simultaneous equations which are linear in a_n if we differentiate ϕ in (4), with respect to a_n's and set them equal to zero.

$$\phi = \sum_v \left[\sum_n a_n S_n(v) - W(v) \right]^2,$$

$$\frac{1}{2}\frac{\partial \phi}{\partial a_n} = \sum_v [S(v) - W(v)]\, S_n(v). \tag{6}$$

Differentiating once again w.r.t a_m

$$\frac{1}{2}\frac{\partial^2 \phi}{\partial a_m \partial a_n} = \sum_v S_m(v)\, S_n(v) = X_{mn} \text{ (say)}. \tag{7}$$

Substituting (7) in (6) and setting $\partial\phi/\partial a_n = 0$

$$\sum_m a_m X_{mn} - \sum_v W(v) = 0.$$

There are n such equations for $n = 1, 2 \ldots . N$.
Defining the matrices

$$\beta_n = \left[\sum_v W(v) S_n(v) \right],$$

$$X_{mn} = \left[\sum_v S_m(v) S_n(v) \right],$$

we get the matrix equation

$$aX = \beta.$$

This can be solved to get the matrix of the coefficients a_n

$$a = X^{-1}\beta.$$

A simple computer program can be written to set up the matrices X and β, finding the inverse of X and then calculating a. These coefficients can then be used to generate the field distribution $P(H)$.

4. Examples of use

A test usage of the program is illustrated in figures 1 and 2. In figure 1, spectrum A is the Mössbauer spectrum simulated for two Gaussian fields of equal intensity as shown in A'. The intensity ratios of the component spectra were constrained in the ratio 3:2:1:1:2:3 and the isomer shift fixed at zero. Using 5 terms in the fourier series expansion of $P(H)$ the field distribution obtained using the program outlined above is shown in B'. The two peaks are unresolved. When 10 terms are included in the Fourier series the distribution marked C' is obtained and the simulated and fitted spectrum agree very well as shown in C.

Figure 2 shows the experimental Mössbauer spectrum for an amorphous sample (Vitrovac 4040 from Vacuumschmelze GMBH, Hanau, Germany) together with the

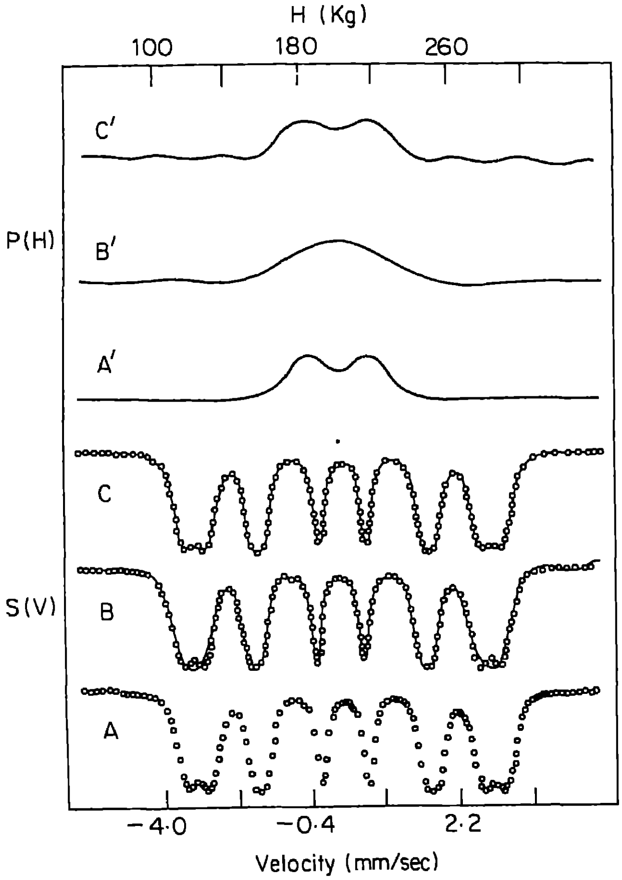

Figure 1. The Mössbauer spectrum A is simulated for two Gaussian peaks shown in A′. The field distribution B′ is obtained using the computer program described here when 5 terms are used in the Fourier series expansion of $P(H)$. The corresponding Mössbauer spectrum is shown in B. For 10 terms in $P(H)$ the distribution C′ is obtained and the corresponding fit is shown in C.

field distributions obtained using this program. In fitting such spectra there is uncertainty in the value of the intensity ratios to be chosen for the elementary spectra. One of the ways generally used is to vary the intensity ratio in the form $3{:}x{:}1{:}1{:}x{:}3$ and use that value of x which gives the best fit to the experimental spectrum. The field distributions for various x values are shown in figure 2. For a value $x = 2{\cdot}5$ one gets a good fit to the spectrum.

The number of terms in the Fourier series that should be retained in the expansion for $P(H)$ also has to be chosen carefully. For a small number of terms the resolution is poor. As seen in figure 1, the two Gaussian peaks are not resolved when only 5 terms are used but are seen separately for 10 terms in the expansion. However if the number of terms is made very large there occurs another difficulty. The distribution tries to fit the statistical fluctuation in data which are unphysical and thereby produces oscillations in the field distribution.

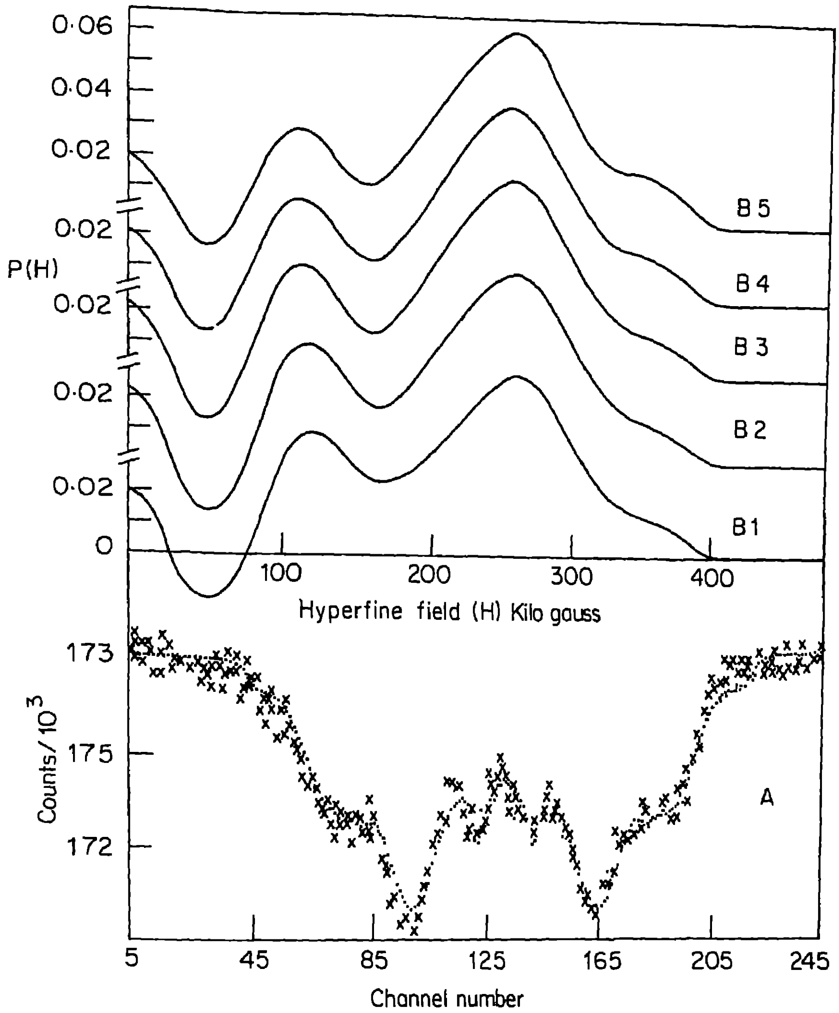

Figure 2. The experimental Mössbauer spectrum for Vitrovac 4040 sample (+) and fitted spectrum (·) for the field distribution in B2. The field distributions for various values of x (intensity ratio of 2nd and 5th lines relative to 3rd and 4th lines) are shown as B1 ($x = 2$), B2 ($x = 2{\cdot}5$), B3($x = 3$), B4($x = 3{\cdot}5$), B5($x = 4$).

5. Conclusions

The program described above is simple to write and can be simply modified to analyse spectra which have a paramagnetic single line in addition to distributions at higher velocities or for situations in which the baseline is parabolic. A listing of the program is available with us and has about 175 statements in Fortran IV.

Acknowledgement

The author is grateful to Dr R G Pillay of the TIFR, Bombay, for help in writing the program and testing it.

References

Bansal C, Ray J and Chandra G 1975 *J. Phys.* **F5** 1663
Bansal C and Chandra G 1979 *Phys. Rev.* **B20** 3357
Hesse J and Rübartsch A 1974 *J. Phys.* **E7** 526
LaCaer G and Dubois J M (1979) *J. Phys.* **E12** 1083
Logan J and Sun E 1976 *J. Noncryst. Solids* **20** 285
Window B 1971 *J. Phys.* **E4** 401
Wivel C and Morup S 1981 *J. Phys.* **E14** 605

Bull. Mater. Sci., Vol. 6, No. 6, December 1984, pp. 1053–1057. © Printed in India.

Spin wave relaxation processes in polycrystalline yttrium iron garnets

S N BHATIA, P B JOSHI and C M SRIVASTAVA

Department of Physics, Indian Institute of Technology, Powai, Bombay 400076, India

MS received 7 May 1983

Abstract. The wavevector and temperature dependence of the spinwave linewidth in yttrium iron garnets has been studied for polycrystalline samples of average grain diameter 12·8 μm and has been compared with the calculated relaxation times of basic three-magnon confluence and four-magnon scattering processes.

Keywords. Relaxation; spin-wave line-widths; yttrium iron garnets

1. Introduction

The nature of the intrinsic relaxation processes which determine the dissipative characteristics of magnetically ordered materials is well understood for the crystalline state (Gurevich and Anisimov 1975). The uniform precession mode which is created in the parallel pumping experiment loses its energy into the degenerate magnon modes. The small wavevector (k) magnons thus generated relax by the three-magnon confluence process ($3c$) while the larger k magnons, $4 \times 10^5 < k < 9 \times 10^5\,\mathrm{cm}^{-1}$, attain equilibrium *via* scattering involving four magnons ($4sc$). The splitting process requiring magnons of high frequencies is therefore restricted to $k > 10^6\,\mathrm{cm}^{-1}$. The observed temperature and k dependences of these processes have been established to be in accord with the theoretical results (Sparks 1967; Vaks *et al* 1968; Gurevich and Anisimov 1975). Such an understanding is lacking for the polycrystalline materials. Vrehan's (1966) transit time model has been used successfully by Patton (1970) and Scotter (1972) to explain the observed relaxation time for the $k \to 0$ limit in large grains but the model fails for finite k and small grain samples. An empirical relation based on the predictions of transit time model for the wavevector dependence of the spin-wave linewidth, obeyed by samples of grain size 1–12 μm has been arrived at by Prakash and Srivastava (1980). However no attempt appears to have been made to correlate such measurements with the fundamental processes involving the magnons. We have measured the spin-wave linewidths of polycrystalline YIG as functions of the wavevector and temperature for samples of various grain sizes and analysed them in terms of the basic scattering processes of the magnons.

2. Experimental

Polycrystalline YIG samples (densities > 99 % average grain diameter 0·9–12·8 μm) were prepared using the normal sintering and hot pressing techniques.

A high power microwave bench giving pulses of 4 μsec duration, 80 kW peak power with a repetition frequency of 50 pulses/sec and operating at microwave frequency 9·391 GHz was used to study the parallel pumping instability threshold (h_c) in these samples. A reflection-type rectangular cavity operating in TE_{104} mode was used and the sample was mounted at its $3\lambda g/2$ position in a vacuum-jacketed glass tube. Liquid nitrogen vapour was blown through this tube to regulate the sample temperature between 120 and 300 K.

3. Results

The instability threshold field (h_c) has been observed as a function of the applied magnetic field H_0. The spin-wave linewidth (ΔH_k) is calculated from h_c through the relation

$$h_c = (\omega_k/\omega_m)/(\Delta H_k/\sin^2\theta_k),$$

where ω_k is the operating frequency, $\omega_m = 4\pi\gamma M$ and θ_k is the angle between the direction of propagation of the spin-waves and H_0. The h_c *vs* H_0 curve was used to calculate ΔH_k up to $(h_c)_{\mathrm{min}}$, the corresponding k value being obtained from the standard dispersion relations. ΔH_k vs k curves for the grain size 12·8 μm are shown in figure 1. Temperature is displayed as a parameter on these curves.

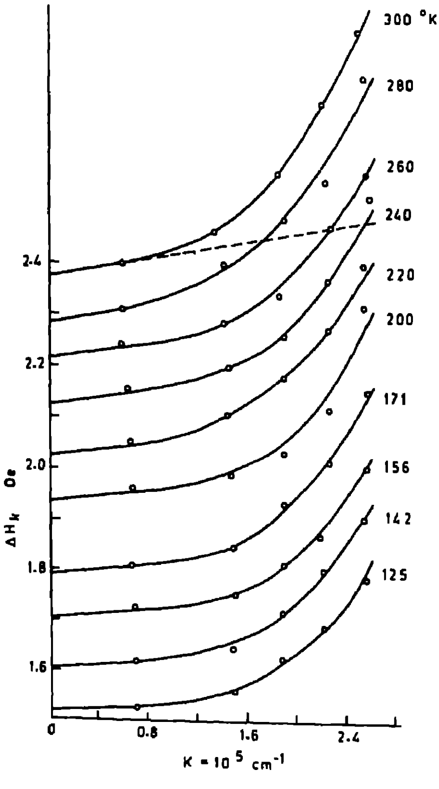

Figure 1. Wavevector dependence of the spin-wave line-width for polycrystalline YIG.

The striking feature of these curves is the nonlinear dependence of ΔH_k on k for all temperatures. This is in contrast to the linear dependence reported earlier (Patton 1970; Prakash and Srivastava 1980) and is attributed to the rather large range of k used in the present graphs. Over the limited range of $1{\cdot}5 \times 10^5 < k < 3 \times 10^5\,\mathrm{cm}^{-1}$ used in earlier studies, the present data also shows an almost linear dependence of ΔH_k on k. A similar linear dependence was also observed by White *et al* (1979) between 88 and 368 K. Their most dense sample appears to have lesser $4\pi M_s$ and therefore more porosity than ours. Pores could be the dominant scattering centres (Scotter 1972).

The initial portion of each curve however appears to be a straight line up to a certain value of the wavevector $k_{\min}$, after which the nonlinearities begin. $k_{\min}$ appears to decrease with increasing temperature. This initial portion of each graph was fitted to the equation,

$$\Delta H'_k = \Delta H_{k\to o}(T) + a(T)k. \tag{1}$$

After substracting $\Delta H'_k$ from the observed ΔH_k for $k > k_{\min}$, the difference $\Delta H_k - \Delta H'_k$ was fitted to

$$\Delta H_k - \Delta H'_k = b(T)k^2, \tag{2}$$

for each temperature. The observed variations of $a(T)$ and $b(T)$ with temperature are shown in figure 2. Also shown in this figure is the number of thermal magnons excited $n(T)$ which is linear with T as the energy of these magnons

$$\hbar w_k \simeq \gamma H_0 + Dk^2 \approx \gamma H_0 \approx 1, k_\beta \ll k_\beta T.$$

The increase in $a(T)$ and $b(T)$ with temperature can be attributed to the larger number of magnons present at higher temperatures. Two processes *viz* the three-magnon confluence and the four-magnon scattering brought on by the dipolar forces, show respectively a linear and a quadratic dependence on both k and T. Their respective contributions to ΔH_k for single crystals are

$$(\Delta H_k)_{3c} = \frac{\pi M \gamma k_B}{2D\omega_k} T k = C_{3c} T k, \tag{3}$$

$$(\Delta H_k)_{4sc} = \frac{1}{3\pi}\frac{\omega_k}{\gamma}\frac{k_\beta^2 T^2}{(4\pi MD)^2}\left(\ln\frac{\hbar w_k}{k_\beta T}\right)^2 k^2 \tag{4}$$

$$= C_{4sc} T^2 k^2.$$

These expressions are valid for magnons with predominant Zeeman energy ($Dk^2 \ll \gamma H_0$) and at high temperatures, ($\hbar\omega_k \ll k_\beta T$). As mentioned above both these conditions are valid here.

We notice from figure 2 that the coefficients $a(T)$ and $b(T)$ are roughly linearly and quadratically proportional to T suggesting that (1) and (2) could be representing the $3c$ and $4sc$ processes and consequently the proportionalities.

$$a(T) \propto C_{3c},$$

$$\text{and} \quad b(T) \propto C_{4sc}.$$

However (3) and (4) which are valid for single crystals cannot be used directly here for polycrystalline materials as their contributions to ΔH_k are an order of magnitude smaller than the experimentally observed values at all temperatures. Thus for

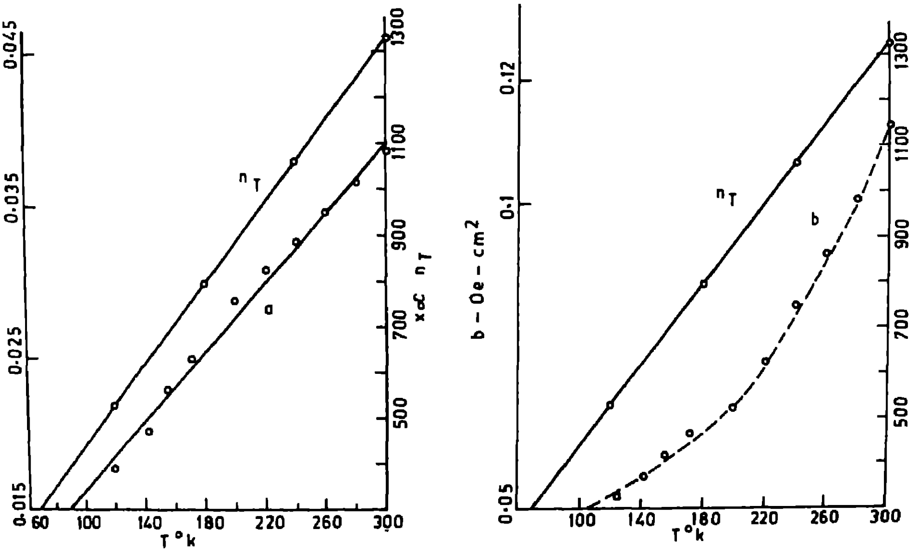

Figure 2. Temperature variation of the coefficients a and b. $n(T)$ is proportional to the number of thermal magnons excited at these temperatures.

$k = 2 \times 10^5\,\mathrm{cm}^{-1}$ experimental ΔH_k values are 0·2 and 0·1 Oe at 300 and 120 K respectively as against 0·02 and 0·004 Oe calculated for the 4*sc* processes. Thus it appears that in changing over from the single crystal to the polycrystalline materials, only the form of these expressions is preserved.

$\Delta H_{k \to 0}$ obtained from figure 1 is plotted against T in figure 3. Again a linear dependence on T is indicated with the data at the lowest temperatures showing some deviations from this line. This is again contrary to the observations of White *et al* (1979) who report an essentially temperature-independent ΔH_k, and is also contradictory to the transit time model. This dissipation parameter contains contributions which may depend upon k but do not vanish as $k \to 0$. In the present case, 3*c* and 4*sc* processes do not contribute to $\Delta H_{k \to 0}$. Major contribution to $\Delta H_{k \to 0}$ is stipulated to come from the Kasuya-LeCraw magnon-phonon processes (Sparks 1964) which show a similar temperature dependence. Here again magnitude-wise the observed $\Delta H_{k \to 0}$ is an order of magnitude larger than that predicted for single crystals (Sparks 1964). However more data at temperatures below 120 K are required to justify this association.

4. Conclusion

For the sample with average grain size 12·8 μm the dissipation processes occurring appear to be identical to those in single crystals with two major differences, (i) the minimum k value at which the 4*sc* processes start contribution is significantly smaller here ($k_{\min} < 1{\cdot}2 \times 10^5\,\mathrm{cm}^{-1}$ at 300 K) than in single crystals (typically $2 \times 10^5\,\mathrm{cm}^{-1}$) and (ii) the magnitudes of the contributions of the respective processes are an order of magnitude greater here than in single crystals. This increased scattering of magnons could be due to the grain boundaries present in the polycrystalline materials. This

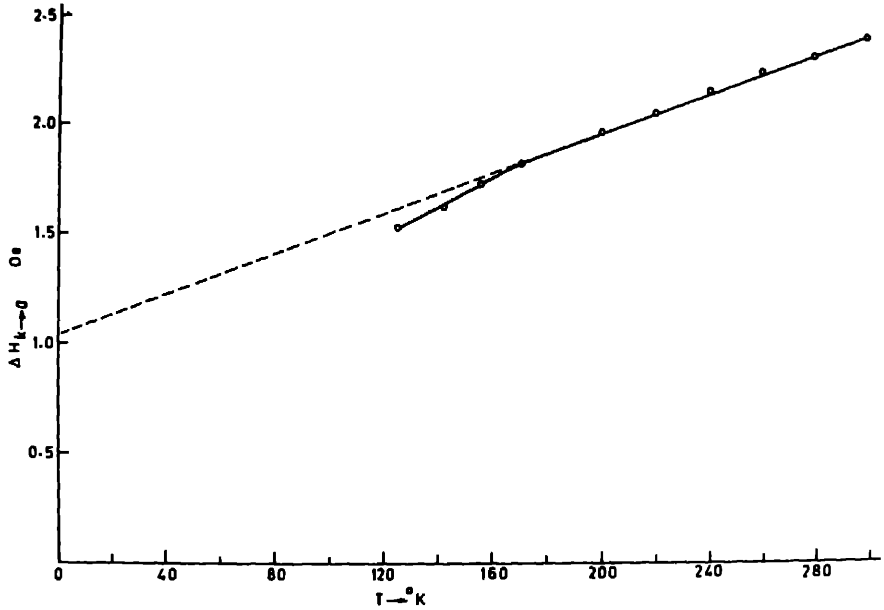

Figure 3. Temperature dependence of the spin-wave linewidth ΔH_k for $k \to 0$. Note the deviations from linearity at the lower temperatures.

scattering should be more intense in smaller grain samples where there are more boundaries which is in qualitative agreement with the previous observations of Prakash and Srivastava (1980). The details of this mechanism are being investigated.

References

Gurevich A G and Anisimov A N 1975 *Sov. Phys.* **41** 336
Patton C E 1970 *J. Appl. Phys.* **41** 1637
Prakash O and Srivastava C M 1980 *Bull. Mater. Sci.* **2** 181
Scotter D G 1972 *J. Phys.* **D5** L93
Sparks M 1967 *Phys. Rev.* **160** 364
Sparks M 1964 *Ferromagnetic relaxation theory* (New York: McGraw-Hill)
Vaks V G, Larkin A I and Pikin S A 1968 *Sov. Phys. JETP* **26** 647
Vrehans Q H F 1966 *J. Appl. Phys.* **40** 1849
White G, Patton C E and Edmondson 1979 *J. Appl. Phys.* **50** 2118

Bull. Mater. Sci., Vol. 6, No. 6, December 1984, pp. 1059–1062. © Printed in India.

Spin-wave excitations in amorphous ferromagnets

ANIL K BHATNAGAR, B BHANU PRASAD, N RAVI and
R JAGANNATHAN*

School of Physics, *School of Chemistry, University of Hyderabad, Hyderabad 500 134, India

MS received 7 May 1983

Abstract. Mössbauer measurements have been performed on a number of metallic glasses. The temperature dependence of average hyperfine or internal magnetic field $H_{\text{eff}}(T)$ arises from long wavelength spin wave excitations in these glasses. Values of $B_{3/2}$ and $C_{5/2}$ are in general much higher than those observed for crystalline ferromagnets indicating higher density of states for spin waves in amorphous ferromagnets.

Keywords. Spin wave excitations; amorphous ferromagnets; Mössbauer measurements; metallic glasses; temperature dependence.

1. Introduction

Amorphous metallic alloys, prepared by rapid quenching of molten alloys, have become an important class of materials from theoretical as well as practical points of view in recent years. There have been extensive studies of magnetic and electrical properties of iron-rich metallic glasses in the past decade. Study of magnetic phenomena in these glasses presents a fascinating field for theorists and experimentalists as magnetism is a structure sensitive property, and therefore, it is expected to be affected in amorphous solids. In this paper we discuss the temperature dependence of hyperfine magnetic field of iron-rich metallic glasses as measured by the ^{57}Fe Mössbauer spectroscopy. Results are interpreted in terms of excitations of long wavelength spin waves.

2. Experimental

Mössbauer spectra of a number of commercially available metallic glasses ($Fe_{81}B_{13.5}Si_{3.5}C_2$, $Fe_{78}B_{13}Si_9$, $Fe_{79}B_{16}Si_5$, $Fe_{40}Ni_{40}B_{20}$ and $Fe_{67}Co_{18}B_{14}Si_1$) were recorded in the temperature range 77–900 K using an Elscint spectrometer coupled with a 256 channel MCA. The spectrometer was used in the constant acceleration mode and the source was ^{57}Co in rhodium matrix. The Curie temperatures of $Fe_{81}B_{13.5}Si_{3.5}C_2$, $Fe_{78}B_{13}Si_9$, $Fe_{40}Ni_{40}B_{20}$ and $Fe_{79}B_{16}Si_5$ were determined by the constant Doppler velocity thermal-scan method (Bhanu Prasad *et al* 1983), while that of $Fe_{67}Co_{18}B_{14}Si_1$ was estimated by plotting hyperfine magnetic field, $H_{\text{eff}}(T)$ *vs* temperature since the Curie temperature, T_c, in this case was larger than the crystallization temperature (Bhanu Prasad *et al* 1980). $H_{\text{eff}}(T)$ values were determined by fitting each spectrum to the Lorentzian line-shape sextet pattern. The spectrometer was calibrated using a thin iron foil.

3. Results and discussion

The decrease in magnetization of a crystalline ferromagnet at low temperatures can be explained if the low lying magnetic excitations are spin waves which obey the following dispersion relation:

$$\hbar w(q) = Dq^2 + Eq^4 + \dots \tag{1}$$

where $\hbar w(q)$ is the energy of spin wave with propagation wave number q, and D and E are the stiffness constants. Usually E is much smaller than D. This dispersion relation leads to the following temperature dependence of magnetization $M(T)$,

$$M(T) = M(O)(1 - BT^{3/2} - CT^{5/2} - \dots), \tag{2}$$

where B and C are constants and are related to D and E as given below.

$$B = 2{\cdot}612[g\mu_B/M(O)]\,(k_B/4\pi D)^{3/2} \tag{3}$$

$$C = 1{\cdot}341[g\mu_B/M(O)]\,(k_B/4\pi D)^{5/2}(15\pi E/D) \tag{4}$$

where k_B is the Boltzmann constant, μ_B is the Böhr magneton and g is the usual g factor. Equation 2 can be rearranged to give

$$\frac{M(T) - M(O)}{M(O)} = -BT^{3/2} - CT^{5/2} - \dots \tag{5}$$

or

$$\frac{M(T) - M(O)}{M(O)} = -B_{3/2}(T/T_c)^{3/2} - C_{5/2}(T/T_c)^{5/2} - \dots \tag{6}$$

Inelastic neutron scattering measurements on some of amorphous ferromagnets have established the existence of long wavelength spin waves obeying the dispersion relation given by (1) (Lynn *et al* 1976; Rhyne *et al* 1979). Similarly magnetization measurements (Tsuei *et al* 1968; Kaul 1981) and ferromagnetic resonance studies (Spano and Bhagat 1981) have shown that the temperature dependence of $M(T)$ follows the behaviour predicted by (2).

From Mössbauer measurements the average internal magnetic field $H_{\text{eff}}(T)$ is determined. It has been found experimentally that for most iron-rich metallic glasses, the average internal magnetic field is directly proportional to the magnetization to a good approximation and the proportionality constant is approximately 135 kOe/μ_B (Chien *et al* 1979). Therefore, (5) and (6) can be expressed in terms of $H_{\text{eff}}(T)$ as follows:

$$\frac{H_{\text{eff}}(T) - H_{\text{eff}}(O)}{H_{\text{eff}}(O)} = -BT^{3/2} - CT^{5/2} - \dots \tag{7}$$

or

$$\frac{H_{\text{eff}}(T) - H_{\text{eff}}(O)}{H_{\text{eff}}(O)} = -B_{3/2}(T/T_c)^{3/2} - C_{5/2}(T/T_c)^{5/2} - \dots \tag{8}$$

where B, C, $B_{3/2}$, and $C_{5/2}$ constants remain the same as in (5) and (6). Thus the temperature dependence of $H_{\text{eff}}(T)$ at low temperatures can also be interpreted in terms of excitations of spin waves. At first it may seem surprising that spin waves can be excited in noncrystalline solids. However, the situation is quite akin to the sound wave propagation in glasses. This is so because the long wavelength modes are not sensitive to the local order or disorder. In particular Herring and Kittel (1951) have shown that long wavelength spin waves can exist even in a ferromagnetic continuum medium.

Average hyperfine magnetic fields of various metallic glasses were determined as explained in § 2. A plot of $[H_{\text{eff}}(T) - H_{\text{eff}}(O)]/H_{\text{eff}}(O)$ *vs* $(T/T_c)^{3/2}$ for various metallic glasses is shown in figure 1. A computer least square fit of (7) and (8) to experimental data yields values of B, C, $B_{3/2}$ and $C_{5/2}$ which are given in table 1. For sake of comparison, the values of these constants for crystalline Fe and Ni, and glassy $Fe_{40}Ni_{40}P_{14}B_6$, $Fe_{80}B_{20}$ and $Fe_{82}B_{12}Si_6$ are also listed in the table. It is observed that $B_{3/2}$ values range from 0·2–0·4 and are much larger than the values for crystalline Fe and Ni. Also $T^{3/2}$ dependence of relative change in $H_{\text{eff}}(T)$ extends to much higher temperatures than observed for crystalline ferromagnets. $T^{3/2}$ plus $T^{5/2}$ dependence, as given by (7) and (8), can be fitted to experimental data over a large temperature interval. Values of $B(B_{3/2})$ and $C(C_{5/2})$ depend upon the temperature interval used to fit the data (Bhatnagar *et al* 1982; Saegusa and Morrish 1982). If data is fitted over a large temperature interval then it has the effect of reducing the $B(B_{3/2})$ value and increasing the $C(C_{5/2})$ value which is expected. It has also been observed that B and C values

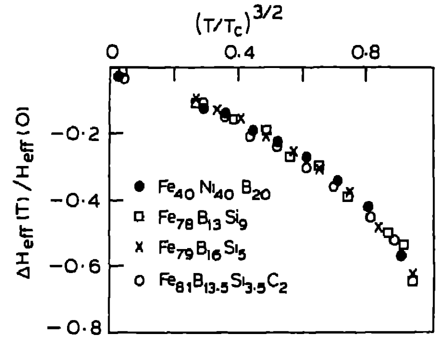

Figure 1. Plot of $[H_{\text{eff}}(T) - H_{\text{eff}}(O)]/H_{\text{eff}}(O)$ vs $(T/T_c)^{3/2}$ for various iron-rich metallic glasses.

Table 1. Sample compositions, Curie temperature T_c, coefficients B, C, $B_{3/2}$ and $C_{5/2}$ for amorphous ferromagnets and crystalline Fe and Ni.

System	T_c(K)	$B(10^{-6}K^{-3/2})$	$C(10^{-8}K^{-5/2})$	$B_{3/2}$	$C_{5/2}$	Reference
$Fe_{80}B_{20}$	685	22	1·2	0·40	0·17	Chien (1978)
$Fe_{40}Ni_{40}B_{20}$	695	22	0·4	0·40	0·06	Present work
$Fe_{40}Ni_{40}P_{14}B_6$	537	38	1·2	0·47	0·08	Chien and Hasegawa (1977)
$Fe_{78}B_{13}Si_9$	733	10	2·4	0·21	0·35	Present work
$Fe_{79}B_{16}Si_5$	730	11	2·3	0·22	0·33	Present work
$Fe_{82}B_{12}Si_6$	658	—	—	0·34	0·21	Ok and Morrish (1980)
$Fe_{81}B_{13.5}Si_{3.5}C_2$	698	16	2·1	0·30	0·27	Present work
$Fe_{81}B_{13.5}Si_{3.5}C_2$	668	—	—	0.30	0.29	Saegusa and Morrish (1982)
Crystalline Fe	1042	3·4	0·1	0·114	0·04	Chien and Hasegawa (1977)
Crystalline Ni	637	7·5	1·5	0·117	0·15	Chien and Hasegawa (1977)

become much smaller after the amorphous material crystallizes (Hasegawa and Ray 1979). Hence, the high $B(B_{3/2})$ and $C(C_{5/2})$ values seem to be the characteristic of the amorphous state. Higher B values in glassy ferromagnets also mean lower values of D, the stiffness constant, for glassy systems as seen from (3). Lower values of D also mean that the density of states for spin waves are higher in the amorphous state. Theoretical calculations do show higher density of states for spin waves in amorphous materials due to fluctuations in the exchange interaction arising from the random atomic arrangement (Montgomery *et al* 1970; Simpson 1974). Thus the existence of spin wave excitations in amorphous ferromagnets is clearly demonstrated by Mössbauer measurements as well as by magnetization (Kaul 1981) and inelastic neutron scattering measurements (Lynn *et al* 1976; Axe *et al* 1977; Rhyne *et al* 1979).

4. Conclusion

The temperature dependence of the average internal magnetic field of a number of ferromagnetic metallic glasses can be described by the expression $H_{\text{eff}}(T) = H_{\text{eff}}(O)$ $(1 - BT^{3/2} - CT^{5/2} - \ldots)$, which is indicative of spin wave excitations in these solids. Values of $B(B_{3/2})$ are much higher than those for crystalline Fe, Ni etc. This observation can be explained if higher density of states for spin waves are assumed in the amorphous ferromagnets. Values of $B(B_{3/2})$ and $C(C_{5/2})$ are found to depend upon the temperature interval used to fit experimental data to the $T^{3/2}$ and $T^{5/2}$ dependence.

Acknowledgements

Authors thank the Science and Engineering Research Council (DST, India) and the Department of Atomic Energy for support.

References

Axe J D, Shirane G, Mizoguchi T and Yamauchi K 1977 *Phys. Rev.* **B15** 2763

Bhanu Prasad B, Bhatnagar A K and Jagannathan R 1980 *Solid State Commun.* **36** 661

Bhanu Prasad B, Bhatnagar A K and Jagannathan R 1983 *J. Appl. Phys.* **54** 2019

Bhatnagar A K, Bhanu Prasad B, Ravi N, Jagannathan R and Anantharaman T R 1982 *Solid State Commun.* **44** 905

Chien C L 1978 *Phys. Rev.* **B18** 1003

Chien C L and Hasegawa R 1977 *Phys. Rev.* **B16** 2115

Chien C L, Musser D, Gyorgy E M, Sherwood R C, Chen H S, Luborsky F E and Walter J L 1979 *Phys. Rev.* **B20** 283

Hasegawa R and Ray R 1979 *Phys. Rev.* **B20** 211

Herring C and Kittel C 1951 *Phys. Rev.* **81** 869

Kaul S N 1981 *Phys. Rev.* **B24** 6550

Lynn J W, Shirane G, Birgeneau R J and Chen H S 1976 *AIP Conf. Proc.* **34** 313

Montgomery C G, Krugler J I and Stubbs R M 1970 *Phys. Rev. Lett.* **25** 669

Ok H N and Morrish A H 1980 *Phys. Rev.* **B22** 4215

Rhyne J J, Lynn J W, Luborsky F E and Walter J L 1979 *J. Appl. Phys.* **50** 1583

Saegusa N and Morrish A H 1982 *Phys. Rev.* **B26** 10

Simpson A W 1974 *Wiss Z. dTH Dresden* **3** 1020

Spano M L and Bhagat S M 1981 *J. Magn. Mag. Mater.* **24** 143

Tsuei C C, Longworth G and Lin S C H 1968 *Phys. Rev.* **170** 603

Bull. Mater. Sci., Vol. 6, No. 6, December 1984, pp. 1063–1067. © Printed in India.

Infrared absorption in spinel ferrites

T T SRINIVASAN, C M SRIVASTAVA, N VENKATARAMANI* and M J PATNI*

Department of Physics, *Materials Science Centre, Indian Institute of Technology, Powai, Bombay 400 076, India

MS received 31 May 1983

Abstract. The IR spectra of a number of ferrites, MFe_2O_4, M(Mn, Fe, Co, Ni, Cu and Zn) have been studied at room temperature in the range 200–1000 cm^{-1}. In all the cases the spectrum consists of four bands, two of which have strong absorption while the other two have weak absorption and often appear as shoulders on the main band. However up to 20 % of the inverse ferrite, the shoulder in the low energy side appears as a band. In this paper we have analysed the origin of the above bands.

Keywords. IR spectrum; ferrites; centre frequency; force constants.

1. Introduction

Infrared spectrum of ferrites has been studied by Waldron (1955). The effect of a Jahn-Teller ion on the lattice vibrational frequencies of nickel ferrite has also been studied by Srivastava and Srinivasan (1982). Waldron has assumed that the 14 atoms in the primitive unit cell of a spinel lattice can be divided into two MO_4 groups and one Fe_4 group of tetrahedral symmetry. This allows the classification of the vibrations into the point group T_d. The conclusions reached by him are not very satisfactory. For example, the force constants K_t for the *t–o* bond for the normal ferrite $ZnFe_2O_4$ and $MnFe_2O_4$ are substantially smaller than that for the inverse spinels like Co, Fe and Ni ferrites. The normal ferrites are formed due to the strong tetrahedral site preference of the divalent ions like Zn^{2+}. As the size of the Zn^{2+} (0·74 Å) ion is larger than the Fe^{3+} (0·64 Å) ion, the overlap and strength of the *t–o* bond is expected to be greater for $ZnFe_2O_4$ than say for Fe_3O_4. We would therefore expect that the increased covalency in the bond would more than compensate for the decrease in the electrostatic energy due to the change for 3+ and 2+ state of the metal ion. Further each of the two broad bands showed asymmetry in the line shape. Waldron (1955) has also reported the presence of low as well as high frequency shoulders in his observations. We have analysed them as additional vibrational modes of the system. The IR frequencies are given in tables 1 and 2.

2. Experimental

The samples were prepared using the normal conventional ceramic technique. All the samples had densities higher than 97 % of their x-ray density. The x-ray analysis showed a single phase and a spinel structure.

Table 1. IR spectral frequencies of ferrites.

MFe_2O_4	Centre frequency (linewidth) cm^{-1}			
M =	T_2^o	T_2^t	E^o	E^t
Mn	330 (88)	400 (100)	545 (78)	640 (90)
Fe*	350 (62)	410 (55)	590 (78)	640 (100)
Co*	340 (67)	390 (50)	570 (75)	650 (78)
Ni	340 (105)	396 (40)	587 (100)	660 (110)
Cu	330 (70)	400 (90)	565 (80)	620 (75)
Zn	338 (105)	415 (120)	550 (85)	660 (160)

*Waldron's (1955) data.

Table 2. IR spectral frequencies of $Zn_{1-x}Ni_xFe_2O_4$ $(0 \leqslant x \leqslant 1)$.

x	Centre frequency of (cm^{-1})			
	T_2^o	T_2^t	E^o	E^t
0	338	415	550	660
0·02	338	415	555	670
0·04	338	420	553	670
0·06	340	420	555	670
0·08	338	421	555	670
0·15	340	421	559	670
0·2	340	422	562	670
1	340	396	587	660

The ferrite powders were dispersed in KBr and pressed to get a clear disc. The spectra in the range of 200–1000 cm^{-1} were recorded at room temperature (SP 2000 IR Spectrameter, TYPE UNICHEM make). In order to examine the effect of the transformation from the normal to the inverse ferrite on the lattice modes of vibration we have studied the IR spectra of $Zn_{1-x}Ni_xFe_2O_4$ $[0 \leqslant x \leqslant 0{\cdot}2$ and $x = 1]$. These are shown in figure 1. The spectrum has been analysed in terms of four bands, each having a Lorentzian shape.

3. Analysis and discussion

Our observations show that the spectrum in all the cases consists of four bands, two of which have strong absorption. The remaining two have weaker absorption, and in some

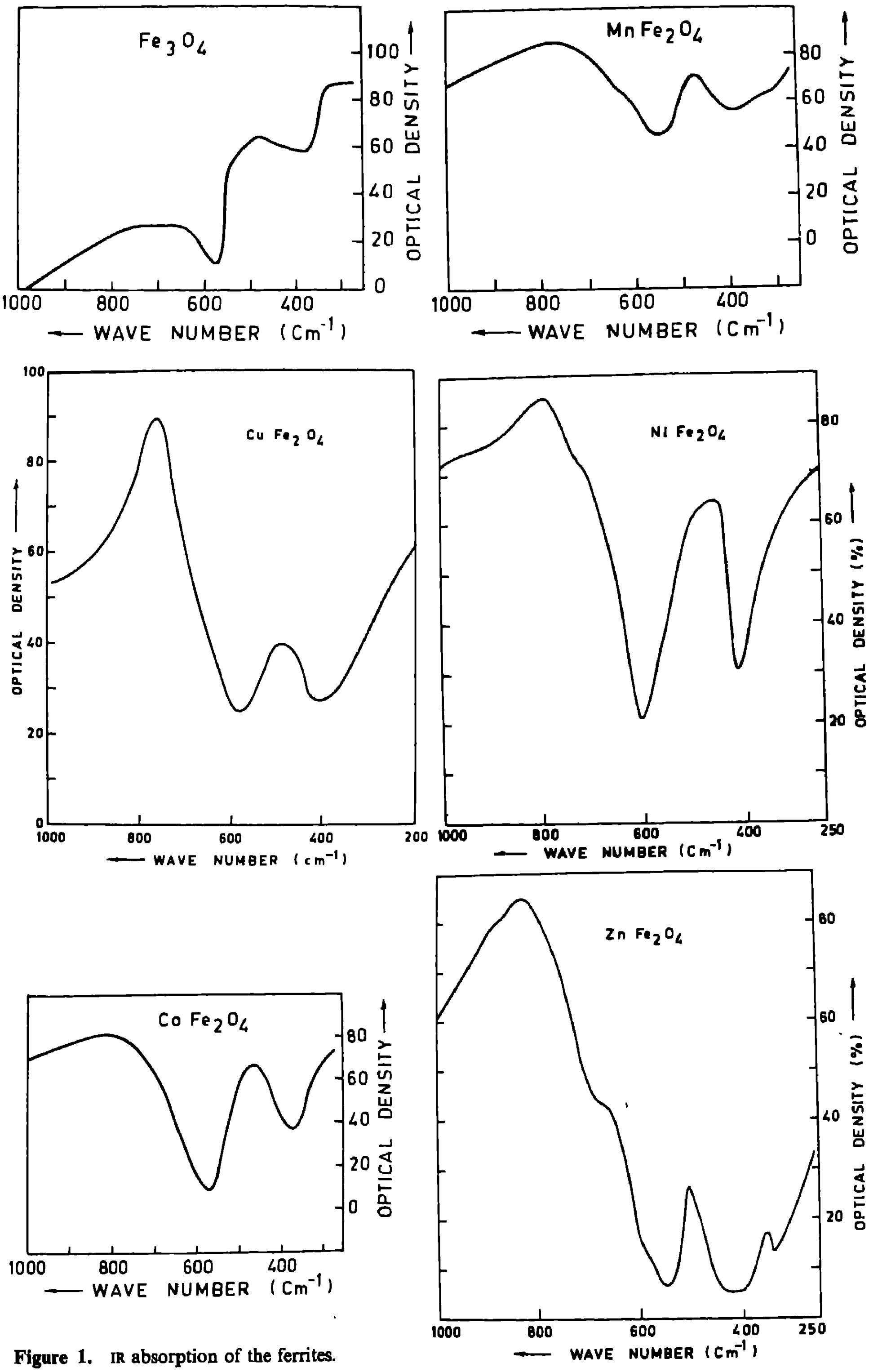

Figure 1. IR absorption of the ferrites.

cases appear as a shoulder to the main bands. We have attributed these to the absorption by lattice vibrations having E and T_2 symmetries. These type of phonon modes have been assumed by Bates and Steggles (1975) for the analysis of EPR data in Fe^{2+} in Al_2O_3. As there are two types of metals in the sites, we have E^o, E^t, T_2^o and T_2^t phonon modes where the superscripts '*o*' and '*t*' indicate the E and T_2 symmetry of the atomic displacements around the octrahedral and tetrahedral metal ions. The bands were identified on the systematics of the observed central frequencies as the metal ion M was changed from d^5 to d^{10} configurations. The frequency increases in the following order

$$\nu(T_2^o) < \nu(T_2^t) < \nu(E^o) < \nu(E^t).$$

It is difficult to assign the precise nature of atomic displacements for these modes of vibrations. We assume that those of the T_2 type would be bond-bending while the E type would be bond-stretching so that in general $\nu(T_2) < \nu(E)$. Again we would assume that the bond stretching for tetrahedral site would lead to a higher force constant than that for the octrahedral site. On this basis we would be able to assign the bands in the order given in tables 1 and 2. The IR frequencies as a function of the number of d electrons in M^{2+} ion are plotted in figure 2. It is seen that with an assignment the stretching mode of the tetrahedral *t–o* bond (E^t) has a larger value for $ZnFe_2O_4$ as compared to others. This mode however has a relatively weak absorption. The stretching modes (E^o) for the normal Mn and Zn ferrites have identical frequencies as these have only Fe^{3+} ions on the B-site. The bond stretching modes (E^o) on the B-site have a strong absorption. For Ni^{2+}, it shows a higher frequency and a narrow band. This seems to be related to the ground singlet state of the ion. Even T_2^t bands in this ferrite ($\Delta\nu \approx 40\,cm^{-1}$) is narrower as compared to others. The bond-bending frequencies T_2^t and T_2^o are nearly the same as expected. In table 2 the variation of centre frequencies as one goes from normal ferrite ($ZnFe_2O_4$) to inverse ferrite ($NiFe_2O_4$) is given for all the four bands.

In an inverse ferrite the octahedral site is occupied by Fe^{3+} and the divalent ion M^{2+}. Due to charge imbalance the oxygen ion is likely to shift towards the Fe^{3+} ion making

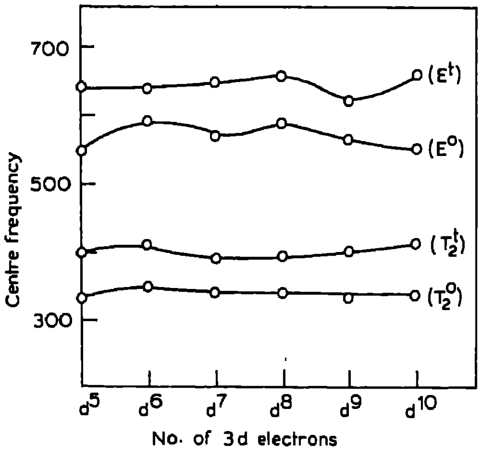

Figure 2. IR frequencies as a function of the number of d electrons in $M^{2+}(MFe_2O_4)$.

the force constant between Fe^{3+} and O^{2-} more. Hence we expect an increase in the bond stretching E^o phonon mode, frequencies as we go from normal to inverse spinels. This is supported by our results on $Zn_{1-x}Ni_xFe_2O_4$ in which we find that $\nu(E^o)$ increase as x is increased and the others T_2^o, T_2^t and E^t do not change with the type of spinel structure, given in table 2.

4. Conclusions

IR spectrum of spinel ferrites in the range of 200–1000 cm^{-1} consists four bands. These bands have been assigned on the basis of E and T_2 phonon symmetries around the crystallographic metal ion sites, A and B. On gradual change from normal to inverse spinel structure only one of the bands is affected as expected.

References

Bates C A and Steggles P 1975 *J. Phys.* **C8** 2283
Srivastava C M and Srinivasan T T 1982 *J. Appl. Phys.* **53** 8148
Waldron R D 1955 *Phys. Rev.* **99** 1727

Bull. Mater. Sci., Vol. 6, No. 6, December 1984, pp. 1069–1074. © Printed in India.

Influence of spin orbit coupling and lanthanide contraction on the exchange interaction in rare earth garnets

C M SRIVASTAVA, C SRINIVASAN and R AIYAR

Department of Physics, Indian Institute of Technology, Bombay 400076, India

MS received 7 May 1983

Abstract. The exchange constants observed in the rare earth iron garnets, obtained from fitting magnetization and paramagnetic susceptibility as a function of temperature have been analysed in terms of Anderson's theory of superexchange. The transfer integrals and covalency parameters have been obtained for various rare earth ions overlapping with oxygen.

Keywords. Exchange constants; superexchange; transfer integrals; covalency parameters; molecular field constants.

1. Introduction

In an earlier paper (Srivastava *et al* 1982) we had reported the simultaneous fitting of saturation magnetisation (M_s) and paramagnetic susceptibility (χ) for the ferrimagnetic garnets $R_3Fe_5O_{12}$ where R is yttrium or a trivalent rare earth ion with configuration $(Xe)\ 4f^n$ ($7 \leqslant n \leqslant 13$). We had used the molecular field constants to determine the exchange constants by means of the equation

$$J_{ij} = \frac{g_i g_j \mu_B^2 n_j \lambda_{ij}}{2Z_{ij}}, \tag{1}$$

where g_i, g_j are the g factors of the sublattices i and j, λ_{ij} are the molecular field constants, n_j is the number of j ions per unit mole and Z_{ij} is the number of $n-nj$ ions to an ion on ith sublattice. But if one of the ions involved is a rare earth ion then (1) is not the correct expression to convert the molecular field constants to J_{ij}. This is because for the rare earths the orbital momentum is not quenched and hence the exchange energy is

$$E_i = -2n_j Z_{ij} J_{ij}(g_i - 1)\bar{J}_i \cdot \bar{S}_j. \tag{2}$$

Here, we have assumed that the ith ion is a rare earth and the factor $(g_i - 1)$ comes because the rare earth spin has to be projected on J_i the angular momentum. In terms of λ_{ij}, E_i is given by

$$\begin{aligned} E_i &= -\mu_i \cdot \mu_j = -g_i \bar{J}_i \mu_B \cdot \lambda_{ij} \bar{M}_j, \\ &= -n_j g_i g_j \mu_B^2 n_j \lambda_{ij}\ \bar{J}_i \cdot \bar{S}_j \end{aligned} \tag{3}$$

From (2) and (3) we get

$$J_{ij} = \frac{g_i g_j \mu_B^2 n_j \lambda_{ij}}{2Z_{ij}(g_i - 1)}. \tag{4}$$

Table 1. Exchange constants (°K) in garnets ($R_3Fe_5O_{12}$).

	Values in °K		
R	$-J_{ac}$	$-J_{dc}$	$-J_{cc}$
Y	0	0	0
Gd	0·60	1·8	0
Tb	1·12	2·0	0
Dy	2·97	2·97	−0·9
Ho	2·64	2·80	0
Er	2·70	3·40	0
Tm	2·64	3·96	0
Yb	21·00	16·1	−0·2

The $-J_{aa}$, $-J_{ad}$ and $-J_{dd}$ values are 6·45, 30·40 and 12·05 respectively in all the cases.

Equation (4) differs from (1) because of the factor $(g_l - 1)$ in the denominator. Hence the exchange constants have to be corrected by dividing the values reported earlier (Srivastava *et al* 1982) by $(g_i - 1)$ where g_i is the g factor of the rare earth site. These are shown in table 1.

2. Exchange constants from Anderson's theory

We give below the calculation of exchange constants from Anderson's theory of superexchange for these garnets. For the exchange between a rare earth and Fe^{3+} ions in garnets Levy (1966) has shown that if the Z axis for the interaction is chosen as the RE-O^{2-} bond direction then the only orbital on the RE ion contributing to the exchange is the one with $m_l = 0$ (*i.e.* f_{z^3} orbital). Following the same convention we find that the only transfer integral in Anderson's expression for 180° superexchange interaction is $b_{\sigma\sigma}$ arising from the overlaps of f_{z^3} orbital on RE ion and $e_g(d_{z^2})$ on Fe^{3+} with a p_z orbital on the O^{2-} ion. Similarly the only transfer integral for the 90° exchange is $b_{\pi\sigma}$ arising from overlaps of t_{2g} and f_{z^3} orbitals with p_z orbital on oxygen. Thus we have (ignoring direct overlap of magnetic orbitals)

$$J_{ij} = -\frac{1}{4(g_i - 1)\, J_i S_j} 2 \frac{b_{\sigma\sigma}^2}{U} \text{ for 180° superexchange} \tag{5a}$$

$$J_{ij} = -\frac{1}{4(g_i - 1)\, J_i S_j} 2 \frac{b_{\pi\sigma}^2}{U} \text{ for 90° superexchange} \tag{5b}$$

In rare earths the spin orbit interaction is very strong compared to the crystal field energy, hence the ground state wavefunction will have admixtures of states with all values of m_l. However, as explained above only the $m_l = 0$ state contributes to the superexchange. Hence if we assume that all the m_l states have equal probability of being occupied then the probability that the state $m_l = 0$ has unpaired electron is $1 - (n - 7)/7 = 2 - (n/7)$ where n is the number of electrons in the $4f$ shell ($n \geqslant 7$). Using this in (5) and noting that J_{ac} is a predominantly 90° exchange while J_{dc} is a 180°

exchange we get for a $f^n - d^5$ superexchange interaction

$$J_{dc} = -\frac{1}{4(g_i - 1)\,J_i S_j}\,2\frac{b^2_{\sigma\sigma}}{U}\left(2 - \frac{n}{7}\right), \tag{6a}$$

$$J_{ac} = -\frac{1}{4(g_i - 1)\,J_i S_j}\,2\frac{b^2_{\pi\sigma}}{U}\left(2 - \frac{n}{7}\right). \tag{6b}$$

The values of the coulomb energy can be estimated by a procedure used by Anderson (1959) to evaluate U for the $3d$ series transition metal ions. Taking the free ion ionisation potential (IP) for these ions we find that $I_4 - I_3$ *i.e.* the difference between the 4th and 3rd IP gives the free ion U. This has to be corrected in the solid. Firstly the transfer of electrons take place through a finite distance and not to infinity as is the case for calculating IP. Anderson estimated this correction to be 4 eV for $3d$ electrons. We shall assume the same correction for R^{3+} ions. The next correction is the dielectric polarisation correction because the coulomb repulsion takes place in a dielectric medium and not in vacuum. This gives another correction of 4 eV. Finally because of covalency another 10 % correction is required. Using the IP calculated by Sugar and Reader (1973) and using the above method we get $U = 10\,\text{eV} \pm 1\,\text{eV}$ for all the rare earth ions except Gd^{3+} as shown in table 2. Since the ground state of Gd^{2+} is $5d^2f^7$ and not f^8, the U value for Gd will reduce if the correct IP for $4f^7$——f^8 transition is taken Hence we can assume $U = 10$ eV for all the heavy rare earths. Using (4) instead of (1) as was used in our earlier work (Srivastava *et al* 1982) to get the correct values of J_{ij} we have obtained the values of $b_{\sigma\sigma}$ and $b_{\pi\sigma}$ using (7) for all these garnets which are given in table 3. In table 3 we also give the distance of closest approach of the rare earth and oxygen orbitals

$$S^{-1} = \frac{r_{R\text{-}O} - (r(R^{3+}) + r(O^{2-}))}{r(R^{3+}) + r(O^{2-})}.$$

The values of $r_{R\text{-}O}$, $r(R^{3+})$, $r(O^{2-})$ are from Tchéou *et al* (1970), Khattak and Yang (1979) and CRC handbook (1980) respectively. Figure 1 gives a plot of b^2 against S^{-1} for both $b^2_{\sigma\sigma}$ and $b^2_{\pi\sigma}$. This curve resembles the curve obtained by Slater (1953) for metals. However, $b^2_{\sigma\sigma}$ does not show the peak in the observed region of overlap. Yb does not fit in the above scheme because as shown by Copland (1970) the $5p$ shell plays a

Table 2. Coulomb energy U (eV) for rare earth ions.

Ion	Ionisation potential (eV) I_3	Ionisation potential (eV) I_4	Free ion $U = I_4 - I_3$ (eV)	Corrected U (eV)	Covalency correction (10%)	Corrected U in solid (eV)
Gd	20·63	44·01	23·78	15·38	1·54	13·84
Tb	21·91	39·79	12·88	9·88	0·99	8·89
Dy	22·79	41·47	18·68	10·68	1·07	9·61
Ho	22·84	42·48	19·64	11·68	1·17	10·57
Er	22·74	42·65	19·91	11·91	1·19	10·92
Tm	23·68	42·69	19·01	11·01	1·10	9·91
Yb	25·03	43·74	18·71	10·71	1·07	9·64

The correction for $n - n$ and dielectric polarization was 8 in all the cases.

Table 3. Transfer integrals in garnets $R_3Fe_5O_{12}$.

R	J_l	$b^2_{\sigma\sigma}$ $(\mathrm{eV})^2$	$b^2_{\pi\sigma}$ $(\mathrm{eV})^2$	S^{-1} $\dfrac{r(R\text{–}O)-r(R^{3+})-r(O^{2-})}{r(R^{3+})+r(O^{2-})}$
Gd	3·5	0·0271	0·0091	0·016
Tb	6·0	0·0295	0·0168	0·022
Dy	7·5	0·0448	0·0448	0·024
Ho	8·0	0·0419	0·0398	0·026
Er	7·5	0·0513	0·0408	0·032
Tm	6·0	0·0596	0·0398	0·035
Yb	3·5	0·0240	1·15	0·037

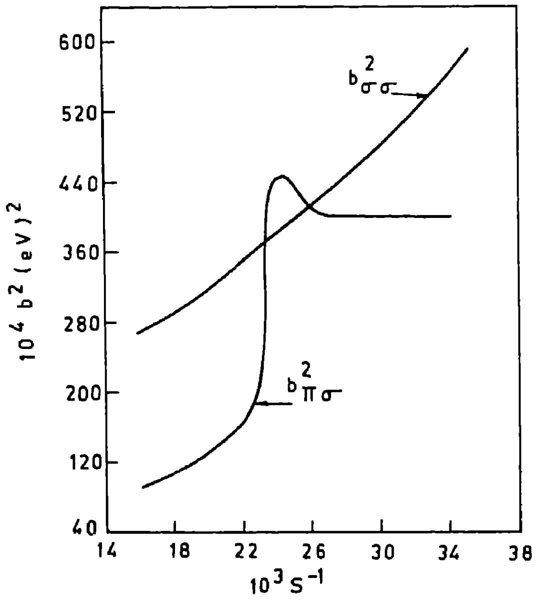

Figure 1. Transfer integrals in garnets.

dominant role in superexchange in YbIG, unlike the other garnets where the 4*f* shell is the dominant orbital contributing to superexchange.

3. Covalency parameters

Zeiger and Pratt (1973) have shown that the transfer integrals b_{ij} are related to the covalency parameters λ_{ic} and λ_{jc}, where c refers to the intervening anion by

$$b_{ij} = \lambda_{ic}\lambda_{jc}\Delta E_c$$

where ΔE_c is the one electron ionization energy of the anion. For the Fe^{3+}-Fe^{3+}

Table 4. Covalency parameters and transfer integrals in garnets.

	Type of exchange	Transfer integral	Value of b_k(eV)	λ_σ (Fe^{3+}-O^{2-})	λ_π (Fe^{3+}-O^{2-})	λ_σ (R^{3+}-O^{2-})
Fe^{3+}	J_{ad}	$b_{\sigma\sigma}$	0·48	0·24		
		$b_{\pi\pi}$	0·18		0·14	
		$b_{\sigma\sigma'}$	0·12	0·12		
	J_{dd}	$b_{\pi\sigma}$	0·30	0·25	0·14	
Gd^{3+}	J_{ac}	$b_{\pi\sigma}$	0·095		0·14	0·078
	J_{dc}	$b_{\sigma\sigma}$	0·16	0·25		0·08
Tb^{3+}	J_{ac}	$b_{\pi\sigma}$	0·13		0·14	0·107
	J_{dc}	$b_{\sigma\sigma}$	0·17	0·25		0·08
Dy^{3+}	J_{ac}	$b_{\pi\sigma}$	0·21		0·14	0·17
	J_{dc}	$b_{\sigma\sigma}$	0·21	0·25		0·098
HO^{3+}	J_{ac}	$b_{\pi\sigma}$	0·20		0·14	0·16
	J_{dc}	$b_{\sigma\sigma}$	0·20	0·25		0.094
Er^{3+}	J_{ac}	$b_{\pi\sigma}$	0·20		0·14	0·17
	J_{dc}	$b_{\sigma\sigma}$	0·22	0·25		0·105
Tm^{3+}	J_{ac}	$b_{\pi\sigma}$	0·20		0·14	0·16
	J_{dc}	$b_{\sigma\sigma}$	0·24	0·25		0·11
Yb^{3+}	J_{ac}	$b_{\pi\sigma}$	1·07		0·14	0·8
	J_{dc}	$b_{\sigma\sigma}$	0·15	0·25		0·07

exchange we have

$$\begin{aligned} b_{\sigma\sigma} &= \lambda_\sigma(\mathrm{Fe}^{3+})\lambda_\sigma(\mathrm{Fe}^{3+})\Delta E_c \\ b_{\pi\pi} &= \lambda_\pi(\mathrm{Fe}^{3+})\lambda_\pi(\mathrm{Fe}^{3+})\Delta E_c \\ b_{\pi\sigma} &= \lambda_\pi(\mathrm{Fe}^{3+})\lambda_\sigma(\mathrm{Fe}^{3+})\Delta E_c \\ b_{\sigma\sigma'} &= \lambda_\sigma(\mathrm{Fe}^{3+})\lambda_{\sigma'}(\mathrm{Fe}^{3+})\Delta E_c \end{aligned} \tag{7}$$

For $Fe^{3+} - R^{3+}$ exchange we have

$$\begin{aligned} b_{\pi\sigma} &= \lambda_\sigma(R^{3+})\lambda_\pi(\mathrm{Fe}^{3+})\Delta E_c \\ b_{\sigma\sigma} &= \lambda_\sigma(R^{3+})\lambda_\sigma(\mathrm{Fe}^{3+})\Delta E_c \end{aligned} \tag{8}$$

The electron affinity of oxygen is -1.47 eV and for O^- it is 7·2 eV so that $\Delta E_c = 8{\cdot}67$ eV. Using this in (7) and (8) we obtain the λ values which are listed in table 4.

We observe that $\lambda_\sigma > \lambda_\pi$ for Fe^{3+} exchange as expected from chemical bond theory. Also λ_σ values for the rare earth ions are generally lower than that for the Fe^{3+} bonds. This also agrees with the chemical theory of covalent bonds where it is known that the covalent bonds involving the 3*d* orbitals are stronger than those involving the 4*f* orbitals.

References

Anderson P W 1959 *Phys. Rev.* **115** 2
Copland G M 1970 *Chem. Phys. Lett.* 7 175

CRC Handbook of Chemistry and Physics 1980–81, 61st (CRC Press Florida) p. F.216
Khattak C P and Yang F F Y 1979 *Handbook of physics and chemistry of rare earths* (ed.) Schneider Jr and L Eyrings (Amsterdam: North Holland) Vol. 3 p. 565
Levy P M 1966 *Phys. Rev.* **147** 311
Slater J C 1953 *Rev. Mod. Phys.* **25** 199
Srivastava C M, Srinivasan C and Aiyar R 1982, *J. Appl. Phys.* **53** 781
Sugar J and Reader J 1973 *J. Chem. Phys.* **59** 2083
Tchéou F, Fuess H and Bertaut H 1970 *Solid State Commun.* **8** 1745
Zeiger H J and Pratt G W 1973 *Magnetic interactions in solids* (Oxford: Clarenden) p. 242

Bull. Mater. Sci., Vol. 6, No. 6, December 1984, pp. 1075–1086. © Printed in India.

Electrical properties of films at microwave frequencies

D C DUBE
Physics Department, Indian Institute of Technology, New Delhi 110016, India

MS received 1 June 1983

Abstract. A technique suitable for the measurement of electrical properties of films/sheets at microwave frequencies has been described. Groups of materials are identified for which the absence of any kind of electrodes in these microwave measurements can be utilised with advantage. Results are presented for a variety of materials such as metal films, superionic conductors, semiconductors and insulating polymers.

Keywords. Microwaves; waveguide; dielectric constant; a.c. conductivity.

1. Introduction

Knowledge of the electrical properties of films at microwave frequencies is helpful in material study and characterization for device fabrication. Thin metal and insulating films, for example, are extensively used in microwave integrated circuits. There, it is of interest to know the attenuation and phase produced by a particular film and variation of these quantities with parameters such as film thickness, temperature etc. Thin semimetal and metal films were studied by several workers (Gunn 1967; D'Aiello and Freedman 1969; Duggal and Rup 1969; Ramey *et al* 1970). The microwave applications of thin metallic films have also gained importance as exemplified by the use of films as microwave mirrors and as large size film reflectors (Korolev and Gridnev 1963). Microwave measurements are essential in the above cases. But in many situations advantage can be taken of the fact that at microwave frequencies the measurements basically are electrodeless and therefore these are recommended to study materials which require special type of electrodes. Groups of materials may be identified where contacts do pose problems, such as *e.g.* (i) semi-conductors (ii) fast ion conducting solids (iii) membranes and other biological systems. Such materials can be conveniently studied at microwave frequencies.

Section 2 describes few techniques including the one developed earlier (Dube and Natarajan 1973), for the measurement of dielectric constant, loss and conductivity of films and foils. Finally the results are presented for a variety of films.

2. Measurement techniques

The most widely used method for microwave measurements of dielectric parameters of solids is the short-circuited line technique of Von Hippel (Von Hippel 1961). The technique involves the measurement of VSWR (voltage standing wave ratio $= E_{\max}/E_{\min}$) on the standing waves set-up when the microwaves are totally reflected from a short circuit. A dielectric specimen in the form of a small block which completely

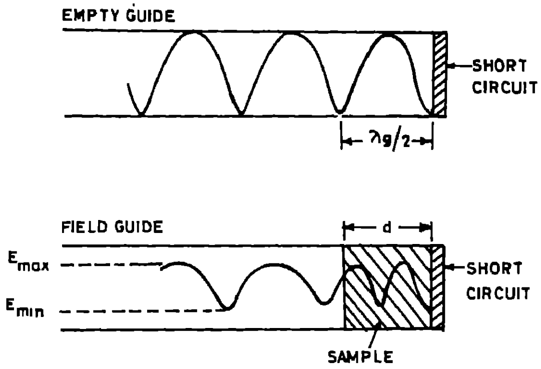

Figure 1. Standing wave pattern in empty and field guide.

fills the section of waveguide is placed next to the short circuit. This alters both the position of standing wave pattern and the size of the voltage ratio by amounts which depend on the dielectric constant and loss of the material and on the length of the 'filled guide' (figure 1).

Von Hippel's method when applied to a very thin specimen does not give accurate results, the reason being the lack of strong interaction between the e.m. wave and the thin specimen. Therefore the presence of the specimen shifts the voltage minima only slightly (often insignificantly) and the change in standing wave ratio is also small (often not measurable accurately).

Recently, Von Hippel's technique has been modified to suit thin samples by measuring impedance not only with short circuit (figure 1) but also using an open circuit and matched terminations (Das Gupta and Pramanic 1982). The method is effective only for high dielectric constant films.

Cavity methods which measure the change in resonance frequency and broadening of resonance response on introduction of the specimen are also not very successful for the same reasons of lack of strong interaction when the specimen is very thin. However, attempts have been made to study thin samples using specific forms of cavities (Conklin 1965; Sobol and Hughes 1967) and other forms of sample holders (Pilipenko *et al* 1970). Cavity perturbation technique has also been used (Rzepecka and Hamid 1972).

3. An accurate and convenient technique

In the above techniques such as that of Von Hippel, the accuracy of measurement is poor due to weak interaction of e.m. wave with the specimen. And the reason for the poor interaction is the fact that in normally used TE_{10} mode of excitation the electric field is maximum at the centre of the waveguide and diminishes to zero at the side walls (figure 2); most of the portion of the specimen lies in the weak field regions. Keeping this in view, a suitable technique was developed (Dube and Natarajan 1973) to study thin film specimens. In this technique the thin specimen is placed longitudinally at the centre of the broad side of a hollow rectangular waveguide excited in the TE_{10} mode so that the whole specimen remains in maximum electric field as shown in figure 3. In this geometry Maxwell's equations can be solved for the TE_{10} mode by taking Z variations of the form $\exp(-i\beta Z)$ (axis of waveguide is along the z-direction). Then by usual

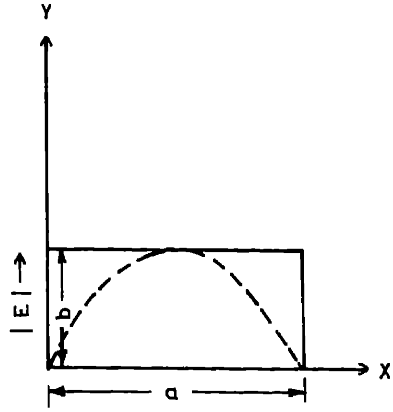

Figure 2. Electric field distribution in a rectangular waveguide in the TE_{10} mode.

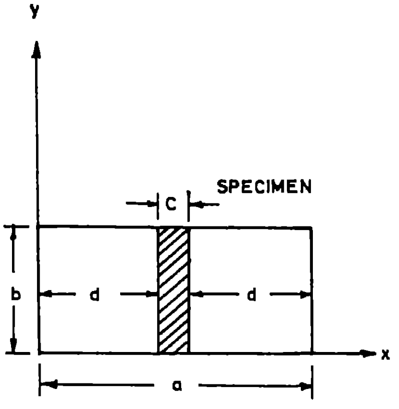

Figure 3. Cross-section of a rectangular waveguide with specimen.

methods (Collin 1960), the following dispersion relation is obtained

$$\tan[d(k^2-\beta^2)^{1/2}]\tan[\tfrac{1}{2}c(\varepsilon k^2-\beta^2)^{1/2}] = \frac{(k^2-\beta^2)^{1/2}}{(\varepsilon k^2-\beta^2)^{1/2}} \tag{1}$$

where $k = \omega/C_0$ is the free space propagation vector and ω is the angular frequency. Equation 1 is a transcendental equation, and its solution can be obtained only by graphical methods. For complex dielectric constants, the solution of (1) is very difficult even graphically. Therefore, we simplify (1) under the approximation $\frac{1}{2}c(\varepsilon k^2-\beta^2)^{1/2} < 1$, which holds very well in the case of thin films; hence using $\varepsilon = \varepsilon_r - i\varepsilon_i$ and $\beta = \beta_r - i\beta_i$, we get the following expressions for the real and imaginary parts of the complex dielectric constant:

$$\varepsilon_r = \frac{1}{k^2}\left((\beta_r^2-\beta_i^2)+\frac{a_1a_3+a_2a_4}{a_3^2+a_4^2}\cdot\frac{1}{\frac{1}{2}cd}\right), \tag{2}$$

$$\varepsilon_i = \frac{1}{k^2}\left(2\beta_r\beta_i-\frac{a_2a_3-a_1a_4}{a_3^2+a_4^2}\cdot\frac{1}{\frac{1}{2}cd}\right), \tag{3}$$

where

$$a_1 = d\,\mathrm{Re}\,(k^2-\beta^2)^{1/2},$$

$$a_2 = d\,\mathrm{Im}\,(k^2-\beta^2)^{1/2},$$

$$a_3 = \frac{2\sin 2a_1}{\exp(2a_2)+\exp(-2a_2)+2\cos 2a_1},$$

and

$$a_4 = \frac{\exp(2a_2)-\exp(-2a_2)}{\exp(2a_2)+\exp(-2a_2)+2\cos 2a_1},$$

and

β_t = attenuation introduced by unit length of the specimen (measured in nepers m^{-1})

$\beta_r = \beta_p + \beta_0$ (measured in radians m^{-1})

where

β_p = phase shift produced by the unit length of the specimen

and

$\beta_0 = 2\pi/\lambda g$, where λg is the guide wavelength in the empty guide,

c = thickness of specimen, and

$d = \frac{1}{2}(a-c)$, a being the width of the waveguide (figure 3).

Thus, in complex dielectrics, the value of ε_r and ε_i can be obtained from (2) and (3). For loss-free dielectrics the solution of (1) can be obtained without any approximations. The two main quantities required to be measured experimentally are the phase and attenuation introduced by the specimen. Two experimental arrangements have been proposed (Dube and Natarajan 1973, 1974). Either may be used for these measurements. Both make use of rectangular waveguide system excited in the TE_{10} mode. One arrangement has been shown in figure 4.

Microwave power is obtained from a Klystron source. The power is divided into two arms at the 10-dB directional coupler. The lower arm contains the standard impedance, *i.e.*, a standard variable attenuator and a standard variable phase shifter (0° → 360°). The upper arm contains the sample holder which is an approximately 10 cm long waveguide having a sharply cut longitudinal slot at the middle. The sample is introduced through this slot. The powers from the upper and the lower arms are again combined at a 3-dB directional coupler. The power output from the directional coupler is fed to the detecting system.

To start with, a null point is obtained in the detector by properly adjusting the variable attenuator and the phase shifter. The introduction of the specimen disturbs the balance. The null conditions are restored by varying the attenuator and phase shifter. Thus the phase shift and attenuation introduced by the sample can be accurately measured. Large sample lengths should be used for producing large phase shifts and attenuations.

Reflections from the edge of the sample are normally extremely small. But these can be detected by a separate experiment and if required, tuner no. 8 in figure 4 may be used for matching purposes.

The minimum detectable phase shift and attenuation in the measuring system were 0·25° and 0·02 dB, respectively.

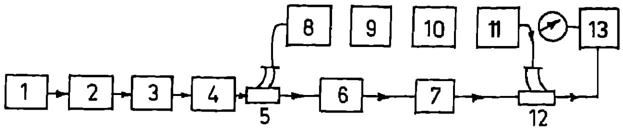

Figure 4. Schematic diagram of the experimental set up: 1. Klystron power source; 2. Frequency meter; 3. Padder attenuator: 4. Ferrite isolator; 5. and 12, Directional couplers; 6. Calibrated variable phase shifter; 8 and 11 tuners; 9. Variable attenuator; 10. sample holder waveguide; 13. Amplifier and meter.

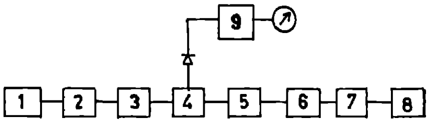

Figure 5. Schematic diagram of the experimental set-up; 1. Klystron power source; 2. Frequency meter; 3. Ferrite isolator; 4. Waveguide travelling detector; 5. variable attenuator; 6. E-H tuner; 7. sample holder waveguide; 8. movable short; 9. Amplifier and meter.

To study dielectric parameters as a function of temperature, the guide section containing the specimen may be cooled by a low temperature bath around the section or may be heated by a cylindrical furnace.

The other experimental set-up (Dube and Natarajan 1974) is shown in figure 5. This is a simpler arrangement and does not require calibrated variable phase shifter and attenuator and is as accurate as the first set-up.

Here the travelling wave detector is used to measure the shift of the voltage minimum when the specimen is introduced. Let the specimen length be L cm and the phase shift produced be X cm, then phase introduced by the specimen per unit length is

$$\beta_s = \beta_0 \frac{X}{L}$$

Thus the total phase constant β_r is given by

$$\beta_r = \beta_0 + \beta_s$$

or

$$\beta_r = \beta_0 \left(1 + \frac{X}{L}\right)$$

For measuring the dielectric loss, the VSWR is taken with and without the specimen. Let these be ρ_1 and ρ_2; then

$$r = \frac{\rho_1 - 1}{\rho_1 + 1} = \exp(-\alpha), \tag{4}$$

and

$$r' = \frac{\rho_2 - 1}{\rho_2 + 1} = \exp - (\alpha + 2\beta_t L), \tag{5}$$

where r and r' are the reflection coefficients of the system with and without the sample and α is the attenuation constant. Hence β_t can be calculated from (4) and (5).

4. Results and discussion

The accuracy of the proposed technique for measuring the dielectric parameters of films was checked by studying two materials namely, myler and teflon whose dielectric properties are well known over a wide frequency range including microwaves. Results are summarised in table 1.

In the recent past the technique has been used to study films/sheets/wafers of varying nature and differing widely in electrical properties. Some of the results are given below.

Complex permittivity and conductivity have been studied for silicon semiconductor (Natarajan *et al* 1978). ε_r and ε_i values for one sample of *p*-silicon for various thicknesses are given in table 2. The thickness of the starting sample was reduced by etching and lapping.

The d.c. conductivities measured by the four-probe technique and the microwave conductivities obtained from the relation $\sigma_{\text{a.c.}} = \omega\varepsilon_0\varepsilon_i$ are compared in table 3 for three samples of *p*-silicon.

The microwave conductivity is slightly less than the d.c. values. This is somewhat

Table 1. Dielectric parameters of teflon and mylar films at 9·375 GHz at room temperature (310°K)

Sample	Sample thickness (μm)	Phase shift per unit length (deg.)	Dielectric constant: Present work	Dielectric constant: Literature
	90	0·61	2·03	2·08[a]
Teflon	130	0·96	2·03	2·07 ± 0·03[b]
	186	1·28	2·02	
	75	1·15	3·13	
Mylar	130	1·91	3·10	3·145[c]
	250	3·74	3·18	

[a] Von Hippel (1961); [b] Pilipenko *et al* (1970); [c] Conklin (1965).

Table 2. Complex permittivity for a *p*-type silicon (5·45 Ω cm) at room temperature (310°K) and at a frequency of 9·410 GHz

Thickness (microns)	Phase shift per unit length (degrees)	Attenuation per unit length (decibles)	ε_r	ε_i
272	15·0	8·6	11·61	30·58
226	13.0	7·5	11·65	32·12
200	12·0	6·9	11·81	33·13
180	10.8	6·1	11·58	32·68
140	8·6	5·1	11·62	34·61
94	5·8	3·4	11·41	34·76
70	4·5	2·4	11·63	32·69

Table 3. Comparison of d.c. and a.c. conductivities for three samples of *p*-silicon

d.c. conductivity by four-probe technique $(\Omega\,\mathrm{m})^{-1}$	Microwave conductivity from $\sigma_{\mathrm{a.c.}} = \omega\varepsilon_0\varepsilon_i$ $(\Omega\,\mathrm{m})^{-1}$
10.26	9.79
15.63	15.17
18.35	17.97

consistant with the usual expressions for a.c. and d.c. conductivities.

$$\sigma_{\mathrm{a.c.}} = \frac{ne^2\nu}{m[\nu^2+\omega^2]},$$

and

$$\sigma_{\mathrm{d.c.}} = \frac{ne^2}{m\nu},$$

where m, e, n and ν are the mass, charge, concentration and collision frequency of the holes in *p*-silicon.

The microwave data may also be used to determine other transport parameters of silicon. The dielectric constant and conductivity in terms of effective mass m^* and relaxation time τ may be written as

$$\varepsilon_r = \varepsilon_L - \frac{ne^2\tau^2}{\varepsilon_0 m^*[1+(\omega\tau)^2]},$$

$$\sigma = \frac{ne^2\tau}{m^*[1+(\omega\tau)^2]} = \omega\varepsilon_0\varepsilon_i,$$

where ε_L is the lattice dielectric constant and ε_0 is the permittivity of free space. From the above two equations, we get

$$\tau = \frac{\varepsilon_L-\varepsilon_r}{\omega\varepsilon_i}.$$

With the present results the relaxation time in silicon comes out to be around 10^{-13} sec, which agrees well with the data ($\simeq 10^{-13}$ sec) produced by Blatt (1968).

The conductivity variations with temperature for *p*-silicon samples (d.c. resistivities 10·5, 40 and 170 ohm cm) in the temperature range 190–525°K are plotted in figure 6. The curves for the three silicon samples exhibit broadly similar characteristics. *viz* the conductivity initially decreases with increase of temperature and later increases very rapidly with temperature. This is, of course, expected, considering the relative predominance of extrinsic and intrinsic conduction mechanisms. The conductivity of the samples (having resistivities 10·5 and 40 ohm-cm) decreases from room temperature to 440°K. In this temperature region lattice scattering by acoustical phonons plays the dominant role (Blackmore 1969). As the temperature is raised further, the concentration of free electrons and holes increases and the intrinsic conduction predominates thereafter. In the case of the third sample (170 ohm cm, the highest resistivity of all the

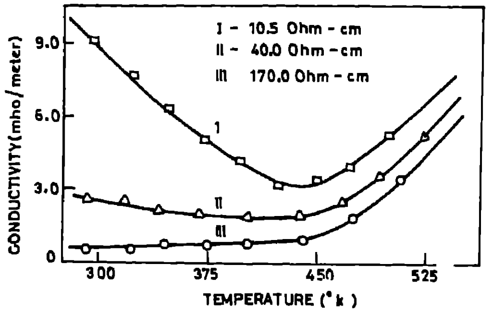

Figure 6. Microwave conductivity variation of silicon wafers in the temperature range 293–523°K.

three) the conductivity rises slowly from room temperature up to 440 K and increases very rapidly subsequently thereby showing its intrinsic behaviour right from room temperature. Bhar (1963) made similar measurements on temperature variations of microwave conductivity for bulk *p*-silicon samples having conductivities 0·7 and 0·1 mho m^{-1} in the temperature range 273–480°K. His results also resemble the curves of figure 6.

Electrical parameters have been measured for metal and semimetal films of thicknesses less than the skin depths deposited on glass substrates by vacuum thermal evaporation technique (Dube *et al* 1978).

Figures 7 and 8 show the phase shift and attenuation constants as a function of film thickness for the semimetal bismuth. Table 4 contains the results for ε_r and ε_i for bismuth films of different thicknesses. The high values of ε_r and ε_i are attributed to the presence of free carriers and are consistent with the results of Rahneberg (1971) for bismuth films measured by a different technique at 14·50 GHz. Gold and aluminium films also show high dielectric parameters of the order of 10^5 (Dube *et al* 1978).

Dielectric behaviour of pure polyvinyl chloride (PVC) and iodine-doped PVC has been studied at microwave frequencies using the proposed technique (Natarajan and Dube 1981). Pure PVC films were obtained by dissolving the polymer powder in tetrahydrofuran and permitting the evaporation of the solvent at room temperature. Iodine-doped PVC samples were prepared from the PVC solution in which a requisite amount of iodine was dissolved. The concentration of iodine in the samples varied from 4–40 % by weight.

Figure 9 depicts the variation of ε_r with temperature for all PVC samples. It is seen that at any fixed temperature, the dielectric constant increases as the iodine content in the sample increases. This effect is more pronounced for iodine concentrations above ~ 5 % (by weight). For temperatures above 90°C the dielectric constant decreases for all samples containing iodine.

The rise in ε_r with iodine concentration may be attributed to the presence of highly polarizable molecular iodine in the specimen. The presence of free iodine was detected in the absorption spectrum in the visible region.

The volume expansion due to transition from glassy to rubbery state seems to account for the decrease of ε_r with temperature in the vicinity of 85°C as the glass transition temperature (T_g) of PVC falls in the region 70–105°C (Brandrup and Immergut 1975). Variation of loss-tangent (tan δ) with temperature for different iodine

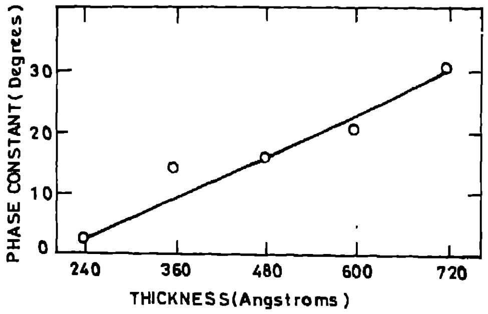

Figure 7. Variation of phase constant as a function of bismuth film thickness.

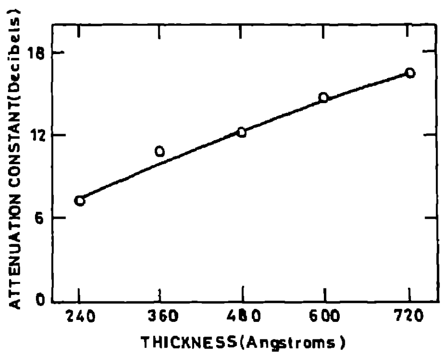

Figure 8. Variation of attenuation constant as a function of bismuth film thickness.

Table 4. Complex permittivity for thin bismuth films for various thicknesses at 310°K and at a frequency of 9·410 GHz.

Thickness (angstroms)	Phase shift/ length (degrees)	Attenuation/ length (decibels)	Dielectric parameters ($\times 10^5$) ε_r	ε_i
240	2·5	7·5	0·36	3·12
360	12·0	10·8	0·91	2·91
480	15·5	12·2	0·89	2·38
600	20·0	13·7	0·83	1·83
720	30·0	16·3	1·05	1·86

dopings has been shown in figure 10. For iodine content of 10% and above, well-defined loss-peak appears at around 90°C in each case. With increasing iodine content, the position of loss peak does not change; however, the peak height changes considerably. The fact that loss tangent maxima does not change in position but only in magnitude with iodine concentration shows that on increasing the doping the number of dipoles participating in the orientation process increases, while the frequency of orientation remains unchanged.

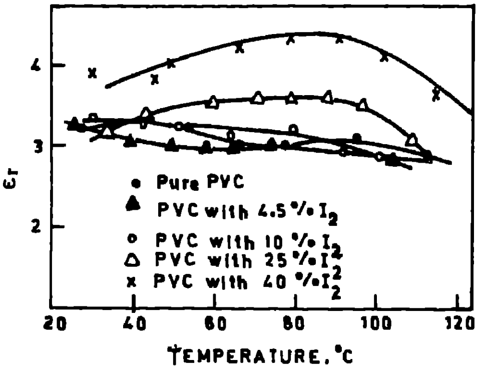

Figure 9. Variation of ε_r with temperature for pure and iodine doped PVC.

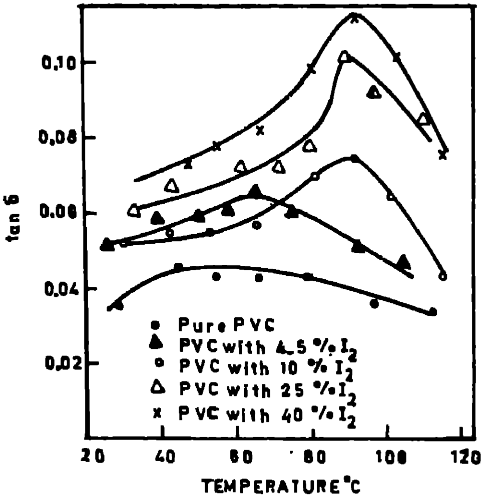

Figure 10. Variation of tan δ with temperature for pure and iodine doped PVC.

Fast ion conducting solids (also called superionic conductors) have become very important in the recent past due to their applications in many electrochemical devices. Electrical measurements on these materials require special attention due to the variety of electrodes (blocking, reversible and their combinations) (Bottelberghs 1978) used making the analysis more complex. The ionic conduction has been studied recently at microwave frequencies (Dube and Saraswat 1982) in silver iodide in the high conductivity α-phase. Thin pellets of AgI of varying packing density were used and dielectric and conductivity data obtained. This data can be transformed to 100 % dense bulk using correlation formulae (Landau and Lifshitz 1960; Leoyenga 1965; Dube 1970).

$$\varepsilon_p'^{1/3} - 1 = \delta(\varepsilon_b'^{1/3} - 1),$$

$$\varepsilon_b'' = \frac{\varepsilon_p''}{\delta}(\varepsilon_b'/\varepsilon_p')^{2/3},$$

Table 5. Conductivity and dielectric constant for α-AgI ($T = 160°C$) at 10 kHz

Packing fraction %	Observed parameters for pellets		Values converted to 100% density by correlation formulae		Values reported in literature in microwave region (Gebhardt *et al* 1980)	
	Dielectric constant	Conductivity $(\Omega\,\text{cm})^{-1}$	Dielectric constant	Conductivity $(\Omega\,\text{cm})^{-1}$	Dielectric constant	Conductivity $(\Omega\,\text{cm})^{-1}$
72	12·0	0·044	21·74	0·092	22·00	1·22
82	15·4	0·076	22·30	0·119		
86	16·9	0·084	22·45	0·110		
92	19·4	0·088	22·75	0·116		

and

$$\sigma_b = \omega \varepsilon_0 \varepsilon_b'',$$

where ε_p' and ε_p'' are the dielectric constant and loss factor for the pellet of packing fraction δ and ε_b', ε_b'' are the corresponding parameters for the bulk. σ_b is the conductivity at angular frequency ω. ε_0 is permittivity of free space ($= 8{\cdot}85 \times 10^{-12}\ \text{Fm}^{-1}$). Various results have been summarised in table 5. It is seen that while the deduced dielectric constant data match with experimentally reported value of 22, the conductivity results are found reduced by an order of magnitude. This reduction in conductivity is attributed to the presence of grain boundaries in the unsintered samples used in the above studies.

In conclusion, it may be said that the microwave technique described is very convenient and accurate and can be used to study electrical transport behaviour of materials differing widely in characteristics.

References

Bhar J N 1963 *Proc. IEEE* **51** 1623
Blakemore J S 1969 *Solid State Physics* (Toronto: Saunders Company)
Blatt F J 1968 *Physics of electronic conduction in solids* (New York: McGraw-Hill)
Bottelberghs P H 1978 in *Solid electrolytes: General principles, characterization, materials, applications* (eds) Paul Hagenmuller and W Van Gool (New York: Academic Press)
Brandrup J and Immergut E M (eds) 1975 *Polymer handbook* (New York: John Wiley) 2nd edn p. 44
Collin R E 1960 *Field theory of guided waves* (New York: McGraw-Hill) Chap. 6
Conklin G E 1965 *Rev. Sci. Instrum.* **36** 1347
D'Aiello R V and Freedman S J 1969 *J. Appl. Phys.* **40** 2156
Das Gupta C and Pramanick P 1982 *Microwave* **76**
Dube D C 1970 *J. Phys.* **D3** 1648
Dube D C and Natarajan R 1973 *J. Appl. Phys.* **44** 4927
Dube D C and Natarajan R 1974 *J. Phys.* **E7** 256
Dube D C, Natarajan R and Tripathi V K 1978 *Indian J. Phys.* **A52** 405
Dube D C and Saraswat A K 1982 *J. Appl. Phys.* **53** 7095
Duggal V P and Rup R 1969 *J. Appl. Phys.* **40** 492
Gebhardt K F, Soper P D, Merski J, Balle T J and Flygare W H 1980 *J. Chem. Phys.* **72** 272
Gunn M W 1967 *IEEE Proc.* **114** 207
Korolev F A and Gridnev V I 1963 *Radiotekh. Electron.* **8** 1480

Landau L D and Lifshitz F M 1960 *Electrodynamics of continuous media* (London: Pergamon) *p*. 46
Looyenga H 1965 *Physica* **31** 401
Natarajan R, Dube D C and Tripathi V K 1978 *Indian J. Phys.* **52** 567
Natarajan R and Dube D C 1981 *Indian J. Pure Appl. Phys.* **19** 675
Pilipenko V V, Polovnikov G G, Sologub V G and Shestopilov V P 1970 *Sov. Phys. Tech. Phys.* **14** 1662
Rahneberg E W 1971 *Measurement of the Complex Permittivity of Thin Bismuth Films within the Ku-band* Ph.D. Thesis, University of Arizona USA
Ramey R L, Landes H S and Manus E A 1970 *IEEE Trans. Microwave Theory Technol.* **MTT-18** 196
Rzepecka M A and Hamid M A K 1972 *IEEE Trans. Microwave Technol.* **MTT-20** 30
Sobol H and Hughes J J 1967 *IEEE Trans. Microwave Technol.* **MTT-15** 377
Von Hippel A R 1961 Dielectric materials and applications (New York: Wiley)

Bull. Mater. Sci., Vol. 6, No. 6, December 1984, pp. 1087–1091. © Printed in India.

Surface modification of polyvinyl chloride towards blood compatibility

GEETHA KURIAN and CHANDRA P SHARMA

Department of Biomedical Engineering, Sree Chitra Tirunal Institute for Medical Sciences and Technology, Trivandrum 695 012, India

MS received 29 January 1983; revised 6 September 1983

Abstract. The surface modification of medical grade polyvinylchloride (PVC) from various sources with the ionic bonding of polyelectrolyte is investigated by exposing the PVC sheets to 1 % zephiran chloride for 10 min and then to 50 mg % solution of polyelectrolyte for 10 min. Surface energy and platelet adhesion studies were carried out to demonstrate the suitability of our improved surface towards blood compatibility. Relative changes due to γ-irradiation are also discussed.

Keywords. Polyvinyl chloride; surface modification; blood compatibility

1. Introduction

Polyvinylchloride (PVC) with a wide choice of additives and ingradients such as plasticizers, fillers, stabilisers etc (Ownes and Read 1979) is being used for various biomedical applications. However the surface of the PVC may change depending upon the additives used. Since the prosthetic blood interaction is dependent on the nature of the surface, various surfaces may behave differently. Therefore, we have attempted in this paper to mention the modification of the medical grade PVC from different sources using polyelectrolyte towards improved blood compatibility.

Polyelectrolytes from synthetic poly (*cis*-1,4 isoprene) possess anticoagulant activity (van der Does *et al* 1979) and have been used for surface modification of polymers (Sederel *et al* 1983). Therefore we have chosen natural rubber, (Source Hevea Brasiliensis "Para Rubber") to obtain the polyelectrolyte for our studies. It seems the effect of surface modification with this method is independent of the PVC type and therefore appears quite promising for future investigations.

2. Experimental work

The PVC sheets of different sources are dipped in 0·1 % soap solution. They are thoroughly cleaned with distilled water, finally rinsed with methanol and dried in vacuum oven. Polyelectrolyte (synthesised from natural rubber, van der Does *et al* 1979) is ionically bound on the various PVC sheets by first exposing to 1 % Zephiran chloride for 10 min and then to polyelectrolyte (50 mgm % in water) for 10 min. The bare as well as the polyelectrolyte coated PVC sheets were irradiated at room temperature (CO^{60} gamma source) with a constant dose rate of 0·25 M rad (strength 843/Rontgen/hr/m) for 4 hr 30 min.

Inherent viscosity of the various bare PVC sheets was compared and the results are given in table 1. Variation of contact angle with time are also studied with a goniometer at room temperature using double distilled water as shown in figures 1–4.

2.1 *Blood coagulation studies*

Calf blood is used for evaluating the recalcification time under controlled pH and temperature with the PVC coated tubes. Glass tubes of 7·5 cm length and 1 cm diameter are coated with 10 % solution of PVC in tetrahydrofuran. The tubes are dried at 60°C in a

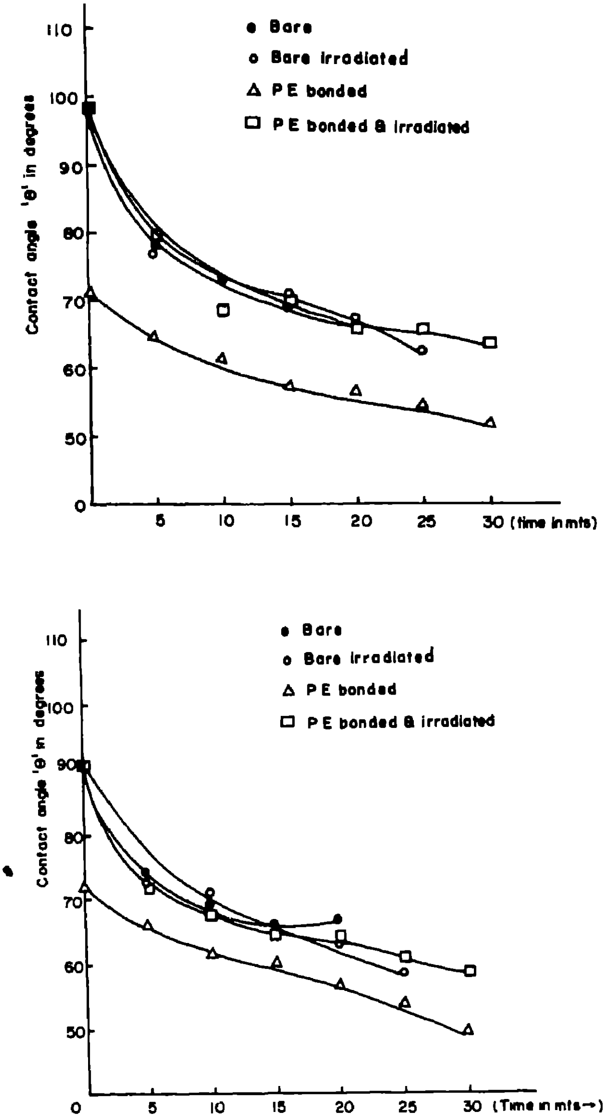

(1)

(2)

Figures 1–2. Change in contact angle with time on PVC surfaces **1.** Bhor **2.** SCTIMIST.

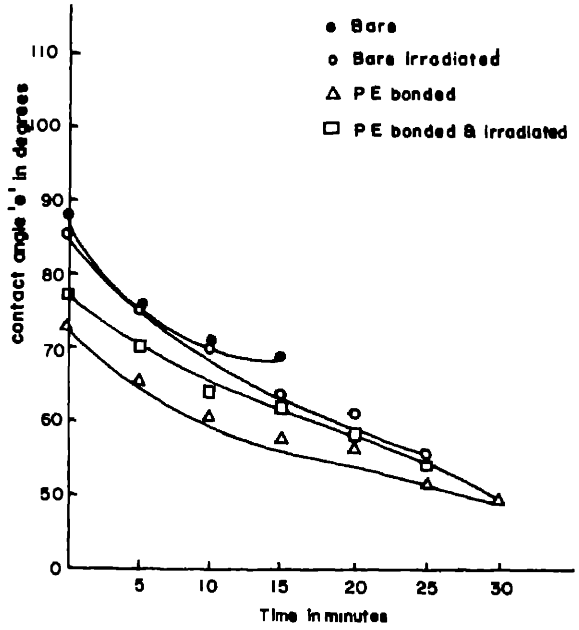

(3)

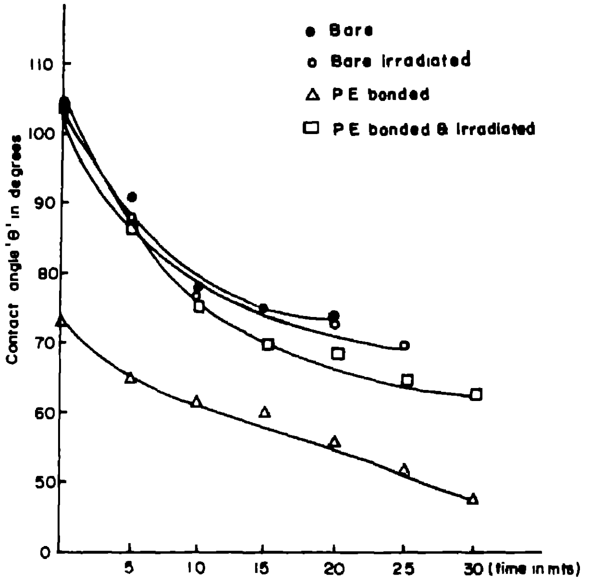

(4)

Figures 3–4. Change in contact angle with time on PVC surfaces 3. TUTA 4. Fenwal.

vacuum oven. The clotting time for the plasma is determined at 37°C (Austen and Rhymes 1975). The results are tabulated in table 2.

2.2 *Platelet adhesion on PVC surfaces: Preparation of platelet suspension*

Washed calf platelets are prepared and suspended in tyrode solution (Sharma and Chandy 1982) for adhesion studies. The washed PVC sheets are exposed to platelet

Table 1. Inherent viscosity data of various PVC sheets.

PVC sheets	Viscosity (dl/g)
I	1·27
II	1·03
III	1·01
IV	1·08

I—Bhor Industry India Product for SCTIMST. II—Polymer Technology Division Product of our Institute for blood bag applications, submitted by S N Pal, SCTIMST. III—Tuta Industry Australia, blood bag. IV—Fenwal, Travenol Inc. (USA), blood bag.

Table 2. Plasma recalcification time

Surfaces	Plasma recalcification time (sec) SD ($n = 5$)
Plain glass	140 ± 2
I	187 ± 5
II	166 ± 11
III	340 ± 3
IV	198 ± 20

I, II, III and IV are as noted in table 1.

Table 3. Platelet adhesion on various PVC sheets.

	Bare PVC sheets		Polyelectrolyte coated PVC sheets	
PVC sheets	Before γ-irradiation ($n = 10$)	After γ-irradiation ($n = 10$)	Before γ-irradiation ($n = 10$)	After γ-irradiation ($n = 10$)
I	5·8 ± 0·8	4·9 ± 0·7	3·6 ± 0·5	4·2 ± 0·4
II	5 ± 0·8	4·9 ± 0·7	3·6 ± 1·2	4·2 ± 0·5
III	5 ± 1·0	4·9 ± 0·7	3·6 ± 0·53	3·8 ± 1·0
IV	5·8 ± 0·8	5 ± 0·7	3·6 ± 1·2	4·4 ± 0·6

I, II, III and IV are as noted in table 1.

suspension for 1 hr, rinsed with phosphate buffer of pH 7·4 under uniform flow for about 3 min and the platelets are fixed with Coomassie Blue G. The number of platelets adhered to the PVC sheets are accounted using an optical microscope. Different fields are read randomly and averaged in a similar fashion for all samples. The results are given in table 3.

3. Results and discussion

Platelet adhesion and contact angle studies were carried out on bare as well as on polyelectrolyte coated PVC surfaces to investigate the effect of polyelectrolyte coating on PVC towards blood compatibility.

It seems when polyelectrolytes are on the surface the material is improved towards blood compatibility. Platelet adhesion is relatively less as indicated in table 3. Although they are different before modification as indicated by our plasma recalcification time (table 2) and the change in contact angle with time (figures 1–4), the contact angle becomes relatively more stable and the behaviour of the various PVC sheets becomes alike (figures 1–4). After irradiation the effect of polyelectrolyte is no longer obvious as shown in figures 1–4. It becomes a part of the PVC structure such that leaching components do not have any additional resistance as it was before irradiation. Therefore we suggest that PVC surfaces can be improved towards blood compatibility like polyelectrolyte as described above, provided the material is already sterilised by γ-irradiation, since for long term applications ionic bonding of polyelectrolytes with PVC surface may not be stable enough. This modification is suggested for all short term medical applications of PVC coming in contact with blood such as oxygenators and blood bags etc. No adverse change in platelet adherance is observed on modified surfaces if autoclaving sterilization (Sharma and Nirmala 1983) is used instead of CO^{60}, γ-irradiation.

Acknowledgement

The authors appreciate the help received from Dr V N Krishnamurthy of Vikram Sarabhai Space Centre, Trivandrum for ^{60}Co γ-irradiation of our samples, Dr A V Lal for providing calf blood, Mr S N Pal for the PVC samples and Mr Thomas Chandy and Mrs M K Sheela for help.

References

Austen D E G and Rhymes I L 1975 *A laboratory manual of blood coagulation* (Oxford: Blackwell Scientific Publications) p. 35.

Owen B D and Read R L 1979 *J. Polym. Sci., Polym. Chem. Ed.* **17** 2719

Sederel L C, van der Does E, Evverman B J, Bantjes A, Kluft C and Kempen H J M 1983 *Biomaterials* **4** 3

Sharma C P and Chandy T 1982 *J. Colloid Interface Sci.* **89** 479

Sharma C P and Nirmala N V 1983 *Polyvinyl chloride compatibility* at National Seminar on *Recent developments in Polymer Science,* AC College Campus, Madras, December 22 and 23rd, Proceedings to follow in honour of Prof. M Santappa

van der Does L, Bengeling T, Frochling P E and Bantjes A J 1979 *Polym. Sym.* **66** 337

Errata

I. "Lithium solid electrolytes and their application" by D N Bose and D Majumdar, *Bull. Mater.* Sci **6** pp. 223–230 May 1984

The paper falls under the subject "Electrical Properties" and not under "Glasses" as printed in the Contents Page of the Journal.

II. "Electrical properties of polycrystalline silicon and zinc oxide semiconductors" by S N Singh, S Kumari and B K Das, *Bull. Mater. Sci.* **6** pp 243–258 May 1984

(i) On page 247 the lines following the description of eq (3) should read as

For a discrete energy level, on the other hand, ϕ_B is obtained from the solution of equation (Martinez and Piqueras 1980)

$$(8\varepsilon N_D q\phi_B)^{1/2} = qN_{is}\left[\frac{1}{1+\exp[(E_T-E_{FG}-q\phi_B)/kT]} - \frac{1}{1+\exp[(E_T-E_{FB})/kT]}\right], \tag{4}$$

and (ii) On page 250, the first line of last paragraph of section 2.2c should read as

"A comparison of (11) and (17) shows that the activation energies of μ_{eff} and σ are not identical."

Bulletin of Materials Science

Volume 6, January–December 1984

SUBJECT INDEX

A.C. conductivity
  Electrical properties of films at microwave frequencies 1075

Accelerator irradiation
  High voltage electron microscope irradiation and observations in metallic glasses 595

Activation energy
  Electron transport in non-crystalline garnet films 53
  DC electrical conductivity of Na_2O-ZnO-B_2O_3 glass system 1009

Alloy design
  Mechanisms and empirical equations for deformation and some principles of alloy design 677

Al-Pu fuels
  Plutonium metallurgy in India 923

Al-rare earth system
  High resolution electron microscopic studies of $HoAl_3$, $Er_{0.5}$ $Gd_{0.5}$ Al_3 and $Y_{0.91}$ $Er_{0.09}$ Al_3 in thin film form 603

Aluminium alloy
  Analytical electron microscopy of aluminium alloys 513

Amorphous character
  Effect of compositional modifications on the piezoelectric properties of spray dried lead zirconate titanate ceramics 83

Amorphous ferromagnets
  Spin-wave excitations in amorphous ferromagnets 1059

Amorphous films
  A novel method of RF powder sputtering 971

Amorphous semiconductors
  Electronic conduction in bulk $Se_{1-x}Te_x$ glasses at high pressures and at low temperatures 231

Analytical microscopy
  Metallic glasses 579

Anelasticity
  Internal friction in hexagonal metals 959

Annealing behaviour
  Annealing behaviour of electron-beam deposited tin dioxide films 1029

Anodic dissolution
  Electrochemical preparation of potassium gold cyanide 165

Antimony film
  Electron diffraction analysis of antimony films 611

Antiphase boundaries
  High resolution electron microscopy of long range ordered alloys 417

As-Sb-Se glasses
  Elastic properties of As-Sb-Se glasses 1001

Atomistic behaviour
  Field ion microscopic observations of LaB_6 on tungsten 573

Austenite
  Structure and properties of an investment—cast austenitic stainless steel 119

BCS theory
  On the mechanism of pairing in the BCS theory 273

Beam broadening
  X-ray microanalysis in the transmission electron microscope 503

Biological molecules
  Investigation of hydrogenous materials using neutrons 151

Biquadratic exchange interaction
  A Mössbauer study of hyperfine interactions in the boroferrite $Fe_{3-x}Ga_xBO_6(x = 0, 0{\cdot}12)$ 33

Blood compatibility
  Surface modification of polyvinyl chloride towards blood compatibility 1087

Boroferrite
  A Mössbauer study of hyperfine interactions in the boroferrite $Fe_{3-x}Ga_xBO_6(x = 0, 0{\cdot}12)$ 33

Boron
  Structural and magnetic investigations of some new boron containing rare earth intermetallic compounds 263

Breakdown process
  Growth of research and development in rare metals extraction in India 901

Burgers vectors
  Grain boundary-dislocation interactions 699

- Carbon-carbon composites
  - Use of coal tar pitch for carbon-carbon composites 91
- Carbon matrix
  - Use of coal tar pitch for carbon-carbon composites 91
- Catalytic oxide
  - MnO_2 catalyzed carbon electrodes for dioxygen reduction in concentrated alkali 259
- Cavity
  - Fracture of particulate composites 799
- Centre frequency
  - Infrared absorption in spinel ferrites 1063
- Ceramic materials
  - Effect of compositional modifications on the piezoelectric properties of spray dried lead zirconate titanate ceramics 83
- Cermet
  - Metal-to-ceramic bonding in $(Al_2O_3 + Fe)$ cermet studied by Mössbauer spectroscopy 13
- Chalcogenide films
  - Photon, electron and ion beam induced physical and optical densification in chalcogenide films 1013
- Chalcogenide glasses
  - Electronic conduction in bulk $Se_{1-x}Te_x$ glasses at high pressures and at low temperatures 231
- Chaos
  - Elementary concepts in chaos and turbulence 807
- Chemical beneficiation
  - Growth of research and development in rare metals extraction in India 901
- Chemical etching
  - Evidence of screw dislocations on (002) cleavages of lithium carbonate single crystals 991
- Classical statistical mechanics
  - Computer simulation of tensile testing 643
- Coal-fired MHD generator
  - High temperature materials for magnetohydrodynamic channels 71
- Cohesive energy
  - Strength and electronic structure 717
- Composite
  - Fracture of particulate composites 799
  - Glass-metal particulate composites 193
  - Some recent advances in materials technology 405
- Computer simulation
  - Computer simulation of tensile testing 643
- Conducting ceramic
  - Preparation and characterisation of β''-Al_2O_3 979
- Conducting polymers
  - Some recent advances in materials technology 405
- CONM model
  - Elastic properties of As-Sb-Se glasses 1001
- Continual mechanical twinning
  - Serrated plastic flow 653
- Convergent beam electron diffraction
  - Scanning transmission electron microscopy and microdiffraction techniques 477
- Cooper pairing
  - On the mechanism of pairing in the BCS theory 273
- Cooperative behaviour
  - Repeated yield drop phenomena as a cooperative effect 665
- Corrosion resistance
  - Structure and properties of an investment cast austenitic stainless steel 119
- Covalency parameters
  - Influence of spin orbit coupling and lanthanide contraction on the exchange interaction in rare earth garnets 1069
- C-periodicity
  - High resolution electron microscopy as a tool for structural investigations 459
- Critical exponent
  - Magnetic structure of zinc ferrite 27
- Critical temperature
  - On the mechanism of pairing in the BCS theory 273
- Crookes dark space
  - A novel method of RF sputtering 971
- Crystal puller
  - Sophisticated equipment developed for growth and evaluation of perfection of nearly perfect crystals 129
- Crystalline solids
  - Relevance of liquid state to solid state properties 773
- Crystallization behaviour
  - Metallic glasses 579
- Crystallization temperature
  - High voltage electron microscope irradiation and observations in metallic glasses 595
- Curie temperature
  - Curie temperatures and 0°K magnetic moments of zinc-substituted lithium ferrites 39
- Curvature tensor
  - Elastic continuum theories of lattice defects: A review 775
- Cycle period
  - Elevated temperature low cycle fatigue studies on AISI 304 steel 111
- Defect characteristics
  - High voltage electron microscope irradiation and observations in metallic glasses 595
- Defects
  - Repeated yield drop phenomena as a cooperative effect 665

Defects
  Effects of mechanical deformation: Exoemission 755

Defect structure
  High resolution electron microscopy of superconductors 453

Deformation mechanisms
  Mechanisms and empirical equations for deformation and some principles of alloy design 677

Delta ferrite
  Structure and properties of an investment cast austenitic stainless steel 119

Delta-stabilised alloys
  Plutonium metallurgy in India 923

Densification mechanism
  Dependence of microstructure on process variables in manganese zinc ferrites 65

Density
  DC electrical conductivity of Na_2O-ZnO-B_2O_3 glass system 1009

Diametral strain
  Elevated temperature low cycle fatigue studies on AISI 304 steel 111

Dielectric constant
  Electrical properties of films at microwave frequencies 1075

Dielectric studies
  Dielectric and pyroelectric studies on triglycine sulphate-polymer composites 105

Diffusional flow
  Superplasticity 689

Dioxygen reduction
  MnO_2 catalyzed carbon electrodes for dioxygen reduction in concentrated alkali 259

Disclinations
  Elastic continuum theories of lattice defects: A review 775

Dislocation
  Etch pit observations on the habit faces of gel grown nickel molybdate crystals 997

Dislocation creep
  Superplasticity 689

Dislocation density correlations
  Elastic continuum theories of lattice defects: A review 775

Dislocation density tensor
  Elastic continuum theories of lattice defects: A review 775

Dislocation dynamics
  Mechanisms and empirical equations for deformation and some principles of alloy design 677

Dislocation interactions
  Grain boundary-dislocation interactions 699

Dislocation-precipitate interaction
  Some aspects of dislocation-precipitate interaction in under-aged aluminium-germanium alloy 1041

Dislocations
  Effects of mechanical deformation: Exoemission 755
  Relevance of liquid state to solid state properties 773
  Elastic continuum theories of lattice defects: A review 775

Disordered materials
  Investigation of hydrogenous materials using neutrons 151

Disordered zones
  Electron microscopy of defect clusters produced by radiation damage 537

Domain structures
  High resolution electron microscopy of long range ordered alloys 417

Dual phase steels
  Applications of scanning transmission electron microscope microanalysis in the study of materials 491

Ductility
  Superplasticity 689

Ductility minimum
  Serrated plastic flow 653

Dynamic strain ageing
  Serrated plastic flow 653

Elastic continuum theory
  Elastic continuum theories of lattice defects: A review 775

Elastic field equations
  Elastic continuum theories of lattice defects: A review 775

Electron emission
  Effects of mechanical deformation: Exoemission 755

Electronic energy
  Strength and electronic structure 717

Electron-mediated interactions
  Strength and electronic structure 717

Electron microscopy
  High resolution electron microscopy of superconductors 453
  Electron microscopy of defect clusters produced by radiation damage 537
  Electron microscopy of layered single crystals grown by direct vapour transport method 549

Electrical conductivity
  Fast ion conducting lithium glasses Review 201
  DC electrical conductivity of Na_2O-ZnO-B_2O_3 glass system 1009

Electrical properties
  Glass-metal particulate composites 193
  Electrical properties of polycrystalline silicon and zinc oxide semiconductors 243

Electrolytic reduction
  Growth of research and development in rare metals extraction in India 901

Electro-optic
  Hydrothermal growth of $A^{II}B^{VI}$ semiconductors 177

Electron beam evaporation
  Annealing behaviour of electron-beam deposited tin dioxide films 1029

Electron diffraction
  Electron diffraction analysis of antimony films 611

Electron exchange
  Influence of the presence of Fe^{2+} ion in nickel-zinc ferrite 7

Electron diffraction
  Formation of lamellar $M_{23}C_6$ on and near twin boundaries in austenitic stainless steels 617

Electron transport
  Electron transport in non-crystalline garnet films 53

Electrochemical preparation
  Electrochemical preparation of potassium gold cyanide 165

Electronic simulation
  Instabilities in yielding 645

Empirical equations
  Mechanisms and empirical equations for deformation and some principles of alloy design 677

Epoxy resin
  Amine-cured epoxy/glass fibre composites 99

Equation of state
  The pressure-volume relation of ytterbium up to 9 GPa 395

Etch pits
  Etch pit observations on the habit faces of gel grown nickel molybdate crystals 997

Exchange constants
  Influence of the presence of Fe^{2+} ion in nickel-zinc ferrite 7
  Influence of spin orbit coupling and lanthanide contraction on the exchange interaction in rare earth garnets 1069

Exchange parameter
  Curie temperatures and 0°K magnetic moments of zinc-substituted lithium ferrites 39

Fast breeder-test reactor
  Plutonium metallurgy in India 923

Ferrimagnetism
  Amorphous state ferroelectricity, magnon scattering and phase stability in microparticle materials 327

Ferrites
  Curie temperatures and 0°K magnetic moments of zinc-substituted lithium ferrites 39
  Infrared absorption in spinel ferrites 1063

Ferroelasticity
  Ferroelasticity 733

Ferroelectric ferroelastics
  Ferroelasticity 733

Ferroelectricity
  Pyroelectric materials 317
  Amorphous state ferroelectricity, magnon scattering and phase stability in microparticle materials 327

Ferroelectrics
  Investigation of hydrogenous materials using neutrons 151

Ferromagnetic resonance
  Ferromagnetic resonance in metallic glasses: study of fracture, stress and thermal stability 1

Field ion microscope
  Details of an imaging atom probe 569

Field ion microscopy
  Field ion microscopic observations of LaB_6 on tungsten 573

First order phase transitions
  Instabilities in first order phase transitions 701

Fissile
  Plutonium metallurgy in India 923

Flow stress
  Serrated plastic flow 653
  Some aspects of dislocation-precipitate interaction in under-aged aluminium-germanium alloy 1041

Fluctuations in materials
  Experimental study of fluctuations in materials 805

Fluorescence and absorption corrections
  X-ray microanalysis in the transmission electron microscope 503

Force constants
  Infrared absorption in spinel ferrites 1063

Fractals
  Fractals 817

Fracture
  Ferromagnetic resonance in metallic glasses: study of fracture, stress and thermal stability 1
  Fracture of particulate composites 799

Frequency-modified life
  Elevated temperature low cycle fatigue studies on AISI 304 steel 111

Gamma Fe_2O_3
  Amorphous state ferroelectricity, magnon scattering and phase stability in microparticle materials 327

Gamma ferric oxide
  Development of pure and doped gamma ferric oxide 59

Garnet
  Mössbauer spectroscopy of titanium-substituted iron garnets 17

Gel grown
  Etch pit observations on the habit faces of gel grown nickel molybdate crystals 997

Glass-forming ability
  Metallic glasses 579

Glass-metal composites
  Glass-metal particulate composites 193

Glass structure
  Fast ion conducting lithium glasses—Review 201

Glassy electrolytes
  Fast ion conducting lithium glasses—Review 201

Gold plating salt
  Electrochemical preparation of potassium gold cyanide 165

Grain boundary
  Superplasticity 689
  Grain boundary—dislocation interactions 699

Grain boundary effects
  Electrical properties of polycrystalline silicon and zinc oxide semiconductors 243

Grains
  Fractals 817

Growth technique
  Electron microscopy of layered single crystals grown by direct vapour transport method 549

Growth temperature
  Preparation of single crystal films of magnetic bubble materials—Rare earth yttrium iron gallium garnets by liquid phase epitaxy and their physical properties 47

Habit faces
  Etch pit observations on the habit faces of gel grown nickel molybdate crystals 997

Hallide metallurgy
  Growth of research and development in rare metals extraction in India 901

Hardness pendulum
  Observations on the physical basis of mechanical behaviour 627

Heat bath
  Experimental study of fluctuations in materials 805

Helium embrittlement
  Radiation effects in nuclear reactor materials—Correlation with structure 339

Hexagonal metals
  Internal friction in hexagonal metals 959

High pressure
  Lithium solid electrolytes and their applications 223
  The pressure-volume relation of ytterbium up to 9 GPa 395

High resolution analysis
  Analytical electron microscopy of aluminium alloys 513

High resolution electron microscopy
  High resolution electron microscopy of long range ordered alloys 417
  High resolution electron microscopy as a tool for structural investigations 459

High resolution electron microscopy
  High resolution electron microscopic studies of HoAl$_3$, Er$_{0\cdot5}$Gd$_{0\cdot5}$Al$_3$ and Y$_{0\cdot91}$Er$_{0\cdot09}$Al$_3$ in thin film form 603

High resolution microscopy
  Metallic glasses 579

High strength and low alloy steels
  Applications of scanning transmission electron microscope microanalysis in the study of materials 491

High temperature electrode
  High temperature materials for magnetohydrodynamic channels 71

High voltage electron microscopy
  High voltage electron microscope irradiation and observations in metallic glasses 595

High voltage pulser
  Details of an imaging atom probe 569

Hot pressing
  Dependence of microstructure on process variables in manganese zinc ferrites 65

Hydrogen sulphide
  Oxidation of thin films of tin at room temperature in hydrogen sulphide atmosphere 1019

Hydrogenous materials
  Investigation of hydrogenous materials using neutrons 151

Hydrothermal growth
  Hydrothermal growth of A^{II}B^{VI} semiconductors 177

Hyperfine field
  Mössbauer spectroscopy of titanium-substituted iron garnets 17
  Magnetic structure of zinc ferrite 27

Hyperfine interactions
  A Mössbauer study of hyperfine interactions in the boroferrite Fe$_{3-x}$Ga$_x$Bo$_6$ ($x = 0$, 0·12) 33

Imaging atom probe
  Details of an imaging atom probe 569

Imide-amine hardness
  Amine-cured epoxy/glass fibre composites 99

Impact resistance
  Mechanisms and empirical equations for deformation and some principles of alloy design 677

Inhomogeneities
  Elastic continuum theories of lattice defects: A review 775

Instabilities
  Instabilities in yielding 645
  Instabilities in first order phase transitions 701

Insulator materials
  High temperature materials for magnetohydrodynamic channels 71

Intensity ratio
  X-ray microanalysis in the transmission electron microscope 503

Internal friction
  Internal friction in hexagonal metals 959

Investment casting
  Structure and properties of an investment—cast austenitic stainless steel 119

Ionic conductivity studies
  Lithium solid electrolytes and their applications 223

Ionic conductor
  Preparation and characterisation of β''-Al_2O_3 979

Iron garnet
  Mössbauer spectroscopy of titanium-substituted iron garnets 17

Irradiation creep
  Radiation effects in nuclear reactor materials—Correlation with structure 339

Irradiation effects
  Radiation effects in nuclear reactor materials—Correlation with structure 339

Irradiation embrittlement
  Radiation effects in nuclear reactor materials—Correlation with structure 339

Irradiation growth
  Radiation effects in nuclear reactor materials—Correlation with structure 339

Irradiation hardening
  Radiation effects in nuclear reactor materials—Correlation with structure 339

IR spectrum
  Infrared absorption in spinel ferrites 1063

Jahn-Teller ion spinels
  Influence of the presence of Fe^{2+} ion in nickel-zinc ferrite 7

Kataoka-Yamada theory
  Temperature dependence of microhardness in mixed crystals 1035

Lamellar $M_{23}C_6$
  Formation of lamellar $M_{23}C_6$ on and near twin boundaries in austenitic stainless steels 617

Lanthanum hexaboride
  Field ion microscopic observations of LaB_6 on tungsten 573

Laser devices
  Hydrothermal growth of $A^{II}B^{VI}$ semiconductors 177

Lattice defects
  Elastic continuum theories of lattice defects: A review 775

Lattice imaging
  High resolution electron microscopy as a tool for structural investigations 459
  High resolution electron microscopic studies of $HoAl_3$, $Er_{0.5}Gd_{0.5}Al_3$ and $Y_{0.91}Er_{0.09}Al_3$ in thin film form 603

Lead zirconate titanate
  Effect of compositional modifications on the piezoelectric properties of spray dried lead zirconate titanate ceramics 83

Lead zirconate titanate
  Amorphous state ferroelectricity, magnon scattering and phase stability in microparticle materials 327

Limit cycle solutions
  Repeated yield drop phenomena as a cooperative effect 665

Liquid metal-cooled fast breeder reactors
  Plutonium metallurgy in India 923

Liquid phase epitaxy
  Preparation of single crystal films of magnetic bubble materials—Rare earth yttrium iron gallium garnets by liquid phase epitaxy and their physical properties 47

Liquid state properties
  Relevance of liquid state to solid state properties 773

Lithium carbonate single crystals
  Evidence of screw dislocations on (002) cleavages of lithium carbonate single crystals 991

Lithium ion conductors
  Lithium solid electrolytes and their applications 223

Localised spin canting
  Curie temperatures and 0°K magnetic moments of zinc-substituted lithium ferrites 39

Long range order
  High resolution electron microscopy of long range ordered alloys 417

Low cycle fatigue
  Elevated temperature low cycle fatigue studies on AISI 304 steel 111

Macroscopically defect free cement
  Some recent advances in materials technology 405

Magnetisation
  Curie temperatures and 0°K magnetic moments of zinc-substituted lithium ferrites 39

Magnetic bubble materials
  Preparation of single crystal films of magnetic bubble materials—Rare earth yttrium iron gallium garnets by liquid phase epitaxy and their physical properties 47

Magnetic properties
  Magnetic properties of metallic glass $Fe_{39}Ni_{39}Mo_4Si_6B_{12}$ 21
  Glass-metal particulate composites 193

Magnetic recording materials
  Development of pure and doped gamma ferric oxide 59

Magnetic structure
  Magnetic structure of zinc ferrite 27

Magnetic susceptibility
  Structural and magnetic investigations of some new boron containing rare earth intermetallic compounds 263

Magnetic hyperfine field distributions
  Evaluation of magnetic hyperfine field distributions from Mössbauer spectra of disordered alloys and metallic glasses 1047

Magnon scattering
  Amorphous state ferroelectricity, magnon scattering and phase stability in microparticle materials 327

Martensitic transformation
  Deformation and martensitic transformation 703

Manganese zinc ferrites
  Dependence of microstructure on process variables in manganese zinc ferrites 65

Mechanical behaviour
  Observations on the physical basis of mechanical behaviour 627
  Experimental study of fluctuations in materials 805

Mechanical deformation
  Effects of mechanical deformation: Exoemission 755

Mechanical properties
  Structure and properties of an investment—cast austenitic stainless steel 119
  Glass-metal particulate composites 193

Melt-quenching
  Metallic glasses 579

Metglasses
  Some recent advances in materials technology 405

Metal-ceramic joint
  High temperature materials for magnetohydrodynamic channels 71

Metal excess systems
  Structure and superconductivity in ternary systems of compounds 283

Metal-hydrogen systems
  Investigation of hydrogenous materials using neutrons 151

Metastable crystalline states
  Electron diffraction analysis of antimony films 611

Metastable phases
  Analytical electron microscopy of aluminium alloys 513

Metallic glasses
  Ferromagnetic resonance in metallic glasses: study of fracture, stress and thermal stability 1
  Magnetic properties of metallic glass $Fe_{39}Ni_{39}Mo_4Si_6B_{12}$ 21
  Metallic glasses 579
  High voltage electron microscope irradiation and observations in metallic glasses 595
  Spin-wave excitations in amorphous ferromagnets 1059
  Evaluation of magnetic hyperfine field distributions from Mössbauer spectra of disordered alloys and metallic glasses 1047

Microanalysis
  Applications of scanning transmission electron microscope microanalysis in the study of materials 491

Microdiffraction
  Scanning transmission electron microscopy and microdiffraction techniques 477

Microemulsion
  Amorphous state ferroelectricity, magnon scattering and phase stability in microparticle materials 327

Microfocus x-ray generator
  Sophisticated equipment developed for growth and evaluation of perfection of nearly perfect crystals 129

Microhardness
  Temperature dependence of microhardness in mixed crystals 1035

Microparticle
  Amorphous state ferroelectricity, magnon scattering and phase stability in microparticle materials 327

Microstructure
  Structure and properties of an investment—cast austenitic stainless steel 119

Microwaves
  Electrical properties of films at microwave frequencies 1075

Mixed crystals
  Temperature dependence of microhardness in mixed crystals 1035

Mixed oxide and carbide fuels
  Plutonium metallurgy in India 923

MnO_2
  MnO_2 catalyzed carbon electrodes for dioxygen reduction in concentrated alkali 259

Modulated phases
  High resolution electron microscopic studies of $HoAl_3$, $Er_{0.5}Gd_{0.5}Al_3$ and $Y_{0.91}Er_{0.09}Al_3$ in thin film form 603

Modulated structure
  High resolution electron microscopy of long range ordered alloys 417

Molecular field constants
  Influence of spin orbit coupling and lanthanide contraction on the exchange interaction in rare earth garnets 1069

Morphotropic phase boundary
  Effect of compositional modifications on the piezoelectric properties of spray dried lead zirconate titanate ceramics 83

Mössbauer measurements
  Spin-wave excitations in amorphous ferromagnets 1059

Mössbauer spectra
  Mössbauer spectroscopy of titanium-substituted iron garnets 17

Mössbauer spectra
  Evaluation of magnetic hyperfine field distributions from Mössbauer spectra of disordered alloys and metallic glasses 1047

Mössbauer spectroscopy
  Metal-to-ceramic bonding in (Al_2O_3 + Fe) cermet studied by Mössbauer spectroscopy 13
  Magnetic properties of metallic glass $Fe_{39}Ni_{39}Mo_4Si_6B_{12}$ 21
  Amorphous state ferroelectricity, magnon scattering and phase stability in microparticle materials 327

Mössbauer study
  A Mössbauer study of hyperfine interactions in the boroferrite $Fe_{3-x}Ga_xBO_6$ ($x = 0, 0{\cdot}12$) 33

Na_2-ZnO-B_2O_3 glass
  DC electrical conductivity of Na_2O-ZnO-B_2O_3 glass system 1009

Neutrons
  Investigation of hydrogenous materials using neutrons 151

Nickel alloys
  Radiation effects in nuclear reactor materials—Correlation with structure 339

Nickel-zinc ferrite
  Influence of the presence of Fe^{2+} ion in nickel-zinc ferrite 7

$NiMoO_4 \cdot xH_2O$ crystals
  Etch pit observations on the habit faces of gel grown nickel molybdate crystals 997

NMR
  Lithium solid electrolytes and their applications 223

Non-crystalline garnet
  Electron transport in non-crystalline garnet films 53

Non-integral dimensions
  Fractals 817

Nonlinear dynamics
  Elementary concepts in chaos and turbulence 807

Nonlinear Langevin equations
  Repeated yield drop phenomena as a cooperative effect 665

Non-local elasticity
  Elastic continuum theories of lattice defects: A review 775

Nuclear electricity
  Plutonium metallurgy in India 923

Nuclear reactor materials
  Radiation effects in nuclear reactor materials—Correlation with structure 339

Optical densification
  Photon, electron and ion beam induced physical and optical densification in chalcogenide films 1013

Optical properties
  Glass-metal particulate composites 193

Ordering kinetics
  Phase transformations—a physicist's perception 837

Overlap integrals
  Magnetic structure of zinc ferrite 27

Oxidation
  Oxidation of thin films of tin at room temperature in hydrogen sulphide atmosphere 1019

Oxide glasses
  Glass-metal particulate composites 193

Pairing interaction
  On the mechanism of pairing in the BCS theory 273

Phase changes
  Electron diffraction analysis of antimony films 611

Phase diagrams
  Phase transformations—a physicist's perception 837

Phase identification
  Analytical electron microscopy of aluminium alloys 513

Phase transformations
  Electron microscopy of layered single crystals grown by direct vapour transport method 549
  Phase transformations—a physicist's perception 837

Phase transitions
  Ferroelasticity 733

Physical beneficiation
  Growth of research and development in rare metals extraction in India 901

Piezoelectric
  Hydrothermal growth of $A^{II}B^{VI}$ semiconductors 177

Piezoelectricity
  Effect of compositional modifications on the piezoelectric properties of spray dried lead zirconate titanate ceramics 83
  Pyroelectric materials 317

Plastic deformation
  Deformation and martensitic transformation 703

Plastic properties
  Elastic properties of As-Sb-Se glasses 1001

Plating
  Electrochemical preparation of potassium gold cyanide 165

Plutonium
  Plutonium metallurgy in India 923

Point defect clusters
  Electron microscopy of defect clusters produced by radiation damage 537

Polycrystalline semiconductors
  Electrical properties of polycrystalline silicon and zinc oxide semiconductors 243

Polymers
  Investigation of hydrogenous materials using neutrons 151

Polysilicon
  Electrical properties of polycrystalline silicon and zinc oxide semiconductors 243

Polytype in SiC
  High resolution electron microscopy as a tool for structural investigations 459

Polytype structures
  Structural disorder and solid state transformations in single crystals of $Zn_xCd_{1-x}S$ and $Zn_xM_{1-x}S$ 369

Polyvinyl chloride
  Surface modification of polyvinyl chloride towards blood compatibility 1087

Potassium gold cyanide
  Electrochemical preparation of potassium gold cyanide 165

Precipitation morphology
  Formation of lamellar $M_{23}C_6$ on and near twin boundaries in austenitic stainless steels 617

Pressure-induced semiconductor-to-metal transitions
  Electronic conduction in bulk $Se_{1-x}Te_x$ glasses at high pressures and at low temperatures 231

Pseudoelasticity
  Deformation and martensitic transformation 703

Pu-Be neutron sources
  Plutonium metallurgy in India 923

Pyroelectricity
  Pyroelectric materials 317

Pyroelectric studies
  Dielectric and pyroelectric studies on triglycine sulphate-polymer composites 105

Quantitative model
  X-ray microanalysis in the transmission electron microscope 503

Quadrupole splitting
  Mossbauer spectroscopy of titanium-substituted iron garnets 17

Radiation damage
  Radiation effects in nuclear reactor materials—Correlation with structure 339
  High resolution electron microscopy of superconductors 453
  Electron microscopy of defect clusters produced by radiation damage 537

Random distribution model
  A Mössbauer study of hyperfine interactions in the boroferrite $Fe_{3-x}Ga_xBO_6$ ($x = 0, 0{\cdot}12$) 33

Rapid solidification techniques
  Metallic glasses 579

Rare earths
  Structural and magnetic investigations of some new boron containing rare earth intermetallic compounds 263

Rare metal extraction
  Growth of research and development in rare metals extraction in India 901

Relaxation
  Spin wave relaxation processes in polycrystalline yttrium iron garnets 1053

Repeated yield drop
  Repeated yield drop phenomena as a cooperative effect 665

Resistance change
  Oxidation of thin films of tin at room temperature in hydrogen sulphide atmosphere 1019

RF sputtering
  A novel method of RF powder sputtering 971

Saturation temperature
  Preparation of single crystal films of magnetic bubble materials—Rare earth yttrium iron gallium garnets by liquid phase epitaxy and their physical properties 47

Scanning electron microscopy
  A novel method of RF powder sputtering 971

Selective surfaces
  Some recent advances in materials technology 405

Semiconductors
  Hydrothermal growth of $A^{II}B^{VI}$ semiconductors 177

Separation process
  Growth of research and development in rare metals extraction in India 901

Serrated flow
  Serrated plastic flow 653

Shape memory effect
  Deformation and martensitic transformation 703

Sheet resistivity
  Annealing behaviour of electron-beam deposited tin dioxide films 1029

Shield
  A novel method of RF powder sputtering 971

Shock deformation
  Shocks and high velocity deformation 633

Shock front
  Mechanisms and empirical equations for deformation and some principles of alloy design 677

Shock melting
  Shocks and high velocity deformation 633

Shock propagation
  Shocks and high velocity deformation 633

Single crystals
  Structural disorder and solid state transformations in single crystals of $Zn_xCd_{1-x}S$ and $Zn_xMn_{1-x}S$ 369

Silicon carbide
  High resolution electron microscopy as a tool for structural investigations 459

Sintering
  Dependence of microstructure on process variables in manganese zinc ferrites 65
  Effect of compositional modifications on the piezoelectric properties of spray dried lead zirconate titanate ceramics 83

Slag ceramic interaction
  High temperature materials for magnetohydrodynamic channels 71

Slip lines
  Some aspects of dislocation-precipitate interaction in under-aged aluminium-germanium alloy 1041

Sodium beta alumina
  Preparation and characterisation of β''-Al_2O_3 979

Solid electrolyte
  Preparation and characterisation of β''-Al_2O_3 979

Solid state batteries
  Fast ion conducting lithium glasses—Review 201

Solid state properties
  Relevance of liquid state to solid state properties 773

Spinel
  Metal-to-ceramic bonding in (Al_2O_3 + Fe) cermet studied by Mössbauer spectroscopy 13

Spinodal decomposition
  Phase transformations—a physicist's perception 837

Spin-reorientation
  A Mössbauer study of hyperfine interactions in the boroferrite $Fe_{3-x}Ga_xBO_6$ ($x = 0, 0{\cdot}12$) 33

Spin wave excitations
  Spin-wave excitations in amorphous ferromagnets 1059

Spin-wave line-widths
  Spin wave relaxation processes in polycrystalline yttrium iron garnets 1053

Spiral etch pits
  Evidence of screw dislocations on (002) cleavages of lithium carbonate single crystals 991

Spray drying
  Effect of compositional modifications on the piezoelectric properties of spray dried lead zirconate titanate ceramics 83

Stacking fault energy
  Electron microscopy of layered single crystals grown by direct vapour transport method 549

Stacking sequence
  High resolution electron microscopy as a tool for structural investigations 459

Stainless steel
  Structure and properties of an investment—cast austenitic stainless steel 119
  Radiation effects in nuclear reactor materials—Correlation with structure 339

STEM
  Applications of scanning transmission electron microscope microanalysis in the study of materials 491

Strain rates
  Elevated temperature low cycle fatigue studies on AISI 304 steel 111

Strength
  Strength and electronic structure 717

Strengthening mechanisms
  Strength and electronic structure 717

Stress
  Ferromagnetic resonance in metallic glasses: study of fracture, stress and thermal stability 1
  Effects of mechanical deformation: Exoemission 755

Stress and strain rate
  Superplasticity 689

Structural characterization
  High resolution electron microscopic studies of $HoAl_3$, $Er_{0{\cdot}5}Gd_{0{\cdot}5}Al_3$ and $Y_{0{\cdot}91}Er_{0{\cdot}09}Al_3$ in thin film form 603

Structural disorder
  Structural disorder and solid state transformations in single crystals of $Zn_xCd_{1-x}S$ and $Zn_xMn_{1-x}S$ 369

Structural investigation
  High resolution electron microscopy as a tool for structural investigations 459

Sublattices
  Influence of the presence of Fe^{2+} ion in nickel-zinc ferrite 7

Superconducting compounds
  Structure and superconductivity in ternary systems of compounds 283

Super conducting materials
  High resolution electron microscopy of superconductors 453

Superconductivity
  On the mechanism of pairing in the BCS theory 273

Superconductors
  Investigation of hydrogenous materials using neutrons 151

Superexchange
  Influence of spin orbit coupling and lanthanide contraction on the exchange interaction in rare earth garnets 1069

Superplasticity
  Superplasticity 689

Superstructure
  High resolution electron microscopy of long range ordered alloys 417

Surface modification
  Surface modification of polyvinyl chloride towards blood compatibility 1087

Surface states
  Observations on the physical basis of mechanical behaviour 627

Surface studies
  Scanning transmission electron microscopy and microdiffraction techniques 477

Structural investigations
  Structural and magnetic investigations of some new boron containing rare earth intermetallic compounds 263

Surface roughness
  Observations on the physical basis of mechanical behaviour 627

Symmetry
  Ferroelasticity 733

Target
  A novel method of RF powder sputtering 971

Temperature dependence
  Spin-wave excitations in amorphous ferromagnets 1059
  Temperature dependence of microhardness in mixed crystals 1035

Tensile testing
  Computer simulation of tensile testing 643
  Instabilities in yielding 645

Ternary systems
  Structure and superconductivity in ternary systems of compounds 283

Theoretical models
  Structural disorder and solid state transformations in single crystals of $Zn_xCd_{1-x}S$ and $Zn_xMn_{1-x}S$ 369

Thermal decomposition
  Development of pure and doped gamma ferric oxide 59

Thermal hysteresis
  A Mössbauer study of hyperfine interactions in the boroferrite $Fe_{3-x}Ga_xBO_6$ ($x = 0, 0{\cdot}12$) 33

Thermal stability
  Ferromagnetic resonance in metallic glasses: study of fracture, stress and thermal stability 1

Thermo-compression bonds
  Metal-to-ceramic bonding in $(Al_2O_3 + Fe)$ cermet studied by Mössbauer spectroscopy 13

Thermoplastic
  Use of coal tar pitch for carbon-carbon composites 91

Thermopower
  Lithium solid electrolytes and their applications 223

Thin films
  Electron transport in non-crystalline garnet films 53
  Oxidation of thin films of tin at room temperature in hydrogen sulphide atmosphere 1019

Tilt boundaries
  Evidence of screw dislocations on (002) cleavages of lithium carbonate single crystals 991

Tin
  Oxidation of thin films of tin at room temperature in hydrogen sulphide atmosphere 1019

Tin dioxide films
  Annealing behaviour of electron-beam deposited tin dioxide films 1029

Torsion tensor
  Elastic continuum theories of lattice defects: A review 775

Transfer integrals
  Influence of spin orbit coupling and lanthanide contraction on the exchange interaction in rare earth garnets 1069

Transition metal dichalcogenides
  Electron microscopy of layered single crystals grown by direct vapour transport method 549

Transmission electron microscopy
  X-ray microanalysis in the transmission electron microscope 503
  A novel method of RF powder sputtering 971

Transport number
  Fast ion conducting lithium glasses—Review201

Triglycine sulphate polymers
  Dielectric and pyroelectric studies on triglycine sulphate-polymer composites 105

Tungsten field evaporation
  Field ion microscopic observations of LaB_6 on tungsten 573

Turbulence
  Elementary concepts in chaos and turbulenCe 807

Twin boundaries
  Formation of lamellar $M_{23}C_6$ on and near twin boundaries in austenitic stainless steels 617

Twinning
  Ferroelasticity 733

Twist boundaries
  Evidence of screw dislocations on (002) cleavages of lithium carbonate single crystals 991

Under-aged
  Some aspects of dislocation-precipitate interaction in under-aged aluminium-germanium alloy 1041

Uranium
  Radiation effects in nuclear reactor materials—Correlation with structure 339

Vacuum casting
  Structure and properties of an investment—cast austenitic stainless steel 119

Void growth
  Fracture of particulate composites 799

Void nucleation
  Fracture of particulate composites 799

Void swelling
  Radiation effects in nuclear reactor materials—Correlation with structure 339

Waveguide
  Electrical properties of films at microwave frequencies 1075

Work hardening peaks
  Serrated plastic flow 653

X-ray diffraction
  The pressure-volume relation of ytterbium up to 9 GPa 395
  Electron microscopy of layered single crystals grown by direct vapour transport method 549

X-ray diffraction topography camera
  Sophisticated equipment developed for growth and evaulation of perfection of nearly perfect crystals 129

X-ray diffractometer
  Sophisticated equipment developed for growth and evaluation of perfection of nearly perfect crystals 129

X-ray microanalysis
  X-ray microanalysis in the transmission electron microscope 503
  Analytical electron microscopy of aluminium alloys 513

Yielding
  Instabilities in yielding 645

Ytterbium
  The pressure-volume relation of ytterbium up to 9 GPa 395

Yttrium iron garnet
  Amorphous state ferroelectricity, magnon scattering and phase stability in microparticle materials 327
  Spin wave relaxation processes in polycrystalline yttrium iron garnets 1053

Zinc ferrite
  Magnetic structure of zinc ferrite 27

Zirconium alloys
  Radiation effects in nuclear reactor materials—Correlation with structure 339

ZnO varistors
  Electrical properties of polycrystalline silicon and zinc oxide semiconductors 243

AUTHOR INDEX

Agarwal M K
Electron microscopy of layered single crystals grown by direct vapour transport method 549

Aiyar R
see Venkataramani N 65
see Srivastava C M 1069

Amelinckx S
High resolution electron microscopy of long range ordered alloys 417

Ananthakrishna G
Repeated yield drop phenomena as a cooperative effect 665

Anantharaman M R
Development of pure and doped gamma ferric oxide 59

Anavekar R V
DC electrical conductivity of Na_2O-ZnO-B_2O_3 glass system 1009

Asundi M K
Internal friction in hexagonal metals 959

Ayyub P
see Multani M S 327

Bahadur D
see Srivastava C M 17
Electron transport in non-crystalline garnet films 53

Balakrishnan V
Summary and outlook 823

Balasubramanian N
see Ramaseshan S 405

Banerjee S
Electron microscopy of defect clusters produced by radiation damage 537
Instabilities in first order phase transitions 701

Bansal C
Metal-to-ceramic bonding in $(Al_2O_3 + Fe)$ cermet studied by Mössbauer spectroscopy 13
Evaluation of magnetic hyperfine field distributions from Mössbauer spectra of disordered alloys and metallic glasses 1047

Bhatia S N
Spin wave relaxation processes in polycrystalline yttrium iron garnets 1053

Bhatnagar Anil K
see Parashar R S 1
see Prasad B Bhanu 21
Spin-wave excitations in amorphous ferromagnets 1059

Bhat T Balakrishna
Mechanisms and empirical equations for deformation and some principles of alloy design 677

Bose D N
Lithium solid electrolytes and their applications 223

Chakravorty D
Glass-metal particulate composites 193

Chandrasekharaiah M N
see Prasad B Bhanu 21

Chatterjee S N
see Kishan Pran 39

Chidambaram R
Shocks and high velocity deformation 633

Chopra K L
Photon, electron and ion beam induced physical and optical densification in chalcogenide films 1013

Cowley J M
Scanning transmission electron microscopy and microdiffraction techniques 477

Dasannacharya B A
Investigation of hydrogenous materials using neutrons 151

Das B K
see Singh S N 243
see Kalsi H S 979

Datta K K
see Seth R L 91

Devaraj N
see Anavekar R V 1009

Dhar Ajay
see Sreenivas K 105

Dhar D
Fractals 817

Dhar S K
see Malik S K 263

Dube D C
Electrical properties of films at microwave frequencies 1075

Embury J D
see Ramachandran T R 513

Ganguly C
see Roy P R 923

Geetha Balakrishnan
see Rao G V Subba 283

Geetha Kurian
Surface modification of polyvinyl chloride towards blood compatibility 1087

Giridhar A
Elastic properties of As-Sb-Se glasses 1001

Goel R C
see Kalsi H S 979

Gopal E S R
see Parthasarathy G 231

Goyal P S
see Dasannacharya B A 151

Gupta Arjeesh
Annealing behaviour of electron-beam deposited tin dioxide films 1029

Gupta C K
see Sundaram C V 901

Gupta M S
see Singh Anand Kumar 603

Harshavardhan K Solomon
see Chopra K L 1013
A novel method of RF powder sputtering 971

Houghton D C
see Ramachandran T R 513

Indira Rajagopal
Electrochemical preparation of potassium gold cyanide 165

Ittyachen M A
see Kurien K V 997

Jagannathan R
see Vithal M 33
see Bhatnagar Anil K 1059

Jebaraj P M
Structure and properties of an investment—cast austenitic stainless steel 119

Joag D B
Field ion microscopic observations of LaB_6 on tungsten 573

Joglekar S M
see Srivastava C M 7

Joshi P B
see Bhatia S N 1053

Kalsi H S
Preparation and characterisation of β''-Al_2O_3 979

Kanitkar M M
see Joag D B 573

Kanitkar P L
see Joag D B 573

Keer H V
see Anantharaman M R 59

Kishan Pran
Curie temperatures and 0°K magnetic moments of zinc-substituted lithium ferrites 39

Kishore
Some aspects of dislocation-precipitate interaction in under-aged aluminium-germanium alloy 1041

Krishna K N
see Harshavardhan K Solomon 971

Krishan Lal
Sophisticated equipment developed for growth and evaluation of perfection of nearly perfect crystals 129

Krishnan R
see Rodriguez P 339

Krishna P
see Sebastian M T 369

Kshatriya J D
see Agarwal M K 549

Kulkarni A R
Fast ion conducting lithium glasses—Review 201

Kumari S
see Singh S N 243

Kurien K V
Etch pit observations on the habit faces of gel grown nickel molybdate crystals 997

Kuzmina I P
see Kuznetsov V A 177

Kuznetsov V A
Hydrothermal growth of $A^{II}B^{VI}$ semiconductors 177

Laddha G S
see Raju K S 991

Lal C
see Seth R L 91

Lal Ramji
Effect of compositional modifications on the piezoelectric properties of spray dried lead zirconate titanate ceramics 83

Landuyt J Van
see Amelinckx S 417

Laroia K K
see Kishan Pran 39

Lorimer G W
X-ray microanalysis in the transmission electron microscope 503

Maiti H S
see Kulkarni A R 201

Majumdar D
see Bose D N 223

Malhotra L K
see Chopra K L 1013

Malik S K
Structural and magnetic investigations of some new boron containing rare earth intermetallic compounds 263

Manoharan R
MnO_2 catalyzed carbon electrodes for dioxygen reduction in concentrated alkali 259

Mansingh Abhai
see Sreenivas K 105

Mittal V P
see Seth R L 91

Mohandas E
see Seshadri V R 569

Mukhopadhyay G
Effects of mechanical deformation: Exoemission 755

Multani M S
Amorphous state ferroelectricity, magnon scattering and phase stability in microparticle materials 327

Muneera C I
Oxidation of thin films of tin at room temperature in hydrogen sulphide atmosphere 1019

Murthy H R Krishna
Relevance of liquid state to solid state properties 773

Nagpaul L K
see Kishan Pran 39

Nandedkar R V
High voltage electron microscope irradiation and observations in metallic glasses 595

Nayar V Unnikrishnan
see Muneera C I 1019

Neelakantan K
see Seshadri V R 569

Om Prakash
see Srivastava C M 17

Palaniswamy M
see Raju K S 991

Palkar V R
see Multani M S 327

Pande C S
High resolution electron microscopy of superconductors 453

Parashar R S
Ferromagnetic resonance in metallic glasses: study of fracture, stress and thermal stability 1

Parthasarathy G
Electronic conduction in bulk $Se_{1-x}Te_x$ glasses at high pressures and at low temperatures 231

Patel J V
see Agarwal M K 549

Patel P D
see Agarwal M K 549

Patni M J
see Srivastava C M 7
see Srinivasan T T 1063

Paul A
see Kulkarni A R 201

Poonam Gupta
see Gupta Arjeesh 1029

Prabhawalker P D
Electron diffraction analysis of antimony films 611

Pragati Mukhopadhyay
Preparation of single crystal films of magnetic bubble materials—Rare earth yttrium iron gallium garnets by liquid phase epitaxy and their physical properties 47

Prasad B Bhanu
Magnetic properties of metallic glass $Fe_{39}Ni_{39}Mo_4Si_6B_{12}$ 21
see Bhatnagar Anil K 1059

Purdy Gary R
Applications of scanning transmission electron microscope microanalysis in the study of materials 491

Raghavan K Srinivasa
Superplasticity 689

Raghunathan V S
see Seshadri V R 569

Rai R S
see Singh G 459

Raj R G
see Varma D S 99

Rajagopalan S
see Chopra K L 1013

Rajagopalan S R
see Indira Rajagopal 165

Rajan K Govinda
Strength and electronic structure 717

Raju K S
Evidence of screw dislocations on (002) cleavages of lithium carbonate single crystals 991

Ramachandran T R
Analytical electron microscopy of aluminium alloys 513

Ramakrishna J
see Anavekar R V 1009

Ramakrishnan P
see Lal Ramji 83

Ramakrishnan T V
see Murthy H R Krishna 773

Ramasamy P
see Raju K S 991

Ramaswamy Ramakrishna
Elementary concepts in chaos and turbulence 807

Ramaseshan S
Some recent advances in materials technology 405
Observations on the physical basis of mechanical behaviour 627

Ranganathan S
Grain boundary-dislocation interactions 699

Rao C N
see Asundi M K 959

Rao K R
Experimental study of fluctuations in materials 805

Rao T Sudersena
see Sreenivas K 105

Rao G V Subba
Structure and superconductivity in ternary systems of compounds 283

Rao B Uma Maheshwar
see Srivastava C M 17
see Pragati Mukhopadhyay 47